CRBR

CDA ENERGETICS.

Independent Assessment

NUREG/CR-3224

3/11/83

TR #4
delete B. White

CLASSES OF CDAs

- UNPROTECTED
  - LOFA ~ 200 K/s Na-C t
  - TOP ~ 200 K/s Na-I
- PROTECTED
  - LOHS ~ 1 K/s Steel- ict

OTHERS

- Severe Seismic : Combination of Above
- Fuel Failure Propagation: No problem.
- TOP / LOF : Extremely Low Probability.

LOFA OVERALL APPROACH.

- STRUCTURAL CAPABILITY
  - Core "Cage" — II.2.
  - Vessel Head — II.2.
- FRAMEWORK FOR RANGE OF PHENOMENOLOGY
  - CDA Initiation — II.3
  - Disruption — II.5
- SEARCH FOR ENERGETIC EVENTS
  - Forced Fuel Motions (Pressures) — II.4
  - Recriticality (Gravity) — II.7
- SCRUTINIZE FOR MILD DISPERSAL
  - Coolant Channels — II.6
  - Gaps, Control Assemblies — II.6

LOFA GENERIC ACCIDENT PROGRESSION

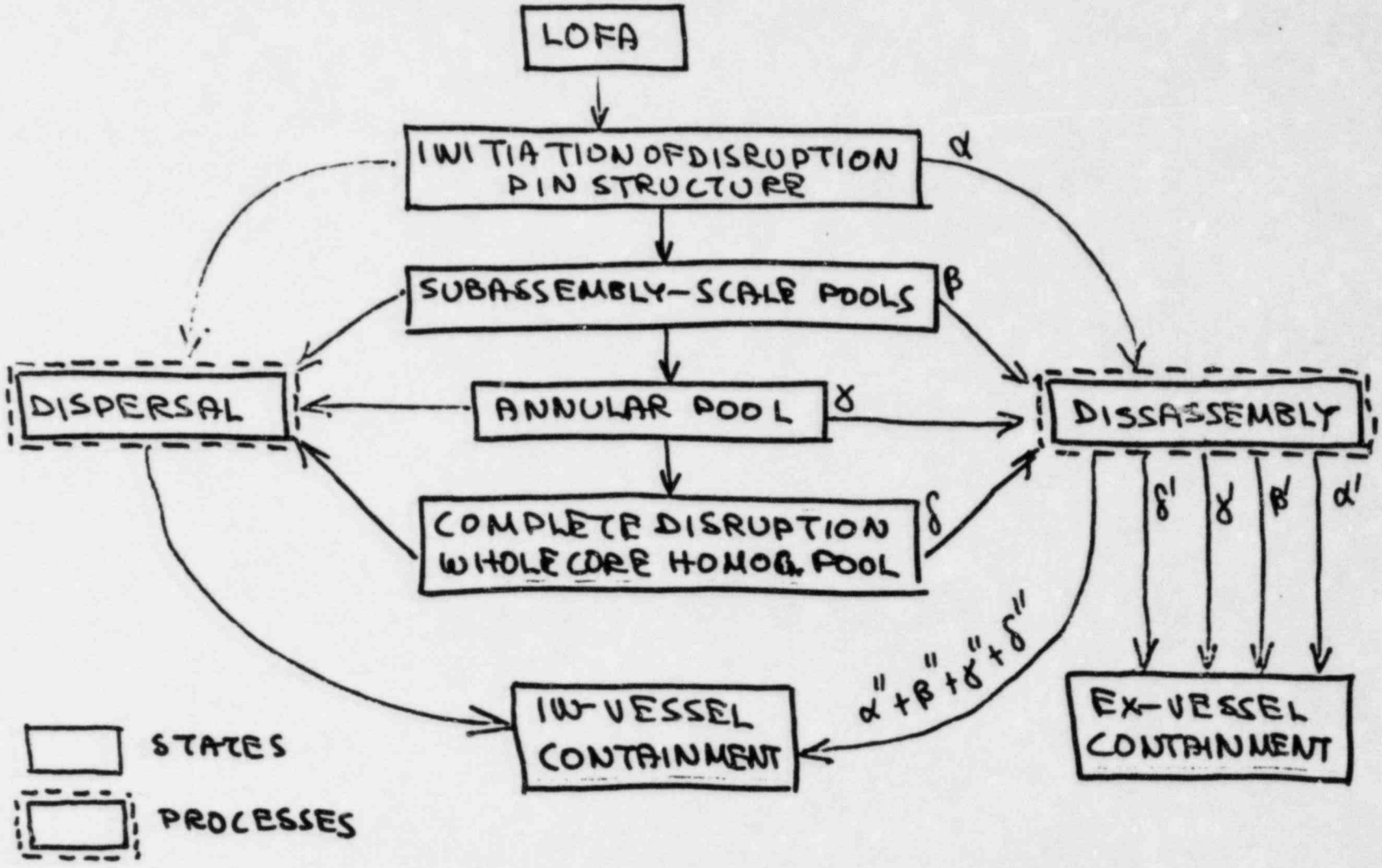

PROBABILISTIC ASSESSMENT PROCEDURE

1. Define Levels of Likelyhood — II.1.
   - 10^{-1} Edge-of-Spectrum.
   - 10^{-2} Out-of-Spectrum
   - $\therefore$ 10^{-3} Physically Unreasonable.
2. Develop Basis for Judgements — II.2-II.7
3. Assign High Confidence Conservative Estimates of Prob. to Branches — II.8
4. Carry-out Arithmetic for Vessel Failure Probability (Conditional on LOFA) — II.8

* 5. Use Definitions to Convert Back to Physical Meaning — II.8

CRBR STRUCTURAL CAPABILITY

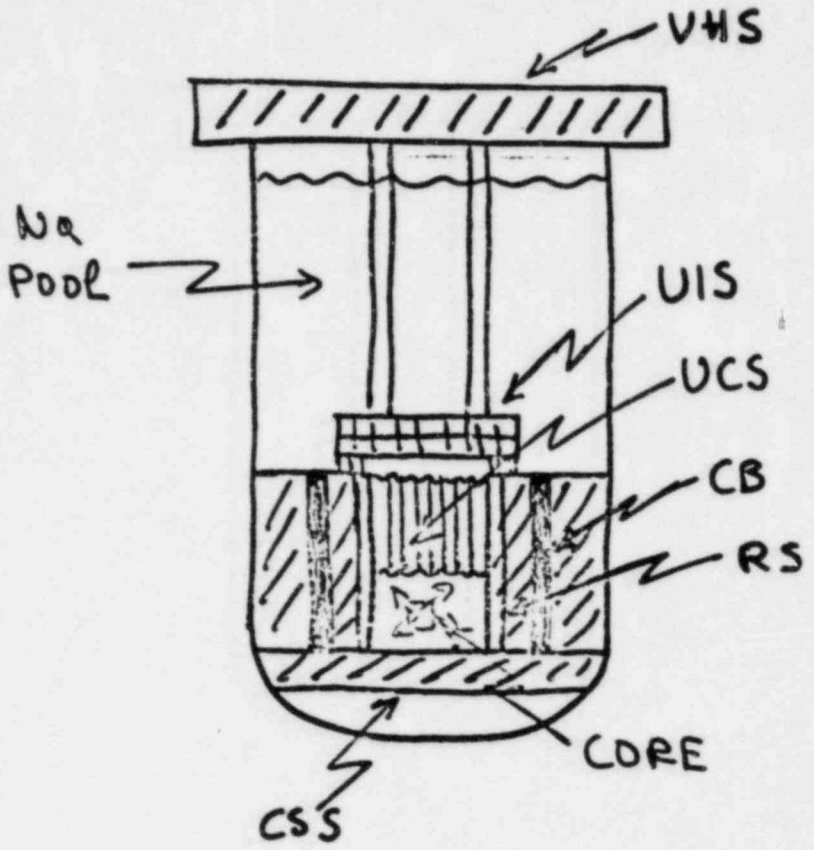

UIS/CB/CSS : Core Envelope "Cage".

Failure Modes

- UIS : Column Buckling } P(t) Needed.
- CB : Radial Strain } 100 #/s 2 ϕ
- VHS : Slug Impact } IKE Needed. 200 #/s 2 ϕ

Reference Yields

100 #/s ⇒ 1,150 MJ UWP

200 #/s ⇒ 2,550 MJ UWP.

Applicant Used 661 MJ Source.

"CAGE" LOADING MECHANISMS.

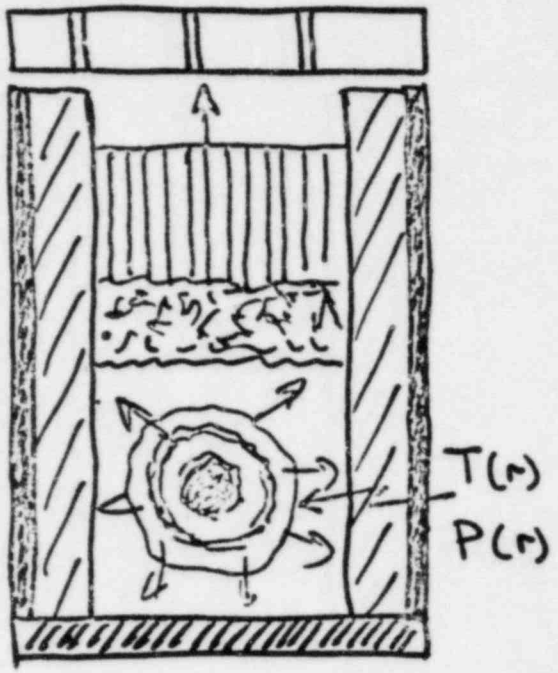

- 2 ϕ Compliance (Energetics and Mitigation)
- UCS Translation } Losses
- CB Radial Strain } Losses
- UIS Delayed Loading } Reduced force.

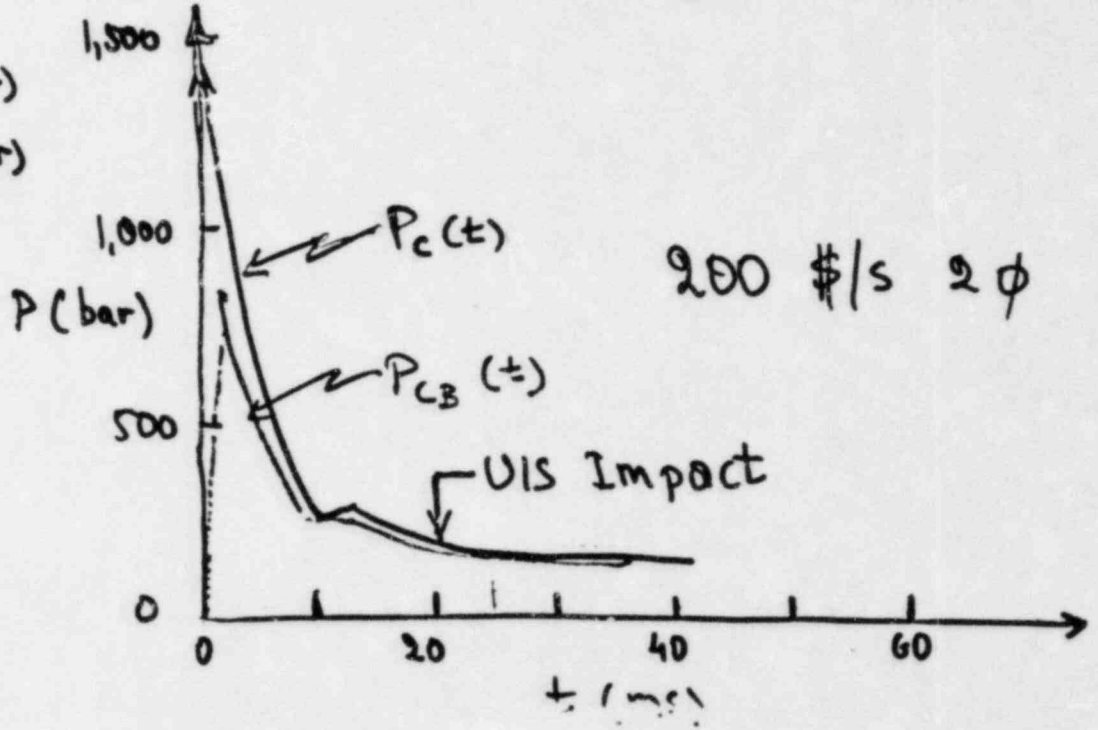

200 $/s 2 ϕ

ENERGY PARTITION: SHORT TERM.

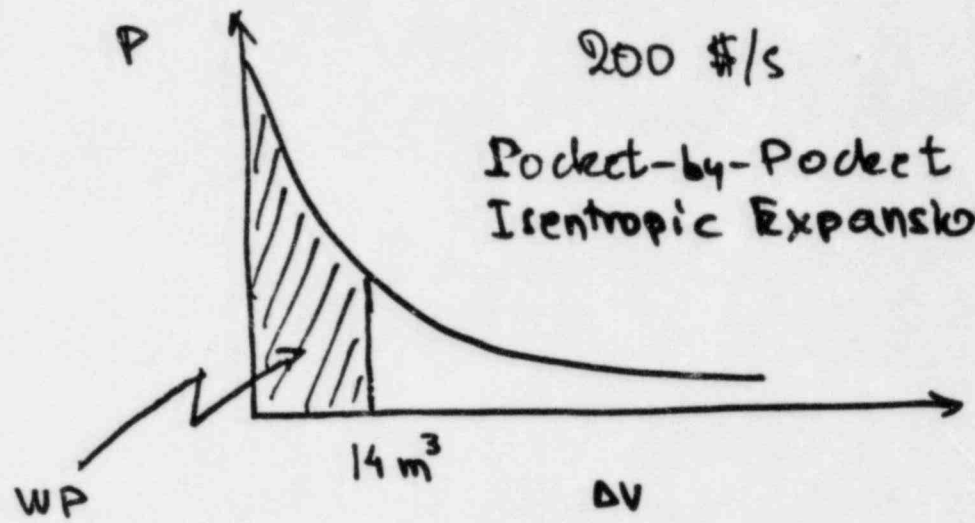

520 MJ → 180 MJ + 340 MJ

CB Strain Energy + UCS kinetic Energy → UIS Impact and Dissipation.

Pool K.E. ~ 0.

VESSEL HEAD LOADING

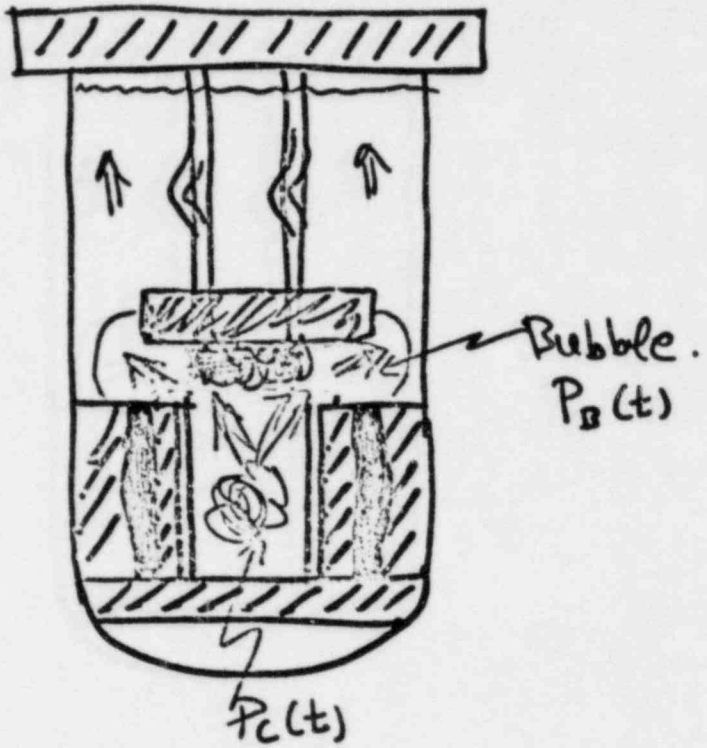

- Throttle Effects $P_B \sim P_c/2$
- 1-D Slug Impact.
- Adiabatic Bubble Wall.

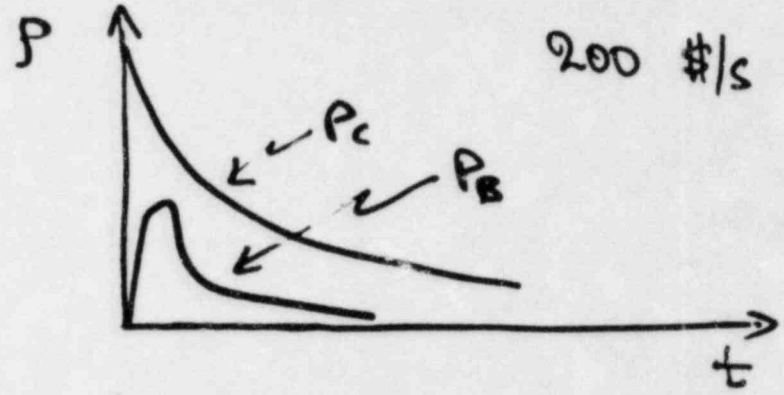

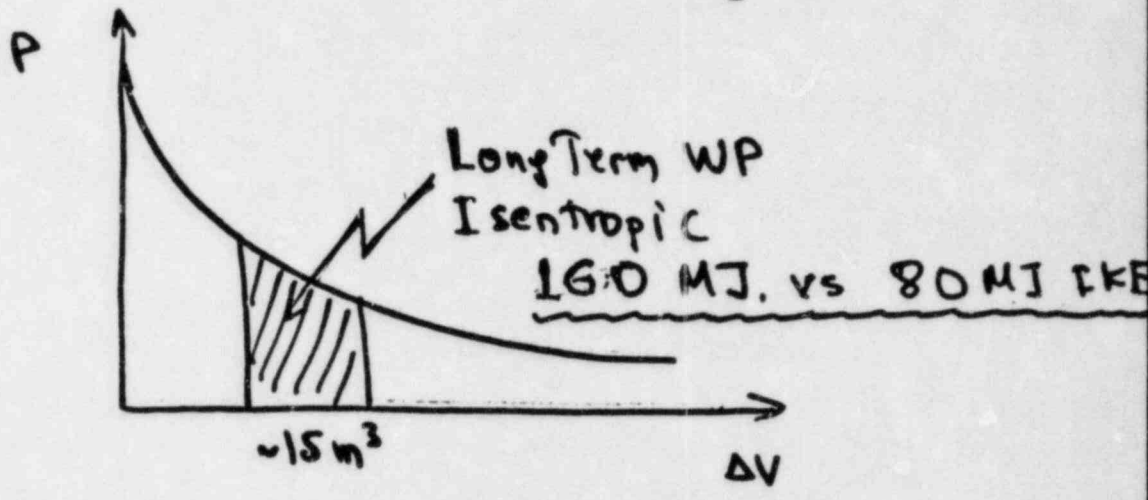

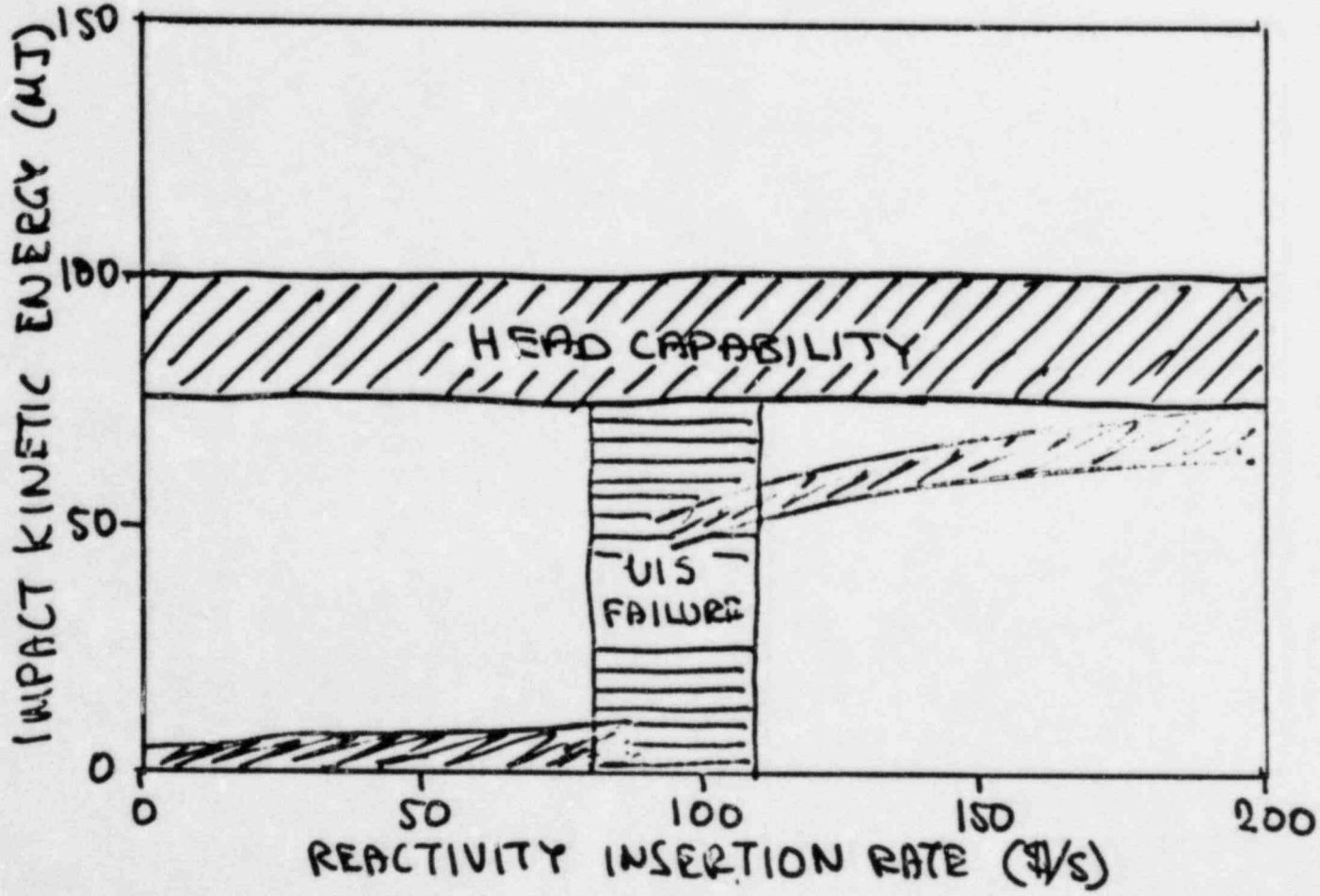
IMPACT KINETIC ENERGY (MJ)
150
100
50
0
HEAD CAPABILITY
UIS FAILURE
0
50
100
150
200
REACTIVITY INSERTION RATE (ft/s)

INITIATING PHASE PHENOMENA.

- SODIUM VOIDING.
- CLAD RELOCATION

} Set the stage for fuel motion.
– Incoherence –

- FUEL MOTION

} Needs to be force fuel to be significant
& Fission Gases Pressures?

- Blockage Formation?
- Power? ⇒ Co-disruption?
- Fuel Failure mode?

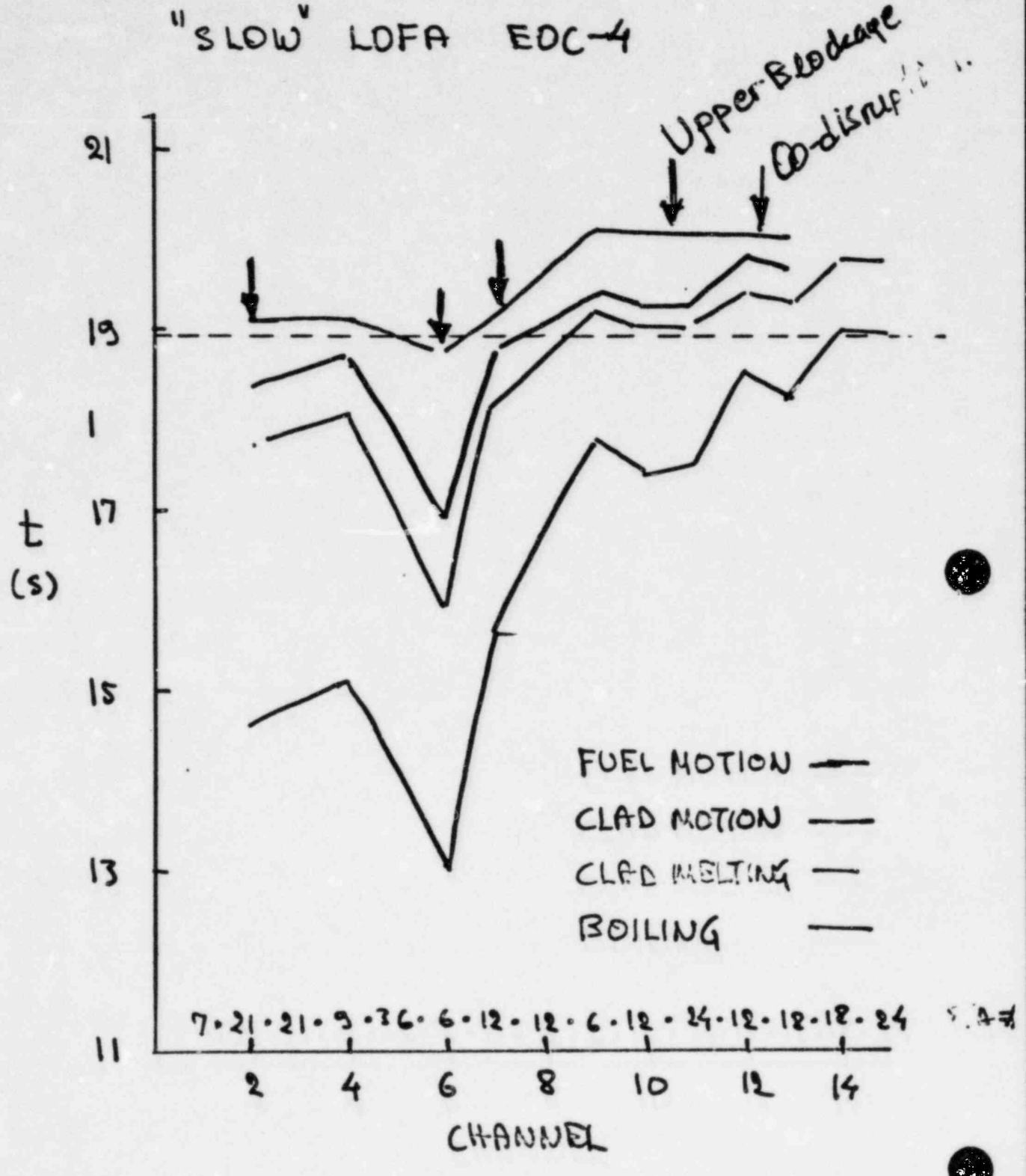
"SLOW" LOFA EOC-4
Upper Blockage
Co-disrup
21
19
1
17
15
13
11
t
(s)
FUEL MOTION
CLAD MOTION
CLAD MELTING
BOILING
7 · 21 · 21 · 9 · 36 · 6 · 12 · 12 · 6 · 12 · 24 · 12 · 18 · 18 · 24
2
4
6
8
10
12
14
CHANNEL

"FAST" LOFA EOC-4.

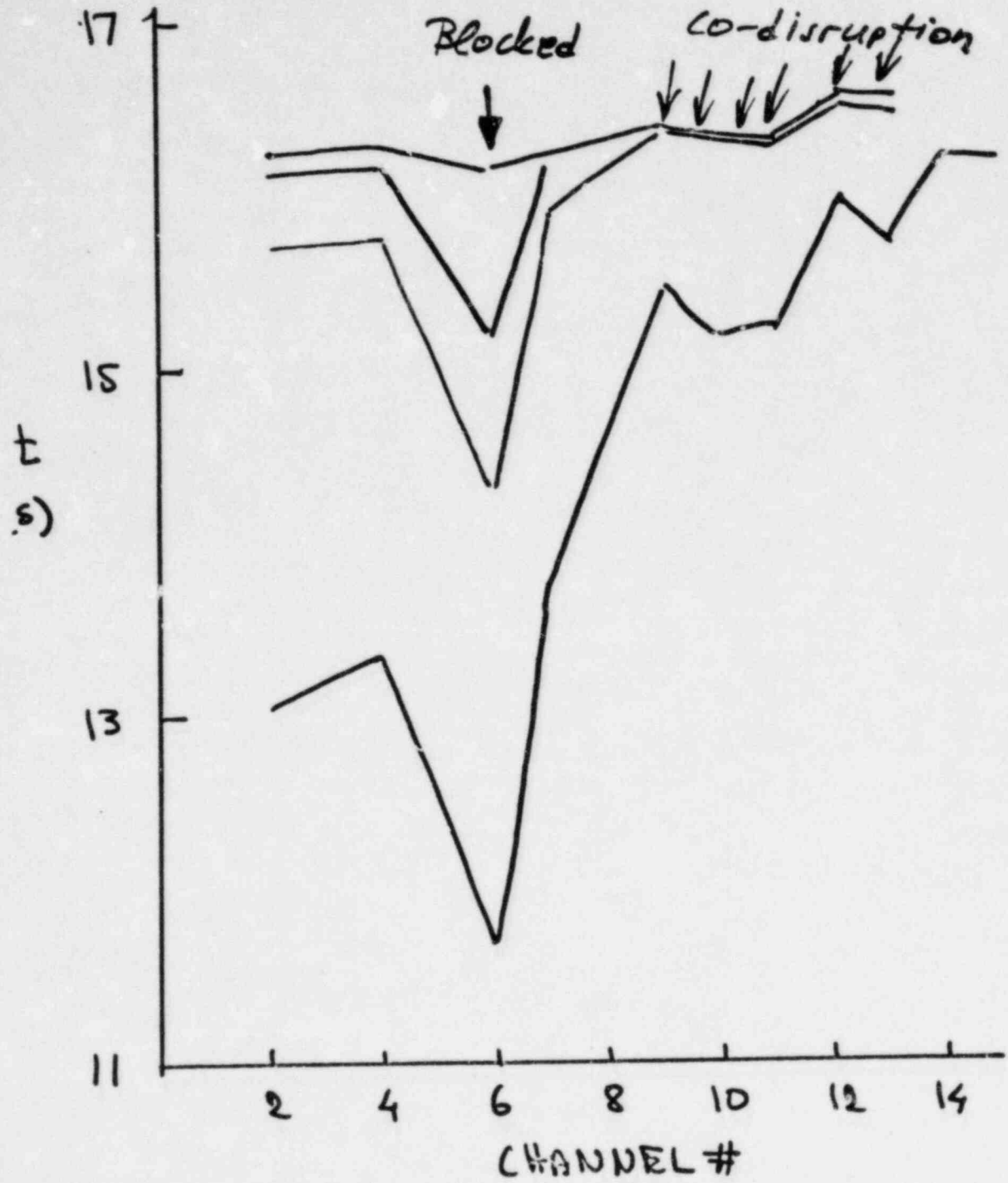

III (C).9 ILLUSTRATION OF CO-DISRUPTION

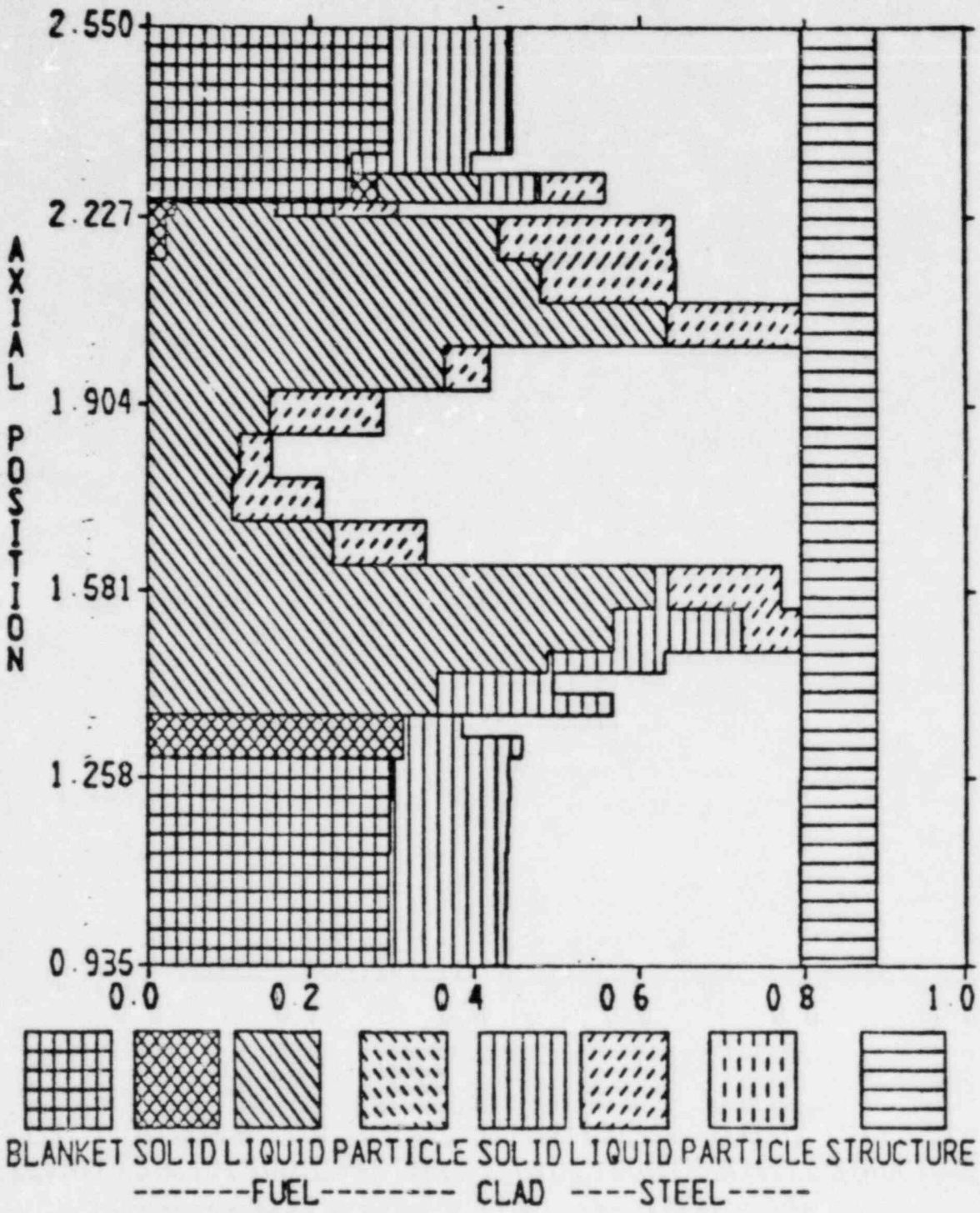

INITIATING PHASE ENERGETICS.

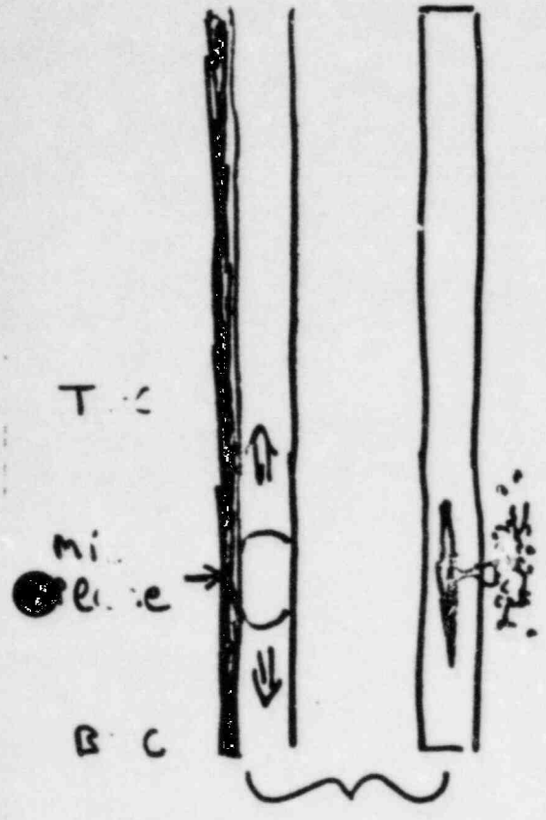

CRBR HETEROG CORE

NO!

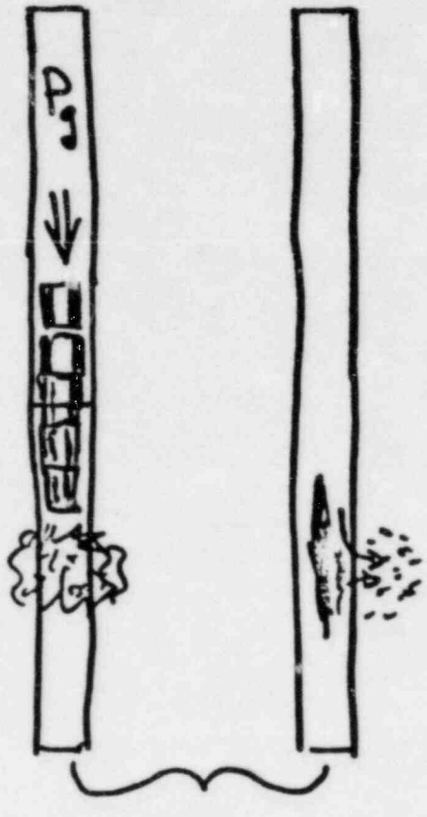

20-50 $/s AUTOCATALYTI

MAYBE.

PLENUM FISSION GAS COMPACTION

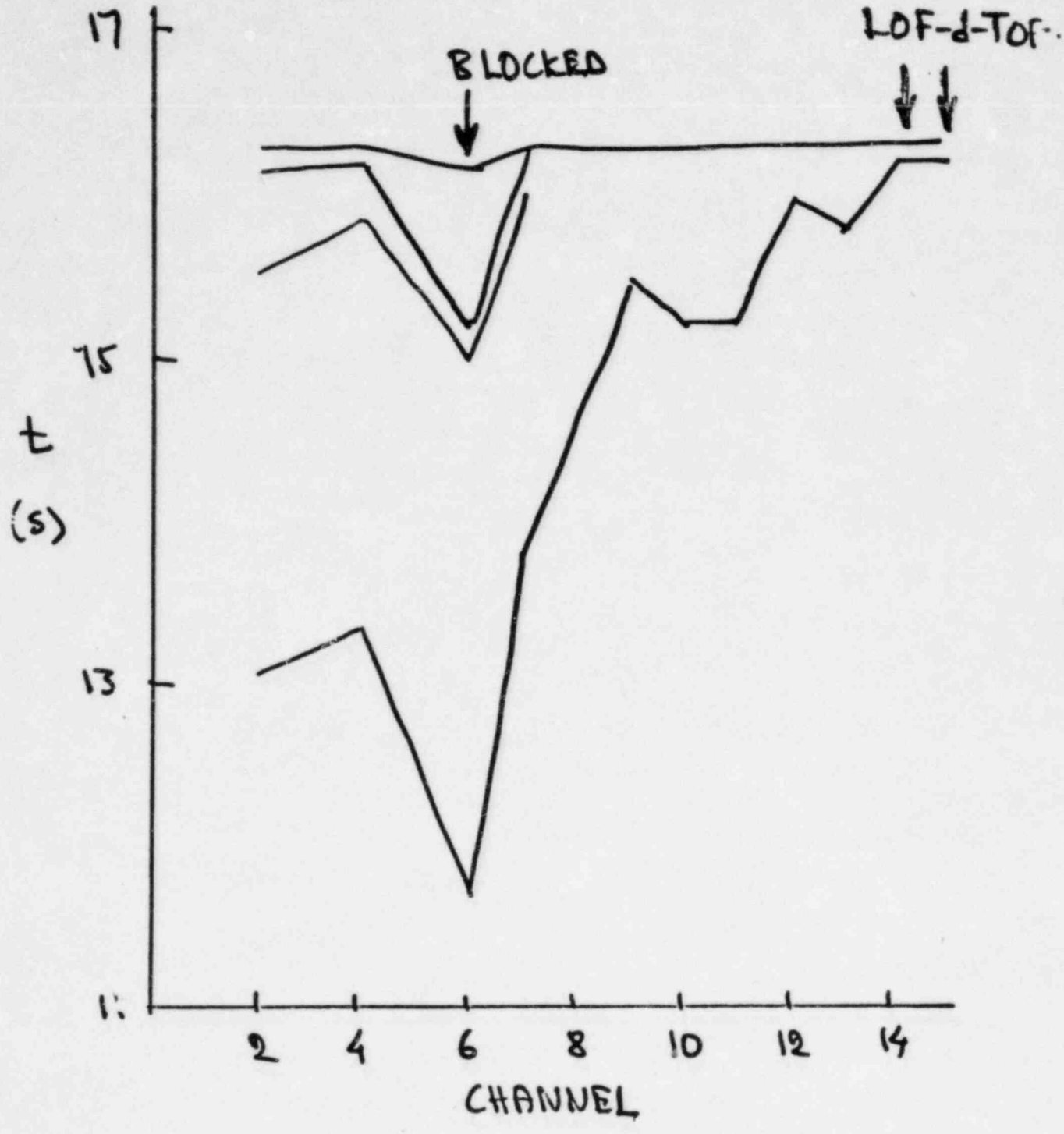

PLENUM FISSION GAS COMPACTION

RESOLUTION

WE RECOMEND TO ELIMINATE PROBLEM BY DESIGN.

- APPLICANT HAS AGREED TO CONSIDER.

DISRUPTION PHASE

- Extended Fuel Motions
- Neutronic Activity
- Transient Pressures and Fuel Expl ions
- Progressive Disruption

  ↳ Addition Fuel Removal Path
  Additional Coherence

↓

RECRITICALITY AMPLIFICATION

?

DISRUPTION PHASE ENERGETICS
(SA Geometry)

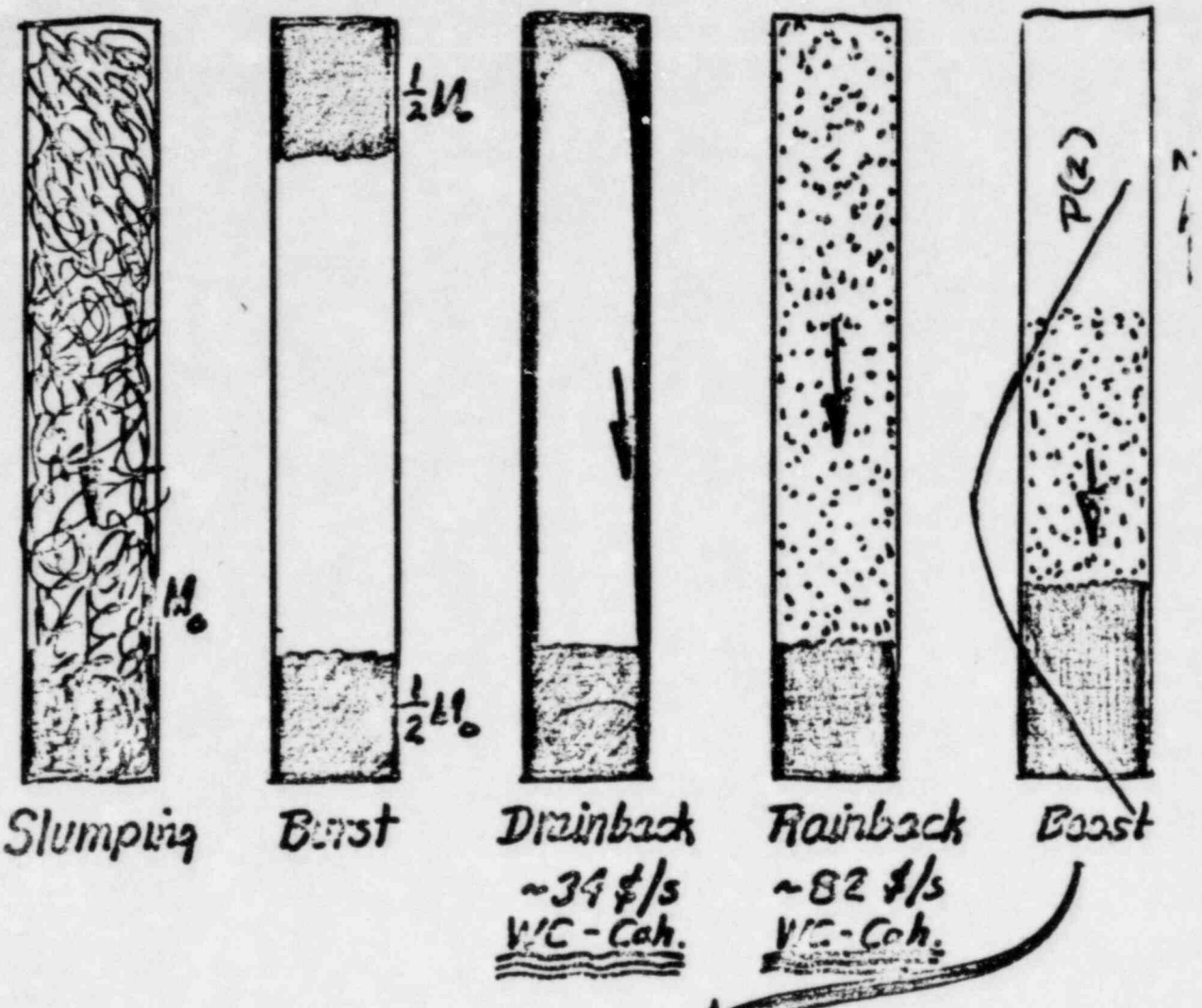

- Only a potential challenge if a coherent WC boost
- Local boosts mild amplication form low energetics event ⇒ no immediate challenge
- Boost requirements:
  - no local compliance (void, voided)
  - puddle to peak flux height < 1
  - bottom blockage
  - narrow inventory range

(SA Geometry Cont.)

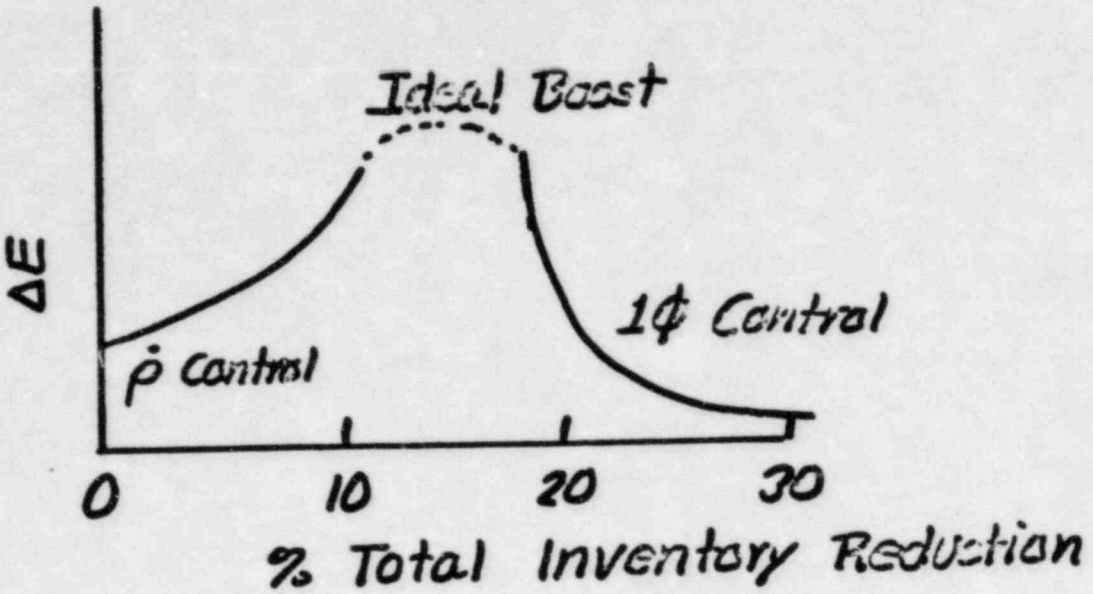

- Ideal rainback only significant b st mode.
  - Drainback requires greater pud ing for criticality (fuel at top effectiv removed)
  - Boilup requires greater puddl g

FLUX PEAK MOVES INTO PUDL E

↓

NO SIGNIFICANT BOOST

+

NO ENERGETICS THREAT

DISRUPTION PHASE ENERGETICS
(Annular Pool)

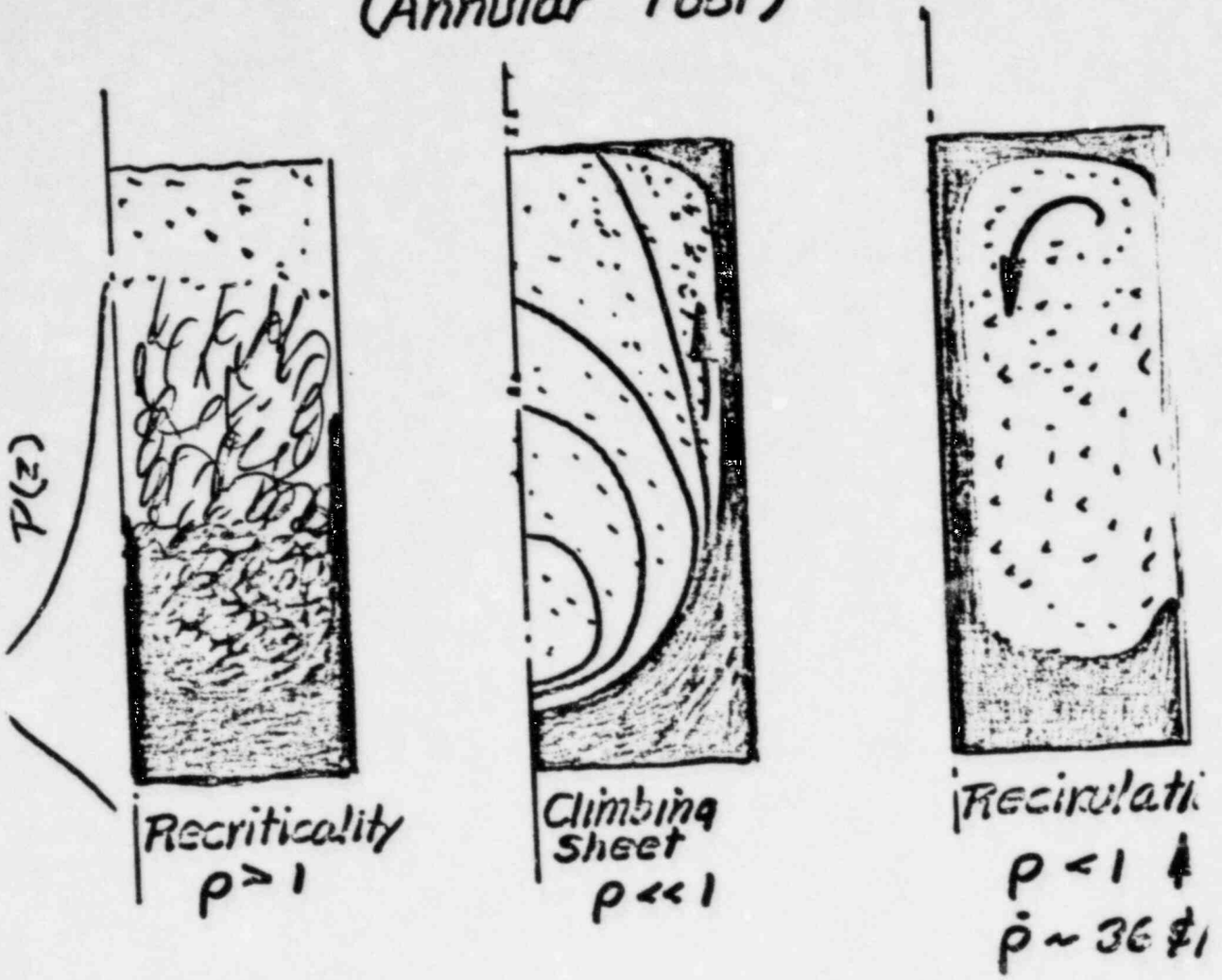

- Ideal rainback ⇒ ~72 ¢/s
- Recirculation ⇒ Reflux str
- Boosts will not occur in real geome ic

⇓

NO SIGNIFICANT ENERGETICS THREAT

DISRUPTION PHASE ENERGETICS
(Whole - core pool)

Early WC Pool Behavior

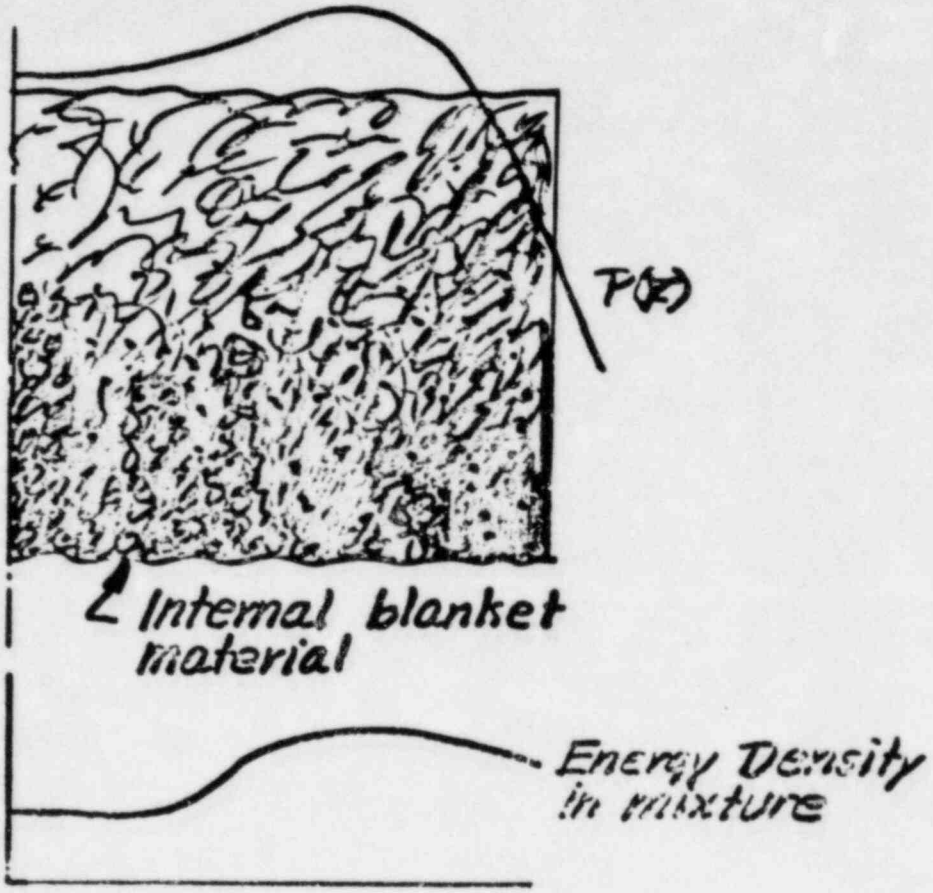

- Early sloshing not central
- Homogenization potential is weak
- Fuel removal paths large
- Neutronic stabilization at < 20.. removal.

DISRUPTION PHASE ENERGETICS
(Whole-core homogenized pool)

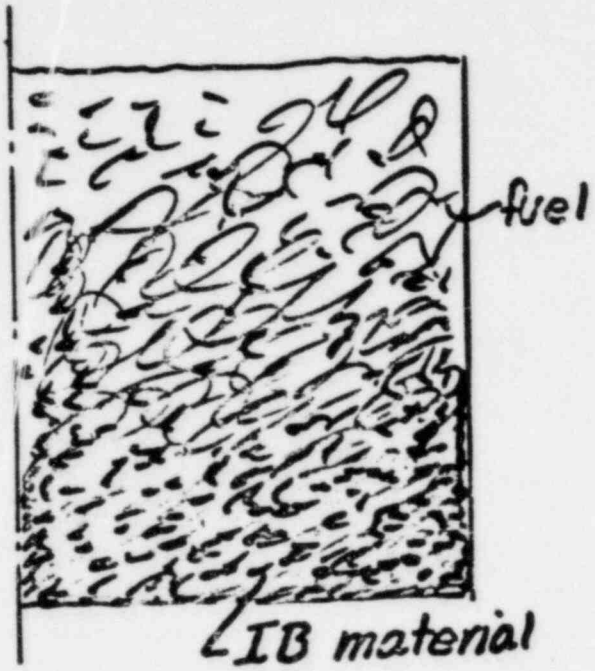

$\rho \simeq 0$ ↑

$\rho << 0$ Post burst

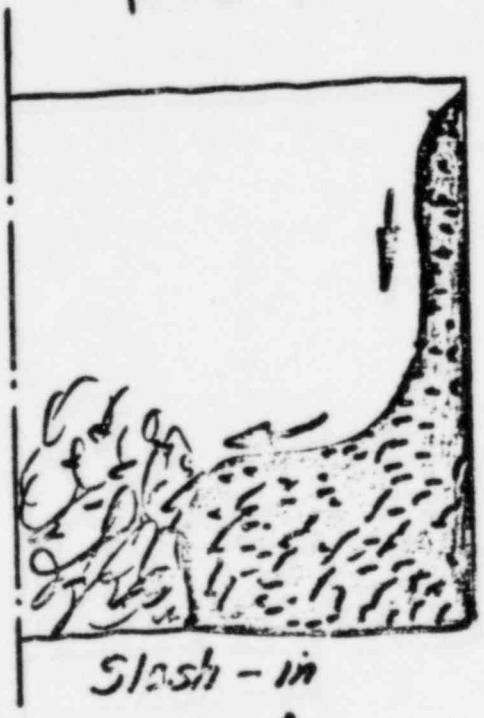

$\rho < 0$ ↑

$\dot{\rho} \simeq 100\ \$/s$

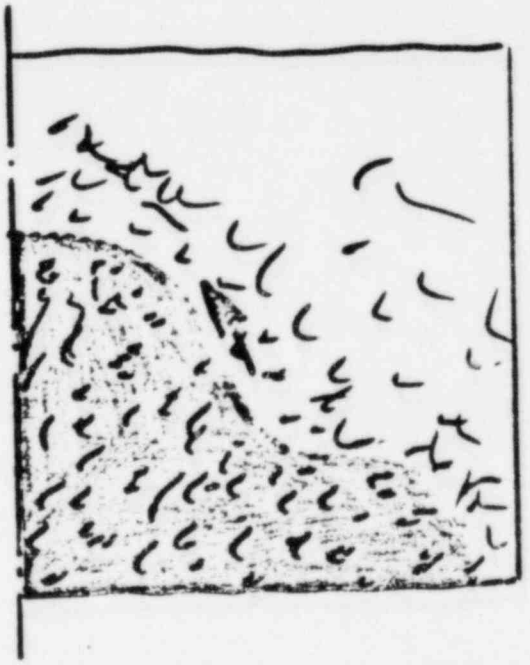

$\dot{\rho} \simeq 300\ \$/s$

1ϕ

W.C. Pool Recriticality

— Non-homogenized —

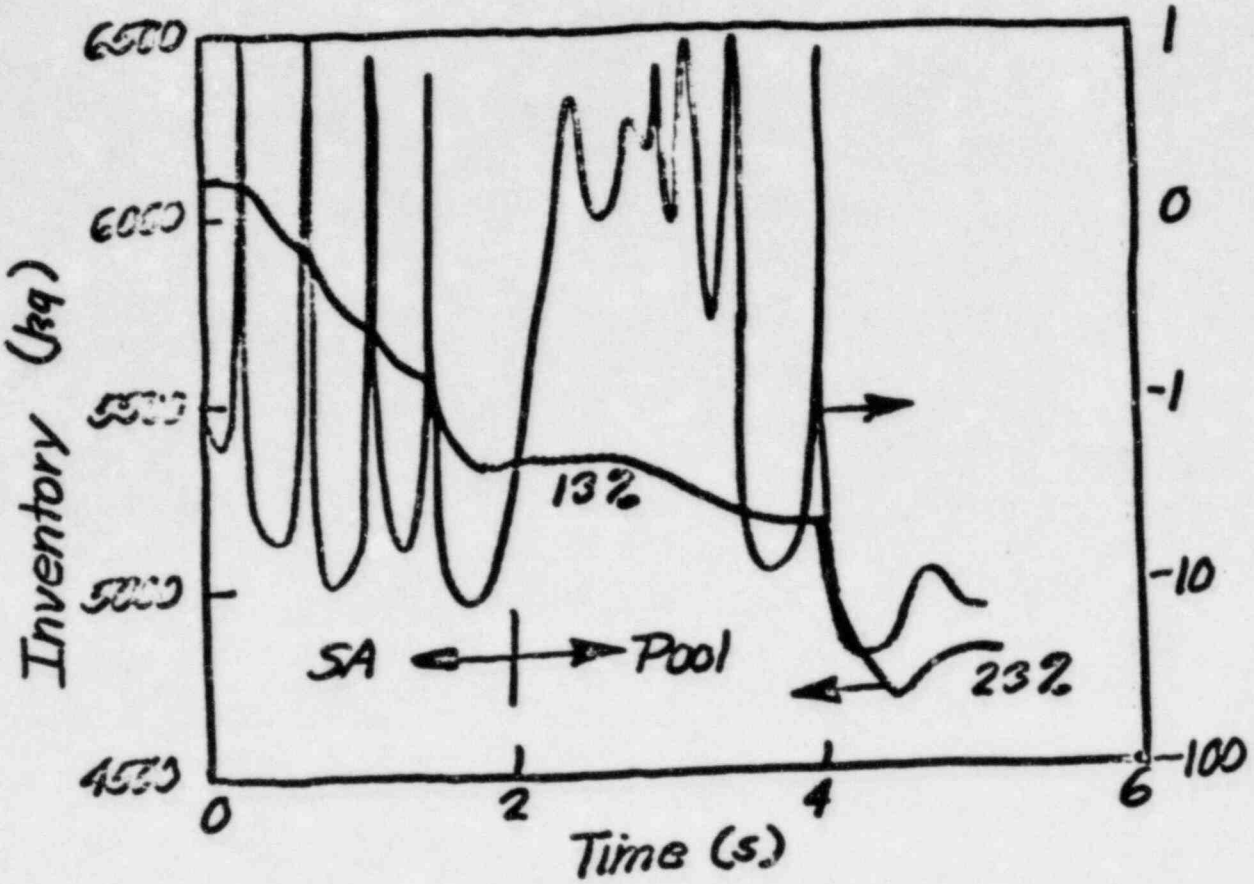

- Unblocked Flow Channel + IB (- p Fuel Removal Only
- Pool Neutronics Stablized
- More time for fuel removal by R.B. gaps + control rod SAs

↓

NO SIGNIFICANT ENERGETICS THREAT

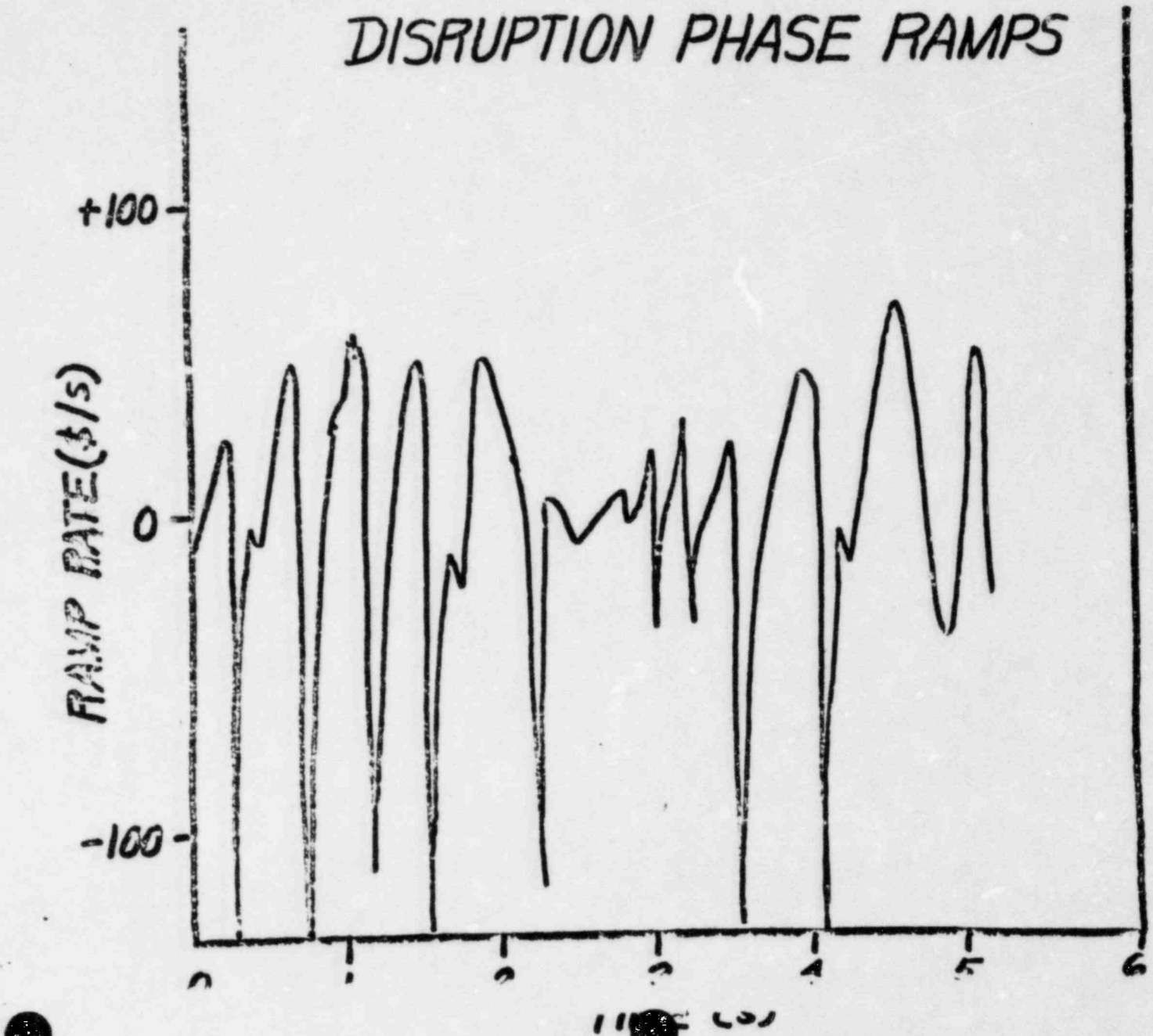
DISRUPTION PHASE RAMPS
+100
0
-100
RAMP RATE(°/s)
0
1
2
3
4
5
6

OUTER REGION POWER PEAKING

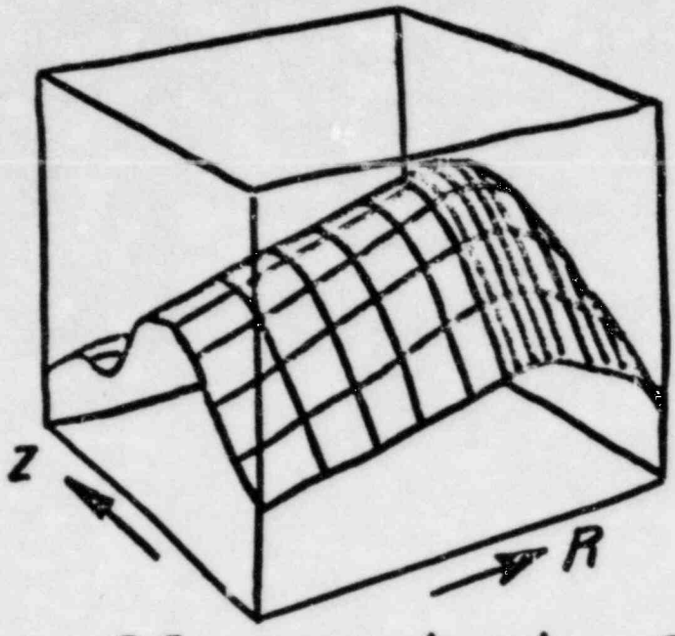

3.0s pre - burst $\rho \Rightarrow 0$

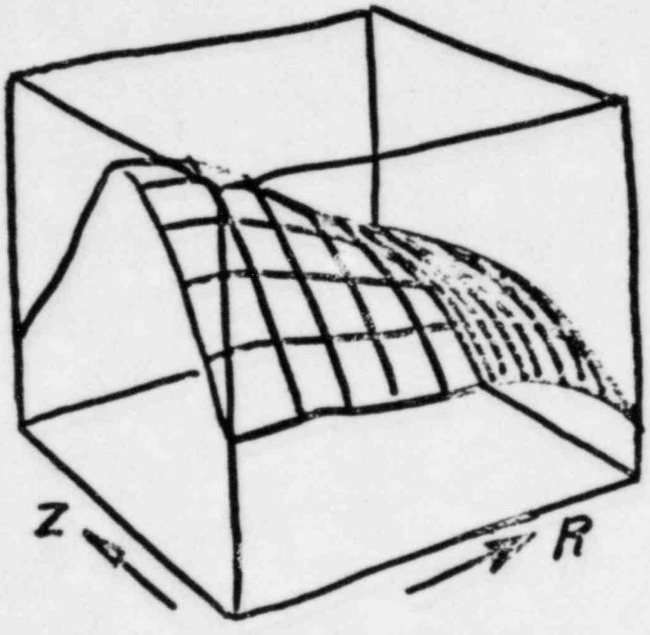

3.7s Post - burst $\rho << 0$

SUMMARY DISRUPTION PHASE ENERGETICS

SA - Phase $\dot{\rho} < 100$ \$/s

Annular Pool Phase $\dot{\rho} < 100$ \$/s

W.C. Pool Phase

- Non-homog. $\dot{\rho} < 100$ \$/s
- Homog. 2ϕ $\dot{\rho} \lesssim 100$ \$/s
  1ϕ $\dot{\rho} < 300$ \$/s Non energetic

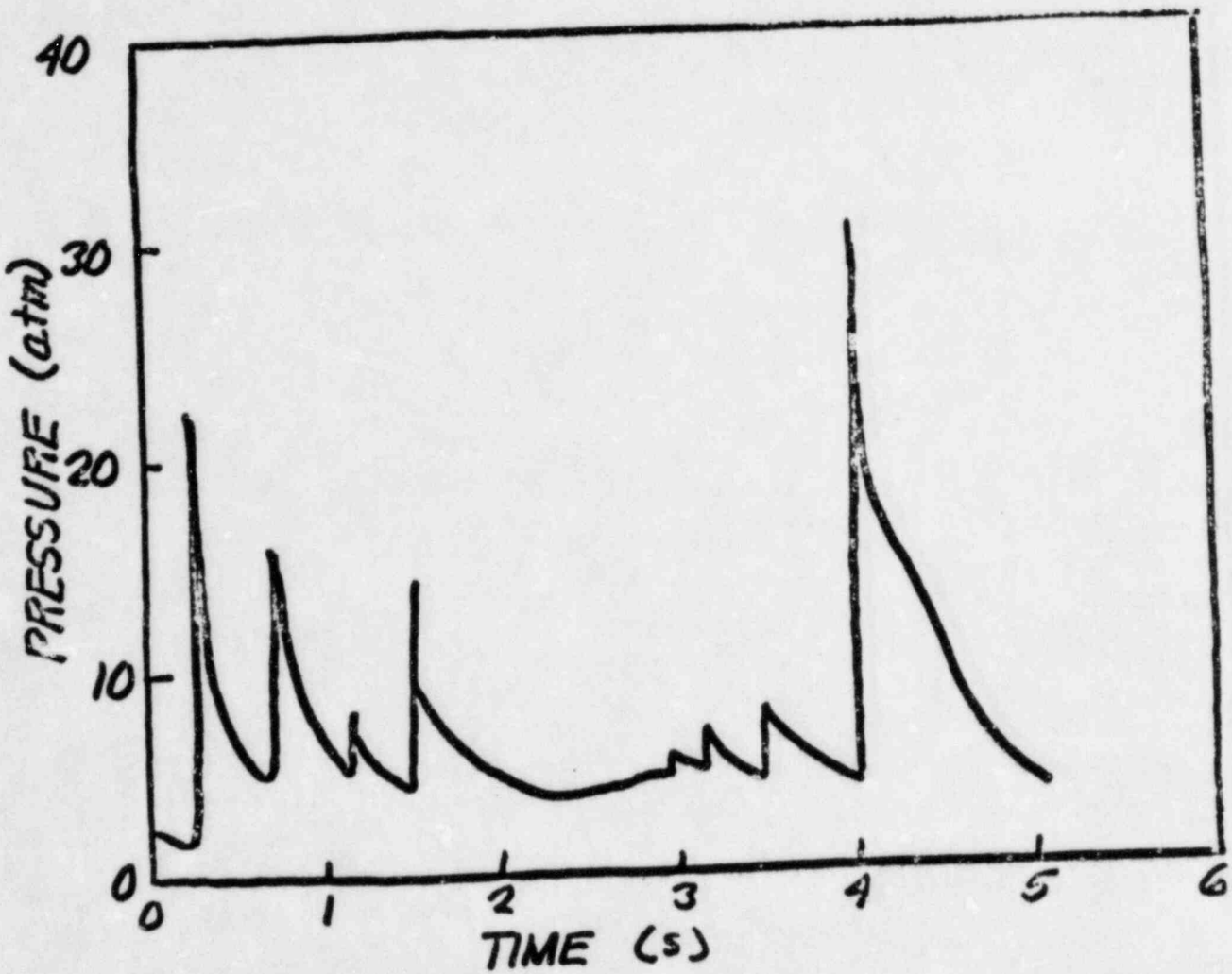

ACTIVE CORE DISRUPTION
PHASE PRESSURE

DISPERSAL BY EXTENDED FUEL MOTION

FUNDAMENTAL ASPECTS

- PATH AVAILABILITY
- MOVEMENT & THROUGHPUT
- PRESSURE

PIN BUNDLE FUEL REMOVAL

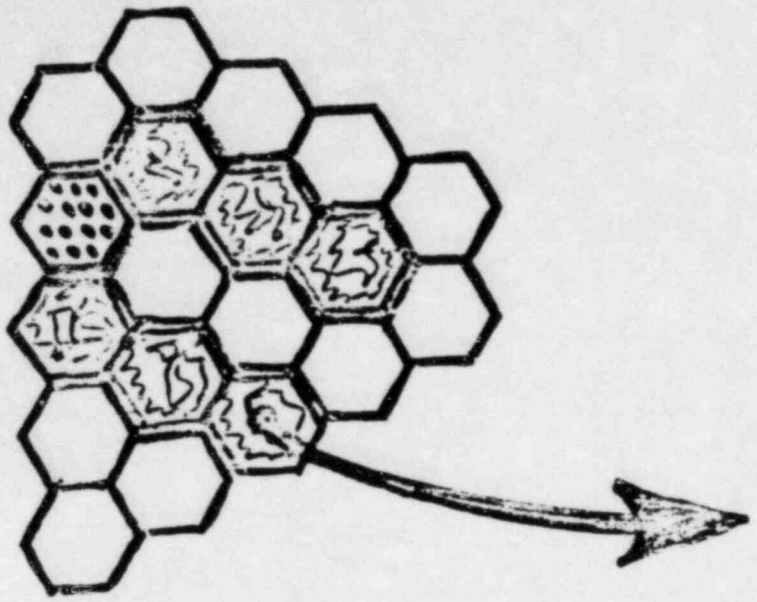

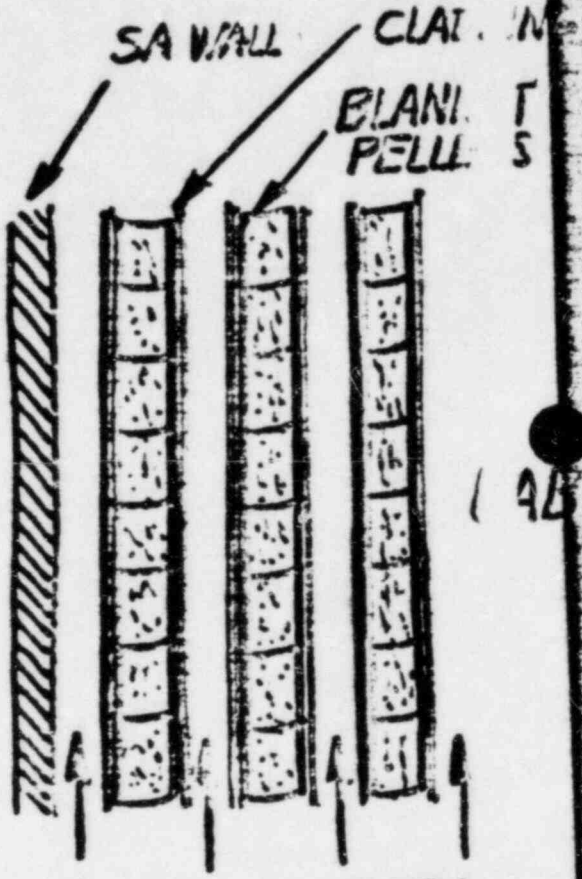

NUMBER OF SAs AVAILABLE DEPENDS ON INITIATING PHASE CLADDING BLOCKAGES

TYPICALLY $\frac{1}{2}$ UAB + $\frac{3}{4}$ LAB

REMOVAL PATH (COOLANT CHANN)

PREDICTION OF PENETRATIONS AS FUNCTION OF PRESSURE.

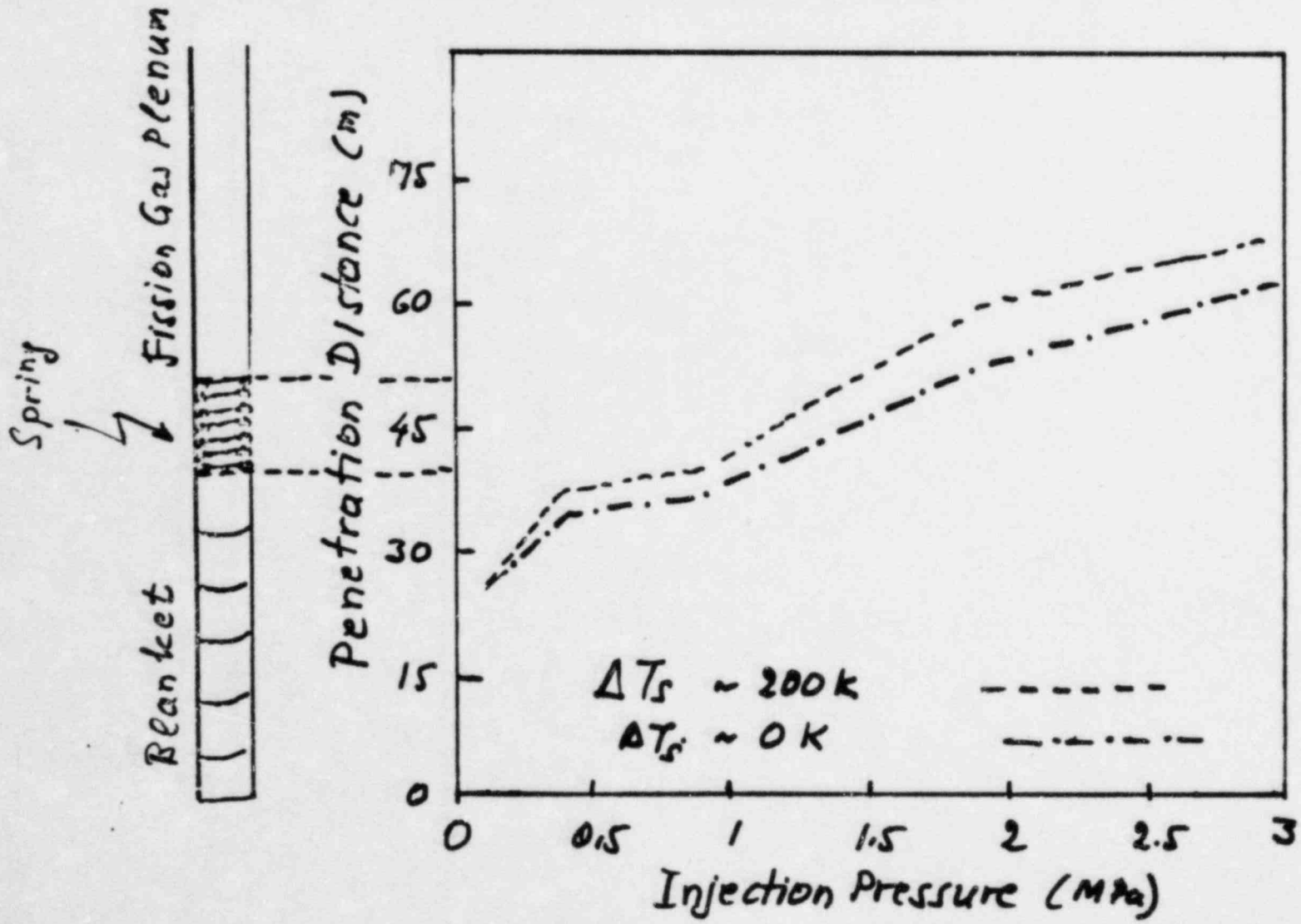

INTERNAL BLANKET GAP REMOVAL

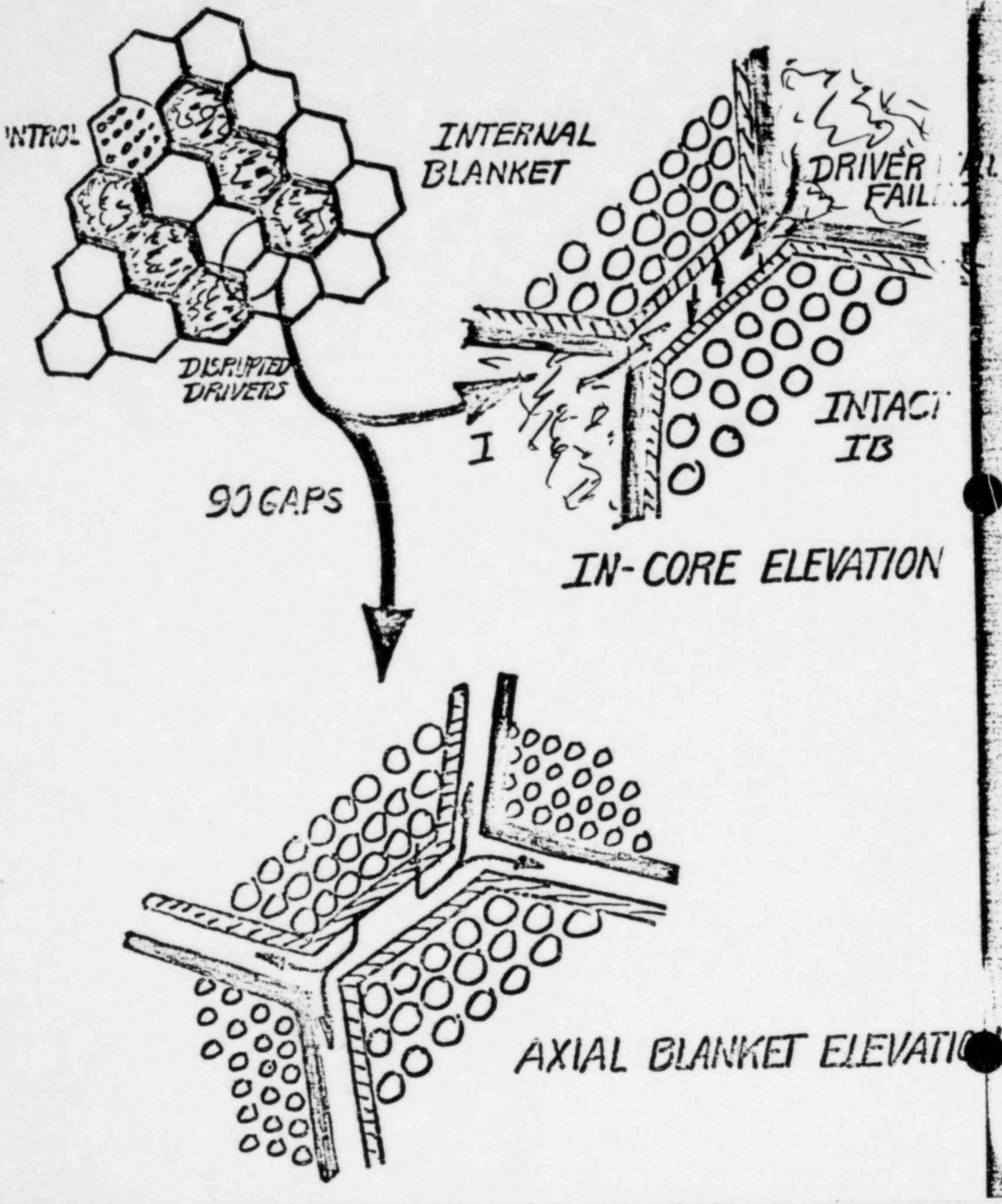

GAP FUEL REMOVAL DYNAMICS

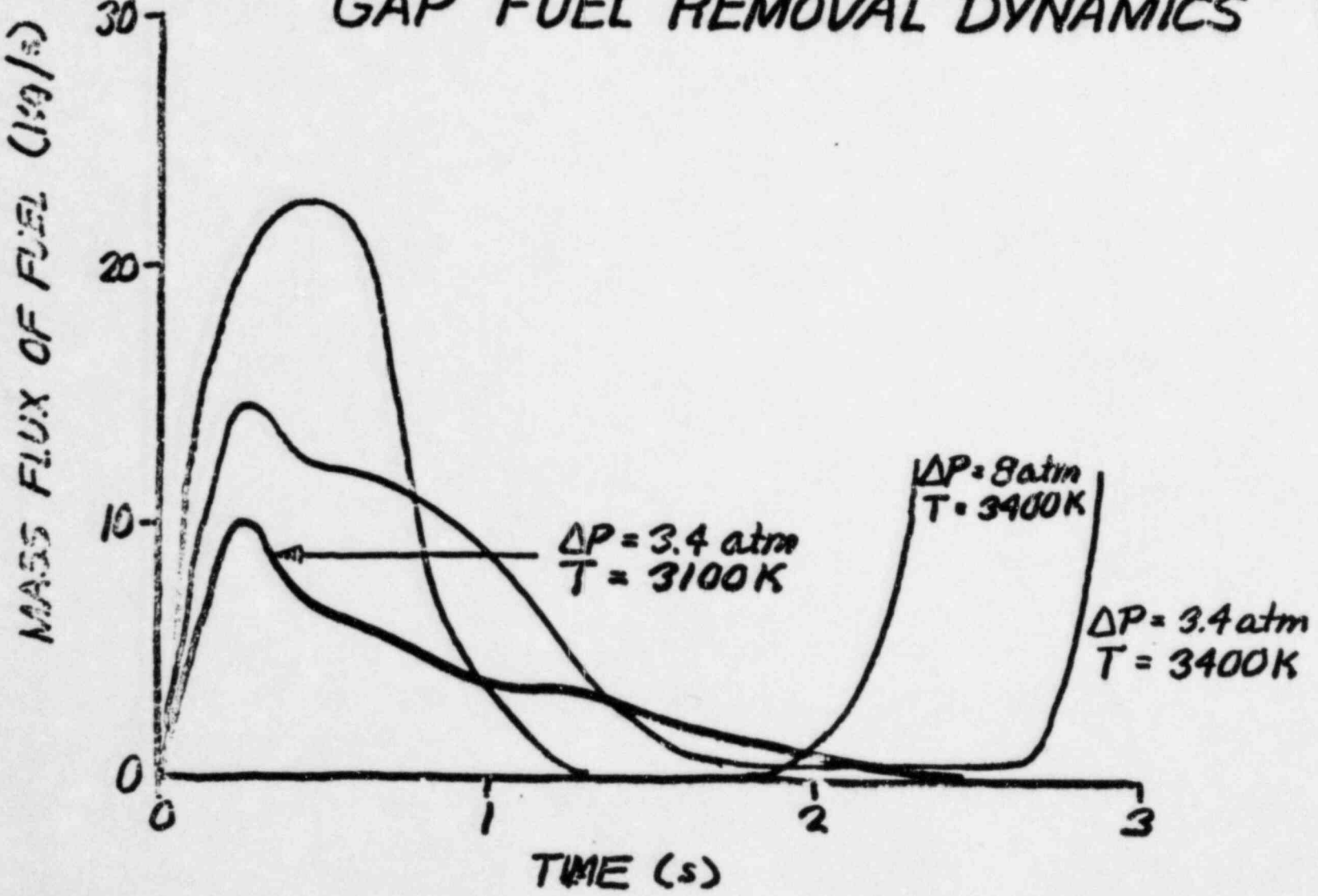

RADIAL BLANKET FUEL REMOVAL

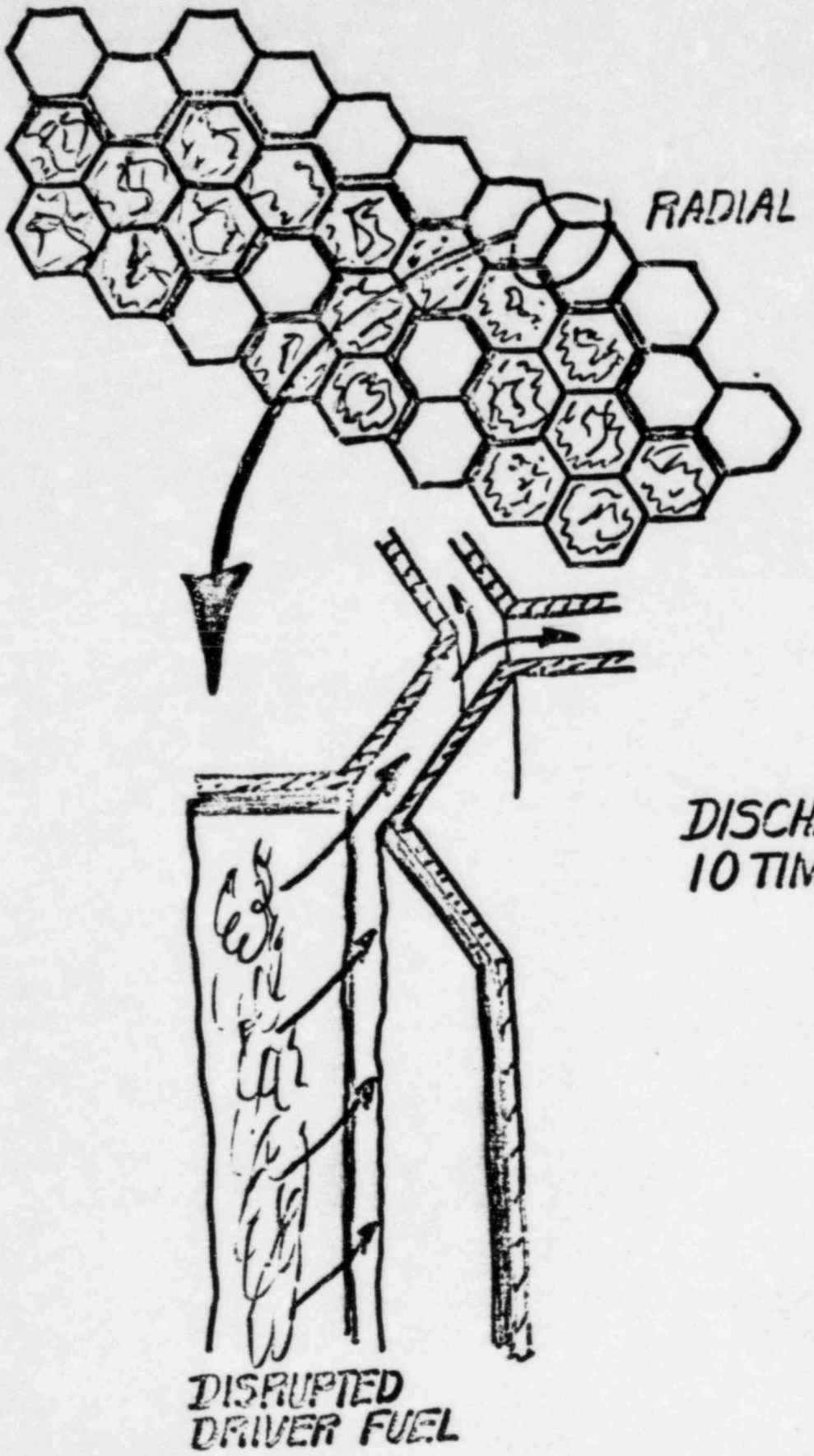

FUEL ESCAPE PATH SUMMARY

PATH	CHARACTERISTICS	ACCESS TIME (s)	COHERENT REMOVAL RATE (%/s) ΔP = 5 atm	CAPACITY @ (%) HOMO-POOL
UAB	Pin-structure	0	6	12
LAB	" "	0	12	25
ID → LAB	Gaps	1-2	21	10
ID → UAB	Gaps	1-2	21	1
RB	Gaps	2-4	200	10
TR	Gaps	2-4	200	>40
Control SA.	Large dia. ducts	3-4	100	>10

FUEL REMOVAL SUMMARY

PATH	ADJUSTED RATE (kg/s)	DISCHARGE TIME (s)	% [illegible]
UAB	3	5	12
LAB	6	5	25
ID/LAB	10	3	10
IB/UAB	10	3	1
RB	20	2	0
RR	20	2	0
Control SAs	10	2	0
		Total	100 %

THEREFORE: DISPERSAL TERMINATION HIGHLY FAVORED

II.1 LOHS CDA INITIATOR

- Core uncovery required for cladding melt.
  - Saturation ~ 10 hrs

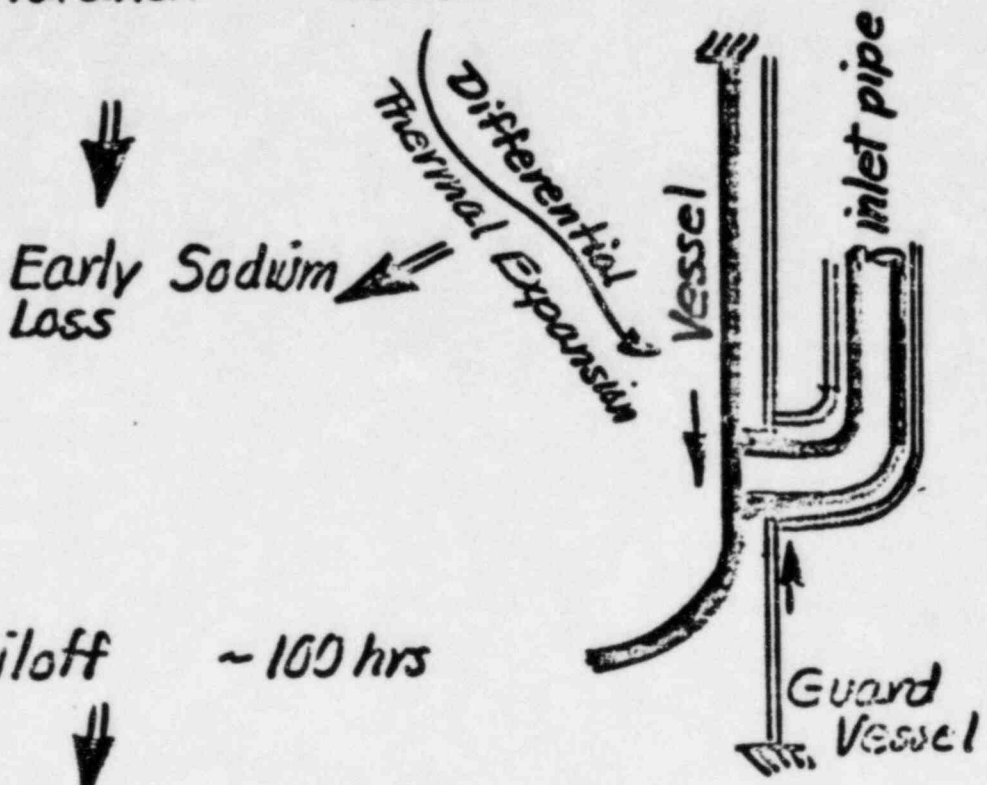

  - Boiloff ~ 100 hrs
    - Possible Recovery
- Heating Rate: 0.5 to 1% of nominal full power

II.2 LOHS CORE DISRUPTION

- Slow steel melting
- Steel draining
- Massive lower blockage

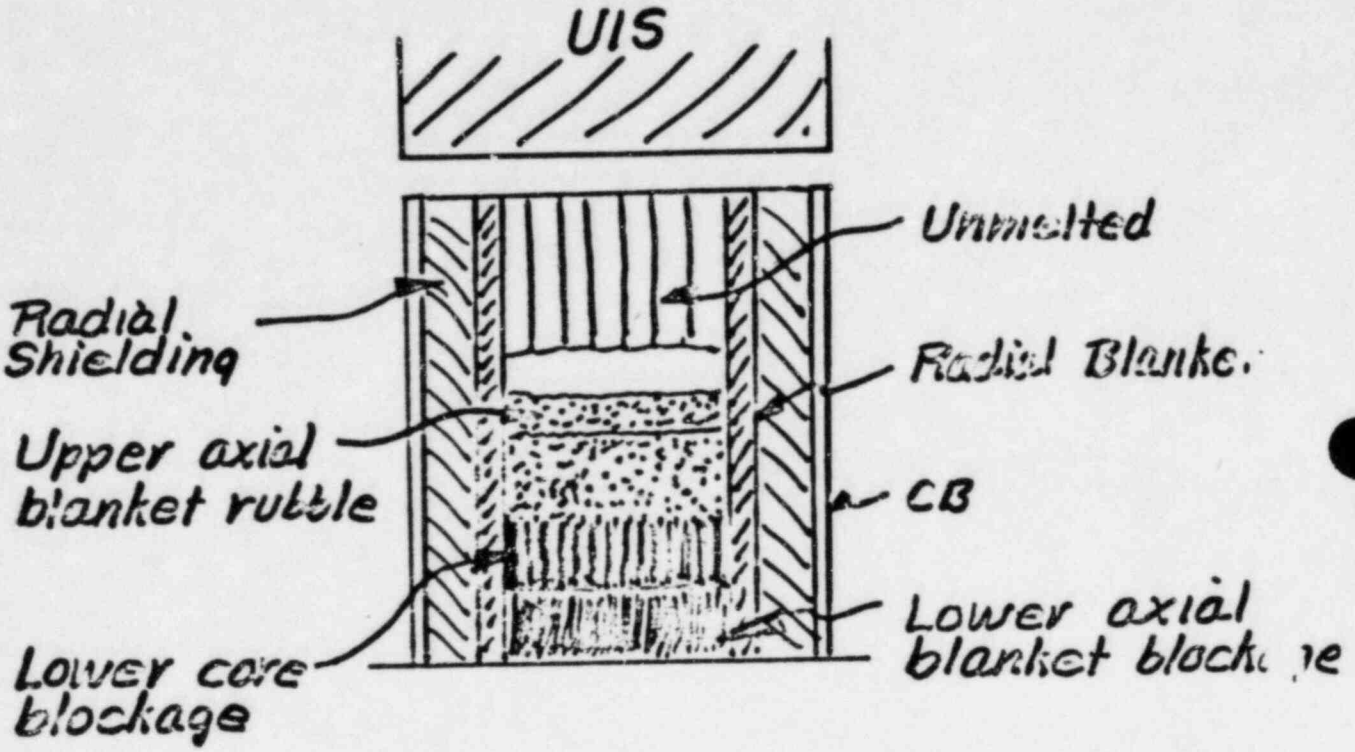

- Slow approach to critical
  - Fuel sagging
  - Fuel melting
  - Control sublimation

II.3 LOHS INITIAL RECRITICALITY

- Power → Rapid melting → Gravity fall

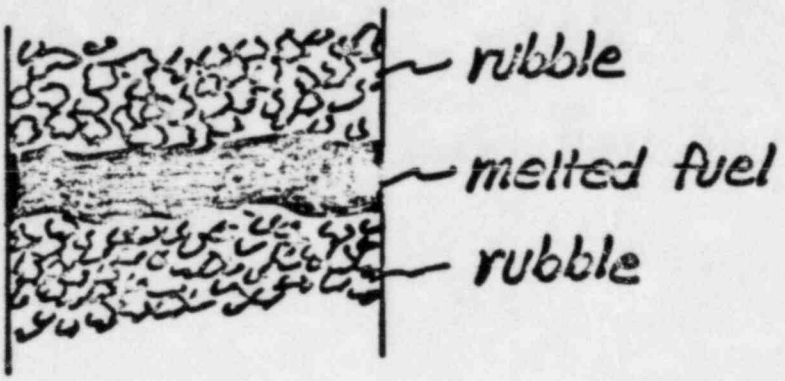

- Key considerations :
  1 to 2 cm displacement ⇒ critical to p[illegible]
  Gravity motion ⇒ 60 $/$ if coher[illegible]
  Local collapse ⇒ low $\dot{\rho}$ ⇒ no termi[illegible]

II.4 LOHS RECRITICALITY TERMINATION

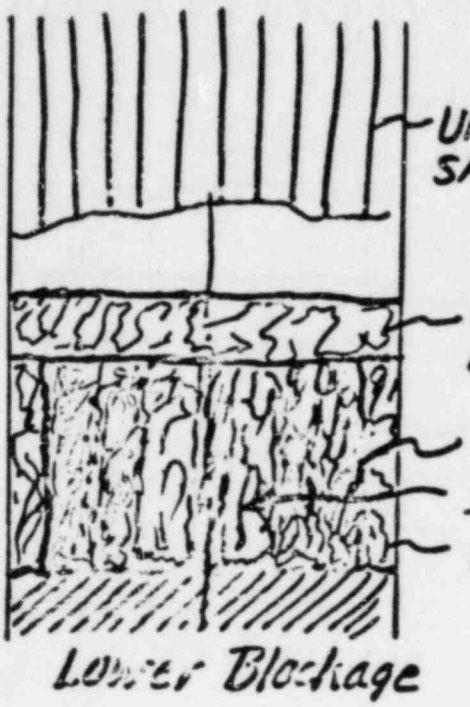

LOF Contrast

- Upper blanket easy mixing
- Easier upward termination

Reactivity Effects:

Homogenize upper axial blk. ⇒ ~ −. 7$
Homogenize internal blk's ⇒ ~ +: 7$
Homogenize ½ radial blk. ⇒ ~ −; 1$
Remove control material ⇒ ~ +; 1$
Complete puddling ⇒ < +1 $

Termination Mode:

Mild recriticalities ⇒ mix UAB
⇒ mix IB's
⇒ mix RB

Final State Slumped & control out
⇓
SUBCRITICAL

II.5 LOHS WHAT IF ENERGETICS ?

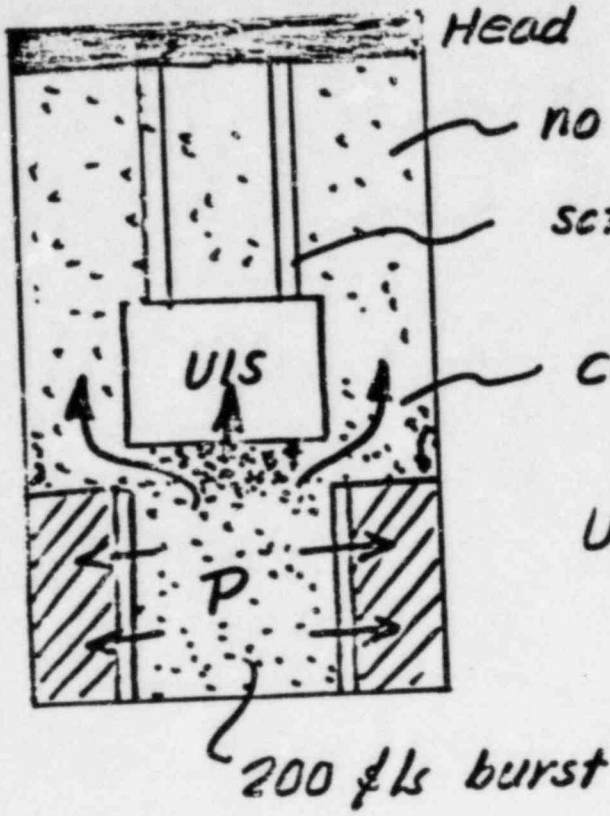

UIS KE ~ 5MJ

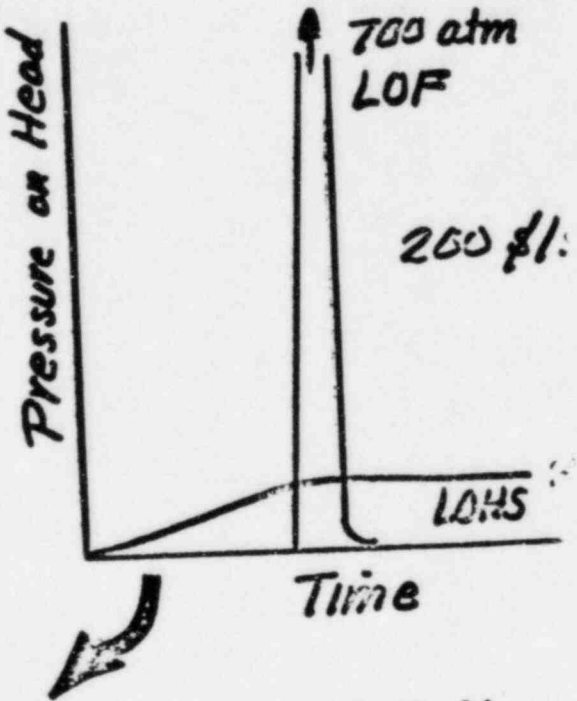

No Vessel Head Failur

LA-9716-MS
NUREG-CR-3224

AN ASSESSMENT OF CRBR CORE DISRUPTIVE ACCIDENT ENERGETICS

by

T. G. Theofanous and C. R. Bell

March 11, 1983

Contributors

W. R. Bohl (LANL)
L. L. Luck (LANL)
T. A. Wehner (LANL)
H. H. Hummel (ANL)
P. Pizzica (ANL)
M. Asprey (LANL)
T. A. Butler (LANL)
R. E. Baars (LANL)

ACKNOWLEDGEMENTS

This work was carried out under the joint sponsorship of the NRC offices of Nuclear Reactor Regulation and of Nuclear Regulatory Research. We are particularly grateful to Mssrs. N. Grace, P. Check, W. Morris, and C. Allen for their support, encouragement, and understanding throughout the period of this study. We also appreciate the support of the LANL management in making available the resources necessary for maintaining the fast pace and tight schedules of this work. Last but not least our sincere thanks to Ms. B. Douglass whose magnificent typing and perseverance removed all pain in the preparation of the final manuscript, and simply, made the meeting of this last deadline possible.

TABLE OF CONTENTS

ACRONYMS

ACRS	Advisory Committee on Reactor Safeguards
ANL	Argonne National Laboratory
BNL	Brookhaven National Laboratory
CB	Core Barrel
CCS	Core Support Structure
CDA	Core Disruptive Accident
CRBR	Clinch River Breeder Reactor Project
FAI	Fauske and Associates Inc.
FFP	Fuel Failure Propagation
FFTF	Fast Flux Test Facility
FPS	Full-Power-Seconds
FTR	Fast Test Reactor
GE	General Electric Co.
HCDA	Hypothetical Core Disruptive Accident
HEDL	Hanford Engineering Development Laboratory
IKE	Impact Kinetic Energy
IRP	Intermediate Rotating Plug
IWP	Impact Work Potential
LANL	Los Alamos National Laboratory
LMFBR	Liquid Metal Fast Breeder Reactor

LOFA	Loss of Flow Accident
LOF-d-TOP	Loss of Flow Driven Transient Overpower
LOHS	Loss of Heat Sink Accident
LWR	Light Water Reactor
NRC	Nuclear Regulatory Commission
PDE	Post Disassembly Expansion
PRA	Probabilistic Risk Assessment
RES	Office of Nuclear Regulatory Research
S/A	Subassembly
SAS3D	Computer Code for Initiating Phase Analysis
SBTF	Sodium Boiling Test Facility
SIMMER-II	Computer Code for Generalized CDA Analyses
SSE	Safe Shutdown Earthquake
SMBDB	Structural Margin Beyond the Design Basis
SNL	Sandia National Laboratory
TER	Technical Evaluation Report
TOP	Transient Overpower Accident
TREAT	The TREAT Test Reactor
UCS	Upper Core Structure
UIS	Upper Internal Structures in CRBR
ULOHS	Unprotected LOHS
UWP	Ultimate Work Potential
VHS	Vessel Head Structure

0. EXECUTIVE SUMMARY

This section contains the results of our independent assessment of the energetic behavior resulting from postulated Core Disruptive Accidents in the CRBR Heterogeneous core design. The object is to define in a reasonably conservative fashion, the magnitude of the mechanical energy releases against which the integrity of primary system, and of the reactor vessel head in particular, should be assessed. This effort began with a detailed review and evaluation of the Applicants' positions, and their technical bases, on the subject and evolved, over a period of nearly 15 months, into a completely independent study with original elements on one or more of the following aspects: (a) accidents, phenomena, or effects taken into account, (b) analysis methods utilized, (c) experimental evidence brought to bear. The results of the independent assessment are briefly summarized in this section and the details are provided in the body of this report. A similar structure and cross-referencing to the original document are utilized in this summary to facilitate the search for additional details.

0.1. Overall Technical Approach

Depending upon whether reactor shutdown has been achieved, core disruption may initiate at powers ranging from near normal to decay levels. The corresponding heating rates vary by two orders of magnitude and define the first major classification of CDAs into "unprotected" and "protected" respectively. Mechanistically a protected CDA is the result of sustained failure to remove decay heat and is commonly referred to as the Loss of Heat Sink Accident (LOHS). In the unprotected CDA case initial core disruption may occur due to either an undercooling or an overpower condition. Mechanistically, the undercooling would be the result of loss of coolant flow, known as the Loss of Flow Accident (LOFA), and the overpower due to an uncontrolled reactivity insertion, which is commonly referred to as the Transient Overpower Accident (TOP). In general terms, these three accidents exemplify the generic behavior over the whole range of the CDA spectra of circumstances, hence, they can be used to adequately characterize the spectra of energetic consequences.

Another class of CDA initiators, that of Fuel Failure Propagation (FFP), has also been identified and extensively studied in the past. The evidence is conclusive now that the attainment of whole core disruption through such a mechanism can be neglected. Finally, various combinations of function failure events (TOP/LOF, etc.) and/or of structural failures (i.e. due to extreme external events such as earthquakes beyond the SSE, yielding core support failures, loss of piping integrity, etc.) have also occasionally been considered. Our review of these areas indicates that those few cases, for which severe energetic behavior cannot be precluded at this time (i.e. TOP/LOF, etc.), are of sufficiently low probability to be neglected.

Our approach consists of realistically following each one of the three generic CDA initiators through the core disruption phases and until accident termination. These so-called mechanistic CDA analyses provide an overall framework against which the potential for energetic phenomena is assessed with due regard for the controlling physical processes. In terms of actual licensing cases, the first efforts along these lines were made during the Regulatory review of the FFTF CDA energetics assessment. The approach further matured with the initial (homogeneous core) CRBR application and licensing review.

It would be in error, however, to expect that such mechanistic analyses can, at this time, predict uniquely the complete evolution of a postulated CDA from initiation to termination. There is considerable complexity in the underlying physical processes that has not yet been appropriately modeled. We believe that such limitations may alter the overall timing of some events, and may even affect the actual character and sequence of the intermediate states. However, we also believe that these uncertainties can be adequately handled within a properly oriented overall effort. With this in mind we do not attempt to associate a simple outcome to a given initiator. Rather, we attempt to establish a "range of phenomenology" consistent with experience and known physical principles. Within this range we search for energetically-prone circumstances, identify the important mechanisms, and quantify the intensity of energy release in a reasonably conservative manner (i.e. avoiding excessive and clearly non-physical conservatisms). Similarly, we scrutinize for termination-favoring phenomena, identify the important mechanisms, and quantify the approach to termination, by the fraction of fuel removed from the core region (at approximately 40% removal permanent subcriticality, i.e. termination, is achieved). Based on these results we complete the assessment by synthesizing sequences and respective likelihoods.

These analyses were carried out by means of the system codes SAS3D (and to a limited extent the most recent version SAS4A) and SIMMER-II. These codes are used as "integrators" of the technical base and their results are guided, scrutinized and/or augmented by employing special purpose analytical techniques, in-pile experimental data, and out-of-pile simulant experiments as appropriate. As in all safety studies, the synthesis of experimental data and analysis techniques to produce a quantified basis for the conclusions requires approximations, involves uncertainties, and must be appropriately focused. Engineering judgement is utilized here to provide overall guidance in this regard.

As an initial step in our independent assessment effort we made the judgement that among all core disruptive accidents the LOFA should be chosen as the subject of our most detailed considerations. This was based on the opinion that: (a) the LOFA phenomenology spans the range of energetically significant CDA behavior, (b) within the LOFA sequences our previous review effort identified specific and significant areas of concern, (c) exploratory examination of all other CDAs indicated an energetically benign behavior as compared to that projected for the LOFA. Furthermore, this emphasis was to reflect the relative complexity of the LOFA sequence as compared to that of the TOP and LOHS accidents rather than the neglect of the unique aspects of these other CDA initiators. Indeed, these unique aspects were also studied in detail and with all assessments complete the choice of this distribution of effort was found appropriate.

0.2. The Loss of Flow Accident

- Generalities

From the initiation of core disruption (i.e. initial clad melting) the LOFA will evolve through a continuum of gradually escalating core disruption states until complete disruption (i.e. melting of all materials found within the original core confines, also known as a whole-core pool) occurs. Energetically this progression is important for as long as a sufficient fraction of the initially present fuel (approximately 60% for the CRBR) remains within the active core region. Neutronically active states are then possible through a variety of rearrangements of driver, blanket, structural, control, and coolant materials. Permanent subcriticality, or "Termination" (i.e. termination of energetic concerns) may occur from any point along the continuum of core disruption states. When the relocation of the appropriate quantity of driver fuel occurs in a forceful manner we speak of "energetic termination" or hydrodynamic

"disassembly." When this relocation is benign we speak of "mild termination" or simply "dispersal." Our overall objective is to determine the relative likelihood of these two termination paths as a function of the degree of core disruption, and to quantify the damage potential of the energetic ones.

Energetic behavior is the consequence of rapid reactivity insertion. For the present CRBR design such reactivity increases can only result from sizable (large mass flux), and generally compactive, fuel motions. When such motions occur from fuel in the process of undergoing disruption we speak of "Initiating Phase Energetics." When such motions occur due to compaction from highly, but temporarily, dispersed fuel states, they are called "Recriticalities." The character of these two energetic phenomena is fundamentally different with regard to both the reactivity-yielding mechanisms as well as the resulting damage potential. The structural capability of the system provides an appropriate perspective against which the damage potential of a given energetic event must be viewed.

- Structural Capability of CRBR

The levels of energetics required to produce significant structural damage in the CRBR were evaluated (Section II.2) taking into account an "inner containment" formed by the Core Barrel/Upper Internal Structure/Core Support Structure envelope. In addition, the pressure transmission characteristics of the two phase expanding core medium and other materials found within were taken into account. These characteristics have important implications on the resulting short term loading of the local structures (Core Barrel and Cove Support Structure). This mitigating behavior is the result of a compliant core state (distributed voids) and it must be taken into account particularly since such compliance is one of the crucial prerequisites for highly energetic behavior to start with. Our structural analyses indicate that a level of energetics equivalent to 1130 MJ (isentropic expansion yield to one atmosphere) would be required to breach this inner containment. That is, minimal energetic release against the boundary of the primary system can be expected for any energetics below this level.

At still higher levels, upwards displacement of the UIS, and a longer-term expansion against the sodium pool would take place. For the heterogeneous CRBR core this is the only sequence leading to the opportunity for large-scale fuel-coolant interactions. Experimental evidence indicates that under the specific contact conditions this interaction would not yield pressure augmentation, and that the energy conversion process would be controlled by two-phase

chocking and a minimal fuel/coolant heat transfer. Evaluations of the long-term expansion phenomena indicate that an energetic event of nearly twice the above magnitude, approximately 2550 MJ, would be required to produce a slug impact kinetic energy close to the vessel head design capability of 75 MJ. The 1130 and 2550 MJ energetic levels correspond to 100 and 200 $/s disassemblies respectively occurring in the two-phase regime.

- Initiating Phase Energetics

A number of SAS3D analyses covering a broad range of the important parameters were carried out to characterize the range of initiating phase LOFA behavior (Section II.3). With the lower coolant void reactivity of the heterogeneous CRBR core, the LOF-d-TOP (LOFA driven TOP), which was a major energetic problem area [1] for the previous homogeneous CRBR core design, is avoided. This LOF-d-TOP situation arises due to the development of high overpower conditions that lead to pin failures in unvoided subassemblies. If such failures occur at the core mid-plane, which, based on available evidence, cannot be excluded, a potentially autocatalytic behavior may result from the rapid in-pin fuel motion towards the failure location (core mid-plane).

Although these analyses revealed insufficient power augmentation to reach the LOF-d-TOP condition, even those cases calculated with the parameter choices favoring a "slow" accident exhibit substantial neutronic activity (overpower condition). This activity is caused by extended fuel motions (i.e. following the initial tendency to disperse due to retained fission gas pressures) and gives rise to a process we call co-disruption. Co-disruption is the result of accelerated core disruption such that there is insufficient time for the molten cladding to separate from the fuel prior to core-wide fuel disruption. Co-disruption favors dispersal since it implies higher (steel) vapor pressures, increased penetration potential into axial blanket areas, and remeltable blockages.

Plenum fission gas induced fuel compaction has been proposed as another mechanism for initiating phase energetics [2]. In the presence of plenum pressure the fuel pin is subjected to unbalanced forces upon fuel disruption resulting in rapid downward ejection of the blanket and undisrupted driver fuel pellets. The Applicant analyzed this mechanism in response to questioning during this review process, and concluded that there would be adequate time for the plenum fission gas to escape prior to fuel disruption. Based on the results of our own analyses we cannot agree with this conclusion (Section II.4). We have been able to bound the reactivity insertion

rates from the fuel compaction process per se at approximately 50 $/s, which as previously indicated, represents a tolerable level of energetics. However, at the time of this energetic event, only one-half of the core has been voided and the resulting high overpower could induce an LOF-d-TOP event on the other half. Such a combination of energetic events is judged as highly undesirable. Even on purely philosophical grounds the unmitigated manifestation of these high pressures cannot be tolerated. It is recommended, therefore, that steps be taken to limit the action of these pressures during the initiating phase of the LOFA.

- Recriticality Energetics

The general behavior of the post-initiation period was examined (Section II.5) both in terms of a SIMMER-II integral system calculation as well as in terms of generic ad hoc evaluations of relevant physical processes.

The integral calculation was a continuation of one of the SAS3D analyses. The overlap portions between these two calculations were in excellent agreement. The results depict a generally active sequence, with regular power bursts corresponding to fuel reassembly motions. Some evidence of progressive coherence or "tuning" is noted, however. The power oscillations in the early portion appear substantially damped. The effect of the associated pressurization transients to force molten fuel (and steel mixture) through the axial blankets and, upon melting of subassembly duct walls that are adjacent to internal blankets, through inter-subassembly gaps, and away from the core region is evident. The modelling allows for freezing and plugging of such paths, and indeed such behavior is observed in the results. Merging of the S/A-scale pools (annular pool geometry) and destruction of the internal blanket barrier (whole-core pool) occur successively within only a few seconds. Upon attainment of a two-dimensional character the power oscillations amplify because of increasingly severe sloshing pool motions. However, homogenization of the internal blanket regions develops slowly, hence radially focused sloshings are inhibited, the system total available reactivity is well below that of a homogeneous pool, and the associated power bursts are non-energetic. This delay is sufficient to allow removal of the final small quantity of fuel required for termination prior to the formation of a homogeneous whole-core pool, even though the inter-assembly gap escape paths of the radial blankets were, conservatively, not modelled in this calculation.

Recognizing that this integral calculation is one of a few ever attempted, the above results must not and were not taken at face value. The mild termination potential was evaluated (Section II.6) in terms of separate effects calculations that model in great detail the flow path, the flow constituents and thermal interactions including freezing and plugging phenomena. Prototypic experimental data were utilized to benchmark these calculations. Even under modest pressures compared to those expected in view of the continuing neutronic activity, adequate fuel removal to assure permanent neutronic termination is estimated to occur prior to the formation of a homogeneous whole-core pool.

Gravity driven recriticalities were examined from the point of view of amplification potential (Section II.7). For the S/A-scale and annular pool phases under power burst perturbations, the fuel column will separate initially into a compact lower mass and a distributed upper segment of approximately equal material quantity. Reassembly under conditions of reduced fuel inventory or low heat losses (minimal boilup) would produce a growing lower liquid puddle within which the peak of the axial power distribution will occur. Hence, reassembly energetics would be mitigated strongly by single phase liquid expansion feedback during the power transient. Reassembly under conditions of high inventory or high heat losses (large-scale boilup) on the other hand would produce low ramp rates and therefore would be effectively controlled by two-phase dispersal during the power transient. In addition the SA phase cannot have core-wide coherence because the time interval to SA wall disintegration permits only a few power cycles which are insufficient to complete the "tuning" of the fluid dynamics. Thus reassembly ramp rates would be small. However, even if we assume complete core-wide coherence, maximum ramp rates of less than 100 $/s are obtained. Therefore no physically reasonable threat to the vessel head structures can be seen from these first two stages of disruption.

For the whole-core, homogeneous pool an amplification mechanism was calculated. Under perfectly symmetric conditions (geometry and power distribution) a radially focused sloshing action is observed which, under certain conditions of material configuration, may produce high reactivity insertion rates. In most such cases single phase expansions dominate and negligible energetics result. For example in one such case considered, an in-slosh with 300 $/s ramp at prompt critical yielded quick, single-phase thermal expansion, shutdown and produced negligible energy release. However, there is also a narrow range of conditions over which substantial energy releases are calculated. This is particularly so when two-phase regions exist. For example in one high-inventory case considered,

prompt criticality was obtained earlier in the in-slosh, while a two-phase field still dominated the central pool portion. The resulting reactivity of 125 $/s produced the energy equivalent of the 100 $/s two-phase disassembly considered in our structural evaluation. The importance of symmetry in such evaluations is highlighted by the integral SIMMER-II calculation of core disruption. This calculation did enter the whole core pool and it did indicate radial sloshing and amplification. However, due to the system non-homogeneity in the early stages of this phase, a non-centered power distribution results, hence radial focusing is absent and a non-energetic behavior is observed. Before there was a chance to obtain homogenization of the internal blanket material, permanent termination of neutronic activity by fuel removal was indicated.

0.3. The Transient Overpower Accident

The TOP-unique behavior (Section III) develops during the very early stages of the initiating phase. As a result of the reactivity insertion the power rises quickly and produces fuel melting and pin failure well before coolant and cladding overheating. For a postulated mid-plane failure location pin-internal fuel motion can have a significant reactivity augmentation effect and unless it is moderated by an equally rapid dispersal of the fuel escaping into the coolant channels, an autocatalytic behavior could potentially develop.

The Applicant has provided extensive analyses for a variety of core burnup states and reactivity insertion rates. Our assessment focused, therefore, on more closely defining the margins for autocatalytic behavior for assumed mid-plane failures. This behavior is controlled by the competition between pin-internal fuel motion and pin-external dispersal usually referred to as sweepout. The relevant time scale is determined by the core-wide coherence of such pin failures which, in turn, is affected by the core configuration and the imposed reactivity ramp rate (coherence increases with ramp rate). For the CRBR the EOC-3 core with the replacement of the six high power driver fuel assemblies with blanket material is the most coherent. On the basis of failure modes and effects analysis of the reactor control system, we concluded that ramp rates of 10-12 ¢/s are more than one order of magnitude less probable than those of 2 ¢/s or 5-8 ¢/s. Furthermore 15-20 ¢/s ramps are more than three orders of magnitude less likely than those of 10-12 ¢/s. We selected therefore the 10-12 ¢/s TOP as a conservative upper limit for this investigation.

The EOC-3 core CRBR TOP accident was simulated with the PLUTO2/SAS4A computer code. A failure incoherence (time between failures) of more than 300 ms for the first six groups of subassemblies was deduced. The PLUTO2 sweepout calculation was adjusted to available experimental data from the L8 TREAT TOP test. The calculated sweepout was seen to successfully cancel pin internal fuel motion reactivity (and a small amount of sodium voiding reactivity) and to produce shutdown within the first 100 ms.

Thus, even under the most limiting conditions of core coherence and pin failure location, no energetic behavior could be found for TOPs of up to 10-12 ¢/s. For TOPs with higher ramp rates energetic behavior cannot be precluded, however, such events are of sufficiently low probability that they can be excluded from consideration.

0.4. The Loss of Heat Sink Accident

The LOHS-unique circumstances (Section IV) originate from core disruption occurring at very low power and in the absence of sodium coolant. The absence of coolant is required since natural convection boiling has been shown adequate to remove heat at decay power levels. Core uncovery may occur either due to coolant boiloff or due to reactor vessel failure at the high temperature LOHS environment. The actual mechanism is not important, affecting only the disruption stage power level which in any case is very small and much more dependent upon the other aspects of the accident scenario. Characteristically, however, disruption would not occur until many hours into the accident, indicating significant margins for recovery.

At the characteristically low heating conditions all steel within the core will melt, relocate downward and form a plug at the lower axial blanket region. The system will remain subcritical, hence will continue to heat slowly, until fuel settling occurs either due to softening of the pellets (as the melting point is approached) or simply due to toppling and compaction at a lower porosity. The initial porosity is approximately 65% and a porosity of approximately 50% would be required to approach criticality. This eventual reaching of criticality would accelerate the melting rate thus producing, at most, a moderate scale recriticality estimated at approximately 60 $/s. Such an event would be sufficient to disperse the core into the vessel and provide permanent neutronic termination. A smaller recriticality, however, i.e. approximately 10-20 $/s, would be considered more likely under these circumstances and it would be insufficient to provide termination. A whole core pool,

with homogenization of all internal, axial and radial blankets would result in this case. The resulting dilution would be adequate to render the system permanently subcritical even in the absence of the steel and control rod materials which will eventually separate out.

Furthermore, in the absence of the sodium pool, even the most severe recriticalities could provide no challenge to the reactor vessel head integrity. As an example we considered the 200 $/s discussed in the LOFA as the energetic level required to substantially challenge the vessel head integrity. The expansion forces on the UIS, assuming absence of significant resistance by its support columns, were evaluated using the SIMMER-II code. An upper bound UIS kinetic energy (in the upward direction) of approximately 5 MJ was thus estimated. Such a missile is of little mechanical consequence to the reactor vessel head.

0.5. Conclusions

- We have systematically evaluated the possible progression of all three classes of CDAs as exemplified by the LOF, TOP, and LOHS accidents. Non-negligible energetic circumstances were identified only within the LOFA sequences, and assuming that the plenum fission gas fuel compaction mechanism becomes inoperative, by design, as recommended, only as a consequence of recriticalities.

- Recriticality events in the S/A-scale and annular pool phases cannot be excluded. However, their magnitudes are limited to the order of 50 $/s or less because of incoherence and the absence of significant amplification. Neutronic activity, throughout both of these stages of core disruption is substantial and contributes to pressurization and fuel dispersal away from the core region. Thus, benign termination prior to entering the whole-core, homogeneous, pool phase, is projected even under restrictive assumptions for fuel removal path availability and fuel removal mechanics.

- Whole-core pool recriticalities exhibit a narrow range of significant energetic behavior. This energetic regime is associated with idealized perfectly symmetric geometry and completely homogeneous pools. The amplification is the result of radial sloshing following a centrally located and symmetrically distributed power pulse. Even so, the resulting level of energetics did not exceed the structural capability of the primary system boundary.

- The levels of energetics required to produce significant structural damage in the CRBR were evaluated, taking into account,

for the first time, the structural enclosure formed by the Core Barrel/Core Support Structure/Upper Internal Structure, and the pressure transmission characteristic of the expanding core medium and other materials found within. We conclude that an 1130 MJ accident (expressed as the isentropic work potential for expansion to one atmosphere) would be required to fail this inner containing structure, and a 2550 MJ accident to substantially challenge the reactor vessel head structure, i.e. produce a slug impact kinetic energy close to the CRBR vessel head design value of 75 MJ. These levels of energetics roughly correspond to two-phase whole-core disassemblies with 100 $/s and 200 $/s driving reactivity ramp rates.

- Based on these results we conclude that a CDA-induced energetic vessel head failure is physically unreasonable.

- Further, based on the projected absence of significant energetic events we conclude that the Applicant's energetic source term of 661 MJ (75 MJ slug impact kinetic energy), as applied by the Applicant, for evaluating the structural margin beyond design basis is adequate.

0.6. References

1. J. F. Meyer, L. Lois, J. L. Carter and T. P. Speis, "An Analysis and Evaluation of the Clinch River Breeder Reactor Core Disruptive Accident Energetics," NUREG-0112, March 1977.

2. T. G. Theofanous, "Multiphase Transients with Coolant and Core Materials in LMFBR Core Disruptive Accident Energetics Evaluations," NUREG/CR-0224, July 1978.

I. INTRODUCTION

Although excluded from the design basis, core-melt accidents in Liquid Metal Fast Breeder Reactors (LMFBRs) have claimed a prominent role in licensing even when relatively little attention was devoted to such accidents in Light Water Reactors (LWRs) (pre-Three Mile Island era). Clearly, the probability of occurrence of such events is in both cases very low. However, in the LMFBR case upon meltdown, and loss of the original core geometry, configurations of higher reactivity are possible. Thus, the theoretical possibility of achieving very high level temperatures and pressures with direct and potentially severe consequences on the containment barriers gives rise to an LMFBR-generic safety issue, that of "energetics." As we experience the current up-stepping (post-Three Mile Island era) of licensing efforts in the beyond the design basis accidents for LWRs, it is important to remember that the LMFBR safety community in general, and our regulatory system in particular, have maintained a balanced overall approach to risk assessments throughout these early stages of LMFBR technology development. Furthermore, just as important differences in system behavior led to an early recognition of the "energetics" issue, similarly important differences point to the expectation of significantly lower probability of core-melt accidents in LMFBRs [1]. It is for these reasons that all energetics considerations must be viewed in the proper probabilistic perspective.

In this report we are concerned with the impact from such accidents given their initiation. That is, we will assume the occurrence of gross power/cooling mismatch or the loss of ability to remove decay heat from the primary system. Such conditions lead to core and coolant materials overheating, and eventual melting and relocation. Typically the reactivity changes associated with such core material relocations yield power transients such that even in the absence of energetics, major core disruption and dispersal away from the original geometric configuration must occur before permanent subcriticality can be achieved. It is for these reasons that core-melt accidents in LMFBRs are more commonly known as Core Disruptive Accidents (CDAs). Available experience indicates that CDA energetics depend strongly on the particular reactor design. In this report we will assess the CDA energetic behavior of Clinch River Breeder Reactor (CRBR) Heterogeneous core design as described in [2].

In the initial licensing application [3] the blanket material was arranged such as to surround the driver fuel region, this being referred today as the homogeneous core design. The assessment of CDA energetics for this design was initially carried out by the General Electric Company (GE) [4]. These analyses were superseded by two Argonne National Laboratory (ANL) studies [5, 6] which were in turn further extended by another GE study [7]. Meanwhile, the licensing review by the Nuclear Regulatory Commission (NRC) staff, which considered the then-available original GE and the first of the ANL studies [5], was discontinued in 1976. The status of the review at this time as summarized in the Denise to Caffey letter [8] indicates a significant divergence of opinion between the NRC staff and Applicant on the subject of energetics. The Applicant's best estimate assessment indicated a negligible level of energetics, while certain "pessimistic" estimates were still insufficient to challenge the structural integrity of the primary system (reactor vessel head). The NRC staff, on the other hand, reached the conclusion that a level of energetics of roughly twice the magnitude chosen by the Applicant as the structural design basis "should be included in the specification of functional requirements for features to protect containment integrity." The basis for this conclusion was documented in [9]. It appears that the concerns over a potentially energetic process referred to as Loss of Flow driven Transient Over Power (LOF-d-TOP) (see Section II.4) provided the main impetus for this assessment.

In 1981 the licensing process for CRBR was reactivated. The core design was changed to include blanket material within the driver fuel region. This is known as the Heterogeneous CRBR core design. In this arrangement the reactivity increase due to coolant voiding the core is significantly smaller than that in the homogeneous design. As a consequence the propensity for certain CDAs to yield the LOF-d-TOP condition is significantly decreased. The Applicant's CDA analysis [10] again argued for negligible energetics of the best estimate case and showed that certain pessimistic ones were well below the 75 MJ slug impact energy (i.e., the whole sodium pool accelerated to a velocity corresponding to a kinetic energy of 75 MJ) which represents the structural design basis for the CRBR [11].

The renewed NRC staff licensing review effort evolved in terms of two distinct phases. The first phase involved a team of consultants (see Table 1) from Los Alamos National Laboratory (LANL), Sandia National Laboratory (SNL) and Universities under the general direction of C. Allen who is the individual in charge of energetics in NRC's CRBR Program Office. This effort took just over six months (12/81-6/82) and was predominantly review-oriented. With the help

of several technical exchange meetings, the NRC consultants endeavored to comprehend and scrutinize the assessment presented by the Applicant. This review effort culminated with the documentation of a rather comprehensive enumeration of their areas of concern in a Technical Evaluation Report (TER) which was authored by the LANL members but included the concerns of all the review team participants. Subsequently, these concerns were summarized in the form of eight questions (see Table 2) which on 6/15/82 were officially transmitted to the CRBR Project Office. At this time it became evident that an independent probing of these eight areas of concern (which spanned the whole range of accident analyses performed by the Applicant) by the reviewers would be beneficial in sharpening their own ability to sort out the important aspects from the details. Thus, the second phase of the review was initiated.

This independent assessment effort involved, by-and-large, the same NRC review team (to be referred to as the Team) under the direction of a Management Group (to be referred to as the Group) consisting of T. G. Theofanous (Purdue) and C. R. Bell (LANL). The purpose of the Group was to focus the technical efforts of the Team such that an independent position on CRBR energetics may be completed under the tight time constraints specified. This effort took roughly six months and it is culminating with the publication of the present report.

For purposes of clarity and continuity, this report is focused on our independent assessment efforts. However, important differences or similarities with the Applicant's methods and/or results are briefly mentioned as appropriate. Additional details on our views of the Applicant's assessment may be found in our TER mentioned above. This TER, together with a massive quantity of other material developed during both phases of the review, have been compiled under one cover and are available upon request. It is intended that this "CRBR Energetics Review Compendium" will make our technical effort scrutable in all its detail. References to particular sections of this Compendium and to specific pages of the TER will be frequently made.

The remaining of this introduction is intended to provide a perspective on the magnitude and depth of the overall effort. Thus, in addition to presenting our overall technical approach, we go into certain organizational and management aspects. In the concluding section of the introduction, the structure of the remaining report is explained and some guidance to facilitate the task of the variously interested audience is offered.

1. Scope and Management of Independent Assessment

The charge given to the Group by the NRC staff, CRBR Program Office, was to develop and document, by March 4, 1983, an independent position on the CRBR energetics issue. This position is to be considered together with the Applicant's updated assessments by the NRC staff in making the necessary licensing decisions. In this licensing context the charge amounts to providing an assessment of the magnitude of CDA energetic events to be "expected" as well as the resulting potential to violate the containment barriers provided in the CRBR.

Towards this goal the major task of the Group was to manage, focus, and integrate the technical activities of the Team members. Complementary to the above efforts, however, the Group sought to elicit additional data and technical contributions from the Applicant. Thus, in parallel with the independent assessment activities, the review effort continued as these additional materials were provided by the Applicant over the same time frame. The essential aspects of this review work are also included in the present report. Finally, the Group maintained a close interaction with the NRC staff and its on-going licensing activities. The Group interactions with the Applicant were carried out through H. K. Fauske of Fauske and Associates Inc. (FAI) who at about the same time was appointed to manage the Applicant's energetics licensing efforts. These main organizational interfaces are schematically illustrated in Figure 1.

In pursuing its task, the Group sought the advice and criticisms of the Team and of the NRC staff CRBR Program Office on a continuing basis. In addition, the Group formally requested comments and criticisms from these two "internal" organizations as well as from the "outside." These formal requests were issued on three occasions. The first was addressed to the Team and to the NRC staff CRBR Program Office upon completion of the detailed definition and scheduling of the technical tasks comprising the independent assessment effort. The responses received were compiled in Section 1 of the Compendium. The second request was issued following the formulation of a preliminary independent assessment position as documented in [12]. This was prepared on the occasion of a status report presentation to the Advisory Committee on Reactor Safeguards (ACRS) CRBR subcommittee (on 11/19/82) by the Group [13]. The final formal request [14] was issued upon the completion of the final draft of the present document. Both of these two formal requests were intended to cover the US LMFBR safety community at large. That is, in addition to the ACRS, the Team, and the NRC staff CRBR Program Office, these requests for feedback were addressed

to the Applicant and the Managements of the NRC's Office of Nuclear Regulatory Research (RES) and of all National Laboratories engaged in LMFBR energetics research (i.e. LANL, SANL, BNL, ANL, and HEDL). Comments from appropriate members of their respective organizations were solicited. These two subject documents [12, 14], together with the responses received, and our disposition of the points raised, are now part of the record and available upon request as Section 2 of the Compendium.

Based upon the level of involvement and their eventual contributions towards this document, Team members are identified as "contributors" and as "consultants" as shown in Table 3. All written contributions received by the "contributors" and "consultants" have been compiled in Section 3 of the Compendium.

2. Philosophy of Overall Technical Approach

In the early considerations of LMFBR energetics, the terminology Hypothetical Core Disruptive Accidents (HCDAs) was in common use. This was not only to connote the extremely low probability of initiation of such accidents, but also the tentative nature of our understanding of their behavior and resulting consequences. Certain out-of-context (Hypothetical?) situations were postulated for the purpose of analytically realizing an energetic behavior and thus attempting to establish "bounds of severity." After nearly twenty years of intensive research and development effort, it appears that there is no longer reason to resort in such examinations of hypothetical circumstances. Rather, a CDA initiator can be realistically followed through the core disruption phases until accident termination. These so-called mechanistic CDA analyses provide an overall framework against which the potential for energetic phenomena may be assessed with due regard for the controlling physical processes. In terms of actual licensing cases the first efforts along those lines were made during the Regulatory review of the FFTF CDA energetics assessment. The approach further matured with the initial (homogeneous core) CRBR application and licensing review.

It would be in error, however, to expect that such mechanistic analyses can, at this time, predict uniquely the complete evolution of a postulated core disruptive accident from initiation to termination. There is considerable complexity in the underlying physical processes that has not yet been appropriately modeled. We believe that such limitations may alter the overall timing of some events and may even affect the actual character and sequence of the intermediate states. However, we also believe that these uncertainties

can be adequately handled within a properly oriented overall effort. With this in mind we do not attempt to associate a single outcome to any given initiator. Rather, we attempt to establish a "range of phenomenology" consistent with experience and known physical principles. Within this range we search for energetically-prone circumstances, identify the important mechanisms, and quantify the intensity of energy release in a reasonably conservative manner (i.e. avoiding excessive and clearly non-physical conservatism). Similarly, we scrutinize for termination-favoring phenomena, identify the important mechanisms, and quantify the approach to termination, by the fraction of fuel removed from the core region (at approximately 40% permanent subcriticality, i.e. termination is achieved). Based on these results we complete the assessment by synthesizing sequences and respective likelihoods.

For these assessments we use the system codes SAS3D [23] and SIMMER-II [24]. These codes are used as "integrators" of the technical base and their results are guided, scrutinized and/or augmented by employing special purpose analytical techniques, in-pile experimental data, and out-of-pile simulant experiments as appropriate. "Engineering judgement" is a very important ingredient of these activities and since the term is so often misused and/or misinterpreted, we would like to elaborate on our usage.

Firstly, judgement was required in identifying the priorities and level of detail (or effort) for assessing the variously initiated CDAs and particular aspects of each. In addition, judgement was applied in synthesizing through various code calculations (including sensitivity studies), auxiliary analyses and considerations of the available experimental evidence, the nominal range of expected accident progression (i.e. ranges of relevant phenomenology). Further, and perhaps most importantly, judgement was utilized in searching within this broad range for energetic-prone circumstances and adequately enveloping their consequences. Finally, judgement was required to synthesize sequences and likelihoods in a manner usable in the licensing context. The implication is that no single element (code, analysis, or experiment) is a sufficiently capable, or in our opinion, even desirable tool for addressing safety concerns associated with CDA energetics. We have approached this task with the recognition that judgement in the above sense would be the central element of our efforts.

3. Structure of Technical Management Plan

Among the variously initiated core disruptive accidents, those resulting from an unprotected Loss-of-Flow event, LOFA (i.e. loss of pumping power in all sodium recirculation pumps with failure of the protection system to scram the reactor), or from an unchecked Transient Overpower condition, TOP (i.e. control rod withdrawal with failure of the protection system to scram the reactor), attracted almost exclusive attention in previous LMFBR safety assessments [3,9,10,19]. Also, historically, the LOFAs seem to have dominated in terms of concerns for energetically-prone mechanisms as well as severity of projected consequences [15,16,17,18]. The propagation of local faults, i.e. Fuel Failure Propagation (FFP) as a mechanism leading to core disruptive accidents has been the subject of persistent investigations although with consistently negative results. The remaining CDA initiator possibilities arise from severe external events, i.e. Earthquakes beyond the Safe Shutdown design limit (SSE) or a variety of Loss Of Heat Sink (LOHS) accidents. A persistent LOHS event, although powered at decay heat levels only (protected accident), leads to coolant boil-off and a CDA eventually nonetheless. A very severe earthquake, in addition to causing failures leading to any combination of the above initiators (i.e. shearing off all primary recirculation lines and causing a LOHS situation), could also introduce core structural perturbations with associated reactivity changes. None of these other possibilities seem to have been the subject of serious study previously. Of particular interest in this regard is the call for attention to the LOHS accident expressed in a recent SNL study [20]. Based on the fact that LOHS accidents, as do all protected accidents, have a significantly higher probability of occurrence, as compared to the unprotected ones (i.e. LOFA, TOP), and on the findings of certain previous BNL reports [21, 22] indicating the potential for recriticality in the CDA sequence of the LOHS, the SNL study concluded that such accidents dominate the risk.

As an initial step in our independent assessment effort, we made the judgement that among all core disruptive accidents, the LOFA should be chosen as the subject of our detailed considerations. This was based on the opinion that: (a) the LOFA phenomenology spans the range of energetically significant CDA behavior, (b) within the LOFA sequences our previous review effort identified specific and significant areas of concern, (c) preliminary scoping examination of all other CDAs, including the LOHS accident, indicated an energetically benign behavior as compared to that projected for the LOFA.

On this basis our technical management plan was formulated in terms of two more-or-less distinct portions. The one was concerned with the in-depth study of the LOFA. The other was to deal with all other CDAs, including probabilistic aspects of the respective initiators, a broad but realistic scoping out of the relevant phenomenologies, and an evaluation of the consequences and/or of the available recovery margins. Detailed analyses on unique and important aspects of these accidents were to be carried out on an as-needed basis.

A set of technical tasks and associated completion milestones for each one of these two portions were defined. The definition and structure of the tasks in the LOFA portion were keyed to a generic visualization of the progression of CDAs, and of the LOFA in particular, as illustrated in Figure 2. In contrast to severe LWR accidents, the energetically significant portion of CDAs (with the possible exception of certain LOHS accidents, which are protected and hence evolve over a considerable time period) is of a very short duration, i.e. less than one minute for the LOFA. As a result there is no means or opportunity for such accidents to be complicated by external actions and typically they will evolve from initiation to termination on their own accord. As a result, a simple and generic structure as shown in Figure 2 indeed exists.

From the initiation of core disruption (i.e. initial clad melting), the accident will evolve through a continuum of gradually escalating core disruption states until complete disruption (i.e. melting of all materials found within the original core confines) occurs. Energetically this progression is important for as long as a sufficient fraction of the initially present driver fuel (typically more than 60% for the CRBR) remains within the core region. Neutronically active states are then possible through a variety of rearrangements of driver, blanket, structural, control, and coolant materials. When such states are obtained by fuel compaction in supercritical configurations following highly but temporarily dispersed fuel states (i.e. subcritical), they are called "recriticalities." Permanent subcriticality, or "Termination" (i.e. termination of energetic concerns), on the other hand, may occur from any point along the continuum of core disruption states. When the relocation of the appropriate quantity of driver fuel occurs in a forceful manner we speak of "energetic termination" or "hydrodynamic disassembly," or simply "disassembly" for short. When this relocation is benign we speak of "mild termination" or simply "dispersal" for short. Our overall objective is to determine the relative likelihood of these two termination paths (processes) as a function of the degree of core disruption, and to quantify the damage potential of the energetic ones.

This dependence on degree of core disruption is explicitly taken into account by assessing at each major stage of core disruption the likelihood of achieving termination against the likelihood of progressing into the next stage. Three groups of tasks (LOF-, TOP-, SP-) addressing questions relevant to these assessments through the initial stages of disruption, and one group (D-) applied to all subsequent disruption states, were identified as shown on Figure 2. The initial stages of disruption are defined to extend through significant loss of fuel pin (rod) structure. The LOF-task pertains to events and phenomena typical of the classical LOFA, the TOP-tasks focus on fuel/coolant dynamics under overpower conditions (including those that may develop as a consequence of a LOFA) and the SP-tasks address special (new) areas of concern. The technical basis for judging the damage potential of the energetic termination path (i.e. "in-vessel" vs. "en-vessel" containment states shown) against the capability of the CRBR primary system is developed in the group of T-tasks. With the exception of the dual-scope TOP-tasks, all other tasks are keyed specifically to the LOFA sequences. The adequacy of this approach including the definition and resolution of any unique circumstances due to other CDA initiators, are developed within the group of I-tasks.

The listing of all tasks is shown in the form of our milestone chart in Table 4. The vertical arrows indicate lines of feedback and/or continuing interaction. The Group was responsible for these integration activities. For each task, a reasonably detailed definition in the format of Table 5 was prepared. These tasks were then matched to individual Team members according to interest and specialty. The list of these assignments, together with the corresponding task definitions and other organizational details contained in the transmittal letter, have been compiled in Section 4 of the Compendium. Responses received to our formal request for feedback on all this technical plan did not indicate any area of difficulty, disagreements, or omissions.

Finally, it would appear proper to comment on the positive phrasing, i.e. "show that autocatalytic behavior is extremely unlikely," utilized in the sample task definition of Table 5, as well as in several of the other task definitions, indeed. This is not to be perceived as a biased outlook from the outset! Rather, it should convey the thought that in July of 1982 the Group did not embank on an openly-defined "research project" to be completed six months later, but rather it undertook to complete an assessment of a case for which it had a reasonably good understanding already (i.e. in addition to the first phase six month review effort, some of the Team members were involved in the CRBR CDA energetics evaluations since the original

applications almost a decade ago!). Furthermore, a few independent studies were carried out by the Team also during the review period. Thus, for the particular example of Table 5, such studies explored expressly for autocatalytic behavior and found none. Last, but not least, the general working atmosphere of the Team was encouraging the pursuit of any aspects for which potential difficulties could be suspected. Indeed, this mode of operation resulted in a number of new elements (as listed in Section 5) that significantly contributed to our understanding of CRBR CDA energetics.

4. Chronology of the Review and Independent Assessment Activities

The essential elements of the review and independent assessment phases of the CRBR energetics evaluations were discussed in the previous sections. A better appreciation of the interrelationships among these different activities and their relative timing may be gained with the help of Figures 3 and 4.

It is hoped that these figures clearly indicate our special efforts to seek "internal" as well as "external" feedback throughout the independent assessment phase for which we were responsible.

5. Major Accomplishments

Our independent assessment studies ranged from simple parametric evaluations carried out within the context of the Applicant's analyses to completely new studies that are original in one or more of the following elements: (a) phenomena or effects taken into account, (b) analysis methods, and (c) experimental evidence. An effort is made in the technical presentation to identify the nature of the contribution on a topic-by-topic basis as the case may be. For now we would like to offer, from our perspective, in summary form the major technical contributions made. The nature of these contributions is identified in the listing of Table 6 where reference to the appropriate report section(s) is made for additional details.

A brief statement on each item on this table is given below.
(a) As a result of the eight questions, the Applicant revised the best estimate value of the sodium reactivity worth in the upwards direction. This revision had a significant impact on the whole LOFA sequence and hence on the energetics potential.

(b) A new mechanism for energetic behavior in the LOFA was brought to the attention of the Applicant as a result of our review.

This mechanism involves the compaction of fuel columns, by the gas pressures in the fission gas plena, following loss of fuel pin integrity (occurring typically around the core axial mid-plane). This mechanism was accepted and eventually addressed also by the Applicant.

(c) Results of original calculations provided important new perspectives on the origin and possible magnitude of recriticalities.

(d) New analyses of recriticalities provided important new insights on the effects of fuel inventory and configuration (especially of the existence of single-phase regions) on the magnitude of the resulting energetics.

(e) We identified and quantified significant energetics mitigating mechanisms in the mechanical constraints provided by the Upper Internal Structure (UIS) and Core Barrel (CB) core "bottle."

(f) Our evaluation of the LOHS accident (the Applicant did not submit such evaluations) indicates the absence of significant energetic behavior.

(g) It is our judgement that our evaluation of CRBR energetics has reached a level of confidence sufficient to allow a first attempt to realistically quantify the probability of energetically-induced vessel failure.

6. Structure of this Report

The technical portion of this report is arranged under four major subheadings. Chapter II covers the detailed evaluation of the LOFA, Chapter III covers the evaluation of the TOP, and Chapter IV covers the evaluation of the LOHS.

The LOFA is treated according to the "generic structure" and the "philosophy of the overall technical approach" discussed above. With reference to Figure 2, the basis for the whole treatment is provided by establishing a range of expected phenomenology through the successive core disruption states. This is done in Sections II.3 and II.5 for the initial and for all the advanced core disruption states, respectively. Plenum fission gas induced fuel compaction (relevant during the initial stages of core disruption), and gravity-driven fuel compaction (relevant during the advanced stages of core disruption) were identified as dominant energetics-yielding mechanisms with

potential to occur over these projected ranges of accident evolution. Our assessments of the energetics potentially resulting from these mechanisms are found in Sections II.4 and II.7, respectively. The relationship between the magnitude of the reactivity excursion and resulting damage potential is developed in Section II.2. Considerations of termination by mild fuel removal from any one state in the core disruption sequence are presented in Section II.6. Finally, the overall framework for converting all these assessments into a quantitative collective judgement is introduced in Section II.1 and is completed in Section II.8.

The other CDAs are handled similarly except not at the same level of detail. Here emphasis is given to the identification and treatment of any unique (as compared to the LOFA sequences) circumstances. The probabilistic aspects of CDA initiator intensity (i.e. rate of control rod withdrawal) and of available recovery margins (i.e. recovery from a LOHS event) also are considered.

As already mentioned, this document is focused on our independent assessment effort. However, Important aspects of the Applicant's positions [10,11,25] are given in the introductory, "objectives and overview," subsection of each major section together with a reference to documents and locations where the positions on the particular topic may be found in original form. In the same references, we cite pages of our Draft TER [26] that contain our detailed evaluations of these positions. References to our supplemental TER [27] containing our evaluations of the Applicant's responses to the eight questions are also made as appropriate.

In the presentation of the technical material several levels of detail are utilized to facilitate the communication at the level of detail chosen by the reader. The "Executive Summary" presents a non-technical abstraction of our main results and conclusions. The "main body" of this report provides a technical presentation emphasizing the essence of the technical arguments and the results obtained. The details of the analysis methods and their bases are covered in the "appendices." Still more detail, including computer program listings, and outputs, data, or other auxiliary material, may be found in the Compendium.

The report is organized on the basis of a "unit" format. Each unit is self-contained and independent with respect to all auxiliary material, i.e. References, Nomenclature, Figures, Tables, as well as page numbering. The set of units is constituted by the main report Sections (I, III, IV, V, VI), the subsection of Section II (II.1, II.2, . . ., II.8), and all Appendices. The Appendices are placed to follow the particular main text unit to which they refer and they

are named by prefixing the letters A, B, C, . . . to the number of this main text unit. The page numbering contains as a prefix the unit number such that with a glance at the Table of Contents the ordering of the units may be visualized and hence any unit be quickly located through the page identification.

TABLE 1
LIST OF CONSULTANTS IN THE
INITIAL REVIEW EFFORT

M. E. Asprey
Los Alamos National Laboratory

R. E. Baars
Los Alamos National Laboratory

C. R. Bell
Los Alamos National Laboratory

W. R. Bohl
Los Alamos National Laboratory

C. A. Erdman
Texas A&M University

T. Ginsberg
Brookhaven National Laboratory

H. H. Hummel
Argonne National Laboratory

M. S. Kazimi
Massachusetts Institute of Tech.

L. B. Luck
Los Alamos National Laboratory

P. K. Mast
Sandia National Laboratory

P. Pickard
Sandia National Laboratory

P. A. Pizzica
Argonne National Laboratory

J. Scott
Los Alamos National Laboratory

T. A. Theofanous
Purdue University

T. R. Wehner
Los Alamos National Laboratory

TABLE 2
THE EIGHT AREAS OF CONCERN

1. Can TOP become prompt-critical in such a way that internal fuel motion in lower power channels is the key factor in the energetics determination? Is such an event possible only for mid-plane failures with low sweepout? How is the degree of sweepout determined? What is the effect of intrasubassembly incoherence on sweepout?

2. An LOF-d-TOP might still occur if the sodium void worth is 50-60 percent higher and internal fuel motion in TOP type channels can occur. What are the reactivity uncertainties of sodium void, Doppler, axial expansion and lead channel fuel motion? How do you interpret the significance of these uncertainties?

3. What is the potential for autocatalysis due to plenum fission gas acting on the fuel column to force axial compaction as disruption occurs in the initiating phase of the LOF?

4. To what extent can steel blockages form throughout the core to prevent fuel removal through normal axial blanket flow channels during the early phase of the LOF? What is the location and character of the steel blockages in these channels?

5. What is the basis for maintaining continuous subcriticality in the high heat loss environment of early meltout phase? What are the fuel losses (quantified) taking into account uncertainties in removal path geometrics, driving pressures and freezing mechanisms?

6. What degree of subcriticality is required to prevent pool recriticality from thermal and fluid dynamics upset conditions? What is your position on the potential for small recriticalities to amplify? What is the justification for your position?

7. In assessing benign termination from the boiled-up pool (upward removal) justify the fuel removal mechanisms and rates. In particular assess the potential for upper pool sodium entry via rapid condensation of steel vapor pressure.

8. What is your estimate of the force required to produce a mechanically induced relief path via upper internals structures displacement?

TABLE 3
THE INDEPENDENT ASSESSMENT TEAM

Contributors

P. A. Pizzica
Argonne National Laboratory

H. H. Hummel
Argonne National Laboratory

W. R. Bohl
Los Alamos National Laboratory

M. E. Asprey
Los Alamos National Laboratory

T. A. Butler
Los Alamos National Laboratory

R. E. Baars
Los Alamos National Laboratory

T. R. Wehner
Los Alamos National Laboratory

L. B. Luck
Los Alamos National Laboratory

Consultants

T. Ginsberg
Brookhaven National Laboratory

C. A. Erdman
Texas A&M University

P. K. Mast
Sandia National Laboratory

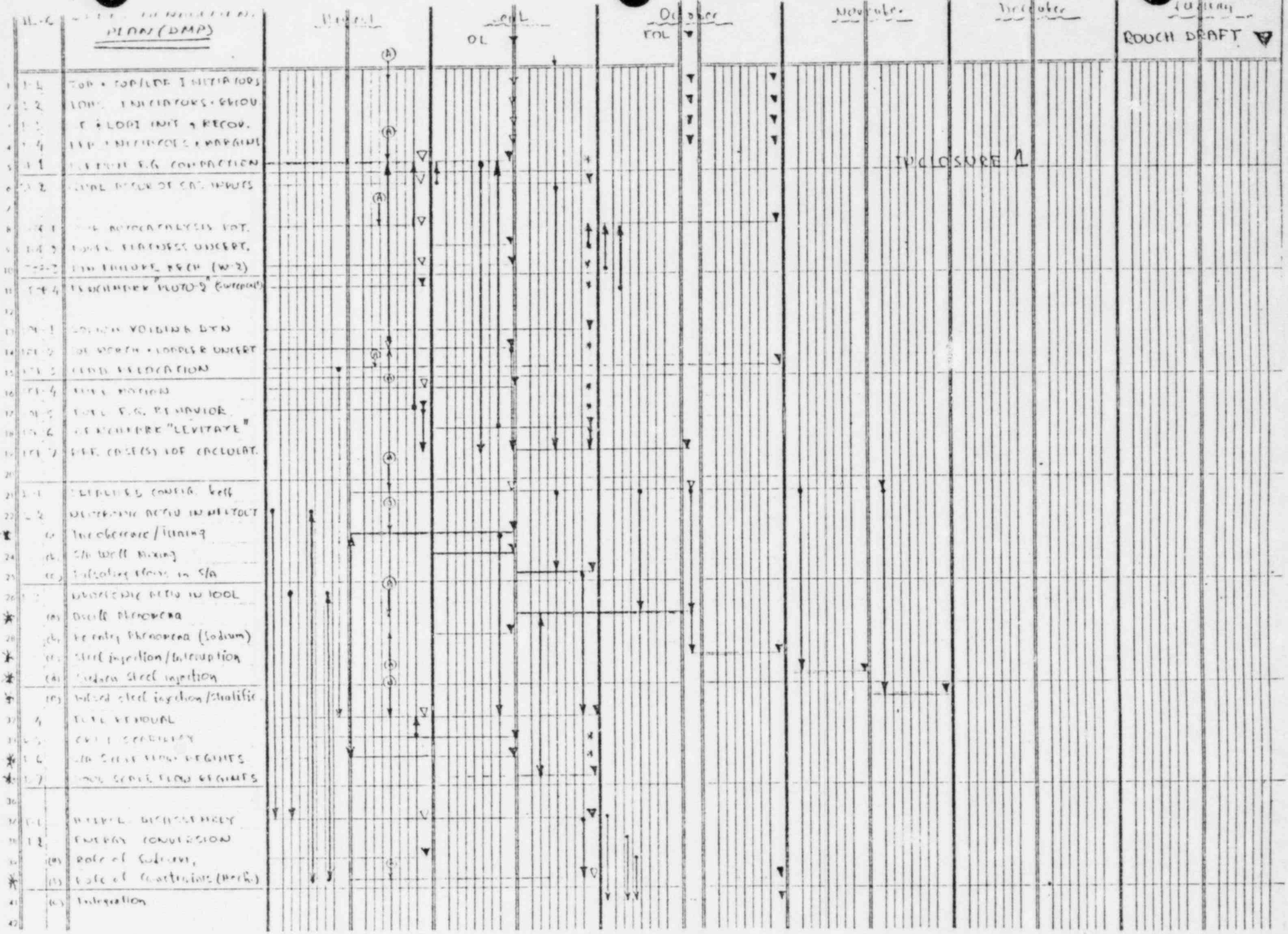

Table 1

II.1

TABLE 5
SAMPLE TASK DEFINITION

SP-1 Plenum F.G. Compaction

Objectives

Show that autocatalytic behavior is extremely unlikely. Establish a range of realistic LOFA initiating-phase power history outcomes.

Scope

Consider in detail fission gas inventories, blowdown constraints and accident timing margins. Consider incoherent core behavior. Consider the effect of fuel motion history (early). Take into account Na worth uncertainties. Consider R8 experimental information.

Output

Provide initiating phase power histories and enthalpy distributions for a range of conditions. Document one or two cases in detail adequate to visualize the scenario and sequence of processes. Highlight remaining areas of uncertainty.

Schedule

Preliminary assessment August 30. Final report September 15.

Resources

SAS3D, LEVITATE (SAS4A)

Inputs

LOF-2, LOF-5, SP-2, LOF-6

TABLE 6

MAJOR REVIEW ACCOMPLISHMENTS

- Revision of Sodium Void Worth Values
- Consideration of Plenum Fission Gas Compaction
- Detailed Consideration of Recriticality Potential
- Inventory and Configuration Effects on Recriticalities
- Energetics Mitigating Mechanisms due Internal Structures
- Consideration of the LOHS Accident
- Relative Likelihood of LOFA Evolution Paths

II. THE LOSS OF FLOW ACCIDENT

II.1. QUALITATIVE PROBABILISTIC FRAMEWORK

1. Objectives and Overview

The purpose of this section is to lay the framework for quantifying the relative likelihood of the various LOFA paths and outcomes (particularly those that produce mechanical vessel failure). Such quantification, of course, can be done at various levels of detail and with varying degrees of rigor. For the results to be of adequate reliability, and thus useful, these choices must be made with a realistic appreciation of the available state of technology vis-a-vis accident sensitivities. At this time no well established procedures or guidelines exist. In fact the available experience in this area is very limited (see next section). Still, there seems to exist little disagreement that the high end of the LMFBR risk spectrum is dominated by the energetics of CDAs. Notwithstanding the above difficulties, therefore, it appeared to us essential that our effort does not stop short of making a serious attempt in this direction. As it turned out, our studies revealed a generally insensitive CRBR energetic behavior, relative to the specified vessel structural capability, such that our final results are in fact considerably "cleaner" (i.e. of less ambiguity) than initially expected.

2. Previous Work

Previous attempts in this direction were made as portions of overall Probabilistic Risk Assessments (PRA) and seem to have been overwhelmed by the magnitude of these efforts. Thus in the recent SNR-300 PRA [1] the treatment of CDA energetics occupies approximately 50 out of the 815 pages of the study. The quantitative aspects on the CDA portion were synthesized from the responses of 18 internationally selected LMFBR safety experts who were polled by mail on certain aspects of the LOFA scenario. The available CRBR PRA [2] was done for the original homogeneous core design and contains also an abbreviated treatment of CDA energetics. The pivotal point in this work was a perceived (and well accepted till now) sensitivity of the energetic outcome to small variations in the assumed, or estimated, disassembly-driving conditions, beyond a low

range considered insignificant for the structural design. The approach, therefore, consisted of arguing that any energetic behavior above a certain low value (i.e. approximately 30 $/s) would be a low probability event. Thus, for initiating phase energetics a number of SAS-3A parametrics for the LOFA were carried out to address the question ". . . to what extent conservative assumptions have to be compounded . . ." for an energetic disassembly outcome. That is, recognizing the absence of experimental information in the LOF-d-TOP, a threshold (on-off) approach, rather than one discriminating on the level of resulting damage, was utilized. Similarly, recriticalities were judged to be low probability events on the basis of the compaction-resistant nature of the volumetrically boiling CRBR core at decay heat levels. Based on these considerations, probability split fractions for three damage levels were assigned to the outcome of each CDA initiator. For the LOFA for example, values of 10^{-1} and 10^{-2} were assigned for "moderate" and "massive" reactor vessel head seal failure respectively. The energy level ranges of 300-800 MJ (i.e. "around the design value of 661 MJ) and of 800-1500 MJ "or higher" were chosen to correspond to these two damage levels. These engineering judgement probability assignments were intended to be conservative and the method included a review ". . . by a number of people who are knowledgeable about the current state of LMFBR accident analysis technology." The most recent Applicant position on the heterogeneous CRBR design contained in GEFG-523 [4] is that "best estimate" CDAs terminate in a benign fashion, and that energetic terminations are comparatively low probability events. No attempt was made, however, to quantify this judgement.

At the other extreme we find the Sandia LMFBR Accident Delineation Study [3]. The major emphasis here is in laying out the currently available understanding, of the phenomenological CDA sequences, in the PRA event-tree formalism. A detailed elaboration of much of the pertinent literature is given, and eventually the study loses itself in its own detail. In fact, the quantitative assessment of CDA energy yields, which is the source of all consequence analysis, is bypassed altogether in the single "quantitative" example given at the end. The LOFA for the CRBR heterogeneous core is chosen for this example. A qualitative discussion of the accident phenomenology concludes with: "For purposes of this illustrative example and its continuation into the Post-Accident Phenomenology Area, it is assumed [emphasis added] that the disassembly causes moderate damage to the vessel head but no secondary containment damage." Presumably the authors did not feel that the state of technology allowed at that time a quantification in terms of their methodology. However, qualitative approaches are not always more "forgiving"

than quantitative ones. Two important issues will be mentioned in this regard. The one, concerns the judgement made in this example that initiating phase energetics in the CRBR heterogeneous core design are negligible. The other, concerning the conclusion (presumably one of the major ones) made in this delineation study that for LMFBR, in general, and CRBR in particular, the LOHS accident represents the dominant CDA energetics contributor. We sharply disagree with both of these two judgements (see Sections II.4 and IV, respectively).

3. Present Procedure

3.1. Generic Structure of Accident Evolution

The essential elements of the LOFA CDA sequence as discussed previously (see Section I.3) are shown in Figure 1. Here the continuum of intermediate core disruption states is discretized into two generic configurations. The one is characterized by extensive fuel disruption although the subassembly (S/A) wall is still largely intact, i.e. many S/A-scale pools. The other acknowledges the existence of core-internal blanket subassemblies as illustrated in Figure 2. Due to the low power level in these regions their disruption due to their own internal heating would lag substantially behind the disruption of all driver fuel. In fact, such a time-lag would be substantially longer than the time required to melt-attack the S/A walls such that their external disruption by the surrounding driver fuel rather than by internal heating is predicted. Hence, the formation of an Annular Pool preceding the state of complete disruption, also known as a Whole-core Pool, is envisioned. It is our view that more detailed considerations including additional intermediate disruption states are unnecessary and beyond the level of detail considered reasonably predictable. On the other hand the assessment proposed here is feasible because the projected high neutronic activity (power transients) in the postinitiation period introduces a strong element of non-determinism (randomness) that results in a chaotic, "long-term" character to the transient along the locus of highly disrupted core states.

On the other hand, both the mechanisms as well as the character of the potential energetic events change as we proceed from the initial stages of core disruption (often called "Initiating Phase") to the whole-core pool stage (named "Transition Phase" [5]). In particular, for all but the initiating phase stages, this character is an important function of the fuel inventory (see sections II.5 and II.7). As shown in Figure 1, Termination via mild Dispersal can

occur from any stage along the disruption path. Similarly, "partial" (insufficient to yield Termination) Dispersals can also occur. Such Dispersals will continue to reduce the core fuel inventory thus affecting the character of all subsequent stages. A "long-term" memory effect is therefore implied.

A detailed appreciation of this "dual character" of the core disruption process provides the key to the quantitative understanding of the potential energetic consequences. Our approach is to separately and conservatively bound the "inventory" effects and the magnitude of energetic events at each step along the disruption path. This is accomplished by enveloping the non-deterministic nature of the sequence by a priori deterministic calculations. This procedure is possible because

(a) the core fuel inventory depends mainly on the integral of the power history rather than its detailed shape, and as the level of disruption increases the fuel dispersal process is overwhelmed by the increasing availability of the escape paths (intersubassembly gaps) i.e. becoming less dependent on pressure driving forces; and

(b) at each stage recriticalities are best bounded not in terms of a precisely interphased calculation to a detailed core disruption history, but rather in terms of a priori specifications of recriticality geometries that span the range of physically possible behavior.
The quantitative aspects of this procedure will be found in sections II.5, II.6, and II.7.

By comparison to the non-determinism introduced by the extended fuel motions in the various advanced core disruption states mentioned above, the early stages of core disruption including coolant voiding, clad melting, and initial fuel disruption (i.e. Initiating Phase) may be viewed as reasonably deterministic. Yet uncertainties in phenomenological behavior (i.e. material motions) give, also here, rise to a need for viewing this early sequence in terms of a range rather than of a single (or even a few discreet) outcome. Our approach here also is to identify energetic mechanisms that can occur within this range and bound the energetic results. The quantitative aspects of this procedure will be found in Sections II.3 and II.4. The core fuel inventory aspects of this phase are also assessed as described in Section II.6.

3.2. Definition and Probabilistic Concepts

In the next few sections we will develop the basis for assigning probability split fractions to each one of the transitions shown in Figure 1. In a full-fledged probabilistic study the transition probabilities would be dependent upon the probability distributions of the various important parameters and, in principle, could be obtained from them through a series of calculations and classification of outcomes according to the definitions taken for each transition path. In addition, by considering the uncertainty ranges in these distributions, uncertainty bounds could be placed on the transition probabilities.

However, this process is not practical for the problem at hand. Several reasons may be cited: (a) The detailed probability distributions for individual parameters for processes are not known; (b) The probability distributions of the deviations of the various analytical (model) predictions from the corresponding reactor behavior are not known; and (c) The sensitive and hence non-deterministic character of the core disruption sequences cannot be probabilistically quantified. Furthermore, it is unlikely that these difficulties could be eliminated at any time in the foreseeable future. As it turns out, all these details can be made unnecessary in characterizing the energetic behavior of the CRBR heterogeneous core.

This is accomplished by aiming to quantify the high (in severity) ends of the probability spectra rather than the complete distributions. That is, at each transition we aim to bound the energetic consequences from above and the dispersal behavior from below. The result is a high confidence level, upper bound, vessel failure probability. Clearly some judgement is required in both developing the technical base as well as assigning the actual numbers for each transition. The role of such judgements and the associated level of confidence can be appreciated only after a careful study of Sections II.2 to II.6.

Probability levels are assigned on an order of magnitude basis according to the following definitions. A transition with 10^{-1} chance is one with an overall behavior within known trends (i.e. adequately characterized by a set of parameters) but obtainable only at the "edge-of-spectrum" of the parameter values. A transition with 10^{-2} chance represents a behavior that cannot be positively excluded although its occurrence would be clearly "outside the spectrum of reason." As a consequence of these two definitions, an outcome with a 10^{-3} chance represents the in-series occurrence of an off-spectrum

and an edge-of-spectrum events and should be characterized as "physically unreasonable." The Dispersal transitions are examined against the 40% core fuel inventory reduction required for permanent subcriticality. The vessel failure transitions are judged by comparing the estimated upper bound mechanical energy releases (measured as sodium slug kinetic energy impacting the vessel head) against the specified design capability of 75 MJ. The Disassembly transitions are counted only among those that result in significant vessel head loading. All these definitions are summarized in Table 1.

3.3. Probabilistic Assessment Procedure

The procedure involves three major steps. In the first step we characterize the accident progression along the various core disruption states (Figure 1), without particular regard for Termination processes. The aim here is to identify and characterize the range of possible behavior in certain important respects. Power behavior, blockage formation, and timing between successive disruption states represents some of these important aspects. This task is accomplished in two segments, Sections II.3 and II.5, for the initiating and all other disrupted core states respectively.

The second step is focused on the Termination processes. The path of core succession states previously established is now searched to identify and quantify (bound) the occurrence of energetic events. The two such mechanisms identified are treated in Sections II.4 and II.7 for the two segments of analysis mentioned above respectively. Similarly fuel dispersal rates at the various stages along the disruption path are estimated to scope out the benign termination potential (Section II.6). Based on the outcome of these studies at each transition in core disruption state a dominant behavior along either of the two termination paths or towards the next disruption state is identified. The remaining two paths are then identified as end of spectrum events.

Finally, in the third step the disassembly paths are carried analytically into their mechanical consequences (Section II.2). Conservative bounds are here again established and vessel failure probabilities assigned, according to previous definitions, to each path according to the implied violation of (or margin from) the design limit.

Table 1 (Section II.1)

~~III.3~~ DEFINITION OF PROBABILITY SPLIT LEVELS

~~1/2 NO PREVAILING EVIDENCE AVAILABLE~~

~1/10 BEHAVIOR WITHIN KNOWN TRENDS BUT OBTAINABLE AT THE EDGE-OF-SPECTRUM PARAMETER VALUES.

~1/100 BEHAVIOR CANNOT POSITIVELY EXCLUDED BUT OUTSIDE THE SPECTRUM OF REASON

~1/1000 ~~INCREDIBLE~~ Physically unreasonable BEHAVIOR VIOLATING WELL-KNOWN REALITY CAN POSITIVELY ARGUE AGAINST ITS OCCURANCE.

II.2. CRBR STRUCTURAL CAPABILITY

1. Overview and Objectives

Due to the dispersive character of matter under high power heating (thermal expansion and vapor pressures), the high pressures characteristic of disassemblies must develop in short, millisecond, time scales. This, in turn, is possible at sufficiently high reactivity insertion rates such that super-prompt criticality and the associated extremely high power levels may be maintained for a sufficiently long time (typically 1-2 milliseconds) to integrate an adequate amount of energy before the self-limiting character (Doppler, rapid outward displacements due to high internal pressures) of these excursions yield neutronic shutdown.

High reactivity insertion rates require rapid material relocations. As we will see in Section II.7 the actual relationship between these two quantities and with the associated energy release is a strong function of the quantity and configuration of the materials involved. Typically for vapor pressure disassemblies (i.e. disassemblies occurring in the two-phase regime) a ramp rate of approximately 30 $/s would be required to produce pressures in excess of a few atmospheres. For purposes of this discussion we will take this ramp rate level to define, roughly, the onset of energetic behavior. In conjunction with material reactivity worths the corresponding material relocation requirements may be identified.

Thus, for the CRBR heterogeneous core with a maximum sodium void worth below 2$, the coherent voiding of the whole core in less than 0.07 s would be required to achieve energetic behavior. In fact, some very early LMFBR LOFA analyses considered such a direct disassembly mechanism, which was postulated to occur by highly superheating and suddenly flashing the core sodium into vapor. Today we know that except in highly controlled laboratory environments such high superheating and associated rapid sodium voiding is truly physically unreasonable and we cite it as an example of our 1/1000 probability category. In fact, we will see (Section II.3) that sodium voiding, in an intact pin geometry, is roughly one order of magnitude slower than required for energetic behavior. On the other hand, sodium voiding in the presence, or due to, fuel pin disruption may be substantially faster. However, in the CRBR

heterogeneous core design such situations arise only under a very particular set of circumstances (see Section II.4) and in any case the overall reactivity transient is dominated by fuel motion.

The core cladding worth is approximately 5 $ and its complete removal in less than 0.17 s could yield the onset of energetic behavior. Again, such behavior is physically unreasonable. Even if all cladding could ever become mobile (molten) within this time (this in itself being impossible) the forces and mechanisms for such rapid relocations simply do not exist (see Section II.3). Furthermore such massive relocations, should they be postulated, would be self-terminating by freezing and plugging the core exit paths.

Finally, a uniform, core-wide, fuel compaction by approximately 1 cm would insert a reactivity of approximately 1$. Uniform compaction velocities in excess of 30 cm/s would be required for energetic behavior, through this mechanism, in CRBR. Alternatively, higher velocities or smaller core fractions could be equally effective. These situations cannot be excluded a priori in the simple manner just done for the sodium and cladding cases and will have, therefore, to be considered in detail.

The essential conclusion is that only substantial fuel compactions are relevant to energetics concerns. Clad and sodium relocations (and associated neutronic feedbacks and thermal effects) on the other hand are also significant in setting the stage for these all-important fuel motions during the initial phases of core disruption. The negative reactivity feedbacks due to Doppler, fuel axial expansion (in pin geometry, prior to disruption), and retained (within the fuel) fission gas and vapor pressures that help moderate positive reactivity insertions should also be mentioned here. Further, due to non-uniformity in power and coolant flow distributions, considerable variations in the timing of material motions across the core develop. Such space-time distributions in voiding, and clad relocation processes directly affect the early accident evolution particularly in promoting fuel motion incoherencies and hence moderating any resulting positive reactivity insertion rates from such motion.

These considerations on the onset of energetic behavior, together with the level required to produce "significant mechanical damage," form a perspective against which the search for energetics must be made. The objective of this section is to quantify this latter aspect. As shown in Figure 1 two structures are relevant in this regard; hence the discussion is carried out in terms of the two levels of energetics that roughly correspond to the onset of potential mechanical damage for these two structures, respectively. From a

risk standpoint the integrity of the Vessel Head Structure (VHS) is significant. Failures in this structure would allow the release of coolant directly into the containment atmosphere with the possibility for spray fires and containment overpressurization. At the extreme of catastrophic failure, one might even be concerned about missile generation and hence direct challenge to the containment boundary integrity. The significance of the "cage" defined by the UIS/CB/CSS enclosure (the term "cage" is used rather than "bottle" to signify the leaky character of this enclosure) on the other hand is in providing an "intermediate containment" so-to-speak with substantial dissipative qualities (i.e., mitigating VHS loadings). The analysis is carried out in two steps.

We begin with the immediate post-disassembly stage (Section 2), that is, with the power excursion terminated, but prior to any significant expansion (i.e., only slight displacements are required for neutronic shutdown) of the high pressure core materials. For the purpose of this discussion, this state will be characterized by the P-V work release through a packet by packet adiabatic expansion down to one atmosphere and will be related to a reactivity ramp rate through a vapor pressure driven (two-phase) disassembly. This ideal P-V work release would be applicable to an uncontained (free) expansion, hence will be called "Ultimate Work Potential" (UWP). An expansion over the cover gas volume, on the other hand, is a more appropriate measure of the VHS damage and will be simply called "Impact Work Potential" (IWP). The effect of material quantity and configuration on the energy yield and the relation to the cases chosen here will be covered in Section II.7. In the first analysis step (Section 3.1), the expansion is allowed to proceed within the UIS/CB/CSS "cage." With the boundaries of this enclosure maintained fixed we can estimate loading histories, and thus evaluate the structural response. This portion we call "short term expansion." The second step (Section 3.2) consists of carrying out the expansion into the sodium pool. This portion we call "long term expansion." Clearly, this expansion is relevant only in the event of substantial failure of the "cage" boundary. The long term expansion would then be forceful, yielding sodium pool acceleration and, eventually, impact with the VHS. This Impact Kinetic Energy (IKE) defines the forcing function against which the structural capability of the VHS can be assessed [1].

The Applicant has taken the position that significant energetic behavior is of extremely low probability. Hence the quantitative aspects of excursion yields, and energy conversions (damage potential) were not emphasized. The Structural Margin Beyond the Design Basis (SMBDB) was based on an arbitrarily defined P-V, fuel

vapor expansion, curve with an UWP of 661 MJ, and an IWP of 100 MJ. The role of the UIS in constraining this expansion was neglected (subsequently in response to our Question #8, see Table 2 of Section I, the Applicant estimated [12] that the UIS would give way under a load of approximately 100 bar), however, a relatively small degree of energy absorption into the CB was taken into account to yield a slug IKE of approximately 75 MJ. One initiating phase (assumed for a TOP sequence) disassembly at 43 $/s was analyzed [2] yielding an UWP of 111 MJ and an IWP of 33 MJ, i.e. well below the SMBDB of the VHS. The Applicant estimated that ramp rates of approximately 80 $/s and of 90-100 $/s for initiating phase and recriticality disassemblies respectively, would be required to produce mechanical energy releases approaching the system structural capability. Our detailed comments on the Applicant's documentation in this area may be found in [3].

2. Energy Yield Characteristics

The two-step analysis method mentioned above will be carried out here for disassemblies of 100 $/s and 200 $/s occurring in the two-phase mode. These two levels are chosen as roughly indicative of the energy required to approach the structural capability limits of the UIS/CB/CSS "cage" and of the VHS respectively, and with no regard for the actual attainability of such conditions. Their relationship to any projected CRBR energetic events will be discussed in Section II.7.

The energetic characterization of these two disassemblies, made according to the methods and results of Section II.7, is graphically depicted in Figures 2 to 4. The work potential figures are not very sensitive to the equation of state utilized, as long as consistency is maintained in the usage between disassembly and expansion calculations; hence they are convenient in expressing in a very loose way, the "severity" of the excursion. The temperature distributions, Figure 3, on the other hand are useful in expressing core internal pressure gradients as shown in Figure 4. The adiabatic, packet-by-packet expansions that have been traditionally utilized [4] to obtain the UWP and IWP values, and the loadings (i.e., shown in Figure 5 for the two cases at hand) on the immediate structures (CB in particular) disregard these internal gradients, and hence the associated dissipative effects.

The mitigating character of these internal pressure gradients results from the existence of void space both within the expanding core as well as within the surrounding material that will, eventually,

transmit the loading to the adjacent structural boundary (i.e., the UIS/CB/CSS "cage"). The core-internal void allows rapid decay of the peak pressures of Figure 4 by a succession of local expansions before these pressures can be transmitted to the boundary. The recognition of this mechanism is important, particularly in view of crucial role of such internal voids (and the associated compliance) in allowing the development of high energetic yields, as compared to low or single-phase systems, in the first place (see Section II.7).

3. Energy Conversions and Damage Potential

3.1. Short Term Expansion

The objective of this first portion of the analysis is to quantify the structural response of the UIS/CB/CSS "cage" subjected to the forces resulting from the relaxation of the thermal energy states depicted in Figure 3. These loads are highly dynamic and a rigorous computation must consider simultaneously the fluid with the structure dynamics. In the absence of an adequate computational tool in this regard we proceed to uncouple the problem.

First we considered the fluid dynamic loads resulting from an expansion constrained within an assumed rigid-boundary enclosure. This assumption will tend to minimize pressure relief due to the displacement of these boundaries, hence it should provide a conservative load definition. The detailed description of the SIMMER-II model utilized in these analyses is given in Appendix A. Briefly, a core-internal void of 1.0 m^3 (approximately 30%) more or less uniformly distributed, and a surrounding material void of approximately 6 m^3 has been utilized as shown schematically in Figure 6. Of this surrounding void the major portion is found within the Upper Core Structure (UCS) region (fission gas plena). These surrounding structures are allowed to "crush" (i.e., void collapse) against the rigid boundaries constrained only by their own inertia. Based upon this conservatively calculated pressure field a preliminary estimation of the CB strain was made according to the procedure discussed in the next paragraph. A second and more realistic calculation of the pressure field was then made by carrying out the expansion described above but with an allowance for core barrel boundary displacement, taken as a conservative fraction of the estimated CB strains, as shown in Figure 6. These second iteration pressure transients, at several key locations within the enclosure, are shown in Figures 7 and 8 for the 100 \$/s and the 200 \$/s cases respectively. Especially note that one would grossly

overestimate the radial, CB, loads if the peak pressure is used rather than the pressure at the edge of the core. The detailed results may be found in Appendix A.

The structural responses of the CB and UIS under the dynamic loads defined above were determined with the help of the finite element model described in Appendix B. The actual calculations were carried out following a successful benchmarking exercise against the SRI CRBR model tests [5] and REXCO calculation [4].

The calculated UIS displacement histories for the two cases considered are shown in Figure 9. We can see that for the 200 $/s case the UIS boundary clearly fails, while a small but measureable (indicating the approach to failure) total displacement is found in the 100 $/s case. As may be seen in Figures 7 and 8 the UIS loading pressures for the corresponding cases are 150-100 bar and 80-60 bar respectively, hence our results are in good agreement with the 100 bar failure threshold provided by the Applicant.

The calculated CB displacement histories are shown in Figure 10. Again, the 100 $/s loads are clearly contained, while the 200 $/s case indicates strains well within the failure range of approximately 10-20%. The CB strain allowed in the expansion seems to have converged for the 100 $/s, however, the 10% allowance (see Figure 6) made in the 200 $/s expansion is still conservative. Furthermore, at these high strains the vessel would establish contact with and expand against the guard vessel; an additional stiffening effect should be considered. Considering everything we judge that the CB failure conditions under a 200 $/s disassembly are only marginally met.

The net result of this short term expansion is to degrade the work potential greatly while little kinetic energy is manifested in the sodium pool. For the 200 $/s case, 505 MJ of mechanical energy was released. This corresponds well with the isentropic work, 535 MJ, for an equivalent expansion indicating that numerical dissipation in our dynamic calculations was minimal. Of that approximately 180 MJ is used in straining the core barrel and vessel. The other 325 MJ is manifested first as kinetic energy in the Upper Core Structure (UCS). After UCS/UIS impact, most of it is dissipated in the inelastic interaction between these two bodies. At most about 80 MJ is given to the UIS which cannot be effectively given to the pool to augment the head impact loads. This kinetic energy is dissipated by column strain and slug rebound.

The magnitude of the conservatism of the present approach may be surmised by comparison with the results of [4]. The 5400°K CRBR case of Table I of [4] corresponds to approximately 10 Full Power Seconds (FPS) or ~ 10,000 MJ. This case is close to our 100 $/s case, and was estimated to yield a 12.5% CB strain. Our estimated strain for this case is much lower (approximately 2.5%). In fact, the pressure transient utilized in loading the CB in [4], as shown in their Figure 2, seems to qualitatively correspond to our 200 $/s case (see Figure 8) and indeed produces CB strains very similar to those we calculated, i.e. 12.5% vs. 18%. It is clear, therefore, that the structural portion of our analysis method is consistent with previous work, while the substantial discrepancy in final results lies in differences in the definition of the forcing functions.

In the SIMMER-II expansions reported herein, the heat exchange among the different constituents of the expanding core region has been neglected. With the exception of the sodium coolant, which would be absent in the post-initiating phase, recriticality type, energetics of interest here (see Sections II.3, II.4, and II.5), these constituents include steel and, depending on the circumstances, blanket materials. These discrete phases will remain essentially "cold" during the extremely short duration of the power burst, hence, they will represent substantial heat sinks in the post-disassembly expansion period. Owing to the complex nature of the underlying physical processes and the variability in the material quantities and configurations involved, the actual quantification of this effect is not straightforward. However, the generally mitigative character of such thermal interactions was established through parametric SIMMER-II calculations [6] and, for now, we will let this effect represent an unquantified conservative element in the adiabatic expansion results reported herein.

3.2. Long Term Expansion

For as long as the structural envelope of the UIS/CB/CSS system remains largely intact, an effective "throttling" of the expansion process is achieved with essentially nil VHS damage potential. On the other hand the massive failure of this "intermediate" containment envelope would release a high pressure expanding fluid at the base of the sodium pool causing its upward acceleration until vessel head impact. Our objective here is to quantify this pressure release and energy conversion processes.

Again, an idealized conceptual model, as shown in Figure 11, was utilized for this purpose. A fixed UIS position, displaced by 0.5 m,

was chosen such as to minimize the flow area restriction and hence any interference with the blowdown process. As may be seen in Figure 9, such a displacement is approached only at 50 ms, i.e. at about the same time that slug impact occurs (see below) and the long-term expansion process is over. The calculation is initialized at the quasi-static core conditions achieved at the end of the constrained, short term, expansion just discussed. Again, the expansion is modelled as an adiabatic process. Other details of the SIMMER-II simulations including an overview of similar model applications to relevant experimental data are provided in Appendix C.

The 200 $/s case yielded peak slug velocities in the 30-40 m/s range, totaling an impact kinetic energy of approximately 80 MJ. The core and bubble pressures that drive these accelerations are shown in Figure 12. These pressure traces indicate, again, a significant non-uniformity within the expansion volume. The reason for this behavior, which has also been observed experimentally [7, 8] in simulant material tests is due to two-phase choking phenomena. Due to its low speed of sound the two-phase expansion (into the vapor bubble) cannot keep up with the rapid rate of growth (pool displacement), hence a rapid pressure decay, as shown in Figure 12, and an associated reduction in pool acceleration with time, as shown in Figure 13, occur. The impact of this effect in limiting the magnitude of the generated impact energy may be readily visualized. In a uniform expansion with an "average" core pressure of approximately 175 bar through an expansion of approximately 20 m^3 (cover gas volume) an impact energy of 350 MJ would be generated. With an "average" bubble pressure of approximately 70 bar (see Figure 12) on the other hand, expansion over the same volume would only generate approximately 140 MJ. The actually computed slug impact energy is somewhat lower than this order-of-magnitude estimate by accounting for deviations from one-dimensional behavior. A more detailed presentation of the results may be found in Appendix C.

As we have seen in the previous section the 100 $/s expansion remained well contained in the short term. It is interesting nevertheless to determine the long term energy release resulting from a postulated early UIS failure. An order-of-magnitude estimate may be obtained from the quasi-static pressures of Figure 7 in the simple P*V manner employed above. A quasi-static pressure of approximately 100 bar implies an "average" bubble pressure of approximately 25 bar which for an expansion of approximately 20 m^3 translates to a slug impact energy of approximately 50 MJ. Indeed, a ratio of results from SIMMER-II calculations for this situation yields approximately 40 MJ, which is a value well below the VHS design specification (SMBDB).

Finally, we must consider the potential augmentation of the long term expansion pressures due to thermal interactions between the fuel and steel bubble contents and the relatively volatile sodium pool. This problem was first considered by Cho and Epstein [9] in terms of a simple parametric pool entrainment model. They concluded that for an "optimum" entrainment rate a maximum augmentation of pool kinetic energy by a factor of x2 could be obtained. The available experimental evidence is preliminary at this time [10, 11], however, it does indicate that pool volatility promotes adiabatic expansions rather than any augmentation processes. Similarly, parametric SIMMER-II simulations allowing for sodium entrainment and heat transfer did not provide evidence for any major effects. In any case, it is important to emphasize that this situation does not even arise at the 100 $/s energetic level.

4. Summary

The potential for incipient structural damage was keyed to two levels of recriticality energetics. At the 100 $/s level (UWP approximately 1130 MJ) the UIS/CB/CSS structural envelope remains largely intact, however, incipient UIS failure is evident. At the 200 $/s level (UWP approximately 2550 MJ) a pool kinetic energy in the neighborhood of the SMBDB is obtained. Large, failure displacements are predicted for the UIS, and substantial CB strains, again in the failure range, are noted. The essence of these conclusions is graphically depicted in Figure 14. The relationship to potential CRBR energetic events is made in Section II.7.

The Applicant's analysis of these damage levels in relation to the originating power excursions (reactivity ramp rates) appears overly conservative in three areas: (a) the mitigating role of the high compliance of the core during the short term expansion was neglected, i.e. the centrally originating high vapor pressures were applied directly to the CB structural boundary, (b) the value of the UIS/CB/CSS structural envelope in "throttling" the high pressure, long term expansion, was also neglected, and (c) the moderation in the magnitude of pool acceleration due to non-uniform expansion (choking effects) was not taken into account. Due to the neglect of these mitigating circumstances, the Applicant's 661 MJ accident corresponds, roughly, in terms of CB strains and slug impact kinetic energy, to our 2550 MJ (200 $/s) energetics level.

APPENDIX A
SHORT TERM EXPANSION

1. Introduction

This Appendix provides the detailed analysis of the short term expansion of the high temperature fuel following core disassembly transients of 100 and 200 $/s. We describe the geometric model used, the assumptions made and the results. Isentropic work potentials are also developed for reference.

2. Geometric Model

The first phase of the Post Disassembly Expansion (PDE) begins directly after disassembly and continues to the point of quasi-static conditions within the core enclosure comprized of the upper internal structure, core barrel, and core support structure. Thus the geometric region of interest is within this enclosure.

The calculational mesh for this first phase or short-term expansion is shown in Figure 1. The core region mesh is identical to that used the disassembly calculations (Section II.7). This permits the thermal/physical data from the disassembly to be used directly in the expansion. Because the early PDE pressures are very large, we have assumed that there is no structural resistance to radial flow within the core.

Initially the UIS does not directly feel the core pressure. The upper axial blanket, and fission gas plena must be translated upward about 30 in. before contact is made. The load transfer from the core is still mitigated because of the crushability of the plena within the subassemblies of the upper core structure (UCS). To simulate this delayed UIS loading, the inertial constraints produced by the UCS mass (approximately 17,000 kg), and the volume available for core expansion, the upper axial blanket and gas plena regions were modeled as solid particulates. The residual sodium in the region above the core was removed based on its easy access to escape paths.

The radial blankets and reflector are also modeled as particulates. If a CB strain is assumed, an equivalent volume is placed between

the radial reflector and CB as shown on Figure 1. The particles then represent the radial inertia. For these expansions the downward direction is blocked.

A special modification to SIMMER-II was required to prevent the radial blanket and radial reflector particulates from convecting axially. As structural members they should move radially only. The modification simply introduced an artificial resistance into the axial momentum equation in these regions.

3. Assumptions

As a result of initial expansions with no assumed CB strain and the analysis of strains from these expansions, second iteration strains of 10% and 2.5% were selected to size the radial void for the 200 $/s and 100 $/s cases respectively. All heat transfer except between fuel and its vapor was eliminated to provide an adiabatic limit. Standard momentum coupling between the liquids, vapors, and particles was assumed.

4. Results

200 $/s adiabatic

The initial core temperature distribution for this short-term post-disassembly expansion is given in Figure 3 of Section II.2. The average value of 5580 K must be interpreted carefully and in the context of the equation-of-state used when comparing with energy levels dealt with in the literature. For our assessment this average temperature represents a very high energy state, i.e. 87% of T_{crit}. The short-term expansion leads to the temperature reduction shown in Figure 2. The energy change associated with this temperature reduction produces the vapor that drives the expansion.

The massive vaporization of fuel associated with the adiabatic expansion is shown in Figures 2 and 4. The final total volume within the UIS/CB/CSS enclosure that fuel and its vapor can occupy is about 15 m^3. Of this 5.5 m^3 is associated with the assumed CB strain of 10%, 4.6 m^3 within the UCS, 2.9 m^3 above the UCS and below the UIS, and 2 m^3 in the active core. Thus this is a relatively large expansion, i.e. of the order of the cover gas volume and is the reason for the large quantity of vapor generated (37% of fuel mass).

The volume provided inside the CB to simulate its strain is shown on Figure 5 as it collapses by radial blanket and shield motions. Note that it is completely collapsed at the same time as the UIS is loaded, i.e. the UCS is driven upward to contact and complete crushing. This coincidence is appropriate because the upper CB does not see pressure until the UCS is translated upward.

The pressure histories of interest are shown on Figures 6 through 8, for the core center, upper core surface, and outer core surface. The later two curves are average pressures over the surface of interest. The pressure transient in Figure 7 drives the UCS upward and ultimately loads the UIS and that shown in Figure 8 loads the CB with an appropriate reduction for the radial inertia and cylindrical geometry. Figure 9 shows the time of UIS engagement. This pressure spike is associated with the assumed fluid nature of the UCS and is therefore somewhat artificial.

The development of the expansion can be seen with the series of three dimensional plots for vapor volume fraction, Figures 10 through 15, and liquid volume fraction, Figures 16 through 21. Figure 11 shows the early movement of material radially opposite the core (radial is to the right and vertical is up to the left--volume fraction is the ordinate). The void grows rapidly upward in the core and the initial void in the UCS is collapsed by the upward movement of the collapsing UCS as time increases. At 0.020 s, Figure 14, the CB void is gone and the UCS is against the upper boundary or UIS. The liquid volume fraction plots simply give a different perspective of the same transient. Note on Figure 20 that the code modification to suppress axial convection in the radial blanket and reflector regions has functioned properly.

A capability to perform an isentropic expansion was developed as part of this assessment. The isentropic results for the 200 $/s case are shown on Figure 22. At the end of this first phase of expansion ($\Delta V \approx 14$ m^3), 535 MJ of work potential have been expended. This is in good agreement with our SIMMER-II results. If the calculated expansion is truly adiabatic, this work potential must be accounted for. In Appendix B the core barrel energy absorption was developed per inch of core barrel at 10% strain. Using the calculated strains for both the core barrel and vessel wall and taking the core barrel length as 100 in. (for strain purposes we use the length from the bottom of the active core to the top of the CB), we obtain 180 MJ. Consider now the work done against the UCS. The UCS contacts the UIS after about 0.02 s. The upper axial blanket must be displaced about 2 m in this time requiring an average velocity of 100 m/s but because of the nearly constant acceleration the impact

velocity would be about 200 m/s. The kinetic energy in the UCS at impact is then 0.5 x (17,000 kg) x (200 m/s)^2 or 325 MJ. Adding this value to the strain energy gives 520 MJ which agree very well with the isentropic value.

The 340 MJ imparted to the UCS for the 200 $/s case is dissipated by inelastic impact with the UIS. The mass ratio of these two bodies is about 3:1, UIS:UCS. The final velocity of the combined masses would be 25% of the impact value or about 50 m/s if no further crushing occurred and the interaction is truly impulsive. The final kinetic energy would be reduced also to 25% or 81 MJ for these assumptions. There is a loss of work or damage potential of at least 245 MJ in this collision process. The UIS columns and control rod drives absorb some of the remaining kinetic energy as strain energy. It is estimated that they can absorb approximately 6 MJ up to a buckling strain of about 5%. The slug impact pressure transient will act downward on the UIS to further destroy its residual kinetic energy. Even if it did reach the head, it would be delayed well beyond the slug impact loading and its damage potential would be small because of the head to UIS mass ratio.

One additional check on internal consistency and on the degree to which nonadiabatic effects such as numerical energy mixing are occurring is to compare the calculated quasistatic pressure with the isentropic value for the change in volume of 14 m^3. This isentropic pressure is 225 atm. The average calculated pressure is 220 atm. Thus the expansion agrees with the isentropic very well.

100 $/s adiabatic

The same procedure was used to generate the pressure loads in the UIS/CB/CSS enclosure. The reduced severity of this accident can be seen from the initial average fuel temperature of only 4940 K or 77% T_{crit}. The characteristics of the expansion are similar to that for 200 $/s. The main difference is the lengthened expansion time. A complete set of results is provided in Figures 23 through 50. The isentropic expansion characteristics are given in Figure 51 for this case. The work potential expended during this stage of expansion (~10 m^3) is 140 MJ and the final pressure is ~90 atm. The final SIMMER-II pressure is also ~90 atm, again in excellent agreement.

Selected Variations

The effects of heat transfer to the residual in-core structures (subassembly walls and internal blankets) and among the liquids and

particulates were evaluated. Using nominal SIMMER-II models for heat transfer, we find that the fuel temperature is rapidly reduced and that the core pressures are reduced to about 2/3 of those for adiabatic expansion. The reduction could be greater if effective heat transfer were permitted to the UCS. The details of this analysis are given in the Compendium [1].

5. Summary

The large amounts of mechanical energy released during expansion within the UIS/CB/CSS enclosure are dissipated within or on this enclosure even if it is induced to fail or is therefore effectively withheld from manifesting itself as kinetic energy in the sodium pool. The expansion against the pool, if it occurs (enclosure must fail in a major way such as UIS buckling), starts from a very degraded condition at which the work potential per unit volume change is much reduced. Thus these structures produce a major mitigating effect on the real expansion.

The results are conservative because they are effectively isentropic. Heat transfer could further mitigate both the structure loads and the subsequent expansion potential.

APPENDIX B
UIS/CB/CSS STRUCTURAL ENVELOPE RESPONSE

1. Introduction

In this appendix we evaluate the response of the CB and UIS to loads generated by the SIMMER-II computer code for the \$100/s and 200 \$/s energetics cases discussed in Section II.2.

The CB is a 2.0 in. thick 304 SS cylinder with an inner radius of 76.0 in. Radial shielding for the core is positioned radially inward from the CB. Proceeding outward from the CB are a 44 in. thick annulus filled with Na and the 2.375 in. thick vessel wall. Outside the vessel wall is a 7.5 in. gap and then the 1.0 in. thick guard vessel wall. Both the reactor vessel and guard vessel are 304 SS.

2. Description of the CB Analytical Model

To simulate the response of the CB during an HCDA we used an axisymmetric finite element model that includes the CB, sodium in the annulus and the reactor vessel wall (Figure 1). The model was developed with the ABAQUS [1] computer code and all components, including sodium, were modeled with the CAX8 eight node element. The CB and vessel wall were modeled with elastic-plastic material properties representing 304 SS at 750°F. An isotropic strain hardening rule with a Von Mises yield surface was used to simulate plastic behavior.

The sodium was modeled as an orthotropic material, incapable of carrying hoop or shear stress. At the CB-Na and vessel-Na interfaces, radial displacements of the sodium and steel boundaries were required to be equivalent, but the sodium was free to move vertically simulating frictionless boundaries. Inertial effects from sodium above the plane of the model were included by lumping the equivalent mass of sodium above this plane at the sodium nodes on the upper plane of the model. This added mass was effective in the vertical direction only.

The model represents the radial dynamic response of the axisymmetric structure while the sodium elements are all in

compression in the radial direction. This suffices to calculate the maximum radial deflection of the CB and vessel wall.

3. Predicted CB Responses

Pressure transients at the core boundary generated with SIMMER-II were used to load the CB. The pressure at the core boundary was reduced by the ratio of the core diameter to the CB diameter before applying it to the model. The core boundary pressure transients for the 100 $/s and the 200 $/s cases respectively as shown in Figures 7 and 8 of Section II.2 were utilized.

Response of the CB and vessel wall to these transients is shown in Figures 2-9 in terms of displacement and hoop strain. For the $100/s case the maximum strain predicted in the CB is 3%. This is well below strain levels that can be expected to fail the CB. A maximum CB hoop strain of 17% is predicted for the 200 $/s case. Reference [2] gives uniaxial ultimate strains of just over 20% for 304 SS between 700°F and 1000°F. Strain rate effects are not important with maximum strain rates predicted to be less than 10 in./in./s. For structures in a biaxial state of stress, such as the CB, this value will be somewhat lower. Therefore, we predict that the CB is likely to fail for the 200 $/s case. The time of failure is difficult to determine but would probably occur between 15 and 20 ms. On the other hand, the vessel wall is predicted to strain approximately 10%. This prediction is high because when the wall has strained 6.5% it will contact the 1.0 in. thick guard vessel wall, which is not included in the model. Therefore, we do not expect the vessel wall to fail.

To get an approximation of the energy absorbed by the CB as it strains, we use the expansion

$$\sigma = 24000 + \frac{8000}{0.03}\ \varepsilon \qquad (1)$$

to represent stress as a function of strain. Considering on the hoop component of strain,

$$P.E. = \int_{\varepsilon} \int_{vol} \sigma\, dV d\varepsilon \qquad (2)$$

or

$$P.E. = V \int \sigma \, d\varepsilon \tag{3}$$

Substituting equation (1) into (3) gives

$$P.E. = V[24000\,\varepsilon + \frac{4000}{0.03}\,\varepsilon^2] \tag{4}$$

where the volume of the CB wall is

$$V = 4\pi\,(76) = 955 \text{ in.}^3 \tag{5}$$

So, for 10% strain, the energy absorbed by a 1.0 in. length of the CB is 3.6×10^6 in.-lb or 0.41 MJ. The same calculation can be used for the vessel wall simply by changing the volume.

4. Benchmarking of the CB Model

To determine whether our model accurately predicts CB response, we have compared its predictions with scale model test results [3]. Because our loads are significantly higher than those for the scale model tests and no pressures were recorded at the CB during the tests, we are constrained to compare the ratio of CB to vessel wall strain. Table 1 lists these ratios for our analyses and for the SM-3, SM-4, and SM-5 model tests. Final plastic strains are used for the test ratios. Note that the comparison is quite good and that it is very close compared to the experimental scatter between test SM-3 and tests SM-4 and SM-5.

The model also was tested against the coupled fluid/structure interaction analysis [6] of REXCO for the CRBR CB under CDA loads. The pressure transient calculated by REXCO at the edge of the active core was used as the loading function for our model. This loading function and the calculated strain transients for both calculations are given in Figure 10. Good agreement is noted.

5. Description of the UIS Models

The UIS is a very rigid steel structure suspended above the Upper Core Structure (UCS). It weighs approximately 105,000 lb and is held in place by four 316 SS cylindrical columns. The columns are approximately 210 in. long with the upper end connected to the Intermediate Rotating Plug (IRP) of the vessel head through a jacking mechanism. For this study we assumed that all components of the UIS are rigid except for the columns.

Two simple models were developed with the ABAQUS computer code to simulate the UIS response during an energetic event. In both models the UIS was represented as one mass lump. In one model it was connected to the vessel head through a single truss element. This model was capable of simulating nonlinear material behavior but could not simulate column buckling. Material properties for the nonlinear truss were developed using data from [3]. For cases where column buckling is important we used a second model where the column stiffness was represented by a spring that includes buckling effects. The spring was based on the force deflection curve generated by the applicant using a more detailed finite element model that included buckling [4]. This model with the nonlinear spring is capable of simulating UIS response as long as the displacement is monotonically increasing. For analyses where unloading occurs, the first model with the truss element had to be used. Both models give very similar results in the regions of response where they both apply.

6. Predicted UIS Responses

The loads applied to the UIS models were based on the core boundary pressures predicted by SIMMER-II. There is a delay in time (approximately 20 ms) before the loads act on the UIS. This delay is from the gap between the UCS and UIS and crushing that occurs in the UCS. To develop a force from the pressures (Figures 7 and 8 of Section II.2) we assumed that the pressure is applied uniformly over 5000 $in.^2$ of the UIS (this corresponds to the core area).

Figure 11 shows the UIS displacement response for the 100 $/s case. The UIS truss model was used for this calculation because some unloading does occur before the maximum displacement is reached. The UIS displaces a maximum of 5.8 in. at 200 ms from when it is initially loaded (228 ms from the start of the accident). This displacement is far below that required for the UCS to be forced out of the core restraint structure (20 in.).

Displacement response of the UIS during the 200 $/s accident is shown in Figure 12. The loads are sufficient in this accident to buckle the columns so the second UIS model with the spring representing the UIS support columns was used. Displacement of the UIS is monotonically increasing and exceeds 20 in. at approximately 30 ms after it is initially loaded. Therefore, the UCS will be dislodged from the core restraint structure at approximately 48 ms after the start of the accident.

7. Benchmarking of the UIS Models

The models have been benchmarked against scale model test ACS2 [5] and shown to conservatively overpredict displacement. In test ACS2 a scale model of the UIS and its support columns was subjected to a pressure volume curve similar to that being used for the Applicant's base case (661 MJ) scenario.

TABLE 1
RATIO OF CB TO VESSEL WALL STRAIN

100 $/s	1.7
200 $/s	1.7
SM-3	1.7
SM-4	2.0
SM-5	2.0

APPENDIX C
LONG TERM EXPANSION

1. Introduction

This Appendix provides the details of the core expansion against the sodium pool following failure of the UIS. It is through this mode that a mechanical threat is delivered to the reactor head. This analysis was performed for the 200 $/s transient.

2. Geometric Model

The geometric and calculational model used for this vessel-scale analysis is shown in Figure 1. The core and part of the above core region (radial mesh 1 to 8 and axial mesh 1 to 8) are expanded to preserve the volume assumed in Appendix A for core barrel strain. A void region has been introduced directly below the UIS (modeled as a jammed-no flow region; radial mesh 1 to 9 and axial mesh 21 to 35) to account for the 0.5 m displacement of the UIS to permit venting to the pool. The cover gas volume was reduced to 15 m^3 to account for the previous voiding of sodium from the core, UCS and plenum region under the UIS. The region below the active core is assumed to be nonparticipating and is not included within the problem boundaries. All boundaries in this assessment are assumed rigid.

3. Initial Conditions

The temperature and pressure throughout the core at the end of the short term expansion are essentially uniform. This uniformity is preserved. The density distributions were transferred by averaging the density in the subregions shown on Figure 1 (called mesh sets) on the mesh used in Appendix A. This enabled the mesh structure to change while roughly maintaining the material arrangement. Total masses are conserved in this transformation. The cover gas is modeled as condensible sodium vapor. Thus there is no gas compression to mitigate the expansion through back pressure buildup. The expansion is forced to be adiabatic as in the short-term portion.

4. Results

The results for this part of the expansion are presented in the same format as those in Appendix A. The masses of liquid and vapor fuel continue to change as long as expansion to larger volume can occur. After expansion to the cover gas volume at about 50 ms, 42 percent of the fuel is vaporized as seen on Figures 2 and 3. The core pressure continues to fall as shown in Figure 4 until slug impact, at which time it levels out at about 100 atm. One important aspect of the transient expansion is the large pressure gradient between the source of pressure in the original core and UCS regions and the expansion bubble where work is done on the pool. Comparing the early pressure histories in Figures 4, 5, and 6 which represent core, bottom of the UIS and expansion bubble respectively we find that at 40 ms the pressures are 190 atm, 80 atm, and 20 atm. Obviously if the high pressures were able to act on the pool interface, 2.7 times more work would be done on the pool. This is precisely the difference between the isentropic and adiabatic/dynamic expansion performed here. In an isentropic expansion inertia is zero and the source material can be visualized as moving with the bubble interface. In reality the high density, two-phase fuel is far removed from the bubble interface (approximately 4 m), it has substantial inertia, it must turn a corner to get to the expansion interface, and it must continually accelerate to stay with the accelerating interface. Thus the pressure drop and thus the large reduction in delivered work potential. The work potential has not been dissipated or otherwise lost. It simply has not developed its work potential in this highly dynamic situation.

The pool velocity is shown on Figure 7. Impact of the pool with the head is at ~47 ms. A small secondary expansion and impact occurs at ~65 ms. The impact pressures shown on Figure 8 should be simply related to the impact velocity and pool density for the sodium hammer situation in a rigid vessel. The simple fluid hammer formula gives a pressure of $6.3(10^7)$ Pa for the sodium properties used in SIMMER-II. The agreement is very good. Figure 9 shows the pressure at the top of the UIS as a result of the compression wave from slug impact propagating downward through the pool.

A more detailed view of the expansion is seen in Figures 10 through 14 for vapor volume fraction, Figures 15 through 19 for liquid volume fraction, Figures 20 through 25 for pressure, Figures 26 through 28 for radial velocity, and Figures 29 through 31 for axial velocity. On Figure 13 we can see some nonuniformity in the pool upper surface. This makes the impact slightly incoherent but it is a second order effect. Figure 19 gives a good view of the bubble at

slug impact. The cover gas volume is so small that the bubble never reaches the vessel wall. Figure 21 shows the pressure decrease from the original active core to the bottom of the UIS where the flow changes direction to enter the bubble radially. The initial fluid impact pressure is seen in Figure 24 and its propagation in Figure 25.

The development of axial kinetic energy in the system and in the sodium pool alone is shown in Figures 32 and 33 respectively. The difference of about 20 MJ is in the high velocity core material as it flows to the expansion bubble. The damage potential to the head derives from the 80 MJ peak shown on Figure 33 for the sodium pool alone because the core material is uncoupled from the sodium pool. The radial kinetic energies are shown in Figures 34 and 35. Most of this kinetic energy, which is also uncoupled from the pool, is in the flow of core material from the UIS to the expansion bubble. The maximum total system kinetic energy is 124 MJ.

Taking the starting point for the ideal isentropic expansion as the end of the short-term dynamic expansion, the isentropic work potential released during the long-term expansion to slug impact is 160 MJ. The dynamic reduction factor is 2. If we compare the 80 MJ to that obtained via an ideal isentropic expansion to 29 m^3 (14 m^3 from short-term and 15 from long-term), a conversion efficiency of 11% results.

Heat transfer among the various materials within the core (steel, fuel, and internal blanket pellets) and expansion bubble (fuel, steel, and sodium) were assessed [7] using nominal SIMMER-II models. Two major effects are noted. First, the dynamic pressure drop between the core and expansion bubble is reduced because of sodium vapor generation in the bubble. Second, the pressure in the core and bubble is reduced as a result of heat transfer from the fuel in the core. The net effect is a factor of 2 reduction in the IKE.

5. Validity of Results

The fluid dynamics in the expansion above is very simple and straightforward. SIMMER-II has been exercised [1-4] extensively on this type of problem and has been tested against data [5, 6] in this regime.

6. Summary

By including some fundamental aspects of the postdisassembly expansion, the effective generation of damage potential to the head (pool axial kinetic energy) is only 11% of thermodynamic maximum possible. These results are not sensitive to modeling uncertainties.

II.3. REFERENCE INITIATING PHASE BEHAVIOR

1. Objectives and Overview

The phenomenological sequence of the LOFA Initiating Phase has been well established, both analytically and experimentally. The flow coast down occurs, typically, with a time constant of ~ 8 s, sodium boiling initiates at ~ 10 s, at near nominal power level and 20% of full flow. This boiling process is unstable, it quickly leads to pressure buildup and liquid sodium expulsion out of both ends of the coolant channel (subassembly). Following this "coolant voiding" the cladding melts within a fraction of a second and the fuel soon after. Relocation of these molten/disrupted materials occurs under the influence of gravity and existing pressure gradients from fission gases, sodium vapor, any residual pumping, and the static liquid sodium head over the voided region. The actual timing of these subsequent processes depends upon the power level which is on the rise because of reactivity increases associated with the sodium voiding process. The power history, in turn, affects the core-wide sodium boiling inception and voiding pattern such that a highly coupled situation develops.

For a sufficiently high sodium void reactivity worth, a near prompt-critical condition may be obtained well before complete core voiding. The resulting high overpower condition induces a TOP-like phenomenology (see Section III) in the unvoided subassemblies (i.e. cooled, strong cladding) and it is known as the Loss-of-Flow driven Transient Overpower or LOF-d-TOP. The potential for such evolution was identified, for the previous CRBR homogeneous core design, as a major safety (energetics) concern [1, 2]. The mechanism is illustrated in Figure 1. It involves near-mid-plane failures and forceful (due to retained fission gases) molten fuel motion towards the failure location. A potentially autocatalytic character is evident. At this time neither the mechanisms of this LOF-d-TOP regime nor its energetic outcome can be predicted with confidence, hence, its occurrence is highly undesirable. The present, heterogeneous, CRBR core design with its lower sodium void reactivity worth is helpful in this regard.

The extent to which the LOF-d-TOP regime is avoided altogether may be conservatively assessed by means of analyses that accentuate the

positive reactivity feedback (i.e. material relocation rates and worths chosen at the upper end of their uncertainty band) and minimize the negative ones, i.e. the magnitude of the axial thermal expansion of the fuel column and the value of the Doppler. On the other hand, such choices leading to a "fast" initiating phase scenario, also yield nearly simultaneous clad melting and fuel disruption in the voided coolant channels and are, therefore, non-conservative with regard to steel blockage formation and hence recriticality potential during the post-initiation (disruption) stages of the accident sequence. This extreme is conservatively explored by means of analyses that accentuate the negative feedbacks while minimizing the positive ones ("slow" scenario). Both of these extremes as well as several in-between choices of parameters were explored (by means of SAS3D calculations) for the EOC-4 core configuration. In addition we considered the EOC-3 core (increased core-wide coherence due to replacement of the six highest power subassemblies by blankets) and the BOC-1 core (low sodium void reactivity, and absence of fission gases in the fuel) to fully span the range of behavior in the initiating phase. Representative results are presented in Section 7 and in more detail in Appendix BII.2.

The initiating phase phenomena are modelled in great detail in the SAS computer code system. This tool pioneered the field over a decade ago and through a continuing research and development effort, and a succession of new and improved versions has remained at, in fact it helped define, the state-of-the-art in this area. However, as it is common with large "system" codes, the fidelity of portraying local behavior is rather limited. There are two aspects to these limitations. The one results from viewing the whole subassembly (217 pins) response in terms of that of an average pin, i.e. neglecting multidimensional effects and associated intra subassembly incoherencies. The other limitation is a consequence of representing the whole core in terms of a relatively small number of these representative pins or "channels" in SAS terminology, i.e. many subassemblies lumped into a single channel, and thus only approximately accounting for inter-subassembly incoherencies. Our views on the nature and possible impact of these limitations are provided in the next few sections as a means of putting the accident analysis results of Section 7 in the proper perspective. All crucial ingredients in our SAS3D analyses are also presented and discussed in these sections.

The Applicant has also considered the initiating phase behavior in some detail. The SAS3D computer code was utilized in these evaluations. Results for various core configurations, parametric effects, and specific analyses carried out in response to our

Questions #2 and #4 (Table 2 of Section II.1) were provided [3, 4]. Our initial review and evaluation of these results has been documented in [5, 6]. At this time, based on our own independent studies we are in a position to agree with the major conclusion of the Applicant concerning the absence of the LOF-d-TOP regime (for an important qualification on this matter see Section II.4). On the issue of exit core blockage formation, our agreement with the Applicant is qualitative and tentative. It is qualitative because we predict a higher degree (although far from complete) of core exit plugging, by relocated molten cladding; and tentative because this agreement is obtained with fundamentally different approaches. According to the Applicant irradiated fuel remains dispersive throughout the initiating phase; and plenum fission gas blowdown interferes sufficiently with the sodium vapor streaming to inhibit upward clad relocation and plugging at the core exit (UAB area). In our view the initial dispersiveness (upon disruption) of irradiated fuel will dissipate, due to expansion pressure loss and de-entrainment, thus allowing, eventually the fall-back of the disrupted fuel under gravity. On the role of plenum fission gas blowdown on clad relocation, our analyses indicate that this effect, by itself, does not preclude net upward relocation. However, taken together with flow redistribution effects due to radial clad melting incoherencies, on a best estimate basis, can help us arrive to this conclusion. Further discussion of these topics is given in the appropriate sections below.

2. Sodium Voiding

The sodium voiding process is important not only in providing the initial driving reactivity for power escalation but also in affecting the mechanism of the clad relocation process (see Section 3). The potential deviations from the simple, SAS, one-dimensional representation has been recognized for some time. However, progress in quantifying these so-called intra-subassembly boiling incoherencies, has been slow. At this time the only analytical predictions available are based on a simplified homogeneous, equilibrium two-phase flow model (HEV-2D) applied to a two-dimensional (cylindrical symmetry assumed) bundle geometry [2]. The essence of the predicted trends is summarized in Figure 2.

First we note the good agreement in the inlet flow transient between the SAS and HEV-1D (i.e. the HEV model applied in one dimensional geometry) predictions. Inlet flow reversal and macroscopic sodium voiding occur within 0.6 s from boiling inception, and the boiling instability process seems to have been overwhelmed by the heat

input as indicated by the agreement between the two widely different two-phase flow models represented in these two calculations (annular flow in SAS, homogeneous flow in HEV). Allowance for two-dimensional effects is seen to contribute to flow stability, although again flow reversal is obtained. A delay by ~1 s is noted between the one-dimensional and two-dimensional analyses. From a slightly different perspective the 2D results may be viewed as causing boiling initiation by about 1 s too early. Indeed the 1D calculation indicates a delay for boiling inception (as compared to the 2D case) by ~1 s, hence on an absolute time frame the results for flow excursion (i.e. rapid drop-off in inlet flow) and reversal are nearly indistinguishable.

The recently run OPERA-15 test [7] also addressed this problem. A 15-pin triangular bundle was arranged such as to represent, by symmetry, a one-sixth segment of a 61-pin bundle, and was subjected to a flow coastdown transient in the ANL OPERA facility. The technical community was invited [8] to submit pre-test (blind) predictions which were to be published together with the test results. The old results [9] discussed above seemed pertinent to the test conditions and were therefore submitted [10] in response to this request. At this time the test results have been published [7]. It is our understanding [11] that the comparisons with all the pre-test predictions submitted will follow shortly. The comparisons with our own results are shown in Figure 3. A satisfactory agreement is indicated. The time to flow reversal in OPERA-15 is 2.3 s versus the 1.8 s predicted by HEV-2D. However, there is some indication [11] that a slight bowing in the "outer" test assembly flat produced approximately a 10% additional bypass and this may be the reason for the somewhat longer delay observed experimentally.

Based on these results we expect that the SAS 1D predictions of the boiling flow excursion do not significantly suffer from neglecting the intra-subassembly boiling incoherencies. Further, based on extensive and well documented calculations of in-pile tests, we expect that the voiding rates in the 1D mode are accurately predicted. The main effect of the boiling incoherencies, then, is to induce a radial temperature distribution, which translates into radial clad melting incoherencies, which, in turn, significantly affect the clad relocation phenomena as discussed in the next section.

3. Clad Relocation

The flow reversal delays (2D boiling effects) mentioned above translate to radial clad melting incoherencies. We will discuss how such effects may be used to explain some apparent inconsistencies observed in in-pile test data. These data are summarized in Table 1.

Simulant material (woods-metal/air) experimental data have been correlated [2] in terms of the dimensionless gas velocity J_g^* as shown in Figure 4. These data indicate the following relocation regimes: (a) $J_g^* \sim 1$ clad suspension and sloshing, (b) $J_g^* < 0.8$ clad draining, and (c) $J_g^* > 1.5$ net and sustained upward relocation. A rough scale of relocation velocities may be estimated, again with J_g^* as the parameter, in terms of the transient film thickness data also shown in Figure 5. The basic characteristics of the R- and P-series tests are compared to those estimated for the CRBR in Figure 6. The radial melting incoherence $\tilde{A}$ is defined as the radial fraction of the pin bundle experiencing clad melting simultaneously. It is interesting that in this respect the 7-pin bundle of the R-series is superior to the 37-pin P-series bundle in simulating the estimated (by HEV-2D) CRBR bundle incoherency. On the other hand the available pressure drop, ΔP, in the R-series was below that present in the P-series and estimated (by SAS3D) for the CRBR for a LOFA. A similar trend is also noted for the magnitude of the chugging velocities, ΔV, and may be thus inferred for the associated pressure pulses.

The clad relocation trends have been quantified [2] in terms of the flow regime map of Figure 7. The quantity $\tilde{L}$ represents the axial melting incoherency and is defined analogously to $\tilde{A}$. The available pressure gradient ΔP is expressed in terms of the number, m, of the static sodium heads as shown. Any point on this map represents a particular incoherency state. The associated clad relocation trend is determined by the value of the J_g^* trajectory passing through this point and the criteria established on the basis of the data of Figure 4. The points of departure and initial trajectories of the R- and P-series bundles are shown in this flow regime map. Due to the heat losses to the adjacent cold duct walls in the 7-pin R-series bundles, melting should progress rapidly downwards rather than radially, i.e. a more or less straight upwards trajectory of melting incoherency states is indicated. The highly one-dimensional P-series bundles on the other hand should begin at $\tilde{A} \sim 1$. Now a straight upward trajectory is only possible. It is seen that the R-series trajectory corresponds to marginal upward relocation criteria, i.e. $J_g^* \sim 2.2 \times 0.7 \sim 1.54$, initially which develop to clearly sloshing

behavior along the indicated incoherency trajectory. Clearly such marginal behavior could be easily reversed by the gas blowdown in R-8 as indeed the data show. The P-series bundles on the other hand are seen to clearly meet the criteria for sustained upward relocation (i.e. $J_g^* \sim 2.5 \times 1.3 \sim 3.25$) as indeed the data demonstrate. The estimated reactor trajectory is also shown. This process is initially characterized by $J_g^* \sim 1.7$, indicating a somewhat greater tendency for upward relocation than in the R-series. This tendency is maintained with time due to the sideways direction of the trajectory. On the other hand both the m-values and initial incoherency states indicate that the P-series tests would greatly overestimate the upward clad relocation and extent of resulting blockage expected in the CRBR.

In addition, the effects of the plenum blowdown in redistributing the available pressure gradient, and thus altering the m-value, need to be taken into account. The plenum fission gases are released near the top of the active core. Except for an initial small portion of the blowdown transient that is immaterial to clad motion (since clad melting follows clad rupture typically by 0.6 s) this gas release is unable to pressurize the coolant channel and reverse the pressure gradient. It rather serves to concentrate the pressure gradient in the fission gas plenum and upper axial blanket regions in which it is flowing with a certain quantity of sodium vapor flow consistent with the overall pressure drop requirements. The effect is to reduce the sodium vapor flow, or the effective m-value within the active core region as illustrated in Figure 8, and hence interfere with the clad relocation process.

This pressure gradient redistribution process was modelled within the framework of the SAS3D code (see Section II.4). The effective m-values were calculated and used in conjunction with the flow regime maps to guide the SAS3D-calculated clad relocation directions and rates. An example of the variation of the m-values calculated as a function of time, for the EOC-4 case, is shown in Figure 9. Following an initial rapid drop the values of m increase as the plenum fission gases deplete. For the example shown, at the time of clad melting, we read $m^{\frac{1}{2}} \sim 1.6$, which in combination with the beginning of the CRBR incoherency trajectory of Figure 7 yields $J_g^* \sim 1$. That is, a sloshing behavior, with no net upward relocation and absence of core exit blockages is predicted. Furthermore, even for the "slow" cases the power level will increase above nominal, thus reducing the time interval between clad failure and clad melting, and, with reference to Figure 9, even smaller values of $m^{\frac{1}{2}}$ (and of J_g^*) will be applicable as these phenomena develop in subsequent groups of subassemblies (or SAS channels).

Another effect of the increased power is to flatten-out the axial temperature distribution, and thus promote the axial clad melting coherence (i.e. increase $\tilde{L}_m$). As may be seen from Figure 7 this effect will tend to further reduce the potential for upward relocation.

A further pressure gradient redistribution effect decreasing the effective m-values develops during the formation of steel blockages in the upper axial blanket region. As a consequence, well before complete blockages are formed the J^*_σ values decrease to the point where they cannot sustain continuing upward relocation.

Tnus, on a best estimate basis we predict minimal net steel relocation and blockage formation during the initiating phase of core disruption. However, certain important qualifications need be mentioned: (a) the fission gas plenum blowdown and its interference with clad relocation are a function of the core burnup. The above estimates were given for conditions maximizing this interference and will reduce to zero for BOL conditions, (b) the radial clad melting incoherence phenomena have not yet been adequately established. Neglecting these effects, for the example of Figure 9 would yield a $J^*_\sigma \sim 1.6 \times 1.3 \sim 2.1$, i.e. a substantial upward relocation regime, and (c) the effects of pressure pulsations due to liquid sodium "chugging" as it attempts unsuccessfully to re-enter the voided region were not taken into account in the above analyses.

To conservatively bound these uncertainties we imposed a moderate upward clad relocation in all our SAS3A calculations. This was accomplished within the SAS3D framework as follows: (a) radial melting incoherencies were neglected, (b) a two phase frictional multiplier of 12 was utilized, (c) the sodium vapor streaming was calculated on the basis of the quasi-static pressure differential across the core (i.e. neglecting the chugging effects) while taking into account the pressure drop redistribution due to fission gas plenum blowdown, and (d) relocation criteria consistent with the trends of Figure 4 were utilized. In this fashion upward clad relocation velocities of ~ 70 cm/s were typically obtained. These are considerably lower than the velocities predicted by the original SAS formulation (CLAZAS subroutine) but in view of the previous discussion still adequately conservative with respect to the prediction of the extent of the exit core blockage.

4. Fuel Motion

Fuel disruption in voided subassemblies has been extensively studied over the past several years in the TREAT reactor. Experimental

conditions have covered single and seven-pin bundles, normal and up to 20x nominal power, reduced and full length fuel pins, and fresh as well as irradiated fuel. The neutron hodoscope was utilized to quantify the transient fuel motion. These measurements were augmented with temperature, pressure, and flow data in order to "reconstruct" the sequence of events in the experiments. More recently, the fundamentally-oriented FD-series of experiments conducted in the ACRR facility at SNL produced direct visual information (high speed movies) of the fuel disruption process under reasonably prototypic conditions.

Based on this cumulative experience it is generally accepted now that the disruption of irradiated fuel under overpower conditions (from a few times nominal and up) is initially dispersive. The exact timing, rate, and extent of this dispersal process depend upon a number of complicated physical considerations and are subject to debate. These considerations include fission gas retention (within the fuel matrix) during steady-state irradiation, transient fission gas redistribution prior to fuel disruption, fission gas behavior subsequent to fuel disruption, fuel failure criteria, and mode of fuel disruption. They are crucial if the fuel dispersal process is viewed as a mechanism for the mitigation of highly overpowered, near prompt critical conditions. This was the case, for example, in the Applicant's approach to the LOF-d-TOP concern for the previous CRBR homogeneous core application. The present heterogeneous core design substantially relaxes this concern, and hence the need to base the safety case on such details. General, and well-established trends will suffice in this case.

The general fuel disruption modes under the power levels of 5 to 10x nominal, typically expected for the CRBR conditions, the phenomenological SNL FD experiments provide some important insights.

(a) For the initial failures, at ~ 5x nominal power, experiment FD 2.6 shows that the disruption mode consists of rapid liquid-state fuel swelling as fuel melting occurs. The expansion process is modeled quite well by simply assuming expansion of the gas in the liquid fuel to relieve the residual overpressure in the bubbles. The observed disruption in the radially unconstrained FD 2.6 geometry is more than sufficient to block the coolant channels. At that point, it is estimated that the trapped fission gas is still significantly (10 s of bars) overpressurized. Fuel dispersal (not modeled in experiment FD 2.6) would be expected from the overpressurized gas trapped in the liquid fuel. Sodium vapor streaming would not be expected to enhance fuel dispersal.

(b) For subsequent failures at higher power levels (5 to 10x nominal), especially in those channels where cladding motion does not significantly precede fuel disruption, the above described liquid fuel expansion is preceded by rapid radial dispersal of the outer, gas-bearing region of the fuel pin (experiments FD 4.3 and FD 2.8). It would appear that sodium vapor flow could provide some axial dispersal of this initially disrupted fuel. However, radial liquid-state swelling of the fuel blocks off the coolant flow channel within 100 ms of the initial solid-state disruption. Thus, one could only consider sodium-vapor-flow induced fuel dispersal for less than the first 100 ms of the dispersal.

(c) There does not appear to be a fundamental change in disruption mode at higher (9% vs. 4%) burnup. However, there is an enhanced likelihood of early, solid-state disruption of the outer gas-bearing fuel. At lower disruption powers, very nonenergetic disruption of the outer solid fuel is observed. Unlike the fine-scale (grain-size) solid-state disruption observed at higher power levels, the lower-power disruption results in large chunks of solid fuel being ejected into the coolant channel.

Fuel disruption in SAS3D analyses is calculated with the SLUMPY module. This is a parametric model and it does not provide a fully mechanistic treatment of fuel disruption and dispersal. Thus, it has to be calibrated in order to reflect the general trends observed experimentally. The TREAT tests L6 and L7 were utilized for this purpose. The details of this calibration/sensitivity study may be found in [12]. The fuel motion reactivity transients obtained with our final choice of these parameters is compared to the experimental data and the results obtained by the Applicant (using a different set of parameters for each fit) in a similar exercise in Figures 10 and 11.

Based on these comparisons we conclude that:

(a) Our fuel dispersal modelling (choice of parameters) may underestimate the early dispersal rates at high power levels (L7) and may not yield the slight initial compaction effect observed at low power levels (L6). The overall trends, however, are adequately depicted.

(b) The long term fuel relative worth increase depicted in our analytical results is the consequence of assuming fission gas de-entrainment and slumping of the previously dispersed fuel under gravity. This process cannot be evaluated on the basis of the L6 and L7 results.

5. Other Processes and Neutronic Feedbacks

We requested and obtained from the Applicant the EOC-3 neutronic data and a re-evaluation of the sodium void reactivity and its uncertainty for the EOC-4 core configuration. Based on these data we created reactivity worth distributions, power distributions, and estimations of the Doppler feedback appropriate for SAS3D input for a fully independent set of calculations (our initial SAS3D calculations were carried out utilizing the Applicant's input data). The calculational techniques, the results, and their contrast to those obtained by the Applicant are presented in Appendix A. It is in the nature of such elaborate calculations that some differences will be expected; however, due to the generally insensitive nature of the initiating phase of the heterogeneous CRBR core, no significant difference in overall accident evolution is noted (see Section 6).

Finally, the last significant neutronic feedback is due to axial thermal expansion of the fuel column. However, this feedback cannot be guaranteed because of possible clad interference, and perhaps more importantly because of the fuel expansion into existing voids (or gaps between the pellets). It is, therefore, common to treat this effect parametrically. Typically a 50% effectiveness (in reactivity feedback) of the expansion process is used as an arbitrary mid-range value. Limiting behaviors for "fast" and "slow" transients are explored by using effectiveness values of 0% and 100% respectively. A similar parametric approach has been followed in our analyses.

6. Accident Analysis Aspects and Results

Our first effort was to delineate the "boundary" of the LOF-d-TOP regime. Several SAS3D calculations with deliberately "fast" scenario assumptions were carried out for this purpose. The combination of: (a) a sodium void worth at the upper 2 σ uncertainty limit of ~ 2 \$, (b) a 0% effective axial expansion, and (c) a near neutral (non-dispersive and non-compactive) fuel motion model, was found necessary to indicate the approaching of the LOF-d-TOP condition. Such a combination of parameters and physical processes is considered extremely unlikely, especially in view of the definitive experimental evidence that indicates a dispersive mode of fuel disruption especially at the high power level that is encountered prior to, and as, the LOF-d-TOP condition is approached. We conclude that LOF-d-TOP energetics in the heterogeneous CRBR core is physically unreasonable. In the remainder of this section we are concerned with establishing the non-energetic aspects of the

initiating phase phenomenology, in particular the extent of core-exit clad blockages, under more reasonable combinations of parameters. The only other energetics mechanism possible in the initiating phase is examined as a special problem in Section II.4.

The essential specifications for the three core configurations analyzed and the two parametric cases on the EOC-4 are given in Table 2. The main sequences of events are summarized in Figures 12 to 15 for the four cases respectively. The reactivity and power histories and the mobile (molten) cladding and fuel patterns at the time of development of an overpower condition sufficient to produce fuel and steel vapor pressures are shown in Figures 16 to 19. The details of the accident sequences are given in Appendix B. Here some of the main trends will be identified.

All cases indicate substantial neutronic activity. The associated power transients reduce the time interval between clad melting and fuel disruption, thus minimizing the extent of fuel/steel separation and core-exit blockage formation. This process is called "co-disruption," and it is schematically illustrated in Figure 20. It is important in enhancing the termination potential by dispersal, because of (a) greater axial path availability, (b) remeltable blockages, and (c) higher vapor (steel) pressures driving the "dispersal" process. Thus, even with pessimistic clad relocation assumptions, the co-disruption is effective in limiting the duration of such relocation processes and hence a good fraction of the core exit paths remain unblocked.

The other general characteristic is that the advanced core disruption sequences are approached in all four cases with (a) absence of liquid sodium from the active core region, (b) a major fraction of cladding and fuel in the molten and intermixed state, and (c) a considerable neutronic activity dominated by gravity-driven, oscillatory, fuel motions and culminating, at the end of these calculations, with power bursts of 10x to 10^3x nominal power. Thus the entry into the S/A-scale pool phase is clearly identified.

7. Summary

The occurrence of the LOF-d-TOP energetic regime in the CRBR heterogeneous core has been shown to be physically unreasonable (for a special qualification of this conclusion see Section II.4). In the absence of initiating phase energetics we have attempted to quantify the range of behavior concerning core-exit, clad, blockage formation, and the system characteristics at the entry to the S/A-scale pool phase. These results are pursued in Sections II.6 and II.5, respectively.

Table 1 (Section II.3)

~~III-c-3~~ IN-PILE CLAD RELOCATION DATA.

• R-series	7-pin	mm-SCALE BLOCKAGES
• R-8	pressurized	NO BLOCKAGE
• P3A	37-pin	2 cm BLOCKAGE
• P3	37-pin	10 cm BLOCKAGE.

TABLE 2
SAS3D INPUT CHANGES

Parameter	Mid-Range EOC-4	Slow EOC-4	EOC-3	BOC-1
Doppler coefficient	As calculated in Appendix A	Adjusted to be 20% above WARD	As calculated in Appendix A	From GEFR-00523
Sodium void coefficient	As calculated in Appendix A	Adjusted to get $1.46 in driver S.A.	As calculated in Appendix A	From GEFR-00523
Fraction of steady state fission gas available	0.51	1.05	1.05	1.05
Fraction of gas available instantaneously upon fuel motion	0.1176	0.1429	0.1429	0.1429
Fuel particle (drop) diameter	0.02 cm	-	-	-
Viscosity parameter	1000	10,000	10,000	10,000
Extra upper segment acceleration	0.	784 cm/s^2	784 cm/s^2	784 cm/s^2
Axial expansion effective for reactivity feedback	~~0.5~~ 50%	~~1.0~~ 100 %	~~0.5~~ 50 %	~~0.8~~ 80 %
Default for lower blockage	35 cm	30 cm	30 cm	25 cm
Default for upper blockage	130 cm	140 cm	140 cm	130 cm
Steel to fuel mass ratio in SLUMPY where cladding moves before fuel	0.	0.001	0.001	0.001

APPENDIX A

DOPPLER, SODIUM VOIDING NEUTRONIC FEEDBACKS AND POWER DISTRIBUTION

1. Introduction

In the loss-of-flow (LOF) accident, sodium voiding provides an early positive feedback mechanism. The impact of the effect depends on the coherence of the sodium voiding and the magnitude of the sodium void reactivity. The positive reactivity effect is mitigated by the negative reactivity effects of Doppler and axial expansion.

The sodium void reactivity effect is produced by two large, competing components: leakage and non-leakage. The non-leakage component results from changes in the distribution of flux with energy (spectrum) as a result of changes in macroscopic scattering cross sections with the removal of sodium, and to a lesser extent from changes in neutron capture. The leakage component results from changes in neutron leakage as a result of changes in the macroscopic scattering cross section with the removal of sodium. The non-leakage component is largest in the central portion of the core where both the real and adjoint fluxes are large. The leakage component is largest near the core-blanket interfaces where the real and adjoint flux gradients are large. Because of these characteristics, calculated sodium void reactivities are sensitive to calculational methods, nuclear cross section data, and core position. For example, typical results [1] for non-leakage component dominated regions can vary 20% for calculations based on ENDF/III versus ENDF/IV cross section data [2]. Results [1] for high leakage component regions may differ as much as 30% when neutron transport corrections are included. Because the sodium void reactivity is highly dependent on the burn-up state of the reactor, the effect of uncertainties in the predicted pre-accident isotopic compositions should be included along with other data and methods uncertainties.

The Doppler reactivity effect provides a negative feedback mechanism resulting from temperature increases in fertile fuel. The effective Doppler feedback in a heterogeneous core reactor is relatively small because the fertile material is concentrated in the blanket regions which do not heat up as rapidly in a transient as the driver regions, due to their lower specific power. The Doppler reactivity

effect is important in the initiating phase, however, because it is a prompt effect, i.e. no time delay due to heat transfer is involved.

The Doppler effect is produced by the effective broadening of fission and capture resonances due to the thermal motion of fertile isotopes. The varying competition among fission, capture, and leakage reactions as the fuel temperature changes produces the effect. Because the affected resonances are mostly below 25 kev in energy, where the spectrum is rapidly falling off in a typical LMFBR, the predicted Doppler effect is sensitive to the shape of the calculated spectrum.

Uncertainties in the predicted Doppler reactivities result from both data and method uncertainties. The effects of typical data uncertainties are smaller than for the sodium void effect because the partial cancellation of competing effects is not involved; however, experimental verification is less extensive. Method uncertainties involve the use of the calculated Doppler coefficients as well as their prediction. For example, because the Doppler effect is characterized as a "1/T" law for the SAS3D initiating phase accident code, while theory predicts a mixture of $T^{-1/2}$ and $T^{-3/2}$ behavior, a temperature dependent bias is introduced. Exponents of -1.1 to -1.2 were calculated [3] for the homogeneous core design of CRBR. As a second example, the Doppler effect will typically decrease 40% upon sodium voiding. This effect is treated as a local effect in SAS3D, i.e. the Doppler reactivity for a given cell depends only upon the amount of sodium in that cell; however, the cell spectrum and thus the Doppler effect is definitely affected by the presence or absence of sodium in adjacent cells. This effect can be expected to be larger in the heterogeneous core reactors.

In the following, our independently calculated results for sodium void reactivity, Doppler constant, and reactor power distribution are reported for both the EOC-4 and EOC-3 of the CRBR. The EOC-4 results are compared with the values used in the General Electric (GE) accident analysis [2]. An evaluation of the differences is provided and sources of uncertainty are identified and evaluated.

2. Calculational Approach

The initiating-phase analysis [1] supplied for our review was developed by General Electric (GE) and was based on calculations performed with the SAS3D code [2], which models initiating-phase accident phenomena and consequent neutronic effects. Input to this code consists of basic geometry and thermo-hydraulics data defined

by the CRBR design, parameters controlling various phenomenological modeling assumptions, and parameters describing the reactor neutronic characteristics.

The SAS3D code can be used with neutronics parameters, such as reactivity worth distributions, calculated separately; this option was used by GE, based on neutronic parameters supported by the Westinghouse Advanced Reactor Division (WARD). Alternatively, basic neutronics data, such as atom densities, can be supplied to SAS3D, which will then determine the required neutronics parameters by using the neutronics code, DIF3DS [3], as part of its initialization procedure. The later option was used for this work. WARD-calculated atom densities by synthesizing the results of Hex-Planar and R-Z burn-up calculations.

For the EOC-4 configuration, atom densities [4] were supplied to us for each of the 997 zones. WARD assumed one-third core symmetry with each subassembly divided into three separate axial regions in the core and two each in the axial blankets. Thermal-hydraulic data for modeling the reactor with 15 core channels, in which all data are averaged over all subassemblies comprising each channel, were supplied by GE. These data are used by the SAS3D models to define the reactor steady state configuration, i.e. material temperature distributions. The following calculational steps were performed based on these data:

1. WARD atom densities were averaged for each channel and axial region and modified for input to SAS3D.

2. LANL nuclear cross sections were collapsed and shielded.

3. The SAS3D steady state calculation was performed without using the fuel categorization option, thus avoiding the iteration of the SAS3D thermal expansion and DIF3DS reactor power distribution calculation.

4. Neutronics parameters required for SAS3D transient calculations were determined by DIF3DS perturbation calculations.

The WARD-supplied atom densities were averaged over groups of subassemblies representing the 15 channels defined in the GE SAS3D representation, and two additional channels not present in the GE setup to represent the radial blanket. This approach resulted in considerable homogenization of spatial detail, i.e. the 997 zones were condensed into 88 SAS3D regions.

The reference cross section data [5] used are the LIB-IV 50 group set of infinitely dilute cross sections and shielding factors. Shielded isotopic cross sections are separately calculated for each SAS3D region to account for background and temperature effects. The required background interpolation of shielding factors is performed by a multi-function cross section code, XSPROC, which was recently developed to facilitate these types of calculations. Cross section sets are constructed for each isotope over a range of temperatures; DIF3DS then performs the final temperature interpolations for each meshpoint. For the purposes of calculating background cross sections, the 88 regions were further condensed to 15 regions. The 50 group set was collapsed to 18 groups by XSPROC, based on a single weighting spectrum, determined by performing a one dimensional transport calculation in radial geometry using ONEDANT [6], and averaging the resulting fluxes over all space points.

The calculational approach used for the EOC-3 configuration was identical to that of the EOC-4 configuration as described above. The procedure used by WARD to determine atom densities was also identical, i.e. by synthesizing the results of Hex-planar and R-Z burnup calculations. However, the SAS3D data were set up for a 33 channel case in order to avoid averaging the azimuthal asymmetry in coolant flow rates. Atom densities were averaged over groups of subassemblies representing the 33 channels; the 997 WARD-defined zones were condensed onto 98 SAS3D regions.

3. Calculated Results

All neutronics parameters needed for the SAS3D initiating-phase calculation were calculated for the EOC-3 and EOC-4 configurations of CRBR. Results for the EOC-4 case are summarized for the channel scheme used by GE in its transient SAS3D calculations. The subassembly to channel layout is shown in Figure 1. The reactivity changes resulting from the voiding of flowing sodium and the addition of clad and fuel to each channel are shown in Table 1, along with the coolant-in and flowing coolant-out Doppler constants. The power distribution and derivative quantities are shown in Table 2.

Because the uncertainty involved in performing burn-up calculations has not been addressed elsewhere up to this time, the magnitude of potential effects has been estimated by two supplementary calculations. Isotopic composition uncertainties were not estimated a priori, but the impact of an assumed 10% uncertainty in the amount of bred Plutonium has been determined by arbitrarily varying the Plutonium content of the internal blanket (with the total actinide content held

constant). The impact of these variations upon the reactor power distribution is shown in Table 3, where a 10% increase in internal blanket Plutonium is assumed, and Table 4, where a 10% decrease is assumed.

The subassembly to channel layout used for the EOC-3 calculations is shown in Figure 2. The reactivity changes resulting from the voiding of flowing sodium, and the addition of clad and fuel to each channel are shown in Table 7, along with the coolant-in and flowing coolant-out Doppler constants. The power distribution and derivative quantities are shown in Table 8.

4. Comparison with WARD/GE Results - EOC-4

The values supplied by WARD and used by GE for the transient SAS3D calculations are shown in Tables 5 and 6, containing the power distribution and the reactivity changes, respectively. These values were calculated with a three dimensional FOP calculation based on diffusion theory and using ENDF/III cross section data.

As a comparison of Tables 2 and 6 shows, our radial power distribution agrees well with the WARD values. The two main differences in our results are a slight shift (approximately 2%) toward the reactor center and higher relative power in blanket subassemblies. The central shift is not expected to be significant in the initiating phase because the leading driver channels keep the same sequence of power-to-flow ratios. The blanket power differences are apparently caused by differences in neutron capture energies used in the two calculations. These differences are not expected to affect the initiating phase because the low specific power in the blankets retards the development of fuel disruption until late in the transient. A further difference in the two power distributions is the axial shape. A comparison for a typical channel is shown in Figure 3. The WARD curve has a truncated shape in the central portion, due to the three axial zone burn-up calculations used to determine the isotopic compositions. In our calculation, the isotopic densities were axially averaged, and thus do not have this characteristic. This is due to a lack of a proper treatment for reactivity feedback from fuel motion in SAS3D if compositions are varied axially. As a consequence of our more peaked distribution, fuel disruption will occur earlier relative to clad melting in the upper portion of the core.

Comparison of our results, Table 1, and WARD results, Table 5, shows significantly higher calculated sodium void reactivities in our case. The two calculations were similar in that both were first order

perturbation results based on three dimensional diffusion theory. Several differences existed in cross section group structure and weighting spectra determination, along with different fission product cross sections. Also the WARD-supplied nuclear densities were averaged axially and over all subassemblies in each channel in our calculation. Finally, the WARD results were based on ENDF/III cross section data, while our results were based on ENDF/IV cross section data. This last difference is considered to be the most important contributor to the differences between these results; for example, comparison of critical experiments calculations for central sodium void coefficients shows ENDF/III results about 20% lower than ENDF/IV results.

5. Uncertainties

Uncertainties exist in the calculational methods and data, in the reactor configuration, and in the proper application of experimentally derived bias factors. Principal uncertainties in the calculational method for the determination of material reactivity worths are the use of first order perturbation versus exact perturbation and the use of diffusion theory calculated fluxes versus transport theory based fluxes. FOP calculations tend to underestimate the positive non-leakage term and to overestimate the negative leakage term because both real and adjoint spectra tend to harden and the spatial distribution to flatten with sodium removal. A further estimation is made if the effect of sodium voiding upon other cross sections (primarily the increase in resonance self-shielding) is neglected, as it is in our calculation. Differences between transport and diffusion results can be expected to become significant for regions near core-blanket or control rod interfaces. Reactivity changes may be either under- or overestimated with diffusion results. Cross section data uncertainties stem from basic data and the methods used to determine resonance self-shielding and collapsing spectra. Calculational uncertainties of these types are difficult to estimate because the impacts are highly regional dependent. However, errors on the order of 10-20% have been quoted due to the use of FOP, errors on the order of 0 to 30% due to the use of diffusion theory, and as indicated previously, a 20% difference can result between calculations with ENDF/III and ENDF/IV.

Uncertainties in the reactor configuration result from two sources: errors in the reactor burn-up state and uncertainty in the global sodium content (due to previous voiding) when a given subassembly is voided. Errors in the reactor burn-up calculation stem from the use of diffusion theory and the use of approximate cross sections

(which do not properly account for the effects of composition changes). Such errors affect the sodium void reactivity primarily because the Pu^{240} fission threshold occurs at a lower energy than that of U^{238} and the capture-to-fission ratio for Pu^{241} is not as steep as that for Pu^{239}. A second effect occurs because the reactor power distribution is affected by Pu buildup in the internal blankets, which in turn affects the subassembly voiding sequence. The effect of uncertainty in the reactor sodium content is comparable to the use of FOP versus EP in the void reactivity calculation, i.e. the flux hardening and flattening due to previous voiding is properly treated. (This effect cannot be incorporated into an accident code such as SAS3D without prior knowledge of the accident path.) The magnitude of uncertainties in the blanket Pu content should be on the order of 10%.

Uncertainties in the calculational/experimental bias correction to the sodium void reactivities reflect the uncertainty in the comparability of critical assembly critical effects versus power reactor physical effects. The most important difference is the use of platelet geometry in CRBR. Other differences include the absence of fission products and the lack of a temperature distribution in the critical assemblies. Comparison of calculational and experimental results for a number of critical assemblies shows that a significant bias factor is necessary to obtain general agreement for both leakage and non-leakage components. Such bias factors definitely reduce the variance in C/E's for critical assemblies. Some effects, such as streaming, however, are not comparable for platelet versus pin geometry. Thus, the use of bias factors determined for critical assemblies may not be justified for use in power reactors. Some have claimed, for example, that the overprediction of the non-leakage component, which is characteristic of the critical assembly sodium void calculation is almost entirely attributable to platelet streaming effects. In this case the non-leakage bias factor should not be applied to power reactors.

6. Conclusions and Recommendations

The results of our independent calculations of CRBR neutronics parameters have been presented and compared to corresponding values by the Applicant for the CRBR initiating-phase analysis. An evaluation of these differences has been presented along with an identification of the sources of uncertainty. An independent quantitative uncertainty analysis has not been performed, however. The uncertainty analysis provided by the applicant in response to question #2 (Table 2; Section I) recommends an uncertainty for the

Doppler effects of ±16% for driver SAs with a positive worth. We believe that these values adequately bound calculational, voiding sequence, temperature distribution, and fission product uncertainties. It has not been clearly established, however, that calculated to experimental bias factors, from critical experiments, should be applied to power reactor calculated results. Thus for EOC-4 the upper bound of total driver void worth reactivity is taken as 2.03$ based on our calculated value of 1.75$ plus 16% for uncertainty applied to all driver SAs. The lower bound is taken as 1.10$ based on a biased value minus 16% for uncertainty. In this assignment we have treated the bias factor as an additional uncertainty in the downward direction.

TABLE 1
SAS3D CHANNEL CHARACTERISTICS at EOC-4

Doppler constants are multiplied by -10000.
reactivities in dollars, based on beta = 0.003311

channel number	type	number of subs	coolant react.	clad react.	fuel react.	Na In Doppler	Na Out Doppler
1	blkt	7.	0.13	-0.22	-1.11	3.06	2.72
2	driv	21.	0.53	-1.27	18.71	2.73	2.13
3	blkt	21.	0.42	-0.76	-3.62	10.68	9.05
4	driv	9.	0.22	-0.53	7.92	1.26	1.00
5	blkt	36.	0.69	-1.26	-5.31	17.62	14.03
6	driv	6.	0.12	-0.34	6.65	0.90	0.65
7	driv	12.	0.24	-0.66	11.26	1.71	1.22
8	blkt	12.	0.15	-0.29	-1.23	4.15	3.16
9	driv	6.	0.05	-0.21	4.85	0.71	0.48
10	driv	12.	0.18	-0.54	10.26	1.52	1.05
11	driv	24.	0.51	-1.30	20.44	3.23	2.35
12	driv	12.	-0.01	-0.19	8.25	1.06	0.72
13	driv	18.	0.18	-0.59	12.55	1.70	1.17
14	driv	18.	-0.20	0.11	9.58	1.10	0.78
15	driv	24.	-0.07	-0.17	12.32	1.53	1.09
16*	blkt	60.	-0.28	0.32	3.92	6.72	5.55
17*	blkt	72.	-0.14	0.18	1.47	2.34	2.15

total driver coolant reactivity	1.75	
total driver clad reactivity	-5.70	
total driver fuel reactivity	122.80	
total internal blanket coolant reactivity	1.38	
total internal blanket clad reactivity	-2.52	
total internal blanket fuel reactivity	-11.27	
total driver Doppler constant (no voiding)	17.46	
total driver Doppler constant (na voided)	12.64	
total internal blanket Doppler constant (no voiding)		35.51
total internal blanket Doppler constant (na voided)		28.96

* Channels 16 and 17 represent the radial blanket in the LANL calculation. Channel 16 consists of blanket subassemblies adjacent driver subassemblies. Channel 17 consists of the remaining blanket subassemblies.

TABLE 2
SAS3D CHANNEL CHARACTERISTICS at EOC-4

channel number	type	number of subs	norm. sub power	mass flux (gm/cc-s)	average rod pow (KW)	pow/flow (J/gm)	norm. sub pow/flow
1	blkt	7.	0.56	381.7	34.23	214.3	1.04
2	driv	21.	1.32	493.5	22.60	229.1	1.11
3	blkt	21.	0.62	434.5	37.95	208.7	1.01
4	driv	9.	1.33	505.6	22.67	224.3	1.09
5	blkt	36.	0.64	434.5	38.94	214.2	1.04
6	driv	6.	1.48	514.7	25.30	245.9	1.19
7	driv	12.	1.34	524.4	22.93	218.7	1.06
8	blkt	12.	0.54	381.7	32.85	205.6	1.00
9	driv	6.	1.22	524.4	20.92	199.5	0.97
10	driv	12.	1.27	524.4	21.69	206.9	1.00
11	driv	24.	1.29	543.3	22.08	203.3	0.98
12	driv	12.	1.10	491.4	18.78	191.2	0.93
13	driv	18.	1.14	496.2	19.44	196.0	0.95
14	driv	18.	0.93	431.2	15.92	184.6	0.89
15	driv	24.	0.95	433.1	16.17	186.8	0.90
16*	blkt	60.	0.28	257.8	17.18	159.3	0.77
17*	blkt	72.	0.11	144.5	6.71	111.0	0.54

* Channels 16 and 17 represent the radial blanket in the LANL calculation. Channel 16 consists of blanket subassemblies adjacent driver subassemblies. Channel 17 consists of the remaining blanket subassemblies.

TABLE 3
SAS3D CHANNEL CHARACTERISTICS at EOC-4
(Increased Inner Blanket Plutonium)

channel number	type	number of subs	norm. sub power	mass flux (gm/cc-s)	average rod pow (KW)	pow/flow (J/gm)	norm. sub pow/flow
1	blkt	7.	0.61	381.7	37.12	232.4	1.11
2	driv	21.	1.34	493.5	22.96	232.8	1.11
3	blkt	21.	0.67	434.5	40.63	223.4	1.07
4	driv	9.	1.34	505.6	22.94	227.0	1.09
5	blkt	36.	0.67	434.5	40.97	225.3	1.08
6	driv	6.	1.47	514.7	25.17	244.6	1.17
7	driv	12.	1.32	524.4	22.70	216.6	1.04
8	blkt	12.	0.56	381.7	33.96	212.6	1.02
9	driv	6.	1.19	524.4	20.47	195.2	0.93
10	driv	12.	1.24	524.4	21.30	203.2	0.97
11	driv	24.	1.28	543.3	21.89	201.6	0.96
12	driv	12.	1.07	491.4	18.32	186.5	0.89
13	driv	18.	1.11	496.2	19.06	192.2	0.92
14	driv	18.	0.90	431.2	15.50	179.8	0.86
15	driv	24.	0.92	433.1	15.81	182.6	0.87
16*	blkt	60.	0.27	257.8	16.71	154.8	0.74
17*	blkt	72.	0.11	144.5	6.51	107.7	0.52

* Channels 16 and 17 represent the radial blanket in the LANL calculation. Channel 16 consists of blanket subassemblies adjacent driver subassemblies. Channel 17 consists of the remaining blanket subassemblies.

TABLE 4
SAS3D CHANNEL CHARACTERISTICS at EOC-4
(Decreased Inner Blanket Plutonium)

channel number	type	number of subs	norm. sub power	mass flux (gm/cc-s)	average rod pow (KW)	pow/flow (J/gm)	norm. sub pow/flow
1	blkt	7.	0.52	381.7	31.41	196.6	0.96
2	driv	21.	1.30	493.5	22.23	225.3	1.10
3	blkt	21.	0.58	434.5	35.29	194.1	0.95
4	driv	9.	1.31	505.6	22.38	221.4	1.08
5	blkt	36.	0.61	434.5	36.88	202.8	0.99
6	driv	6.	1.49	514.7	25.43	247.2	1.21
7	driv	12.	1.36	524.4	23.16	220.9	1.08
8	blkt	12.	0.52	381.7	31.68	198.3	0.97
9	driv	6.	1.25	524.4	21.37	203.9	1.00
10	driv	12.	1.30	524.4	22.08	210.6	1.03
11	driv	24.	1.31	543.3	22.25	204.9	1.00
12	driv	12.	1.13	491.4	19.25	195.9	0.96
13	driv	18.	1.16	496.2	19.82	199.8	0.98
14	driv	18.	0.96	431.2	16.34	189.6	0.93
15	driv	24.	0.97	433.1	16.54	191.0	0.94
16*	blkt	60.	0.29	257.8	17.67	163.8	0.80
17*	blkt	72.	0.11	144.5	6.91	114.3	0.56

* Channels 16 and 17 represent the radial blanket in the LANL calculation. Channel 16 consists of blanket subassemblies adjacent driver subassemblies. Channel 17 consists of the remaining blanket subassemblies.

TABLE 5
WARD CALCULATION of
SAS3D CHANNEL CHARACTERISTICS at EOC-4

Doppler constants are multiplied by -10000.
reactivities in dollars, based on beta = 0.003403

channel number	type	number of subs	coolant react.	clad react.	fuel react.	Na In Doppler	Na Out Doppler
1	blkt	7.	0.10	-0.17	-1.16	3.55	3.27
2	driv	21.	0.39	-0.98	16.73	3.82	3.23
3	blkt	21.	0.33	-0.61	-3.86	12.24	10.64
4	driv	9.	0.16	-0.41	7.11	1.78	1.53
5	blkt	36.	0.56	-1.03	-5.86	20.37	16.43
6	driv	6.	0.08	-0.27	6.05	1.24	0.93
7	driv	12.	0.16	-0.51	10.20	2.29	1.74
8	blkt	12.	0.13	-0.24	-1.46	4.84	3.70
9	driv	6.	0.03	-0.16	4.43	0.92	0.67
10	driv	12.	0.11	-0.42	9.35	2.00	1.46
11	driv	24.	0.37	-1.03	18.69	4.45	3.47
12	driv	12.	-0.04	-0.12	7.62	1.39	1.01
13	driv	18.	0.12	-0.47	11.61	2.30	1.69
14	driv	18.	-0.20	0.15	8.96	1.51	1.14
15	driv	24.	-0.08	-0.10	11.61	2.15	1.63

total driver coolant reactivity	1.10	
total driver clad reactivity	-4.31	
total driver fuel reactivity	112.35	
total internal blanket coolant reactivity	1.11	
total internal blanket clad reactivity	-2.05	
total internal blanket fuel reactivity	-12.34	
total driver Doppler constant (no voiding)	23.83	
total driver Doppler constant (na voided)	18.49	
total internal blanket Doppler constant (no voiding)		41.00
total internal blanket Doppler constant (na voided)		34.04

TABLE 6
WARD CALCULATION of
SAS3D CHANNEL CHARACTERISTICS at EOC-4

channel number	type	number of subs	norm. sub power	mass flux (gm/cc-s)	average rod pow (KW)	pow/flow (J/gm)	norm. sub pow/flow
1	blkt	7.	0.54	381.7	32.50	203.4	1.00
2	driv	21.	1.30	493.5	21.89	221.9	1.09
3	blkt	21.	0.61	434.5	36.36	200.0	0.99
4	driv	9.	1.31	505.6	21.99	217.5	1.07
5	blkt	36.	0.63	434.5	37.54	206.5	1.02
6	driv	6.	1.46	514.7	24.59	239.0	1.18
7	driv	12.	1.32	524.4	22.16	211.4	1.04
8	blkt	12.	0.54	381.7	32.56	203.8	1.00
9	driv	6.	1.22	524.4	20.57	196.2	0.97
10	driv	12.	1.26	524.4	21.22	202.4	1.00
11	driv	24.	1.29	543.3	21.73	200.1	0.99
12	driv	12.	1.12	491.4	18.87	192.0	0.95
13	driv	18.	1.16	496.2	19.51	196.7	0.97
14	driv	18.	0.96	431.2	16.17	187.6	0.92
15	driv	24.	0.98	433.1	16.56	191.3	0.94

TABLE 7
SAS3D CHANNEL CHARACTERISTICS at EOC-3

Doppler constants are multiplied by -10000.
reactivities in dollars, based on beta = 0.003311

channel number	type	number of subs	coolant react.	clad react.	fuel react.	Na In Doppler	Na Out Doppler
1	blkt	1.	0.01	-0.02	-0.20	0.31	0.30
2	blkt	6.	0.07	-0.14	-1.27	2.32	2.17
3	driv	3.	0.05	-0.14	2.46	0.39	0.33
4	driv	9.	0.14	-0.41	7.28	1.04	0.87
5	blkt	15.	0.21	-0.42	-3.77	6.81	6.11
6	blkt	6.	0.10	-0.17	-1.53	2.63	2.29
7	driv	6.	0.11	-0.29	5.08	0.68	0.54
8	driv	6.	0.11	-0.30	5.27	0.76	0.60
9	driv	6.	0.11	-0.29	5.19	0.78	0.63
10	blkt	6.	0.09	-0.17	-1.52	2.90	2.39
11	blkt	12.	0.19	-0.35	-3.07	5.62	4.72
12	blkt	12.	0.19	-0.37	-3.20	6.12	5.18
13	driv	6.	0.09	-0.29	6.14	0.85	0.62
14	driv	12.	0.21	-0.62	12.09	1.76	1.31
15	driv	6.	0.10	-0.30	6.30	0.87	0.64
16	driv	3.	0.02	-0.12	3.05	0.40	0.28
17	driv	6.	0.07	-0.28	6.27	0.85	0.59
18	blkt	12.	0.20	-0.40	-3.19	5.90	4.54
19	driv	12.	0.19	-0.61	12.17	1.75	1.27
20	driv	6.	0.08	-0.29	6.43	0.87	0.60
21	driv	3.	0.02	-0.12	3.13	0.41	0.28
22	driv	6.	-0.09	0.05	4.69	0.50	0.35
23	driv	6.	-0.02	-0.11	5.39	0.63	0.43
24	driv	6.	0.05	-0.22	5.39	0.65	0.45
25	blkt	12.	0.16	-0.33	-2.67	4.92	3.74
26	driv	6.	0.06	-0.23	5.50	0.70	0.48
27	driv	6.	0.05	-0.22	5.52	0.67	0.46
28	driv	6.	-0.02	-0.11	5.53	0.64	0.43
29	driv	12.	-0.19	0.14	7.97	0.85	0.60
30	driv	12.	-0.06	-0.07	8.03	0.92	0.65
31	driv	12.	-0.05	-0.09	8.20	0.95	0.67
32*	blkt	60.	-0.37	0.45	4.04	8.15	6.69
33*	blkt	72.	-0.16	0.22	1.47	2.60	2.37

total driver coolant reactivity	1.03	
total driver clad reactivity	-4.92	
total driver fuel reactivity	137.09	
total internal blanket coolant reactivity		1.21
total internal blanket clad reactivity		-2.37
total internal blanket fuel reactivity		-20.42
total driver Doppler constant (no voiding)		17.92
total driver Doppler constant (na voided)		13.09
total internal blanket Doppler constant (no voiding)		37.51
total internal blanket Doppler constant (na voided)		31.44

* Channels 32 and 33 represent the radial blanket; Channel 32 consists of blanket subassemblies that are adjacent to drive subassemblies and Channel 33 consists of the remaining blanket subassemblies.

TABLE 8
SAS3D CHANNEL CHARACTERISTICS at EOC-3

channel number	type	number of subs	norm. sub power	mass flux (gm/cc-s)	average rod pow (KW)	pow/flow (J/gm)	norm. sub pow/flow
1	blkt	1.	0.33	385.2	19.92	123.6	0.62
2	blkt	6.	0.37	385.2	22.63	140.4	0.71
3	driv	3.	1.31	513.5	22.59	220.1	1.11
4	driv	9.	1.29	484.8	22.18	228.9	1.15
5	blkt	15.	0.41	438.3	25.14	137.1	0.69
6	blkt	6.	0.40	438.3	24.75	134.9	0.68
7	driv	6.	1.31	513.5	22.61	220.2	1.11
8	driv	6.	1.34	513.5	23.11	225.2	1.13
9	driv	6.	1.34	513.5	23.11	225.1	1.13
10	blkt	6.	0.43	339.6	26.62	187.3	0.94
11	blkt	12.	0.44	438.3	26.67	145.4	0.73
12	blkt	12.	0.45	438.3	27.57	150.3	0.75
13	driv	6.	1.42	551.8	24.51	222.1	1.12
14	driv	12.	1.43	551.8	24.62	223.2	1.12
15	driv	6.	1.44	513.5	24.83	241.9	1.21
16	driv	3.	1.40	551.8	24.12	218.7	1.10
17	driv	6.	1.43	551.8	24.62	223.2	1.12
18	blkt	12.	0.49	438.3	30.08	164.0	0.82
19	driv	12.	1.43	551.8	24.64	223.3	1.12
20	driv	6.	1.45	513.5	24.93	242.8	1.22
21	driv	3.	1.42	513.5	24.42	237.9	1.19
22	driv	6.	1.16	445.5	19.90	223.4	1.12
23	driv	6.	1.28	513.5	22.12	215.5	1.03
24	driv	6.	1.32	513.5	22.66	220.7	1.11
25	blkt	12.	0.45	385.2	27.33	169.5	0.85
26	driv	6.	1.34	513.5	23.01	224.1	1.13
27	driv	6.	1.33	484.8	22.92	236.5	1.19
28	driv	6.	1.30	484.8	22.39	231.0	1.16
29	driv	12.	1.06	434.2	18.22	210.0	1.05
30	driv	12.	1.10	434.2	18.93	218.2	1.10
31	driv	12.	1.12	445.5	19.20	215.6	1.03
32*	blkt	60.	0.26	239.2	16.01	159.9	0.80
33*	blkt	72.	0.10	139.6	6.19	106.1	0.53

* Channels 32 and 33 represent the radial blanket; Channel 32 consists of blanket subassemblies that are adjacent to drive subassemblies and Channel 33 consists of the remaining blanket subassemblies. These channels are not included in the power normalization used in the table.

APPENDIX B
SAS3D ANALYSIS OF THE LOF INITIATING PHASE

1. Introduction

In this Appendix we describe the geometric models, assumptions, and results for four representative SAS3D [1] analyses. These particular cases were selected to investigate the general tendencies of the CRBR heterogeneous core design to produce extensive core-wide steel blockages in the upper and lower axial blankets, extensive co-disruption of fuel and cladding, sustained or cyclic neutronic activity, and significant ramp rates during the initial stages of disruption. The emphasis is on determining and quantifying those characteristics that are of greatest importance to the subsequent disruption-phase behavior particularly fuel dispersal or removal.

The four cases analyzed were BOC-1, EOC-3, EOC-4 (fast), and EOC-4 (slow). Thus the set spans the burnup range and also an uncertainty range for EOC-4. Many more cases obviously could be performed to map the detailed response characteristics to phenomenological uncertainties and initial condition variations. However, we can see from both the Applicant's analysis [2] and our own preliminary work that the response spectrum to uncertainties and variations is continuous, largely monitonic, and weakly coupled to the uncertainties and variations. Therefore it is sufficient to consider only these representative cases that are formulated in a way that highlight and promote conservative conditions for the disruption phase.

2. BOC-1 Analysis

Geometric Model BOC-1

The fundamental idea in an SAS3D representation of the CRBR core is to lump groups of subassemblies into SAS "channels." Each channel is modeled by a representative fuel pin and its associated structure. The starting point for the BOC-1 input was the GEFR-00523 setup. The 15 channels used in this setup are shown in Figure 1. Within an individual channel the axial subassembly dimensions were taken from ANL/RAS 75-29 [3]. The coolant mesh is shown in Figure 2, while the region of the fuel pin containing the

fertile and fissile fuel is given in Figure 3. Pin radial dimensions and the surface areas for heat transfer were taken from GEFR-00523.

Also of importance in the geometric modeling is the primary loop model. A schematic of this model is given in Figure 4. The input values for this model were taken from GEFR-00523. Of particular interest is the size of the inlet plenum, which is a primary variable in determining the backpressure felt by the core during voiding. The volume input was 5.35×10^8 cm^3. This is approximately six times the actual CRBR plenum volume and is used so that sodium compressibility can be used to represent the capacitance effects induced by the changing strain on the primary vessel wall and core support structure as pressure changes. A calculation for these effects is given in ANL/RAS 76-5 [4]. The actual curve for the pump head coastdown as a function of time was taken from ANL/RAS 75-29 as

$$\Delta p_{head} = \Delta p_o \exp[-0.358t + 0.012t^2 - 0.00014t^3],$$

where Δp_o corresponds to 11.08 atm with the current input.

Results BOL-1

Boiling initiates in Channel 11 at 11.66 s. Power stays below nominal until cladding motion, which begins at 15.31 s. Cladding motion reactivity is increased over that in GEFR-00523. This results from the earlier motion initiation and the input and model changes (see Section II.3) which tend to lead to an accumulation of cladding at the core-blanket interface. Fuel motion begins at 17.94 s at 2.1 times nominal power. A series of power pulses then results from fuel slumping. However, as a result of intersubassembly incoherence and the mitigating effects of entrained fission gas (a 30 day burnup was assumed), a prompt critical burst does not develop before fuel vapor is produced in lead subassemblies, producing temporary neutronic shutdown.

Figure 5 gives the overall power and reactivity traces showing the influence of cladding relocation and fuel slumping in raising the power. Figure 6 shows the three power bursts when prompt critical was approached. Figures 7 and 8 give the individual reactivity components, illustrating the negligible influence of voiding reactivity on this transient. Clad relocation produces the reactivity rise while fuel motion controls the power oscillations. Figures 9, 10 and 11 give a channel breakdown of coolant voiding reactivity, indicating the eventual complete voiding in all driver subassemblies. Figures

12 and 13 give a channel breakdown of cladding relocation reactivity, showing little cladding relocation in low-power channels thereby setting the stage for co-disruption. Figures 14 and 15 give a channel breakdown of fuel motion reactivity showing that only Channels 9 and 11 develop appreciable positive reactivity which tends to be offset by simultaneous dispersal in other channels.

Channel 11 is the highest power channel. The final calculated configuration of Channel 11 has cladding blockages above and below the core. A maximum of about 4 atm of fuel vapor pressure exists. Channel 12 is a typical medium power channel. Its final configuration suggests an above core cladding blockage, although molten cladding is still 10 cm away from the lower core/blanket interface. Some co-disruption is indicated. Channel 2 is the last channel to void. Partial cladding and fuel melting have occurred at the termination of the calculation in Channel 2. Any further power burst might be expected to give rise to appreciable co-disruption in this situation.

The final core state is summarized in Figure 19 of Section II.3.

3. EOC-4 Analysis

Geometric Model EOC-4

The only difference in the geometric model for the EOC-4 analysis relative to the BOC-1 is the channel arrangement. We used the channel arrangement of GEFR-00523 [2] which is shown in Figure 16.

Case Assumptions

Two cases were assessed for the EOC-4 state. The first is labeled "mid-range" or "fast" because it was set up with mid-range assumptions for the primary uncertainties such as sodium void, Doppler, thermal expansion feedback, fission gas release behavior, and fuel viscosity. These assumptions are summarized in Table 2 of Section II.3. It is termed "fast" because the voiding and subsequent disruption occur rapidly as a result of the elevated power. The second is labeled "Mod 6" or "slow" because it is the sixth in a series of modifications to the mid-range case both in terms of assumptions and modelling. It represents a "slow" end-of-spectrum set of assumptions for Doppler, expansion feedback, and fission gas release characteristics along with a reduced value of void worth. The intent was to minimize, within reason, the net reactivity and therefore power escalation during early disruption. This case should maximize the clad blockage potential and minimize co-disruption.

Results ECC-4 Mid-range (Fast)

Boiling initiates first in Channel 6 at 11.66 s. The positive voiding reactivity leads to a slow progressive power increase. The power is 1.84 times nominal by the time cladding motion starts in Channel 6 at 15.18 s. This is about the time voiding begihs in a typical medium power channel, e.g., Channel 10. The rapidly increasing voiding reactivity following sodium flow reversal in the medium power channels gives little time for cladding melting and relocation before fuel motion. Fuel motion initiation occurs at 16.13 s with the reactor 10.49 times nominal power. Initial fuel motion is mainly dispersive, reducing the power to below three times nominal by 16.5 s. However, pressure equilibration does allow the SLUMPY upper segments to fall, producing a power burst reaching a peak power about 200 times nominal and marginally prompt critical. This burst leads to co-disruption in the medium power subassemblies, and SAS termination with fuel vapor pressure produced in Channel 6.

Figure 17 gives the power and reactivity traces for the voiding and fuel slumping induced bursts of this transient. Figure 18 shows how closely the net reactivity follows the fuel motion reactivity after 16.1 s. Figure 19 shows that the voiding ramp rate before fuel motion is about $1.5/s, and that most of the cladding relocation reactivity occurs after fuel motion initiation and also after the power burst suggesting extensive co-disruption. Figures 20, 21, and 22 give a channel breakdown of coolant voiding reactivity. They show that the internal blankets are beginning to void at the end of the transient, and the rather late voiding initiation in low power subassemblies. Figures 23 and 24 give a channel breakdown of cladding relocation reactivity. Only the higher power drivers (2, 4, 6 and 7) go into cladding relocation. Even here most of the cladding segment motion is a result of being carried along with or being pushed by the dispersing fuel. Figures 25, 26 and 27 give a channel breakdown of fuel motion reactivity, and indicate that fuel motions in several lead channels are combining to drive the second burst.

The final configurational results for the highest power channel, Channel 6, are given in Figures 28, 29, 30 and 31. The location of the SAs of Channel 6 in the core is shown in Figure 28. The distributions of all materials are shown in Figure 29 in terms of volume fractions. The fuel temperature distribution and channel pressure distribution are shown in Figures 30 and 31 respectively. A tendency is indicated to form cladding blockages above and below the active core. Fuel is shown to have vaporized in the center of the core, with fuel slugs being pushed toward the cladding

blockages. Figures 32, 33, 34 and 35 give the final configurational results in the same form for a typical medium power channel, Channel 10. No motion of cladding independent from fuel is calculated, and the pressures observed are those from the entrained fission gas. Channel 14 is the last channel to void. At the termination of the calculation the maximum fuel melt fraction is 0.46. The cladding temperature at the location of maximum fuel melt fraction is 1300 C. Fuel swelling and co-disruption are expected in this situation as the LOFA progresses into the transition phase.

Results EOC-4 Slow (MOD 6)

With reduced void reactivity and increased negative reactivity feedback, voiding begins at 12.91 s in Channel 6. The power is only 1.1 times nominal when cladding relocation starts in Channel 6 (16.87 s). Approximately 0.50$ of cladding reactivity is inserted by the time fuel motion starts (18.72 s), and the overall net reactivity at this time is 0.63$, which is similar to the EOC-4 cases in GEFR-00523. Only the four lead channels (2, 4, 6 and 7) disrupt on the first burst. Gas de-entrainment and the resulting fuel slumping lead to a second power burst, however. This second power burst does reach prompt critical, causing co-disruption in medium power subassemblies, and generating fuel vapor pressures in Channel 6, terminating the SAS transient. The SIMMER-II case described in Section II.5 was started at 19.75 s, after voiding in all the driver subassemblies, but before the second burst.

Figures 63 and 64 give the power and reactivity traces for this case. The delay between the first and second bursts is evident. Figure 65 shows how dependent the net reactivity is on fuel motion. This dependency is, further illustrated in Figure 66. While the cladding relocation reactivity inserted is appreciable, the changes are slow enough that it does not have a noticeable effect on the instantaneous time derivative of the net reactivity. Figures 67-69 give a channel breakdown of the voiding reactivity, and illustrate how the lower power driver subassemblies are voiding during the quiescent period following the first burst. Figures 70-72 give the cladding relocation reactivities as a function of time. They illustrate how most of the dramatic increases in such reactivities are associated with sodium chugging. Until the voiding of driver subassemblies is complete, and the inlet plenum is calculated to depressurize, quasi-steady-state considerations are apparently not enough to assure cladding relocation velocities below 1 m/s if appreciable flooding is presumed to occur. Figures 73-75 give the channel breakdown of fuel reactivity versus time. Important initial dispersal reactivity is introduced by a sodium re-entry event forcing fuel up in Channel 2. Subsequent

gas de-entrainment is an important contributor to the later power burst. The actual magnitude of the first power burst is controlled by Channel 6. Following some initial fuel dispersal in this channel, fission gas release at the ends of the pin force a limited degree of fuel compaction. This compaction is probably exaggerated by this version of SAS3D. However, the co-disruption observed in this case is judged not to be dependent on this burst augmentation mechanism. All that is required is for fuel not to be monotonically dispersive, with fuel puddling as gas de-entrains and vapor condenses to maintain neutronic activity.

Figures 76-79 give the final configuration results for Channel 6, the highest power channel. These results are similar to the mid-range case, with suggestions of an upper and lower cladding blockage restraining the vaporizing fuel. Figures 80 to 83 give results for a typical medium power channel, Channel 10. Co-disruption is seen to be reduced over the mid-range case, but some steel is present with the fuel. More co-disruption is observed in Channel 12, which voids about 0.8 s after Channel 10. This can be seen in Figures 84 to 87. Finally, the lowest power channel, Channel 14, is experiencing both simultaneous cladding and fuel melting at the end of the calculated transient.

4. EOC-3 Analysis

Geometric Model EOC-3

The SAS3D channel geometry for the EOC-3 analysis is identical to the previous cases. The subassembly channel grouping was changed however. Thirty-three channels were assigned as illustrated in Figure 88. The driver subassemblies were grouped into channels within the orifice zones indicated in the PSAR [5]. Because the heterogeneous CRBR core only has one-third symmetry, more channels were required than might seem obvious for a core with a batch reloading scheme. The internal blankets were also separated by orifice zone and power. Although several blanket channels are not necessary to compute initiating phase LOFA behavior, such a division was judged desirable to improve the accuracy of the neutronics calculations as well as providing spatial detail for the TOP analysis in Section III.

Results EOC-3

Channel 20 has the highest power-to-flow ratio, and starts to void at 12.91 s. However, all the initial subassemblies to void are in the

outer fuel annulus region, and little positive voiding reactivity is obtained until about 15.85 s. At this point sodium flow reversals are beginning to occur in the inner subassemblies, which have higher void worths. The power is up to 1.3 times nominal at the start of cladding motion (16.37 s) and 4.2 times nominal at the start of fuel motion (17.53 s). This later power level is similar to that in the slow EOC-4 case. Indeed, some of the subsequent features of the reactivity traces are similar in the two cases, which might not be too surprising with the use of identical fuel motion modeling. Two bursts are observed; the peak power reached in the first burst is similar; and while appreciable cladding relocation reactivity is seen, the reactivity shape is dominated by fuel motion. The second burst does exhibit reduced energy integration because of the incoherence introduced by the detailed channel arrangement; more subassemblies enter cladding motion because of the core-wide coherence of the EOC-3 state; and Channel 20 does not develop subassembly wall melting during the SAS3D transient as does Channel 6 in the slow EOC-4 case because of the reduced radial power factor. However, in both cases appreciable co-disruption is seen. To produce an appreciable reduction in co-disruption in the EOC-3 case probably requires both adjustments in the neutronics parameters (e.g. reduced void worth, etc.) and at least some further delay in fuel compaction following initial fuel dispersal.

Figures 89 and 90 give the power and reactivity profiles showing the double burst. Figures 91 and 92 give the reactivity components demonstrating again that the large cladding motion reactivity contribution is easily compensated by fuel motion. Figures 93-98 give the channel-dependent voiding reactivity traces showing that all driver subassemblies have at least gone into sodium flow reversal by the time of fuel motion initiation in Channel 20. Figures 99-104 give the channel-dependent cladding motion reactivity traces. In the EOC-3 case all channels (except Channel 16) enter the cladding relocation model. Figures 105-110 give the channel-dependent fuel motion reactivity traces. It is the lead subassemblies (Channels 15 and 20) which exhibit the largest gas de-entrainment and slumping, although there are many small contributions to the second burst, which starts about 18.7 s.

Conditions at the end of the calculation for the lead channel, Channel 20, are given in Figures 111-114. This material reconfiguration is similar to the previous cases. Conditions in a typical medium power channel, Channel 13 (Figures 115-118), are similar to those in Channel 10 of the slow EOC-4 case. Finally, the final conditions in the coldest driver subassembly, Channel 29, are shown in Figures 119-122. While cladding motion has started, cladding relocation

velocities are very limited due to the inlet plenum pressure reduction following voiding completion in the driver subassemblies. Again co-disruption or the potential for co-disruption is seen in the medium and low power channels. A core-wide summary of the final state is given in Figure 18 of Section II.3.

5. Summary

The results of these SAS3D analyses indicate a general pattern in which negative neutronic feedback from sustained fuel dispersal (in contrast to initial dispersal followed by gas de-entrainment and slumping) is of insufficient magnitude to offset the neutronic effect of total removal of cladding (~5$). Therefore cladding relocation over the entire core is not calculated. Typically the high power-to-flow channels, which lead the voiding and disruption process, have calculated blockages in the upper axial blanket as well as some medium power channels. These latter channels generally do not have solid blockages at the lower core interface however. The medium and low power channels typically have incomplete cladding separation prior to fuel disruption thereby establishing a co-disrupted state or the potential for such state in 1/3 to 1/2 of the core in all cases. Thus the potential for some steel-vapor assisted dispersal or removal during the subsequent disruption phase is seen as essentially universal.

Another characteristic of the calculated responses is the fuel motion domination of the net reactivity following initial fuel disruption and the resulting strong neutronic activity. This is not surprising in that the fuel worth is about 20 times that of the cladding. Thus the fuel fluid dynamics over periods greater than 0.5 s and in SA-scale geometry is important fundamentally. This is even more true for the "slow" situations where the time interval of disruption is extended.

II.4. PLENUM FISSION GAS COMPACTION

1. Objectives and Overview

A mechanism for rapid fuel compaction during the initial phases of disruption [1] is possible due to the high pressure plenum fission gases accumulated during irradiation. These pressures may build up to 30 bar during normal operation and heat up to even higher levels during the accident. Following sodium voiding and clad melting, fuel disruption occurs in the highest power-to-flow ratio subassemblies. Upon such disruption the fuel column already under compression due to the plenum fission gases becomes susceptible to axial compaction. The geometry is illustrated in Figure 1. The top portion of the severed cladding cannot withdraw upwards due to the physical constraints at the subassembly exit. Rather it forms a gun-barrel through which the fission gas pressures may eject the upper axial blanket together with any non-disrupted portion of the fuel column beneath it forcefully downwards. The resulting increases in reactivity and power accelerate the accident causing an avalanche of additional fuel disruptions and ejections. The concern of a potentially autocatalytic behavior and high energetics is obvious.

Clearly, substantial blanket pellet/clad mechanical interaction could strongly interfere and might even mitigate this compaction mechanism. However, there is no basis for claiming such behavior. Also, the rapid dissipation, by blowdown, of the plenum pressure prior to fuel disruption could help alleviate this concern. This mitigating mechanism may be evaluated analytically.

The Applicant considered this energetic mechanism in response [2] to our Question #3 (see Table 2 of Section I), and concluded that an energetic outcome would not be expected. This result was based on SAS3D analyses that indicate gas blowdown prior to fuel disruption. We do not agree with this assessment.

2. Key Parameters

The key parameters affecting such a sequence of events are summarized in Table 1. The initial plenum fission gas pressure is a function of the fuel burnup. However due to the blowdown following

clad failure (typical time constants for associated pressure decay estimated at approximately 0.5 to 1.5 s) only a fraction of this pressure will be available for fuel compaction upon disruption of the fuel column. This delay between clad failure and fuel motion is in turn affected by a number of parameters as listed in Table 1. Finally, the ejection potential would depend by the degree of friction between the intact upper portion of the cladding and the sliding pellets.

The variation of the plenum gas pressure with burnup is shown in Figure 2. We observe that reasonably high pressures dominate for nearly one-half of the fuel exposure time period. The mass of retained fission gases accumulated during irradiation is also shown in the same figure. We note that within the relative short exposure of 25-50 days the fuel is reasonably "gasee" such that dispersal (i.e. TREAT experiments L6 and L7) rather than slumping would be expected upon disruption. We conclude that the end-of-cycle (EOS) range of the spectrum is appropriate in this assessment and for consistency dispersive fuel behavior will be assumed. In fact the sensitivity to fuel motion assumptions is not great as long as one stays away from the reasonably unexpected compacting (slumping) behavior.

3. Analysis Methods

The SAS3D computer code was utilized in these evaluations. The incorporation of the plenum fission gas effects on the clad relocation phenomena was already described in Section 3 of II.3. Here we will summarize the modelling and benchmarking of the blowdown model.

Our experience with plenum fission gas effects is limited to the TREAT R-8 test. It was run with prepressurized pins and, as mentioned earlier, it produced no upper clad blockages. The blowdown occurred within ~1 s, and well before fuel disruption, hence it did not provide any information on the compaction mechanism of concern here. However, the plena pressure transients were reported and although the geometry is not exactly applicable to the problem at hand (i.e. inconel reflector and depleted UO_2 insulator pellets in the R8 versus blanket pellets in the CRBR), these results can be used, at least, as a convenient frame of reference.

The R8 geometry is shown in Figure 3. The reported diametral gap of 10 mills appears inconsistent with the indicated clad failure location (top of active core) and the observed blowdown rates.

Consequently, for best estimate purposes we assumed the clad failure occurred ~2" below the top of the active fuel. This failure site was displayed by one pin in the post test examination.

Because the flow was turbulent, the pressure drop was assumed to scale as $L/D^{1.25}$, where L is the flow length and D is the hydraulic diameter. The routine used to calculate depressurization was the SAS3D subroutine PIPFLO. Because PIPFLO cannot accommodate multiple flow areas, the effective length is determined by

$$L_{eff} = D_{fuel}^{1.25} \left[(L/D^{1.25})_{reflector} + (L/D^{1.25})_{insulator} + (L/D^{1.25})_{fuel} \right]$$

Table 2 gives the relevant quantities for this equation leading to an effective length of 4.785 in. or 12.16 cm.

This leads to the comparison to the test data shown in Figure 4, if a friction factor, f, is defined by

$$f = 0.1264\ Re^{-0.25}$$

where Re is the Reynolds number. This friction factor is 1.6 times the standard Fanning friction factor. A plot of this friction factor relationship on a tube flow chart is given in Figure 5.

Extrapolating to the reactor case, calculated depressurization time constants are given in Figure 6. These were obtained under EOC LOF conditions assuming pin failure at the top of the active fuel. The best estimate time constant is seen to be 0.4 s. Because the cold fabricated gap was used in the correlation to the R8 experiment, the best-estimate gap calculation did not take credit for thermal expansion in the reactor situation.

The clad failure was calculated to occur when its circumferential stress at the top active core node exceeded the failure stress. This failure stress was based on the un-irradiated 20% cold-worked 316 stainless steel data of [3]. The correlation used is given in Figure 7.

Upon fuel disruption (at ~ 50% radial melt fraction criteria) the upper pin segment, including the axial blanket, were subjected to the fission gas plenum pressure. The motion was calculated as if only limited by the pellet inertia, i.e. neglecting friction with the cladding.

4. Accident Analysis Results

We have carried out extensive parametric evaluations using the SAS3D code. At the low level of early reactivity feedbacks, the LOFA evolves slowly allowing sufficient time between clad failure and fuel disruption to assure complete plenum blowdown prior to loss of fuel column integrity and hence negligible compaction potential. At the high level of assumed reactivity feedback, the accident proceeds fast and essentially undiminished plenum gas pressures are available for compaction. However, the reactivity prior to the initiation of such compactions is already near prompt critical and insufficient pellet acceleration time (and thus reactivity augmentation) is available prior to disassembly by fuel vapor pressures. That is over the space of the important reactivity feedbacks an intermediate maximum of the accident severity occurs as schematically illustrated in Figure 8. Our effort here will be to provide an upper limit to this intermediate maximum.

The results of such a bounding calculation are summarized in Figures 9 and 10. The details are given in Appendix A. This case study is a restart of the mid-range EOC-4, reference, initiating phase calculation (see Table 2 of Section II.3), at the time of initial fuel disruption, but now taking into account the plenum fission gas compaction effects.

The power burst shown in Figure 9 is characterized by a net reactivity ramp rate of ~ \$50/s. The core material configurations at the time of this power burst are schematically depicted by the bar-charts of Figure 10. The sodium void maps indicate that the core is about half voided and autocatalytic fuel pin failures in sodium-filled channels, known as LOF-d-TOP, cannot be excluded. Also shown on this figure are remaining plenum gas pressures together with radial melt fraction for each one of the 11 driver subassembly groups. From this figure the important core-wide incoherency effects in limiting the extent of the fuel compaction process may be visualized. As may be seen from the clad melt fraction maps both core axial ends remain unblocked providing escape paths for the high pressure fuel/steel mixtures in the post burst period. That is, accident termination is projected provided the LOF-d-TOP is avoided.

5. Summary and Recommendations

Due to intrasubassembly incoherencies we expect that only about one-half of the pins producing compaction in our calculations would in fact be able to do so. As a consequence the already modest level of energetics given here as an upper bound may in reality be limited to values as low as 35 $/s, i.e. barely qualifying as an energetic event. However, the potential for an LOF-d-TOP is troublesome and highly undesirable. We recommend, therefore, that a design fix be implemented to inhibit the precipitous manifestation of the high gas pressures upon the fuel column as disruption occurs. No particular difficulties are envisioned with development of such a design change.

TABLE 1
KEY PARAMETERS FOR THE PLENUM FISSION GAS COMPACTION CONCERN

- Stored Fission Gas Plenum Pressure
- Timing Between Clad Failures & Fuel Melting
  - Sodium Void Worths and Voiding Rates
  - Clad Failures and Relocation Rates
  - Relocation Trends of Disrupted Fuel
- Pellet/Cladding Friction

TABLE 2
QUANTITIES FOR DETERMINING THE EFFECTIVE LENGTH
FOR PIPFLO IN FITTING THE R8 TEST

Quantity	Length	Hydraulic Diameter	$L/D^{1.25}$
Reflector	5.7 inches	0.0101 inches	1780.22
Insulator Pellets	0.792 inches	0.0096 inches	263.56
Fuel Column	2 inches	0.0051 inches	1467.46
Effective Values Used	4.7854	0.0051 inches	3511.2

APPENDIX A
SAS3D ANALYSIS OF PLENUM FISSION GAS COMPACTION

1. Introduction

In this appendix the SAS3D [1] analysis of a representative case with plenum fission gas compaction of the fuel is presented. The process itself is described in Section II.4. The reference case selected is identical to the "mid-range" or "fast" case of Section II.3, Appendix B. A number of cases with other assumptions and conditions were explored during the review period preceding this independent assessment. It was found that the general behavior was not unique to a narrow band of assumptions or conditions except that it is most important in the latter part of the burnup cycle.

Because the SAS3D geometric model is identical to that of Section II.3, Appendix B, it will not be repeated here. A brief discussion of the treatment of plenum gas blowdown and plenum gas acceleration of the fuel column is provided along with detailed results.

2. Unique Modeling

The unique modeling introduced for this analysis consists of 1) transient gas blowdown through the annular gap between upper axial blanket pellets and their cladding, 2) triggering of the blowdown process, 3) fuel column dynamics with plenum pressure as the upper boundary condition, and 4) triggering of the fuel column motions. The modeling of the blowdown and its benchmarking is discussed in Section II.4. The blowdown is triggered when the cladding of the uppermost core node reaches a high temperature burst condition based on pin pressure and cladding temperature. The resistance to gas flow in the annulus of the active core fuel column is assumed to be too large to permit significant blowdown for earlier, in-core cladding failures. The fuel column dynamics is achieved by modifying the SAS3D upper-pin-segment model to utilize the plenum pressure as an acceleration term in addition to gravity. The column motion is triggered when the fuel column in the active core is disrupted locally (melt fraction criterion) and the cladding at the core/UAB interface is failed axially (torn off).

3. Results EOC-4 Fission Gas Compaction Case

As calculated with the best-estimate plenum fission gas release model described in Section II.4, the Channel 7 plenum pressure, when Channel 7 enters fuel motion, is 25 atm. In this mid-range (fast) case, Channel 7 is the second channel to initiate fuel motion. If the remaining plenum gas pressure is postulated to compact the fuel below it, a power burst should be obtainable. Such a burst was calculated for the current parametric case. The power and reactivity traces for this burst are shown in Figure 1. The burst starting at 16.26 s inserts about 7 full-power-seconds. Figure 2 delineates the fuel motion reactivity, and can be used to obtain about a \$50/s ramp rate near prompt critical. Figure 3 shows the negligible reactivity contributions of voiding and cladding motion on the burst. Figures 4, 5 and 6 give the channel details of the voiding reactivity during the power burst. Only Channel 13, which is in the process of flow reversal at elevated power, shows any real change during this time. Figures 7 and 8 show the influence of the development of dispersal fuel pressures on cladding motion in the lead subassemblies. Figures 9, 10 and 11 give the channel dependent fuel reactivity traces. Channels 2 and 4 are seen to undergo some plenum fission gas induced compaction. Channels 12, 14, and 15 are predicted to enter TOP-type behavior (based on a 50% melt fraction pin failure criterion) during the burst.

Figures 12-15 give the final conditions for the highest power channel, Channel 6. The most interesting feature is the presence of sodium in the lower axial blanket. The moving cladding segments are prevented from entering this sodium by the SAS3D model. In turn, these cladding segments are limiting the degree of downward fuel motion. An interaction with liquid sodium can also be inferred from the final configuration shown in Channel 10 (Figures 16-19). Here co-disruption has occurred with both steel and fuel overlapped into liquid sodium. Finally, Figures 20-27 show the results in the unvoided channels. Because the SAS/FCI model of SAS3D was judged to be physically unrealistic, the analysis was not pursued directly. The concurrent failure of pins into the unvoided or recently voided channels was explored with SAS3D/EPIC [2]. As would be expected, the power burst is sufficiently large to cause coherent failure of all pins with a potential failure location bias toward the mid-plane. The internal fuel motion in the pins then dominates the subsequent reactivity leading to unacceptable results.

4. Summary

The results of this representative calculation indicate the potential for severe consequences if the pellets of the upper axial blanket are capable of free slip motion. These consequences are not the direct result of the compacting fuel (autocatalytic propagation by this mechanism does not occur because of the inertia of the pellet columns) but from the induced, coherent LOF-d-TOP in the low power channels. Thus it appears prudent to eliminate or de-rate this mechanism by an appropriate means.

II.5. REFERENCE DISRUPTION PHASE BEHAVIOR

1. Objectives and Overview

The mechanistic analysis of the LOFA beyond the initiating phase is a formidable task and one for which there are few precedences and limited experience. However, the nature of the neutronically active disruption phase is such that its treatment by simple, quasi-static approaches may be misleading, overly conservative (if conservative in this context even can be defined a priori), and necessarily speculative. An integral perspective on the complex, transient, coupled, nonlinear disruption process can be very valuable for guidance and orientation. Therefore we have attempted such a whole-core, coupled (fluid dynamically and neutronically), transient analysis of a CRBR disruption sequence to establish a reference viewpoint for simpler scoping and bounding analyses.

The modelling approach and major assumptions are described in Appendix A. The calculated results are discussed in the following section. We have found these limited results very useful in the overall assessment of the CRBR energetics potential and have made numerous links to other sections of this report.

2. Reference Disruption Phase Analysis

The results of a reference whole-core disruption phase calculation for EOC-4 are presented in this section. The model used for this analysis is described in Appendix A. The initial conditions were obtained directly from SAS3D for the "slow" EOC-4 case of Section II.3. The transformation of this voluminous detailed data also is discussed in Appendix A along with the crucial modeling assumptions.

These types of analyses are very complex and are difficult to portray without the aid of a variety of graphics. We will attempt to highlight the progression of the disruption and in particular trace the movements of materials with time. Because the material motions are strongly related to the neutronic behavior, we have overlaid the reactivity response on the global material inventory records.

The driver fuel configuration at time zero for SIMMER-II (19.75 s for SAS3D) is shown in Figure 1. Most of the core's outer channels have not disrupted at this time. The SAS3D results (see Section II.3) show a burst at about twenty seconds or about 0.25 s on the SIMMER-II time scale. The reactivity history shown on Figure 2 also shows a burst at this time and is roughly the same magnitude as seen from Figure 3 which shows the power history. This provides some confidence that the overall behavior has been preserved through the transformation between codes.

The overall neutronic history shown on Figures 2, 3 and 4 for reactivity, power, and integrated energy, respectively, show three distinct behavioral characteristics. The first 1.5 s shows a very repetitive cyclic pattern with a period of 0.4 s. This is very consistent with the gravity drainback time constants. We can see the connection between the neutronic and fluid behavior in Figure 5 showing the total driver fuel inventory in the bottom four nodes of the core. The reactivity responds each time this inventory increases indicating slumping. The inventory is reduced following each power pulse as expected because of the upward discharge from the slumped region. During this period the temperature of the fuel is high and the heating of subassembly walls is rapid. This is evident on Figure 6 which shows the driver fuel that enters the internal blankets. The time at which the curves depart from zero is when gap flow begins indicating that driver walls are at the solidus energy state. As seen, all gaps are accessed within the first second. This is consistent with the greatly increased extent of disruption evidenced in Figure 7. From Figures 6 and 8 we can see that internal blanket begins to fail at about 1 s.

Another characteristic of the behavior during this early period is the tuning of the fluid dynamic response on a core-wide extent. We can see the result of it in Figure 8 and the synchronization of the fluid responses before and after each power pulse in Figure 9.

A change in character occurs after 1.5 s. The cyclic neutronic response terminates. The core is now capable of large radial motions as seen on Figure 10 from the radial interchange between the two regions of the annular pool and on Figure 11 which shows the breakdown at the internal blankets. The failing walls are permitting fuel to fill the voided coolant volume of the internal blankets. Because there is more of this volume in the central region of the core, a radial in-flow occurs to establish a new common level. The reactivity swings back to supercritical as a result. The inward material motion can be seen by comparing Figures 12 and 13. The process is slow because of internal blanket stubs inhibiting the in-slosh.

By 3.5 s we have established the full-core pool as seen in Figure 14 and suffered a substantial out- and up-slosh with a deep subcritical neutronic state. It falls back as seen from the reactivity response in Figure 2 at 3.7 s. The subsequent in-slosh can be seen in Figure 10 as interchange between regions 3 and 4. It appears that the central region participates only weakly in this radial sloshing. The central region still contains more blanket material (it hasn't homogenized or equilibrated) and has a reduced temperature because of this large heat sink. The general location of the fertile blanket material is shown in Figure 15. The curves give the inventory of blanket material in each blanket/driver region pair. The central three regions (curves 1, 2 and 3) all increase slightly with time until about 4 s. It is only after the final slosh at 4 s that appreciable additional blanket material appears in the outermost region.

A further explanation for the weak participation of the central region in the sloshing process and indeed an explanation for the weak sloshing behavior itself between 3 and 4 s can be seen from the distribution of specific power in the core. A sequence of these distributions is shown in Figure 16. As more fuel slumping occurs in the outer regions and as internal blanket slumping occurs in the inner region (0-2 s) the peaking of the specific power in the outer slumped region becomes very dramatic (compare Figures 16a through 16c). As radial sloshing occurs in the 2-4 s time interval, the outer peaking still exists but is reduced by the out-sloshes that increase neutron leakage. This is very evident in Figure 16f where we see a complete reversal of the peak location. However, as the pool reassembles, the outer peaking returns as seen in Figure 16g. Its magnitude is greatly diminished at this time. Again the reversal is seen in Figure 16h after another out-slosh. The important finding in this calculated behavior is that the sloshes are incoherent radially because of the outer power peaking thereby preventing the occurrence of the radially focused, coherent in-sloshes with their attendent large ramp rates.

There is a clear tendency for the sloshing to amplify in the time interval from 2.5 to 5 s as seen in both the reactivity and ramp rate histories shown in Figures 2 and 17 respectively. The ramp rates grow from the order of 10 \$/s up to about 70 \$/s before the critical state is lost because of fuel removal (see Figure 19). The growing height of the sloshes as seen in Figure 18 from 3.5 to 5 s also attests to the amplification.

The core inventory history, given on Figure 19, provides major insight into the core behavior. The burst at 4 s causes approximately 500 kg of fuel to discharge from the core. This additional loss causes the reactivity state to decrease by about 10 \$ thereby

preventing the system from suffering a recriticality on the slosh back. Because the internal blanket material has not homogenized, the system will be unable to go recritical again. Fuel loss will continue, however, until core pressures decay. As seen in Figure 20 much of the fuel removal has taken place in the lower axial blanket. The IB gap removal is not very efficient in this model because of the closed reservoirs that simulate the LAB gaps (see Appendix A). Recall also that removal into radial blanket and reflector gaps is prevented by the modeling assumptions.

We can obtain a feel for the potential for fuel removal to the radial blanket and reflector regions by considering the availability of these gaps (when do the outermost driver walls reach their solidus energy) and the pressure for removal. The radial gap availability is seen from Figure 21 showing the outer driver SA wall temperature at several near mid-plane locations. The solidus condition is met at about 2 s. Thus these large paths would be available for a major part of the transient and would therefore have a major influence on the termination tendency (i.e. would promote dispersal). The complete pressure history for the 1/3 elevation in the core for each driver region is given in Figure 22. Each power pulse produces a pressure transient that is similar in character but of different magnitude depending on the incremental energy added (see Figure 4). The mean pressure level is abut 5 to 6 atm which is sufficient to produce substantial fuel removal.

3. Summary

The reference disruption phase calculation was intentionally selected as a conservative representation of a spectrum of initial conditions. In addition, the analysis itself was performed very conservatively by using a high effective component viscosity for particles to restrain fuel discharge, neglecting radial blanket removal paths, control rod removal paths, derating internal blanket gap removal, allowing a high quenching potential for the disrupted internal blanket material, and fixing initiating phase blockages to be completely passive and indestructible. Even with all these conservative aspects, the analysis produced sufficient fuel removal to terminate the neutronic activity (~ 22% removed). The cylindrical pool was entered. Growing neutronic oscillations occurred but the incoherent sloshing induced by outer region power peaking and the low void in the critical pool mitigated the ramps and the yields. A major aspect of the results is the role of internal blankets, even if completely disrupted, in suppressing the neutronic state and amplification potential prior to homogenization. A more realistic analysis would have produced substantially more fuel removal and therefore shown even more support for dispersal favored termination.

APPENDIX A
WHOLE-CORE DISRUPTION PHASE MODEL

1. Introduction

The capability to perform an integrated analysis of the disruption phase is relatively new and has not been utilized widely. It was previously attempted by Bohl [1] for the CRBR homogeneous core, Luck [2] for the conceptual design study and Maschek [3] for SNR-300. Experience has been gained and many valuable insights obtained. This appendix describes the application of this mechanistic capability to the heterogeneous core of CRBR with the objective of gaining a reference viewpoint on the complex coupling between the fluid dynamics and neutronics and the disruption progression in general.

2. Geometric Model

The purpose of an analysis of this type is to continue in a reasonably mechanistic manner the detailed treatment of the initiating phase treatment by SAS3D. This requires preservation of geometry in a general way in terms of SAS3D channel volumes and approximate radial location. This latter desire is not achievable in practice because SAS3D groups scattered subassemblies into channels and for SIMMER-II we must transform that channel into an annulus. Axial geometry is preserved and expanded to include some of the sodium pool and UIS.

The case analyzed is the mild or slow EOC-4/LOF. This case was selected as a conservative attempt to envelop the disruption phase energetics potential. Of particular importance in selecting an appropriate case is the blockage distribution (should be maximized), the expected lifetime of the internal blankets (radial power shape and blanket power), and the likelihood of early fuel removal to the radial blankets. We made the choice to use the slow EOC-4/LOF initiator. It is expected to have rapid melt attack on internal blankets (minimum time to whole-core pool), delayed access to the radial blankets (delayed massive fuel removal), but not necessarily the maximum flow channel blockage extent (BOL is worse).

The SAS3D channel arrangement is shown in Figure 1 for the case of interest. The resulting SIMMER-II geometric model is shown in Figure 2 with correspondence between SAS3D channels and SIMMER-II rings given in Table 1.

The simulated inlet plenum provides a common and connected boundary condition at the inlets to the subassemblies. Thus fluid dynamic events that occur in a particular channel have the opportunity to influence other channels or rings. The plenum is obviously too small compared to CRBR but this size, coupled with an enhanced sodium compressibility, has been chosen to give a reasonably prototypic dynamic response.

SIMMER-II does not have a primary loop model so we elected to provide a length of inlet pipe to produce a proper static head on the inlet plenum. The loop flow has largely stopped at this time anyway.

The collector plenum above the core and the UIS simulation are provided to permit sodium re-entry and a dynamic boundary condition in terms of inertia and thermal characteristics.

The internal blankets IB1, IB2, IB3 and IB4 are modeled as gap channels. This means that the interiors of the IB's are fluid dynamically passive and the gaps are active. The IB gaps connect to the gaps in the axial blanket part of the IB's and into reservoirs in the lower reflectors of IB1, IB2, and IB3. These reservoirs are sized to correspond to the volumes of the lower axial blanket gaps of the neighboring drivers.

3. Initial Conditions

The transformation from SAS3D was made at 19.75 s on the SAS3D time frame. It was selected because it is a quasistatic state as seen on Figure 3 and provides for overlap of the two methods thereby permitting a check on the validity of the transformation.

The thermal/physical state is transformed mechanistically with an interface code called SASSIM [4]. It bridges the various calculational meshes within SAS3D and between SAS3D and SIMMER-II. It also bridges the material property differences and modeling differences according to predefined prescriptions. Examples of these prescriptions are preservation of pressure, preservation of crucial geometry such as blockages, and elimination of artificial mixtures of liquid sodium and liquid fuel or steel.

The cladding blockage (assumed complete) extent is as follows: rings 2, 4, 6, 7, 8, 9, and 10 are blocked at the top, and rings 6 and 7 are blocked at the bottom. These blockages are shown on Figure 2.

4. Modeling Assumptions

The neutronic approach used is the same as used for other transient neutronics aspects of this assessment. Transport theory is used with 18 group cross-sections. The neutronics mesh extends over the active core and surrounding blankets only. Some of the larger fluid-dynamic meshes are subdivided as shown on Figure 2.

The fluid dynamics model assumptions are consistent with standard engineering correlations or the standard SIMMER-II models [5]. The specific important assumptions are: (1) the effective component viscosity for solid particles has been selected as 10 to be consistent with the discussion in Section II.6, (2) intact pin disruption is assumed to occur at a melt fraction of 50%, (3) subassembly walls are assumed to permit radial flow at the solidus energy, (4) gap flow is initiated when the neighboring driver wall is at the solidus energy, (5) the Los Alamos fuel equation of state is used, (6) maximum liquid dispersion size is 1 cm diameter, (7) solid particle diameters are set at 1 mm, and (8) thermal attack occurs on the interior of blanket subassemblies subsequent to complete wall melting in the gap channel.

TABLE 1
CHANNEL TO RING CORRESPONDENCE

SIMMER-II Ring Number	Type	SAS3D Channel	Number of Subassemblies
1	IE	1	7
2	D	2	12
3	IB	3	18
4	D	4	18
5	IB	5	36
6	D	6	6
7	D	7	12
8	D	11	12
9	D	11	12
10	D	10	18
11	IB	5	30
12	D	13	18
13	D	12	12
14	D	15	24
15	D	14	18
16	RB	16	60
17	RB	12	72

II.6. DISPERSAL BY EXTENDED FUEL MOTION

1. Objectives and Overview

In the previous section we saw that neutronic activity persists throughout the progression of core disruption states. However, we also saw a natural tendency of the system to resist development of large recriticalities. Both of these trends strongly favor a "dispersal" rather than a "disassembly" termination. In order to establish a common frame of reference as well as a conservative bias to the relative trend between these two termination modes, the manifestation of "dispersal" was deliberately minimized in the analysis of the previous section. Indeed, the insensitivity to obtaining large recriticalities translates into an insensitivity in timing margins for fuel removal, and the neutronic activity implies the persistence of "pumped-up" conditions and that of driving forces for dispersal. In addition, dispersal path availability would increase with time (and level of core disruption) as more fuel, blanket and control rod assembly duct walls melt and as old blockages remelt either by direct heating (fuel-containing blockages) or by melt attack (steel blockages). It is the purpose of this section to quantify these effects and hence to estimate more realistically the tendency for the "dispersal" path, as a function of the degree of core disruption.

The fundamental prerequisites for timely "dispersal" are the availability of fuel escape paths, the ability of core materials to move through these paths, and the existence of discharge pressure to provide the required rates. Each of these aspects is considered in the subsequent sections and generic fuel removal estimates are made.

Fuel escape paths may be found in the inter-pin (available to start with) and the inter-S/A-gap (becoming available as S/A duct walls melt) spaces as illustrated in Figure 1. In the latter category blanket-to-blanket gaps would be particularly effective since their heating lags considerably behind the melt through of fuel assembly duct walls. In the heterogeneous CRBR core design, in view of the internal blankets, such effective gaps would be considerably more numerous than in the homogeneous design, providing thus a considerably enhanced potential for mild termination. This subject of initial escape path availability is addressed in the next section. On the

other hand, the continuing availability over the time required for termination is equally important.

Steel (cladding or duct wall) boundaries define both kinds of paths, hence, as a minimum, the escaping molten fuel (or fuel/steel mixture) will be subjected to approximately 1,000°K cooler temperatures (i.e., difference between the fuel and steel melting points) at these boundaries. As a consequence of this strong cooling effect, the effectiveness of these paths in allowing the required fuel removal must be assessed against the potential for re-freezing and plugging during this dispersal process. Owing to dimensional (characteristic dimensions: inter-pin path approximately 3.5 mm, inter-gap paths approximately 5.5 mm) and geometric differences, between the two path types, the propensity for such behavior will differ. A generic characterization in this regard is attempted in Section 3 below. Finally, in Section 4, these results are integrated with a representative range of driving pressure transients, as deduced from Section II.5, to quantify the "dispersal" potential.

The Applicant's analyses considered this topic in substantial detail [1, 2] and concluded that "dispersal" ("meltout" in his terminology) would occur prior to the disruption of the internal blankets (i.e. prior to the formation of a whole-core, cylindrical pool). Our evaluation of these analyses is documented in [3, 4]. The present independent study differs from that of the Applicant not only in the use of considerably more sophisticated analysis tools, but also by its attempt to more closely quantify the forces available to drive the "dispersal" (i.e., Sections 4 and II.5). Our results indicate that internal blanket disruption could occur substantially sooner than expected by the Applicant. However, the fuel escape rates appear capable of keeping pace, especially in view of the massive creation of new escape paths into the radial blanket gaps just about simultaneously with entry into the whole-core pool phase. Thus avoidance of the whole core homogeneous pool is similarly (with the Applicant) concluded.

2. Fuel Escape Path Availability

In this section we summarize the fuel removal path characteristics, sizes, and general availability during the disruption sequence. The various reservoir sizes are also delineated.

The first fuel removal paths available are the normal flow channels from the active core into the upper and lower axial blankets. Their

availability on a core-wide basis is primarily determined by the initiating phase transient response. From Section II.3 the SAS3D predicted cladding blockages can be obtained. Because the upward cladding relocation tendency is moderate to weak, upper clad blockages will tend to be of the order of centimeters in thickness and perhaps initially incomplete. With the relatively short time duration of the disruption phase, meltout of such blockages will not occur in general. In addition, the partial occlusion of the channel by the blockage will act as a strong inhibitor to all but superheated fuel flow at the leading edge. Therefore, it is appropriately conservative to consider such blockages "effectively" complete and sustained.

The flow channel volume in the axial blankets is relatively large, particularly when the freezing and plugging process effectively ablates the cladding and convects it to a downstream location as discussed in Appendix A. The resulting volume for core materials is about 50%. Assuming a fuel steel mixture of nominal proportions, the two axial blanket could accommodate 70% of the core fuel.

The other path for early fuel removal is through the blanket-blanket or blanket-control gaps within the core. We restrict this removal mode to these gaps alone because the driver walls will tend to deform against each other and against the internal blankets and control assemblies as illustrated on Figure 2, because the drivers lead in pressure and temperature. These gaps (one side of a hex assembly) allow for axial removal to the upper and lower axial blanket gaps and total about 90. The flow will generally initiate in the gap channel when the wall of the discharging subassembly approaches its melting point. This can occur anywhere along the height of the core as thermal conditions dictate. Thus, channel access is virtually guaranteed.

In the reactor case (EOC-4), the gaps will be narrowed partially by radiation-induced swelling and will have increased "effective" heat capacity at the lower-core/lower-axial-blanket interface because of sodium in the gaps and within the lower part of the internal blankets. The in-core swelling is not a concern because the gap can be accessed at virtually all axial elevations at the cost of some minor time delay. Also, any in-core fuel occlusion will be remelted at each power burst. Therefore, the primary issue is the potential for occlusion at the exit of the gap channel where it discharges into the lower axial blanket gaps. As the neutronic activity continues during the early disruption phase, fuel in the lower active core is heated to a disruption criterion of partial melting. Any frozen fuel in an adjacent gap will be disrupted also by remelting, because the flux

shifts toward the core bottom for slumping recriticalities. Even frozen fuel in the top of the lower axial will receive sufficient heat for remelting. This can be seen from the strong flux shape changes for the slumping configurations of Section II.7 and from the reference disruption phase analysis of Section II.5. As a result the gap channel will remain open for fuel removal.

In order for gap fuel removal to occur in a timely and substantial way, the reservoir for fuel deposition must be large and it must be available. The volume fraction of gaps in the lower axial blankets is about 8%. The resulting gap volume including the axial blanket section of the radial blankets is 0.109 m^3. The mix of material will typically be in proportion to the nominal ratio in the core except for density changes at melting and previous cladding relocation. If we use a liquid fuel to steel liquid volume ratio of 1.36 and assume that this mixture will occupy the gaps, the lower axial blanket reservoir will hold a maximum of 600 kg or approximately 10% of the driver fuel.

The third major avenue for fuel removal is into the gaps of the radial blanket following failure of the peripheral driver subassembly walls. This occurs late in the annular pool phase or at the beginning of the cylindrical pool phase. The flow channels are radially outward and contain changes in direction. The total outward flow area is on the order of 0.3 m^2 which is an order of magnitude larger than the total IB gap flow area. The volume in the gaps of the radial blanket for the active core height is 0.118 m^3 and it would contain about 600 kg of fuel (approximately 10%).

A very large volume is available in the radial reflector region such that the reservoir appears unlimited in terms of accommodating sufficient fuel for permanent subcriticality.

The rate of fuel expulsion is, of course, related to the magnitude of the driving pressure, taking into account the presence of sodium in the gaps initially and the flow resistance across the load pad planes that controls its escape. For example, based on simple steady-state flow approaches with a nominal total flow area at the load pad planes of about 0.06 m^2 and a hydraulic diameter based on load pad clearances, several atmospheres of pressure would be required to discharge 1 m^3 of sodium in 2 s. However, if the inventories of the lower and radial blanket gaps are of primary interest, then about 0.2 m^3 of sodium would need to be displaced requiring perhaps 0.1 atm.

The final fuel removal paths are the empty control rod assemblies. They are nominally cold relative to the disrupted core and protected by residual sodium flow. However, some are located directly adjacent to peak power driver subassemblies. Estimates have been made of the time to fail the control subassembly walls but are uncertain. We can be sure that they will not survive for very long if corner cracks develop and cause rapid voiding by small scale fuel injection through the cracks. They represent a large shunt for core material transport, particularly downward. More than 10% of the core inventory can be accommodated downward without requiring flow through the inlet orifices.

We can conclude, therefore, that because of the porosity represented by voided coolant channels, intersubassembly gaps, and withdrawn control rods, and because the volume necessary to accommodate approximately one-third of the core is small (approximately 0.5 m^3 if steel included), there is no problem with reservoir capacity. The available paths to access this capacity increase with disruption extent such that large scale disruption with sustained high inventory retained in the core must be difficult to maintain.

3. Freezing and Plugging Behavior

The problem of quantifying freezing in, and plugging of, fuel escape paths under reactor conditions has been a controversial one for the better part of the last decade. The fundamental difficulty arises because the fuel solidifies at a temperature of more than 1,000°K higher than the steel melting point, such that substrate melting may occur during the fuel freezing process. Such melting is important because it may imply destruction of the insulating fuel crusts (due to the much lower fuel thermal conductivity as compared to that of the steel) and hence much higher heat losses and freezing and plugging potential. As far as predictability is concerned this behavior transforms an otherwise straightforward heat transfer calculation (conduction controlled crust growth and plugging by channel occlusion) to an extremely complicated, interactive, fluid flow and heat transfer problem including the phenomena of slurry formation, substrate entrainment and mixing, and crust stability. Further complications include variable fuel/steel inlet composition, variable compositions along the channel length due to preferential deposition and/or entrainment, transient pressure driving forces and complicated flow path geometries. It is our opinion, therefore, that the conduction model is an oversimplified and, hence, inappropriate tool for such applications.

After the rejection of this fundamentally-derived tool only prototypic material and geometry tests, under carefully controlled conditions, can provide the basis for quantifying fuel removal. Such experimental basis is at present very limited, but work is continuing in several laboratories. Our approach at this time is based on a generalized multiphase, multicomponent flow and heat transfer model that accounts for all complications mentioned above and that automatically reduces to the conduction model when the appropriate conditions apply (i.e. one component flow, stable crusts). This model is described in detail in Appendix A. It was benchmarked against the available prototypic material experimental data, as discussed in the same Appendix. In this section we present and discuss the fuel removal and penetration trends predicted by this model for the reactor geometry and conditions.

- Pin Bundle Geometry

The geometric model used for the one-dimensional benchmarking against the 7-pin thermite tests (Appendix A) was modified to represent a 217 pin, CRBR subassembly from the active core mid-plane to the top of the fission gas plenum. The thermite injector was replaced with the active core section. The same 5 cm noding was used. This "real" geometry and "real" material model together with our generalized freezing and plugging model were used to investigate the fuel removal potential through CRBR pin bundles for a spectrum of conditions and discharge transients.

The first series of results, Figure 3, show the effects of discharge pressure and initial fuel superheat. All these results assume an isothermal, single phase, fuel discharge driven by a constant pressure at the core mid-plane. An effective component viscosity of 200 times the liquid fuel value is used for the solid phase in a particulate slurry. The effect of superheat is seen to be small as expected because crust thickness does not dominate this process nor does the somewhat higher initial fuel energy. The early part of the penetration shown on Figure 3 is more inhibited by fuel superheat because it causes earlier cladding ablation and subsequent fuel particle formation. The significant point to note from these results is that nearly all of the fuel of the upper half of the core can be discharged quickly if pressures of the order of 5 atm are sustained for about 0.5 s.

Generally the figure-of-merit considered in assessing freezing and plugging models and data is fuel penetration distance. For recriticality potential we are more interested in mass discharged. Obviously penetration and removal are related directly in the

subassembly geometry. For these same cases we have plotted the penetration distance versus pressure in Figure 4. A penetration of about 35 cm corresponds to complete removal of one-half the subassembly contents (we consider 1/2 upward and 1/2 downward because the motivating neutronic activity roughly divides the fuel mass after each burst). There is a plateau in penetration versus pressure response because of the tendency to freeze large steel occlusions in the "spring" region if the spring heat capacity is included as part of the wall. The spring does not have good contact with the cladding (line contact if any) and therefore should not be included as rapid response heat capacity. The result is greater, more reliable, penetration into the low heat capacity, high flow area region above the blanket pellets. This can be seen for the "burst driven" results on Figure 4. In reality the "no spring" curve would be off-scale if the hot material could flow inside the cladding in the fission gas region as it did in Spencer's [1] 2.0 kg, hot wall test.

The second set of results shows the fuel removal potential for a discharge following a burst during the early subassembly disruption phase. The core material is assumed to be a mixture of cladding steel (co-disruption) and fuel that is 50% solid and 50% liquid. The steel and fuel are thermally equilibrated at the fuel melting point. The discharge is driven by power bursts of different magnitudes with a representative CRBR axial power shape. Thus small bursts produce low discharge pressures and have particulates at the leading edge. The cladding steel is assumed to be physically distributed on a scale for rapid heating by the fuel (in less than 0.2 s) and is therefore the pressurizing material. The correspondence between burst energy in full-power-seconds (FPS) and steel vapor pressure can be seen on Figure 4. The relationship is exponential because of the Clapeyron equation.

The results in terms of penetration distance are given on Figure 4. The "with spring" and "constant press" results agree well up to 10 atm (3 FPS) and then diverge as the superheat effect becomes dominant at high burst energies. Figure 5 shows rapid and complete discharge in all cases.

The third set of results, shown on Figure 6, indicate the influence of the effective component viscosity for solid particles on removal assuming no superheat and a constant pressure of 5 atm. Even with a high assumed value of 2,000 times the liquid fuel value, a high fraction of the fuel in the upper 1/2 subassembly is removed. The rate is greatly reduced, however. This lengthened removal time is important if the lifetime of the discharge pressure is short compared to the discharge interval.

- Subassembly Gap Geometry

A large set of calculations was performed with our model to determine the discharge characteristic of fuel and fuel/steel mixtures through gap channels under a variety of conditions. A detailed discussion of one particular calculation is given below to provide a view of the general problem. Then some additional results are provided to characterize the general fuel removal potential of the gaps.

The analyses have been oriented toward the fuel discharge through the gaps between internal blankets. These gaps are important as early removal paths. They can be visualized as channels connecting the active core to the reservoir space represented by the gaps in the lower axial blanket. As such, the discharge will not be short-term. We can expect it to continue until occlusion, reservoir fill-up, or channel disruption by wall melt-through.

The calculational model represents a slab as shown in Figure 7. A plane of symmetry is placed at the middle of the gap. Typically the channel length of interest (core mid-plane to lower axial blanket) is about 0.5 m. The gap lateral length is undefined in two-dimensional slab geometry but is implied to be 1 m. Thus for the calculational channel to represent one side of a hex subassembly, the calculated mass discharges were multiplied by the true hex-side dimension in meters.

Consider first a multicomponent discharge that is representative of a disruption phase that is energy starved or has had some upper internal blanket breakup to give perhaps 35% by volume particles in the stream material. Also, subassembly wall melting has occurred to raise the steel content to 40% by volume. The remainder of the stream is liquid fuel (25%). All materials are assumed to be at the fuel melting point which is typical for such slurries. The gap wall is assumed to have an axial temperature distribution running from 860 K at the exit to near the melting point at the inlet. These are conditions that could exist for an EOC-4 core where the sodium has boiled out of the internal blankets and further heatup has occurred by conduction from a neighboring driver wall that is in physical contact. An injection pressure of 0.4 atm is assumed. This pressure is of the order of the gravity head of the fuel/steel pool.

The results are portrayed visually on volume fraction plots. The solid materials are layered from right to left and the mobile materials (liquids and particles) from left to right. Figure 8 indicates the initial state. A 1 m channel is used to demonstrate the freezing and

plugging potential. The reservoir at the end of the channel is of arbitrary size. Figures 8 through 15 show the evolution of the flow and channel characteristics. Figure 9 shows the fuel crust forming on the ablating wall. In this calculation the molten steel under the crust is assumed to entrain into the stream as it forms. This is a major uncertainty in calculations of this type. It is difficult to justify a completely stable crust and at the same time complete, instantaneous entrainment. The choice used here is conservative with respect to quenching the stream (forming more particles) but nonconservative from the standpoint of continually opening the chanrel by wall meltout. This situation has been considered at both extremes and the uncertainty is not a major influence because of the opposing effects.

Figure 10 shows the downstream steel blockage being generated at a position where the fuel particle/steel slurry has cooled by convective heat loss to the wall. The crust does not grow at the downstream location because the liquid fuel has been depleted by plate-out and bulk freezing (the particles from this mode are shown as indicated on Figure 9). Also seen is the particulate "blowby" generally seen in experiments. In the calculation the steel is depleted by plateout leaving only particles to convect downstream. At 1 s a substantial occlusion has formed and the steel/particle slurry is accumulating on its upstream side. The crust does not grow rapidly in this case because the low liquid fuel volume fraction is preventing full access of the liquid to the crust surface.

In the longer time frame the channel fills behind the blockage which is at a distance of about 0.7 m. Thus in the reactor situation the occlusion would be well within the lower axial blanket and would permit radial flow into the neighboring gaps. Other calculations at higher driving pressures (1 to 2 atm) completely ablate the channel with no stoppage.

If we return to the internal blanket geometry with a channel 0.5 m long and calculate the fuel removal capability for different situations, we obtain the results on Figure 16. The areas under the curves represent the mass removed through the 0.5 m length channel with a lateral extent equal to one side or flat of the hex subassembly. The injection in these cases is fuel only. The effect of superheat is to increase throughput initially because of delayed crust growth. The wall ablates and introduces large quantities of liquid steel into the stream which reduces the velocity throughput until it is transported out of the channel. Then the throughput increases rapidly because of the open, non-ablating channel. The increased pressure produces higher throughput initially, more rapid

wall ablation, and a quicker return to high flow. Typical fuel removal quantities for the superheat cases is approximately 15 kg/gap, occurring within approximately 1 s, even if the later flow re-establishment is neglected. Given the large number of gaps (see Section 2) an important fraction of the core inventory potentially can be removed in this way.

4. Fuel Discharge Pressures

From the mechanics of freezing and plugging discussed in Appendix A, it is clear that high discharge pressures are desirable for assuring large quantities of fuel discharge from the core. Most estimates of fuel removal are made on a quasi-static basis for simplicity and clarity. To make estimates of whole-core fuel removal on this basis requires some insight into the general characteristics of the discharge pressures in heat loss environments and transient neutronic heating.

We have seen from both the reference initiating phase and reference disruption phase analyses that the general environment for fuel removal is non-uniform, complex, and highly transient. The disruption begins with the core in an energy-poor state relative to all molten and at an average temperature incapable of producing a sustained pressure differential of 5 atm. This pressure would generally assure massive fuel removal if paths are available and the time frame is a couple seconds. Thus an absolute pressure of approximately 7 atm is required. If fuel vapor must supply this pressure, a temperature of approximately 4230 K is necessary. On the other hand, if steel is available, its temperature need only be about 3570 K.

These temperatures are such that heat losses to any remaining structures would be very high (crusts would not be present). Thus these states will tend to exist locally and temporarily only. Indeed their localness and temporaryness are the causes of the subsequent recriticalities. This implies that the loss of locally high temperature is a non-sustainable state if a potentially critical inventory still exists and fission gases are largely de-entrained (fuel is not levitated by noncondensible gas). What we need to know is a typical pressure decay history between the power, temperature, and pressure spikes associated with recriticalities. We would not expect this history to be linear because of the exponential relation between pressure and temperature.

To obtain a characterization of this pressure history a number of subassembly scale calculations were performed with various initial conditions, power pulses and heat loss assumptions. These calculations are described below.

The geometric model for the analysis is based on single subassembly dimensions as shown in Figure 17. The nominal subassembly wall is included at a temperature of 1240 K. This would be consistent with an early disruption phase state. The calculations were performed with SIMMER-II in a non-neutronic mode. A programmed power pulse was used along with the power distribution shown in Figure 17. The calculational mesh is also given.

The calculations are initiated from a slumped state that implies a possible recriticality. All boundaries are closed. The pressure decay is a function of fluid mixing (hot into cold--this should be minimal in this one-dimensional representation), heat loss to the wall, and heat loss to entrained wall steel.

The results for this group of calculations indicate characteristics that are generally similar. Following the power burst the upper part of the mass is driven upward typically reaching the top in 0.1 s or less depending on the bubble pressures. Gravity then acts to reflux the upward displaced mass into the original pool region. For the various cases listed in Table 1, this reflux process is shown on Figures 18a through 26a. The reflux time interval is made up of a waiting time (time between initial dispersal and initiation of refluxing) and a reflux interval (time for upper slug spreading). In nearly all cases the overall reassembly time is 0.5 to 0.6 s. For the initial wall condition chosen, wall steel entrainment has little influence on the fallback time because the initial crust formation delays surface melting by more than 0.6 s. The cases with the small amount of entrained steel initially are representative of subassemblies that disrupt somewhat earlier and have just begun to entrain steel. These situations are much more dynamic because there is insufficient steel to cause quenching. Case 32 represents a case with 30% cladding steel from initiating-phase co-disruption. These cases with steel exhibit very different characteristics on a time scale greater than 0.6 s but in their early response they are similar to the others.

The pressure available for fuel discharge is the pressure near the location of peak power. The pressures at these locations for the various cases are shown on Figures 18b through 26b. Clearly the discharge pressures are enhanced and sustained if small quantities of steel are present. The limiting situations are associated with fuel

vapor pressure when no non-condensible gas is present as in Case 21. Here pressure decays rapidly because of more expansion (no gas to take up volume). Even for this case the average pressure (see Table 2) is 6 atm.

The situation will clearly be different if a subassembly has massive distributed heat sinks such as large quantities of unequilibrated particles and/or steel. If many subassemblies are in this condition, neutronic activity will continue if the need for removal still exists.

Because low pressure conditions cannot be sustained in a neutronically active system, fuel removal pressure sufficient for at least periodic removal is available. As seen in the previous section, the time for pin bundle penetration is a few tenths of a second if pressures are in the 5 to 10 atm range. During early disruption, bursts of the necessary magnitude to produce 5 to 10 atm of fuel vapor pressure are common for lead subassemblies (see Sections II.5 and II.7). Because co-disruption occurs for the majority of situations, particularly in low power subassemblies, steel vapor pressure enhancement will be commonplace.

Similarly, using the conservative estimate of 15 kg/gap over a period of approximately 1 s, obtained for the range of pressures shown in Table 2, we can estimate that approximately 13% of the driver fuel would escape through the 90 gaps within the lifetime of the pressure pulse. It is important, however, to recognize that another pressure pulse will follow within a fraction of one second, remelting some of the frozen fuel in the gaps and thus allowing the removal process to continue.

5. Summary

Based on the fuel discharge characteristics predicted by our physically based, detailed, and benchmarked model, we have estimated the whole-core fuel dispersal potential as summarized in Table 3. The various paths are identified along with the times of availability (Section II.5). The rates of removal for each path are maximums because all paths of a particular type are assumed to act simultaneously. To be conservative we should assume that the rates are only one-half of those listed to account for incoherence. There are special cases that involve the rapid removal of sodium from the paths prior to or coincident with fuel discharge. These are the high rate or high area paths, RB and RR gaps and control SAs. To be conservative and to be consistent with the only existing integral analysis [5] of fuel discharge into sodium filled gaps with prototypic

load pad resistance, we will assume rates 1/10 as large as those listed in Table 3 for these three paths. The capacities listed in Table 3 are those conservatively associated with each path and are available prior to the homogenization of the whole-core pool. The bottom-line estimate of likely dispersal prior to the energetics prone homogeneous pool phase is obtained by applying the reduced rates over the time intervals for removal (5 s minus the path access time) for each path to obtain the removal per path (cannot exceed the available capacity) and then summing over the paths. The results are presented in Table 4. The distribution of removal capability is such that neutronic termination can be achieved prior to the availability of radial blanket and control SA removal paths. However, the margin would not be large. The later removal through the large area paths provides large margin to assure a dispersal termination prior to the formation of the homogeneous pool.

TABLE 1
VARIATION MATRIX FOR SUBASSEMBLY DISRUPTION ANALYSIS

Case #	C02	C03	C04	C06	C13	C14	C21	C32	C33
Noding	1x39	1x39	1x39	1x39	4x39	4x39	1x39	1x39	1x39
Energy Input (FPS)	3	3	3	3	3	1.5	3	3	3
Initial Pool Void (%)	5	5	5	5	5	5	5	5	5
Cover Gas	NC	NC	NC	NC	NC	NC	C	NC	NC
Initial Steel (% Cladding)	0	0	0	0	0	0	0	0.30	0.02
Wall Heat Transfer	Yes	Yes	Yes	Yes	Yes	Yes	Yes	Yes	Yes
Steel Entrainment Melt Fraction (%)	100	0	100	0	70	70	0	0	0
Entrained Steel Effective Dispersion Size (m)	0.01	0.01	0.0001	0.0001	0.0001	0.0001	0.0001	0.0001	0.0001

TABLE 2
RESULTS FOR THE SUBASSEMBLY DISRUPTION ANALYSIS

Case #	Peak Press (MPa)	Fallback Time t_f(s)	Press (t_f) (MPa)	P_{avg} (MPa)
C02	0.8	0.6	0.6	0.7
C03	0.8	0.6	0.6	0.7
C04	0.8	0.6	0.6	0.7
C06	0.8	0.6	0.6	0.7
C13	2.5	0.5	2.5	2.5
C14	9.5	0.6	8.5	0.9
C21	0.8	0.5	0.4	0.6
C32	2.7	0.5 + boilup	0.6	1.6
C33	2.2	0.5 + boilup	0.6	1.4

TABLE 3
FUEL ESCAPE PATH AVAILABILITY AND CAPABILITY FOR EOC-4

Path	Characteristics	Access Time (s)	Removal Rate[1] (% of Inventory/sec at 5 atm)	Capacity at Initiation of Homogeneous Pool Phase (~ 5 s) (%)
Upper Axial Blanket	Pin-structure	0	6	12[2]
Lower Axial Blanket	Pin-structure	0	12	25[3]
IB gaps to LAB gaps	Vertical Gaps/Horizontal Gaps	1-2	21[6]	10
IB gaps to UAB gaps	Vertical Gaps/Horizontal Gaps	1-2	21	1[7]
Gaps in RB	Horizontal Gaps/Vertical Gaps	2-4	200[8]	10
RB gaps to RR gaps	Horizontal Gaps/Vertical Gaps	2-4	200[8]	>40
Control rods	Large diameter (0.1 m)	3-4	100[4]	10[5]

(1) Rates based on all available paths acting simultaneously.
(2) ½ SAs initially blocked plus 0.5 long-term removal effectiveness - based on Figure 6.
(3) Reduced penetrations assumed for colder walls of LAB (UAB x 0.5).
(4) Rate of removal if sodium previously removed below orifices.
(5) Assumes no upward removal or downward flow through inlet orifices.
(6) Based on Figure 16 with 90 gaps and no gap sodium impedance.
(7) Load pads block gaps plus a 0.5 factor for effective long-term removal.
(8) Assumes no gap sodium impedance.

TABLE 4
ESTIMATE OF TOTAL FUEL DISPERSAL
PRIOR TO THE HOMOGENEOUS POOL PHASE

Path	Discharge Time (s)	Adjusted Rate (% inventory/s)	Maximum Removal (% of inventory)
UAB	5	3	12
LAB	5	6	25
IB/UAB	3	10	10
IB/LAB	3	10	1
RB	2	20	10
RB/RR	2	20	40
CONTROL	2	10	10
		Total	100

APPENDIX A
THE MODELLING OF FREEZING AND PLUGGING

1. Introduction

Fuel dispersal was evaluated by means of a transient flow model taking into account freezing and plugging phenomena. This model is described in some detail in this appendix. The overall approach is to include in the formulation all flow and phase-change processes that are expected, on physical grounds, to participate, and to deduce certain quantitative aspects of this model definition by comparison with prototypic material experimental data, and exact analytical results that are available for certain idealized, limit conditions. This benchmarking procedure is also included here.

2. Freezing and Plugging Model

The model is composed of a number of submodels for heat transfer, momentum transfer, mass transfer, configurations of solid structures and liquids, and equation of state all tied together by the conservation equations. The multiphase, multifield, numerical treatment is implemented within the basic SIMMER-II framework.

2.1. Configuration

Within a local region solids are characterized primarily in terms of mass, surface area, intact geometry (for original structures) or supporting substrate (for frozen crusts) and temperature. The liquid components are characterized primarily by their masses and temperatures. All the liquid components in a mesh cell are assumed to exist as discrete droplets moving with a common velocity. The droplet radius for each component is determined by the minimum of five constraints: (1) fluid-dynamic breakup based on a Weber number criterion, (2) the hydraulic diameter, (3) the liquid mass available, (4) flashing breakup, and (5) droplet coalescence. The droplet radius and component mass determine the total surface area for each component in the mesh cell. Because solids can break up below the liquidus energy and droplets can freeze within the liquid phase, solid particles are represented in the liquid phase as spheres with radii specified by the model user. The vapor components are assumed to have a common temperature and velocity and a single set of thermophysical properties determined by the thermophysical properties and relative amount of each component in the mixture. Figure 1 depicts a typical local region.

2.2. Conservation Equations

a. Mass Conservation

In the solid phase the mass conservation equation for each component is

$$\frac{\partial \bar{\rho}_{Sm}}{\partial t} = -\Gamma_{Sm} \tag{1}$$

In the liquid phase each component is subject to the following

$$\frac{\partial \bar{\rho}_{Lm}}{\partial t} + \nabla \cdot (\bar{\rho}_{Lm} \vec{V}_L) = -\Gamma_{Lm} \tag{2}$$

while the conservation of mass for the gaseous components results in

$$\frac{\partial \bar{\rho}_{Gm}}{\partial t} + \nabla \cdot (\bar{\rho}_{Gm} \vec{V}_G) = -\Gamma_{Gm} \tag{3}$$

The mass transfer terms Γ_{Sm}, Γ_{Lm} and Γ_{Gm} can be positive or negative depending on the net mass transfer rates from all sources, i.e. freezing/melting, vaporization/condensation, etc. The mass transfer models are described in Section 2.3b.

b. Energy Conservation

In the solid phase the energy conservation equation for each component is

$$\frac{\partial \bar{\rho}_{Sm} e_{Sm}}{\partial t} = Q_{Sm} + {}^{N}Q_{NSm} \tag{4}$$

where

$$Q_{Sm} = q_{HSm} + q_{\Gamma Sm} + q_{KSm} \tag{5}$$

In the liquid phase the energy conservation equation for each component is

$$\frac{\partial \bar{\rho}_{Lm} e_{Lm}}{\partial t} + \nabla \cdot (\bar{\rho}_{Lm} e_{Lm} \vec{V}_L) = Q_{Lm} + NQ_{Lm} \quad (6)$$

where

$$Q_{Lm} = q_{HLm} + q_{\Gamma Lm} + q_{KLm} + q_{VLm} \quad (7)$$

Because each component in the gaseous phase is assumed to have the same temperature, the mixture is treated as a single component subject to the following energy conservation equation

$$\frac{\partial \bar{\rho}_G e_G}{\partial t} + \nabla \cdot (\bar{\rho}_G e_G \vec{V}_G) = - p \nabla \cdot (\alpha_G \vec{V}_G + \alpha_L \vec{V}_L)$$

$$+ Q_G + N \sum_m \bar{\rho}_{Gm} Q_{NGm} \quad (8)$$

where

$$Q_G = q_{HG} + q_{\Gamma G} + q_{KG} + q_{VG} \quad (9)$$

and the first term on the right side of Equation (8) represents the pressure-volume work (expansion or compression) which is assigned entirely to the gaseous phase. The energy transfer terms in Equations (5), (7) and (9) are described in Section 2.3a with the exception of the cell-to-cell viscous heating terms, q_{VLm} and q_{VG}.

c. Momentum Conservation

The solid phase is assumed to be an infinite momentum sink. Because each component in the liquid phase is assumed to have the same velocity, the mixture can be treated as a single component with respect to the conservation of momentum.

$$\frac{\partial \bar{\rho}_L \vec{V}_L}{\partial t} + \nabla \cdot (\bar{\rho}_L \vec{V}_L \vec{V}_L) = - \alpha_L \nabla p + \bar{\rho}_L \vec{g} + \Gamma_{GL} \vec{V}_G$$

$$- (\Gamma_{LS} + \Gamma_{LG}) \vec{V}_L + K_{GL} (\vec{V}_G - \vec{V}_L) - K_{LS} \vec{V}_L$$

$$+ \nabla \cdot (\overleftrightarrow{\pi}_L \cdot \vec{V}_L) \quad (10)$$

The last term on the right side of Equation (10) describes the viscous drag between adjacent mesh cells. The gaseous phase can be described similarly with a single momentum equation because all the components have the same velocity

$$\frac{\partial \bar{\rho}_G \vec{V}_G}{\partial t} + \nabla \cdot (\bar{\rho}_G \vec{V}_G \vec{V}_G) = -\alpha_G \nabla p + \bar{\rho}_G \vec{g} + \Gamma_{LG} \vec{V}_L - \Gamma_{GL} \vec{V}_G \cdot$$

$$+ K_{GL}(\vec{V}_L - \vec{V}_G) - K_{GS} \vec{V}_G + \nabla \cdot (\vec{\vec{\tau}}_G \cdot \vec{V}_G) \qquad (11)$$

where, again, the last term on the right side of Equation (11) describes cell-to-cell viscous drag. The interphase drag terms, K_{LS}, K_{GS} and K_{GL} are described in Section 2.3c.

2.3. Transfer Process Models

a. Heat Transfer

Heat transfer can occur between solid components in contact with one another at a rate determined by the following

$$q_{HSmSk} = A_{Skm} \frac{h_{Sm}\, h_{Sk}}{h_{Sm} + h_{Sk}} (T_{Sk} - T_{Sm}) \qquad (12)$$

where

$$h_{Sm} = h_{Smo} (\alpha_{Smo} / \alpha_{Sm}) \qquad (13)$$

The initial heat transfer coefficient, h_{Smo}, is specified by the user, and Equation (13) shows that the heat transfer coefficient, h_{Sm}, increases if the thickness of the solid (proportional to α_{Sm}) decreases.

Heat transfer can occur between liquid components and solid components exposed to the flow (with the exception of solid particles in the liquid). The solid component heat transfer coefficient is given by the product of the pure liquid heat transfer coefficient and a multiplier that accounts for multicomponent, multiphase effects

$$q_{HLmSk} = A_{Sk} \frac{h_{LSm}\, h_{Sk}}{h_{LSm} + h_{Sk}} (T_{Lm} - T_{Sk}) \quad (14)$$

$$h_{LSm} = h_{LSmo} \left[\frac{\alpha_{Lm}}{\alpha_L} f(\alpha_G, \alpha_L, R) \right] \quad (15)$$

where

$$h_{LSmo} = \frac{k_{Lm}}{D_h} \left[C_{HL1m} \left(\frac{\rho_{Lm} V_L D_h}{\mu_{Lm}} \right)^{C_{HL2m}} \left(\frac{\mu_{Lm} C_{pLm}}{k_{Lm}} \right)^{C_{HL3m}} + C_{HL4m} \right] \quad (16)$$

and

$$f(\alpha_G, \alpha_L, R) = \frac{\alpha_G \max(0, 2R-1) + \alpha_L \min(1, 2R)}{\alpha_G + \alpha_L} \quad (17)$$

The two-phase weighting factor, R, in Equation (17) can be varied from 0 to 1 to simulate flow regimes with increasing contact between the liquid and wall.

Heat transfer between liquid components is based on a droplet collision model similar to the droplet coalescence model used in the calculation of droplet radii. The total heat-transfer rate is the product of the collision frequency and the energy exchange per collision

$$q_{HLmLk} = R_{mk} \frac{45}{8} \frac{1}{\frac{r_{pm}}{k_{Lm}} + \frac{r_{pk}}{k_{Lk}}} \frac{\alpha_{Lm}\, \alpha_{Lk}}{(1 - \alpha_S)^2} \frac{r_{pm}^2 + r_{pk}^2}{r_{pm}^3\, r_{pk}^3}$$

$$\cdot (r_{pm} + r_{pk}) [\min(r_{pm}, r_{pk})]^2 (T_{Lk} - T_{Lm}) \quad (18)$$

or if r_{pm} is very small

$$(q_{HLmLk})_{max} = 15 \frac{\alpha_{Lk}}{1 - \alpha_s} \frac{\alpha_{Lk}}{r_{pk}^2} (T_{Lk} - T_{Lm}) \quad (19)$$

Heat transfer between the vapor and liquid or solid is assumed to occur only during phase transition. The heat transfer coefficients are calculated from standard correlations with adjustable parameters similar to Equation (16). The determination of vapor-structure surface area contains logic to preclude phase transition on the structure if α_G is less than $\alpha_{GS\Gamma}(1 - \alpha_S)$, where $\alpha_{GS\Gamma}$ is specified by the user. The determination of liquid-vapor surface area contains logic to switch from a droplet flow regime to a bubble flow regime representation when α_G is less than α_L; however, in such cases it is assumed that the bubble radius is equal to the droplet radius calculated for each component.

b. Mass Transfer

Mass is transferred between the liquid and solid phases by melting and freezing. Liquid component m will freeze on a solid when the interfacial temperature between the two phases is less than the freezing temperature of liquid component m and $(\alpha_{Lm}/\alpha_L)f$ is greater than 10 percent, where f is the two-phase weighting function defined by Equation (17). The interfacial temperature is determined by balancing the convection from all the liquid components with the conduction in the solid

$$(T_i)_{SkL} = \frac{h_{Sk}\, T_{Sk} + \sum_m h_{LSm}\, T_{Lm}}{h_{Sk} + \sum_m h_{LSm}} \qquad (20)$$

where h_{Sk} is given by Equation (13) and h_{LSm} is given by Equation (15). If freezing is occurring the interfacial temperature is set equal to the freezing temperature in the heat transfer calculations, and the imbalance in the heat fluxes from liquid convection and solid conduction determines the freezing rate

$$\Gamma_{LmsN} = \frac{h_{Sk}\,(T_{MELT,m} - T_{Sk}) + \sum_p h_{LSp}\,(T_{MELT,m} - T_{Lp})}{h_{FUS,m} + C_{vLm}\,(T_{Lm} - T_{MELT,m})} \qquad (21)$$

In Equation (21), Γ_{LmSn} is the freezing rate of liquid component m on solid component n; the two components must be the same material, e.g. water/ice, liquid steel/solid steel, etc. However, before an appreciable amount of liquid has frozen, conduction in the solid phase is based on conduction in the solid substrate (Sk) on which the frozen crust is forming. After a significant amount of crust has

formed, Sn replaces Sk for determining the subsequent freezing rate from Equation (21). The sensible heat term in the denominator of Equation (21) appears because liquid component m must be desuperheated before it can freeze.

If the interfacial temperature from Equation (20) exceeds the solid components' melting temperature and none of the liquid components are predicted to freeze, then the interfacial temperature is set equal to $T_{MELT,k}$ and the melting rate becomes:

$$\Gamma_{SkLj} = \frac{h_{Sk}(T_{MELT,k} - T_{Sk}) + \sum_{p} h_{LSp}(T_{MELT,k} - T_{Lp})}{h_{FUS,k} + C_{vSk}(T_{MELT,k} - T_{Sk})} \quad (22)$$

where Sk and Lj must represent the same material. The sensible heat term in the denominator of Equation (22) appears because solid component k must be heated to the melting point before it will melt.

If the interfacial temperature exceeds the solid melting temperature, but a liquid component is freezing, then the energy of the solid will increase beneath the freezing crust. Because the mechanical integrity of the solid becomes dubious above the solidus energy, a failure model has been incorporated to address this situation. The user sets the failure energy between the solidus and liquidus, and when the solid's energy exceeds this point the solid is assumed to begin failing. Additional modelling flexibility is provided by allowing the user to specify the proportion that fails as liquid rather than particles, and this proportion also applies to the interfacial freezing/melting model described above. Because the melted material and particles enter the liquid phase at the liquidus and solidus energies, respectively, while the solid remaining after failure initiation is assumed to be at the failure energy, energy conservation requires that the liquidus proportion exceed the fraction of the latent heat of fusion that defines the failure energy.

Within the liquid phase the components transfer heat to one another, so that the particle volume fraction may increase or decrease as liquids freeze or particles melt, respectively.

Vaporization and condensation can occur at liquid-vapor and vapor-structure interfaces as previously mentioned. The simple vaporization/condensation model is similar to the interfacial freezing/melting model because it is based on setting the interfacial temperature equal to the saturation temperature and comparing the resulting heat fluxes into and out of the interface. A net heat flux

into the interface results in vaporization, while the converse results in condensation. Because the saturation temperature depends on the partial pressure of the vapor component, the vaporization/condensation model is more complicated than the freezing/melting model.

The mass fluxes associated with freezing/melting and vaporization/condensation also transport energy

$$q_{\Gamma Sm} = e_{SOL,m} \sum_k (\Gamma_{LkSm} - \Gamma_{SmLk}) \tag{23}$$

$$q_{\Gamma Lm} = e_{LIQ,m} \sum_k (\Gamma_{SkLm} - \Gamma_{LmSk} + \Gamma_{LkLm} - \gamma_{LmLk} + \Gamma_{GkLm} - \Gamma_{LmGk}) \tag{24}$$

$$q_{\Gamma Lm} = e_{SOL,m} \sum_k (\Gamma_{SkLm} + \Gamma_{LkLm} - \Gamma_{Lmk}) \tag{25}$$

$$q_{\Gamma G} = \sum_m [e_{VAP,m} \sum_k (\Gamma_{LkGm} - \Gamma_{GmLk})] \tag{26}$$

Equation (24) applies to liquids, and the Γ_{LkLm} terms apply to liquid-particle freezing/melting transfer. Equation (25) applies to particles, and the Γ_{LmSk} term is absent because particles cannot go directly into the solid (structure) phase. Because sublimation is not modelled, no such terms appear.

c. Momentum Transfer

Momentum transfer between the phases is caused by drag forces and mass exchange. The pressure drop caused by drag between the two-phase, gas-liquid mixture and the structure is given by the Martinelli correlation.

The friction factors and correlation exponent are given by the following correlations

$$\nabla_{p2\phi} = \phi_L^2 \nabla p_L = \phi_G^2 \nabla p_G \tag{27}$$

where

$$\nabla p_L = -\frac{2f_L}{D_h} \rho_L |j_L| \vec{j}_L \tag{28}$$

$$\nabla p_G = -\frac{2f_G}{D_h} \rho_G |j_G| \vec{j}_G \tag{29}$$

and

$$\phi_L^2 = \left[1 + (1/X^2)^{1/n}\right]^n$$

$$\phi_G^2 = [1 + (X^2)^{1/n}]^n \tag{30}$$

with

$$X^2 \equiv \frac{\phi_G^2}{\phi_L^2} = \frac{f_L \rho_L |j_L|^2}{f_G \rho_G |j_G|^2} \tag{31}$$

The friction factors and correlation exponent are given by the following correlations

$$f_L = 16/Re_L, \quad Re_L \leq 2000 \tag{32}$$

$$f_L = C_{fL1} Re_L^{CfL2}, \quad Re_L \geq 2000 \tag{33}$$

$$Re_L = \frac{\bar{\rho}_L D_h |j_L|}{\sum_m \alpha_{Lm} \mu_{Lm}} \tag{34}$$

$$f_G = 16/Re_G, \quad Re_G \leq 2000 \tag{35}$$

$$f_G = C_{fG1} Re_G^{CfG2}, \quad Re_G \geq 2000 \tag{36}$$

$$Re_G = \frac{\bar{\rho}_G D_h |j_G|}{\alpha_G \mu_{G,mix}} \tag{37}$$

$$n = 4.0, \quad Re_G \geq 2000 \quad \text{and} \quad Re_L \geq 2000 \tag{38}$$

If the liquid and gas momentum equations are added together and the acceleration, phase change and body force (gravity) terms are neglected, the result is

$$(\alpha_L + \alpha_G) \nabla p_{2\phi} = - (K_{LS} \vec{V}_L + K_{GS} \vec{V}_G) \tag{39}$$

Substituting Equation (27) into Equation (39) yields

$$\alpha_L \phi_L^2 \nabla p_L + \alpha_G \phi_G^2 \nabla p_G = - (K_{LS} \vec{V}_L + K_{GS} \vec{V}_G) \tag{40}$$

This suggests the following general interphase coupling coefficients

$$K_{LS} = \frac{\phi_L^2 \nabla p_L}{|V_L|} (\alpha_G + \alpha_L) f(\alpha_G, \alpha_L, R) \tag{41}$$

$$K_{GS} = \frac{\phi_G^2 \nabla p_G}{|V_G|} (\alpha_G + \alpha_L) [1 - f(\alpha_G, \alpha_L, R)] \tag{42}$$

where the two-phase weighting factor, R, can be varied from 0 to 1 to simulate flow regimes with increasing contact between the liquid and wall.

A particle viscosity model has been developed to simulate the frictional effects of particles in the liquid phase. Because of both the theoretical and practical complexity of modelling particle effects from first principles, the particle viscosity model is heuristic in nature. In addition to a user specified value for the particle viscosity used in Equation (34), the model includes logic for determining when the particle radius exceeds the local hydraulic diameter or when the particle volume fraction exceeds a user specified maximum packing fraction. In either case, the liquid-structure momentum coupling coefficient given by Equation (41) is increased by the following multiplier

$$K_{jam} = \begin{cases} 10^{10} \max[10^{-10}, (\min(1, \bar{\rho}_{Lg}/|\nabla P|))^5], & 2r_p \geq D_h \\ \dfrac{\max^{10^{-10}}, (\min(1, \bar{\rho}_{Lg}/|\nabla P|))^5], \quad 2r_p < D_h}{\max[10^{10}, \quad 1 - \dfrac{\alpha_p/(1-\alpha_s)}{\alpha_{p,\,max}}]} \end{cases} \quad (43)$$

The dimensionless pressure gradient term in Equation (43) rapidly decreases K_{jam} to unity as $|\nabla p| \, 100 \, \bar{\rho}_L g$, and it simulates the tendency of large pressure gradients to dislodge blockages.

The liquid-vapor momentum coupling coefficient is given by

$$K_{GL} = \frac{3\bar{\rho}_G}{2\alpha_G \left(\frac{\alpha_G}{1-\alpha_s}\right)^{\lambda-1} \left[\frac{\alpha_G}{1-\alpha_s} - \alpha_0\right]} \left(3\nu_G \sum_m \frac{\alpha_{Lm}}{r_{pm}^2} + \frac{C_o}{4} |V_{LG}| \sum_m \frac{\alpha_{Lm}}{r_{pm}} \right) \quad (44)$$

which is based on stokes flow over a sphere for low Reynolds numbers and form drag on spheres for high Reynolds numbers. α_0 is the value of α_G at the transition between single-phase and two-phase flow, and α_G^2 accounts for drag in highly packed particle beds.

2.4. Equations of State

The system of equations consisting of the conservation equations from Section 2.2 and the constitutive equations from Section 2.3 is not a closed system. The system is closed with the addition of material equations of state.

The equation of state for material m is given by

$$e_{Sm} = C_{vSm} \, T_{Sm}, \quad T_{MELT,m} \quad (45)$$

$$e_{SOL,m} = C_{vSm} \, T_{MELT,m} \quad (46)$$

$$e_{LIQ,m} = e_{SOL,m} + h_{FUS,m} \quad (47)$$

$$e_{Lm} = e_{LIQ,m} + C_{vLm} (T_{Lm} - T_{MELT,m}) \tag{48}$$

when $T_{Lm} \leq 2/3\ T_{CRIT,m}$

$$e_{Lm} = e_{LIQ,m} + C'_{vLm}(T_{Lm} - 2/3\ T_{CRIT,m}) + a_{Lm} - 1/2\ h^{+}_{VAP,m} \tag{49}$$

when $T_{Lm} \geq 2/3\ T_{CRIT,m}$

$$e_{CON,m} = e_{LIQ,m} = C_{vLm} (T_{SAT,m} - T_{MELT,m}) \tag{50}$$

when $T_{SAT,m} \leq 2/3\ T_{CRIT,m})$

$$e_{CON,m} = e_{LIQ,m} + C'_{vLm}(T_{SAT,m} - 2/3\ T_{CRIT,m}) + a_{Lm} - 1/2\ h_{VAP,m} \tag{51}$$

when $T_{SAT,m} \geq 2/3\ T_{CRIT,m}$

$$e_{VAP,m} = e_{CON,m} + h_{VAP,m} - p\nabla V_m \tag{52}$$

$$e_{G,m} = e_{VAP,m} + C_{vGm} (T_G - T_{SAT,m}) \tag{53}$$

$$e_G = \sum_m e_{G,m} \overline{\rho}_{Gm} / \sum_m \overline{\rho}_{Gm} \tag{54}$$

where

$$p_{v,m} (T_{SAT,m}) = p^*_m e^{-T^*_m/T_{SAT,m}} \tag{55}$$

is the assumed pressure-temperature saturation curve and

$$h_{VAP,m} = h^{*}_{VAP,m} \left(1 - \frac{T_{SAT,m}}{T_{CRIT,m}} \right)^{\varepsilon_m} \qquad (56)$$

when $T_{SAT,m} \leq T_{CRIT,m}$

$$h_{VAP,m} = 0 \qquad \text{when } T_{SAT,m} \geq T_{CRIT,m}$$

$$h^{+}_{VAP,m} = h^{*}_{VAP,m} \left(\frac{T_{Lm}}{1 - T_{CRIT,m}} \right)^{\varepsilon_m} \qquad (57)$$

when $T_{Lm} < T_{CRIT,m}$

$$h^{+}_{VAP,m} = 0, \qquad \text{when } T_{Lm} \geq T_{CRIT,m}$$

$$a_{Lm} = 1/2\ h^{*}_{VAP,m}\ (1/3)^{\varepsilon}_{m} + C_{vLm}\ (2/3\ T_{CRIT,m} - T_{MELT,m}) \qquad (58)$$

$$C_{VLm} = 3(e_{CRIT,m} - e_{LIQ,m} - a_{Lm})/T_{CRIT,m} \qquad (59)$$

$$p\Delta V_m = \frac{T_{SAT,m}}{T^{*}_{m}} h_{VAP,m} \qquad (60)$$

All starred (*) quantities in Equations (45)-(60) are material correlation constants.

The pressure in two-phase cells is the sum of partial pressures of the gaseous components

$$p_{2\phi} = \sum_{m} \rho_{Gm} R_m T_G \qquad (61)$$

where R_m, the gas "constant," is dependent on the quantity $\rho_{Gm} T_G$.

For $\alpha_G < \alpha_o$, the cell is assumed to be single-phase liquid, and the pressure is given by

$$p_{1\phi} = \hat{p}_L + \hat{c}^2 \left(\frac{\alpha_L - \alpha_{Lo}}{\alpha_L} \right) \rho_L \qquad (62)$$

where $$\hat{p}_L = \sum_m \hat{p}_{vm} \quad (63)$$

$$\hat{p}_{vm} = P_{v,m}(T_{Lm}) \quad (64)$$

$$1/\hat{C}^2 = \frac{\alpha_L}{\alpha_{Lo}} \sum_m \frac{\alpha_{Lm}}{C^2_{Lm}} \quad (65)$$

where α_{Lmo} and α_{Lo} are equal to α_{Lm} and α_L at the transition point between single-phase nd two-phase flow, respectively.

At the transition between single-phase and two-phase flow the energy of each vapor component is set equal to $e_{VAP,m}(T_{Lm})$ and $\rho_{Gm}R_mT_G$ is set equal to $P_{v,m}(T_{Lm})$ to uniquely determine ρ_{Gm} and T_g.

For small amounts of individual components, the changes in these relationships are given in Appendix B of the SIMMER Manual [8].

3. Model Benchmarking

3.1. Pin Bundles

The freezing and plugging model described above has been applied [1] to a number of experiments involving a range of materials, conditions and geometries. The general success was reasonable over this wide range. The most important data currently available for benchmarking the model in pin bundle geometry is that of Spencer [2]. In reference [1] the model testing was performed in a two-dimensional manner. Because it is applied in a one-dimensional manner for the CRBR assessment, it must be benchmarked accordingly.

The test apparatus shown in Figure 2 was represented completely as were the details of the test pins shown in Figure 3. The one-dimensional model homogenizes the seven pins and the duct wall while

preserving the overall flow channel and local heat transfer characteristics. The noding structure utilized a 5 cm node length in the test section to be comparable to that generally used in the full scale reactor analysis. The test selected was number 1 which represents the upper axial blanket conditions and the expected quantity of fuel.

Four calculations were performed to test different model assumptions. The main mass of fuel stopped in all cases between 30 and 35 cm which is the length of the blanket pellet region. Large steel blockages were formed in all cases downstream of the fuel. Some particulate fuel was blown downstream into the fission gas plenum region prior to steel blockage formation. The general characteristics of the freezing and plugging process were the same as found previously with the two-dimensional modeling. As the fuel entered the test section, the cladding rapidly ablated and entrained into the flowing stream. The entrained steel cooled the fuel in a bulk freezing mode producing a steel-fuel particle slurry. The bulk temperature of the slurry decreased as it flowed downstream sluggishly. The steel froze at the walls at a downstream location, generally at the simulated spring retainer location where the wall heat capacity is high. Even a partial occlusion by steel freezing acts as a blockage in that the particulate slurry has a very difficult time flowing through it. There is some support for using an effective particle viscosity of 10 instead of 1 because from these analyses it permits less particulate material to proceed beyond the blockage in better agreement with the experiment.

3.2. Gap Channels

At the present time there are only a few experiments on fuel injections into gap channels. These are the GAP 1, 2, 3, 4, and 5 experiments at ANL performed in 1978 and more recently GAP3 and 4 [6]. For our benchmarking objective GAP3 and 4 are of interest because of their prototypicality and low injection pressures. The test results are somewhat surprising in that they produced short penetrations, 10 to 30 cm, in an environment that was expected to be controlled by conduction controlled freezing. Long penetration was expected therefore. It is believed to be caused by the stratification of the molybdenum to the leading edge of the injection.

We attempted to scope these experiments with the above model to see if any guidance could be obtained as well as possible benchmarking. The straightforward application of the model led to penetrations of greater than 30 cm. The model ultimately causes the flow to stop by

the amplification of local fluid viscosity resulting in increased flow resistance. Therefore the timing and magnitude of this enhanced viscosity during the flow transient are of major importance. The terminal velocity of the gravity driven flow in the laminar regime is:

$$V = \frac{g \rho D_h^2}{32 \mu}$$

where g is the acceleration due to gravity,
ρ is the fluid density,
D_h is the channel hydraulic diameter,
μ is the fluid viscosity, and
V is the terminal velocity.

For normal liquid fuel this velocity becomes 47 m/s for a gap channel. Obviously the viscosity must be enhanced greatly to cause flow stoppage. If the effect of particles in the stream is to increase the effective stream viscosity to the order of 2 instead of 0.005 (SI units) for liquid, the terminal velocity becomes 0.1 m/s. This suggested that with a specific particle viscosity of 10, a volume fraction of particles of greater than 20% is required to slow and stop the flow. To achieve this fraction of frozen material in the stream before significant penetration and velocity establishment, rapid heat transfer must occur to the walls or particles must pre-exist in the injected stream.

The nominal model with its convective heat transfer treatment produces the material penetration and compositions shown in Figures 4 through 7 for liquid fuel, liquid molybdenum, fuel particles, and fuel crust respectively, when applied to GAP3 with an assumed molybdenum stratification of 60% and no fuel superheat. Similar results are obtained for other stratification assumptions up to 100%. All values are in kilograms per cubic meter (mean density). At a time of 0.1 s the flow should be stopped to be consistent with the experiment, however in the calculation it is greater than 1 m/s. The particulate fraction, formed by molybdenum heat transfer to the wall and concurrent cooling and freezing of the liquid fuel in the mixture in the stream is only about 10% at this time. The stream is only now decelerating. The heat rejection rate from the leading edge of the stream must be larger by at least a factor of 3 to get agreement with GAP3. If, on the other hand, the stream initially contains 5 percent by volume of particles, the average stream penetration velocity would be reduced to less than 0.5 m/s thereby permitting a longer time for particle generating heat transfer and rapid stream stoppage. GAP4 may not have had these particles because of the reduced waiting time. The predicted behavior using this model agrees well with this test.

Although a unique match to these experiments is not possible because the conditions in the leading edge of the discharge cannot be determined, the model does suggest plausible explanations for both results without major model adjustment.

The other benchmarking that has been performed for gap geometry is classical freezing of stable crusts from the wall to occlude the channel. Figure 8 shows the comparison of results from our model and from conduction theory. The agreement is excellent. A further check was made of the integrated fuel througput until occlusion for a net driving pressure of 3.4 atm. The calculated mass discharge as a function of time is shown on Figure 21 as the solid curve. This result compared very well with that calculated by Sandia National Laboratory with a specialized and more sophisticated freezing method that uses transient conduction in the wall and crust (see compendium).

4. Freezing and Plugging Analysis

4.1. Pin Bundles

The geometric model used for the one-dimensional benchmarking against the 7-pin thermite tests was modified to represent a 217 pin, CRBR subassembly from the active core midplane to the top of the fission gas plenum. The thermite injector is replaced with the active core section. The same 5 cm noding is used. This "real" geometry and "real" material model together with our generalized freezing and plugging model were used to investigate the fuel removal potential through CRBR pin bundles for a spectrum of conditions and discharge transients.

The first series of results, Figure 9, show the effects of discharge pressure and initial fuel superheat. All these results assume an isothermal, single phase, fuel discharge driven by a constant pressure at the core mid-plane. A particle viscosity of 1 is used. The effect of superheat is seen to be small as expected because crust thickness does not dominate this process nor does the somewhat higher initial fuel energy. The early part of the penetration shown on Figure 9 is more inhibited by fuel superheat because it causes earlier cladding ablation and subsequent fuel particle formation. The significant point to note from these results is that nearly all of the fuel of the upper half of the core can be discharged quickly if pressures of the order of 5 atm are sustained for about 0.5 s.

Generally the figure-of-merit considered in assessing freezing and plugging models and data is fuel penetration distance. For recriticality potential we are more interested in mass discharged. Obviously penetration and removal are related directly in the subassembly geometry. For these same cases we have plotted the penetration distance versus pressure in Figure 10. A penetration of about 35 cm corresponds to complete removal of one-half the subassembly contents (we consider 1/2 upward and 1/2 downward because the motivating neutronic activity roughly divides the fuel mass after each burst). There is a plateau in penetration versus pressure response because of the tendency to freeze large steel occlusions in the "spring" region if the spring heat capacity is included as part of the wall. The spring does not have good contact with the cladding (line contact if any) and therefore should not be included as rapid response heat capacity. The result is greater, more reliable, penetration into the low heat capacity, high flow area region above the blanket pellets. This can be seen for the "burst driven" results on Figure 10. In reality the "no spring" curve would off scale if the hot material could flow inside the cladding in the fission gas region as it did in Spencer's [5] 2.0 kg, hot wall test.

The second set of results shows the fuel removal potential for a discharge following a burst during the early subassembly disruption phase. The core material is assumed to be a mixture of cladding steel (co-disruption) and fuel that is 50% solid and 50% liquid. The steel and fuel are thermally equilibrated at the fuel melting point. The discharge is driven by power bursts of different magnitudes with a representative CRBR axial power shape. Thus small bursts produce low discharge pressures and have particulates at the leading edge. The cladding steel is assumed to be physically distributed on a scale for rapid heating by the fuel (in less than 0.2 s) and is therefore the pressurizing material. The correspondence between burst energy in full-power-seconds (FPS) and steel vapor pressure can be seen on Figure 10. The relationship is exponential because of the Clapryon equation

The results in terms of penetration distance are given on Figure 10. The "with spring" and "constant press" results agree well up to 10 atm (3 FPS) and then diverge as the superheat effect becomes dominate at high burst energies. Figure 11 shows rapid and complete discharge in all cases.

The third set of results, shown on Figure 12, indicate the influence of particle viscosity on removal assuming no superheat and a constant pressure of 5 atm. Even with a high assumed value of 10,

a high fraction of the fuel in the upper 1/2 subassembly is removed. The rate is greatly reduced, however. This lengthened removal time is important if the lifetime of the discharge pressure is short compared to the discharge interval. In Appendix (Dispersal Press) we see that pressure decay may be on the order of 0.5 to 1 s for a range of assumption and conditions. Thus the high viscosity may cause a slower average rate of fuel removal than that shown in Figure 12 depending on the timing of subsequent bursts. If the bursts reoccur as a result of depressurization and slumpback, the pressure will be re-established. Therefore, in the coupled neutronic framework the removal will be substantial even for the conservatively high particle viscosity of 10.

4.2. Subassembly GAPS

A large set of calculations has been performed with our model to determine the discharge characteristic of fuel and fuel/steel mixtures through gap channels under a variety of conditions. A detailed discussion of one particular calculation is given below to provide a view of the general problem. Then some additional results are provided to characterize the general fuel removal potential of the gaps.

The analyses have been orientated toward the fuel discharge through the gaps between internal blankets. These gaps are important on early removal paths. They can be visualized as pipes to transfer fuel from the active core to the reservoir space represented by the gaps in the lower axial blanket. As such, the discharge will not be short-term. We can expect it to continue until occlusion, reservoir fill-up, or channel disruption by wall melt-through.

The calculational model represents a slab as shown in Figure 13. A plane of symmetry is placed at the middle of the gap. Typically the channel length of interest (core mid-plane to lower axial blanket) is about 0.5 m. The gap laterla length is undefined in two-dimensional slab geometry but is implied to be 1 m. Thus for the calculational channel to represent one side of a hex subassembly, the mass discharge need be multiplied by the true hex-side dimension in meters.

Consider first a multicomponent discharge that is representative of a disruption phase that is energy starved or has had some upper internal blanket breakup to give perhaps 35% by volume particles in the stream material. Also, subassembly wall melting has occurred to raise the steel content to 40% by volume. The remainder of the

stream is liquid fuel (25%). All materials are assumed to be at the fuel melting point which is typical for such slurries. The gap wall is assumed to have an axial temperature distribution running from 860 K at the exit to near the melting point at the inlet. These are conditions that could exist for an EOC-4 core where the sodium has boiled out of the internal blankets and further heatup has occurred by conduction from a neighboring driver wall that is contacting. An injection pressure of 0.4 atm is assumed. This pressure is of the order of the gravity head of the fuel/steel pool.

The results are portrayed visually on volume fraction plots. The solid materials are layered from right to left and the mobile materials (liquids and particles) from left to right. Figure 14 indicates the initial state. A 1 m channel is used to demonstrate the freezing and plugging potential. The reservoir at the end of the channel is of arbitrary size. Figures 15 through 20 show the evolution of the flow and channel characteristics. Figure 15 shows the fuel crust forming on the ablating wall. In this calculation the molten steel under the crust is assumed to entrain into the stream as it forms. This is a major uncertainty in calculations of this type. It is difficult to justify a completely stable crust and at the same time complete, instantaneous entrainment. The choice used here is conservative with respect to quenching the stream (forming more particles) but nonconservative from the standpoint of continually opening the channel by wall meltout. This situation has been considered at both extremes and is not a major influence because of the opposing effects.

Figure 16 shows the downstream steel blockage being generated at a position where the fuel particle/steel slurry has cooled by convective heat loss to the wall. The crust does not grow at the downstream location because the liquid fuel has been depleted by plate-out and bulk freezing (the particles from this mode are shown as indicated on Figure 15). Also seen is the particulate "blowby" generally seen in experiments. In the calculation the steel is depleted by plateout leaving only particles to convect downstream. At 1 s a substantial occlusion has formed and the steel/particle slurry is accumulating on its upstream side. The crust does not grow rapidly in this case because the low liquid fuel volume fraction is preventing full access of the liquid to the crust surface.

In the longer time frame the channel fills behind the blockage which is at a distance of about 0.7 m. Thus in the reactor situation the occlusion would be well within the lower axial blanket and would permit radial flow into the neighboring gap. Other calculations at higher driving pressures (1 to 2 atm) completely ablate the channel with no stoppage.

If we return to the internal blanket geometry with a channel 0.5 m long and calculate the fuel removal capability for different situations, we obtain the results on Figure 21. The area under the curves is the mass removed through the 0.5 m length channel with a lateral extent equal to one side or flat of the hex subassembly. The injection in these cases is fuel only. The effect of superheat is to increase throughput initially because of delayed crust growth. The wall ablates and introduces large quantities of liquid steel into the stream which reduces the velocity throughput until it is transported out of the channel. Then the throughput increases rapidly because of the open, non-ablating channel. The increased pressure produces higher throughput initially, more rapid wall ablation, and a quicker return to high flow. Typical fuel removal quantities for the superheat cases is approximately 15 kg/gap if the later flow re-establishment is neglected. Given the large number of gaps (see Appendix A) an important fraction of the core inventory potentially can be removed in this way.

5. Summary

Based on the mechanics of generalized freezing and plugging, fuel removal in pin bundles and gaps between cold subassemblies should be large if availability versus time is established as acceptable. The gap removal potential is about 15 kg per hex side of a blanket-blanket gap assuming the reservoir inventory is available and the pin bundle removal potential is about 10 kg/subassembly open end. The generalized model used to assess fuel removal is benchmarked against available prototypic materials experimental data, is capable of treating the complexities of the reactor situation, and is compatible with the disruption analysis method. Additional experimental work is under way at Sandia National Laboratory [7] that can be used to further confirm the model adequacy and fuel removal in general.

A BRIEF SUMMARY OF THE THERMAL-HYDRAULIC MODELS

Nomenclature

α_{sm}, α_s	solid component m, solid volume fraction
α_o	value of α_G at single-phase, two-phase transition
$\alpha_{p,max}$	maximum particle packing fraction in Equation (41)
Γ_{Sm}, Γ_{SL}, Γ_{SkLm}	net mass transfer rate from solid component m, mass transfer rate from solid to liquid phase, mass transfer rate from solid component K to liquid component m.
ρ_{Sm}, $\bar{\rho}_{Sm}$, ρ_S, $\bar{\rho}_S$	microscopic and macroscopic densities of solid component m ($\bar{\rho}_{Sm} = \alpha_{Sm}\rho_{Sm}$) and microscopic and macroscopic densities of the solid phase ($\bar{\rho}_S = \alpha_S\rho_S$ and $\bar{\rho}_S = \sum_m \bar{\rho}_{Sm}$)
ϕ_G^2, ϕ_L^2	gas and liquid two-phase friction multipliers used in the Martinelli correlation, Section 2.3c
μ_{Lm}, $\mu_{G,mix}$	liquid component m and vapor mixture viscosities
A_{Sk}, A_{SKm}	surface area of solid component K exposed to the fluid, interfacial surface area between solid components k and m
CpSm, C_{vSm}	specific heats of solid component m at constant pressure, constant volume
C_{fLn}, C_{fGn}	correlation parameter for the liquid-structure, vapor-structure friction factors, Equation (16)
D_h	hydraulic diameter
e	specific energy
f	two-phase weighting function defined by Equation (17)
g	acceleration of gravity

h_{Sm}, h_{LSm}	solid component m heat transfer coefficient, liquid component m to structure heat transfer coefficient
j_G, j_L	gas, liquid superficial velocities $\left(j_G = \frac{\alpha_G}{1 - \alpha_S} \lvert \vec{V}_G \rvert\right)$
k_{Sm}	solid component m thermal conductivity
K_{LS}, K_{GL}, K_{GS}	liquid-structure, gas-liquid and gas-structure momentum coupling coefficients
n	parameter used in Martinelli correlation
N	power generation amplitude function
p, ∇p	pressure, pressure gradient q_{HLm}, q_{rLm}, q_{KLm}, q_{VLm} energy transfer rate to liquid component m from heat transfer, mass transfer, drag and viscous friction
Q_{Lm}, Q_{NLm}	net energy transfer rate to liquid component m, power generated by liquid component m
R	two-phase weighting factor used in Equation (17)
R_m	gas "constant" for gas component m
T	temperature
$\vec{V}_G$, $\vec{V}_L$	gas, liquid velocities
X^2	Martinelli parameter defined by Equation (31)
S, L, G	solid, liquid and gas
Sm, Lm, Gm	solid, liquid and gas component m
SOL, LIQ, CON	solidus liquidus, condensate, vapor, critical
VAP, CRTI	energies

II.7. RECRITICALITY BY EXTENDED FUEL MOTION

1. Objectives and Overview

According to the results of the previous two sections, mild termination by "dispersal" is, by far, the likely path, as compared to a large energetic termination (recriticality). However, recriticalities cannot be ruled out, in fact, they were calculated to occur, albeit only at relatively mild levels (Section II.5). Recognition of the limitations of current understanding and experience in this area, however, provides strong incentives for a better clarification of the potential severity of such events in CRBR. It is the purpose of this section to provide this clarification.

All three of the post-initiation core disruption states (see Figure 2 of Section II.1) are considered. Postulated recriticality events are specified as limiting conditions of the type of oscillatory material motions observed in the "nominal" disruption phase calculations of Section II.5. This oscillatory behavior is a consequence of the unstable character of subcritical states, as well as, of course, of the critical (and supercritical) ones. Under these conditions a limit cycle behavior is possible only in the presence of adequate damping which as we have seen in Section II.5 seems indeed present. On the other hand, the limits (or bounds) of behavior may be explored by removing the damping and/or considering ad hoc perturbations that "overdrive" the system. Thus the extent of possible amplification accounting for uncertainties in modelling the damping effects or in the nature and magnitude of perturbations generated in the integral analysis can be explored. This is the approach adopted here.

Obviously, a great deal of judgement is required to define conditions that adequately explore the limits of behavior yet avoiding those that are physically unreasonable. The rationale for our choices will be given on a case by case basis. Certain general aspects, however, that may be helpful as a background in this regard, are mentioned below.

In principle, fuel material may be driven to recriticality by pressure and/or gravity forces. We already saw one example of pressure-driven fuel motions (Section II.4) during the initiating phase. However, even with a flow limiter, these plenum fission gas

pressures will dissipate well within the S/A-pool stage, and would be of no consequence to recriticality considerations. Pressures due to intense coolant boiling, i.e. rapid fuel/coolant thermal interactions, remain the other possibility. However, if such interactions were to occur, they would, immediately following co-disruption and the associated forceful injection of the high temperature fuel into the sodium-containing coolant channels at the upper and lower extremities of the subassemblies. Available experimental evidence with reasonably prototypic materials indicates the absence of any significant pressure generation events under such conditions. But even if such events were possible, core-wide incoherences being substantial at the early core disruption stages, would dicate local, isolated, occurrences, hence a limited significance for energetic recriticalities. At later times, coherence may develop, however, recriticality concerns for such times presuppose the existence of a "bottled-up" core, hence, again, the impossibility of such fuel/coolant interactions at the immediate core boundary. Re-melting of these blockages is possible, and likely, of course. However, such re-melting most likely will occur under power burst conditions yielding a blowout rather than a fuel re-entry condition. Based on this reasoning, pressure-driven recriticalities are ignored (we will discuss pressure induced pool sloshing in Sections 3.3 and 5.3).

As we will see later in this section, the energetically significant recriticalities pertain to small core fuel inventory depletions. Under such conditions the difference in whole-core compaction states between criticality and prompt criticality is of the order of 1 cm (i.e. approximately 1 \$/cm fuel worth gradient). That is, for an approach velocity corresponding to a 100 \$/s recriticality (approximately 100 cm/s) there would only be approximately 10 ms of significant, at and above nominal levels, power production prior to reaching "disassembly" conditions. Taken at an average power of 10x nominal this pre-disassembly condition could only deposit 0.1 full-power seconds, i.e. 100 MW which is equivalent to a fuel energy deposition of approximately 10 J/g. With a fuel heat capacity of approximately 0.5 J/g°K this heating corresponds to approximately 20°K and a vapor pressure change by only 0.1 MPa (14.7 psia). It is easy to see, therefore, that the commonly held view that criticality can provide a recriticality-mitigating mechanism is true only in principle. In practice, the mechanism of pre-disassembly heatup is effective only for small magnitude recriticalities. For those that matter energetically the compressed (spatial and temporal) scale of this interval severely limits its mitigating character.

A couple of corollary interpretations of this highly nonlinear damping mechanism are also possible. (a) Since the damping may be

effective for low recriticalities the higher nonlinear regime may not be physically relevant, and (b) Any ad hoc choice of analytical perturbations that drive the system outside the early well-damped regime must be carefully scrutinized and interpreted in terms of the likelihood of its occurrence. The evaluation of the recriticalities studied with regard to both of these topics will be made along with each case considered.

The Applicant's treatment of the post-initiating phase core disruption sequence has emphasized the "dispersal" phenomena [1, 2]. The issue of recriticality was qualitatively considered to conclude that: (a) mild recriticality events of the S/A-pool stage are possible but of limited amplitude and they do not amplify, and (b) the accident sequence will terminate benignly without the development of a large-scale confined pool. Our evaluation of these positions is documented in [3, 4].

Our assessment begins with the consideration of certain idealized "disassembly" situations that help generate a perspective on certain crucial aspects of neutronic shutdown (Section 2). In particular the effects of voids and associated role of the equation of state are considered. Also, these simple test cases are used as a convenient basis for comparison between the Eulerian hydrodynamics of our SIMMER-II results, and the Lagrangian methods of the VENUS-II code [5] that has been the standard tool in this area for the past decade. The hydrodynamic responses of the various scale pools and material configurations to postulated perturbations are examined in Section 3. These hydrodynamic re-assembly conditions are then converted to recriticality estimates (Section 4) through the use of criticality estimates and the associated fuel worth gradients. Finally, coupled neutronic hydrodynamic calculations are carried out (Section 5) to quantify the excursion yields and thus order the recriticality events considered in terms of their respective severity and likelihood.

2. Neutronic Shutdown Mechanisms

At super prompt critical conditions the power doubles every 0.01 ms, approximately. Hence, it can reach many thousands of times the nominal level within 1 or 2 ms. This intense heating is self-terminating by the combined action of Doppler (a negative reactivity feedback, related to temperature rise which is a prompt effect) and of outward fuel motion, i.e. "disassembly." This latter effect is not prompt since such motions result only after fluid inertia is overcome. Although relatively slight displacements are adequate for shutdown,

the time-scale imposed by the high power levels requires extremely high acceleration and consequently enormous pressures. Such pressures develop due to heating either by thermal expansion or by the build-up of vapor pressures. However, due to the centrally-peaked flux shape, the generation of such pressures also will be centrally peaked, and since for shutdown we are concerned about a global system expansion rather than a local one, pressure pulse propagation (and relief due to expansion) must be considered. Fluid compressibility is the important parameter in this regard. Indeed, it is well recognized that single-phase liquid (highly incompressible) disassemblies terminate very quickly and produce low yields even at extremely high ramp rates [6].

Single-phase, liquid conditions also may develop, however, from two-phase disassemblies. For example, with an initial, near the melting point, fuel density of 8 g/cm^3, a 50% voided fuel-vapor system will hit, as shown in Figure 1, the liquid saturation line at a temperature of approximately 6250°K (corresponding to approximately 1200 bar). However, as shown in Figure 1 at these elevated temperatures the liquid compressibility has increased substantially, hence the "single-phase" condition may not be as effective in limiting the yield. A parametric evaluation of this effect was carried out using a simple one-dimensional, uniform void, hydrodynamic, SIMMER-II model (a special case of that described in Appendix A) equivalent to one CRBR subassembly including the full steel inventory. A fixed power generation rate was imposed on this model and, based on the calculated fluid displacements and a given (fixed) fuel worth distribution, the time duration multiplied by the power level utilized provides the "yield" of this idealized disassembly.

The results are summarized in Figure 2. Note that the single-phase effects dominate for cases with an initial void fraction up to approximately 15 to 20% in agreement with previous studies with a different code and model [7]. As the quantity of distributed steel decreases, the above limit range of initial void fractions would increase. The above cases imply a single-phase effect for a fuel-to-void volume ratio of approximately 0.5, hence in the absence of steel, single-phase disassembly-limiting effects should be observable up to void fractions of approximately 30%. A representative case from the range with a strong void effect is compared to one from the asymptotic range in terms of calculated detailed responses in Appendix A. From these comparisons the important aspects of the hydrodynamic shutdown mechanism(s) may be visualized. The shutdown behavior for one such case is shown in Figure 3 in comparison to that calculated using VENUS-II. The agreement is excellent.

3. Molten Pool Fluid Dynamics

3.1. Subassembly Scale Pools

As discussed in Section II.5 this phase is dominated by oscillations in fuel mass (axial) distribution and associated power pulses. Although amplification and "tuning" did not occur to any significant extent in that one calculation, their possibility cannot altogether be excluded at this time. To quantitatively explore such possibilities the basic fluid mechanical behavior of such oscillatory fuel motions within a subassembly scale geometry (sealed at both ends) needs to be characterized.

The oscillations originate in the unstable character of a subassembly scale pool dispersed at a subcritical configuration. The high heat loss environment due to the presence of solid (SA walls) or freshly molten steel (i.e. cooler by approximately 1,000°K) and/or equilibration of vapor pressures in the sealed geometry are primarily responsible for this behavior. Upon the subsiding of the dispersive vapor pressures, downward relocation under the influence of gravity must occur. It is the character of this "collapse" of the dispersed state that we seek to establish.

Let us first consider the extreme case depicted in Figure 4. It represents a micro-scale of the classical Bethe-Tait recriticality regime; a power pulse has previously separated (due to the centrally peaked flux) the fuel column into two parts. The upper half, t_1, approaches, under free-fall, and as a coherent mass, the lower half, t_2. If the velocity at prompt critical is j_{pc} and the liquid density ρ_ℓ, the rate of reassembly (i.e. the reactivity ramp rate) would be proportional to j_{pc}. In addressing the situation of a more realistic level, we need to consider what factors influence this simple reassembly expression.

Under free-fall conditions (constant acceleration, g), the velocity j_{pc} is related to the displacement, s_{pc}, to achieve prompt criticality by

$$j_{pc} \sim 1.4(gs_{pc})^{\frac{1}{2}}$$

As a result, the recriticalities from near-critical initial states should be more benign than those from highly subcritical ones. On the other hand, the fallback configuration at t_2, resembling the well-known experiment of turning a full glass of water over, will be highly unstable. It is well known that under these conditions liquid slug breakup will occur within a traveled distance of approximately

1 slug length [8]. The breakup has the appearance of a large vapor (gas) bubble penetrating the slug. In a frame of reference fixed on the subassembly wall, the process has the appearance of the slug running around a large central void space as shown in Figure 5. The relative velocity at fully developed flow conditions will be given [9] by

$$u_\infty \sim 0.35(gD)^{\frac{1}{2}}$$

where D is the subassembly hydraulic diameter. This relative velocity is defined with reference to the bubble nose and the undisturbed liquid slug ahead and implies a substantial liquid slug holdup as compared to that estimated in the undisturbed, free-fall, regime. If the local (area average) void fraction over the draining portion is α and the local liquid velocity over the same portion is u, the reassembly rate, now represented by the superficial velocity at time t, is given by

$$j_{pc} = (1 - \alpha)u$$

A conservative estimate of this reassembly rate may be obtained assuming steady-state, fully developed flow. Then by continuity we obtain

$$j_{pc} \sim u_\infty \sim 0.35(gD)^{\frac{1}{2}}$$

which for a subassembly diameter of approximately 10 cm yields $j_{pc} \sim 35$ cm/s.

As another, somewhat artificial limit, we may think of the upper slug breaking up, again due to instabilities, while in the process of separating, and reversing direction <u>just in time</u> to avoid re-agglomeration of the top (i.e. hypothesizing the presence of a non-condensible gas at the top). For a more-or-less uniform dispersion, an average void fraction of $\alpha \sim 65\%$ would result (see volume ratios of Figure 4). The reassembly rates obtained from such conditions would be given by

$$j_{pc} \sim 1.4(1 - \alpha)(gS_{pc})^{\frac{1}{2}}$$

In the limit of a highly diluted system $S_{pc} \sim 60$ cm, $j_{pc} \sim 114$ cm/s. We can see that this "rain-back" process is considerably more forceful than the "drain-back" considered previously. However, at this limit the differential worth would be considerably smaller than the typical upper range of approximately 1 \$/cm (on a whole core basis), hence, the reactivity insertion effects of this considerably

higher reassembly rate are substantially mitigated (see Section 4 below). For a rainback of approximately 30 cm, as another example, where the 1 $/cm value may be applicable, a reassembly rate of approximately 82 cm/s is estimated.

Subassembly scale pool fluid dynamic behavior was also explored with SIMMER-II calculations, including the thermal aspects of the problem (i.e. vapor production and condensation). These calculations utilized somewhat coarse noding as regards to resolving the details of fluid dynamics, and a special attempt was made to test the code performance in this regime. However, the results presented in Appendix CII.6 indicate substantial agreement with the positions formulated above, and in particular they show no evidence of substantially altered behavior in the presence of heat transfer effects.

3.2. Annular Pool

The fluid dynamic response of the annular pool to power perturbations (neutronic slosh) is examined here. Significant differences with the S/A-scale pools examined above arise due to strongly two-dimensional character of the flow field. Indeed, based on the power peaking, as shown in Figure 6, the fuel vapor bubble (torroidal) would grow at a position less than one pool width from the free surface (L/D < 1). The available upward displacement space, Z, corresponds to roughly two slug lengths (Z/L ~ 2). Some experience with such geometries is available from experiments in Mark III pressure suppression containments. They indicate that preferential upwards bubble growth, as opposed to growth in the radial direction, will occur, leading to breakthrough (of the liquid slug) and bubble venting before a net displacement of 1 to 2 slug lengths. Unfortunately, these experimental data are limited in detail and are not openly available. Specific aspects of interest to our problem include: (a) the quantitative aspects of the breakthrough phenomenon, (b) the flow regime aspects of the arrest and reversal of upwards moving liquid masses at the time of breakthrough, and (c) the existence of any secondary breakup flow regimes. Our approach is based on a combination of SIMMER-II modelling and phenomenological simulant material experiments.

The experiments were carried out in the Omega facility (Purdue) modified by the addition of a central cylinder to form an annular pool (OD ~ 1 m, ID ~ 30 cm, L ~ 60 cm). With these dimensions, and a pool height of 20 cm, the whole CRBR annular pool was modelled at full scale, except for the radius of curvature of the

annulus being at twice the actual. The water pool was driven by nitrogen gas pressure chosen such as to match the expected acceleration of the fuel pool. The experimental results confirmed the breakthrough trends expected and SIMMER-II calculations seem to provide an adequate representation of the global fluid dynamics as documented in Appendix B. However, the calculations are not intended to, and they cannot, portray the fine scale breakup and intense mixing conditions that were observed experimentally to follow breakthrough. Such phenomena would tend to impede liquid fallback, hence their neglect should provide a conservative estimate of reassembly rates.

The CRBR annular pool response to triangular power pulses, at amplitudes of 100X, and 300X nominal power and a half-width of 10 ms, was modelled with a similar SIMMER-II model as described in Appendix B. The power levels chosen represent barely prompt critical conditions, hence, they cannot be considered gross overdrives. The overall behavior is similar to that observed in the calculation of the Omega experiments. A schematic representation of a flow regime evolution is given in Figure 7. The important aspect of the bubble breakthrough phenomenon is to distribute the rising portion of the liquid along the outer wall of the pool, and hence, spread out, in time, the reassembly process. Driven by its momentum, acquired during the bubble growth phase, this wall jet will continue to rise, while decelerating under gravity, impacting the upper boundary, turning around, and jetting downwards along the inner wall of the annulus. At a certain time also the outer wall jet will reverse motion, and accelerate under gravity downwards, however, typically this process occurs near the end of the whole process, hence it is not likely to greatly contribute to the reassembly rate produced by the inner, and more forceful jet. The quantitative aspects of these processes are depicted and discussed in Appendix B. The overall result from a total of seven simulations is a reassembly rate of approximately 25-35 cm/s; which, interestingly enough is a result quite close to that obtained for S/A-scale pools.

However, a substantially higher degree of breakup, than portrayed by the two coherent jet structures in the SIMMER-II results, is evident in the experimental results. Unfortunately, due to time constraints, this aspect could not be quantified experimentally. It is clear, however, that during the jet deflection process, as well as during the subsequent flow, hydrodynamic instabilities will tend to produce a spray-type rainback rather than a jetting-type drainback. Furthermore, substantial momentum dissipation would occur during the deflection process (in the present calculations perfectly elastic collision was assumed) along a rough upper wall, composed, in the

reactor case of exposed pin stubs, wall section ends and crusts of solidified material. Both of the processes would tend to further reduce the rate of reassembly, hence the rates cited above are deemed to be conservative. At the other extreme of complete breakup we expect an average void fraction of $\alpha \sim 65\%$ and free-fall velocities, hence, as in the S/A-scale pool case, reassembly rates in the 80 to 110 cm/s range depending on the applicable free-fall distances. As emphasized previously, however, this kind of situation is highly artificial, especially in the annular pool case in which, due to breakthrough, the material becomes distributed on its way up and no mechanisms can be identified for total re-aglomeration prior to fallback.

3.3. Whole-Core Pool

The aspect that sets this case apart from the previous two considered is the possibility of significant radial motions aggravated by radial convergence of inward flows. This topic, together with its recriticality implications, was first discussed by Bohl [10]. Additional studies were carried out early in the CBBR review process [11]. The basic idea is schematically illustrated in Figure 8. The generally symmetric geometry and equally symmetric flux distribution impose, following a mild recriticality event (assumed perturbation), bubble growth and fuel mass separation around a point of radial and axial symmetry. The breakthrough still occurs and generates an outwardly peaked mass distribution, which, upon fallback, would tend to run in, filling the void generated by the venting vapor bubble. This inward slosh is augmented by radial convergence to produce a mass accumulation just around the area of peak flux, hence a high ramp rate. Our objective here is to study the physical behavior and quantify these radial slosh phenomena. Our approach similar to that followed in the case of the annular pool and consisted of SIMMER-II calculations augmented by simulant material experiments.

The Omega facility (without the central structure present in the annular pool studies) was utilized to benchmark the SIMMER-II sloshing model as in the previous case. In this case also, the expansion phase was successfully modeled. Details may be found in Appendix C.

For the CRBR case, two different perturbation modes, each provoking in a, somewhat, different fashion this radial sloshing mode, were examined. Coupled neutronic/hydrodynamic SIMMER-II computations were carried out in these two cases. The neutronic

feedback was suppressed in subsequent calculations to allow the in-slosh to proceed well beyond initial criticality so that the characteristics of the more extensive in-slosh could be observed. The methods employed are summarized, together with the detailed results, in Appendix C. The in-sloshes observed, in both cases, were of constant rate equivalent to increasing the mass in the central 1/4 portion of the core at the rate of approximately 2,500 kg/s and 6200 kg/s for the neutronic and pressure driven sloshes respectively.

4. Recriticality CRBR Neutronics

The fluid-mechanic reassembly rates developed in the previous section may be converted to reactivity ramp rates by the use of differential fuel reactivity worth values at the critical condition. As we will see shortly, the results obtained are sensitive to the fuel material configuration, particularly to the existence of low void or liquid-only regions. Our approach, therefore, is to span a broad range of possible configurations in terms of the simple three-step procedure employed here, rather than carry out a few of the considerably more involved, complex, neutronic/hydrodynamic recriticality calculations. It is believed that in this fashion we can develop a better understanding of the important trends, and thus be able to more intelligently seek out the recriticality regimes of significance.

Four whole-core recriticality configurations were selected with reference to the S/A-scale pool and annular pool configurations. These configurations are illustrated in Figure 9. Configuration "0" represents a uniformly, core-wide collapsing two-phase disassembly. The other three configurations represent partial slumps at various radial degrees with puddling at the bottom. A series of k_{eff} calculations were carried out for each configuration by compacting the fuel while removing an appropriate amount of fuel mass to achieve criticality. Similarly, a set of k_{eff} calculations were carried out for the cylindrical pool case to simulate, in an idealized form, the in-slosh configuration, as shown in Figure 10. The neutronic treatment in these calculations is identical to that presented in Appendix C. The results are summarized below.

Let us begin with the vertical slumping configurations "2" and "5," which give results that are essentially the same. An examination of the flux (power) shapes as a function of the degree of slumping in conjunction with the associated puddle depths, as shown in Figure 11, reveals a new and interesting "disassembly" phenomenon. This phenomenon is due to the existence of conditions at which the

peak power position is outside the liquid puddle. A disassembly from this condition would involve the rapid single phase response to rapid heating, as discussed in Section II.7.2, except that, assuming that downwards movement is constrained (due to blockages), this would represent a reactivity "boost" rather than a shutdown mechanism. The range of puddle depths over which this boost mode exists is shown in Figure 12. We can see that puddle depths in excess of approximately 10 cm at prompt critical would be required to avoid this mechanism. Combining this result with that of Figure 13 we conclude that such puddle depths are allowed after removal of approximately 15-20% of the fuel inventory. As we have seen already (Section II.6), such a situation is indeed most likely. Conversely, for puddle depths greater than approximately 10 cm, the single-phase shutdown mechanism should enter strongly to significantly limit the energy release. The total reactivity and the differential reactivity are shown in Figure 14. Note that the differential worth is maximized at a pool height of approximately 20 cm, however, the value is within ±40% from the 1 $/cm value utilized on several instances previously. The results for configuration 3 are similar except quantitatively different due to the considerably smaller quantity of fuel involved. Thus the differential worths are considerably smaller at approximately 0.25 ± 0.1 $/cm and the boost occurs for puddle depths up to approximately 20 cm. However, a dispersal of only 1-2% of the core inventory would be necessary to dispel such a concern. Such small quantities of fuel losses are virtually guaranteed to occur even in the short time period appropriate to considering the configuration 3 type recriticality. Finally, the completely homogeneously collapsing mode represented by configuration 0 is characterized also by a differential worth of approximately 1 $/cm ± 40% while, of course, it does not exhibit any of the threshold-type behavior of the puddled configurations.

The results for pool in-slosh states indicate low differential worth of approximately 0.6 ¢/kg through the inward translation until the fluid contacts the pool axis. Beyond this point further radial inward motion results, by continuity, in a central upward bulging, that has a differential worth of approximately 5 ¢/kg.

5. Bounding CRBR Recriticality Yields

The purpose of this section is to combine the fluid mechanics results of Section 3 with the differential worths determined in Section 4 and corresponding disassembly calculations (to be presented here) in order to scope out the various ranges of recriticality yields and respective likelihoods.

A SIMMER-II disassembly model similar to that utilized in the calculations of Appendix A was utilized to establish the excursion yield as a function of the reactivity ramp rate for the range of configurations examined in the previous section. The modelling details are provided in Appendix D and the results of these parametric studies are summarized in Figure 15. The 100 and 200 $/s two-phase (configuration 0) yields that were examined in Section II.2 with reference to structural damage should provide a reference frame for judging the magnitude of the various effects as they are considered below.

Configurations 2 and 3 were calculated with fuel inventories that imply the existence of the boost regime. The substantial augmentation of energetic behavior is clearly evident. On the other hand the configuration 5 inventory lies at the other side of the boost threshold, hence, a benign behavior even for extremely high ramp rates is noted.

Another interesting view of these results may be obtained by cross-plotting yields as a function of the fuel inventory reduction for a given ramp rate. For example, the 100 $/s case is shown in Figure 16. Indeed, it appears that although a fuel removal by approximately 40% is required for permanent subcriticality, for any removal more than approximately 20% (corresponding to the inventory loss for which the peak in flux coincides with the puddle depth at the critical condition) significantly energetic behavior from puddle-type recriticalities (S/A-scale and annular pools) may be ruled out. Furthermore, the significant portion of the boost regime seems to exist on a narrow inventory depletion "window." The physical reasoning for this behavior may be explained in terms of the relative puddle-flux shape position, an example of which is shown in Figure 11. In order for the boost mode to be manifest, a certain minimum puddle height would appear necessary, since: (a) the single phase region must extend well into the high flux region if it is to be heated and expand prior to the inception of disassembly motions in the two-phase region, and (b) the puddle depth must be of adequate size if thermal expansion (which is a fractional effect) is to produce a substantial, reactivity-augmenting, net displacement into the higher worth region. However, it is a consequence of this requirement also that the resulting boost be self-limiting since such rapid displacements will quickly take over the peak worth position, thus transforming into a shutdown mechanism.

Returning to Figure 15, additional important trends may be discerned. The magnitude of the single-phase boost (taken as the difference in yield from the homogeneous two-phase case at the same

ramp rate) increases with the fraction of the core involved in the recriticality as expected. The saturation in the magnitude of this boost with ramp rate also is expected because the sharp disassembly part of the transient begins at a particular displacement of the puddle (through the flux peak). Once the yield level for this displacement is reached further yield increases are inhibited. This characteristic indicates that for puddling-type recriticalities an "effectively asymptotic" behavior exists. This is particularly so in light of the view, developed below, that puddling reactivity insertion rates in excess of approximately 80 $/s would appear totally unreasonable on physical grounds.

As a final step we will attempt to relate the above concepts and trends to the CRBR core disruption sequence. The goal is to more closely explore the likelihood/severity relationship for energetic recriticalities. That is, for purposes of this discussion we will examine all three stages of the core disruption sequence, regardless of the likelihood for achieving such states. Thus the whole treatment here must be viewed in the perspective of the potential for mild termination provided in Sections II.5 and II.6.

5.1. S/A-Scale Pool Recriticalities and Yields

In view of the relatively short time, of 1-2 s, required to melt-attack the S/A duct walls (see Section II.5), as compared to the period of the gravity oscillations (approximately 0.4 s), only a small number of recriticalities are possible within the S/A-scale pool stage. As a consequence the degree of tuning achievable is rather limited. The first mode of recriticality would be due to the slumping of the first-to-disrupt high power channels, i.e. configuration 3. The 1-2% inventory loss required to avoid the boost mode, translated to approximately 10% on a local basis (configuration 3 represents approximately 20% of core). This represents a substantial fuel removal and its occurrence would appear problematical in view of the flow path availability, plugging potential, and timing requirements. In fact, in view of the possibility of some steel blockages at the core exit in these lead disruption channels, it would appear that the boost mode would be avoided due to insufficient fuel loss (see Figure 16). Furthermore, the incoherence may still be substantial, and the negative feedback from continuously disrupting lower power channels would also help avoid the boost mode.

At near full inventory, the "rainback" reassembly rate of 82 cm/s consistent with a rough differential worth of approximately 1 $/cm should apply. The resulting 82 $/s on a whole core basis implies a

reactivity insertion rate of approximately 15 $/s for this smaller slumping region, i.e. an energetically negligible event. On the other hand, if substantial fuel removal is postulated, the 114 cm/s reassembly velocity may be more appropriate. However, at this limit a differential worth of approximately 0.5 $/cm would apply resulting in a (local) reactivity insertion rate of only approximately 10 $/s. The drainback regime would be considerably more probable and would yield approximately 7 $/s. It is doubtful that even in the very unlikely circumstance of fuel inventory reduction within the boost window, actual boosting could ever occur under such low driving initial rates.

Subsequent disruptions will gradually lead into configuration 2 and eventually 5. We have seen already that these two configurations have quite similar neutronic characteristics, i.e. a boost regime at approximately 10-20% inventory reduction and an approximate differential worth of approximately 1 $/cm. Around the boost regime a value of approximately 0.8 $/cm would be more appropriate. At higher fuel inventories a still lower value in the range 0.4-0.6 $/cm would apply. For inventory losses greater than 20%, the reactivity worth may be as high as 1.2 $/cm, however this regime yields negligible energetics. Finally, from Figure 14 we deduce an "average" differential fuel reactivity worth of approximately 1 $/cm. This value would be applicable to a system of uniformly distributed voids undergoing a uniform reassembly. Configuration 2 represents recriticalities from only the three inner driver rings, which include roughly one-half of the core subassemblies. Hence, the above differential worth values must be modified by a factor of approximately 1/2 when applied to this case.

For configuration 2 the boost regime corresponds to a local loss of approximately 20-40% of the fuel. Considering the results of Section II.6 and associated uncertainties, it is highly doubtful that the boost mode can be avoided at this stage <u>if</u> a strong puddling-type recriticality was to occur. Let us consider the various possibilities.

For a "rainback" reassembly rate of 82 cm/s and fuel content around the boost regime (approximately 0.8 $/cm) we estimate that a totally coherent recriticality would yield approximately 38 $/s. Considering the short time available for tuning a value approximately 20 $/s might be more appropriate. At a higher inventory the reactivity worths would be approximately 0.5 $/cm, hence ramp rates of approximately 10 $/s result. For drainback conditions a velocity of approximately 35 cm/s would apply producing, for a totally coherent recriticality, only 18 $/s. All cases represent similarly small recriticalities and as may be seen in Figure 15, even with the boost

the yield would be only marginally over the zero vessel damage boundary and well below the vessel head failure limit.

Finally, in the configuration 5 case the boost regime would be represented by a 10-20% local (same as total for this case) fuel inventory loss. As seen in Section II.6 the additional time margins at this stage of disruption virtually guarantee losses greater than this range, hence the single-phase shutdown, rather than the boost regime, should prevail (i.e. negligible energetics). Furthermore, the disruption of the outer duct wall of driver region #4 would open up new fuel escape paths into the radial blankets, hence, the energetically significant lifetime of this phase (assuming that it exists) would be extremely small. Further, even if despite all these energetics-mitigating reasons we postulate inability to remove 20% of the fuel inventory and coherent reassembly phenomena, still, no large energetic events are envisioned. The results of configuration 2 (previous paragraph) apply except multiplied by a factor of 2X to account for the quantity of fuel involved. Assuming total coherence values of approximately 72 $/s, 36 and 20 $/s for "rainback," "drainback," and high-inventory "rainback," result. Taking into account the short time available for tuning (typically a few cycles before walls melt) a reasonable upper limit ramp is judged at approximately 40 $/s (see Section II.5). With these kinds of recriticalities a straight, two-phase disassembly would yield zero vessel head damage. However, even with a boost we do not see a clear (see Figure 15) challenge to the reactor vessel head structure.

5.2. Annular Pool Recriticalities and Yields

The annular pool would also be short-lived, however, a substantial degree of coherence would be expected here. With an average differential worth of approximately 1 $/cm reactivity insertions of approximately 35 $/s and approximately 110 $/s are estimated for "drainback" and "rainback" reassemblies respectively. As seen in Figure 15 for two-phase disassemblies, such recriticalities would barely approach the zero vessel energetics boundary. Due to significant radial power profiles and pressure relief zones (voided IBs and RBs), the one-dimensional boost mode discussed previously does not apply here.

5.3. Whole-Core Pool Recriticalities and Yields

The differential worths of approximately 5 ¢/kg for radial pool in-sloshes developed in Section 4 can be combined with the

reassembly rates of 2,500 kg/s and 6,200 kg/s estimates for the neutronic and pressurization sloshes respectively (Section 3.3) to yield approximately 125 $/s and approximately 310 $/s. Compared to the recriticalities examined previously, these represent relatively high ramp rates. However, the original SIMMER-II calculations that lead to this particular concern [10] did not take into account single-phase liquid expansion. This deficiency was corrected in the present investigations.

The result of including the single-phase effects as in the puddling-type reassemblies reflect a combination of boost and rapid shutdown effects. However, here again, the boost regime seems to be associated with a narrow range of unique circumstances, and the shutdown regime prevails more universally. The two idealized cases examined yielded the equivalent (based on driver fuel only) of approximately 10 (for the 125 $/s case) and approximately 5 (for the 310 $/s case) full power seconds. Thus the neutronic slosh gives rise to a yield equivalent of a classical two-phase disassembly, while the pressurization slosh is energetically negligible. In fact, in terms of Figure 15 it lies on the extension of the similarly benign configuration 5 trend. The pressurization slosh suppressed boiling almost completely yielding an essentially single-phase reassembly configuration. It is such single-phase behavior that can lead to very high ramp rates, however, it is also responsible for early neutronic shutdown. Additional results on these two case calculations may be found in Appendix C.

In the light of these results it appears that the highly visible, in the past 2-3 years, "whole-core pool concerns" have been reduced and their yields are not beyond accommodation. In addition, the extraordinary circumstances assumed in the two case calculations that lead to this conclusion need be mentioned: (a) pressurization events at the boundary due to fuel/coolant interactions are speculative and (b) pool homogenization as assumed in these calculations requires time to develop (as shown in Section II.5), hence additional margins exist for fuel removal beyond the time of disruption of the internal blankets and the existence of this state therefore is very questionable.

6. Another View of Severe Recriticality Amplification

The boost mode of disassembly was discovered during the course of this work as a consequence of including the single-phase (liquid) equation of state in SIMMER-II. The aim of these studies was to explore the amplification potential of recriticalities along the lines of our Question #6 (see Table 2 of Section II.1) to the Applicant. By

the time our investigations into the single-phase boost phenomena were complete we were ready, based upon the understanding developed from this work, to reevaluate our approach concerning amplification. The results of this reevaluation are presented in this section. These results indicate that results presented in the previous section for amplification by axial motions (i.e. S/A-scale and annular pools) are extremely conservative. In our opinion the development presented in this section adequately addresses the problem of S/A-scale and annular pool recriticality energetics. The presentation in the previous sections is intended as an introductory exercise, however, there may be readers that will interpret these previous results as complementary to those given here.

As discussed above, the whole subject of energetic recriticalities arises due to the unstable character of both permanent subcriticality as well as, of course, of criticality (and supercriticality). The concern is that power oscillations could amplify into the highly energetic regime. Indeed, the results of the previous two sections showed that such a statement would not imply the violation of physical reality as far as the nature of the forces and phenomena involved are concerned. Yet with the exception of the energetically benign recriticalities (single-phase shutdown) and possibly of the two whole core pool cases examined, these results, and particularly those that exhibit the boost phenomenon, are the artifact of very specialized initial conditions. These initial conditions (configurations 0, 2, 3, 5) are in any case highly idealized but they are generally inappropriate for the neutronically active situations of highest likelihood.

The key idea is that under a power perturbation the system will "separate" at the peak flux position (mass centroid). In a core-wide, one-dimensional sense such an event will separate the fuel mass into two equal parts. The lower portion already being in a state of rest will remain in same until and unless boilup occurs. The upper portion as we saw in Sections 3.1 and 3.2, will distribute itself, more or less, over the available space and will proceed to reassemble. Due to the increased overall separation between the two fuel masses, criticality will occur only after some puddling of the falling back fuel mass has taken place. But this is precisely the condition for the peak worth (flux) location to move toward and even within the puddle, thus narrowing strongly the boost regime. If a small fraction of the core is puddling, the flux peak may be at a higher position making a limited boost possible (low puddling ramp). If a large fraction of the core is puddling coherently, then the flux peak will move into the puddle as criticality is achieved and results similar to those for configuration 5 apply. If boilup occurs in the

lower puddle because of pressure reduction by quenching in the upper SA, the puddling ramp is reduced and the single phase region is further removed from the peak power zone thereby making the boost impotent.

The above reasoning cannot be applied to the whole core pool since its two-dimensional character can allow axial-to-radial slosh conversion. However, as we have seen, other limitations apply in this case.

7. Summary

Even for postulated severe rates of reassembly, S/A-scale pools and the annular pool recriticalities will show no severe amplification and should be considered energetically benign. The essence of the basis for this conclusion is that under conditions physically consistent with power perturbations, recriticality shutdown generally would be accelerated by a single-phase effect. A single-phase boost phenomena with significant potential for energetic behavior is physically possible, however, such events can only occur under very specialized initial conditions. The homogeneous whole-core pool yields are the most important from the standpoint of potentially damaging energetics. Several recriticality events were considered with varying degrees of extraordinarily contrived conditions. In no case, however, was the structural boundary of the primary system significantly threatened.

APPENDIX A
NEUTRONIC SHUTDOWN MECHANISMS

1. Introduction

In this Appendix we explore in detail the range of fluid dynamic/ thermodynamic phenomena that are operative in the generation of the necessary fluid motions for neutronic shutdown. A series of simple, one-dimensional calculations were performed with high heating rates typical of high ramp rate, prompt critical excursions and a range of initial void fractions from zero to 40 percent. The model used is discussed along with the analysis approach. The results of the series of calculations are given with two particular cases discussed in sufficient detail to indicate clearly the operative phenomena.

2. Calculational Model and Analysis Approach

The calculations were performed in one-dimension to provide maximum visibility to the operative mechanisms and to permit a simple figure-of-merit for neutronic shutdown to be applied for case to case comparisons. The model used for the SIMMER-II [1] calculations is shown in Figure 1. A single SA is represented with one radial node and 39 equal axial nodes. The boundaries are assumed open and at a pressure of one atmosphere (10^5 Pa). The material represented is that normally present in the core (fuel, cladding, wire wrap, and SA wall) but at an initial state of 3100 K for the all-liquid mixture. This mixture has the volume fraction ratio of 0.377:0.314:0.309 for fuel:steel:void. The corresponding smear densities are 3290 kg/m^3 and 1860 kg/m^3 for fuel and steel respectively. As the void is changed in the following calculations, this ratio is held constant to simulate compaction of the core.

A power distribution from channel 7 of the EOC-4, SAS3D analysis (Section II.3) was used along with consistent fuel and steel specific reactivity (Δk/kg) worth distributions. These distributions are slightly skewed toward the bottom of the SA because of the control rod induced flux depression in the upper core. A simple integration of the change in reactivity is performed over the SA as the materials move. When a total reactivity change of -1.0¢ (based on the nominal densities above) is observed, we pronounce neutronic shutdown. This is equivalent to a change of approximately -1.6$ for the whole-core and is sufficient to decrease the reactivity to below critical.

The energy yields for the various cases can be very simply obtained because of the manner in which the analyses were performed. The power is not calculated from the point-kinetics equations normally applied in disassembly analyses. This coupled procedure would produce very transient power histories thereby adding to the difficulty of clearly discerning the operable fluid dynamics causing neutronic shutdown. Therefore we chose to apply constant powers of different magnitudes that are representative of severe disassembly events. Then by obtaining the time to shutdown as defined by the required reactivity change of 1.0¢, the yield becomes the power times this shutdown time. In the following section we use power in terms of multiples of nominal full power and excursion energy yield in terms of full-power-seconds (FPS).

3. Analysis Results

Our objective in this series of calculations was to determine clearly the influence of initial void on the disassembly energy yields for different excursion severities. The excursion severity was varied through the power level applied. For a calibration against whole-core disassemblies driven by specific ramp rates, we turn to Section II.2 where 100 $/s and 200 $/s produced peak powers of 10,000 and 27,000 times nominal respectively. Therefore we chose a power range of 10,000 to 30,000 for this investigation. We chose a void range from 0 to 0.4 which spans the situations of interest in the LOFA sequence.

The matrix of cases analyzed is shown in Table 1 and the energy yields are tabulated in Table 2. It is clear that a wide range of yields are calculated as initial void varies. This trend can be visualized better on Figure 2 of Section II.7. A saturation effect occurs at a void of about 0.2 for the range of power levels indicating a yield mitigating effect for initial voids below 0.2. If we relate this to the fuel volume fraction, we find this void threshold at a volume fraction ratio of 0.45:0.2 (fuel:void) or approximately 2:1. In a fuel rich region mitigation would occur up to about 30% void.

We proceed now to consider the phenomena that lead to the trends calculated. We will do this by following the progression of the transient in detail for cases 31b and 33b which represent conditions on each side of the threshold. An overall perspective for case 31b is obtained by seeing the time evolution of several key output variables such as material worth, fuel temperature, mid-plane pressure, and mid-plane void fraction shown in Figures 2 through 5 respectively. The time interval for shutdown activity is from 0.4 to 0.6 ms from Figure 2. The key to the rapid shutdown (fuel axial

motion) can be seen on Figures 4 and 5. The single-phase condition is reached at about 0.3 ms at which time the temperature is only about 4700 K. For the equation-of-state [2] used in this analysis (see Figure 6), the liquid fuel density change is about 20%. With an initial fuel volume fraction of about 50% for this case, we should see a void change of 0.2 x 0.5 or 10% and we do in Figure 5. At 4700 K the sonic velocity of the fuel is still high, approximately 1300 m/s, and should cause large pressure increases as the liquid continues to expand with further heating. The pressure response is shown in Figure 4 (the flat top is a built-in limit of the plotting routine) and it is indeed high (greater than 10,000 atm). The pressure reduction at 0.7 ms is the result of the decompression waves returning from the open boundaries. The neutronic shutdown is achieved before this occurs thereby making the results independent of this decompression process. Thus we see the manifestations of the classical single-phase liquid disassembly.

The progression of the disassembly process in time and space is shown in Figures 7 through 11. The nonsymmetry in all of these plots is the result of the skewed axial power profile mentioned previously. The temperature distribution is shown in Figure 7. It simply elevates with time because the liquid specific heat changes only slightly with temperature over this range. Shutdown is complete at about 0.5 ms with a peak temperature of about 5500 K. At the mid-plane location (0.46 on the horizontal axis) the sonic velocity has decreased to about 900 m/s at this shutdown temperature. The axial progression of the single phase region is seen in Figure 8. The entire SA is single phase at the time of shutdown. The pressure propagation is shown in Figure 9. The rarefaction wave can be seen moving inward from the lower boundary in Figures 9b through 9d. Its speed is about 1000 m/s as it should be. The velocities induced in the materials are shown in Figure 10. Velocities of about 50 m/s are generated rapidly. The local density changes are seen in Figure 11. The initial uniform density was 4470 kg/m^3. We can see the material being displaced from the central region to the ends and even out of the lower boundary.

A very different situation results for case 33b. We can see the key differences by comparing the time histories for material worth, fuel temperature, mid-plane pressure, and mid-plane void fraction for this case (Figures 12 through 15 respectively) with corresponding ones for case 31b (Figures 2 through 5). The reduction in reactivity occurs much later (approximately 0.8 ms compared to 0.5 ms for case 31b) thereby allowing 6 FPS (an additional temperature rise of approximately 1000 K) of additional energy to be added to the material. As seen in Figure 13 the critical temperature of 6400 K is reached. The change in slope prior to 0.8 ms is the result of the

increased heat capacity of the liquid fuel as the critical point is approached. The initial void at the mid-plane is not closed by the expanding liquid until 0.65 ms as compared to about 0.25 ms for case 31b. Furthermore the establishment of the single-phase state does not generate pressures, Figure 14, that are nearly as high. This is the result of the reduced sonic velocity (increased compressibility) in the critical point regime. Typical values are 400 m/s for sonic velocity or a factor of about 2-2.5 below that for case 31b. Thus the compressibility is 4-6 times greater. For this case the initial fuel volume fraction is about 0.4. Therefore the fuel had to expand by 75% to fill the void corresponding to a density of about 5 gm/cm^3. From Figure 6 we can see that this does not occur until the critical point is approached.

The progression of the disassembly in space and time provides additional insight into the mechanics of disassembly for this case. The temperature distributions, Figure 16, are similar to case 31b except they proceed to a higher level. The progression of void closure shown on Figure 17 is delayed as expected because of the higher initial value. Also it is important to note that at the time of shutdown the single phase region has not progressed to the ends of the SA. This means that the shutdown fluid dynamics is not dominated by the acoustic characteristics of the single-phase region over the entire SA as in case 31b with the associated generation of large boundary discharges. In this high-void case the fuel is moved locally from the mid-plane region to the end regions where there is still local void or accommodation space. This is seen in Figures 18 through 20 in which the evolution of the distributions of pressure, velocity, and fuel smear density are shown. The large pressure gradients are only at the edges of the single phase regime. They cannot effectively propagate into the two-phase regime.

For still larger initial voids such as 40%, the behavior is very similar because the additional energy required to close 1/3 more void is small (see Figure 6). Indeed this is in agreement with the results in Table 2. This void to fuel ratio is about as high as can exist in the core and still produce criticality.

4. Summary

These results show that single-phase behavior is to be expected in all realistic disassembly events that are sufficiently severe to be a threat to the vessel head structure as defined in Section II.2. However, the mitigating effect is substantial only for fuel to void volume fraction ratios greater than 2:1 or for typical voids of about 20% for the nominal mixture of fuel and steel.

TABLE 1
MATRIX OF CASES FOR THE
1-D DISASSEMBLY INVESTIGATION
(Case numbers)

Power \ Void	0	0.1	0.2	0.3	0.4
10,000	30a	31a	32a	33a	34a
20,000	30b	31b	32b	33b	34b
30,000	30c	31c	32c	33c	34c

TABLE 2
ENERGY YIELDS FOR THE 1-D DISASSEMBLY
INVESTIGATION (FPS)

Power \ Void	0	0.1	0.2	0.3	0.4
10,000	2.4	8.7	12.2	13.0	13.0
20,000	4.0	10.4	14.6	16.4	16.5
30,000	5.1	11.5	16.8	18.6	19.5

APPENDIX B
ANNULAR POOL FLUID DYNAMICS

1. Introduction

In this Appendix an assessment is made of the characteristics of the fluid motion in the annular pool geometry. Based on the reassembly or puddling rates, ramp rate estimates are made for a variety of situations and modeling assumptions. These are not coupled neutronic/fluid dynamic analyses but rather fluid dynamic calculations with assumed initial conditions and simulated initial recriticalities. The material is presented in four sections: analysis model and assumptions, analysis results, experimental benchmarking, and a summary.

2. Analysis Model and Assumptions

The transient fluid dynamics behavior of the annular pool was investigated using SIMMER-II [1] on a simplified pool geometry. Because a neutronic analysis is not being performed, portions of the reactor outside of the annular pool need not be represented. The calculational model is shown in Figure 1. The fluid dynamic region (radial mesh 3 through 12 and axial mesh 1 through 20) represents the driver subassemblies between the third internal blanket ring and the radial blanket (132 subassemblies). The boundaries are assumed to be blocked. The annular pool is assumed to consist of about 85% of the driver fuel and all of the subassembly wall steel. All cladding steel is assumed removed.

The starting configuration assumes that the molten core materials are slumped into the bottom half of this annular core region. An initial temperature of 3100 K is assigned to both fuel and steel. The pool is perturbed with an assumed power transient with a triangular shape and a half width of 0.01 s. The assumed power distribution is shown in Figure 2. It is biased toward the inner edge because of the fuel in the other driver regions. This radial distribution is in reasonable agreement with that calculated for similar configurations in Section II.7.

2. Analysis Results

A number of calculations of these annular pool transients have been performed to assess variations in initial configuration, perturbation strength, and model assumptions. One case will be discussed in detail and the results of the other cases will be tabulated only.

The case chosen for detailed discussion is representative of all the other but has greater numerical resolution because the calculational node sizes in both directions were reduced to one-half of those shown on Figure 1 (four times as many nodes). The applied power transient has a peak power of 300 times nominal full power thereby adding about three full-power-seconds or about 700 K to the pool. Heat transfer between the fuel and steel in the pool occurs moderately fast and is characteristic roughly of a dispersion size with a characteristic size of about 0.001 m diameter. The results indicate a thermal equilibration time of about 0.05 s for the mixture following the preferential heating of the fuel. The liquid/vapor momentum coupling is characterized by a dispersion size of 0.01 m diameter and a multidroplet augmentation parameter of 2.5. This parameter is the exponent on the void fraction which appears in the denominator of the interfield momentum coupling function. As the void fraction decreases the overall coupling increases dramatically.

An overall perspective on the predicted fluid dynamics is given in a sequence of contour plots, Figure 3, for the pool liquid. The "L" and "V" indicate regions of liquid and vapor respectively. Figure 3a shows the initial liquid pool. At 0.020 s all the energy from the assumed power pulse is in the pool but little motion is seen in Figure 3b. Small pockets of vapor are shown. These are the result of locally amplified heat transfer between the fuel and steel. As a vapor region forms the liquid fuel is calculated to flash, break up into a smaller dispersion, and create more area and less resistance to heat transfer. The scattered pattern is the result of local pressure nonuniformities. These scattered bubbles have merged in Figure 3d as the effects of the power profile begin to dominate the fluid dynamics.

The rapid heating of the fuel can be seen in Figure 4. The fuel vapor pressure associated with the maximum fuel temperature is about 2 atm. Figure 5 indicates that a pressure much higher than this is generated rapidly. The steel that is heated to about 3800 K produces a vapor pressure of nearly 15 atm, however, and is therefore the pressure source for perturbing the pool.

The expansion region breaks the pool surface at about .04 s as seen in Figure 3c, but the imparted momentum at that time causes most of the material that is smeared in the breakthrough process to proceed to the top of the region as shown in Figure 3d. Significant upward momentum is imparted to the upper half of the pool prior to breakthrough. This liquid continues to move as a climbing film along the outer wall, circulate around the top of the annulus, and flow downward along the inner surface as shown in Figures 3e through 3i. At 0.16 s the original pool has been distributed completely around the periphery of the annulus. Reassembly of the pool from this point on is highly incoherent because the outer film is moving upward while the inner one produces a mass reflux to the pool region. The subsequent pool reassembly is shown in Figures 3j through 3l. A vortex is generated in the pool as the film enters the pool and causes a large vapor bubble to be entrapped at 0.32 s.

The severity of a secondary recriticality from this mild initial event can be quantified approximately from the mass reflux to the pool (and associated puddling rate) and the differential worths for an annular pool configuration. A secondary event can occur only for conditions that constitute a neutronically critical system. This depends on the inventory of fuel in the system. Even for an inventory of 100%, criticality will not occur until the fuel is concentrated locally or redispersed to nearly its nominal distribution. The configuration at 0.2 s (Figure 3k) is highly subcritical. A transient neutronics calculation was performed to scope these neutronic states. Criticality is approached when about two-thirds of the total mass is in the lower pool region.

The fuel inventory in the lower half of the annulus (corresponding to the original pool) is shown in Figure 6 as a function of time. Because the instantaneous slopes (reflux rates) are not uniquely related to differential reactivity at a critical state due to inventory considerations, and arbitrary selection of maximum slope and maximum differential worth is inappropriately conservative and assumes a level of detailed resolution incompatible with our approach. Therefore, an average slope or reflux rate is used as well as an average differential worth. The average mass reflux rate is approximately 3400 kg/s. This produces an equivalent puddling rate of approximately 27 cm/s. Using an average differential worth from Figure 7 of approximately 1.0 \$/s leads to a ramp rate of 27 \$/s.

Other cases that were calculated are tabulated in Table 1. The reassembly transients are shown on Figures 8 through 13 and the results tabulated in Table 2. The results indicate that mild initiators do not cause the large circulation around the top of the

annulus but instead produce a sheet along the outer radius which simply drains back by gravity. Variation of the vapor-liquid momentum coupling has a small effect as seen by comparing cases C02 with C10 and C06 with C08. The initial pool configuration appears to have the largest effect in the direction of larger ramps. The partially two-phase situation permits a more rapid radial bubble growth initially and therefore lifts the upper half of the pool mass more coherently. The reflux is then also more coherent. It appears that the increased calculational resolution adds more incoherence to the process by resolving the film flows better.

3. Experimental Benchmarking

Because the pool states have a greater potential for larger ramps, it is important to provide an experimental calibration of our ability to assess the pool transients. To this end a timely set of experiments has been performed in the existing OMEGA facility [2] at Purdue University. This facility is designed for postdisassembly expansion experiment in 1/7 CRBR vessel scale. Its application to the active core provides approximately full annulus scale and full axial scale. Therefore it is ideal for this benchmarking.

The experiments performed to date, with a gas source at the annulus inner radius for the pool perturbation source, indicate gross upward and outward movements of the upper half pool initially. Breakthrough does occur with substantial dispersal of liquid. Pressure transducers at the top plate provide an indication of initial liquid contact time and a rough estimate of mass flux.

SIMMER-II analysis of this type of experiment produces fluid dynamic characteristics that are in general agreement with the data. The time that material reaches the top-plate agrees well with the data as do the initial bubble growth patterns and breakthrough time. The bulk material motions are reasonable but the dispersiveness is difficult to compare and would not be expected to be in agreement because the SIMMER-II modeling of these processes is lacking detailed physics. However, if the reflux rate to the puddled regions is controlled more by the bulk or gross motion than by the dispersal, the SIMMER-II analyses should be adequate for providing estimates. In fact, they should provide conservative results because massive dispersiveness would only impede the reflux to the pool.

4. Summary

The analysis of annular pool fluid dynamic following an assumed mild recriticality indicates a tendency for this geometry to produce ramp rates less than that for coherent "rainback." This mitigation comes from the spreading of the upper half pool into a film or sheet type flow that has a reduced reflux rate. Benchmarking experiments provide the basis for assigning credibility and adequacy to these analyses.

TABLE 1
ANNULAR POOL ANALYSIS MATRIX

Case #	Peak Power (xP_0)	Momentum Coupling: Void Exponent	Momentum Coupling: Dispersion Radius (m)	Noding	Fuel-Steel Heat Transfer Multiplier	Initial Pool Configuration
C02	300	2.5	0.005	10 x 20	100	Full Puddled
C04	100	2.5	0.005	10 x 20	100	Full Puddled
C06	300	2.5	0.001	10 x 20	0	Full Puddled
C08	300	2.5	0.005	10 x 20	0	Full Puddled
C10	300	6.0	0.005	10 x 20	100	Full Puddled
C12	300	2.5	0.005	20 x 40	100	Full Puddled
C14	300	2.5	0.005	10 x 20	100	Half Puddled & Half Distributed

TABLE 2
ANNULAR POOL ANALYSIS RESULTS

Case #	Reflux Rate (kg/s)	Puddling Rate (cm/s)	Ramp Rate ($/s)
C02	4460	35	35
C04	3076	24	24
C06	4470	35	35
C08	4590	36	36
C10	3570	28	28
C12	3400	27	27
C14	5545	42	42

APPENDIX C
WHOLE-CORE TRANSIENT POOL RECRITICALITY

1. Introduction

In this Appendix an assessment of the coupled fluid-dynamic/neutronic, transient response of a postulated, homogeneous cylindrical pool is presented. The material is presented in four sections: analysis model and assumptions, analysis results, experimental benchmarking, and a summary.

2. Analysis Model and Assumptions

The analysis of the cylindrical pool behavior was performed with the SIMMER-II code [2]. The calculational model for the CRBR active core and surrounding regions was adapted from that used for a previous intersubassembly gap fuel removal investigation [1]. The calculational mesh is shown on Figure 1. The regions within the mesh represent local regions in the reactor where geometry or thermal-physical conditions do not differ initially. They are used for specifying the local conditions and physical characteristics to the code. The modeling characteristics of these regions are listed in Table 1.

The specific characteristics of all regions surrounding the active core, regions 20 through 67, are unimportant in this assessment except that they contain the true material smear densities to provide proper neutronic boundary conditions for the active core. They were treated as non-flow regions thereby producing a sealed pool configuration.

The active core, regions 1 through 16, was treated as a completely homogenized pool. The fuel and subassembly wall steel of internal blanket and driver subassemblies were mixed at the fuel liquidus temperature of 3100 K. This mixture was assigned to the core region with an assumed uniform void except for the two top node rows which were assumed totally voided. Because the homogenization produces a large positive reactivity effect and some slumping was assumed, the full inventory of core materials could not be utilized in conjunction with the specification of a neutronically critical system.

Adjustments were made in the inventory to provide the initial critical state. The resulting initial pool void fraction was 48% and the fuel inventory was approximately 75% of nominal. This implies a prior fuel loss equal to 25% of the nominal inventory. The cladding steel, assumed to have been removed, was placed in the axial blankets equally. The removed fuel was assumed to be neutronically inert and therefore is assumed to be physically removed beyond the axial and/or radial blankets.

The neutronics treatment is 18-group, space-time, transport theory. The isotopic mixtures and distributions used in this assessment were obtained from Westinghouse (see Appendix A of Section II.3) for the EOC-4 core state. The neutronics calculational mesh overlays the fluid dynamic mesh from node 7 to node 28 axially and node 1 to node 18 radially. The larger radial fluid dynamic mesh-cells are subdivided for the neutronic analysis.

The aspects of the SIMMER-II modeling that are of primary importance in this assessment are the interfacial smearing of material, void collapse, and the liquid-vapor momentum coupling.

The interfacial smearing that occurs in SIMMER-II is a known result of the donner-cell differencing of the Eulerian fluid dynamics equations. Its true extent is proportional to mesh-cell size and, in a two-phase system, to liquid-vapor momentum coupling, in addition. If interfacial interactions dominate the physical problem of interest, considerable care must be exercised in the analysis. The primary interfacial physics of concern in this analysis are fluid dynamic breakup and dispersion by instability mechanisms. If a large portion of the fluid is highly dispersed during the initial out-slosh, the reassembly rates and resulting yield characteristics can change significantly. This was discussed in detail in Appendix B for the annular pool. The adequacy of the SIMMER-II treatment or, more appropriately, simulation of this process is addressed below in the benchmarking section.

Void collapse in this assessment is associated with condensation because of the assumption of fuel and steel vapors only in the pool initially. As the pool is compressed by the perturbing pressure source, the vapors in the pool are compressed and supersaturated, thus producing a condensation potential. If the vapors condense on a time scale that is smaller than the sloshing interval, the spring-back characteristics of a two-phase, compressed system will be mitigated. It would then occur only as a result of reboilup which may be suppressed by a slightly increased over-pressure in the core, the natural result of the initial pressure perturbance. Thus, rapid void collapse will result in an essentially single-phase slosh-in.

In SIMMER-II the condensation is treated as a heat transfer limited process at the liquid-vapor interfaces. The local saturation temperature is computed from the vapor density and temperature (vapor may be superheated). This saturation temperature exists at the condensing interface and is the thermal "force" to drive the condensation energy into the liquid. This condensation is calculated to occur only at the liquid interface of the condensing specie in a multicomponent situation such as the fuel-steel pool. In the absence of local noncondensibles, this model is straightforward and adequate with the primary uncertainty being the interfacial or condensing area. The areas are computed in SIMMER-II based on the local liquid dispersion size from fluid dynamic breakup, flashing, or input constraint and on the local liquid volume fractions. For this assessment the time scale available for condensation is a few tenths of a second and therefore the uncertainties in the detailed modeling are not a factor in the overall results.

The modeling of liquid-vapor momentum coupling is important primarily in determining the effectiveness of the initial pressure perturbation in creating the coherent out-slosh. SIMMER-II treats this coupling as an effective drag resulting from the relative velocity between the liquid and vapor each of which is treated with its own momentum equation. The effective drag depends on the local dispersion of the material and void fraction. This coupling has been tested [3, 4, 5] over a wide range of conditions representing a range of flow regimes and found to be very reasonable for predicting overall fluid motions. For this application we postulated or produced initial pressure perturbations that assure the out-slosh. Therefore, these details are not of major importance.

3. Analysis Results

Two cases are presented which represent two regimes of initial pool perturbations, mild recriticality and local sodium interaction. The results are presented in terms of the reactivity and power histories, sequences of liquid fraction plots, and integral mass redistribution plots.

3.1. Recriticality Sloshing

This case was initiated by gravity slumping of the pool leading to a prompt-critical burst yielding approximately 5 full-power-seconds. This results in a rapid out-slosh which drops the reactivity to a highly negative value as shown on Figure 2. The associated power

transient and energy yield is shown on Figures 2 and 3, respectively. The subsequent pool motion is shown on the sequence of distributions in Figure 5. The classical post disassembly distribution is seen in Figure 5b. The material discharged to the top is seen draining back in Figures 5c and 5d. The material at the outer wall is draining at 0.8 s. The initial void has been eliminated in most of the core mass. During this period the material at the outer periphery is draining downward and turning inward at the bottom. At approximately 1.0 s, criticality is reached at a ramp of approximately 120 \$/s. By suppressing the reactivity state at about 0.99 s, the fluid motion can be observed beyond 1.0 s. This is shown in Figures 5h and 5i. The main mass of material continues to move inward at a nearly constant rate as seen on Figure 6. This figure gives the inventory of fuel in a central cylinder (radial nodes 1 through 5) having the full core height. This constant mass in-flux (approximately 2500 kg/s) to the center of the reactor suggests an increasing ramp rate as the in-slosh proceeds because of the increased differential worth that develops as the mass accumulates in the central region. This effect does not become pronounced however until material begins to peak in the central region (see Section II.7).

The two-phase mass in the central region of Figure 5i is seen to remain two-phase and to be displaced upward by the in-slosh instead of collapsing. The fuel temperature in this region is higher than that at the outer periphery. Thus there is a vapor flux generated that maintains the dispersed state in this region.

Figures 7 and 8 show the fuel inventory and the average void fraction in the central region but over a height of approximately one-third of the core (axial nodes 12 through 16). The average void in this region is important from the standpoint of energy yield for a given ramp. We saw in Appendix A that a void in the range of 20% or less will moderate the yield and its dependence on ramp rate. The recriticality at about 1.0 s had an average void in this region of about 30% and did generate a relatively large yield of about 15 full-power seconds. The mass of the pool includes the internal blankets in this case instead of the driver fuel alone that was used for the disassembly results in Appendix A and Section II.7. Thus the equivalent energy deposition per unit mass is very similar to the 100 \$/s case discussed there for the normal high void situation. The important trend to note is that larger ramps require central pile-up and associated reduced void. Thus the yield is strongly moderated. This is very evident in the result of case 2.

3.2. Sodium Induced Sloshing

This case was initiated by assuming that 250 g of liquid sodium interacted at the bottom of the pool at its axis. The neutronic transient is shown on Figures 9 through 11. The reactivity ramp changes very rapidly from 0.40 to 4.5 s. Following the sloshing behavior in Figure 12 shows the reassembly at the center during this time. The resulting ramp rate is approximately 300 \$/s. The integrated amplitude or energy yield is only 8 full-power-seconds.

The mass influx into the central cylinder is seen to be essentially constant from Figure 13. Comparison of Figures 9 and 13 implies the rapid change in differential fuel worth as this central region is filled.

Figure 14 shows the reason for the small energy yield for this large ramp, i.e. low void fraction at high ramp. This result is also consistent with those of Appendix A and Section II.7.

4. Experimental Benchmarking

To benchmark the capability of SIMMER-II to adequately assess sloshing behavior (fluid dynamics), a series of experiments is being conducted in the existing OMEGA facility [6] (see Figures 15 and 16) at Purdue University. One experiment simulating whole-core, centerline perturbed sloshing has been completed and analyzed with SIMMER-II.

The experiment was run with a 0.9 m diameter by 0.3 m deep water pool. The cover gas space above the pool was also 0.3 m. This pool depth and cover gas space represent in full scale the reactor with a mid-plane (in the pool) induced slosh such as a recriticality. The diameter is about one-half of full reactor scale. Thus we have a very fine representation of the reactor core. The slosh is induced by introducing nitrogen gas at the bottom centerline of the pool through a rupture disc arrangement. The volume of gas (0.005 m^3) and the initial pressure ($\sim$ 7 atm) were selected to give a gentle perturbation to the pool thereby assuring good data resolution (high speed photography) during the initial expansion phase. This was accomplished indeed with very clear results for bubble growth, pool surface displacement, and bubble collapse. The bubble growth contours as a function of time are shown in Figure 17 and the upper surface displacement at the centerline is shown in Figure 18. The upper surface shape is given in Figure 19.

A SIMMER-II model of the experiment was generated that included the nitrogen source and the complete pool (and cover gas). Node sizes in the pool and cover gas were 2 cm axially and 2.5 cm radially. The calculation was initiated at the time of rupture disc failure in the experiment.

The calculated upper surface displacement at the centerline is shown in Figure 18 as the circles. The agreement is excellent. We can get a better view of the agreement by comparing Figures 17 and 19 with the sequence of calculated bubble and surface contours in Figure 20. The initial state is shown in Figure 20a. The growth shape in both experiment and calculation is very close to hemispherical. The maximum growth occurs at about 30 ms in both and the bubble collapse is nearly identical in both.

These results indicate that SIMMER-II performs very well in the early bubble growth phase of a slosh. It is during this phase that the momentum is produced in the liquid thereby setting the stage for the subsequent in-slosh.

5. Summary

Whole-core, centerline induced sloshing does have the potential to produce high ramp rate events. The configuration and extent of the in-slosh are of major importance in determining the magnitude of the ramp rate and the energy yield. There is a connection between the high ramp rates (300 $/s) and the accumulation of a dense (low void) mass of fuel at the centerline of the pool. The dense mass produces large worth gradients near the centerline region such that further influx of mass has a large reactivity effect. The existence of this dense region offsets, however, the large ramp in terms of energy yield.

The benchmarking activity performed as part of the independent assessment of CRBR energetics indicates that SIMMER-II is very capable of adequately addressing and quantifying pool sloshing recriticalities.

TABLE 1
REGION CHARACTERISTICS IN THE SIMMER-II
WHOLE-CORE MODEL FOR ANALYZING
CYLINDRICAL POOL BEHAVIOR

Region Number	Reactor Region	Modeling Characteristics
1 through 12	Active core	Homogenized pool
13 through 16	Internal blanket (IB)	Homogenized pool
17 and 18	Radial blanket (RB)	Interconnected gaps - closed
19	Radial reflector (RR)	Interconnected gaps - closed
20 through 23	Lower axial blanket-driver	Complete blockage
24 through 27	Lower axial blanket-IB	Interconnected gaps - closed
28	Lower axial blanket-RB	Interconnected gaps - closed
29 through 32	Lower axial blanket-driver	Interconnected gaps - closed
33	Lower shield	Interconnected gaps - closed
34	Radial reflector nozzles	No structure
35 through 38	Upper axial blanket-IB	Interconnected gaps - closed
39	Upper axial blanket-RB	Interconnected gaps - closed
40 through 43	Upper axial blanket-driver	Complete blockage
44 through 47	Upper axial blanket-driver	Interconnected gaps - closed
48 through 51	Upper axial blanket -IB load pad	Interconnected gaps - closed
52	Upper axial blanket -RB load pad	Interconnected gaps - closed
53 through 56	Upper axial blanket -driver load pad	Interconnected gaps - closed
57	Radial reflector load pad	Interconnected gaps - closed
58 through 61	Upper axial blanket-IB	Interconnected gaps - closed
62	Upper axial blanket-RB	Interconnected gaps - closed
63 through 66	Upper axial blanket-driver	Interconnected gaps - closed
67	Radial reflector	Interconnected gaps - closed

APPENDIX D
WHOLE CORE DISASSEMBLY ANALYSIS

1. Introduction

In this appendix we present the model used to assess the energy yield characteristics of whole-core disassemblies for postulated disrupted core states. We also discuss the initial conditions used and the method of reactivity insertion. The four configurations investigated are shown in Figure 9 of Section II.7. They will be described in more detail in the following.

2. Analysis Model

The analysis model for these disassembly calculations with SIMMER-II [1] was adapted from that used for a previous assessment of intersubassembly gap fuel removal [2]. The calculational model is the same as that shown in Figure 1 of Appendix C. The region characteristics are the same as in reference [2] except for the active core regions 1 through 12. The specific characteristics of these regions will vary depending on the configuration being simulated (intact pin structure, totally disrupted, or totally disrupted and partially slumped).

This model was used because it permitted a partially mechanistic representation of an advanced core state (both geometric and thermal) for a starting point. The state selected was that at the 5 s point in the transient of reference [2]. This state was reproduced for this investigation by automatically generating a new SIMMER-II input file from the output of that analysis. Reasonable temperatures were thus obtained for the internal and external blankets as well as for any intact fuel in the outermost driver regions 9 through 12. All driver regions are assumed blocked and completely voided.

The neutronic model is the same as that used in Appendix C. Prior to performing these analyses a check was made on the effective Doppler feedback because it is very important in determining disassembly energy yields and because it cannot be explicitly monitored in the transport theory formulation of SIMMER-II. These checks were performed through K-effective calculations for core temperature changes of 1000 K (intact, voided core with a fuel

temperature distribution typical of that at initiation of clad melting). The results were in excellent agreement with those calculated in Appendix A of Section II.3.

The ramp rates were generated in these calculations in a way that approximates the expected mode of recriticality during the disruption phase, namely fuel slumping into the lower part of the core. Once a slumping region was defined a slumping velocity was determined that provided the desired ramp. By using material motion instead of a programmed ramp, a natural mitigation of the ramp is permitted from local pressure gradient development as the power rises during the approach to prompt critical. This approach worked very well and very predictably although the mitigation effects were not significant for ramp rates of 25 $/s and larger.

3. Configurations

A total of four configurations were used in this investigation. The reference configuration, labeled "0," is an idealized arrangement through which the classical two-phase disassembly yields could be established. These yields for various ramp rates provide a baseline against which the yields of the disrupted core situations can be related to get a relative sensitivity of yield to configuration. Configuration "0" is shown in Figure 9a of Section II.7. The driver subassembly walls are generally unmelted but are assumed to have little strength such that they have deformed to close the adjacent intersubassembly gaps. Thus the driver regions consist of about 10% SA wall steel, 34% liquid fuel, and 56% void. The cladding and wire wraps are removed to the axial blankets. As seen in Appendix A this material arrangement should guarantee classical two-phase disassembly mechanics. It is an idealized arrangement in that it can never develop in a neutronically active system as seen in Section II.5.

Configuration "2" represents an attempt to be somewhat more realistic by assuming some initial slumping in the central three driver regions (a puddle depth of about 0.14 m). This could be considered as representative of the SA disruption phase. The material above the single-phase puddle is assumed to be of the same composition as in configuration "0." This two-phase material was assigned the appropriate "rainback" velocity to deliver the desired reactivity ramp. The disassembly was initiated at a critical state and nominal full power. To provide a critical state, approximately 10% of the total driver fuel inventory had to be removed (~ 20% of the central three drivers). This configuration is also idealized

because the "rainback" is uniform axially and radially, a clean interface is assumed between the single-phase and two-phase regions, the ramp rates are arbitrarily assigned, and no disruption is assumed in driver region 4. It is a perfect arrangement for quantifying the magnitude of any potential "boost" phenomenon.

Configuration "3" represents the situation that might be expected in the late initiating phase or early SA disruption phase. A small group of SAs (12 in this case) are assumed to be slumping to produce the driving ramp. The purpose of this configuration is to determine the extent to which very localized slumping and radial flux shape changes could alter the yield spectrum. The arrangement is identical to configuration 0 except that driver 4 is intact and driver 1 only is given a uniform downward velocity to provide the desired ramp. This configuration is not highly unrealistic if strongly leading SAs are involved as in EOC-4. Their radial position in this arrangement is somewhat in error, however. The idealization in this configuration relates to the arbitrary specification of slumping velocity (24 m/s to achieve 100 $/s). This is clearly unreasonable on physical grounds for blocked SAs. However this configuration should quantify the relative sensitivity of the yields to this configuration when compared to the others.

Configuration "5" represents a late stage of the SA or perhaps annular pool disruption phase. The core is uniformly slumped with a puddle depth of 0.21 m. The "rainback" is nearly complete. It is constituted as in configuration 0. In order for this configuration to be critical, about 36% of the fuel had to be removed. This situation is near the permanent neutronic shutdown condition. Again the ramps are delivered by the velocity of the rainback. The region above the "rain" region is void. This should provide insight into the yields at the opposite configuration extreme from configuration 0.

4. Results

The results in terms of yields (FPS) are shown in Figure 15 of Section II.7 as a function of ramp rate and configuration. The results show the existence of the "boost" for the high inventory configurations in which bottom puddling occurs (configurations 2 and 3). They also show the presence of strong mitigation for low inventory, highly puddled configurations (configuration 5) as would be expected from the single-phase disassembly dominance discussed in Appendix A. These results are in total agreement with the expectations generated from the K-effective assessments of these configurations that show the relation between inventory, flux peak/puddle alignment, and boost potential.

Two sets of results are given in Figures 1 through 3 and Figures 4 through 6 for configuration 0 and 2 respectively. Both sets are for a 50 $/s initiating ramp. Figures 1 and 4 show the reactivity transients. The reactivity for the two-phase disassembly levels out because of Doppler and turns down rapidly because of fuel motion or classical disassembly. The reactivity history for configuration 2 is very different in that it levels out because of Doppler feedback but then spikes upward before the rapid turndown. This is characteristic of the single-phase "boost" phenomenon. The power transients also show a very different character (compare Figures 2 and 5). The boost causes the power to rise to a much higher level and then decrease very rapidly as in a single-phase disassembly. This is exactly what is occurring. The difference in energy added to the materials or yield can be seen by comparing Figures 3 and 6. This difference is about a factor of 2.

5. Summary

There appears to be a significant configuration effect on disassembly yields when considering these postulated configurations. It is reasonable that these phenomena occur under the specified conditions. The major question to be addressed is the realism of these configurations in the neutronically active, disrupting core.

TABLE 1
REGION CHARACTERISTICS IN THE SIMMER-II MODEL FOR ANALYZING WHOLE-CORE DISASSEMBLY ENERGY YIELDS

Region Number	Reactor Region	Modeling Characteristics
1 through 12	Active core	Variable per configuration
13 through 16	Internal blanket (IB)	Interconnected gaps
17 and 18	Radial blanket (RB)	Interconnected gaps
19	Radial reflector (RR)	Interconnected gaps
20 through 23	Lower axial blanket-driver	Complete blockage
24 through 27	Lower axial blanket-IB	Interconnected gaps
28	Lower axial blanket-RB	Interconnected gaps
29 through 32	Lower axial blanket-driver	Interconnected gaps
33	Lower shield	Intersubassembly gaps
34	Radial reflector nozzles	No structure
35 through 38	Upper axial blanket-IB	Interconnected gaps
39	Upper axial blanket-RB	Interconnected gaps
40 through 43	Upper axial blanket-driver	Complete blockage
44 through 47	Upper axial blanket-driver	Interconnected gaps
48 through 51	Upper axial blanket-IB load pad	Interconnected gaps
52	Upper axial blanket-RB load pad	Interconnected gaps
53 through 56	Upper axial blanket-driver load pad	Interconnected gaps
57	Radial reflector load pad	Interconnected gaps
58 through 61	Upper axial blanket-IB	Interconnected gaps
62	Upper axial blanket-RB	Interconnected gaps
63 through 66	Upper axial blanket-driver	Interconnected gaps
67	Radial reflector	Interconnected gaps

II.8. CONCLUSIONS

On the technical bases developed in the previous six sections we now proceed to assign probability split levels at each bifurcation of our generic accident sequence path (Figure 1). The procedure has been described in Section II.1. The rational for these assignments will also be briefly given. Also, we have presumed that the Applicant will follow our recommendation for a design fix to eliminate the precipitous manifestation of the plenum fission gas pressure upon the fuel column upon disruption, and that the vessel head capability will be restored to its originally specified value of 75 MJ sodium slug impact kinetic energy. Since this probabilistic exercise is carried out on an order-of-magnitude basis we assign only the 1, 10^{-1}, 10^{-2} and 10^{-3} levels on each branch, that is, the sum of branch probabilities from any state should add up to unity within 0.111. The discussion below is carried with reference to Figure 1.

- The sodium void worth, including uncertainties, is adequately low to guarantee, presuming the design fix for the plenum fission gas compaction problem, the absence of LOF-d-TOP. The only remaining mode for energetic behavior is by fuel slumping under gravity. The assured incoherent nature of this process within the initiating phase guarantees the absence of significant energetic events at this stage. Hence, a value of 1/1000 (physically unreasonable) was assigned to path α. Having assured ourselves that no mechanisms exist to drive an energetic initiating phase behavior it would appear even more difficult to identify energetic events of sufficient magnitude to challenge the substantial vessel head structure (VHS) capability. Hence, a value of 1/1000 was assigned to path α'.

- The subassembly and annular pool stages do not favor amplification of mild recriticalities to substantial energetic events. This statement is based on inherent physical behavior arguments and analysis, and it is insensitive to gross uncertainties in detail phenomenology of fuel motions. It is for this reason that energetic VHS failure is considered physically unreasonable and the value of 1/1000 was assigned to paths β' and γ'. For the same reasons, in fact, it is difficult to achieve any recriticality of magnitude greater than that of a 30 \$/s two-phase disassembly, which we chose to define as the lower limit for this path. Clearly, the events here are of more detailed nature, and we hesitate to claim that an out-of-spectrum characterization would be adequately conservative. Hence, an edge-of-spectrum value of 1/10 is assigned to both path β and γ.

- For the whole core pool we have identified mechanisms yielding amplification of mild recriticalities and, associated energetic releases approaching the structural capability of the VHS. Although the conditions under which these mechanisms may become operative are highly idealized, i.e. perfect symmetry and homogeneous pool, we cannot at present rule out such behavior. However, we also found that only special pool configurations are potentially susceptible, that only short time intervals are required to obtain the incremental fuel removal through the radial blanket gaps for termination, and that the strongly non-homogeneous and chaotic character of this pool following its initial formation dampen its neutronic response. Therefore, its tendency for energetic termination is not midspectrum but clearly edge-of-spectrum. Thus we assign to the path δ a value of 1/10. However, recognizing that even our idealized calculations have failed to produce energetic releases exceeding the capability of the VHS we cannot assign a high conditional probability for head failure. We hesitate claiming anything less than end-of-spectrum, however, primarily because we wish to maintain the high level of confidence in the conservative estimation of these numbers as specified. Thus, a value of 1/10 is chosen for path δ'.

- We quantified the transient pressure histories that drive the dispersal as well as the associated fuel removal rates. Due to co-disruption and sustained neutronic activity we believe favorable conditions exist for mild "dispersal" termination throughout the core disruption phases. For such termination from the initiating phase, we remain skeptical primarily because the judgement depends on details of behavior with substantial uncertainty band and absence of corresponding margins. However, such an evolution should not be considered outside of expectation completely. Hence a value of 1/10 in probability is assigned. Termination from the S/A-scale pool phase is similarly uncertain. The reason is that at this stage the competition, between opening up into the annular pool phase and expelling fuel for termination, is still strong. In the absence of sustained pressures driving these motions (an oscillatory character is expected), we hesitate to conservatively call the expectation for such termination any more likely than edge-of-spectrum. However, as the core disruption develops further, clearly more escape paths open up; new ones into the radial blankets and the control rod assemblies and old ones by remelting blockages (especially those formed in many of the axial blanket regions due to co-disruption). The process of dispersal is overwhelmed by the continuously increasing path availability especially in the time interval between destruction of internal blankets (entry into the cylindrical pool) and mixing of this material that is required to yield the homogeneous whole-core pool. Hence an out of spectrum choice is made for this latter path (1/100) while termination from both of these advanced core disruption states (annular and whole-core pools) is assigned a probability of unity.

- Based on the above the total vessel head failure probability, conditional to the occurrence of the LOFA, is approximately 3×10^{-4}. Returning to our definitions this number indicates that such an event should be considered physically unreasonable. We recall that the assignment of numbers for each path was intended as a high level of confidence, conservative, bound with regard to the key accident branch points (i.e. virtual assurance that the assigned probability number would not be exceeded). Still this final result indicates considerable margin before the "physically unreasonable" threshold in probability definition is met.

- It is emphasized that these probabilistic estimates given are an integral part of the primary definitions utilized in assigning branch probabilities and they should only be utilized in conjunction with these definition. An example was provided above, whereby the final probability for energetic head failure was converted back to a physical meaning of expectation. As another example, the probability of experiencing a whole core, homogeneous, pool given a LOFA is 10^{-2}. This number is converted to words to conclude that "the occurrence of a homogeneous whole-core pool given a LOFA should be considered as very unlikely and outside the spectrum of reason." Also, it is important that our numbers not be used as inputs directly into PRA studies. Rather the word interpretations mentioned above should be converted to PRA input numbers in a manner physically consistent with other qualitative inputs.

III. TRANSIENT OVERPOWER INITIATED CDAs

1. Objectives and Overview

Overpower conditions (as initiating events) result from unchecked reactivity increases. Such increases may occur in step-like or continuous fashion. Mechanistically, a step-like reactivity increase may result from sudden changes in core geometry due to severe external forcing (typically a severe earthquake), or from sudden changes in core composition due to reduction in coolant content (typically a rapid formation of a fission gas bubble). A continuous reactivity insertion on the other hand would be the consequence of sustained removal of poison material (typically a withdrawal of control rod(s)). In this section we are concerned with this latter mode. Step changes of reactivity will be considered in the context of earthquake events in Section 3.

Clearly, only unprotected TOP events can lead to core disruption. Inherent negative reactivity feedbacks are inadequate to compensate the continuously imposed reaction insertion. The power level rises quickly, typically reaching the primary and secondary scram trip levels of 115% and 130% power respectively in just a few seconds, and for all but the smallest imposed reactivity ramps rates fuel melting and pin failure would occur before coolant boiling. We have already encountered a similar sequence of events in the TOP driven by the LOFA-initiated material relocations (LOF-d-TOP, Section II.4). The energetics mechanisms and concerns for autocatalysis are also similar (i.e. mid-plane failures and pin-internal fuel motion). The distinguishing characteristics in the present situation are full coolant flow (as opposed to approximately 20% in the LOF-d-TOP) and low reactivity insertion rates (as opposed to many $/s in the LOF-d-TOP). The lower ramp rates would be less likely to cause mid-plane failures and the higher coolant flow would favor (in both rate and extent) sweepout. However, the potential availability of the whole core for such failures in the present case (as opposed to only a fraction in the LOF-d-TOP case) suggests that a careful delineation of the autocatalysis-prone range of conditions needs to be made nevertheless.

Various combinations (cases) of core conditions (burnup), driving reactivity ramp rates, and parametric variations in key phenomena (i.e. Doppler feedback, failure location, etc.) were examined by the

Applicant [1]. The SAS3D [2] code was used in these evaluations. The two extremes of the core burnup states, i.e. BOC-1 and EOC-4; were combined with the "design ramp rate of 4.1 ¢/s" (i.e. uncontrolled withdrawal of the peak worth control rod at its design speed) as well as with the arbitrarily higher rates of 10 ¢/s and 50 ¢/s. In addition, parametrics with "pessimistic" Doppler and material worth values, and "forced" midplane failures (in the 4.1 ¢/s - BOC and 10 ¢/s - EOC cases) were considered. Only the 10 ¢/s - EOC case with forced midplane failure and SAS/FCI modelling of post-failure fuel motion and fuel-coolant interactions evolved into an energetic event. Reanalysis of these events using the PLUTO2 code (coupled to SAS3D) did not yield such superprompt critical conditions, however. All other cases produced benign termination, neutronic shutdown or power stabilized at some level, by fuel sweepout. In fact, at best estimate only partial core damage was projected.

Our detailed evaluation of these analyses [3] raised a couple of important concerns in the areas of failure location and core-wide pin failure coherence. The location of pin failure under TOP conditions has always been a subject of controversy. The situation was aggravated in favor of mid-plane failures by the results of the most recent (released during the course of our review), intended as prototypic, SLSF W-2 TOP-simulation test. We took, therefore, the position that midplane failures, during low ramp rate TOPs, not only could not be excluded but that they might even represent the best-estimate choice. The subject of core-wide coherence is important particularly if mid-plane failures are assumed. Specifically the time-scale between successive pin failures (pin failure coherence) must be long compared to the characteristic sweepout time (typically approximately 30 ms) if the escalation of the overpower condition is to be interrupted. The cases examined by the Applicant did not adequately envelope the expected CRBR core-wide coherence. Specifically, we identified an intermediate burnup core configuration, the EOC-3, in which the six highest power fuel subassemblies in cycle 4 are replaced by blanket material, as a more appropriate case for consideration in this respect.

An update of the Applicant's arguments in this area was provided [4] in response to our Question #1 (Table 2 of Section I) during the early stages of the independent assessment stage of our review. This assessment addressed the above concerns and arrived to the same position, namely, that "a prompt-critical response would be very unlikely even for combinations of pessimistic assumptions" on failure location and reactivity insertion rates. The principal effort in this documentation is to show the effectiveness of analytically

predicted sweepout mechanism by comparisons to available in-pile experimental data. These results which are in reasonable agreement with those of our own independent assessment are examined and discussed in detail in [5].

Based on the above reservations our independent assessment efforts attempted to more closely delineate the boundaries of autocatalysis. Although, upon closer examination the W-2 test has been found non-prototypic [6], we chose to maintain, in the absence of reliable evidence to the contrary, a mid-plane failure assumption throughout. As a consequence pin failure coherence assumes a position of central importance. Clearly, the failure time delay between any two groups of pins depends upon the relative power at the two respective locations (power distribution) as well as upon the absolute power level. As mentioned above the cycle 3 configuration envelops the power distribution aspect. The power level on the other hand will depend upon the assumed driving reactivity ramp rate. Hence, these evaluations must be placed in the proper context (probabilistic) of the control system failure mode and effects analysis. We begin, therefore, the detailed considerations, with this topic, in Section 2. The competition between pin-internal fuel motion and sweepout dictating the essential aspects of the phenomenological progression is discussed in Section 3. Certain peripheral issues such as the potential for achieving advanced core disruption states akin to those found in the LOFA progression are also included here. Finally, the TOP unique energetic circumstances identified on the basis of this discussion are dealt with in Section 4.

2. Driving Ramp Rates and Relative Likelihoods

Various combinations of the control rod subsystem failures were examined [7] with the object of ordering the relative likelihood of reactivity insertion rates.

Because of multi-levels of overspeed protection incorporated in different subsystems of the control rod system, the rate of reactivity insertion may be divided into discrete levels corresponding to multifailures up to an overspeed protection failure. Starting with the rod withdrawal accidents in group mode, the first overspeed protection is in the reactor controller system. This limiter will limit the rod withdrawal at speeds below 4"/min. Thus at the first level is the control rod bank withdrawal at the speed of up to 4"/min. Five subsystems are required to fail for this occurrence that results in a reactivity ramp rate of 5.6 ¢/s.

of a mechanical common mode failure of five secondary control rods. Compared to the electrical failure of the secondary system (required for the classical TOP), this common mode mechanical failure of the secondary shutdown system is judged to be very unlikely. The combined TOP/LOF event was not, therefore, considered any further.

3. Ranges of Phenomenological Progression

All available accident analysis experience [1, 8, etc.] suggests that the energetically significant TOP phenomenology is dominated by Initiating Phase events. We concur with this conclusion. The discussion in this section will therefore follow this emphasis. As mentioned above a central aspect of this phenomenology is the competition between pin failure coherence on the one hand and fuel sweepout on the other. In assessing the outcome we utilized the codes PLUTO2 [9], SAS/EPIC [10] and the PLUTO2/SAS4A [11] which are the most advanced computational tools currently available in this area. A summary of this assessment is provided below. Additional details may be found in [12]. In what follows we have presupposed mid-plane failures. A discussion of this topic is given in Appendix A. Our rationale is that in view of the uncertainties such a choice is necessary to adequately explore the margins for energetic behavior. Clearly, failures well above the core mid-plane would be benign and as already documented by the Applicant would lead to early termination.

3.1. Pin Failure Coherence

Pin failure under TOP conditions is the result of thermal and mechanical clad loadings which in turn are driven by the overheating of the fuel contained within. That is, notwithstanding the uncertainties in failure mechanisms, and hence in the prediction of failure location(s) (see Appendix A), the relative timing of failures of pins for the same core and imposed transient can accurately quantified from their respective fuel enthalpy rise histories. This method was utilized in this study.

In addition to the BOC-1 and EOC-4 cases examined by the Applicant, the EOC-3 core was also studied here. The results, for an imposed 10 ¢/s TOP for BOC-1 and EOC-4 and 12 ¢/s for EOC-3, are illustrated in Figures 1 to 3 for these three cases respectively. As expected maximum coherence is observed in the EOC-3 case. The BOC-1 configuration appears only slightly more incoherent; however,

the low fuel fission gas content in this fresh core could not support as extensive pin-internal fuel motion and was judged of significantly lower energetics potential (as compared to the EOC-3 case). The EOC-4 case is clearly highly incoherent (channel 6 leading by more than 500 ms). In fact even though in this calculation the negative reactivity from sweepout in channel 6 subassemblies was arbitrarily suppressed, a significant incoherence (approximately 100-200 ms, i.e. ample time for manifestation of the sweepout negative reactivity effects) between the next group of failures (channel 7) and the remaining of the core could be seen. Thus for the BOC-1 and EOC-4 cases, in agreement with the Applicant, we can see no credible evidence for development of autocatalytic behavior. The more limiting EOC-3 scenario, however, needs to be discussed in greater detail.

To better resolve the coherence behavior the EOC-3 case [13] was analyzed with a 34 channel core discretization. From Figure 3 we deduce a pin failure incoherence of more than 300 ms for the first 6 groups of subassemblies (6, 6, 3, 6, 6 and 3 subassemblies respectively). Significant fuel sweepout must occur within about 100-200 ms of the failure of the first group of subassemblies to assure avoidance of self-accelerating trends. Furthermore, in this case the sweepout reactivity (negative) must be of sufficient magnitude to effectively counter the positive contributions due to pin internal fuel motion that needs to be considered in the light of the significant fission gas pressure driving forces present. In fact for the case shown, this additional reactivity insertion following the failure of the first 12 subassemblies may reduce the time interval to failure of the next group of subassemblies to as little as 100 ms. These sweepout requirements increase with the magnitude of the driving reactivity ramp rate. Thus for a 4 ¢/s TOP the failure incoherence becomes approximately 600 ms, while for a 20 ¢/s TOP only approximately 25 ms are available.

3.2. Sweepout Time Scales

Several in-pile and out-of-pile experiments are available and useful in addressing the sweepout question. In all cases rapid and extensive sweepout was measured. However, since none of these tests adequately matched the conditions of interest here, these data cannot be directly and quantitatively applied. The PLUTO2 code was utilized by the Applicant to bridge this gap [4]. With an appropriate selection of phenomenological parameters PLUTO2 results provided a fairly good match of observed fuel sweepout for in-pile, irradiated-pin, TOP TREAT tests H6 and L8. Similarly satisfactory

results were obtained for the E8 TOP test using PLUTO, the predecessor of PLUTO2. In order to assess how well these parameters could be determined we have utilized the PLUTO2 code for additional sensitivity studies on these parameters for the L8 test. The details of these evaluations are summarized in Appendix B. Our findings support the Applicant's position that PLUTO2 in conjunction with tests H6, E8, and L8 provide an adequate basis for predicting sweepout reactivities in CRBR TOP events.

Among the three available in-pile tests only in L8 were full length pins used, and it is therefore the best suited for supplying the fuel motion reactivity data necessary in our present evaluations. However, in this experiment there was a high driving reactivity ramp rate (approximately 7 $/s, initial period 0.08 s, peak power 75 x nominal) chosen to simulate an LOF-d-TOP event. It is important, therefore, to examine the applicability of these results to the much lower ramp rate TOP cases of interest here. This was accomplished by means of several PLUTO2 and SAS4A/PLUTO2 simulations as follows.

The total reactivity change transient due to fuel motion was measured in the L8 experiment. By neglecting the contribution due to in-pin motion, this same result may be taken to represent the sweepout reactivity. This assumption is based on the non-prototypically shorter (molten) cavity found in the L8 as compared to that expected in CRBR, at the same radial melt fraction. Furthermore this assumption leads to a conservative measure of the sweepout reactivity. This inferred experimental sweepout reactivity is compared to the PLUTO2 simulation in Figure 4. The choice of "specific" reactivity, i.e. expressed in terms of ¢ per subassembly per gram of fuel ejected from each pin, made for these comparisons is convenient in expressing a "removal" quality, i.e. more or less independently of the quantity of the fuel involved. In the very early period the calculation overestimates the data, however in the most critical 30-60 ms time period produces conservative results and a fair overall agreement is noted. This early overprediction could be the result of neglecting the contribution (positive) due to pin-internal motion in the L8 data. The simulation, again overpredicts the sweepout beyond 75 ms, however, the total fuel ejection (in L8) at this time is far outside the range of interest for a slow TOP. This is demonstrated in Figure 5 comparing the amount of fuel ejected in L8 (i.e. approximately 7 $/s), as simulated by PLUTO2, with the amount that would have been ejected if the L8 experiment was run at 10 ¢/s instead. Also, as shown, this latter amount would be very close to what would be expected in a CRBR 10 ¢/s TOP transient as predicted by a SAS4A/PLUTO2 simulation. Note that all

cases agree up to approximately 30 ms as they should since the ejection up to this time corresponds to the fuel contained in the (molten) cavity at the time of failure. In the high ramp TOP continuing melting and ejection is observed, however, the 10 ¢/s ramp is too slow to generate significant additional molten fuel in the time frame of interest for sweepout. This is a key point in assessing sensitivity of autocatalysis potential to uncertainties in the phenomena of sweepout.

The effect of other L8 non-prototypic aspects on sweepout can be analytically deduced by comparing the PLUTO2 L8 simulations for a 10 ¢/s TOP to those obtained with SAS4A/PLUTO2 for the CRBR geometry. One such result is shown in Figure 6. The results agree well up to 20 ms. Then the SAS4A/PLUTO2 results go higher (more efficient sweepout) as expected because less fuel is ejected from the CRBR pin (see Figure 5). It is important, however, that in both cases the major sweepout feedback of -0.15 ¢/SA/g/pin is obtained within approximately 20-30 m/s and continues generally to rise well into the 80-90 ms time frame. This general increase in specific sweepout reactivity in the 10 ¢/s case of Figure 6 should be contrasted to the leveling off observed in the 7 $/s case of Figure 4. The explanation is contained in the total amount of fuel involved as shown in Figure 5.

On the basis of this discussion we conclude that for a 10 ¢/s TOP in the CRBR a specific sweepout reactivity of -0.15 ¢/SA/g/pin occurring within approximately 60 ms from the time of failure represents a reasonably conservative estimate consistent with available experimental data.

3.3. Accident Analysis Aspects

On the basis of the above, the determination of the TOP outcome really happens within 50-100 ms from pin failure and can be deduced rather simply as follows. With a specific sweepout reactivity of -0.15 ¢/g/pin/SA (Figure 6) and a fuel mass ejected of approximately 20 g/pin (Figure 5), a net reactivity reduction by approximately 3 ¢/SA at 50 ms is estimated. The associated reactivity increase because of sodium voiding is typically ~1 ¢/SA and that due to pin-internal fuel motion (of approximately 20 g/pin) is approximately 2 ¢/SA. Thus the failure of the 12 subassemblies of Channels 20 and 15 (EOC-3 core) would produce a negative feedback countering that due to voiding and in-pin motion of approximately 36 ¢ within approximately 50 ms. One actual transient as depicted by SAS4A/PLUTO2 is shown in Figure 7. Even a conservative envelope

above the net reactivity curve on Figure 7 indicates a subcritical state of about -30¢ at 90 ms. The next group of SAs (Channel 21 with 3 SAs) fails at about 135 ms. The projected reactivity state at that time is well below -30¢ while the maximum positive from Channel 21 is only about +5¢. It is seen that the sweepout reactivity rate of > -5 $/s for the 12 SAs by far cancels the 12 ¢/s insertion rate beyond 50 ms. Thus ample sweepout exists in this 12 ¢/s CRBR TOP case to assure termination even under the most restrictive coherence conditions and pessimistic failure location assumptions. A large number of parametric whole-core CRBR TOP simulations were carried out to further support this conclusion. Two different codes, EPIC and PLUTO2, were utilized. The effects of pin-internal fission gas pressure at failure (50 to 600 bar) and the intensity of fuel-coolant heat transfer following failure were particularly explored. The results are documented in [12] and support the simple derivation provided above.

The longer term evolution will depend on the coolability of the disrupted and swept-away fuel. All available experimental evidence indicates that for the wire-wrapped pin design, in-core blockages are not to be expected. The Applicant has addressed the question of blockage formation and coolability and concluded that stable (coolable) conditions would prevail. We did not independently assess this problem. However, with the relatively small number of subassemblies affected and the relatively small degree of pin disruption predicted for the 12 ¢/s TOP, we cannot visualize an advanced core disruption and/or associated energetics even if non-coolable, in-core blockages were to be arbitrarily postulated. The so-called TOP-derived Transition Phase has been of some concern in the past regarding such evolution. We chose not to further pursue this topic on the following bases: (a) The heterogeneous core design provides fuel escape paths especially for isolated (subassembly-scale) molten regions (see also Section II.6), (b) Transition phase energetics have been adequately bounded for the LOF case (Section II.7) and no unique aspects could be identified for a TOP-derived (arbitrarily postulated) advanced core disruption.

4. Treatment of Unique Energetic Circumstances

As indicated in the previous section, an energetic TOP would be primarily the consequence of mid-plane failures and inadequate sweepout. We have also established that such behavior would not be expected even under the most limiting conditions consistent with physical reality and experimental evidence. Conversely, if one was to arbitrarily postulate the existence of such energetic behavior for

consistency reasons, one should expect a self-accelerating condition (autocatalysis) at least up to a certain level. Thus, although at initial escalation the tendency would be to increasingly favor mid-plane failures and, of course, coherence, there may be a power level at which the pressure build-up within the pin is rapid enough to cause ripping along its length, thus terminating the reactivity augmenting pin-internal (towards the core mid-plane) fuel motion. However, any of such inherent limits are difficult to support or quantify at this time. Thus the unique energetic circumstances, should one postulate such, consist of autocatalytic tendencies and the presence of sodium in the core. Both of these aspects were discussed in connection with the LOF-d-TOP (Section II.4). Given that at the present context we are even further removed from the realm of possibility, we will let discussion of Section II.4 suffice.

5. Summary

The potential for energetic TOP-initiated behavior was assessed for a limiting imposed ramp in the 10-12 ¢/s range. Even under the most limiting core-coherence conditions (EOC-3), such an energetic behavior is judged as an off-spectrum occurrence.

Additional work to further clarify the matters of pin failure mechanism and location under low ramp TOPs is recommended. This work would be useful in clarifying failure assumptions utilized herein possibly revealing additional margins of safety.

APPENDIX A
TIME AND LOCATION OF MOLTEN FUEL EXPULSION

1. Status of Fuel Rod Failure Prediction Methods

Extensive effort has been expended on experimentation and development of predictive methods for the time and location of fuel expulsion under transient overpower (TOP) conditions [1, 3]. The predictive process involves predicting expansion of the fuel relative to the cladding, predicting the interaction (load generated) between the two when they are in contact, and predicting the response of the cladding to the load that is generated. The behavior of fuel involves the range from temperatures characteristic of brittle ceramic behavior up to temperatures exceeding the liquidus point of fuel. The behavior of cladding must be predicted for a range of irradiation damage and for a wide range of strain rates, temperatures and temperature rates of change. Clearly, the subject is very complex.

The current understanding is that initially the fuel expands differentially against the cladding, generating high loads until the uncracked fuel at the center of the pin creeps, is thinned sufficiently, or is softened enough because of increasing temperature that it can no longer sustain the load. Cladding loading then decreases until the build-up of cavity pressure caused by release of fission gas from the fuel during the transient, by reduced cavity volume, or both, and augmented by increased fuel vapor pressure, again loads the cladding.

Empirical correlations having the form of stress-rupture formulations (Larson-Miller or Dorn parameters) are used to predict when the time-load-temperature history will cause cladding failure. These parameters collapse time and temperature into a single parameter that is correlated as a function of loading experimental tests.

These predictive methods involve modeling several individual processes and properties both in the fuel and the cladding. Particularly for fuel processes and properties, there are virtually no really applicable data. Accordingly, much of the properties and models are "calibrated" simultaneously against integral fuel pin tests. This effectively means that each of the predictive methods has several adjustable knobs, or correlating constants. There is no really good way to determine whether any of these methods can

extrapolate correctly outside their range of correlating data. Yet, they must necessarily be extrapolated because of inadequate coverage of the data base and because of factors in the tests that are atypical to the CRBR. These deficiencies in the data base are discussed in [1].

The most serious specific deficiencies in the predictive models are considered to be as follows:

- The cladding failure criteria do not specifically model the behavior of the fuel adjacency effect. The fuel adjacency effect, the term given to the more severe reduction of strength in cladding irradiated near fuel as compared to cladding irradiated to the same fluence but not near fuel [4], may significantly affect the location of expulsion. This is particularly true because of data that indicate the effect either does not exist or is much less severe [5, 6] above irradiation temperatures of 1050 to 1100°F.

- Current predictive methods do not address whether early cladding failures occurring prior to significant fuel melting may subsequently influence the location of expulsion.

- Current methods assume molten fuel expulsion is synonymous with cladding breach, probably a good assumption for TREAT tests. However, the mechanics of the molten fuel reaching the breach site, the opening or extension of the breach site from a small crack, and prerequisites for these processes to occur may be very important for slow overpower or LOF-initiated events.

- No generally recognized integrated thermal model now exists for fuel-cladding gap conductance and fuel thermal conductivity, particularly for transient conditions.

- Cladding failure models do not now directly address the possible influence of annealing or strain rate on the location or time of expulsion.

- There is a wide diversity in the modeling of fission gas phenomena in predictive methods, including the pre-transient distribution of retained gas, if the phenomena are modeled at all.

- There is virtually no way to verify the correctness of expulsion location predictions, and no data at all exist for the ramp rate range of greatest concern (the vicinity of 5 to 12 ¢/s).

2. Review of he W2 Test

The W2 test was a transient overpower test conducted by the Hanford Engineering Development Laboratory (HEDL) in the Sodium Loop Safety Facility (SLSF) in the Engineering Test Reactor (ETR) late in 1980 [7]. The test was conducted on a bundle of seven full length pins. The center pin was fully prototypic of the FFTF and nearly prototypic of the CRBR, except for the use of highly enriched uranium (93%) in the UO_2 portion of the mixed oxide. The peripheral pins used less highly enriched UO_2 and were designed with a large fuel-cladding gap to minimize the possibility of a peripheral pin failing before the central pin. The test as planned was of particular interest because of the following:

- The test transient was initiated at true steady-state conditions.
- The test simulated a credible ramp rate (5 ¢/s).
- Full length (0.91 meter fuel column) pins were used.

The test was probably as nearly prototypic as any that have been conducted. Nevertheless, there were atypical factors in the test, including the following:

- The high enrichment caused a pronounced radial power depression in the center pin, and a markedly asymmetric power distribution in the peripheral pins.
- Despite filtering to harden the neutron spectrum, it was still very soft and the cladding at the transient had less than one-tenth the fluence corresponding to typical fluences for the fuel exposure.

Pre-test predictions for the test with several of the available predictive methods agreed well with the observed time of expulsion in the test, but did not agree at all as to the location of expulsion, which was determined to be at axial midplane.

Subsequent post-test examinations and analyses by the experimentor [8] have established that for unknown reasons the flux collar was ineffective in obtaining the desired axial power distribution. The axial peak to average ratio was 1.39 rather than a desired 1.25. The radial power split between the central and peripheral pins was also more biased in favor of the peripheral pins than was desired. These differences further accentuated an already certain peripheral pin bowing tendency. The experimentor makes a good case for

explaining the oscillating thermocouple temperatures that were observed in terms of peripheral pins bowing in and out. It is not obvious, however, why the pins would osciliate back and forth dynamically.

The Applicant explains the mid-plane fuel expulsion as resulting from a melt-through of cladding on a peripheral pin caused by molten fuel contacting the cladding where it was jammed against the fluted tube and starved for coolant. This is probably the most rational explanation of the events; however, no data were found that would conclusively prove this hypothesis.

We believe enough doubt has been cast on the applicability of the W2 mid-plane failure that it should not be considered in determining the propensity toward mid-plane failure. The following briefly reviews the principal points of why the W2 failure should not be considered:

- Severe pin bowing does appear to have occurred.
- The factors that caused a marked tendency toward outward pin bowing in W2 were more pronounced than anticipated and will not be present in CRBR.
- The maximum amount of channel constriction possible in CRBR may be comparable to that achieved in W2 by jamming a pin between flutes; however, such an eventuality would clearly be an atypical mode of failure in a CRBR TOP-initiated CDA.

3. A Criterion for Molten Fuel Expulsion

The available systems for predicting the time of molten fuel expulsion, whatever their other problems, generally use methods that are impractical for large CDA analysis codes. Accordingly, the results obtained by these systems need to be correlated in some simple manner for use in the CDA codes. For this reason as well as to provide a criterion with some basis in the real world, we propose use of the axial peak fuel enthalpy as the key parameter, with a value of 1140 kJ/kg (277 cal/g) referred to room temperature as the criterion. By axial peak fuel enthalpy we mean the maximum value of the mean energy content at any radial slice along the fuel column.

Fuel enthalpy has been proposed as a failure criterion before, but never received general acceptance. This proposal is based on the discovery that the calculated values of peak fuel enthalpy at the observed time of fuel expulsion for nine TREAT tests [9-14] could

be correlated by a single value (1140 kJ/kg) with a standard deviation of only 76 kJ/kg (6.7%). Calculations were performed with the LAFM [15] code. These same calculations produced good agreement with thermal data taken in the tests, and the mechanically based cladding failure predictions agreed well with observed times of fuel expulsion. The tests for which calculations were performed are tabulated in Table 1 along with the calculated enthalpies and mass fractions of fuel in the liquid phase at the time of expulsion.

These tests among them covered a range of burn-ups of 30 to 120 MWd/kg, of fluence from 3 to 8 x 10^{22} nvt/cm^2 ($E \geq 0.1$ Mev), of linear power rating from 6 to 12 kW/ft, and of ramp rate from 50 ¢/s to 3 $/s. We believe that the fact that this wide range of conditions could be correlated by a single value of fuel enthalpy at expulsion implies that fuel conditions may be more important to fuel expulsion than previously thought, and that use of the criterion for slow overpower and LOF-initiated TOP conditions may be reasonable.

4. Location of Expulsion: TOP-Initiated CDA

The ramp rate range of interest in the TOP-initiated CDA is bounded on one side by the rate below which location of expulsion is unimportant to the outcome and on the other side by the maximum credible ramp rate. This range of interest is quite narrow, and includes from about 5 ¢/s to about 12 ¢/s, with some allowance for overlap.

There are no experimental data on the response of integral pins to ramp rates in the range of interest, and we must rely on other means of assessment. Our principal concerns about applying the predictive methods to this problem are that 1) the methods do not address the possible impact of no fuel adjacency effect above irradiation temperatures of 1050 to 1100°F, and 2) the methods do not address what influence, if any, breaches predicted prior to significant fuel melting might have on the location of expulsion.

Calculations were performed with the LAFM code to explore the predicted response of a peak power pin to ramp rates in the range of interest under various conditions. Fuel creep was considered in these calculations by setting the temperature at which fuel is strengthless to 2700 K, the same value as was used in the previously reported analyses of TREAT tests. Because the TREAT tests were all in the 50 ¢/s to 3 $/s range, use of the same value of TCREEP should be conservative (overestimate cladding loading) for slower ramp rates.

The analyses were performed for a pin with a peak linear heat rating of 11 kW/ft, estimated to be the nominal peak power pin at end-of-cycle 3 (EOC-3), at inlet temperatures of 750 and 600°F. The peak cladding midwall temperatures corresponding to these inlet temperatures were 1220 and 1070°F, respectively. Cladding breach predictions were made using the life fraction approach with the HEDL Dorn parameter correlation [16]. This correlation as used assumed that damage saturated at a fluence of 6×10^{22} nvt/cm^2 ($E \geq 0.1$ Mev) and that damage was not a function of irradiation temperature.

In all cases analyzed, initial breaches occurred prior to significant fuel melting. By the time the peak fuel enthalpy had reached the enthalpy criterion proposed previously, life fractions had exceeded one over virtually the entire pin and from mid-plane higher had exceeded one by several orders of magnitude. To assess the probability of mid-plane expulsion because of the influence of an early breach, we reviewed the axial profile of life fraction at the time of initial breach--that is, the earliest time that a life fraction of one was achieved anywhere on the pin. The location of the peak life fraction at that time, coupled with the gradient of the life fraction either way from the peak, provides some guidance as to the possibility of the early breach significantly affecting the subsequent site of expulsion. The life fraction profiles for the two inlet temperatures are shown in Figure 1.

To assess the impact of the fuel adjacency effect being markedly diminished above a particular temperature, one need only look at the axial location on the cladding of the presumed temperature at which the change occurs and assume that expulsion would occur only below that location. This presumes that the effect is a cliff--that is, that the effect disappears over a narrow temperature range. The steady-state temperatures are compared in Figure 2 for the two inlet temperatures.

Finally, to assess the location of expulsion in the absence of the foregoing two biases, one approach would be to review the axial profile of the life fraction at the time the fuel enthalpy criterion is reached. This approach may be risky because it assumes that the fuel itself plays a significant role and that the actual expulsion of fuel does not occur at the very instant that both molten fuel is available in the pin and the cladding has breached. Clearly, if the foregoing is true, then the mechanics of how molten fuel reaches the breach site, how the breach site opens, and what conditions are necessary for this process to proceed are all important factors, and factors about which we have essentially no knowledge. The life fraction and life fraction profile may reflect something about this

process when the life fraction is orders of magnitude greater than one, but such is not guaranteed at this time. The life fraction profiles near achievement of the enthalpy criterion are shown in Figure 3 for the two inlet temperatures.

The life fraction profiles shown in Figure 1 indicate a clearly greater bias toward cladding breach above mid-plane for the 600°F inlet temperature than for the 750°F inlet temperature. If the early cladding breach or damage does influence the subsequent location of fuel expulsion, then the low inlet case would clearly entail a lesser reactivity gain, if any, than the high inlet case. Similarly, a review of Figure 2 clearly demonstrates that if the fuel adjacency effect is markedly diminished above the 1050 to 1100°F range of irradiation temperature, the adverse impact of favoring an expulsion site low on the pin would be considerable for the high inlet temperature but would not be a factor at the low inlet temperature.

Reviewing Figure 3, both life fraction profiles appear to strongly favor an expulsion site high on the pin. However, we have previously pointed out that if expulsion is indeed delayed until a fuel enthalpy of 1140 kJ/kg is reached, it is not clear that the accumulated life fractions several orders of magnitude over the breach criterion of one are meaningful. Accordingly, we have not attached much significance to Figure 3.

We conclude that 1) at the high inlet temperature (750°F) expulsion high on the fuel pin is not assured and mid-plane may be the preferred site, and 2) at the low inlet temperature expulsion seven to ten inches above mid-plane appears more likely than expulsion at mid-plane.

5. Location of Expulsion: LOF-Initiated TOP CDA

The LOF-initiated TOP event is primarily concerned with the behavior of low-powered pins that would not disrupt during the LOF-initiating phase. These pins experience elevated cladding temperatures during the LOF phase, followed by a mild TOP (about five times steady-state power in the order of two seconds), and then a very rapid burst. The concern with when and where fuel expulsion would occur from these pins is over whether the reactivity consequences of their behavior during the rapid burst would significantly add to the dimensions of the overall event.

There are very few data on how integral pins will respond to such specialized extreme conditions. Currently available analytical

methods coupled with recent data on the response of cladding to such conditions must be relied on to assess the response of these pins.

We have explored the behavior of integral fuel pins under these conditions using both the LAFM and DSTRESS [17] codes. The cladding flow stress model in LAFM was modified to provide cladding strength predictions in accordance with the data in [18]. In general, we assumed that the cladding in this application would behave as if it had not been irradiated, because of the high temperatures experienced in the LOF phase and the evidence that such high temperatures would erase the fuel adjacency effect [5].

The calculations were performed for a pin with a 6 kW/ft peak linear heat rating and an inlet temperature of 700°F. The pin was assumed to undergo the undercooling transient described in [2] out to 16 seconds, then embark on an exponentially increasing TOP transient to five times steady-state power in two seconds, and then finally a rapid burst. Bursts were analyzed with periods ranging from two to ten milliseconds. Fission gas was assumed to be released during the LOF transient in accordance with the LAFM model, but to escape to the plenum. During the mild TOP, released fission gas was assumed to be retained in the central cavity. It was assumed during the rapid burst that effectively no fission gas was released because of the rapidity of the event.

The DSTRESS code was used primarily because it models strain rate effects in the cladding. The code does model fuel creep. LAFM does not model fuel creep explicitly, but does allow fuel creep to be simulated by specifying a fuel temperature above which the fuel is strengthless.

We found that the pin being analyzed would not have closed the fuel-cladding gap during steady-state operation (according to the SIFAIL code [19]). The gap was just beginning to close at the start of the rapid burst, and incipient fuel melting was also reached at that time. Neither code appeared to provide reasonable predictions during the rapid burst. The gap in the top third of the pin never did close and was only barely closed at mid-plane in the DSTRESS calculation. The problem appeared to be caused by a combination of cladding thermal creep and densification of the outer fuel when reasonable plenum pressures were used. Even when reduced plenum pressures were used we could not get significant fuel-cladding mechanical interaction and the gaps in the upper half of the pin tended to oscillate from closed to open. The LAFM code gave similar results when the fuel creep parameter was set to the solidus

temperature. However, the fuel during most of the burst was either above 2700 K or radially cracked, so that when the parameter was set to 2700 K, the fuel was moved out to the cladding and the cavity pressure was applied directly to the cladding. Cladding loading was significantly increased under this behavior.

We conclude that these mechanical predictive methods were never intended to be used for the type of conditions being analyzed, and that the mechanical predictions are not trustworthy. We do note that the LAFM cladding breach predictions all were for earlier times than the time at which the fuel enthalpy criterion in Section 4.2 was satisfied. This was the result whether the HEDL Dorn stress-based criterion or the strain criterion in [18] was used. We believe that under the circumstances the fuel enthalpy criterion is the most realistic criterion to use for predicting the time of fuel expulsion. There is no alternative, we believe, but to assume that expulsion would begin at axial mid-plane.

Other studies have shown that when expulsion begins at mid-plane the consequences are significantly mitigated when the expulsion site is assumed to extend upward along the top half of the fuel pin in a time frame of a few milliseconds [20]. We studied this possibility for the current application and concluded that we could not now support its use, at least on the time frame necessary to mitigate the event. We reached this conclusion because of the following:

- Data clearly show that unstable rip propagation is very unlikely at the high temperatures encountered in this application [21].

- Assuming that the enthalpy criterion can be applied locally, the axial rate at which additional sites reach the criterion and presumably open for expulsion (beyond the original site) exceeds the speed of the internal decompression wave only out to 0.15 m from the original site. That the extension rate falls below the decompression wave propagation rate does not mean that the site would not open, only that it could be delayed. We were not in a position to evaluate that delay.

6. Conclusions

- Several predictive systems [1, 3] are available that predict the time of expulsion from TREAT TOP tests with acceptable accuracy. Verification of prediction accuracy for the location of expulsion is not possible because the location of expulsion is known for only three of the TREAT tests. None of these

methods addresses how molten fuel reaches the cladding breach site, nor what conditions are required for molten fuel to be expelled once the cladding is predicted to have breached.

No data are available to verify either time or location of expulsion for slow overpower conditions (the TOP event most likely to initiate a CDA), or for fuel pins irradiated with significant portions of the cladding above 1050 to 1100°F. The latter phenomenon could involve significant portions of the highest powered CRBR pins. The relevance of these phenomena is identified in the following point.

- Two possible significant phenomena not now addressed could mandate mid-plane failure. These are as follows:

  - Cladding breaches or severe damage incurred near mid-plane early in the transient when there is little or no molten fuel, as may occur in slow overpower transients, may subsequently influence the location of fuel expulsion [1].

  - Current data for the fuel adjacency effect (a phenomenon wherein cladding irradiated next to fuel is more severely degraded than cladding irradiated remote from fuel) indicate that the effect for fueled cladding irradiated at temperatures above 1050 to 1100°F is either not present or is much less severe [4-6] . If true, cladding breach and fuel expulsion would be virtually guaranteed to occur below the locations on the pin corresponding to those temperatures.

- In the absence of the foregoing influences, the major phenomenon biasing the location of fuel expulsion (other than the two factors previously listed) is believed to be cladding temperature and would favor an expulsion site high on the pin.

- A fuel enthalpy of 272 cal/gm (1140 j/gm) is recommended as a criterion for determining the time of fuel expulsion under all TOP conditons.

- The minimum conceivable cavity driving force to cause fuel expulsion is believed to be 50 atmospheres. This bound is based on calculations with the LAFM code for several TREAT tests assuming that no fission gas was released so that cavity pressure increased only because of heating and compression at the observed time of expulsion.

- Based on TOP calculations for a peak power CRBR pin in the 5 to 15 ¢/s ramp rate range, with appropriate consideration for biasing agents so far listed, we conclude that mid-plane failure cannot be precluded at normal CRBR operating conditions and may be the preferred location. If operating temperatures were lowered so that no more than the top ten percent of any fuel pin were irradiated above a temperature of 1050°F, the most probable location of fuel expulsion would be seven to ten inches above the fuel column mid-plane. For these conditions, the probability of expulsion at mid-plane would definitely be less than the probability of expulsion above mid-plane, but would still be finite.

- LOF-induced TOP conditions involve pins of low linear heat rating (about six kW/ft) coupled with much higher cladding temperatures than are encountered in a straight TOP-initiated event. Our studies of this event show many similarities with the slow overpower regime in that cladding breach is likely much earlier than the availability of significant amounts of molten fuel. The expulsion of molten fuel, both as to time and location, will probably be determined by processes in the fuel rather than in the cladding. All of the location biases identified for the TOP-initiated event are likely to be muted if operable at all, further supporting the likelihood of the event being dominated by fuel processes. We recommend that the fuel enthalpy criterion previously cited for use in TOP-initiated events also be used for determining when molten fuel would be expelled in a LOF-initiated TOP event, with an axial mid-plane location presumed.

- We cannot now support rip extensions of more than 0.15 meters for the LOF-initiated TOP event, at least on a time scale that would mitigate the outcome of the event. Data have shown that unstable rip propagation is very unlikely at elevated temperatures. Calculations show that axial extension of multiple expulsion sites more rapidly than the propagation of the decompression wave (inside the fuel pin) away from the original expulsion site is unlikely beyond 0.15 meters from the original site.

TABLE 1

CALCULATED VALUES OF SELECTED PARAMETERS

AT OBSERVED TIMES OF FUEL EXPULSION

Test	Peak Fuel Enthalpy (kJ/kg)	Fraction of Fuel in Liquid Phase
HUT-37B	1127.6	0.63
HUT-36B	1121.3	0.64
HUT-32A	1221.6	0.78
HUT-57B	1073.0	0.49
HUT-55A	1169.4	0.63
HUT-52B	1228.2	0.69
E6	1197.4	0.68
E7	989.5	0.29
E8	1132.2	0.62

APPENDIX B
PLUTO2 ANALYSES OF L8 EXPERIMENT

1. Introduction

An analysis of the L8 experiment using a stand-alone version of the PLUTO2 code was presented by Bowers, Tentner, and Wider [1]. In that analysis the following parameters were adopted as best fitting the experimental results:

- Pin failure pressure 150 atm (adjusted by varying cavity gas volume).
- Fuel particle radius for particulate flow in coolant channel 170 μm.
- Fuel/coolant heat transfer proportional to the square of the liquid sodium volume fraction.
- Grain boundary fission gas (instantly available on fuel melting) 0.1 to 0.5 of the retained gas.
- Coalescence time constant for gas in grains at fuel melting 60 ms.
- Initial clad rip 3 nodes (18.5 cm) about core mid-plane, increasing with time.

In order to assess how well these parameters are determined by the experiment, a series of variations has been performed on the case previously reported (referred to here as the "base case"). The version of PLUTO2 used in the previous work has been made available to us by courtesy of H. Wider for performing these studies. Because of some minor changes and corrections made recently by Wider the newly calculated base case does not give exactly the same results as the previous one.

2. Parametric Variations

Parametric variations to the base case, Case 1 in Table 1, are as follows. In Case 2, all FCI heat transfer was eliminated in the

particulate flow regime. Some fuel-coolant heat transfer still takes place in the annular flow regime, however. In Case 3, the transition from the original particulate flow in the coolant channel to annular flow for molten fuel and sodium/fission gas was suppressed in order to simulate the modeling in EPIC, which is restricted to particulate flow. In the base case this transition was specified by input to occur when the liquid sodium volume fraction dropped to 0.33. In Case 4, the molten fuel/sodium heat transfer coefficient was assumed proportional to the first power instead of the square of the liquid sodium volume fraction. In Case 5, the initial cavity pressure was tripled by tripling the initial fission gas content. In Case 6, the initial cavity fission gas content was divided by three to reduce the initial cavity pressure by one third. In Case 7, the initial cavity pressure was tripled by reducing the void volume by three, and in Case 8 the initial pressure was reduced by a factor of three by tripling the void volume at pin failure. In Case 9, the fraction of retained fission gas assumed to be on grain boundaries and thus immediately available was reduced to zero. In Case 10, the time constant for coalescence of gas entering the pin cavity and thus becoming available was reduced from 60 ms to 30 ms. In Case 11, the first power of the sodium volume fraction was assumed for the heat transfer coefficient, and the initial fission gas and void fraction were both tripled, the failure pressure remaining at 150 atm.

3. Results and Discussion

The new results for total fuel reactivity as a function of time following pin failure normalized to original fuel worth are given in Table 1 and are also compared to the experimental values. Comparison of experiment and Case 1 illustrates the trend found previously [2] for the calculated fuel sweepout to be too large up to about 30 ms and to be too small at later times.

A comparison of the results for Case 1 and Case 2 indicates that the FCI is not calculated to have much effect on fuel reactivity, and that sweepout is actually greater when the heat transfer is turned off, apparently because the sodium liquid volume fraction is greater in this case, so that the particulate flow regime is retained longer and the ejected fission gas moves fuel more efficiently. When the EPIC modeling was simulated by suppressing the development of annular flow in Case 3, excessive fuel sweepout developed even with the assumption of fuel/coolant heat transfer proportional to the square of the liquid volume fraction, particularly at times later than 50 ms. As discussed in Section III, with EPIC this excess in sweepout becomes even larger if the heat transfer is assumed proportional to

the first power of the sodium volume fraction. With PLUTO2 when all flow regimes are allowed, however, because of the development of annular flow, whether the first power or the square of the volume fraction is used makes little difference, as is seen by comparing Cases 1 and 4.

Early reactivity change is quite sensitive to the amount of initial fission gas in the cavity when the void fraction is kept constant, as is seen comparing Cases 5 and 6 with the base case. These effects tend to wash out at later times because of the growth of the cavity in this rapid transient, causing further fission gas release from newly melted fuel. The early reactivity change is far too negative with an initial pressure of 450 atm but is about right at later times. With an initial pressure of 50 atm the calculated early reactivity change is still too large up to 20 ms, after which it becomes much too small. When the initial pressure is varied by varying the void volume rather than the gas content, as in Cases 6 and 7, the effects are smaller. Intermediate results are obtained when the gas content and void volume are varied simultaneously, as seen by comparing Cases 4 and 11.

A common problem in all of these cases is the one pointed out by Bowers et al. [1] that the lower sodium slug velocity as calculated by PLUTO2 is lower than the measured one, particularly at times later than 30 ms after pin failure. None of the parametric variations was of such help in improving this situation.

On the basis of these studies it appears that the most important factors affecting fuel sweepout up to 50 ms after pin failure in the L8 experiment are the transition from particulate to annular flow and the initial cavity fission gas content. The ratio of fission gas to fuel used in the calculations of Bowers et al. [1] appears to be in a reasonable range but may be somewhat low considering the underprediction of fuel sweepout in the base case calculation.

In addition to an increase in gas content, it might also be appropriate to use a lower sodium liquid volume fraction than the currently assumed 0.33 for the transition from particulate to annular flow. This would increase sweepout at times up to 50 ms.

Within the context of the PLUTO2 modeling the FCI did not have a large effect on fuel sweepout in the L8 experiment and parameters relating to it are not determined with great precision. Only modest total pressures up to about 15 atm were generated in these calculations, but these were sufficient to generate the required fuel velocities. Pressures of the same order were observed in the

experiments, except that for the fourth event in H6 a stronger FCI apparently took place, with a peak pressure measured at 124 atms. In their analysis of this event with PLUTO2, Wider and Semenza [3] used a 100 m fuel particle radius instead of 170 m, but sodium vapor pressures were not significantly higher than in the L8 calculations, so that the analysis did not reproduce the experimental pressure history.

4. Conclusions

The parametric PLUTO2 studies of the L8 experiment reveal certain modelling deficiencies, however, the benchmarking thus achieved is adequate for conservative modelling of fuel motion reactivity effects in TOP accidents.

5. References

1. C. H. Bowers, et al., "Analysis of TREAT Tests L7 and L8 with SAS3A, LEVITATE, and PLUTO2," Specialists' Workshop on Prediction Analysis of Material Dynamic in LMFBR Safety Experiments, March 13-15, 1979, Los Alamos Scientific Laboratory, LA-7938C, p. 242.
2. H. U. Wider, et al., "The PLUTO2 Overpower Excursion Code and a Comparison with EPIC," Proceedings of the ANS/ENS International Meeting on Fast Reactor Safety Technology, Seattle, WA, August 19-23, 1979, p. 120.
3. H. U. Wider and L. A. Semenza, "Analysis of TREAT Transient Overpower Experiments Using the PLUTO Codes," Specialists' Workshop on Prediction Analysis of Material Dynamic in LMFBR Safety Experiments, March 13-15, 1979, Los Alamos Scientific Laboratory, LA-7938C, p. 153.

TABLE 1
TOTAL FUEL REACTIVITY IN L8 RELATIVE TO ORIGINAL

Case		Time after pin failure, ms 10	20	30	40	50	60	70	80	90	100
	Experiment	1.01	0.99	0.96	0.93	0.90	0.88	0.88	0.88	0.86	0.85
1.	Base Case	0.984	0.961	0.951	0.951	0.948	0.935	0.918	0.901	0.886	0.866
2.	No FCI	0.984	0.957	0.938	0.928	0.923	0.913	0.900	0.892	0.900	0.861
3.	All Particulate Flow	0.984	0.959	0.942	0.929	0.905	0.874	0.835	0.803	0.779	0.757
4.	FCI $\propto$ (NaVF)	0.983	0.964	0.953	0.949	0.941	0.929	0.913	0.898	0.883	0.861
5.	Initial FG x 3 (P = 450 atm)	0.977	0.929	0.919	0.918	0.912	0.903	0.894	0.890	0.883	0.863
6.	Initial FG x 1/3 (P = 50 atm)	0.993	0.979	0.972	0.970	0.961	0.949	0.936	0.924	0.906	0.882
7.	1/3 Initial Void (P = 450 atm)	0.980	0.953	0.944	0.942	0.93[illegible]	0.920	0.903	0.891	0.881	0.871
8.	Initial Void x 3 (P = 50 atm)	0.989	0.969	0.962	0.960	0.953	0.945	0.935	0.930	0.917	0.893
9.	0 Grain Boundary Gas	0.984	0.959	0.945	0.943	0.936	0.924	0.907			
10.	30 ms Coalescence Time	0.984	0.957	0.948	0.943	0.931	0.915	0.898	0.887	0.883	0.882
11.	FCI $\propto$ (NaVF), Initial FG x 3, Initial void x 3 (P = 150 atm)	0.975	0.944	0.933	0.932	0.927	0.930	0.905	0.892	0.882	0.869

Case 1 parameters: Failure pressure 150 atm
Particle radius 170 μm
Fuel/coolant heat transfer $\propto (NaVF)^2$ unless otherwise noted

IV. LOSS OF HEAT SINK INITIATED CDAs

1. Objectives and Overview

We have already examined in detail CDAs initiated by coolant overheating (LOF). We have also considered CDAs initiated by overheating of the fuel (TOP). Here we will be concerned with the consequences of a third generic CDA initiator mechanism that leads to simultaneous fuel and coolant overheating. This situation arises as a result of loss in heat rejection capability from the primary system. Such loss is normally considered in conjunction with the achievement of neutronic shutdown and is known as the Loss-of-Heat Sink (LOHS) accident.

The LOHS may also occur in conjunction with failure of the reactor protection system (unprotected accident, ULOHS) [1, 2]. However, the likelihood of such occurrence would be anywhere from one [2] to more than two [2] orders of magnitude lower (than the protected LOHS). Furthermore, we would expect that the ULOHS phenomenological evolution would contain elements of both the LOHS and the LOFA and in fact it would easily revert to either of the two by tripping either the primary coolant pumps and/or the reactor shutdown system. Such transitions are particularly likely in view of the relatively long time margins available (large system heat capacity) for recovery actions. In other words, from the point of view of providing the fullest coverage of the CDA phenomenologies in a generic sense it would appear that the "protected" aspect of the LOHS would provide the most meaningful complement to the unprotected LOFA and TOP cases covered already. On this basis we chose to not consider further the ULOHS here.

The essential character of the LOHS is that core disruption takes place at decay power levels. The relevant degradation processes occur on the time scale of many hours to many minutes, as compared to the fractions of a minute pertaining to the unprotected CDAs. This slow evolution taken together with a well subcritical initial core state indicate an extremely sluggish neutronic behavior at least during the first approach to criticality. Such approach to criticality would appear inevitable since continuing fuel and control material degradation would yield increased fuel compaction states and eventually melting (or sublimation) and separation of the considerably lighter absorber material. Just as in the other CDAs

considered previously, our objective here is to establish the LOHS core disruption path, to identify termination mechanisms and to explore for energetic behavior during such evolutions.

The unique character of the LOHS CDA was emphasized by the first study of the topic appearing in 1977 [3]. A handful of others followed [4, 5] but not all unique aspects of behavior appear to have been pursued in the past. These studies originated with the homogeneous CRBR core design and agree in concluding that eventual recriticality is to be expected, but disagree on the timing of such events.

The Applicant's CDA analyses did not specifically address this topic. Thus, our own efforts in this area will have to stand alone at this time. It is important, therefore, that we place our results in the proper perspective of this limited extent of previous work available. This is accomplished in Section 2. The possible ranges of phenomenological progression are examined in Section 3 and our assessment of the LOHS-unique energetic circumstances is presented in Section 4.

2. Previous Work

Previous work on LOHS CDAs has been very scarce indeed. The first such study carried out for the homogeneous CRBR core design is due to Chan, Min, and Okrent [3]. They modeled the natural circulation between the inlet and outlet plena assumed to continue through sodium boiling and until core uncovery (i.e. sodium escaping as vapor from primary system relief paths). They estimated durations of 5.6 hrs and 32 hrs for reaching coolant boiling and upper plenum depletion respectively. Following core uncovery and melting, SA wall melting and fuel disruption occurred sequentially. The sodium vapor velocities were found inadequate to levitate the molten cladding, hence a downward steel relocation process was projected (i.e. absence of core-exit blockages). Failure of the core wall was taken to signal "gross fuel motion wherein fuel pellets can be arranged into a more compact geometry before they start to melt." Criticality calculations were carried out for several hypothesized core geometries including fuel compaction states with 30% and 50% void fraction, and the presence or absence of steel at the upper core boundary. In the absence of control material all cases indicated supercriticality ($k_{eff} > 1$), while a homogeneous mixture of fuel with the control materials produced a subcritical pile. The view expressed in their conclusion was that further study of the core disruption stages of this rather different class of CDAs would

be worthwhile, although no projections on the potential for energetic behavior were given.

The LOHS accident was also studied by Bari and co-workers at BNL. The first study [4] appeared a little after that of Chan et al. [3]. It presented the ALOHA code modelling and preliminary results up to the point of clad melting and relocation. In these calculations natural convection was assumed to terminate following saturation and boiling inception, i.e. sodium boiloff and subsequent heatup were considered from heat capacity standpoint at the (isolated) subassembly scale. As a result dryout was calculated to occur in less than 10 minutes. Clad melting and relocation into the lower axial blanket (plugging) followed soon after. A more complete presentation of the ALOHA predictions was given in a follow-on study [5]. However the previous dryout concept was retained leading again to core disruption soon after reaching saturation conditions (i.e. approximately 3.3 hrs into the accident). The clad is predicted to melt within 5 minutes after dryout and the fuel and control assembly duct walls melt a few minutes later. A non-mechanistic equilibrium nodal heat capacity model was utilized to predict steel draining and plugging the core inlet. The resulting, steel-free core was examined for recriticality events. The possible effects of core fuel crushing by the weight of the above-core structures was discounted. However, compaction in the solid state by toppling fuel and/or control material pellets, including the possibility of fragmentation of the latter due to retained fission gases, was identified as a very likely mechanism for recriticality. The criticality compaction boundaries were estimated for the CRBR homogeneous core design as shown in Figure 1. In conclusion, the qualitative judgement was offered that "the core disruption process is rather slow and sluggish" and, therefore, small ramp rates (< 10 $/s) are to be anticipated.

Quite a different interpretation of these results was suggested by Williams [6]. Such sluggish recriticalities were viewed as the prelude to the formation of a whole-core, transition phase pool. Based on recent SIMMER results [7] indicating a potent energetic behavior of such pools (but see Section II.7 for an update), and the judgement that the energetic behavior of such pools would overshadow all other aspects of the LOFA energetic behavior, he concluded that the LOHS accident consequences would be comparable to those of the LOF. This coupled with the conclusion of another related Sandia study [2] indicating a two orders of magnitude higher probability for the LOHS accident lead to the conclusion that the major energetics contributor to the risk had been badly neglected in the past.

The assumptions of Chan et al. [3] and Bari et al. [4, 5] concerning the onset of dryout were examined, by Perkins et al. [8], in terms of the stability of the boiling process. By comparing the two-phase (boiling) pressure drop to the available static sodium head, the coolability power limits could be established. However, uncertainties in predicting the frictional losses yielded a wide range of predicted dryout power levels. In fact the decay heat power levels of interest to LOHS assessments fell well within the quoted dryout power uncertainty range of 0.2-4%. At about the same time as this study, direct experimental evidence on the subject became available [9]. An average subchannel of the Fast Test Reactor (FTR) was simulated in the radiantly heated Sodium Boiling Test Facility (SBTF) at Oak Ridge National Laboratory. With the exception of a longer inlet section, closely prototypic thermal-hydraulic characteristics were achieved. With an inlet subcooling of approximately 500°C, stable natural convection boiling was achieved up to a power level equivalent to 15% of the FTR power (17 w/cm^2 or 200 w/cm^3). These experimental coolability limit results were recently interpreted [11] in terms of the same flow stability considerations mentioned above. However, here a slip flow model (for $\alpha > 0.4$) and the homogeneous friction factor were utilized as opposed to the Barockzy correlation (for two-phase friction) utilized before. This study concluded that typical LMFBR subassemblies can be safely cooled under natural convection conditions for heat fluxes corresponding to 8-10% of the average nominal power.

The energetics implications for these dryout requirements were recently discussed by Fauske [12]. He suggested that "the steel-blanket fuel pin structure above the core would melt almost simultaneously with the fuel and steel materials that comprise the active core, as if the subassembly structure just above the core was subjected directly to the core volumetric power level." Thus he ruled out the possibility of core exit plugging and thus the bottled-up whole-core pool recriticality concerns of Williams [6]. Furthermore he suggested that even if a severe recriticality event were to be postulated in the absence of the upper plenum sodium pool there would exist no mechanism to focus the fuel expansion work into the reactor vessel head.

3. Range of Phenomenological Progression

3.1. The Pre-dryout Period

The decay power behavior of the CRBR following a full cycle of operation is shown in Figure 2. We see that within 1 second from

shutdown the power is under 10% and within 10 seconds it is below 6%. At these times the inlet sodium is well subcooled and the experimental results from the SBTF directly apply indicating comfortable coolability. In a LOHS accident the primary system will continue to heat and will approach coolant saturation in the 3-5 hr time frame. In this near saturation regime no directly applicable experimental data are available. However, the following considerations apply: (a) Even with the 500°C subcooling utilized in the SBTF experiments, only 7% of the total power (at near dryout conditions) was absorbed as sensible heat (bringing the sodium flow to saturation) while 93% was utilized for vaporization, i.e. the subcooling should not have been a significant contributor to the coolability limits, (b) The previous conclusion is supported by analytically accounting for the effect of subcooling [11], (c) As may be seen from Figure 2 at times where the coolant approaches saturation the decay power has declined to the value of approximately 1%, i.e. this whole order of magnitude margin from the measured dryout fluxes should overshadow any detail effects.

Clearly, we rely heavily on the SBTF experimental results in formulating the position presented above. It is worthwhile therefore to consider in more detail any possible limitations of their applicability to the problem at hand. The authors [9] emphasize in particular the non-prototypicality resulting from an SBTF loop inertance (proportional to inlet length) that is considerably larger than that of the fuel assembly inlet module. This would have the effect of resisting flow reversal and indeed only sporadic reversals were measured. However, at such low heat fluxes it is doubtful that flow reversals, even if possible (especially limited under inlet subcooling) would be of much consequence on coolability. The authors mention two additional limitations: (a) a relatively high, ±17%, power level uncertainty (at the dryout limits), and (b) an axial temperature profile anomaly that was attributed to non-uniform (inlet peaked) power distribution which moved the saturation point upstream and into the inlet (unheated) section. This anomaly had not been resolved but was deemed as a conservative aspect of the experiment, i.e. an increased requirement in pressure drop for the two-phase flow. The potential differences in frictional characteristics between the simple tube geometry in the test and the 217-pin wire-wrapped fuel bundle should also be mentioned. Such differences are known to exist for grid-spaced bundles where grids are known to disrupt the wall film, causing a lower frictional pressure drop but a premature dryout [13]. Although no experimental data for wire-wrapped bundles exist for two-phase flow, experience with single-phase flows and the non-obstructing character of the wire-wrap indicate that no significant deviation from simple channel behavior should be expected.

Thus we conclude that the core will remain coolable for as long as it is covered by sodium. Even if the LOHS initiator left the primary system intact, at the high boiling point of sodium the shear ring seals will fail creating a sodium vapor relief path. Under these conditions sodium boil-off will continue with stable natural convection boiling through the core until the whole upper plenum inventory has been depleted. The time duration for this process was estimated by Chan et al. [3] at approximately 32 hours. Indeed at approximately 1% power level (approximately 10 MW) sodium vaporization would occur at approximately 2.7 kg/s (5.4 lbm/s) yielding depletion of the whole primary system inventory of 0.7 million pounds (mostly in the upper plenum) in approximately 30 hours.

Such long exposures at the high (sodium boiling) temperatures of approximately 880°C raise the question of mechanical integrity of the load-bearing reactor vessel components. We utilized the recently available high temperature creep data of [14] to evaluate the response of the reactor vessel/flange-support juncture. With a total dead-weight bearing of 2×10^6 lb_f we estimated a lifetime in excess of 1,000 hrs [10]. Similarly the vessel sidewall would survive high temperature creep for as long as 10,000 hrs. Our concern for such failures stems from the possibility of producing vessel slump upon the guard vessel and onto the reactor cavity floor, i.e. core falling away from the still-latched control rods. Although, based on the above such failures would appear unlikely, we emphasize the need for procedures to scram the reactor, thus unlatching the control rods upon any indication of a LOHS occurrence.

Consideration, however, quite different from those discussed above, did yield a potential mode of vessel failure [10]. As the primary system heats up slowly, as a whole, the reactor vessel will expand downwards, while the surrounding guard vessel will expand upward slightly in the manner indicated in Figure 3. Such differential thermal expansion may cause mechanical interference and failure at the inlet nozzle position. Such failure would be expected at near saturation conditions and would result in rapid draining of the whole primary system sodium inventory into the reactor cavity. Such a scenario would imply a considerably earlier entry into the core disruption phase as compared to the boil-off scenario developed earlier. This would imply a somewhat higher decay power (approximately 1% vs. 0.4%, see Figure 2), however, we are still concerned with a very gradual disruption and the absence of sodium coolant throughout this process.

3.2. Core Disruption

Upon uncovery the core disruption phase will commence with clad melting at approximately 1% power level. Even if vessel failure and coolant draining did not occur, sodium vapor velocities are clearly inadequate to produce cladding levitation (see Section II.3), hence, gradual slumping will occur. Soon after, also, the fuel and control duct walls will melt and will relocate into the lower blanket space. The details of this seemingly complicated process are not important. The important point is that the control material (B_4C) melts at 2350°C and fuel at 2700°C, that is, at temperatures of more than 1,000°C above the steel melting temperature (1,400°C). At the extremely low power levels of interest core-internal thermal gradients would be minimal, thus complete melting of all steel and draining would be expected well before any fuel or absorber material melting.

This behavior would also be true for at least a portion of the above core structure (i.e. blanket and fission gas plenum cladding and corresponding duct wall). The upper axial blanket pellets will, therefore, be released on the top of the fuel pellets which by this time should be found in a randomly packed rubble-bed configuration. Most likely the remaining above core steel structure will also dislodge coming to rest on the top of the blanket rubble. Now, the possibility of continuing melt attack through conduction and radiation processes should be mentioned. The resulting molten steel would trickle down the fuel bed providing a cooling mechanism and eventually filling up the available interstitial space. However, in view of the insulating properties of the blanket layer and the large heat capacity of the steel structure (behaving in a thermally lumped manner due to its order of magnitude higher thermal conductivity than that of the blanket material) the degree of this additional melt attack occurring prior to fuel melting may be minimal. An upper limit of the available time, assuming approximately 1% power and adiabatic core heatup, is estimated at approximately 10 min [5]. At the other extreme, a prior recriticality would significantly shorten or essentially eliminate this time interval. Indeed, such recriticality seems entirely possible.

3.3. Recriticality Considerations

A schematic of the material configuration described above is shown in Figure 4. The lower steel plug was assumed to penetrate the whole LAB, i.e. all incore and UAB cladding and duct wall material was taken to fill the available space thus reaching approximately 20 cm into the active core region. With the fuel, blanket, and control

material pellets in their respective operating positions the pile would be approximately 30 $ subcritical. A uniform compaction by approximately 20 cm, corresponding to a decrease of the void fraction (porosity) from its initial 65% value to approximately 50%, as shown in Figure 4, would be required to approach criticality. These criticality calculations, carried out in the manner described in Section II.7, indicate a similar reactivity worth gradient of approximately 1.5 $/cm of compaction. That is, a uniform collapse velocity of approximately 100 cm/s would be required to achieve a 150 $/s ramp. Clearly, such situations would be incredible given the material configurations of interest here (i.e. Figure 4).

However, a mild recriticality will be achieved sooner or later; if not by toppling of the unclad fuel and control pellets (note that sintering during power operation will tend to inhibit such topplings) then by a gradual melting and draining mechanism. Upon first reaching a fission power level (criticality) neutronic activity would accelerate with the increasing rate of fuel melting and collapse. An upper bound example of reactivity ramp rates associated with such a collapse may be obtained by assuming a free-fall process uniformly across the whole rubble pile. The mechanistic concept of this collapse is illustrated in Figure 5. Starting from critical a net displacement by only 1-2 cm would be required to achieve prompt criticality. Under free-fall conditions the velocity at prompt critical will therefore be approximately 40 cm/s which with the worth gradient of approximately 1.5 $/cm quoted above translates into approximately 60 $/s. On the other hand if neutron precursors are not available because of the long time after shutdown, the higher power condition might be obtained at a supercritical or perhaps a prompt critical state. In this event even less acceleration time is available, hence a lower level of energetics is obtained.

3.4. Termination Considerations

With respect to termination the essential aspects of the above scenario is that the plugging prone, high heat capacity UAB region, would be disrupted well before the onset of neutronic activity. However, the blanket layer and plenum cladding/duct steel combination as shown in Figure 4 may still represent a formidable obstacle for sustained blowdown and dispersal in the upward direction for the low range of recriticality intensities. Indeed, the 60 $/s estimate was presented above as a high margin upper bound. That is, taking into account radial melting incoherencies due to presence of blankets and the non-uniform, radially, power distribution we would expect only a fraction of this upper bound ramp rate to manifest

itself. As the core becomes mobile by melting the UAB will mix rapidly (greater density) to lower the reactivity state, off-set control material loss, and dampen any neutronic activity. The higher energy state of the core will melt the wall and cladding steel from the radial blanket, if it hadn't occurred earlier, leading to radial blanket entrainment into the pool. At this point the core is immune neutronically to any type of reconfiguration, homogenization, or material removal. It is permanently subcritical.

4. Energetics Margins for LOHS

Although no significant energetics events for the LOHS accident sequence have been identified, we will discuss the characteristics of a postulated event to establish a point of reference and to highlight the generic margin the system possesses to accommodate events of this type.

Contrary to all cases of energetic behavior examined up to this point, in the LOHS accident, the mechanical impact of an energetically expanding core will take place without the intervening sodium pool. As we have seen for the cases of unprotected CDAs (i.e. LOFA, TOP), the role of the pool is to provide a medium for focusing this expansion work into a sharp, and hence potentially damaging mechanical impact on the reactor vessel head. Here we will consider an example of this energy conversion process in the absence of the sodium pool.

The methods of Section II.2 are applied here also, however, the loss of mechanical strength of certain structural components in the high temperature LOHS environments needs be taken into account. Thus, we assume that the UIS support columns can offer no resistance to the upwards UIS displacement driven by the core expansion process. Similarly, the core barrel is assumed to offer no resistance to core expansion in the radial direction. Indeed failure of the core support structures and expansion in the downward direction might even be possible under these conditions.

Based on the above, the conceptual model consists of an expansion in all directions constrained only by the inertia of the intervening masses. A schematic is shown in Figure 6. The UCS is also considered only as a strengthless inertia constraint, which is visualized to crush upon contract with the UIS. With an initial void fraction (porosity) within the UCS of approximately 75%, at full compaction against the UIS core venting would be expected. Such venting would further accelerate the rate of pressure decay within the

expansion zone thus moderating the continuing acceleration of the inertia masses. Our first order concern is to evaluate the vessel and containment damage potential due to the associated missile generation and impacts.

From the point of view of containment integrity, the question is whether the UIS impact upon the reactor vessel head could generate a secondary missile of energy sufficient to reach the containment boundary. A highly conservative upper bound on the UIS impact velocity was obtained as follows. The maximum level of energetics examined in the presence of the sodium pool (Section II.2) was chosen for this evaluation. The lower and radial components of the expansion were conservatively neglected. The venting was also conservatively minimized by assuming that the UIS does not move, i.e. the UCS upon crushing clears the initially present venting passage of approximately 30 inches shown in Figure 6. A SIMMER-II expansion of the high pressure core into the empty reactor vessel was carried out and the resulting pressure transients across the UIS thickness as well as their algebraic sum (net) are shown in Figure 7. As shown on this figure the net impulse may be approximated by a constant approximately 40 bar pressure over the duration of approximately 40 ms. The mass of the UIS is taken at 4.75×10^4 kg and the area over which the pressure force is applied is taken as approximately 4.5 m^2. A peak velocity of approximately 15 m/s corresponding to a kinetic energy of approximately 5 MJ is estimated on the basis of the above multiple conservative assumptions. Such missile energies are clearly of no consequence to the reactor vessel head integrity, and much less of course to the generation of secondary missiles. Similarly radial or downward vessel failures could be of no consequence to containment integrity.

5. Summary

Severe energetic behavior in the LOHS accident can be ruled out at this time. An evaluation of the inherent margin to accommodate such events indicates a negligible challenge to the reactor vessel head even if severe events are postulated because of the absence of the sodium pool.

V. CONCLUSIONS

- We have systematically evaluated the possible progression of all three classes of CDAs as exemplified by the LOF, TOP, and LOHS accidents. Non-negligible energetic circumstances were identified only within the LOFA sequences, and assuming that the plenum fission gas fuel compaction mechanism becomes inoperative, by design, as recommended, only as a consequence of recriticalities.

- Recriticality events in the S/A-scale and annular pool phases cannot be excluded. However, their magnitudes are limited to the order of 50 $/s or less because of incoherence and the absence of significant amplification. Neutronic activity, throughout both of these stages of core disruption is substantial and contributes to pressurization and fuel dispersal away from the core region. Thus, benign termination prior to entering the whole-core, homogeneous, pool phase, is projected even under restrictive assumptions for fuel removal path availability and fuel removal mechanics.

- Whole-core pool recriticalities exhibit a narrow range of significant energetic behavior. This energetic regime is associated with idealized perfectly symmetric geometry and completely homogeneous pools. The amplification is the result of radial sloshing following a centrally located and symmetrically distributed power pulse. Even so, the resulting level of energetics did not exceed the structural capability of the primary system boundary.

- The levels of energetics required to produce significant structural damage in the CRBR were evaluated, taking into account, for the first time, the structural enclosure formed by the Core Barrel/Core Support Structure/Upper Internal Structure, and the pressure transmission characteristic of the expanding core medium and other materials found within. We conclude that an 1130 MJ accident (expressed as the isentropic work potential for expansion to one atmosphere) would be required to fail this inner containing structure, and a 2550 MJ accident to substantially challenge the reactor vessel head structure, i.e. produce a slug impact kinetic energy close to the CRBR vessel head design value of 75 MJ. These levels of energetics roughly correspond to two-phase whole-core disassemblies with 100 $/s and 200 $/s driving reactivity ramp rates.

- Based on these results we conclude that a CDA-induced energetic vessel head failure is physically unreasonable.

- Further, based on the projected absence of significant energetic events we conclude that the Applicant's energetic source term of 661 MJ (75 MJ slug impact kinetic energy), as applied by the Applicant, for evaluating the structural margin beyond design basis is adequate.

I.1 ORGANIZATIONAL INTERFACES. (Section I)

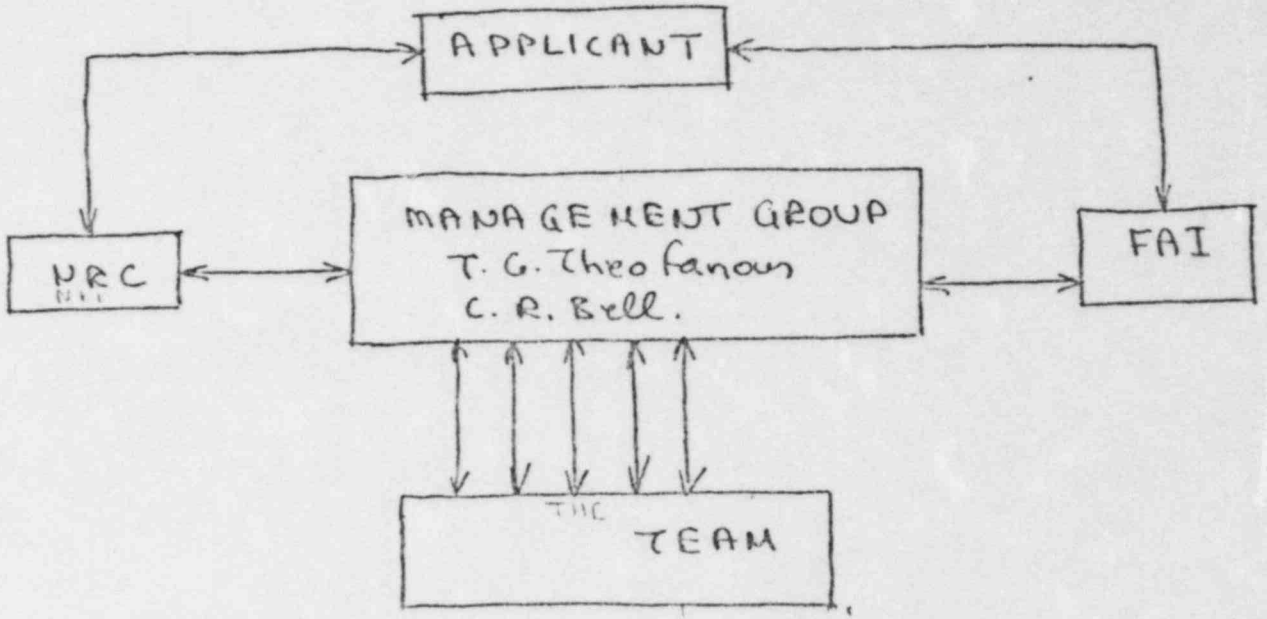

I ✓

I Fig 2

II MANAGEMENT PLAN STRUCTURE.

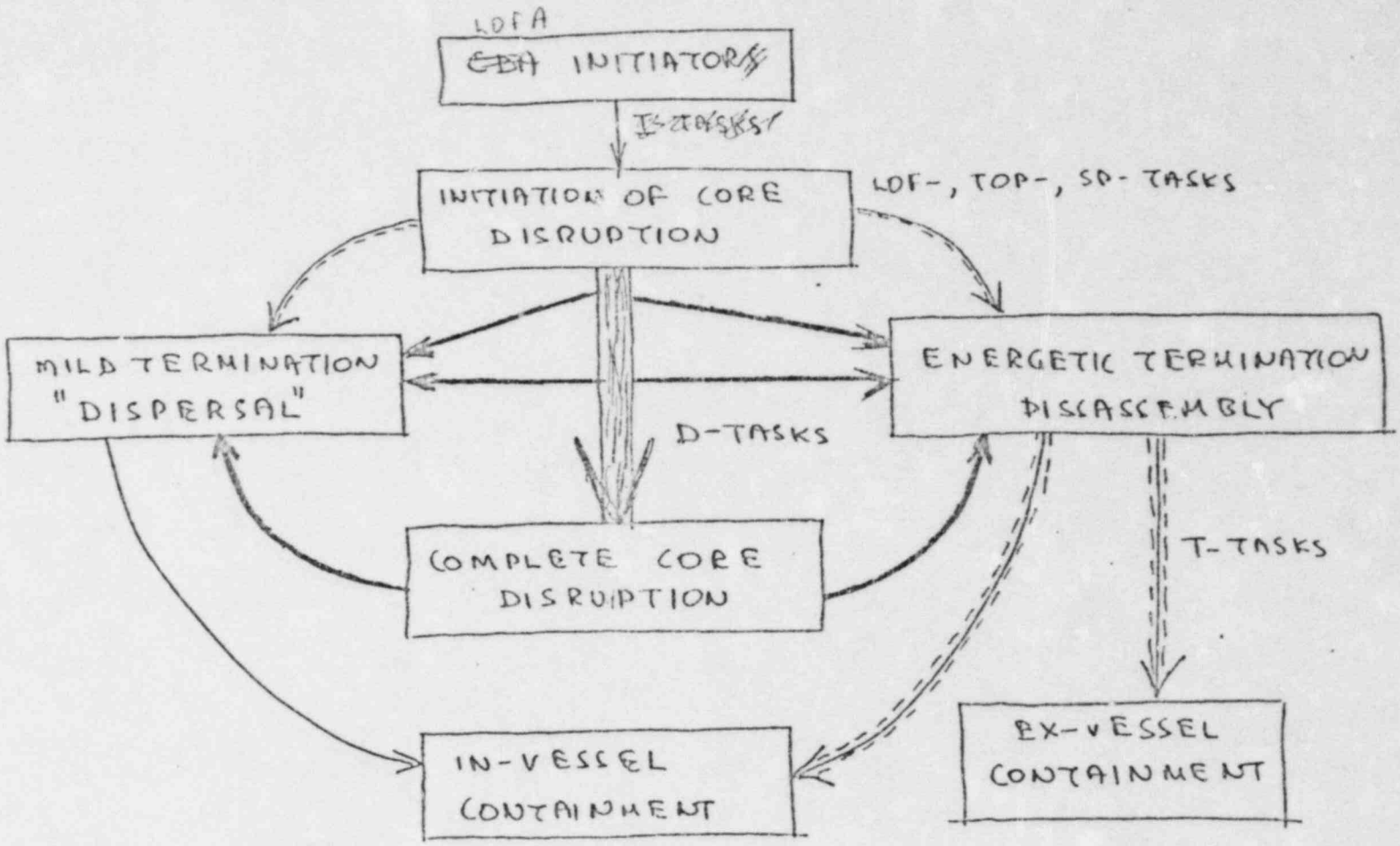

I

~~Fig~~ Fig 3

~~THE~~ THE REVIEW PATH.

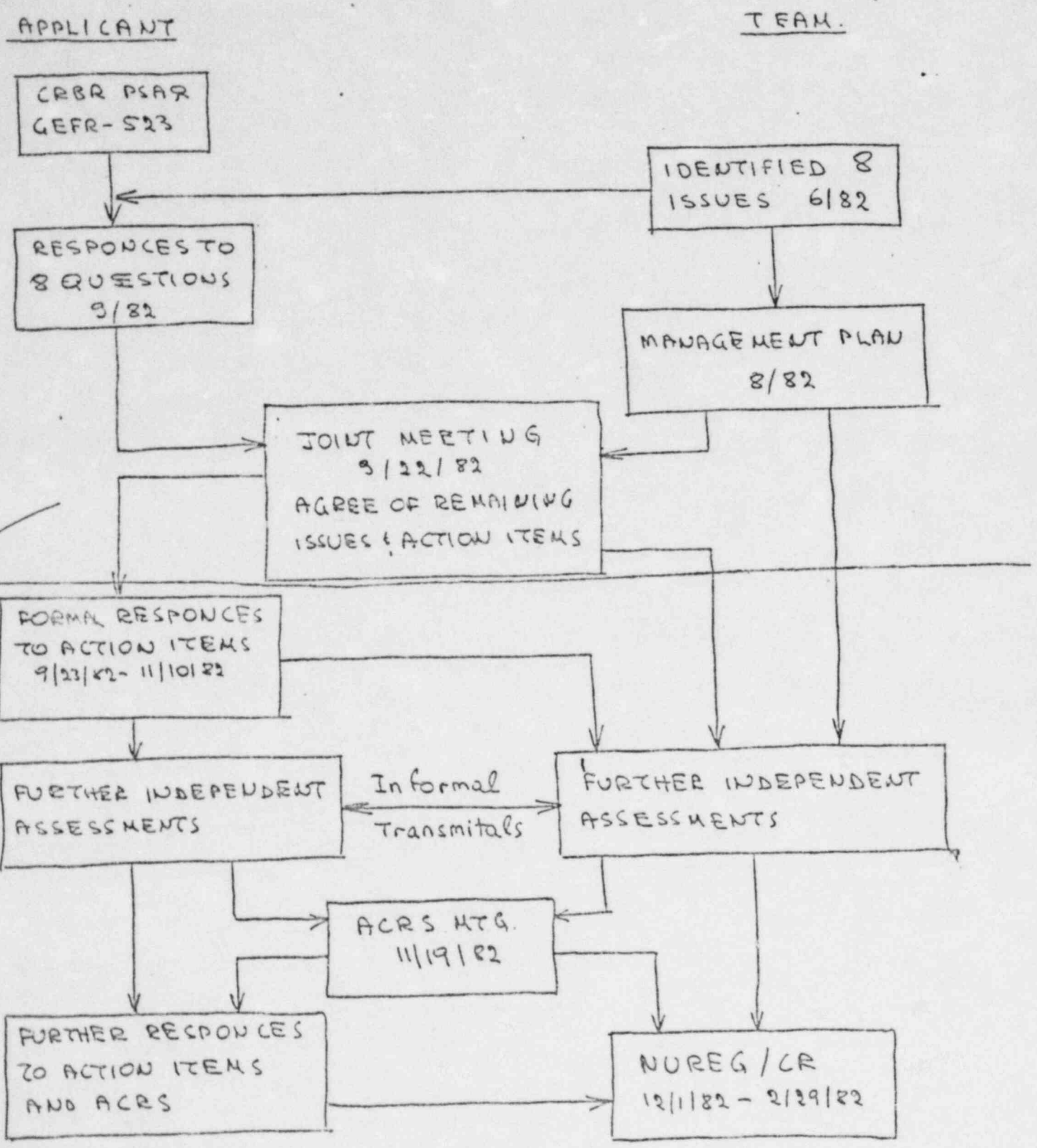

✓ Fig 4 I.4

I

Fig 1 (Section II.1)

FIG 1. QUALITATIVE PROBABILISTIC FRAMEWORK

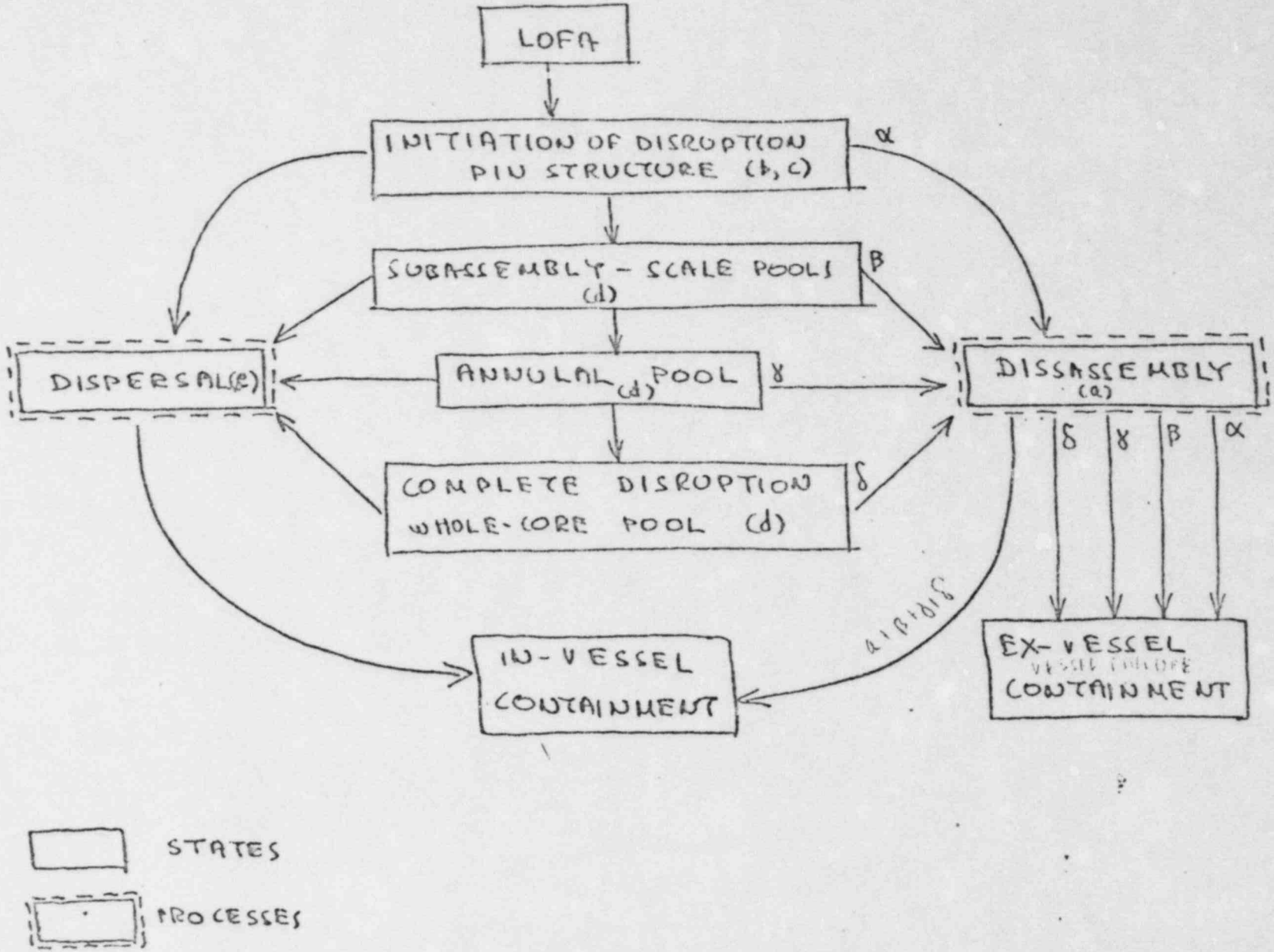

II.1

II

Fig 2

CRBR CORE CONFIGURATION

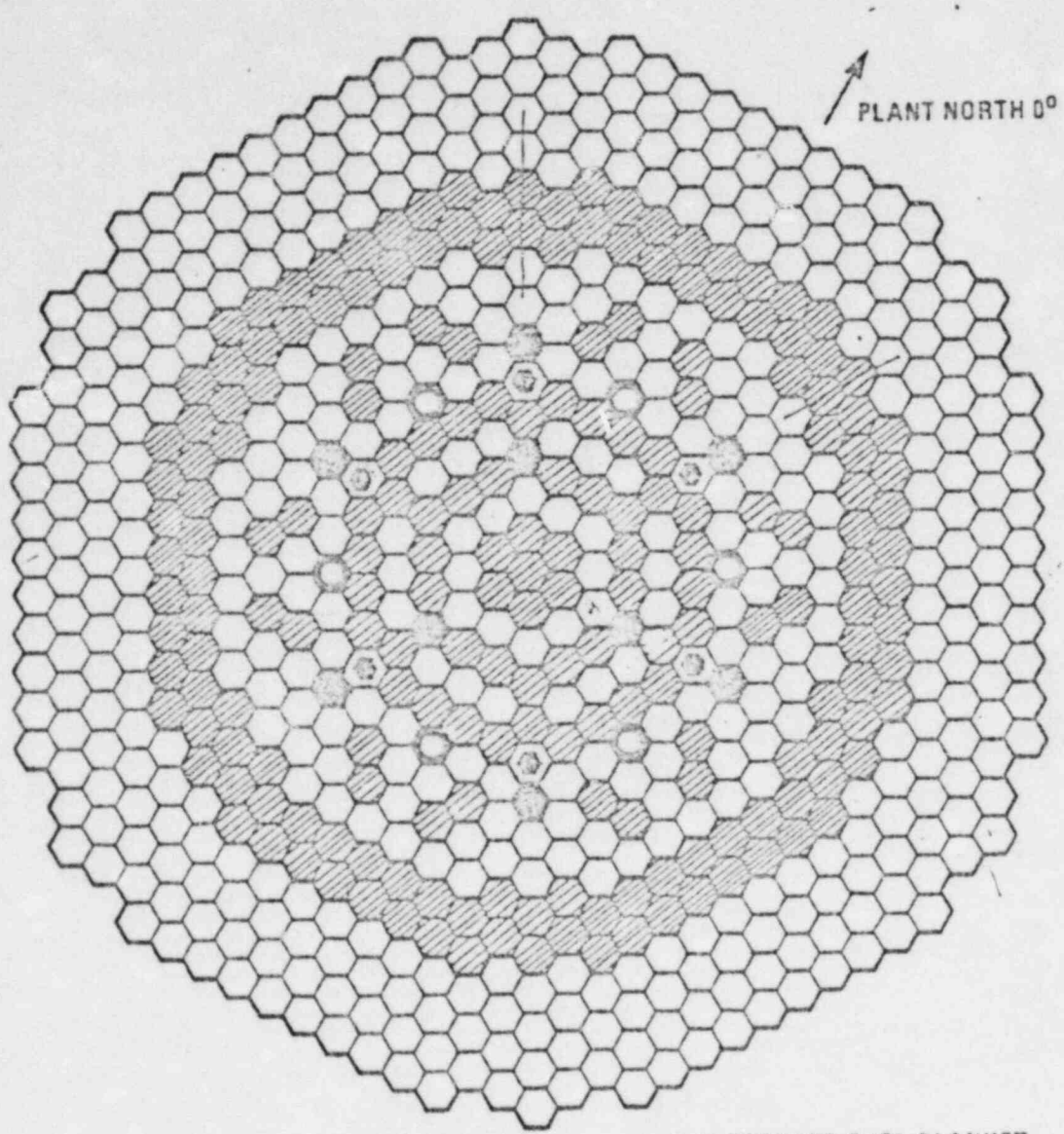

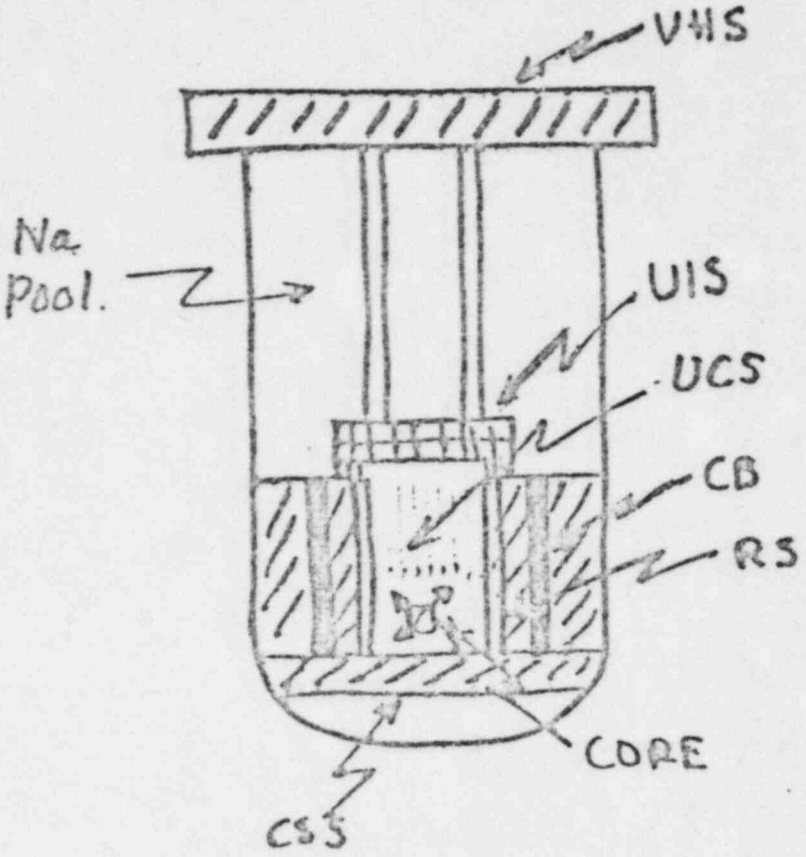
VHS
Na
Pool.
UIS
UCS
CB
RS
CORE
CSS

Fig 1

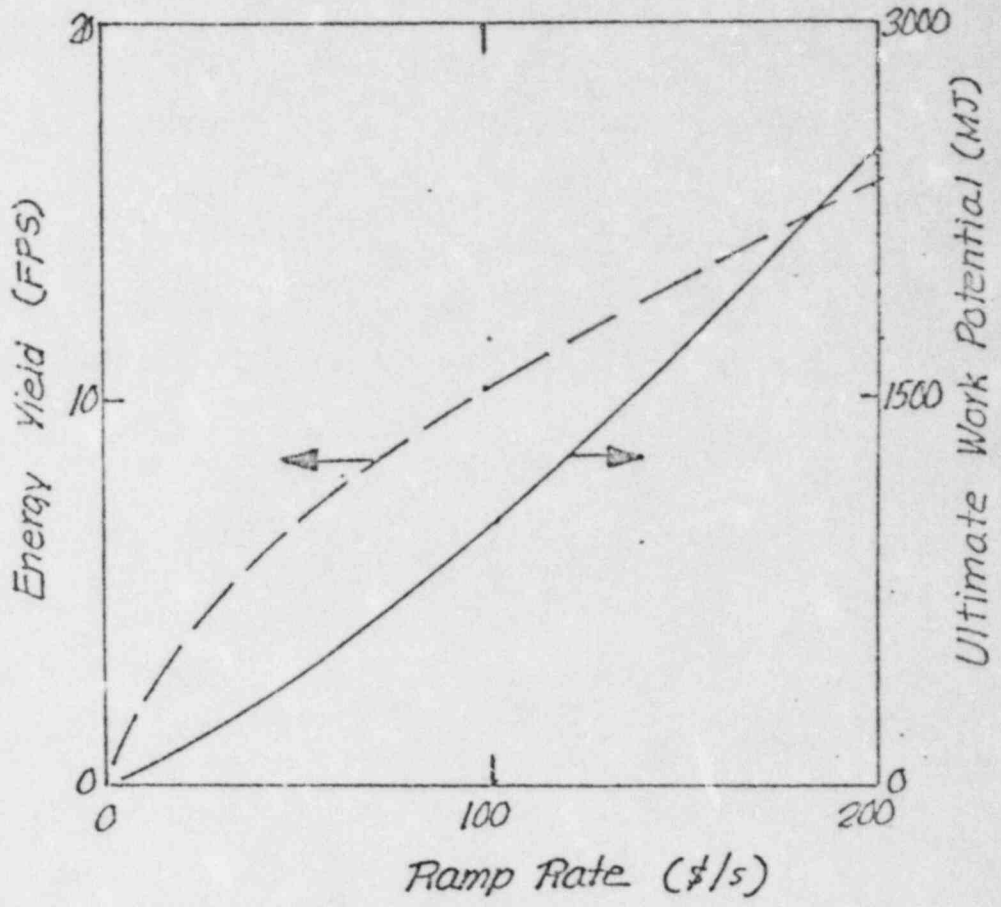
20
10
0
0
100
200
3000
1500
0
Energy Yield (FPS)
Ultimate Work Potential (MJ)
Ramp Rate ($/s)

Fig 2

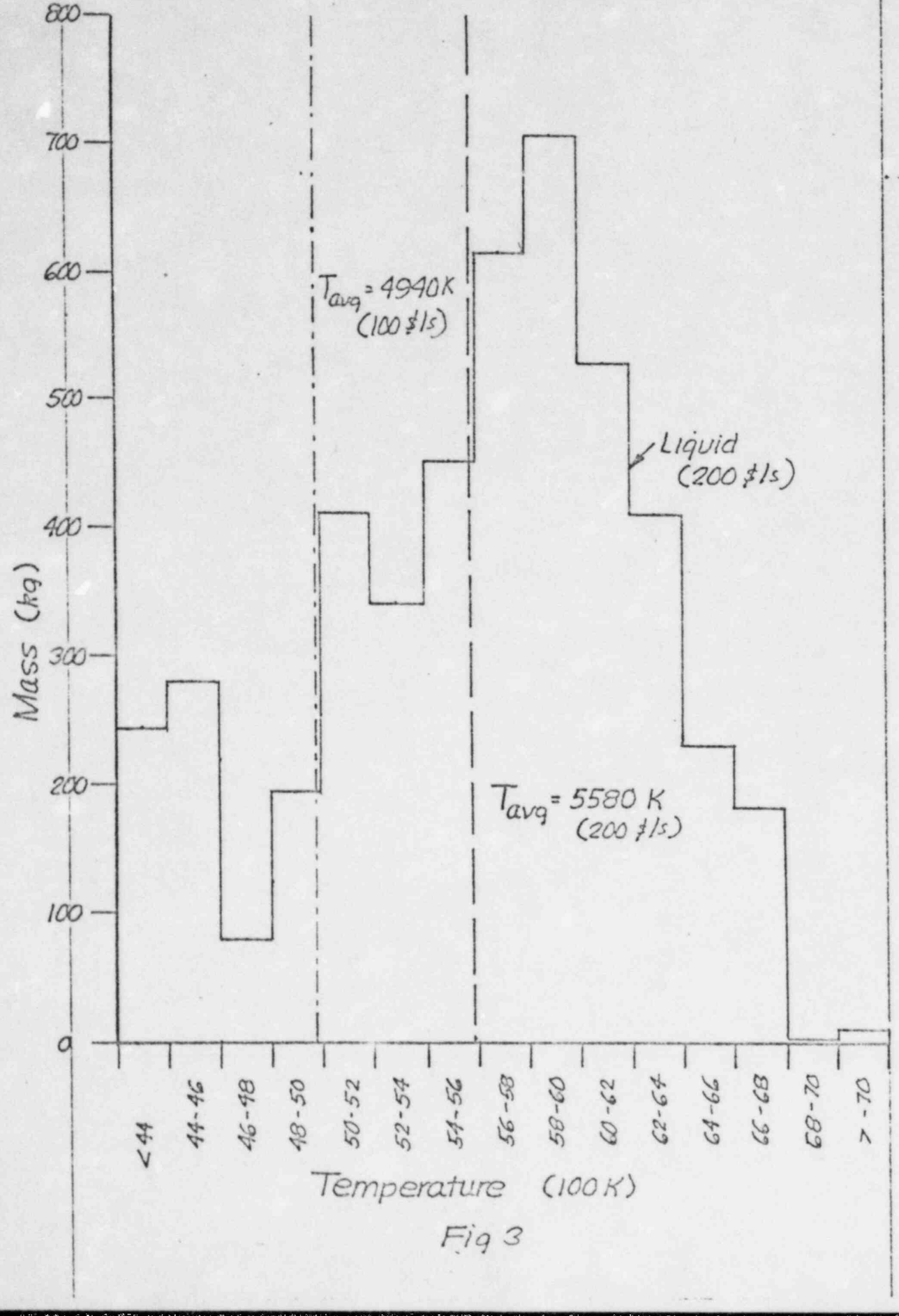
800
700
600
500
400
300
200
100
0
Mass (kg)
T_{avg} = 4940K
(100 #/s)
Liquid
(200 #/s)
T_{avg} = 5580 K
(200 #/s)
<44
44-46
46-48
48-50
50-52
52-54
54-56
56-58
58-60
60-62
62-64
64-66
66-68
68-70
>70
Temperature (100K)

Fig 3

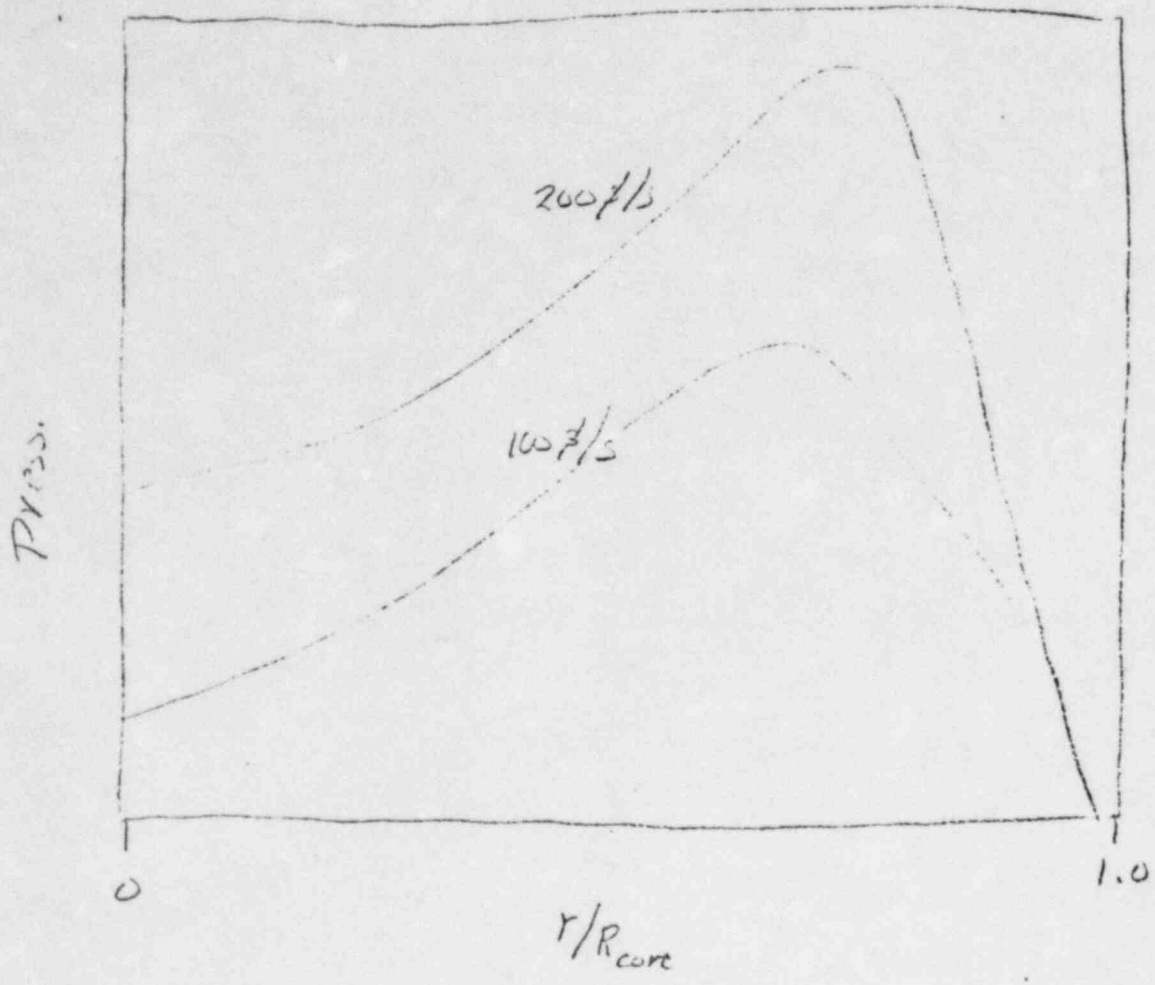

Fig 4

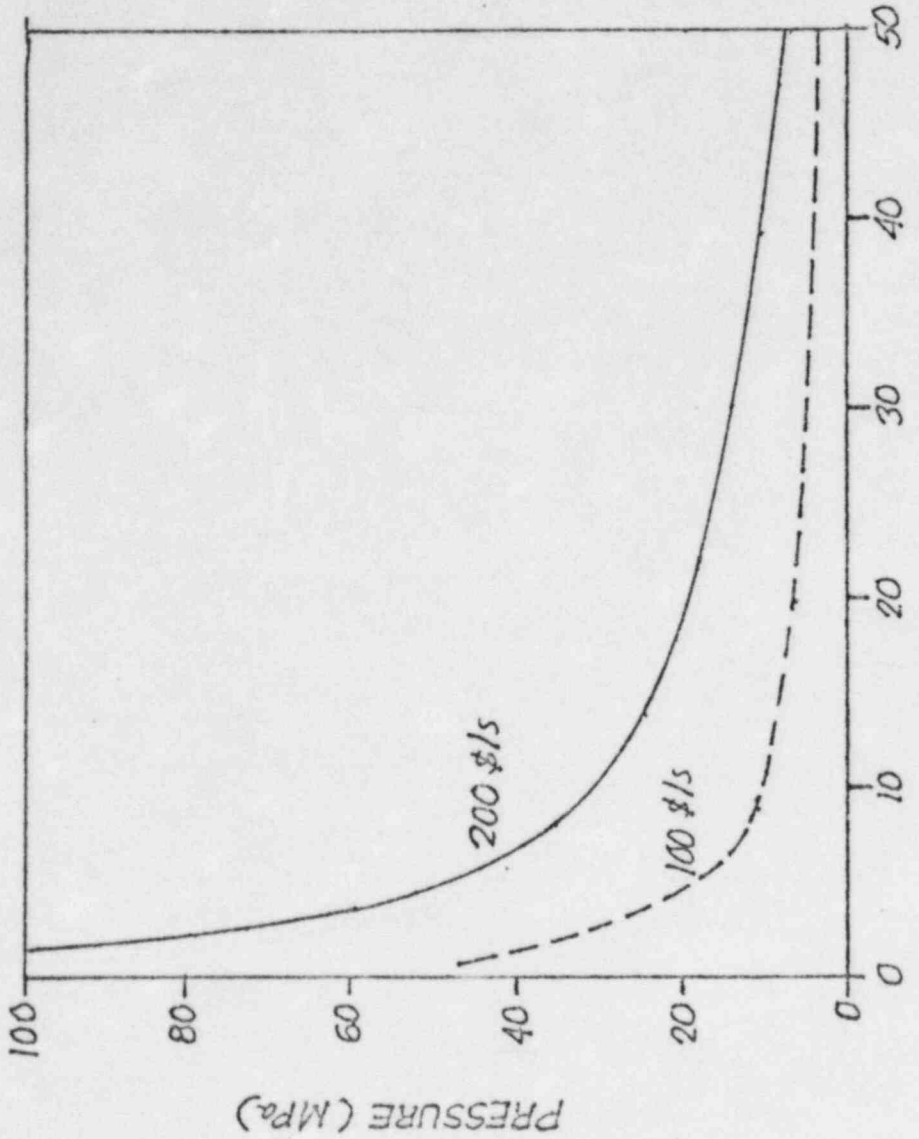
PRESSURE (MPa)
100
80
60
40
20
0
200 $/s
100 $/s
0
10
20
30
40
50
VOLUME CHANGE (m³)

Fig 5

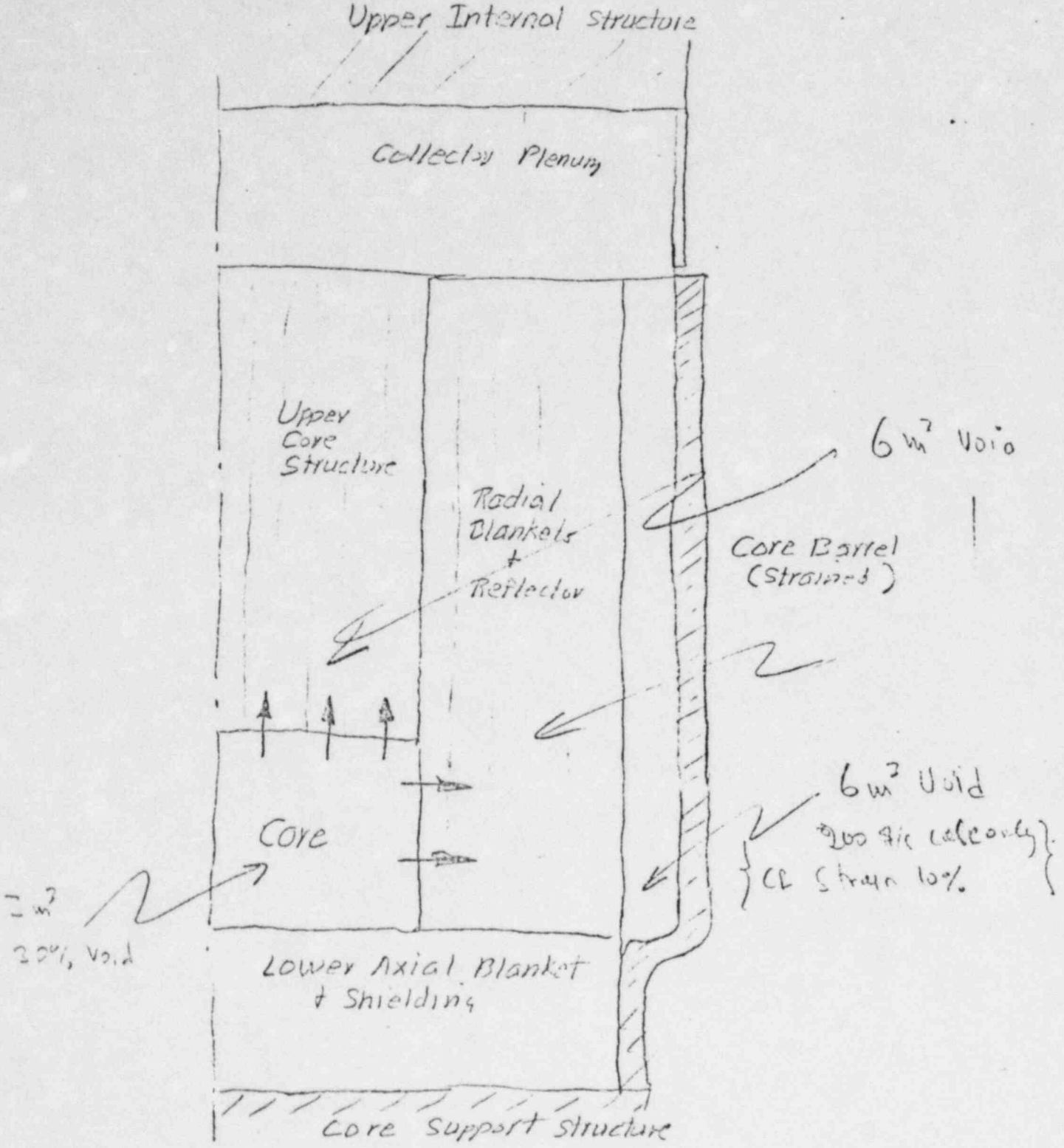
Upper Internal Structure
Collector Plenum
Upper Core Structure
Radial Blankets + Reflector
6 m³ Void
Core Barrel (Strained)
6 m³ Void
Core
Lower Axial Blanket + Shielding
Core Support Structure

Fig. 6

PRESS AT 6-7,15-20 C03 100 $/s

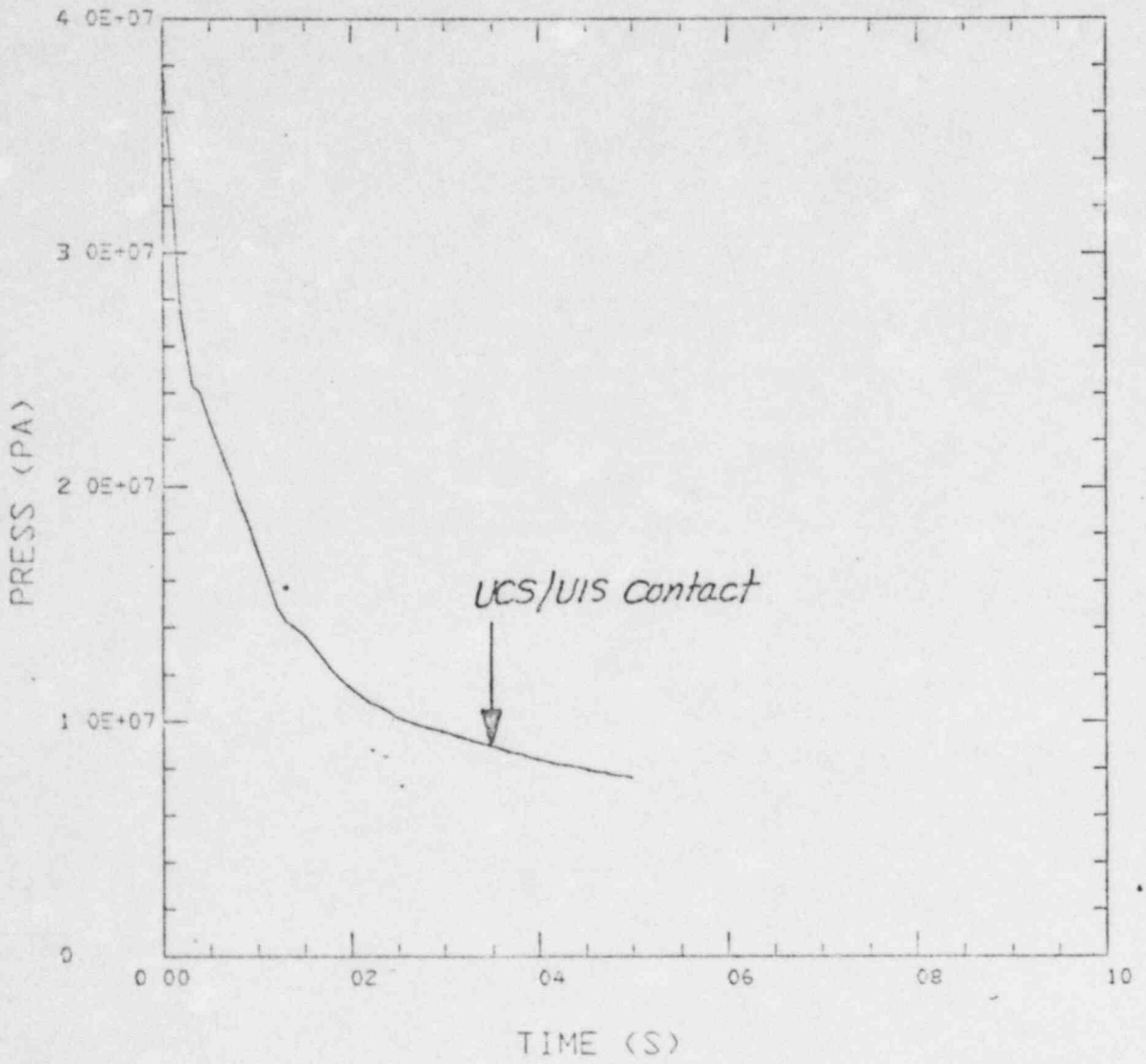

Fig 7a

PRESS AT 16.12-24 C08 100 $/s

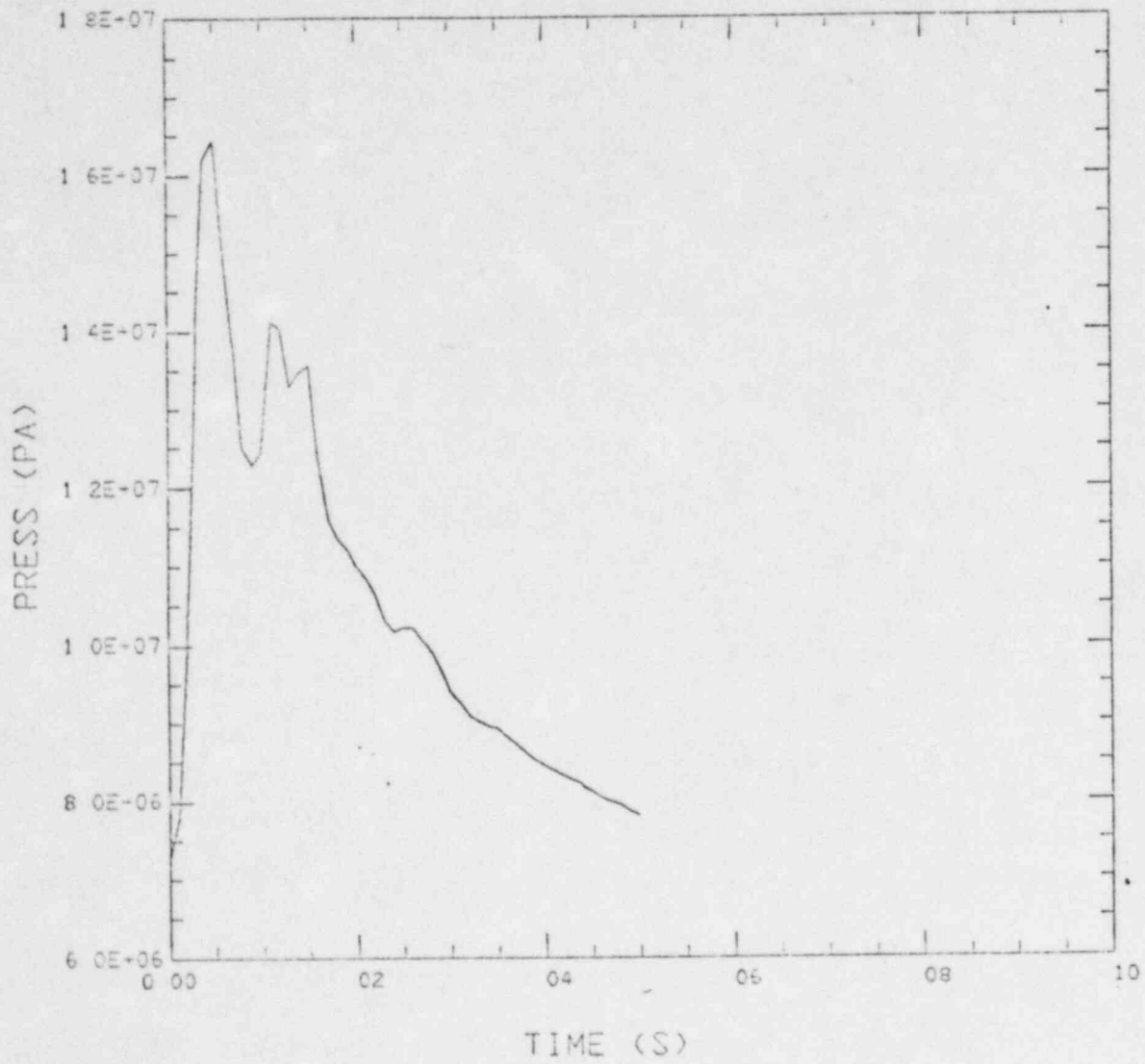

Fig 76

PRESS AT 6-7,16-20 C07 200 $/s

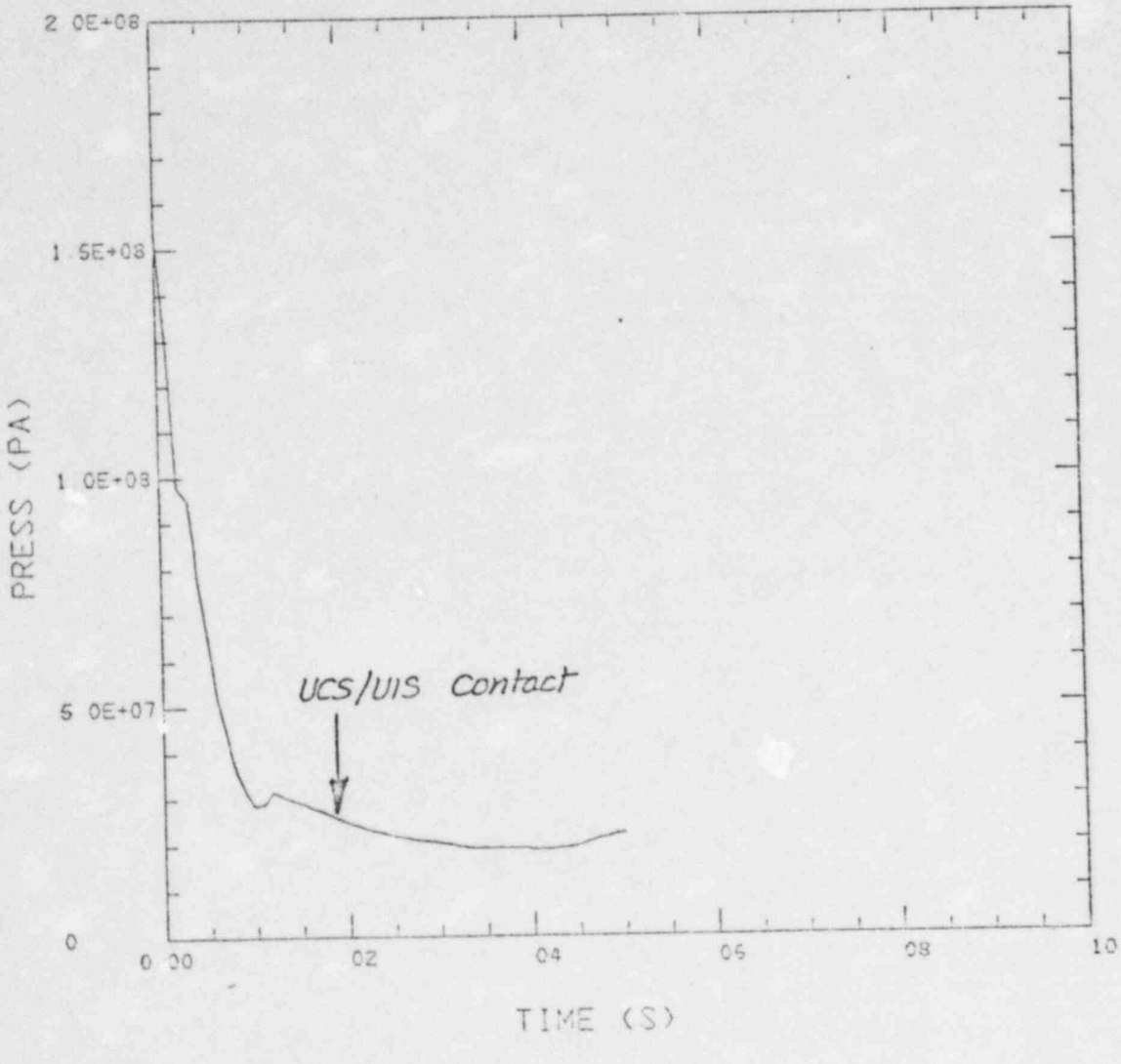

Fig 8a

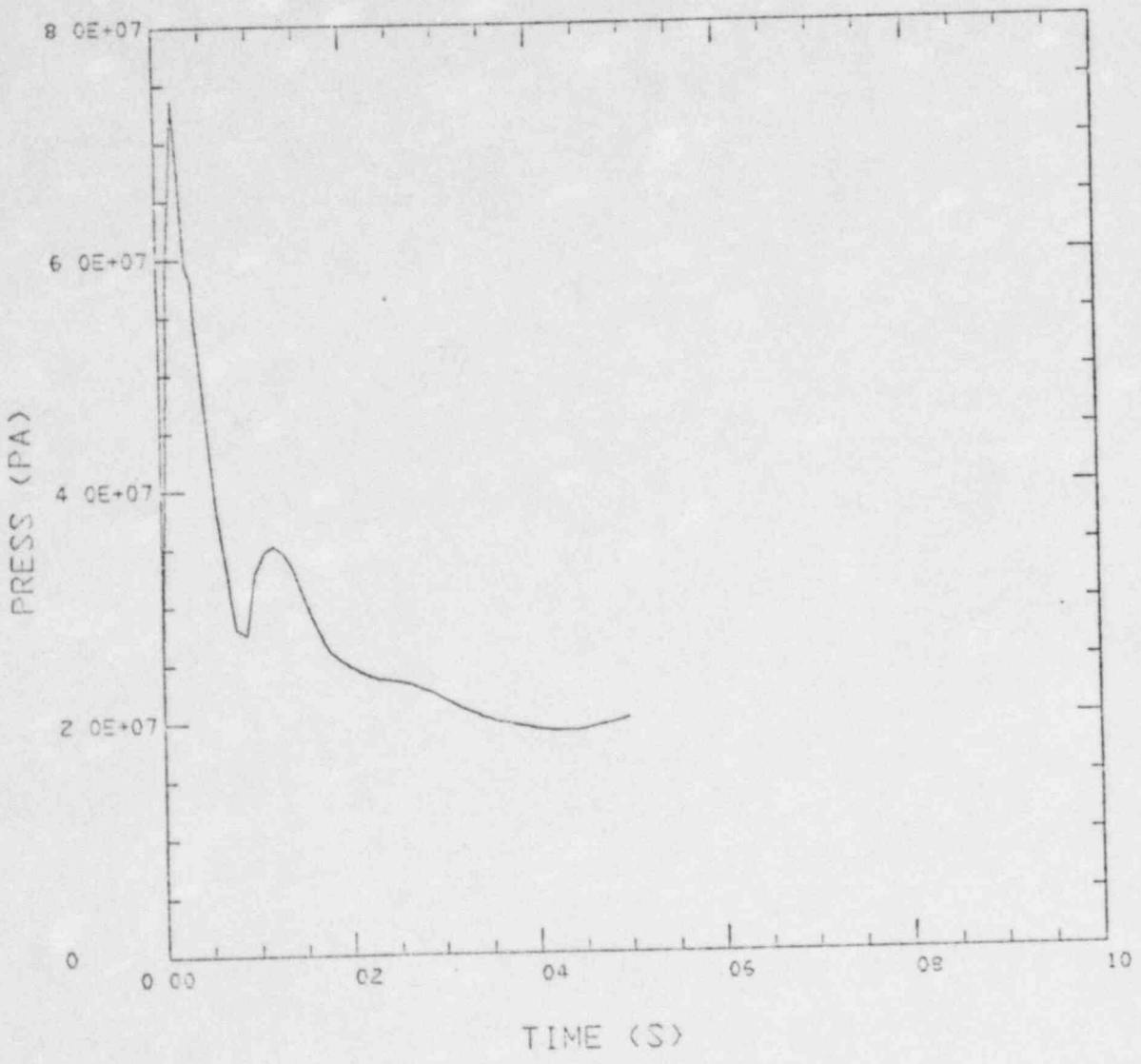
PRESS AT 16,12-24 C07 200 #/s
8 0E+07
6 0E+07
4 0E+07
2 0E+07
0
PRESS (PA)
0 00
02
04
06
08
10
TIME (S)

Fig 9b

(3)

UIS Dis.

C03

100 $/s
Adiabatic

Fig 9a

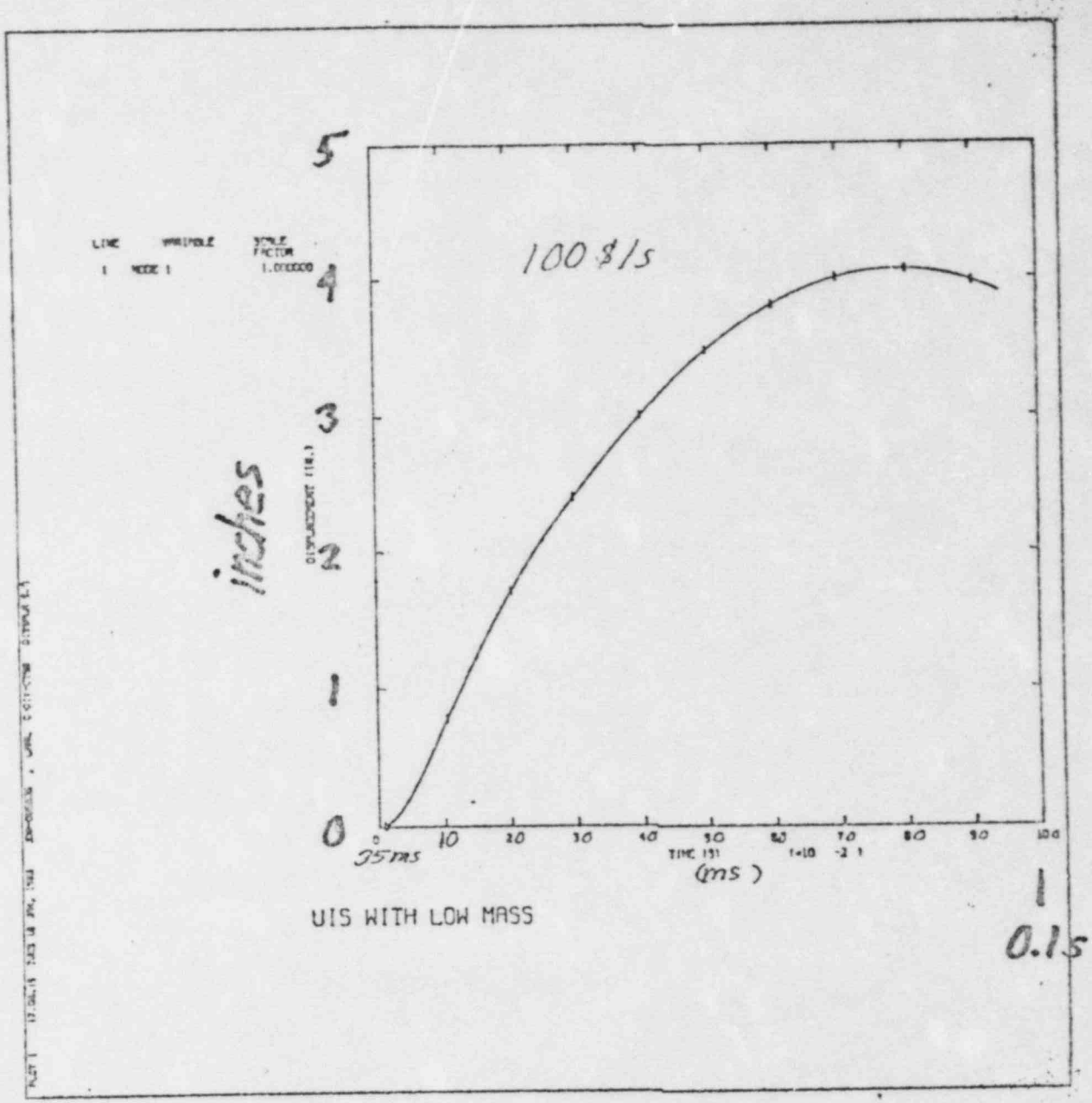

UIS WITH LOW MASS

II.2

Fig 96 HCDA.

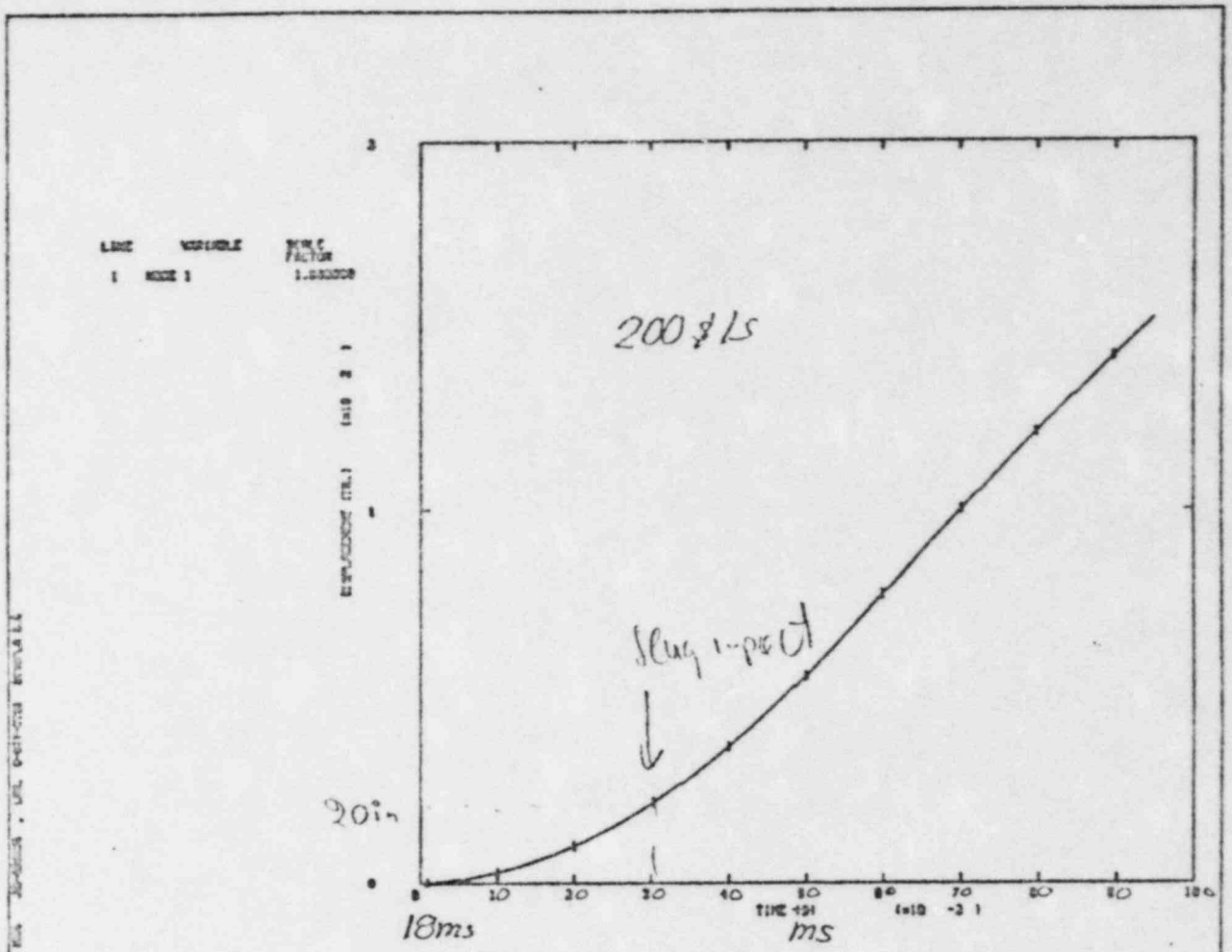

UIS WITH SPRING (CO7UIS)

Fig 10a

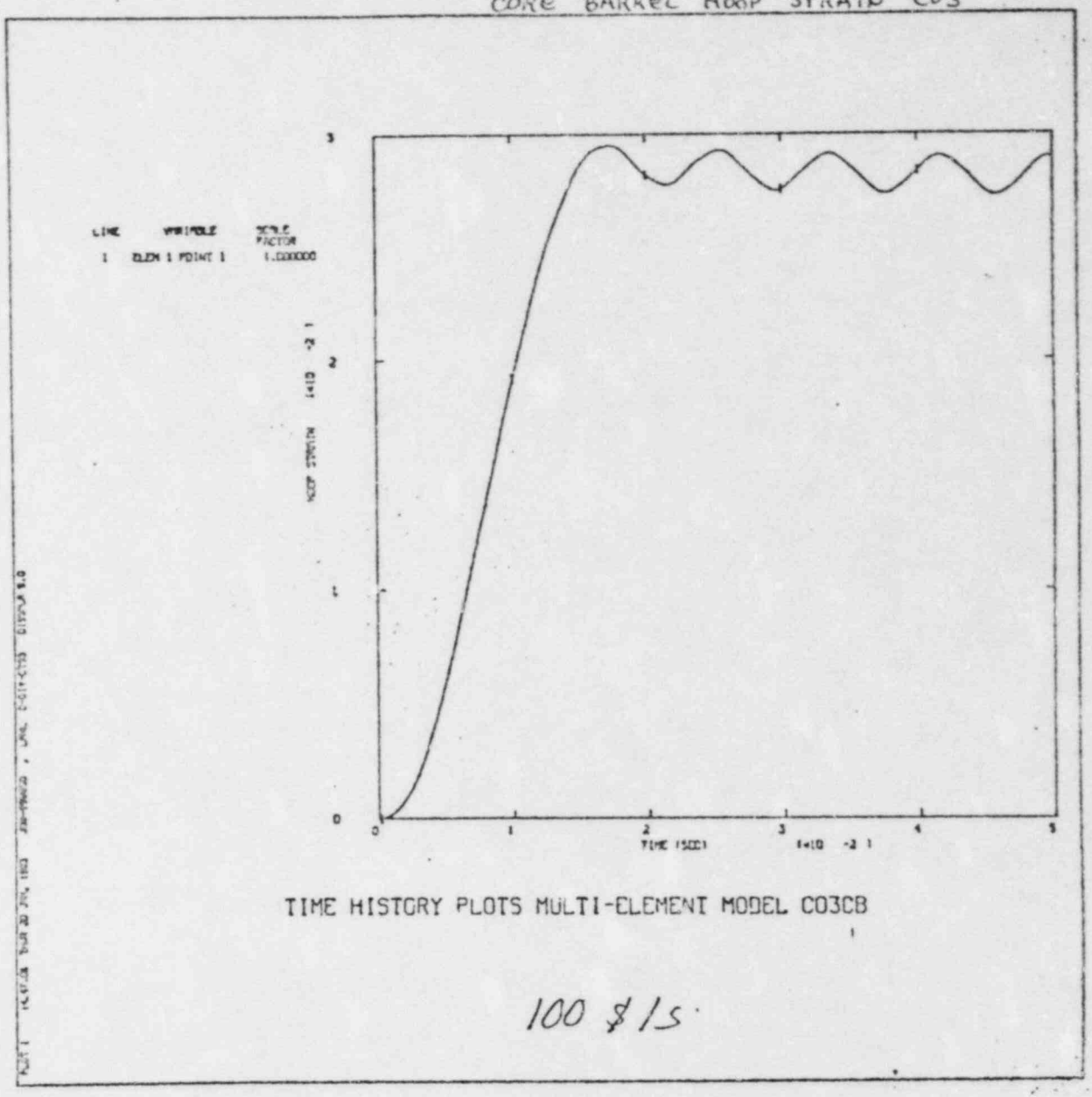
CORE BARREL HOOP STRAIN C03
LINE VARIABLE SCALE FACTOR
1 ELEM 1 POINT 1 1.000000
HOOP STRAIN (+10 -2)
TIME (SEC) (+10 -2)
0
1
2
3
4
5
TIME HISTORY PLOTS MULTI-ELEMENT MODEL C03CB
100 $/s

II.23

Fig 10b HCDA

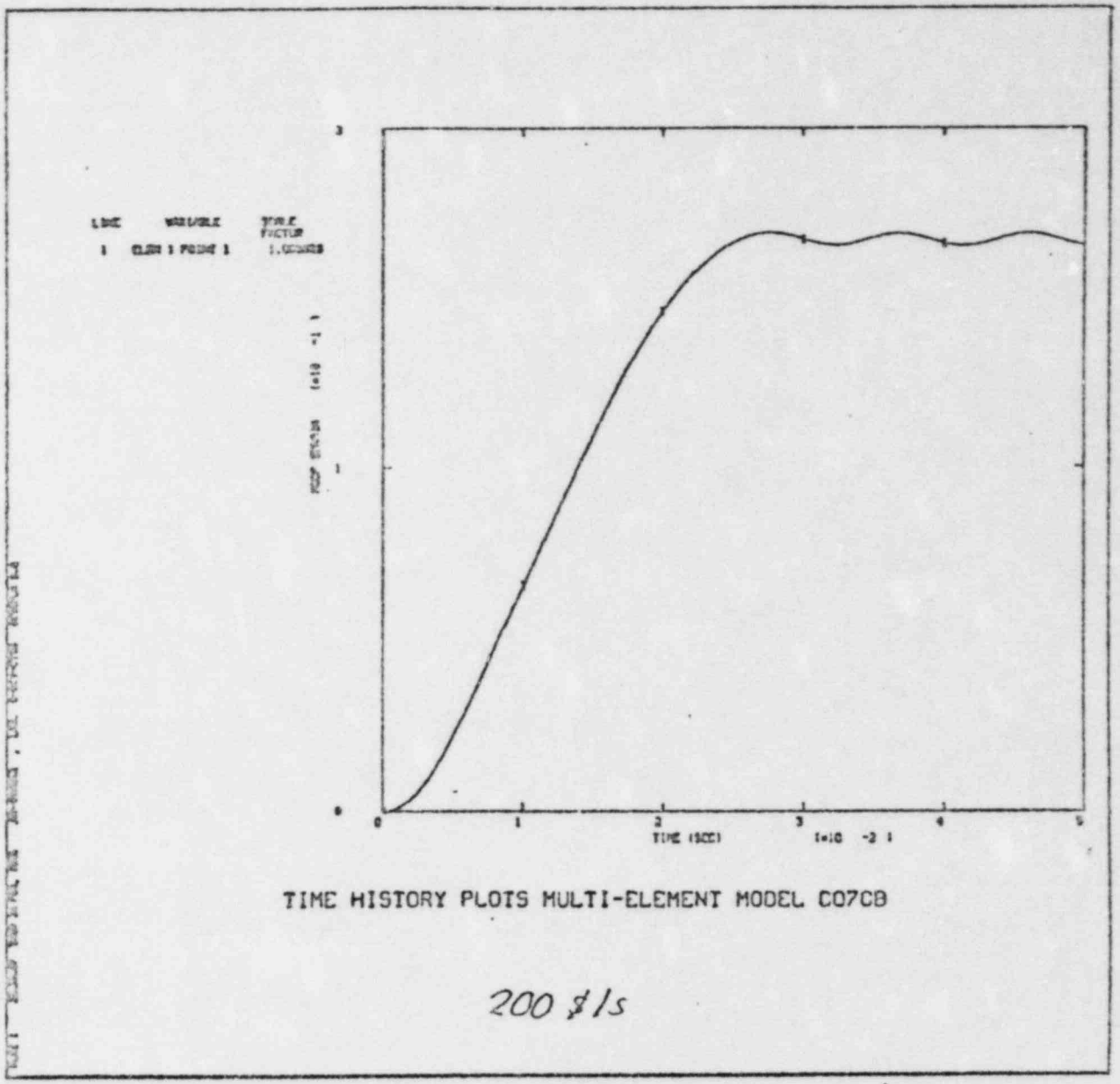

200 #/s

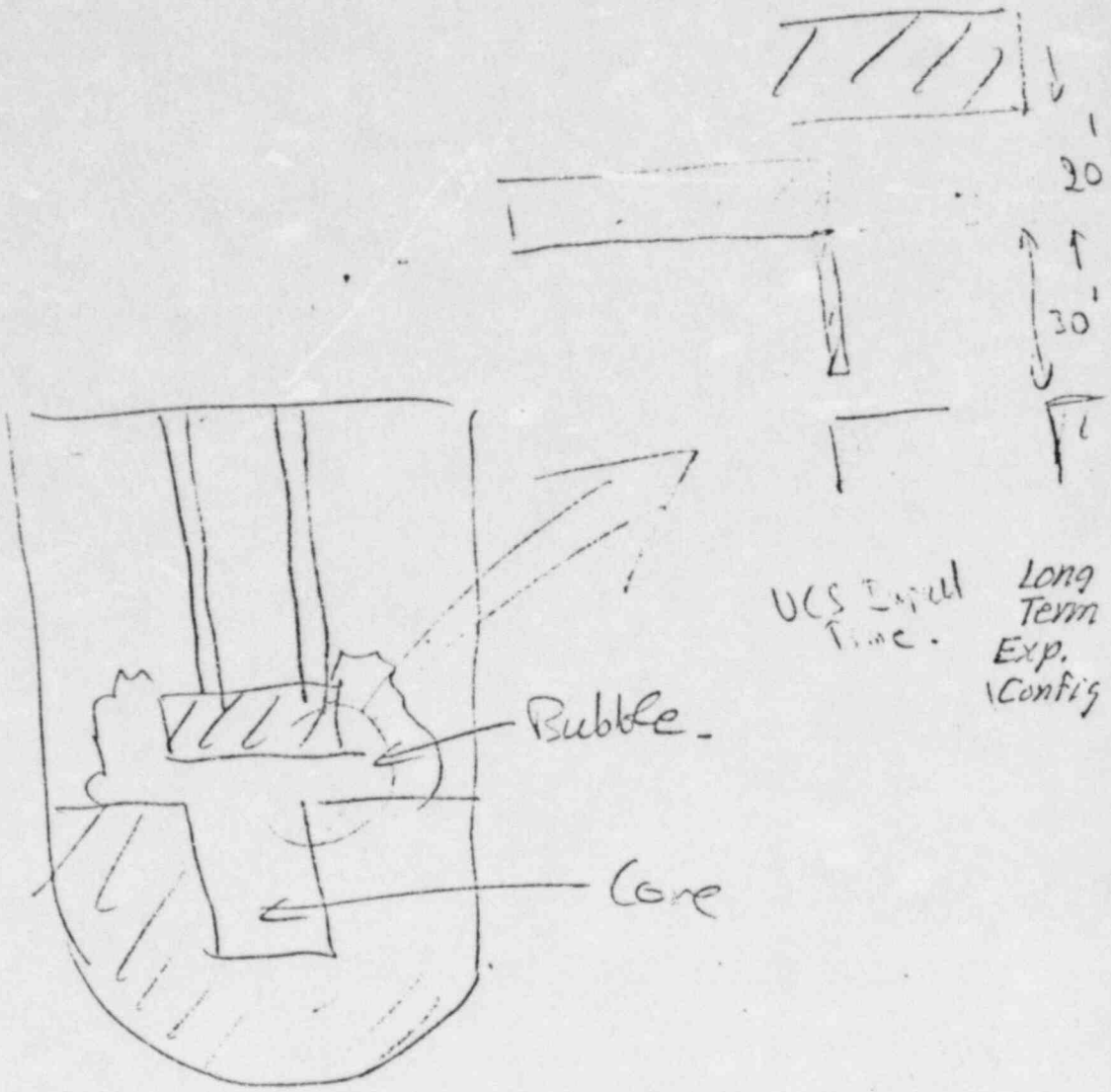

Fig. 11

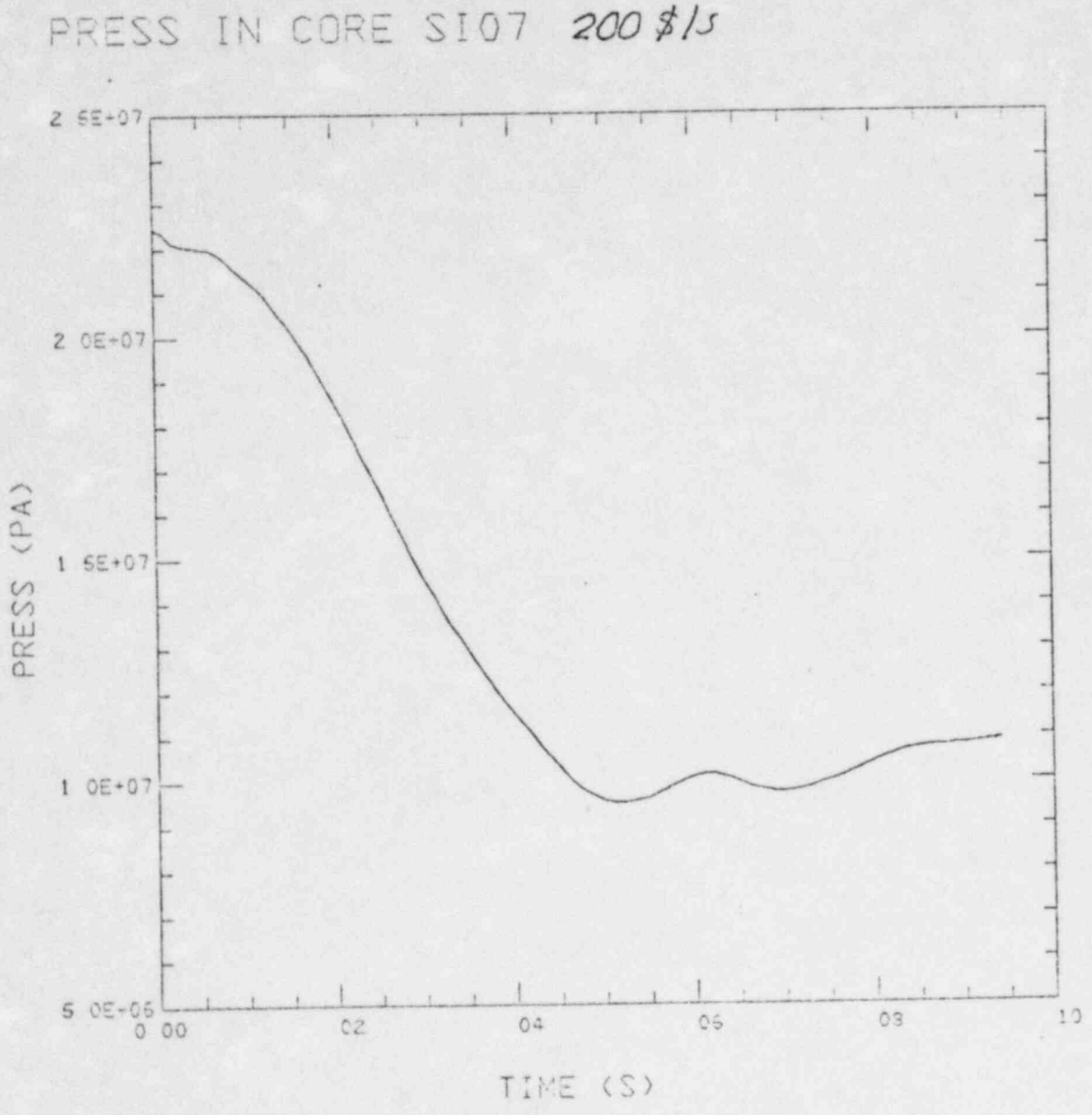
PRESS IN CORE SI07 200 $/s
2 5E+07
2 0E+07
1 5E+07
1 0E+07
5 0E-06
PRESS (PA)
0 00
02
04
06
08
10
TIME (S)

Fig 12a

PRESS IN EXP BUBBLE SI07 200 $/s

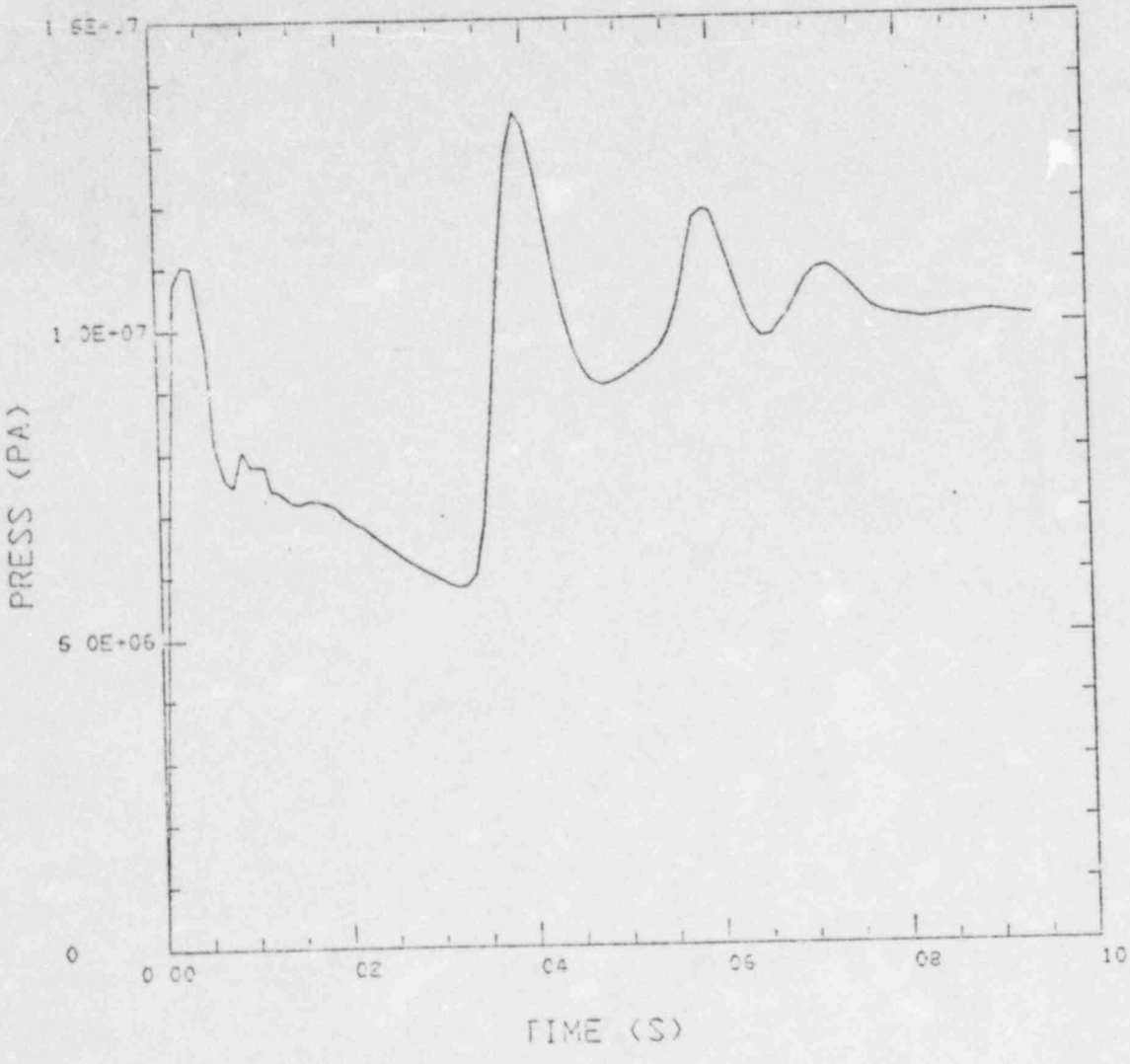

Fig 12b

POOL VELOCITY SI07 200 #/s

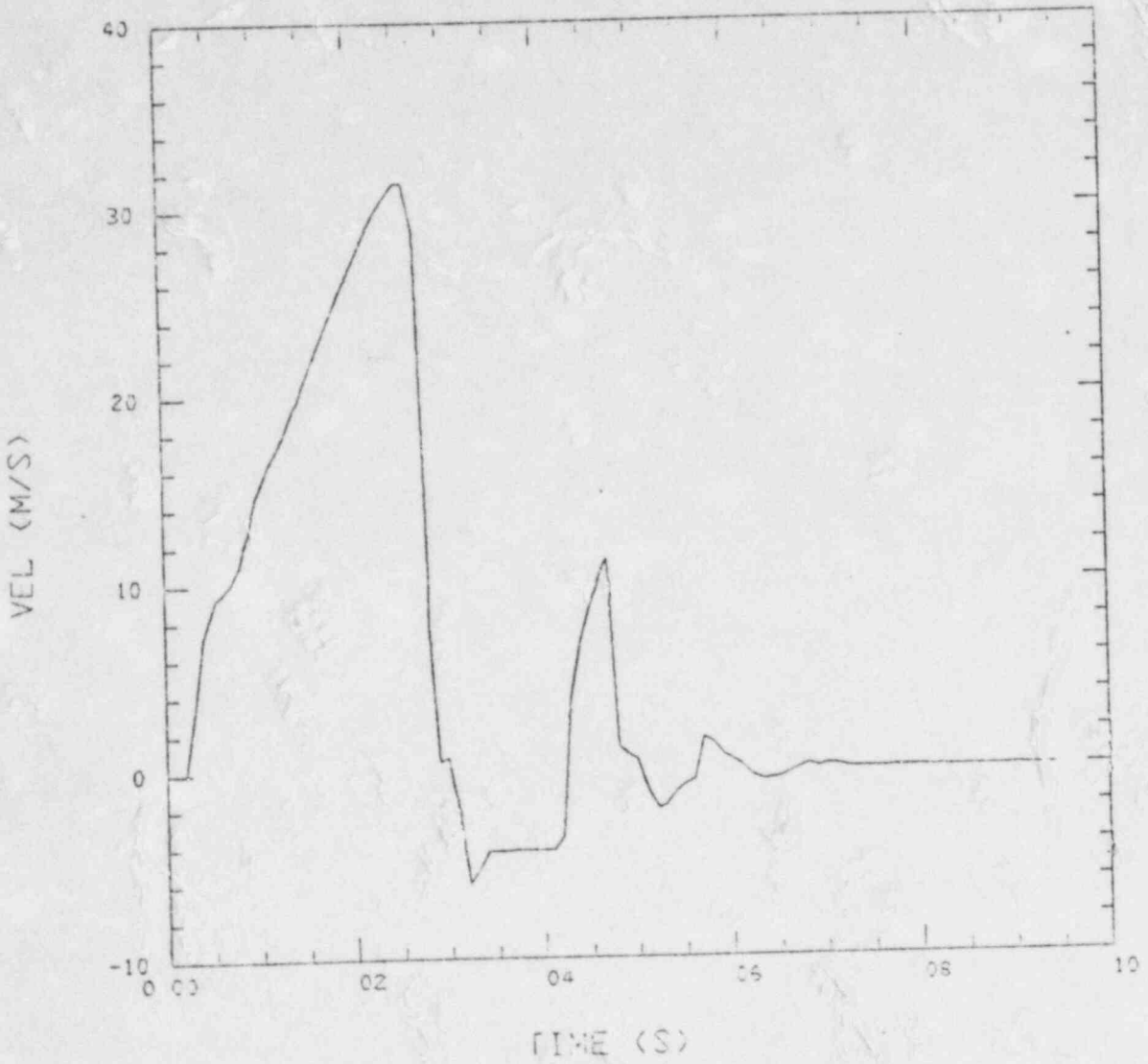

Fig 13

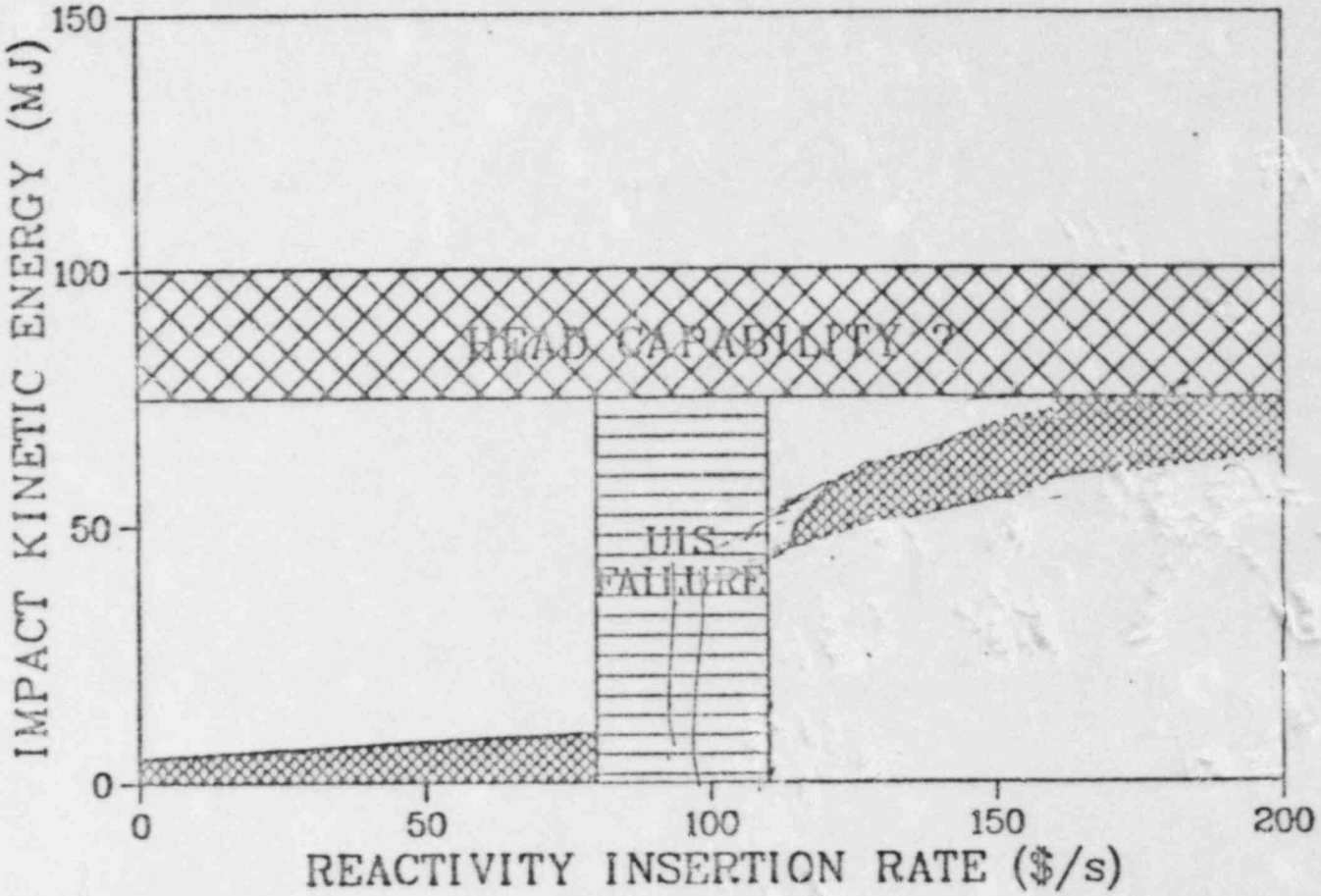
IMPACT KINETIC ENERGY (MJ)
150
100
50
0
HEAD CAPABILITY ?
UIS FAILURE
0
50
100
150
200
REACTIVITY INSERTION RATE ($/s)

Fig 14

Fig 1
(Section AII.2)

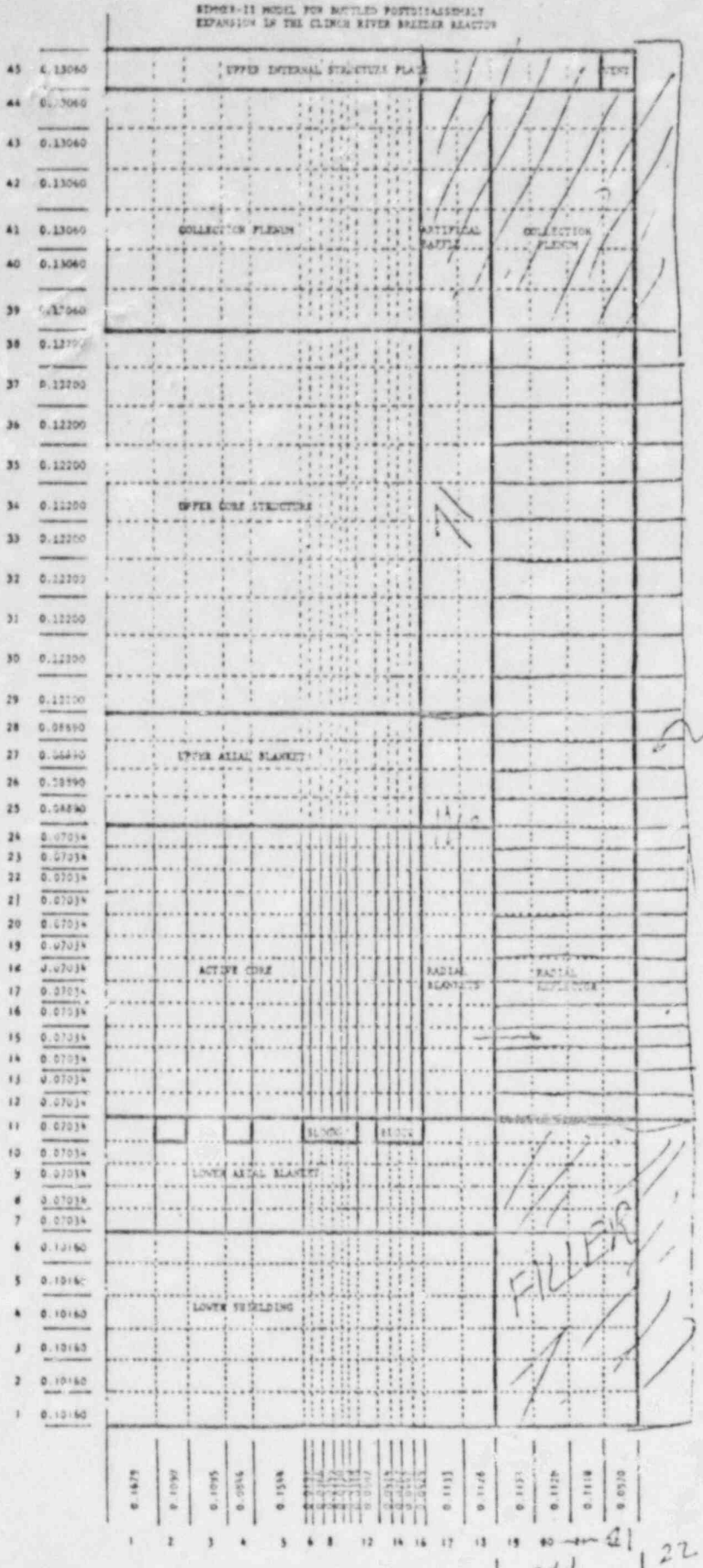

a Void.

AII.2

AVG LIQ FUEL TEMP C07 200 #/s

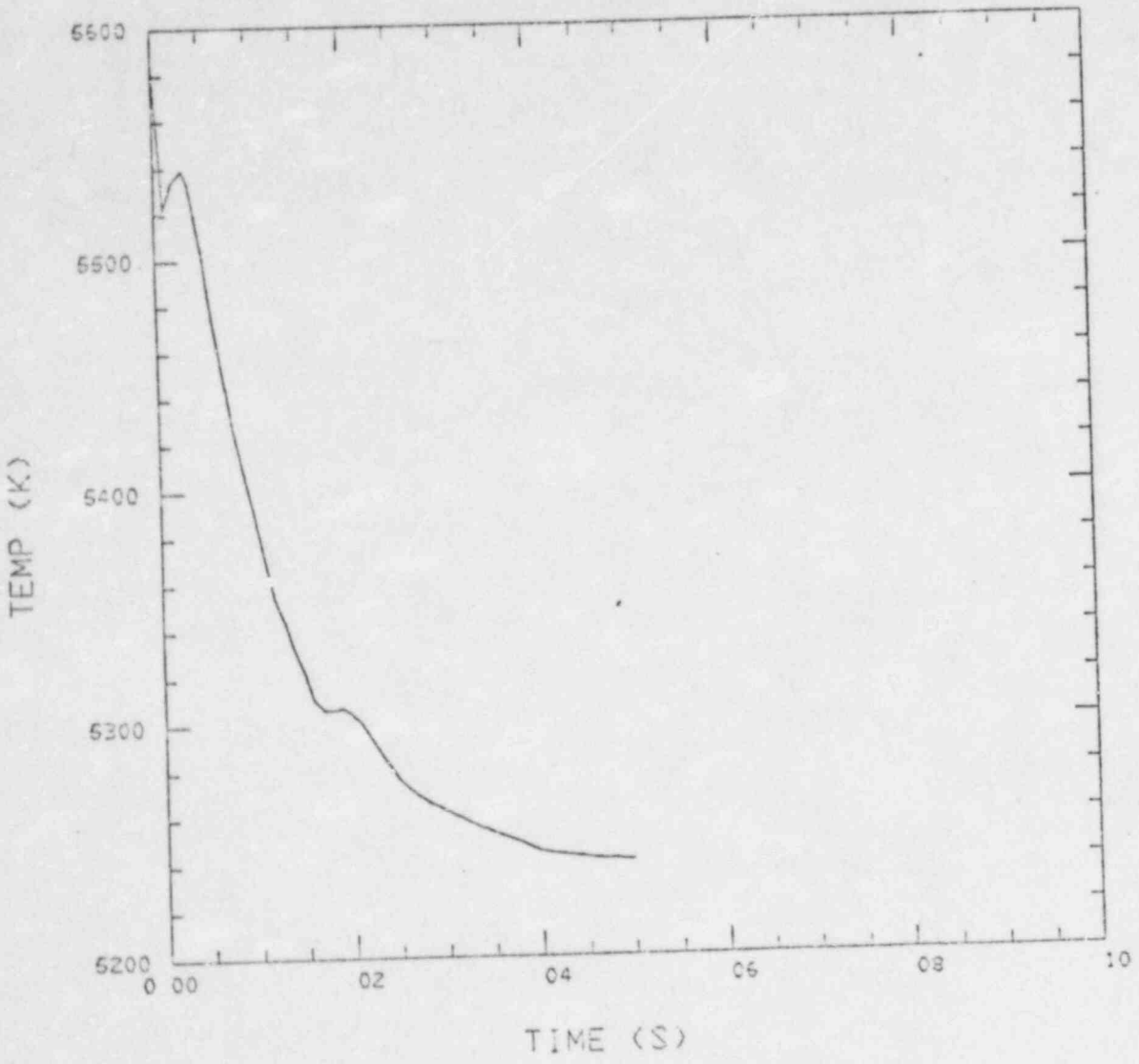

Fig 2

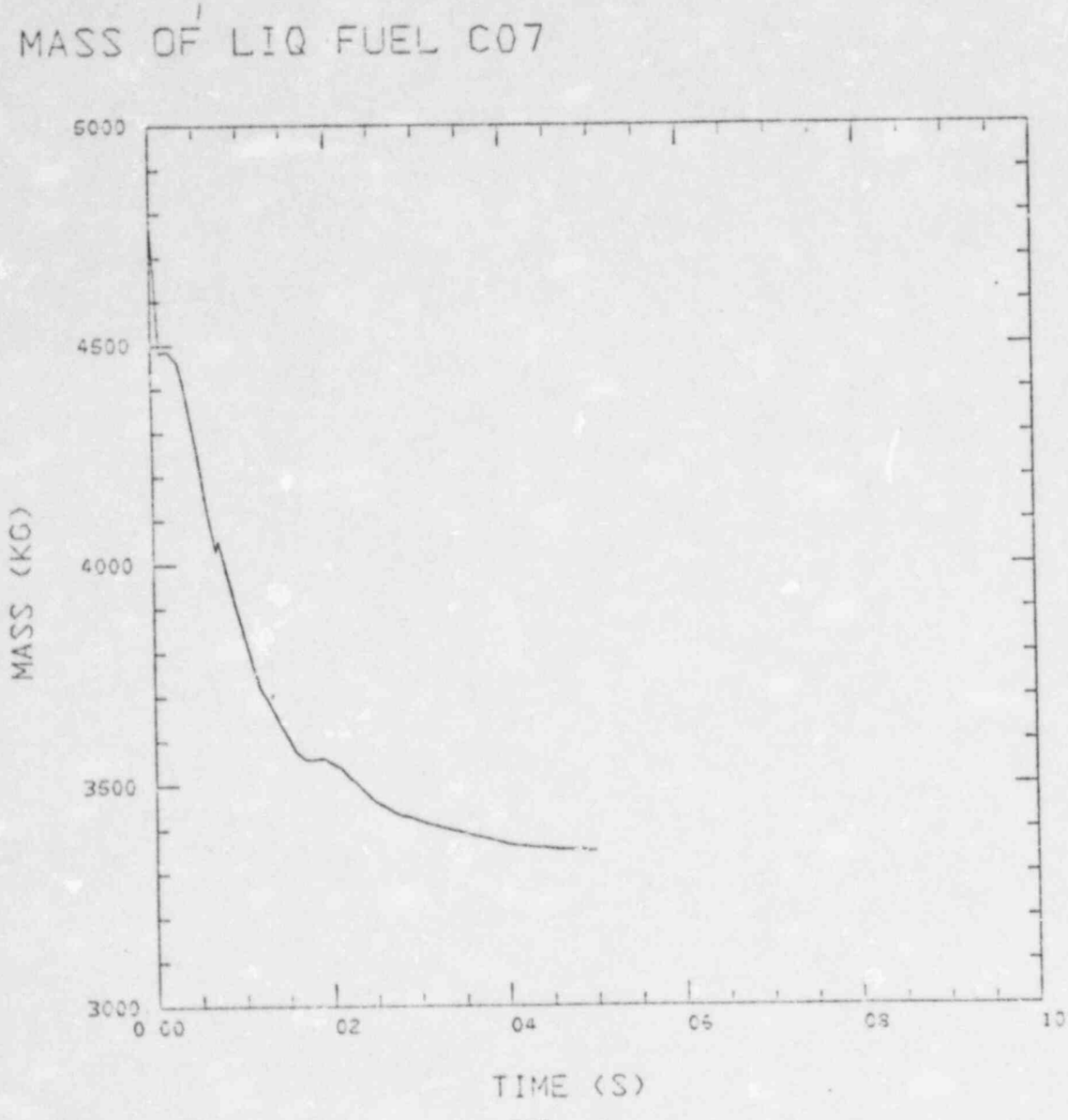
MASS OF LIQ FUEL C07
5000
4500
4000
3500
3000
MASS (KG)
0 00
02
04
06
08
10
TIME (S)

Fig 3

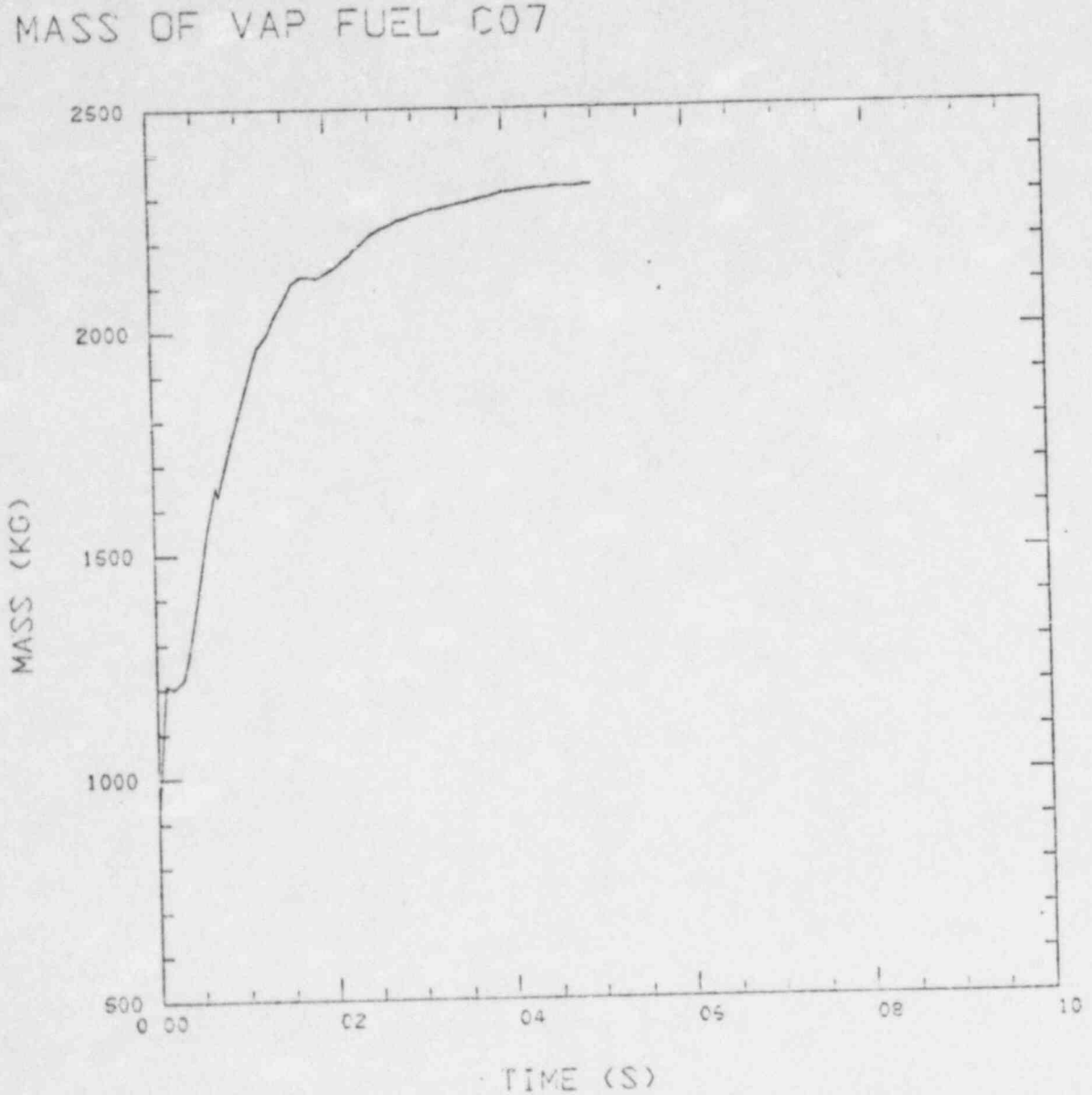
MASS OF VAP FUEL C07
2500
2000
1500
1000
500
0
MASS (KG)
00
02
04
06
08
10
TIME (S)

Fig 4

STRAIN

CORE BARPEL^ VOLUME

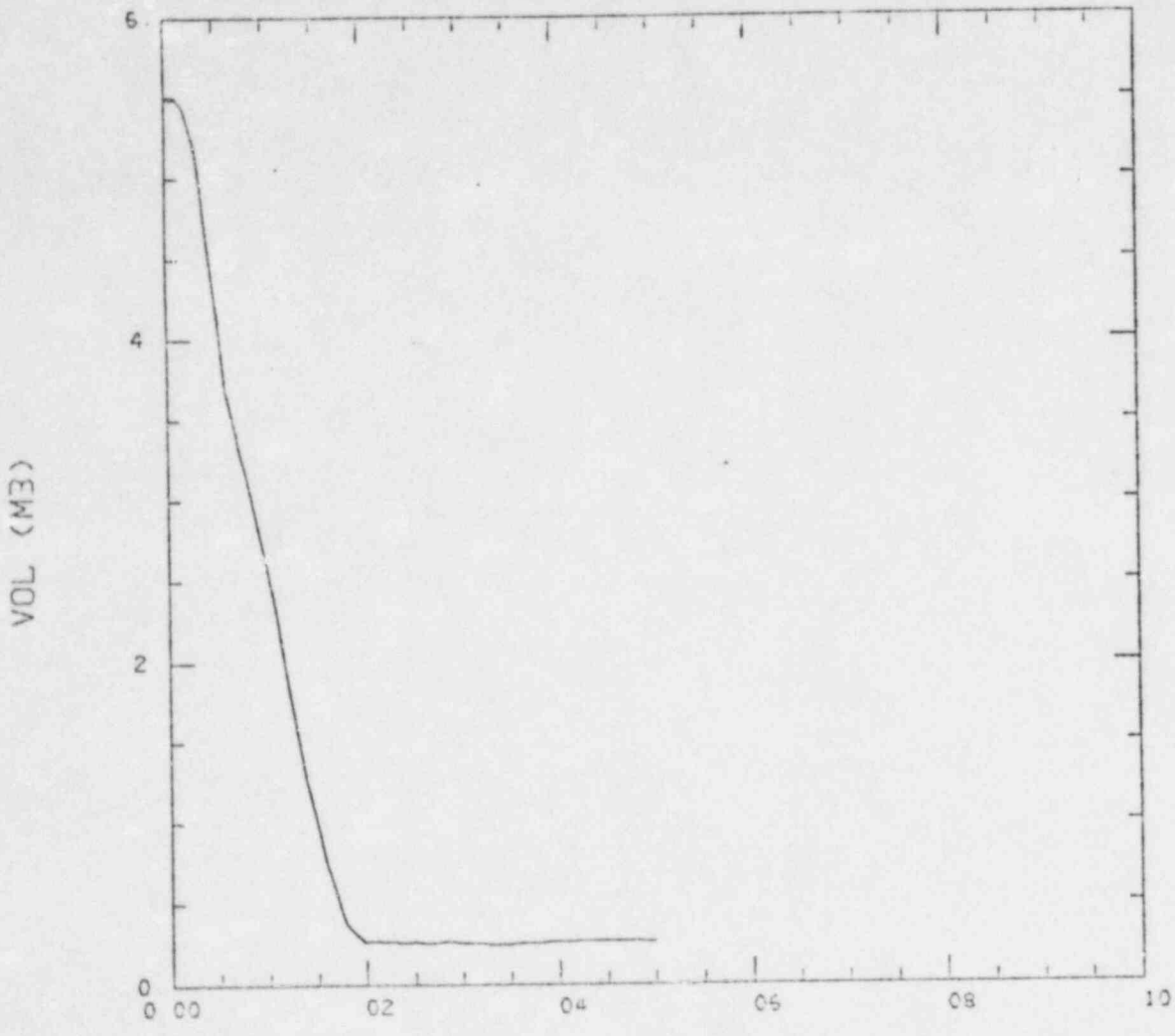

Fig 5

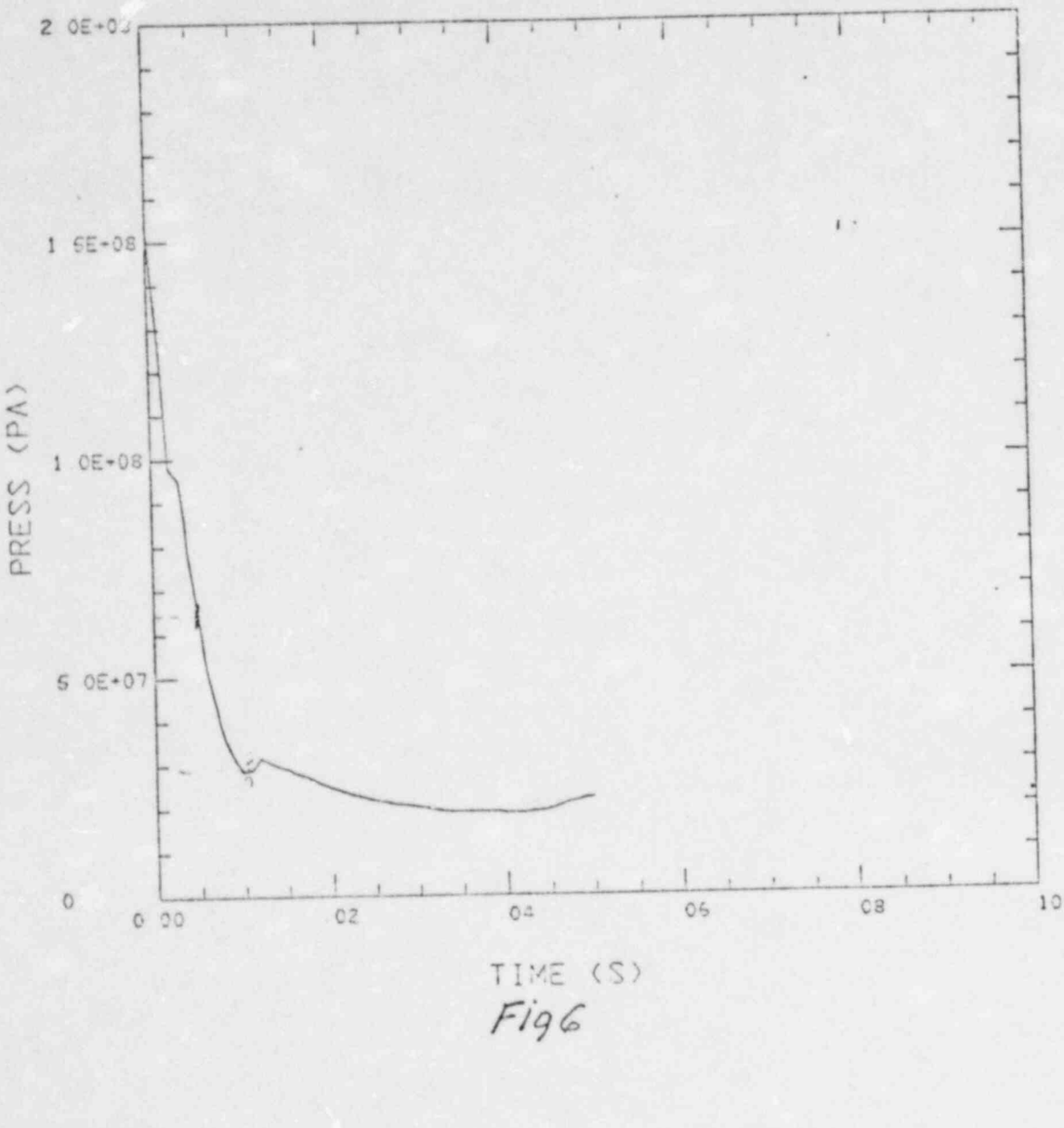
PRESS AT 6-7,16-20 C07
2 0E+00
1 5E-08
1 0E-08
5 0E-07
0
PRESS (PA)
0 00
02
04
06
08
10
TIME (S)

Fig 6

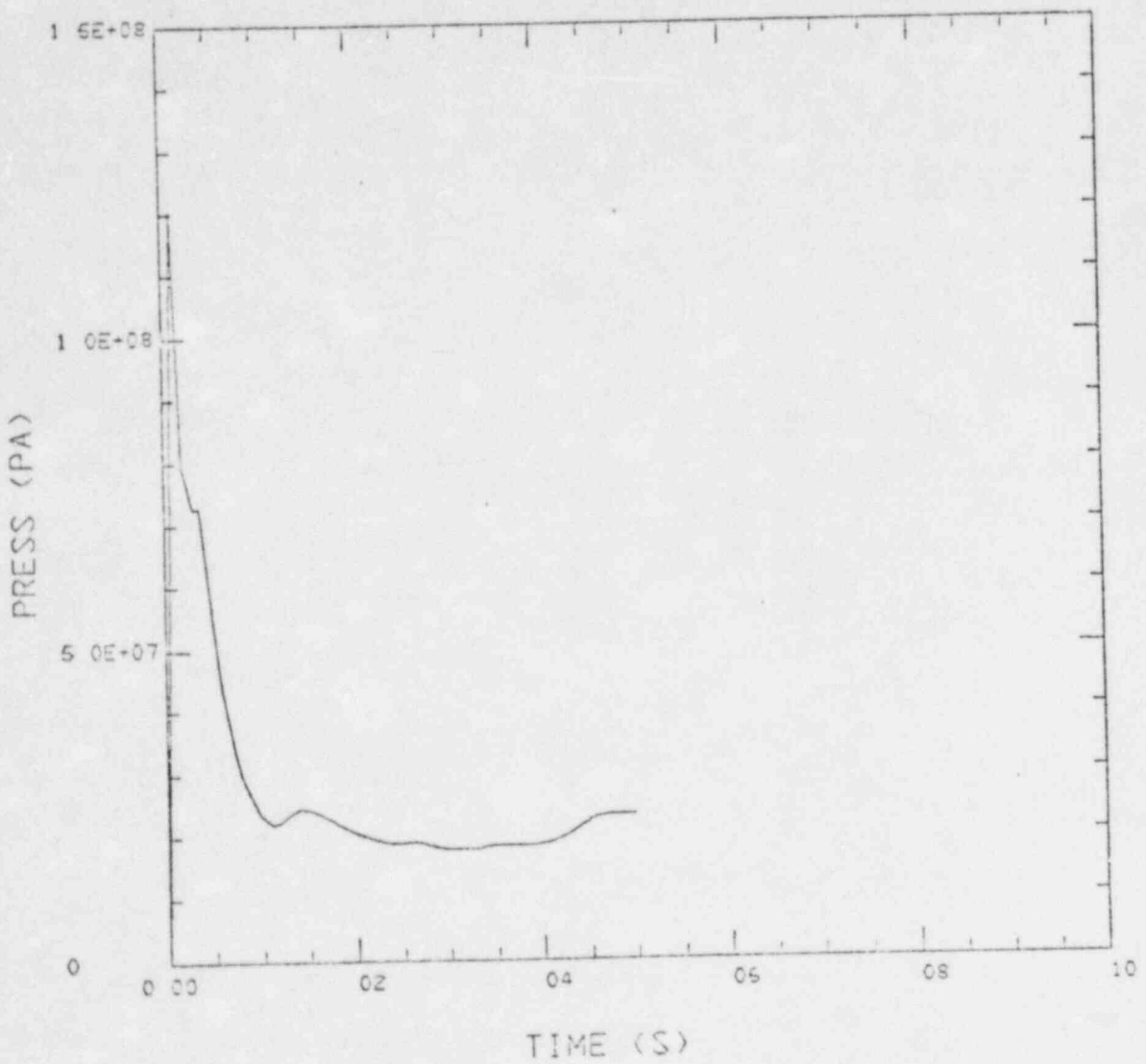
PRESS AT 1-16,24 C07
1 5E+08
1 0E+08
5 0E+07
0
PRESS (PA)
0 00
02
04
06
08
10
TIME (S)

Fig 7

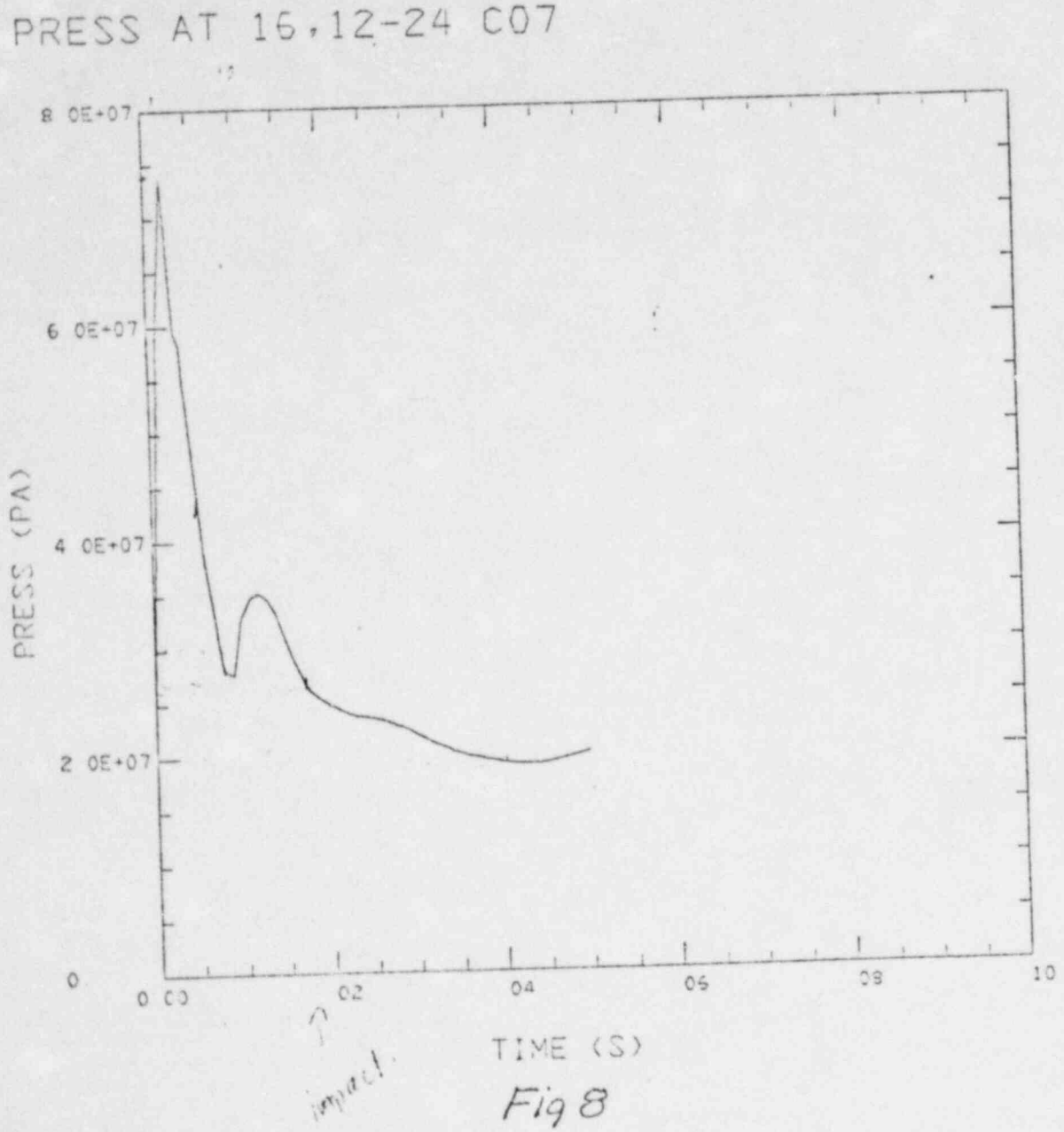
PRESS AT 16,12-24 C07
8 0E+07
6 0E+07
4 0E+07
2 0E+07
0
PRESS (PA)
0 00
02
04
06
08
10
TIME (S)
impact

Fig 8

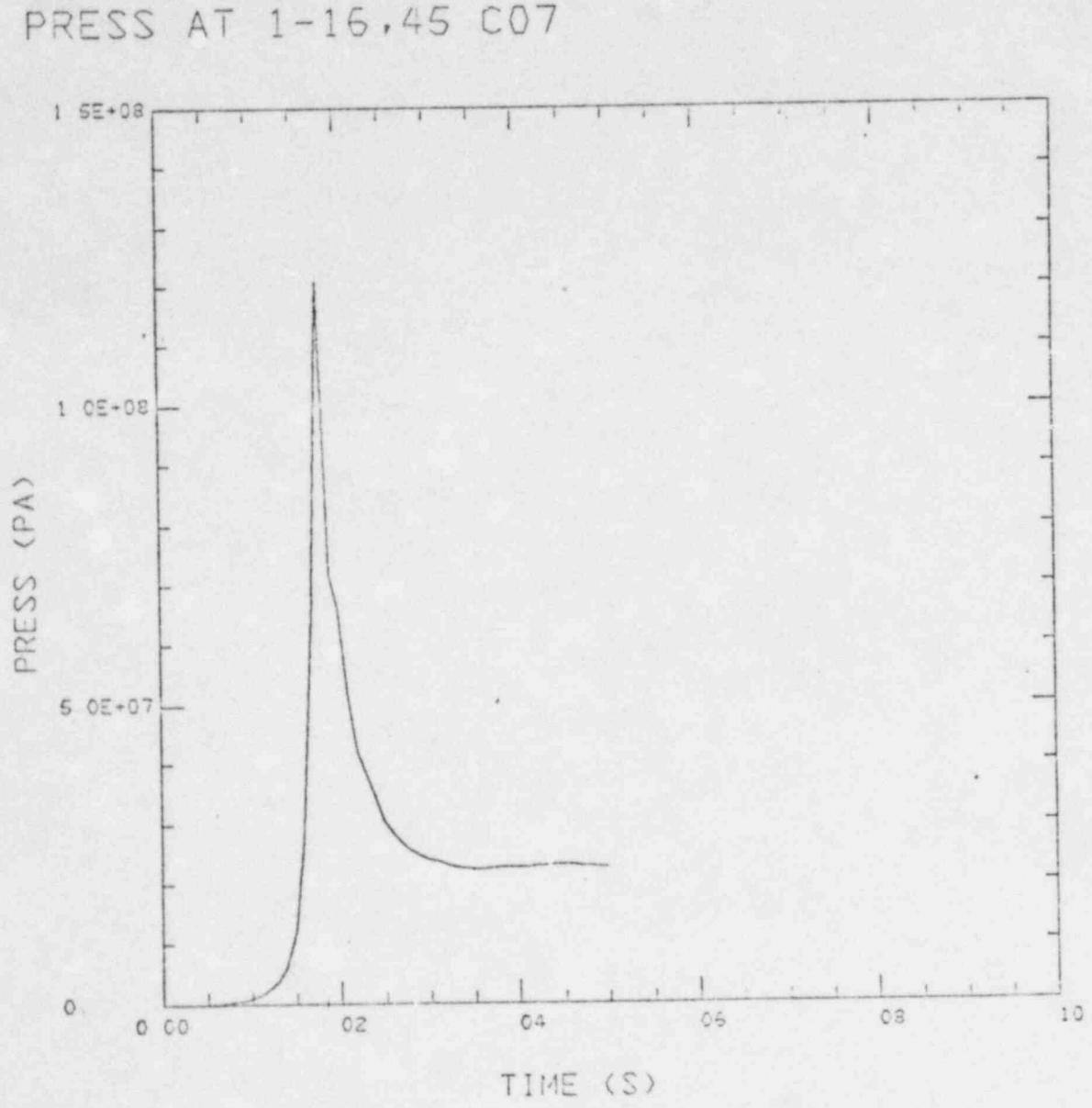
PRESS AT 1-16,45 C07
1 5E+08
1 0E+08
5 0E+07
0
PRESS (PA)
0 00
02
04
06
08
10
TIME (S)

Fig 9

TIME .000 MSEC

TI

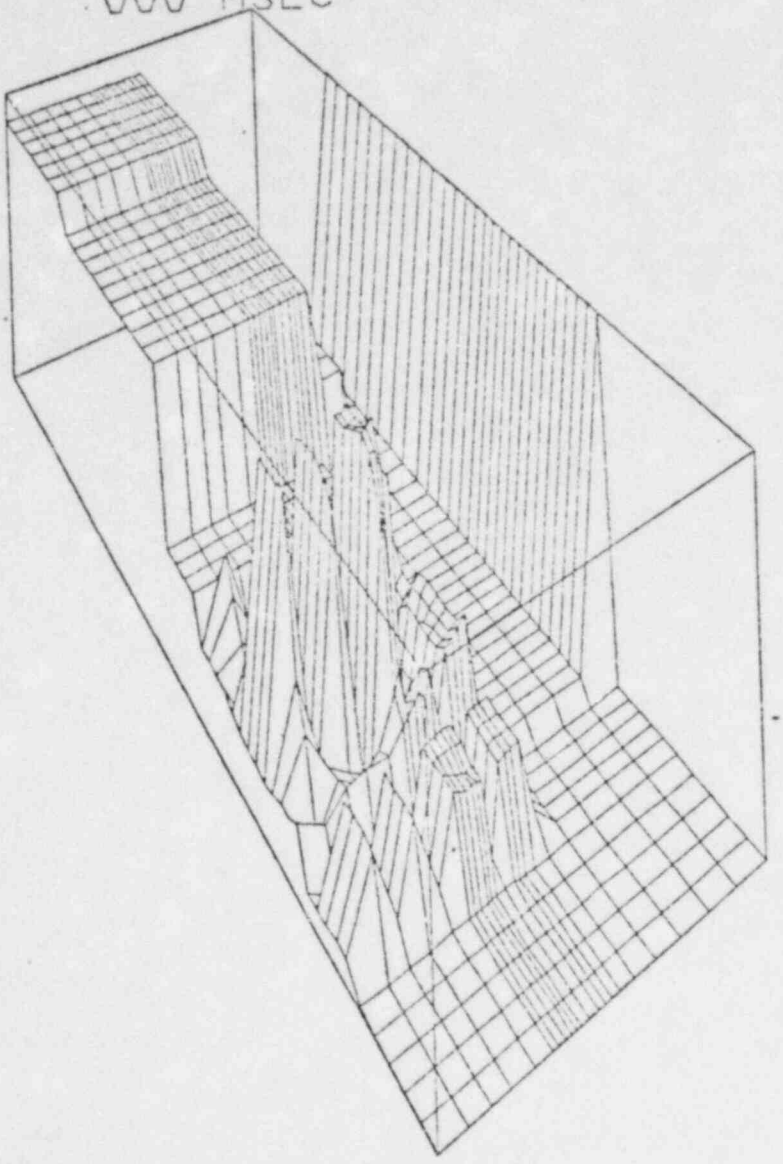

V

VOLUME FRACTION OF VAPOR
MINIMUM = 1.00000E-06 MAXIMUM = 9.98644E-01

Fig 10

TIME 5 000 MSEC

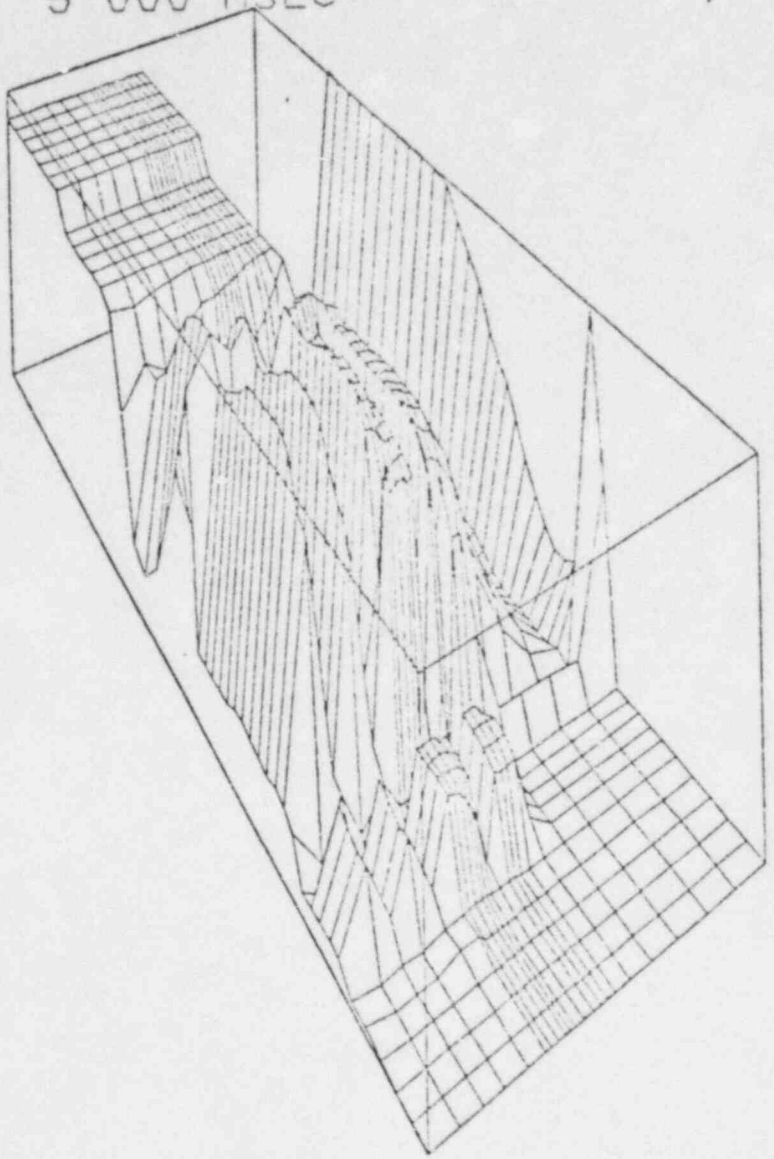

VOLUME FRACTION OF VAPOR
MINIMUM = 1 0000E-06 MAXIMUM = 9 9854E-01

Fig 11

TIME 10 000 MSEC

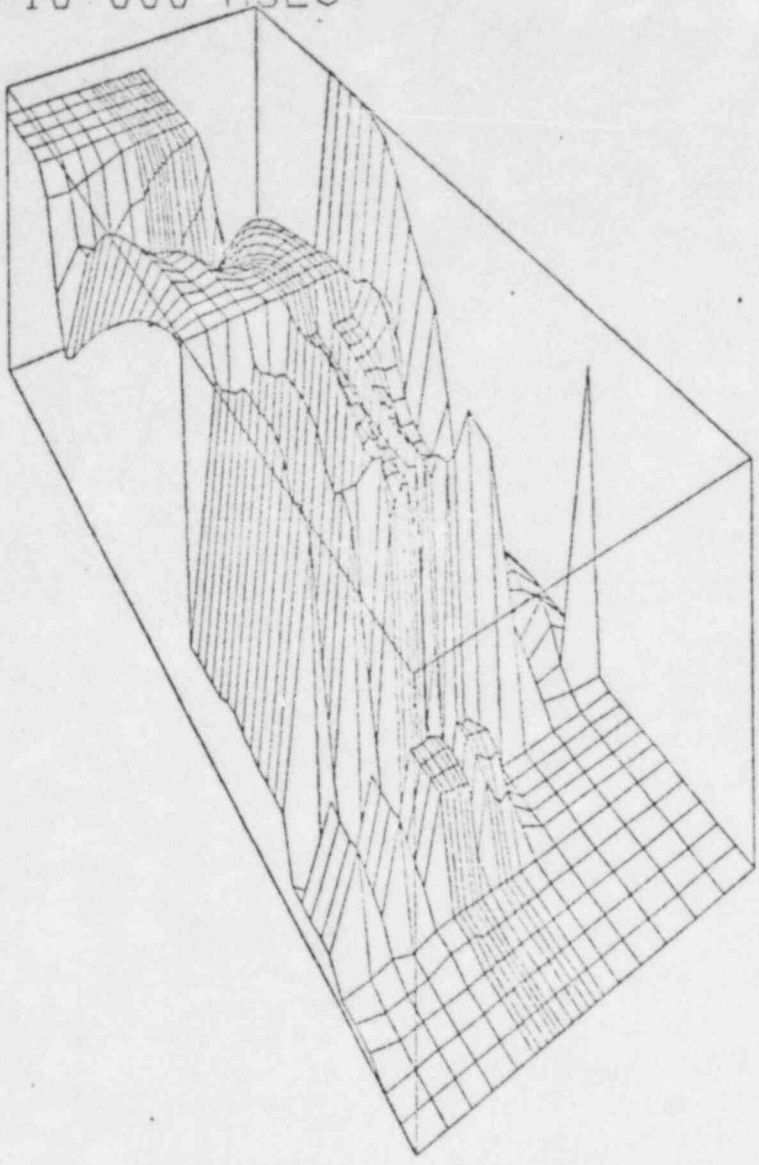

VOLUME FRACTION OF VAPOR
MINIMUM = 1 00000E-05 MAXIMUM = 9 98644E-01

Fig 12

TIME 15.000 MSEC

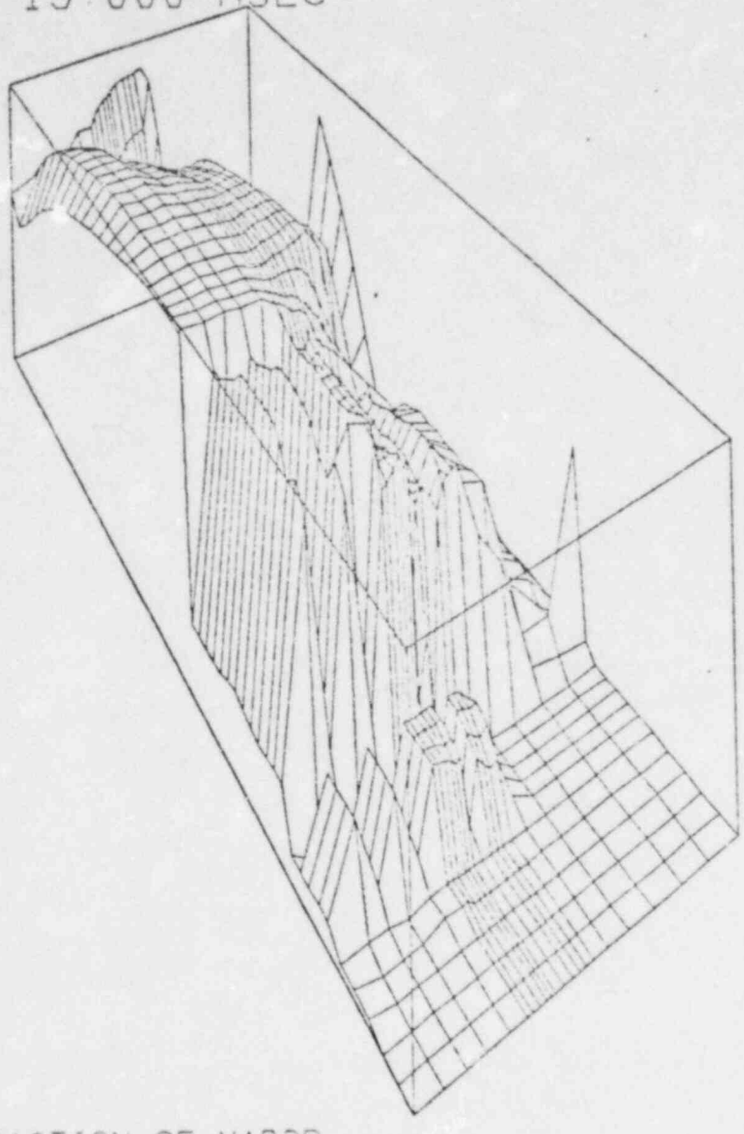

VOLUME FRACTION OF VAPOR
MINIMUM = 1.00000E-05 MAXIMUM = 9.98644E-01

Fig 13

TIME 20 000 MSEC

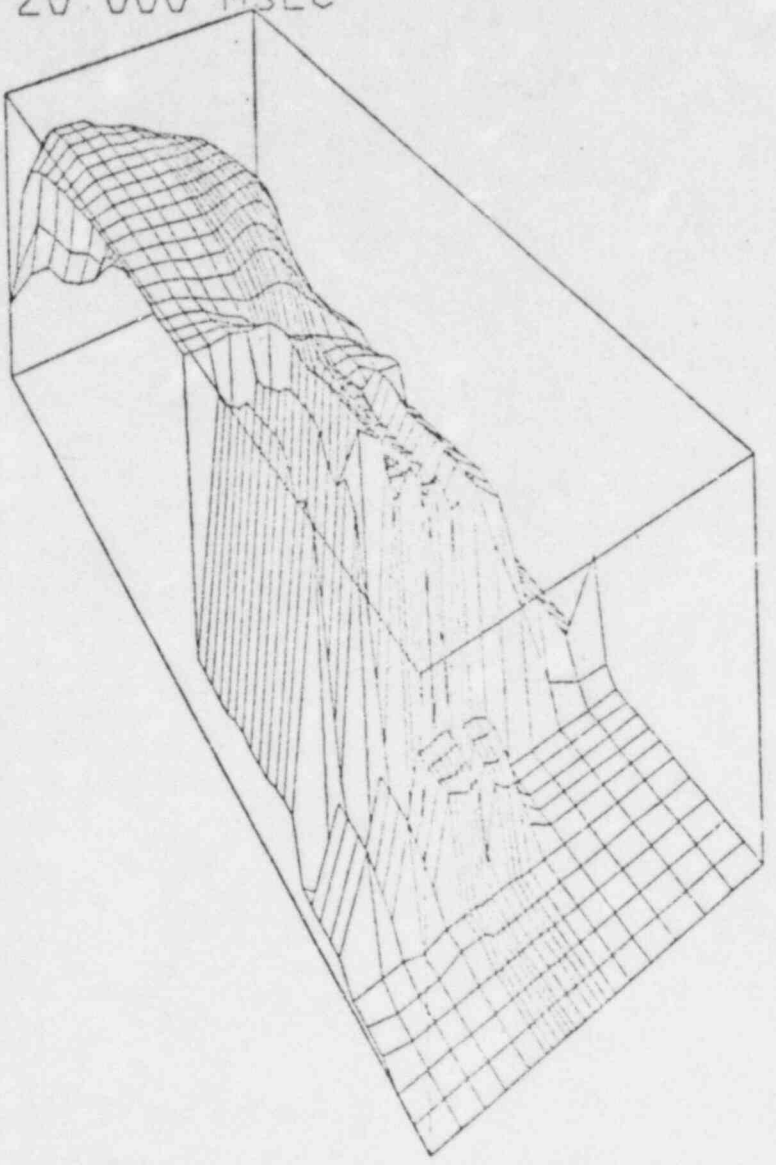

VOLUME FRACTION OF VAPOR
MINIMUM = 1 00000E-05 MAXIMUM = 9 98544E-01

Fig 14

TIME 25.000 MSEC

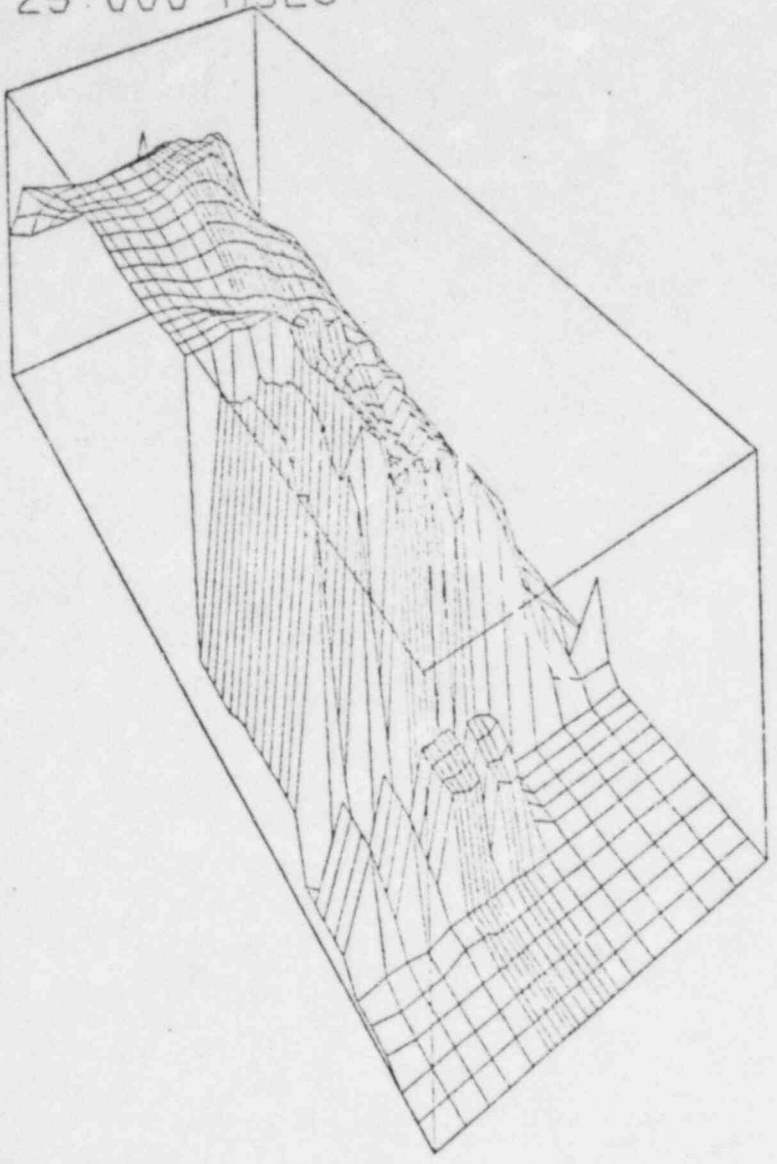

VOLUME FRACTION OF VAPOR
MINIMUM = 1.00000E-05 MAXIMUM = 9.98644E-01

Fig 15

TIME .000 MSEC

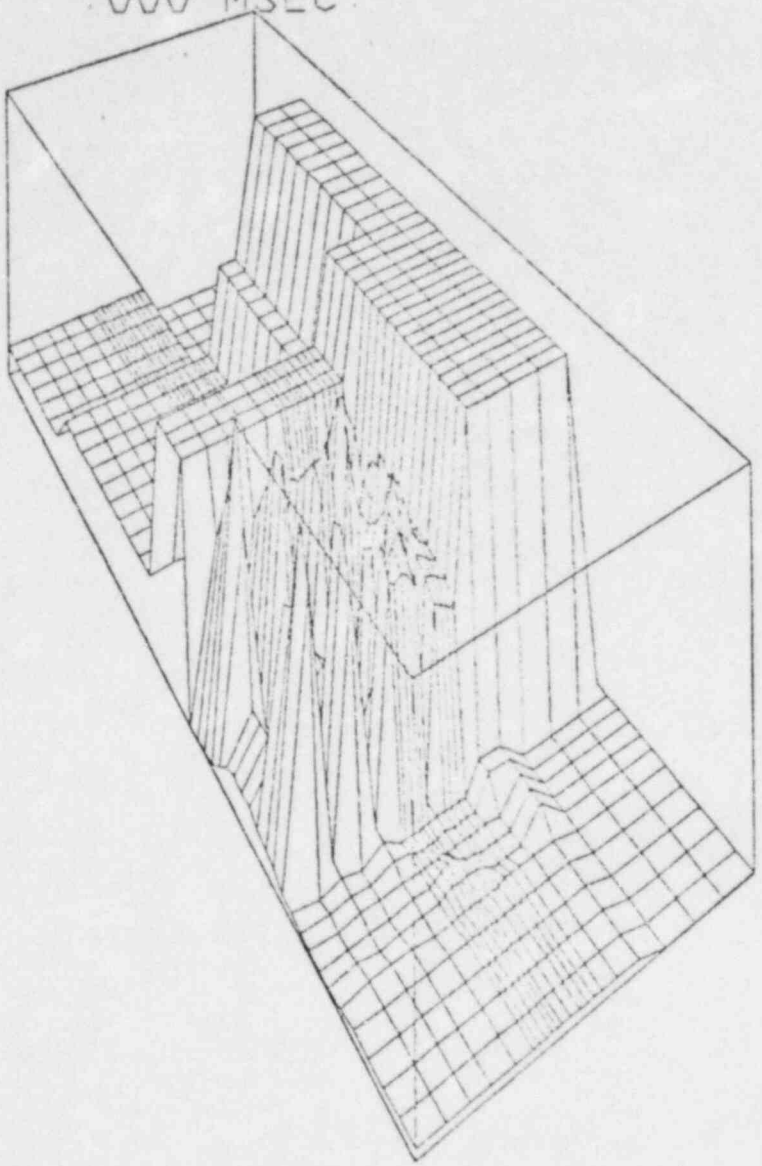

VOLUME FRACTION OF LIQUID
MINIMUM = 1.85195E-05 MAXIMUM = 9.99999E-01

Fig 16

TIME 5 000 MSEC

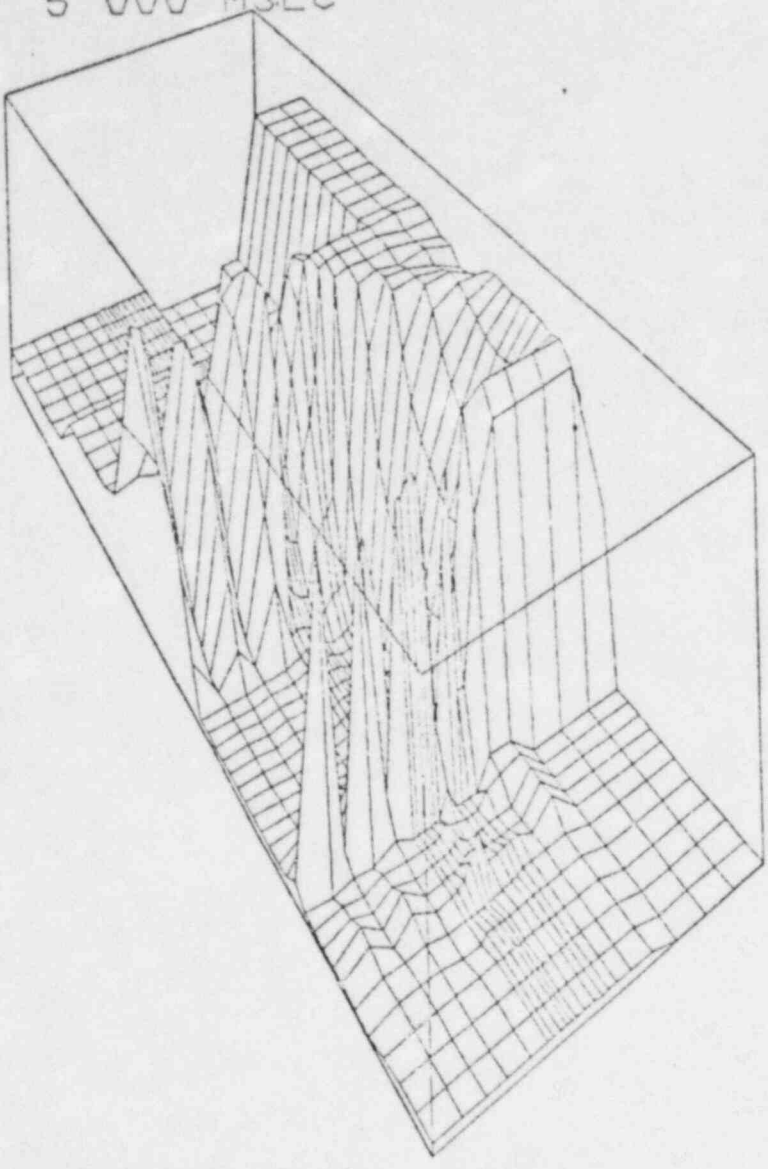

VOLUME FRACTION OF LIQUID
MINIMUM = 1 85195E-05 MAXIMUM = 9 99999E-01

Fig 17

TIME 10.000 MSEC

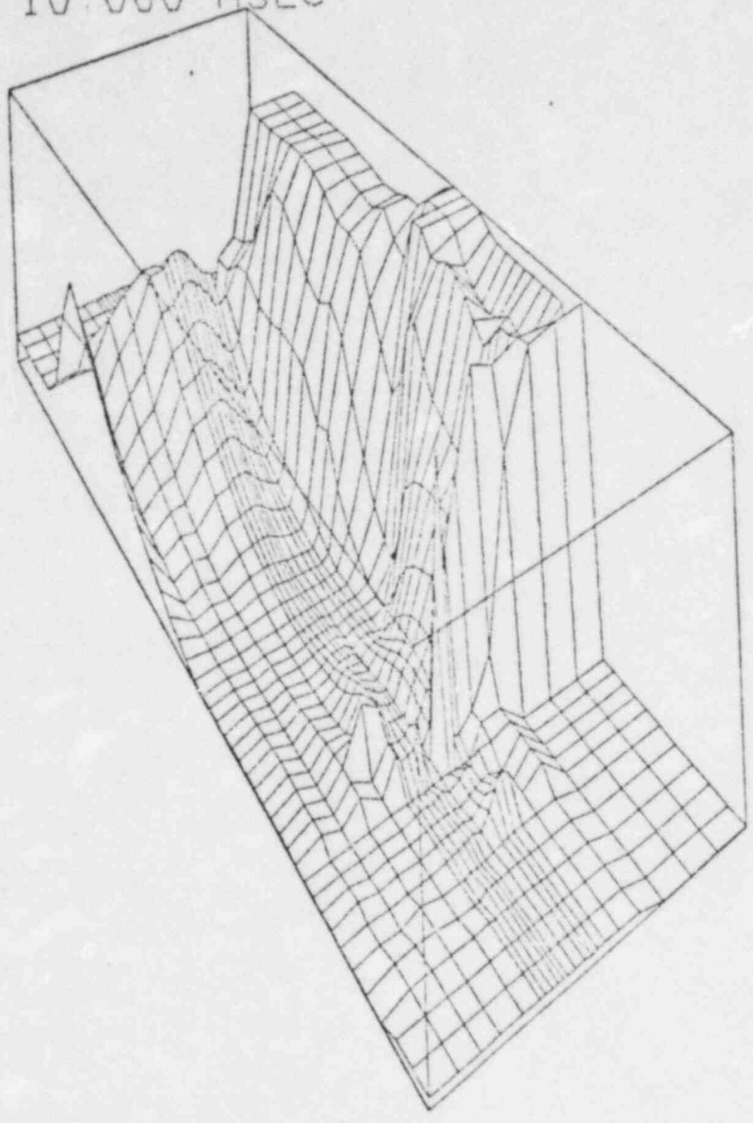

VOLUME FRACTION OF LIQUID
MINIMUM = 1.85195E-05 MAXIMUM = 9.99999E-01

Fig 18

TIME 15 000 MSEC

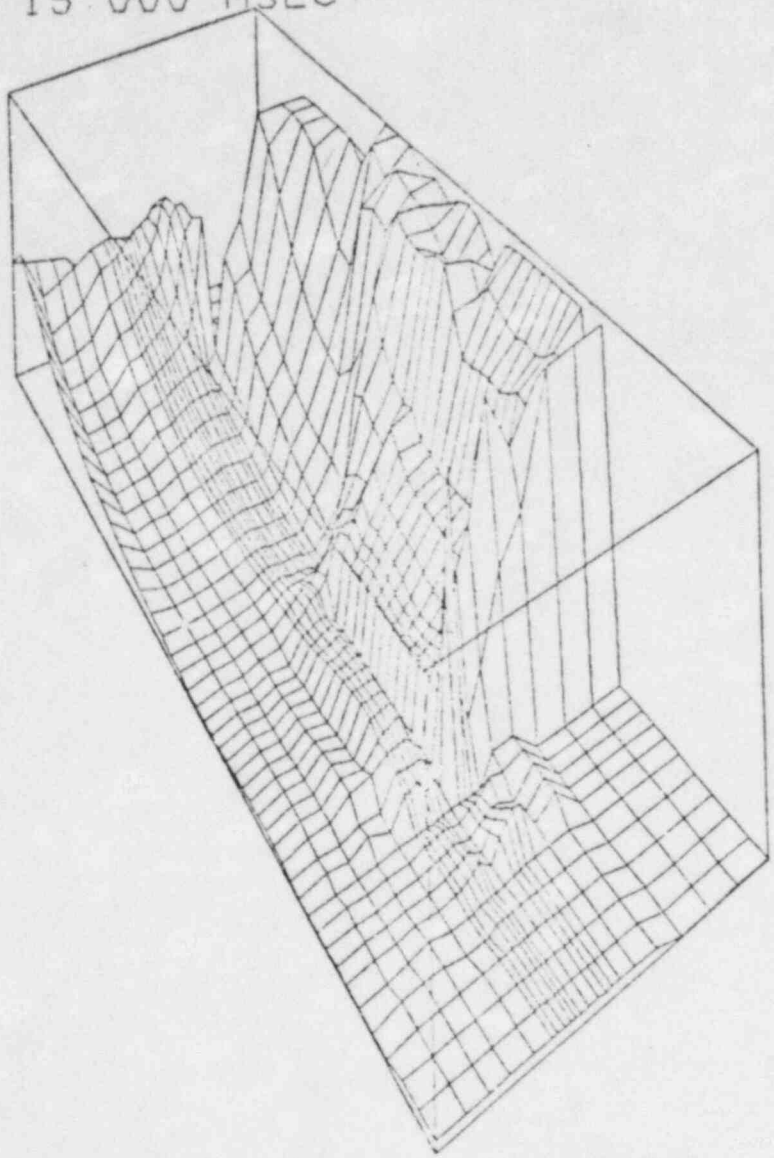

VOLUME FRACTION OF LIQUID
MINIMUM = 1 85195E-05 MAXIMUM = 9 99995E-01

Fig 19

TIME 20 000 MSEC

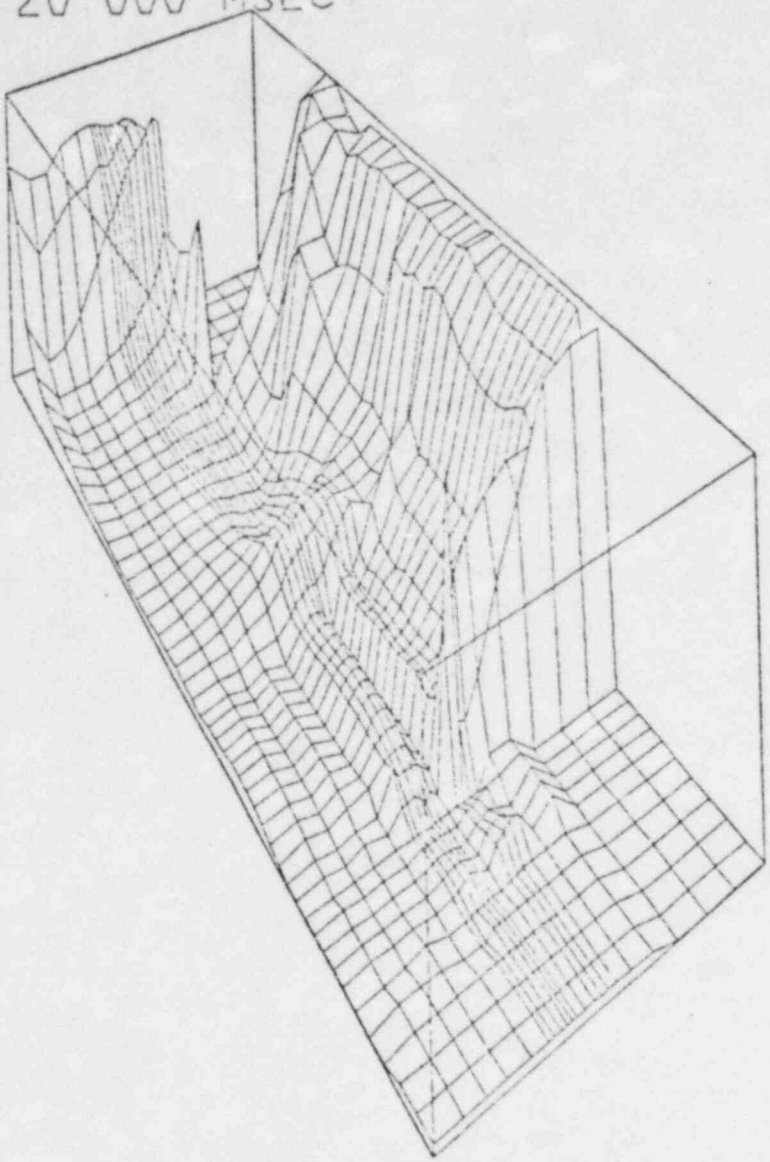

VOLUME FRACTION OF LIQUID
MINIMUM = 1 85195E-05 MAXIMUM = 9 99999E-01

Fig 20

TIME 25 000 MSEC

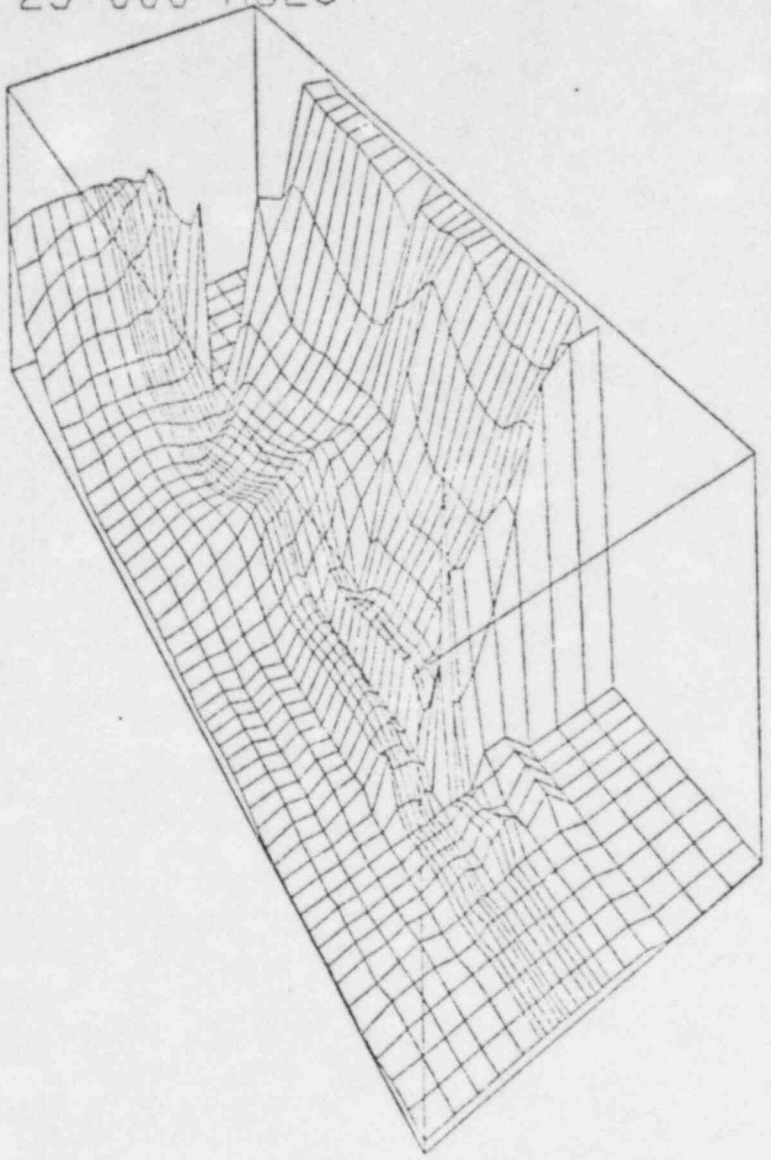

VOLUME FRACTION OF LIQUID
MINIMUM = 1 85195E-05 MAXIMUM = 9 99999E-01

Fig 21

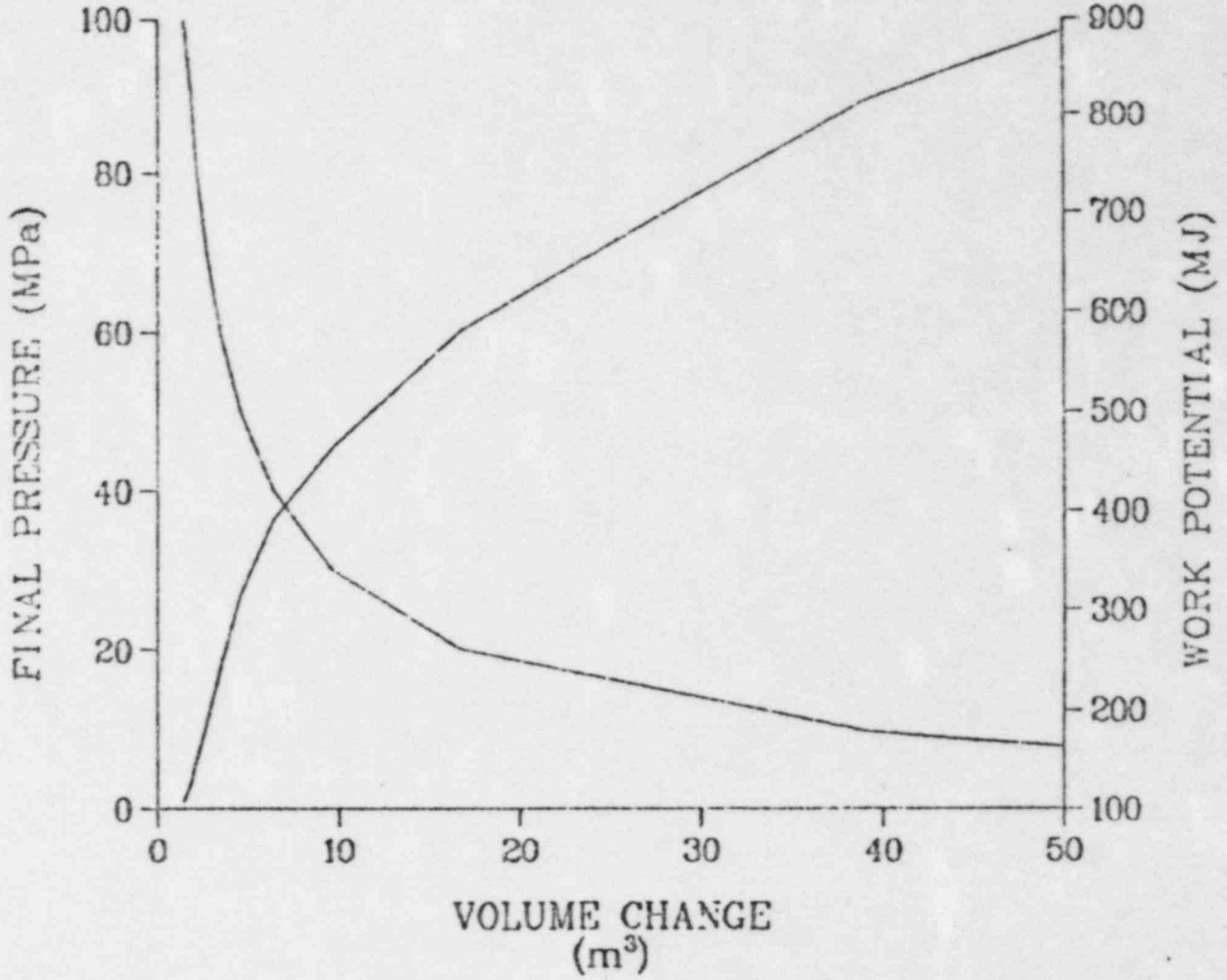
FINAL PRESSURE (MPa)
100
80
60
40
20
0
WORK POTENTIAL (MJ)
900
800
700
600
500
400
300
200
100
0
10
20
30
40
50
VOLUME CHANGE
(m³)

Fig 22

AII.2

AVG LIQ FUEL TEMP C08 100 $/s

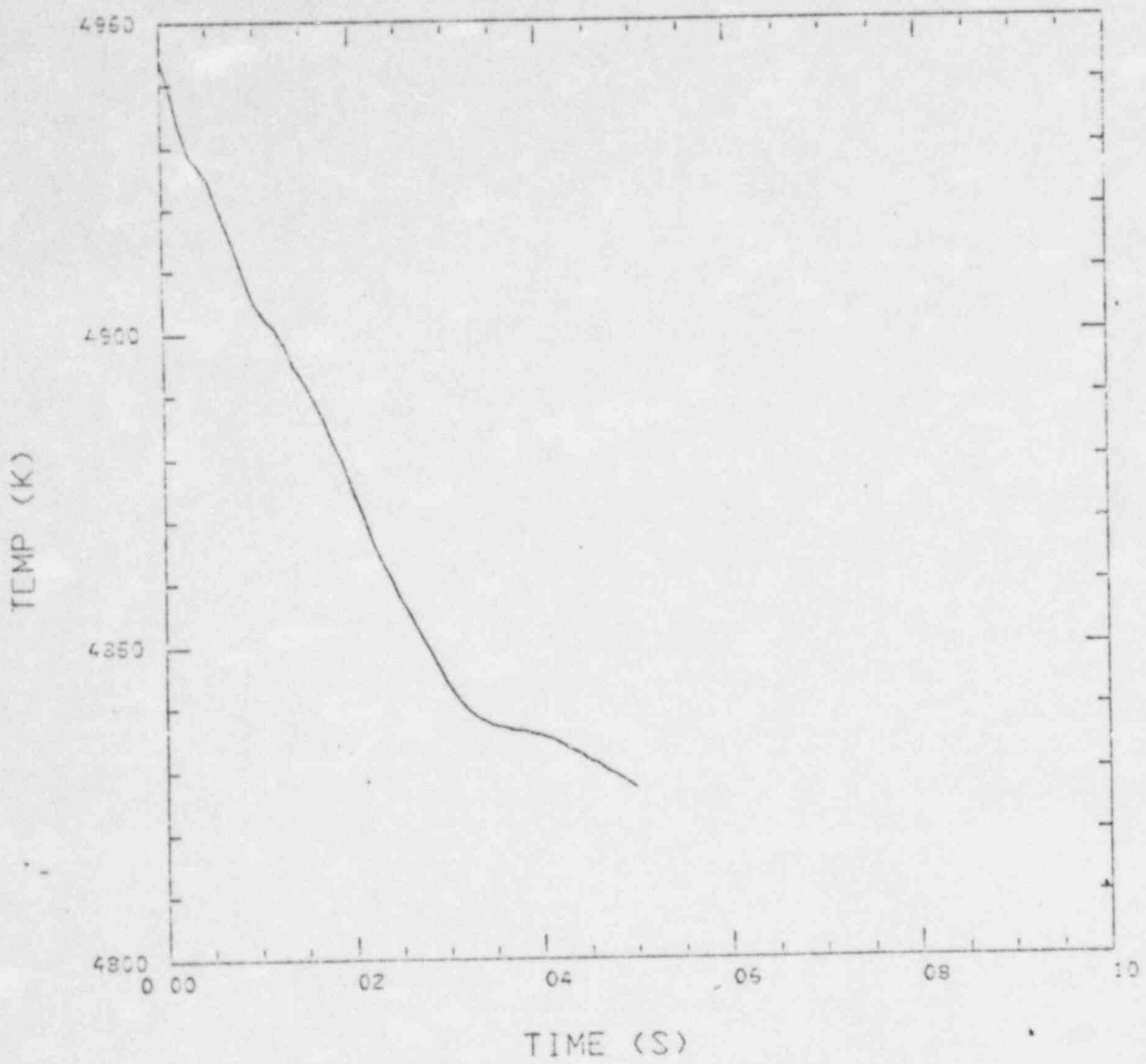

Fig 23

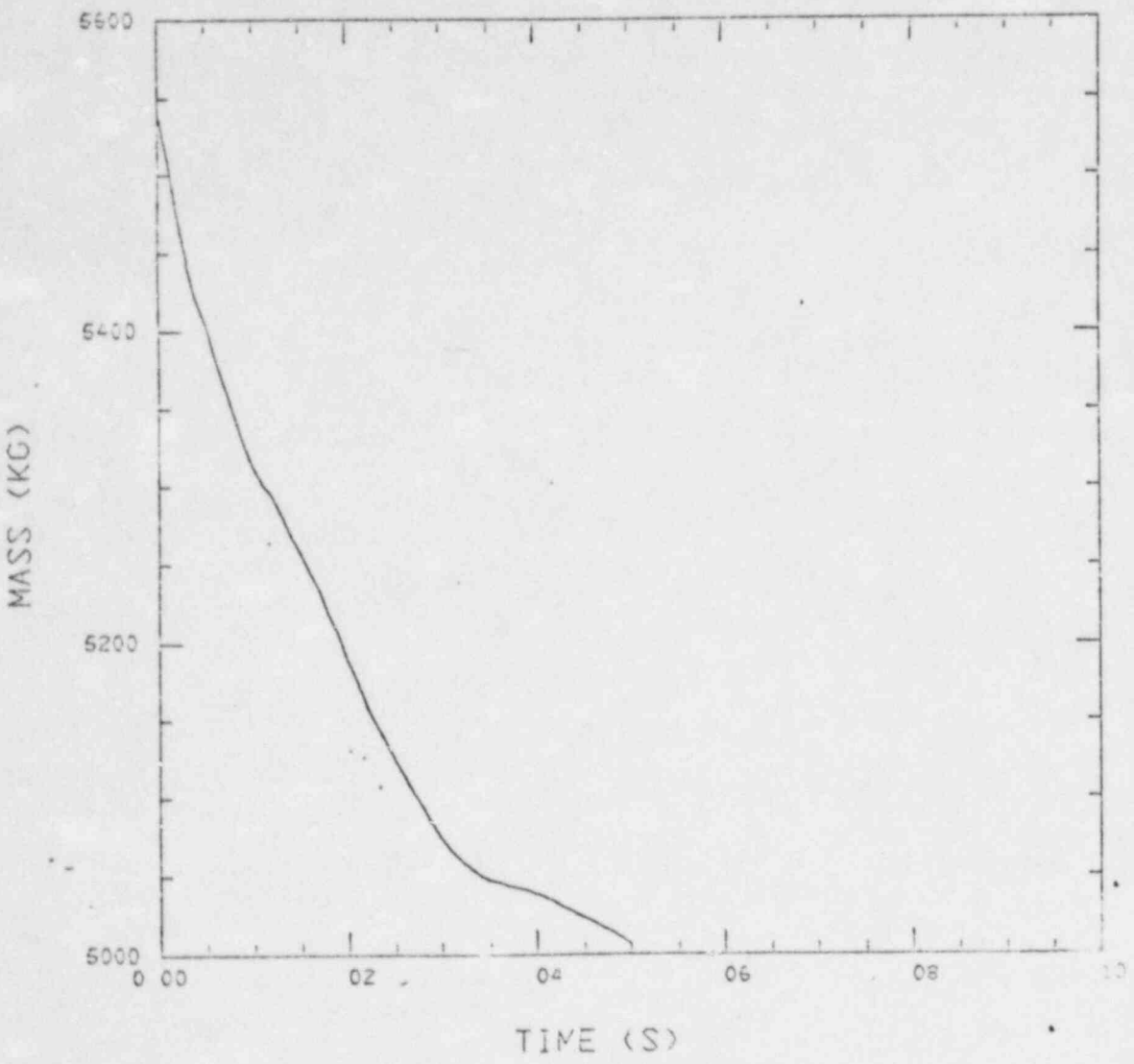
MASS OF LIQ FUEL C08
5600
5400
5200
5000
MASS (KG)
0 00
02
04
06
08
10
TIME (S)

Fig 24

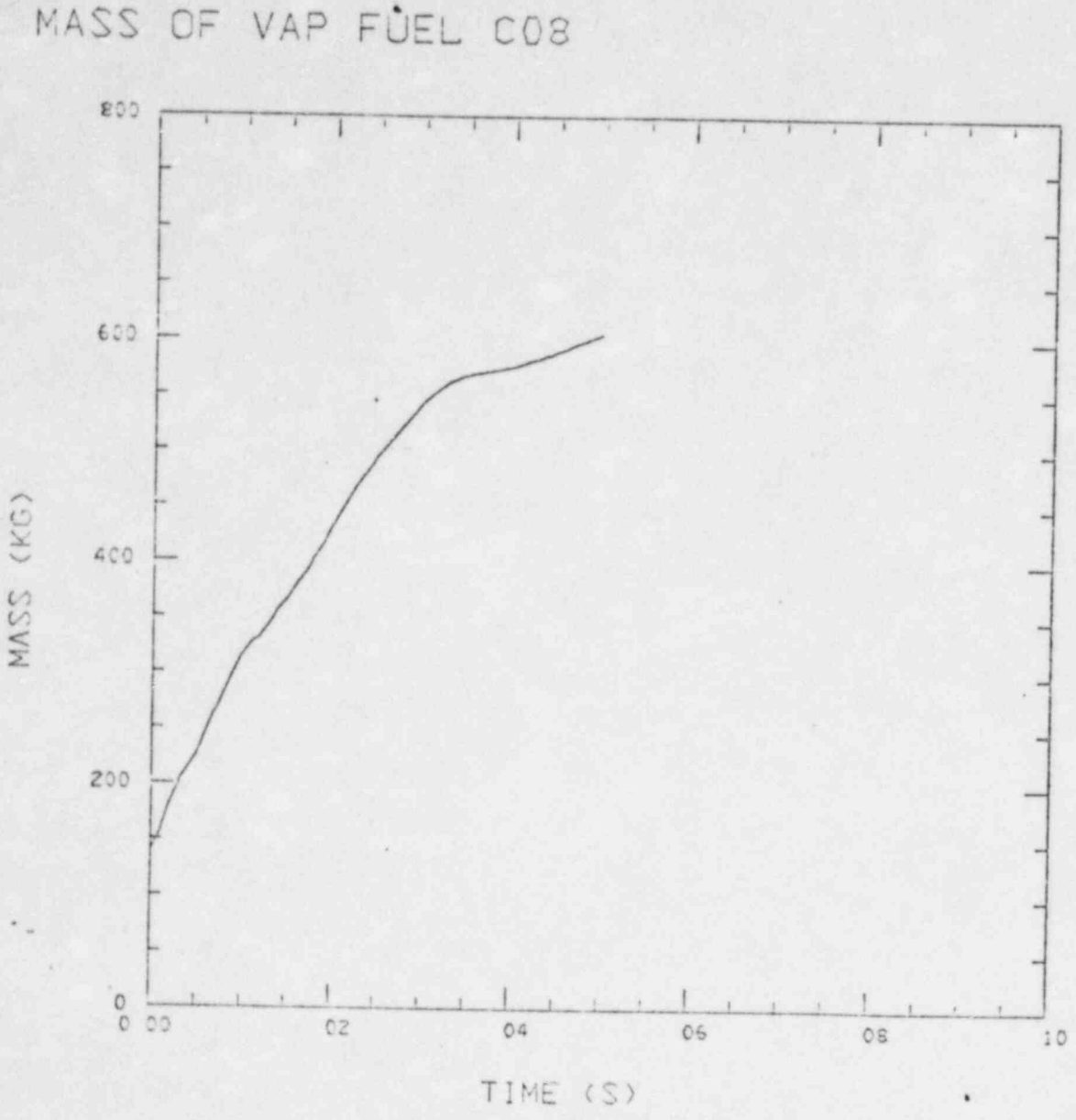
MASS OF VAP FUEL C08
800
600
400
200
0
0 00
02
04
06
08
10
MASS (KG)
TIME (S)

Fig 25

CORE BARREL VOLUME

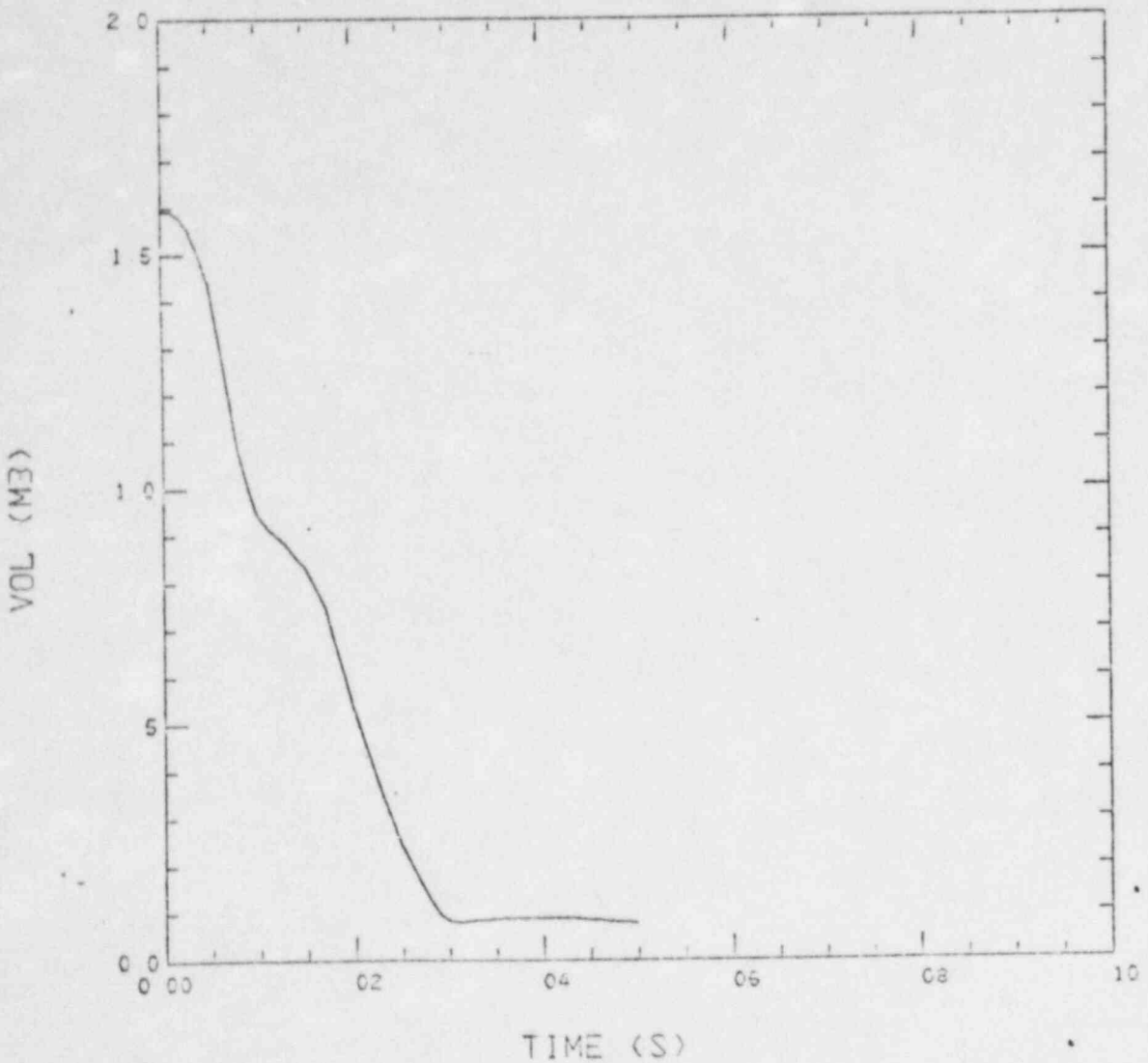

Fig 26

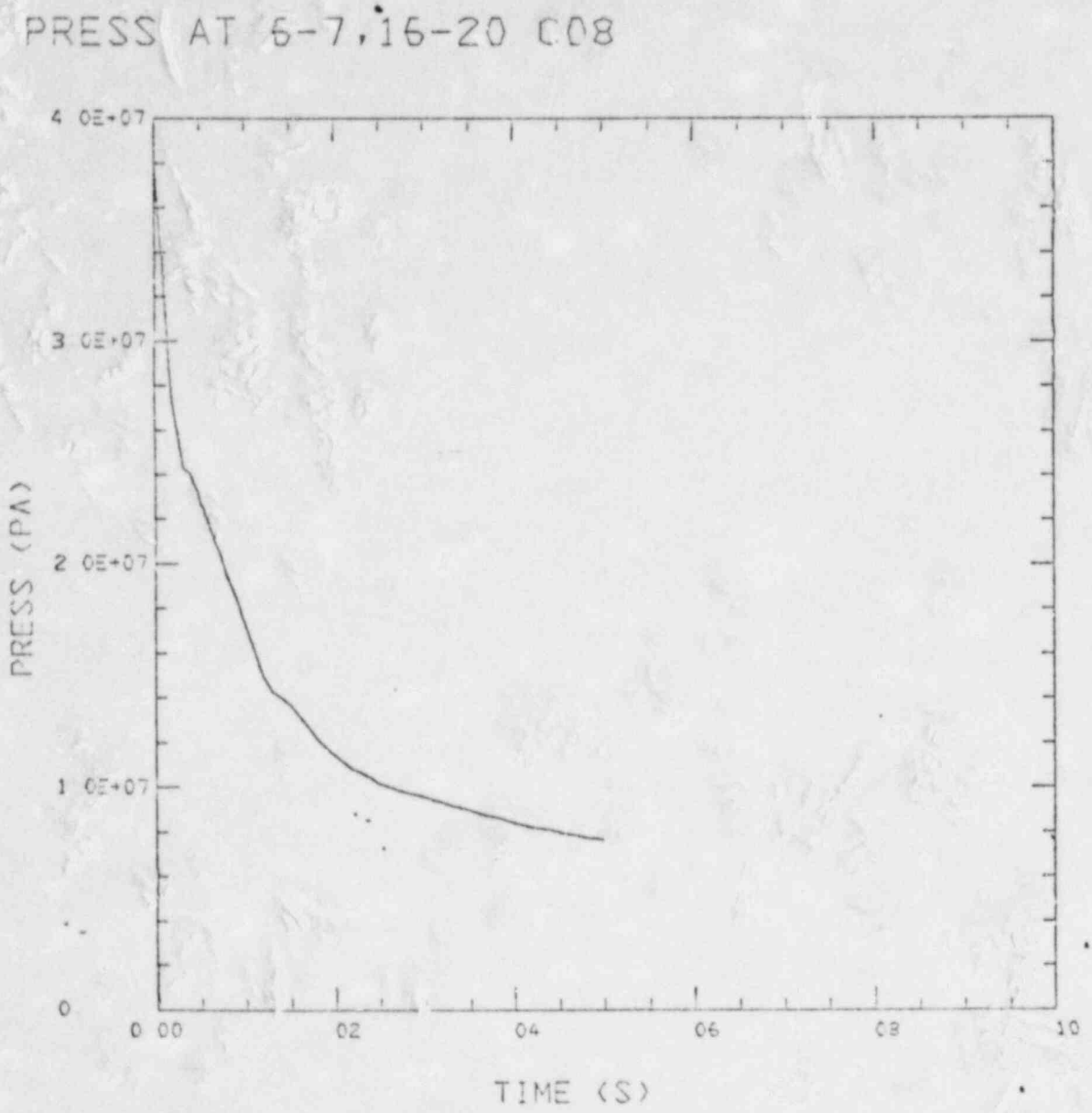
PRESS AT 6-7,16-20 C08
4 0E+07
3 0E+07
2 0E+07
1 0E+07
0
PRESS (PA)
0 00
02
04
06
08
10
TIME (S)

Fig 27

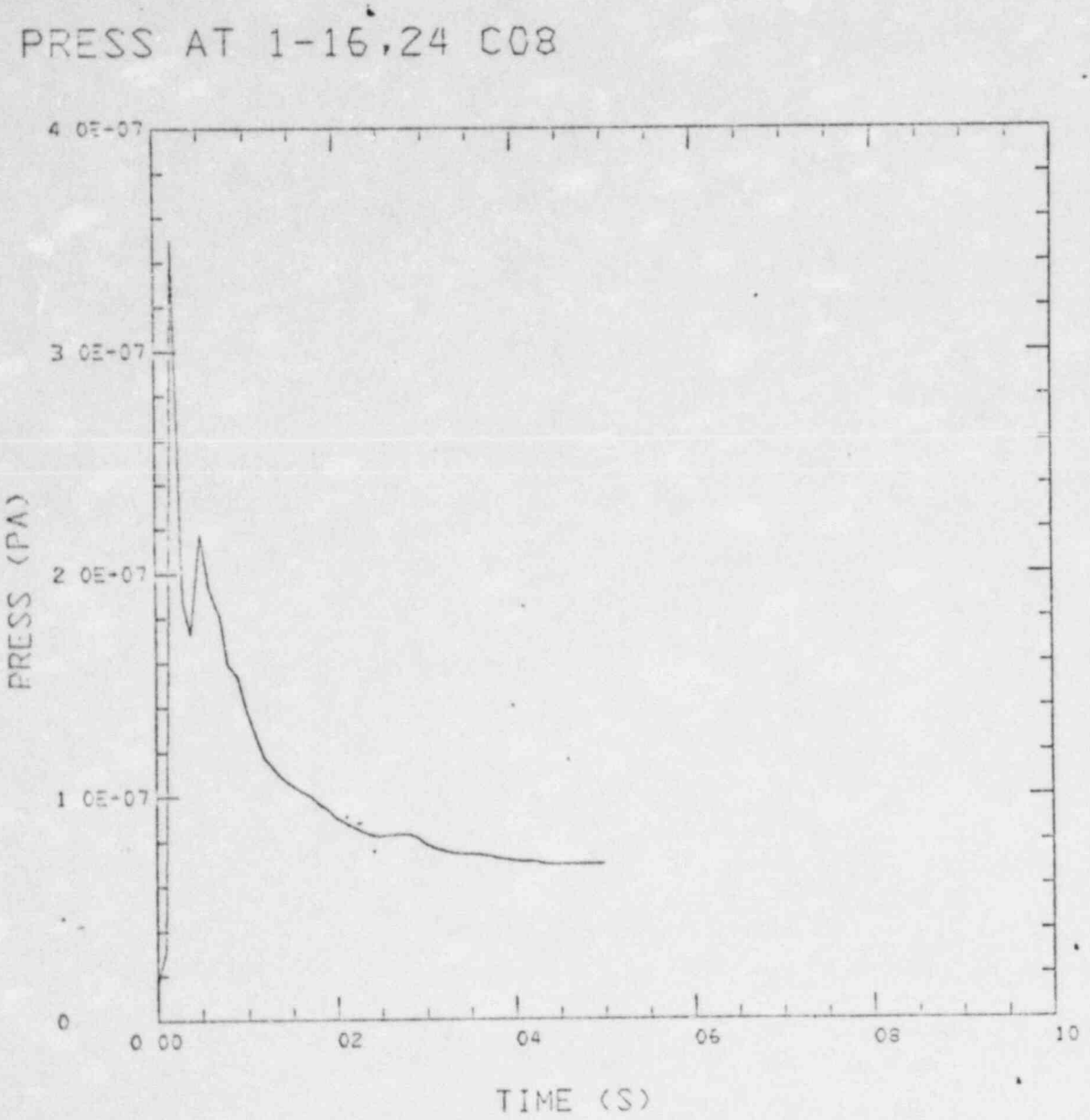
PRESS AT 1-16,24 C08
4 0E-07
3 0E-07
2 0E-07
1 0E-07
0
PRESS (PA)
0 00
02
04
06
08
10
TIME (S)

Fig 28

PRESS AT 16,12-24 C08

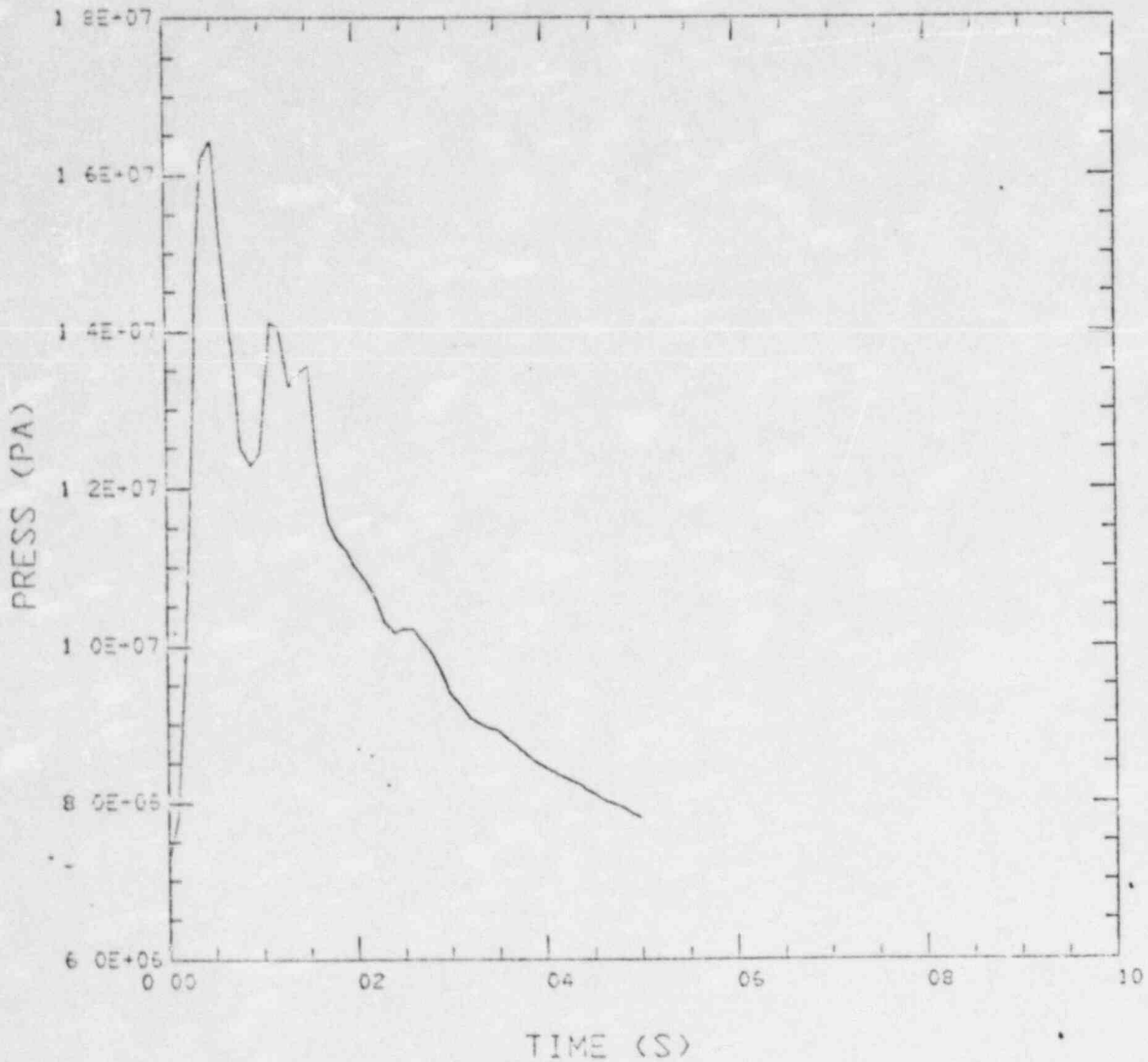

Fig 29

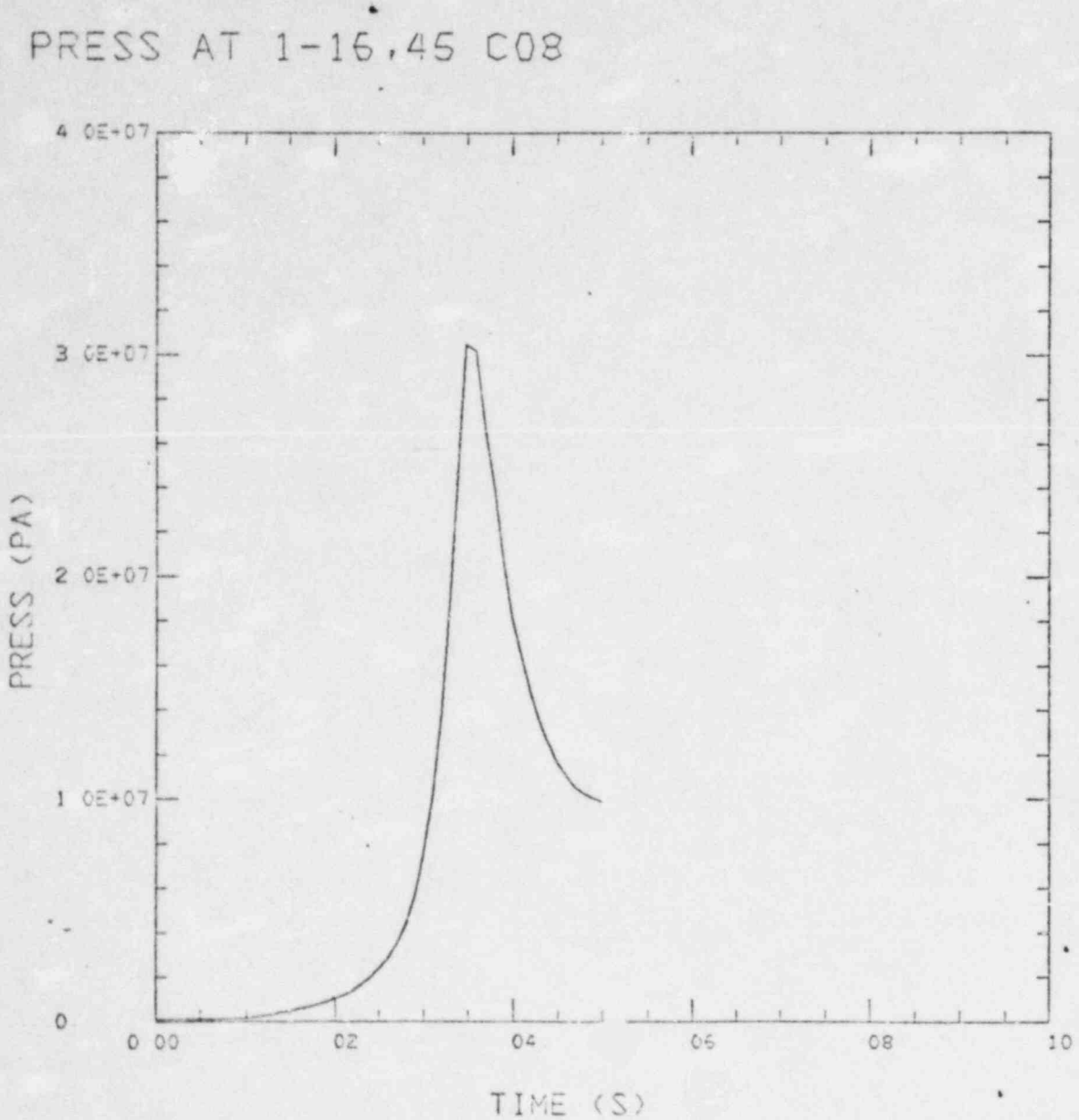
PRESS AT 1-16,45 C08
4 0E+07
3 0E+07
2 0E+07
1 0E+07
0
PRESS (PA)
0 00
02
04
06
08
10
TIME (S)

Fig 30

TIME .000 MSEC

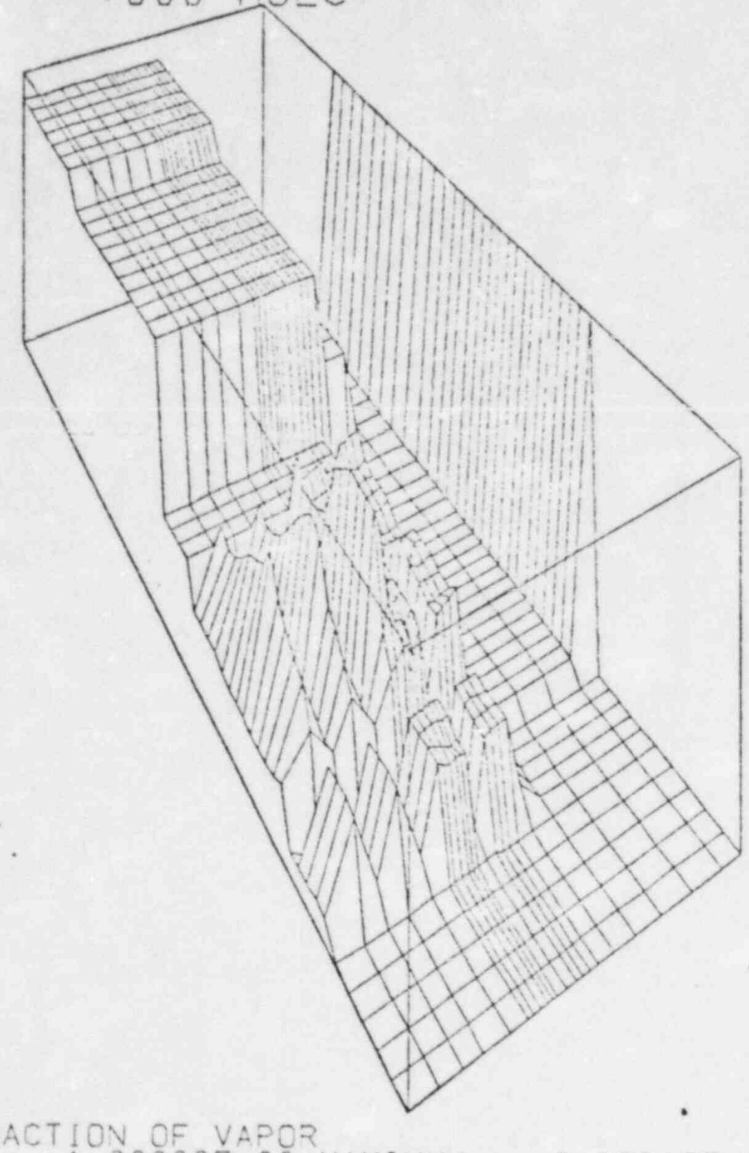

VOLUME FRACTION OF VAPOR
MINIMUM = 1 00000E-06 MAXIMUM = 9 99019E-01

Fig 31

TIME 5 000 MSEC

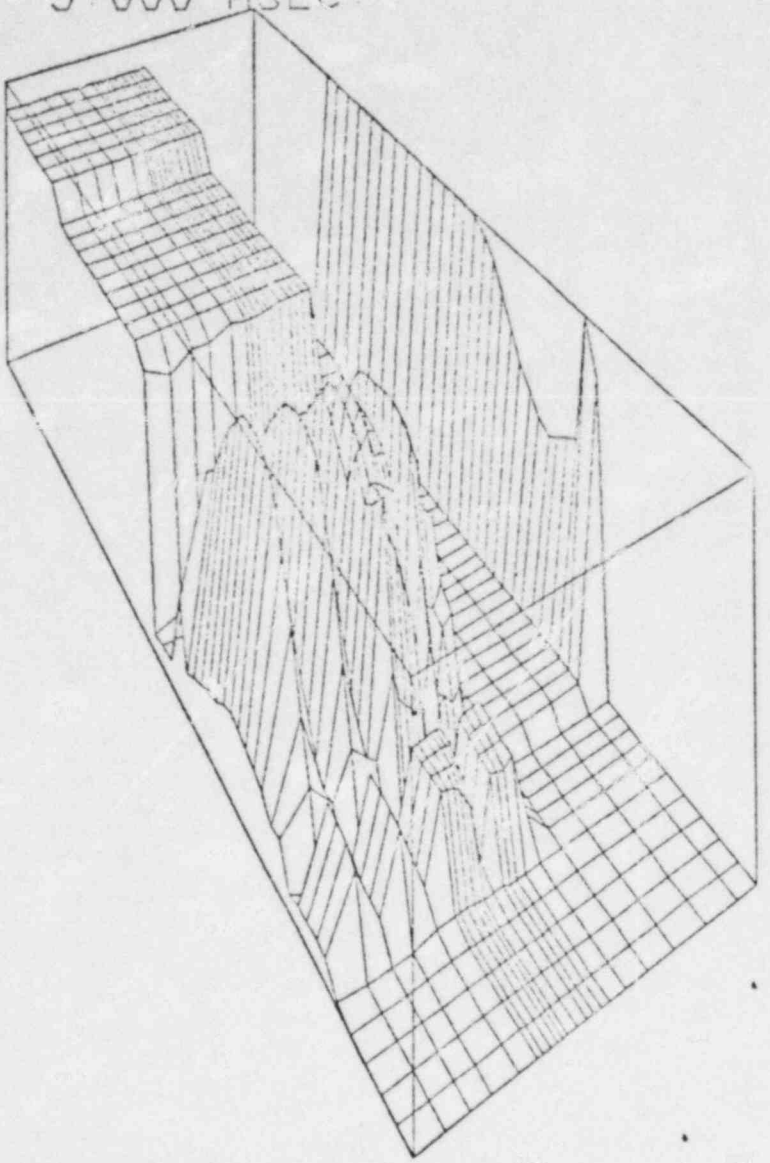

VOLUME FRACTION OF VAPOR
MINIMUM = 1 00000E-05 MAXIMUM = 9 99019E-01

Fig 32

TIME 10 000 MSEC

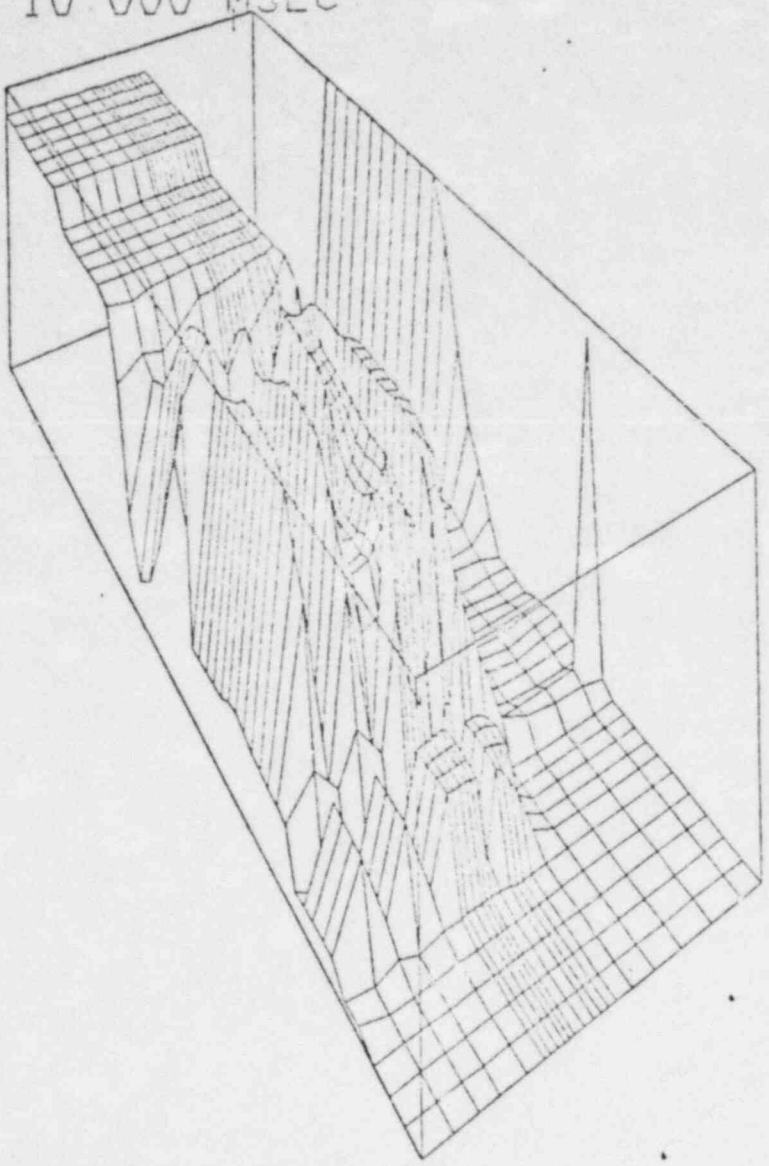

VOLUME FRACTION OF VAPOR
MINIMUM = 1 00000E-05 MAXIMUM = 9 99019E-01

Fig 33

TIME = 15.000 MSEC

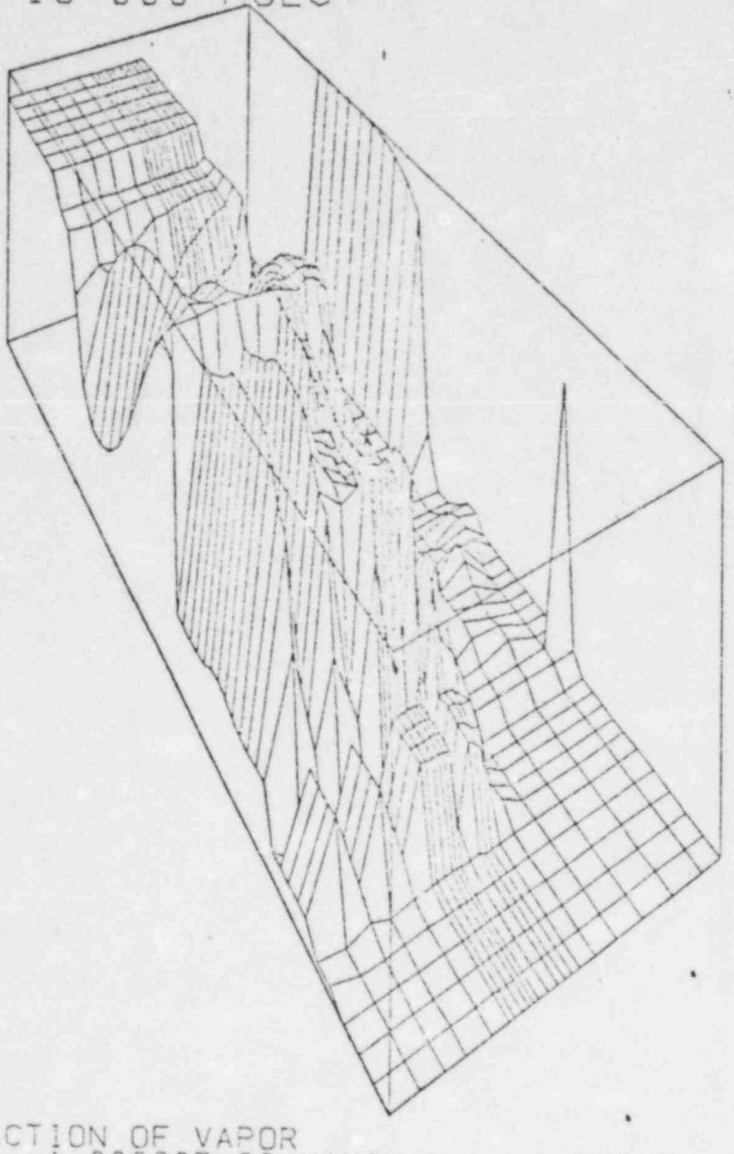

VOLUME FRACTION OF VAPOR
MINIMUM = 1.00000E-05 MAXIMUM = 9.99019E-01

Fig 34

TIME = 20.000 MSEC

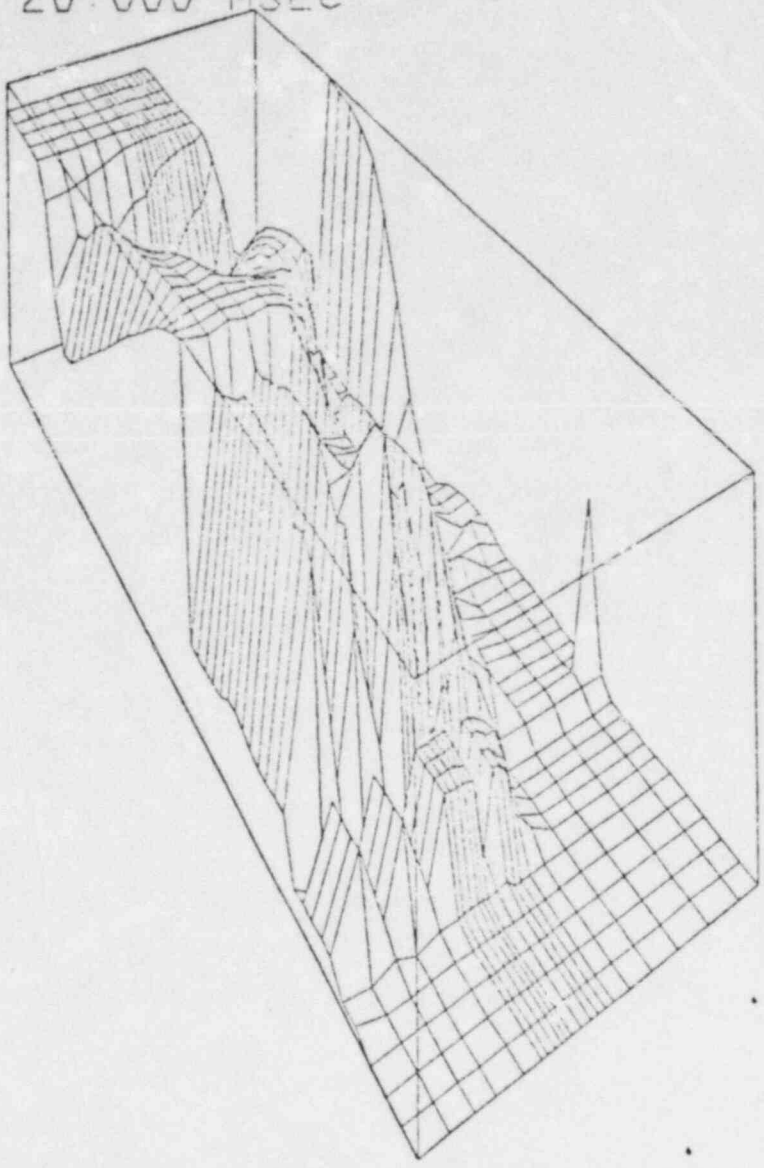

VOLUME FRACTION OF VAPOR
MINIMUM = 1.00000E-05 MAXIMUM = 9.99019E-01

Fig 35

TIME 25 000 MSEC

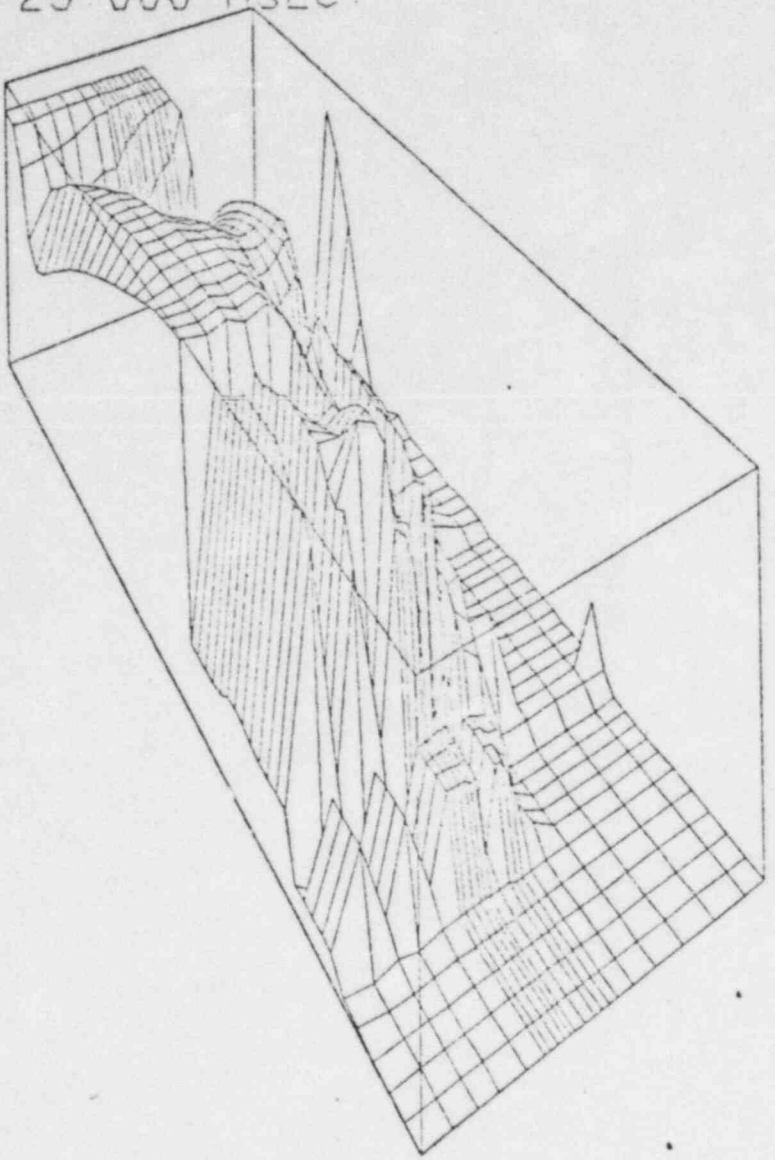

VOLUME FRACTION OF VAPOR
MINIMUM = 1 00000E-06 MAXIMUM = 9 99019E-01

Fig 36

TIME 30 000 MSEC

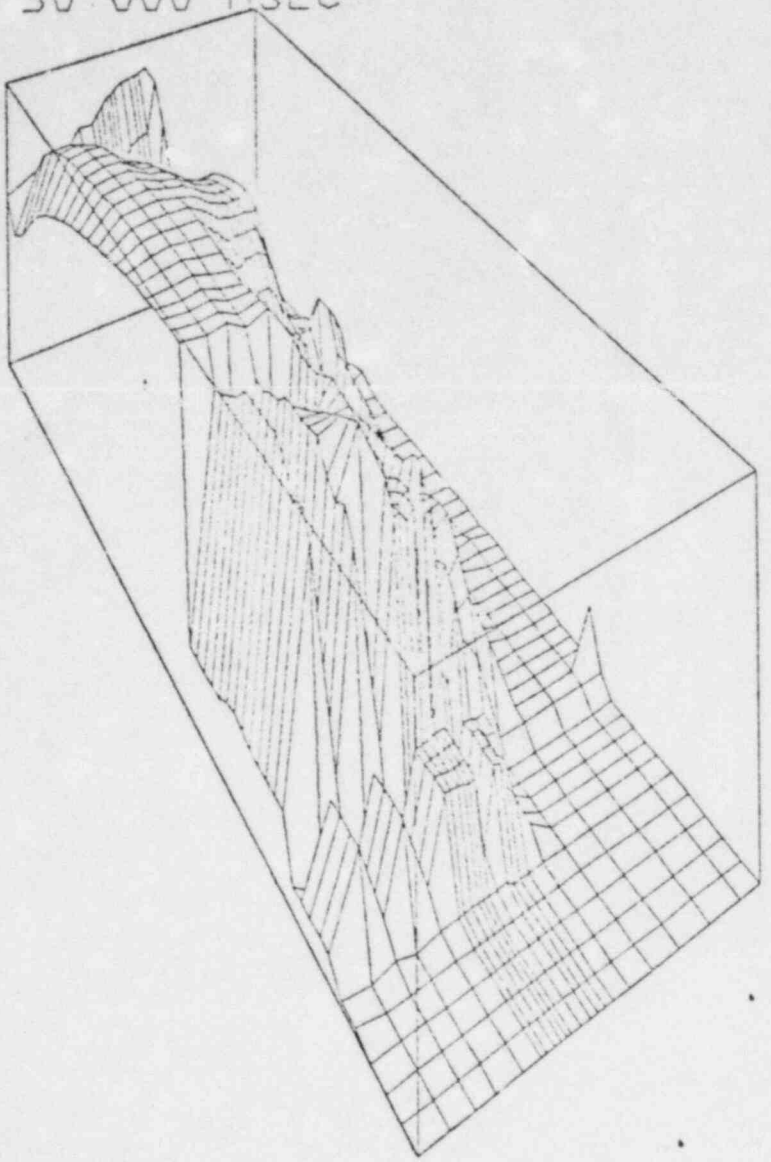

VOLUME FRACTION OF VAPOR
MINIMUM = 1 00000E-05 MAXIMUM = 9 99019E-01

Fig 37

TIME 35 000 MSEC

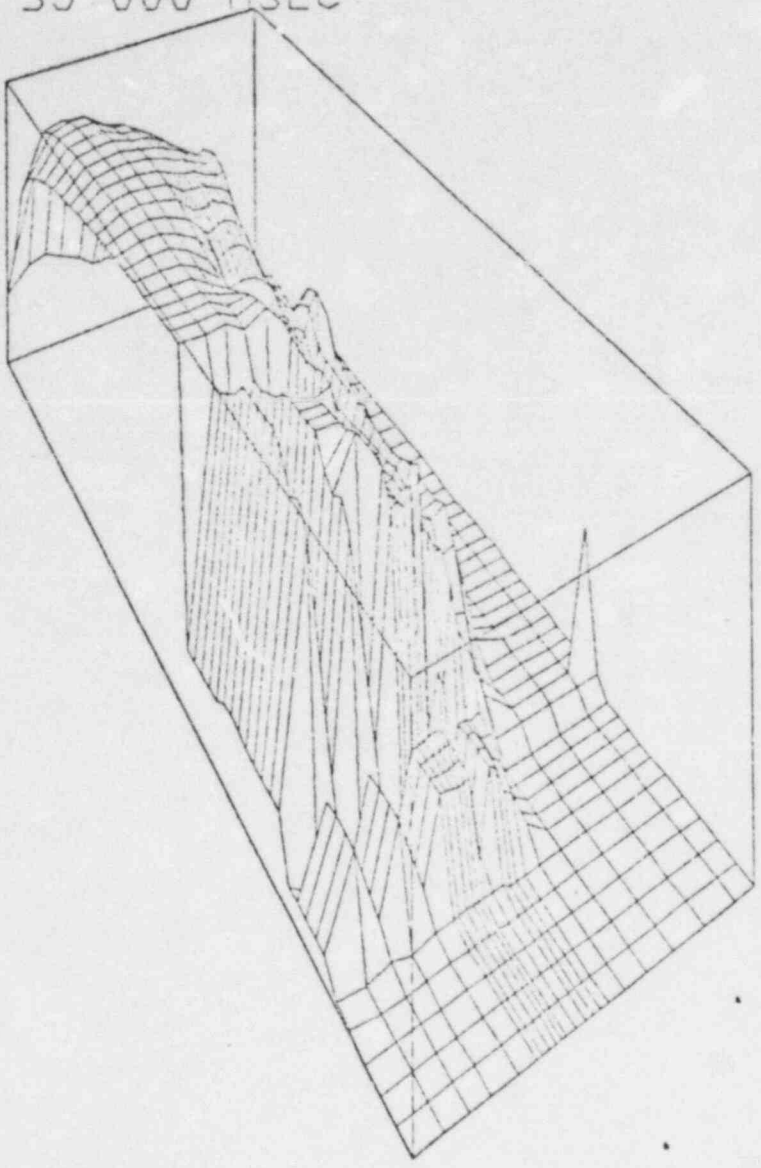

VOLUME FRACTION OF VAPOR
MINIMUM = 1 00000E-05 MAXIMUM = 9 99019E-01

Fig 38

TIME 40.000 MSEC

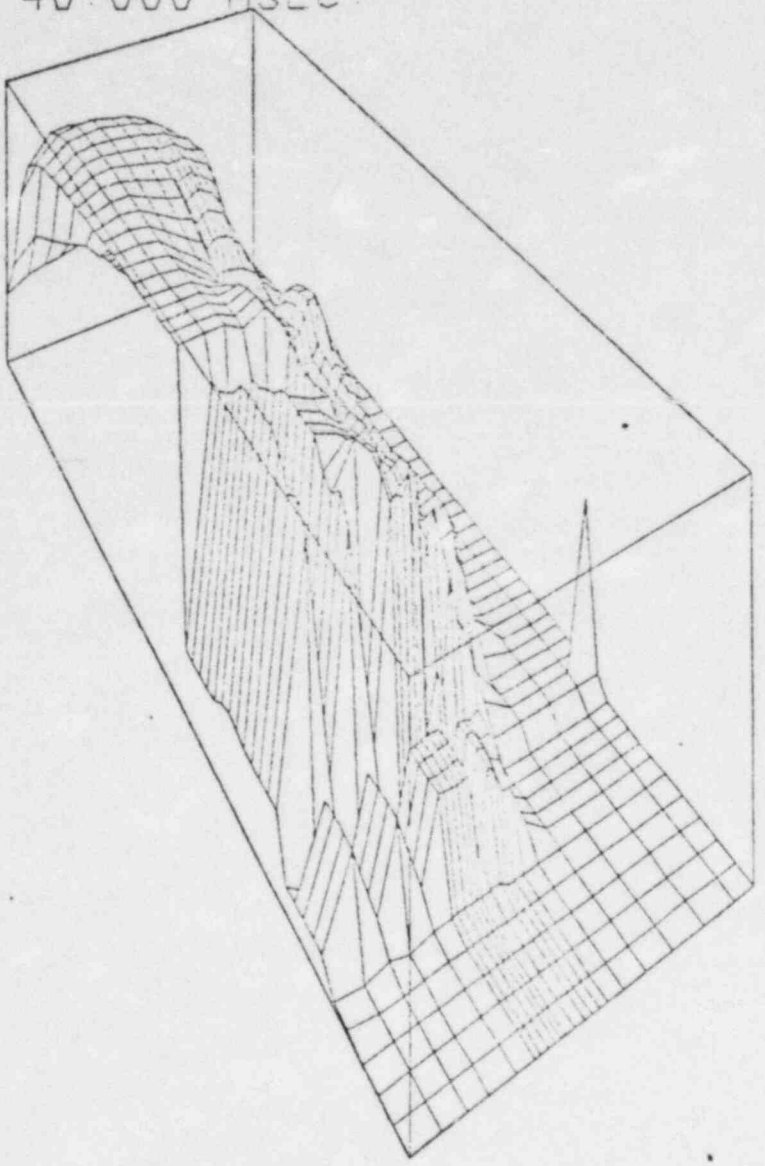

VOLUME FRACTION OF VAPOR
MINIMUM = 1.00000E-06 MAXIMUM = 9.99019E-01

Fig 39

TIME .45 000 MSEC

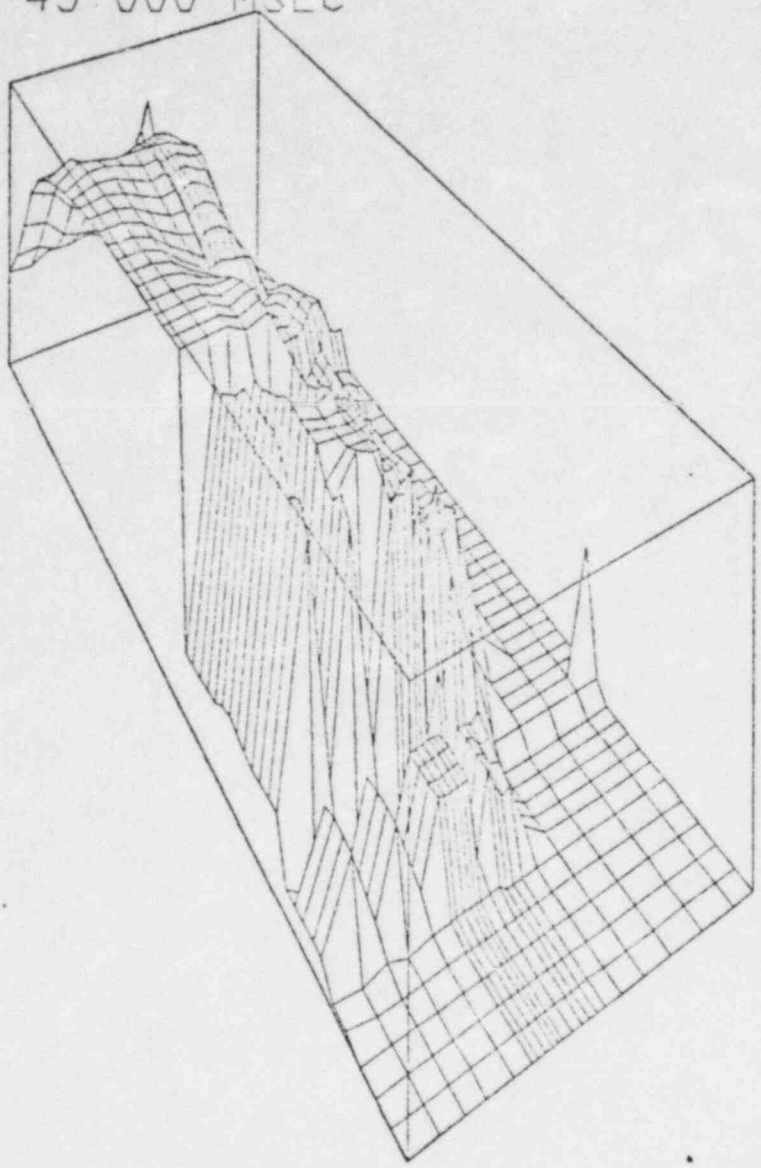

VOLUME FRACTION OF VAPOR
MINIMUM = 1 00000E-06 MAXIMUM = 9 99019E-01

Fig 40

TIME .000 MSEC

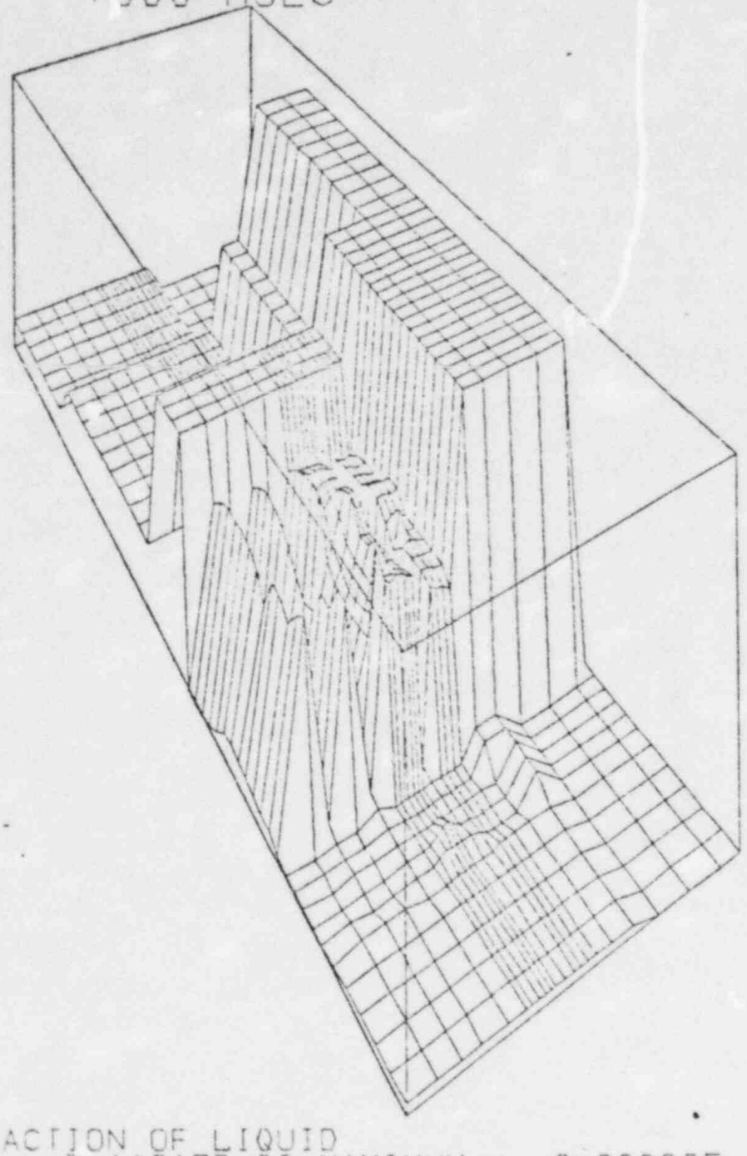

VOLUME FRACTION OF LIQUID
MINIMUM = 7.14217E-05 MAXIMUM = 9.99999E-01

Fig 41

TIME 5 000 MSEC

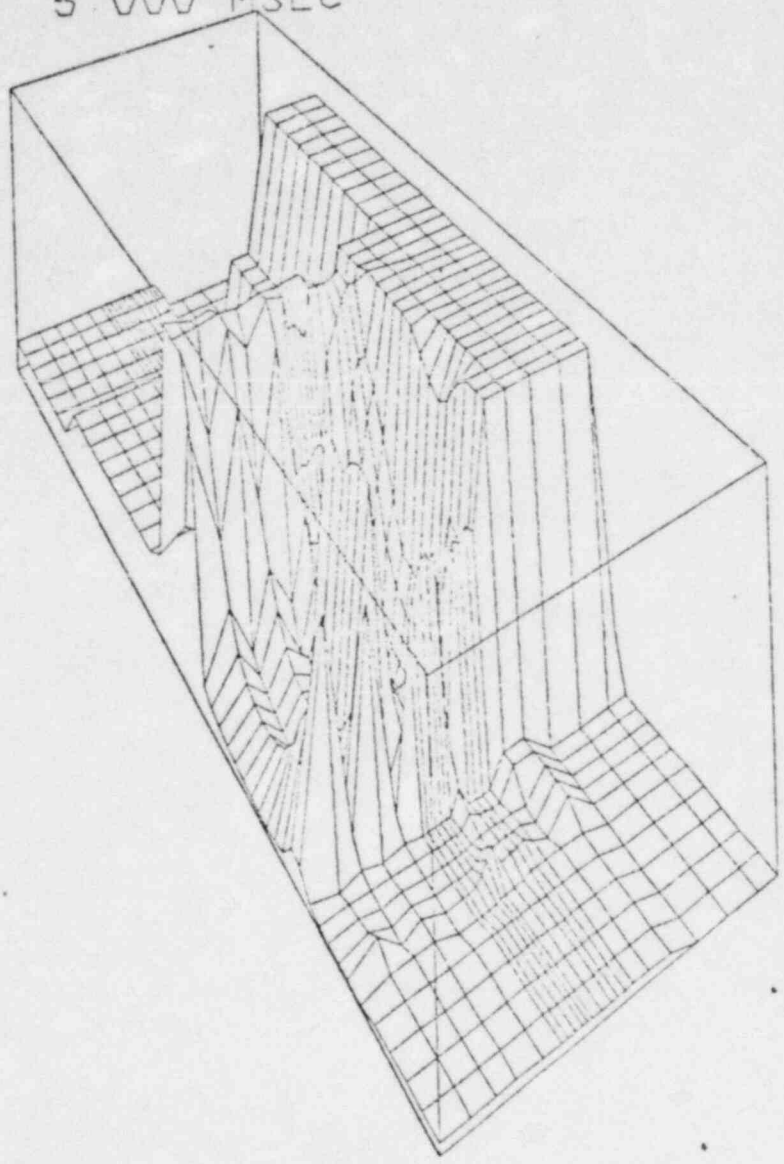

VOLUME FRACTION OF LIQUID
MINIMUM = 7 14217E-05 MAXIMUM = 9 99999E-01

Fig 42

TIME 10.000 MSEC

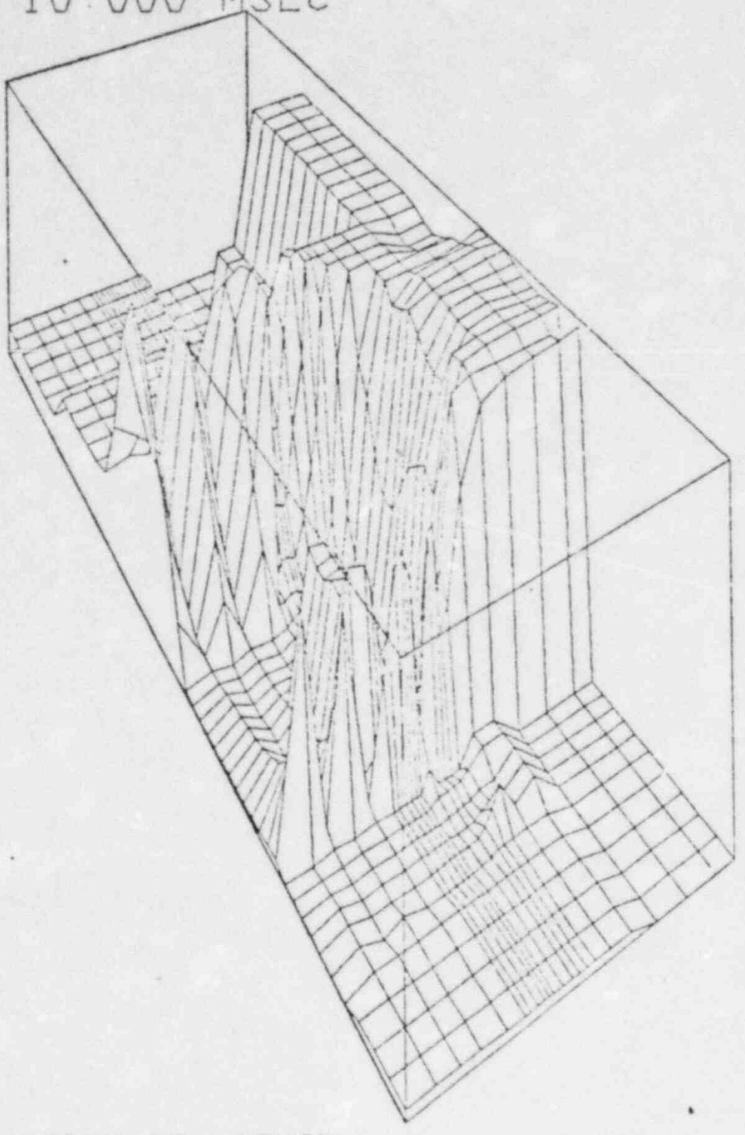

VOLUME FRACTION OF LIQUID
MINIMUM = 7.14217E-06 MAXIMUM = 9.99999E-01

Fig 43

TIME 15 000 MSEC

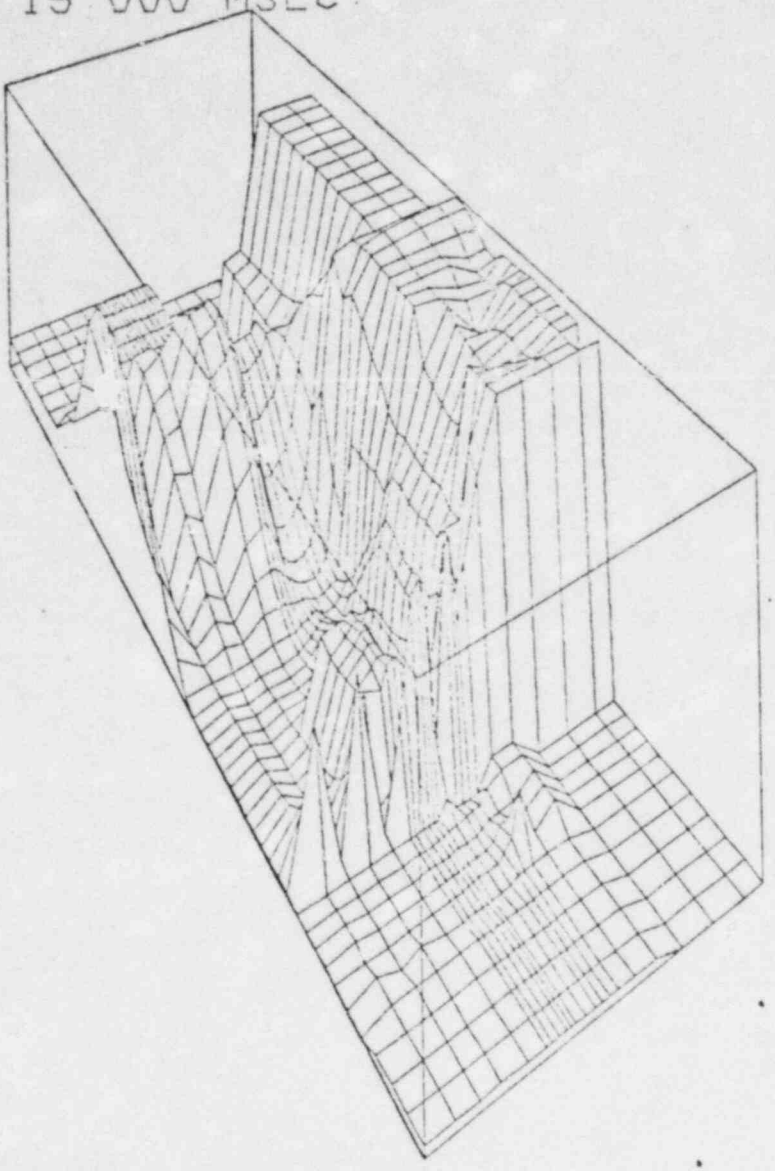

VOLUME FRACTION OF LIQUID
MINIMUM = 7 14217E-05 MAXIMUM = 9 99999E-01

Fig 44

TIME 20.000 MSEC

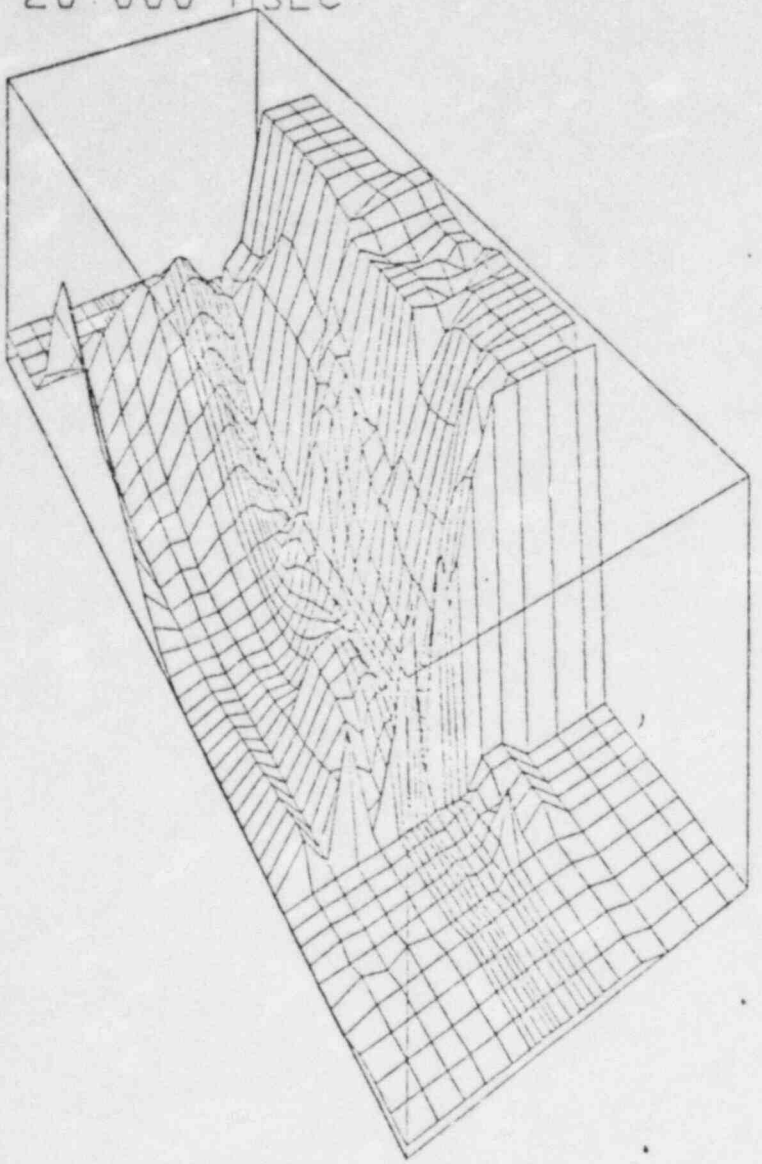

VOLUME FRACTION OF LIQUID
MINIMUM = 7.14217E-06 MAXIMUM = 9.99999E-01

Fig 45

TIME 35 000 MSEC

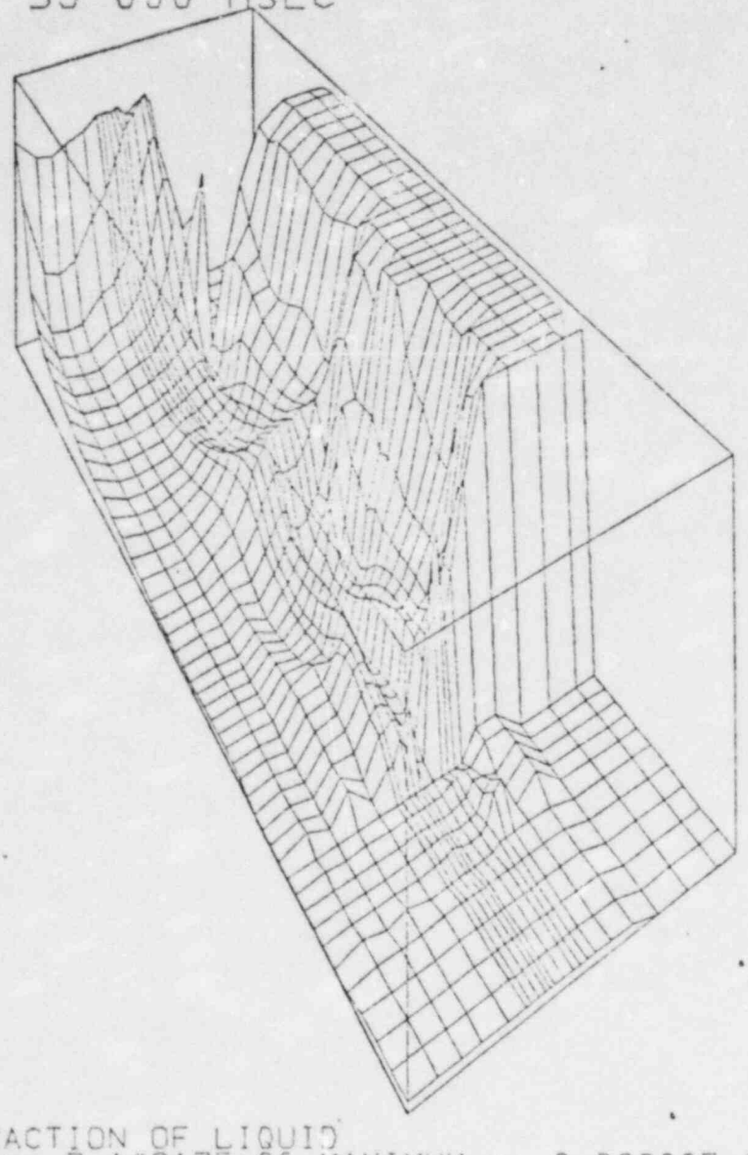

VOLUME FRACTION OF LIQUID
MINIMUM = 7 14217E-06 MAXIMUM = 9 99999E-01

Fig 48

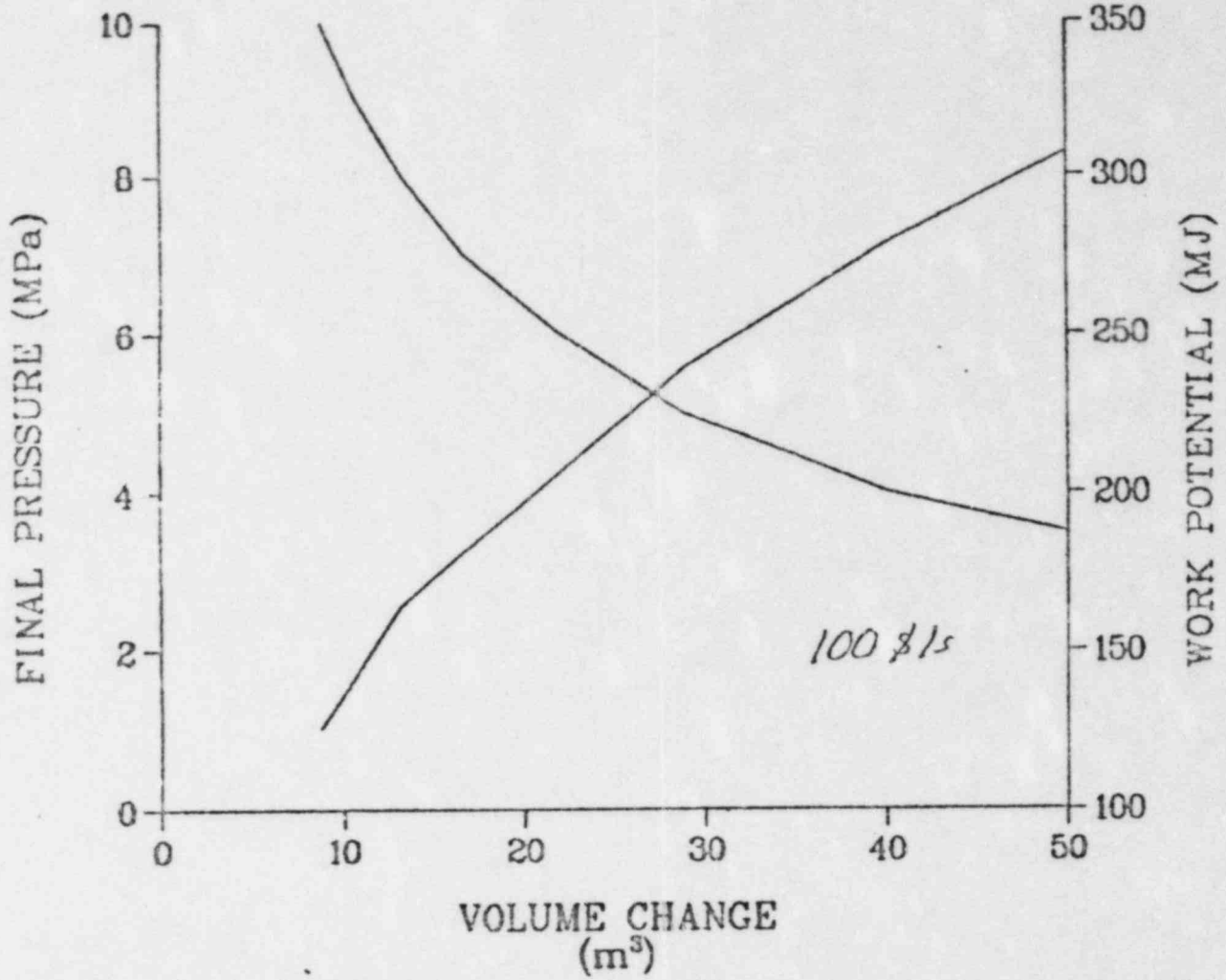
FINAL PRESSURE (MPa)
WORK POTENTIAL (MJ)
VOLUME CHANGE
(m³)
0
2
4
6
8
10
100
150
200
250
300
350
0
10
20
30
40
50
100 ℓ/s

Fig 51

A.II.2

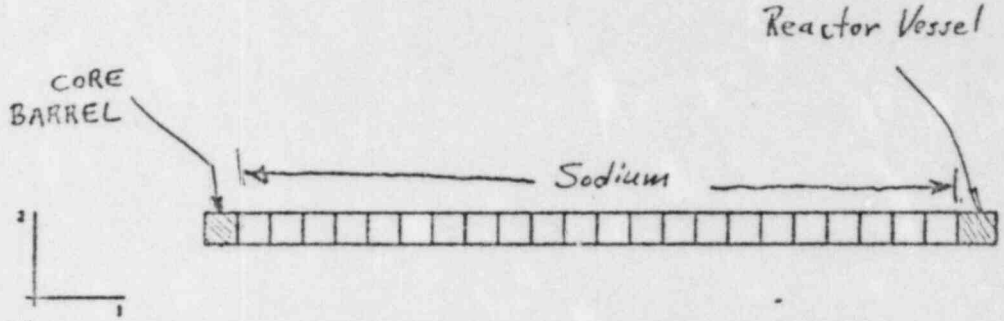

Fig. 1. CRBR RADIAL CORE STRUCTURAL RESPONSE MODEL

B II.2

CB displacement for 100 ft/s HCDA.

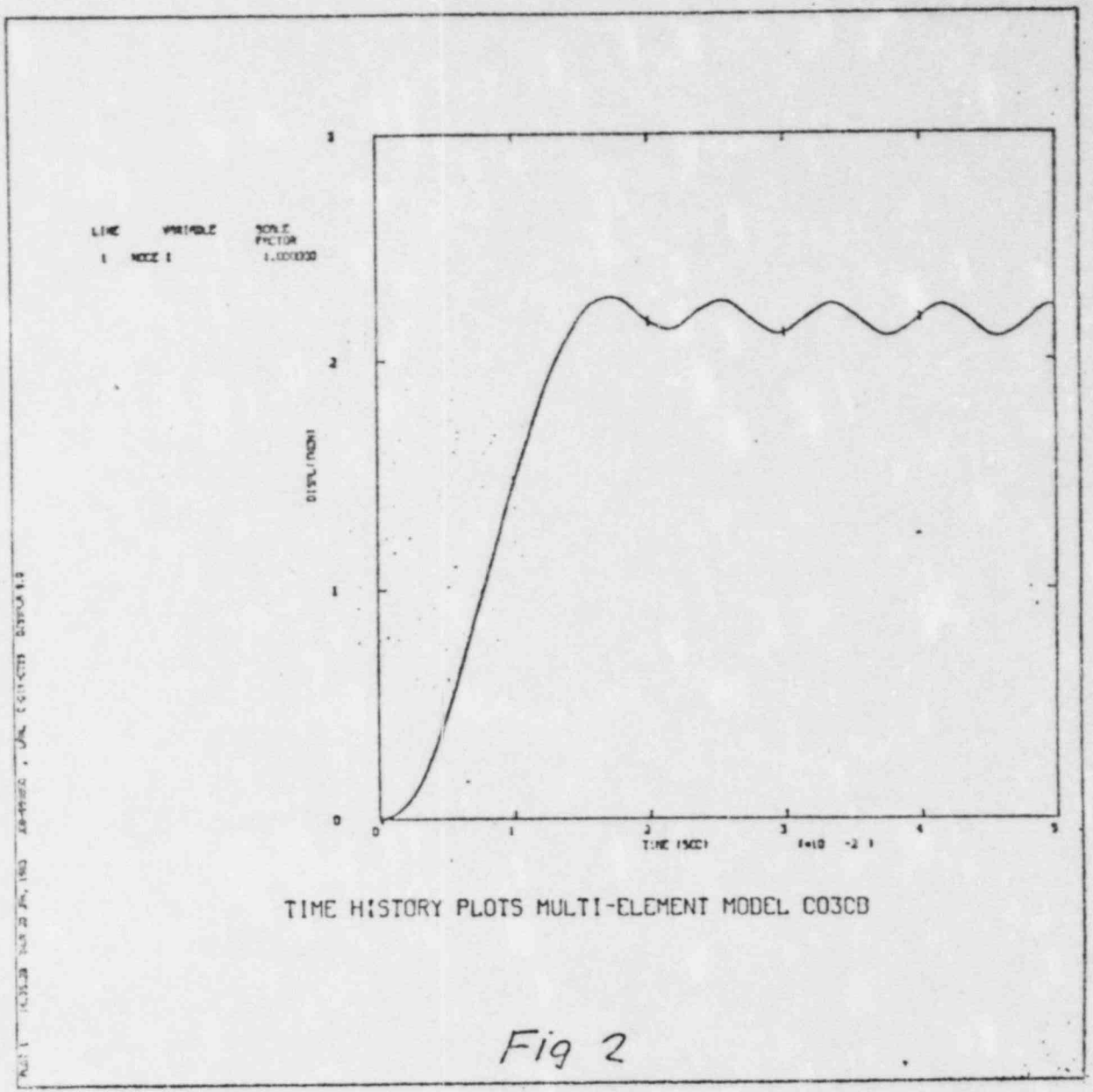

TIME HISTORY PLOTS MULTI-ELEMENT MODEL CO3CB

Fig 2

B.II.2

Vessel wall displacement up to 100 ft/s HCDA.

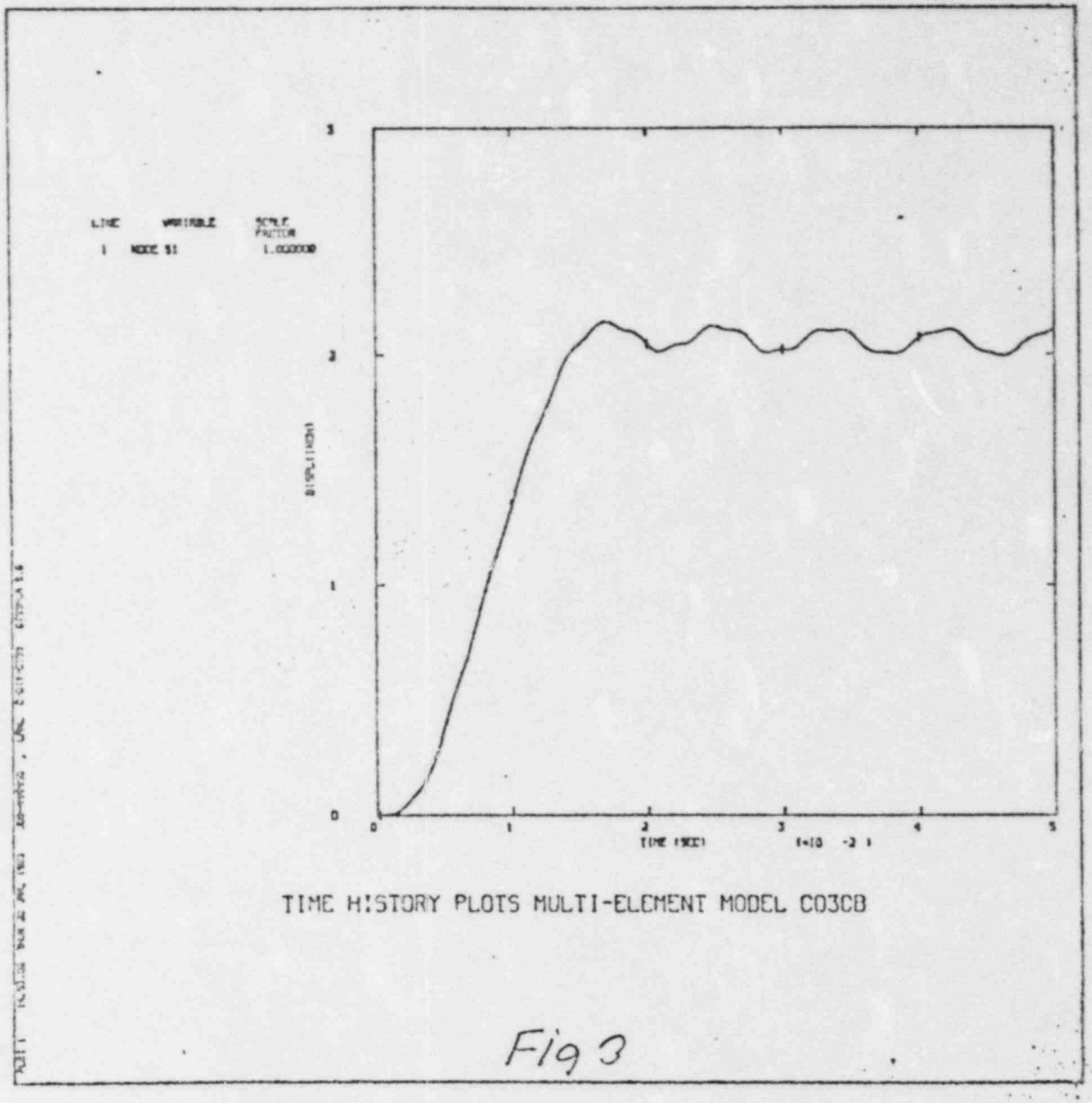

TIME HISTORY PLOTS MULTI-ELEMENT MODEL CO3CB

Fig 3

<8 strain for 100 #/s N

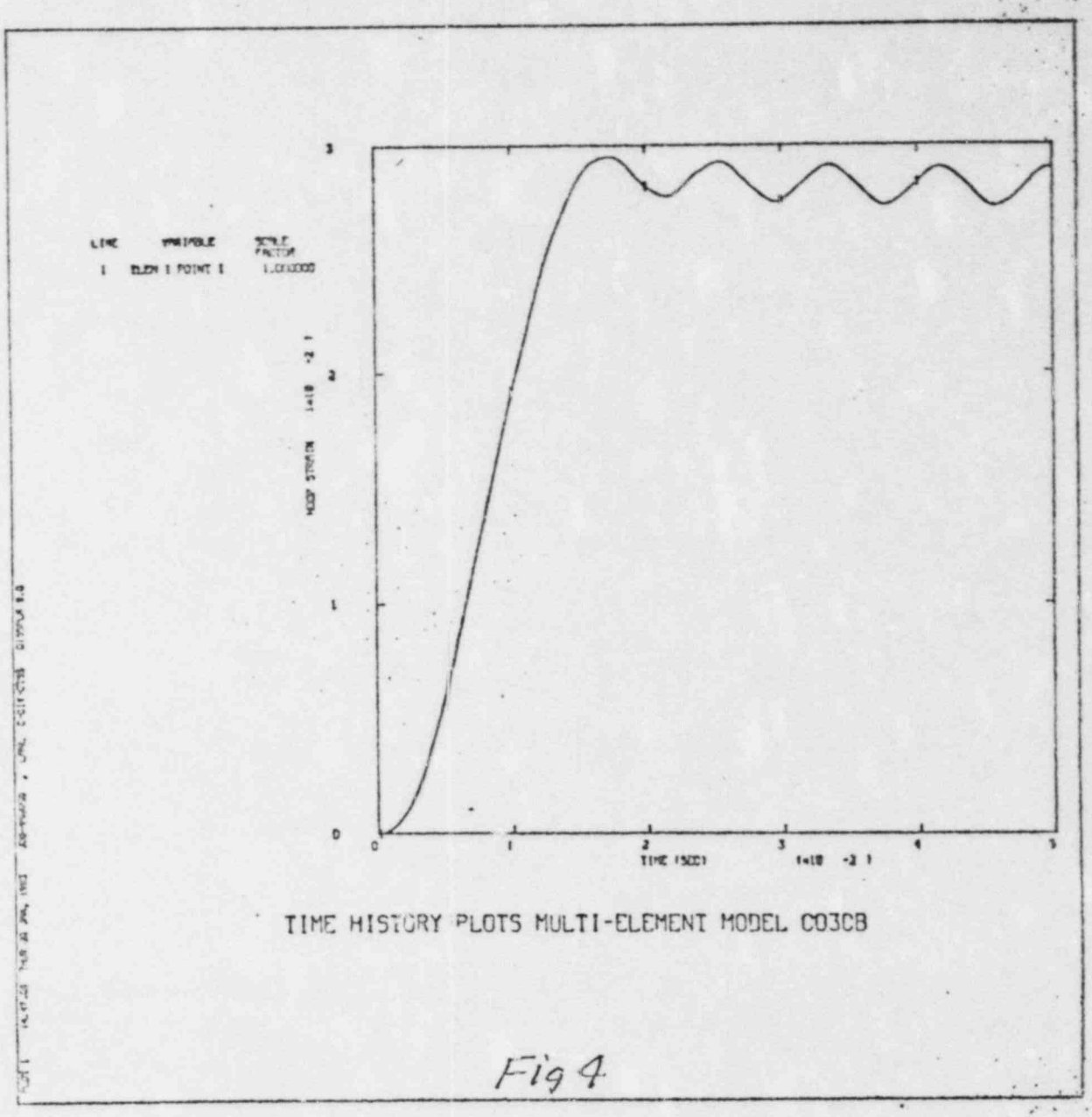

TIME HISTORY PLOTS MULTI-ELEMENT MODEL C03CB

Fig 4

B II.2

Vessel wall strain for R[illegible]/s ATCDA

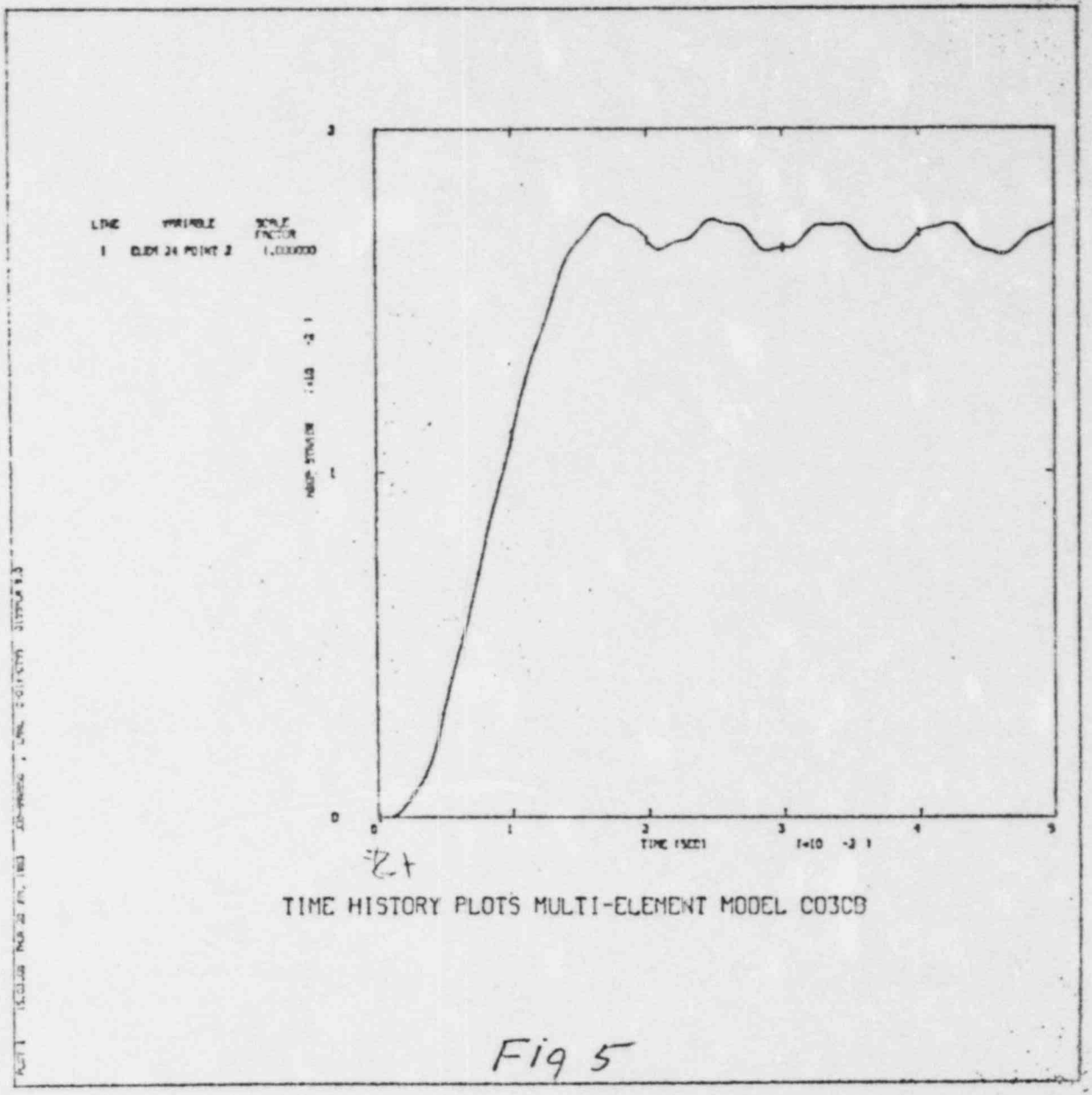

TIME HISTORY PLOTS MULTI-ELEMENT MODEL CO3CB

Fig 5

B.II.2

CB displacement for 200 $/$ HCDA

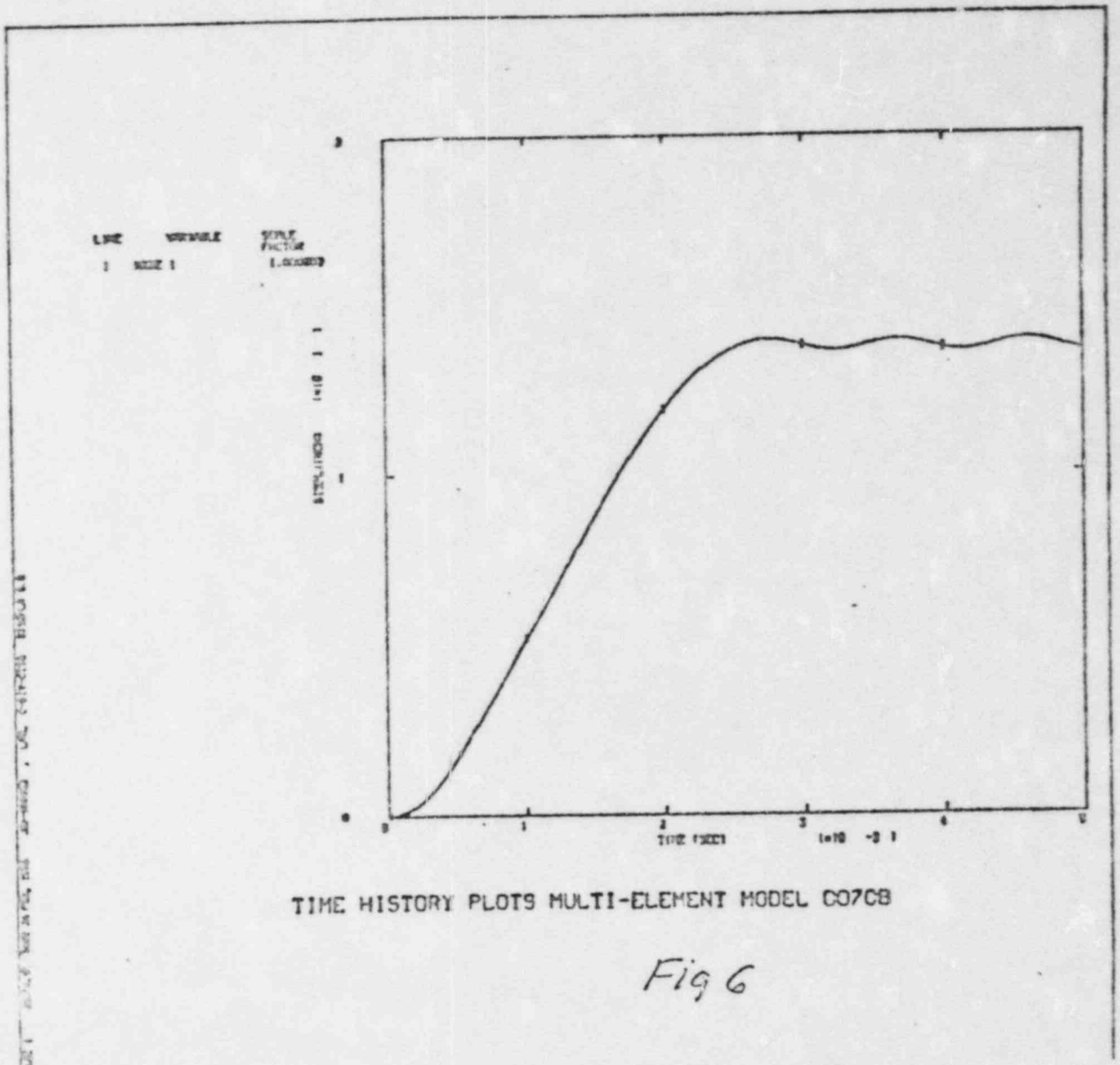

TIME HISTORY PLOTS MULTI-ELEMENT MODEL CO7CB

Fig 6

Vessel wall displacement for
$1200/5 NCDA.

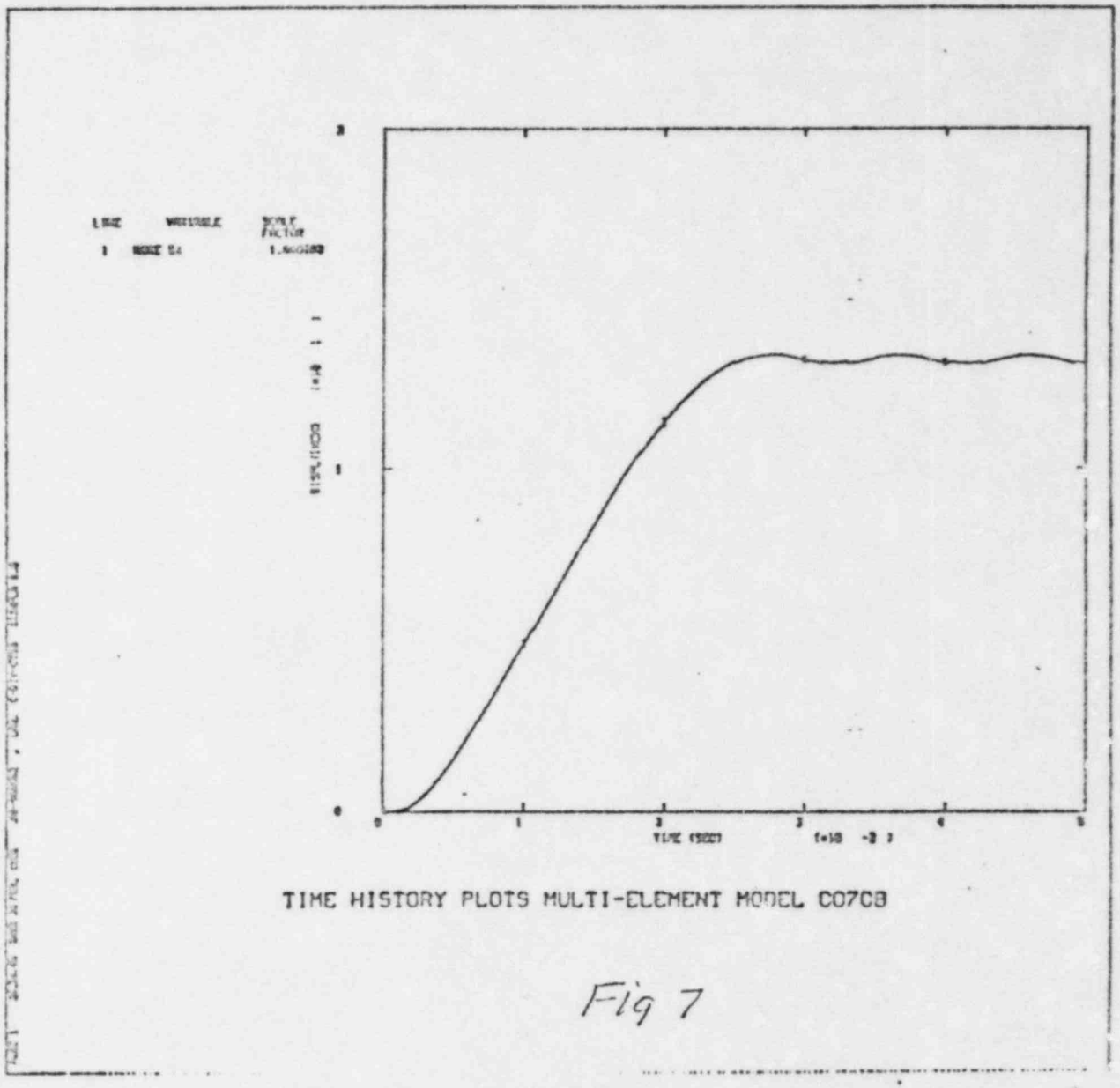

TIME HISTORY PLOTS MULTI-ELEMENT MODEL C0708

Fig 7

B II.2

CB Strain for #/5
HCDA

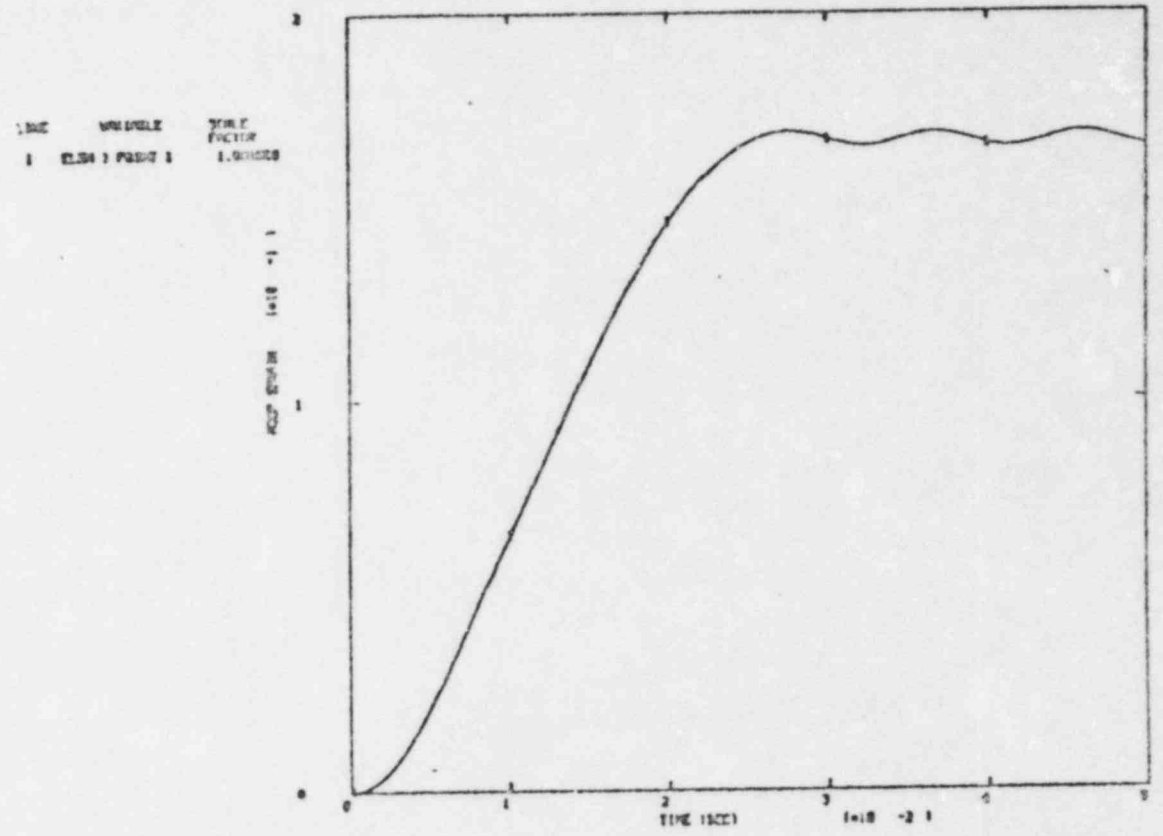

TIME HISTORY PLOTS MULTI-ELEMENT MODEL CO7CB

Fig 8

B.II.2

Vessel wall strain
200 s/s HCDA.

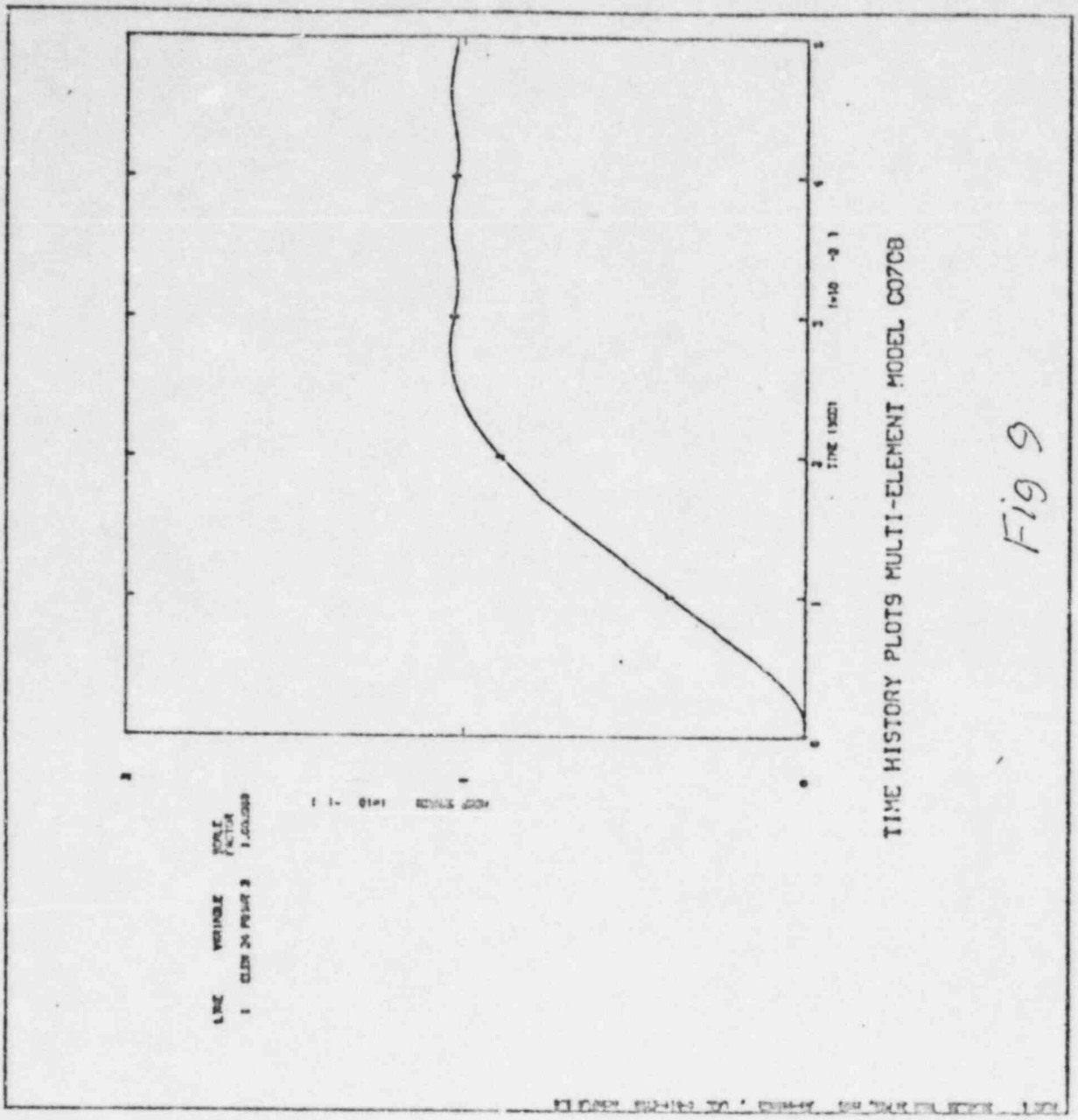

Fig 9

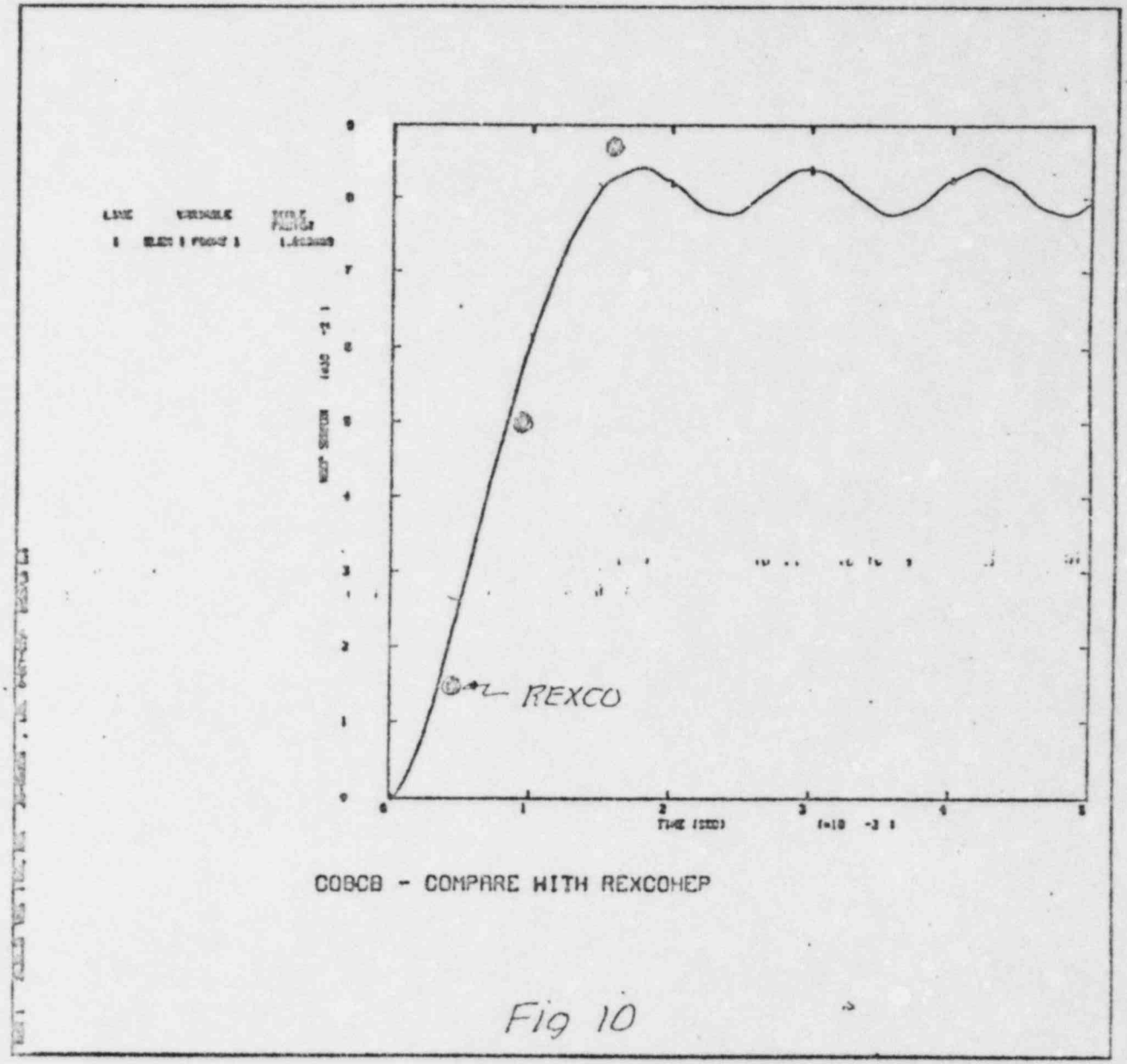

COBCB - COMPARE WITH REXCOHEP

Fig 10

COSMIC - TRUSS

UIS response during 100 $/s
NCOA.

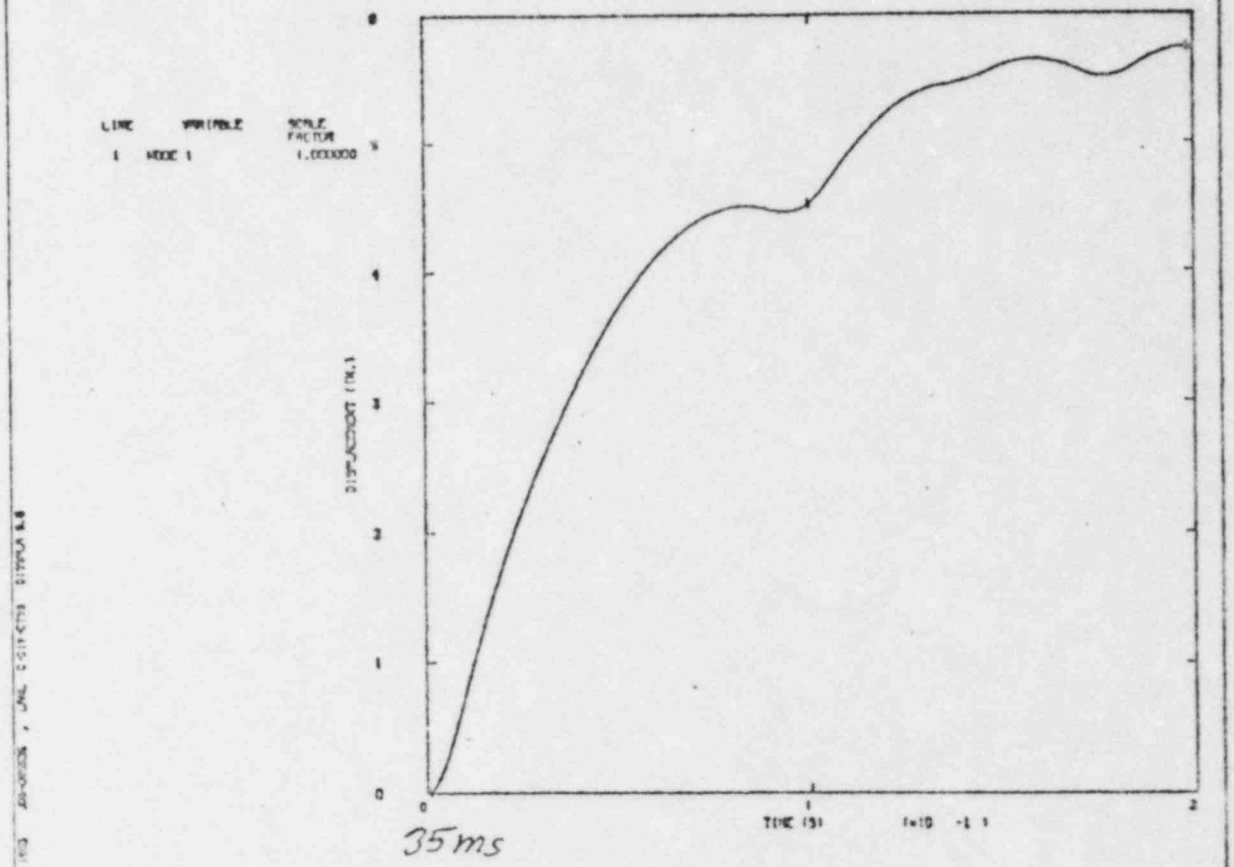

UIS WITH LOW MASS

Fig 11

B.II. 2

UIS response during 200 ft/s HCDA.

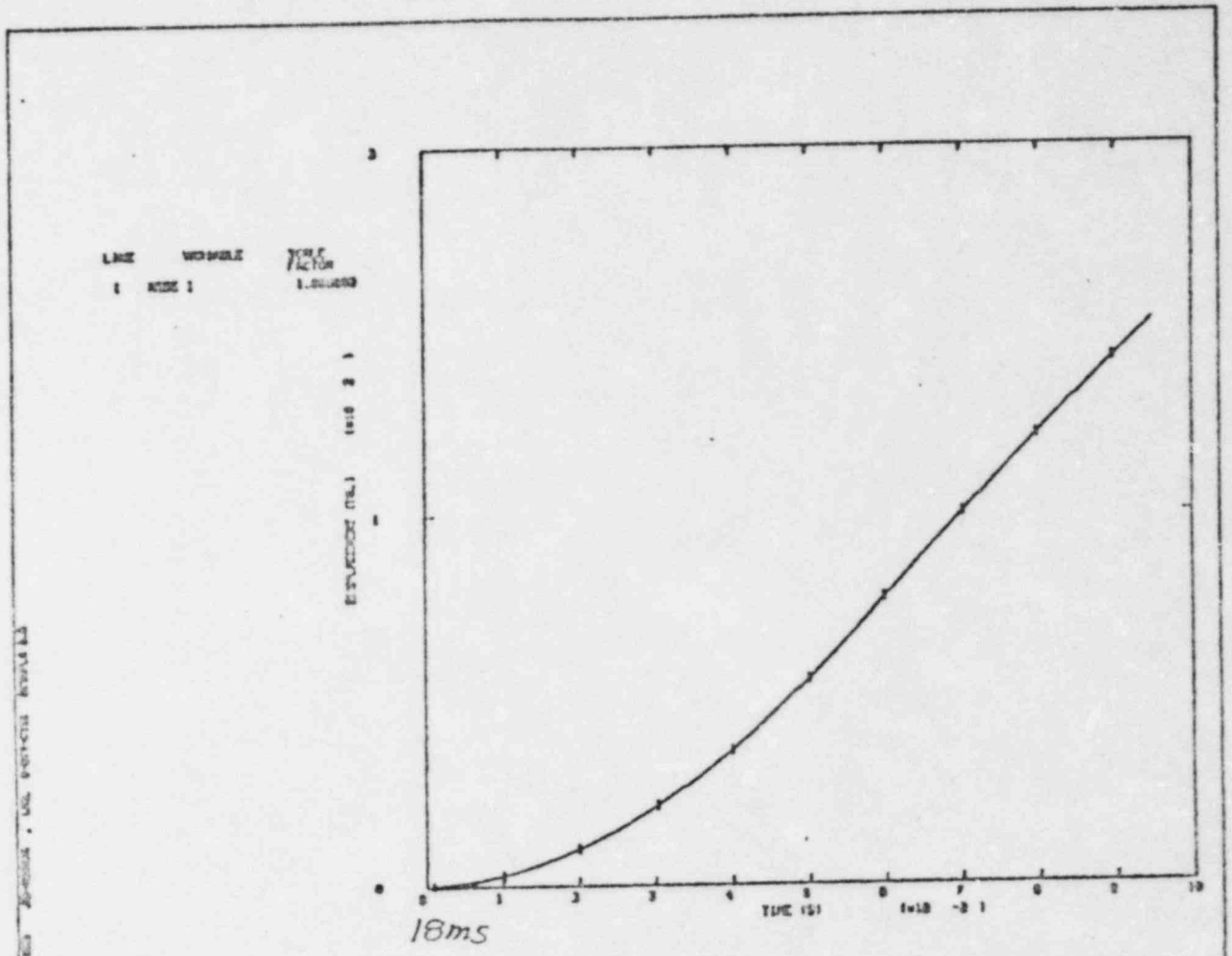

UIS WITH SPRING (C07UIS)

Fig 12

B.II.2

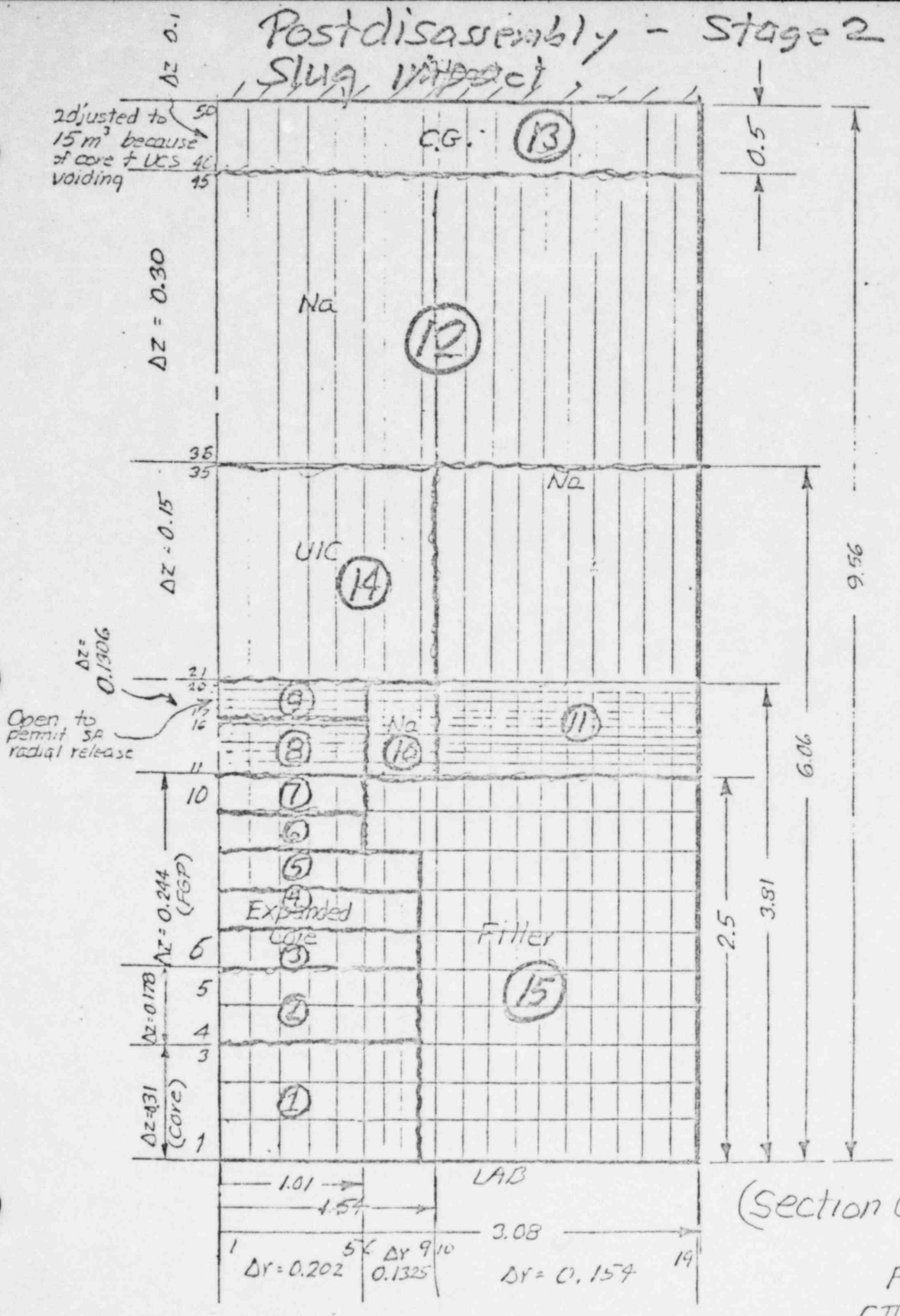
Postdisassembly - Stage 2
Slug Impact
Δz 0.1
adjusted to 15 m³ because of core + UCS voiding
50
45
C.G.
13
0.5
Na
12
Δz = 0.30
35
35
Na
UIC
14
Δz = 0.15
Δz = 0.1906
21
20
17
16
11
Open to permit SP radial release
9
8
Na
10
11
10
7
6
5
4
Expanded Core
Filler
6
3
15
Δz = 0.244 (FGP)
Δz = 0.178
5
4
3
2
Δz = 0.31 (Core)
1
1
9.56
6.06
3.81
2.5
LAB
1.01
1.54
3.08
1
5
9
10
19
Δr = 0.202
Δr 0.1325
Δr = 0.154
(Section CII.1

Fig 1
CII.2

MASS OF LIQ FUEL SI07 200 $/s

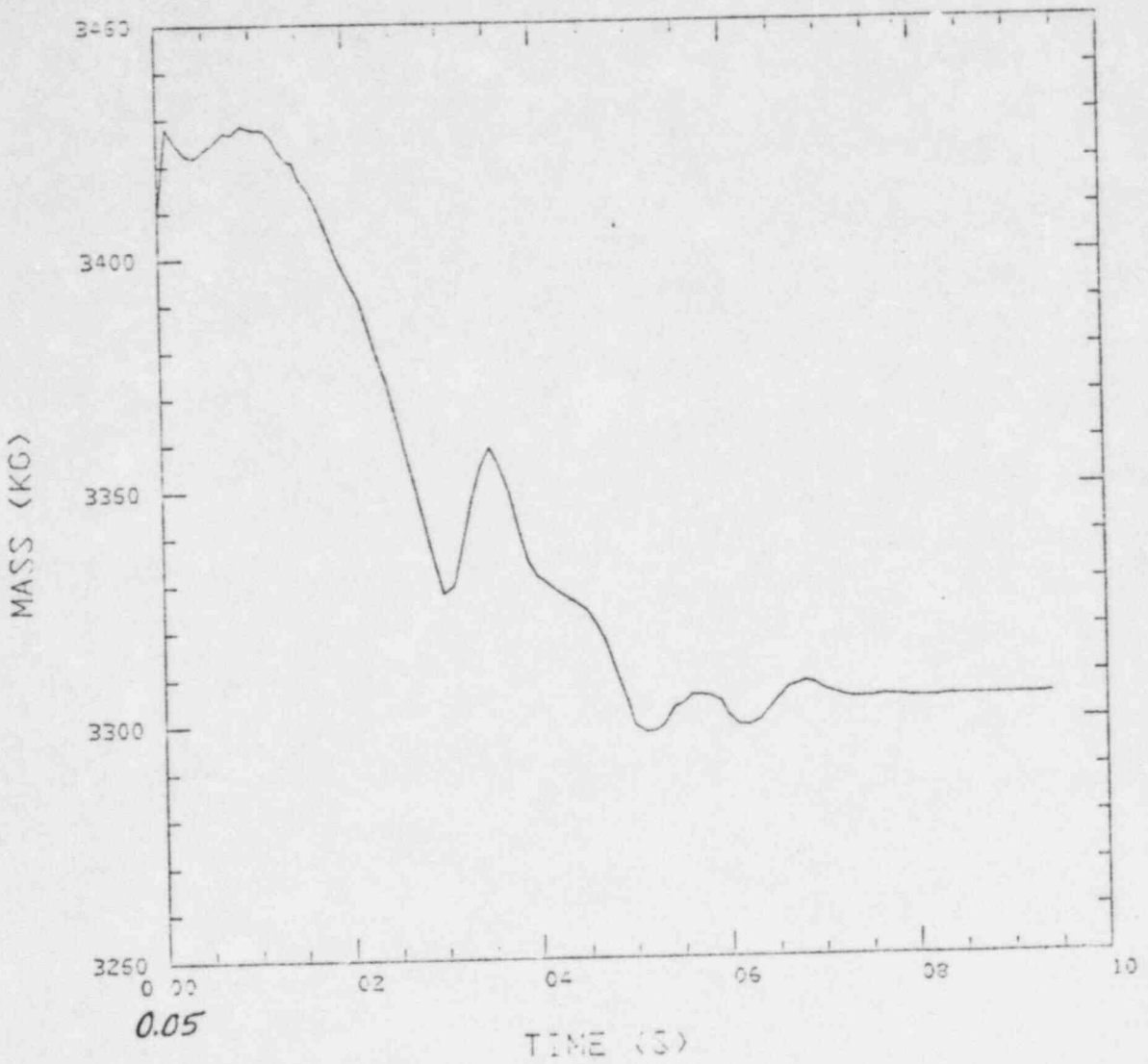

Fig 2

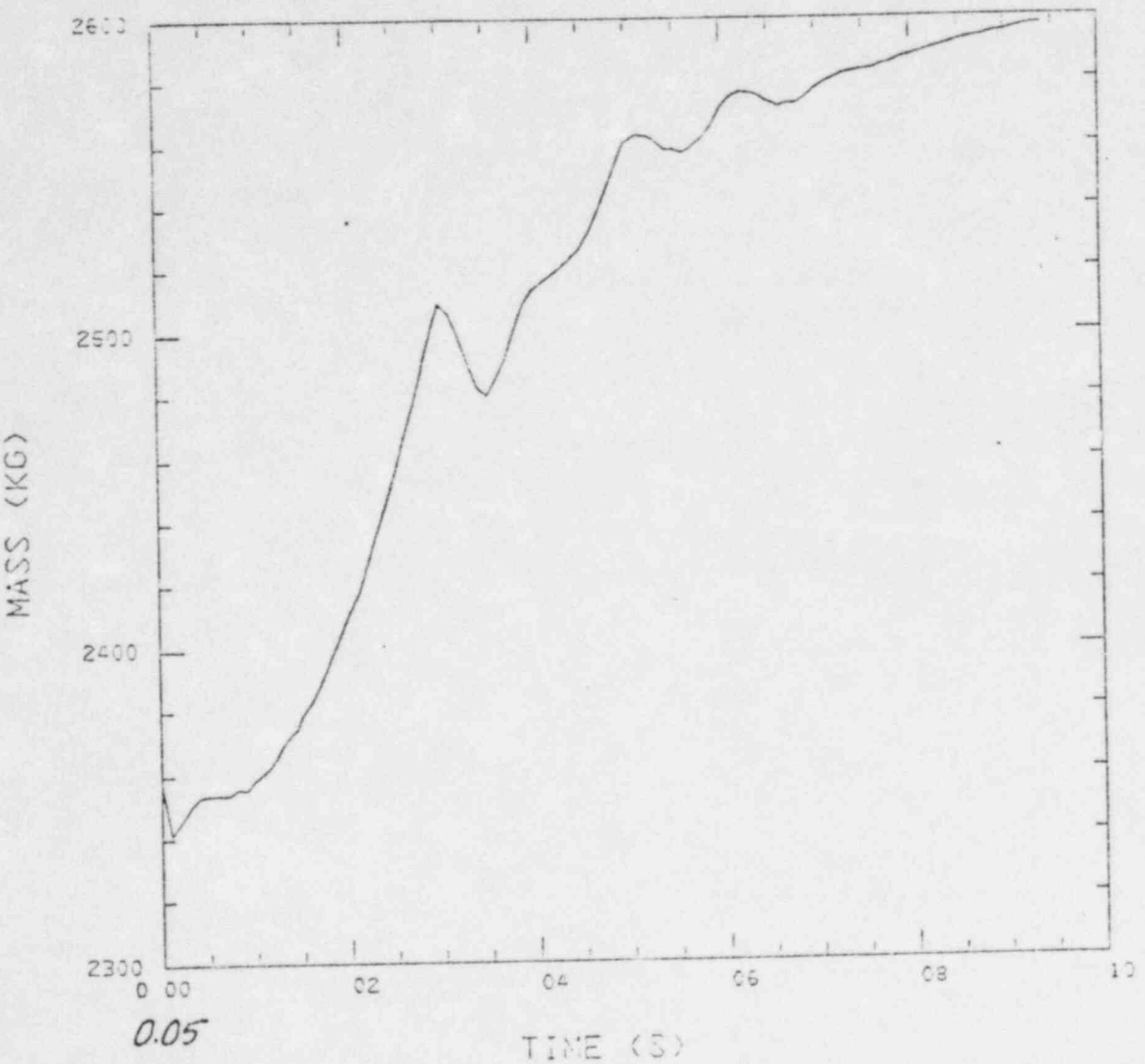
MASS OF VAP FUEL SI07
2600
2500
2400
2300
MASS (KG)
0 00
02
04
06
08
10
0.05
TIME (S)

Fig 3

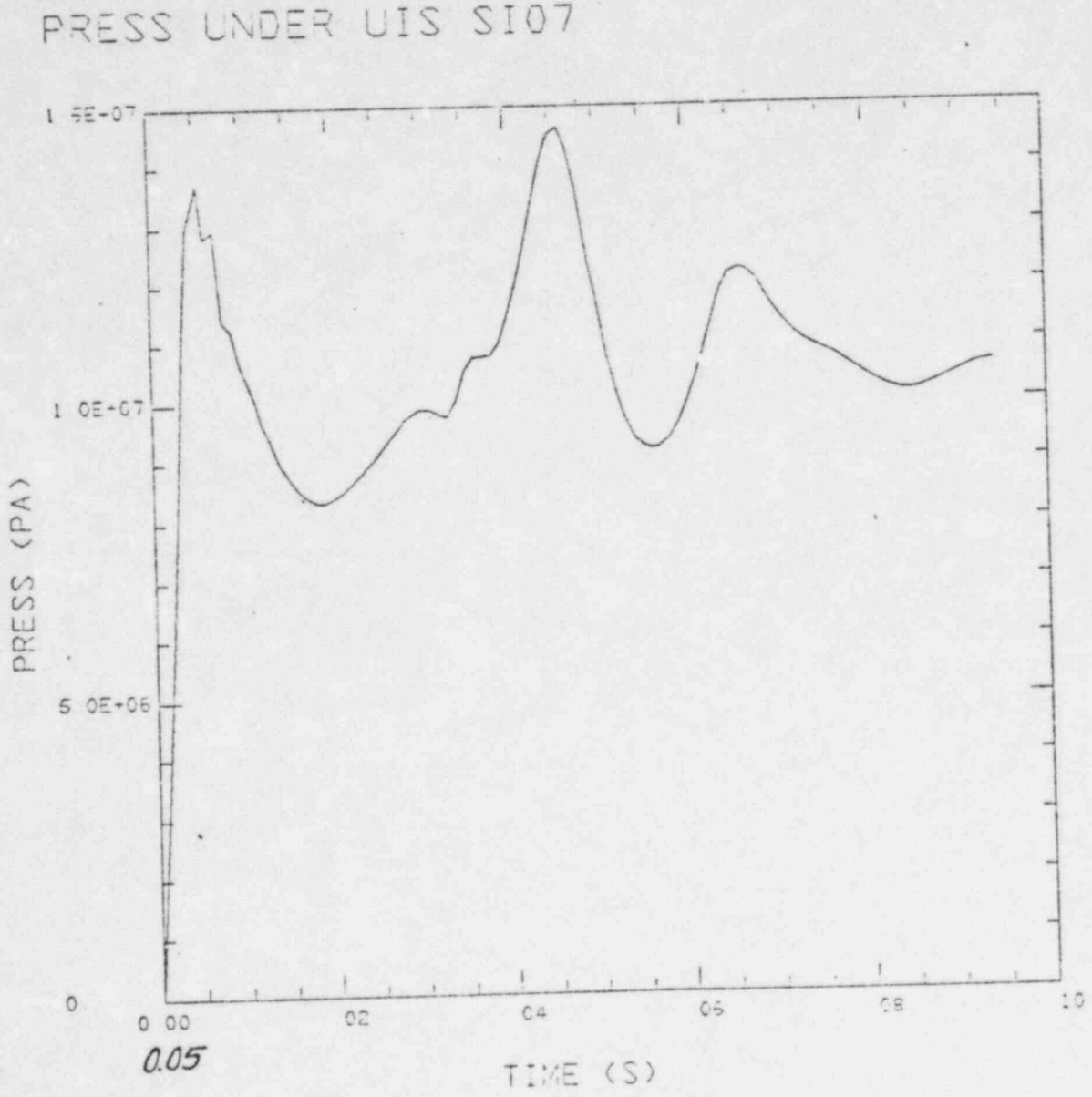
PRESS UNDER UIS SI07
1 5E-07
1 0E+07
5 0E+06
0
PRESS (PA)
0 00
02
04
06
08
10
0.05
TIME (S)

Fig 5

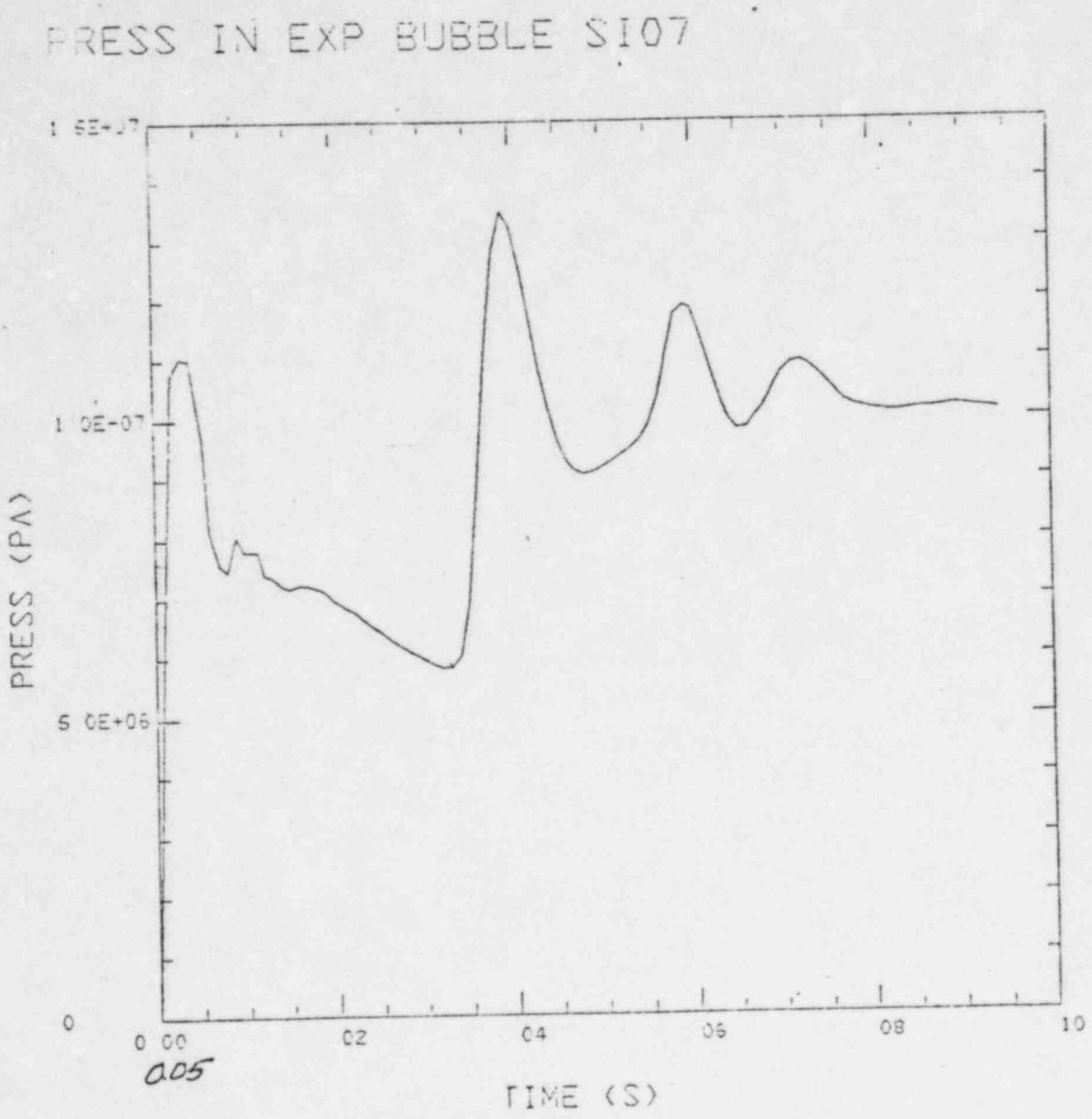
PRESS IN EXP BUBBLE SI07
1 5E+07
1 0E-07
5 0E+06
0
PRESS (PA)
0 00
02
04
06
08
10
005
TIME (S)

Fig 6

POOL VELOCITY SI07

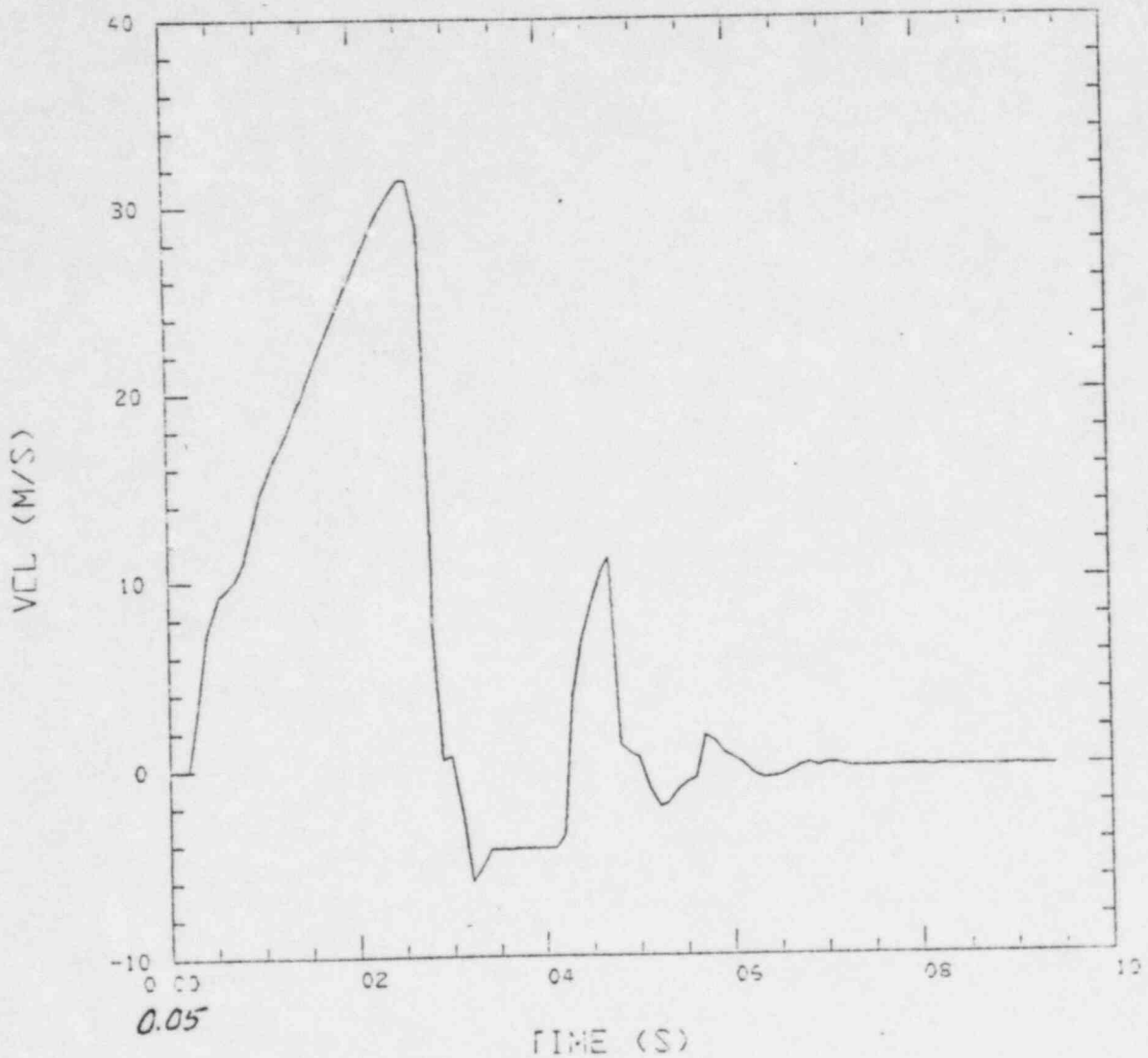

Fig 7

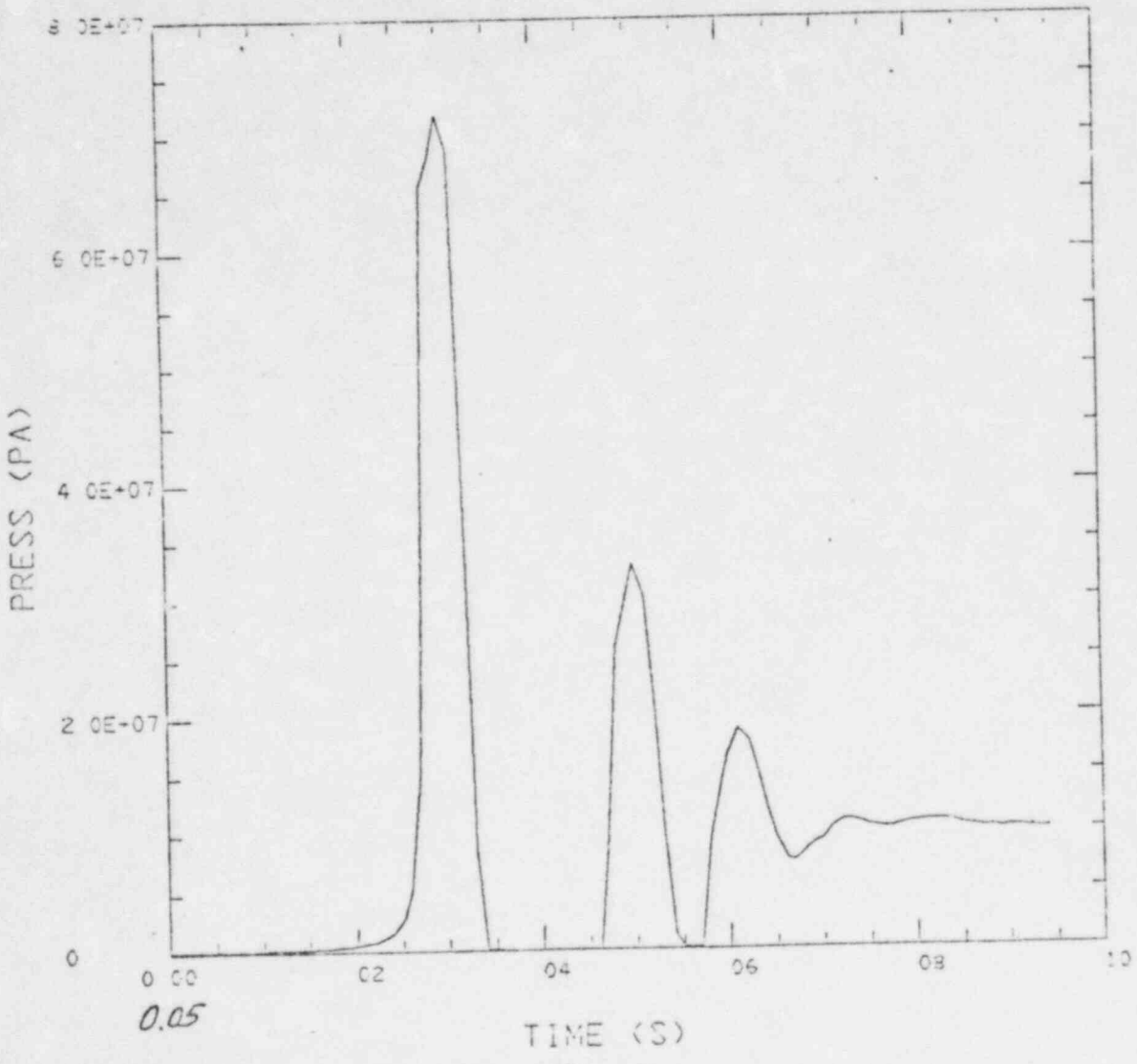
PRESS AT HEAD SI07
8 0E+07
6 0E+07
4 0E+07
2 0E+07
0
PRESS (PA)
0 00
02
04
06
08
10
0.05
TIME (S)

Fig 8

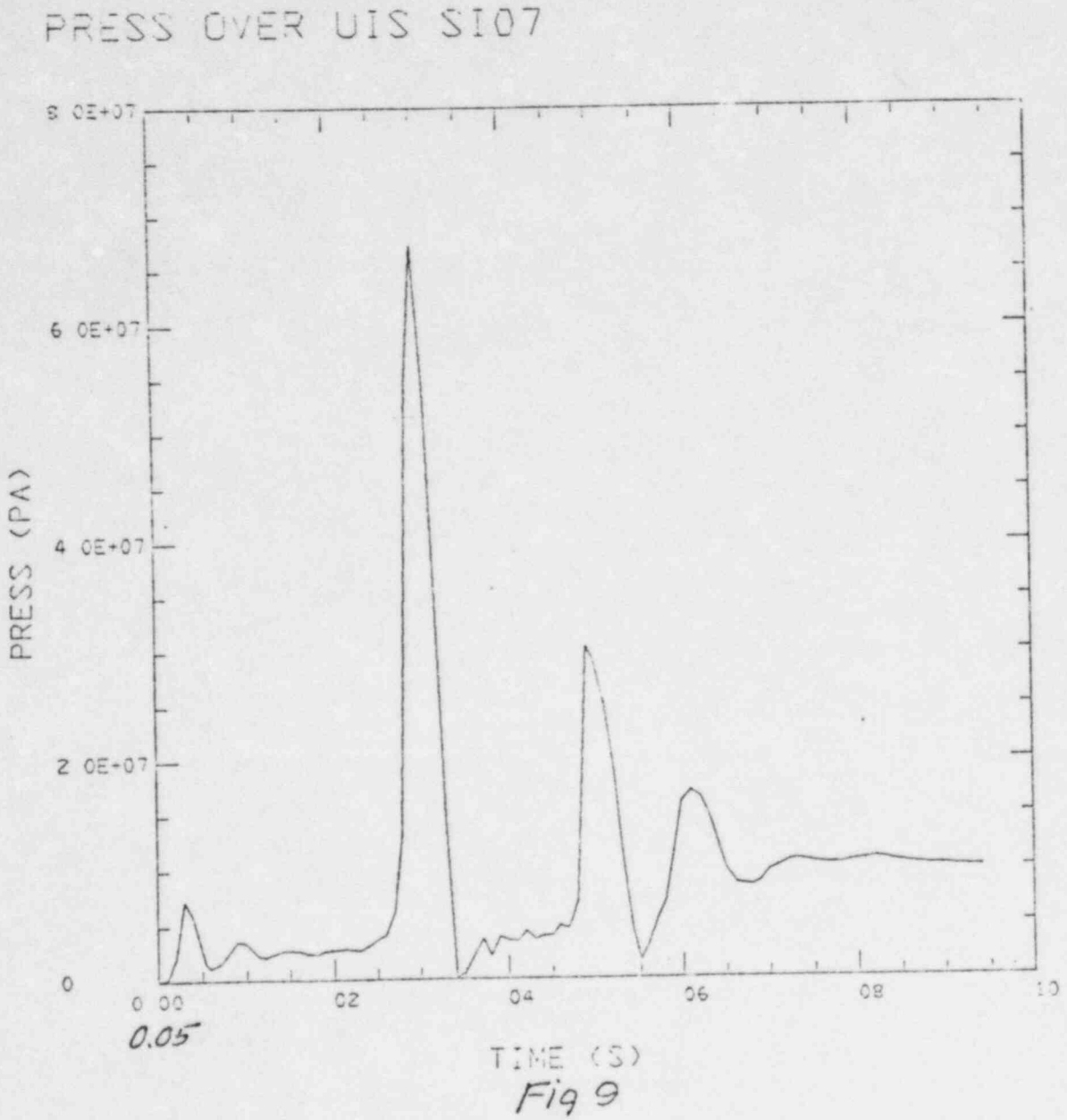
PRESS OVER UIS SI07
8 0E+07
6 0E+07
4 0E+07
2 0E+07
0
PRESS (PA)
0 00
02
04
06
08
10
0.05
TIME (S)

Fig 9

TIME = 000 MSEC + 50

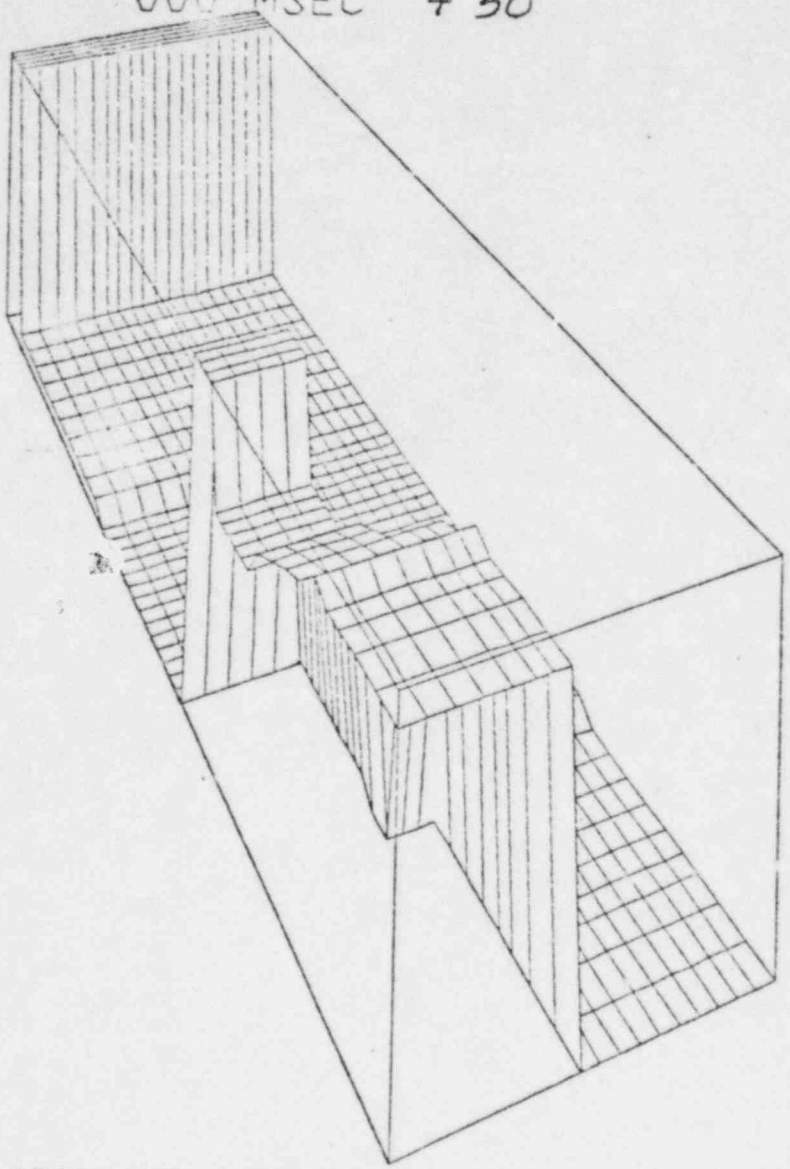

VOLUME FRACTION OF VAPOR
MINIMUM = 1 56134E-03 MAXIMUM = 9 99216E-01

Fig 10

TIME 10 000 MSEC +50

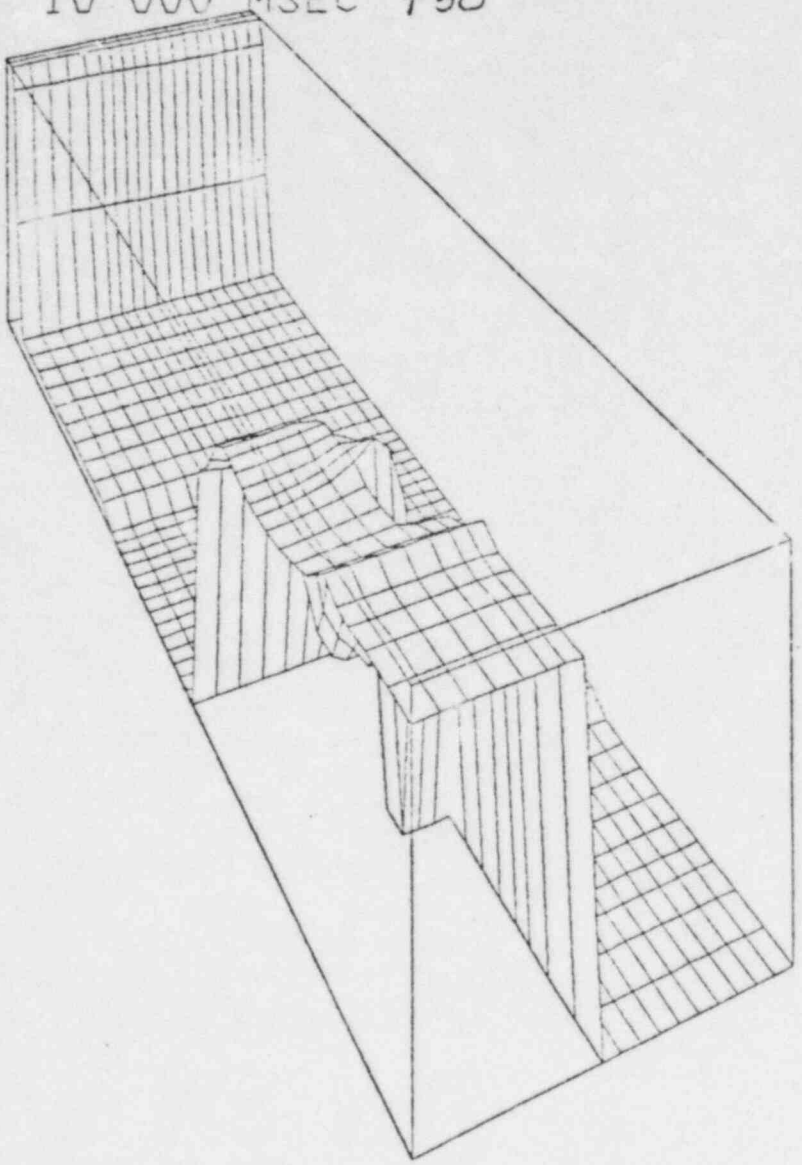

VOLUME FRACTION OF VAPOR
MINIMUM = 1 56134E-03 MAXIMUM = 9 99216E-01

Fig 11

TIME 20 000 MSEC +50

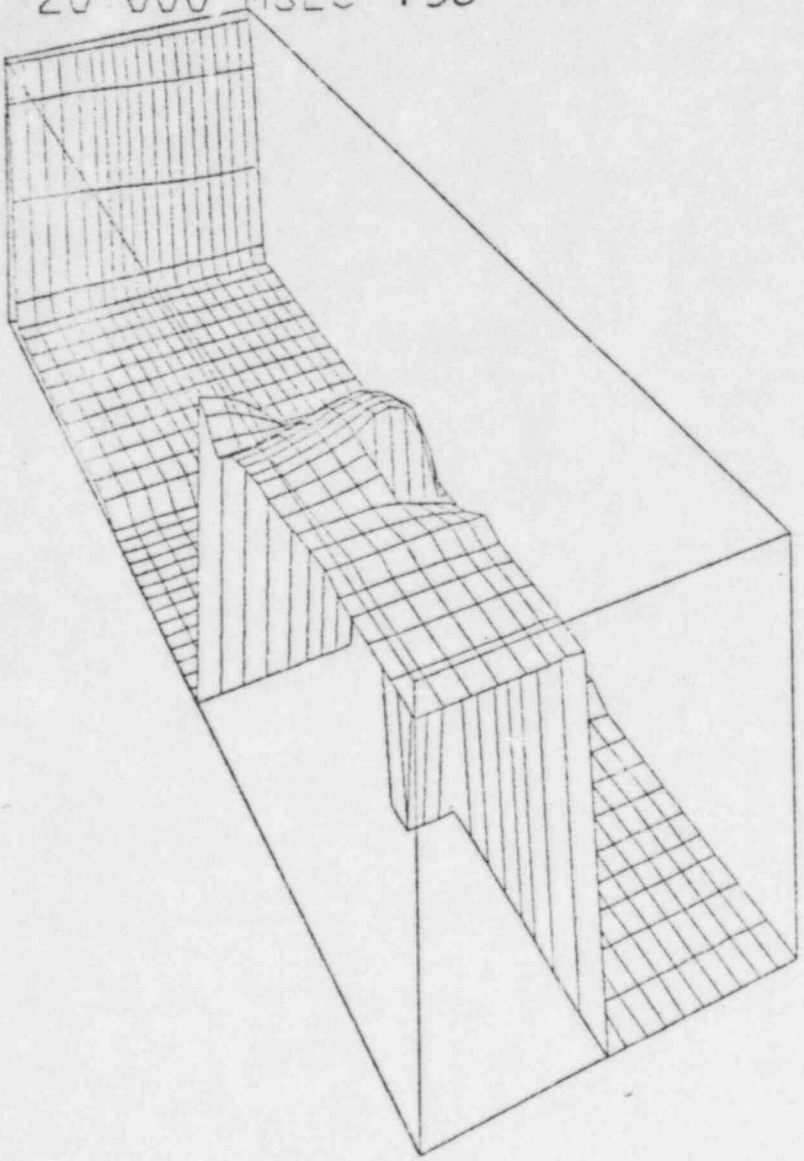

VOLUME FRACTION OF VAPOR
MINIMUM = 1 56134E-03 MAXIMUM = 9 99216E-01

Fig 12

TIME 26 000 MSEC + 50

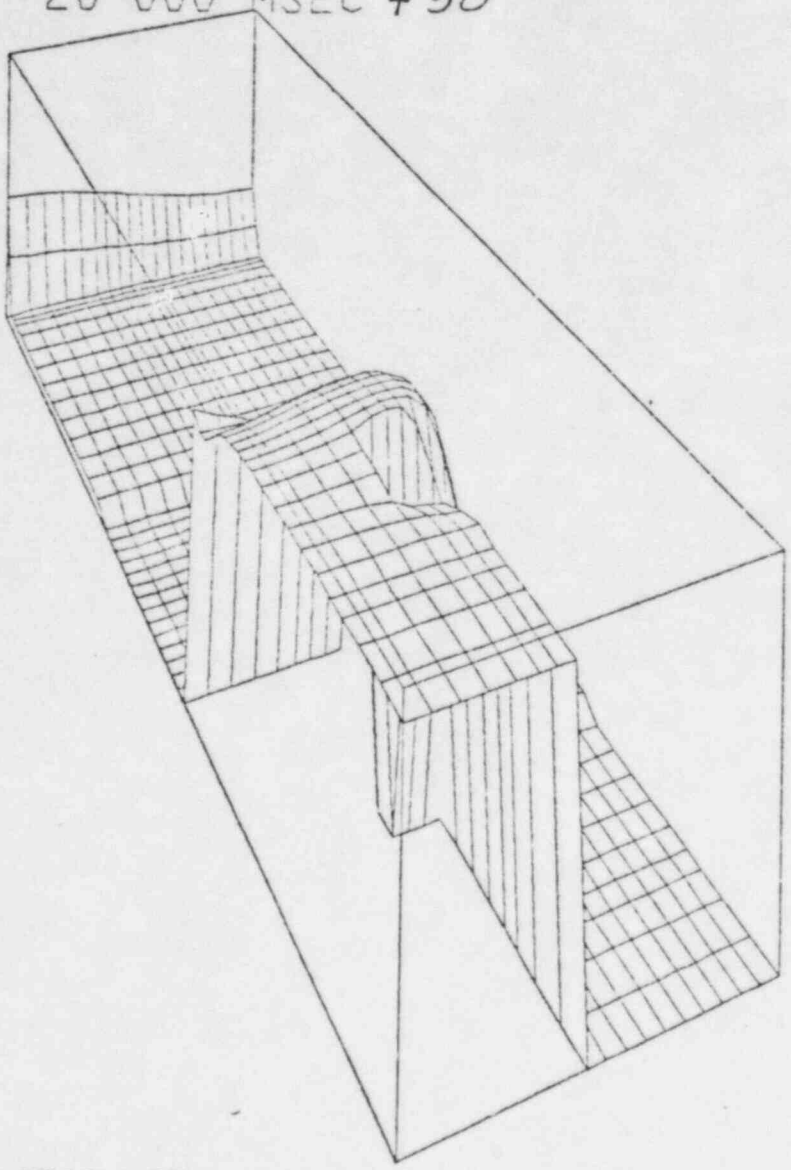

VOLUME FRACTION OF VAPOR
MINIMUM = 1 56134E-03 MAXIMUM = 9 99216E-01

Fig 13

TIME 28 000 MSEC + 50

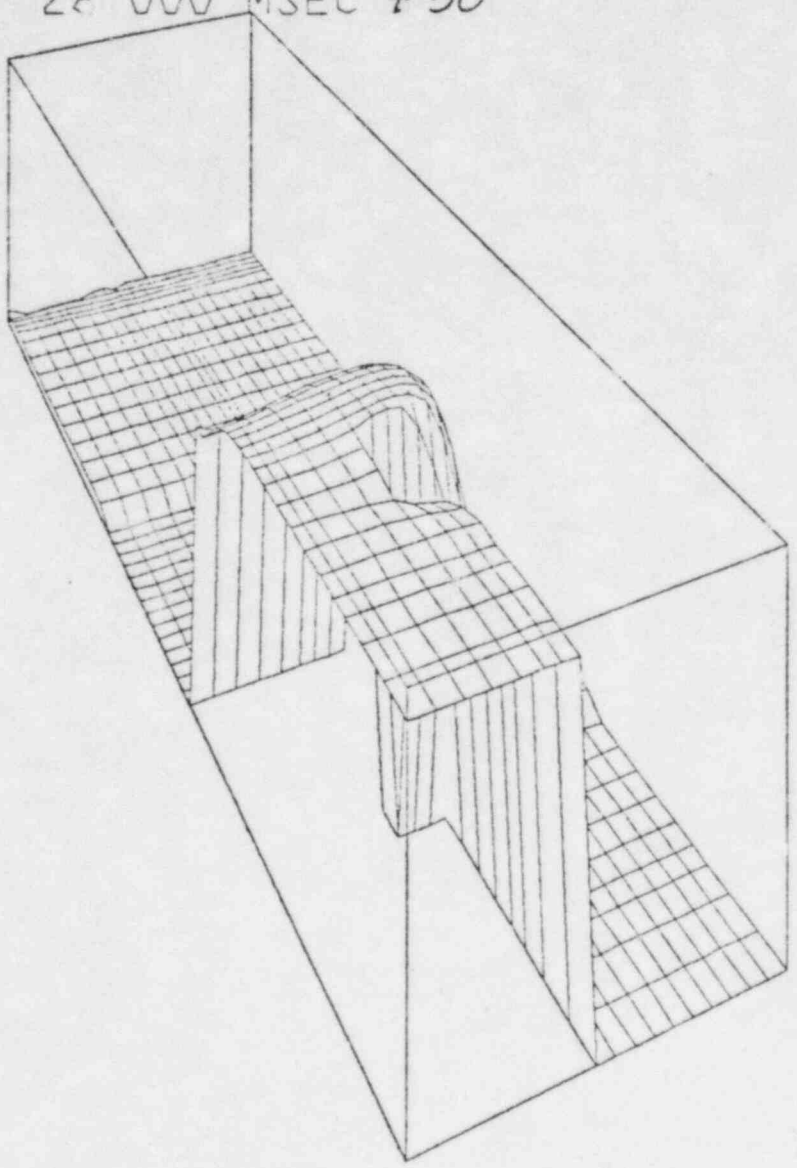

VOLUME FRACTION OF VAPOR
MINIMUM = 1 56134E-03 MAXIMUM = 9 99216E-01

Fig 14

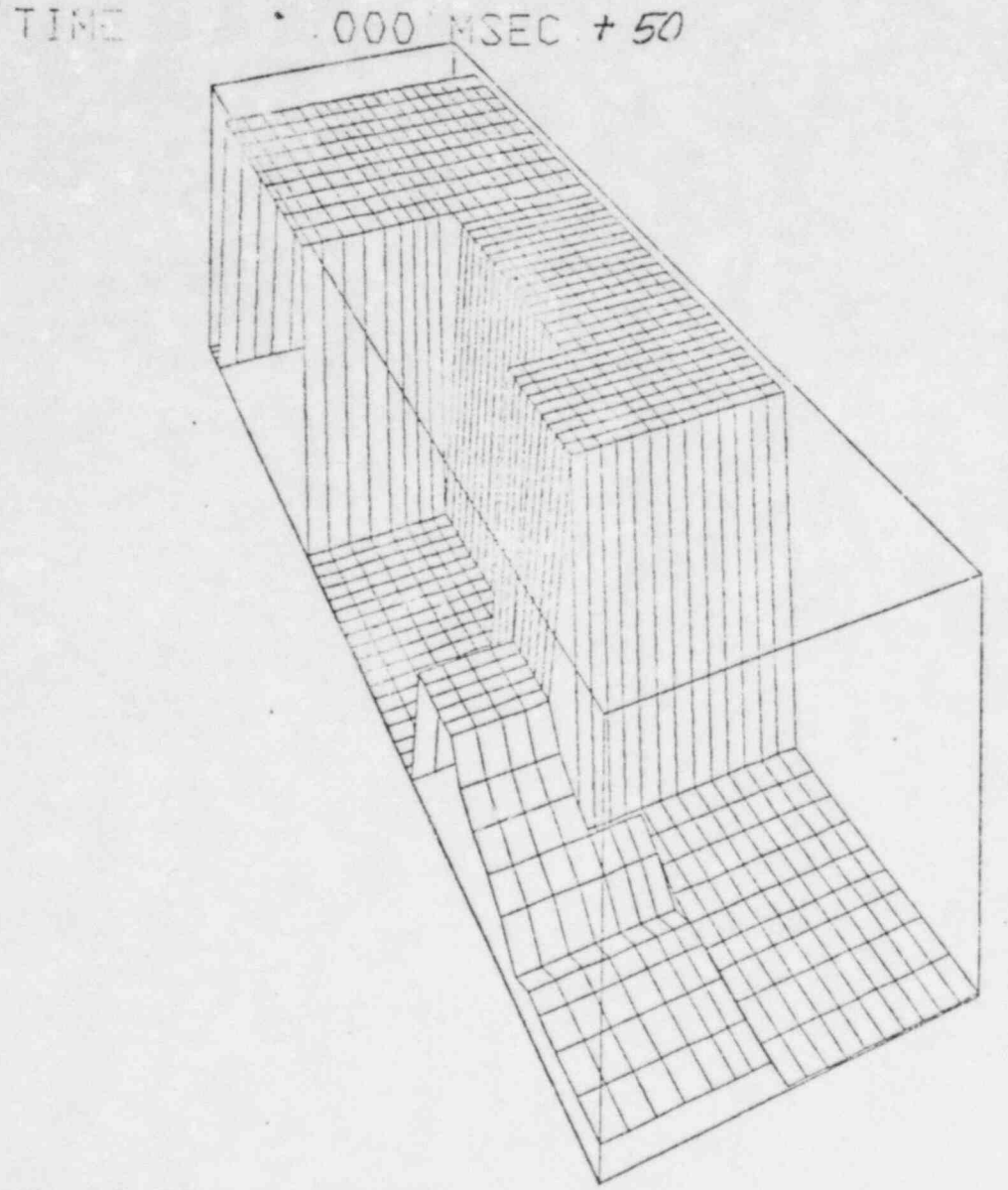
TIME .000 MSEC +50
VOLUME FRACTION OF LIQUID
MINIMUM = 7 84014E-04 MAXIMUM = 9 94051E-01

Fig 15

TIME 10 000 MSEC +50

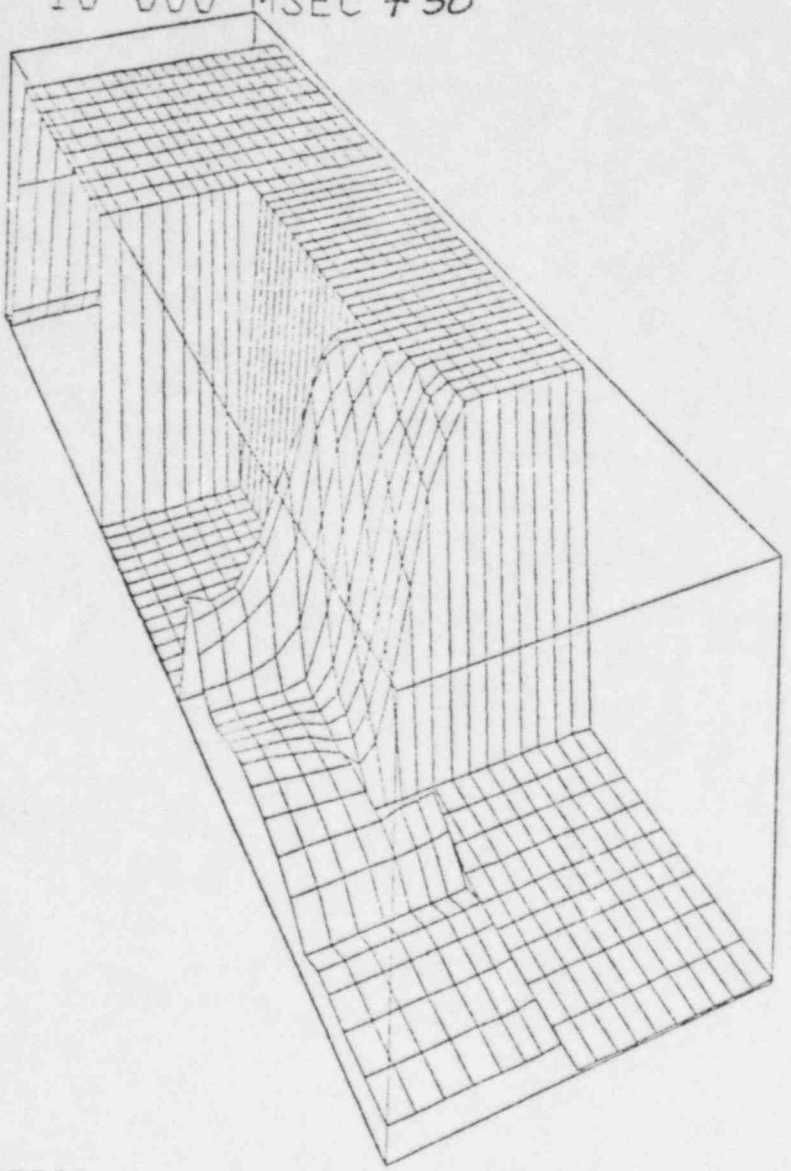

VOLUME FRACTION OF LIQUID
MINIMUM = 7 84014E-04 MAXIMUM = 9 94051E-01

Fig 16

TIME 20 000 MSEC + 50

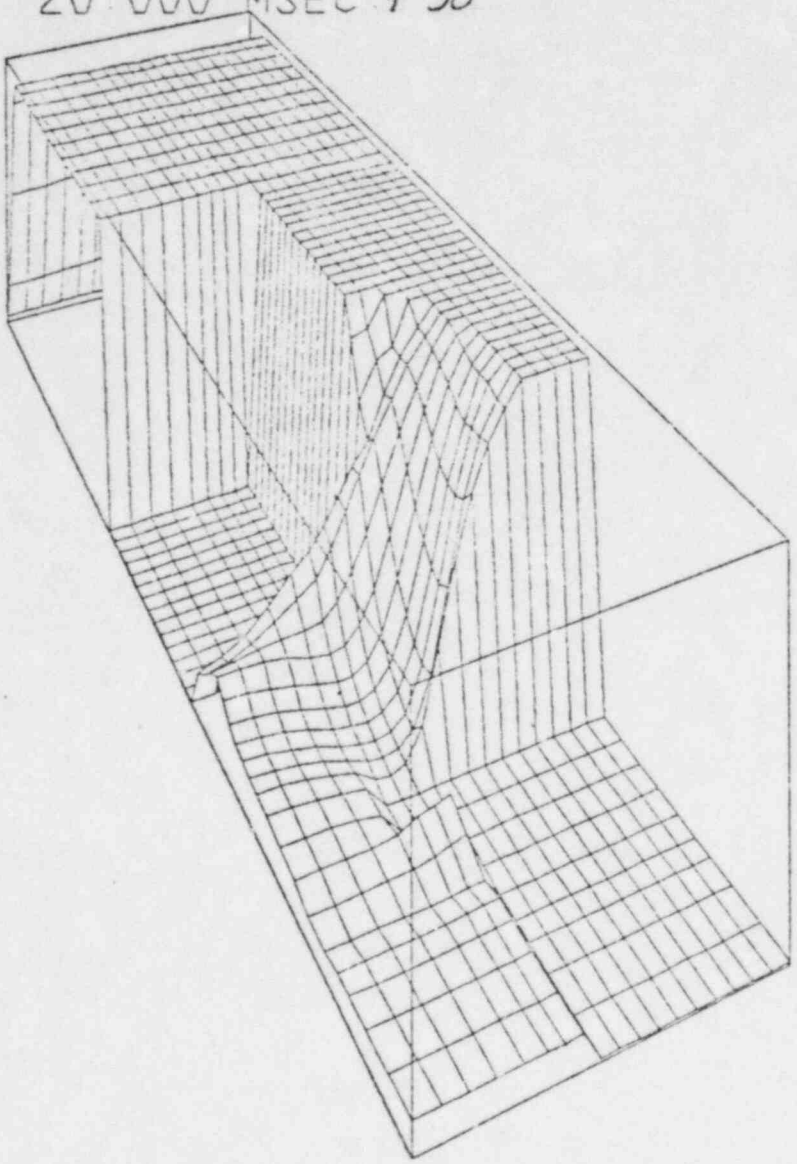

VOLUME FRACTION OF LIQUID
MINIMUM = 7 84014E-04 MAXIMUM = 9 94051E-01

Fig 17

TIME 26.000 MSEC + 50

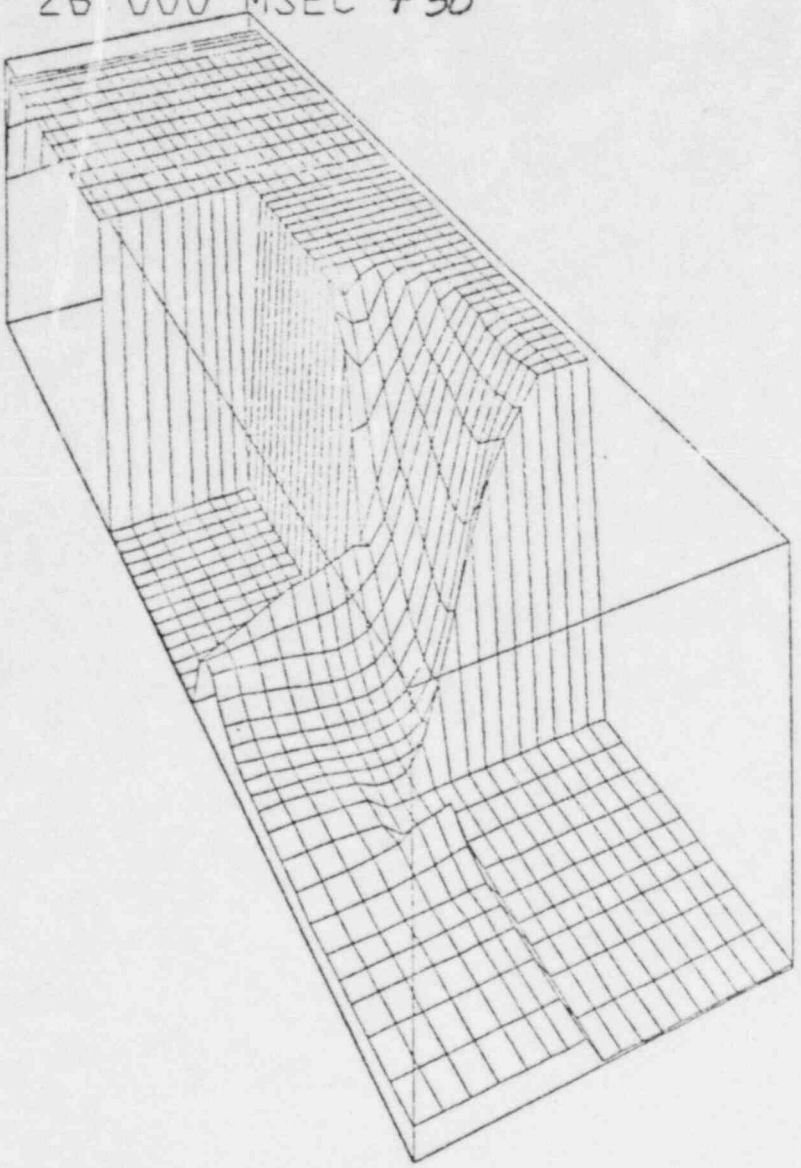

VOLUME FRACTION OF LIQUID
MINIMUM = 7.84014E-04 MAXIMUM = 9.94051E-01

Fig 18

TIME 28.000 MSEC +50

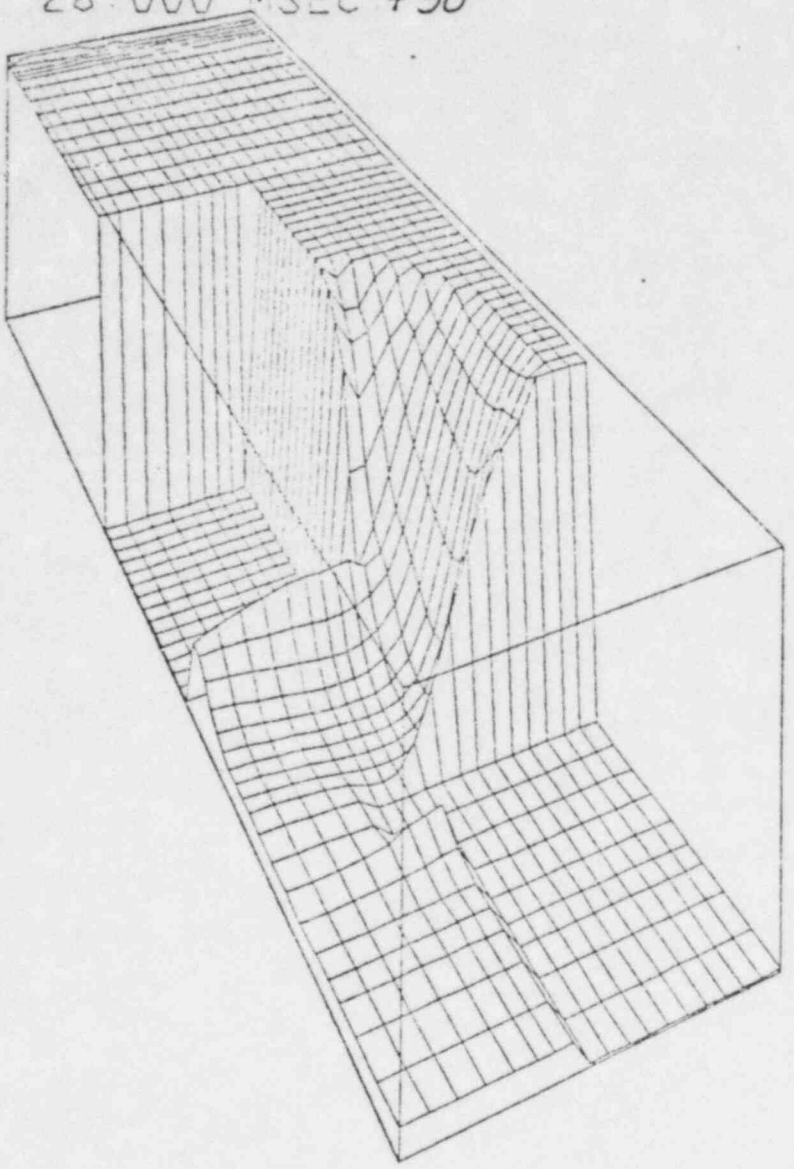

VOLUME FRACTION OF LIQUID
MINIMUM = 7.84014E-04 MAXIMUM = 9.94051E-01

Fig 19

TIME 000 MSEC +50

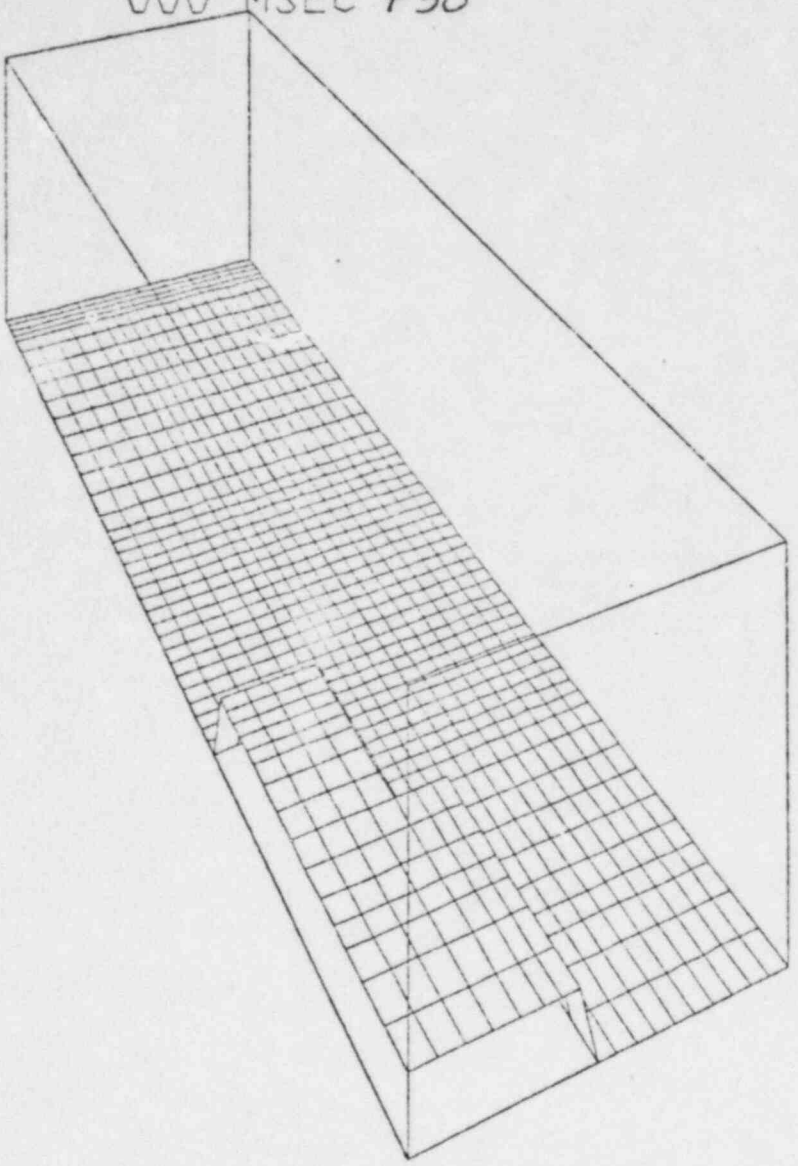

PRESSURE
MINIMUM = 2 68947E+04 MAXIMUM = 1 22011E+08

Fig 20

TIME 10 000 MSEC + 50

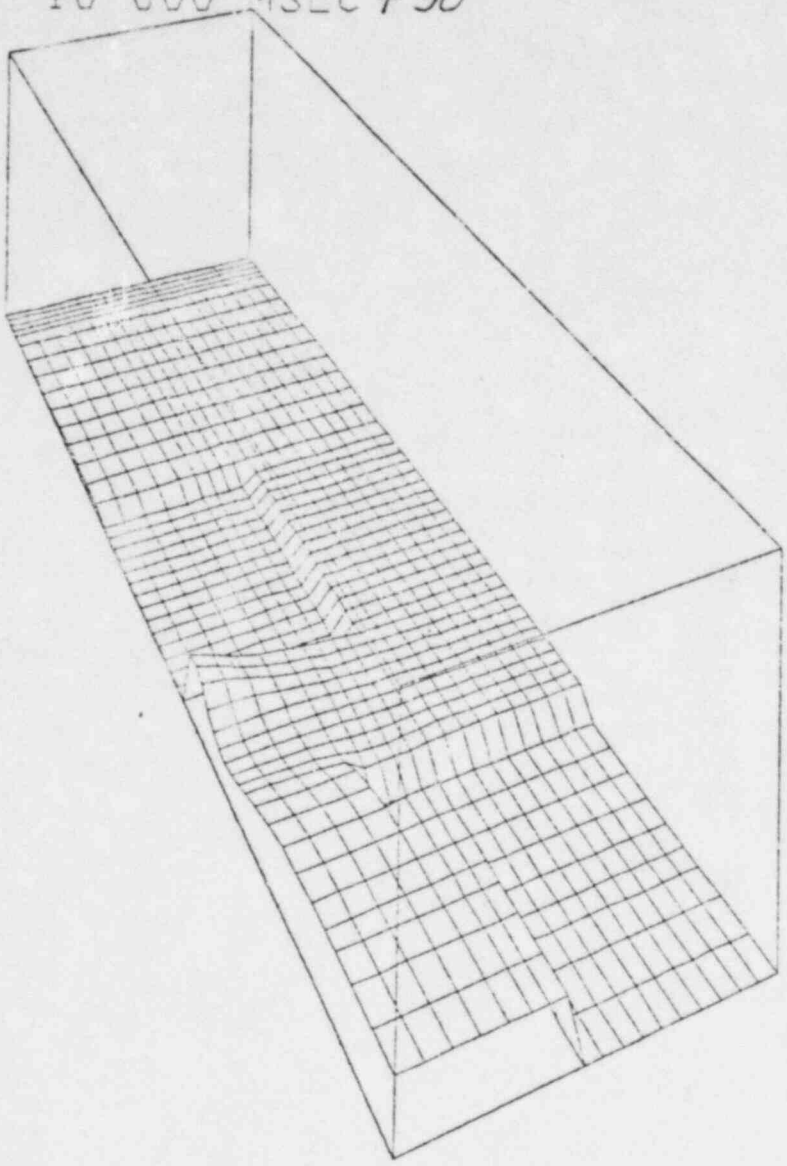

PRESSURE
MINIMUM = 2 68947E+04 MAXIMUM = 1 22011E+08

Fig 21

TIME 20 000 MSEC + 50

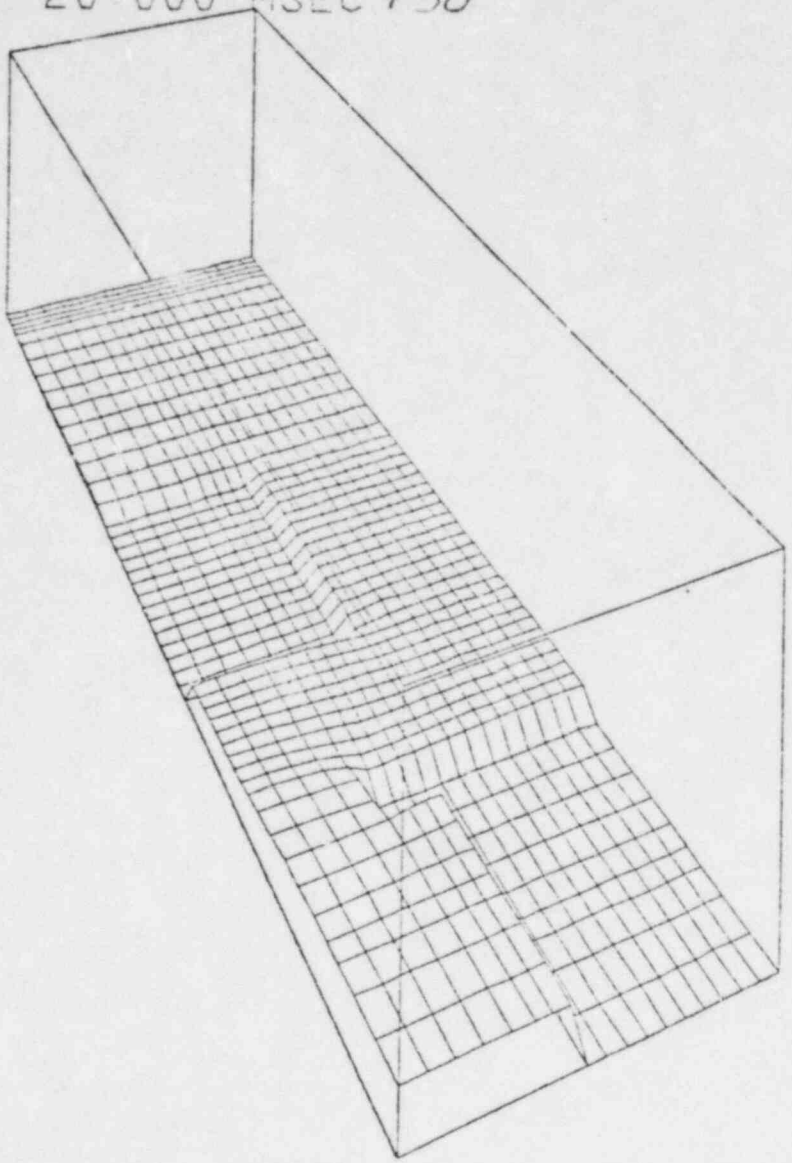

PRESSURE
MINIMUM = 2 68947E+04 MAXIMUM = 1 22011E+03

Fig 22

TIME 26 000 MSEC +50

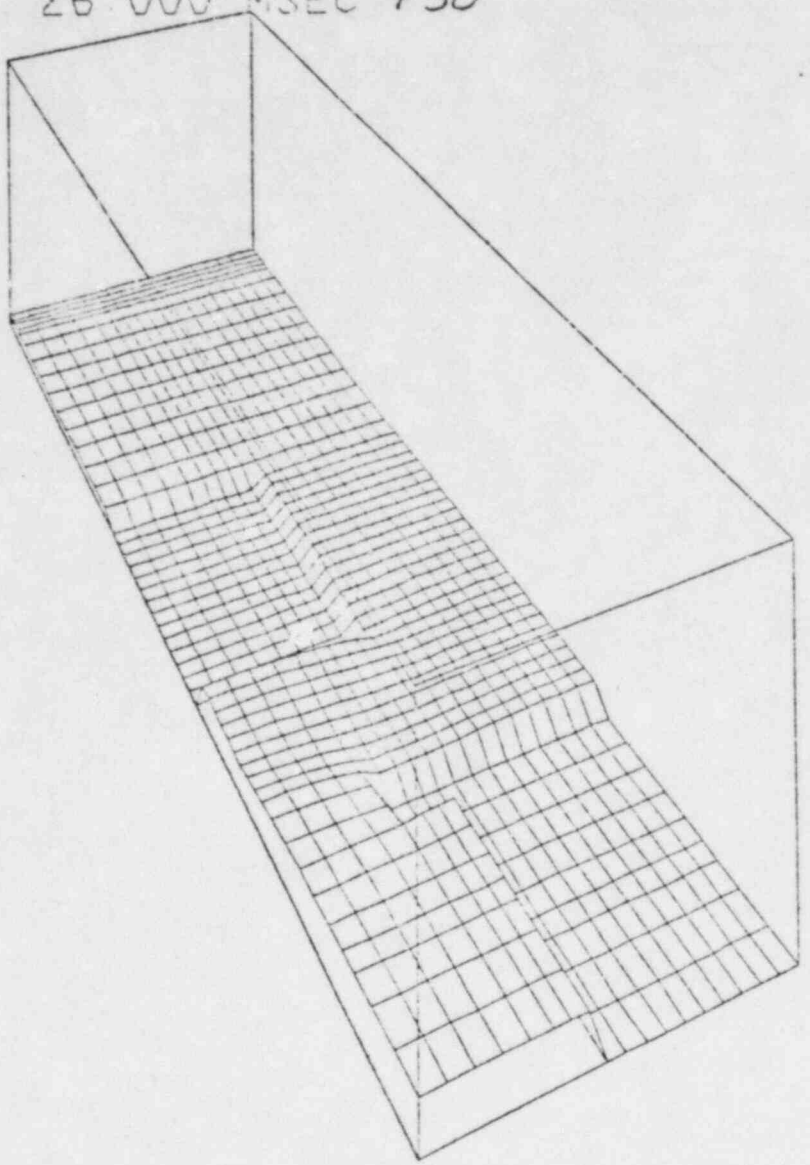

PRESSURE
MINIMUM = 2 68947E+04 MAXIMUM = 1 22011E+08

Fig 23

TIME 28 000 MSEC +50

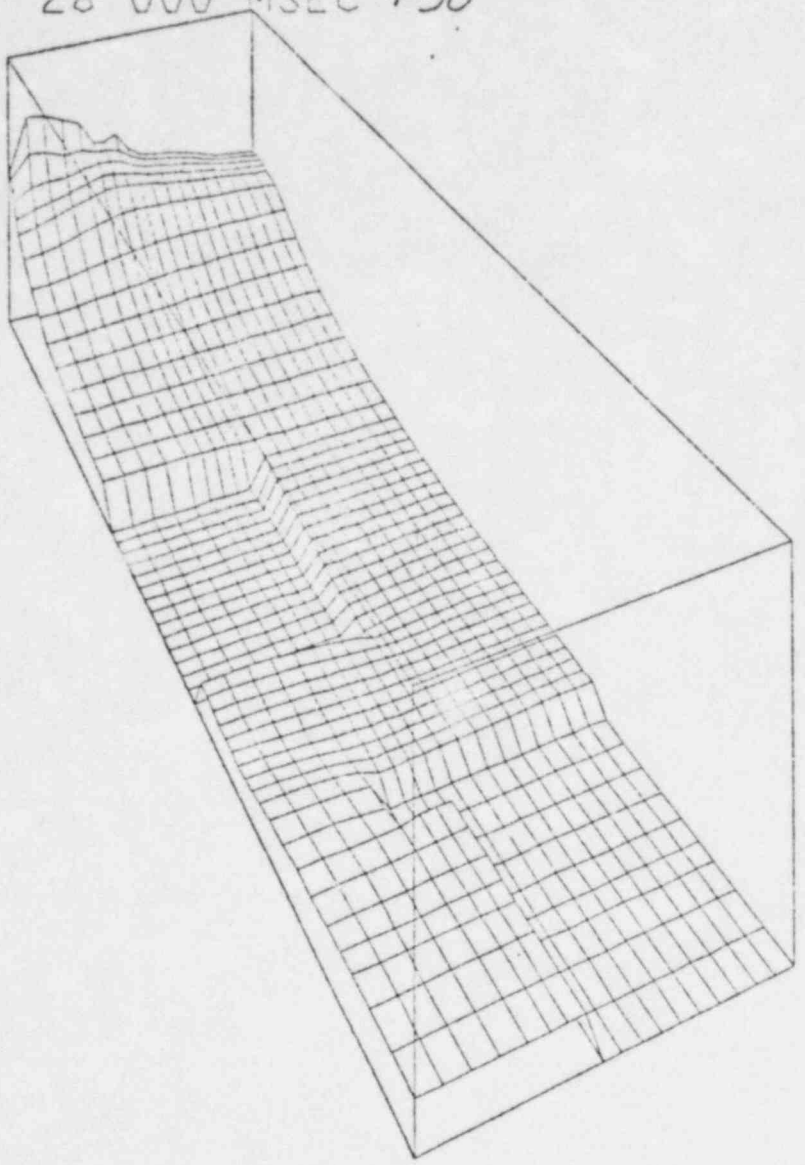

PRESSURE
MINIMUM = 2 68947E+04 MAXIMUM = 1 22011E+03

Fig 24

TIME 30 000 MSEC +50

TIME

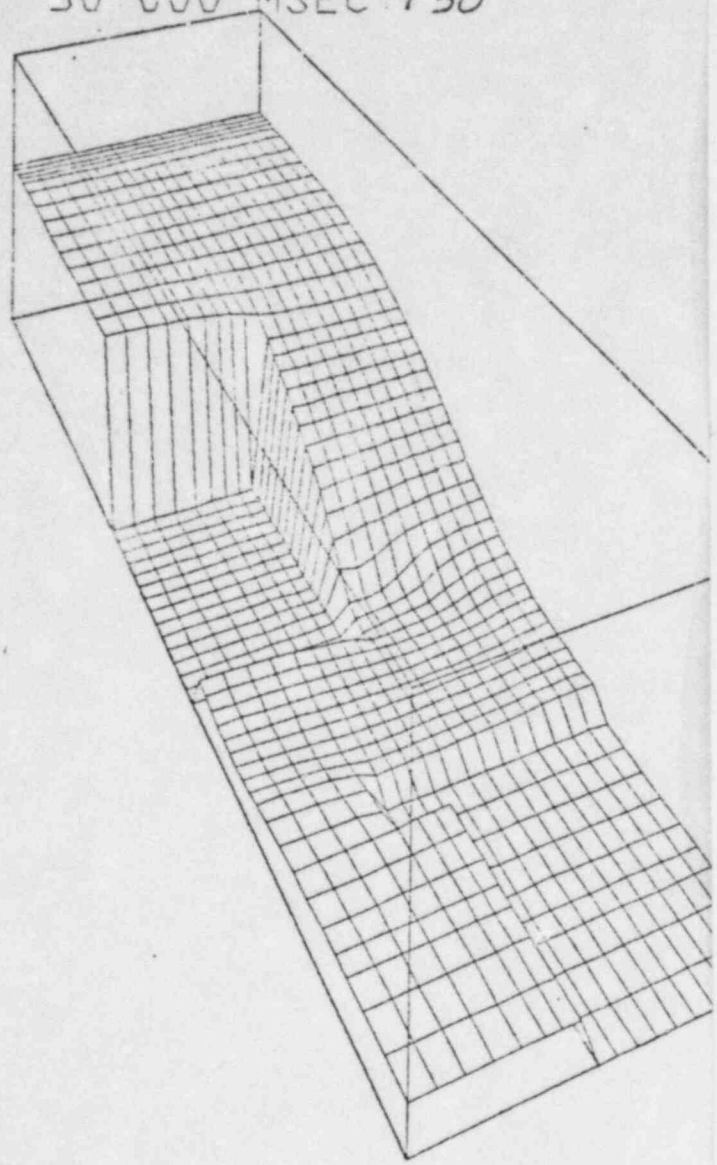

PRESSURE
MINIMUM = 2 68947E+04 MAXIMUM = 1 2201

RADIAL
MINIM

Fig 25

TIME 30 000 MSEC +50

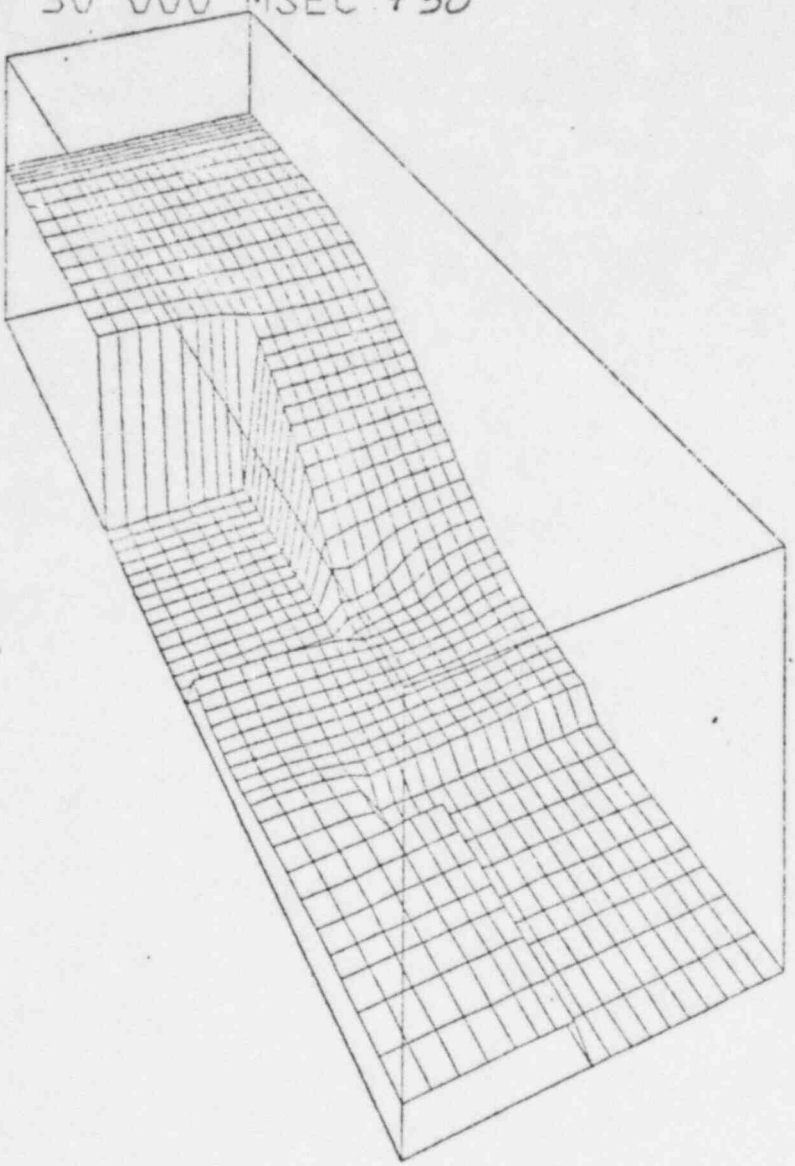

PRESSURE
MINIMUM = 2 68947E+04 MAXIMUM = 1 22011E+08

Fig 25

TIME 10 000 MSEC +50

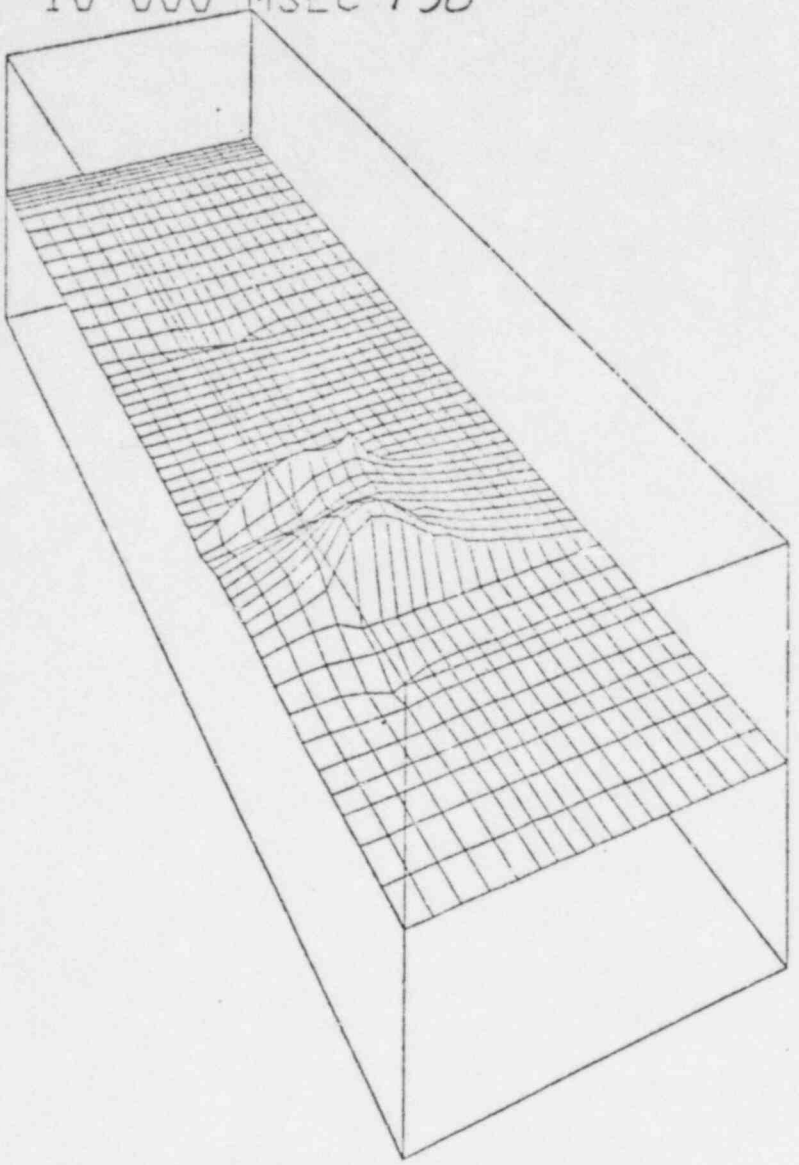

RADIAL VELOCITY OF LIQUID
MINIMUM = -1 18355E+02 MAXIMUM = 1 26921E+02

Fig 26

TIME 20.000 MSEC +50

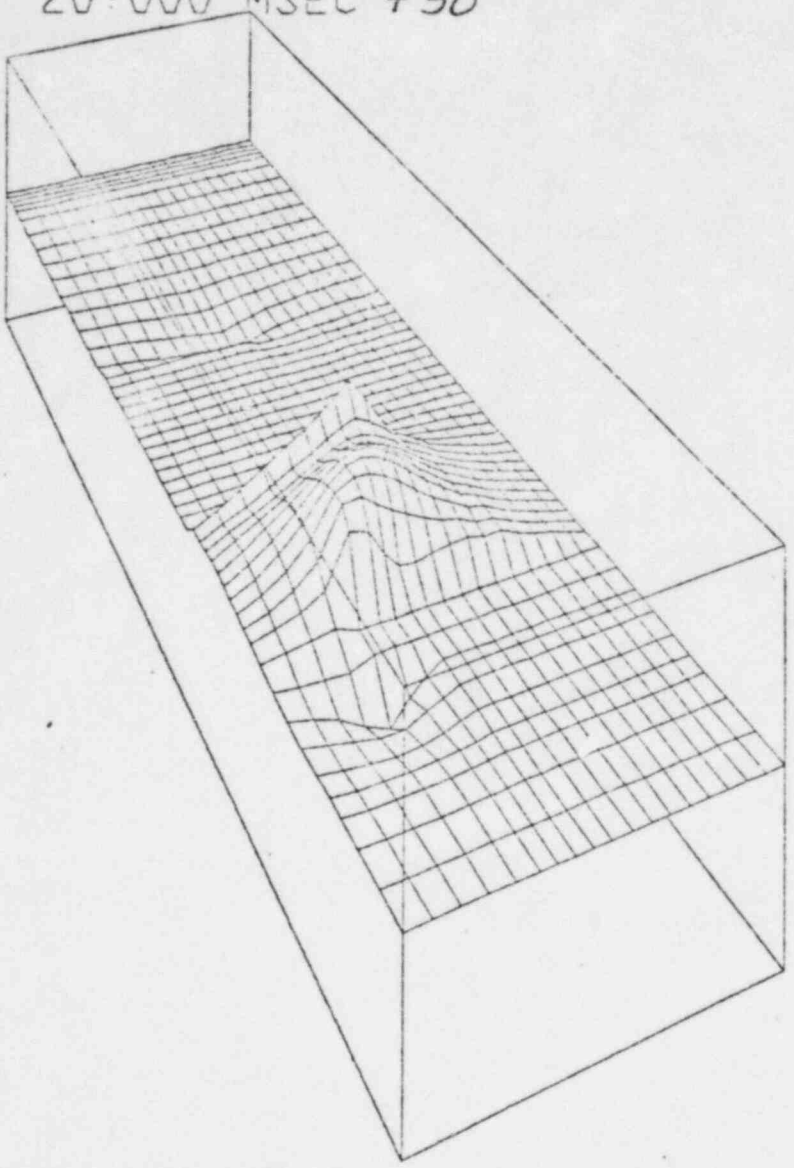

RADIAL VELOCITY OF LIQUID
MINIMUM = -1 18355E+02 MAXIMUM = 1 26921E+02

Fig 27

TIME 28.000 MSEC +50

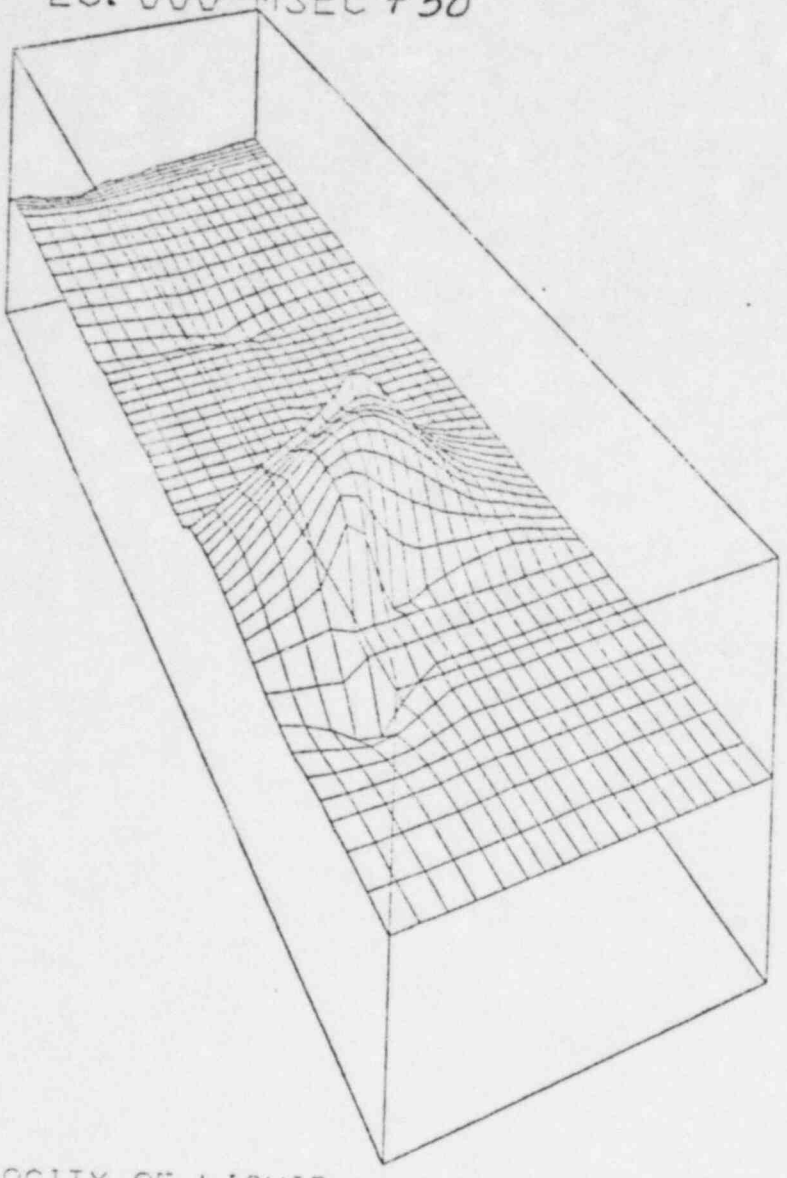

RADIAL VELOCITY OF LIQUID
MINIMUM = -1 18355E+02 MAXIMUM = 1 26921E+02

RA
M

Fig 28

TIME 10.000 MSEC +50

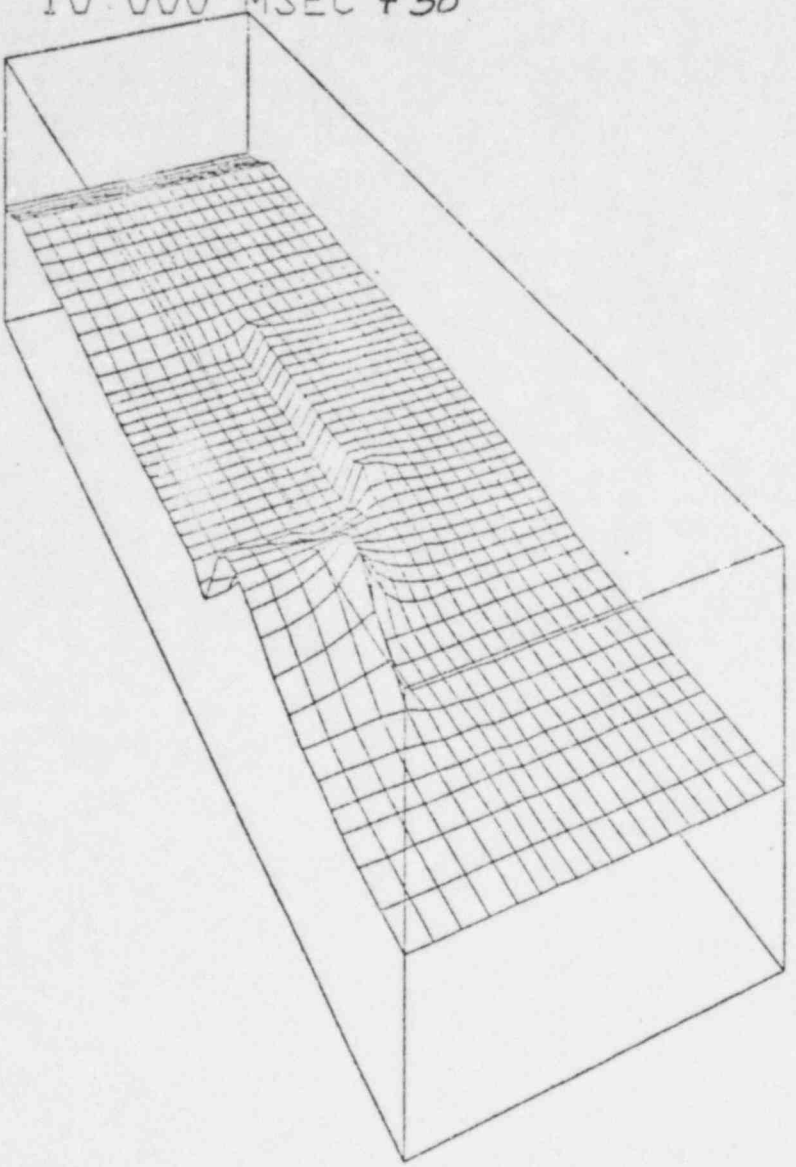

AXIAL VELOCITY OF LIQUID
MINIMUM = -1.21025E+02 MAXIMUM = 1.56316E+02

Fig 29

TIME 20.000 MSEC + 50

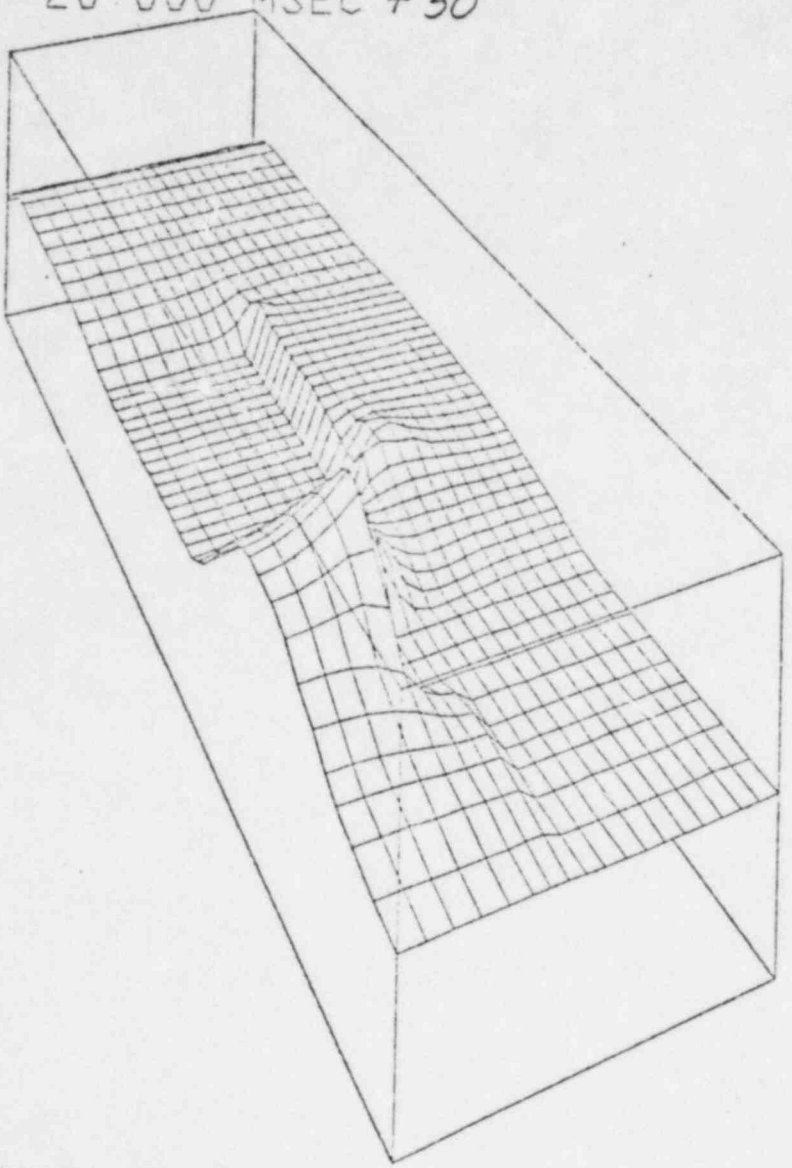

AXIAL VELOCITY OF LIQUID
MINIMUM = -1 21026E+02 MAXIMUM = 1 55316E+02

Fig 30

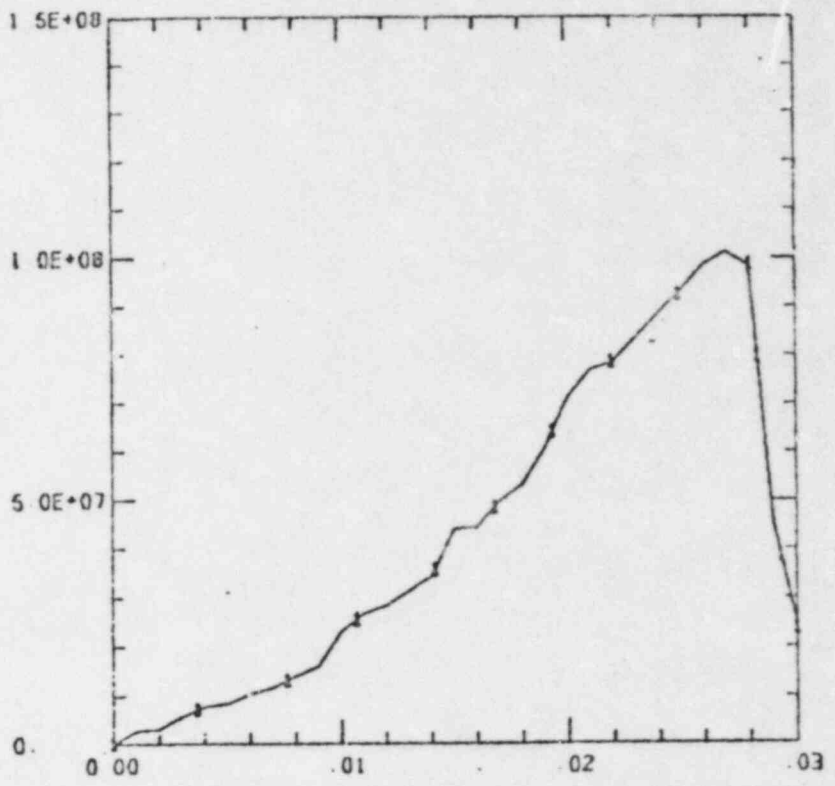

GROUP SUMS AXIAL KENITIC OF ALL LIQUIDS
5*(RLF1+RLF2+RLB3+RLB4+RLB8)*VL**2
MINIMUM VALUE = 0 MAXIMUM VALUE = 1.01E+08

Fig 32

CII.2

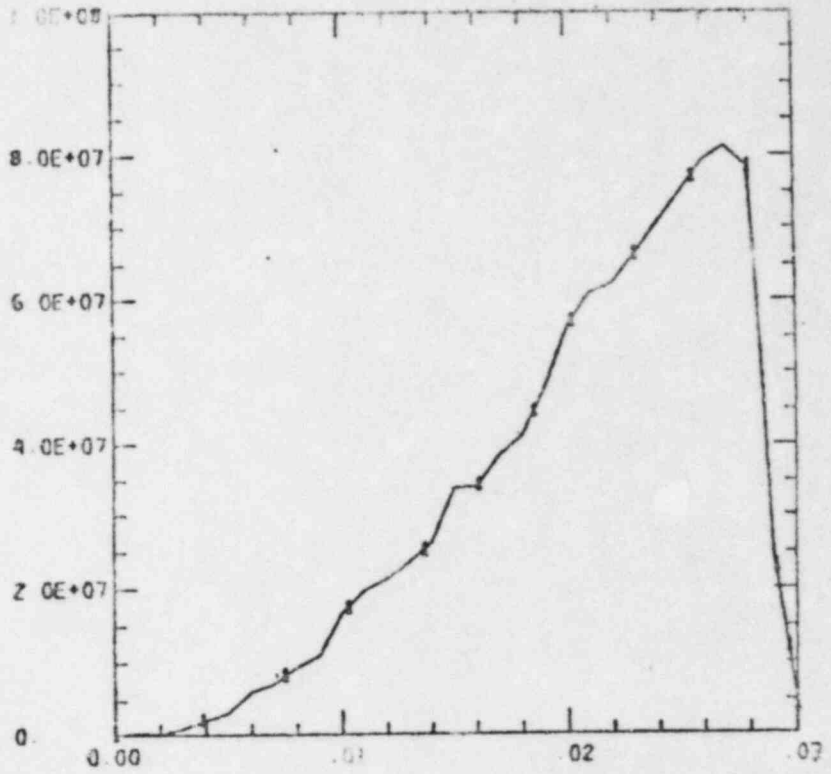

TIME (S)

GROUP SUMS AXIAL KINETIC ENERGY OF LIQUID SODIUM
.5*RLB4*VL**2
MINIMUM VALUE = 0 MAXIMUM VALUE = 8.12E+07

Fig 33

C.II.2

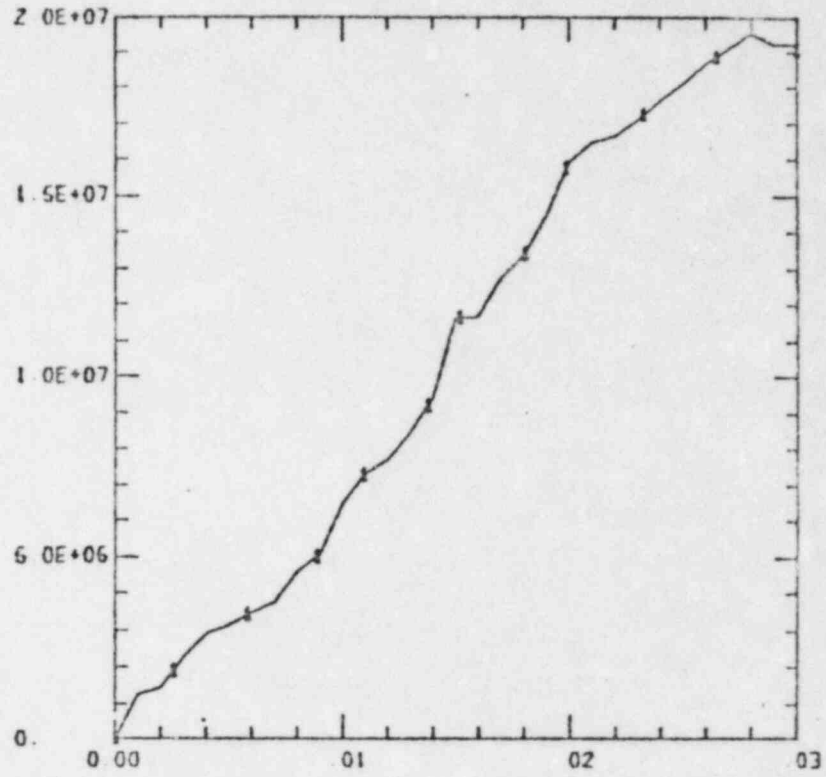

GROUP SUMS RADIAL KENITIC OF ALL LIQUIDS
5*(RLF1+RLF2+RLB3+RLB4+RLB8)*UL**2
MINIMUM VALUE = 0 MAXIMUM VALUE = 1.96E+07

Fig 34

C.II.2

SI07

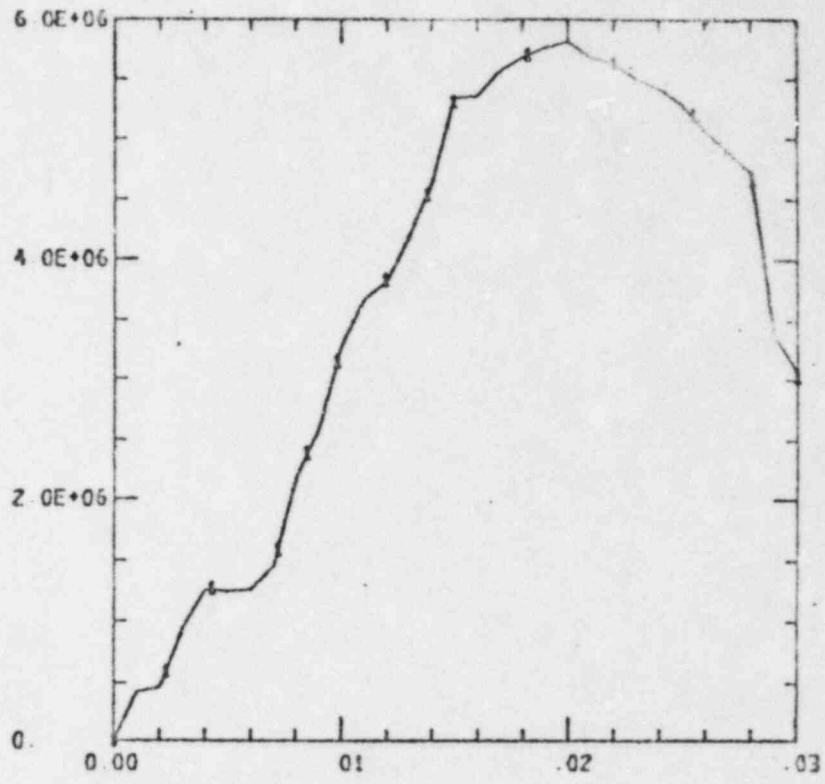

GROUP SUMS RADIAL KINETIC ENERGY OF LIQUID SODIU
.5*RLB4*UL**2
MINIMUM VALUE = 0. MAXIMUM VALUE = 5.81E+06

Fig 35

CII.2

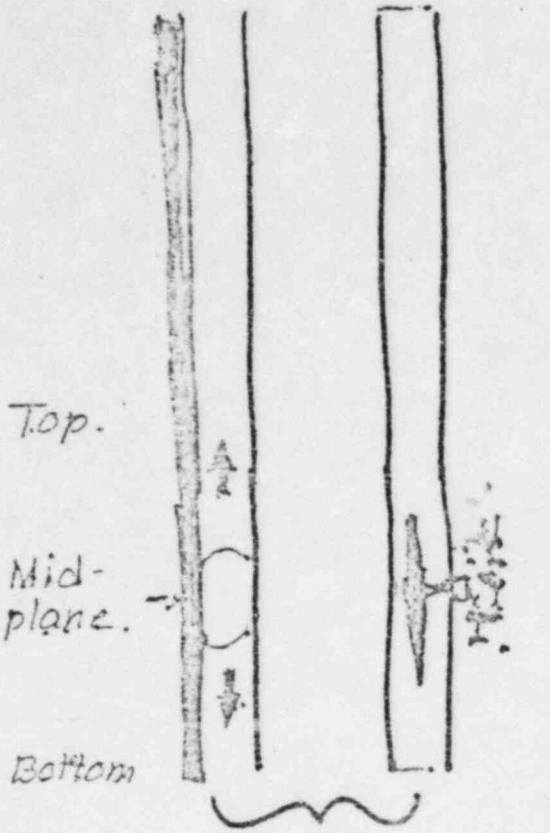

Fig 1

2.

Fig 2

~~III(c)-2~~ (CONT'D)

COMPARISONS OF HEV-1D & -2D at 100% and 85% Power with SAS

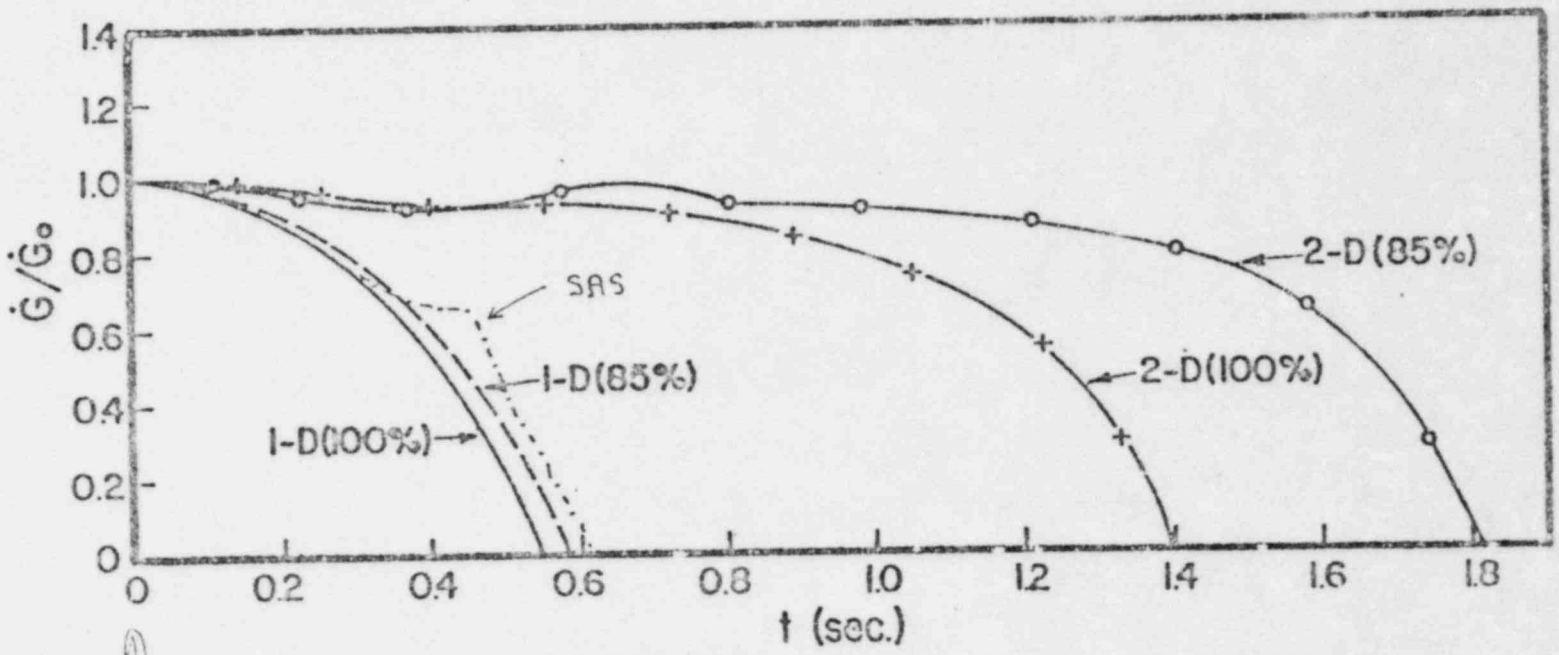

↑ boiling inception

Fig 3 (Section) II.B

~~III (6) 2~~ TIMING & RATE OF VOIDING

HEV-2D Pretest Predictions of OPERA-15 Inlet Flow Transient.

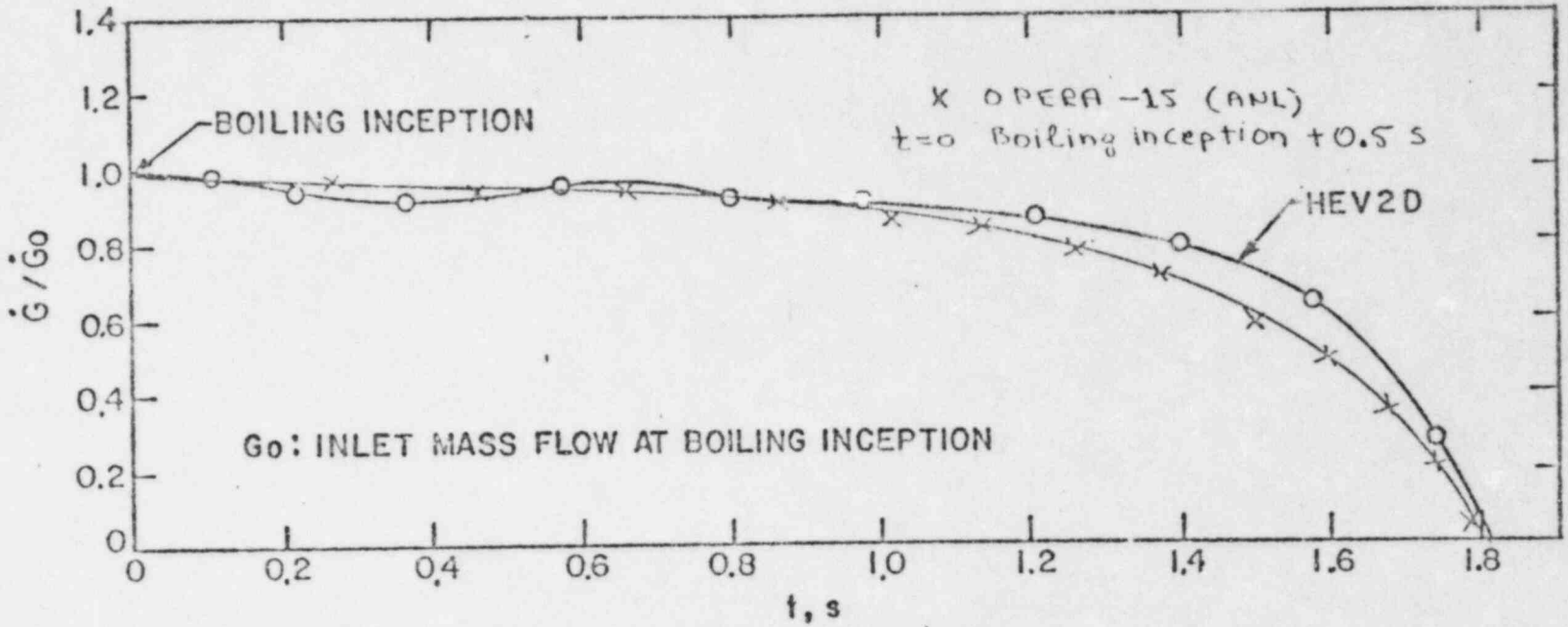

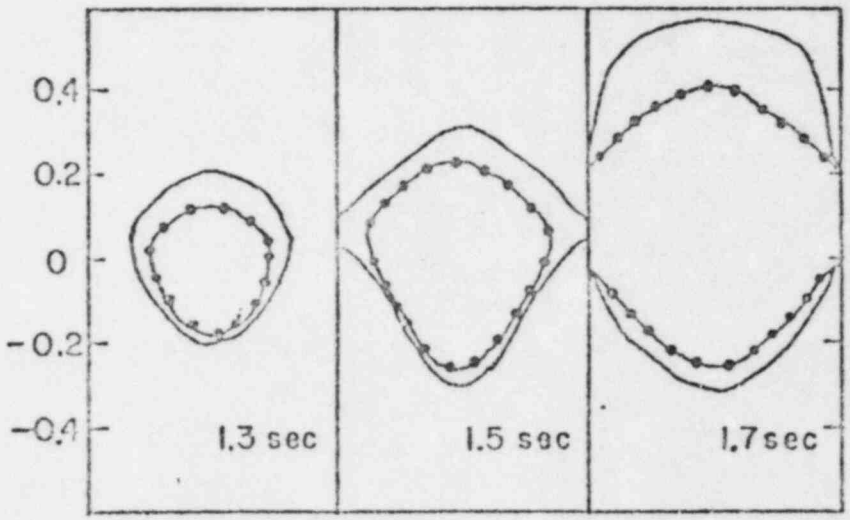

OPERA-15
1.6 s

10% VOID FRACTION
75% VOID FRACTION

Time to reach 1-D behavior

II.C.3

Fig 4

~~III-(c)-4~~ QUANTIFICATION OF RELOCATION TRENDS

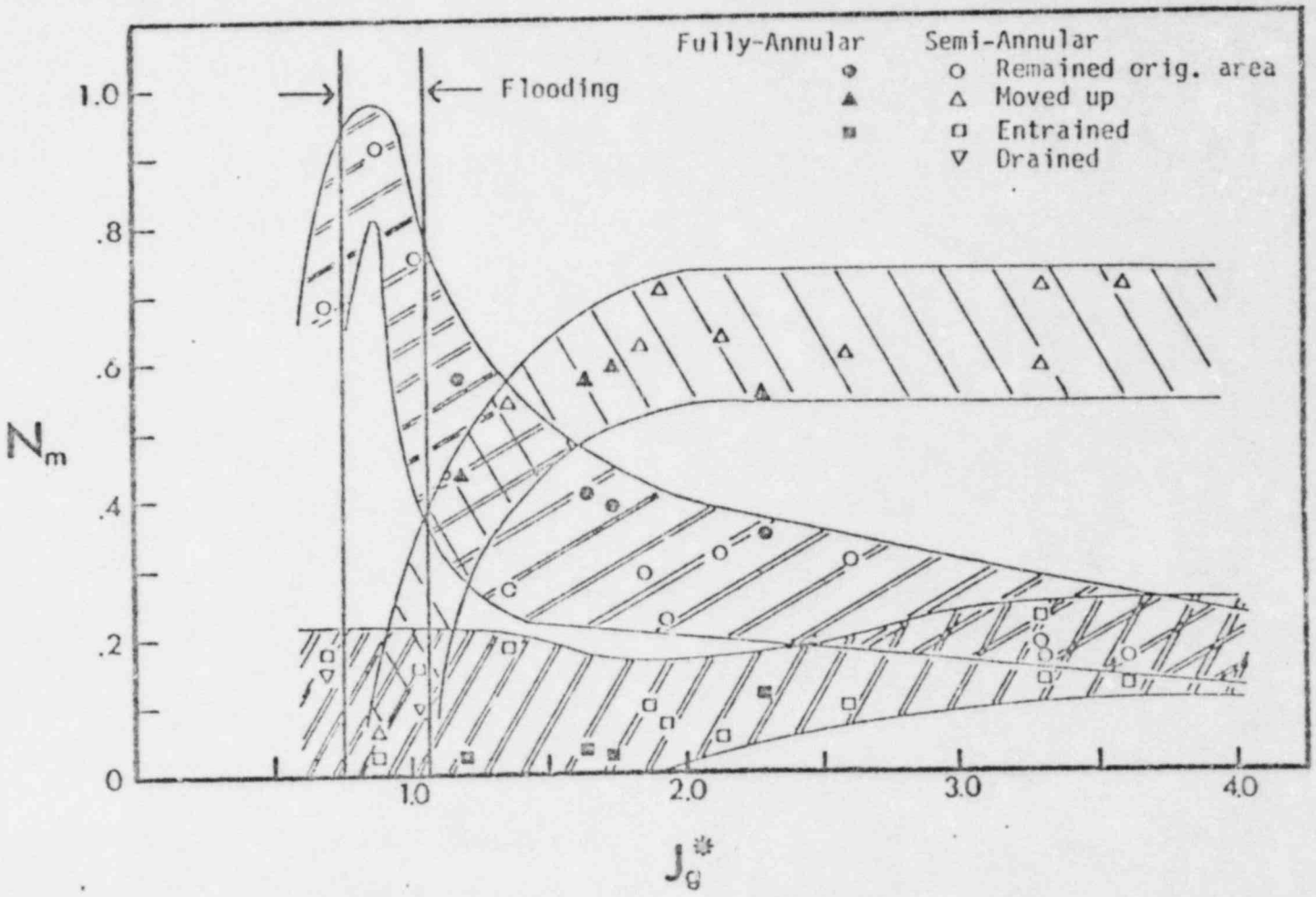

4.5

Fig 3b

Define J_g^*

~~III (C) 1~~ (CONT'D) QUANTIFY RELOCATION RATES

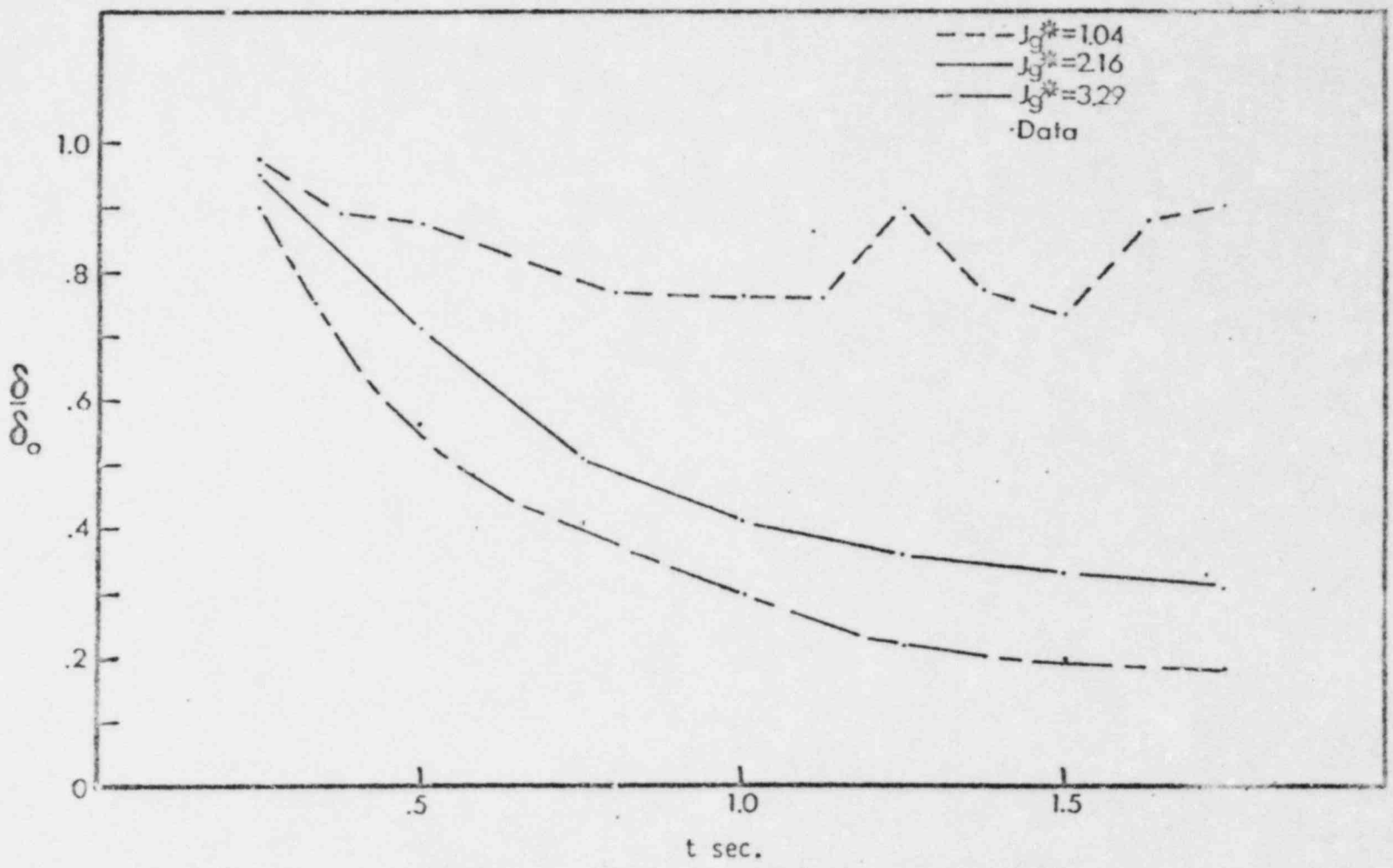

II.3

Fig 6

IN-PILE TEST PARAMETERS

R-SERIES (TREAT)	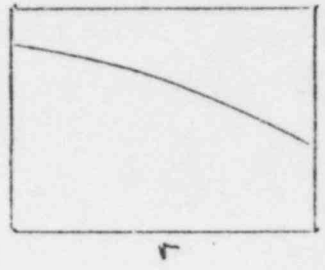	$\check{A} \sim 0.4$	$\Delta P \sim 11.5$ psi $\Delta V \sim \pm 0.9$ m/s
P-SERIES (SLSF)	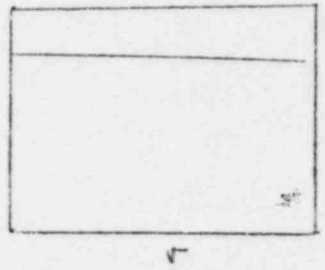	$\check{A} \sim 1$	$\Delta P \sim 16$ psi $\Delta V \sim \pm 1.61$ m/s
REACTOR (CRBR)	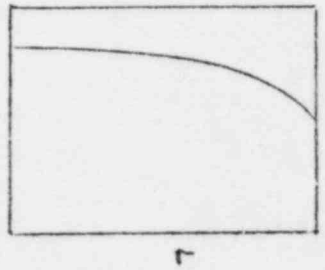	$\check{A} \sim 0.6$	$\Delta P \sim 15$ psi $\Delta V \sim \pm 1.3 - 2.4$ m/s

Fig

QUANTIFY INCOHERENCY EFFECTS

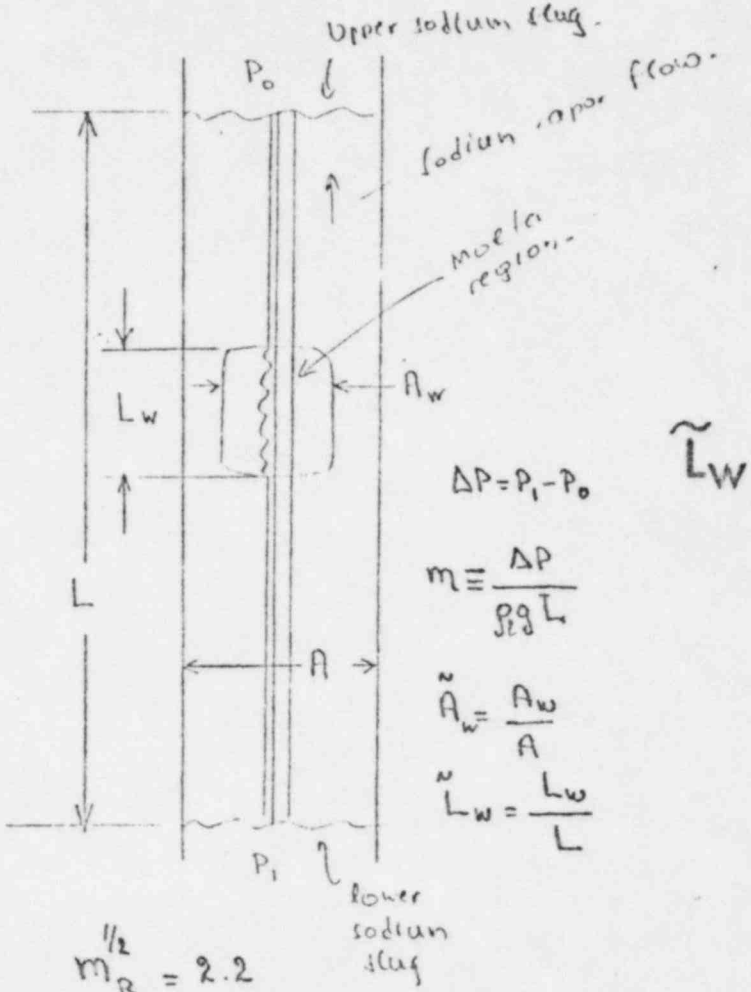

$$\Delta P = P_i - P_o$$

$$m \equiv \frac{\Delta P}{\rho_\ell g L}$$

$$\tilde{A}_w = \frac{A_w}{A}$$

$$\tilde{L}_w = \frac{L_w}{L}$$

$m_R^{1/2} = 2.2$

$m_P^{1/2} = 2.5$

$m_{Rec}^{1/2} = 1.9$

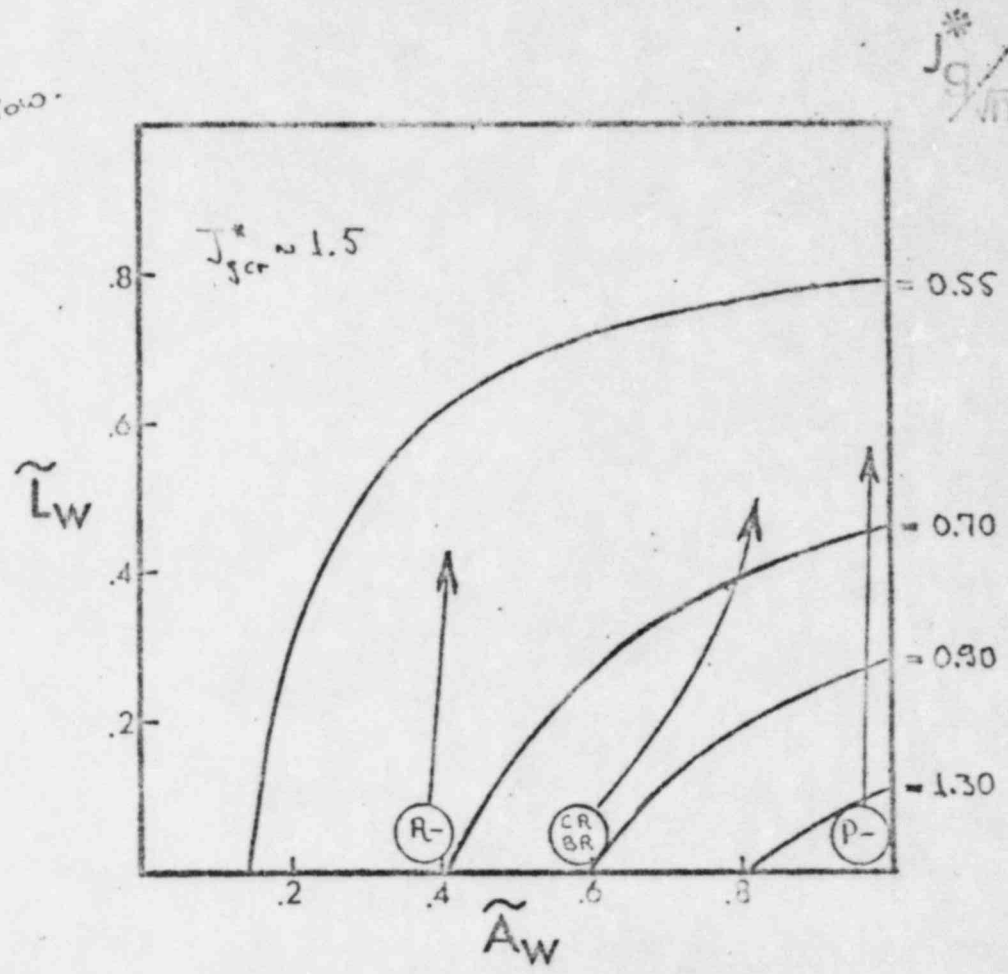

PLUS : CHUGGING RANDOMNESS.

II.3

Fig 9

EFFECT OF GAS BLOWDOWN ON $\dot{m}$.

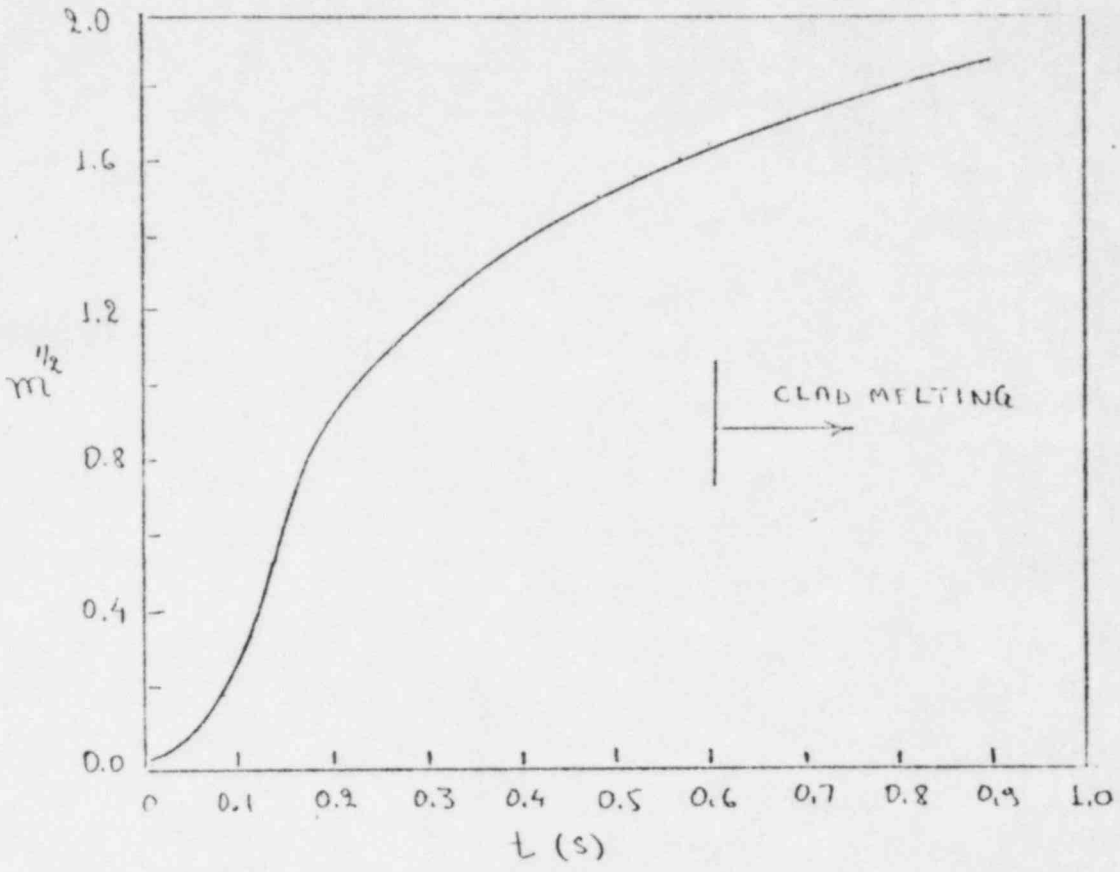

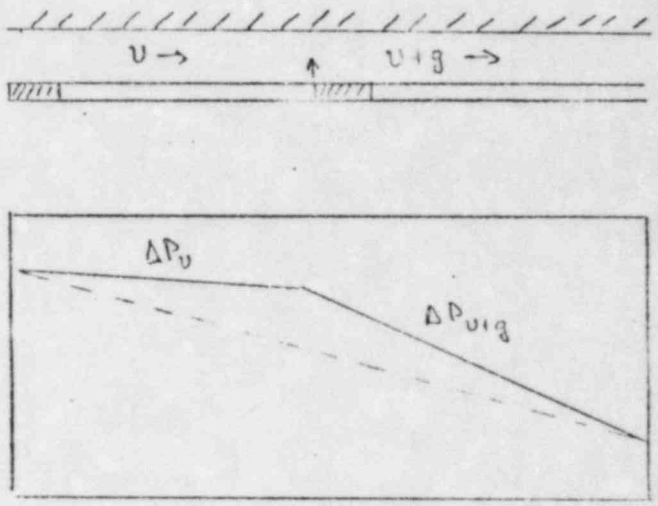

Fig 8

. At inlet of lead channel

II.3

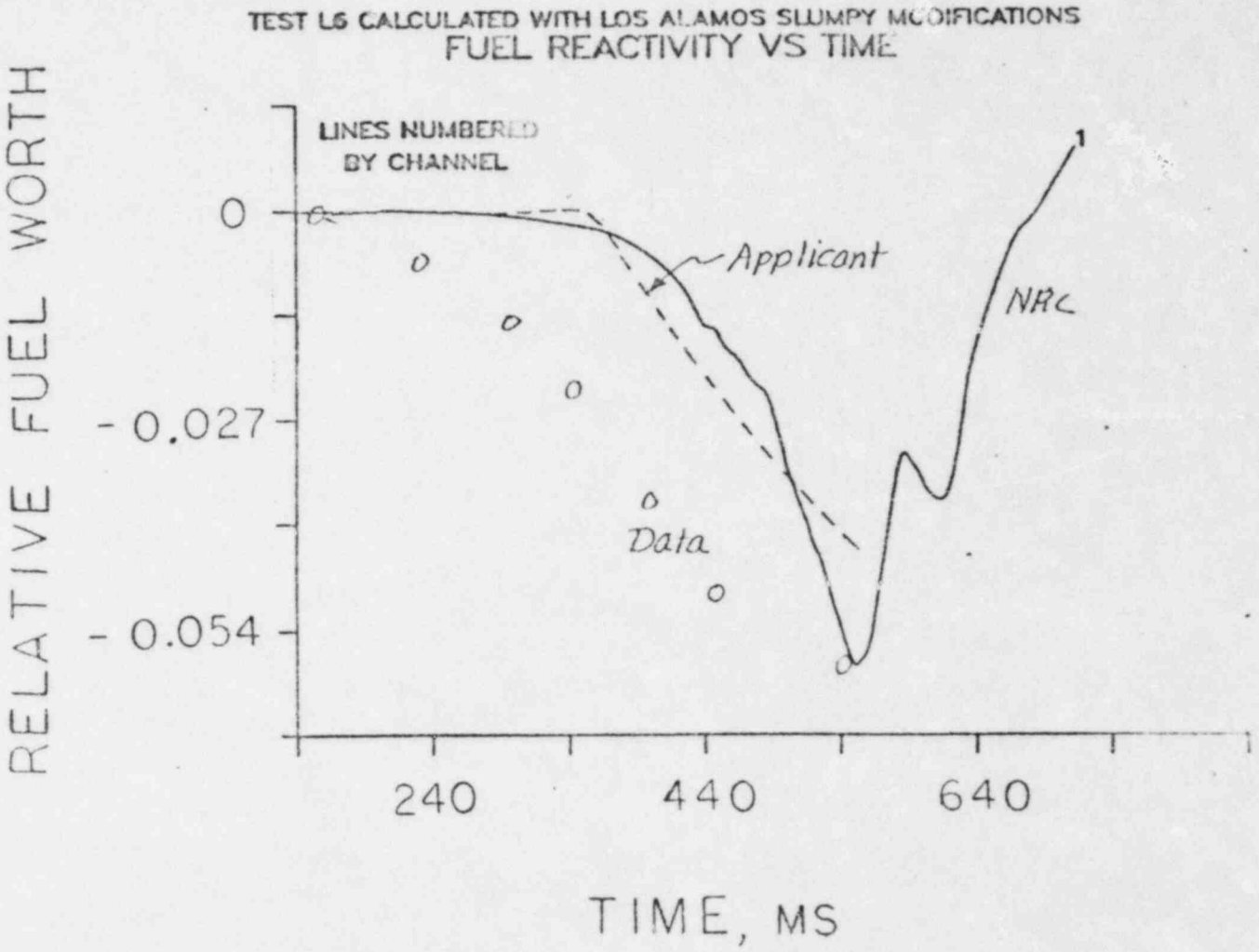
TEST L6 CALCULATED WITH LOS ALAMOS SLUMPY MODIFICATIONS
FUEL REACTIVITY VS TIME
LINES NUMBERED BY CHANNEL
RELATIVE FUEL WORTH
0
- 0.027
- 0.054
Applicant
NRC
Data
1
240
440
640
TIME, MS

Fig 10

II.3

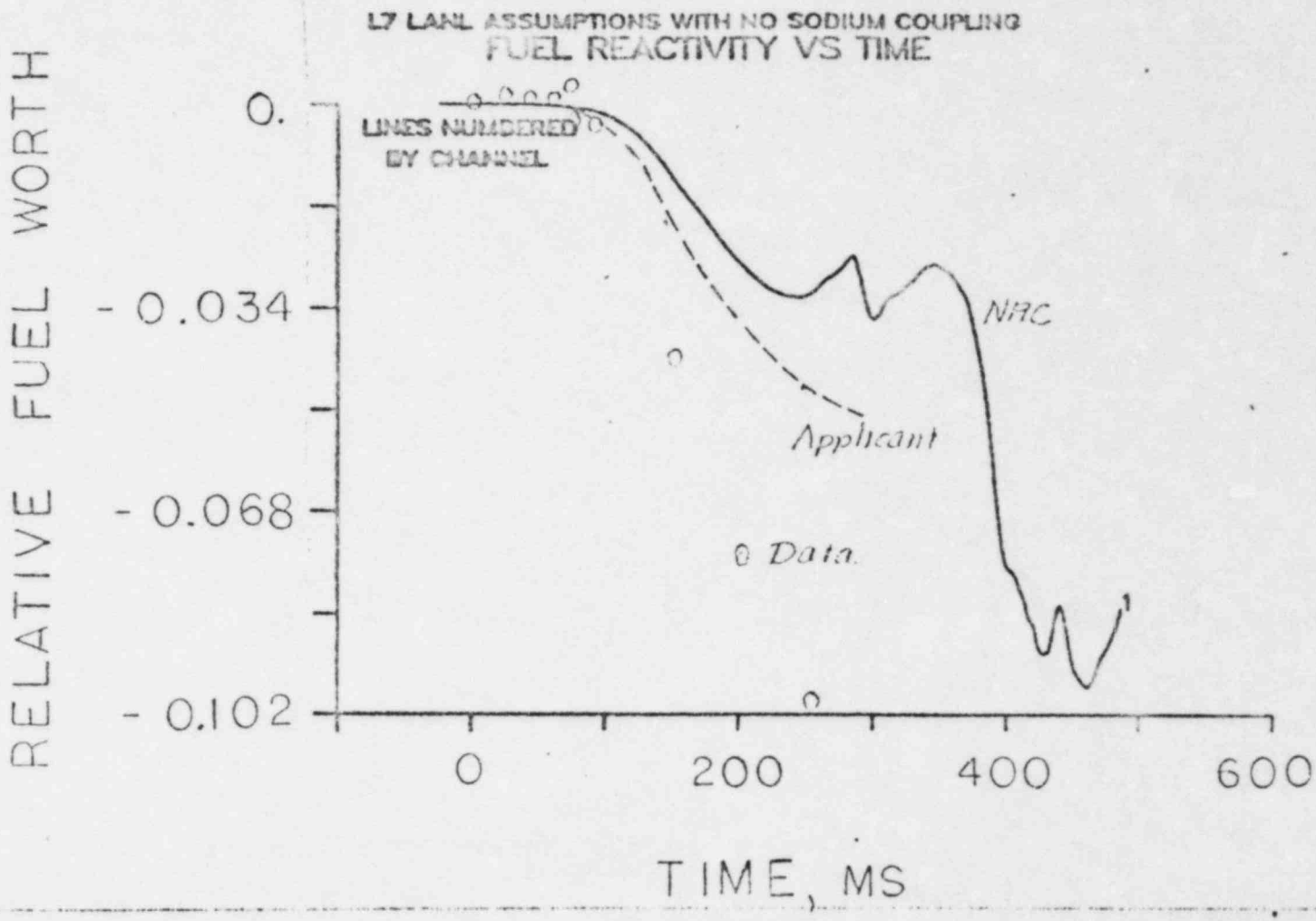
L7 LANL ASSUMPTIONS WITH NO SODIUM COUPLING
FUEL REACTIVITY VS TIME
LINES NUMBERED BY CHANNEL
NRC
Applicant
Data
RELATIVE FUEL WORTH
0.
- 0.034
- 0.068
- 0.102
0
200
400
600
TIME, MS

Fig II

FAST LOF EOC-4

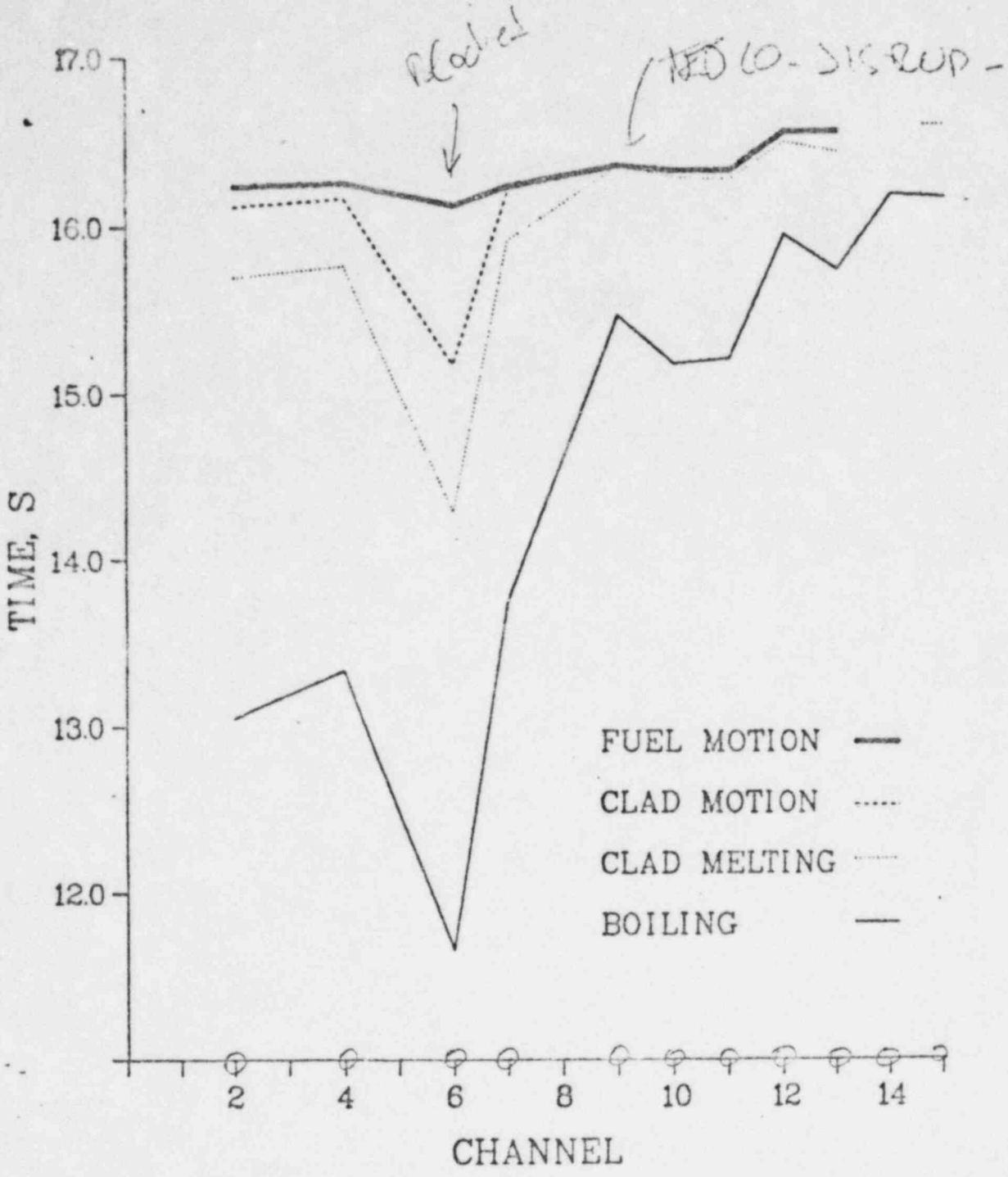

Fig 12

SLOW LOF EOC-4

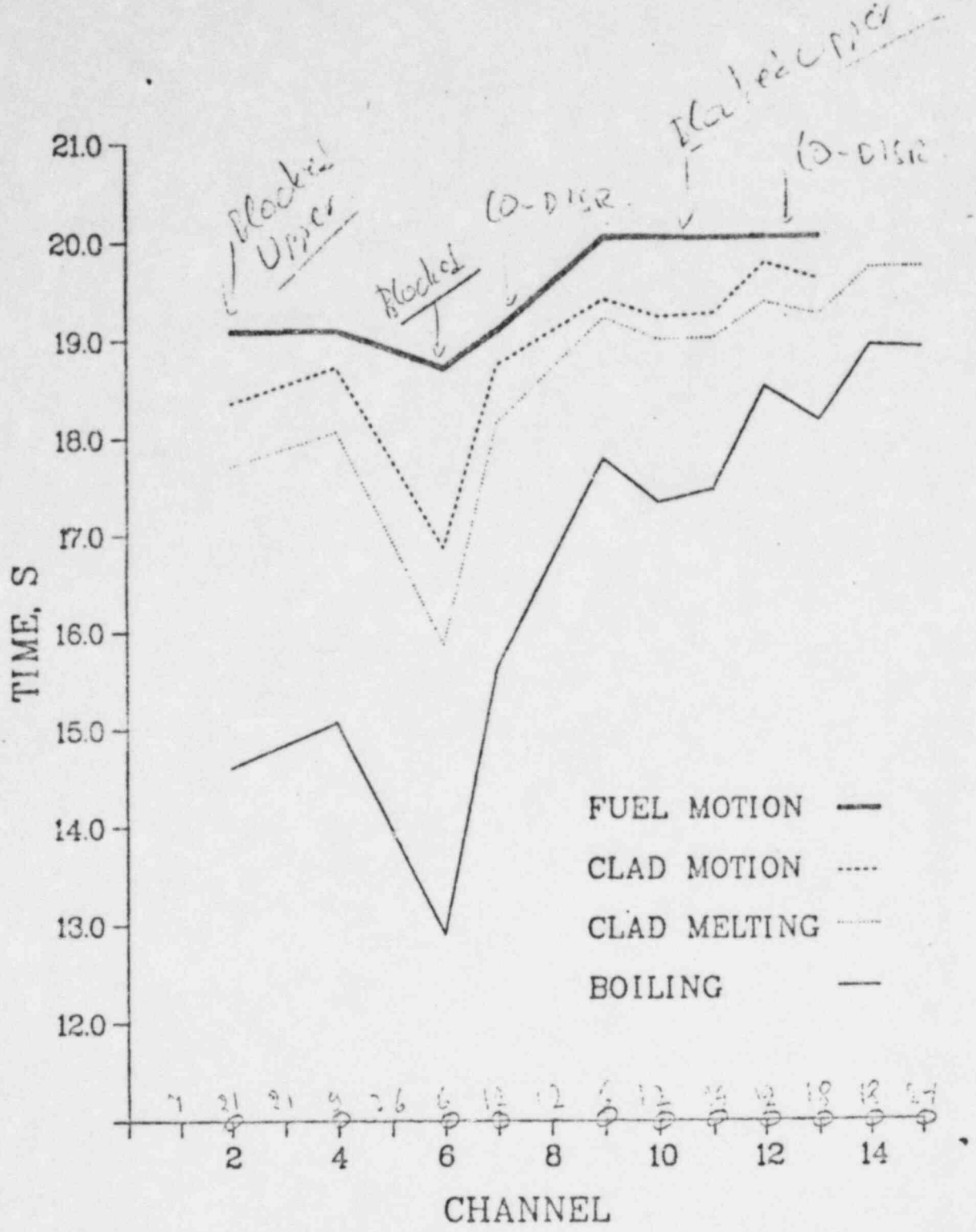

Fig 13

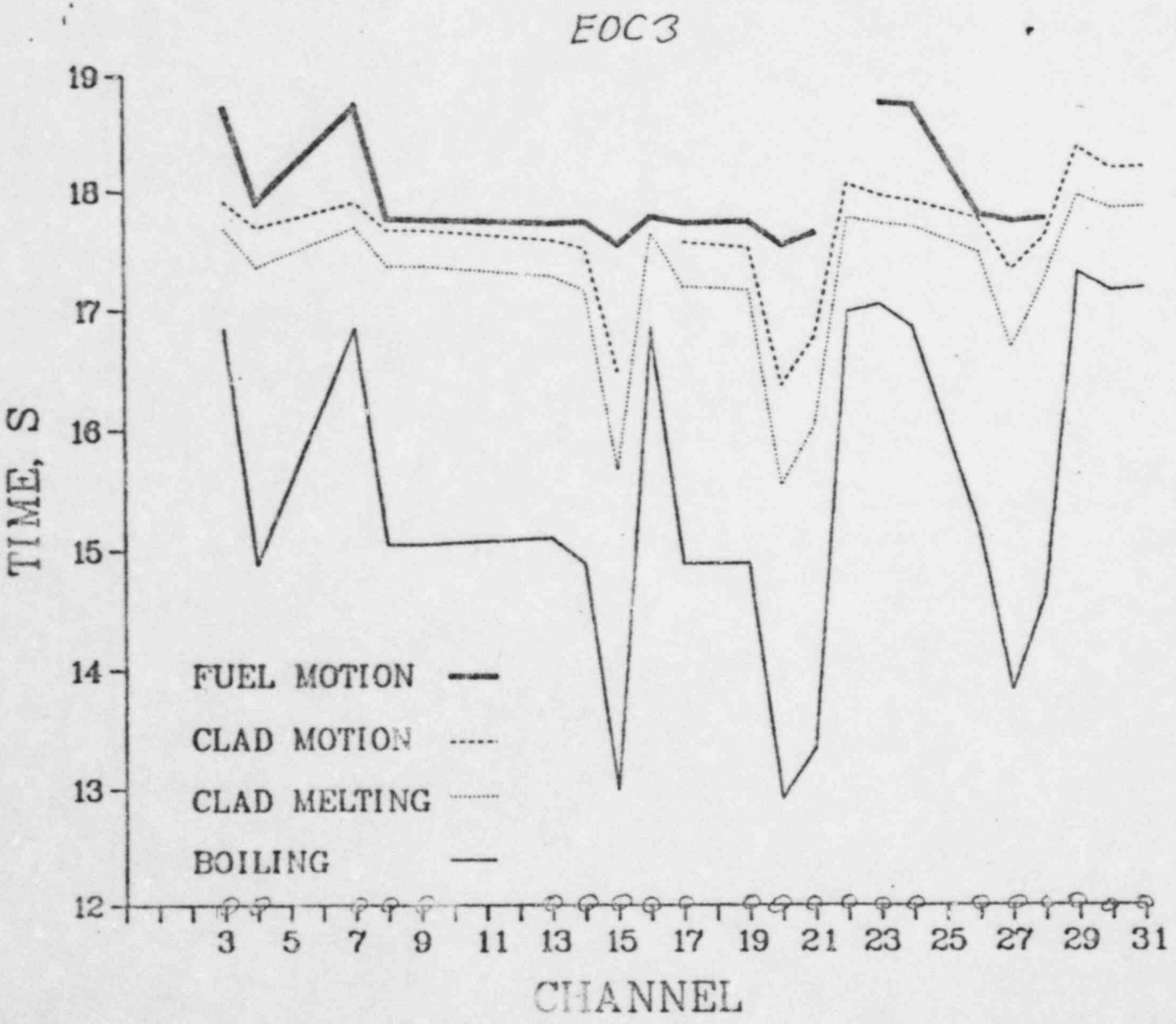
EOC3
TIME, S
19
18
17
16
15
14
13
12
FUEL MOTION
CLAD MOTION
CLAD MELTING
BOILING
3 5 7 9 11 13 15 17 19 21 23 25 27 29 31
CHANNEL

Fig 14

II.3

BOL

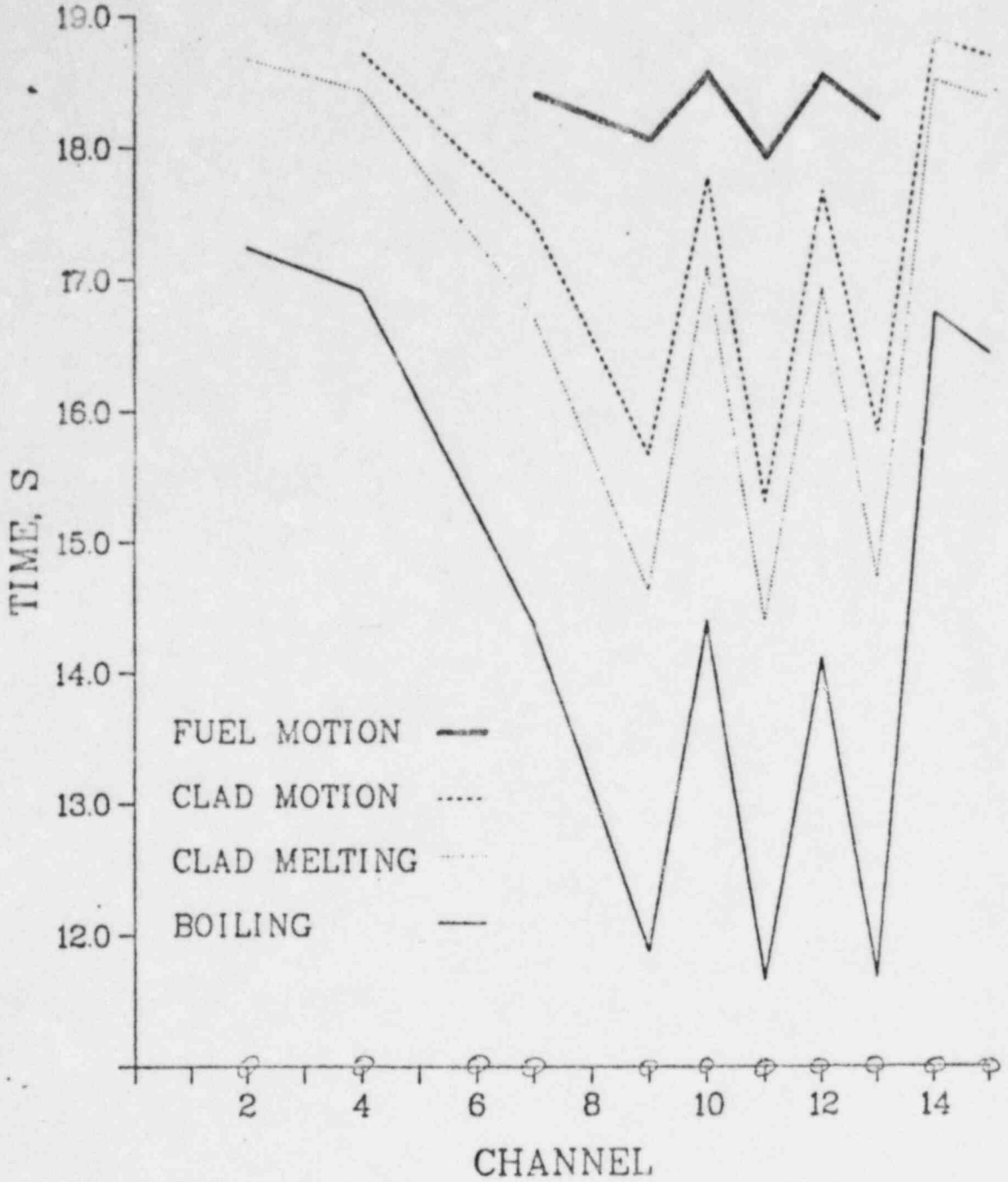

Fig 15

II.3

III(c).10 CO-DISRUPTION FOR CASE B.

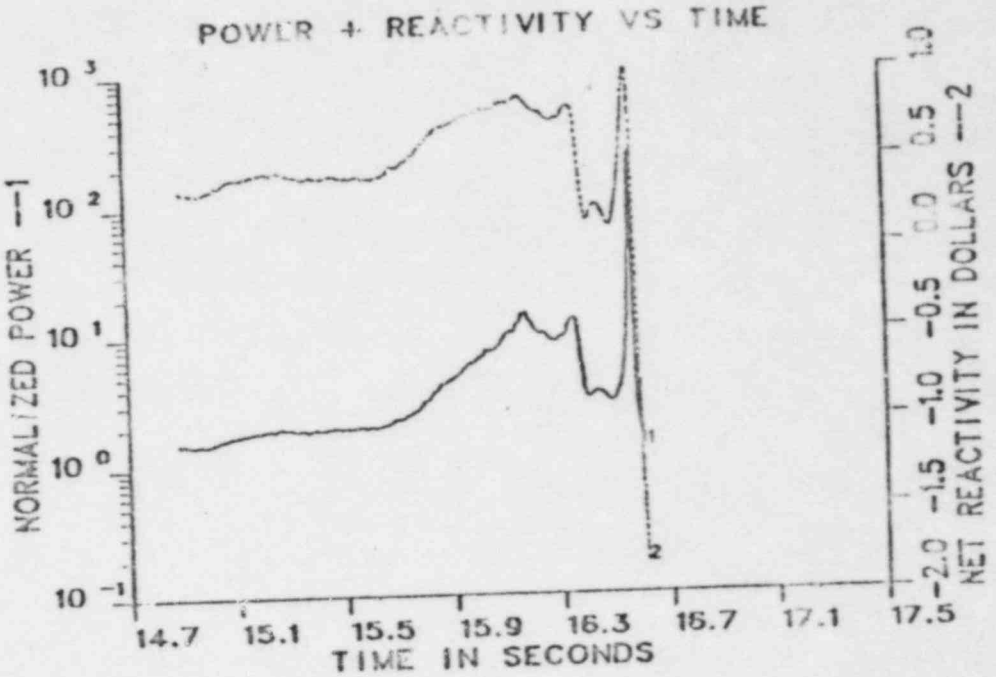

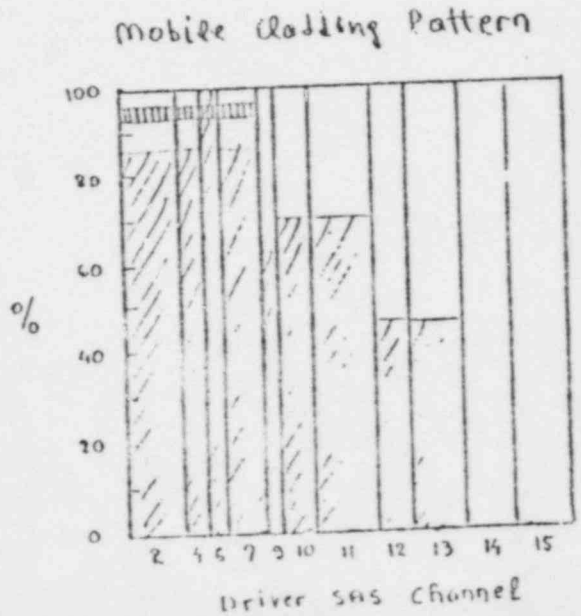

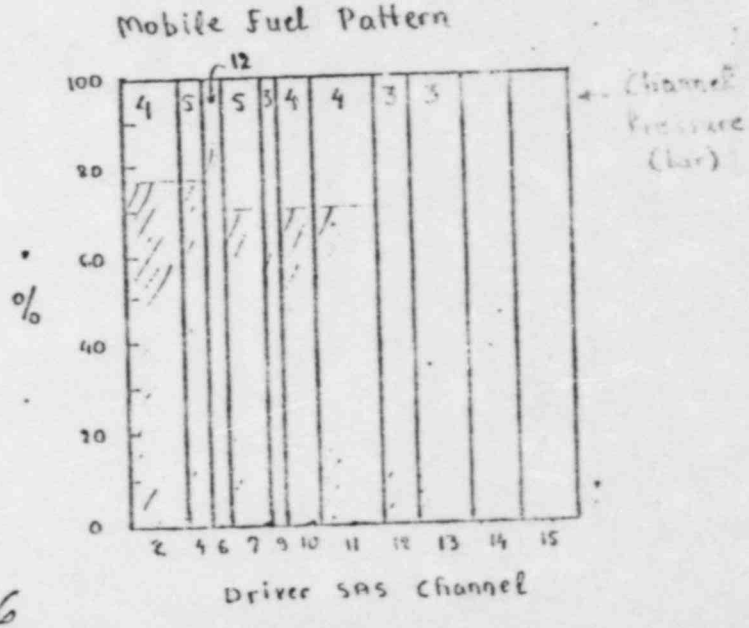

Fig 16

II.3

III (c).10 CO-DISRUPTION FOR CASE G

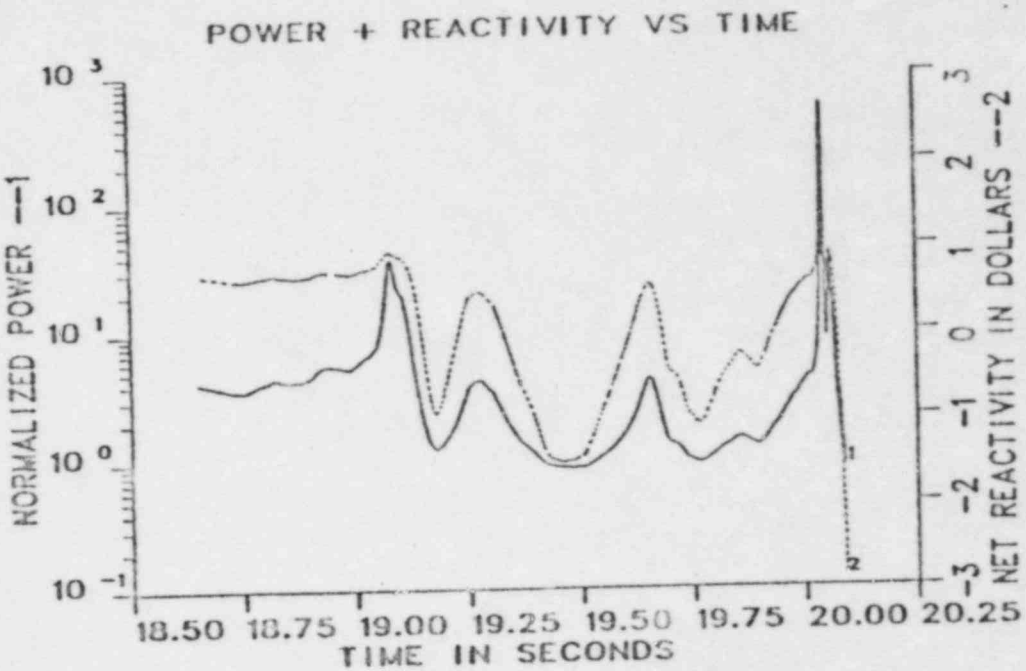

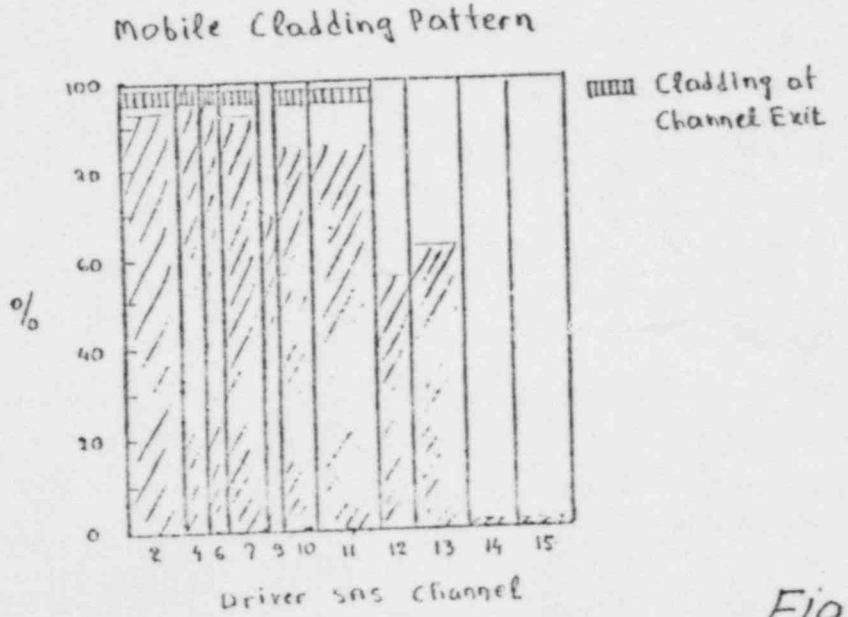

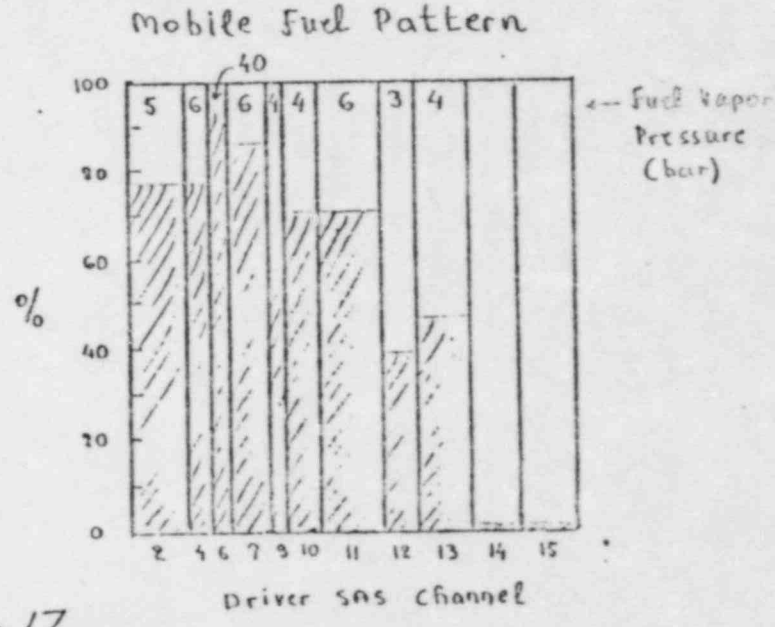

Fig 17

II.3

Mobile Cladding Pattern

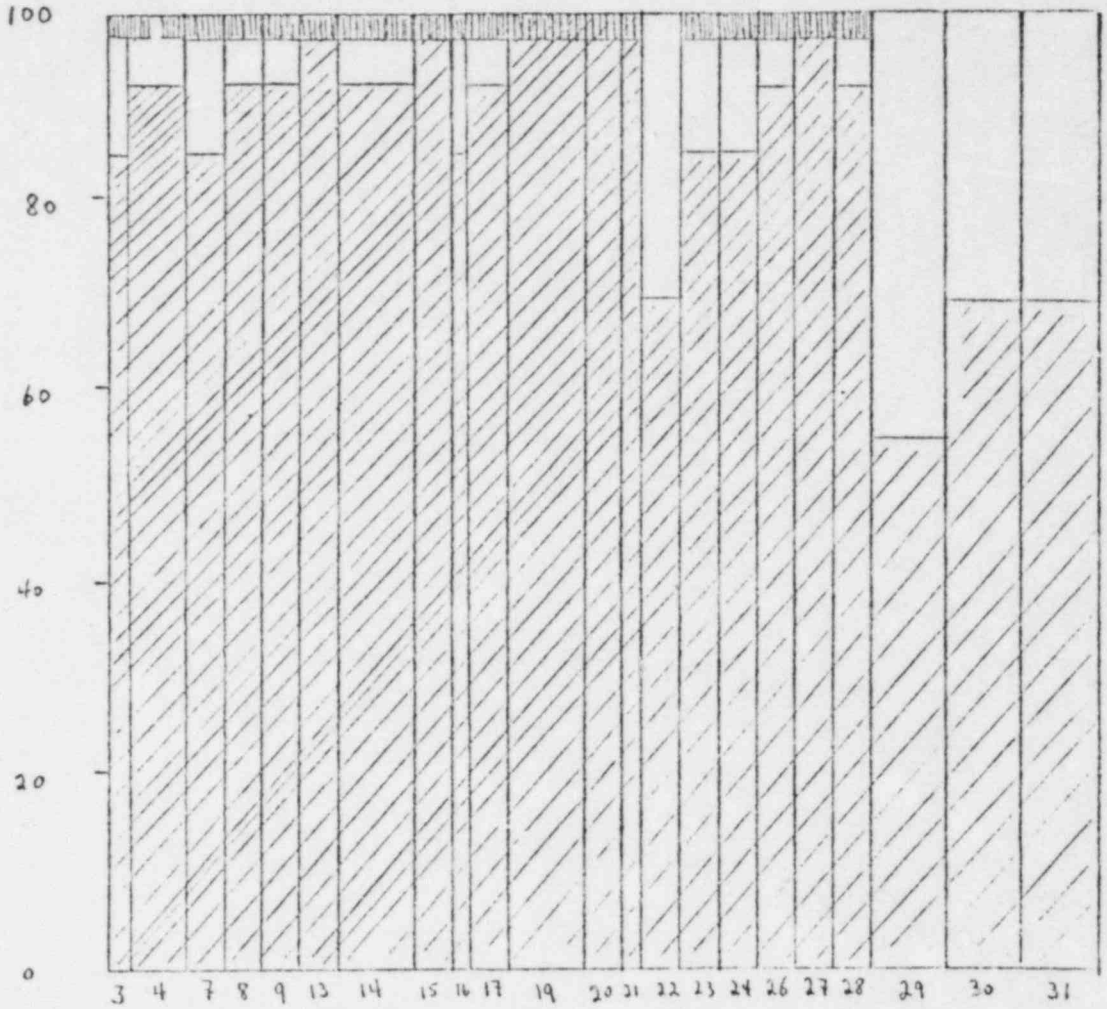

Cladding At Channel Exit

Fig 18a

C.II

Mobile Fuel Pattern

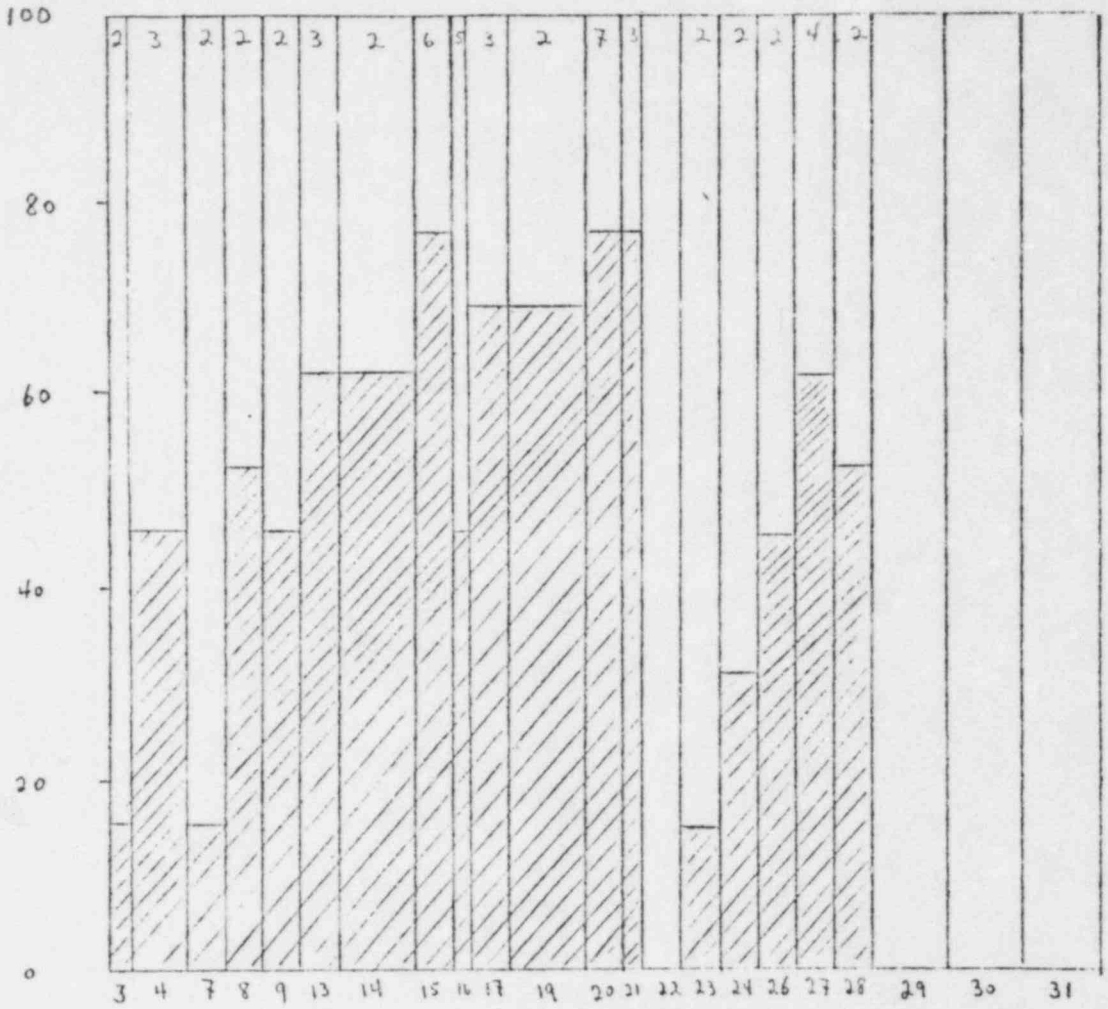

Channel Pressure In Disrupted Fuel Region (Bar)

Fig 18b

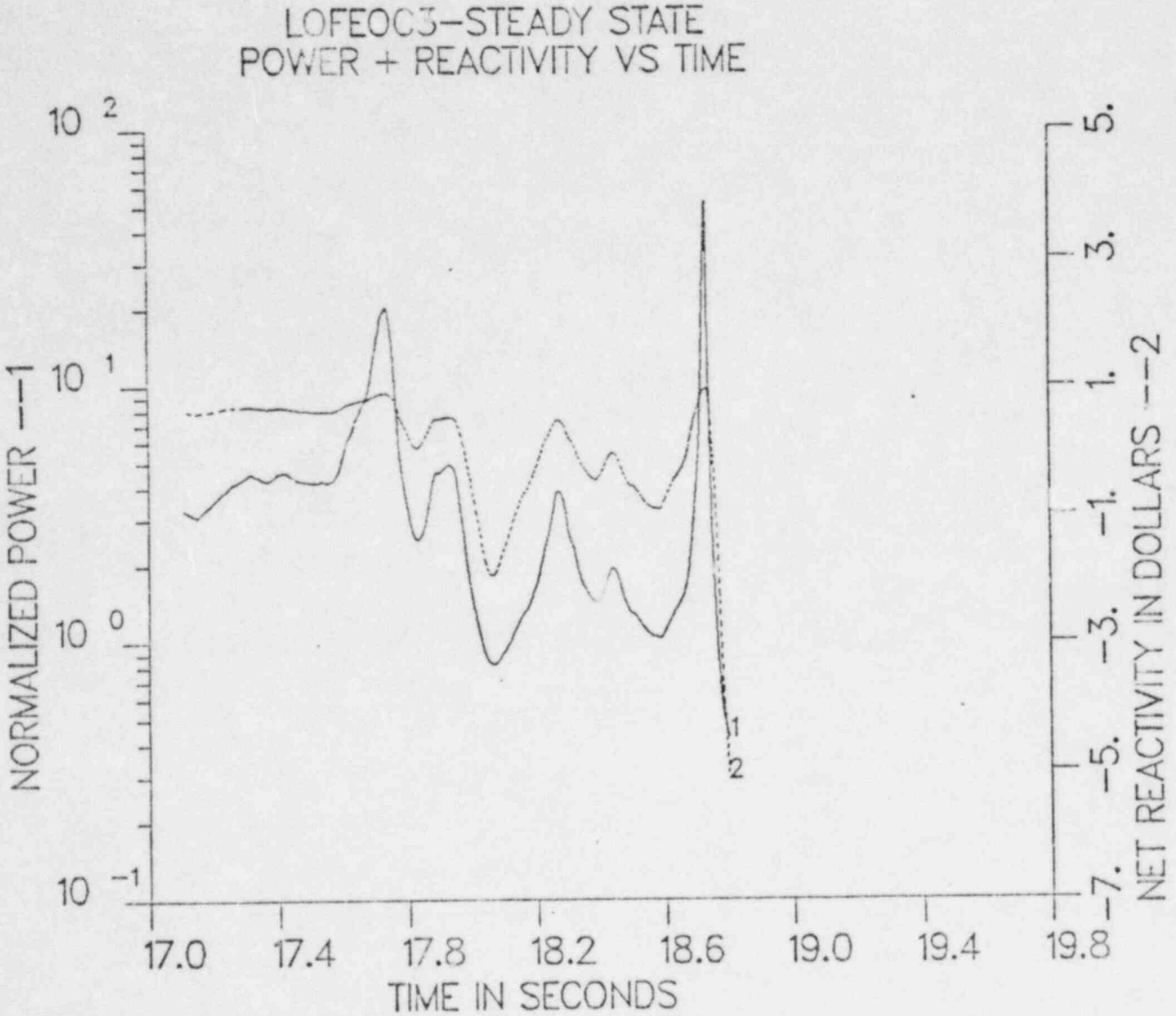
LOFEOC3–STEADY STATE
POWER + REACTIVITY VS TIME
NORMALIZED POWER --1
10 2
10 1
10 0
10 -1
NET REACTIVITY IN DOLLARS --2
5.
3.
1.
-1.
-3.
-5.
-7.
17.0
17.4
17.8
18.2
18.6
19.0
19.4
19.8
TIME IN SECONDS
1
2

Fig 18c

III (C).10 CO-DISRUPTION FOR CASE A

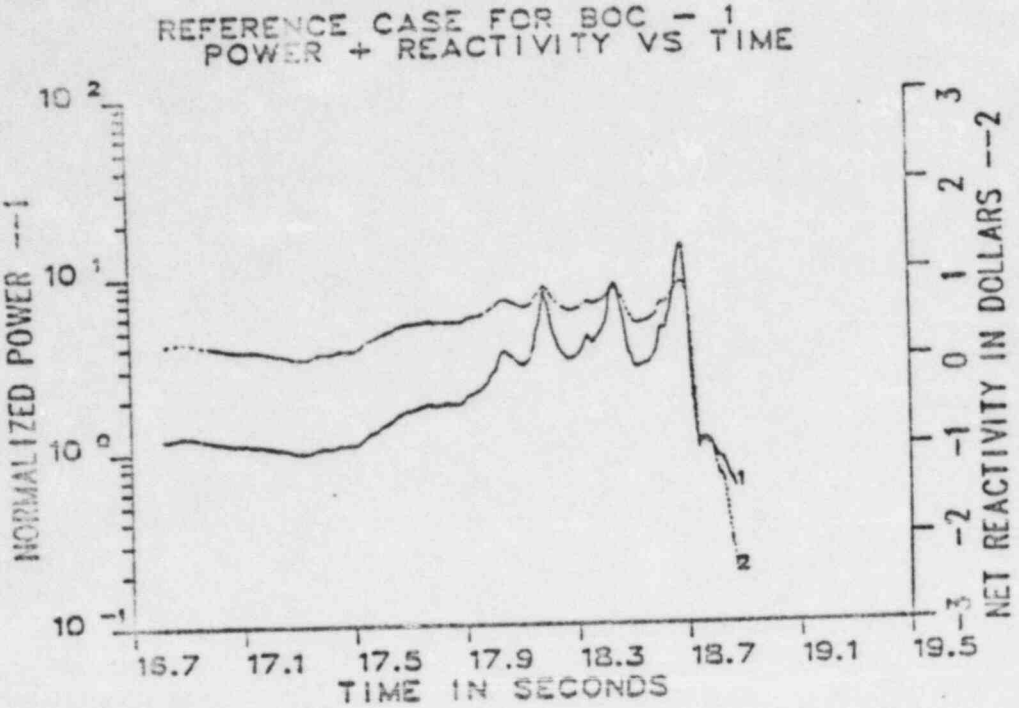

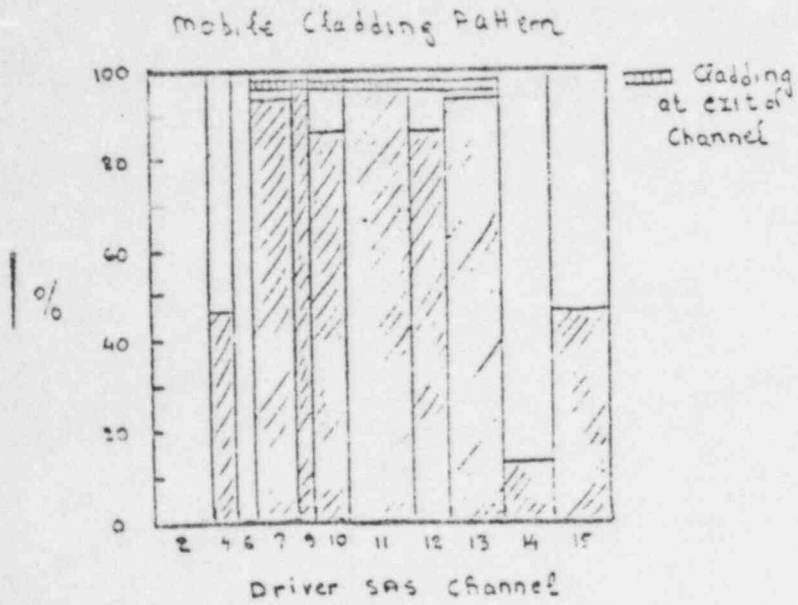

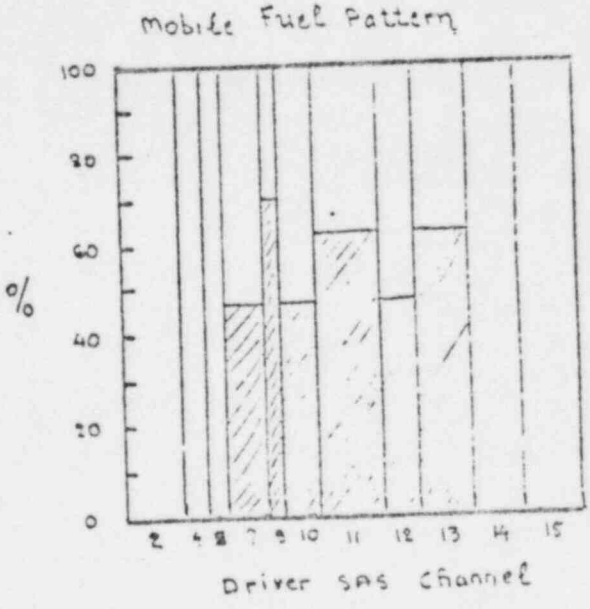

Fig 19

ILLUSTRATION OF CO-DISRUPTION

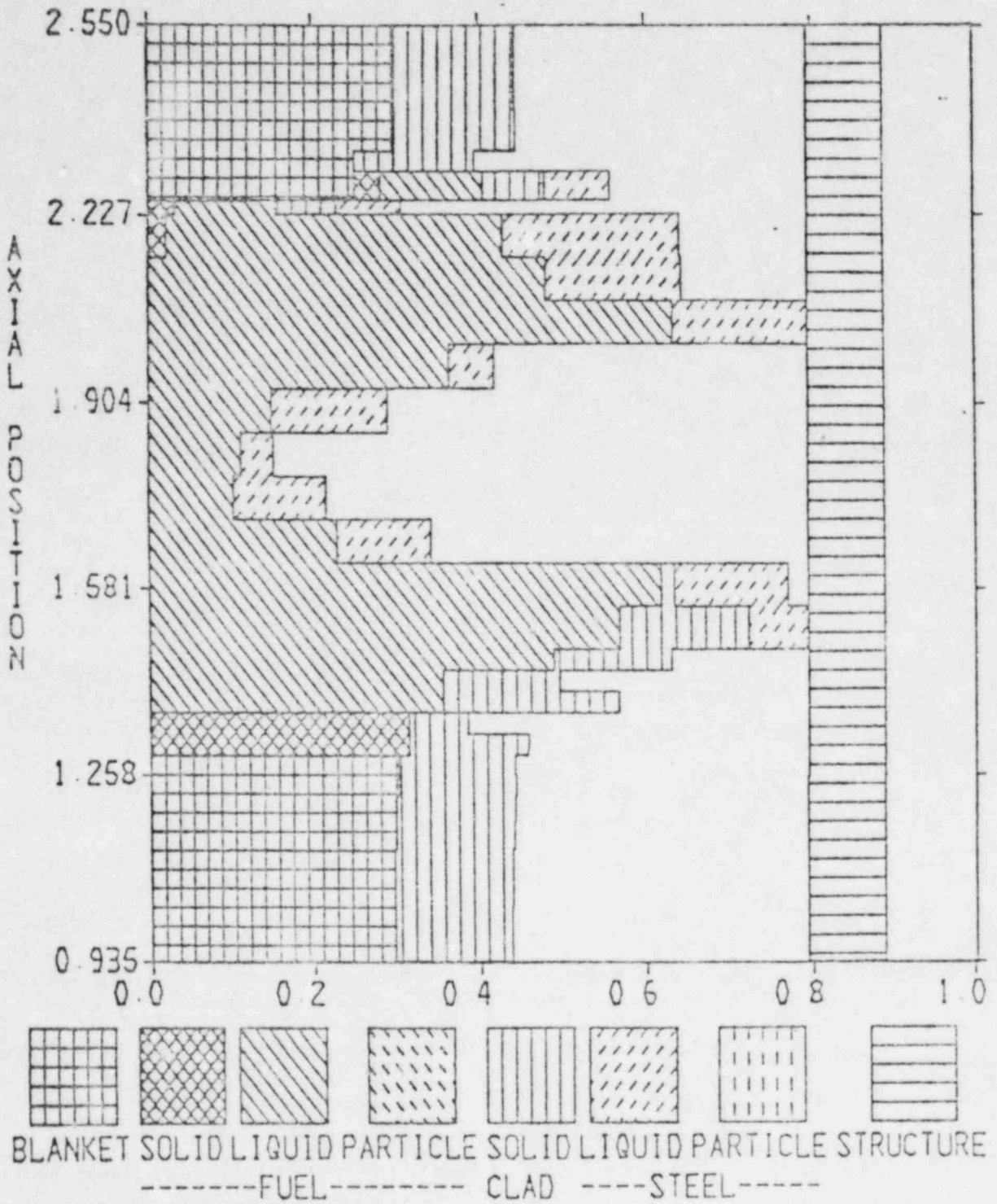

Fig 20

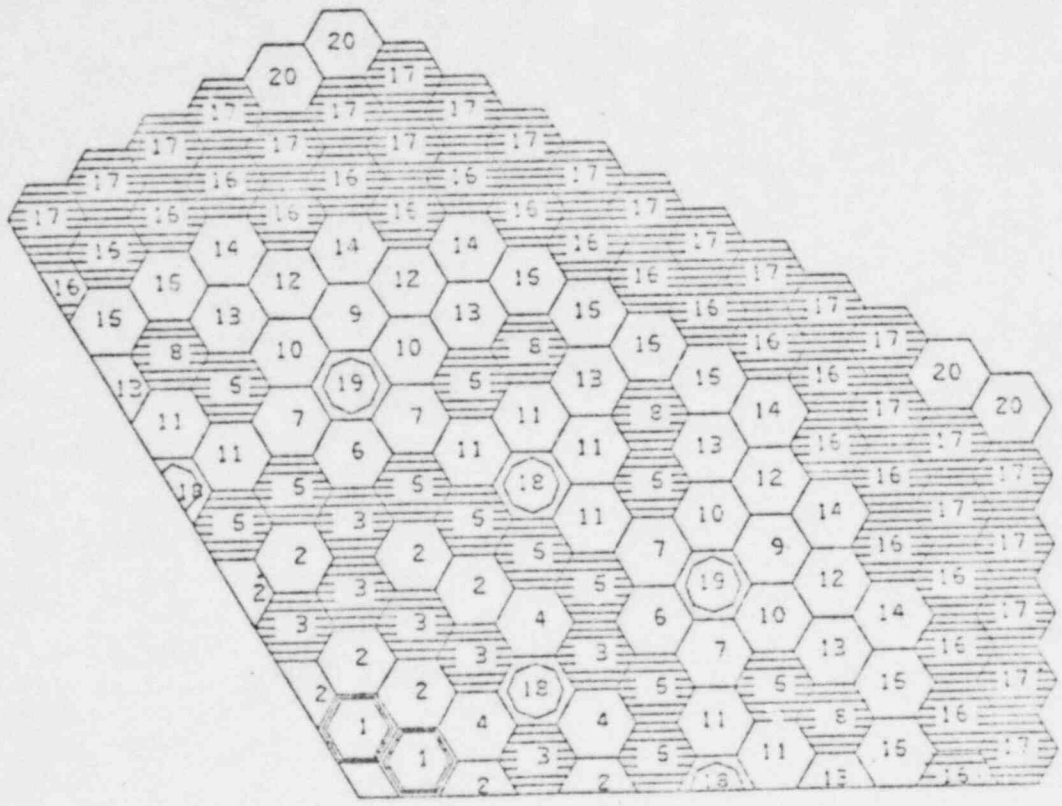

Fig 1

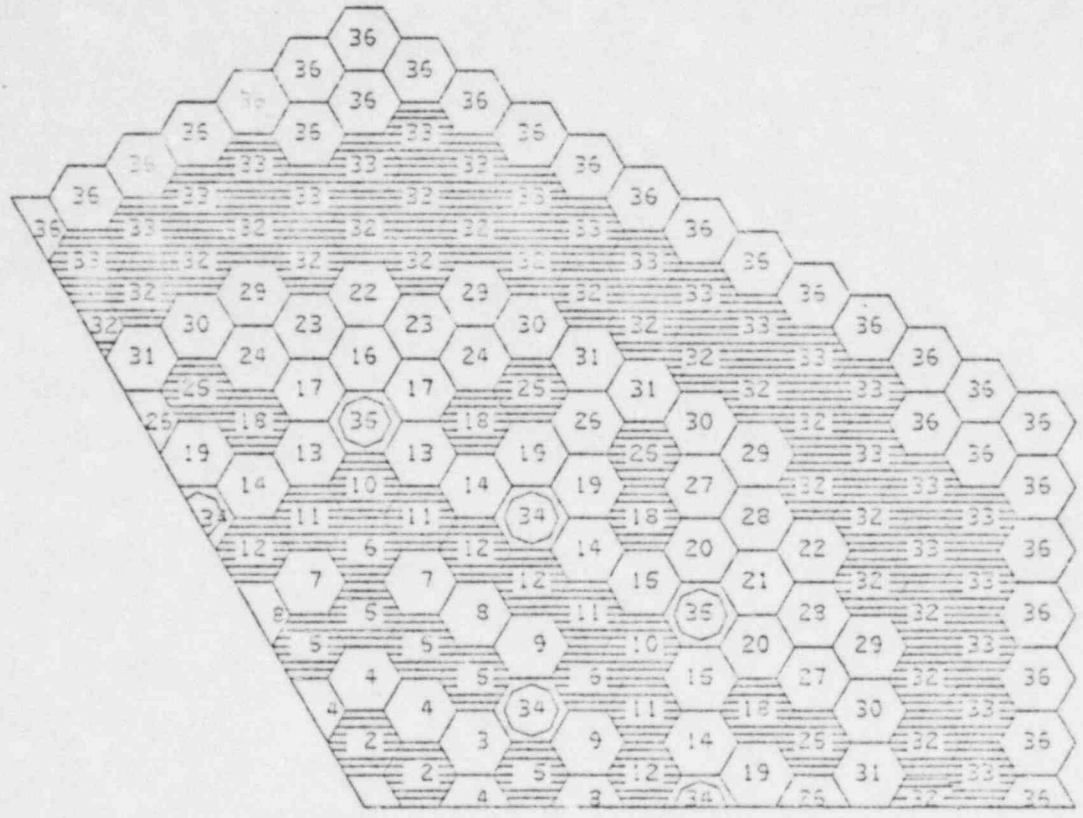

Fig 2

AII.

CRBR EOC4 CONFIGURATION

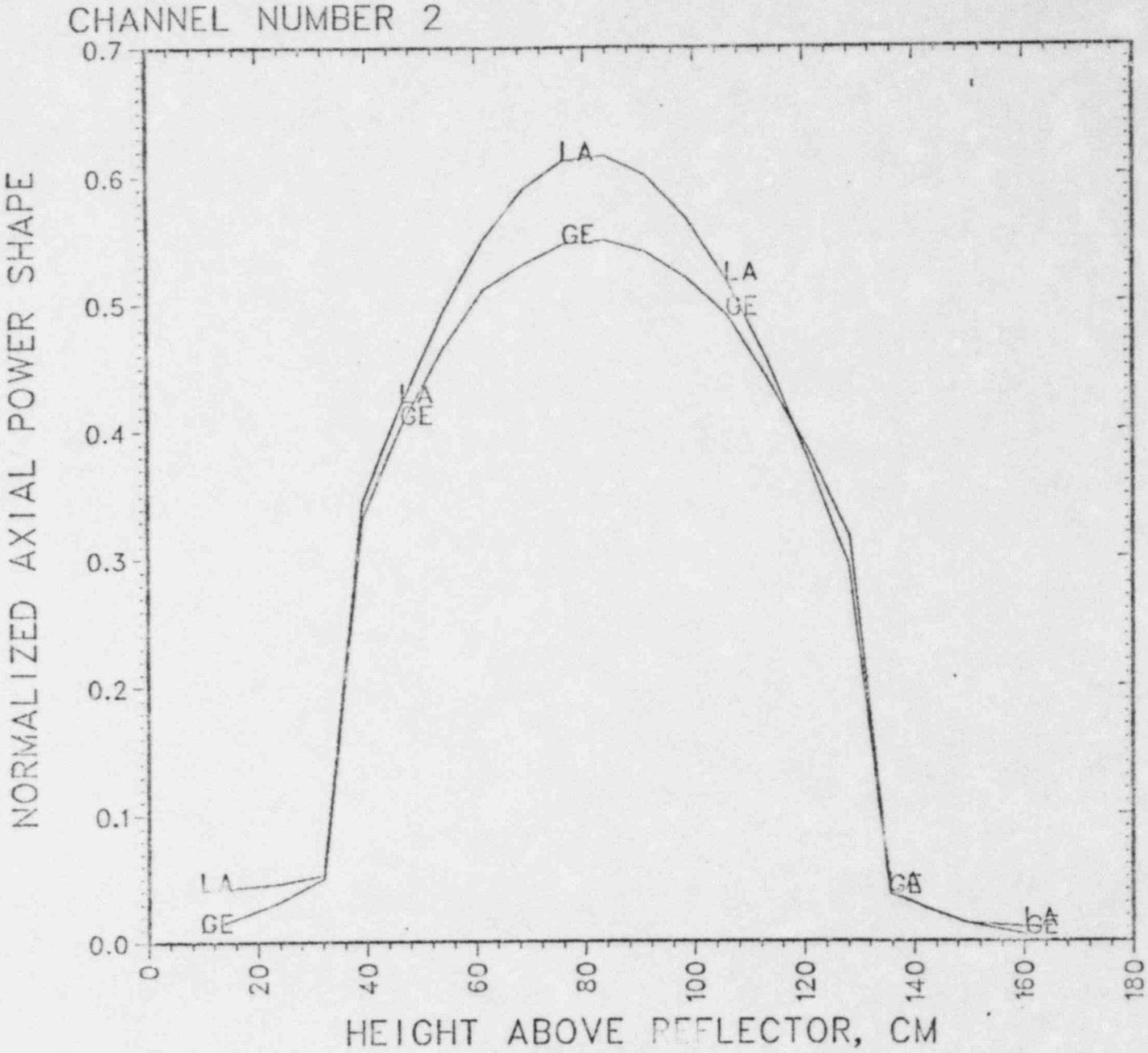

Fig 3

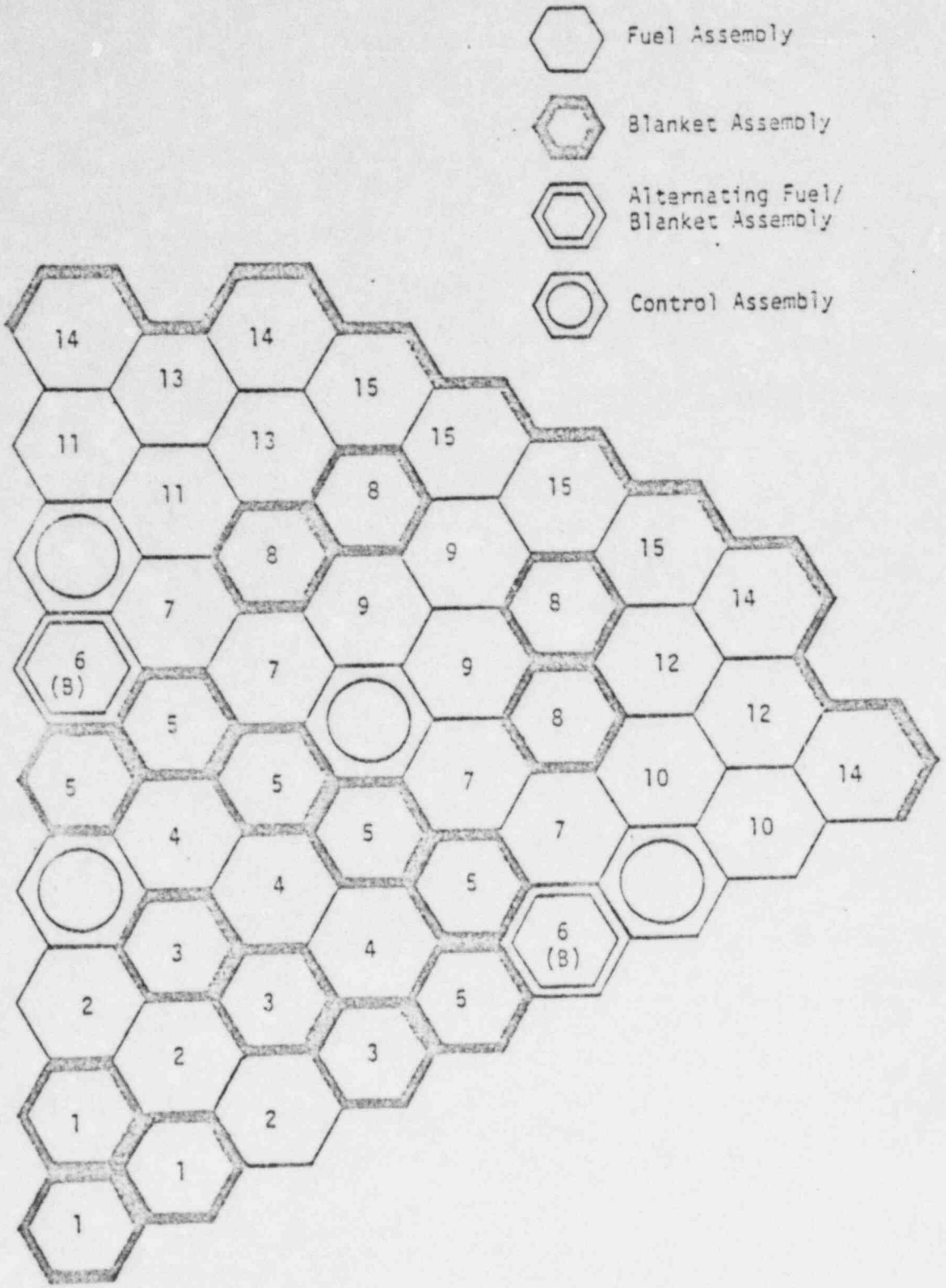

Fig. 4-8 SAS3D 15 Channel Representation of CRBRP Heterogeneous Core at BOC-1

B.II.3

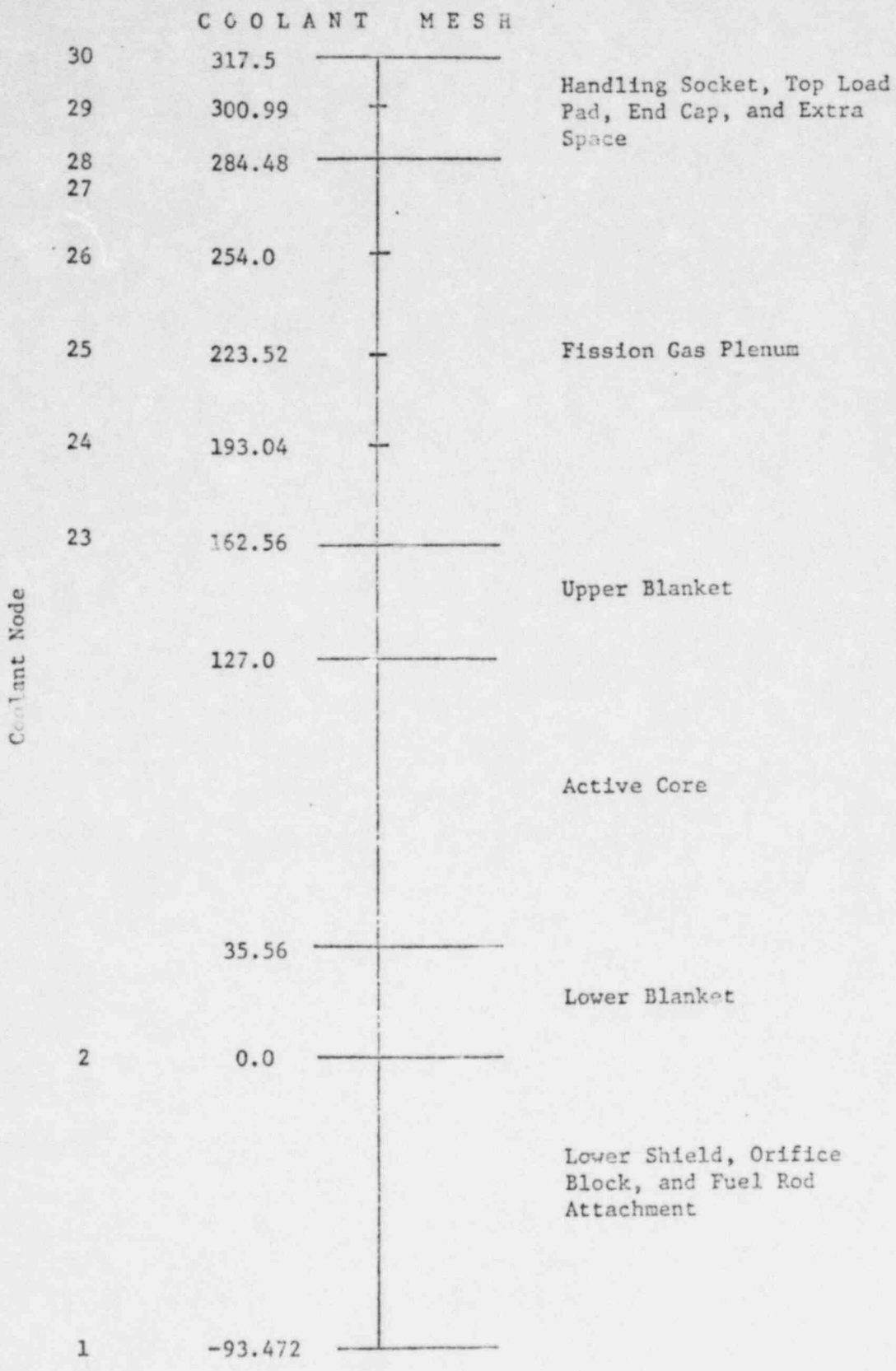

FIG. 2 SAS Coolant Mesh Used for Representation of the CRBR Core

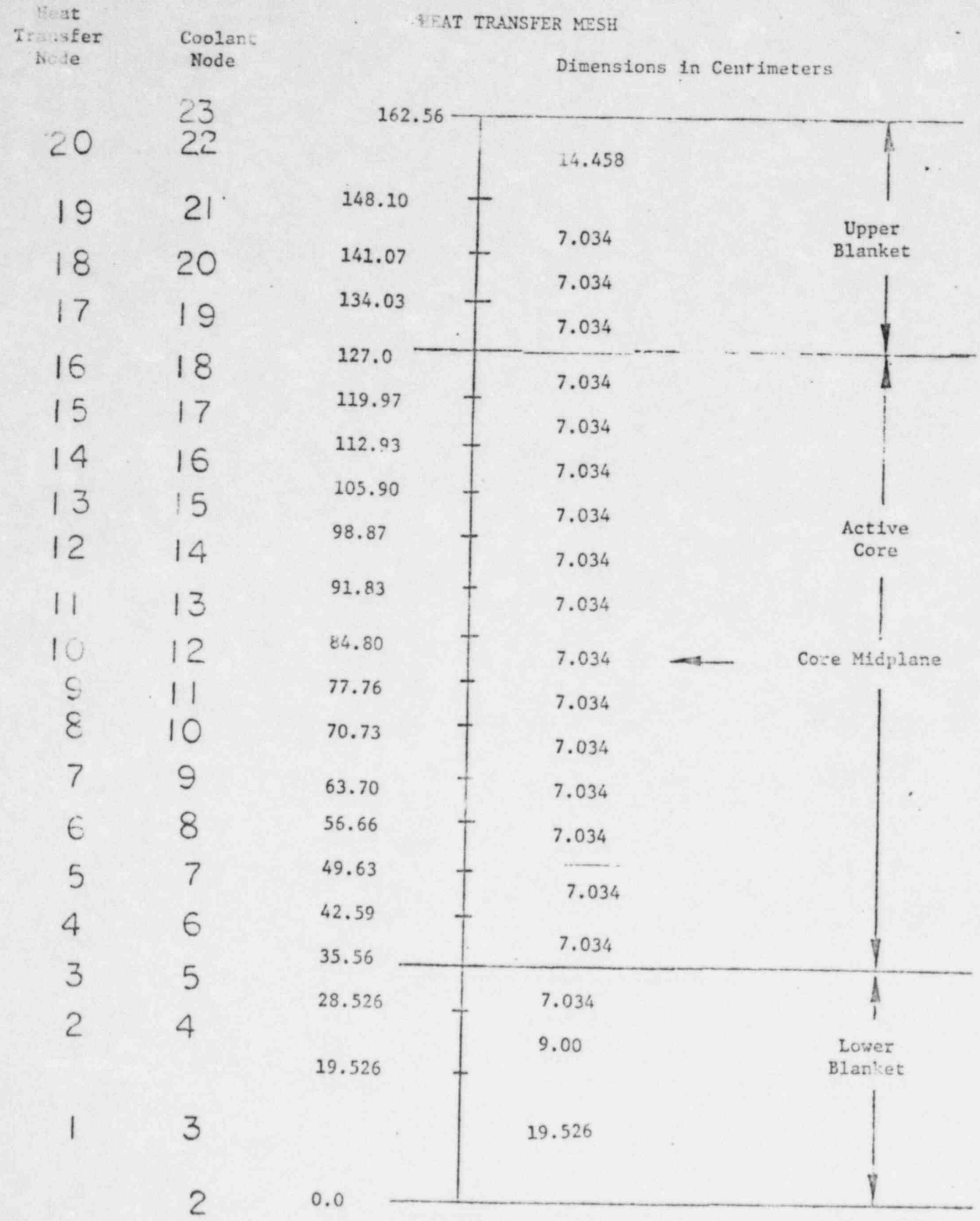

FIG. 3 Core and Blanket Mesh Spacing for SAS3A

BII.3

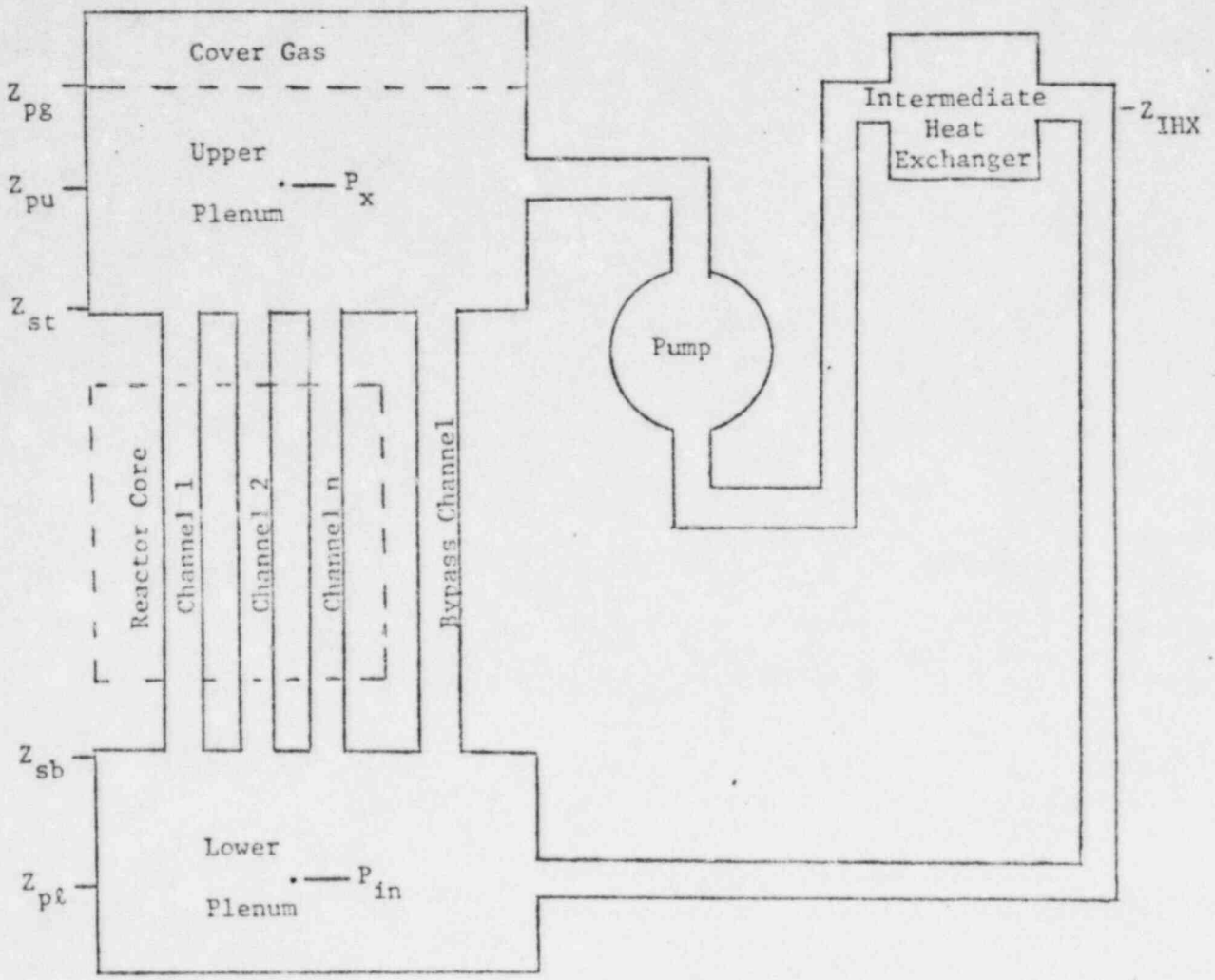

FIG. 4 Primary-Coolant Loop.

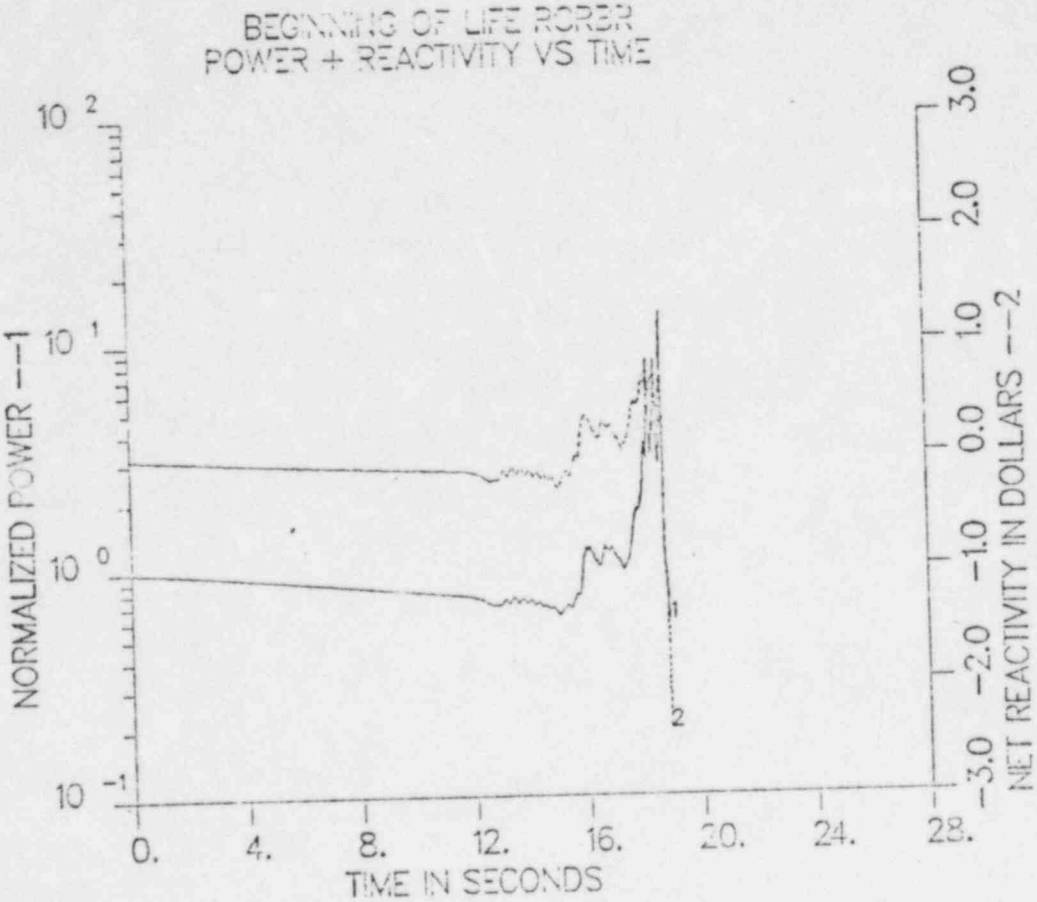
BEGINNING OF LIFE RORSR
POWER + REACTIVITY VS TIME
NORMALIZED POWER --1
10 2
10 1
10 0
10 -1
0.
4.
8.
12.
16.
20.
24.
28.
TIME IN SECONDS
3.0
2.0
1.0
0.0
-1.0
-2.0
-3.0
NET REACTIVITY IN DOLLARS --2

Fig 5

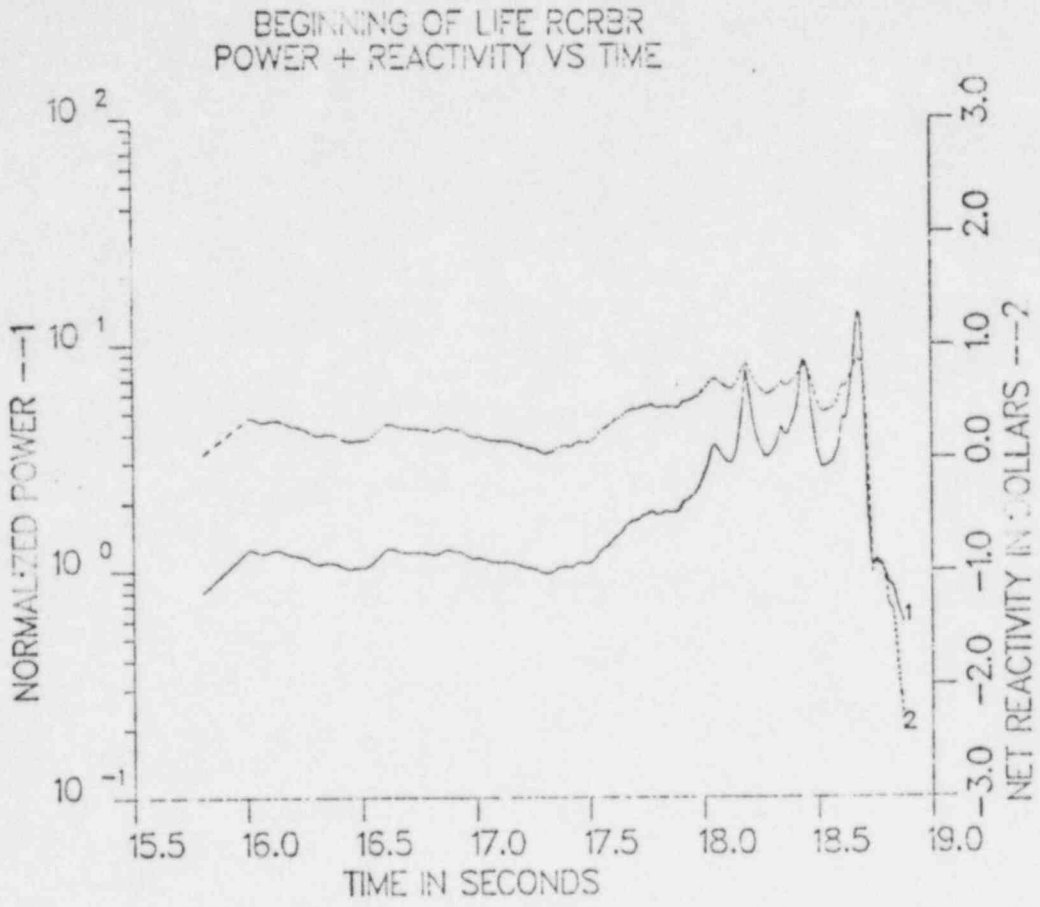
BEGINNING OF LIFE RCRBR
POWER + REACTIVITY VS TIME
NORMALIZED POWER --1
NET REACTIVITY IN DOLLARS --2
TIME IN SECONDS
10 2
10 1
10 0
10 -1
15.5
16.0
16.5
17.0
17.5
18.0
18.5
19.0
3.0
2.0
1.0
0.0
-1.0
-2.0
-3.0

Fig6

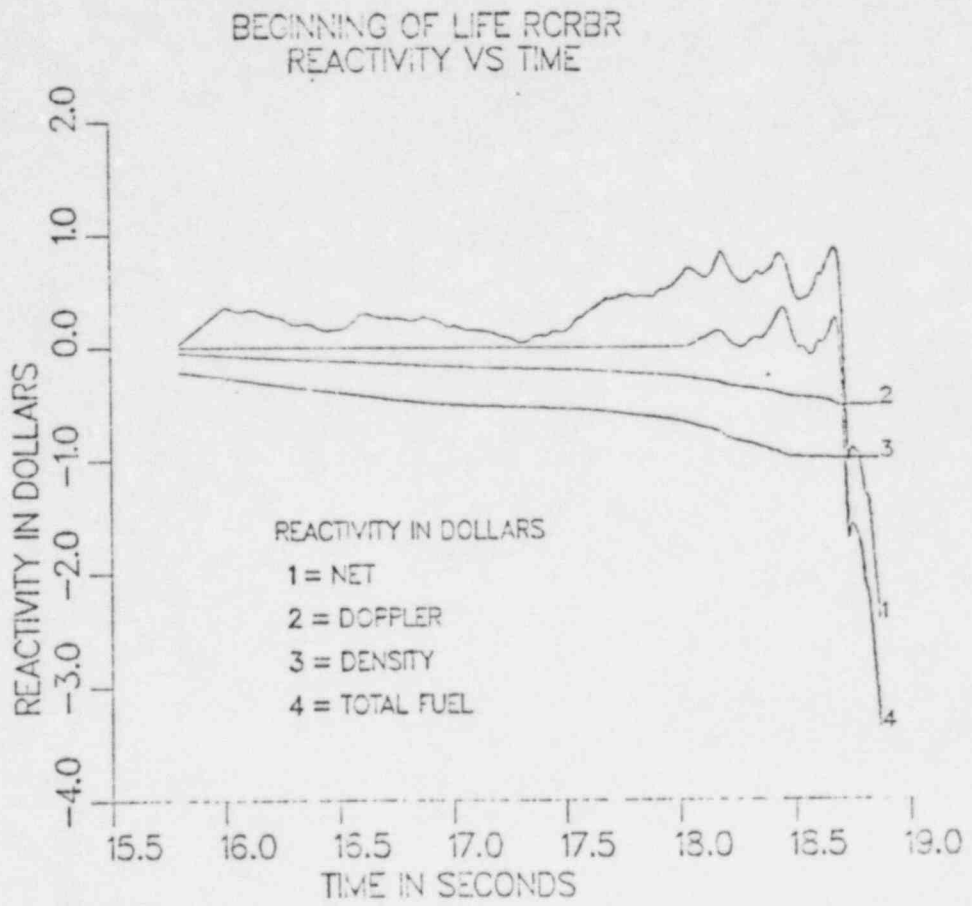
BEGINNING OF LIFE RCRBR
REACTIVITY VS TIME
REACTIVITY IN DOLLARS
2.0
1.0
0.0
-1.0
-2.0
-3.0
-4.0
REACTIVITY IN DOLLARS
1 = NET
2 = DOPPLER
3 = DENSITY
4 = TOTAL FUEL
1
2
3
4
15.5
16.0
16.5
17.0
17.5
18.0
18.5
19.0
TIME IN SECONDS

Fig 7

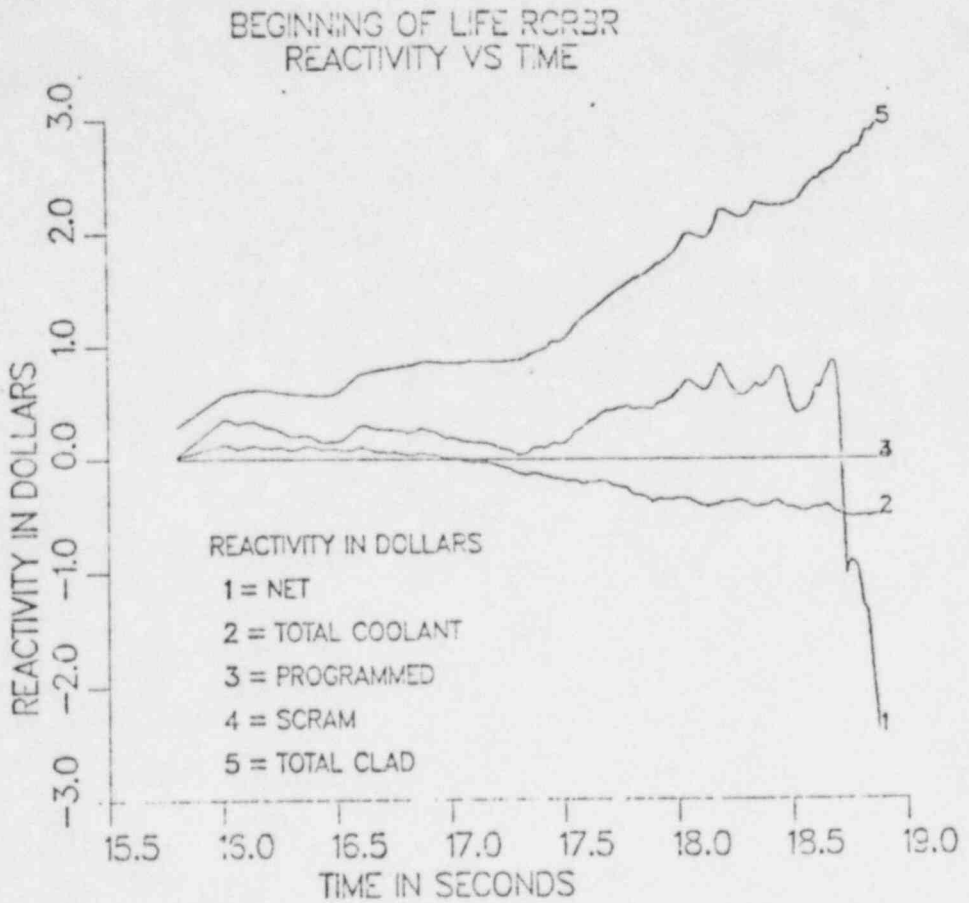
BEGINNING OF LIFE RCRBR
REACTIVITY VS TIME
REACTIVITY IN DOLLARS
3.0
2.0
1.0
0.0
−1.0
−2.0
−3.0
15.5
16.0
16.5
17.0
17.5
18.0
18.5
19.0
TIME IN SECONDS
REACTIVITY IN DOLLARS
1 = NET
2 = TOTAL COOLANT
3 = PROGRAMMED
4 = SCRAM
5 = TOTAL CLAD
1
2
3
5

Fig 8

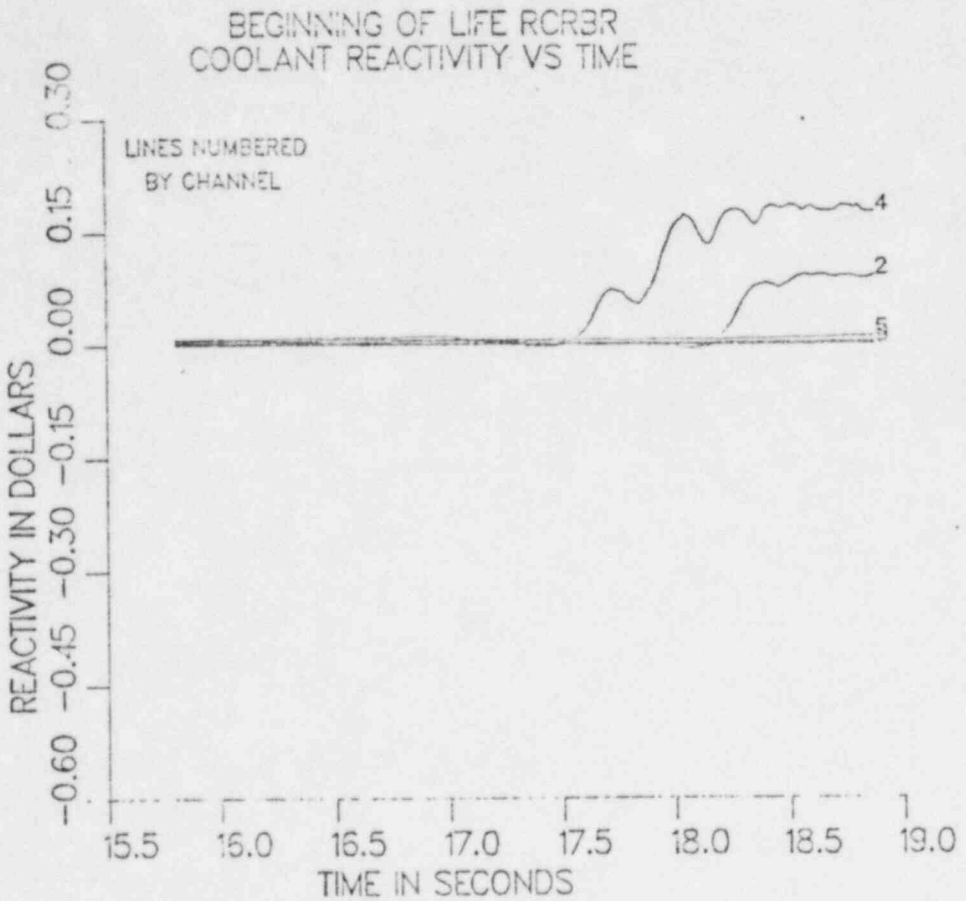
BEGINNING OF LIFE RCRBR
COOLANT REACTIVITY VS TIME
LINES NUMBERED
BY CHANNEL
4
2
5
REACTIVITY IN DOLLARS
0.30
0.15
0.00
-0.15
-0.30
-0.45
-0.60
15.5
16.0
16.5
17.0
17.5
18.0
18.5
19.0
TIME IN SECONDS

Fig 9

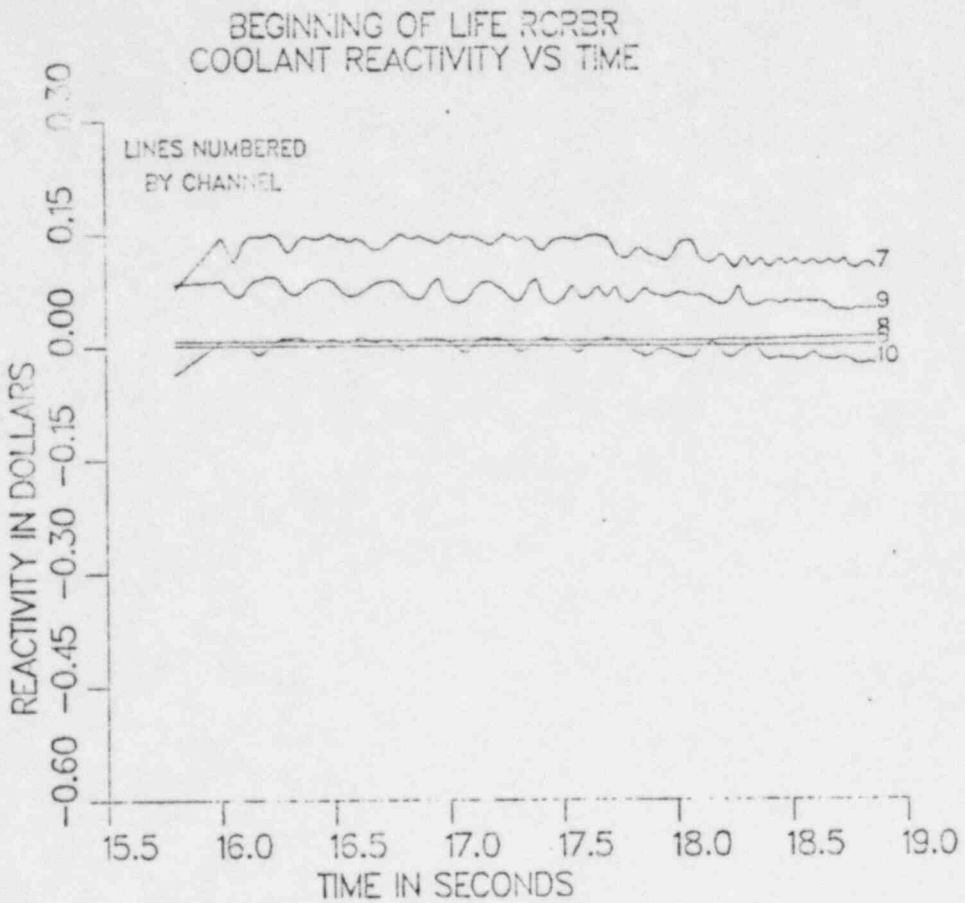
BEGINNING OF LIFE RORBR
COOLANT REACTIVITY VS TIME
LINES NUMBERED
BY CHANNEL
7
9
8
10
REACTIVITY IN DOLLARS
0.30
0.15
0.00
−0.15
−0.30
−0.45
−0.60
15.5
16.0
16.5
17.0
17.5
18.0
18.5
19.0
TIME IN SECONDS

Fig 10

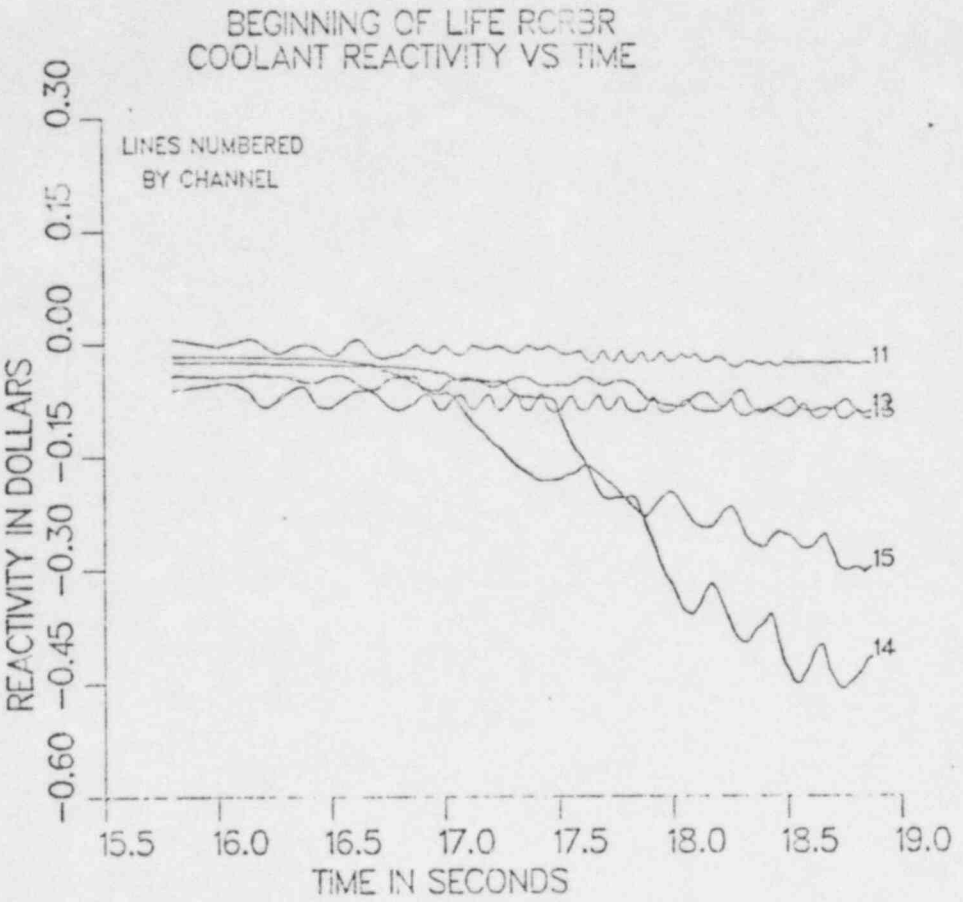
BEGINNING OF LIFE RCRBR
COOLANT REACTIVITY VS TIME
LINES NUMBERED
BY CHANNEL
REACTIVITY IN DOLLARS
0.30
0.15
0.00
-0.15
-0.30
-0.45
-0.60
11
13
15
14
15.5
16.0
16.5
17.0
17.5
18.0
18.5
19.0
TIME IN SECONDS

Fig 11

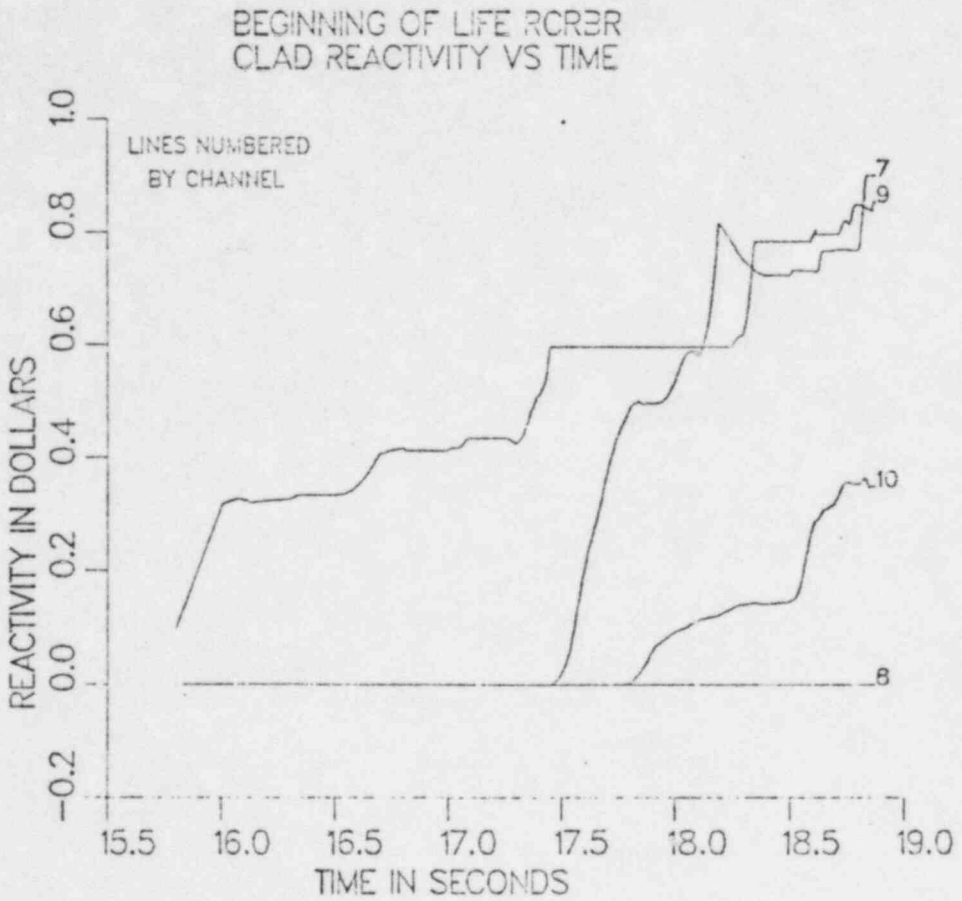
BEGINNING OF LIFE RCR3R
CLAD REACTIVITY VS TIME
LINES NUMBERED
BY CHANNEL
7
9
10
8
REACTIVITY IN DOLLARS
1.0
0.8
0.6
0.4
0.2
0.0
−0.2
15.5
16.0
16.5
17.0
17.5
18.0
18.5
19.0
TIME IN SECONDS

Fig 12

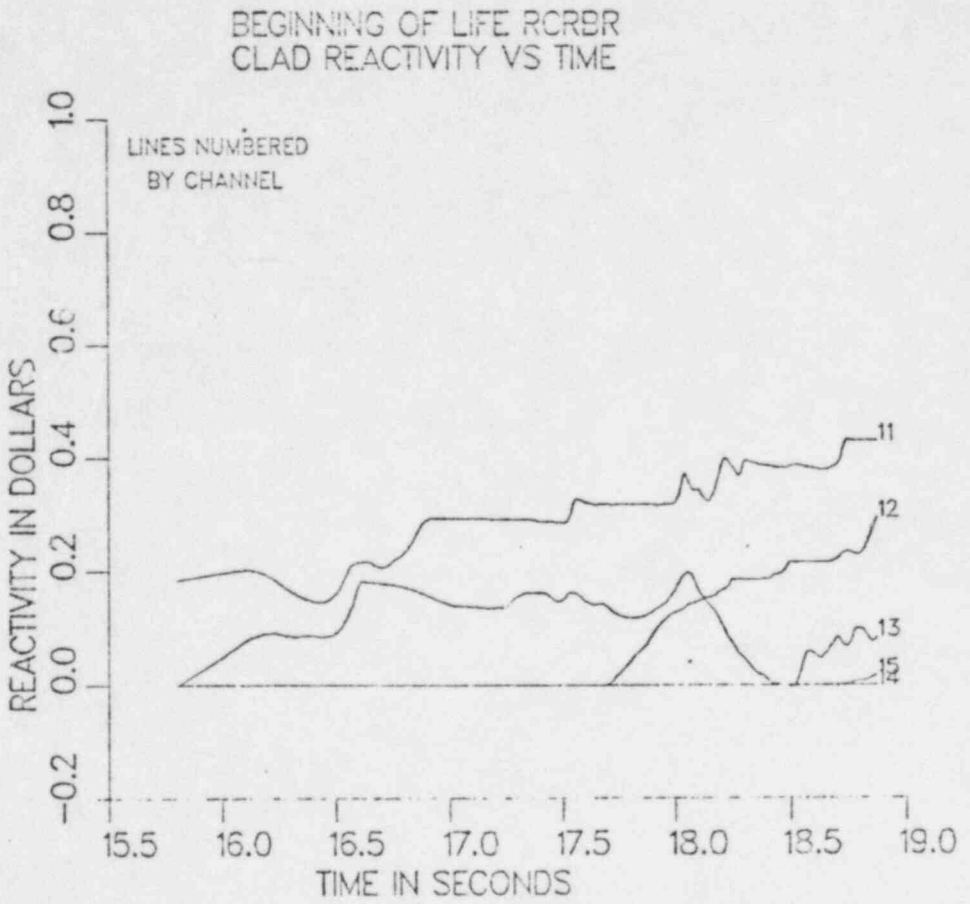
BEGINNING OF LIFE RCRBR
CLAD REACTIVITY VS TIME
LINES NUMBERED
BY CHANNEL
REACTIVITY IN DOLLARS
1.0
0.8
0.6
0.4
0.2
0.0
−0.2
11
12
13
14
15
15.5
16.0
16.5
17.0
17.5
18.0
18.5
19.0
TIME IN SECONDS

Fig 13

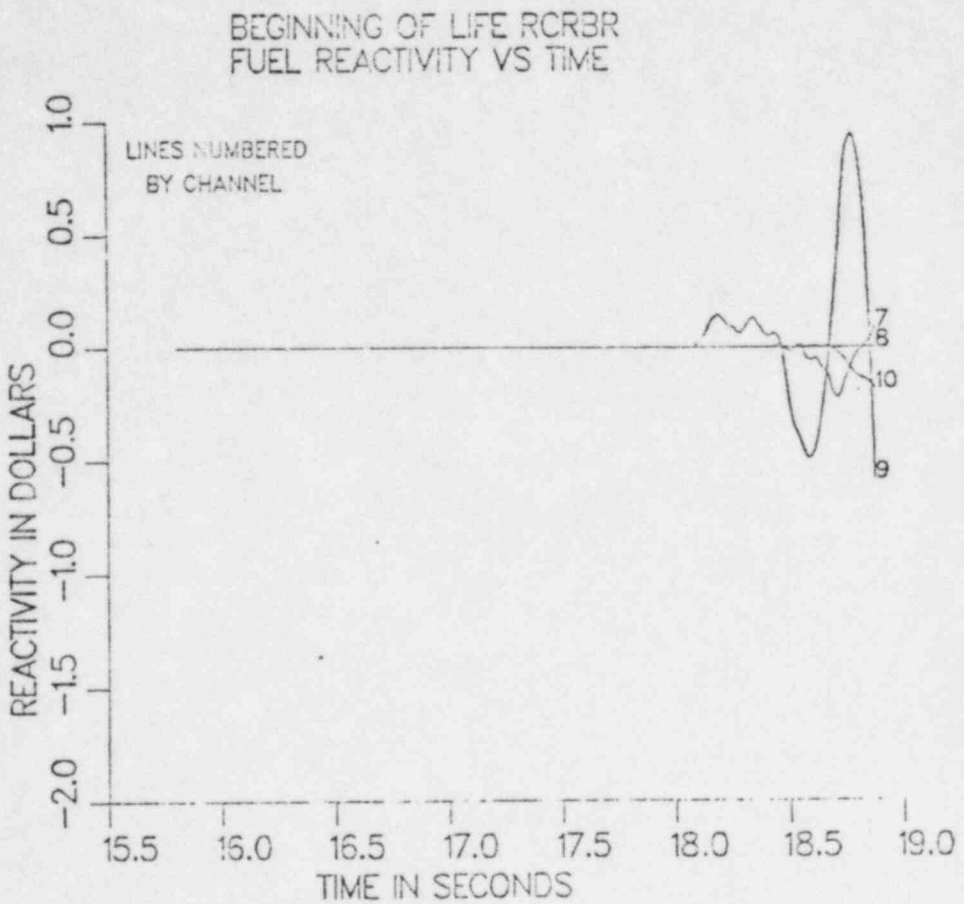
BEGINNING OF LIFE RCRBR
FUEL REACTIVITY VS TIME
LINES NUMBERED
BY CHANNEL
7
8
10
9
REACTIVITY IN DOLLARS
1.0
0.5
0.0
-0.5
-1.0
-1.5
-2.0
15.5
16.0
16.5
17.0
17.5
18.0
18.5
19.0
TIME IN SECONDS

Fig 14

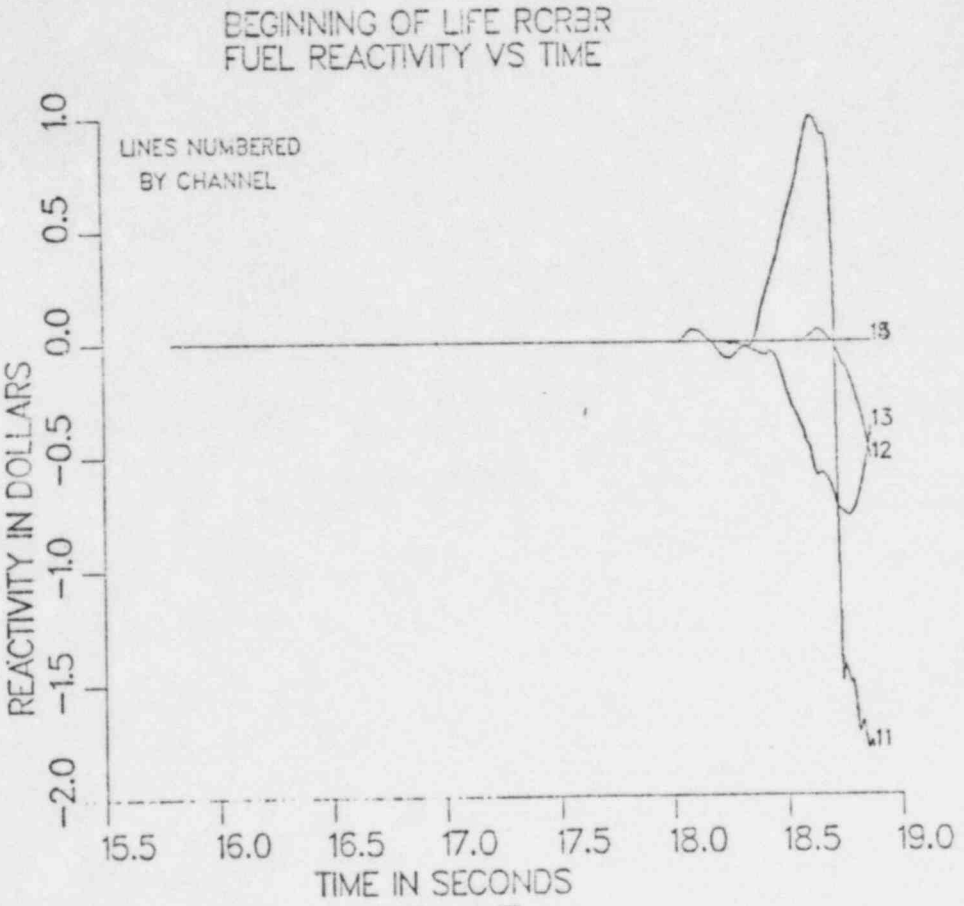
BEGINNING OF LIFE RCR3R
FUEL REACTIVITY VS TIME
LINES NUMBERED
BY CHANNEL
REACTIVITY IN DOLLARS
1.0
0.5
0.0
-0.5
-1.0
-1.5
-2.0
15.5
16.0
16.5
17.0
17.5
18.0
18.5
19.0
TIME IN SECONDS
13
13
12
11

Fig 15

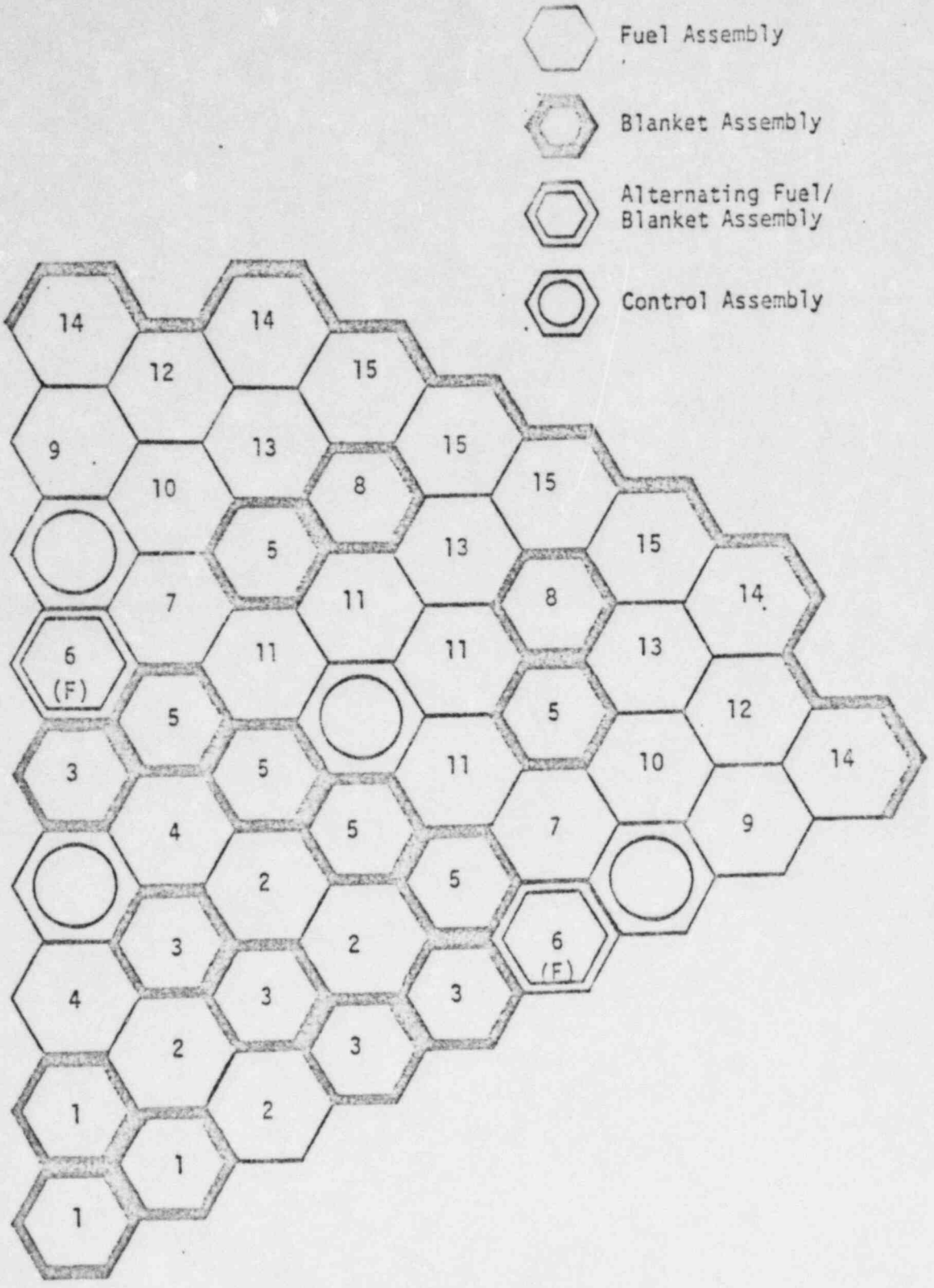

Fig. 4-9 (16) SAS3D 15 Channel Representation of CRBRP Heterogeneous Core at EOC-4

B II.3

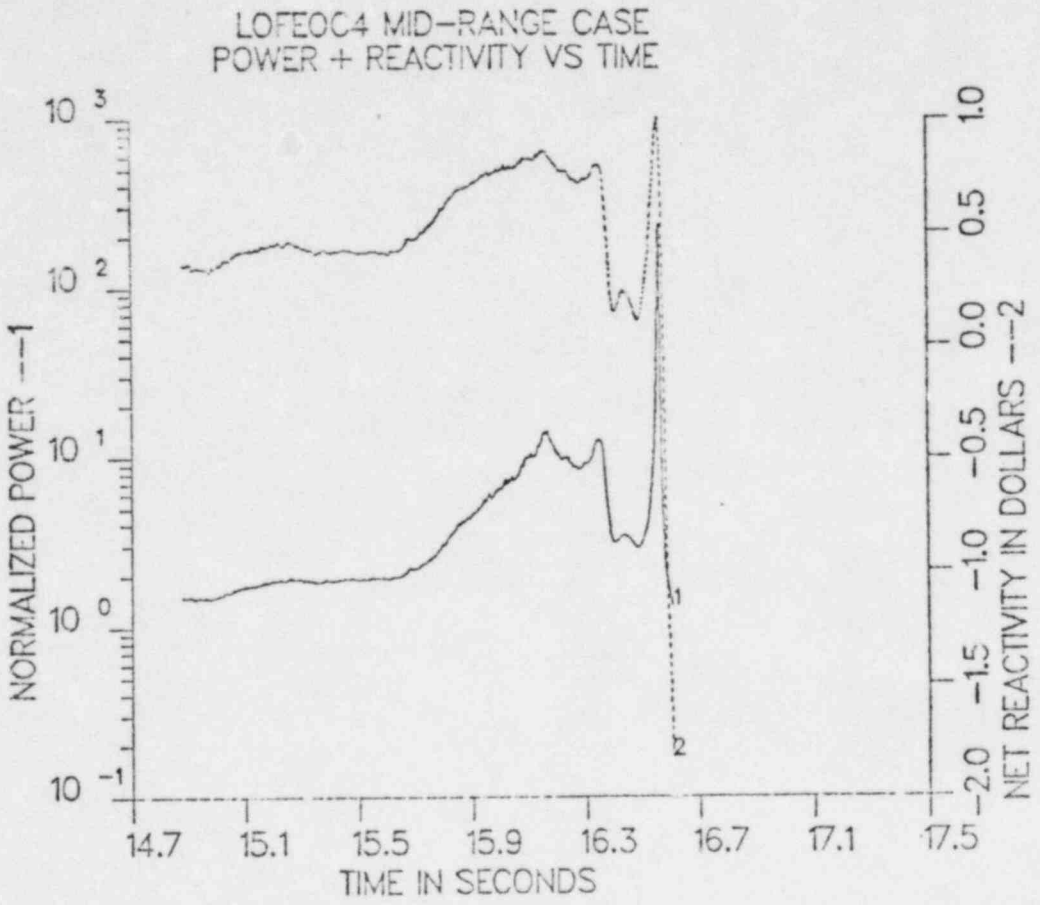
LOFEOC4 MID-RANGE CASE
POWER + REACTIVITY VS TIME
NORMALIZED POWER --1
10 3
10 2
10 1
10 0
10 -1
14.7
15.1
15.5
15.9
16.3
16.7
17.1
17.5
TIME IN SECONDS
1.0
0.5
0.0
-0.5
-1.0
-1.5
-2.0
NET REACTIVITY IN DOLLARS --2
1
2

Fig 17

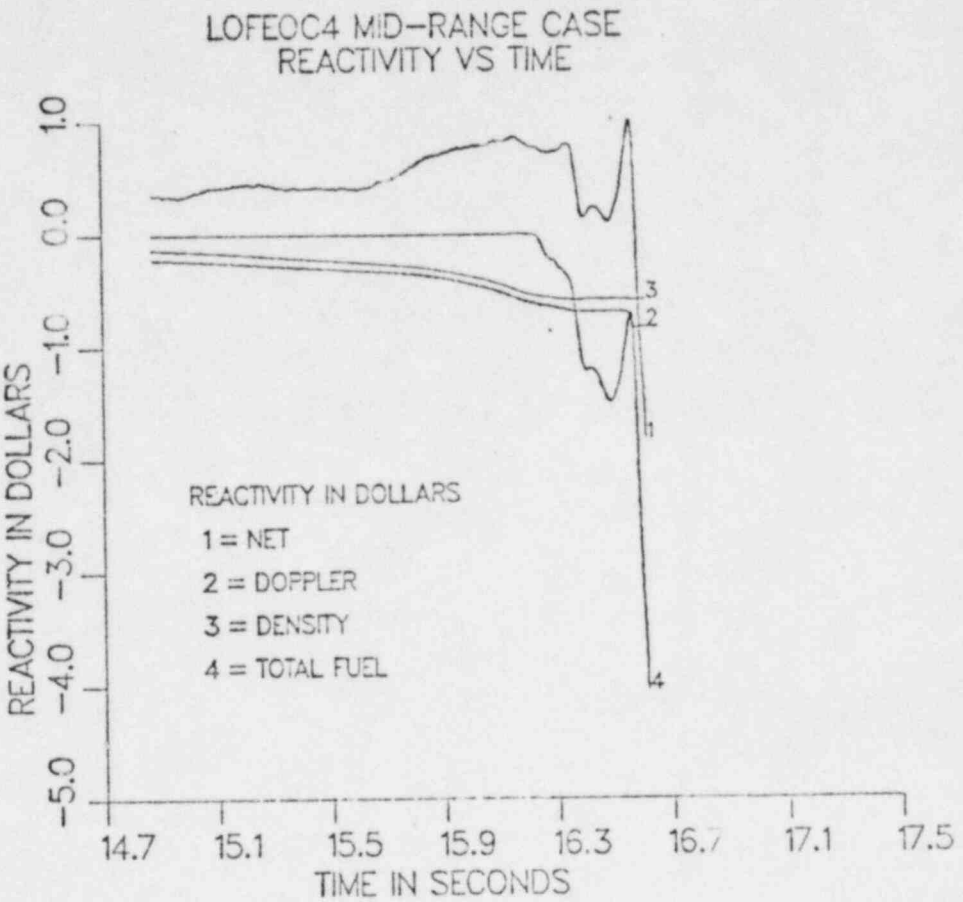
LOFEOC4 MID-RANGE CASE
REACTIVITY VS TIME
REACTIVITY IN DOLLARS
1.0
0.0
-1.0
-2.0
-3.0
-4.0
-5.0
REACTIVITY IN DOLLARS
1 = NET
2 = DOPPLER
3 = DENSITY
4 = TOTAL FUEL
1
2
3
4
14.7
15.1
15.5
15.9
16.3
16.7
17.1
17.5
TIME IN SECONDS

Fig 18

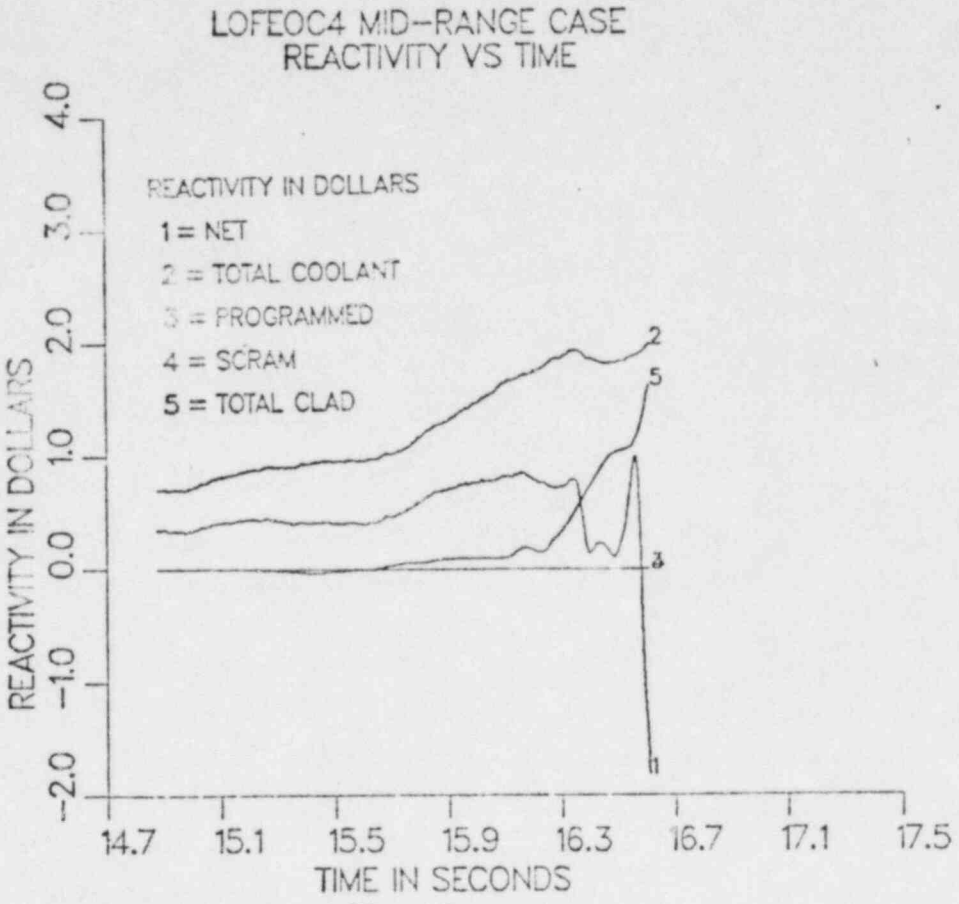
LOFEOC4 MID-RANGE CASE
REACTIVITY VS TIME
REACTIVITY IN DOLLARS
1 = NET
2 = TOTAL COOLANT
3 = PROGRAMMED
4 = SCRAM
5 = TOTAL CLAD
REACTIVITY IN DOLLARS
4.0
3.0
2.0
1.0
0.0
-1.0
-2.0
14.7
15.1
15.5
15.9
16.3
16.7
17.1
17.5
TIME IN SECONDS

Fig 19

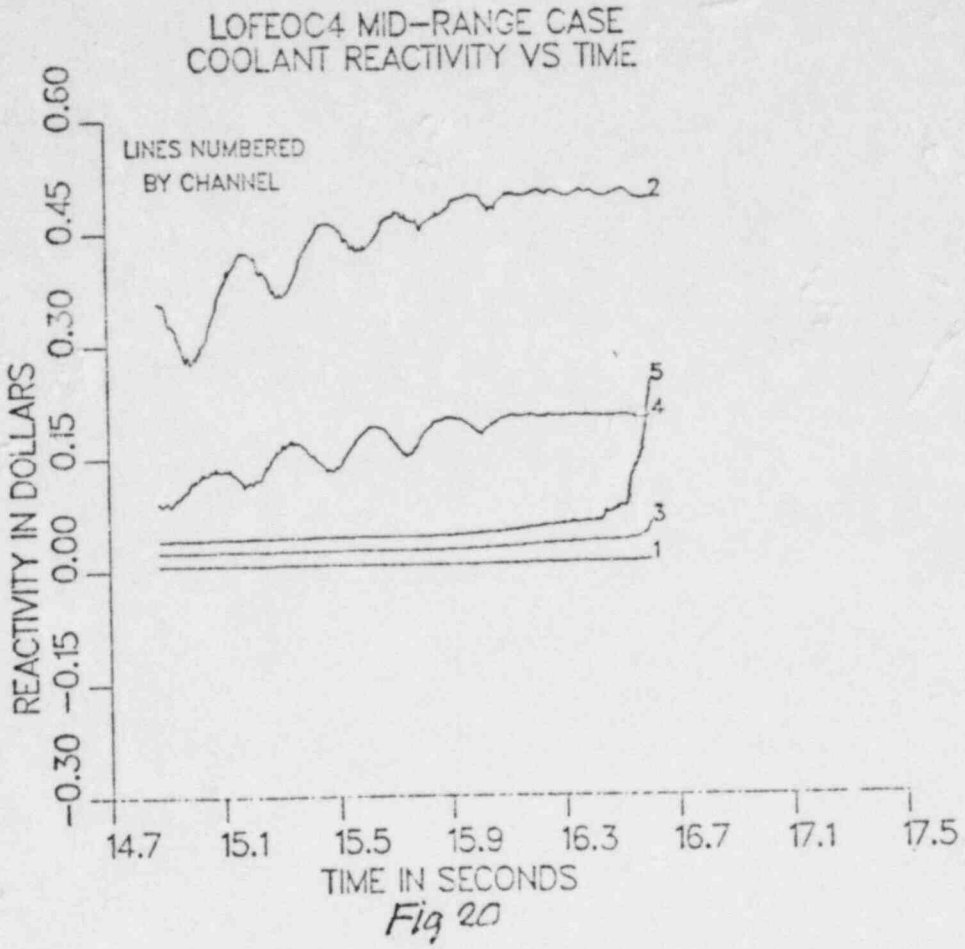
LOFEOC4 MID-RANGE CASE
COOLANT REACTIVITY VS TIME
LINES NUMBERED
BY CHANNEL
REACTIVITY IN DOLLARS
0.60
0.45
0.30
0.15
0.00
-0.15
-0.30
2
5
4
3
1
14.7
15.1
15.5
15.9
16.3
16.7
17.1
17.5
TIME IN SECONDS

Fig 20

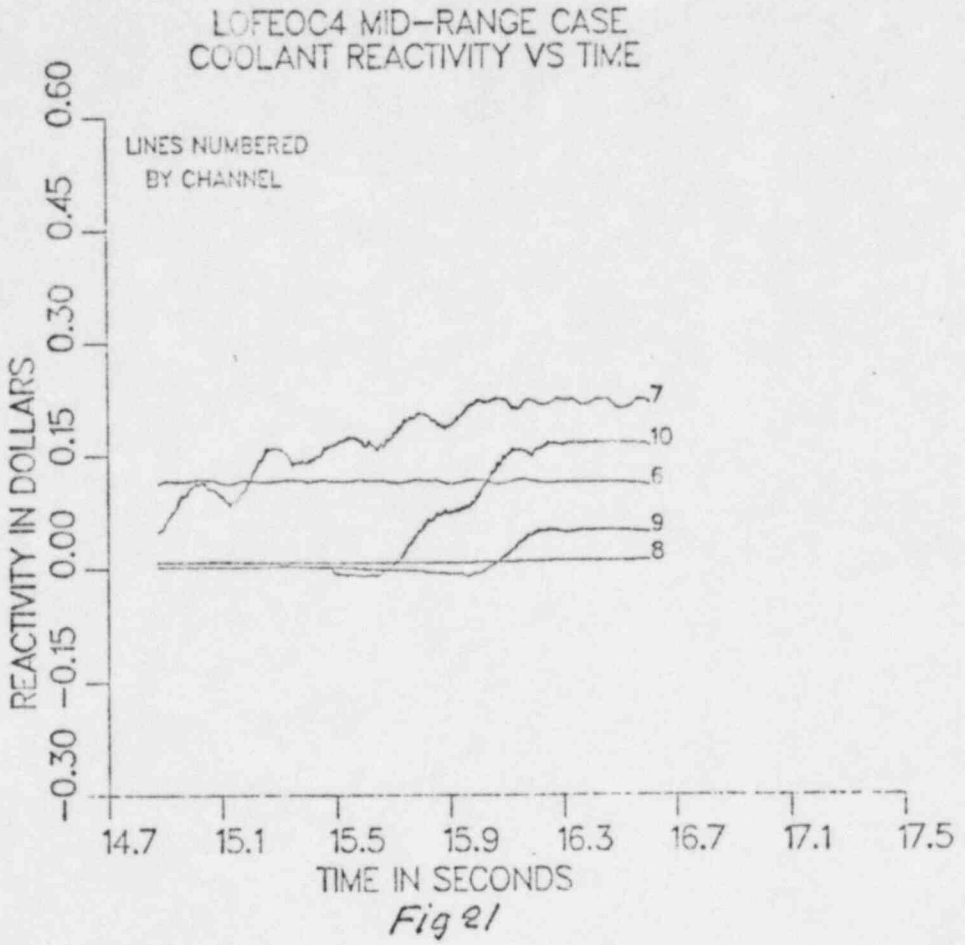
LOFEOC4 MID-RANGE CASE
COOLANT REACTIVITY VS TIME
LINES NUMBERED
BY CHANNEL
REACTIVITY IN DOLLARS
0.60
0.45
0.30
0.15
0.00
-0.15
-0.30
7
10
6
9
8
14.7
15.1
15.5
15.9
16.3
16.7
17.1
17.5
TIME IN SECONDS

Fig 21

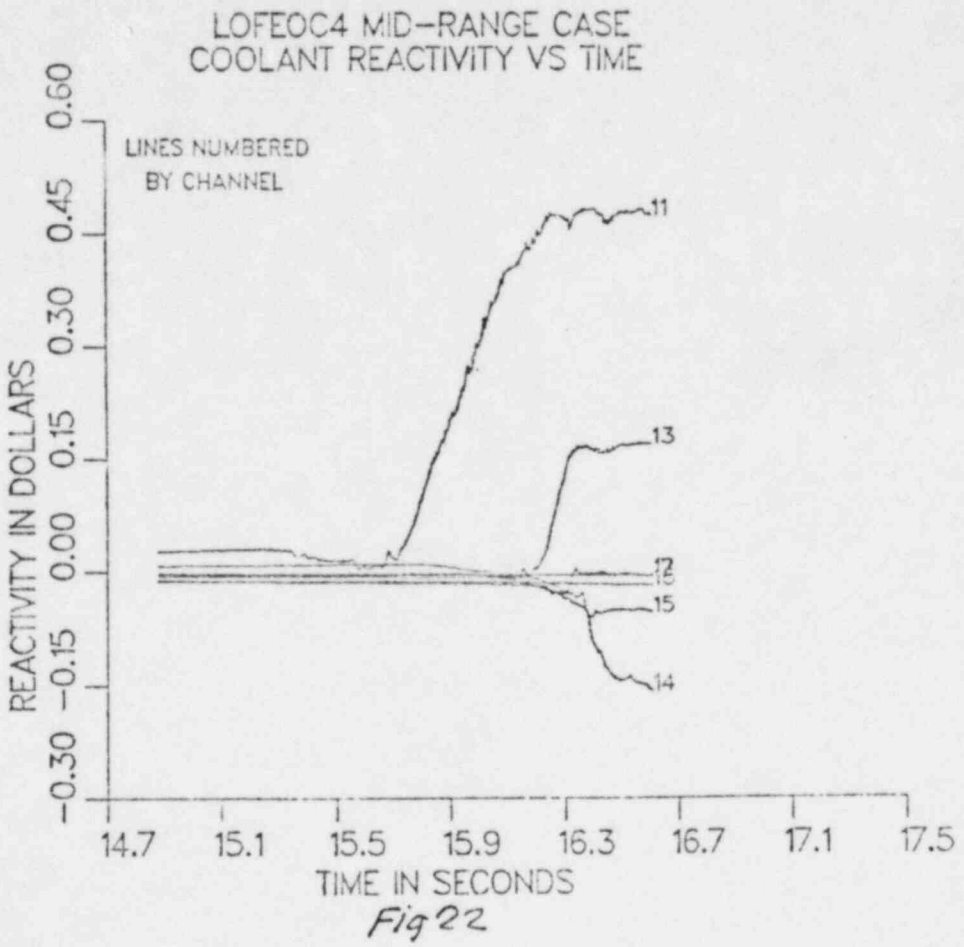
LOFEOC4 MID-RANGE CASE
COOLANT REACTIVITY VS TIME
LINES NUMBERED
BY CHANNEL
REACTIVITY IN DOLLARS
0.60
0.45
0.30
0.15
0.00
-0.15
-0.30
11
13
12
16
15
14
14.7
15.1
15.5
15.9
16.3
16.7
17.1
17.5
TIME IN SECONDS

Fig 22

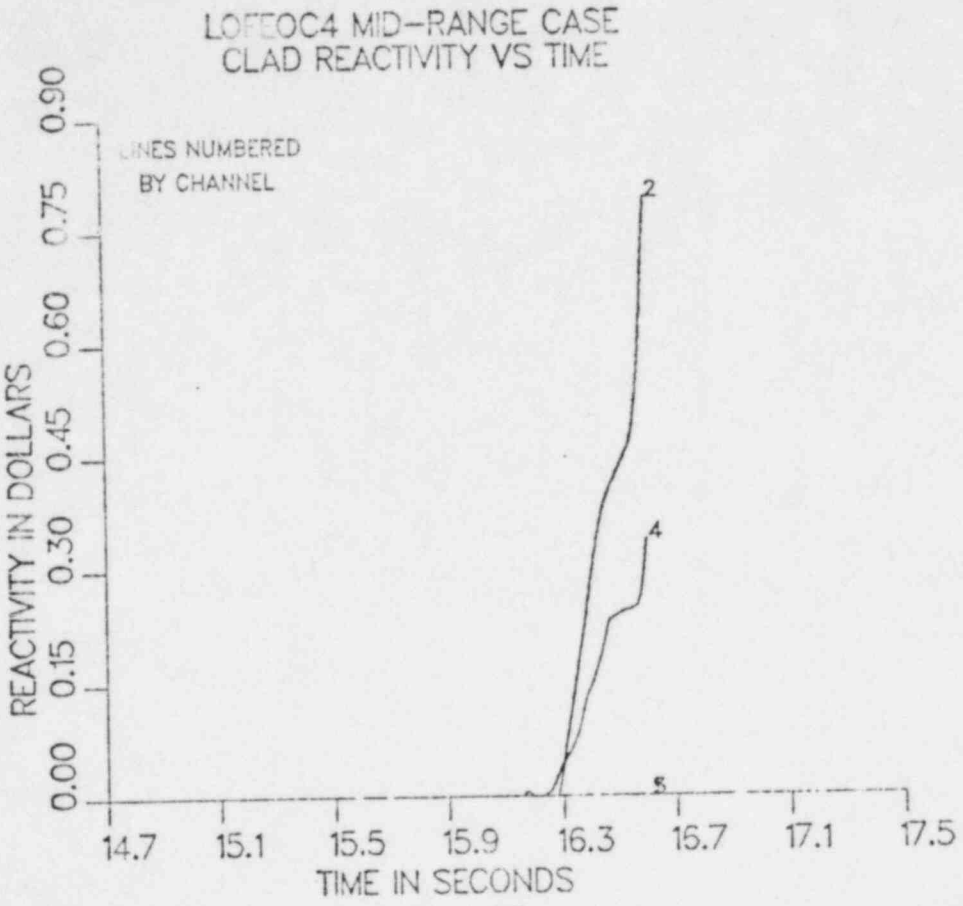
LOFEOC4 MID-RANGE CASE
CLAD REACTIVITY VS TIME
LINES NUMBERED
BY CHANNEL
2
4
5
REACTIVITY IN DOLLARS
0.00
0.15
0.30
0.45
0.60
0.75
0.90
14.7
15.1
15.5
15.9
16.3
16.7
17.1
17.5
TIME IN SECONDS

Fig 23

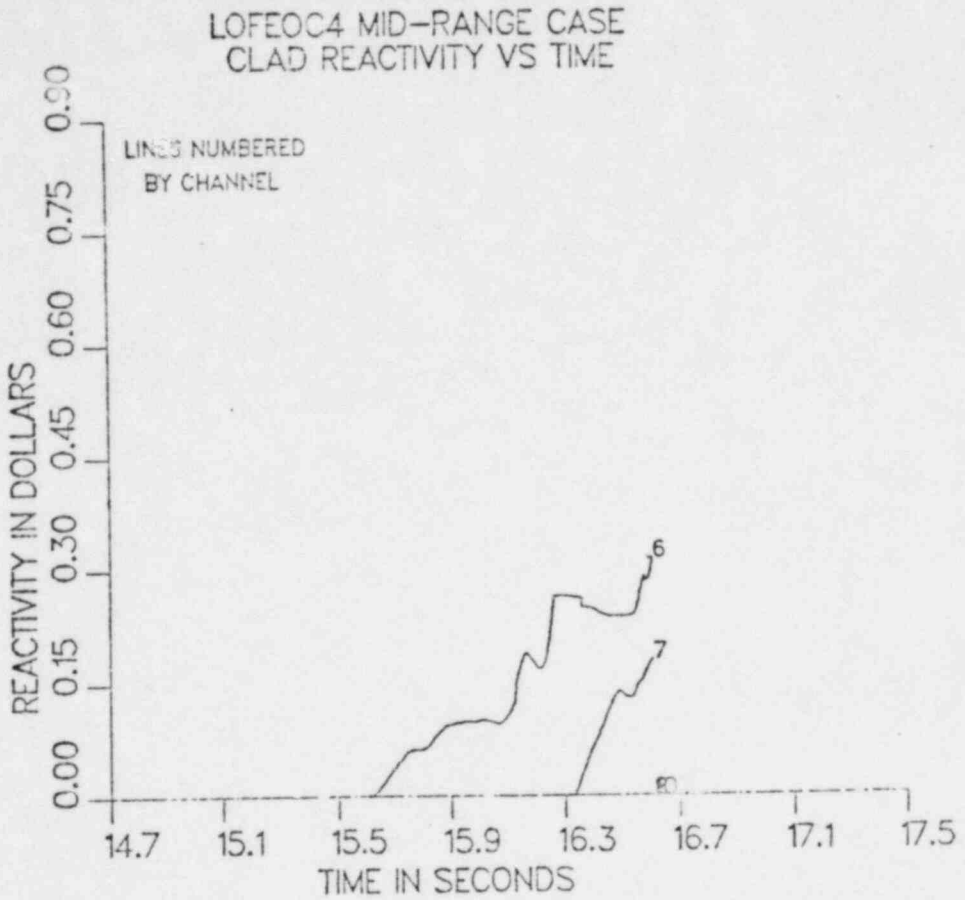
LOFEOC4 MID-RANGE CASE
CLAD REACTIVITY VS TIME
LINES NUMBERED
BY CHANNEL
REACTIVITY IN DOLLARS
0.00
0.15
0.30
0.45
0.60
0.75
0.90
6
7
80
14.7
15.1
15.5
15.9
16.3
16.7
17.1
17.5
TIME IN SECONDS

Fig 24

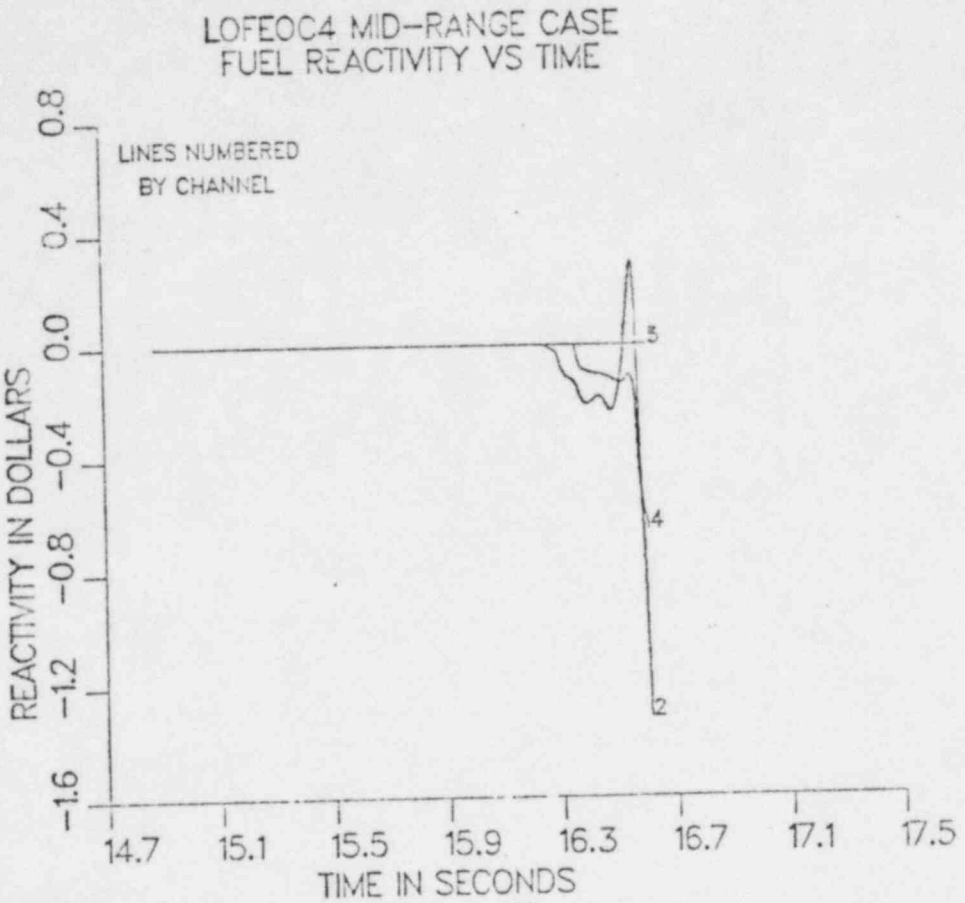
LOFEOC4 MID-RANGE CASE
FUEL REACTIVITY VS TIME
LINES NUMBERED
BY CHANNEL
REACTIVITY IN DOLLARS
0.8
0.4
0.0
-0.4
-0.8
-1.2
-1.6
3
4
2
14.7
15.1
15.5
15.9
16.3
16.7
17.1
17.5
TIME IN SECONDS

Fig 25

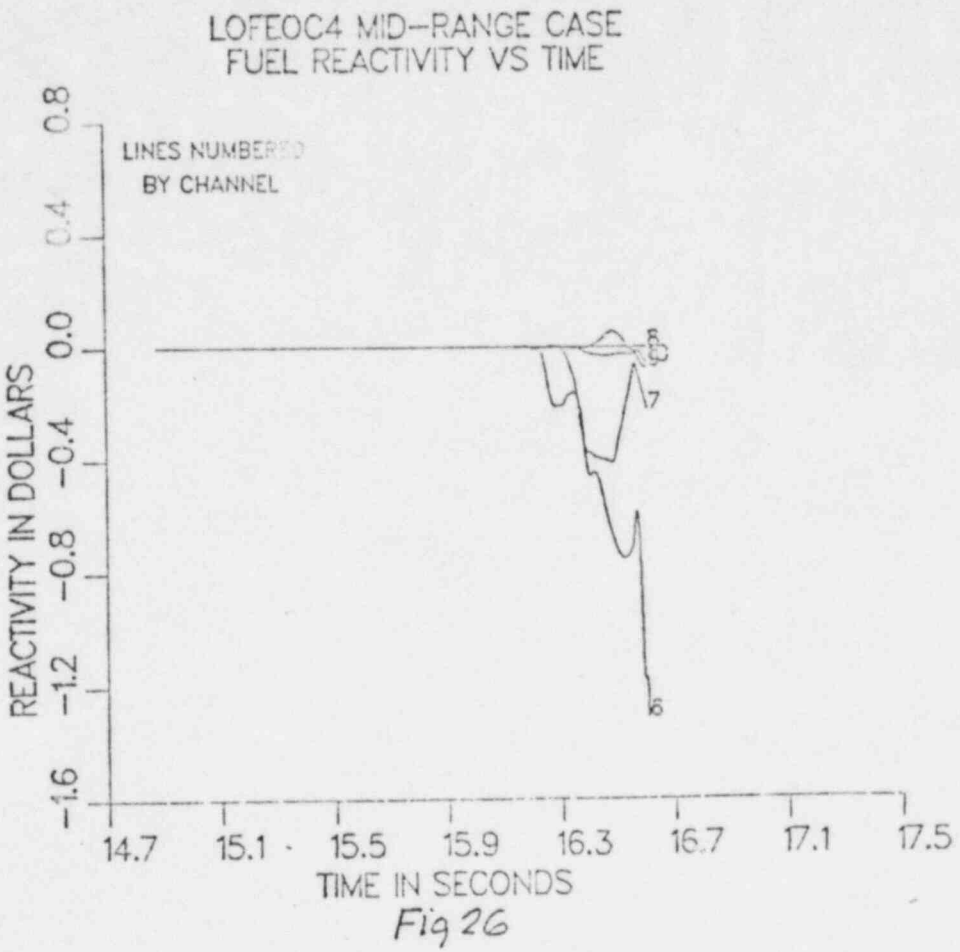
LOFEOC4 MID-RANGE CASE
FUEL REACTIVITY VS TIME
LINES NUMBERED
BY CHANNEL
REACTIVITY IN DOLLARS
0.8
0.4
0.0
-0.4
-0.8
-1.2
-1.6
14.7
15.1
15.5
15.9
16.3
16.7
17.1
17.5
TIME IN SECONDS

Fig 26

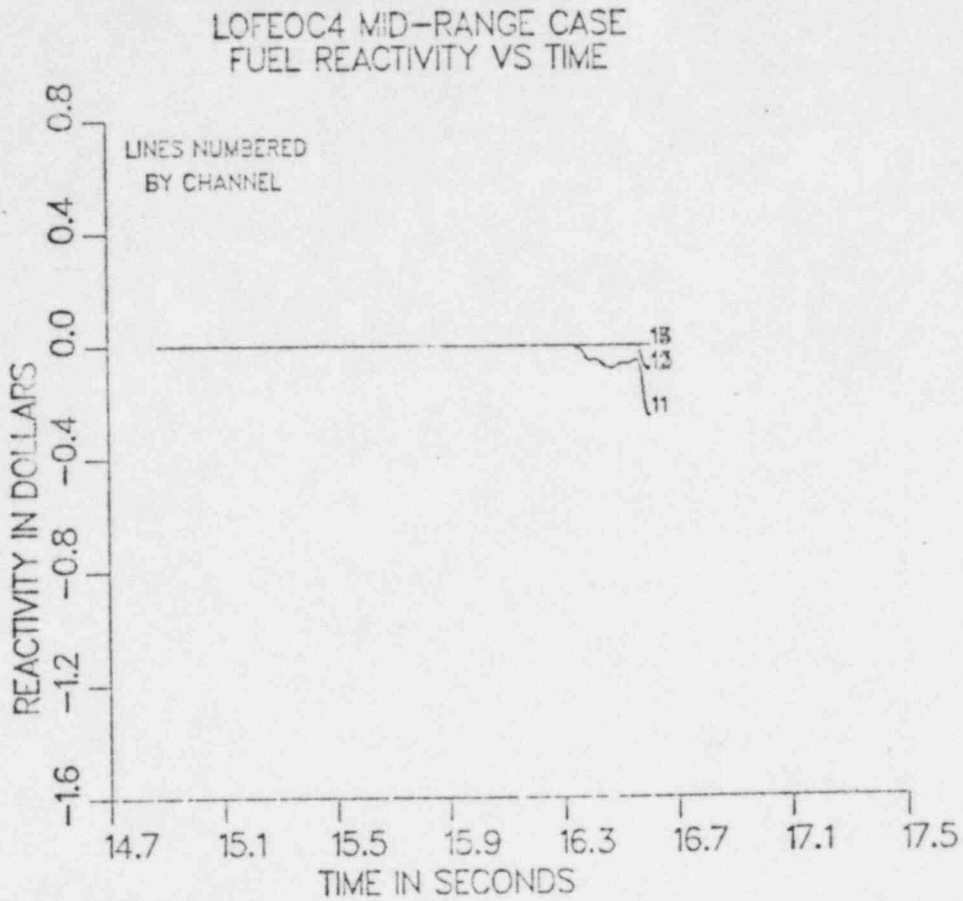
LOFEOC4 MID-RANGE CASE
FUEL REACTIVITY VS TIME
LINES NUMBERED
BY CHANNEL
REACTIVITY IN DOLLARS
0.8
0.4
0.0
-0.4
-0.8
-1.2
-1.6
13
12
11
14.7
15.1
15.5
15.9
16.3
16.7
17.1
17.5
TIME IN SECONDS

Fig 27

MID-RANGE CASE FOR THE HETEROGENEOUS CORE AT EOC - 4
SUBASSEMBLIES FOR CHANNEL 6

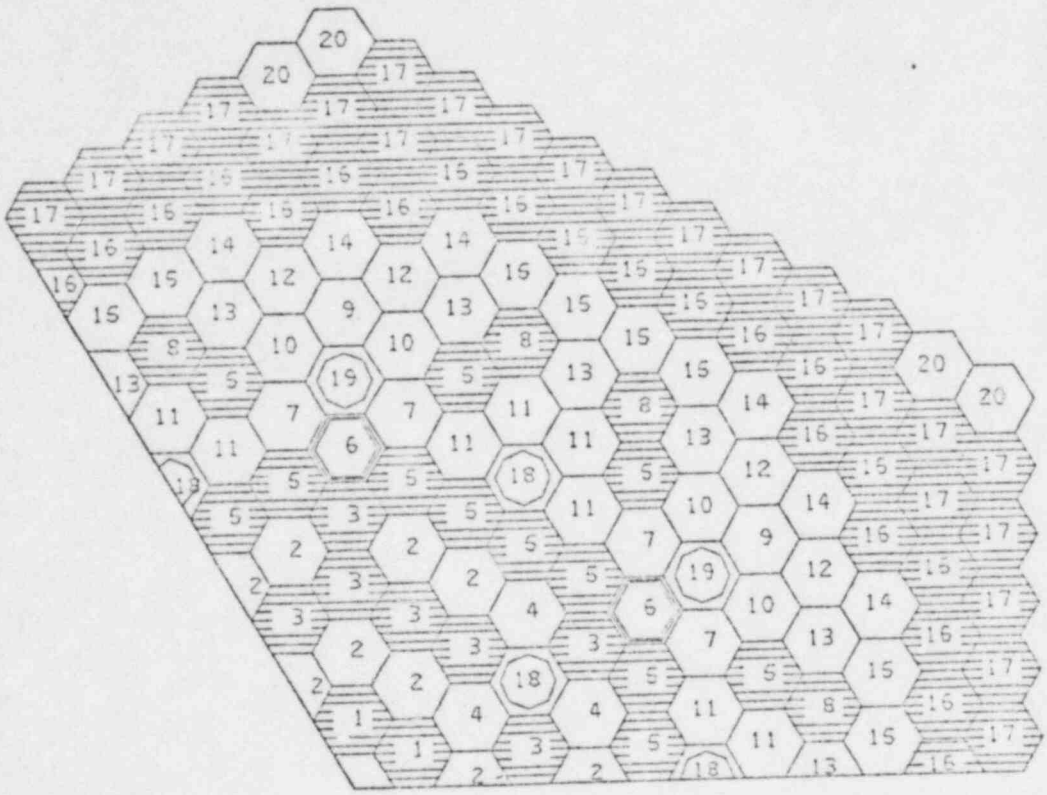

Fig 28

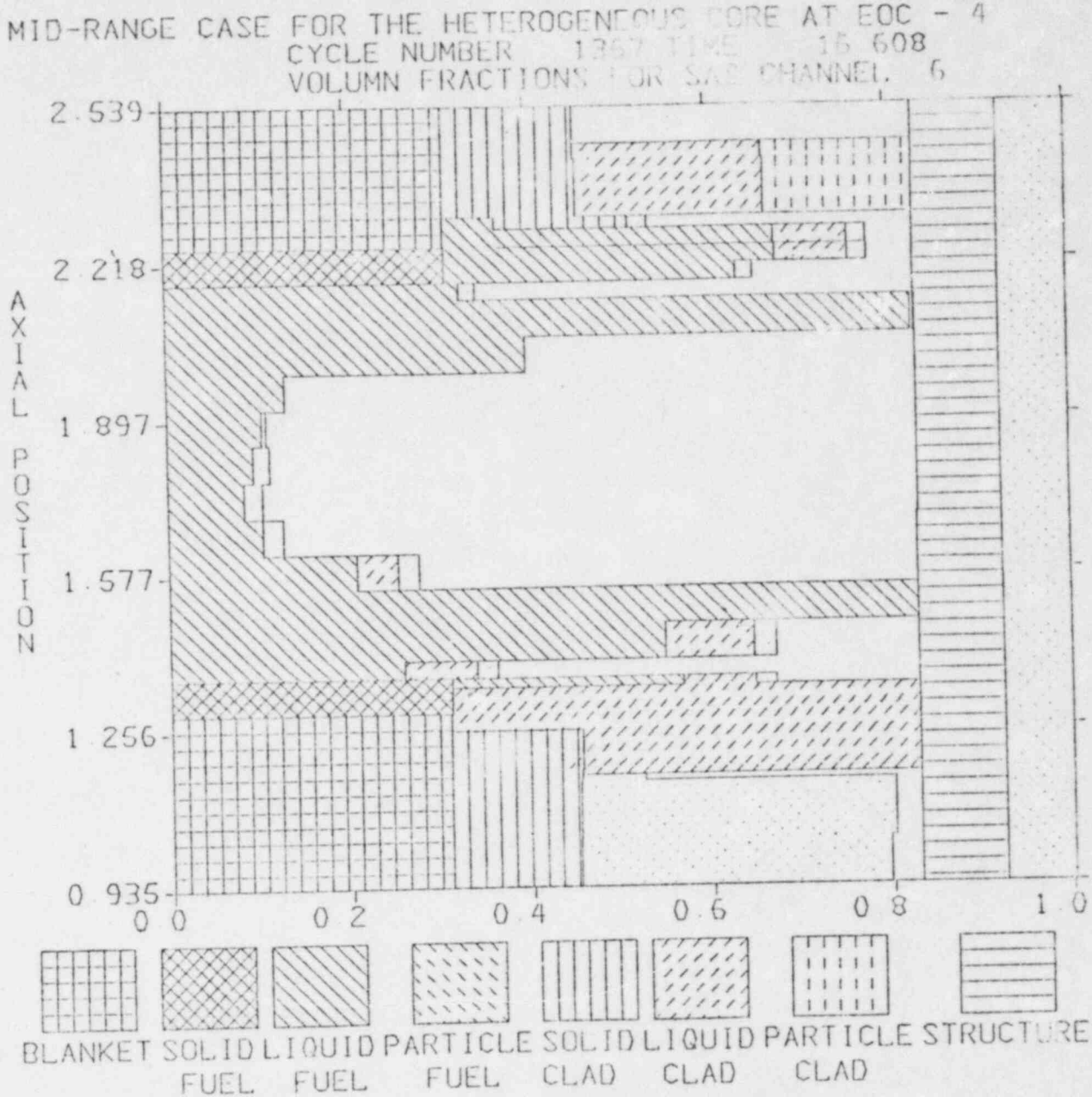
MID-RANGE CASE FOR THE HETEROGENEOUS CORE AT EOC - 4
CYCLE NUMBER 1367 TIME 15 608
VOLUMN FRACTIONS FOR SAS CHANNEL 6
2 539
2 218
1 897
1 577
1 256
0 935
AXIAL POSITION
0 0
0 2
0 4
0 6
0 8
1 0
BLANKET
SOLID FUEL
LIQUID FUEL
PARTICLE FUEL
SOLID CLAD
LIQUID CLAD
PARTICLE CLAD
STRUCTURE

Fig 29

B.II.9

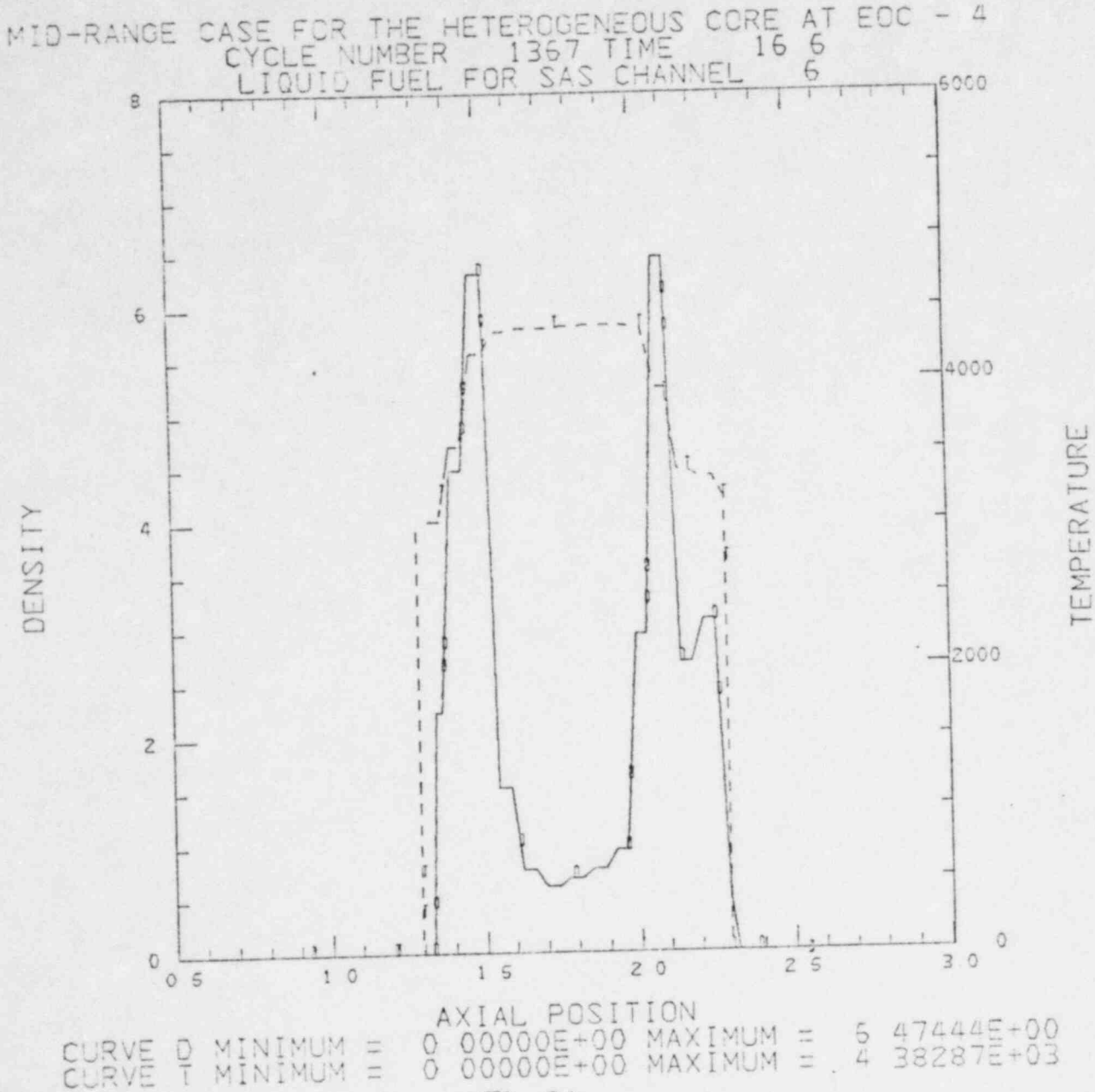
MID-RANGE CASE FOR THE HETEROGENEOUS CORE AT EOC - 4
CYCLE NUMBER 1367 TIME 16 6
LIQUID FUEL FOR SAS CHANNEL 6
DENSITY
TEMPERATURE
AXIAL POSITION
0
2
4
6
8
0
2000
4000
6000
0 5
1 0
1 5
2 0
2 5
3 0
CURVE D MINIMUM = 0 00000E+00 MAXIMUM = 5 47444E+00
CURVE T MINIMUM = 0 00000E+00 MAXIMUM = 4 38287E+03

Fig 30

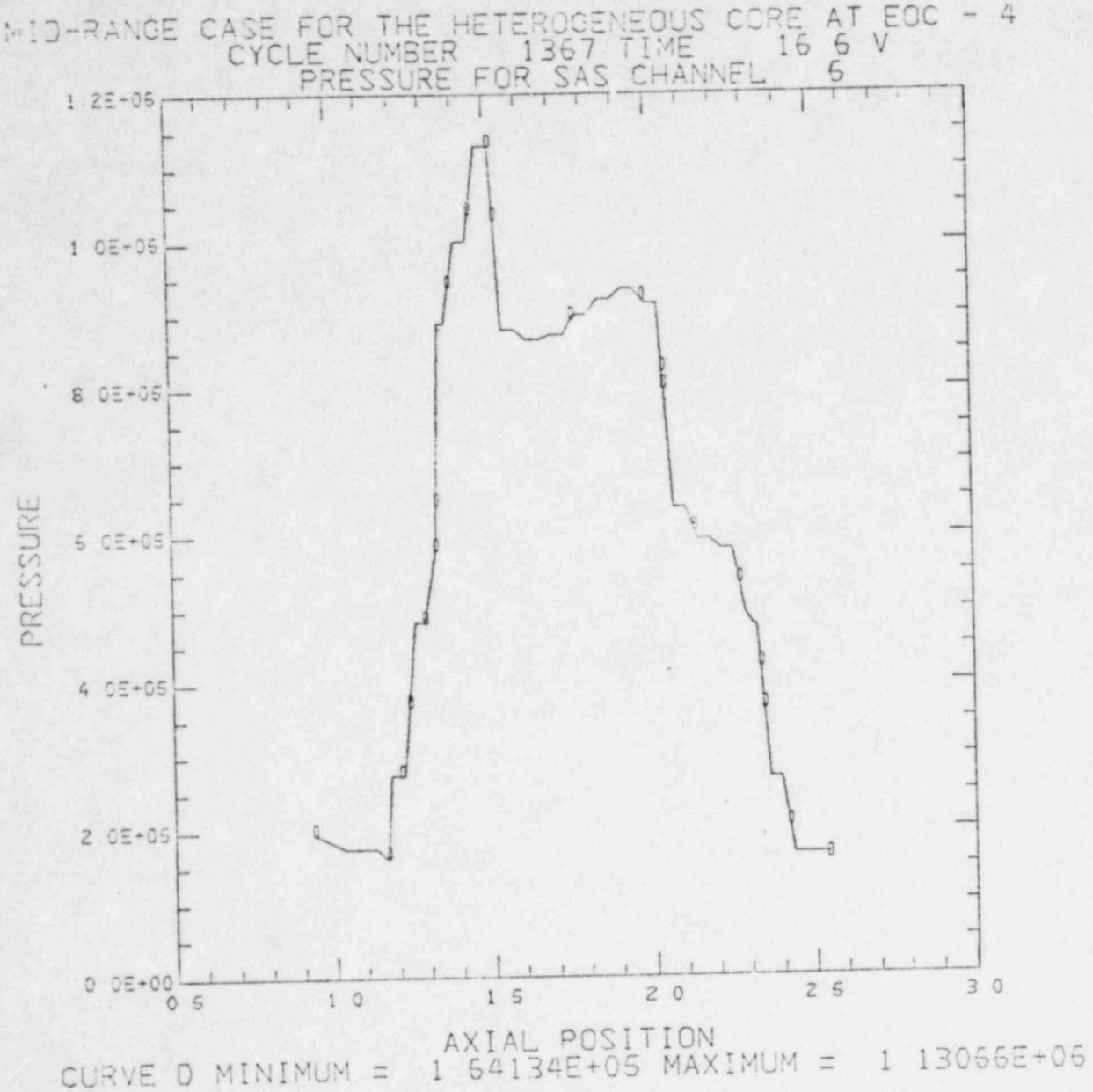
MID-RANGE CASE FOR THE HETEROGENEOUS CORE AT EOC - 4
CYCLE NUMBER 1367 TIME 16 6 V
PRESSURE FOR SAS CHANNEL 6
1 2E+06
1 0E+06
8 0E+05
6 0E+05
4 0E+05
2 0E+05
0 0E+00
PRESSURE
0 5
1 0
1 5
2 0
2 5
3 0
AXIAL POSITION
CURVE D MINIMUM = 1 64134E+05 MAXIMUM = 1 13066E+06

Fig 31

MID-RANGE CASE FOR THE HETEROGENEOUS CORE AT EOC - 4
SUBASSEMBLIES FOR CHANNEL 10

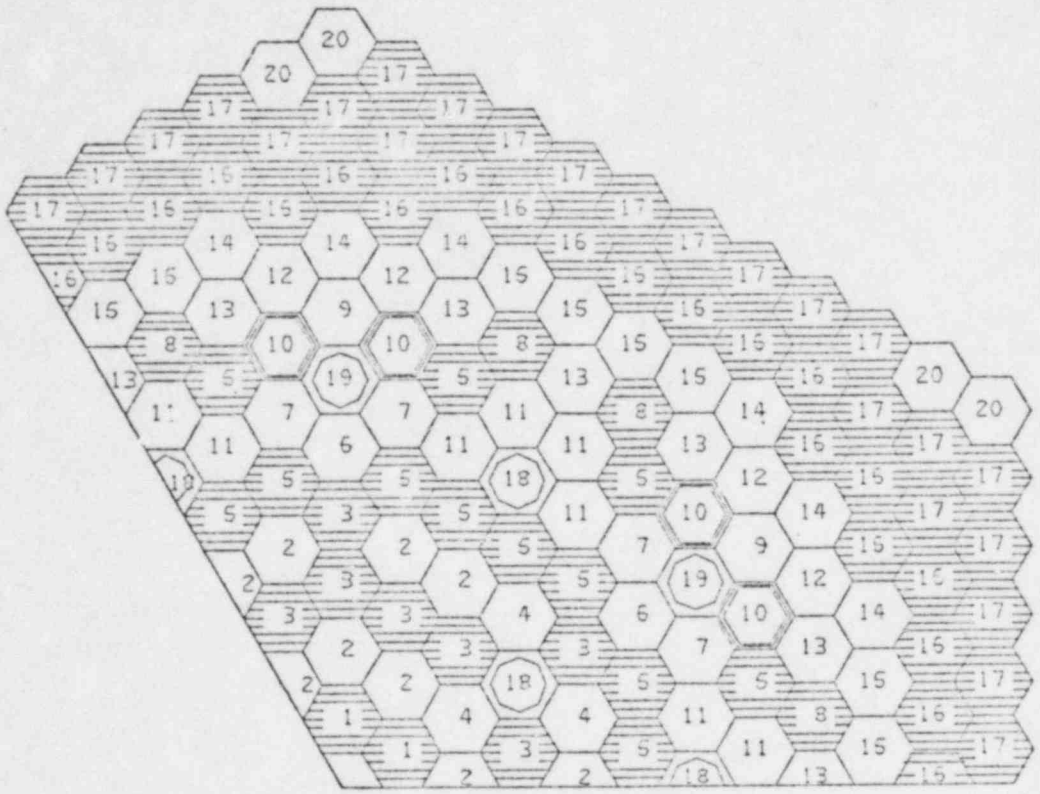

Fig 32

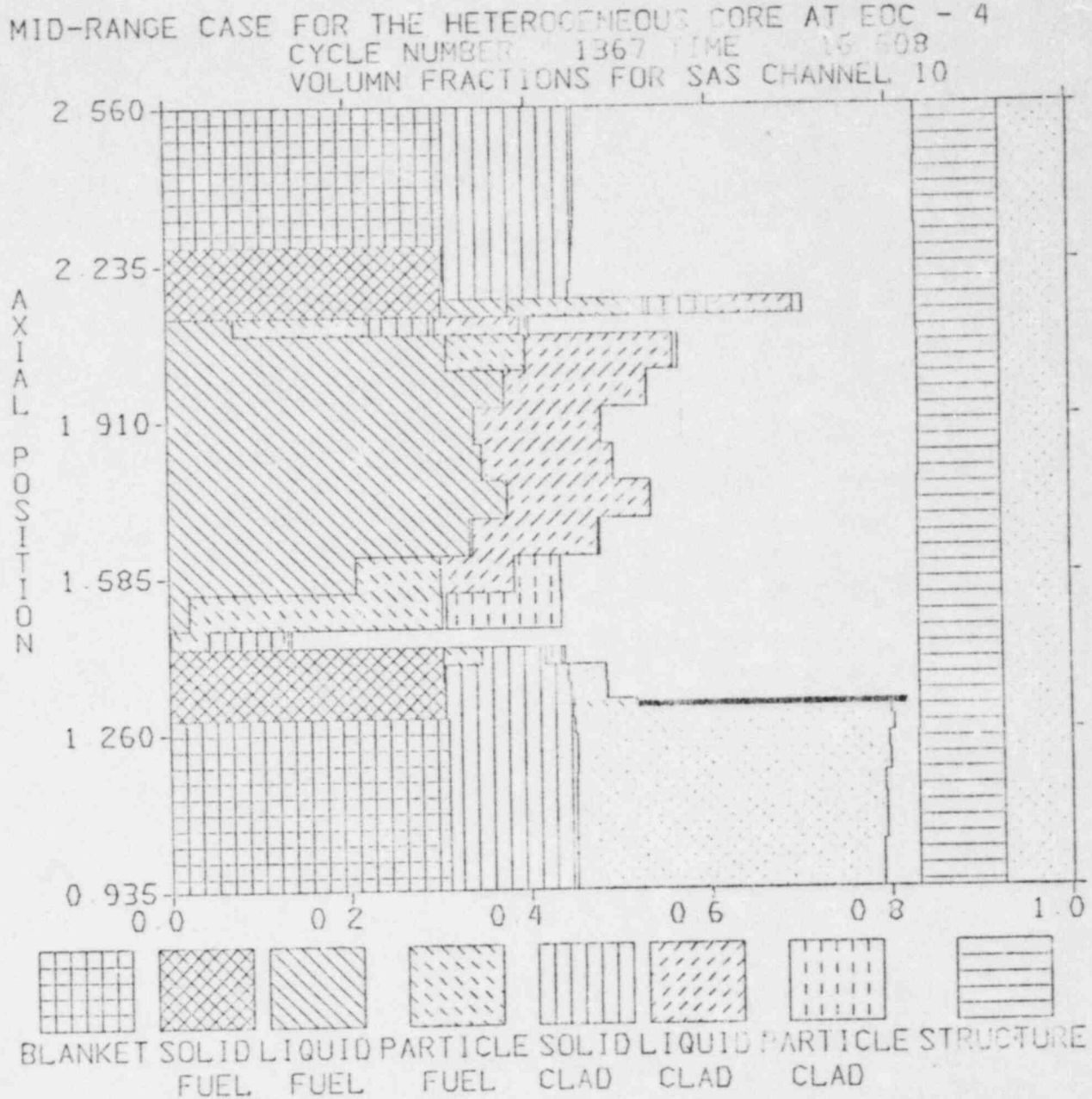
MID-RANGE CASE FOR THE HETEROGENEOUS CORE AT EOC - 4
CYCLE NUMBER 1367 TIME 15 608
VOLUMN FRACTIONS FOR SAS CHANNEL 10
AXIAL POSITION
2 560
2 235
1 910
1 585
1 260
0 935
0 0
0 2
0 4
0 6
0 8
1 0
BLANKET
SOLID FUEL
LIQUID FUEL
PARTICLE FUEL
SOLID CLAD
LIQUID CLAD
PARTICLE CLAD
STRUCTURE

Fig 33

BII.3

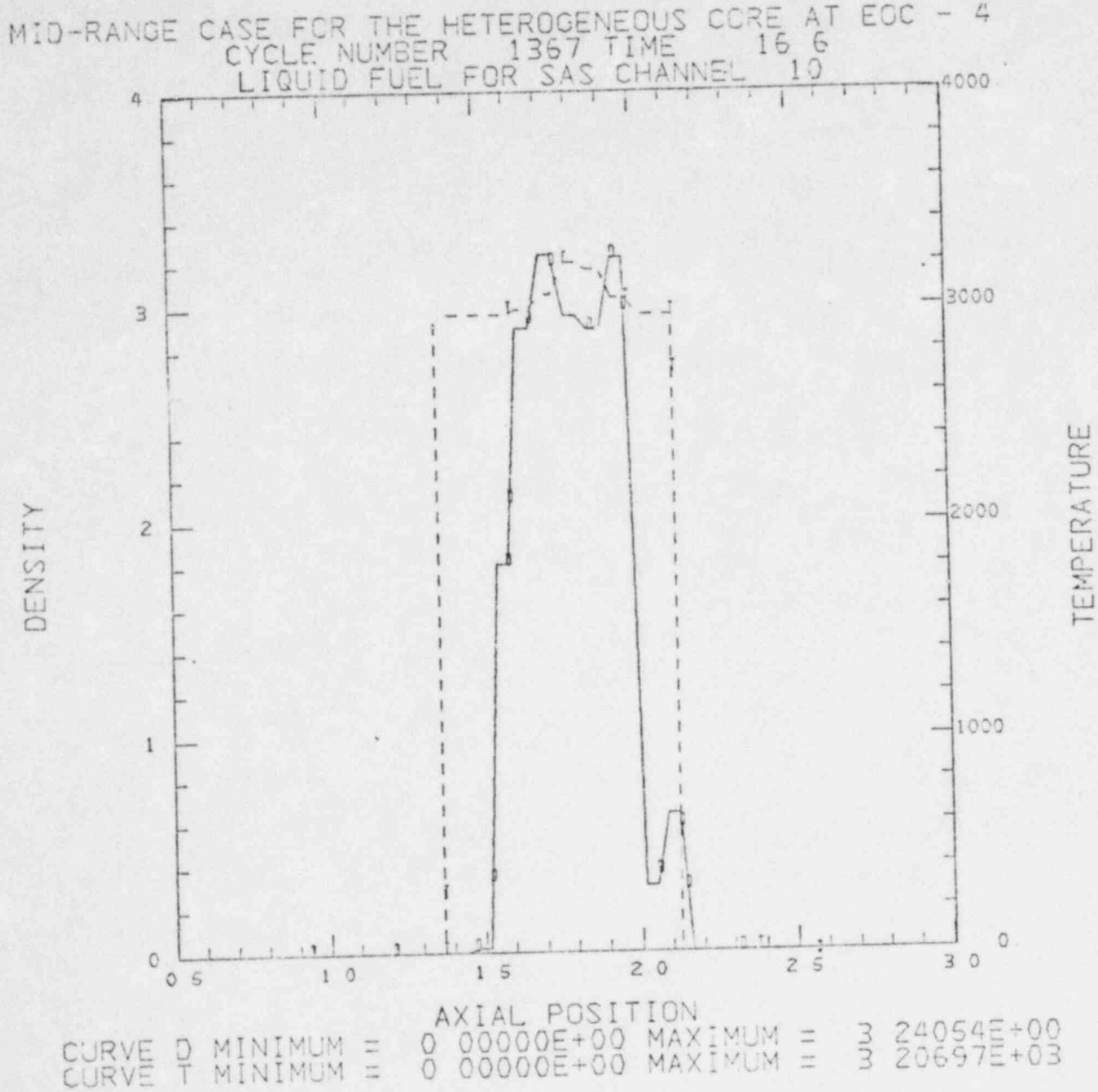
MID-RANGE CASE FOR THE HETEROGENEOUS CORE AT EOC - 4
CYCLE NUMBER 1367 TIME 16 6
LIQUID FUEL FOR SAS CHANNEL 10
DENSITY
TEMPERATURE
AXIAL POSITION
0
1
2
3
4
0
1000
2000
3000
4000
0 5
1 0
1 5
2 0
2 5
3 0
CURVE D MINIMUM = 0 00000E+00 MAXIMUM = 3 24054E+00
CURVE T MINIMUM = 0 00000E+00 MAXIMUM = 3 20697E+03

Fig 34

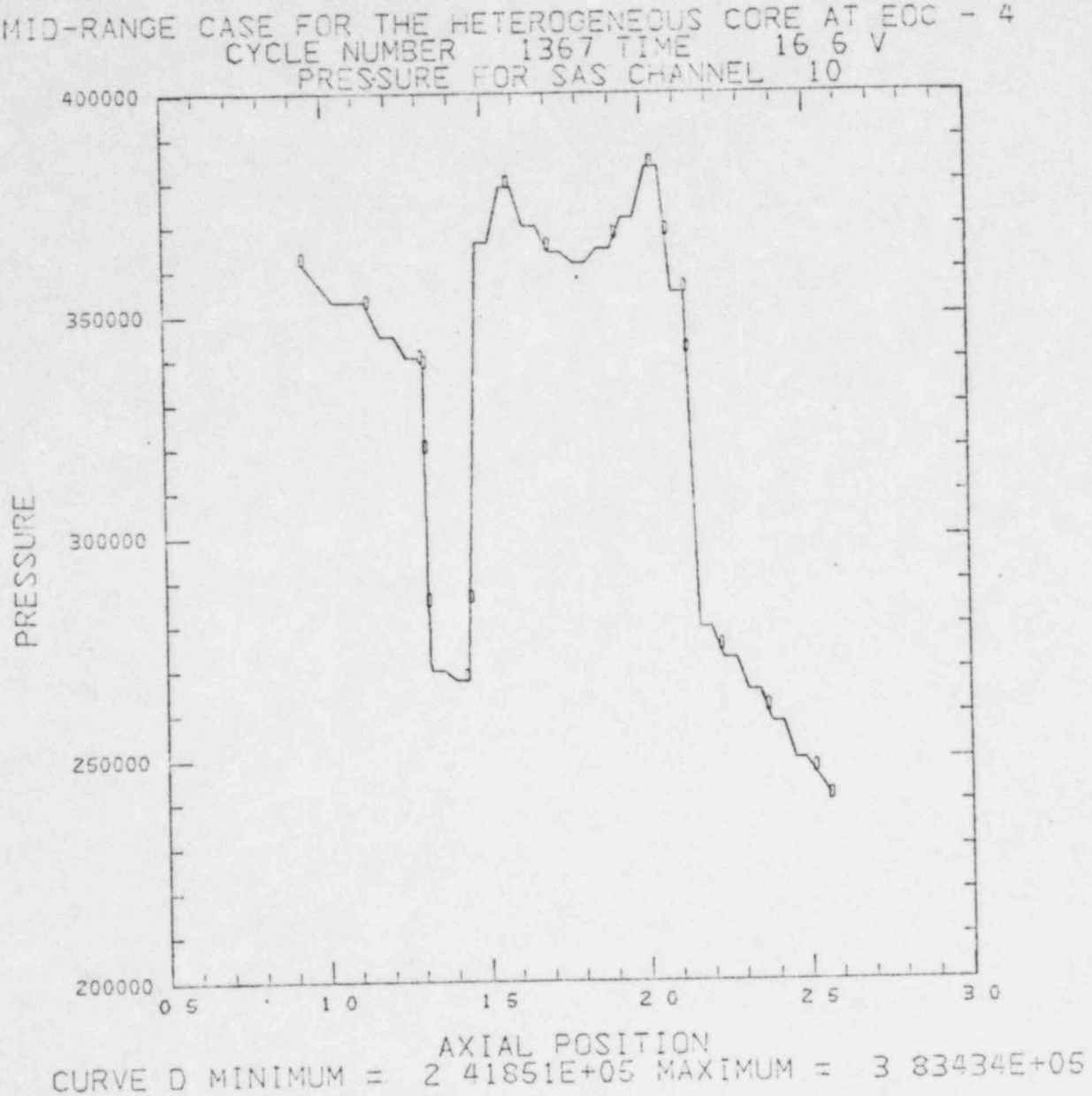
MID-RANGE CASE FOR THE HETEROGENEOUS CORE AT EOC - 4
CYCLE NUMBER 1367 TIME 16 6 V
PRESSURE FOR SAS CHANNEL 10
400000
350000
300000
250000
200000
PRESSURE
0 5
1 0
1 5
2 0
2 5
3 0
AXIAL POSITION
CURVE D MINIMUM = 2 41851E+05 MAXIMUM = 3 83434E+05

Fig 35

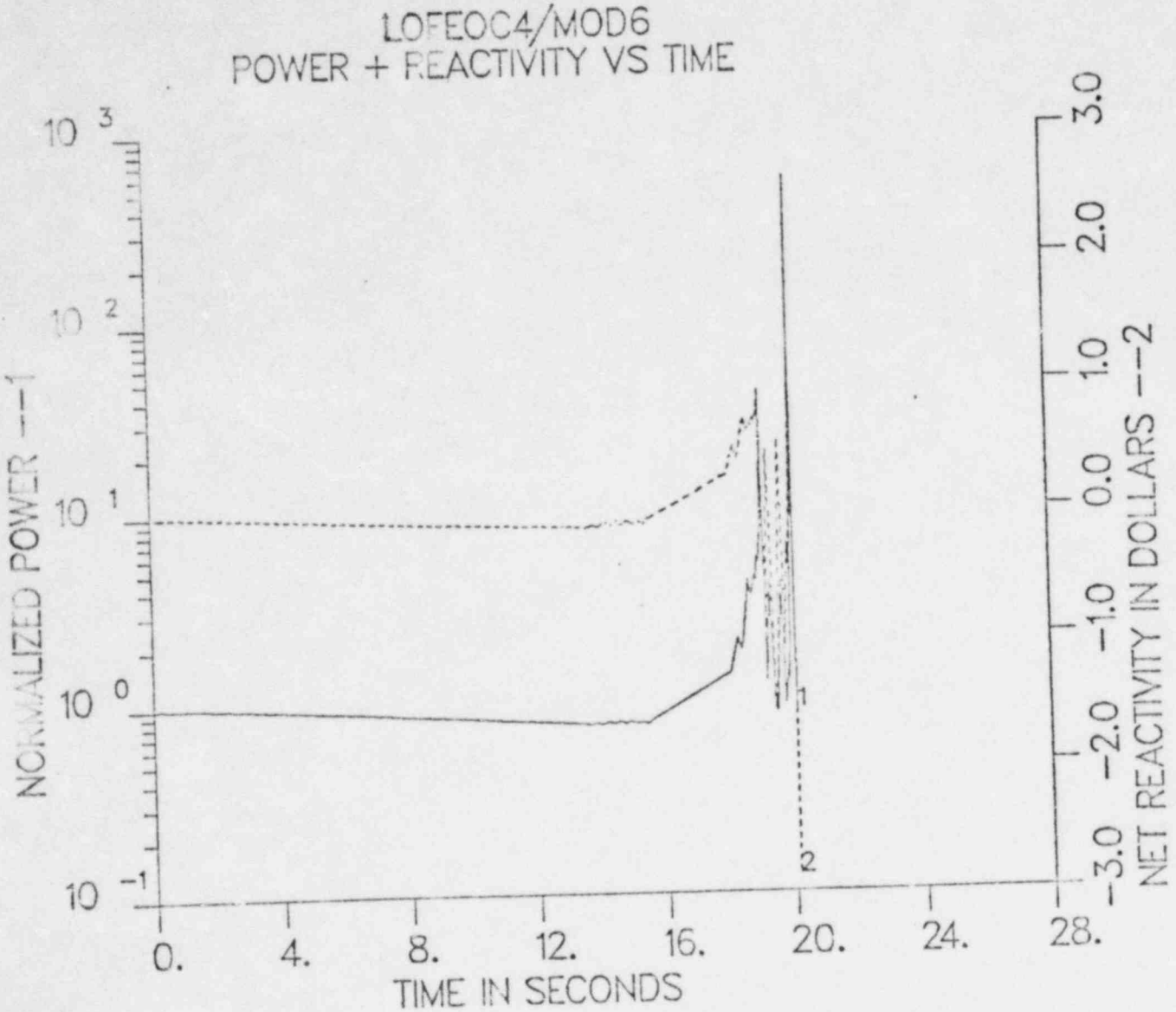
LOFEOC4/MOD6
POWER + REACTIVITY VS TIME
NORMALIZED POWER --1
10 3
10 2
10 1
10 0
10 -1
0.
4.
8.
12.
16.
20.
24.
28.
TIME IN SECONDS
3.0
2.0
1.0
0.0
-1.0
-2.0
-3.0
NET REACTIVITY IN DOLLARS --2
1
2

Fig 63

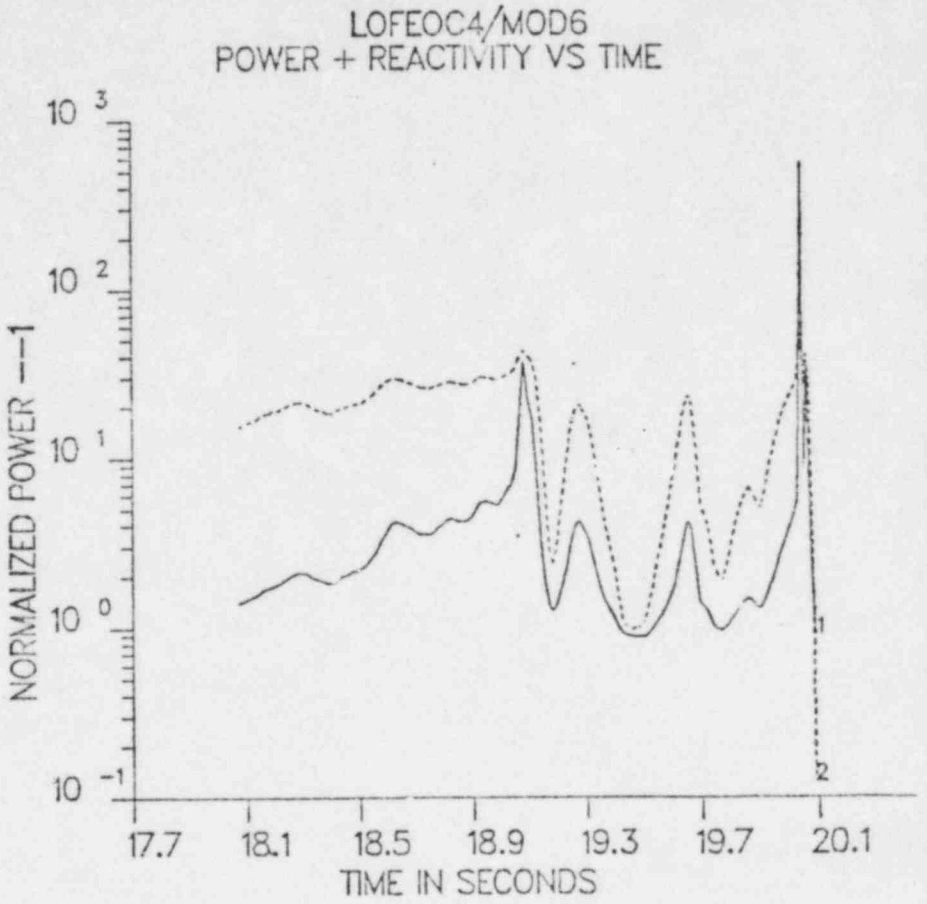
LOFEOC4/MOD6
POWER + REACTIVITY VS TIME
NORMALIZED POWER —1
10 3
10 2
10 1
10 0
10 -1
17.7
18.1
18.5
18.9
19.3
19.7
20.1
TIME IN SECONDS
1
2

Fig 64

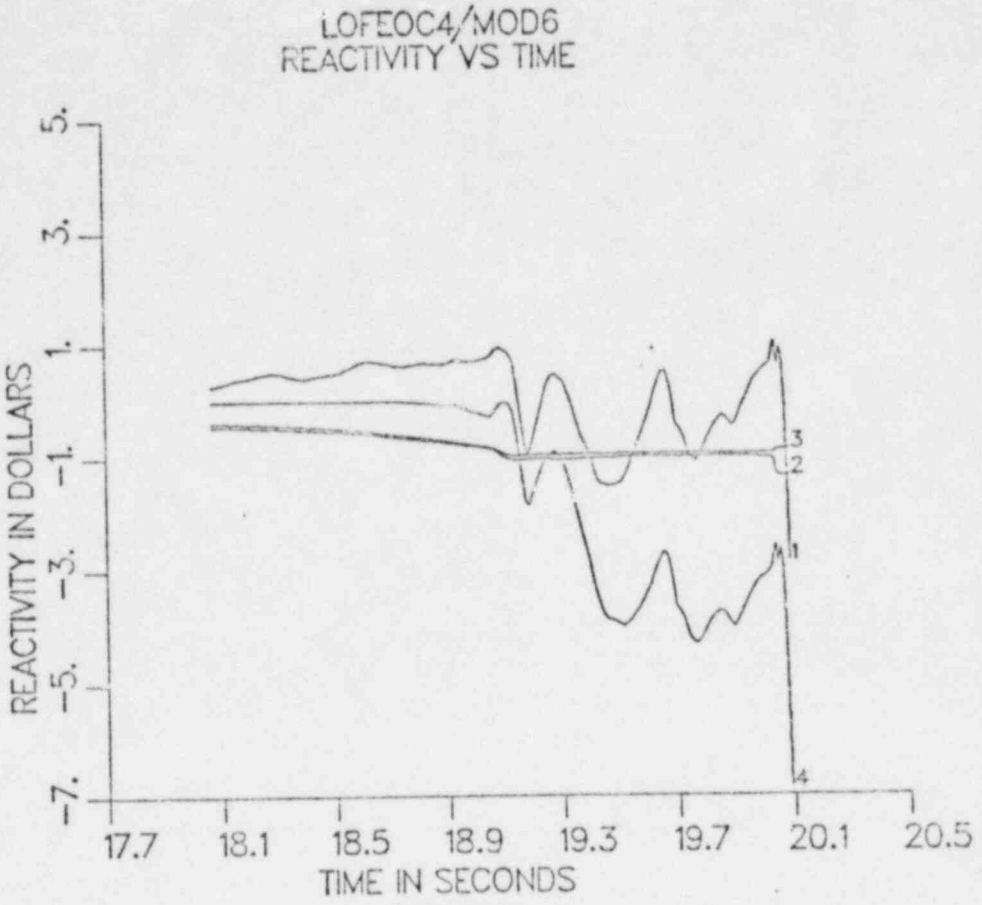
LOFEOC4/MOD6
REACTIVITY VS TIME
REACTIVITY IN DOLLARS
5.
3.
1.
-1.
-3.
-5.
-7.
17.7
18.1
18.5
18.9
19.3
19.7
20.1
20.5
TIME IN SECONDS
1
2
3
4

Fig 65

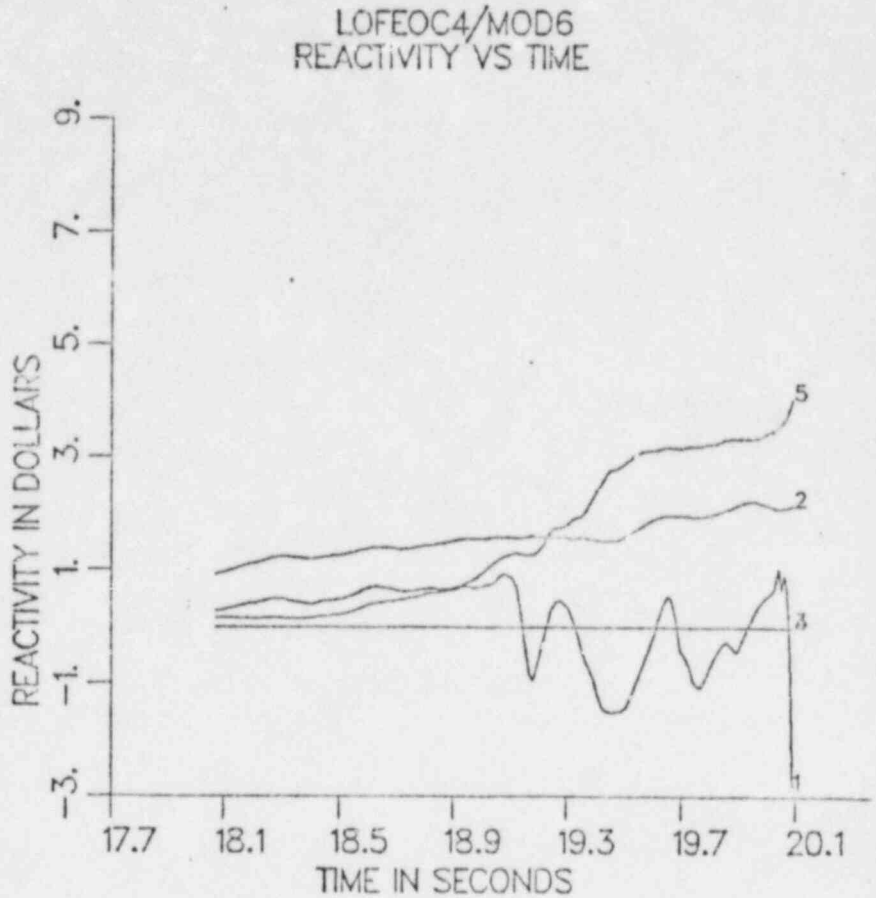
LOFEOC4/MOD6
REACTIVITY VS TIME
REACTIVITY IN DOLLARS
9.
7.
5.
3.
1.
-1.
-3.
17.7
18.1
18.5
18.9
19.3
19.7
20.1
TIME IN SECONDS
5
2
3
1

Fig 66

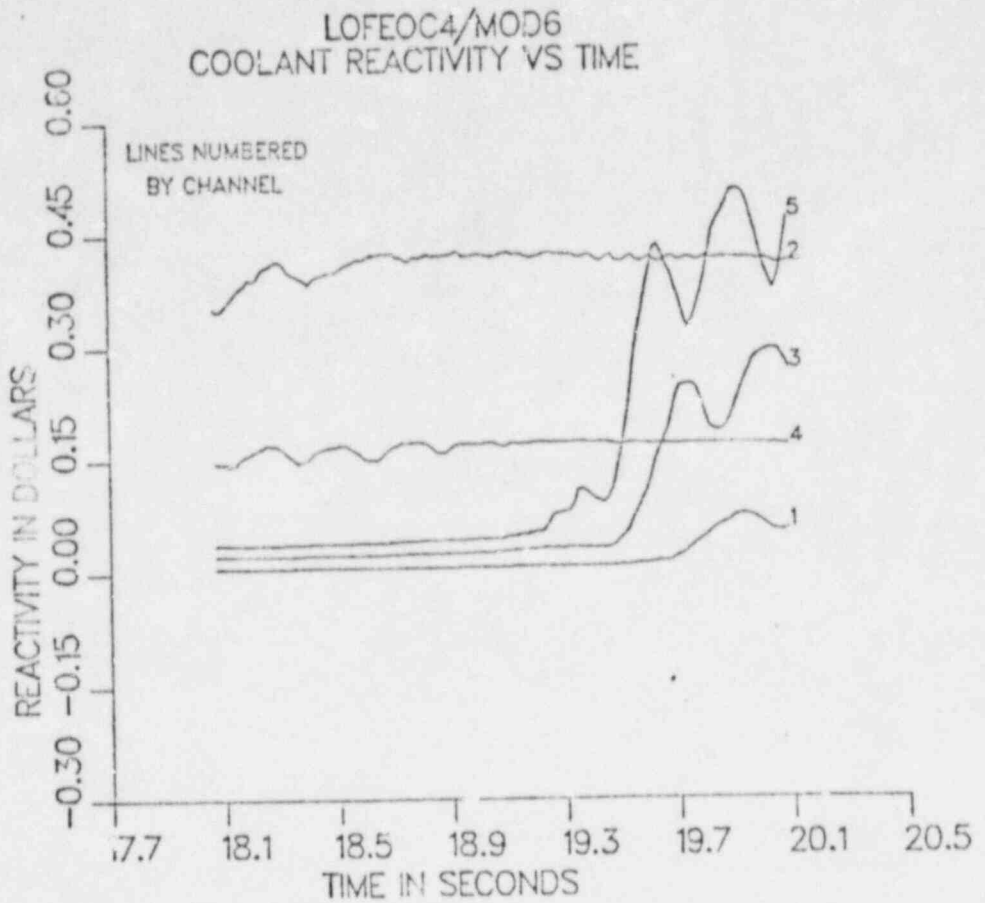
LOFEOC4/MOD6
COOLANT REACTIVITY VS TIME
LINES NUMBERED
BY CHANNEL
5
2
3
4
1
REACTIVITY IN DOLLARS
0.60
0.45
0.30
0.15
0.00
−0.15
−0.30
17.7
18.1
18.5
18.9
19.3
19.7
20.1
20.5
TIME IN SECONDS

Fig 67

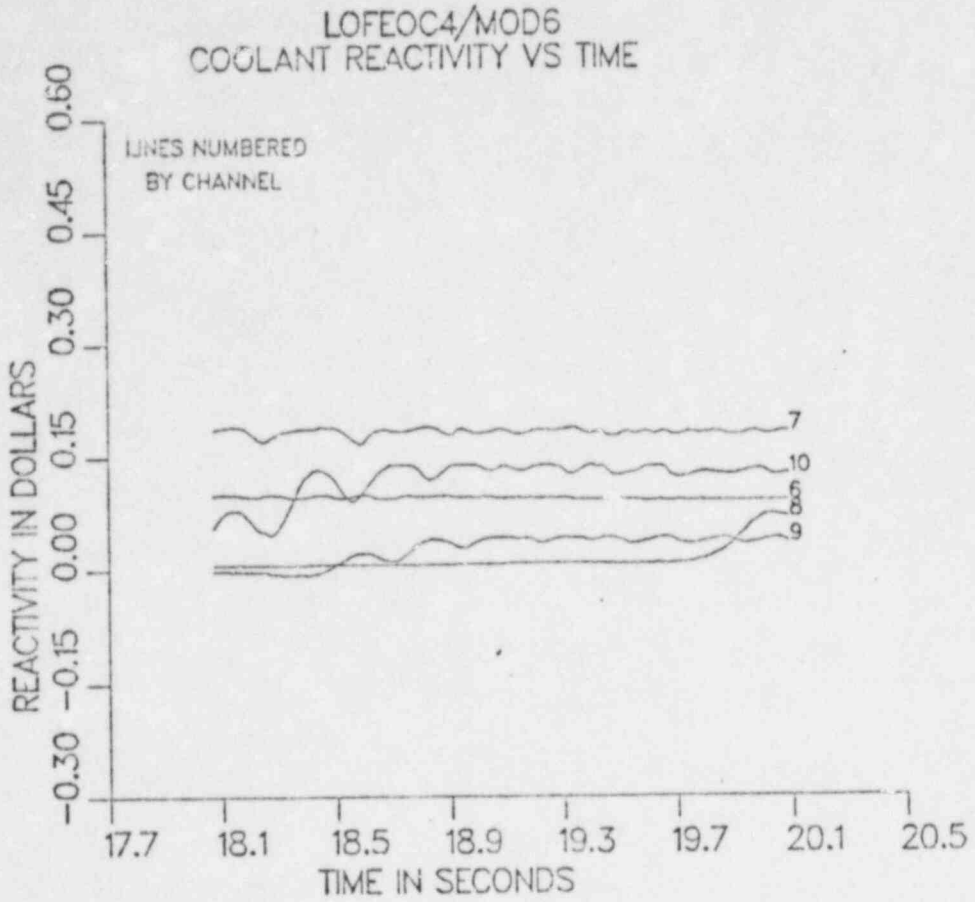
LOFEOC4/MOD6
COOLANT REACTIVITY VS TIME
LINES NUMBERED
BY CHANNEL
REACTIVITY IN DOLLARS
0.60
0.45
0.30
0.15
0.00
-0.15
-0.30
7
10
8
9
17.7
18.1
18.5
18.9
19.3
19.7
20.1
20.5
TIME IN SECONDS

Fig 68

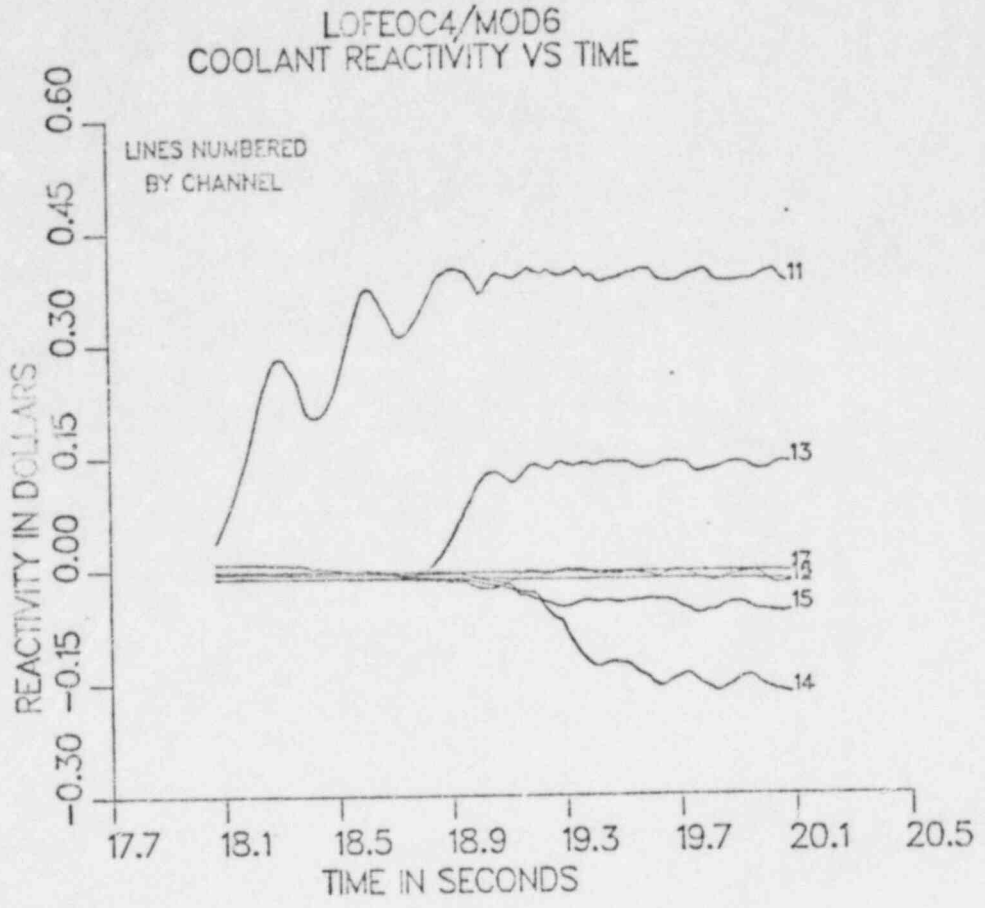
LOFEOC4/MOD6
COOLANT REACTIVITY VS TIME
LINES NUMBERED
BY CHANNEL
REACTIVITY IN DOLLARS
0.60
0.45
0.30
0.15
0.00
−0.15
−0.30
11
13
17
12
15
14
17.7
18.1
18.5
18.9
19.3
19.7
20.1
20.5
TIME IN SECONDS

Fig 69

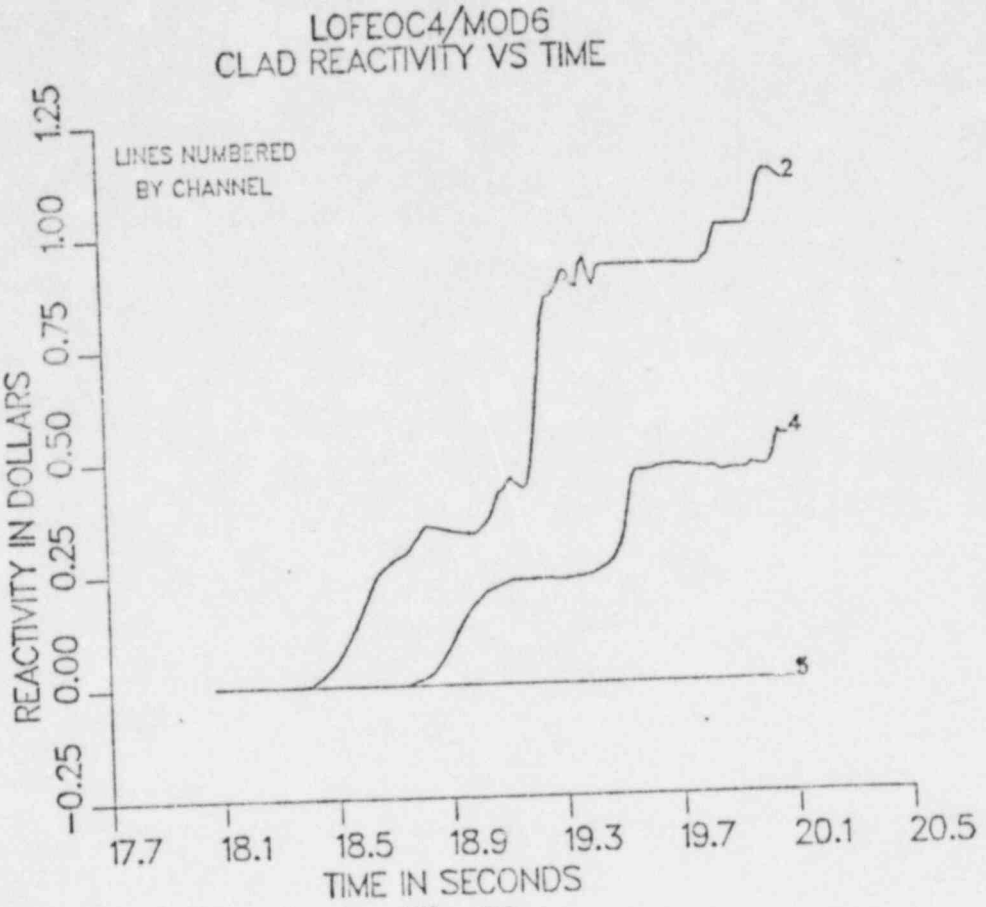
LOFEOC4/MOD6
CLAD REACTIVITY VS TIME
LINES NUMBERED
BY CHANNEL
REACTIVITY IN DOLLARS
1.25
1.00
0.75
0.50
0.25
0.00
−0.25
2
4
5
17.7
18.1
18.5
18.9
19.3
19.7
20.1
20.5
TIME IN SECONDS

Fig 70

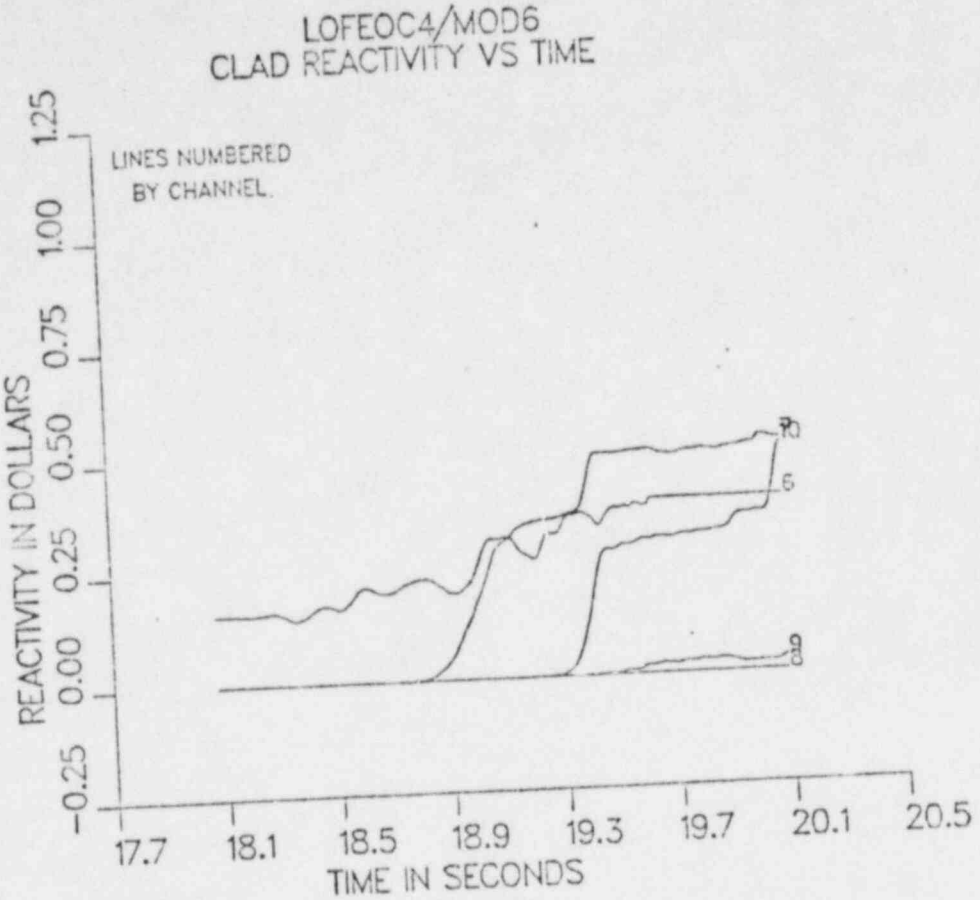
LOFEOC4/MOD6
CLAD REACTIVITY VS TIME
LINES NUMBERED
BY CHANNEL.
REACTIVITY IN DOLLARS
1.25
1.00
0.75
0.50
0.25
0.00
-0.25
17.7
18.1
18.5
18.9
19.3
19.7
20.1
20.5
TIME IN SECONDS
10
6
9
8

Fig 71

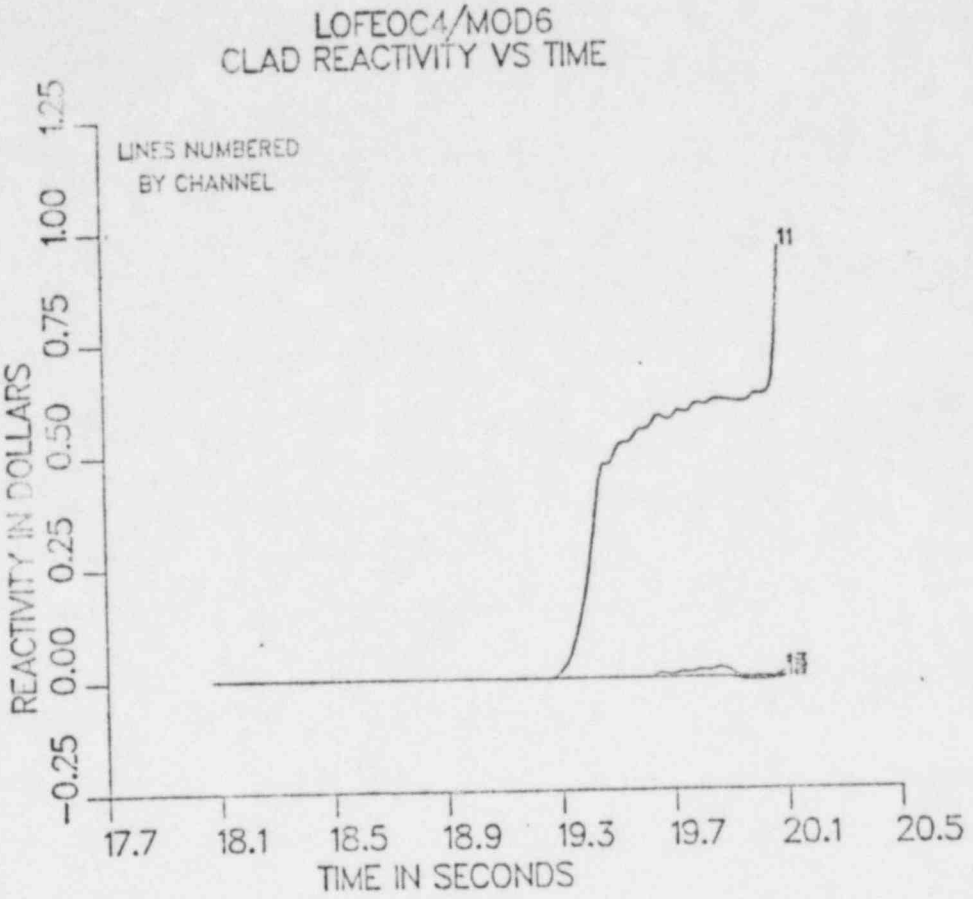
LOFEOC4/MOD6
CLAD REACTIVITY VS TIME
LINES NUMBERED
BY CHANNEL
REACTIVITY IN DOLLARS
-0.25
0.00
0.25
0.50
0.75
1.00
1.25
11
13
17.7
18.1
18.5
18.9
19.3
19.7
20.1
20.5
TIME IN SECONDS

Fig 72

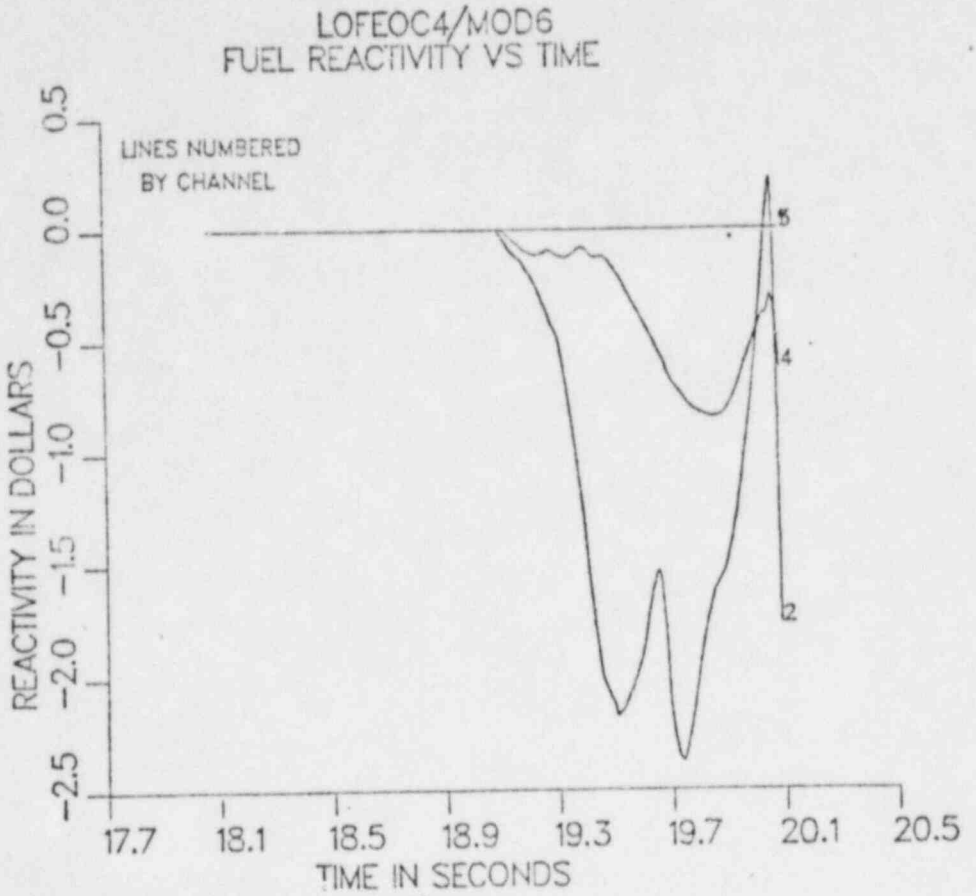
LOFEOC4/MOD6
FUEL REACTIVITY VS TIME
LINES NUMBERED
BY CHANNEL
REACTIVITY IN DOLLARS
0.5
0.0
-0.5
-1.0
-1.5
-2.0
-2.5
5
4
2
17.7
18.1
18.5
18.9
19.3
19.7
20.1
20.5
TIME IN SECONDS

Fig 73

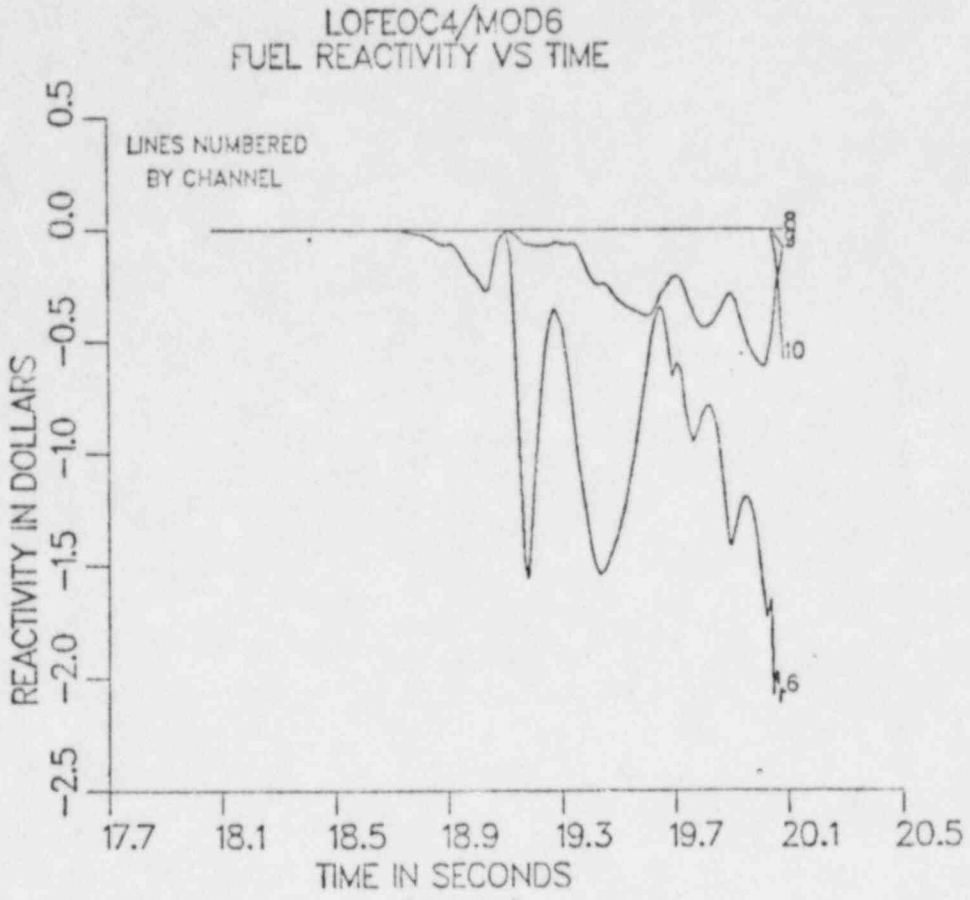
LOFEOC4/MOD6
FUEL REACTIVITY VS TIME
LINES NUMBERED
BY CHANNEL
REACTIVITY IN DOLLARS
0.5
0.0
-0.5
-1.0
-1.5
-2.0
-2.5
17.7
18.1
18.5
18.9
19.3
19.7
20.1
20.5
TIME IN SECONDS
8
10
6

Fig 74

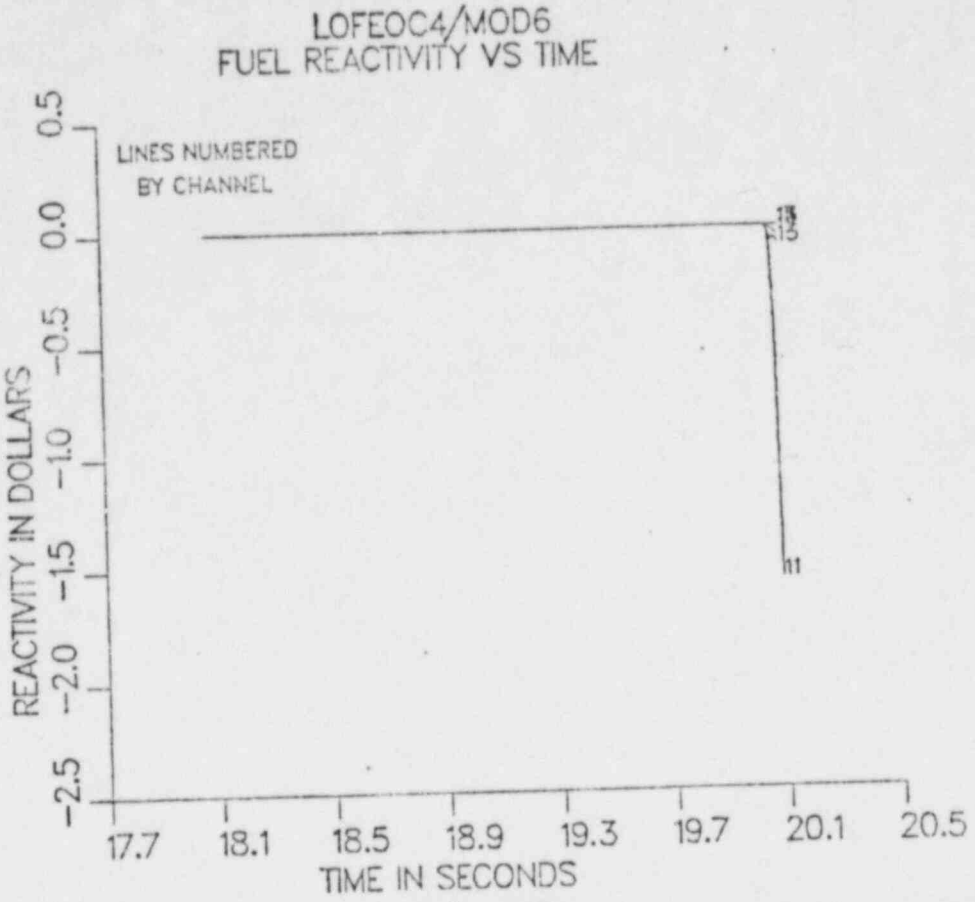
LOFEOC4/MOD6
FUEL REACTIVITY VS TIME
LINES NUMBERED
BY CHANNEL
REACTIVITY IN DOLLARS
0.5
0.0
-0.5
-1.0
-1.5
-2.0
-2.5
13
11
17.7
18.1
18.5
18.9
19.3
19.7
20.1
20.5
TIME IN SECONDS

Fig 7.5

MODS. REF CASE FOR THE HETEROGENEOUS CORE AT EOC - 4
SUBASSEMBLIES FOR CHANNEL 6

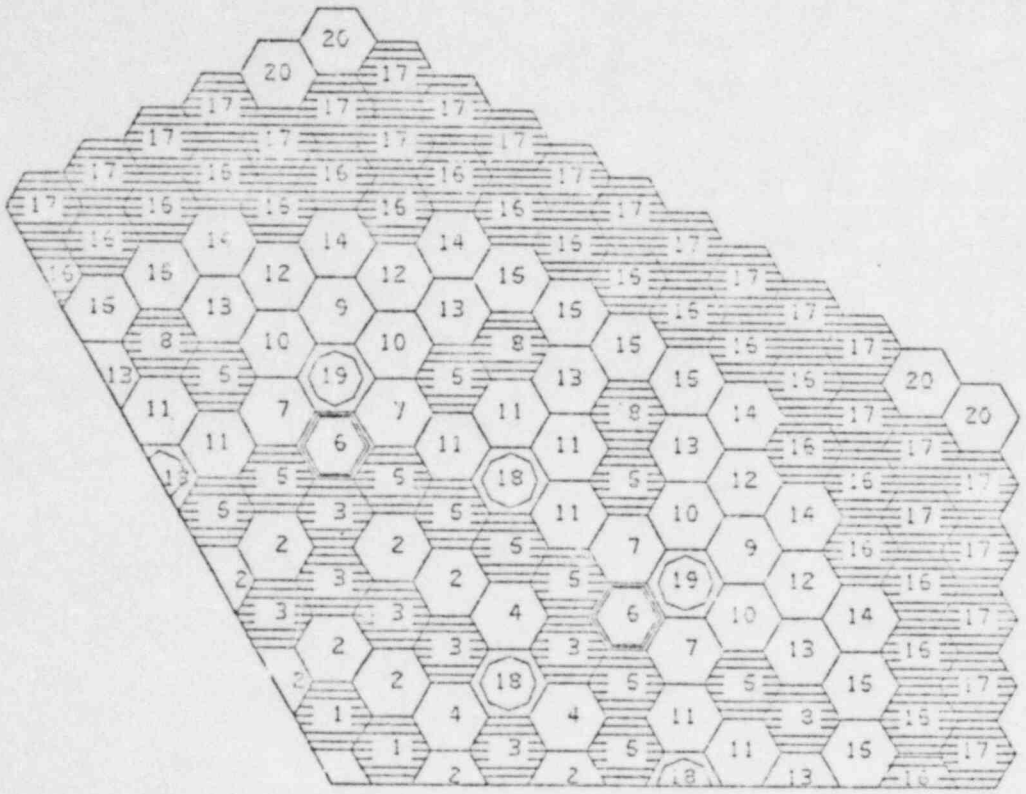

Fig 76

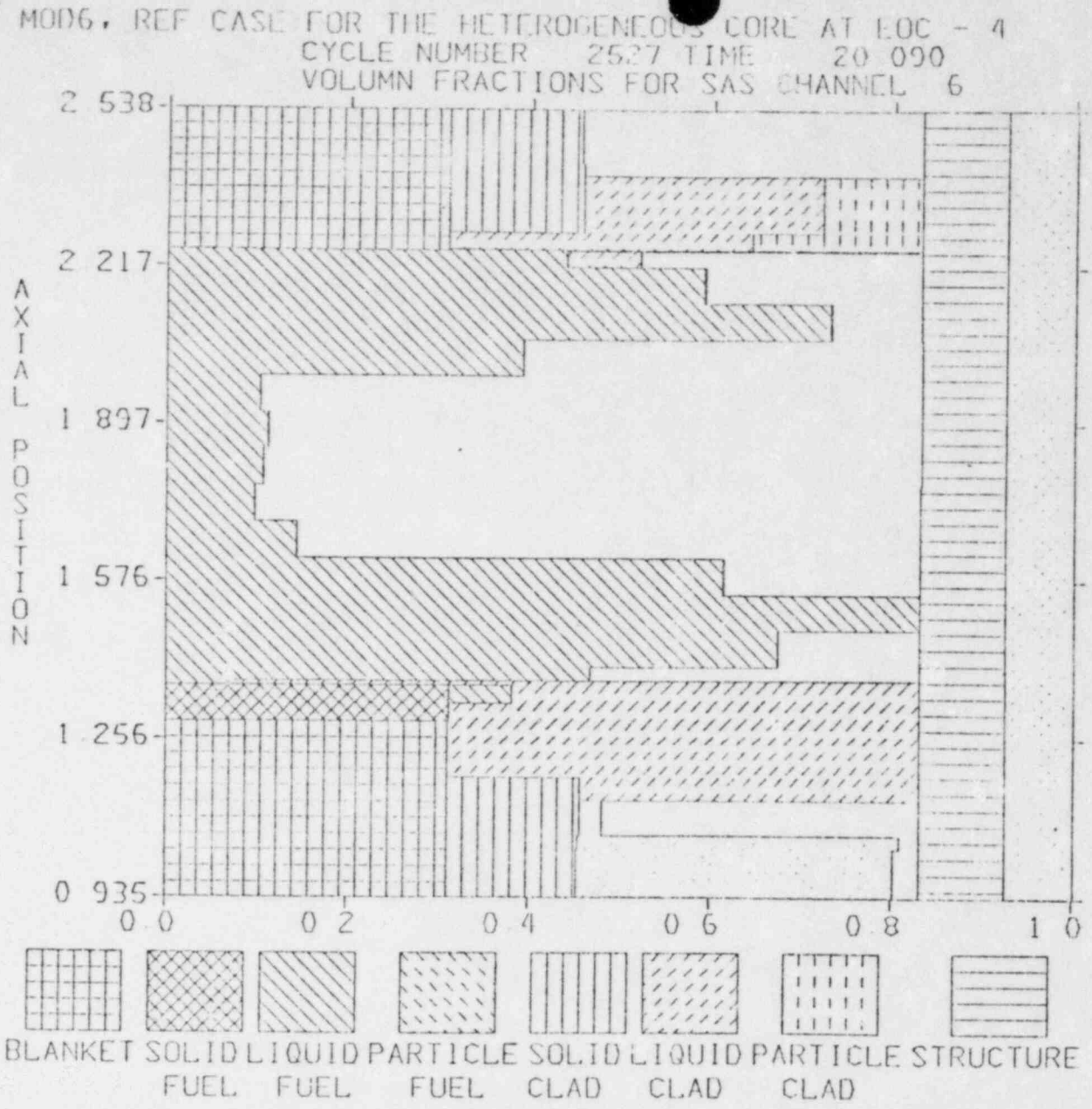
MOD6, REF CASE FOR THE HETEROGENEOUS CORE AT EOC - 4
CYCLE NUMBER 2527 TIME 20 090
VOLUMN FRACTIONS FOR SAS CHANNEL 6
AXIAL POSITION
2 538
2 217
1 897
1 576
1 256
0 935
0 0
0 2
0 4
0 6
0 8
1 0
BLANKET
SOLID FUEL
LIQUID FUEL
PARTICLE FUEL
SOLID CLAD
LIQUID CLAD
PARTICLE CLAD
STRUCTURE

Fig 77

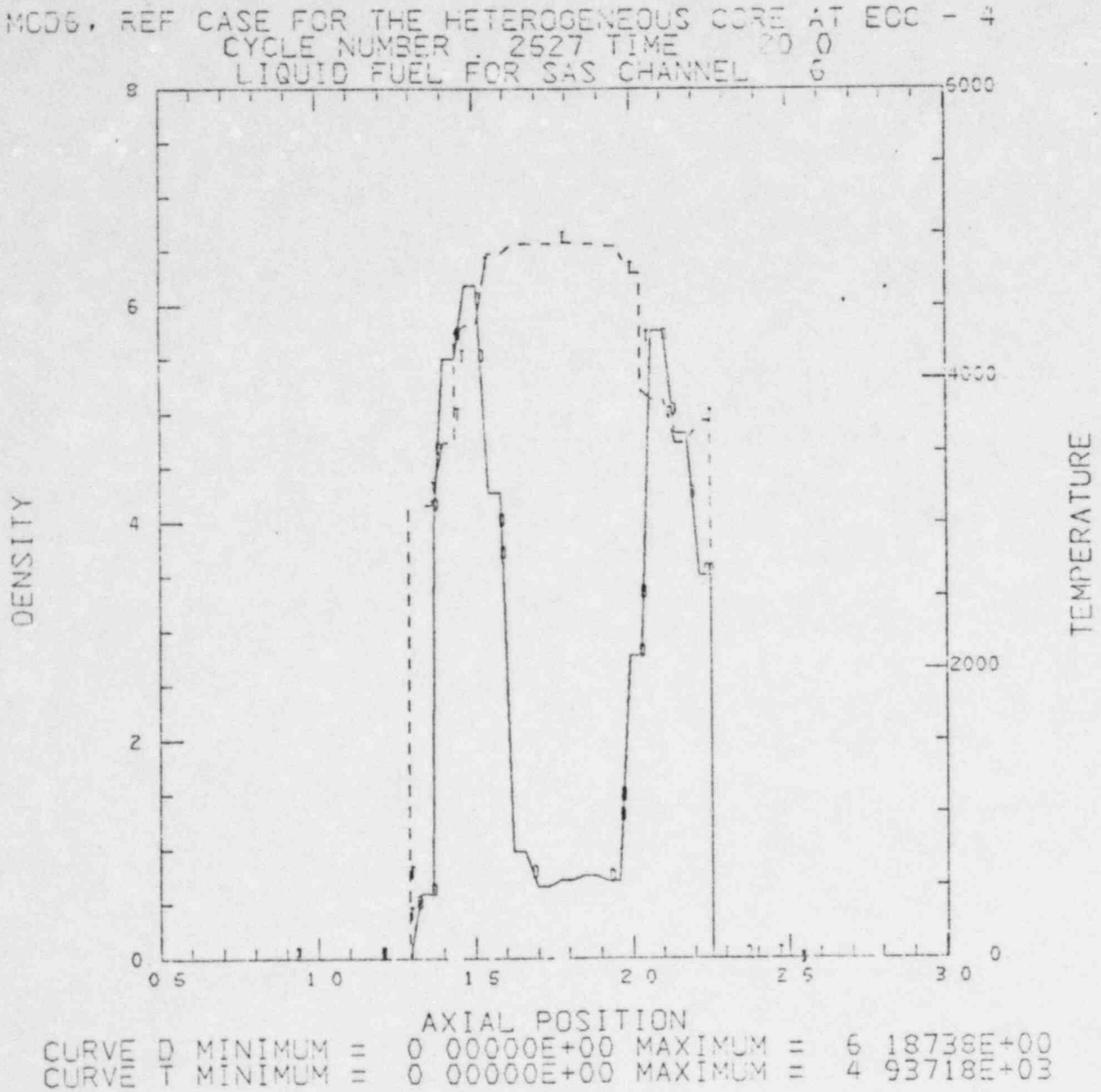

CURVE D MINIMUM = 0 00000E+00 MAXIMUM = 6 18738E+00
CURVE T MINIMUM = 0 00000E+00 MAXIMUM = 4 93718E+03

Fig 78

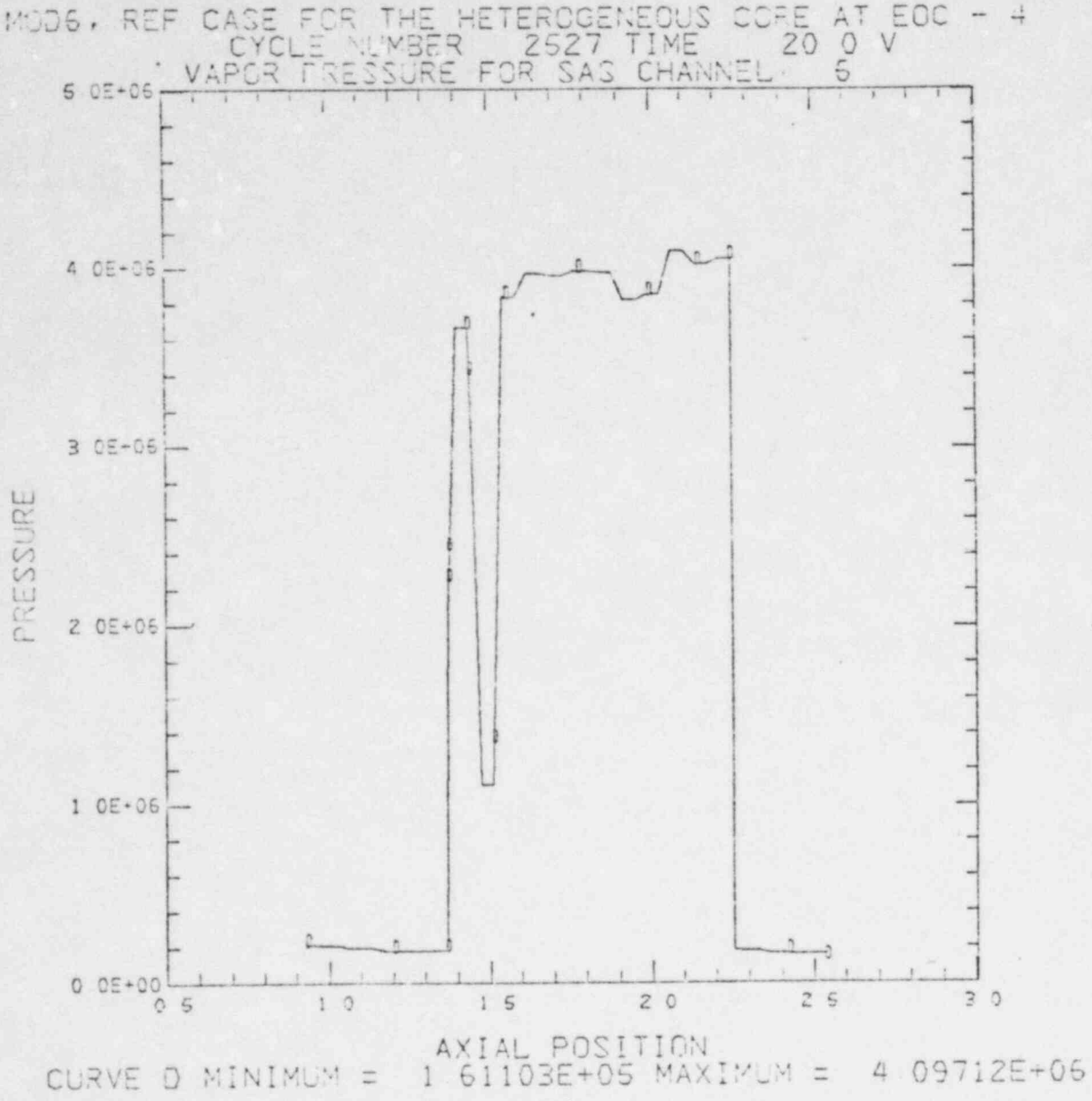
MOD6, REF CASE FOR THE HETEROGENEOUS CORE AT EOC - 4
CYCLE NUMBER 2527 TIME 20 0 V
VAPOR PRESSURE FOR SAS CHANNEL 5
5 0E+06
4 0E+06
3 0E+06
2 0E+06
1 0E+06
0 0E+00
PRESSURE
0 5
1 0
1 5
2 0
2 5
3 0
AXIAL POSITION
CURVE D MINIMUM = 1 61103E+05 MAXIMUM = 4 09712E+06

Fig 79

MOD6, REF CASE FOR THE HETEROGENEOUS CORE AT EOC - 4
SUBASSEMBLIES FOR CHANNEL 10

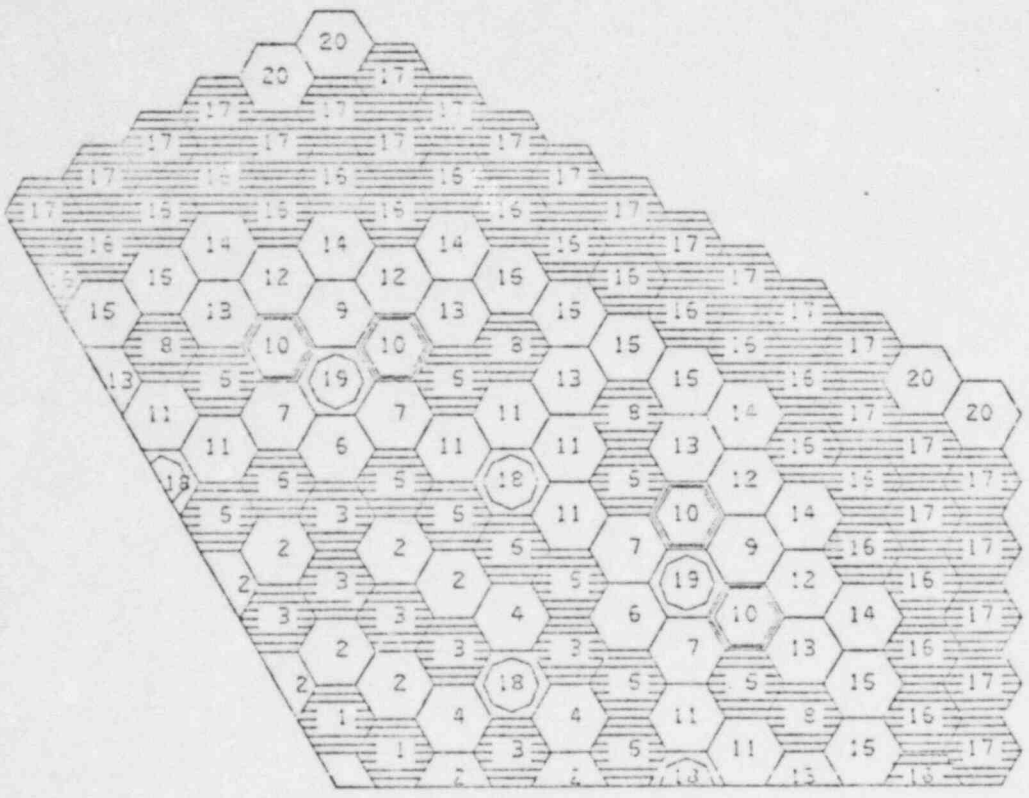

Fig 80

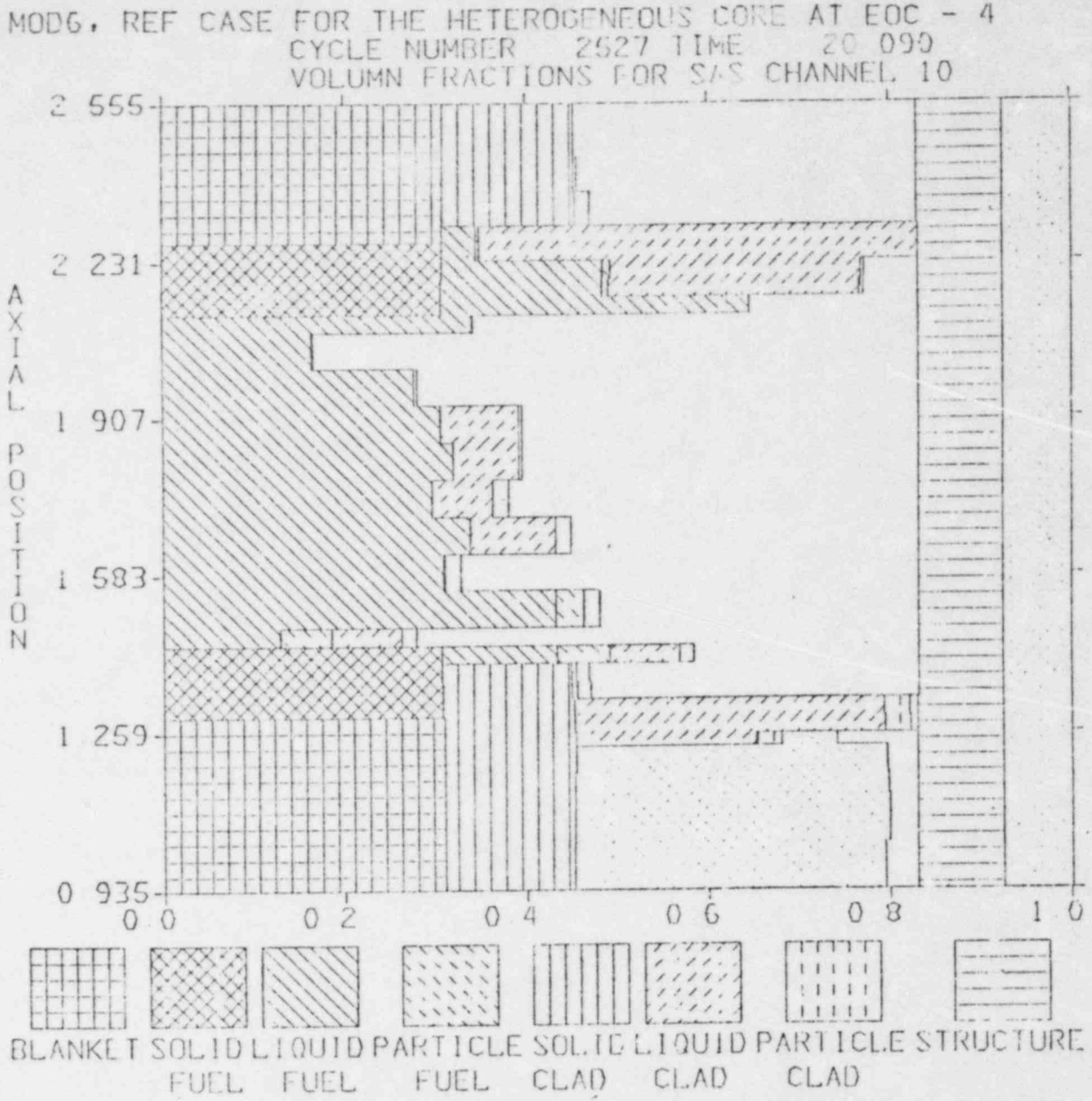
MOD6, REF CASE FOR THE HETEROGENEOUS CORE AT EOC - 4
CYCLE NUMBER 2527 TIME 20 090
VOLUMN FRACTIONS FOR S/S CHANNEL 10
AXIAL POSITION
2 555
2 231
1 907
1 583
1 259
0 935
0 0
0 2
0 4
0 6
0 8
1 0
BLANKET
SOLID FUEL
LIQUID FUEL
PARTICLE FUEL
SOLID CLAD
LIQUID CLAD
PARTICLE CLAD
STRUCTURE

Fig 81

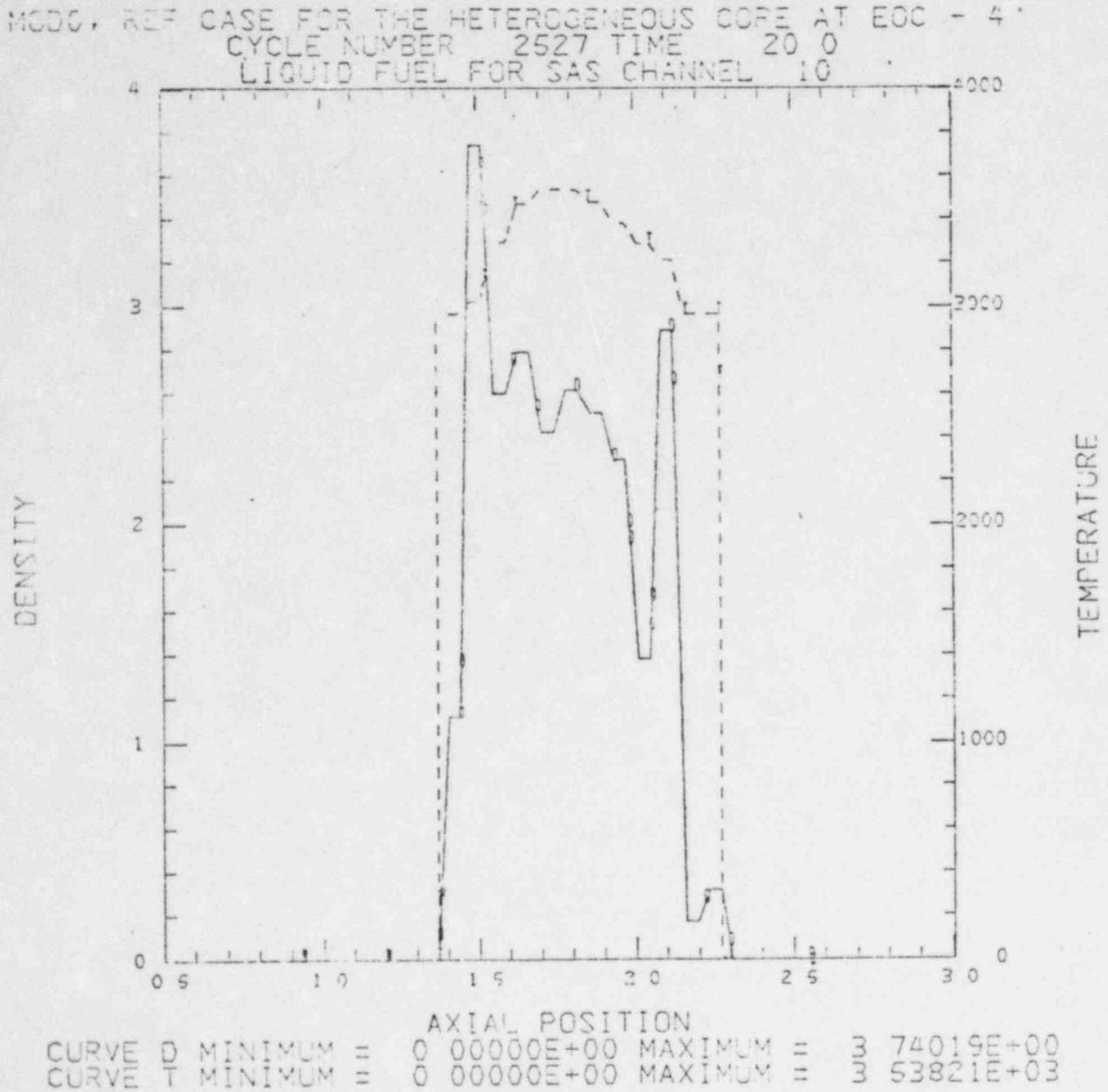

CURVE D MINIMUM = 0 00000E+00 MAXIMUM = 3 74019E+00
CURVE T MINIMUM = 0 00000E+00 MAXIMUM = 3 53821E+03

Fig 82

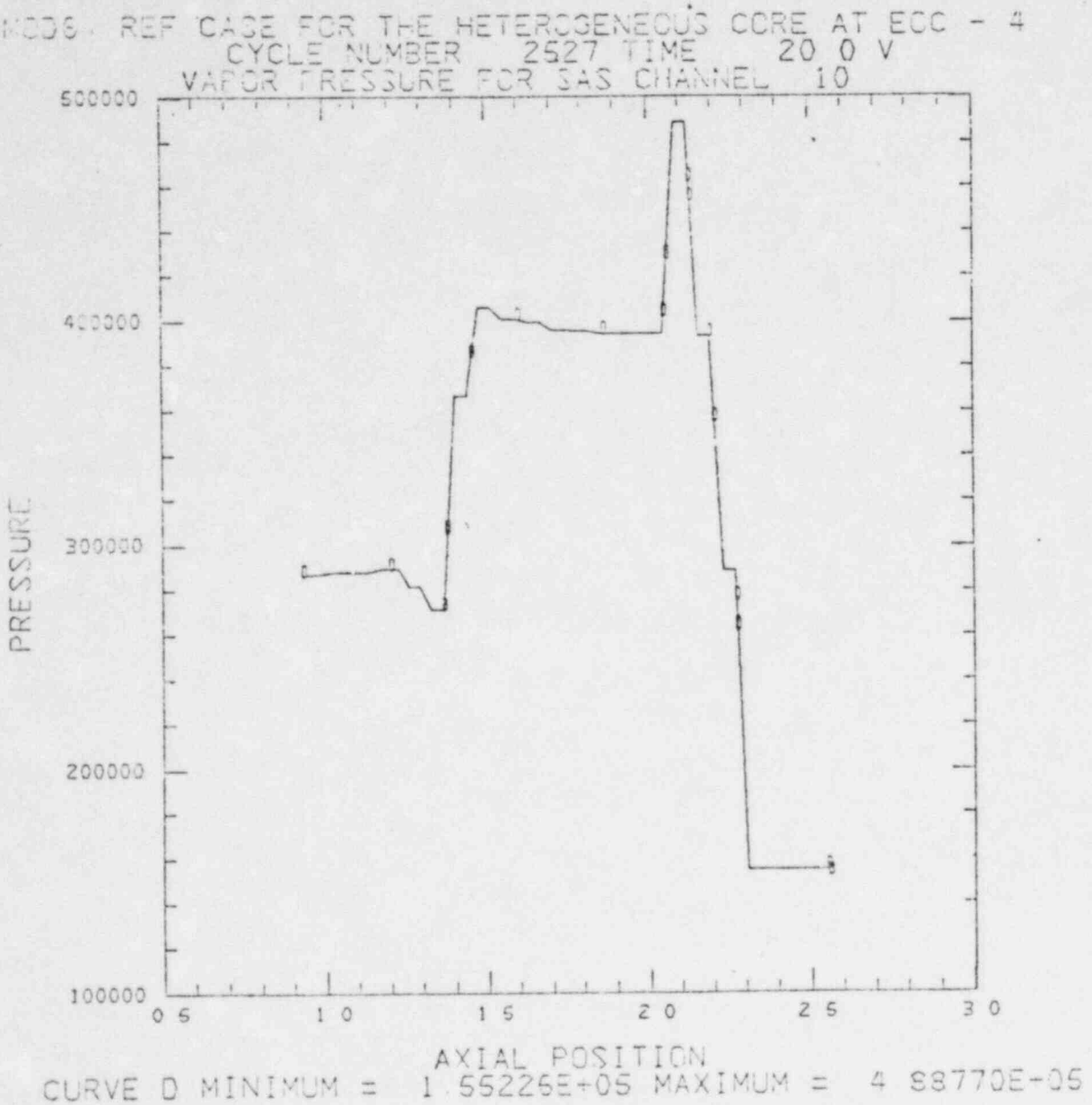
MOD6 REF CASE FOR THE HETEROGENEOUS CORE AT ECC - 4
CYCLE NUMBER 2527 TIME 20 0 V
VAPOR PRESSURE FOR SAS CHANNEL 10
500000
400000
300000
200000
100000
PRESSURE
0 5
1 0
1 5
2 0
2 5
3 0
AXIAL POSITION
CURVE D MINIMUM = 1 55226E+05 MAXIMUM = 4 88770E-05

Fig 83

MOD5, REF CASE FOR THE HETEROGENEOUS CORE AT EOC - 4
SUBASSEMBLIES FOR CHANNEL 12

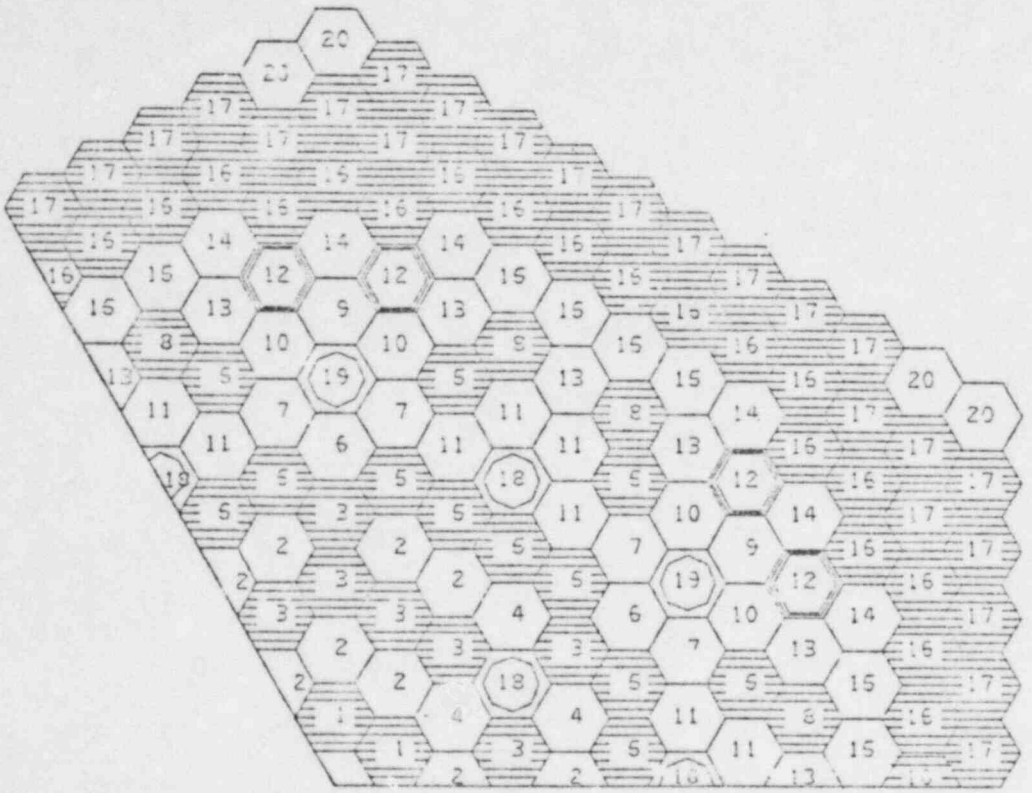

Fig 84

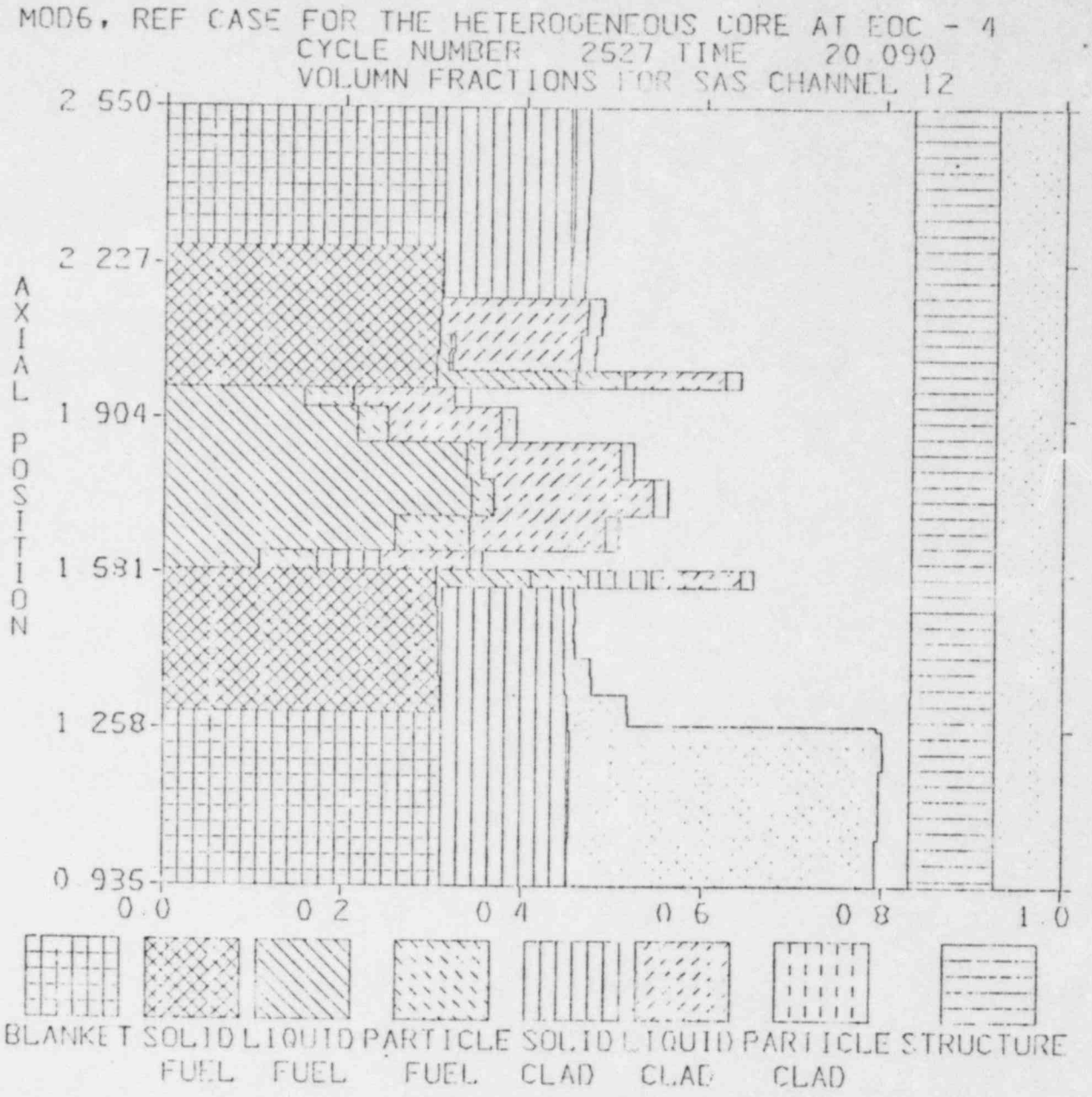
MOD6, REF CASE FOR THE HETEROGENEOUS CORE AT EOC - 4
CYCLE NUMBER 2527 TIME 20 090
VOLUMN FRACTIONS FOR SAS CHANNEL 12
AXIAL POSITION
2 550
2 227
1 904
1 581
1 258
0 935
0 0
0 2
0 4
0 6
0 8
1 0
BLANKET
SOLID FUEL
LIQUID FUEL
PARTICLE FUEL
SOLID CLAD
LIQUID CLAD
PARTICLE CLAD
STRUCTURE

Fig 85

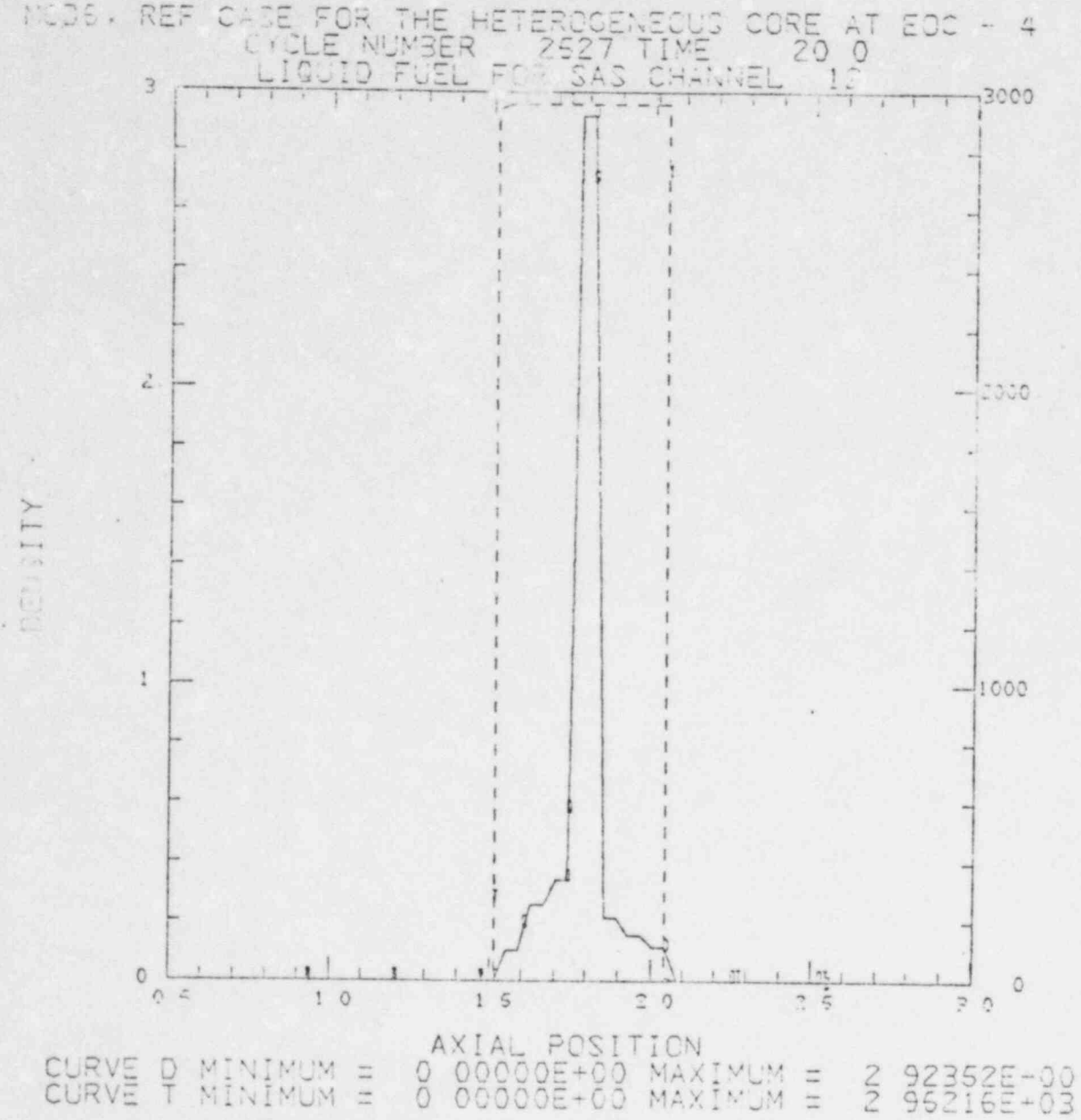

CURVE D MINIMUM = 0 00000E+00 MAXIMUM = 2 92352E-00
CURVE T MINIMUM = 0 00000E+00 MAXIMUM = 2 95216E+03

Fig 86

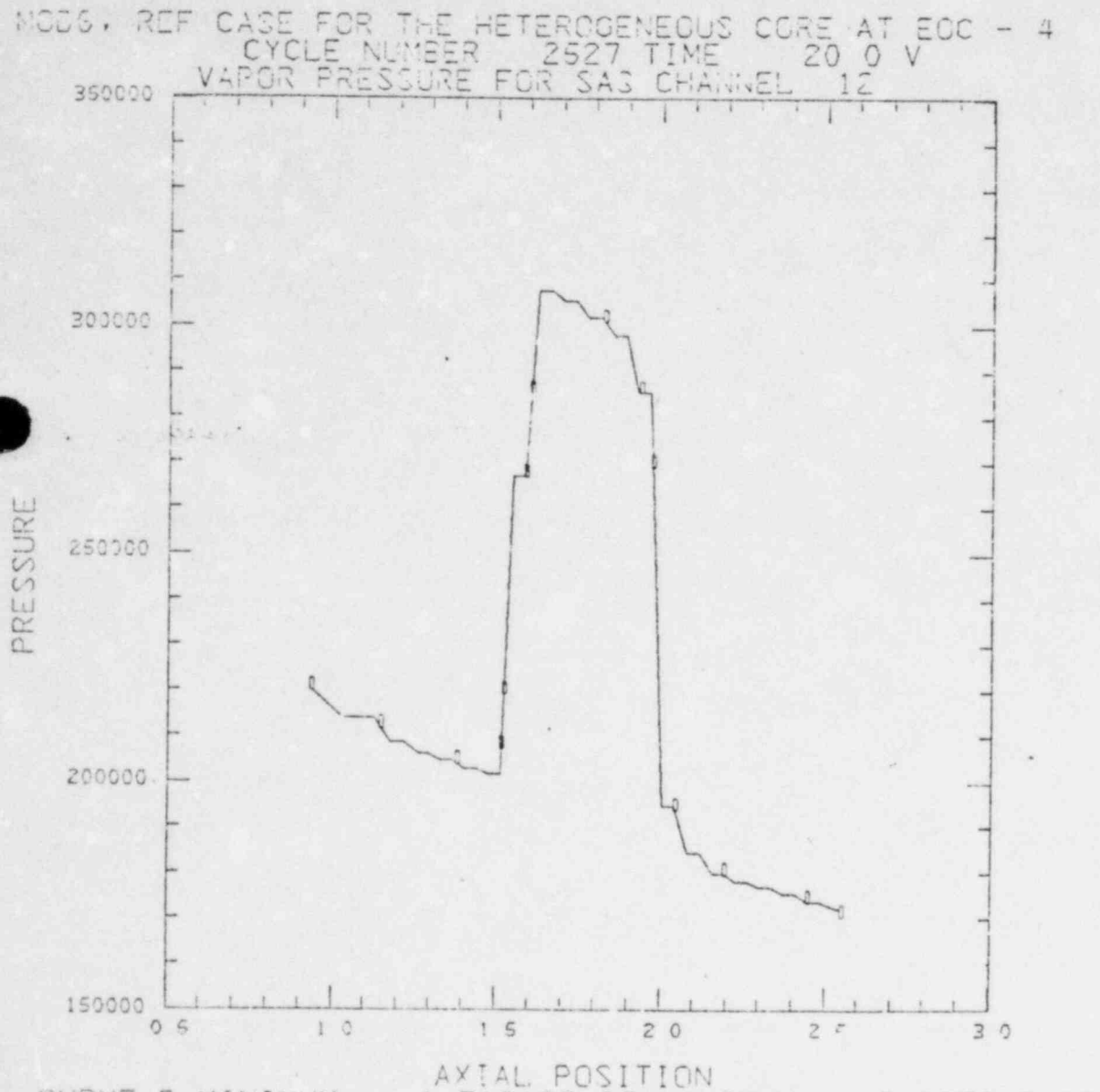
MOD6, REF CASE FOR THE HETEROGENEOUS CORE AT EOC - 4
CYCLE NUMBER 2527 TIME 20 0 V
VAPOR PRESSURE FOR SAS CHANNEL 12
350000
300000
250000
200000
150000
PRESSURE
0 5
1 0
1 5
2 0
2 5
3 0
AXIAL POSITION
CURVE D MINIMUM = 1 71919E+05 MAXIMUM = 3 07701E+05

Fig 87

CORE MAP

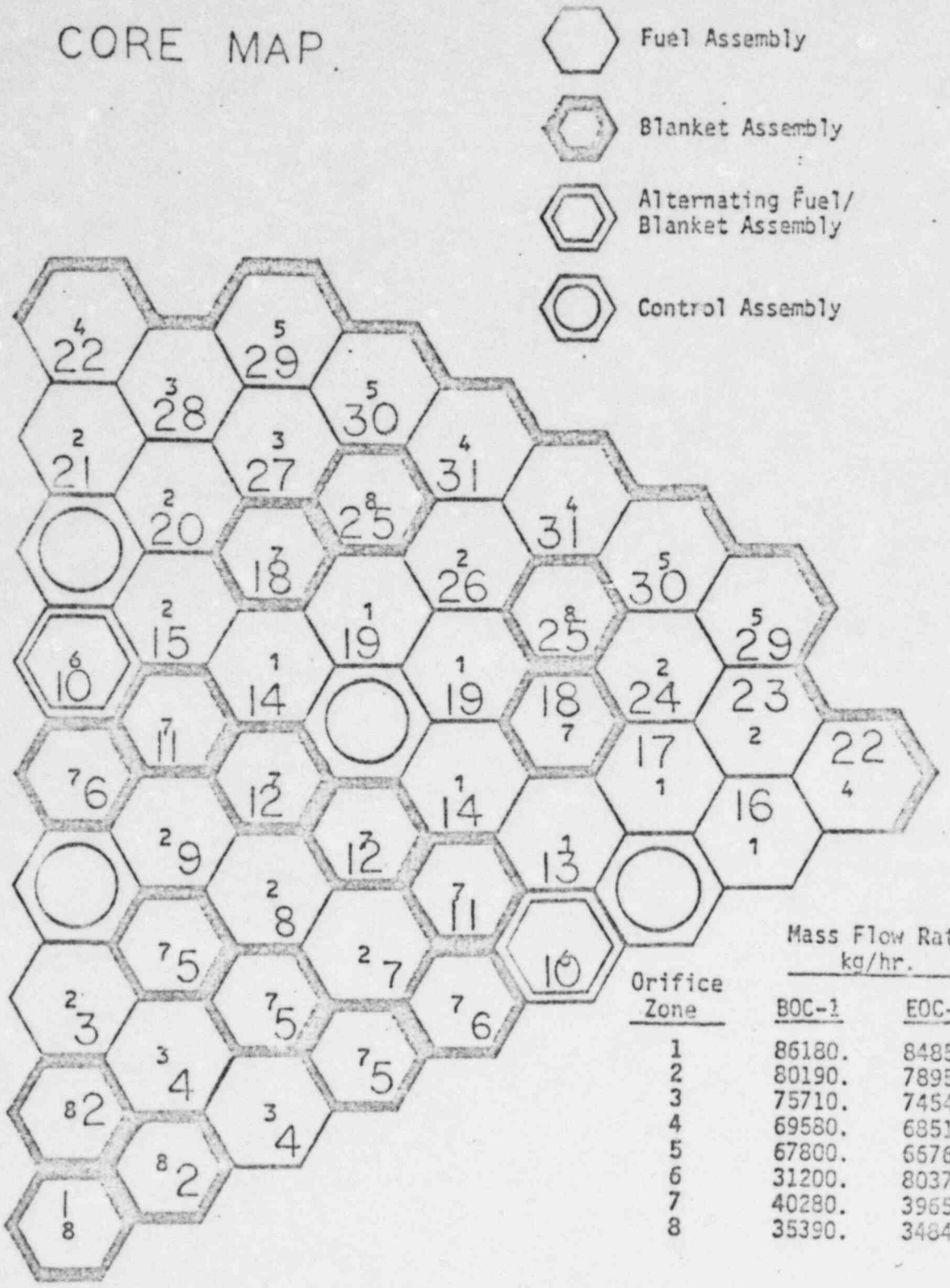

Orifice Zone	Mass Flow Rate, kg/hr. BOC-1	EOC-4
1	86180.	84850.
2	80190.	78950.
3	75710.	74540.
4	69580.	68510.
5	67800.	66760.
6	31200.	80370.
7	40280.	39650.
8	35390.	34840.

88

Fig. 4-7 Orifice Zones and Mass Flow Rates for CRBRP Core CHANNELS FOR EOC-3

CHANNELS 32 + 33 ARE RADIAL BLANKETS

BII.3

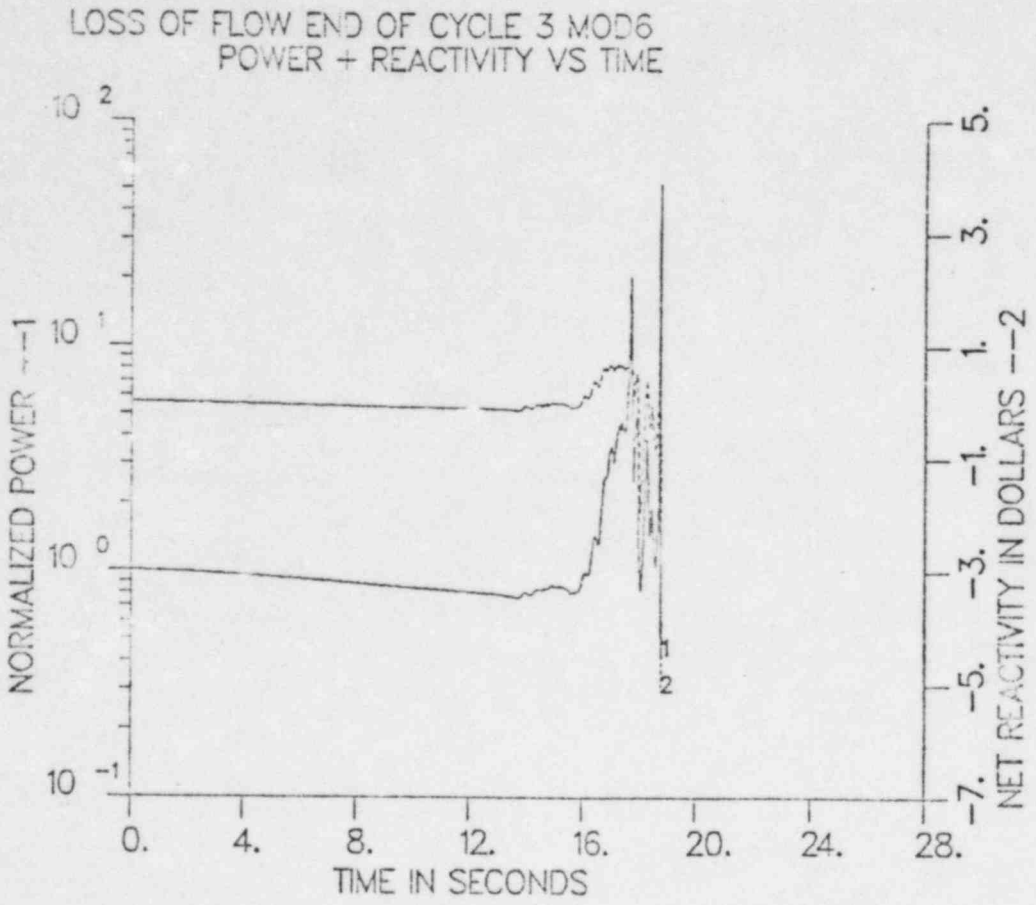
LOSS OF FLOW END OF CYCLE 3 MOD6
POWER + REACTIVITY VS TIME
NORMALIZED POWER --1
10 2
10 1
10 0
10 -1
0.
4.
8.
12.
16.
20.
24.
28.
TIME IN SECONDS
5.
3.
1.
-1.
-3.
-5.
-7.
NET REACTIVITY IN DOLLARS --2
2
1

Fig 89

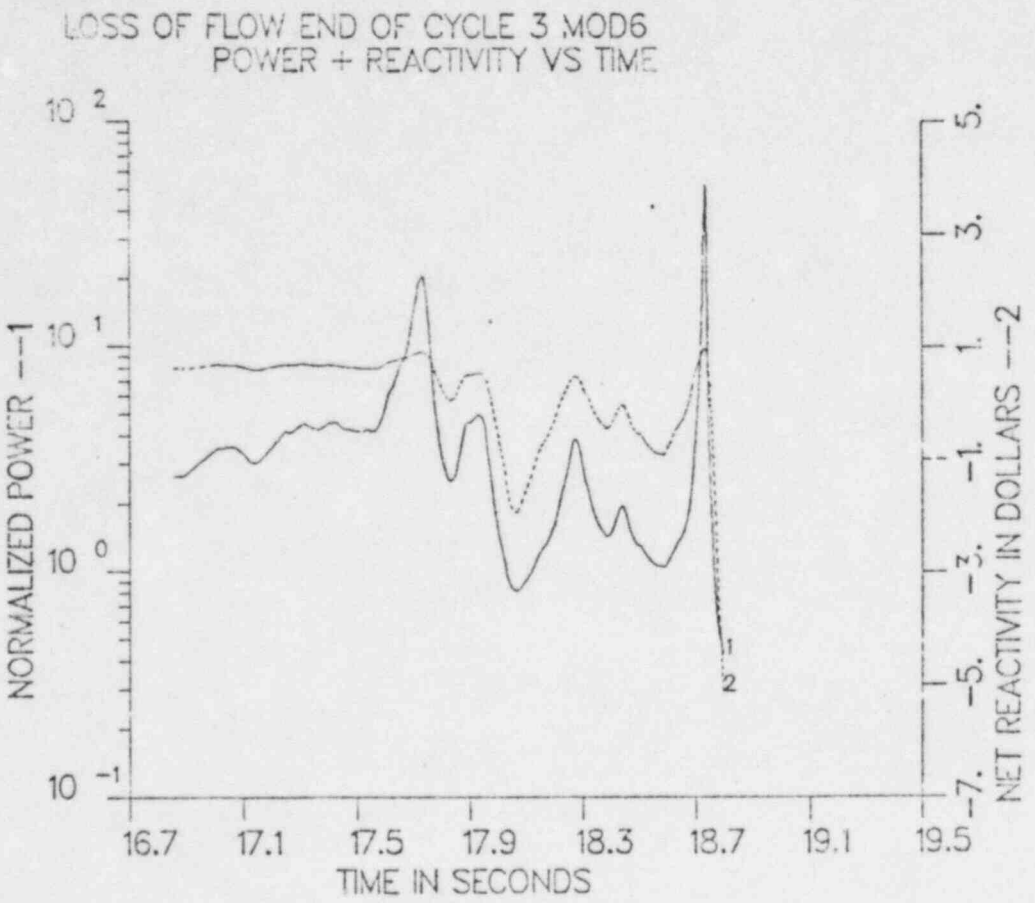
LOSS OF FLOW END OF CYCLE 3 MOD6
POWER + REACTIVITY VS TIME
NORMALIZED POWER --1
10 2
10 1
10 0
10 -1
NET REACTIVITY IN DOLLARS --2
5.
3.
1.
-1.
-3.
-5.
-7.
16.7
17.1
17.5
17.9
18.3
18.7
19.1
19.5
TIME IN SECONDS
1
2

Fig 90

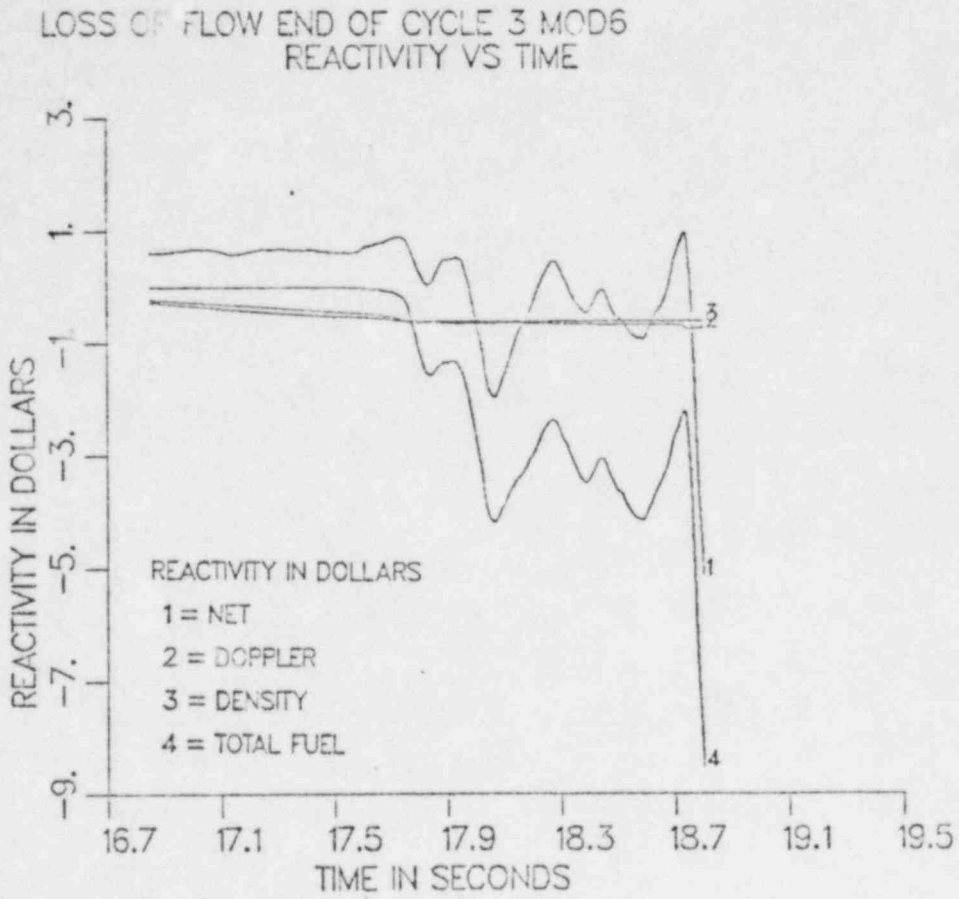
LOSS OF FLOW END OF CYCLE 3 MOD6
REACTIVITY VS TIME
REACTIVITY IN DOLLARS
3.
1.
-1.
-3.
-5.
-7.
-9.
16.7
17.1
17.5
17.9
18.3
18.7
19.1
19.5
TIME IN SECONDS
REACTIVITY IN DOLLARS
1 = NET
2 = DOPPLER
3 = DENSITY
4 = TOTAL FUEL
1
2
3
4

Fig 91

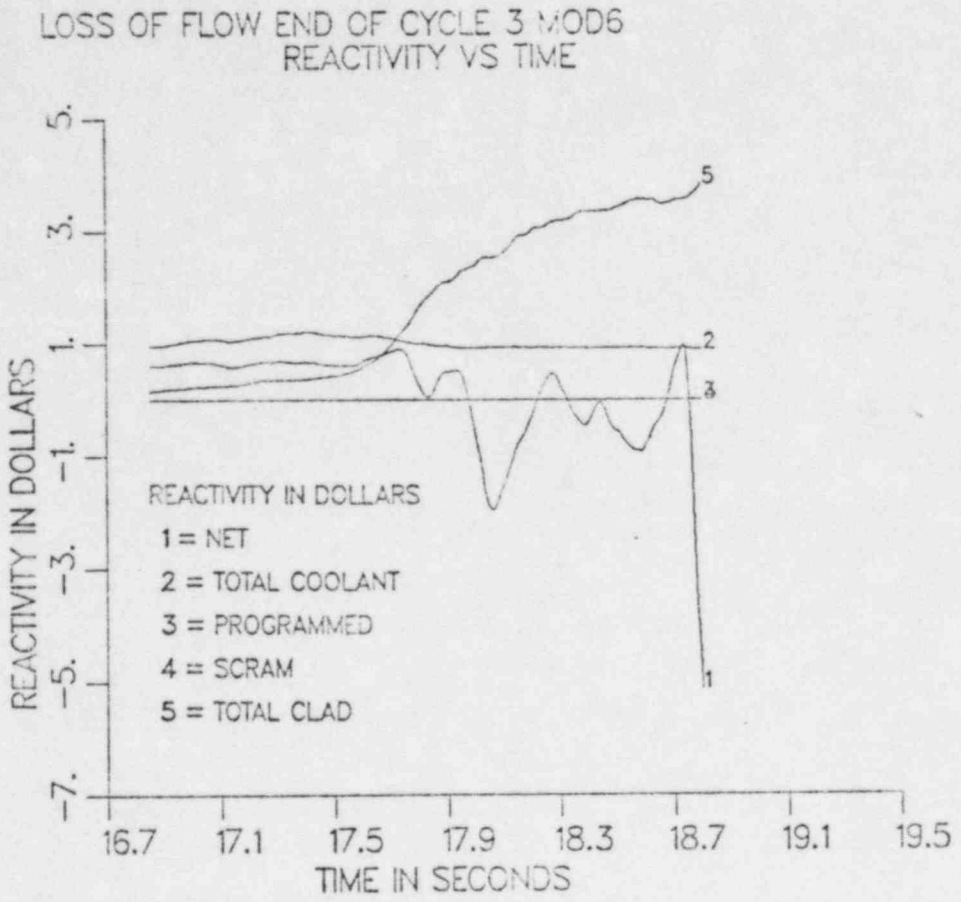
LOSS OF FLOW END OF CYCLE 3 MOD6
REACTIVITY VS TIME
REACTIVITY IN DOLLARS
5.
3.
1.
-1.
-3.
-5.
-7.
16.7
17.1
17.5
17.9
18.3
18.7
19.1
19.5
TIME IN SECONDS
REACTIVITY IN DOLLARS
1 = NET
2 = TOTAL COOLANT
3 = PROGRAMMED
4 = SCRAM
5 = TOTAL CLAD
5
2
3
1

Fig 92

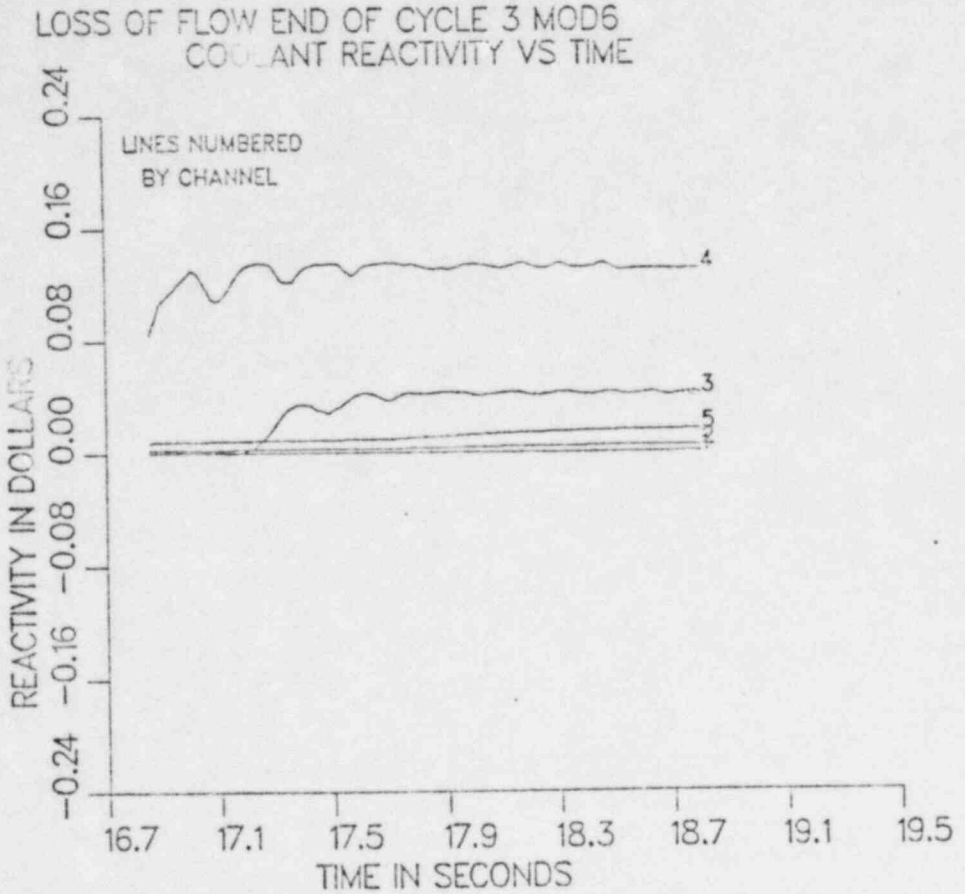
LOSS OF FLOW END OF CYCLE 3 MOD6
COOLANT REACTIVITY VS TIME
LINES NUMBERED
BY CHANNEL
REACTIVITY IN DOLLARS
0.24
0.16
0.08
0.00
−0.08
−0.16
−0.24
4
3
5
2
16.7
17.1
17.5
17.9
18.3
18.7
19.1
19.5
TIME IN SECONDS

Fig 93

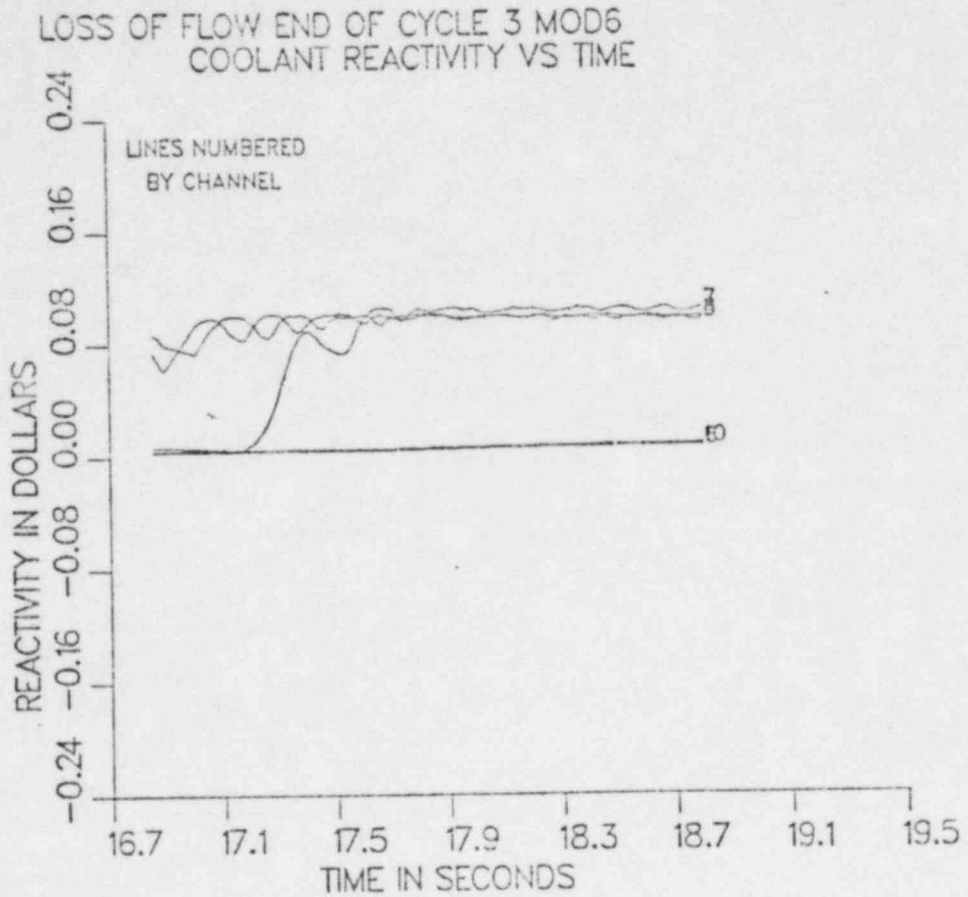
LOSS OF FLOW END OF CYCLE 3 MOD6
COOLANT REACTIVITY VS TIME
LINES NUMBERED
BY CHANNEL
REACTIVITY IN DOLLARS
0.24
0.16
0.08
0.00
-0.08
-0.16
-0.24
16.7
17.1
17.5
17.9
18.3
18.7
19.1
19.5
TIME IN SECONDS

Fig 94

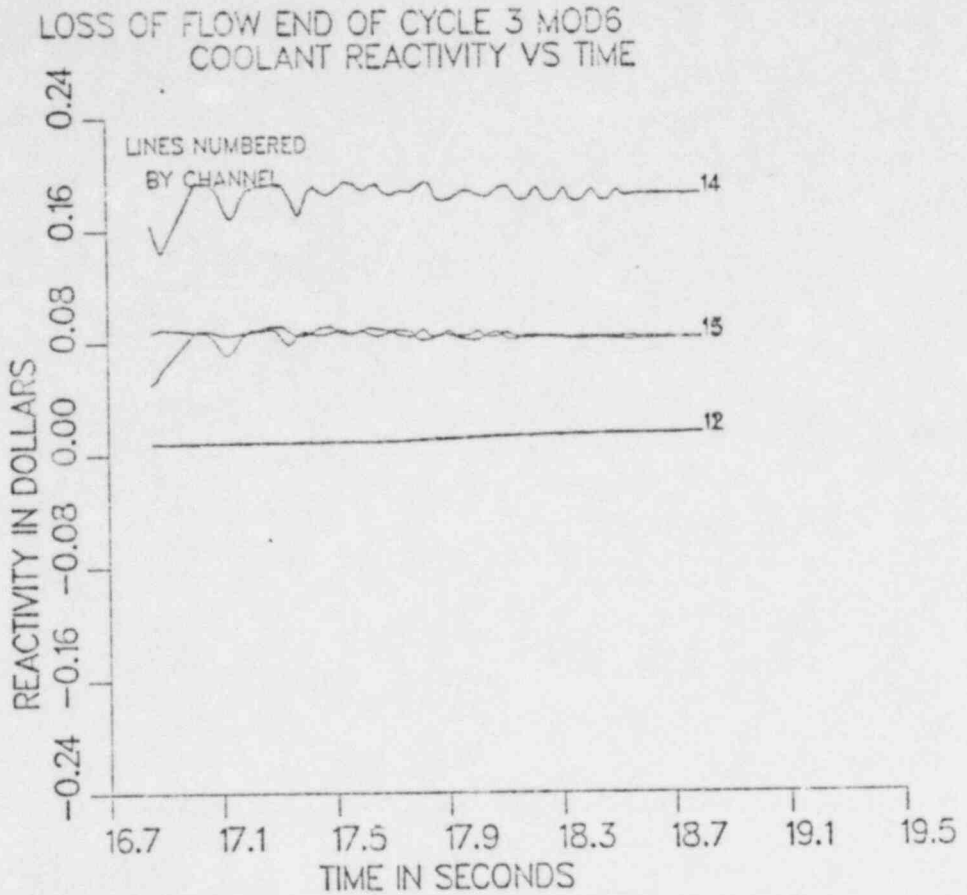
LOSS OF FLOW END OF CYCLE 3 MOD6
COOLANT REACTIVITY VS TIME
LINES NUMBERED
BY CHANNEL
14
13
12
REACTIVITY IN DOLLARS
0.24
0.16
0.08
0.00
-0.08
-0.16
-0.24
16.7
17.1
17.5
17.9
18.3
18.7
19.1
19.5
TIME IN SECONDS

Fig 95

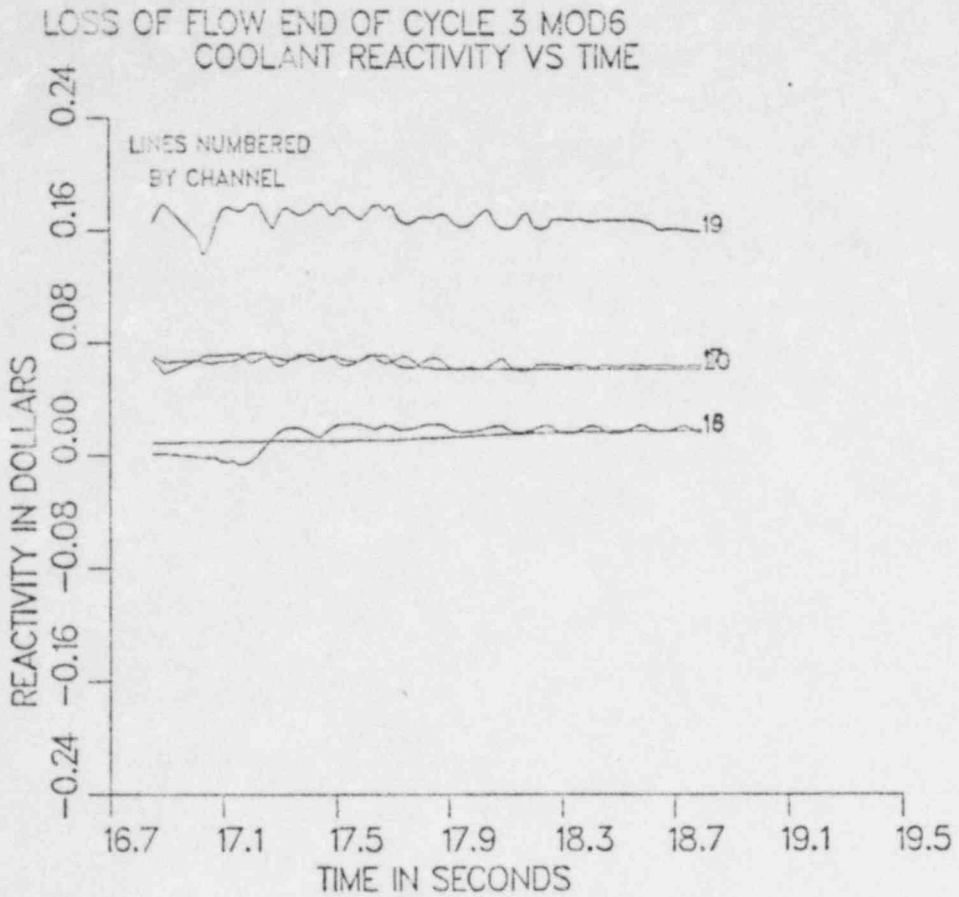
LOSS OF FLOW END OF CYCLE 3 MOD6
COOLANT REACTIVITY VS TIME
LINES NUMBERED
BY CHANNEL
19
20
16
REACTIVITY IN DOLLARS
0.24
0.16
0.08
0.00
-0.08
-0.16
-0.24
16.7
17.1
17.5
17.9
18.3
18.7
19.1
19.5
TIME IN SECONDS

Fig 96

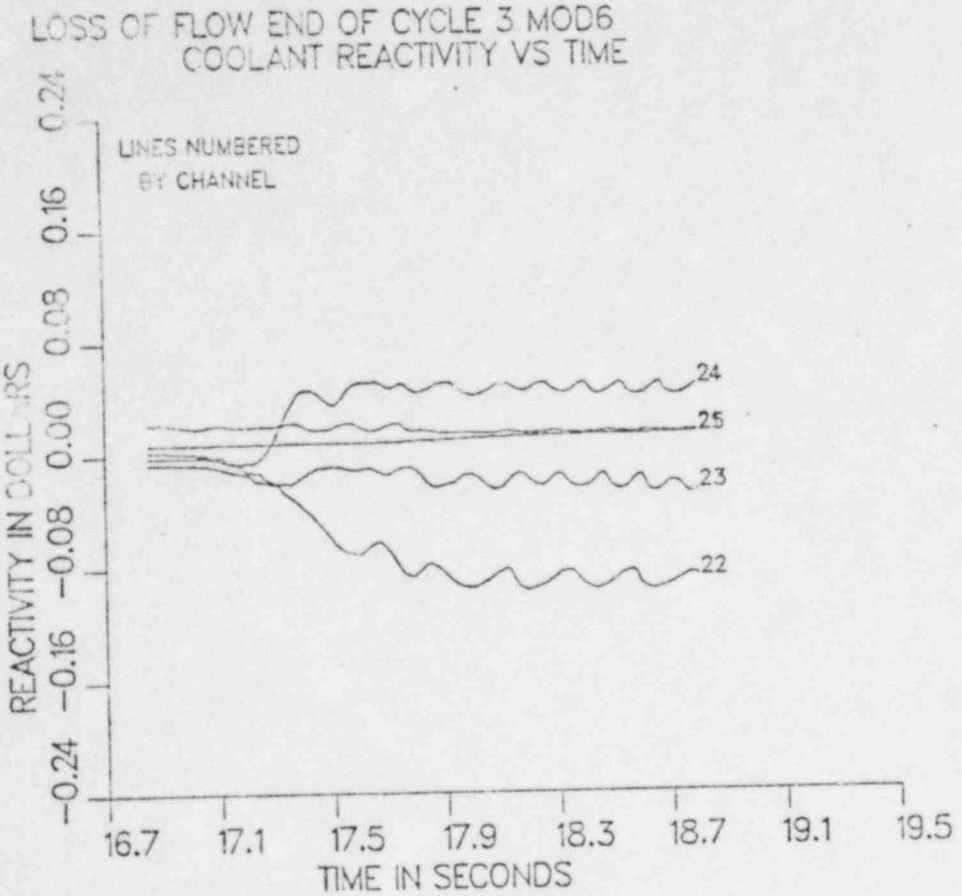
LOSS OF FLOW END OF CYCLE 3 MOD6
COOLANT REACTIVITY VS TIME
LINES NUMBERED
BY CHANNEL
REACTIVITY IN DOLLARS
0.24
0.16
0.08
0.00
-0.08
-0.16
-0.24
24
25
23
22
16.7
17.1
17.5
17.9
18.3
18.7
19.1
19.5
TIME IN SECONDS

Fig 97

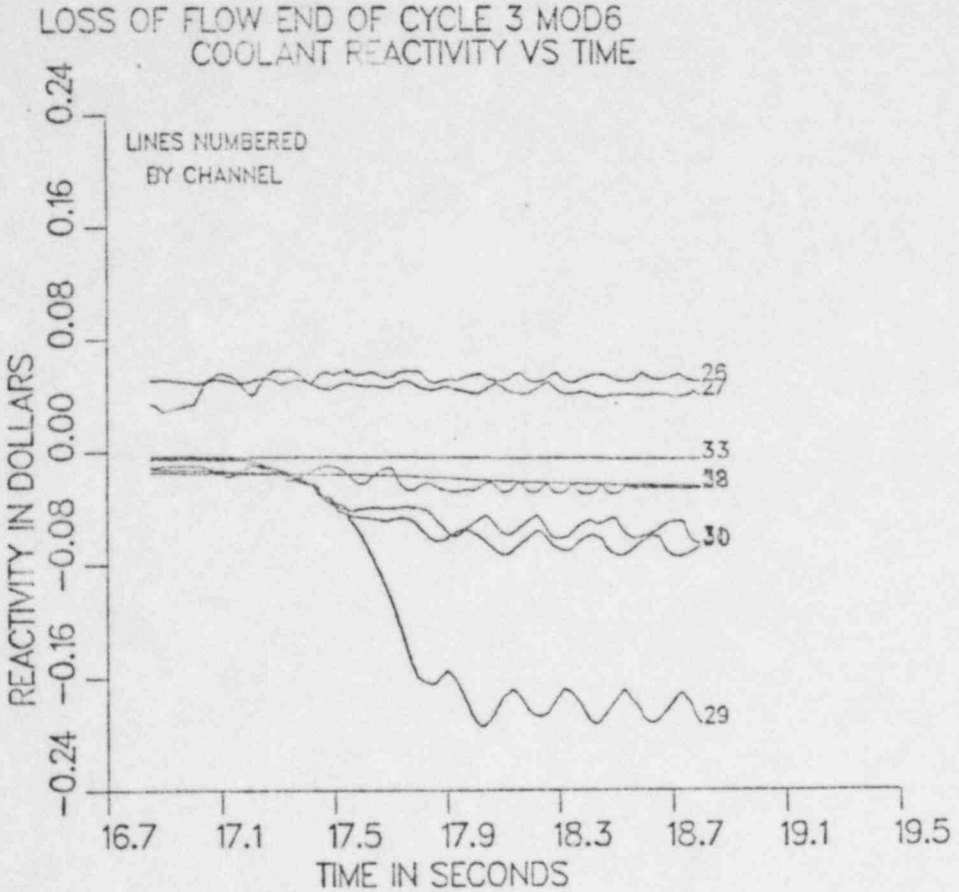
LOSS OF FLOW END OF CYCLE 3 MOD6
COOLANT REACTIVITY VS TIME
LINES NUMBERED
BY CHANNEL
REACTIVITY IN DOLLARS
0.24
0.16
0.08
0.00
−0.08
−0.16
−0.24
26
27
33
38
30
29
16.7
17.1
17.5
17.9
18.3
18.7
19.1
19.5
TIME IN SECONDS

Fig 98

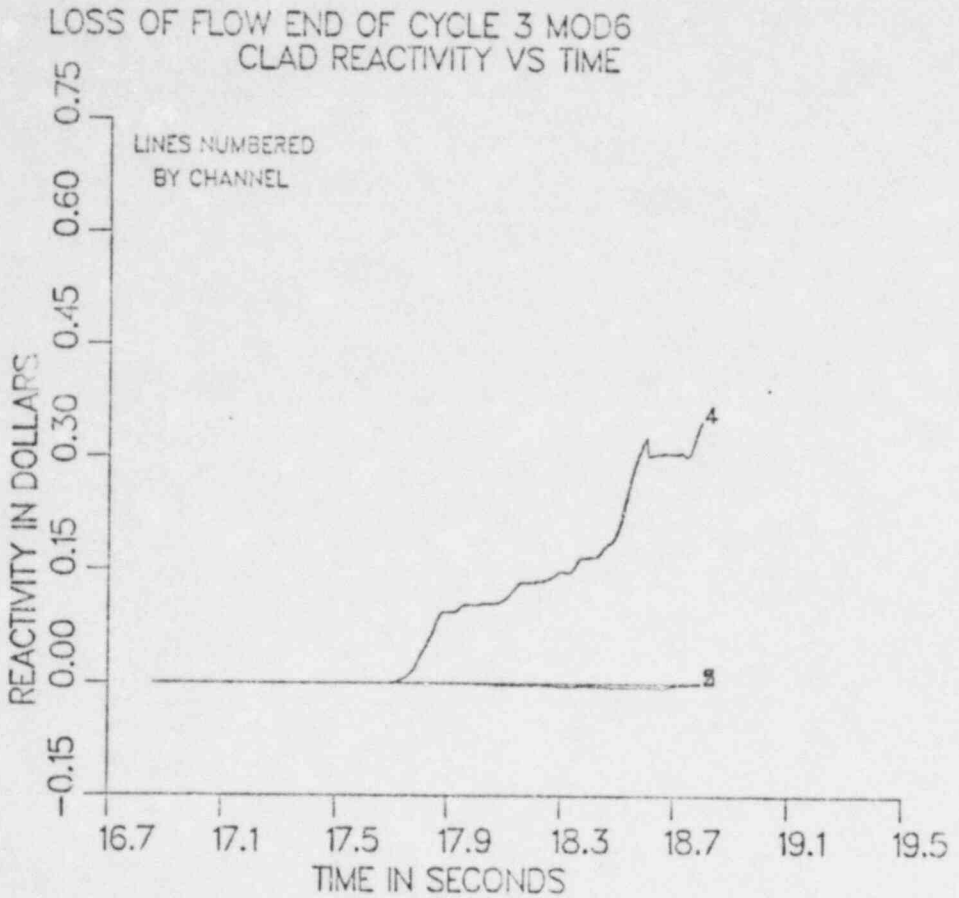
LOSS OF FLOW END OF CYCLE 3 MOD6
CLAD REACTIVITY VS TIME
LINES NUMBERED
BY CHANNEL
REACTIVITY IN DOLLARS
0.75
0.60
0.45
0.30
0.15
0.00
-0.15
4
3
16.7
17.1
17.5
17.9
18.3
18.7
19.1
19.5
TIME IN SECONDS

Fig 99

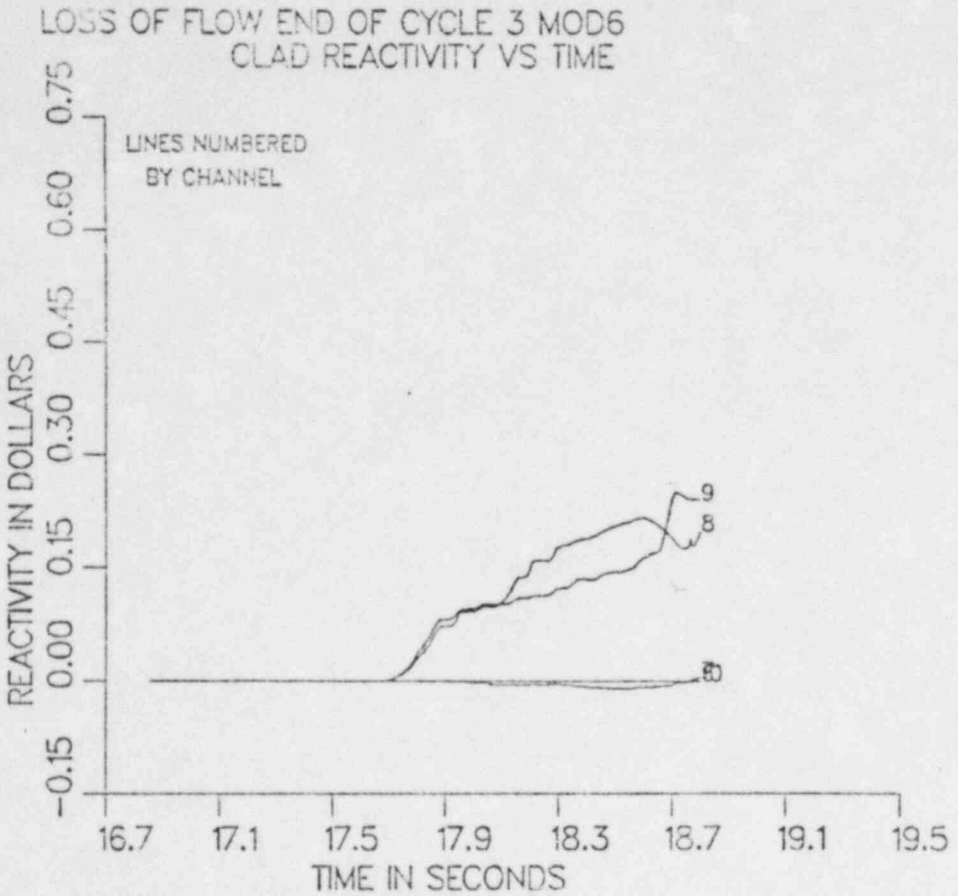
LOSS OF FLOW END OF CYCLE 3 MOD6
CLAD REACTIVITY VS TIME
LINES NUMBERED
BY CHANNEL
REACTIVITY IN DOLLARS
0.75
0.60
0.45
0.30
0.15
0.00
-0.15
9
8
50
16.7
17.1
17.5
17.9
18.3
18.7
19.1
19.5
TIME IN SECONDS

Fig 100

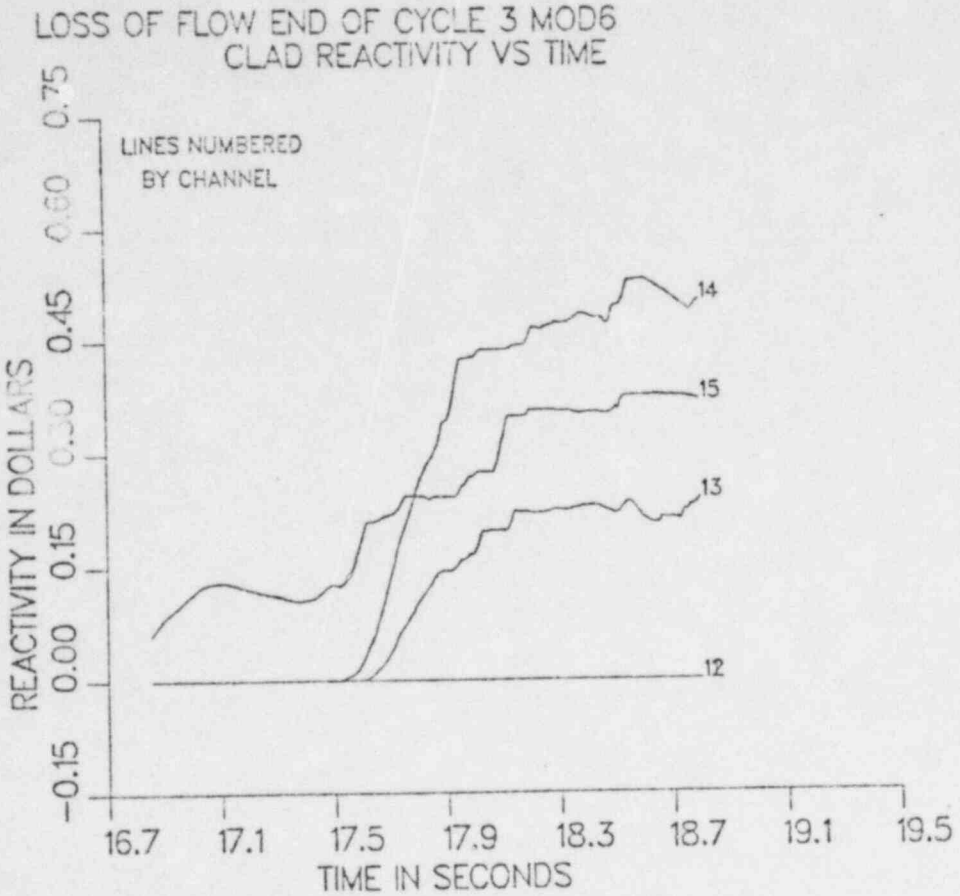
LOSS OF FLOW END OF CYCLE 3 MOD6
CLAD REACTIVITY VS TIME
LINES NUMBERED
BY CHANNEL
REACTIVITY IN DOLLARS
0.75
0.60
0.45
0.30
0.15
0.00
-0.15
14
15
13
12
16.7
17.1
17.5
17.9
18.3
18.7
19.1
19.5
TIME IN SECONDS

Fig 101

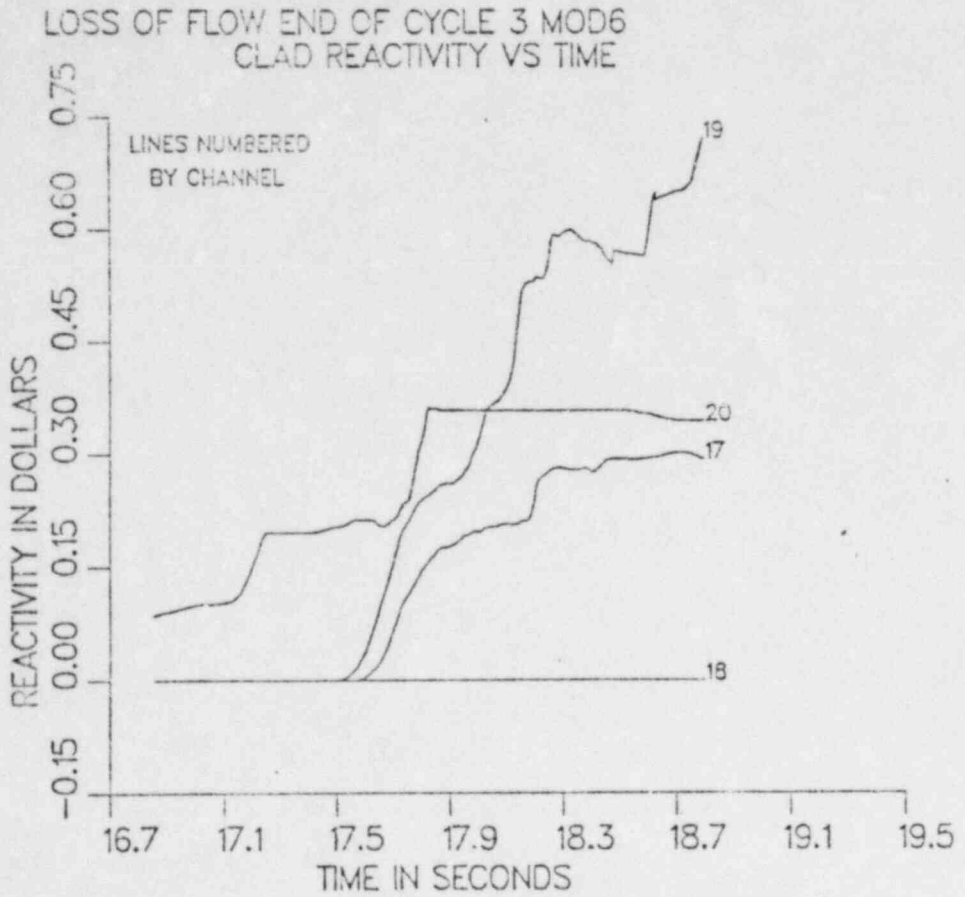
LOSS OF FLOW END OF CYCLE 3 MOD6
CLAD REACTIVITY VS TIME
LINES NUMBERED
BY CHANNEL
19
20
17
18
REACTIVITY IN DOLLARS
0.75
0.60
0.45
0.30
0.15
0.00
-0.15
16.7
17.1
17.5
17.9
18.3
18.7
19.1
19.5
TIME IN SECONDS

Fig 102.

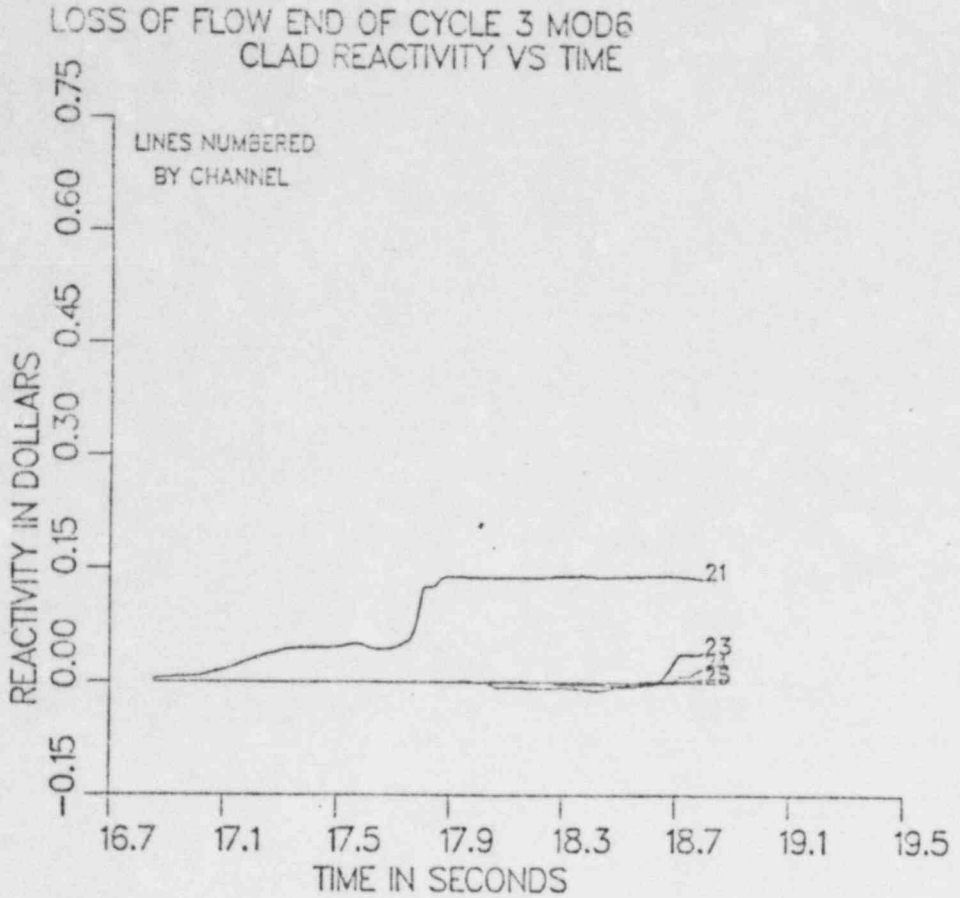
LOSS OF FLOW END OF CYCLE 3 MOD6
CLAD REACTIVITY VS TIME
LINES NUMBERED
BY CHANNEL
REACTIVITY IN DOLLARS
0.75
0.60
0.45
0.30
0.15
0.00
-0.15
21
23
25
16.7
17.1
17.5
17.9
18.3
18.7
19.1
19.5
TIME IN SECONDS

Fig 103

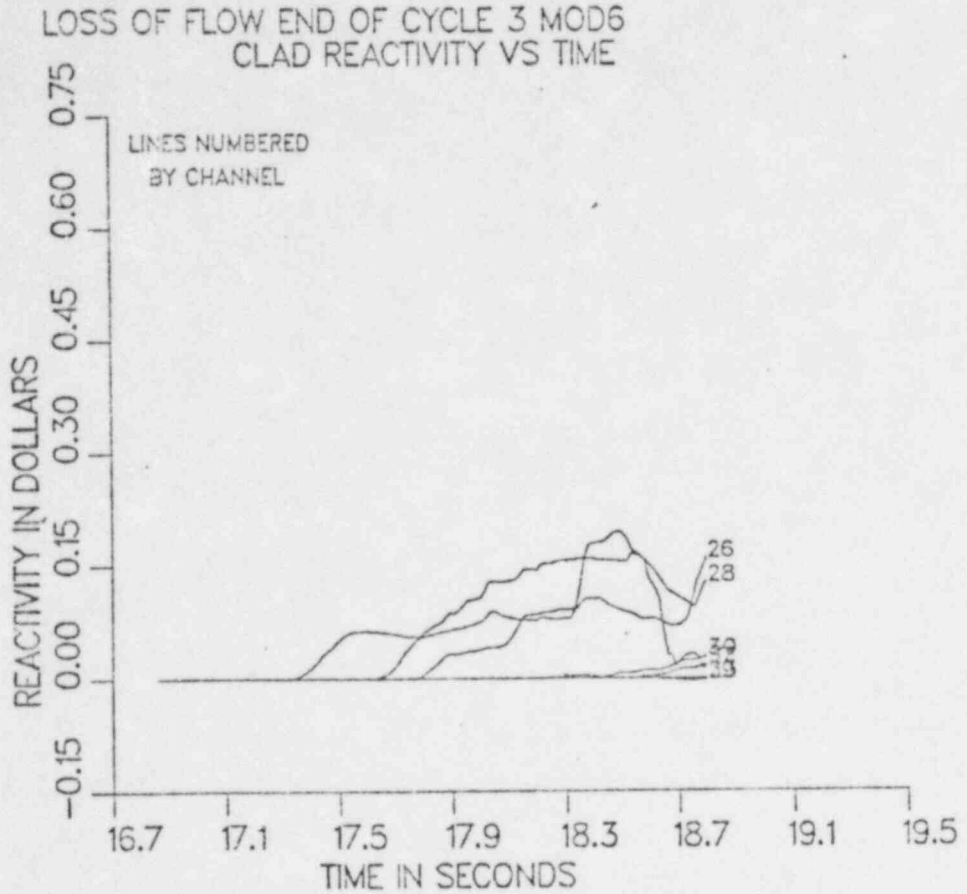
LOSS OF FLOW END OF CYCLE 3 MOD6
CLAD REACTIVITY VS TIME
LINES NUMBERED
BY CHANNEL
REACTIVITY IN DOLLARS
0.75
0.60
0.45
0.30
0.15
0.00
−0.15
26
28
16.7
17.1
17.5
17.9
18.3
18.7
19.1
19.5
TIME IN SECONDS

Fig 104

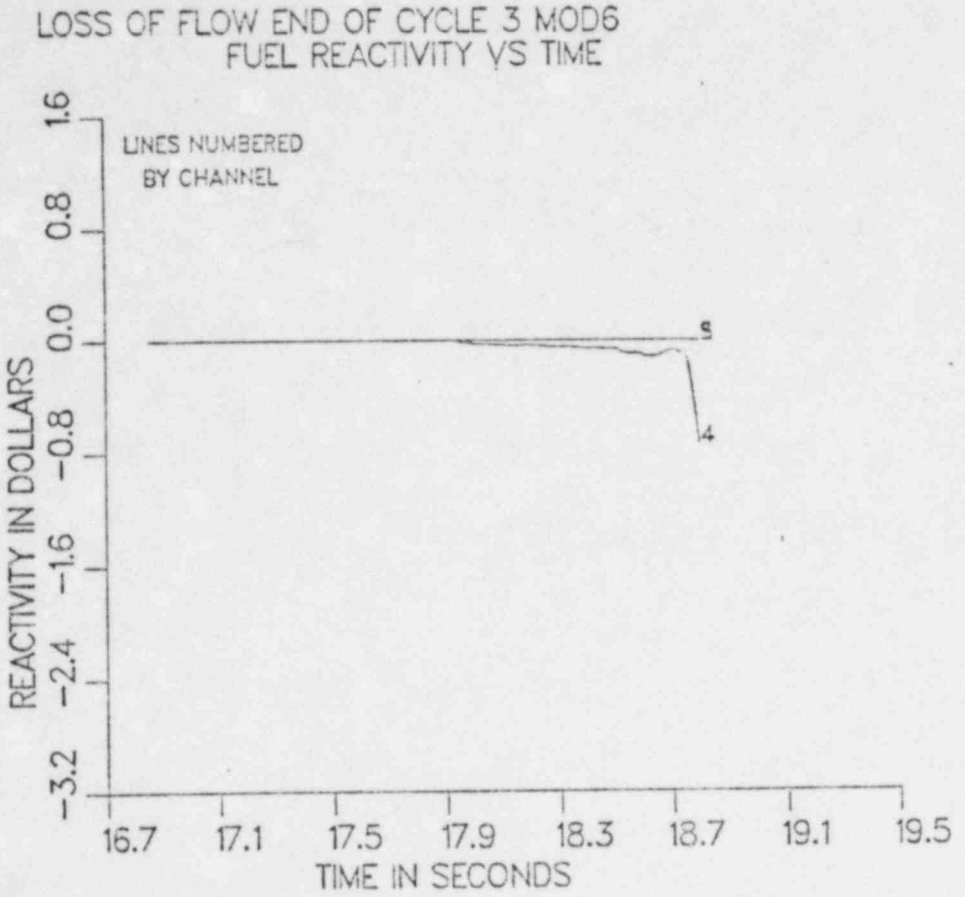
LOSS OF FLOW END OF CYCLE 3 MOD6
FUEL REACTIVITY VS TIME
LINES NUMBERED
BY CHANNEL
REACTIVITY IN DOLLARS
1.6
0.8
0.0
-0.8
-1.6
-2.4
-3.2
5
4
16.7
17.1
17.5
17.9
18.3
18.7
19.1
19.5
TIME IN SECONDS

Fig 105

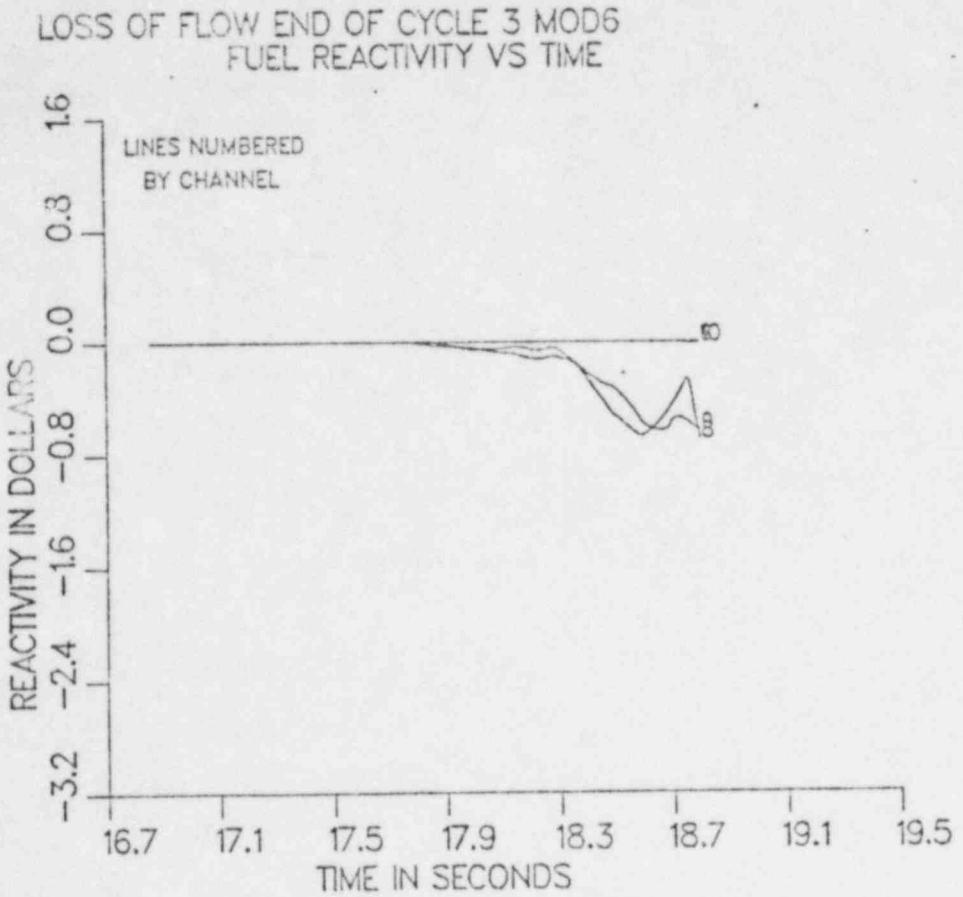
LOSS OF FLOW END OF CYCLE 3 MOD6
FUEL REACTIVITY VS TIME
LINES NUMBERED
BY CHANNEL
REACTIVITY IN DOLLARS
1.6
0.3
0.0
-0.8
-1.6
-2.4
-3.2
16.7
17.1
17.5
17.9
18.3
18.7
19.1
19.5
TIME IN SECONDS

Fig 106

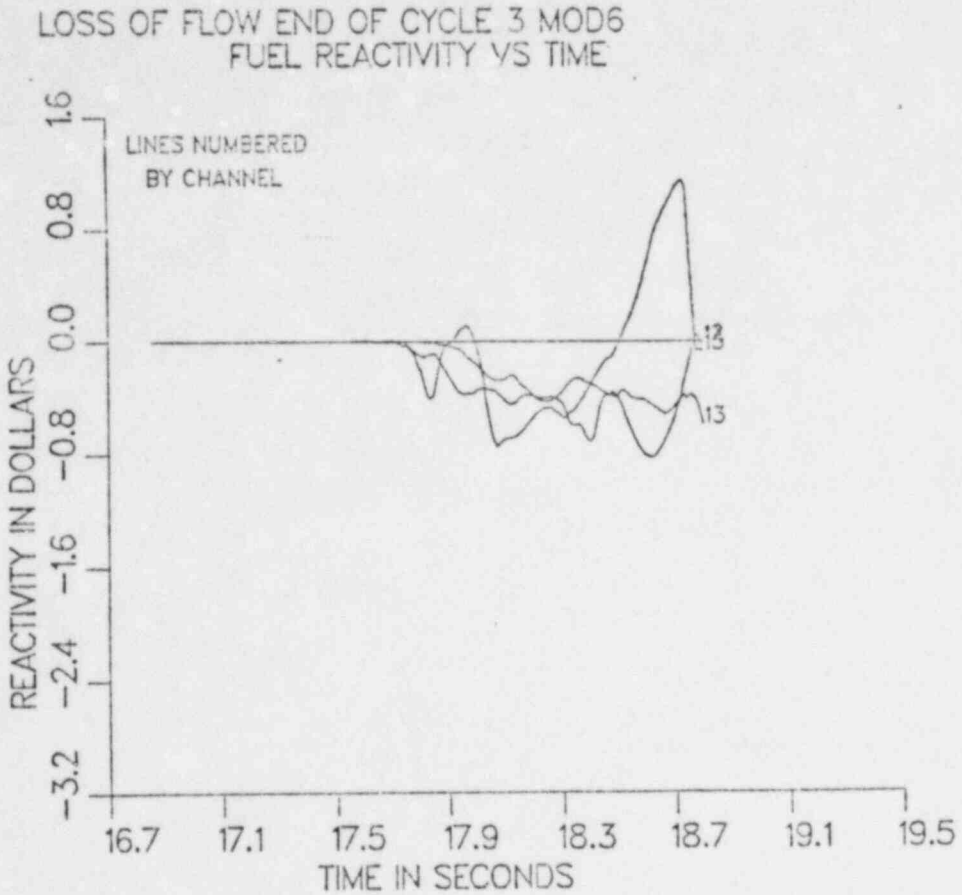
LOSS OF FLOW END OF CYCLE 3 MOD6
FUEL REACTIVITY VS TIME
LINES NUMBERED
BY CHANNEL
REACTIVITY IN DOLLARS
1.6
0.8
0.0
-0.8
-1.6
-2.4
-3.2
13
13
16.7
17.1
17.5
17.9
18.3
18.7
19.1
19.5
TIME IN SECONDS

Fig 107

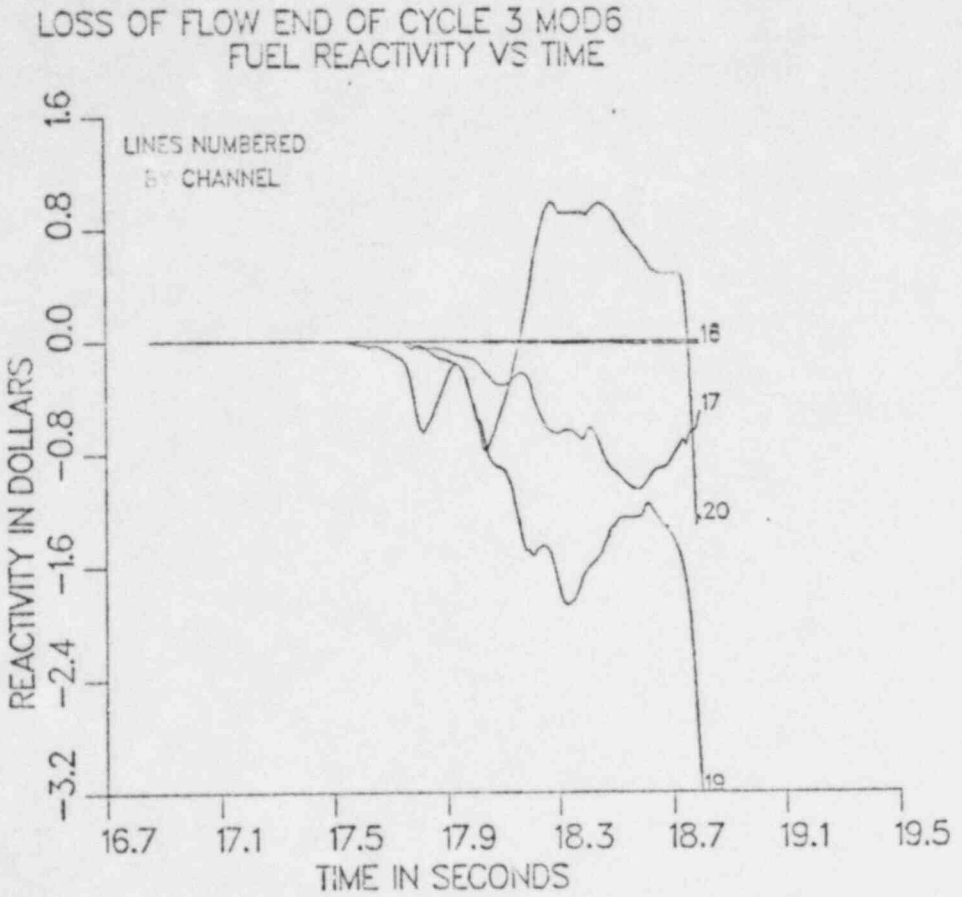
LOSS OF FLOW END OF CYCLE 3 MOD6
FUEL REACTIVITY VS TIME
LINES NUMBERED
BY CHANNEL
REACTIVITY IN DOLLARS
1.6
0.8
0.0
-0.8
-1.6
-2.4
-3.2
16
17
20
19
16.7
17.1
17.5
17.9
18.3
18.7
19.1
19.5
TIME IN SECONDS

Fig 108

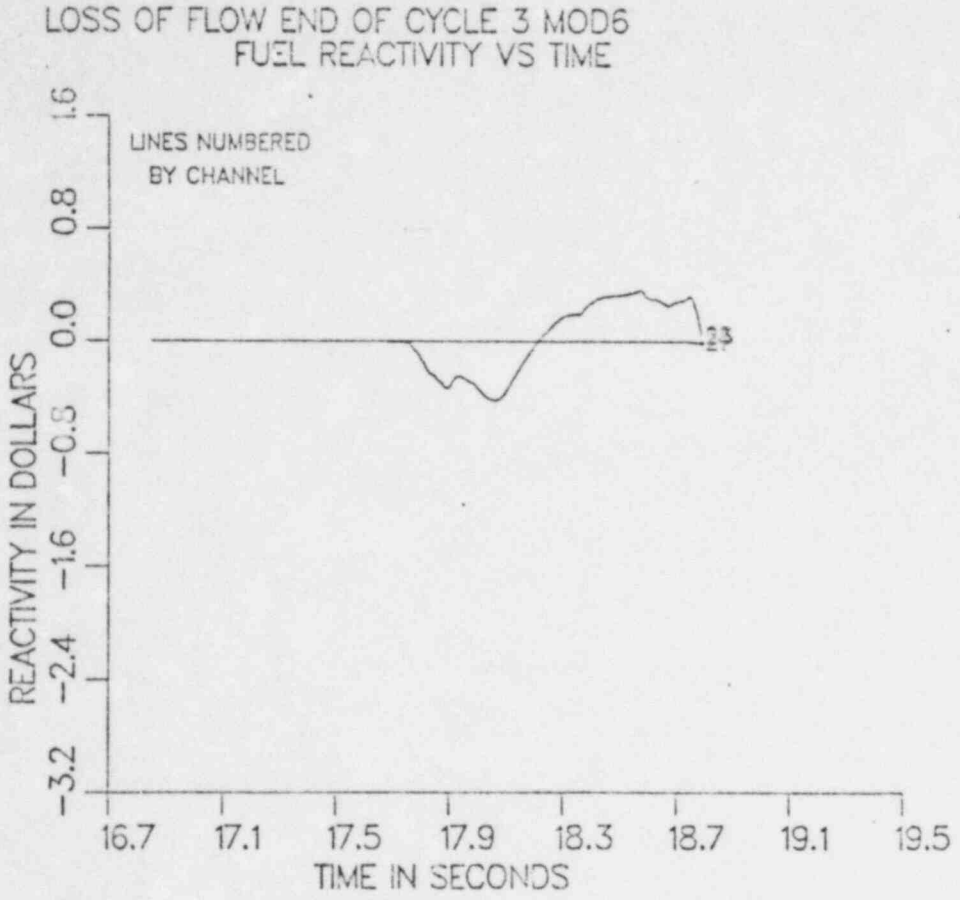
LOSS OF FLOW END OF CYCLE 3 MOD6
FUEL REACTIVITY VS TIME
LINES NUMBERED
BY CHANNEL
REACTIVITY IN DOLLARS
1.6
0.8
0.0
-0.8
-1.6
-2.4
-3.2
23
27
16.7
17.1
17.5
17.9
18.3
18.7
19.1
19.5
TIME IN SECONDS

Fig 109

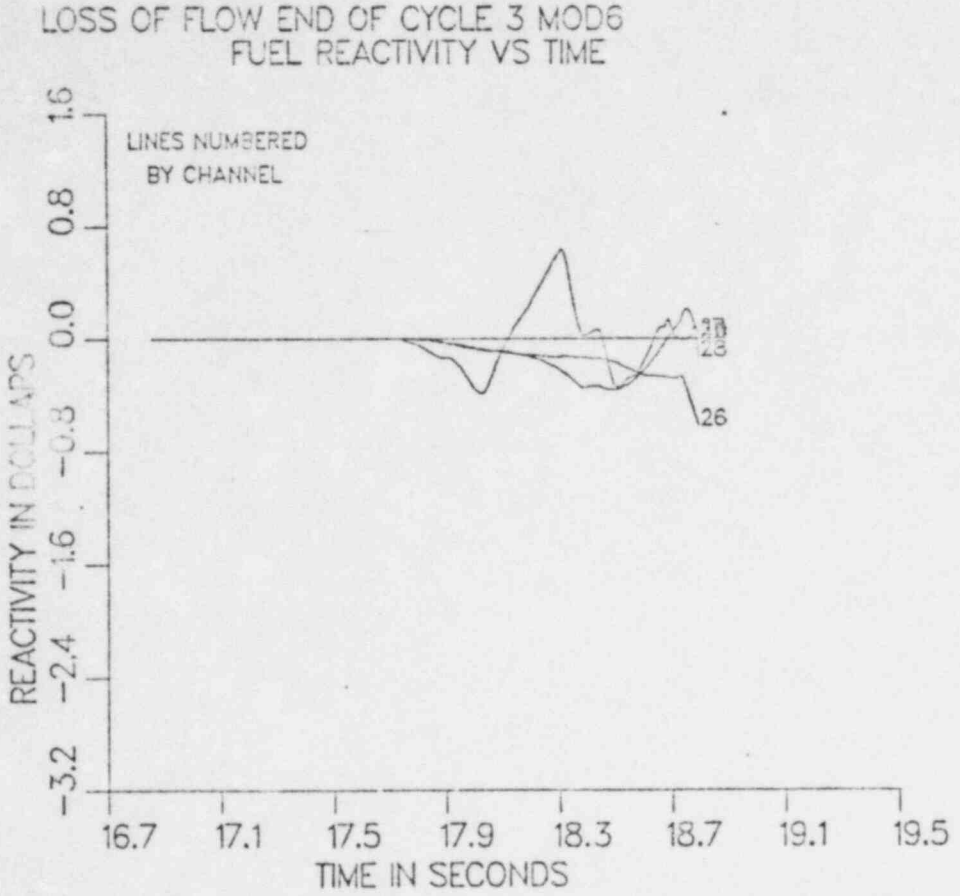
LOSS OF FLOW END OF CYCLE 3 MOD6
FUEL REACTIVITY VS TIME
LINES NUMBERED
BY CHANNEL
REACTIVITY IN DOLLARS
1.6
0.8
0.0
-0.8
-1.6
-2.4
-3.2
26
16.7
17.1
17.5
17.9
18.3
18.7
19.1
19.5
TIME IN SECONDS

Fig 110

REFERENCE CASE FOR THE HETEROGENEOUS CORE AT EOC - 3
SUBASSEMBLIES FOR CHANNEL 20

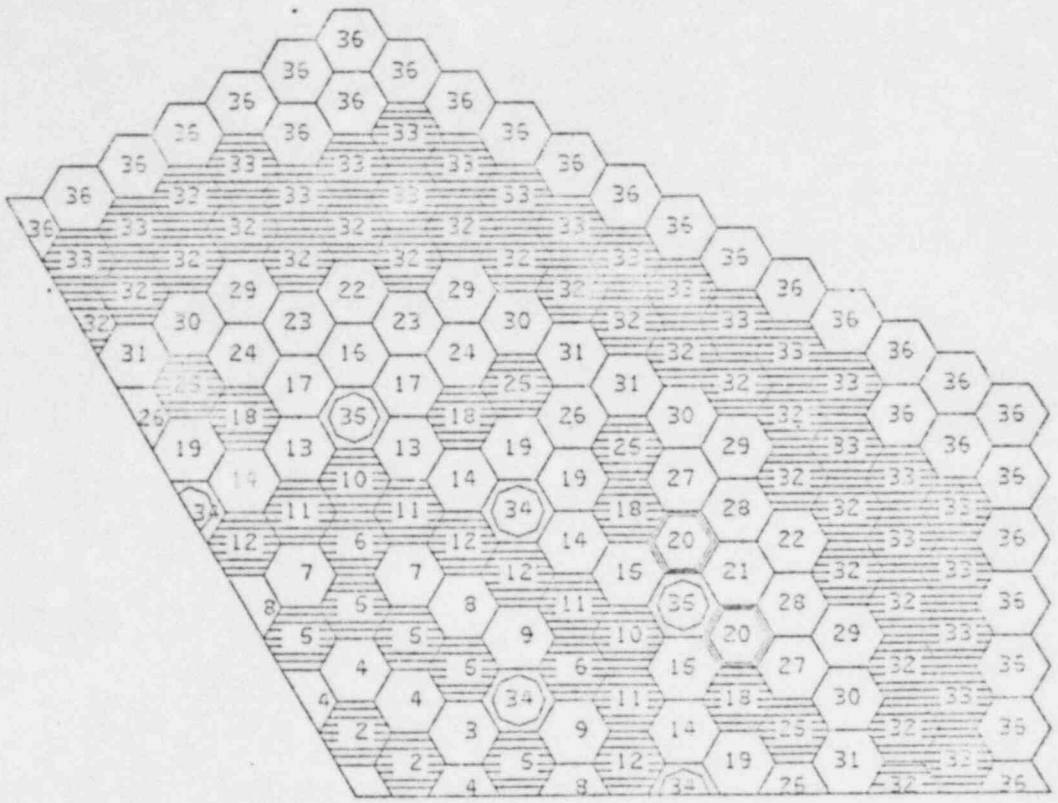

Fig III

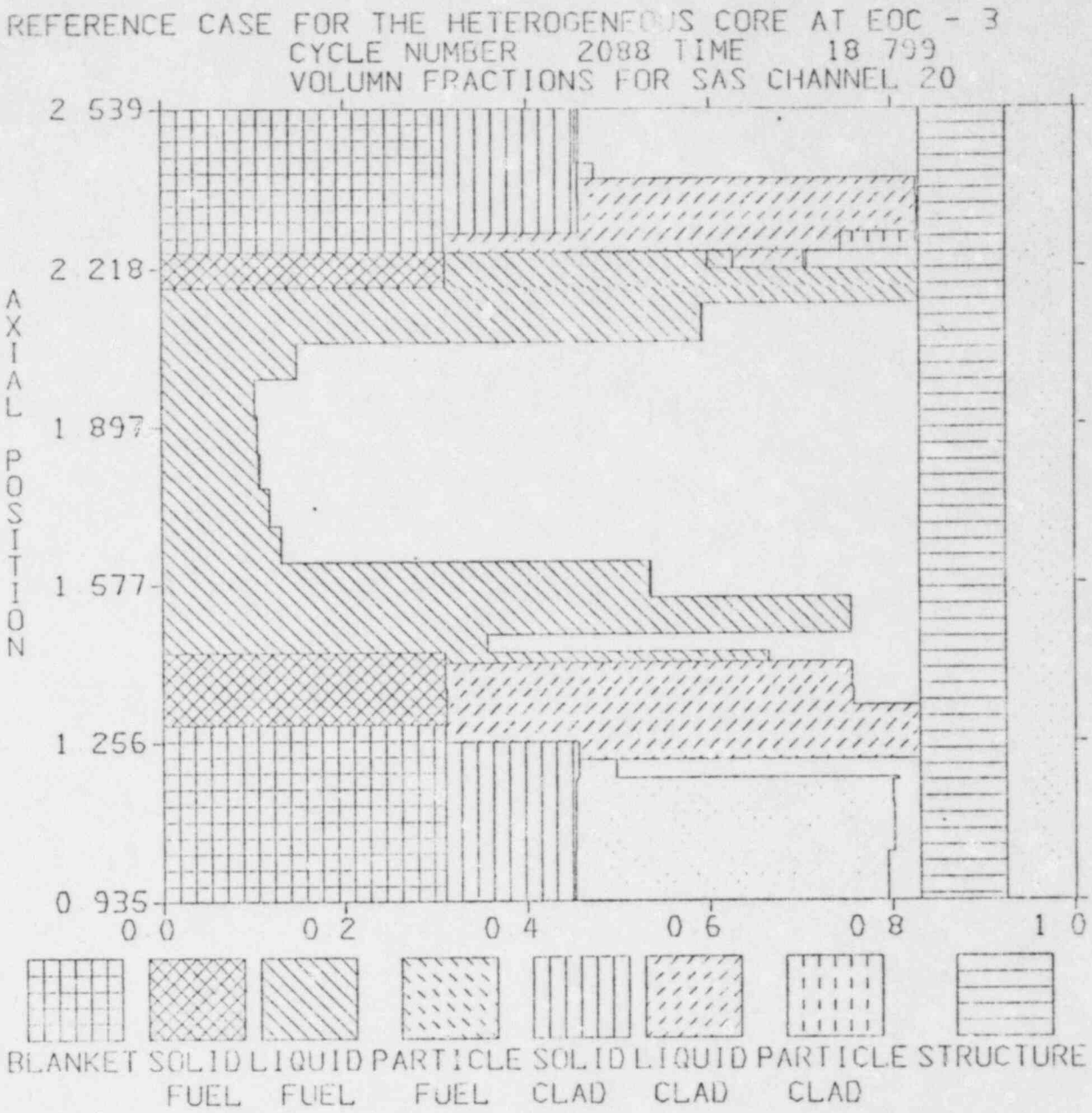
REFERENCE CASE FOR THE HETEROGENEOUS CORE AT EOC - 3
CYCLE NUMBER 2088 TIME 18 799
VOLUMN FRACTIONS FOR SAS CHANNEL 20
AXIAL POSITION
2 539
2 218
1 897
1 577
1 256
0 935
0 0
0 2
0 4
0 6
0 8
1 0
BLANKET
SOLID FUEL
LIQUID FUEL
PARTICLE FUEL
SOLID CLAD
LIQUID CLAD
PARTICLE CLAD
STRUCTURE

Fig 112

Figures 113 & 114

Channel 20 - High power SA
Final fuel temp - Fig 113
Final Pressure - Fig 114

To be supplied.

REFERENCE CASE FOR THE HETEROGENEOUS CORE AT EOC - 3.
SUBASSEMBLIES FOR CHANNEL 13

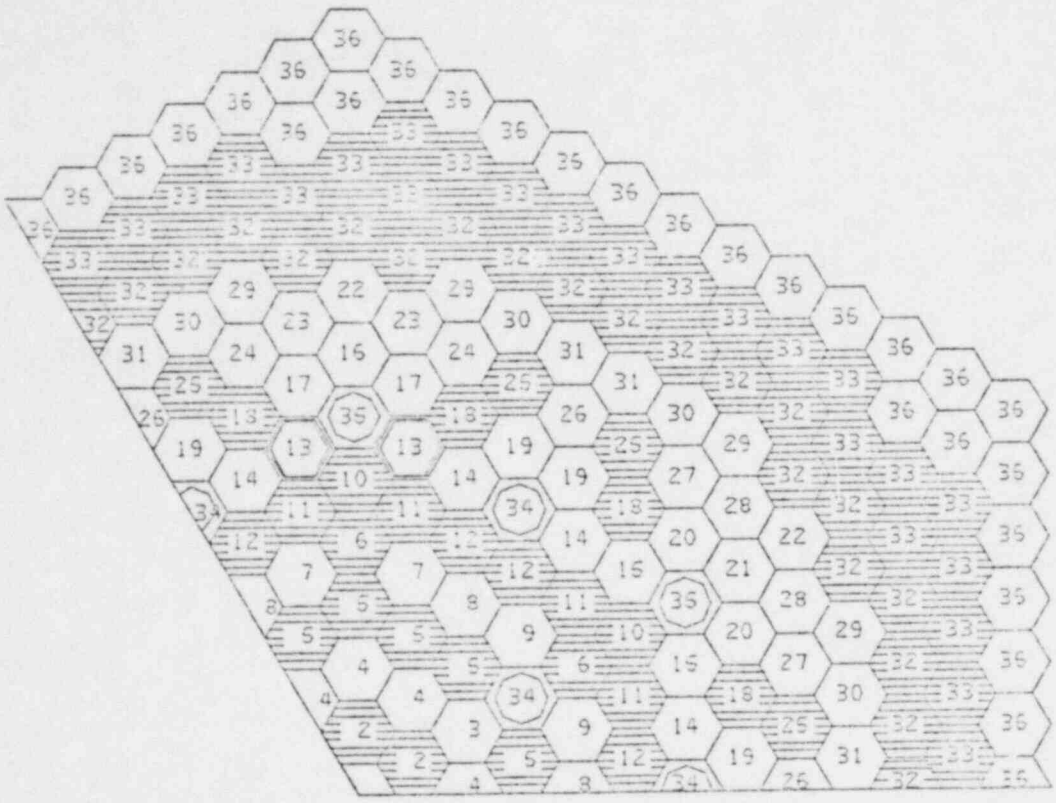

Fig 115

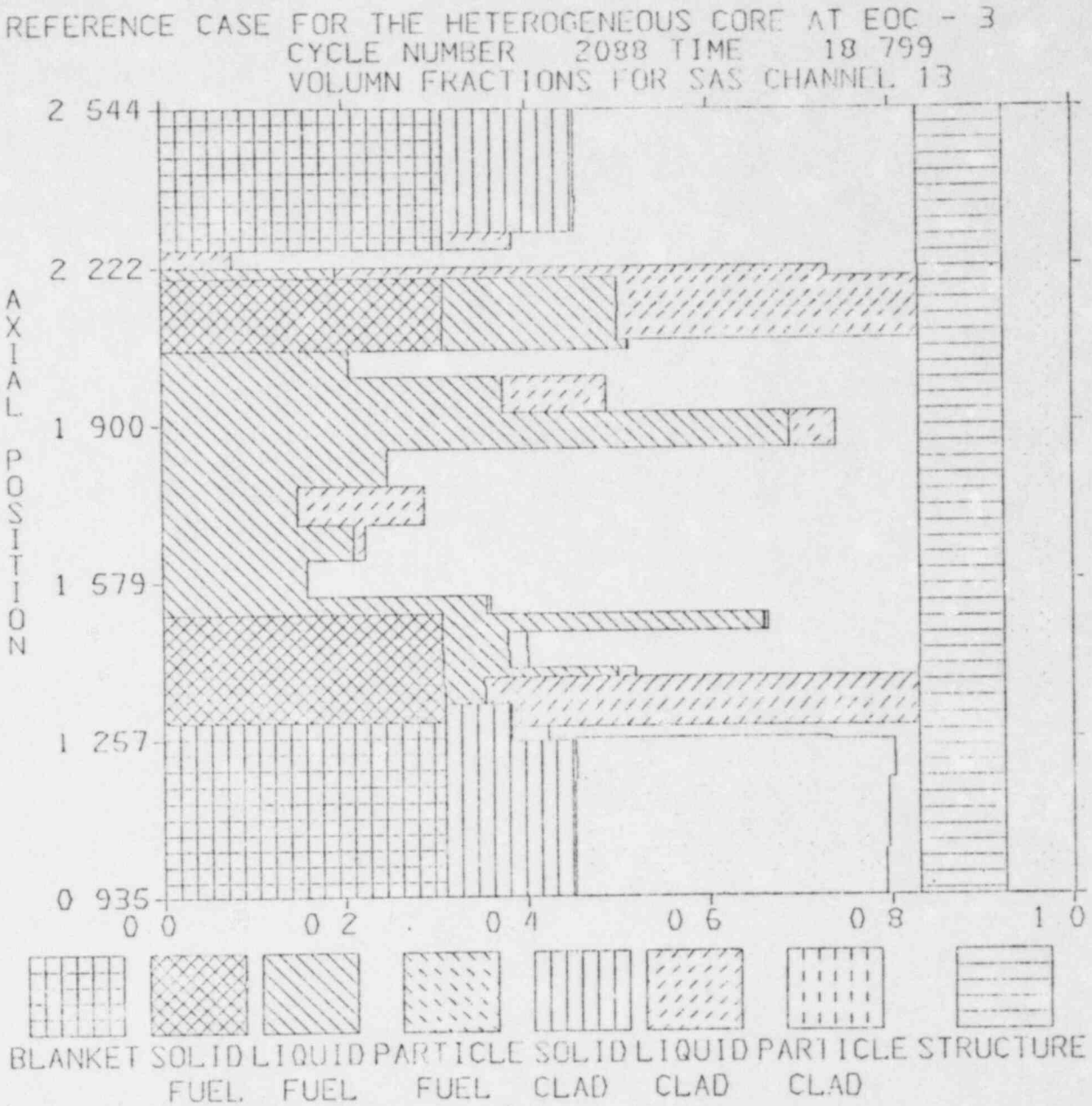
REFERENCE CASE FOR THE HETEROGENEOUS CORE AT EOC - 3
CYCLE NUMBER 2088 TIME 18 799
VOLUMN FRACTIONS FOR SAS CHANNEL 13
AXIAL POSITION
2 544
2 222
1 900
1 579
1 257
0 935
0 0
0 2
0 4
0 6
0 8
1 0
BLANKET
SOLID FUEL
LIQUID FUEL
PARTICLE FUEL
SOLID CLAD
LIQUID CLAD
PARTICLE CLAD
STRUCTURE

Fig 116

B.II.3

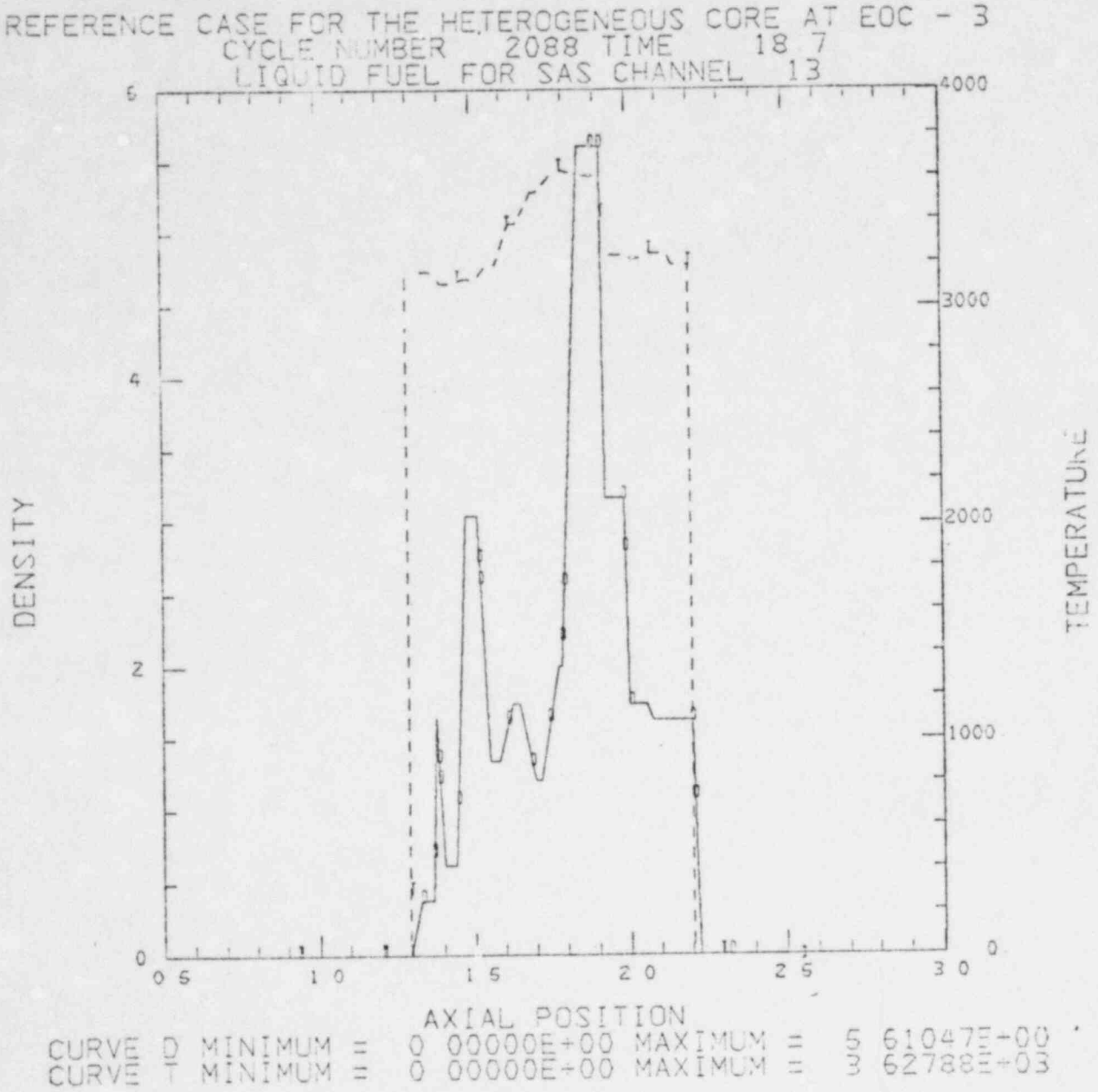
REFERENCE CASE FOR THE HETEROGENEOUS CORE AT EOC - 3
CYCLE NUMBER 2088 TIME 18.7
LIQUID FUEL FOR SAS CHANNEL 13
DENSITY
TEMPERATURE
AXIAL POSITION
0
2
4
6
1000
2000
3000
4000
05
10
15
20
25
30
CURVE D MINIMUM = 0.00000E+00 MAXIMUM = 5.61047E+00
CURVE T MINIMUM = 0.00000E+00 MAXIMUM = 3.62788E+03

Fig 117

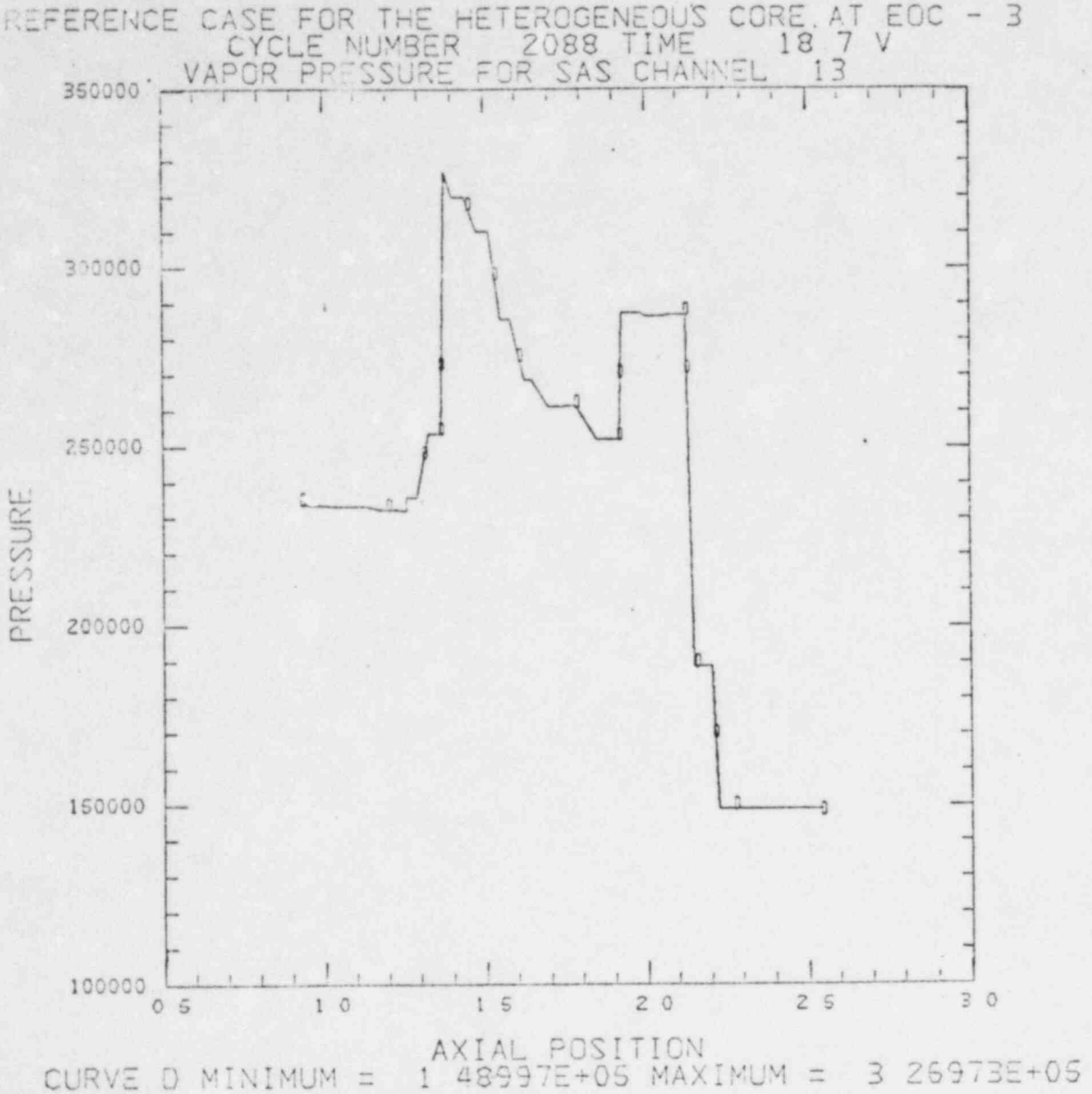
REFERENCE CASE FOR THE HETEROGENEOUS CORE AT EOC - 3
CYCLE NUMBER 2088 TIME 18 7 V
VAPOR PRESSURE FOR SAS CHANNEL 13
350000
300000
250000
200000
150000
100000
PRESSURE
0 5
1 0
1 5
2 0
2 5
3 0
AXIAL POSITION
CURVE D MINIMUM = 1 48997E+05 MAXIMUM = 3 26973E+05

Fig 118

REFERENCE CASE FOR THE HETEROGENEOUS CORE AT EOC - 3
SUBASSEMBLIES FOR CHANNEL 29

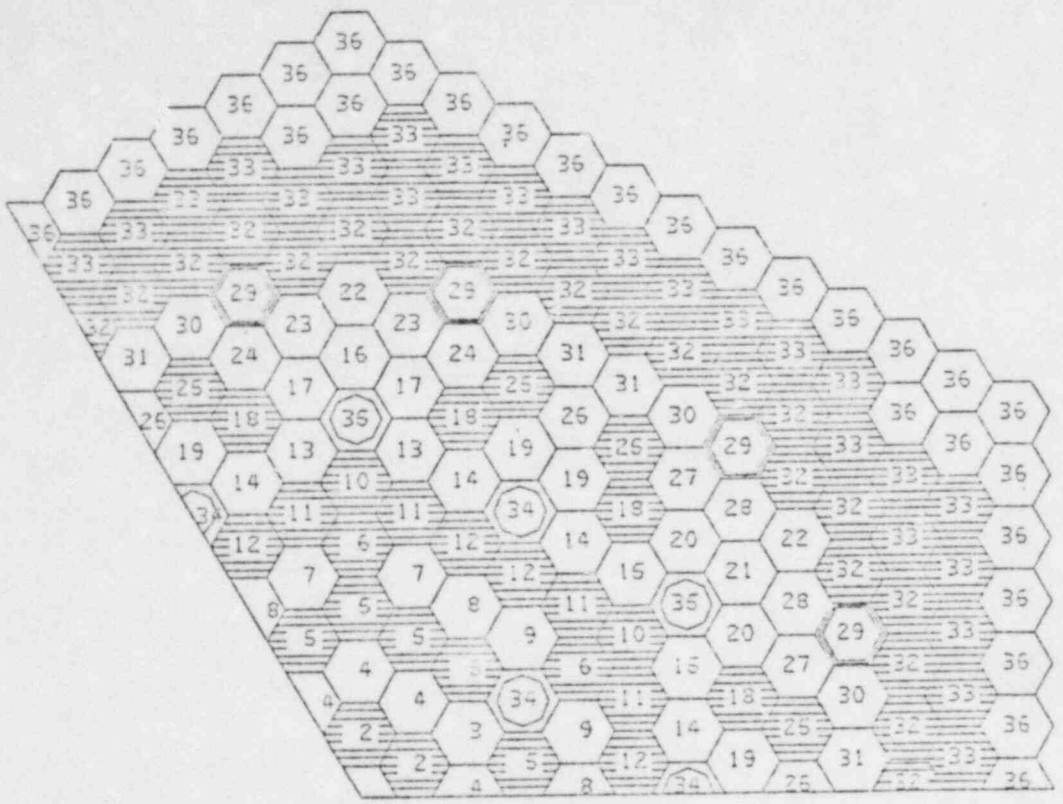

Fig 119

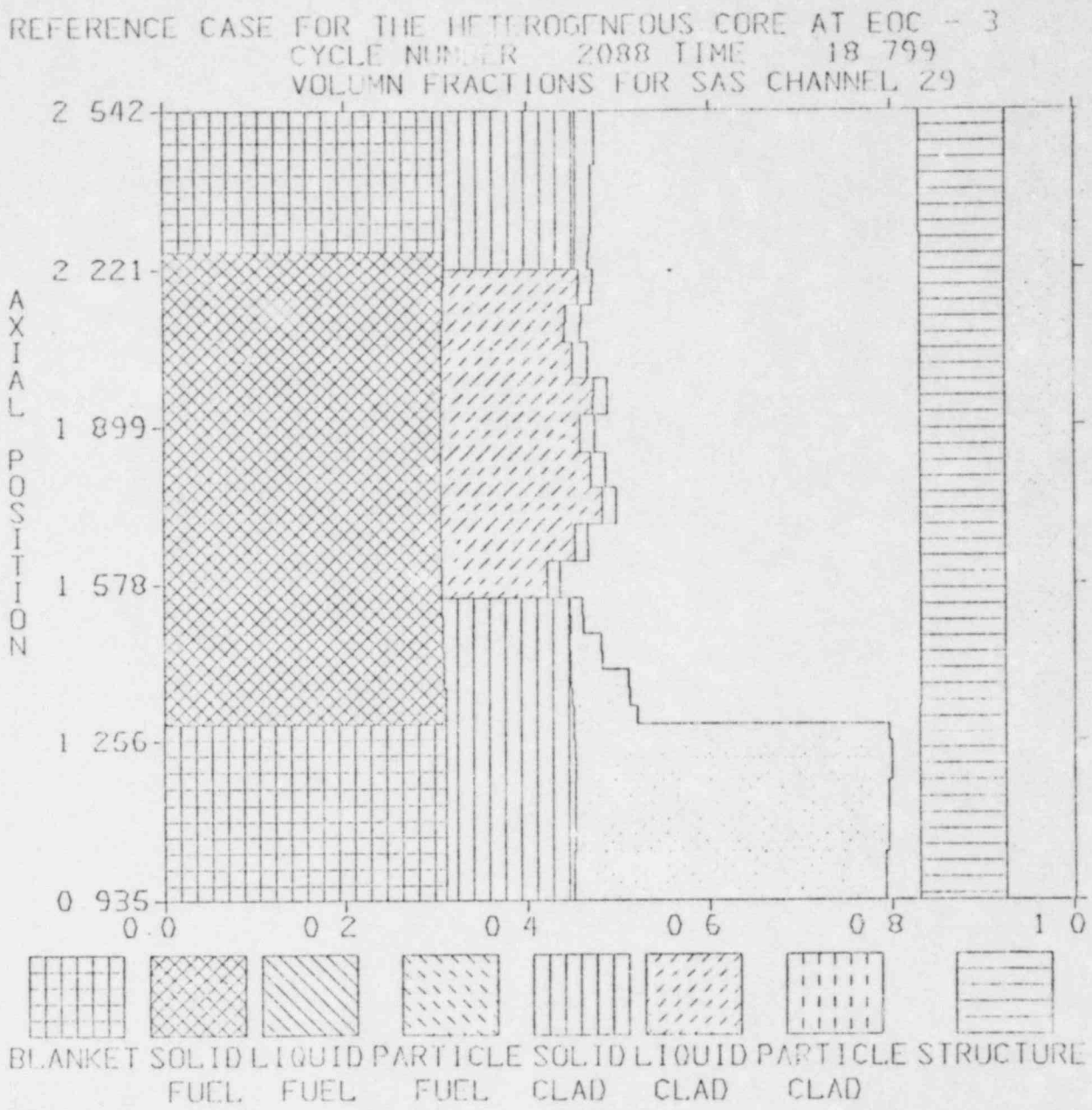
REFERENCE CASE FOR THE HETEROGENEOUS CORE AT EOC - 3
CYCLE NUMBER 2088 TIME 18 799
VOLUMN FRACTIONS FOR SAS CHANNEL 29
AXIAL POSITION
2 542
2 221
1 899
1 578
1 256
0 935
0 0
0 2
0 4
0 6
0 8
1 0
BLANKET
SOLID FUEL
LIQUID FUEL
PARTICLE FUEL
SOLID CLAD
LIQUID CLAD
PARTICLE CLAD
STRUCTURE

Fig 120

B.II.3

Figures 121 & 122

Channel 29

Final Fuel Temp - Fig 121
Final Pressure - Fig 122

To be supplied.

PLENUM FISSION GAS INDUCED FUEL COMPACTION

THE MECHANISM

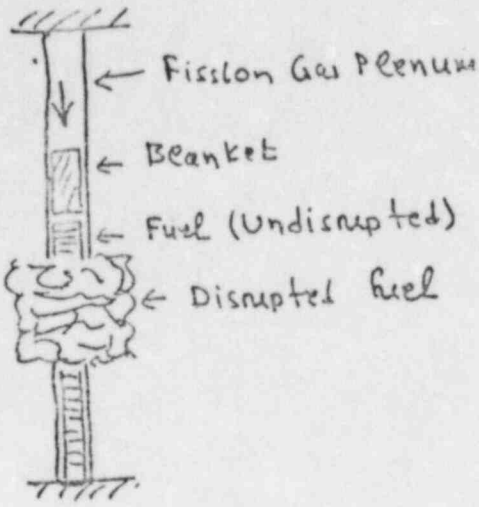

Fig 1

Fig 2

KEY PARAMETERS (CONT'D).

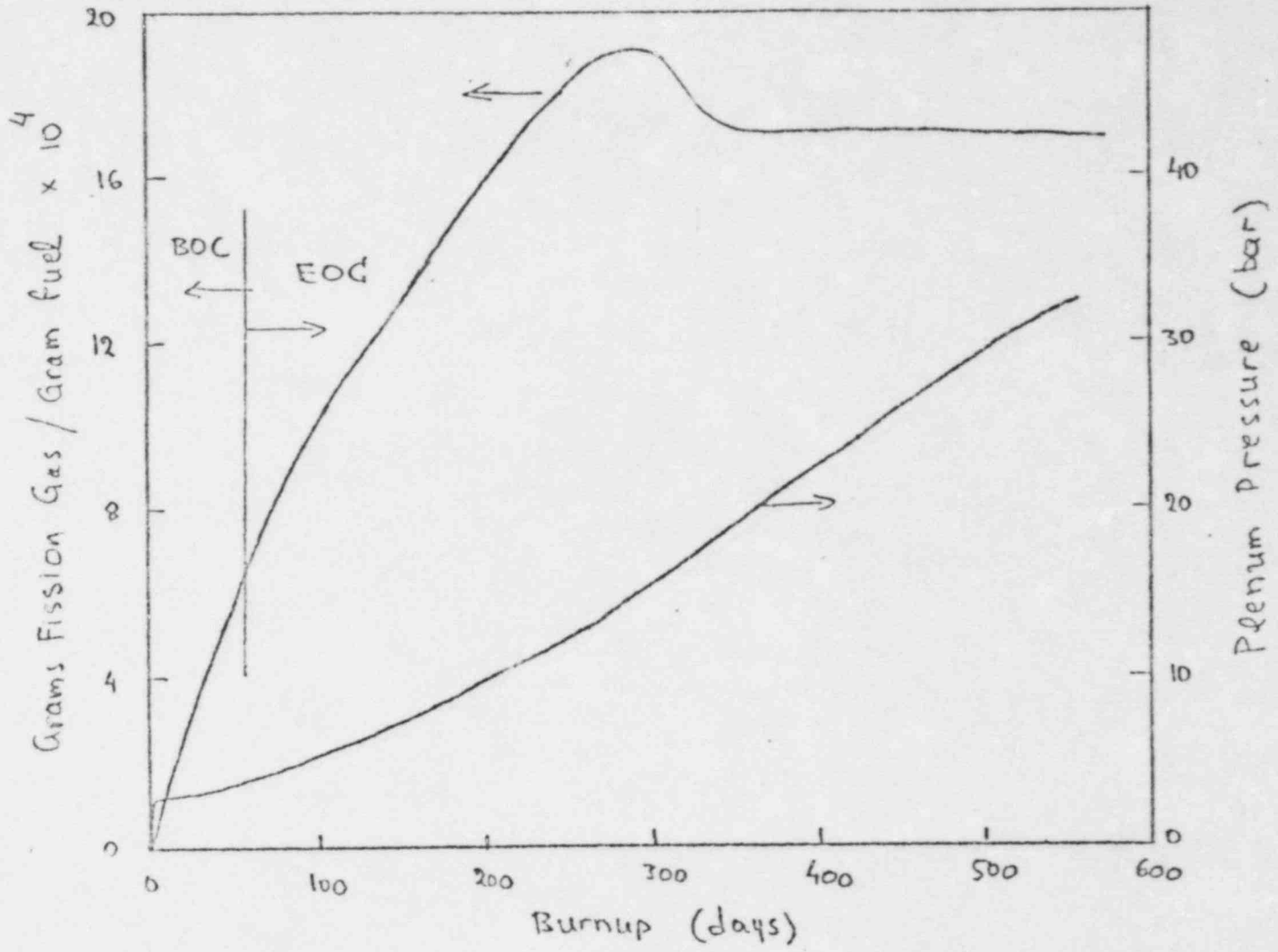

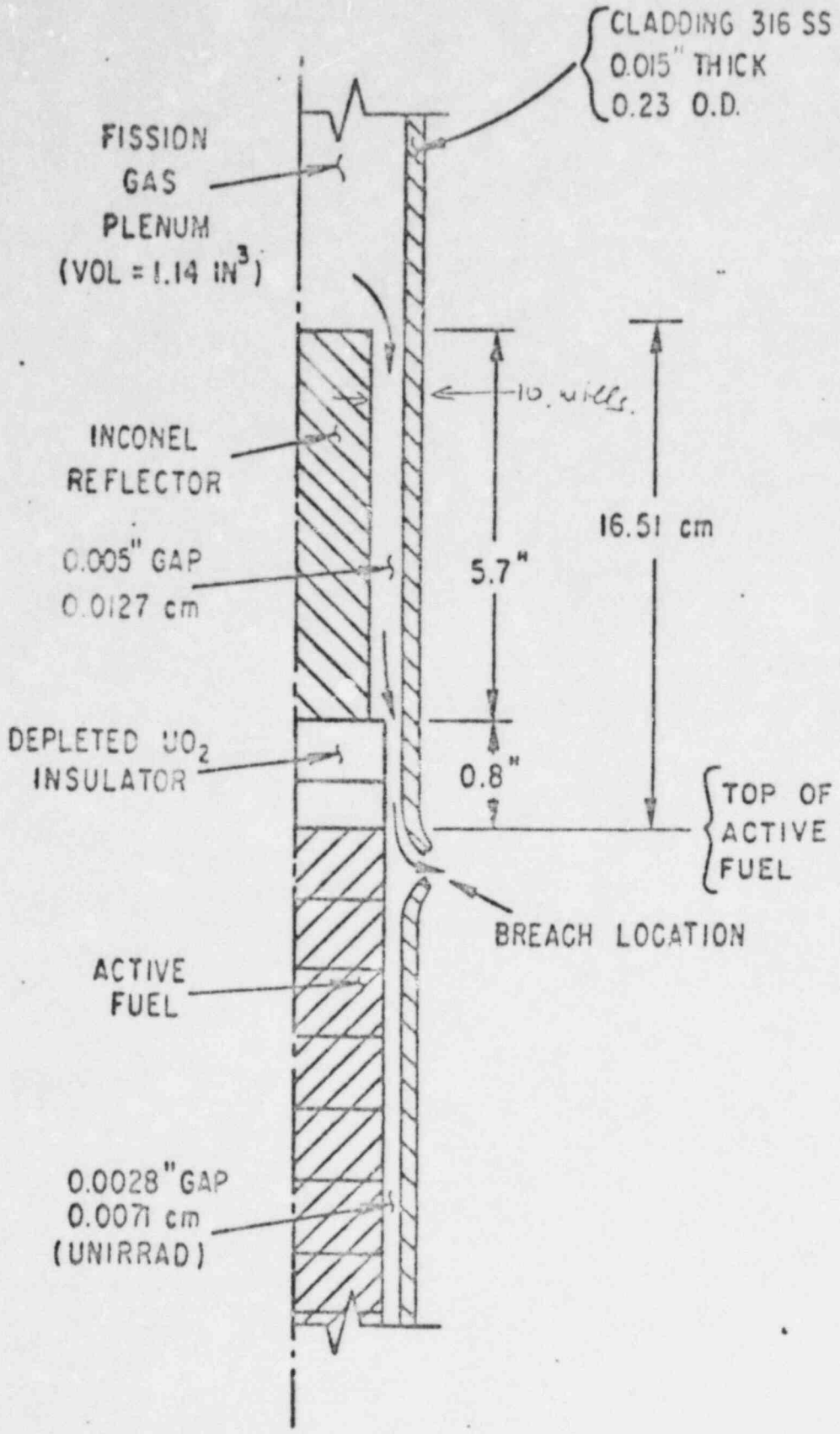

FIG 3 MODEL FOR TEST R8

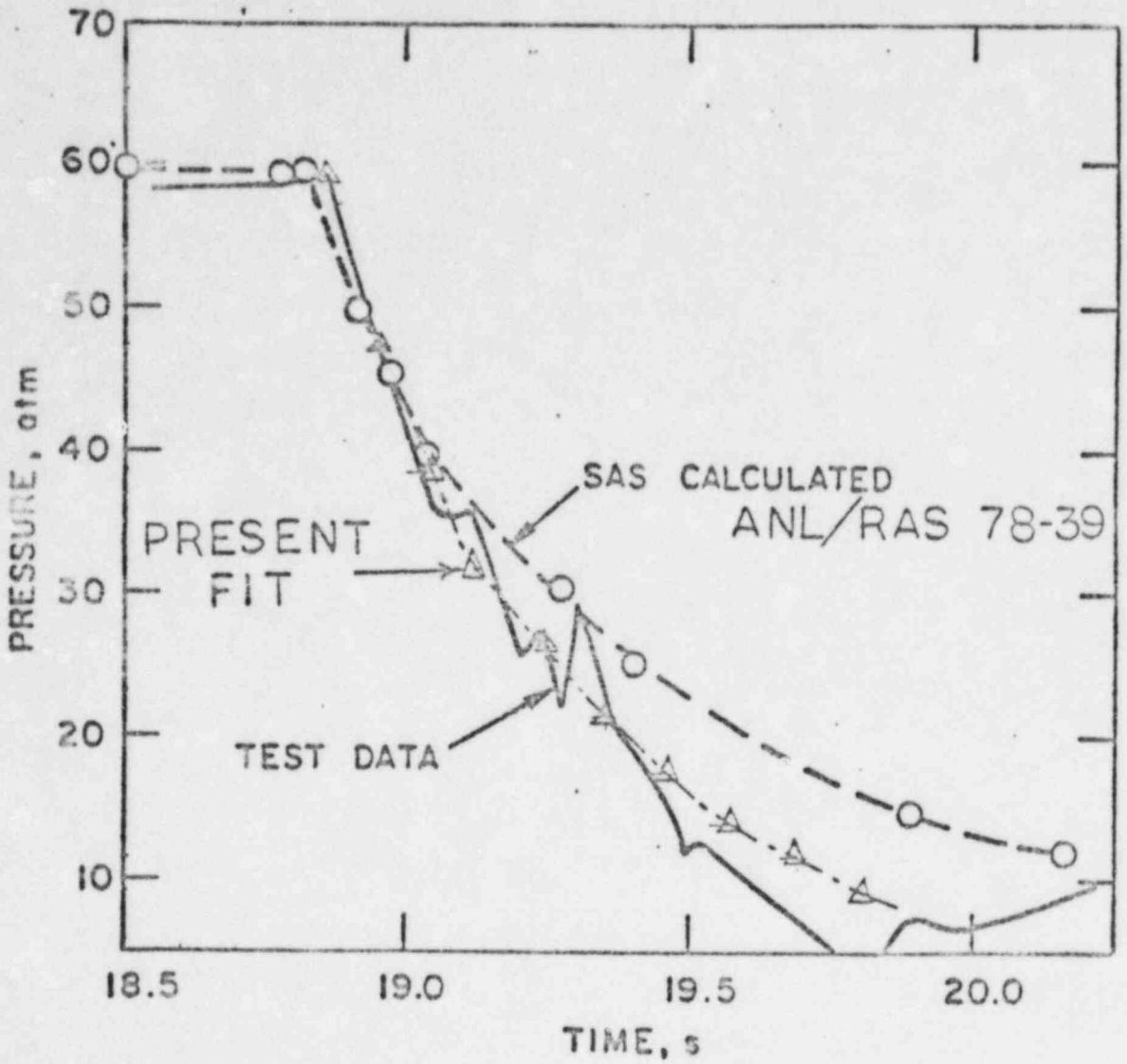

FIG. 4 R8 BLOWDOWN RATES

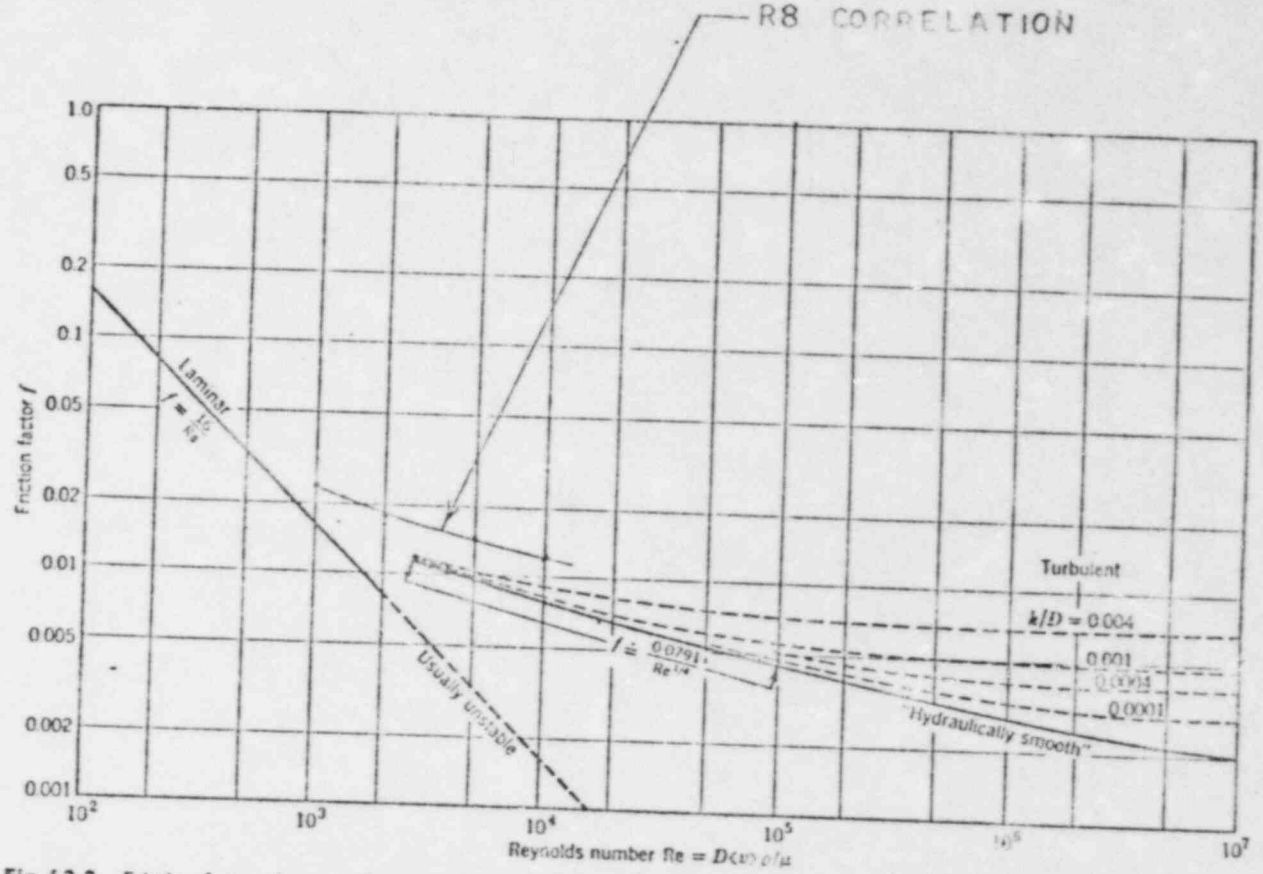

Fig. 4.2-2. Friction factors for tube flow (see definition of f in Eqs. 6.1-2 and 6.1-3. [Curves of L. F. Moody, *Trans.* ASME, 66, 671 (1944) as presented in W. L. McCabe and J. C. Smith, *Unit Operations of Chemical Engineering*, McGraw-Hill, New York (1954).]

FIG. 5

DEPRESSURIZATION WITH PIPFLO

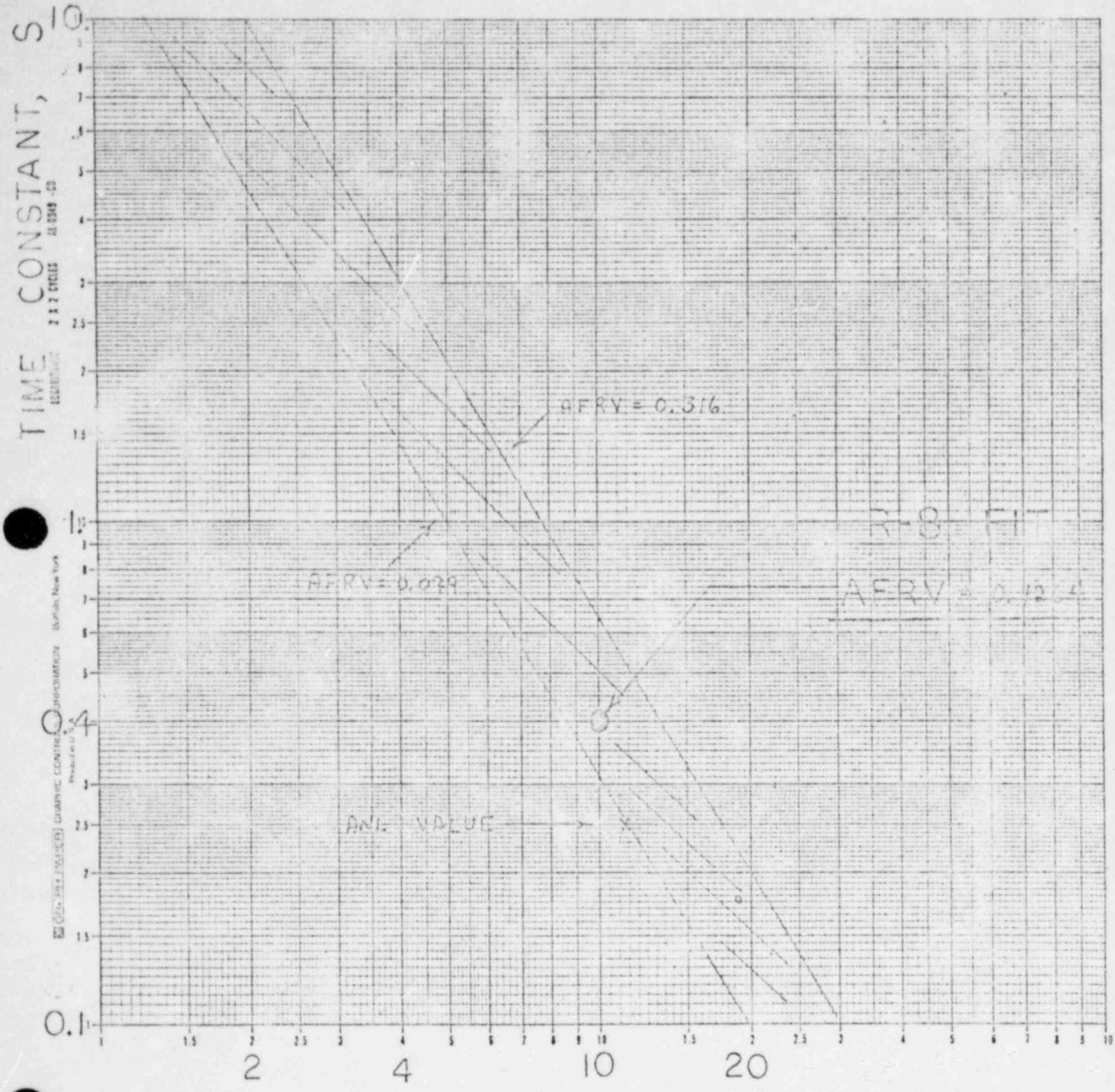

FIG 6

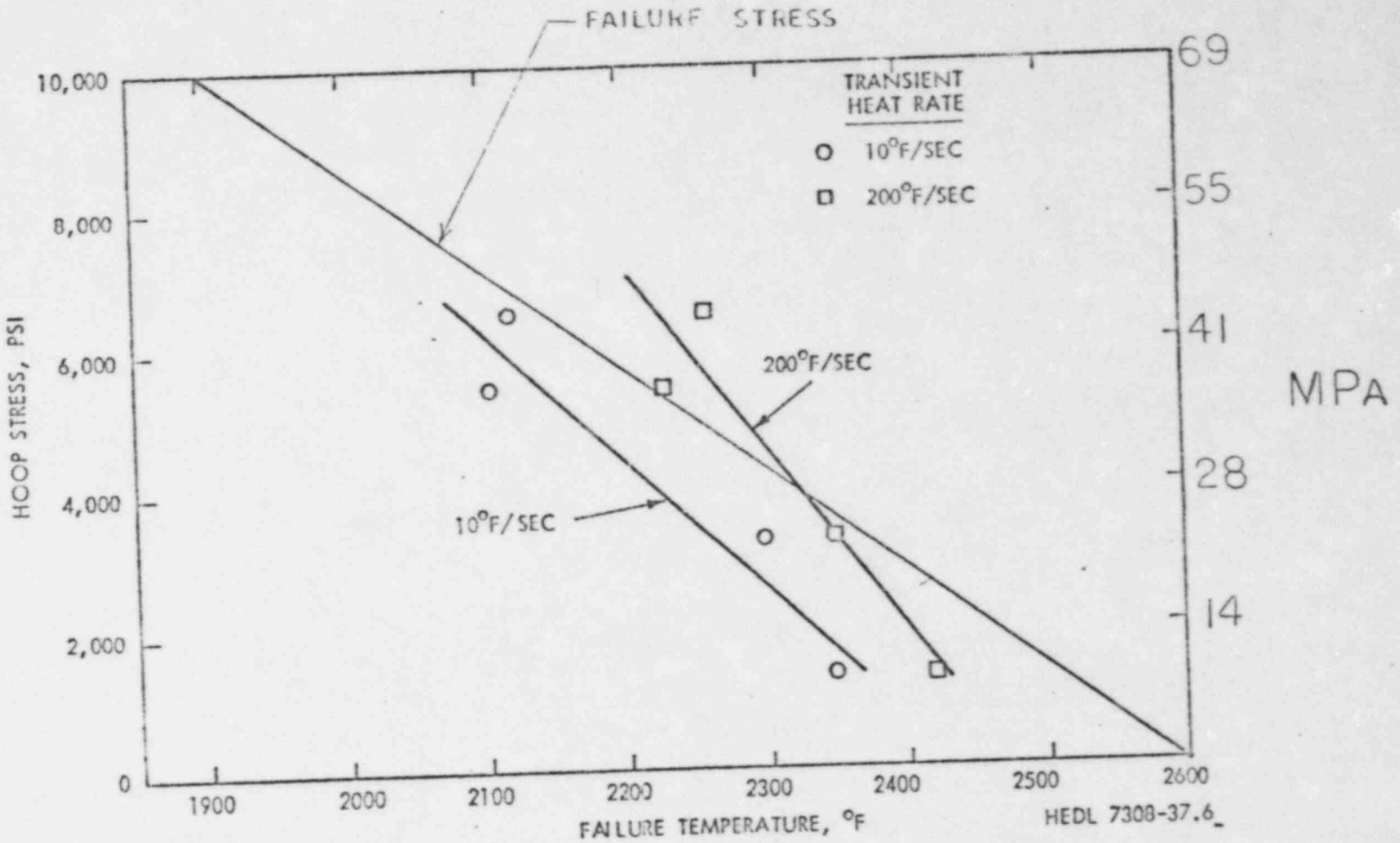

FIGURE 2. Effect of Hoop Stress on the Failure Temperature of Unirradiated 20% C.W. Type 316 Stainless Steel Cladding During High Temperature Transients.

FIG 7

571

II.4

Fig 8

KEY PARAMETERS (CONT'D).

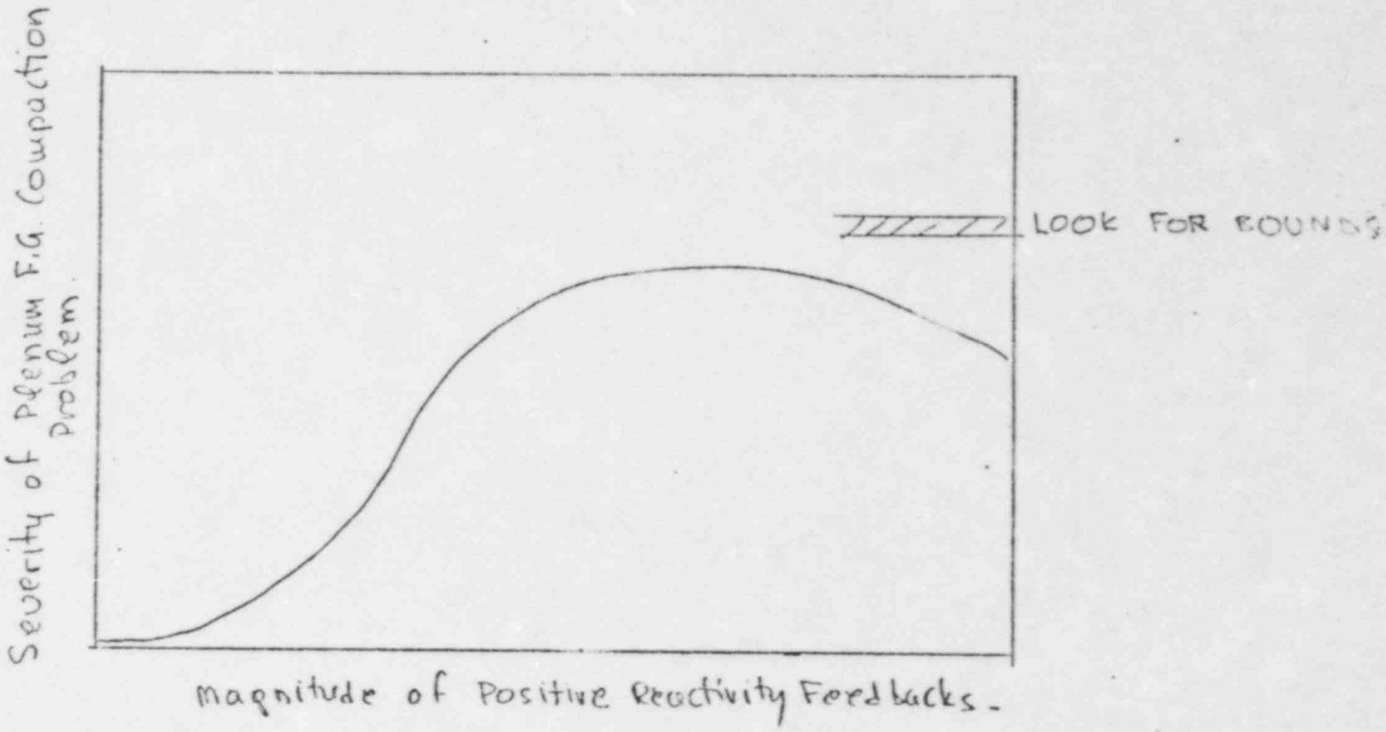

Fig 9

-SAS3D PREDICTED BOUNDS OF POWER AND REACTIVITY TRANSIENTS FOR PLENUM F.G. COMPACTION.

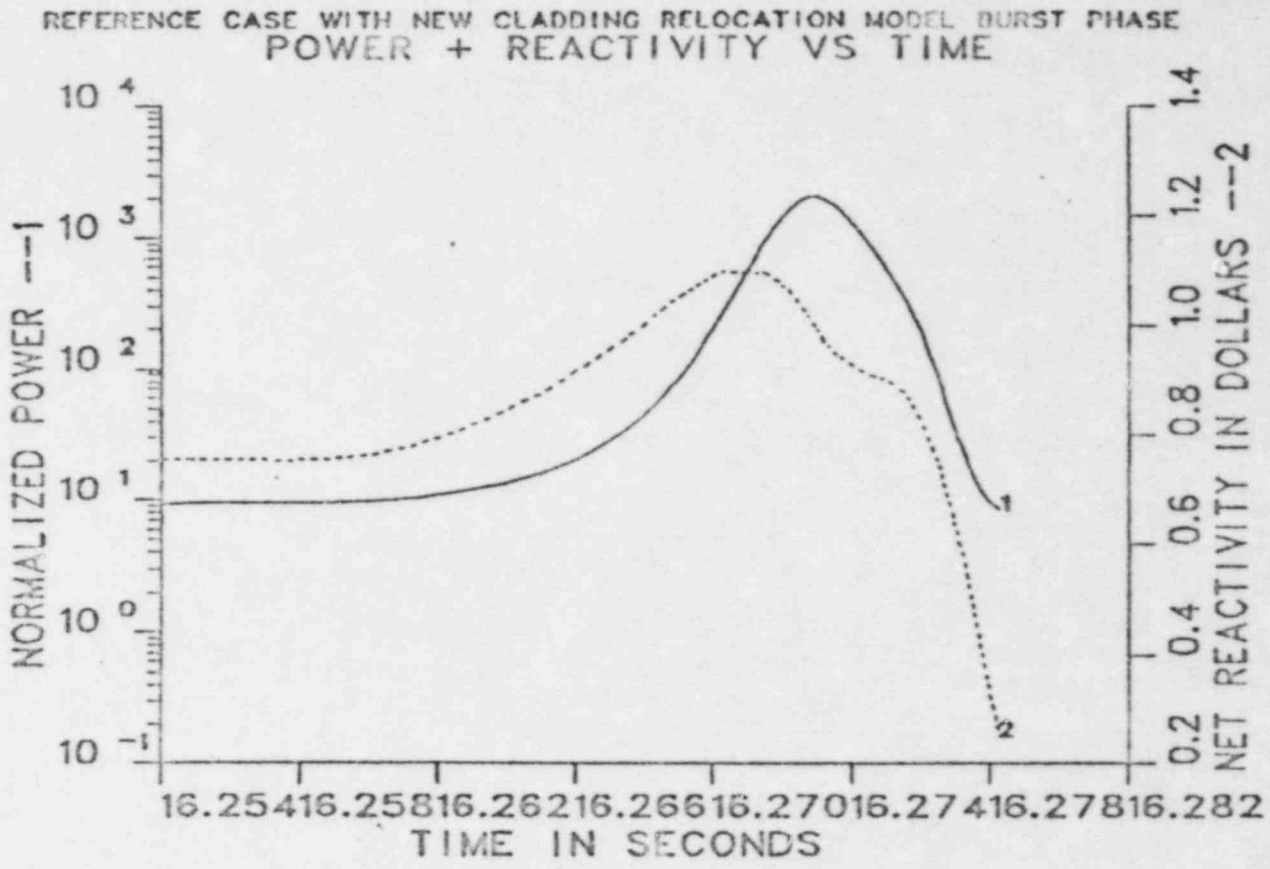

Fig 55

~~III (6).5.~~ SAS3D MATERIAL PATTERNS

Sodium Void Pattern.

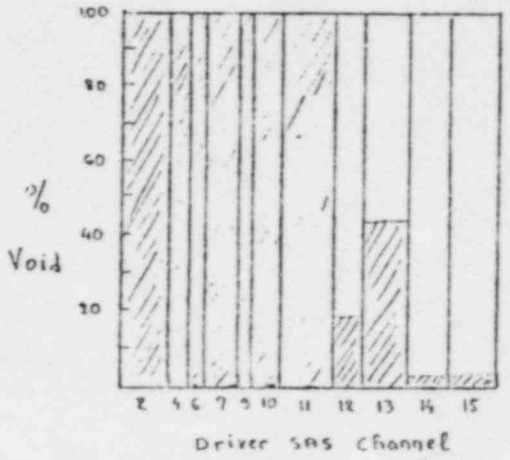

Cladding Melt Pattern.

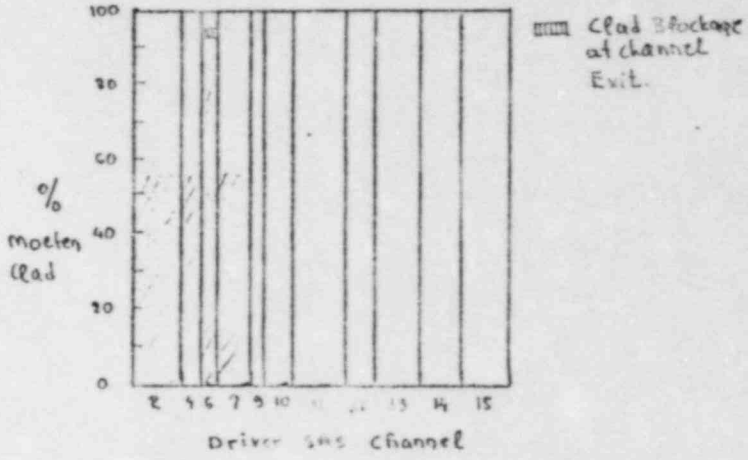

Max. Radial Fuel Melt Fraction

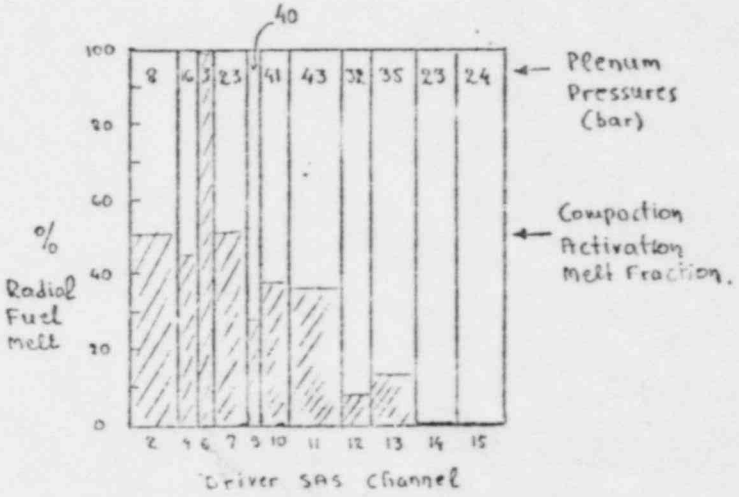

Post-Burst Fuel Melt Pattern.

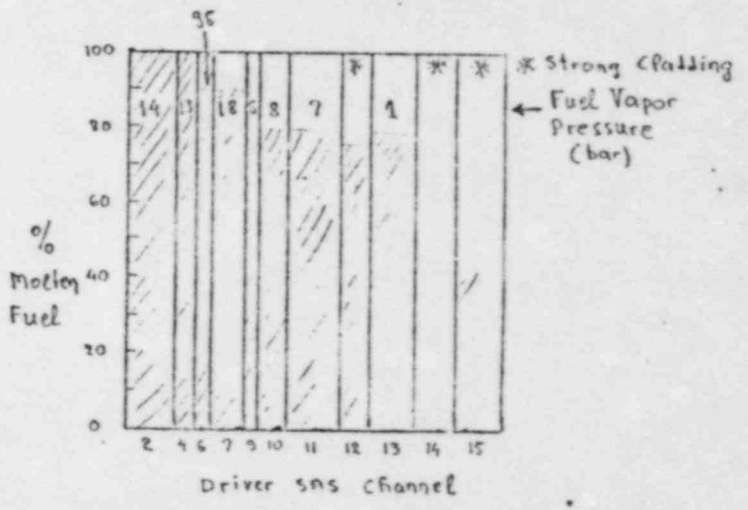

II.4

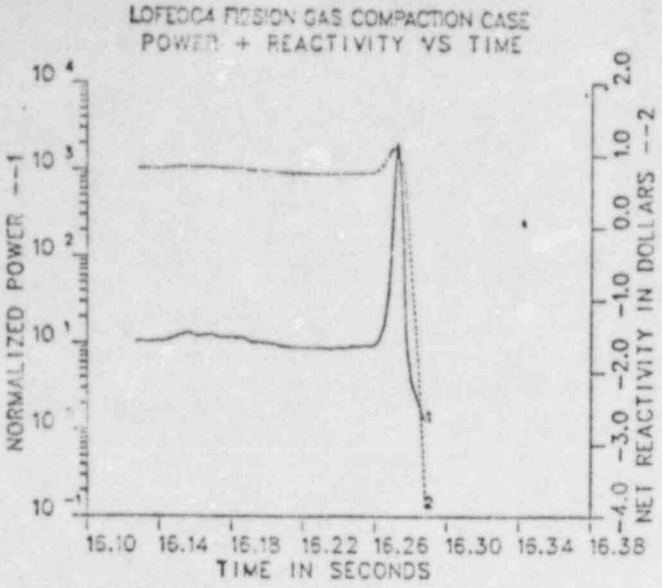

Fig 1

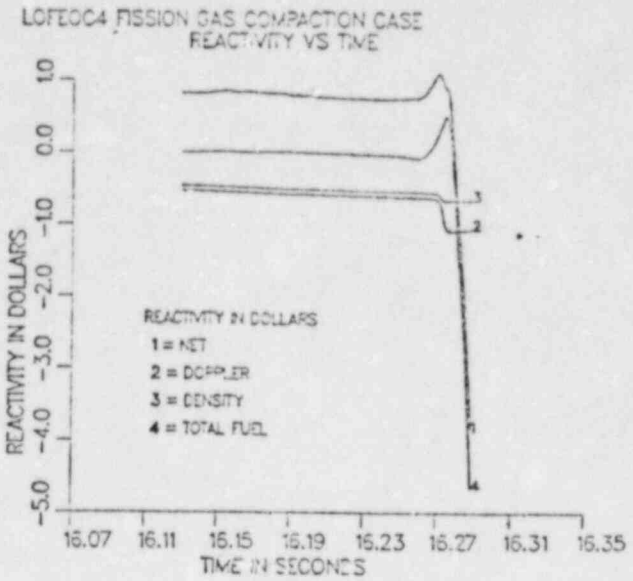

Fig 2

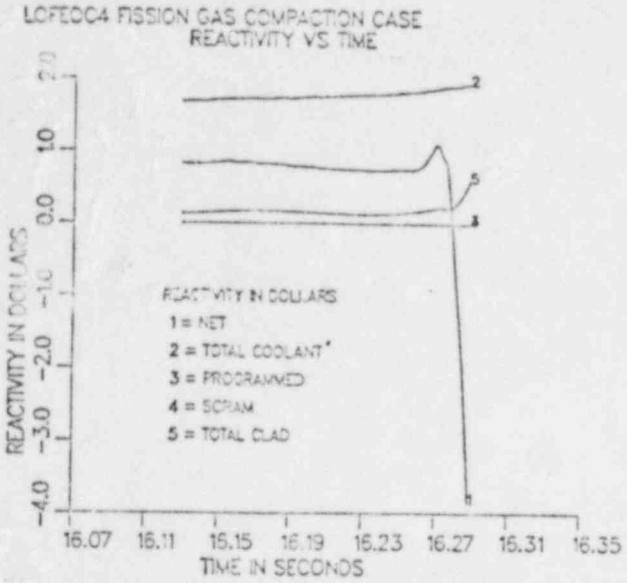

Fig 3

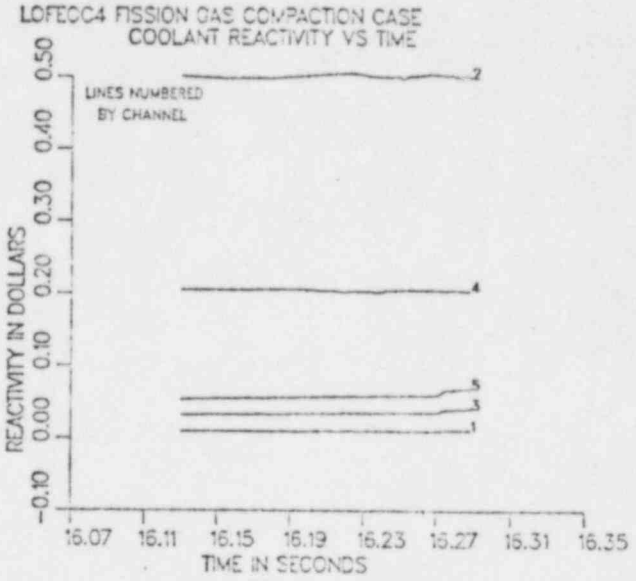

Fig 4

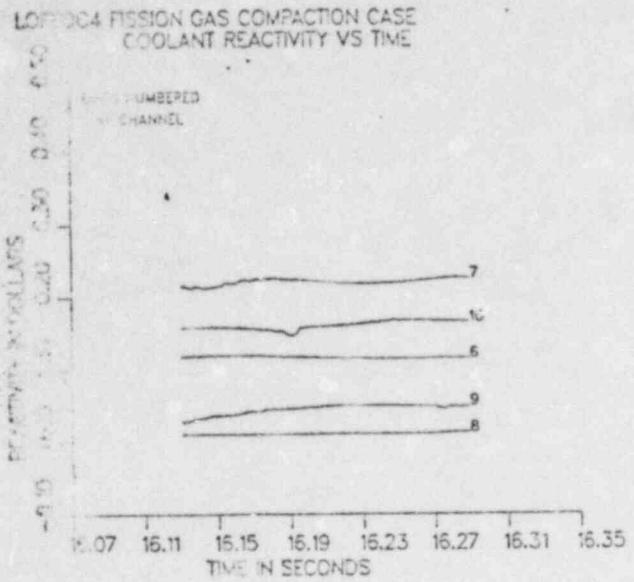

Fig 5

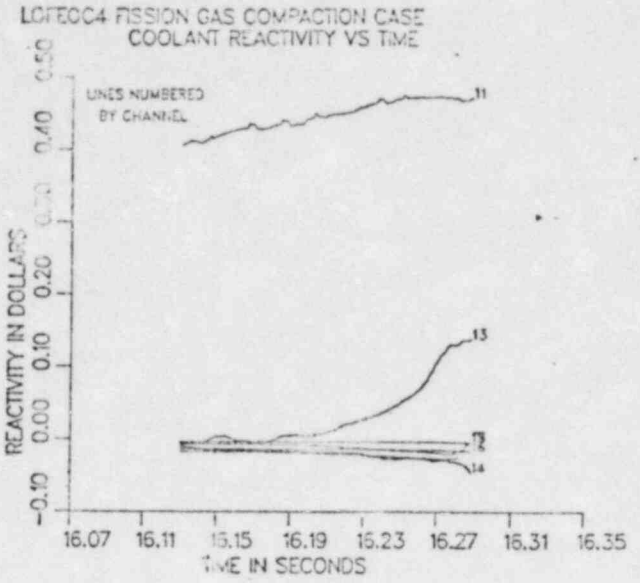

Fig 6

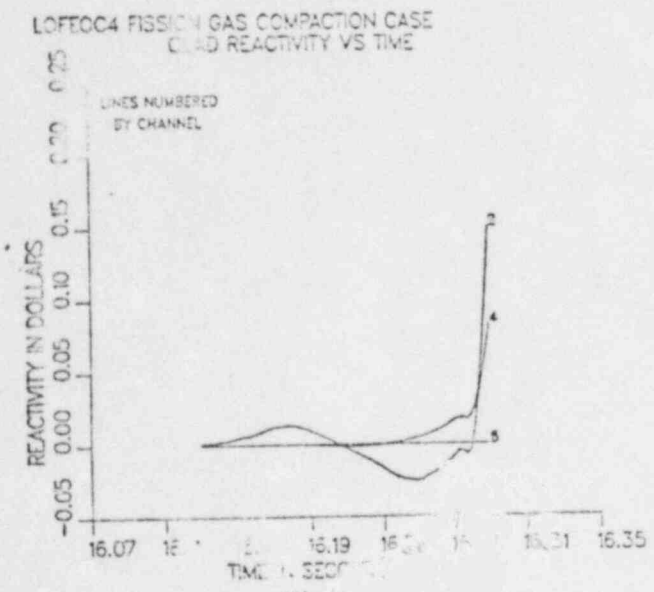

Fig

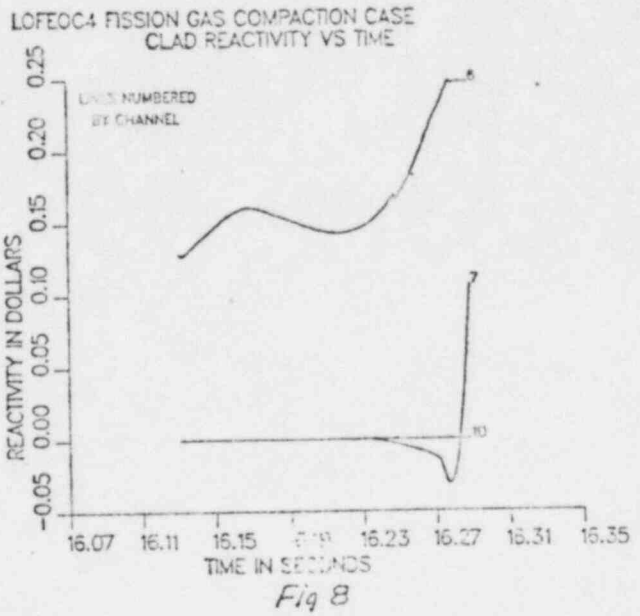

Fig 8

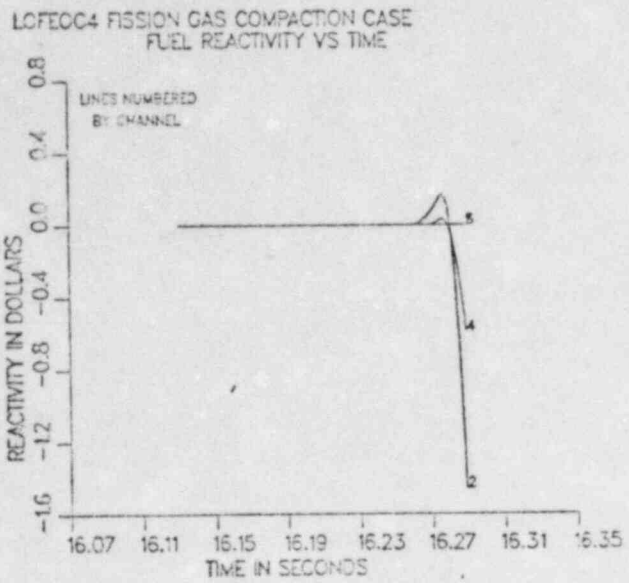

Fig 9

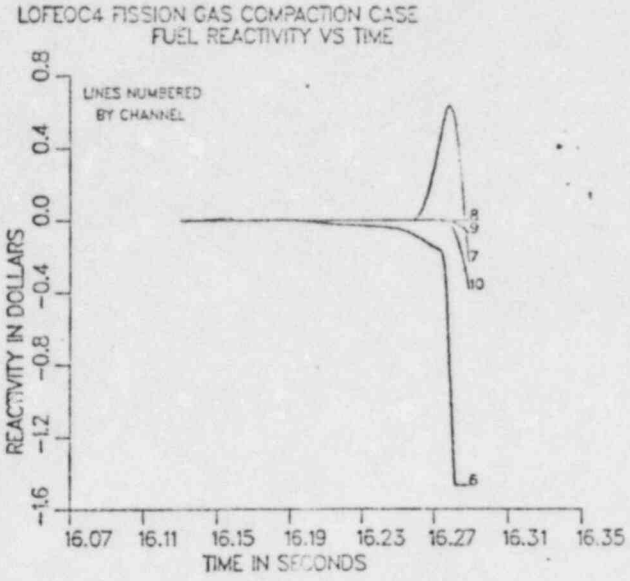

Fig 10

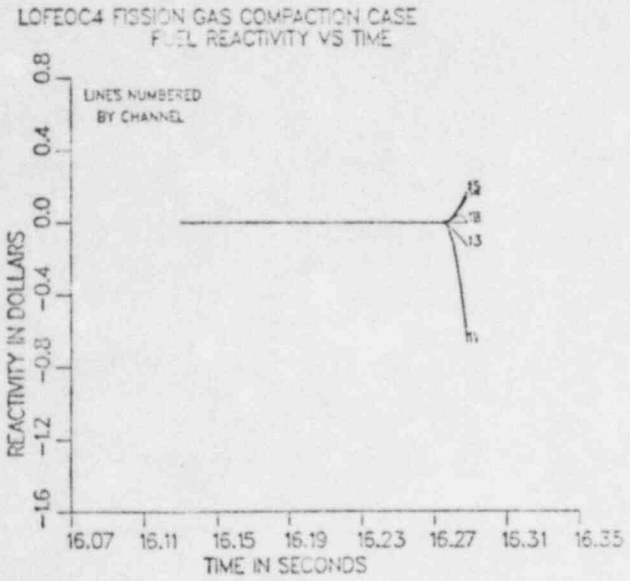

Fig 11

MODS. REF CASE FOR THE HETEROGENEOUS CORE AT EOC - 4
SUBASSEMBLIES FOR CHANNEL 6

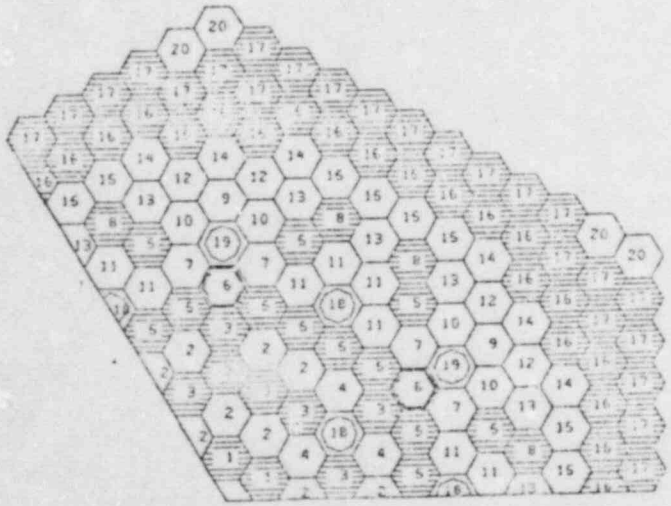

Fig 12

FISSION GAS COMPACTION CASE FOR THE HETEROGENEOUS CORE
CYCLE NUMBER 1164 TIME 16 289
VOLUMN FRACTIONS FOR SAS CHANNEL 6

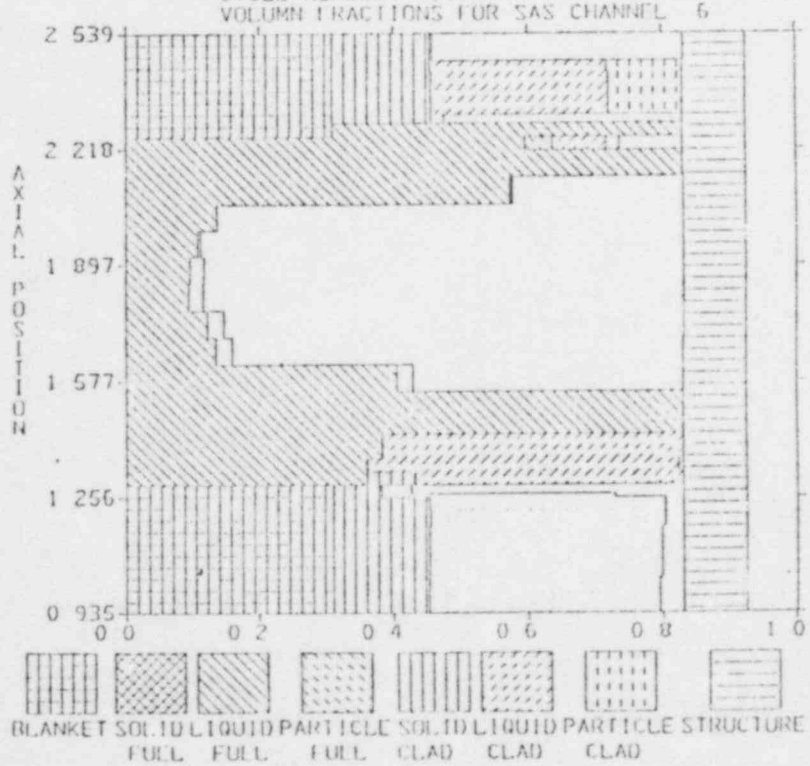

Fig 13

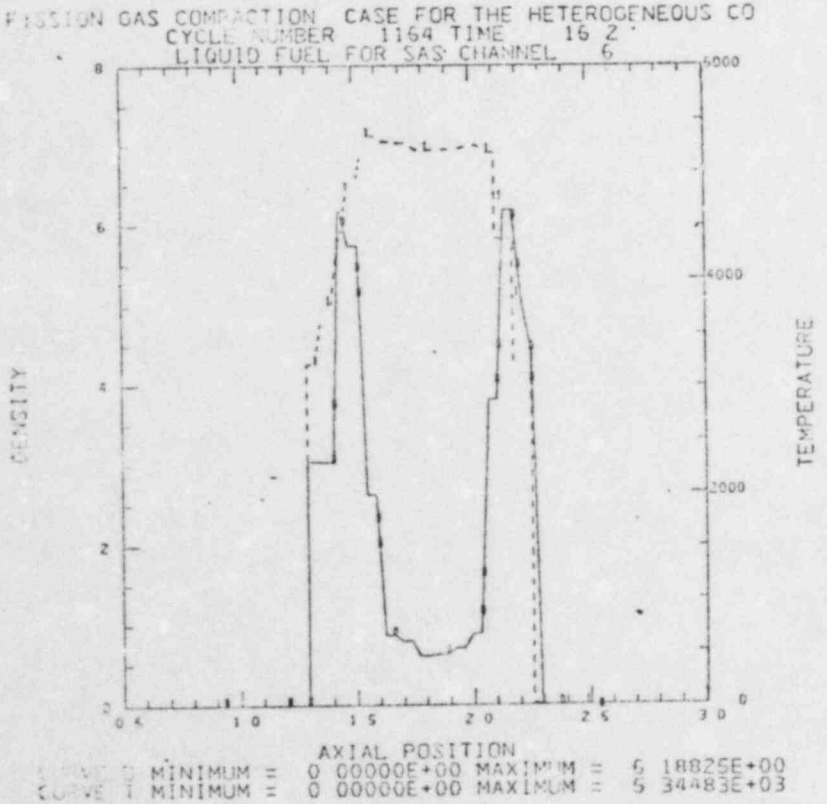
FISSION GAS COMPACTION CASE FOR THE HETEROGENEOUS CO
CYCLE NUMBER 1164 TIME 16 2
LIQUID FUEL FOR SAS CHANNEL 6
DENSITY
TEMPERATURE
AXIAL POSITION
CURVE D MINIMUM = 0 00000E+00 MAXIMUM = 6 18825E+00
CURVE T MINIMUM = 0 00000E+00 MAXIMUM = 5 34483E+03

Fig 14

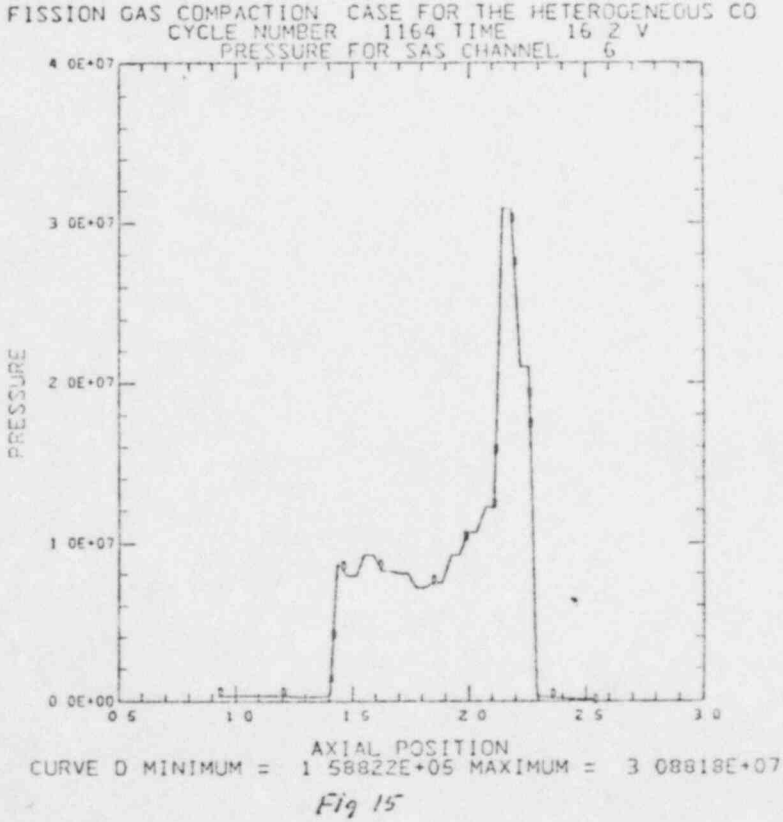
FISSION GAS COMPACTION CASE FOR THE HETEROGENEOUS CO
CYCLE NUMBER 1164 TIME 16 2 V
PRESSURE FOR SAS CHANNEL 6
PRESSURE
AXIAL POSITION
CURVE D MINIMUM = 1 58822E+05 MAXIMUM = 3 08818E+07

Fig 15

MOD6. REF CASE FOR THE HETEROGENEOUS CORE AT EOC - 4
SUBASSEMBLIES FOR CHANNEL 10

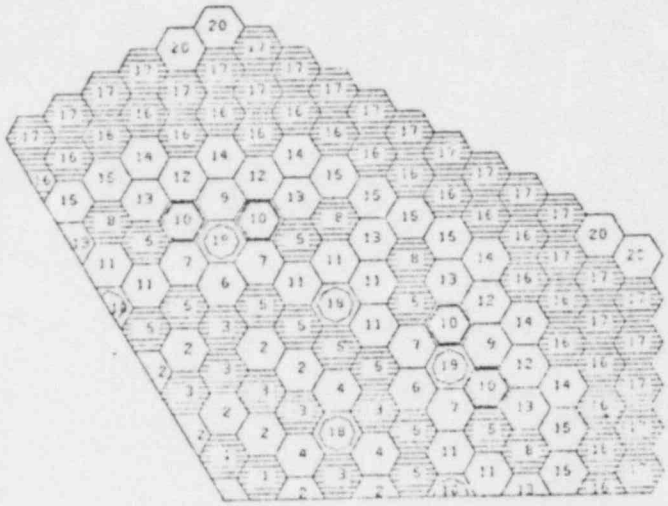

Fig 16

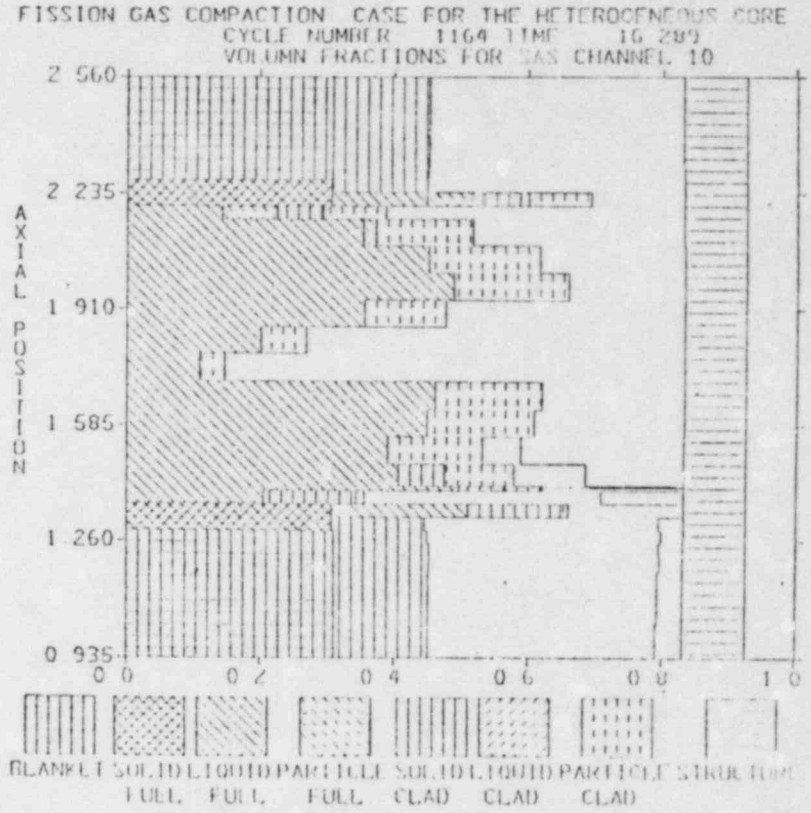

Fig 17

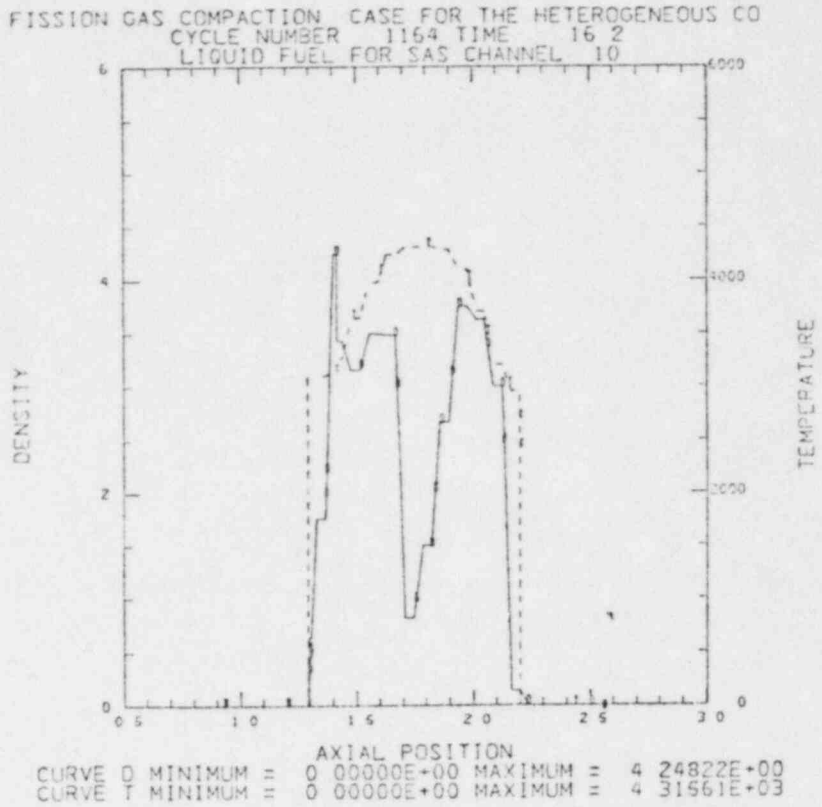

CURVE D MINIMUM = 0 00000E+00 MAXIMUM = 4 24822E+00
CURVE T MINIMUM = 0 00000E+00 MAXIMUM = 4 31561E+03

Fig 18

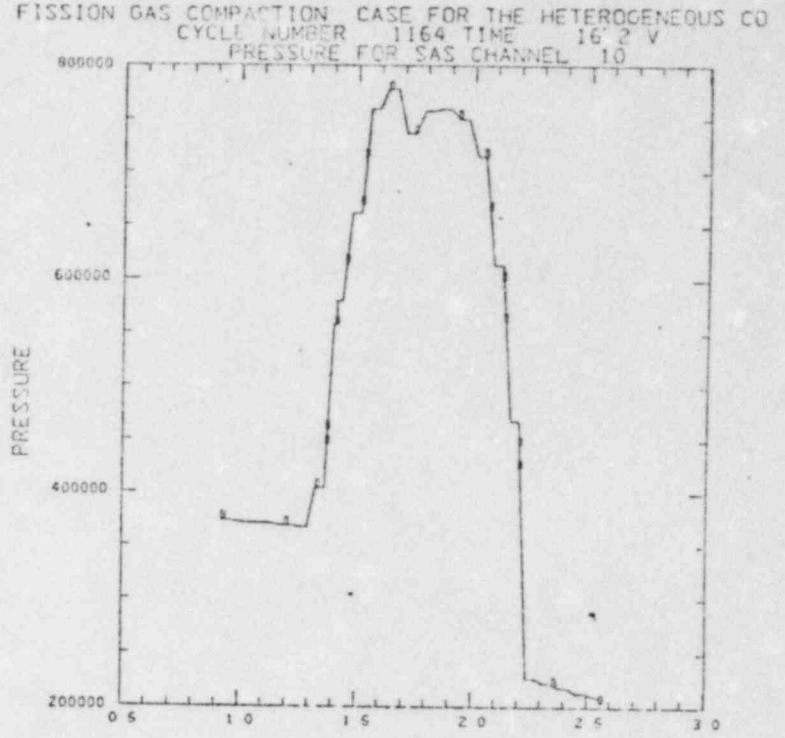

CURVE D MINIMUM = 2 09199E+05 MAXIMUM = 7 78556E+05

Fig 19

X006. REF CASE FOR THE HETEROGENEOUS CORE AT EOC - 4
SUBASSEMBLIES FOR CHANNEL 12

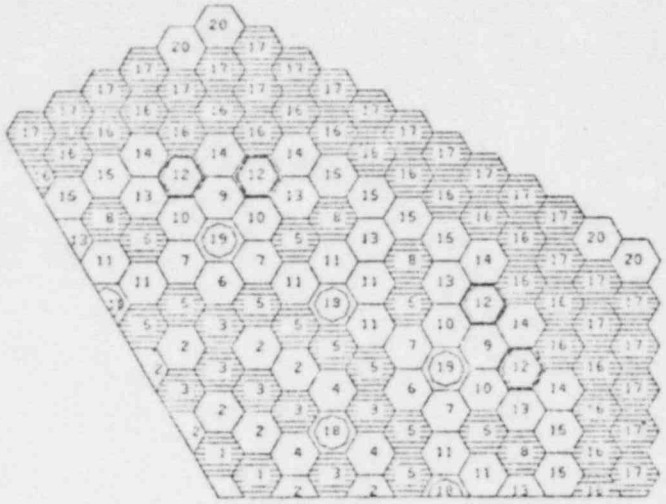

Fig 20

FISSION GAS COMPACTION CASE FOR THE HETEROGENEOUS CORE
CYCLE NUMBER 1164 TIME 16 289
VOLUMN FRACTIONS FOR SAS CHANNEL 12

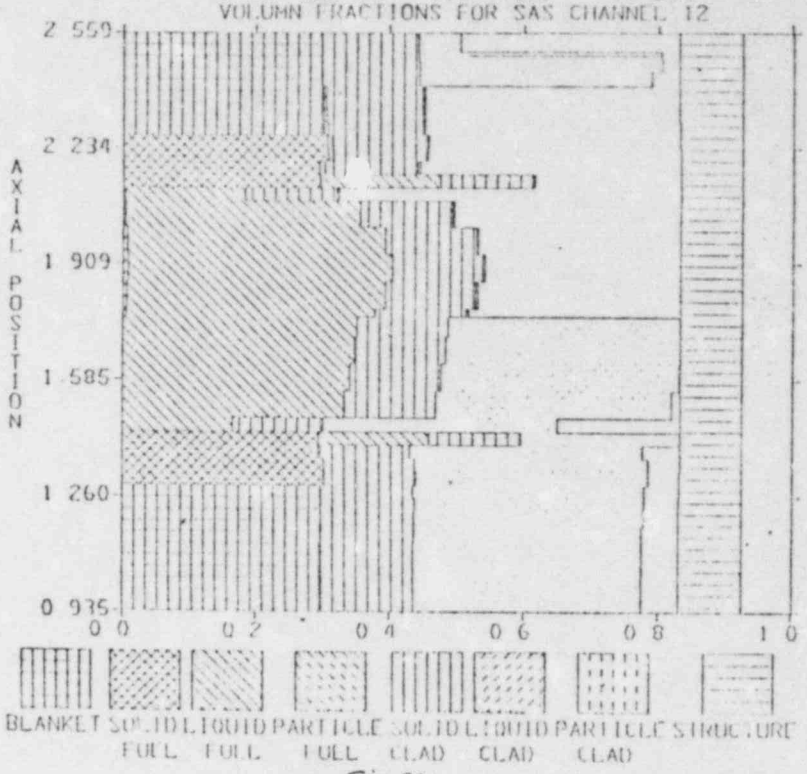

Fig 21

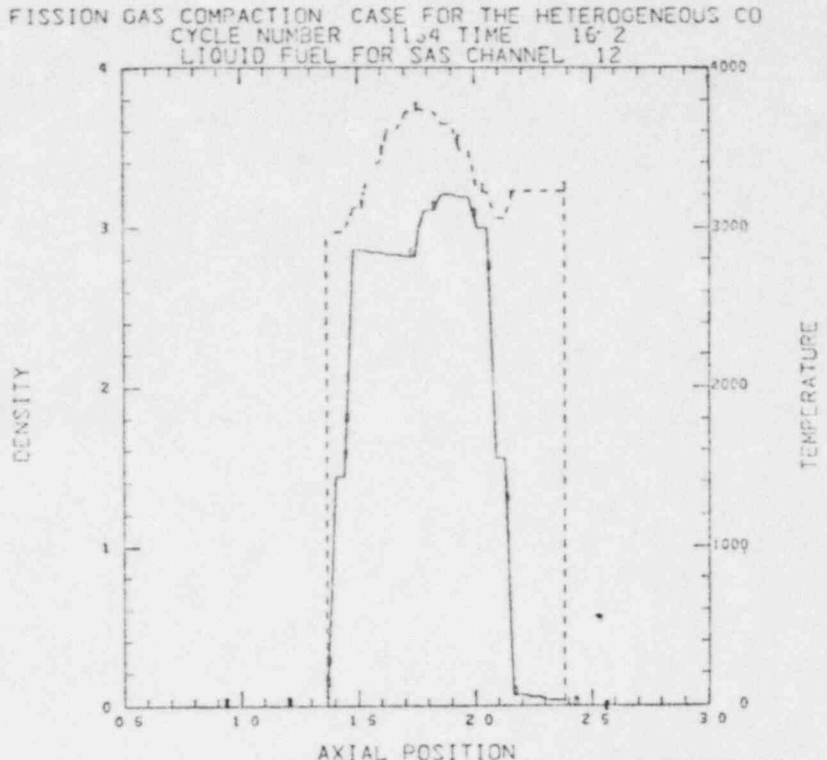

Fig 22

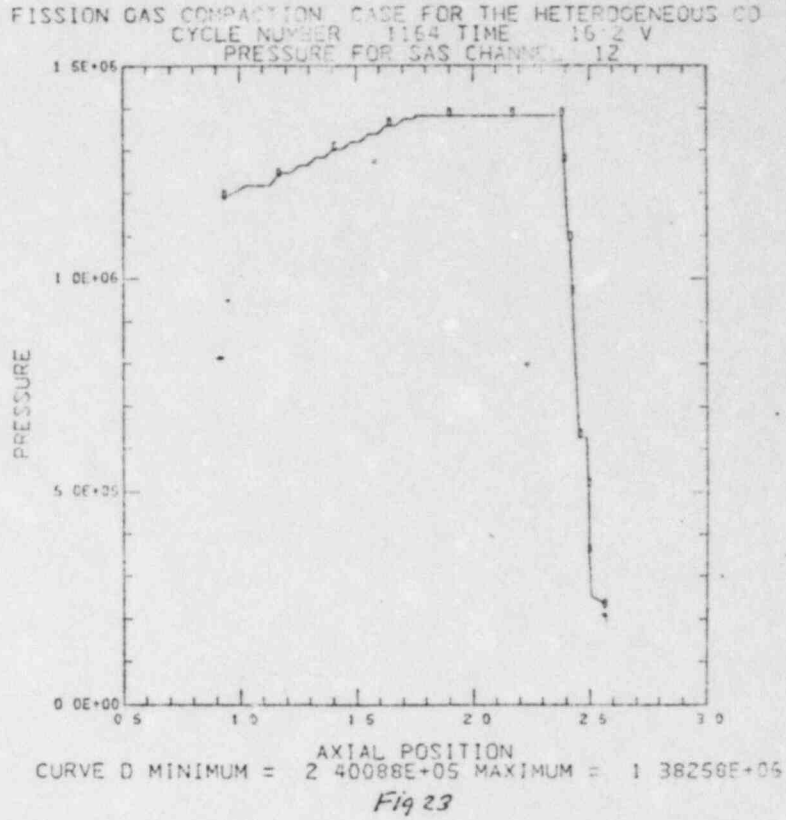

Fig 23

A II.4

MOD6. REF CASE FOR THE HETEROGENEOUS CORE AT EOC - 4
SUBASSEMBLIES FOR CHANNEL 14

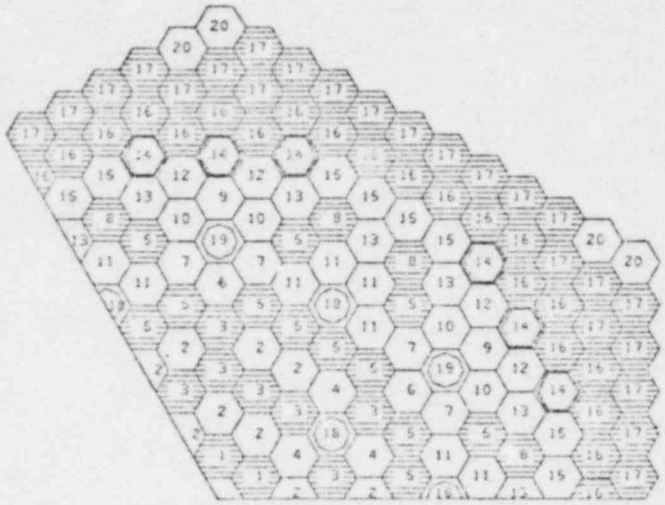

Fig 24

FISSION GAS COMPACTION CASE FOR THE HETEROGENEOUS CORE
CYCLE NUMBER 1164 TIME (4 280)
VOLUMN FRACTIONS FOR SAS CHANNEL 14

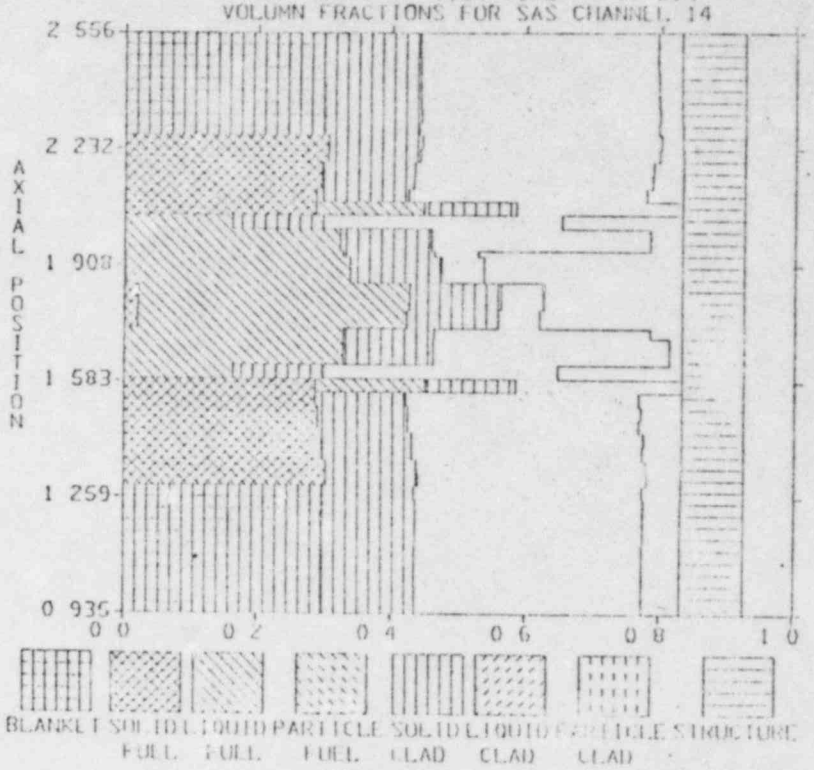

Fig 25

MOD6. REF CASE FOR THE HETEROGENEOUS CORE AT EOC - 4
SUBASSEMBLIES FOR CHANNEL 15

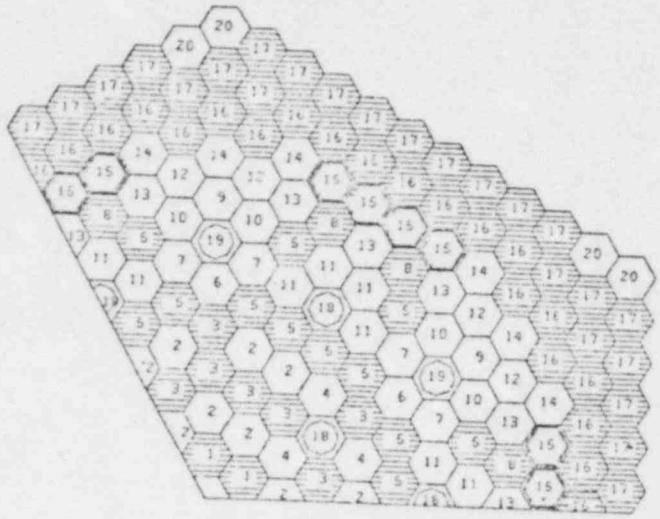

Fig 26

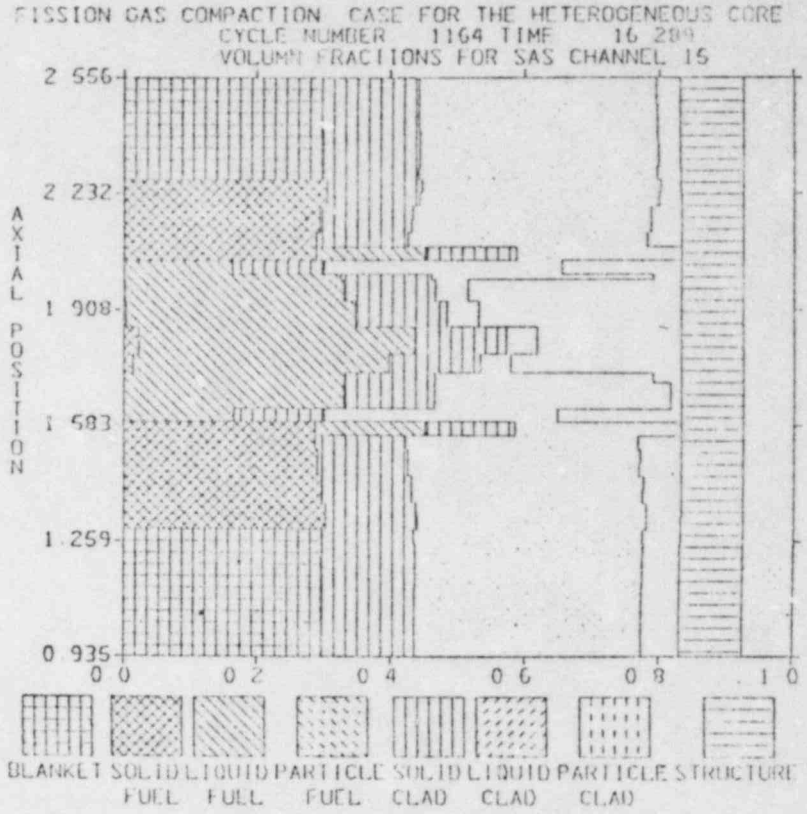

Fig 27

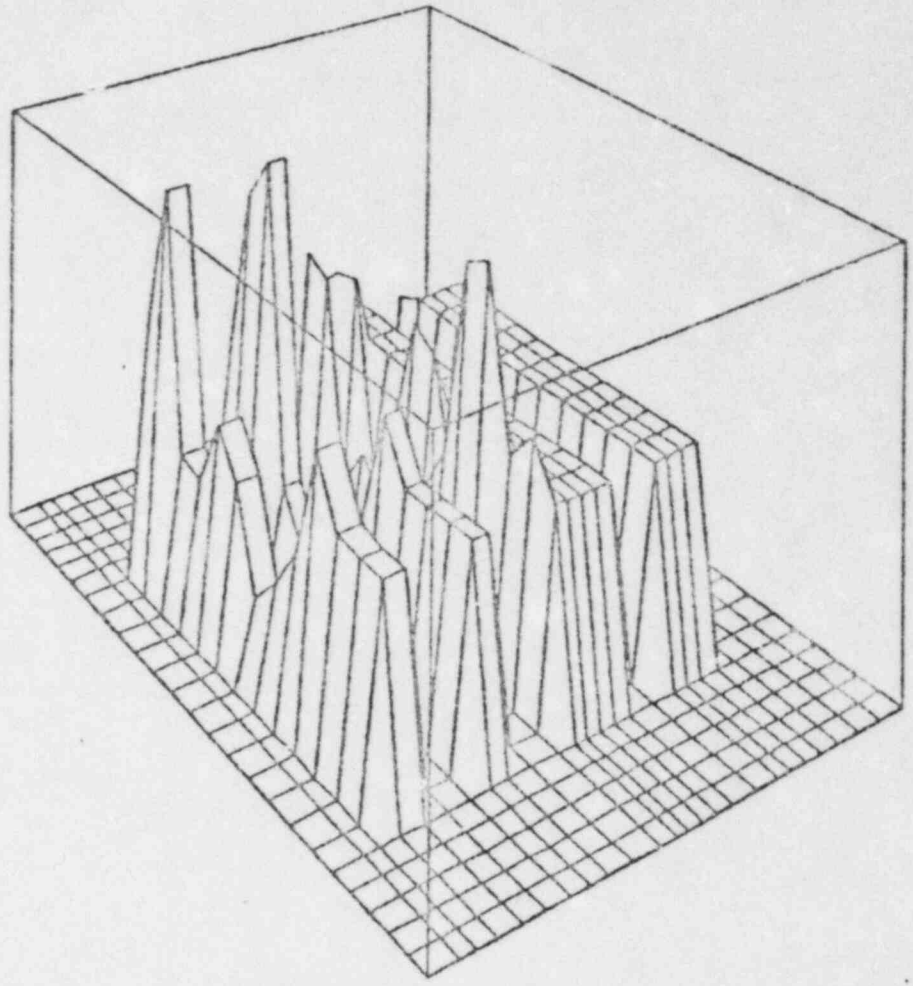

DENSITY OF FISSILE FUEL
MINIMUM VALUE = 0.
MAXIMUM VALUE = 6.5748E+03 TIME = 0.000 MS

Fig 1

II.5

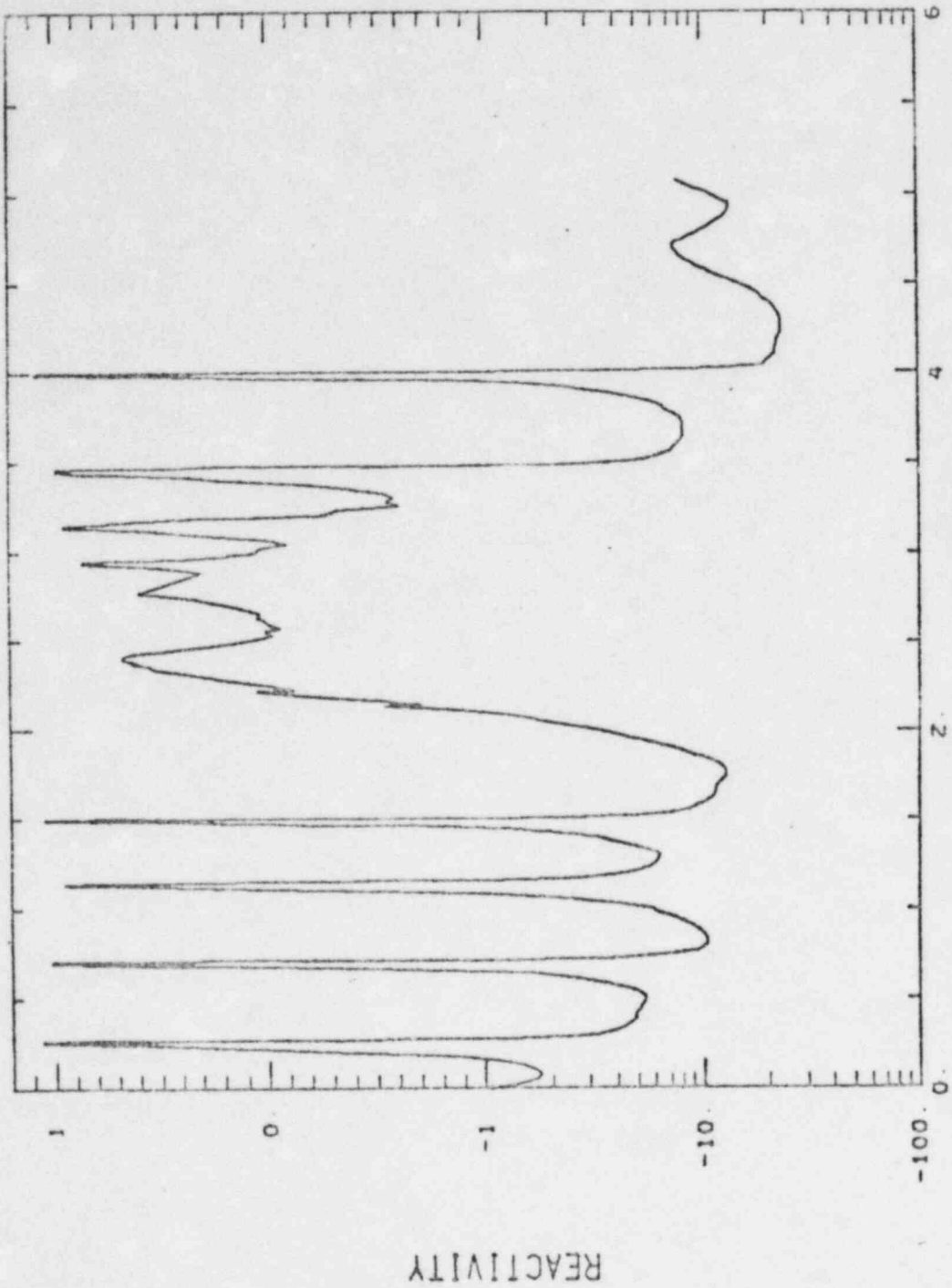
REACTIVITY
1
0
-1
-10
-100
0
2
4
6
TIME(S)
MINIMUM VALUE= -2.27864E+01
MAXIMUM VALUE= 1.08363E+00

Fig 2

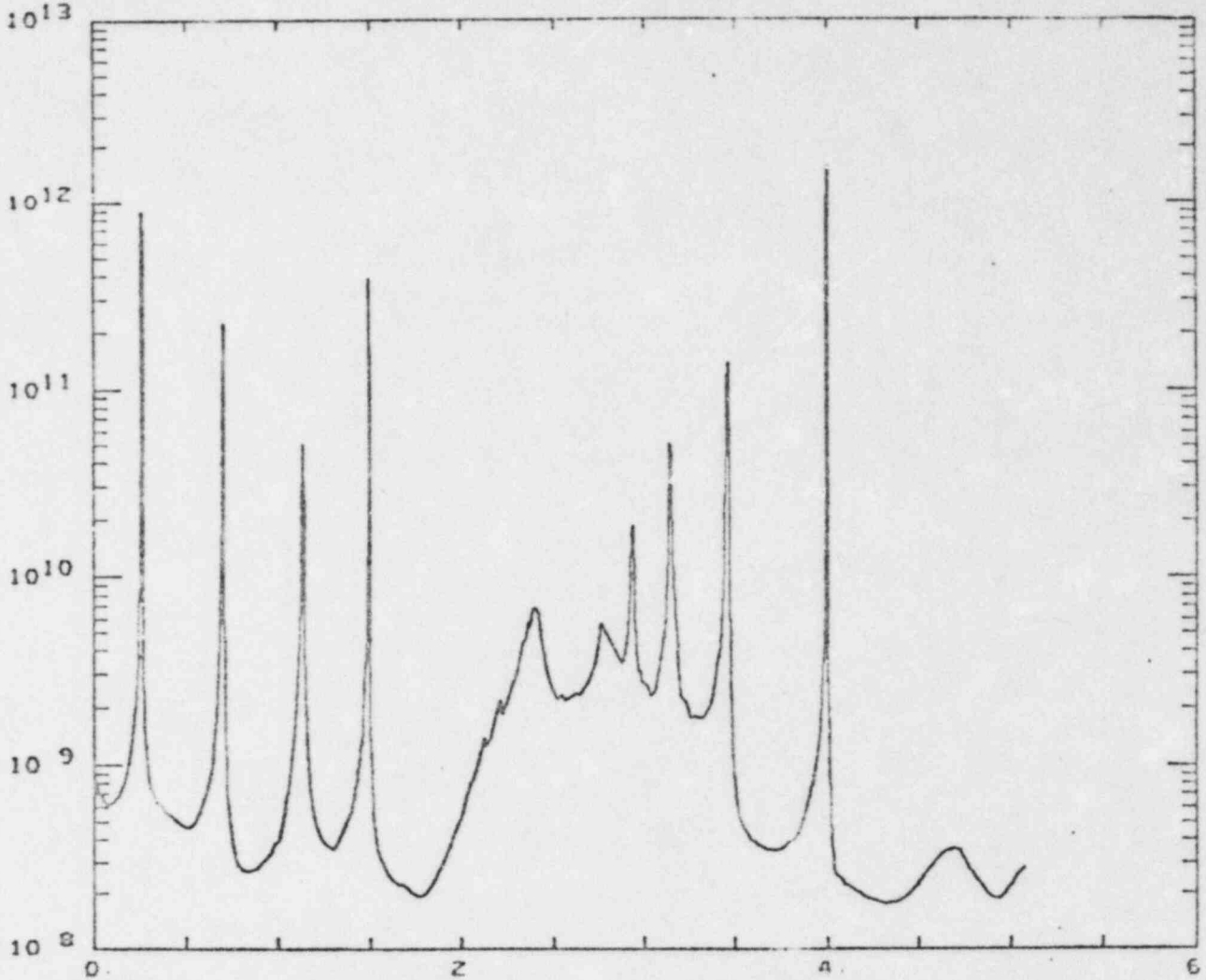

MINIMUM VALUE= 1.80417E+08
MAXIMUM VALUE= 1.52604E+12

Fig 3

II.5

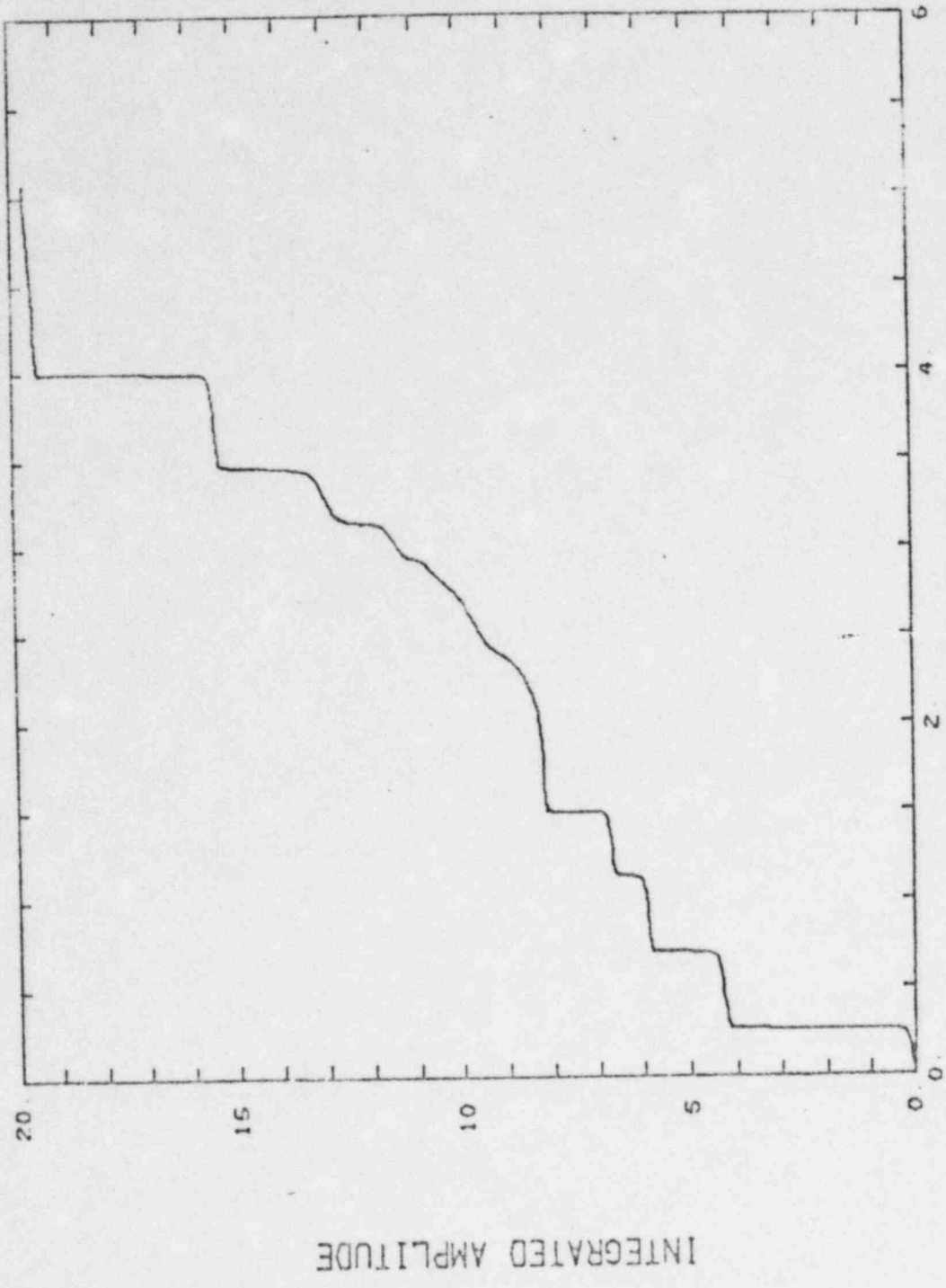
INTEGRATED AMPLITUDE
20
15
10
5
0
0
2
4
6
TIME (S)
MINIMUM VALUE= 9.22988E-04
MAXIMUM VALUE= 1.97200E+01

Fig 4

REGIONS/GROUP - 5
HR IL IU JL JU
1 1 25 7 10

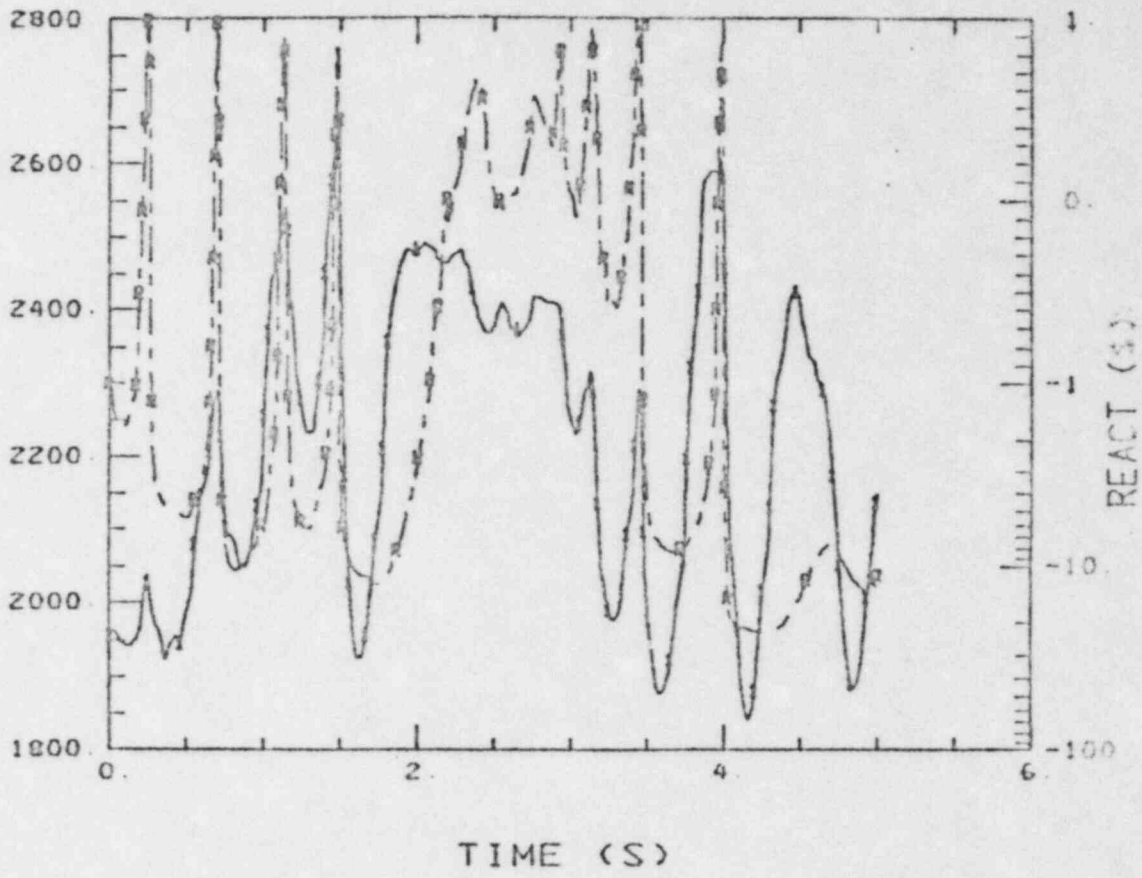

REGION SUMS/GROUP- 5
DENSITY OF FISSILE FUEL
MINIMUM VALUE = 1.84E+03 MAXIMUM VALUE = 2.64E+03

Fig 5

II.5

REGIONS/GROUP - 4

NR	IL	IU	JL	JU
1	1	3	7	19
2	6	7	7	19
3	10	11	7	19
4	17	17	7	19
5	22	25	7	19

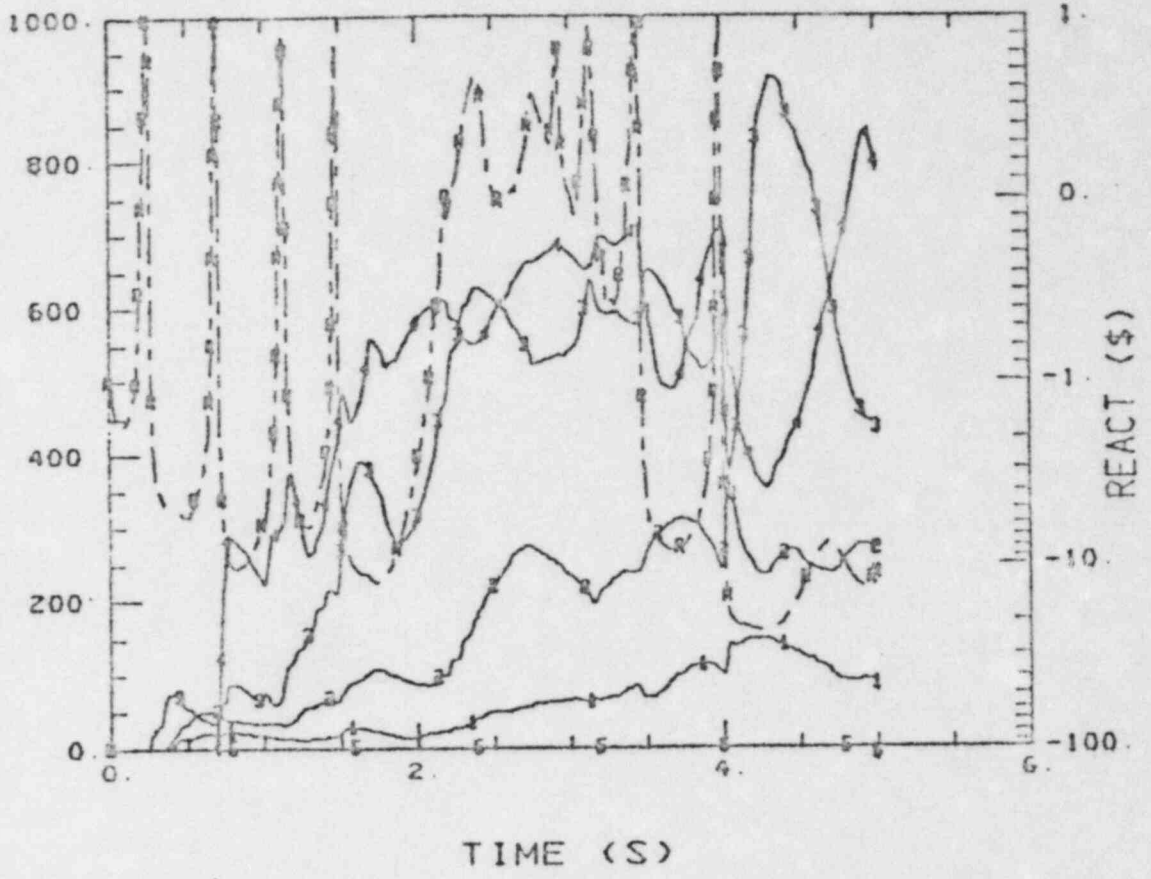

REGION SUMS/GROUP- 4
DENSITY OF FISSILE FUEL
MINIMUM VALUE = 0. MAXIMUM VALUE = 9.14E+02

Fig 6

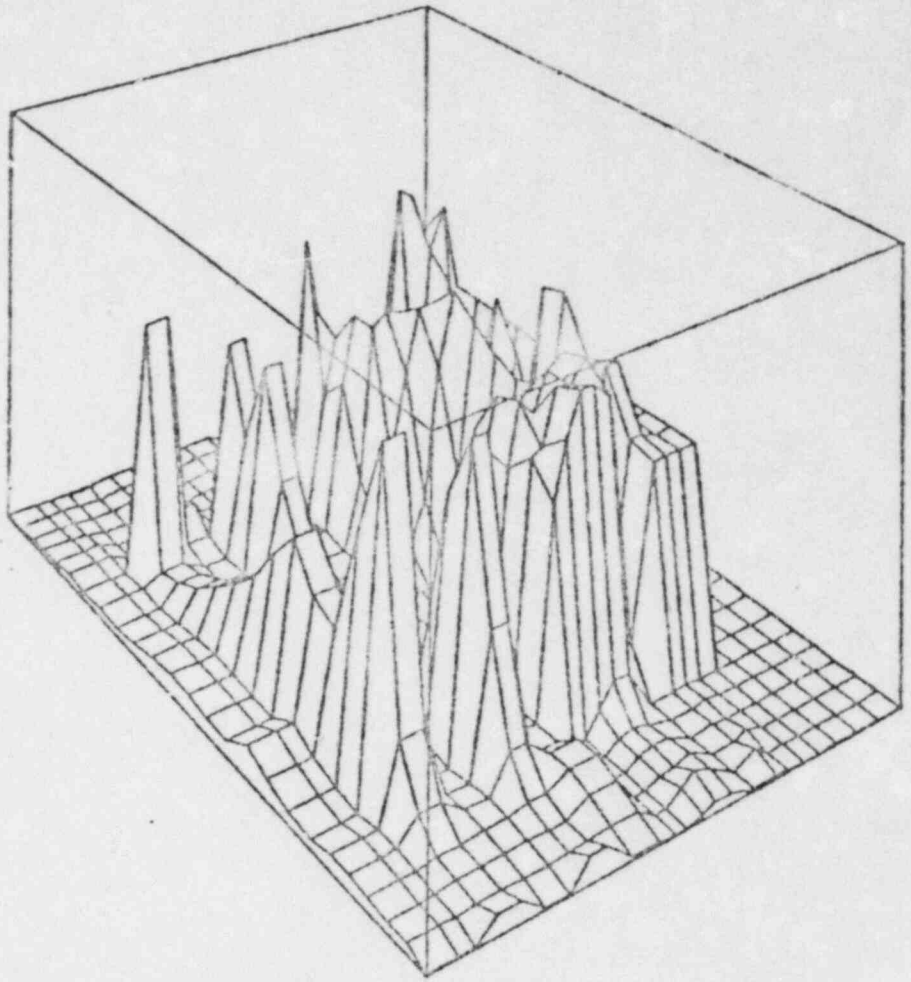

DENSITY OF FISSILE FUEL
MINIMUM VALUE = 0.
MAXIMUM VALUE = 6.5748E+03 TIME = 1000.000 MS

Fig 7

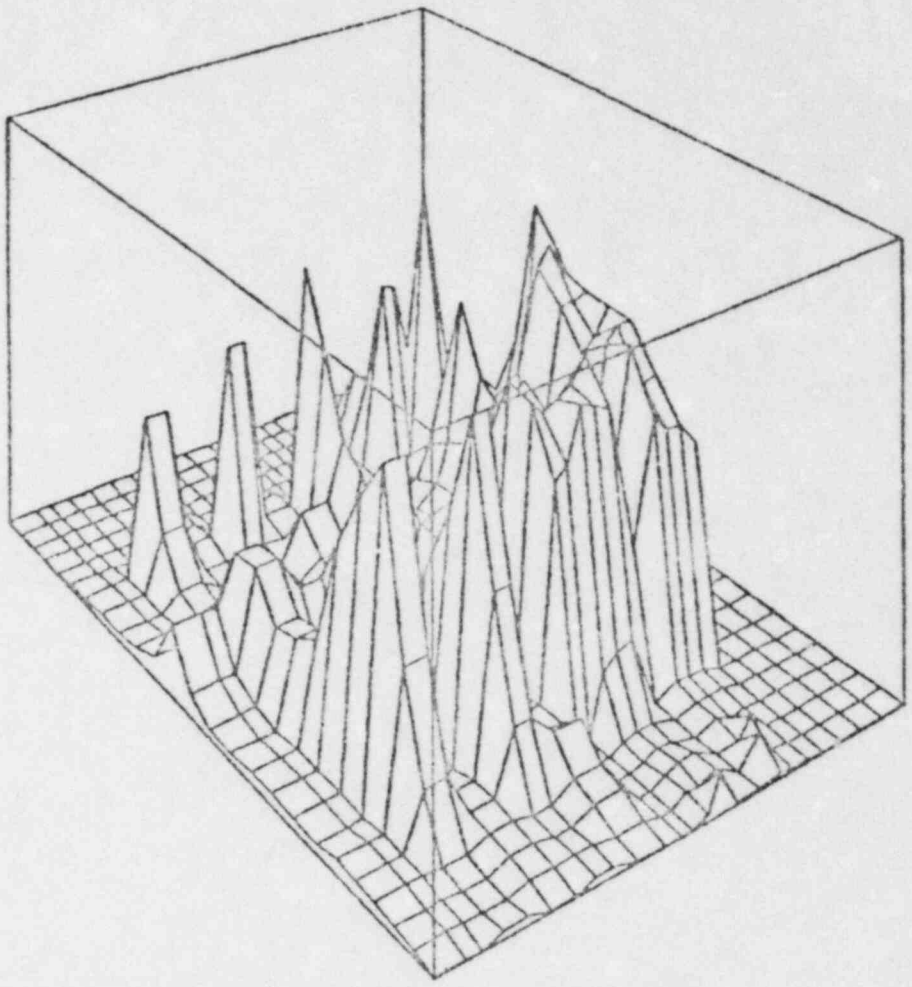

DENSITY OF FISSILE FUEL
MINIMUM VALUE = 0.
MAXIMUM VALUE = 6.5748E+03 TIME = 1500.000 MS

Fig 8.

REGIONS/GROUP - 1

KR	IL	IU	JL	JU
1	4	5	7	10
2	8	9	7	10
3	12	16	7	10
4	18	21	7	10

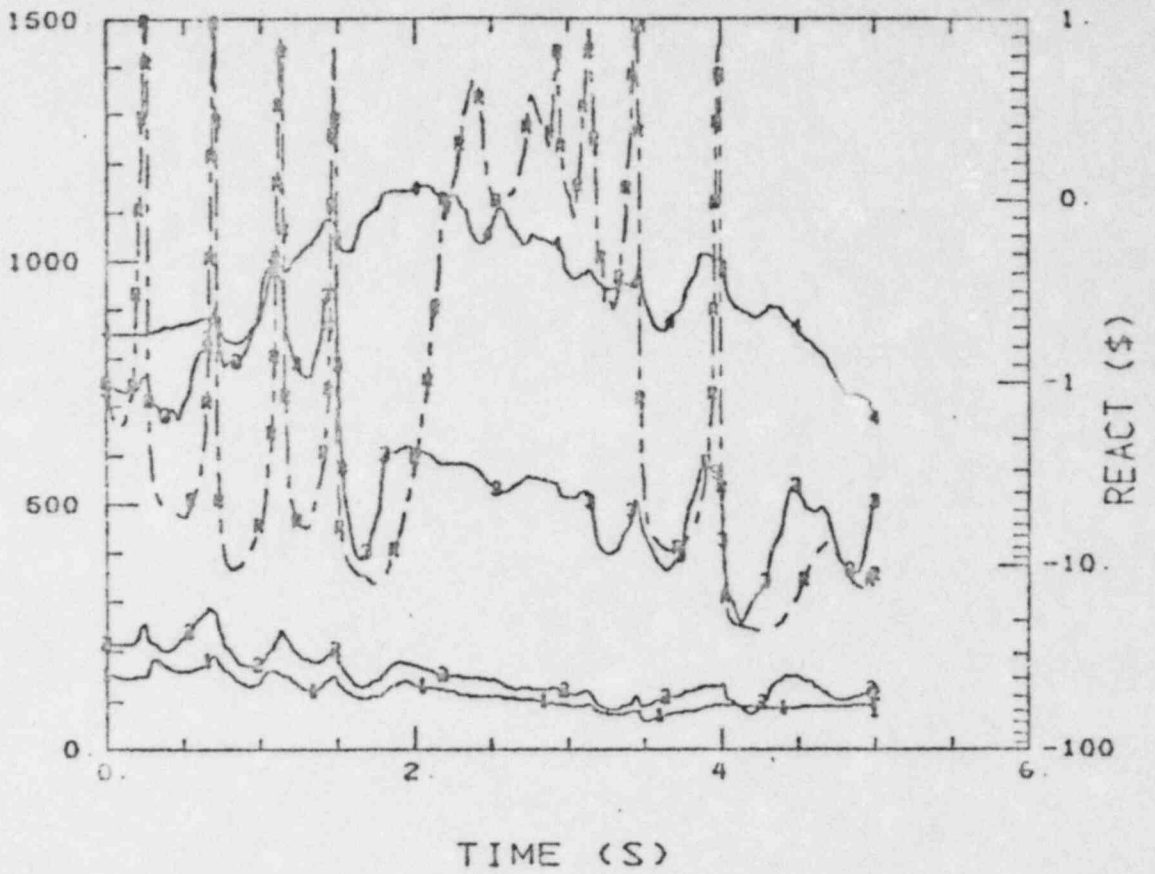

REGION SUMS/GROUP- 1
DENSITY OF FISSILE FUEL
MINIMUM VALUE = 6.36E+01 MAXIMUM VALUE = 1.16E+03

Fig. 9

REGIONS/GROUP - 1

KR	IL	IU	JL	JU
1	4	5	7	19
2	8	9	7	19
3	12	16	7	19
4	18	21	7	19

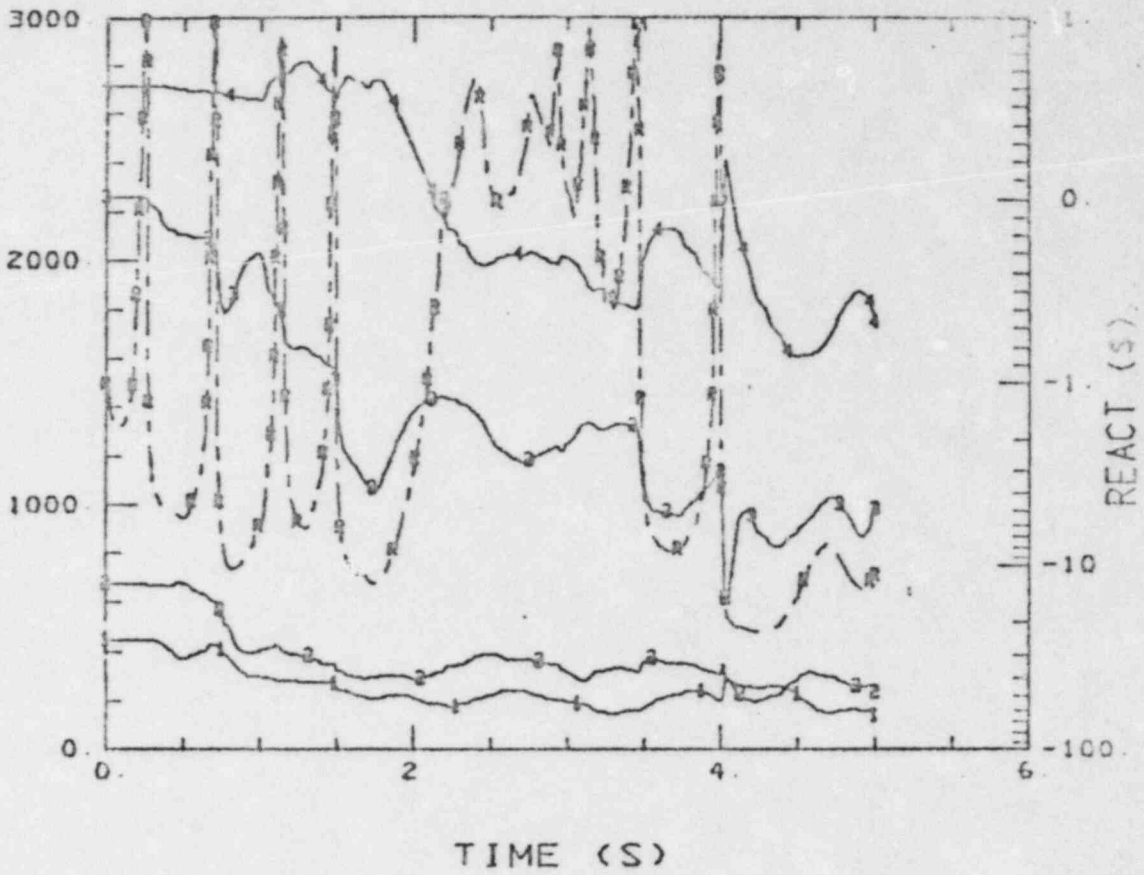

REGION SUMS/GROUP- 1
DENSITY OF FISSILE FUEL
MINIMUM VALUE = 1.53E+02 MAXIMUM VALUE = 2.82E+03

Fig 10

REGIONS/GROUP - 1

NR	IL	IU	JL	JU
1	1	3	7	19
2	6	7	7	19
3	10	11	7	19
4	17	17	7	19

1 = IB1

2 = IB2

3 = IB3

4 = IB4

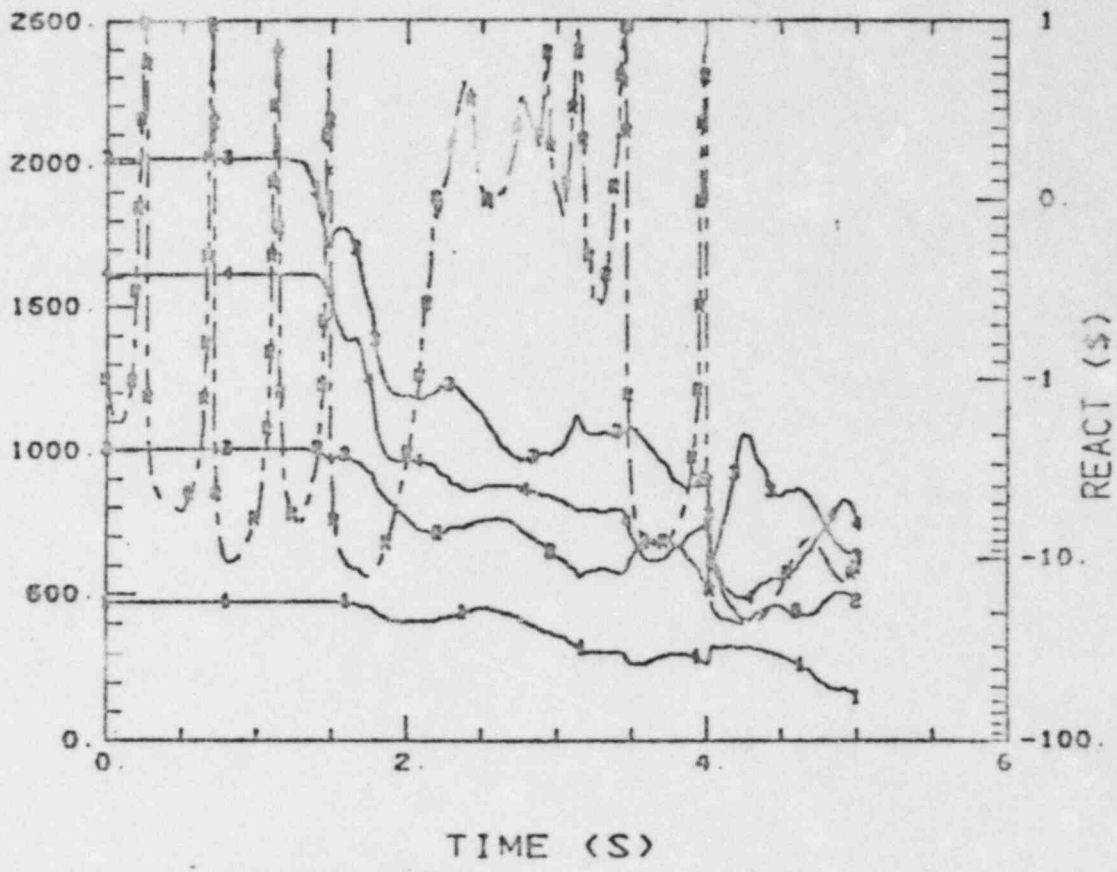

REGION SUMS/GROUP- 1 MASS
DENSITY OF FERTILE FUEL
MINIMUM VALUE = 1.73E+02 MAXIMUM VALUE = 2.02E+03

Fig 11

T.S.

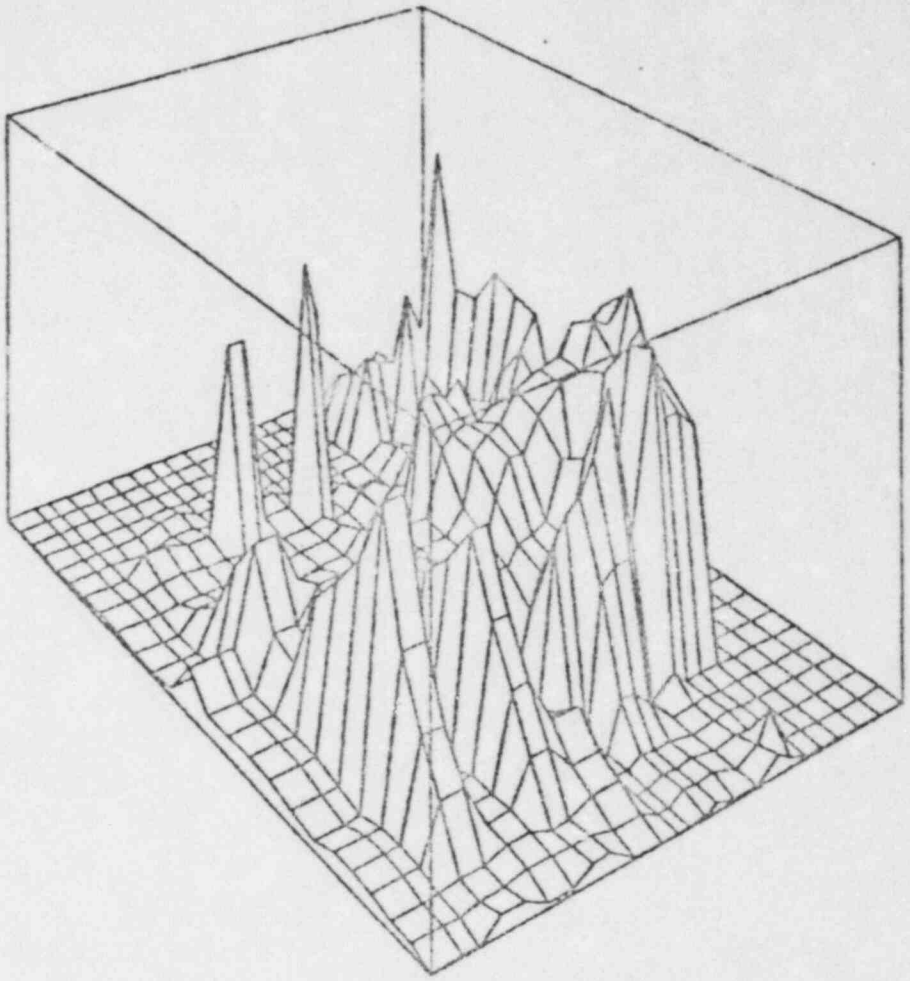

DENSITY OF FISSILE FUEL
MINIMUM VALUE = 0.
MAXIMUM VALUE = 6.5748E+03 TIME = 2000 000 MS

Fig 12

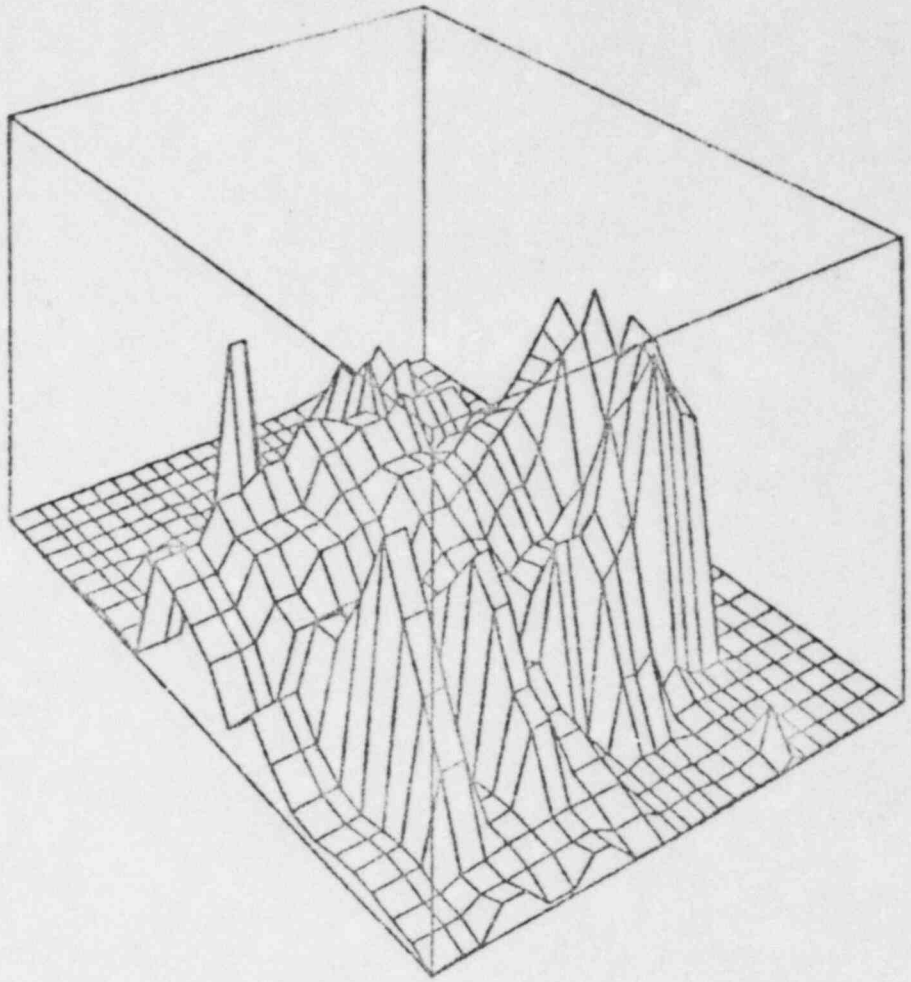

DENSITY OF FISSILE FUEL
MINIMUM VALUE = 0.
MAXIMUM VALUE = 6.5748E+03 TIME = 2500.000 MS

Fig 13

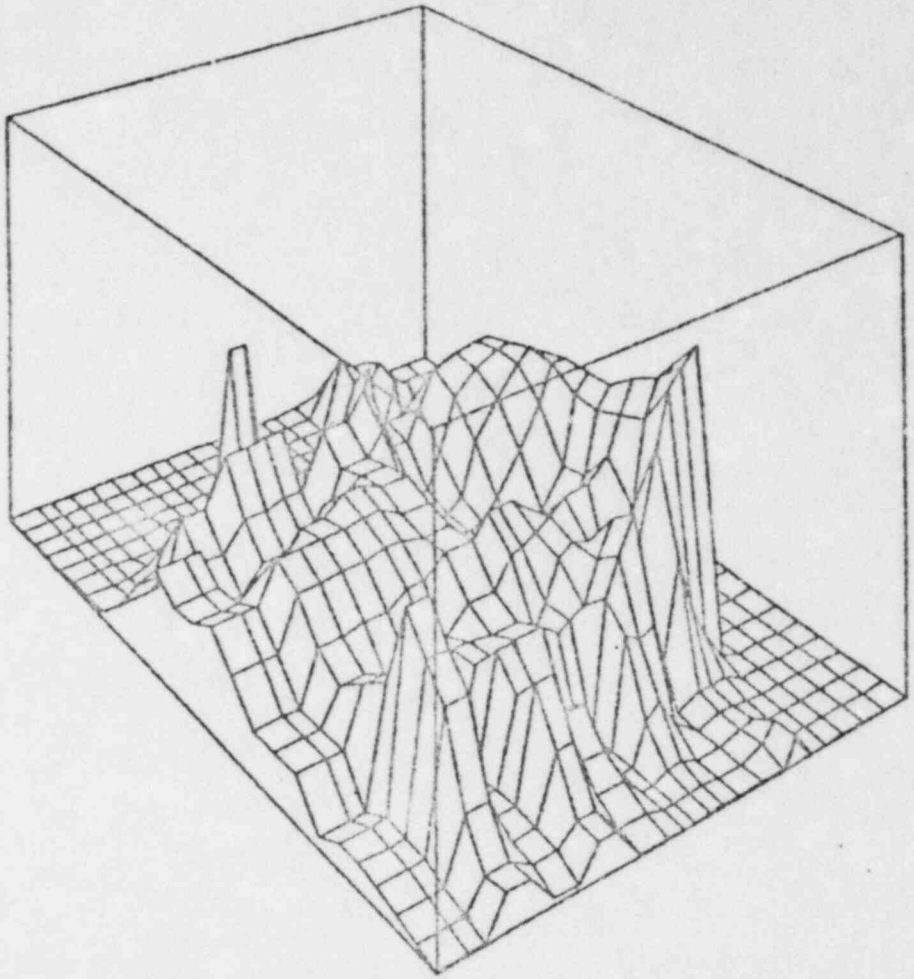

DENSITY OF FISSILE FUEL
MINIMUM VALUE = 0
MAXIMUM VALUE = 6.5748E+03 TIME = 3500.000 MS

Fig 14

1 = IB1 + DR1

2 = IB2 + DR2

3 = IB3 + DR3

4 = IB4 + DR4

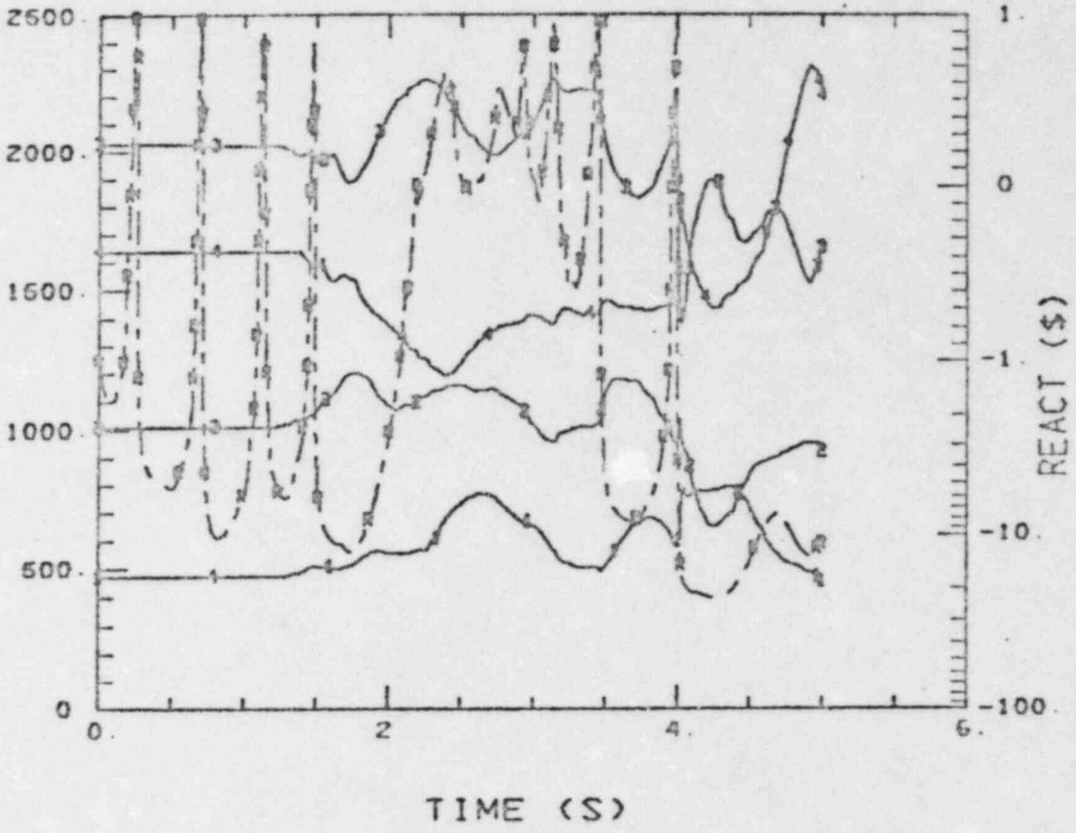

GROUP SUMS MASS
DENSITY OF FERTILE FUEL
MINIMUM VALUE = 4.77E+02 MAXIMUM VALUE = 2 31E+03

Fig 15

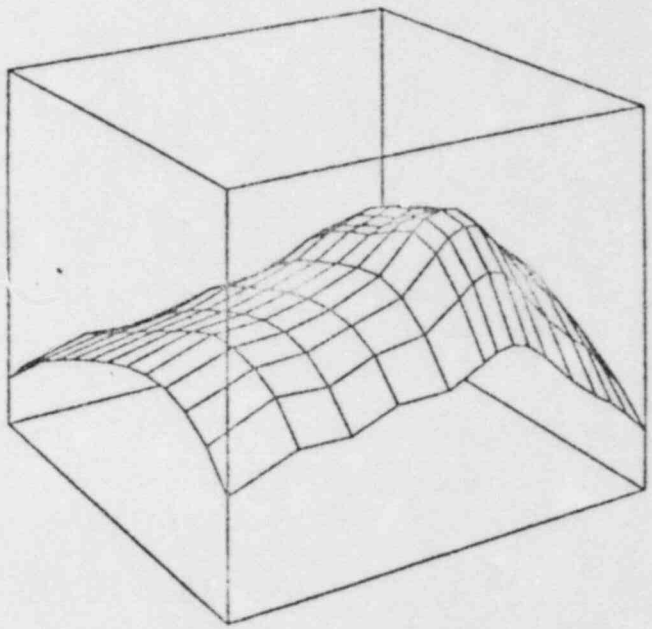

REGIONS IL= 1 IU=16 JL=14 JU=26

FISSILE FUEL INTERNAL ENERGY RATE

MINIMUM VALUE = 4.2717E+04

MAXIMUM VALUE = 2.2816E+05 TIME = 1000 000 MS

Fig 16a

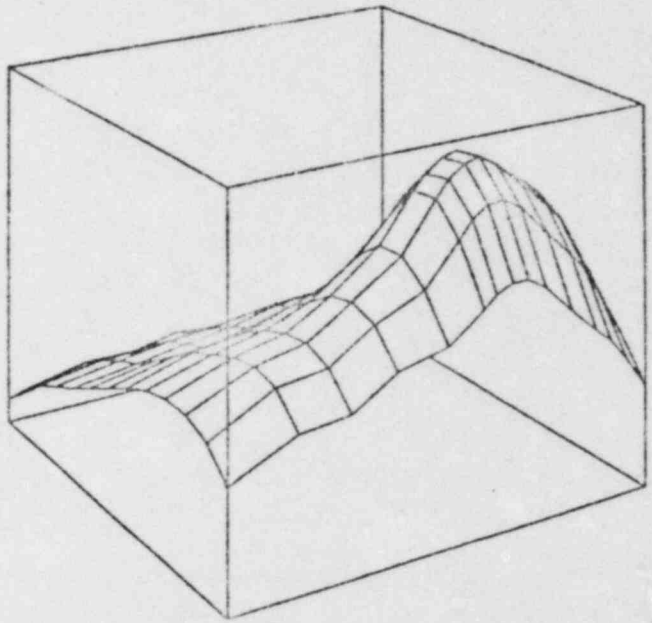

REGIONS IL= 1 IU=15 J =14 JU=26
FISSILE FUEL INTERNAL ENERGY RATE
MINIMUM VALUE = 4 2717E+04
MAXIMUM VALUE = 2 2816E+05 TIME = 1500 000 MS

Fig 16b

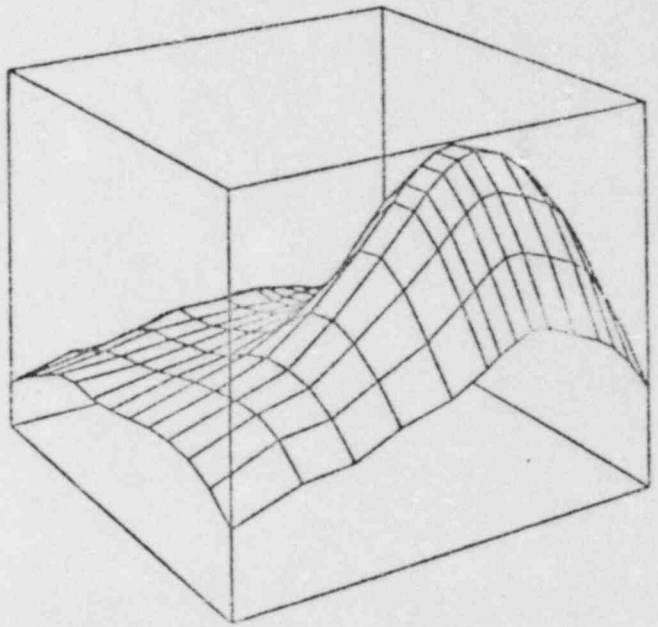

REGIONS IL= 1 IU=16 JL=14 JU=26
FISSILE FUEL INTERNAL ENERGY RATE
MINIMUM VALUE = 4.2717E+04 TIME = 2000.000 MS
MAXIMUM VALUE = 2.2816E+05

Fig 16c

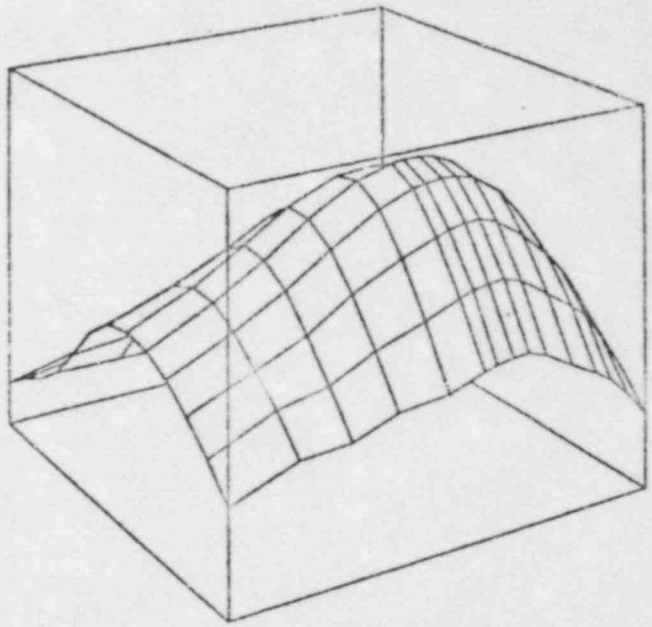

REGIONS IL= 1 IU=15 JL=14 JU=26
FISSILE FUEL INTERNAL ENERGY RATE
MINIMUM VALUE = 4.2717E+04 TIME = 2500.000 MS
MAXIMUM VALUE = 2.2816E+05

Fig 16d

II.5

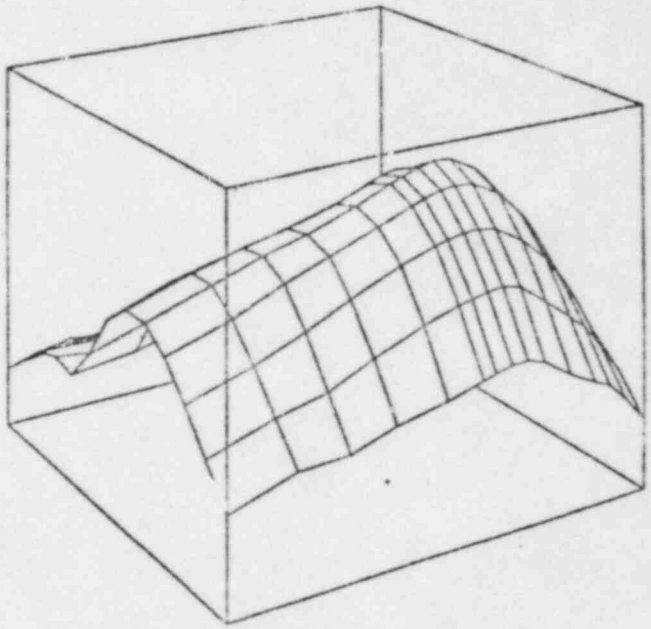

REGIONS ILo 1 IU=18 JL=14 JU=25
FISSILE FUEL INTERNAL ENERGY RATE
MINIMUM VALUE = 4 2717E+04
MAXIMUM VALUE = 2 2816E+05 TIME = 3000.000 MS

Fig 16e

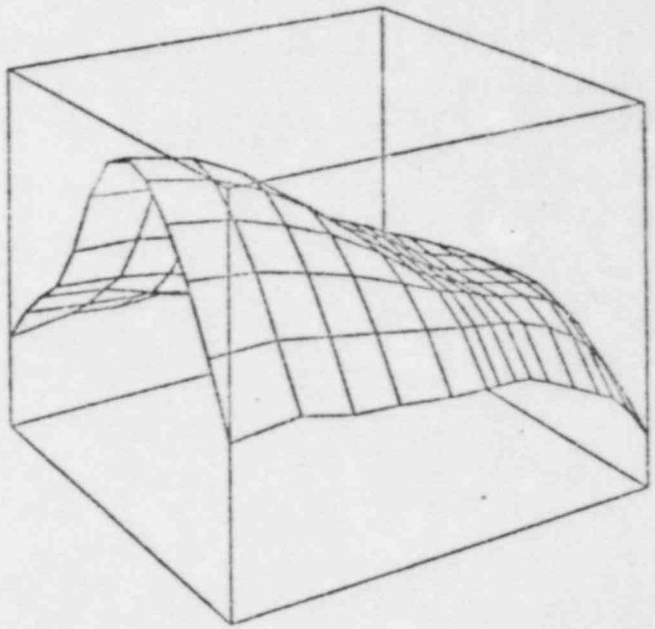

REGIONS IL= 1 IU=15 JL=14 JU=26
FISSILE FUEL INTERNAL ENERGY RATE
MINIMUM VALUE = 4.2717E+04 TIME = 3700.000 MS
MAXIMUM VALUE = 2.2816E+05

Fig 16f

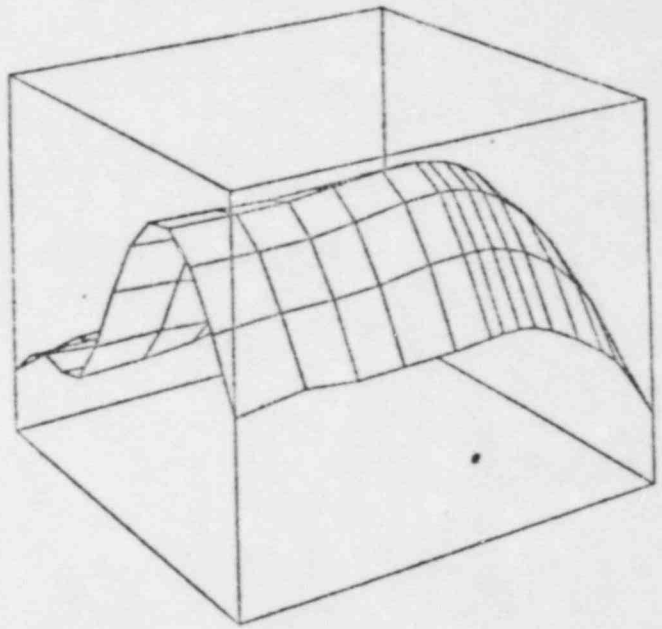

REGION2 IL= 1 IU=16 JL=14 JU=26
FISSILE FUEL INTERNAL ENERGY RATE
MINIMUM VALUE = 4 2717E+04 TIME = 4000 000 MS
MAXIMUM VALUE = 2 2816E+05

Fig 16g

II.5

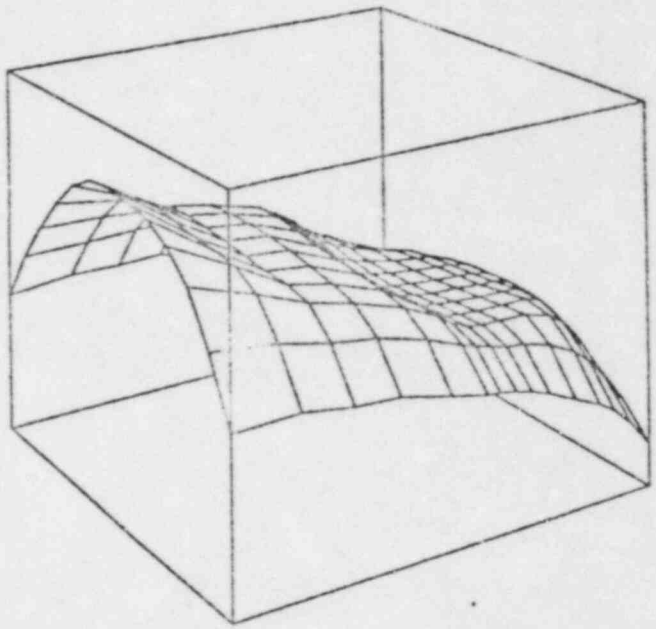

REGIONS JL= 1 JU=15 JL=14 JU=25
FISSILE FUEL INTERNAL ENERGY RATE
MINIMUM VALUE = 4.2712E+04
MAXIMUM VALUE = 2.2816E+05 TIME = 4200.000 MS

Fig 16h

II.5

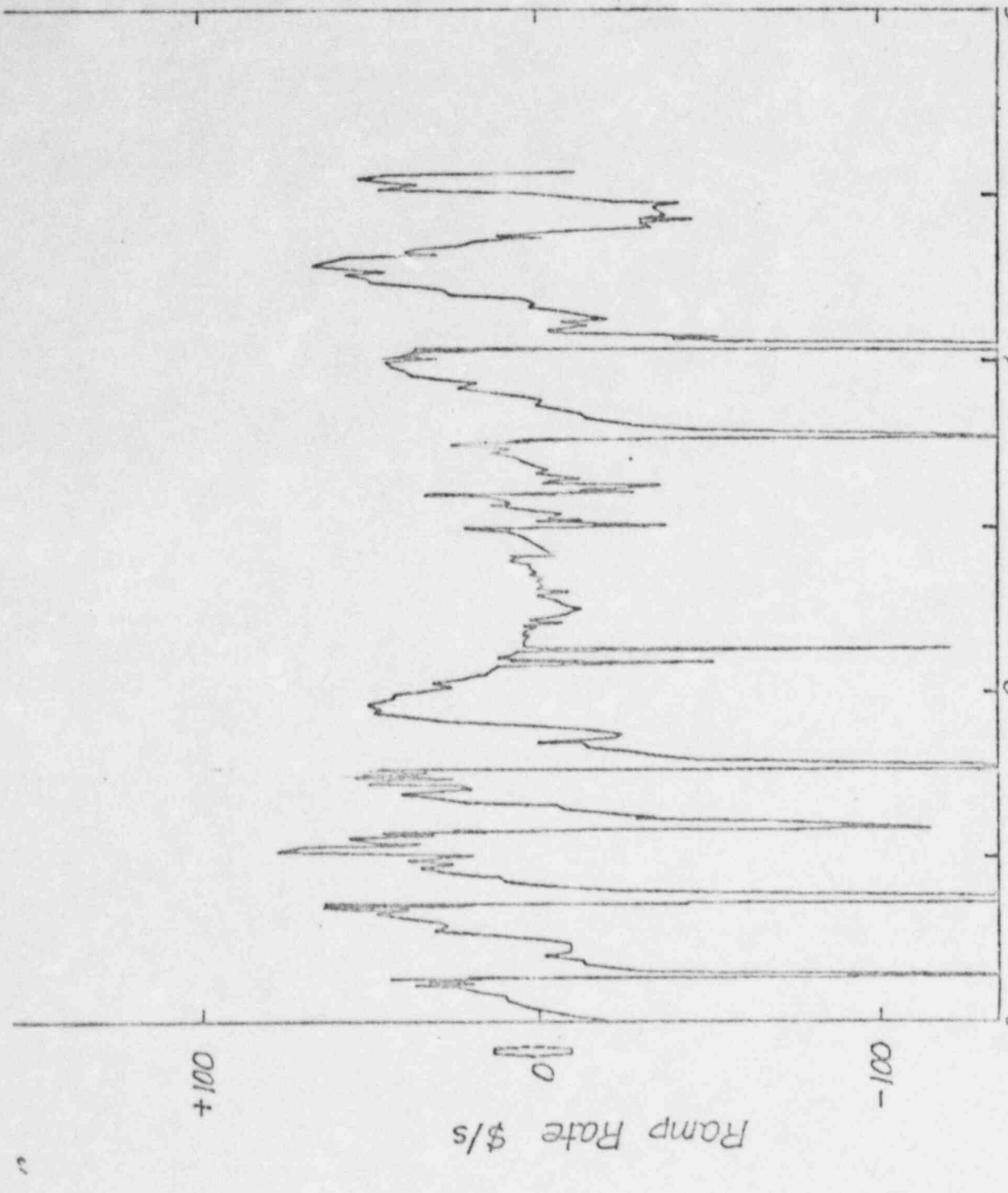

Fig 17

REGIONS/GROUP - 1

KR	IL	IU	JL	JU
1	4	5	16	19
2	8	9	16	19
3	12	16	16	19
4	18	21	16	19

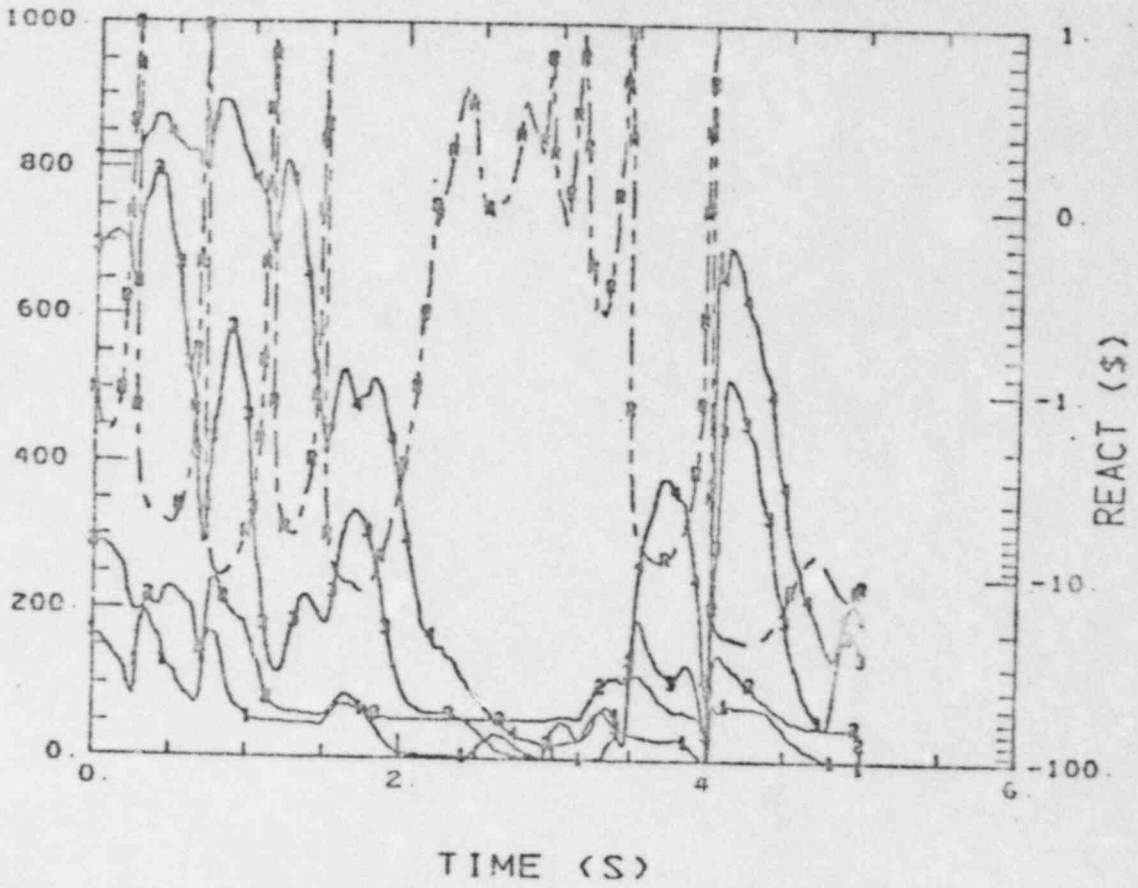

REGION SUMS/GROUP- 1
DENSITY OF FISSILE FUEL
MINIMUM VALUE = 2.00E-01 MAXIMUM VALUE = 8.93E+02

Fig 18

II.5

REGIONS/GROUP - 5
KR IL IU JL JU
1 1 25 7 19

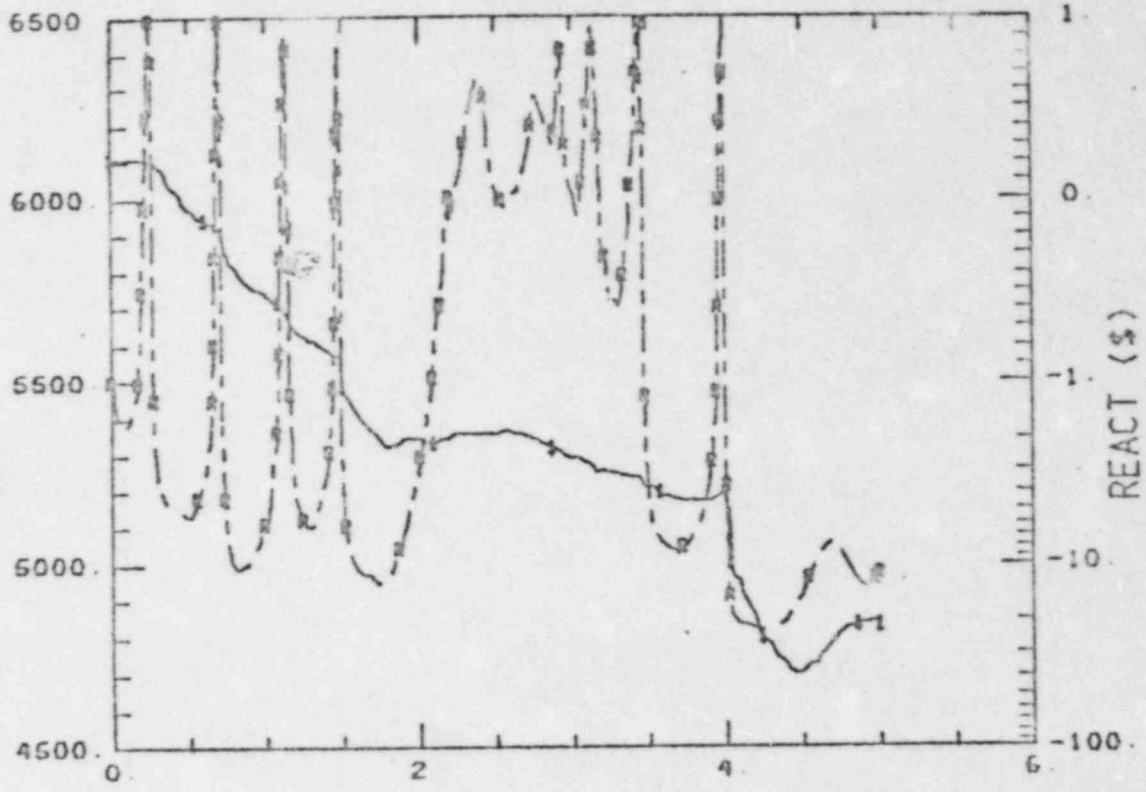

REGION SUMS/GROUP- 5
DENSITY OF FISSILE FUEL
MINIMUM VALUE = 4.71E+03 MAXIMUM VALUE = 6.11E+03

Fig 19

II.5

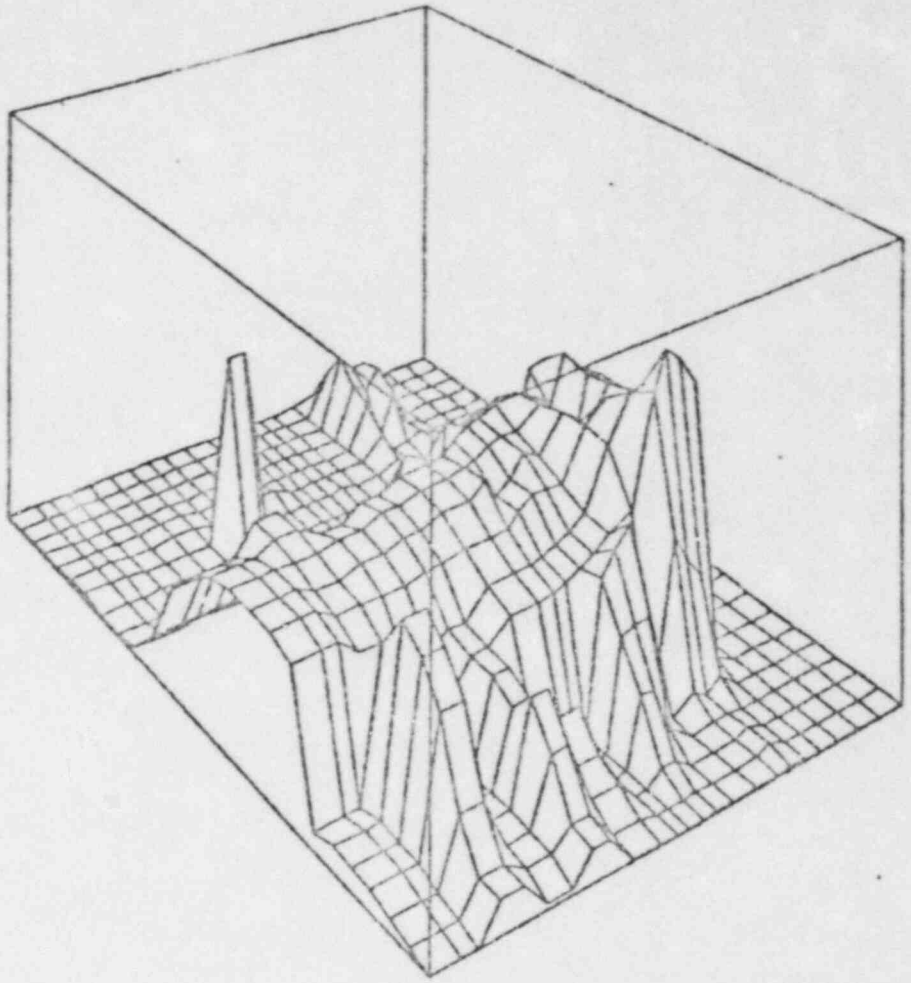

DENSITY OF FISSILE FUEL
MINIMUM VALUE = 0.
MAXIMUM VALUE = 6.5748E+03 TIME = 4000.000 MS

Fig 20

/8 /8 /8

CELLS

KR	I	J
1	15	18
2	15	19
3	15	20
4	15	21
5	15	22

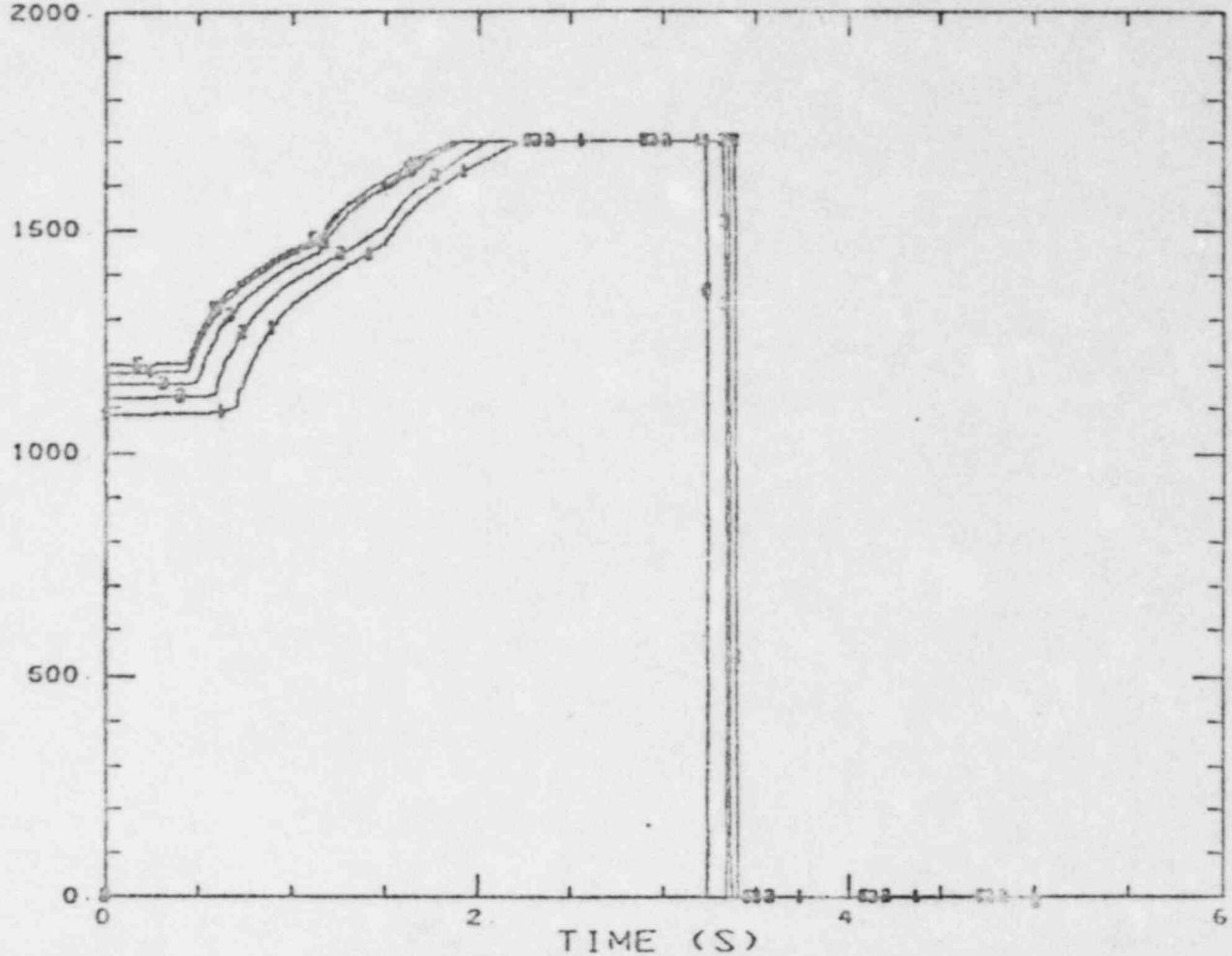

TEMPERATURE OF SUBASSEMBLY CAN WALL
MINIMUM = 0 MAXIMUM = 1.700E+03

Fig 21

T.S

CELLS
KR I J
1 2 18
2 4 18
3 6 18
4 10 18
5 14 18

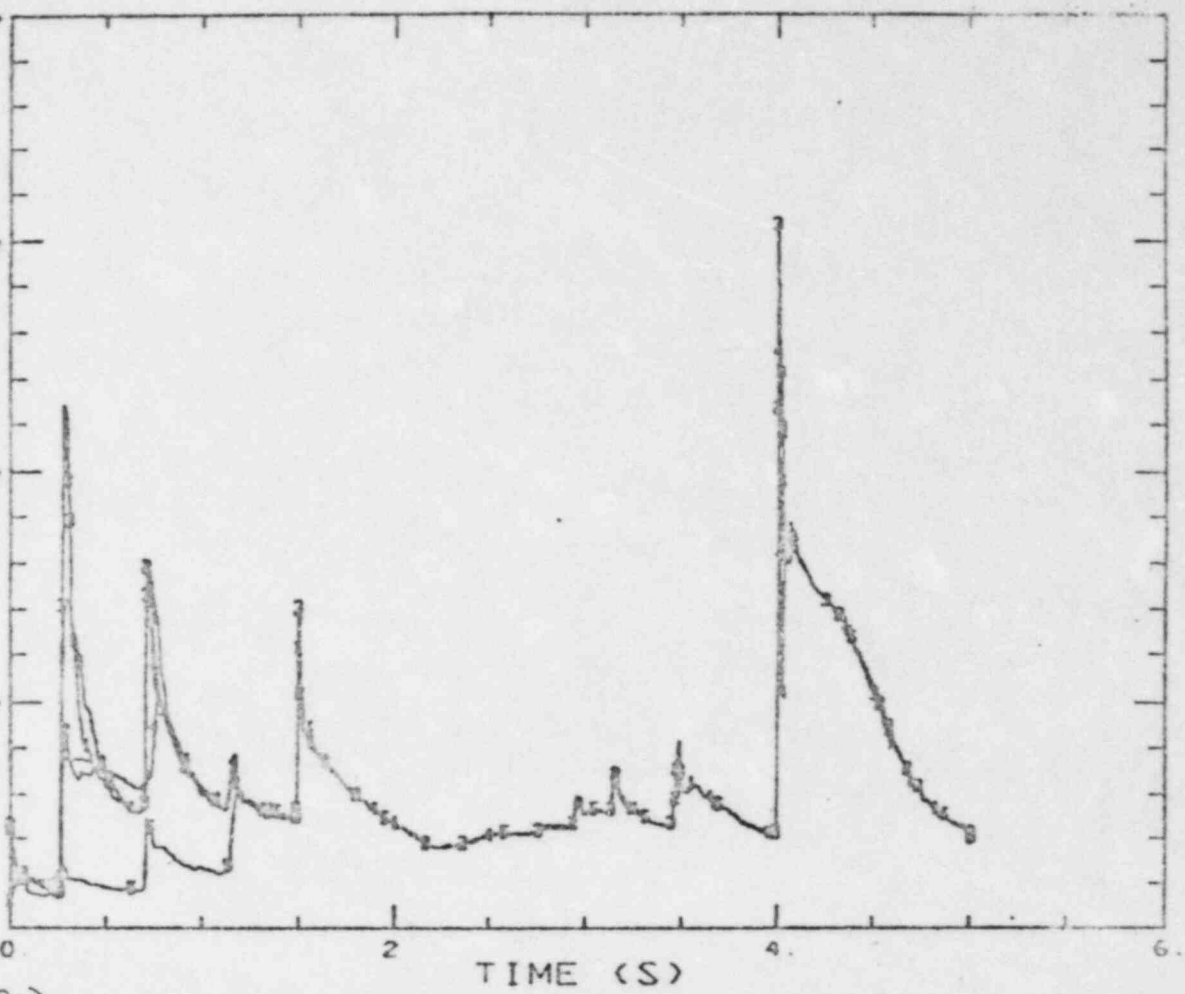

PRESSURE (Pa)
MINIMUM = 1.296E+05 MAXIMUM = 3.070E+06

Fig 22

Fig 1

MOD6. REF CASE FOR THE HETEROGENEOUS CORE AT EOC - 4
SUBASSEMBLIES FOR CHANNEL 1

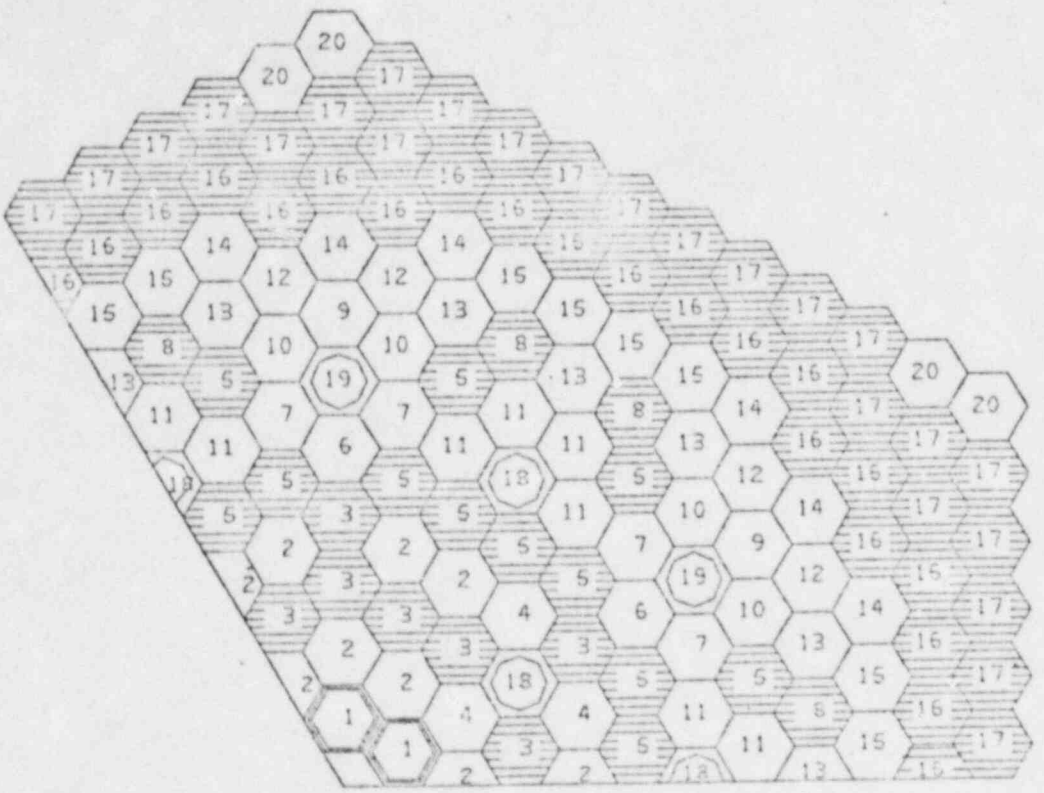

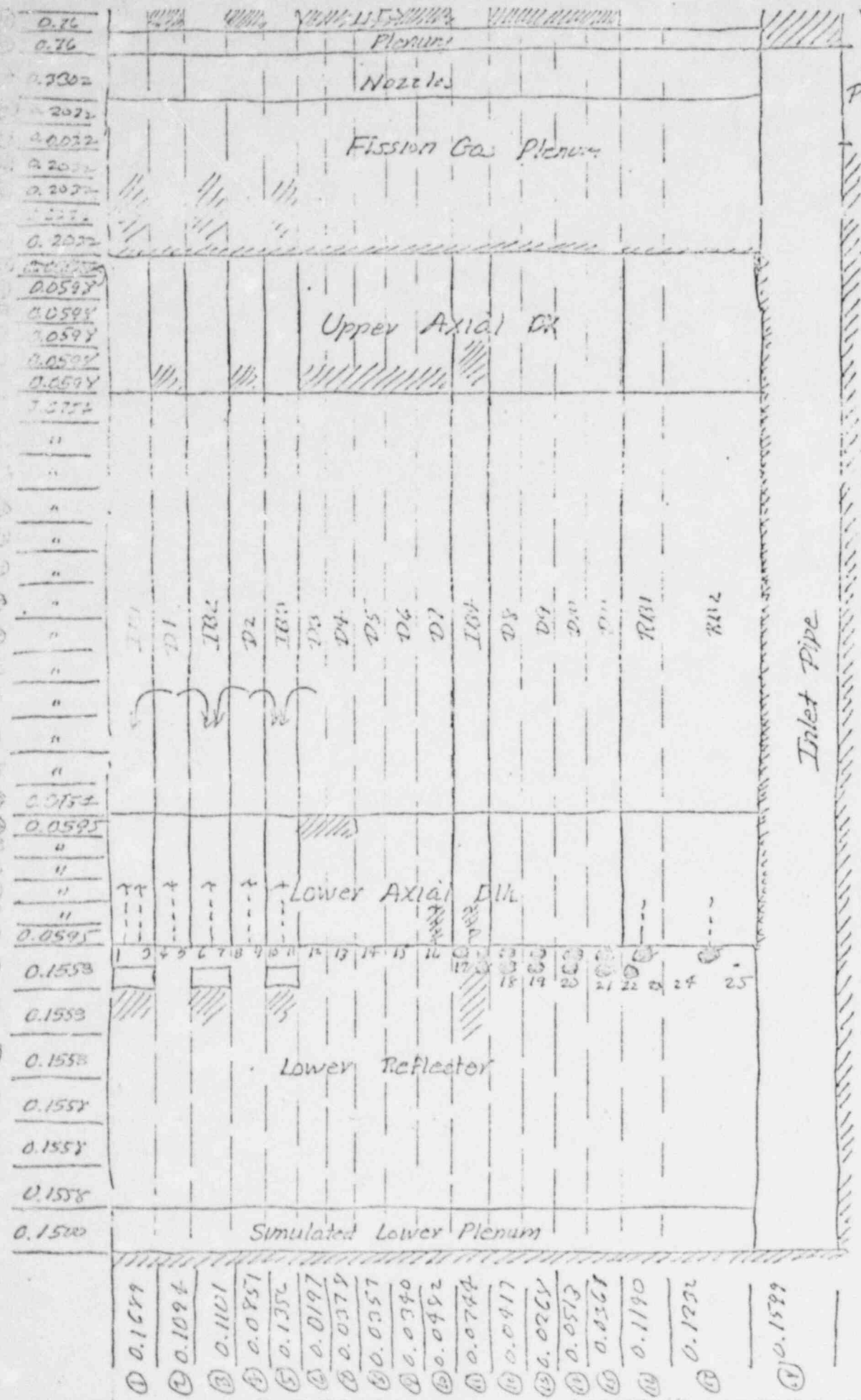

Fig 2 Geometric and Calculational Model for the Whole-core Disruption Phase Analysis

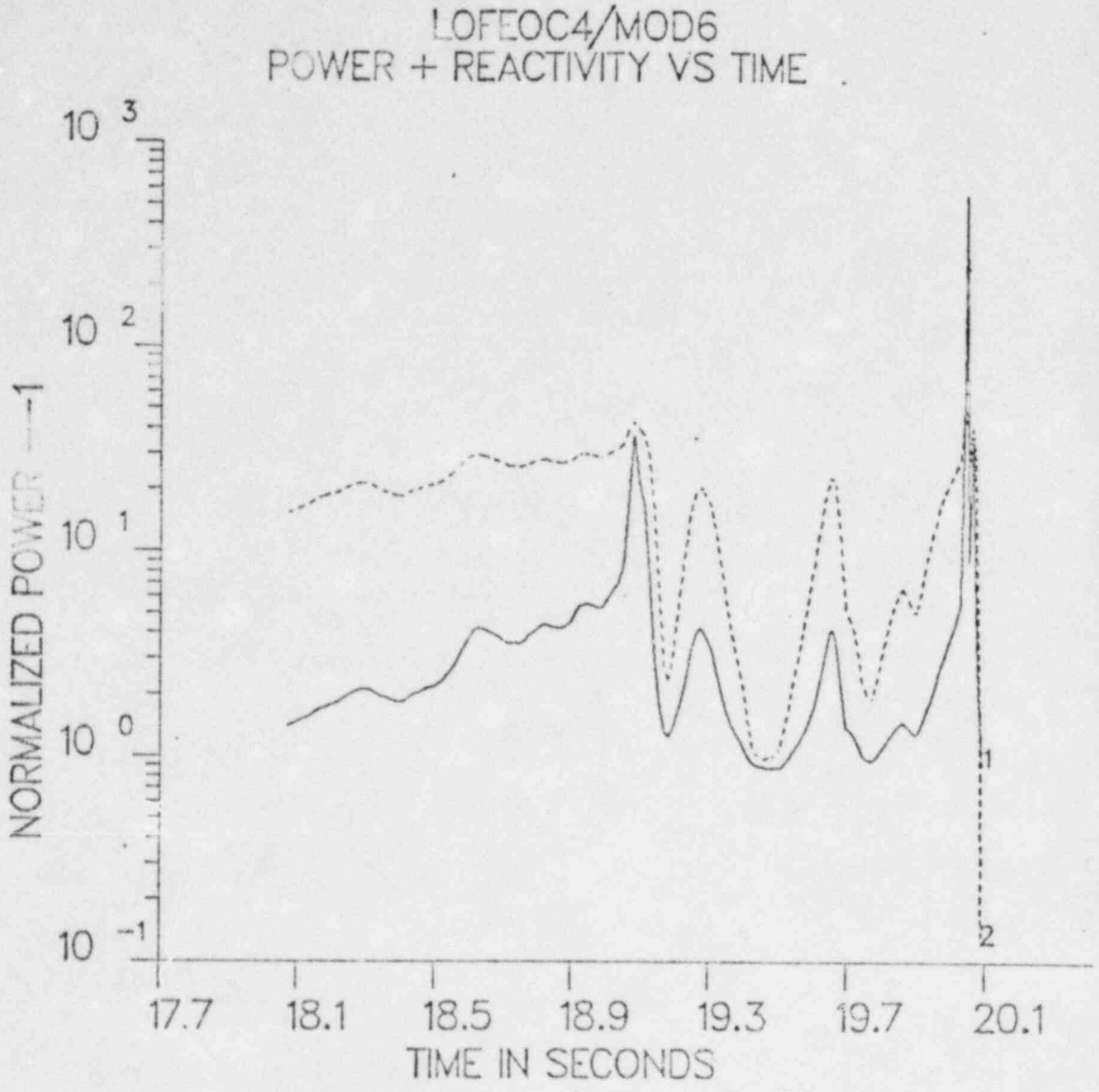
LOFEOC4/MOD6
POWER + REACTIVITY VS TIME
NORMALIZED POWER —1
10 3
10 2
10 1
10 0
10 -1
1
2
17.7
18.1
18.5
18.9
19.3
19.7
20.1
TIME IN SECONDS

Fig 3

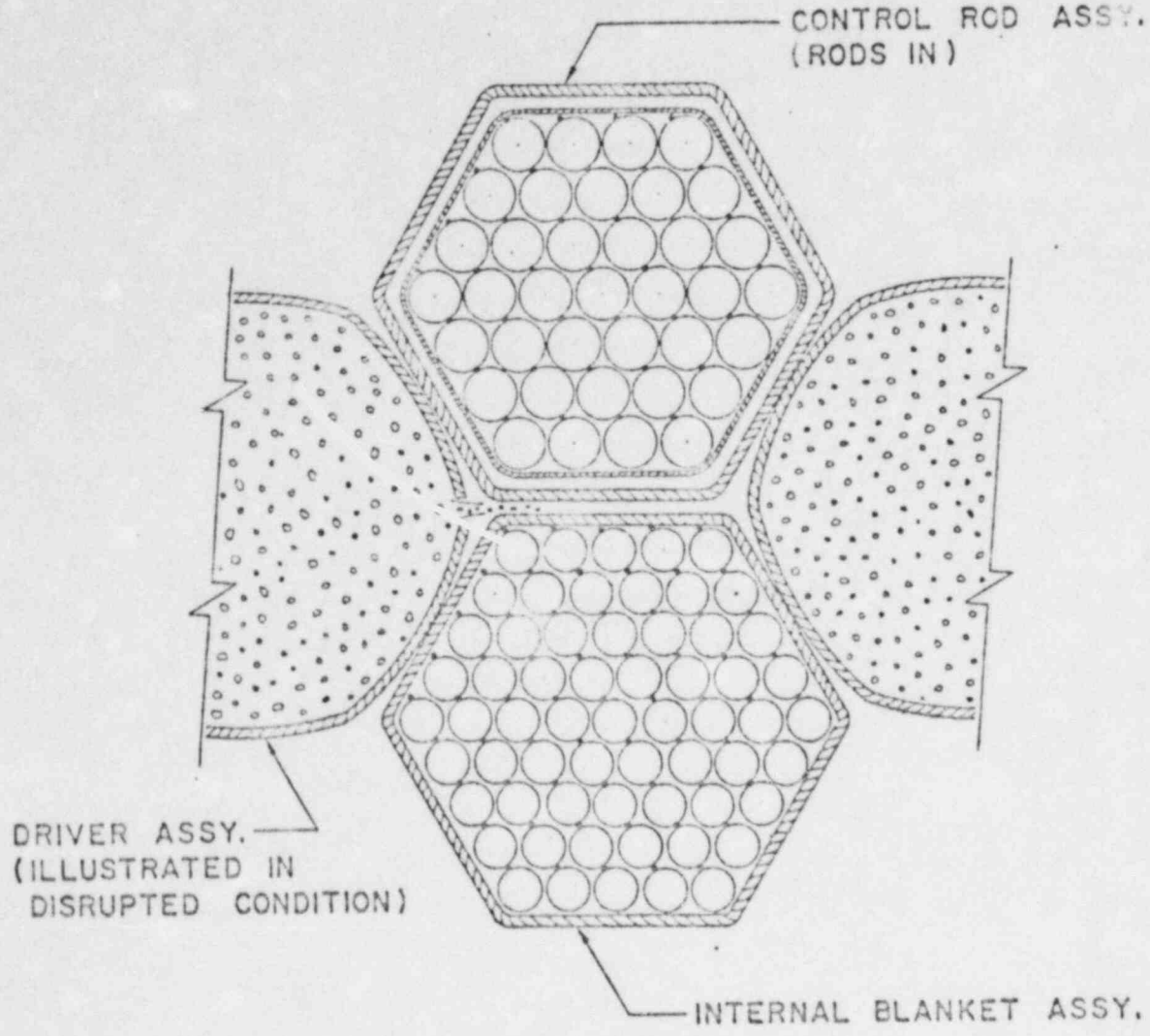

Illustration of Dispersal Process Involving Molten Fuel
from Disrupted Fuel Assembly Entering Intersubassembly Gap Volume

Fig 1

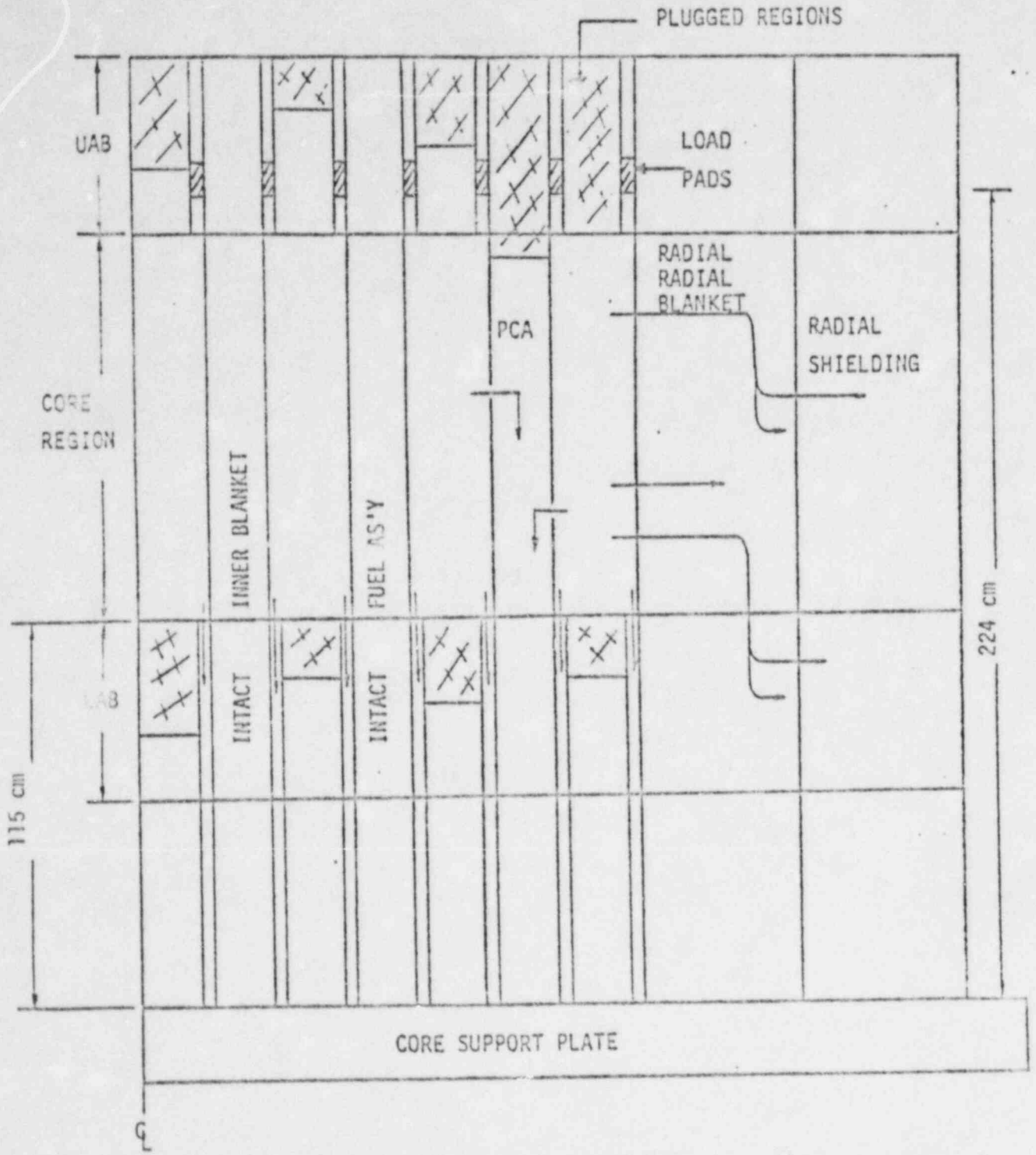

Side View of Early Fuel Escape Paths (not to scale)

Fig 2

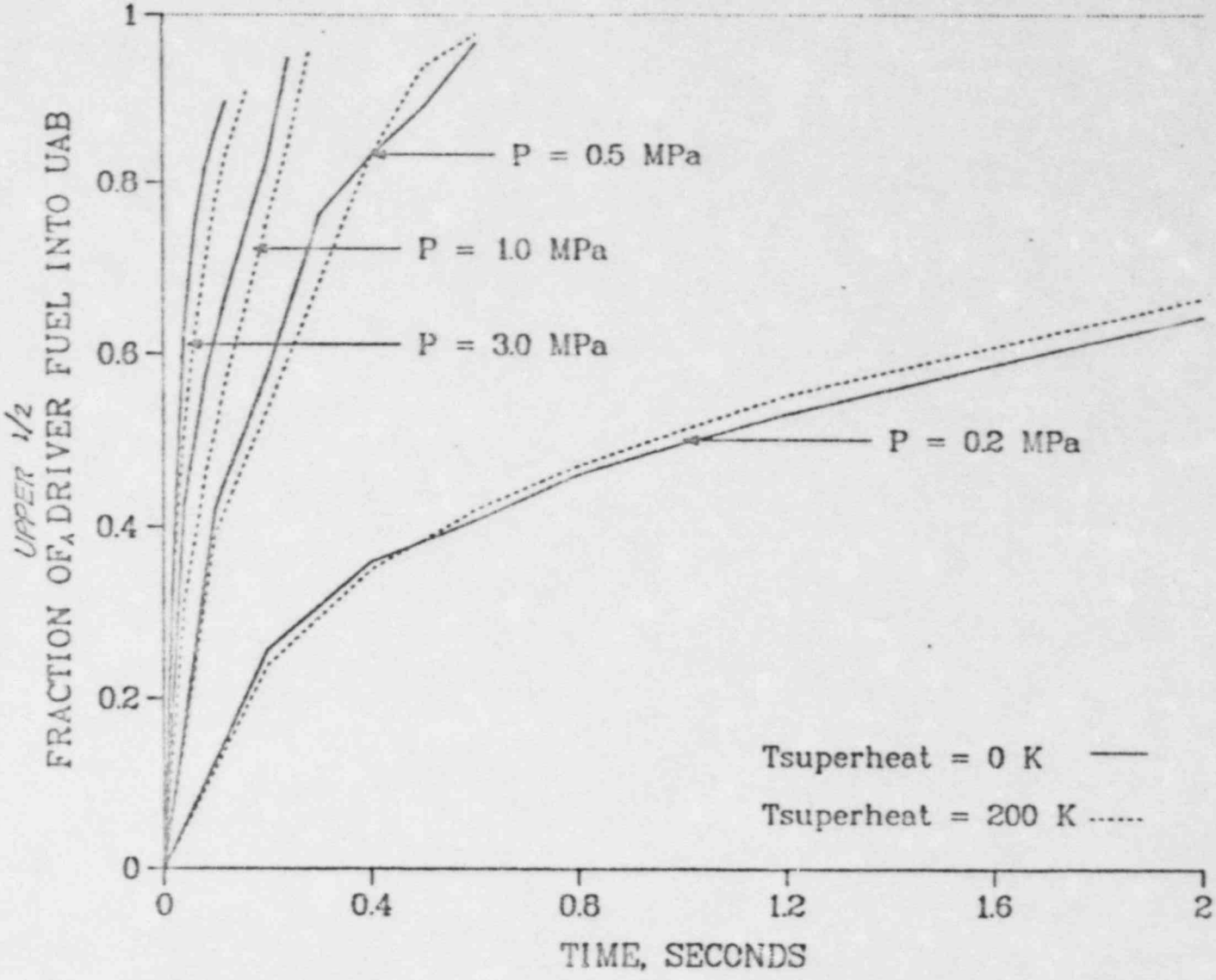
FRACTION OF UPPER 1/2 DRIVER FUEL INTO UAB
1
0.8
0.6
0.4
0.2
0
P = 0.5 MPa
P = 1.0 MPa
P = 3.0 MPa
P = 0.2 MPa
Tsuperheat = 0 K
Tsuperheat = 200 K
0
0.4
0.8
1.2
1.6
2
TIME, SECONDS

Fig 3

II

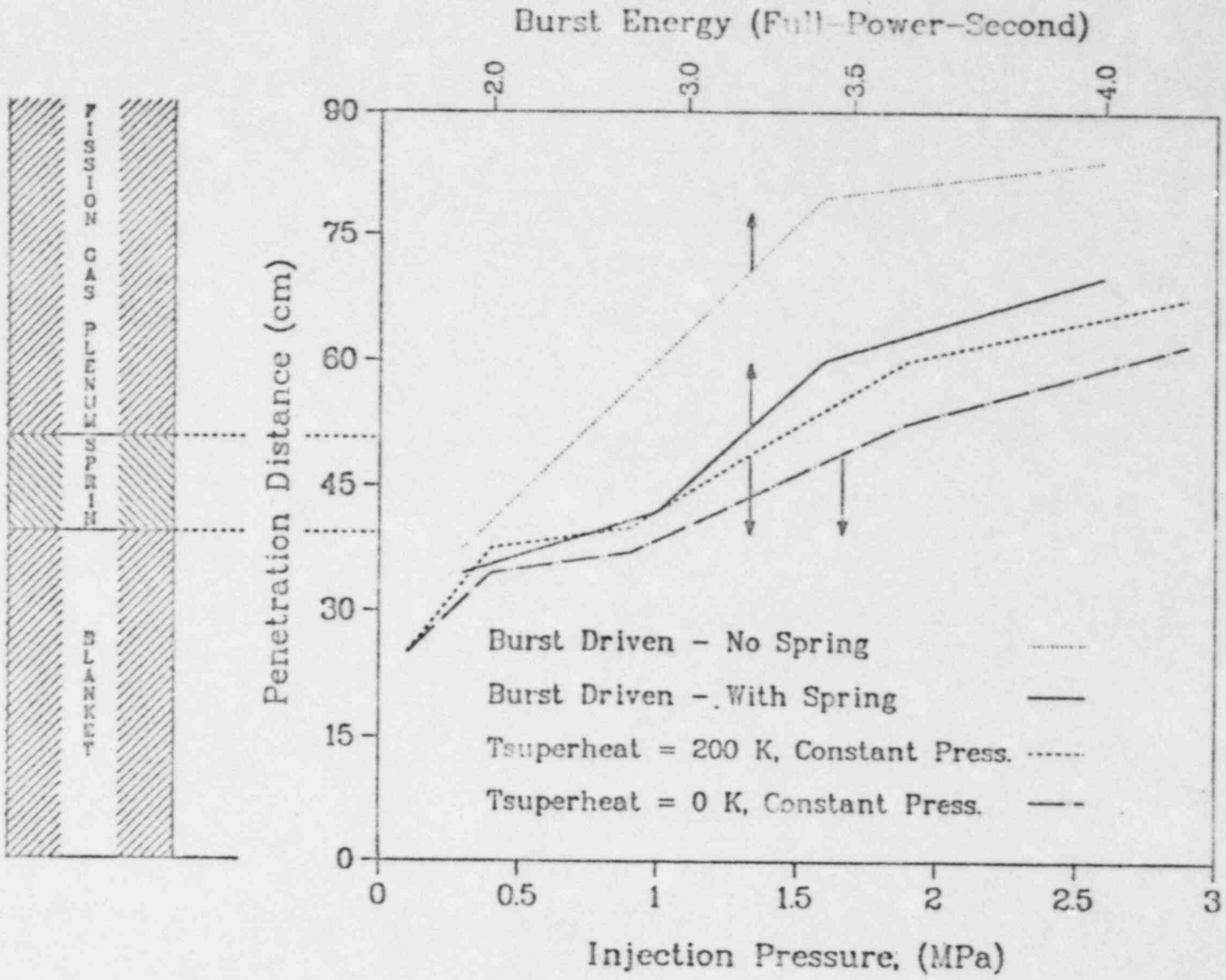
Burst Energy (Full-Power-Second)
2.0
3.0
3.5
4.0
90
75
60
45
30
15
0
Penetration Distance (cm)
FISSION GAS PLENUM SPRING
BLANKET
Burst Driven - No Spring
Burst Driven - With Spring
Tsuperheat = 200 K, Constant Press.
Tsuperheat = 0 K, Constant Press.
0
0.5
1
1.5
2
2.5
3
Injection Pressure, (MPa)

Fig 4

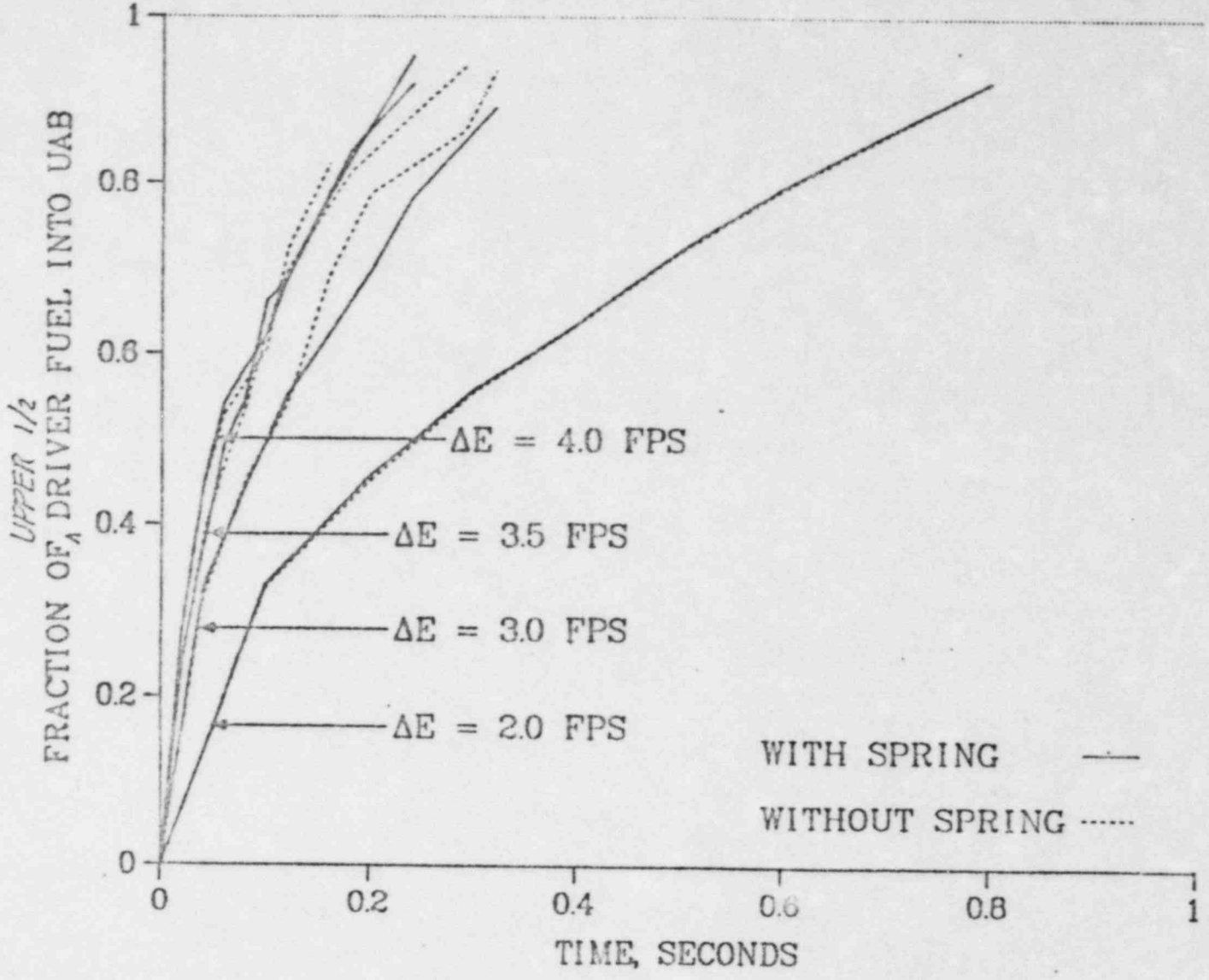
FRACTION OF UPPER 1/2 DRIVER FUEL INTO UAB
1
0.8
0.6
0.4
0.2
0
ΔE = 4.0 FPS
ΔE = 3.5 FPS
ΔE = 3.0 FPS
ΔE = 2.0 FPS
WITH SPRING
WITHOUT SPRING
0
0.2
0.4
0.6
0.8
1
TIME, SECONDS

Fig 5

7'II

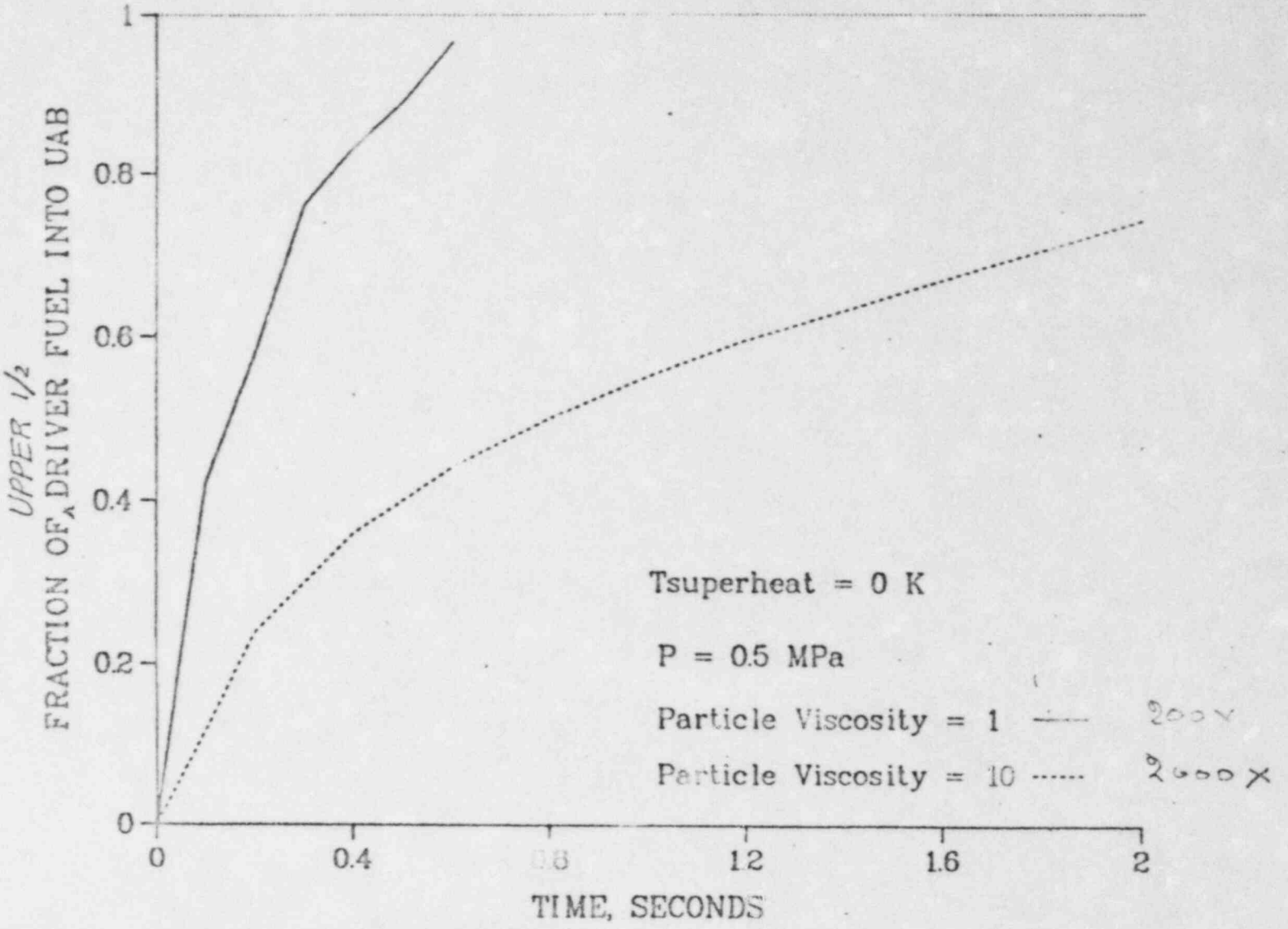
FRACTION OF DRIVER FUEL INTO UAB
UPPER 1/2
1
0.8
0.6
0.4
0.2
0
0
0.4
0.8
1.2
1.6
2
TIME, SECONDS
Tsuperheat = 0 K
P = 0.5 MPa
Particle Viscosity = 1
Particle Viscosity = 10

Fig 6

II.6

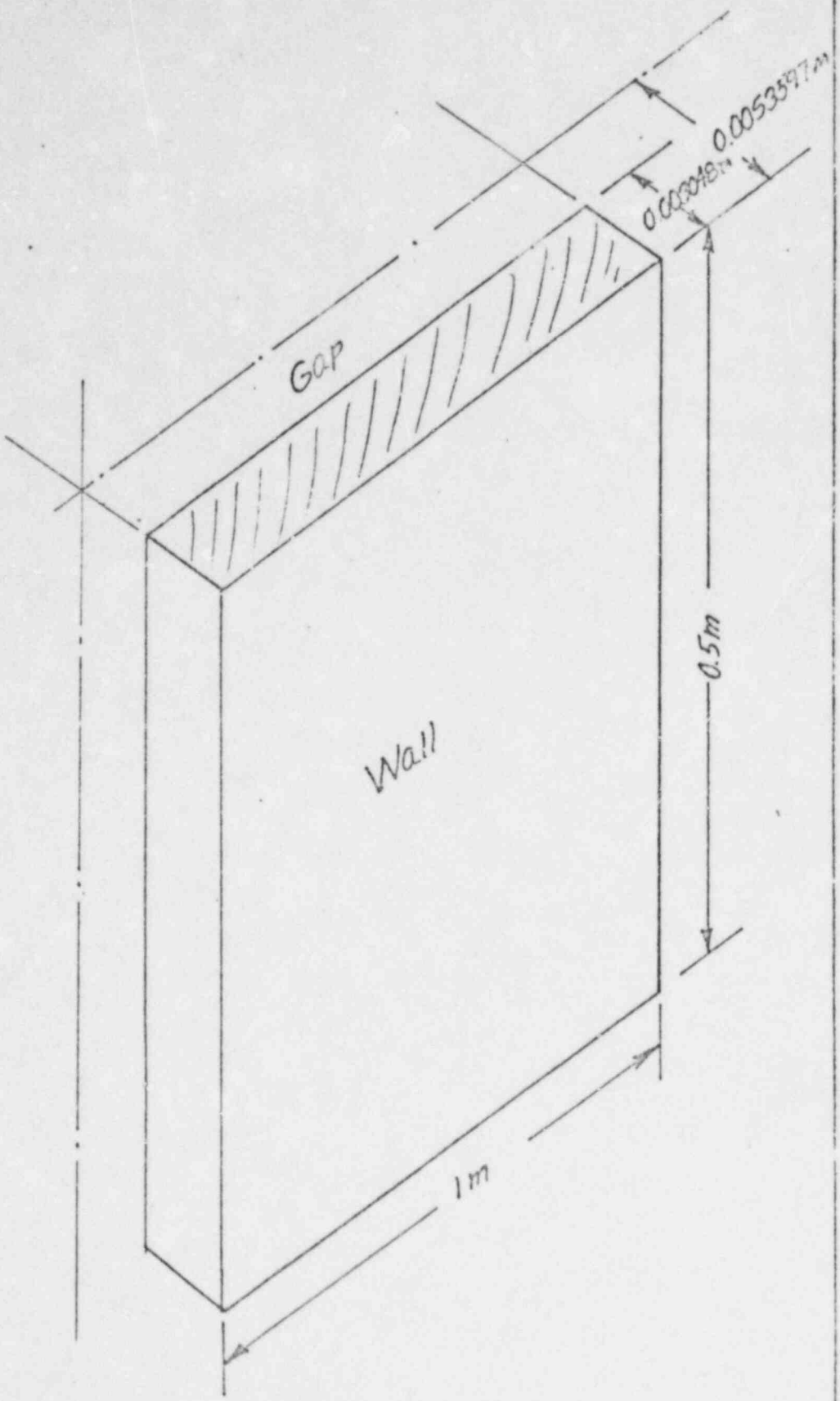

Fig 7

TIME 000 MSEC

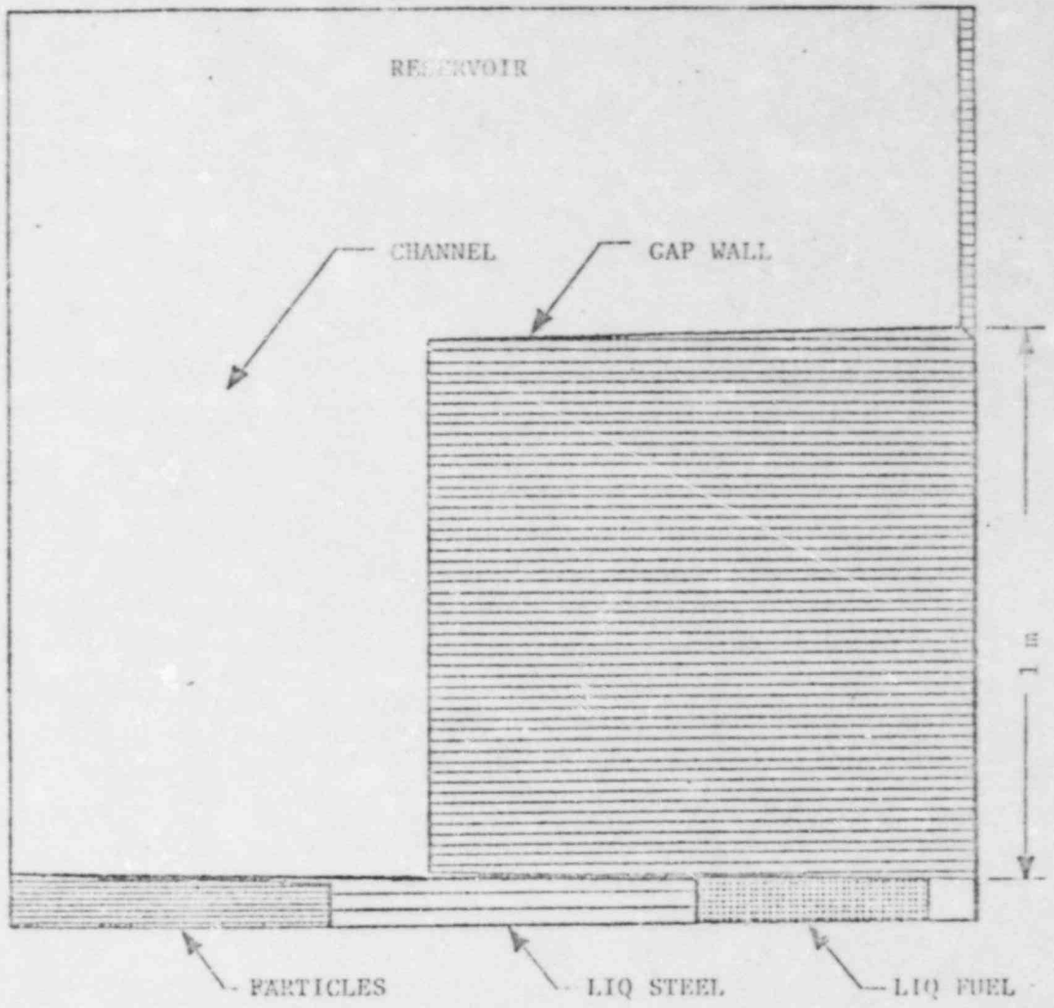

Fig 8

II.2

TIME 200 000 MSEC

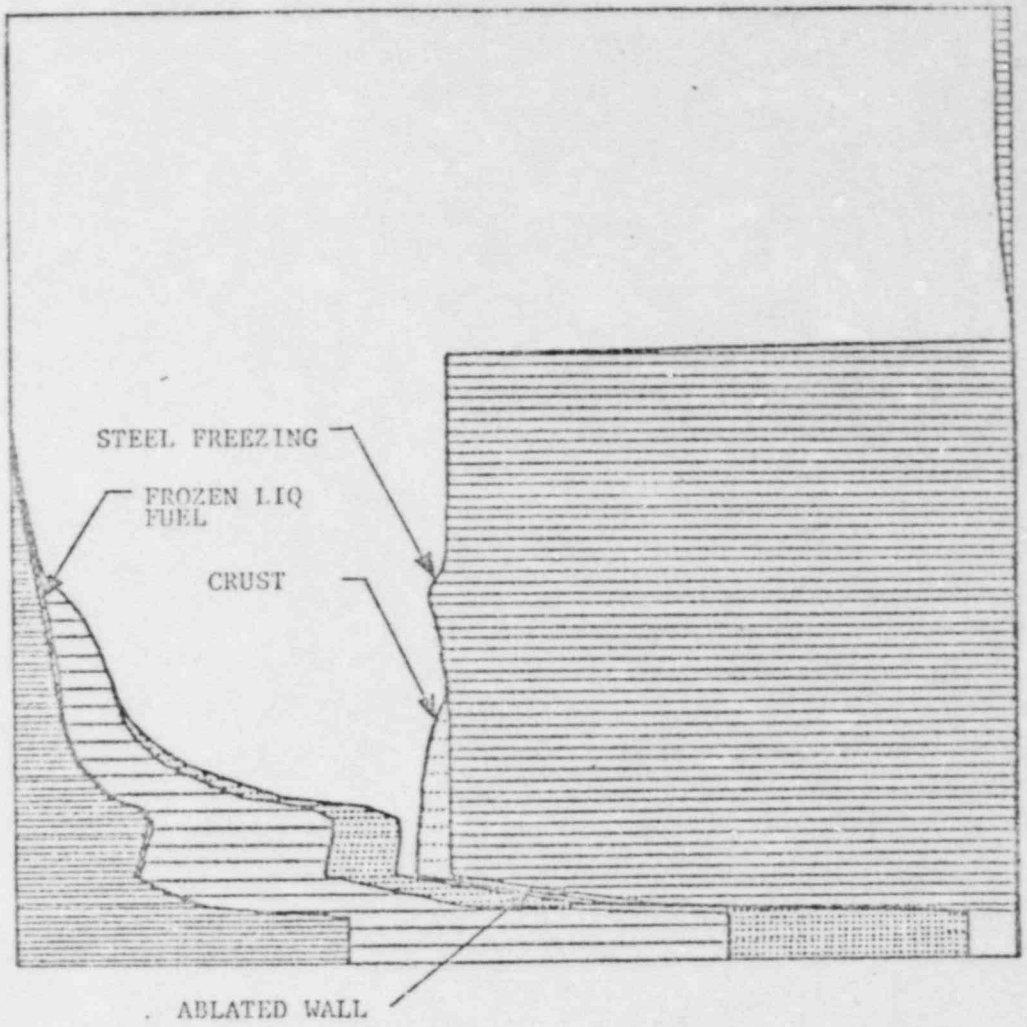

Fig 9

II.C

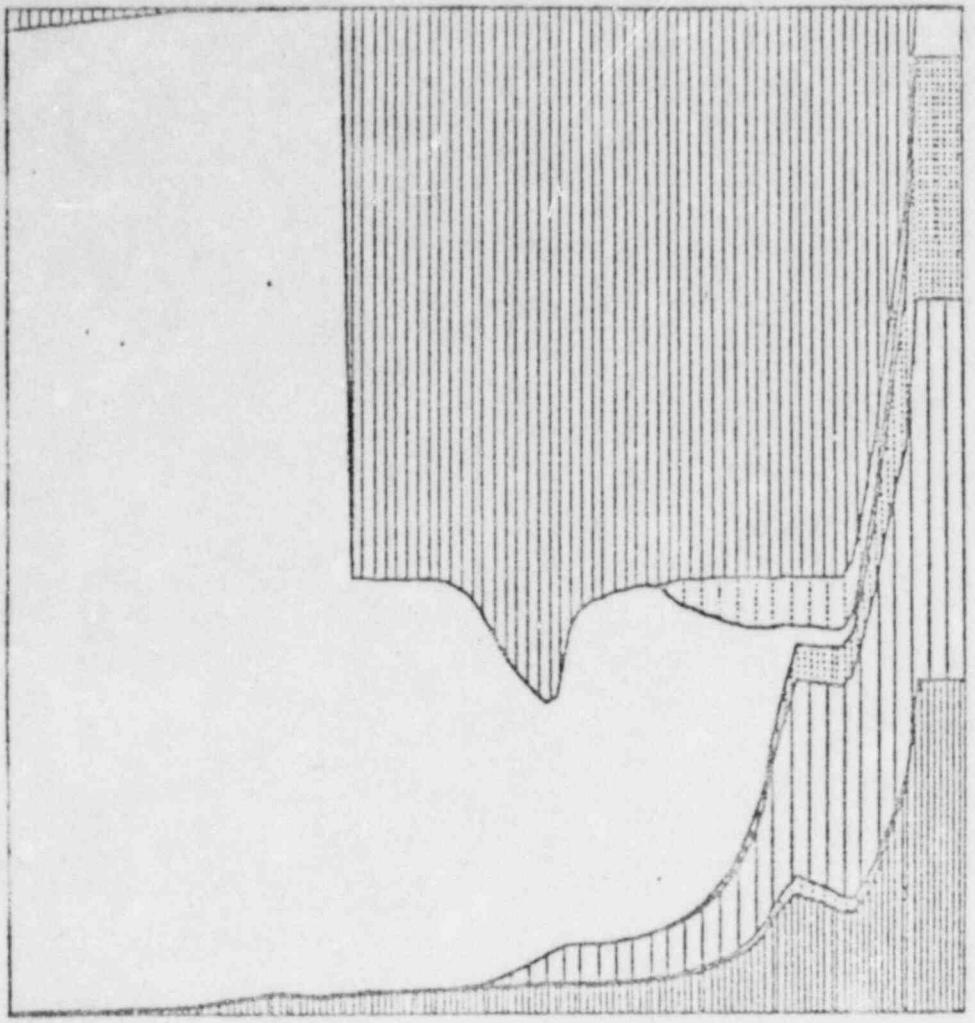

Fig 10

TIME 600 000 MSEC.

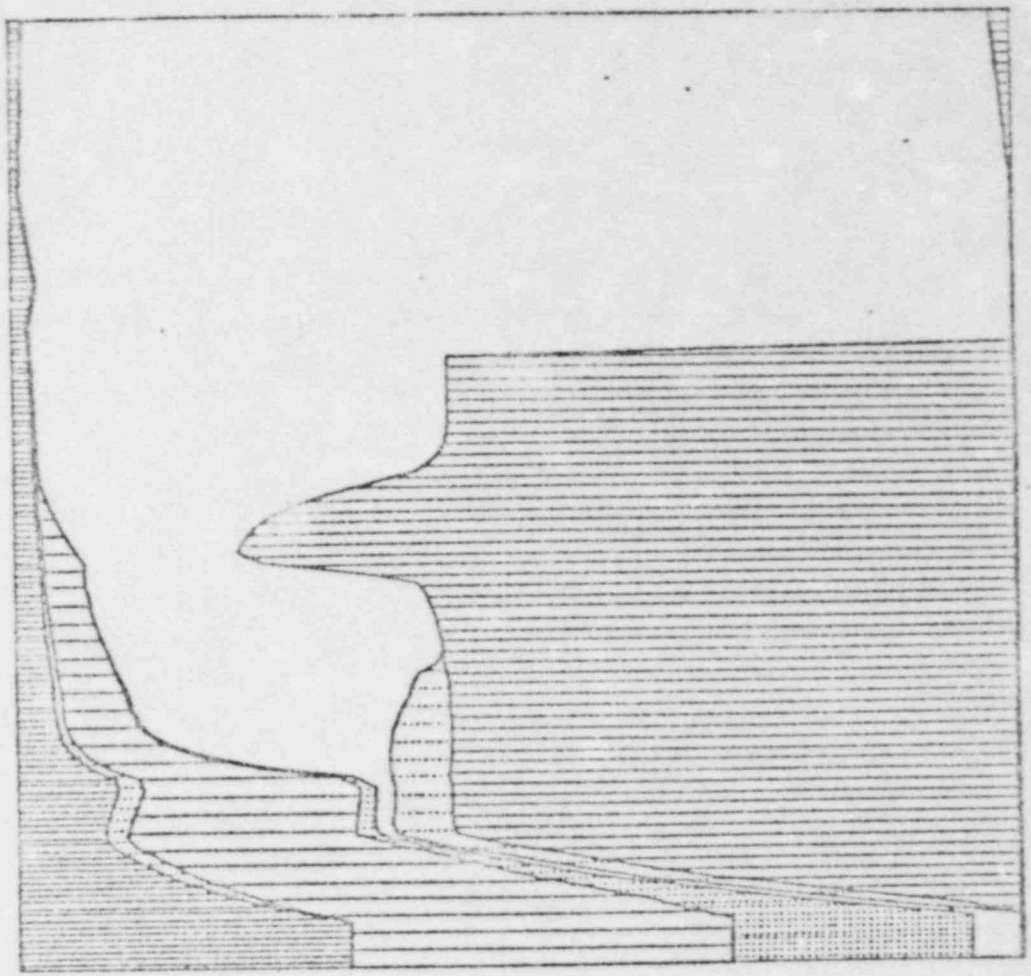

Fig 11

TIME 800.000 MSEC.

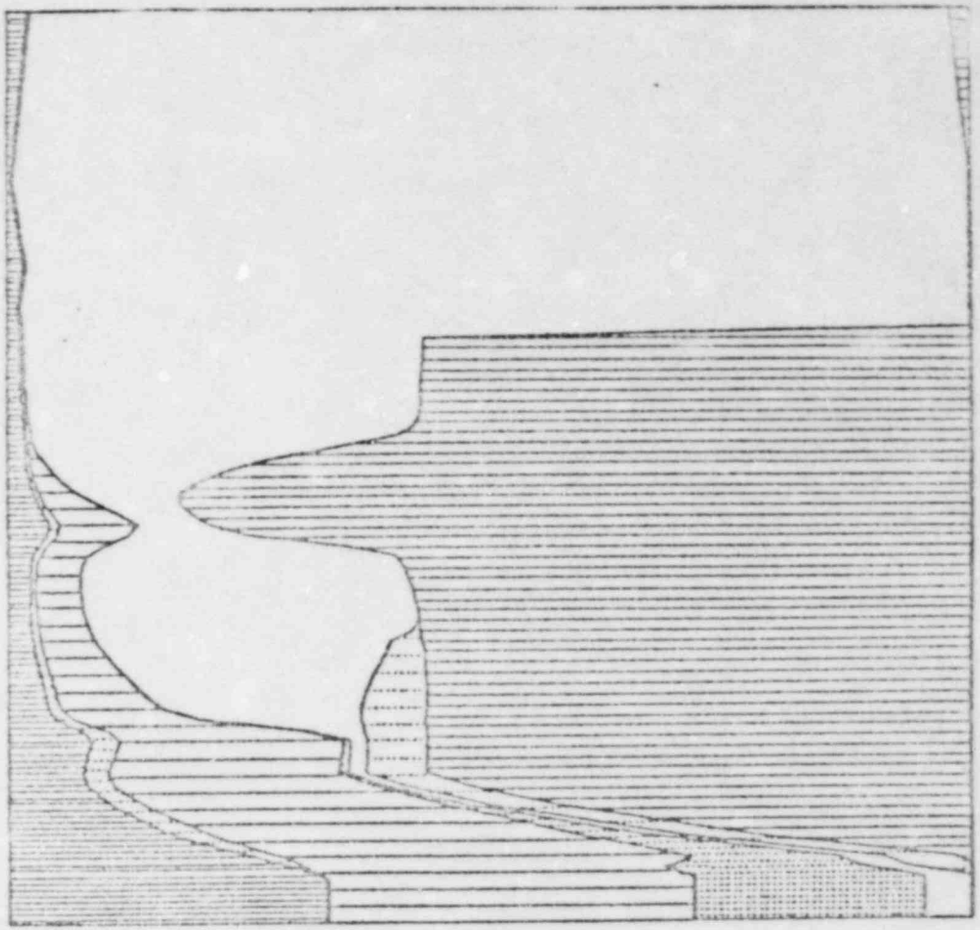

Fig 12

II.4

TIME 1000 000 MSEC

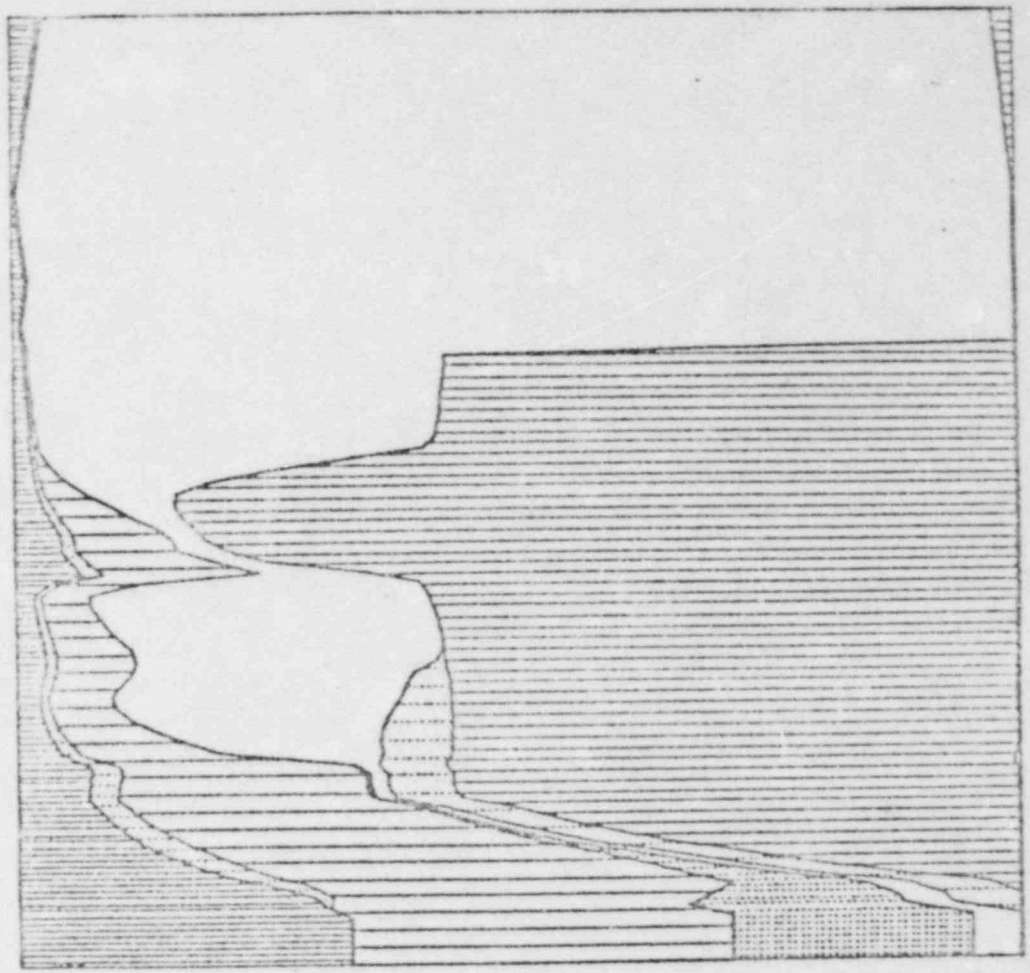

Fig 13

II.6

TIME 1200 000 MSEC

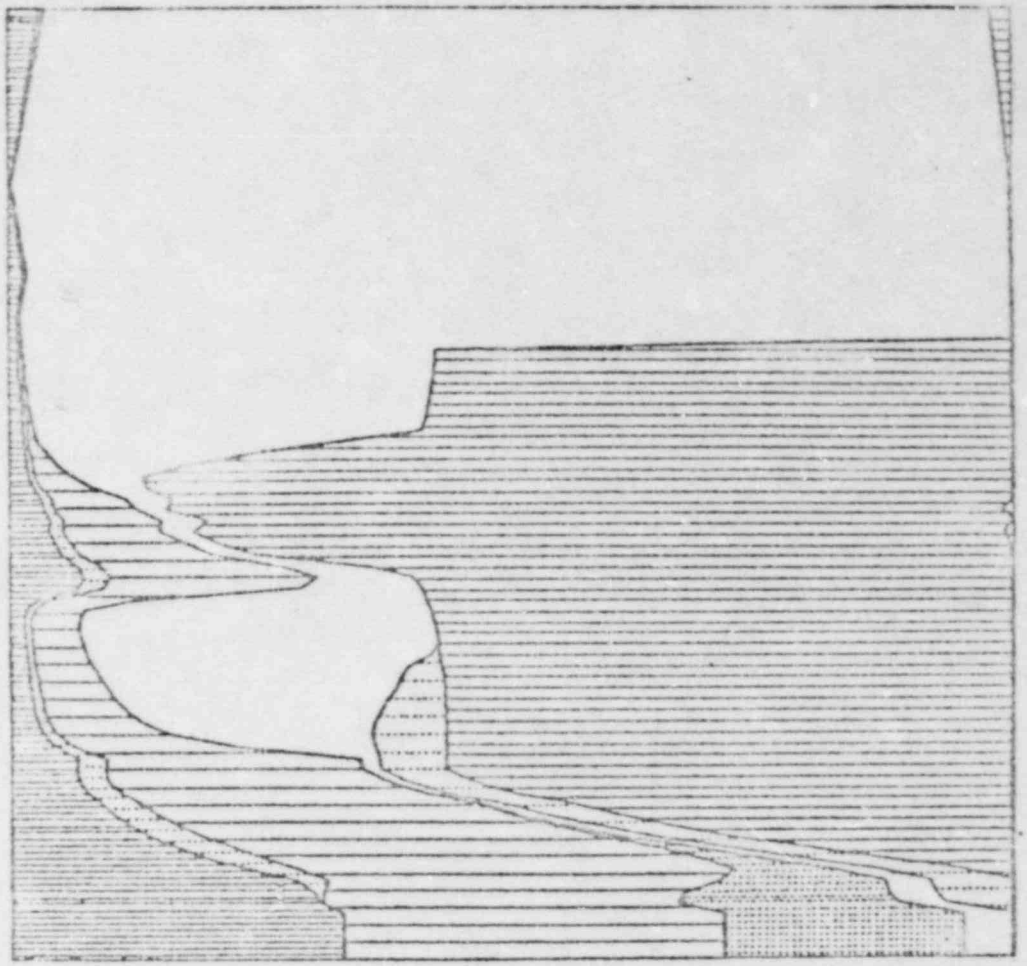

Fig 14

II.6

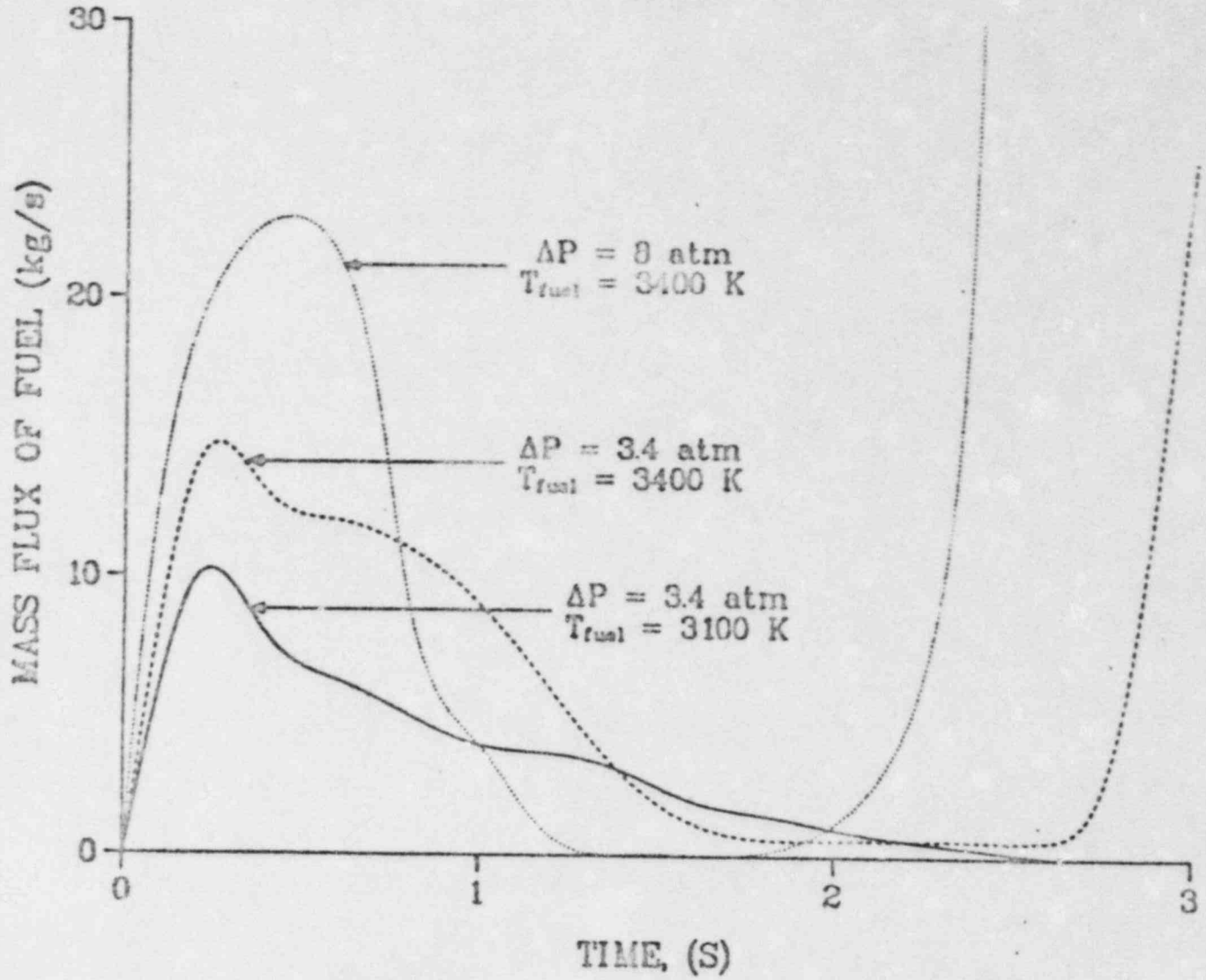
30
20
10
0
0
1
2
3
MASS FLUX OF FUEL (kg/s)
TIME, (S)
ΔP = 8 atm
T_fuel = 3400 K
ΔP = 3.4 atm
T_fuel = 3400 K
ΔP = 3.4 atm
T_fuel = 3100 K

Fig 16

II.9

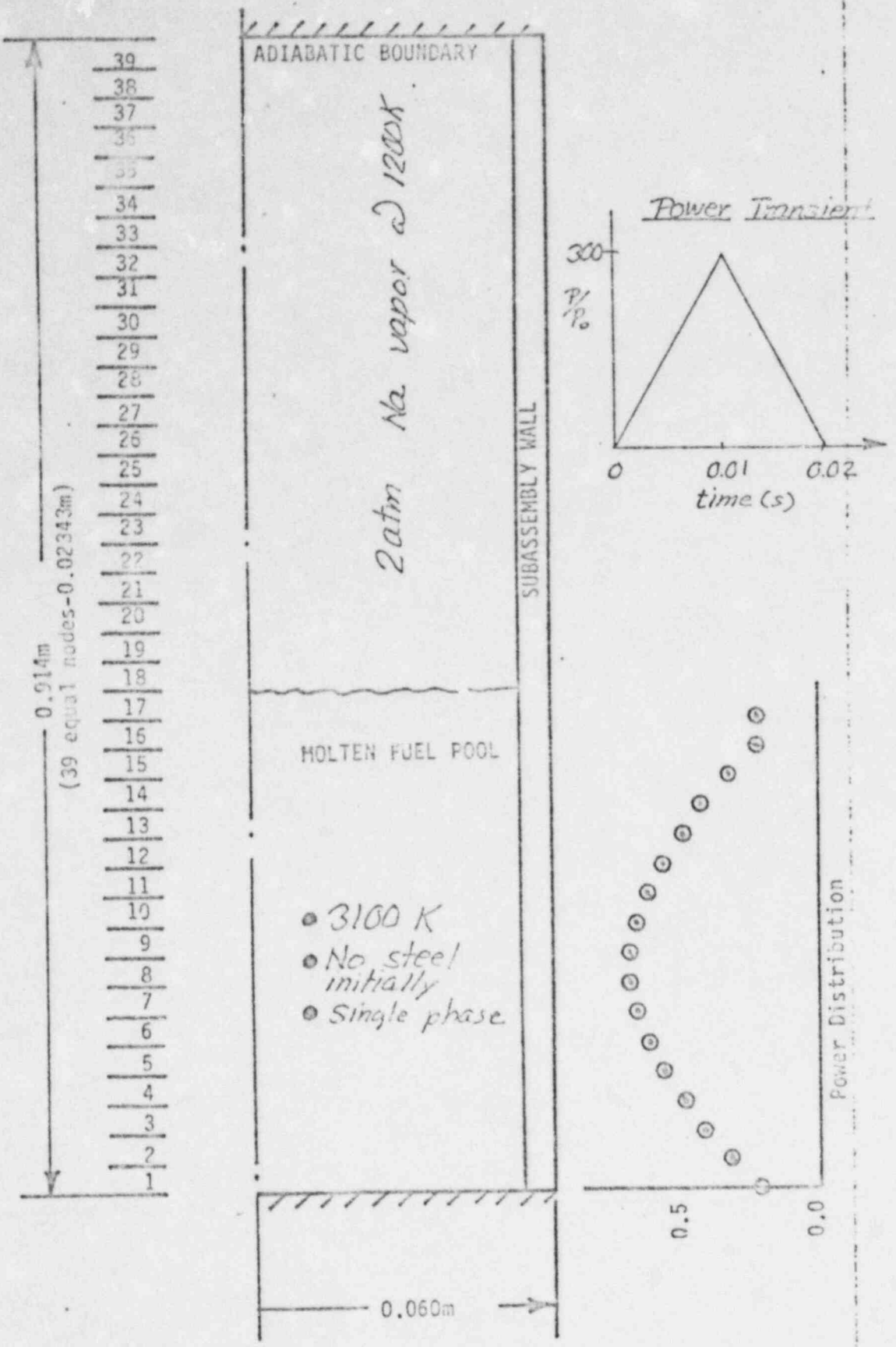

Fig 17

GEOMETRIC MODEL FOR SUBASSEMBLY DISRUPTION ANALYSIS

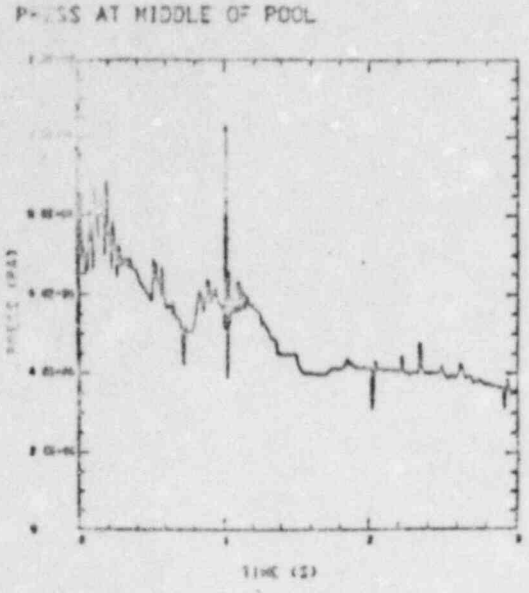

(a)

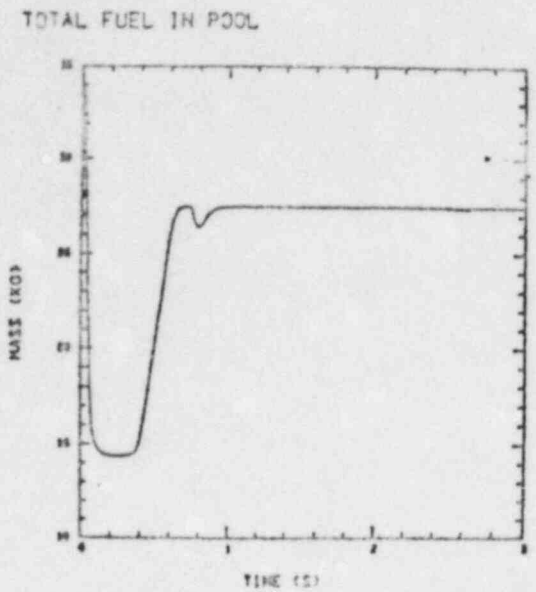

(b)

Fig 10 (co2)

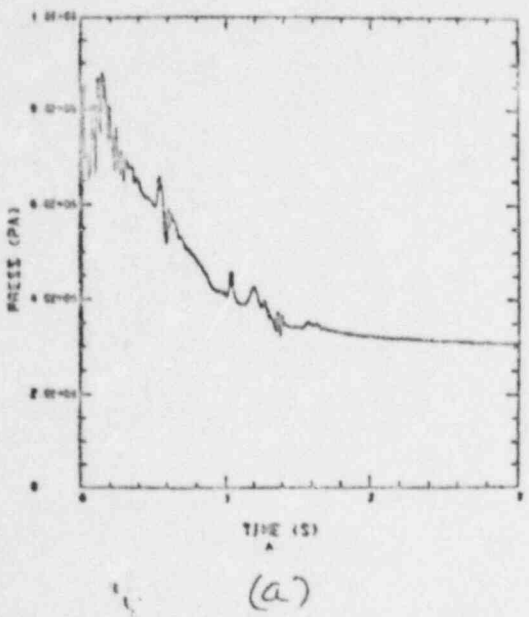

(a)

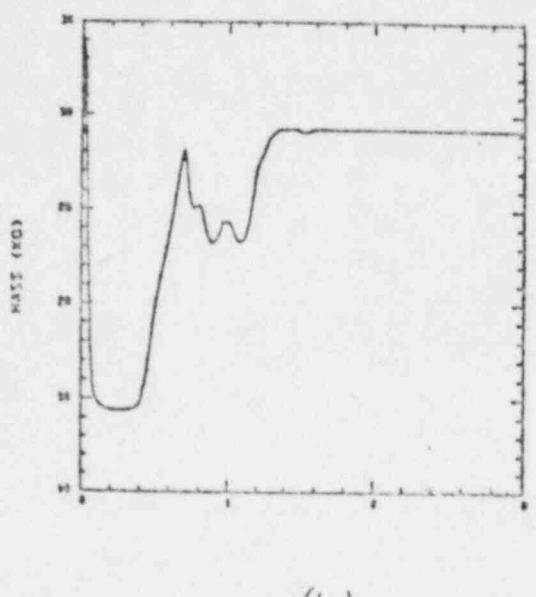

(b)

Fig 9 (co3)

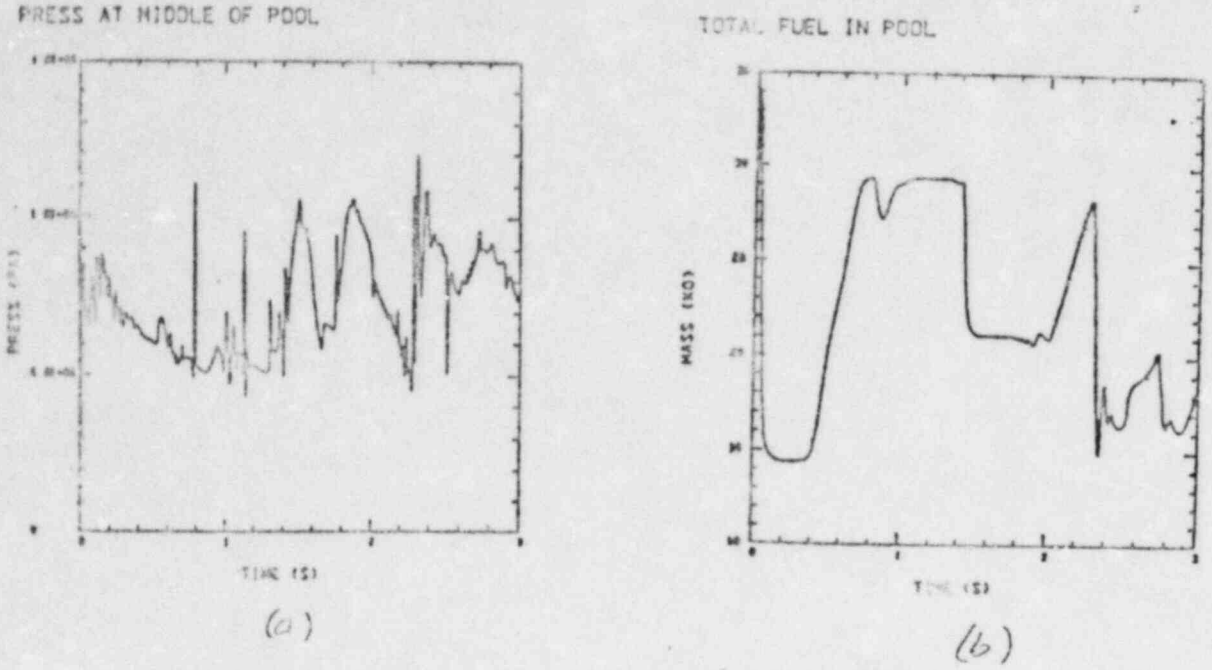

(a) (b)

Fig 20 (co4)

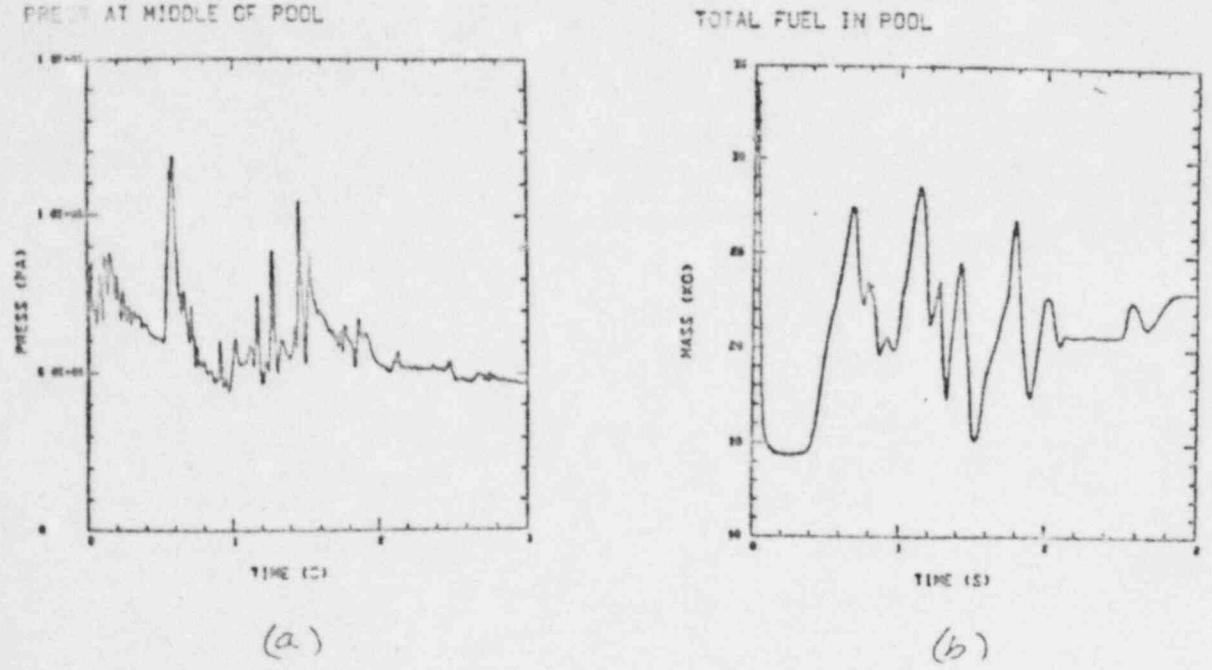

(a) (b)

Fig 21 (co6)

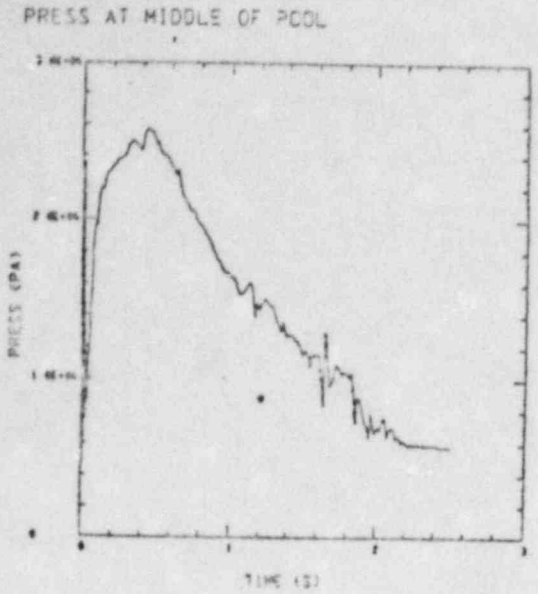

(a)

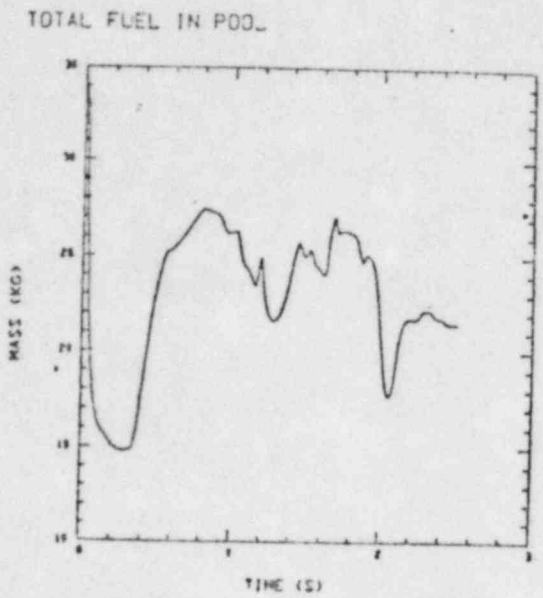

(b)

Fig 22 (C13)

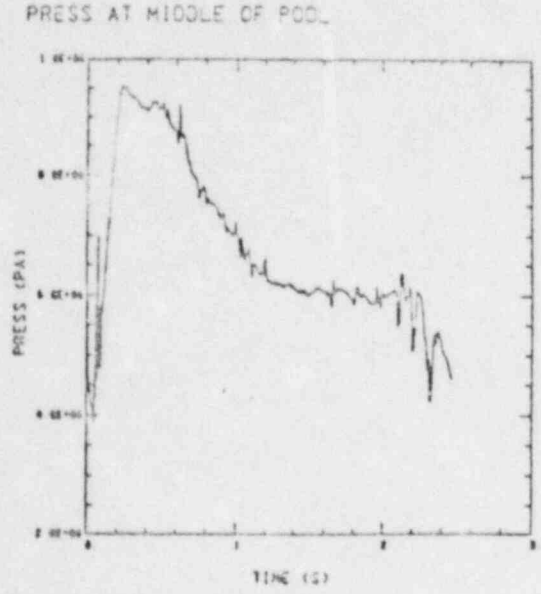

(a)

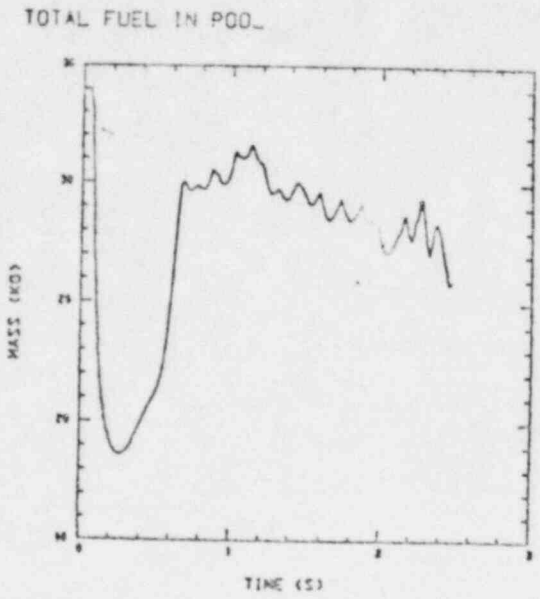

(b)

Fig 20 (C19)

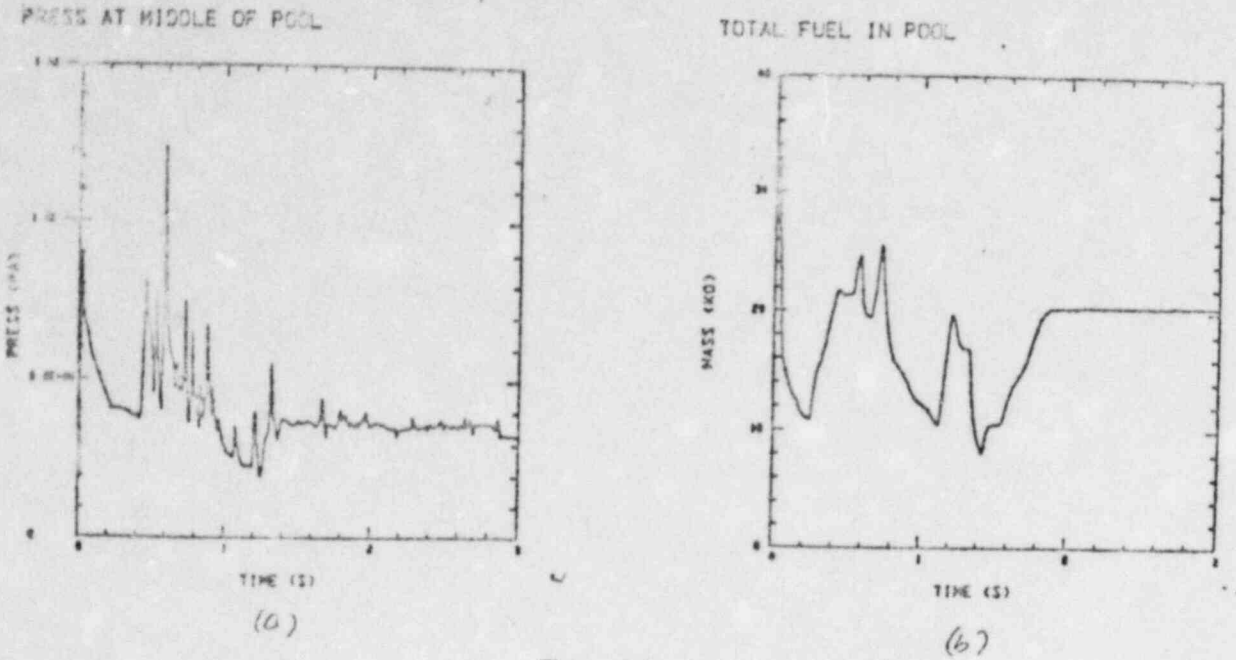

(a) (b)

Fig 24 (C21)

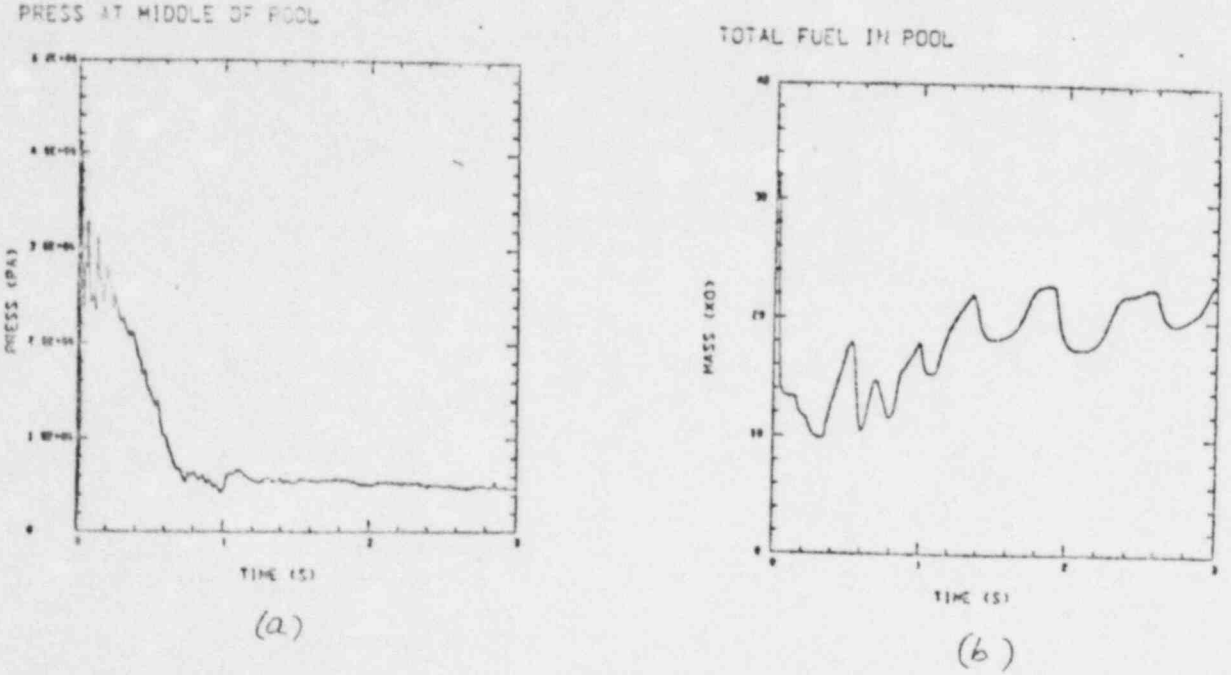

(a) (b)

Fig 25 (C22)

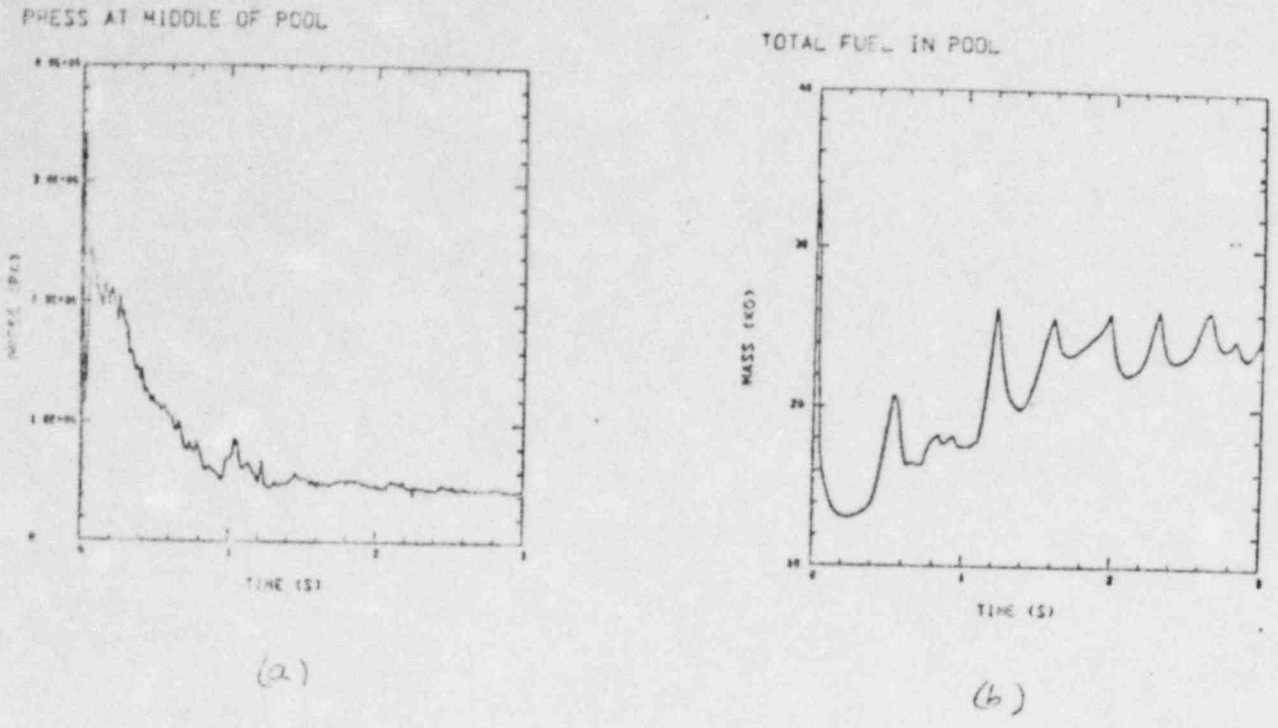
PRESS AT MIDDLE OF POOL
TIME (S)
TOTAL FUEL IN POOL
MASS (KG)
TIME (S)

(a)

(b)

Fig 26 (C93)

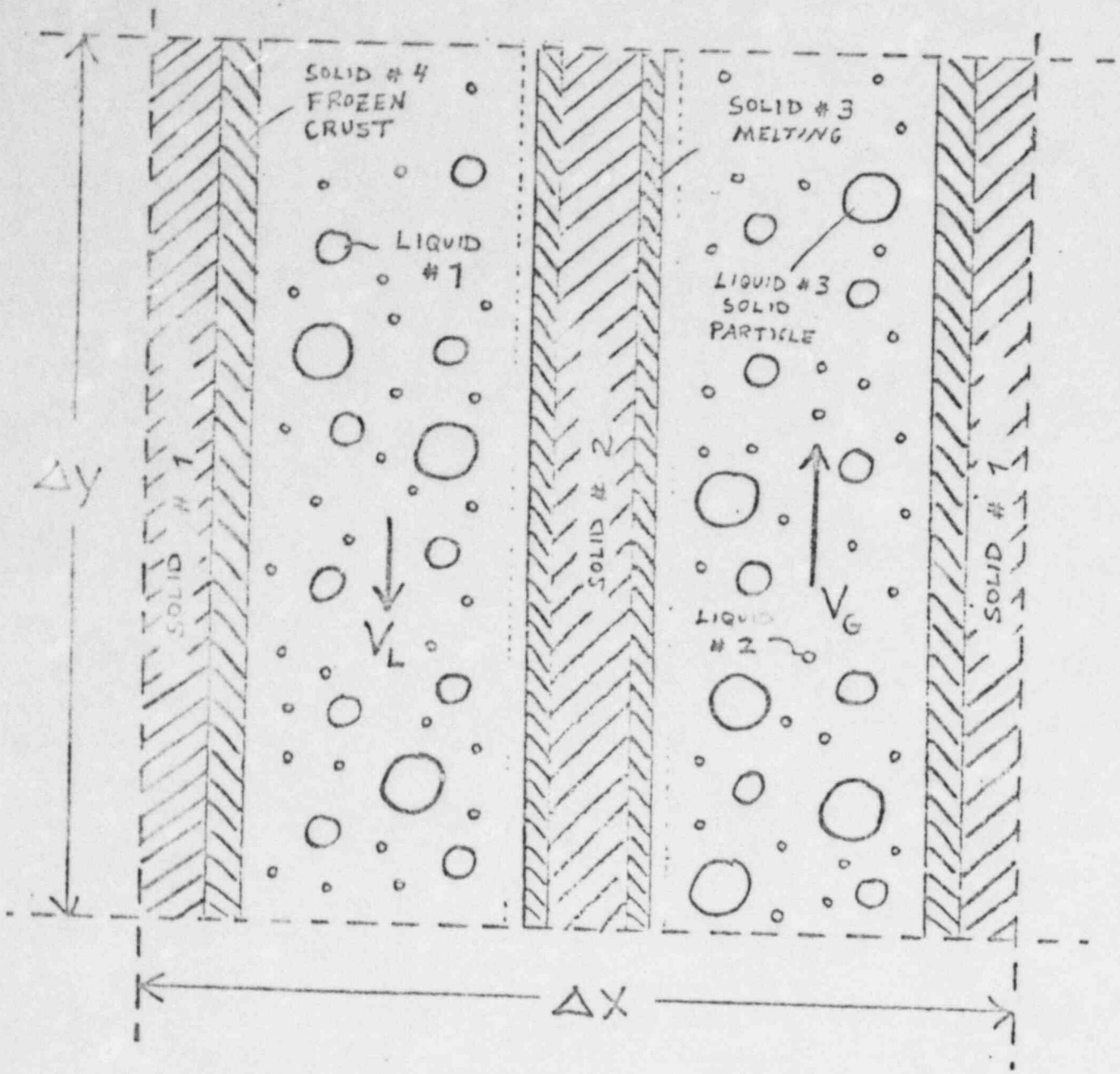

Fig. 1.
Typical ~~mesh cell and component configuration in crab geometry.~~ local region in the freezing and plugging model.

(SECTION A II. 6)

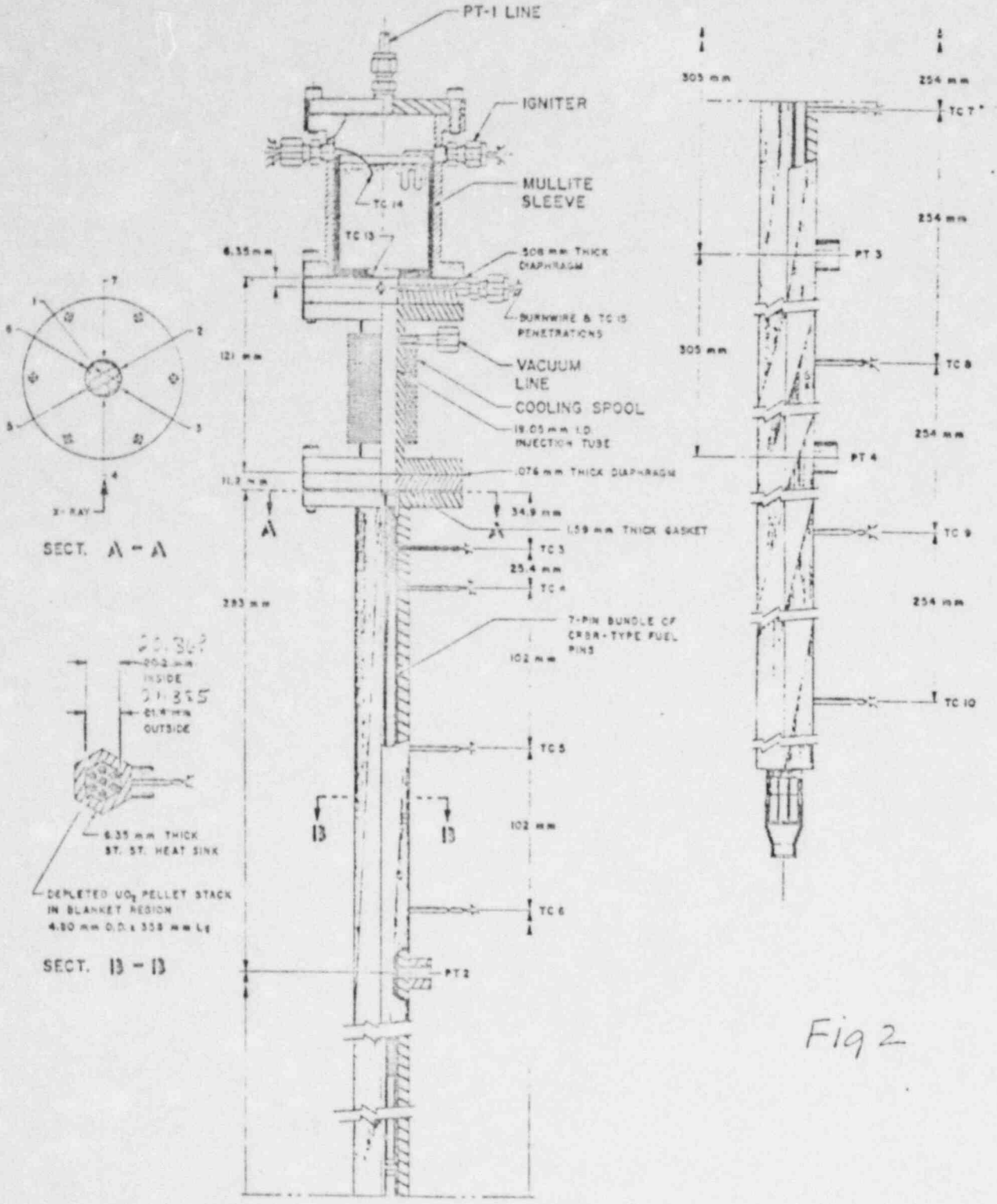

Fig 2

Fig. 1. Experimental apparatus used for CRBR-series fuel freezing experiments. Neg. No. 900-78-395. (X)

AII.6

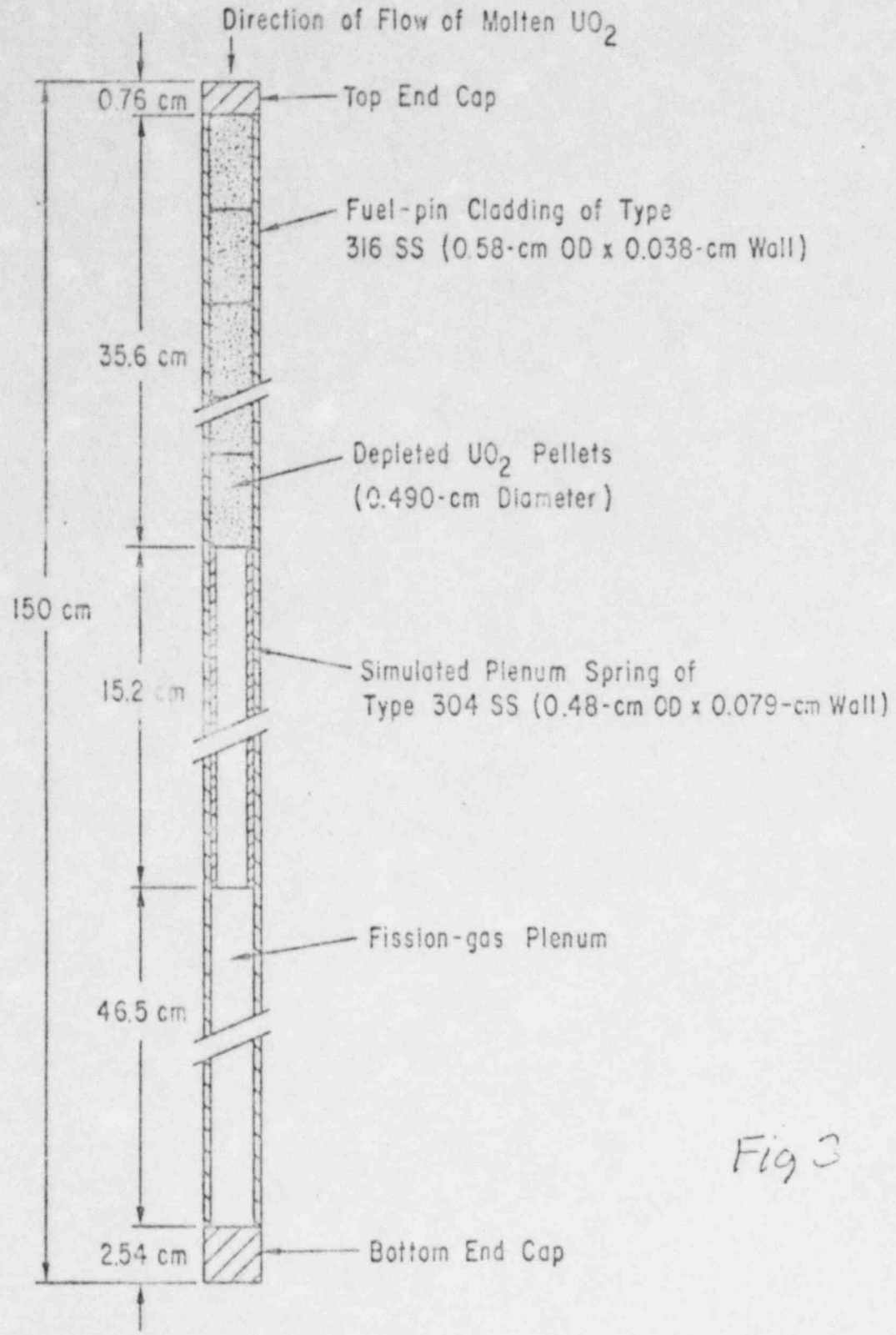

Fig 3

Fig. 3. Configuration of CRBR-type pins used in fuel freezing tests. Neg. No. 900-78-1150.(z)

A.II.6

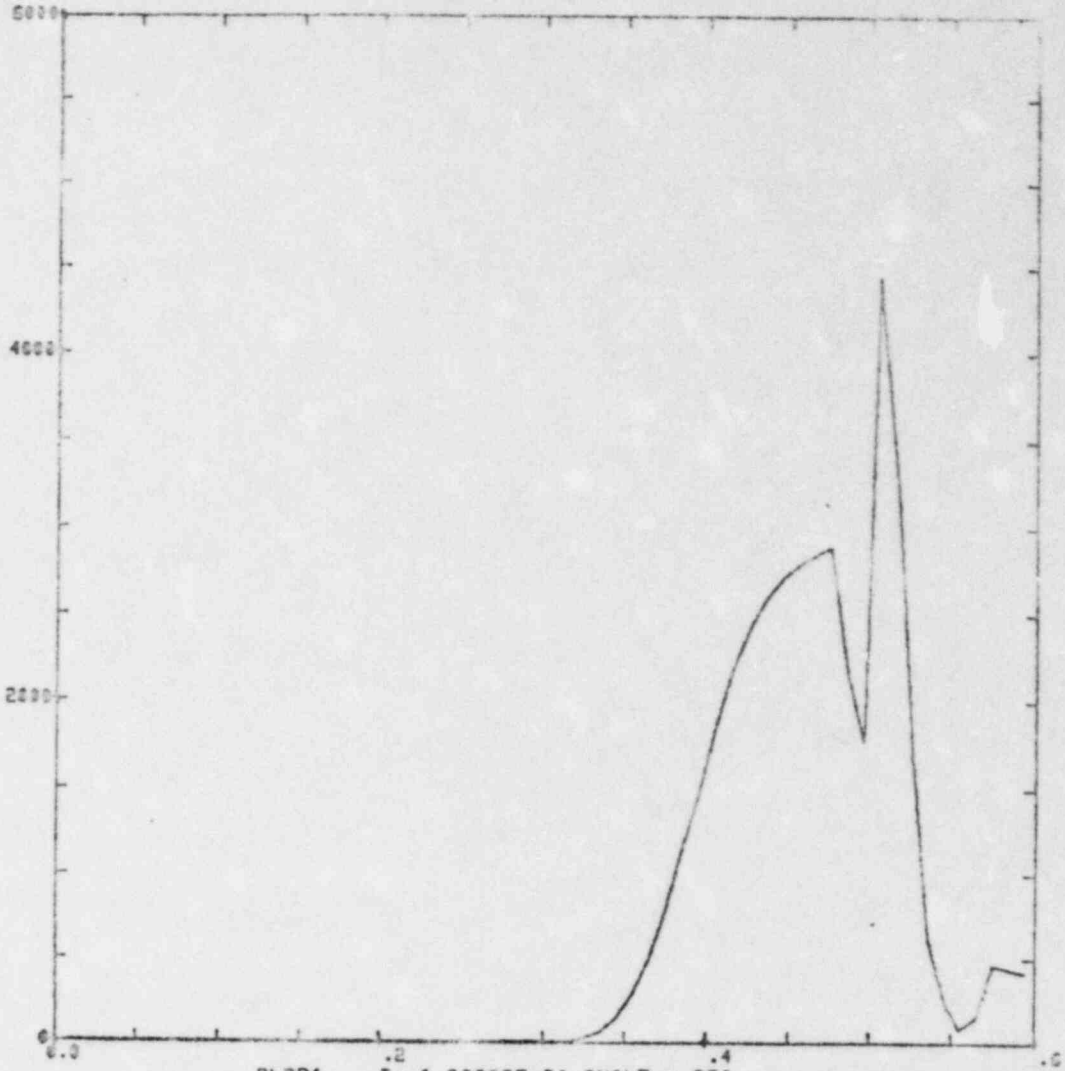
6000
4000
2000
0
0.0
.2
.4
.6
RLBR1 T= 1.00000E-01 CYCLE = 254
MIN= 4.05833E-07 MAX= 4.44000E+03
GAP TEST INVESTIGATION TD5G

Fig 4

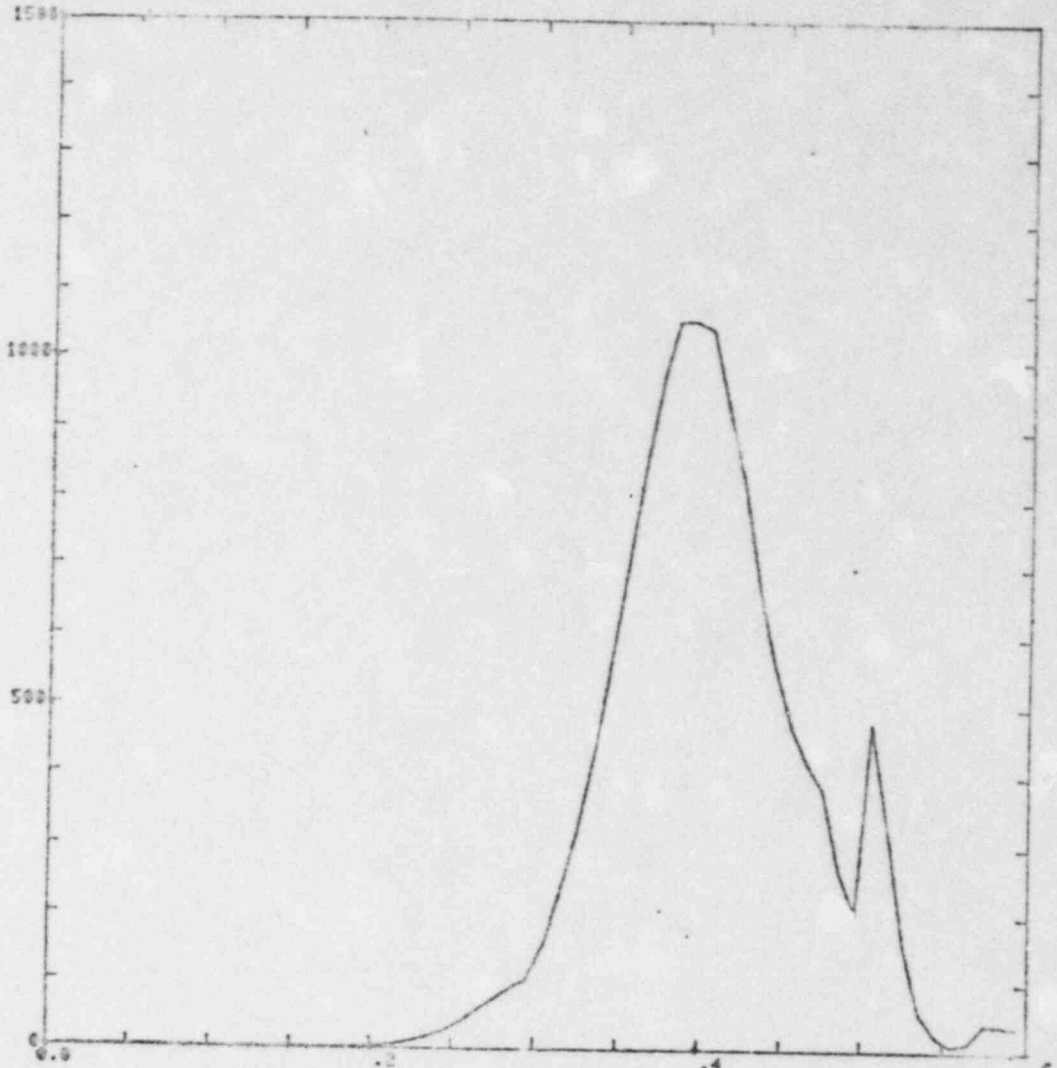
1500
1000
500
0
0.0
.2
.4
.6
RLBR3 T= 1.000000E-01 CYCLE = 254
MIN= 5.81730E-05 MAX= 1.05520E+03
GAP TEST INVESTIGATION T050

Fig 5

A.II.6

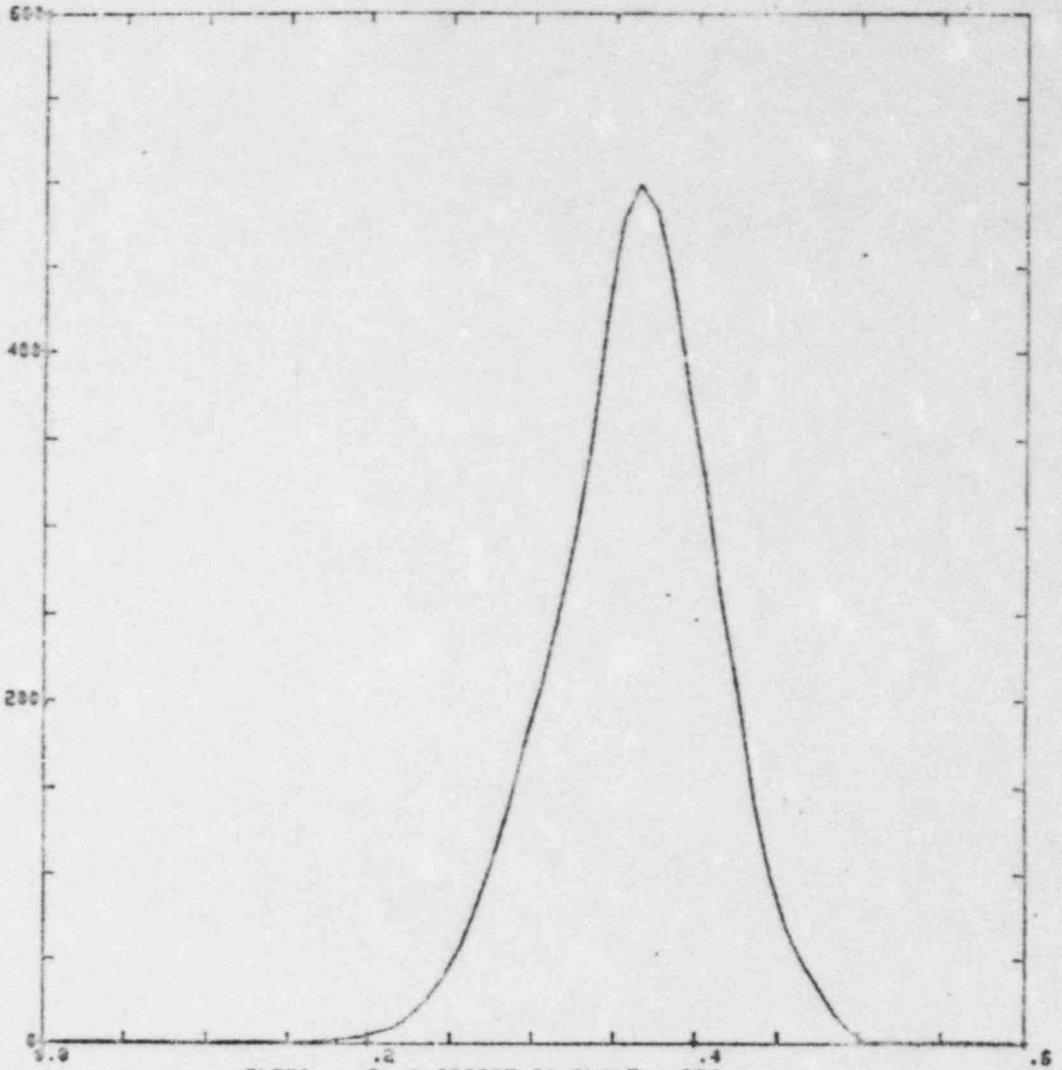
600
400
200
0
0.0
.2
.4
.6
RLBM6 T= 1.00000E-01 CYCLE = 254
MIN= 3.33279E-04 MAX= 4.97670E+02
GAP TEST INVESTIGATION T05G

Fig 6

AII.G

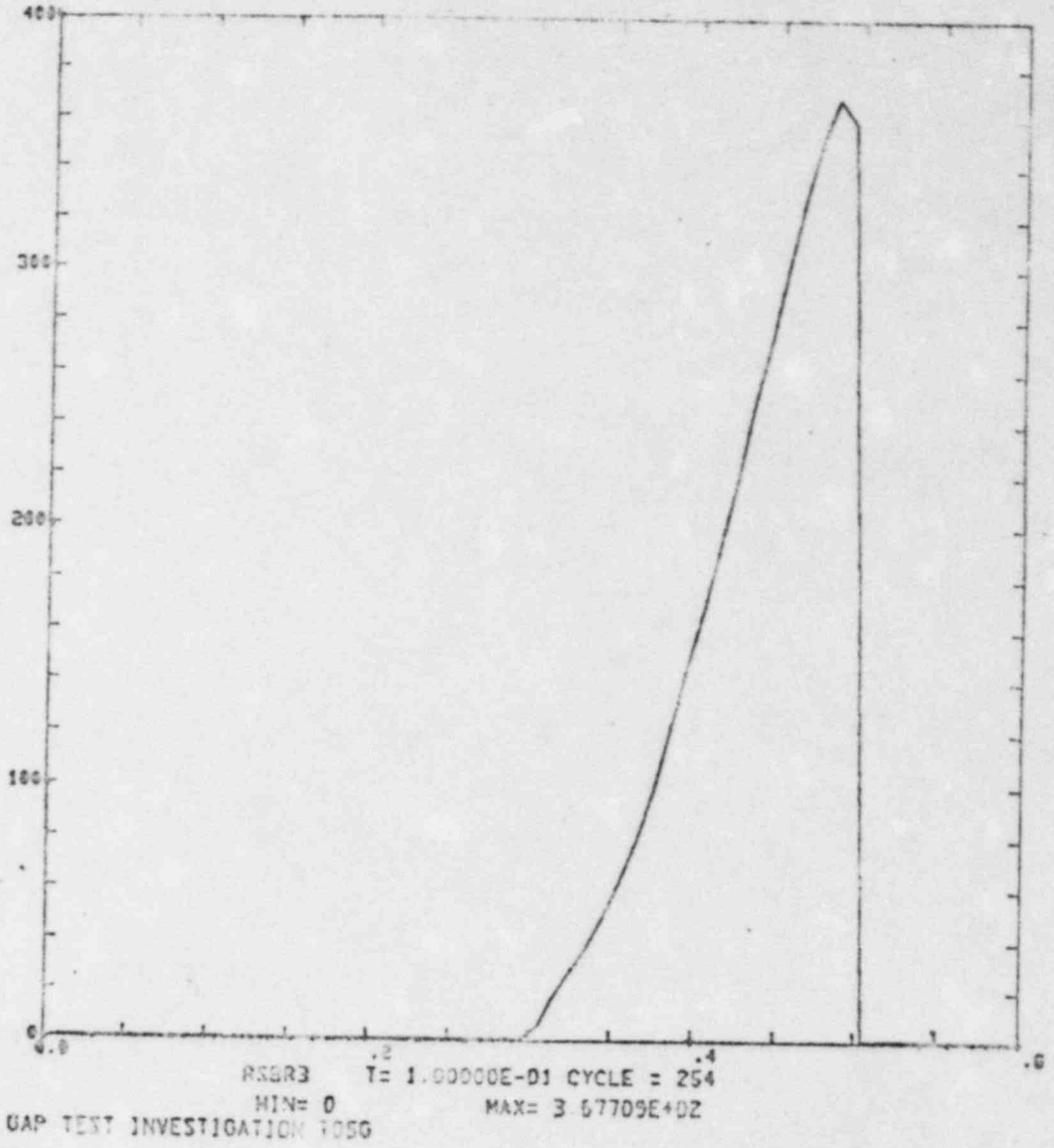
400
300
200
100
0
.0
.2
.4
.6
RSGR3 T= 1.00000E-01 CYCLE = 254
MIN= 0 MAX= 3.67709E+02
GAP TEST INVESTIGATION RDSG

Fig 7

A.M.C

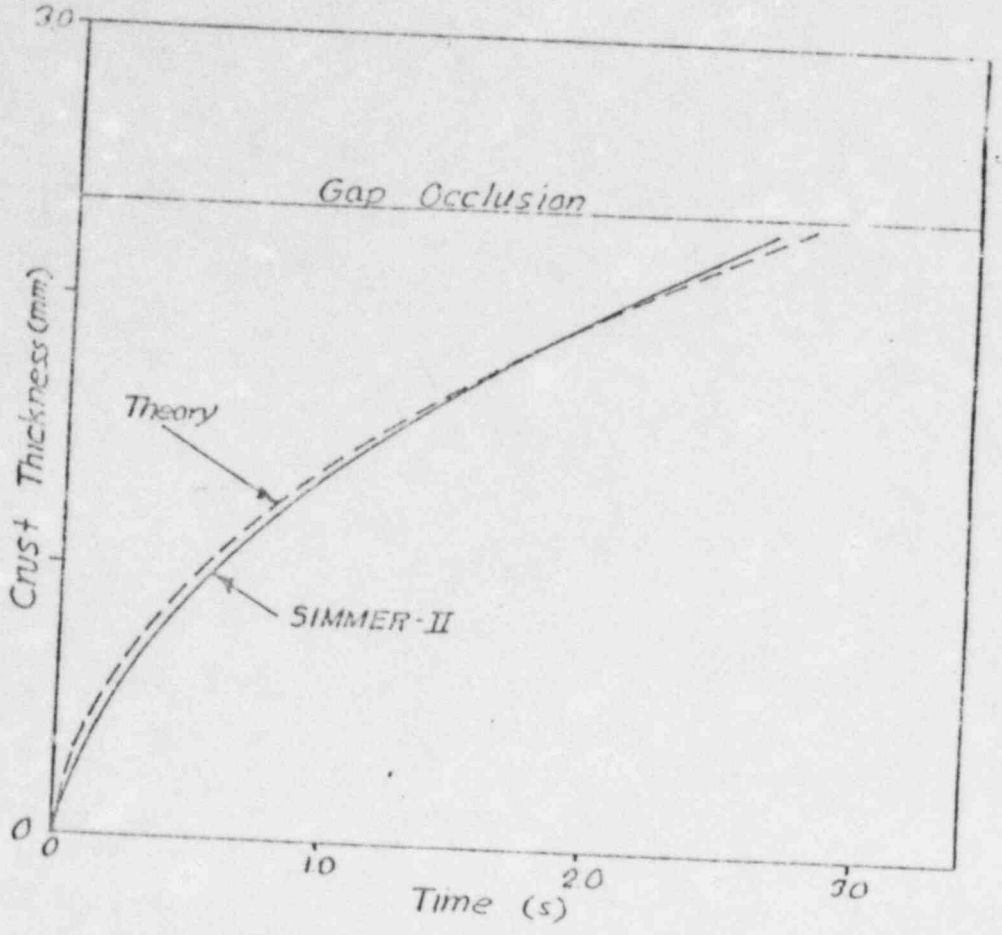
30
Gap Occlusion
Crust Thickness (mm)
Theory
SIMMER-II
0
0
10
20
30
Time (s)

Fig 8

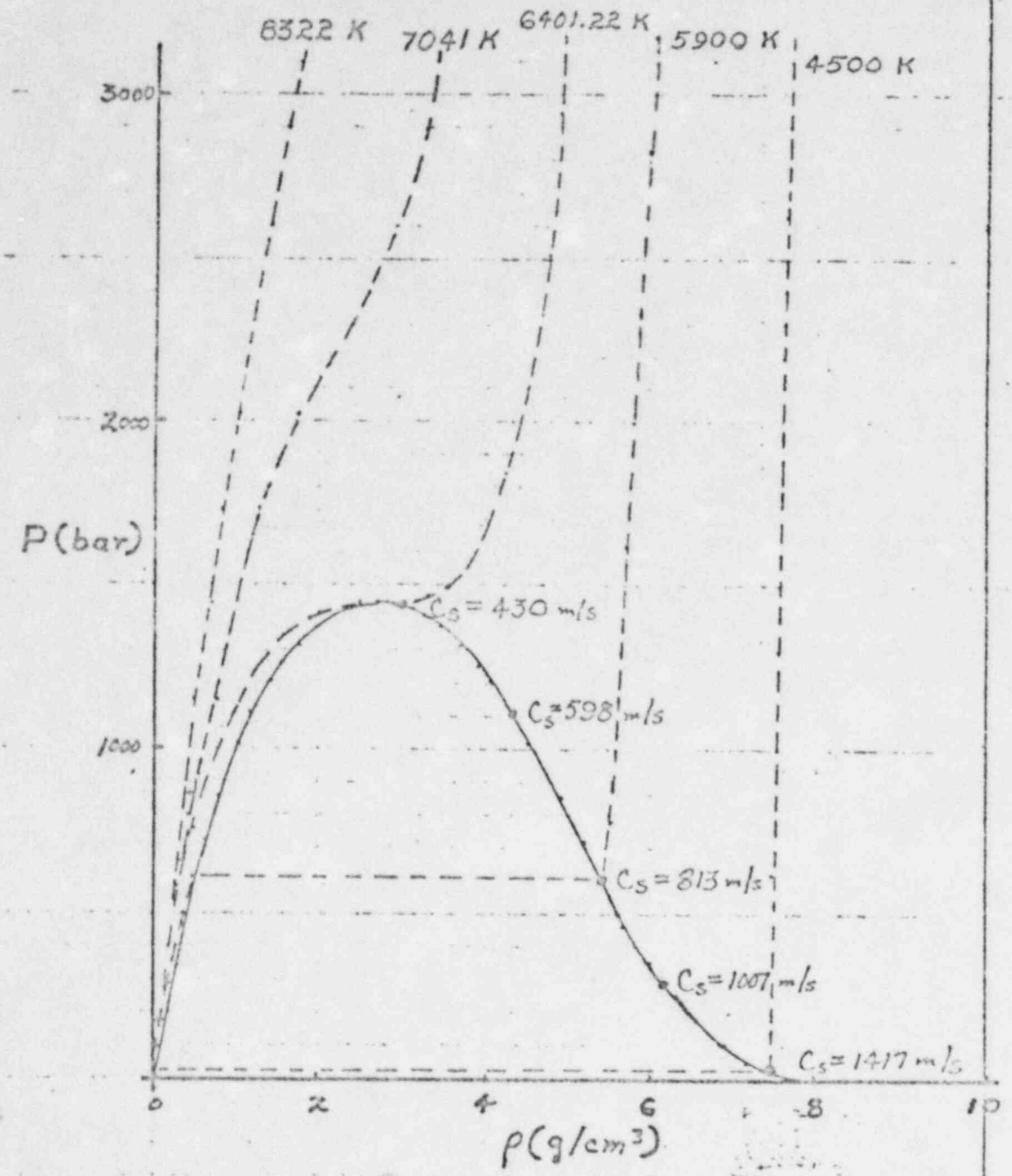
8322 K
7041 K
6401.22 K
5900 K
4500 K
3000
2000
1000
P(bar)
C_s = 430 m/s
C_s = 598 m/s
C_s = 813 m/s
C_s = 1007 m/s
C_s = 1417 m/s
0
2
4
6
8
10
ρ(g/cm³)

Fig. 1

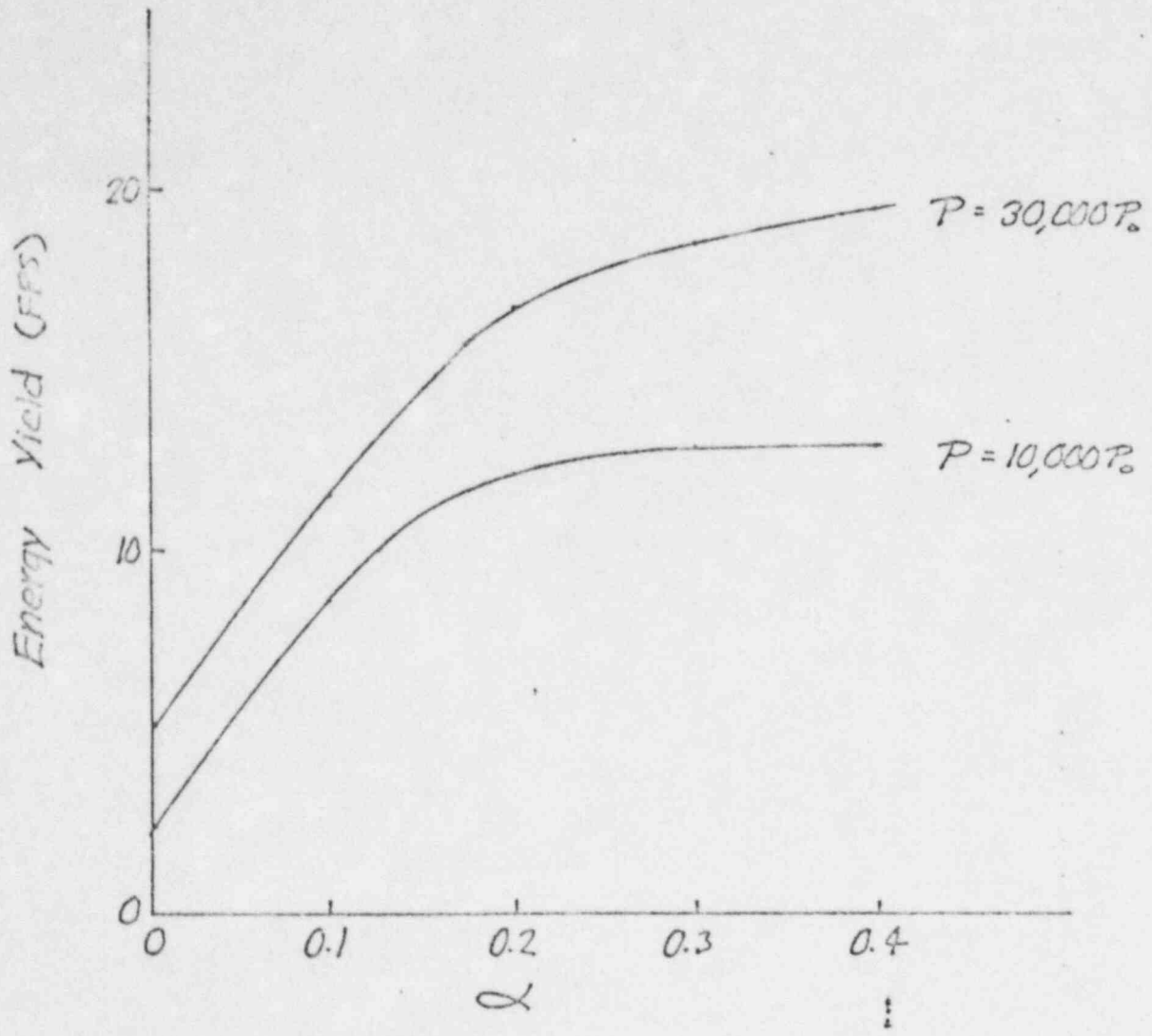

Fig 2

WORTH OF FUEL AND STEEL 1DD26C

$\alpha_{steel} = 0.24$

$\alpha_{fuel} = 0.39$

$\alpha_{void} = 0.37$

$c = f(T)$; min = 400m/s

$P = 10{,}000\ P_o$

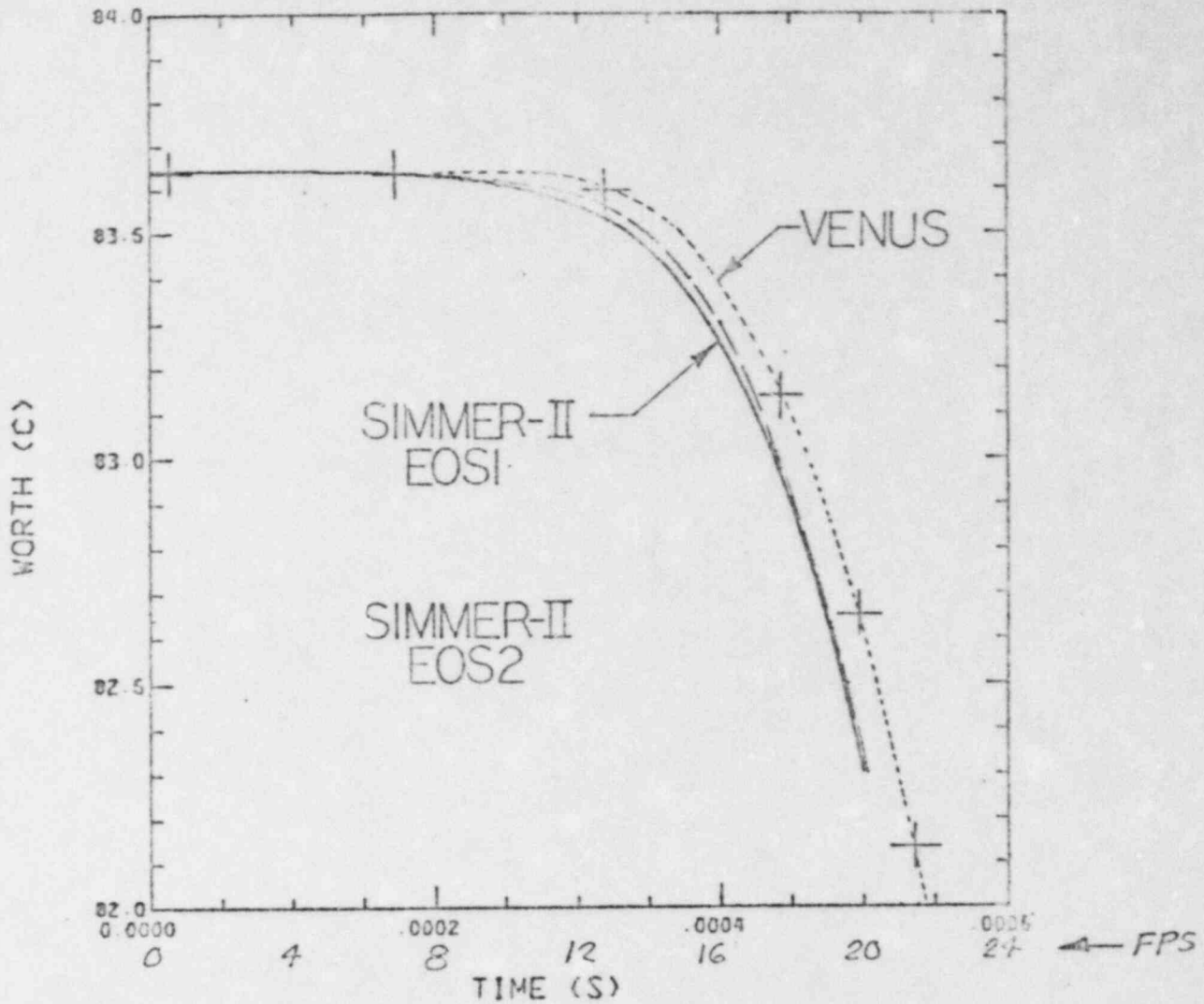

Fig 3

II.7

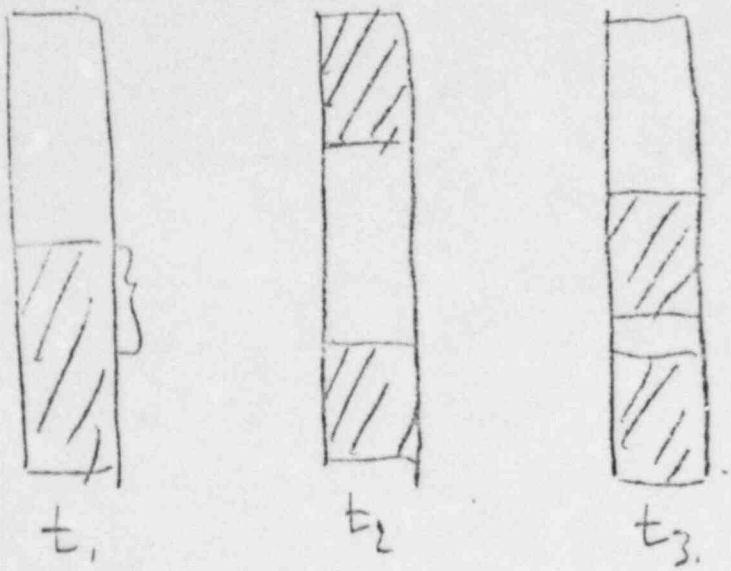

Fig 4

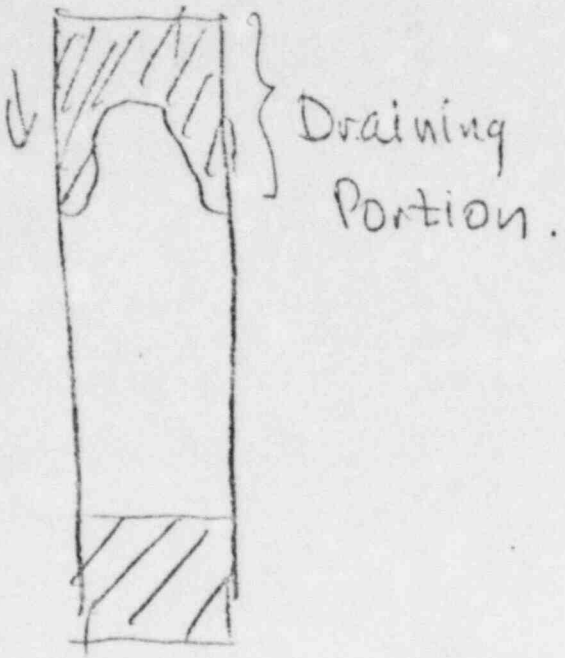

Fig. 5

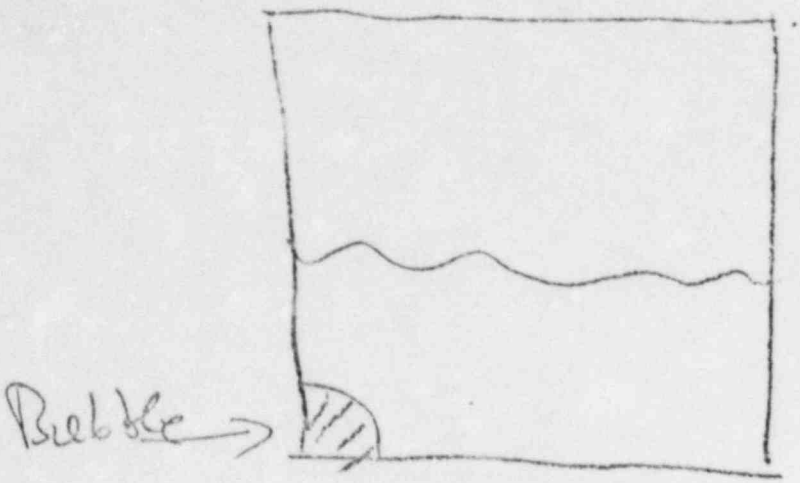

Fig. 6

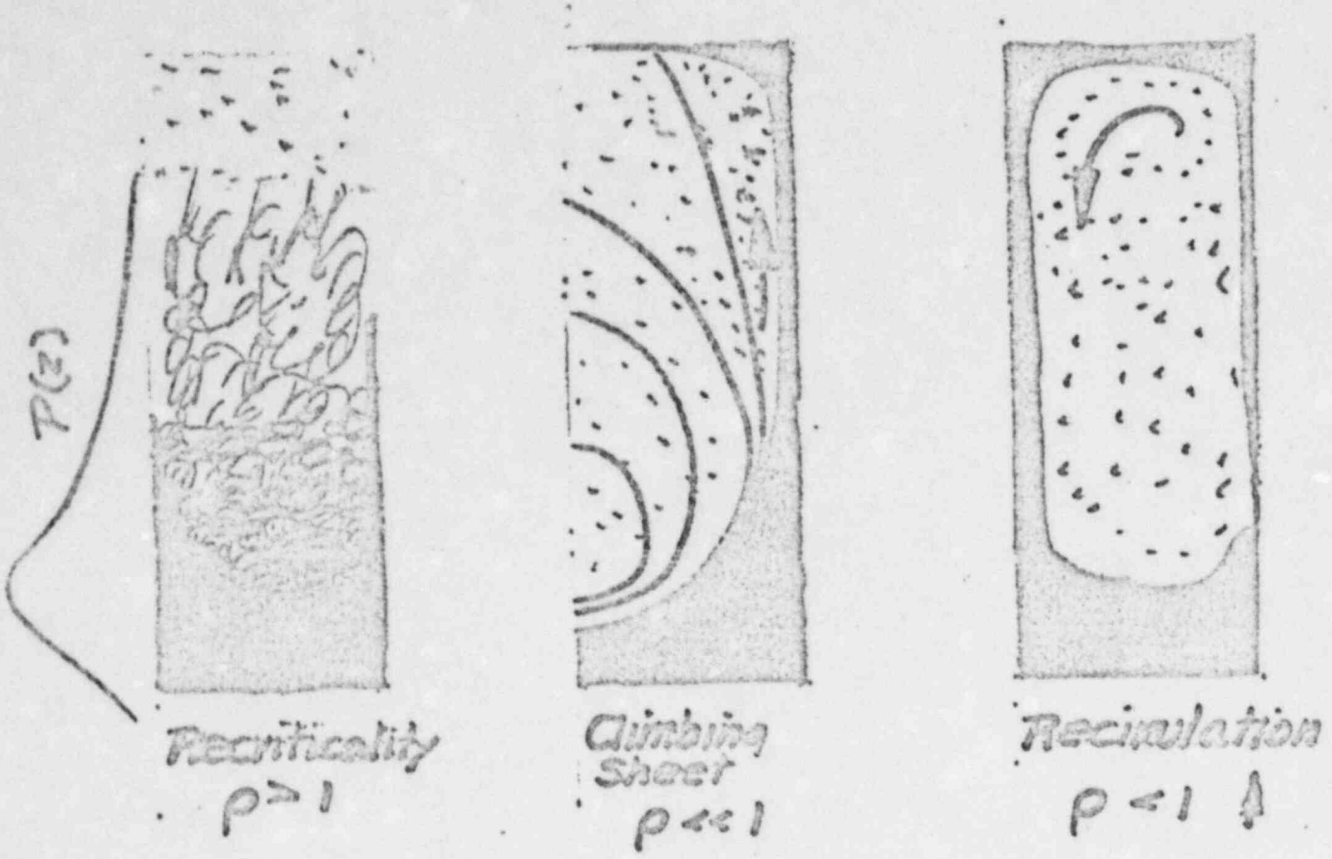

Fig. 7.

DISRUPTION PHASE ENERGETICS
(Whole-core homogenized pcol)

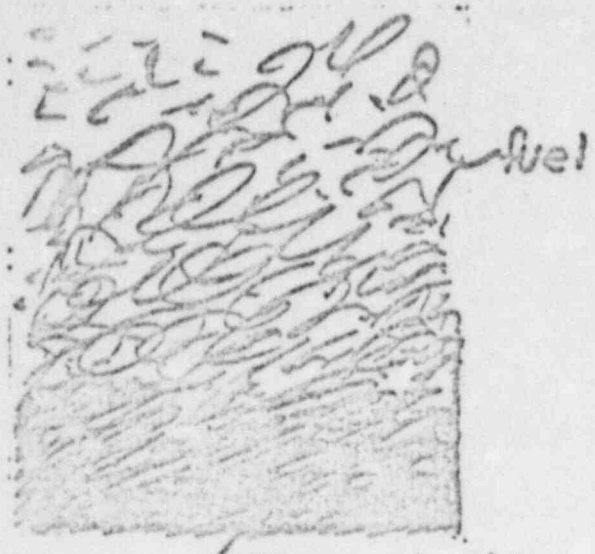

LIB material
$\rho = 0$ ↑

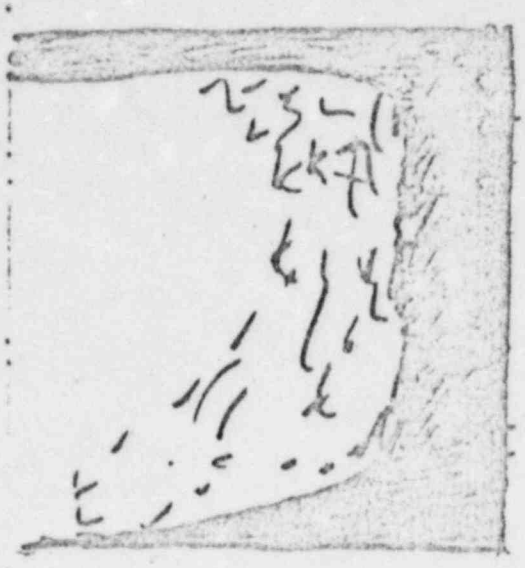

$\rho << 0$ Post burst

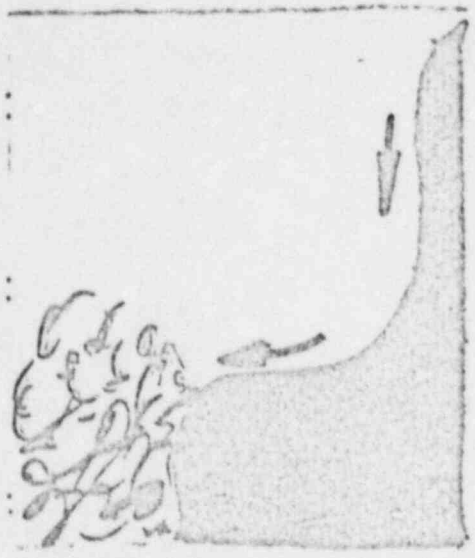

Slash-in
$\rho < 0$ ↑
$\dot{\rho} = 100$ $/s

$\dot{\rho} = 300$ $/s
10

Fig 8

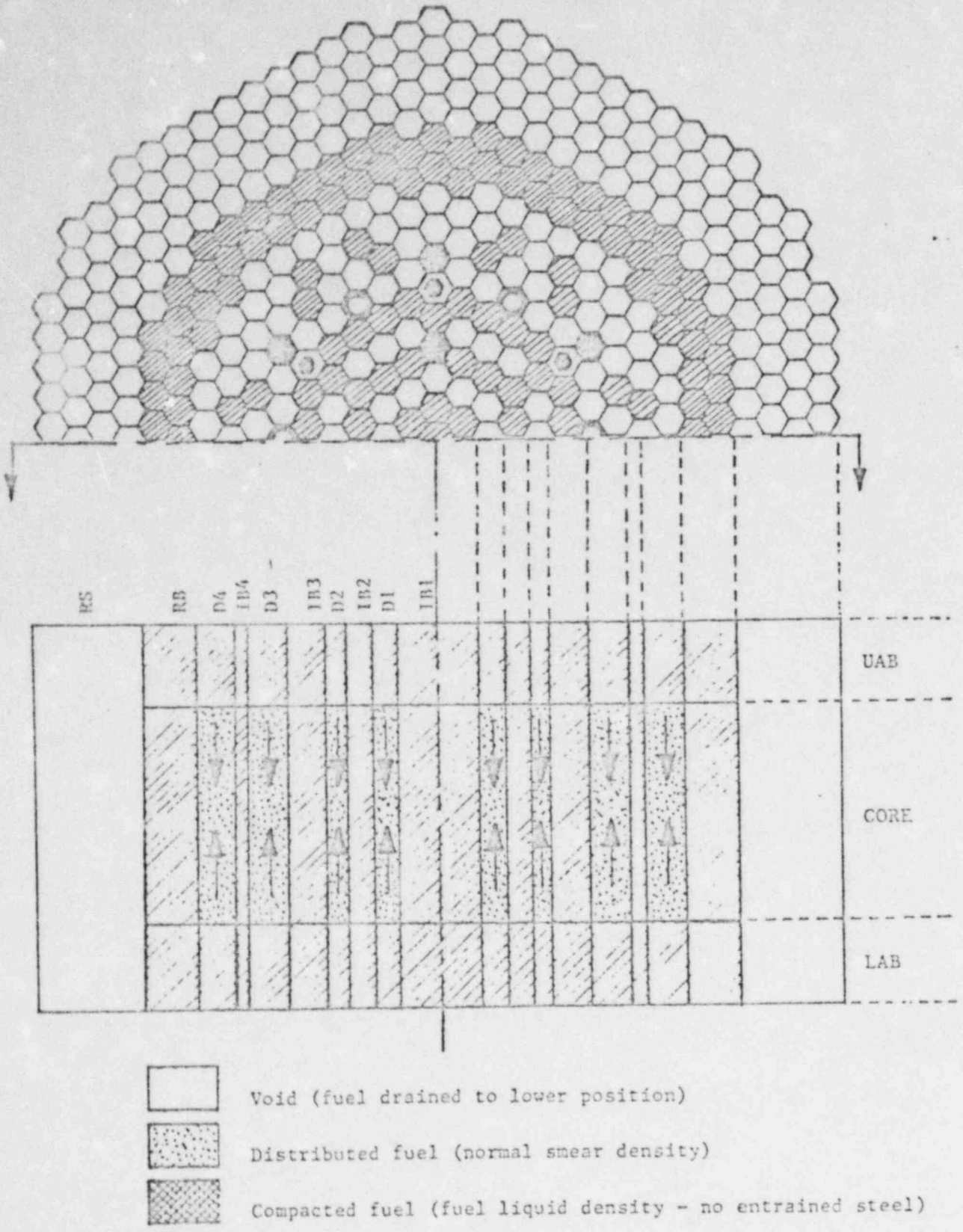

(2)

Config 0

Initialing Phase fuel configuration with total coherent

Fig. 9a

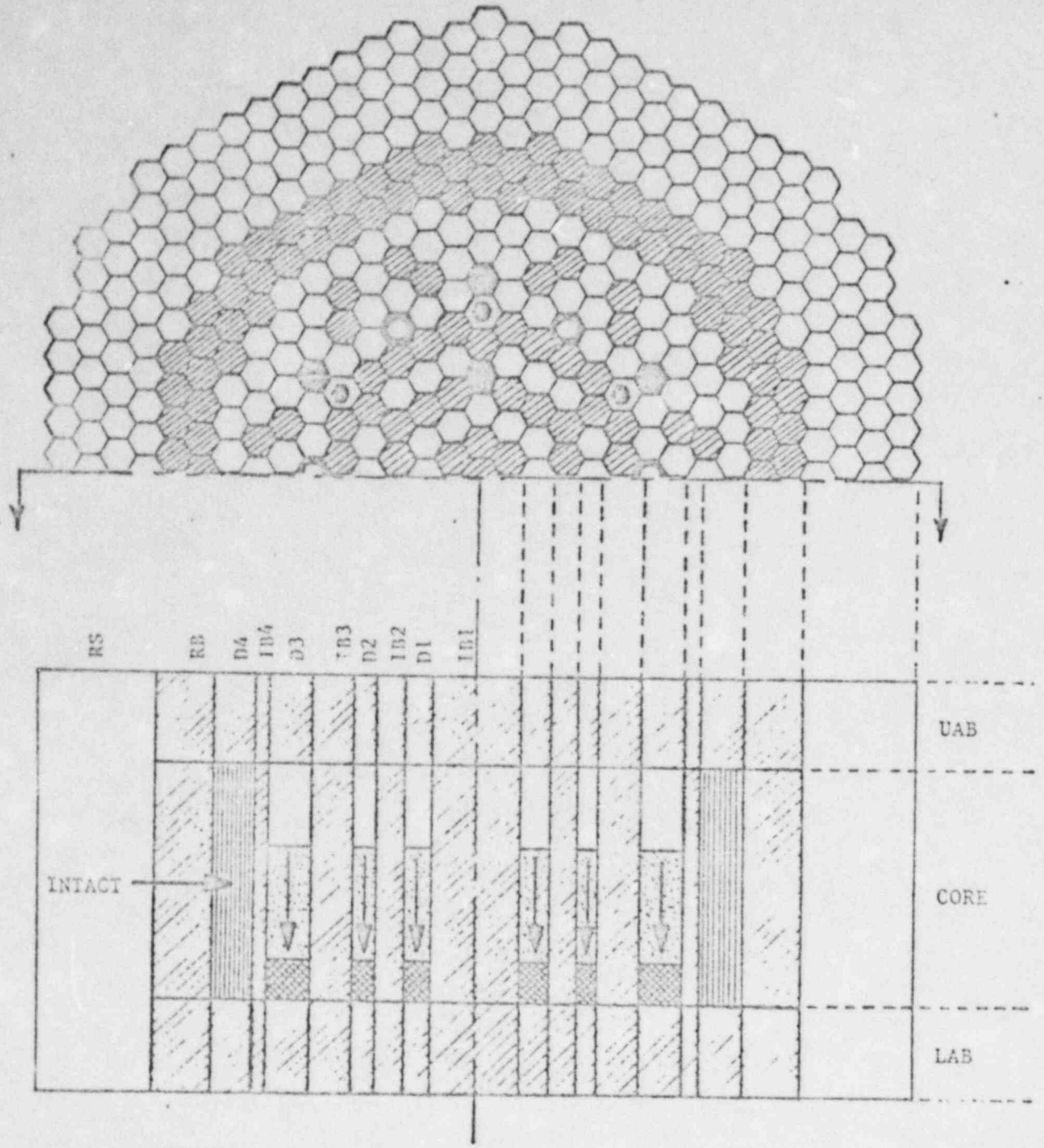

(4)

Config 2
Early M.P. with
reduced inventory
88 2.

Fig 9L

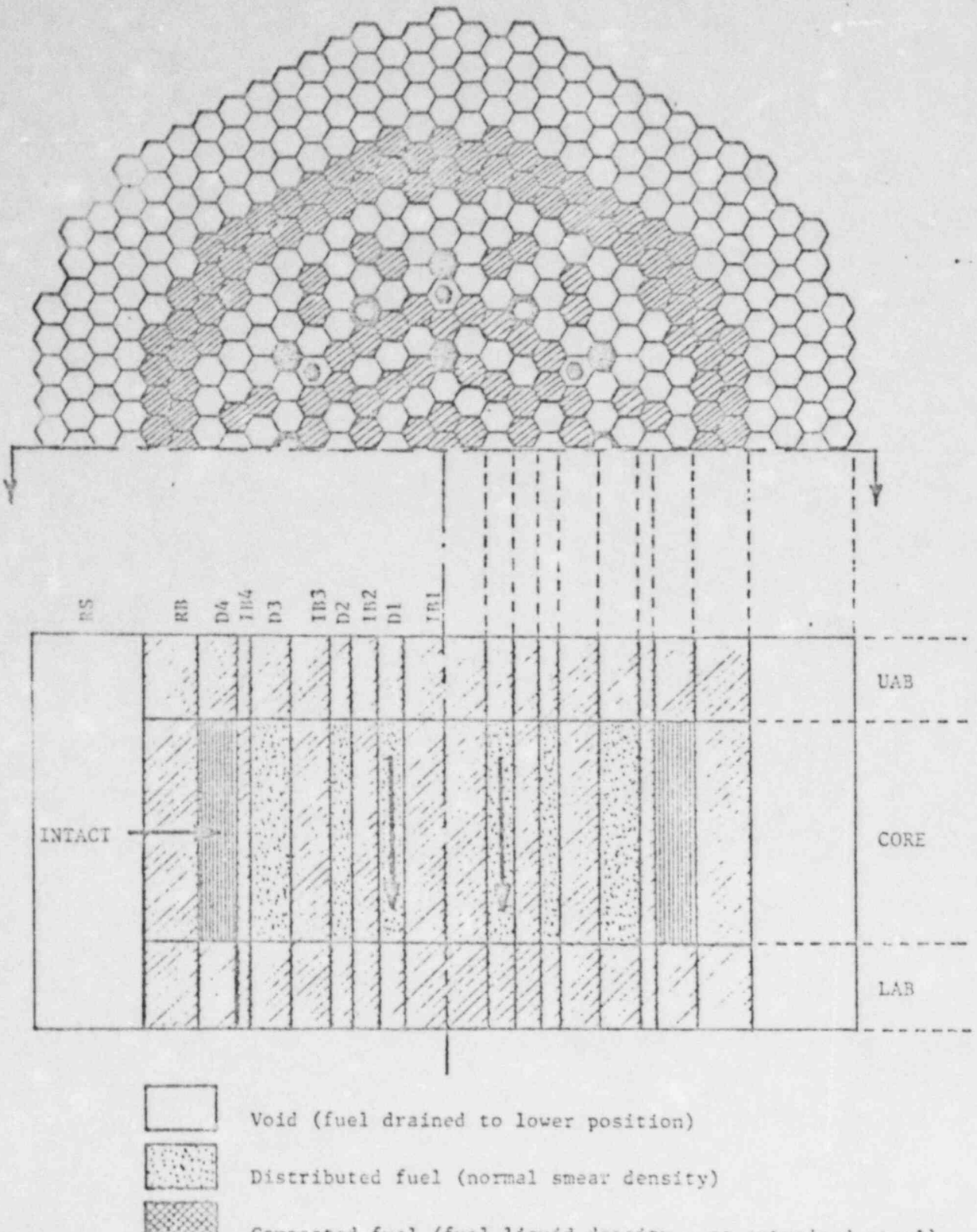

(5)
Config 3
Early disruption
- local compaction
event.

Fig. 9c

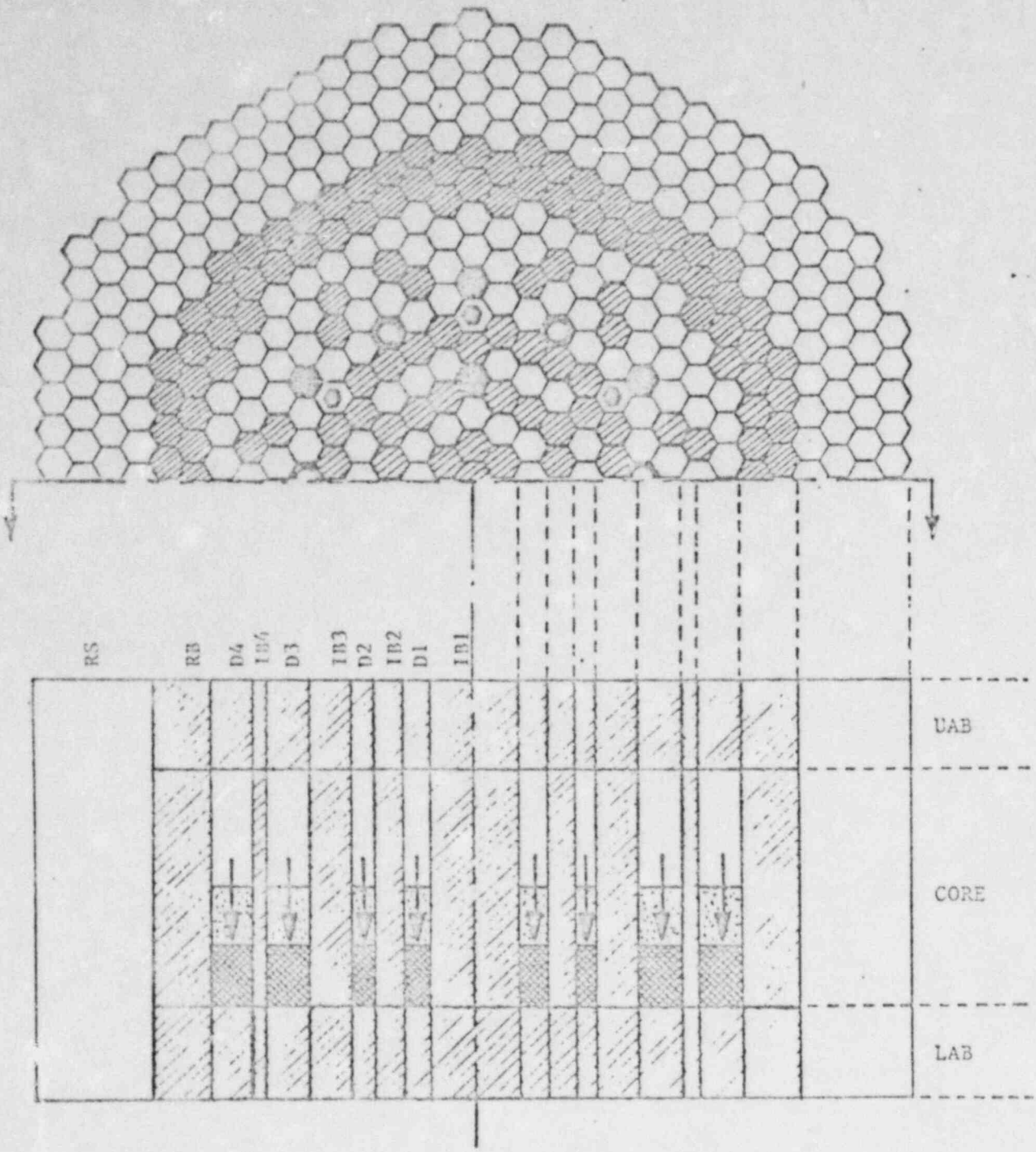

Void (fuel drained to lower position)

Distributed fuel (normal smear density)

Compacted fuel (fuel liquid density - no entrained steel)

(a)
Config 5
late M.P.
reduced invent.
70%

Fig. 9d.

MESH SETS

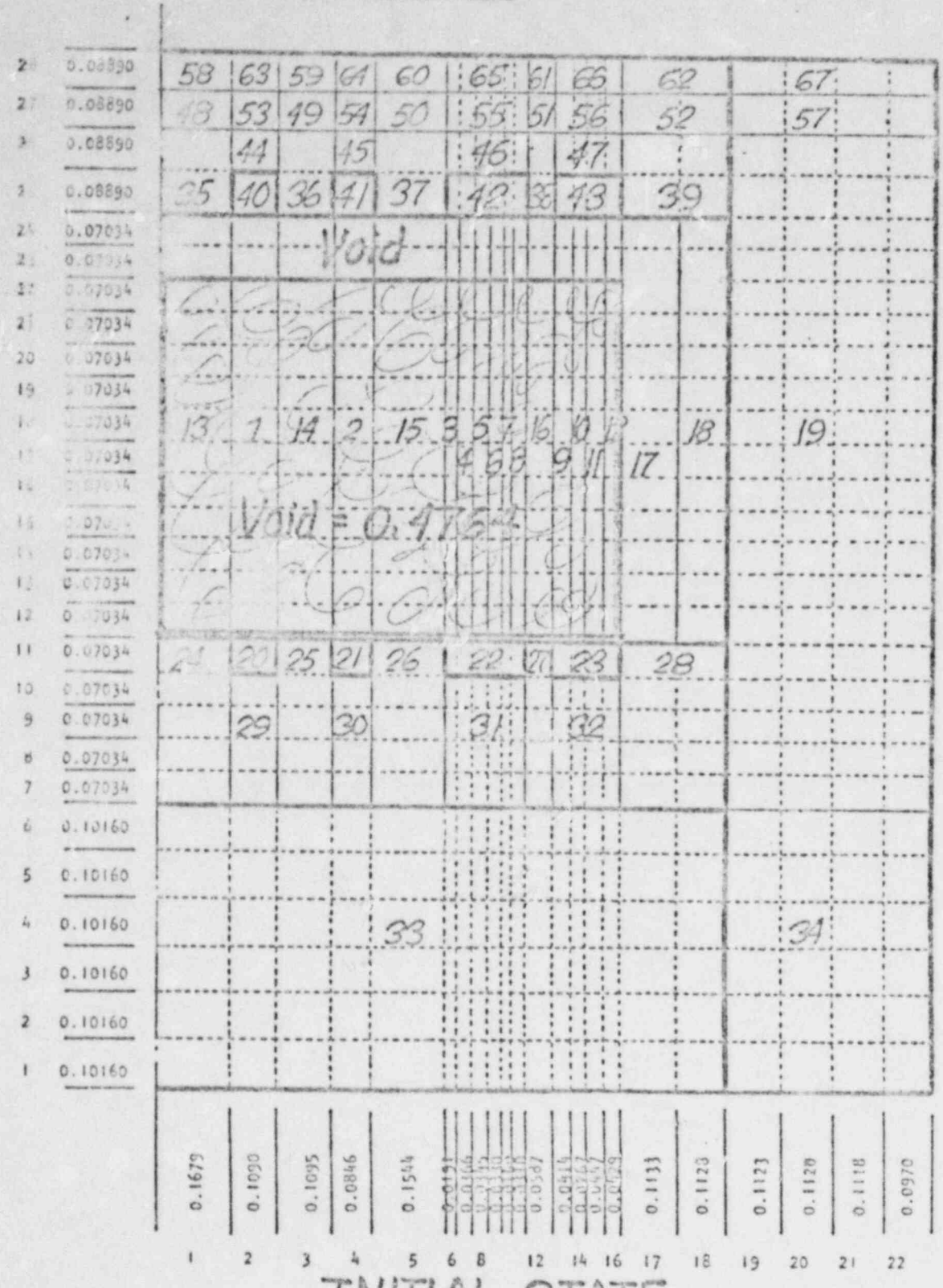

INITIAL STATE

K_{eff} = 1.01957

fig 10a.

MESH SETS

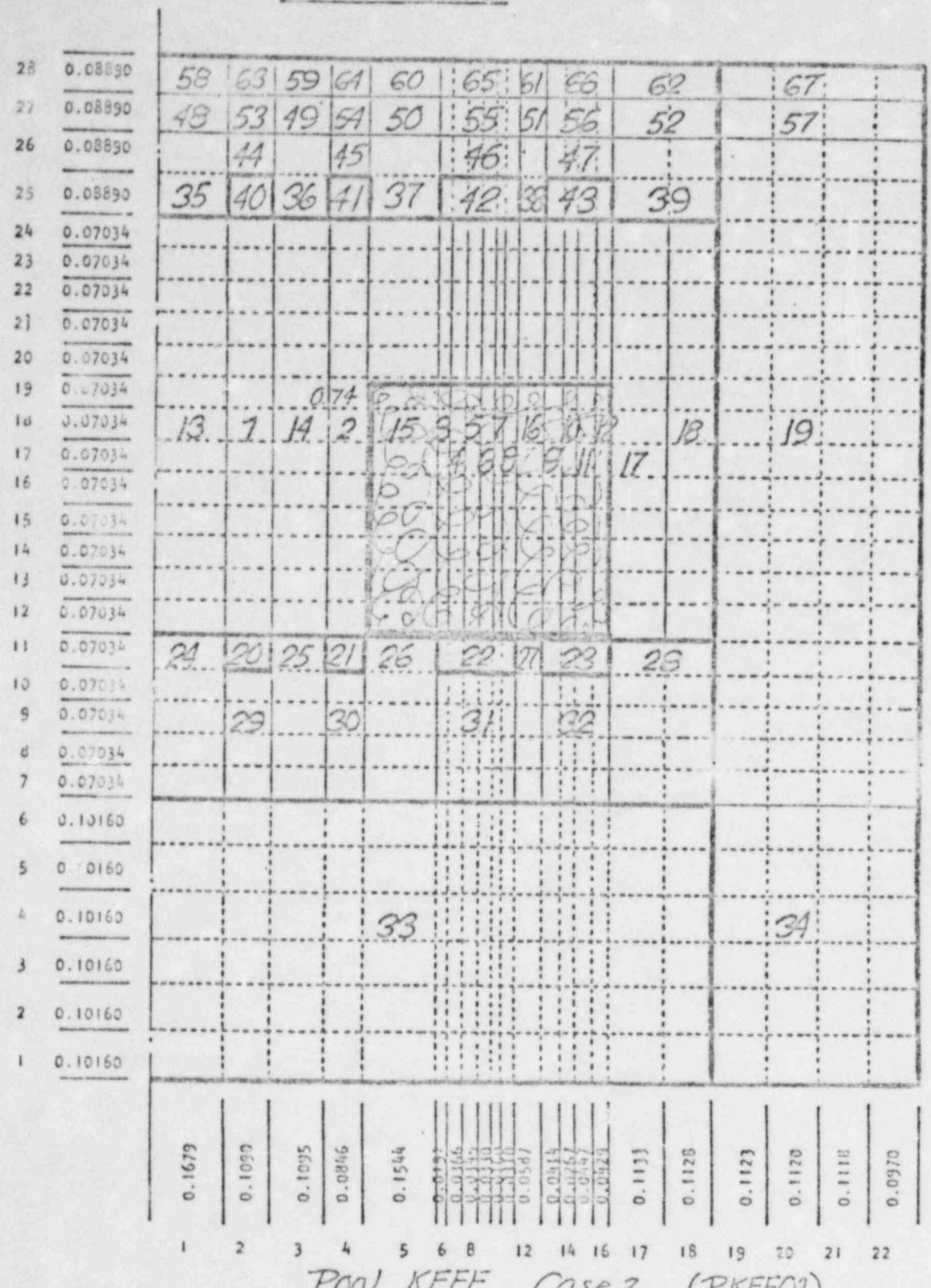

Pool KEFF Case 2 (PKFF02)

Fig 10.b

CALCULATIONAL MODEL FOR SIMMER-II ANALYSIS OF GAP FUEL REMOVAL
DURING HYPOTHETICAL CORE DISRUPTIVE ACCIDENTS IN THE CRBR

MESH SETS

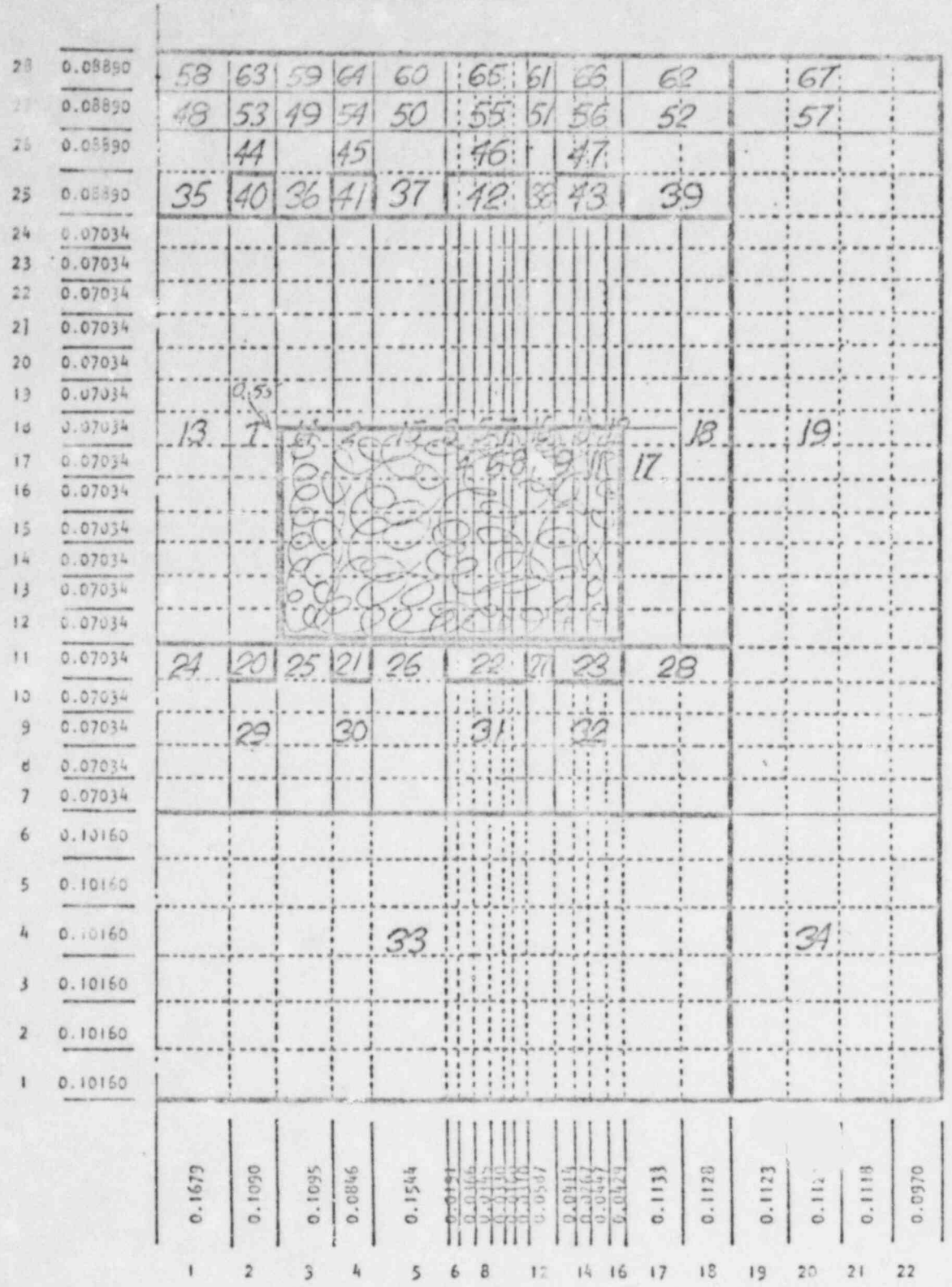

Pool KEFF Case 2a (PKEFF2a)

Fig. 10.c

CALCULATIONAL MODEL FOR SIMMER-II ANALYSIS OF GAP FUEL REMOVAL
DURING HYPOTHETICAL CORE DISRUPTIVE ACCIDENTS IN THE CRBR

MESH SETS

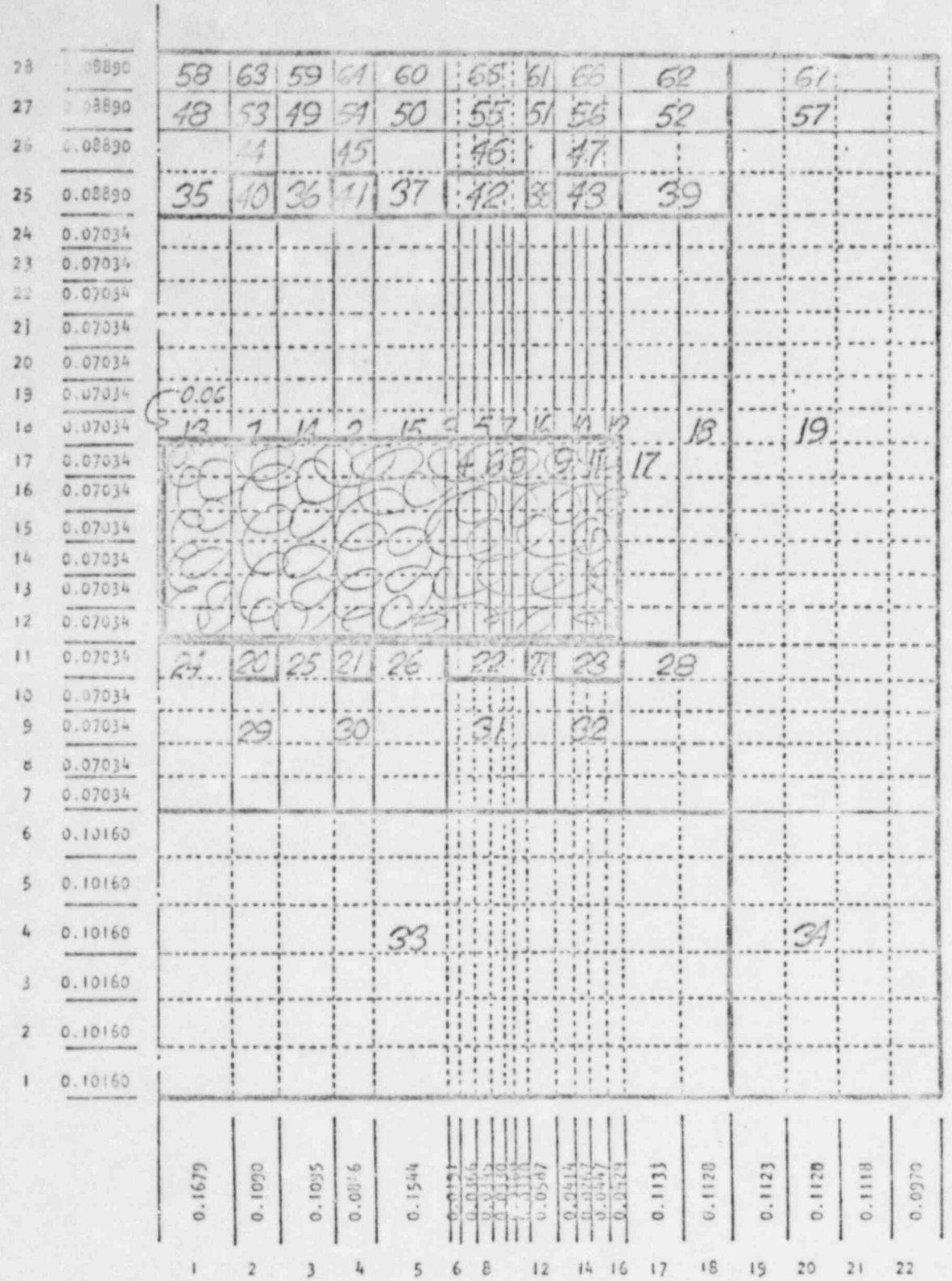

Pool KEFF Case 2b (PKEFF2b)

Fig. 10.d

CALCULATIONAL MODEL FOR SIMMER-II ANALYSIS OF GAP FUEL REMOVAL
DURING HYPOTHETICAL CORE DISRUPTIVE ACCIDENTS IN THE CRBR

MESH SETS

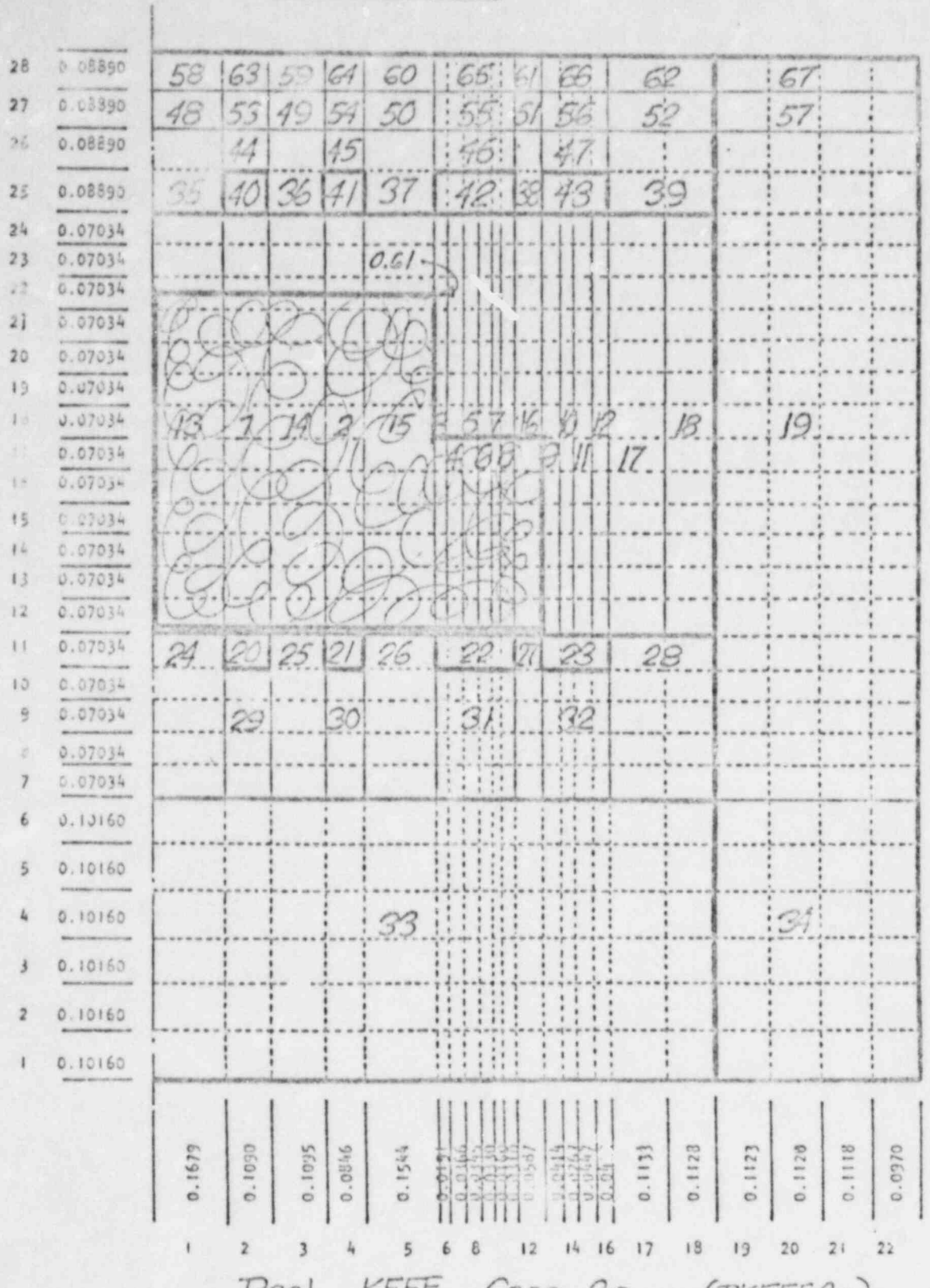

Pool KEFF Case 2c (PKEFF2c)

10.e

II.7

POOL DEPTH ON AXIAL SPECIFIC POWER PLOTS
IN SLUMPED POOLS FORMED BY
ALL DRIVERS

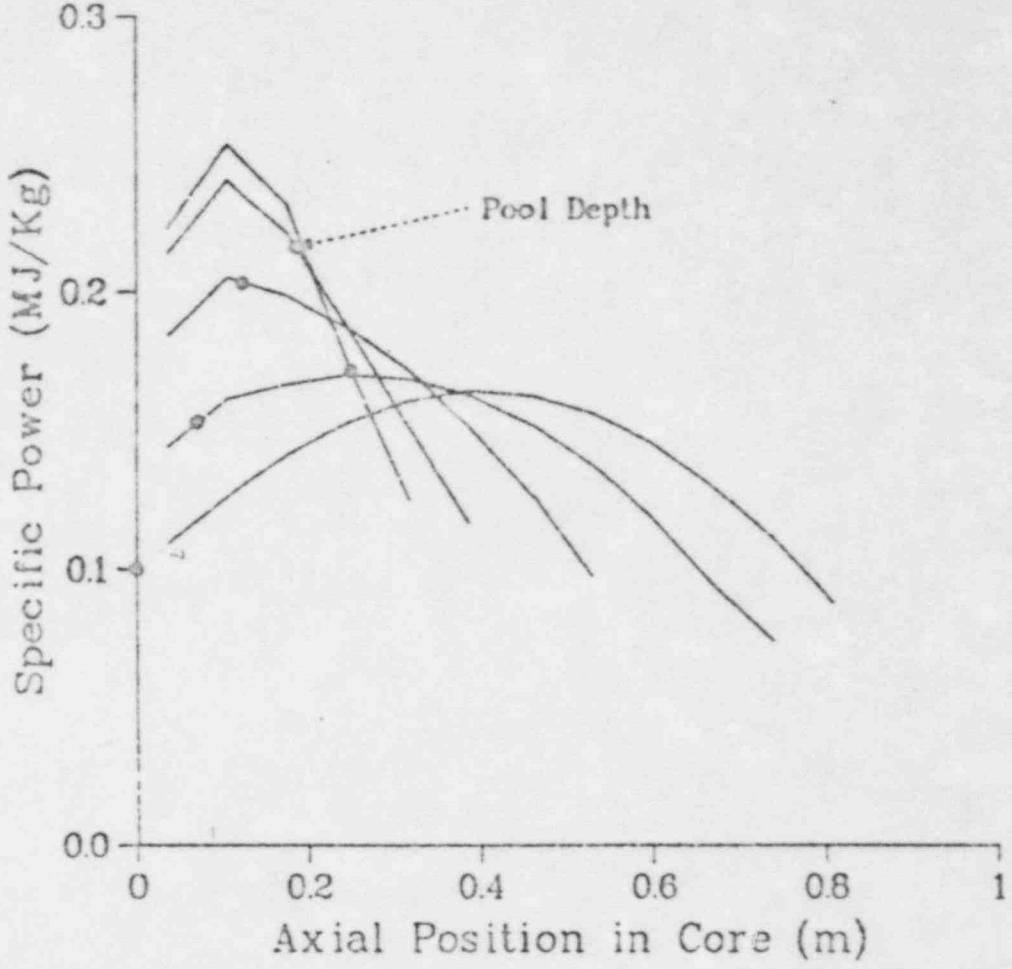

Fig 11

PEAK FLUX LOCATION RELATIVE TO POOL DEPTH
IN ALL DRIVERS

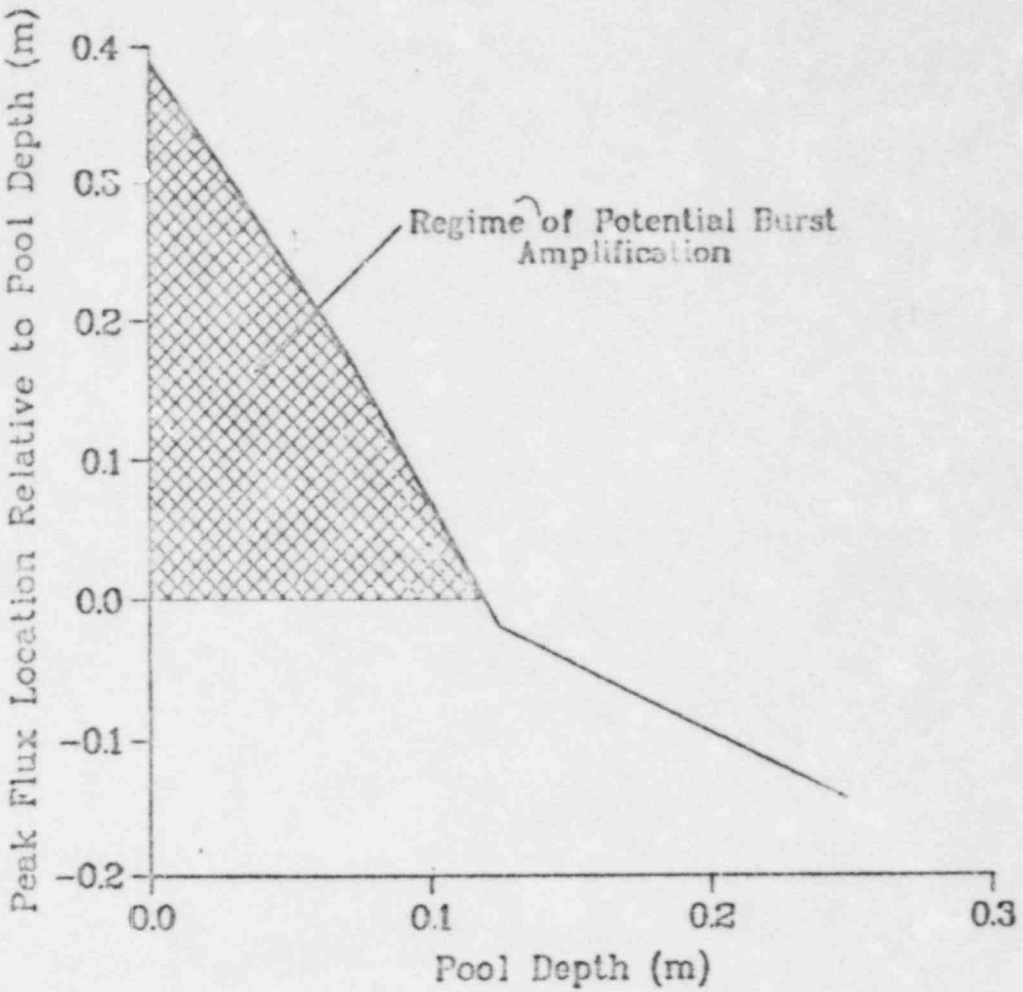

Fig 12

II.7

FISSILE INVENTORY REDUCTION REQUIRED (Δm) vs
POOL DEPTH FOR ALL DRIVERS

(Nominal = 6151 kg)

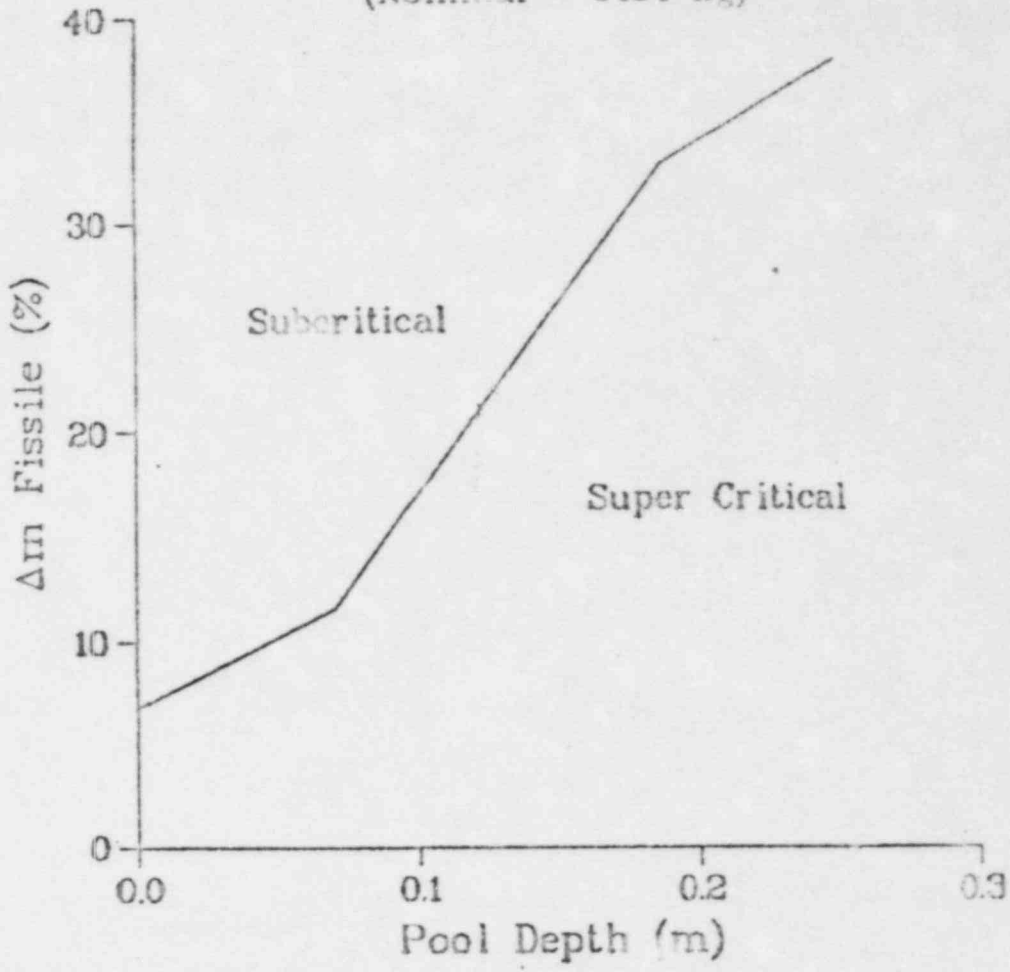

Fig 13

REACTIVITY vs POOL DEPTH FOR SLUMPING OF ALL CRBR DRIVERS

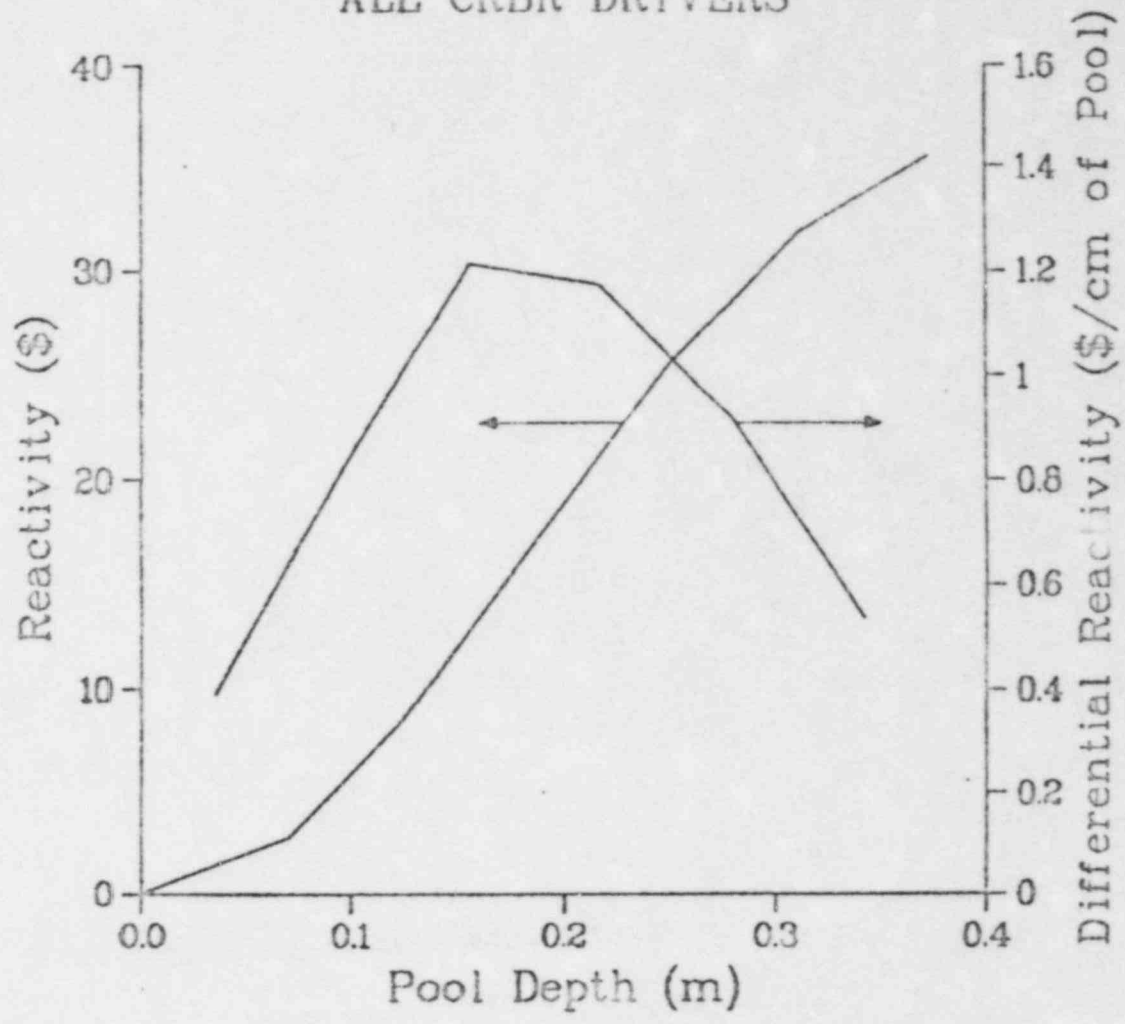

Fig 14

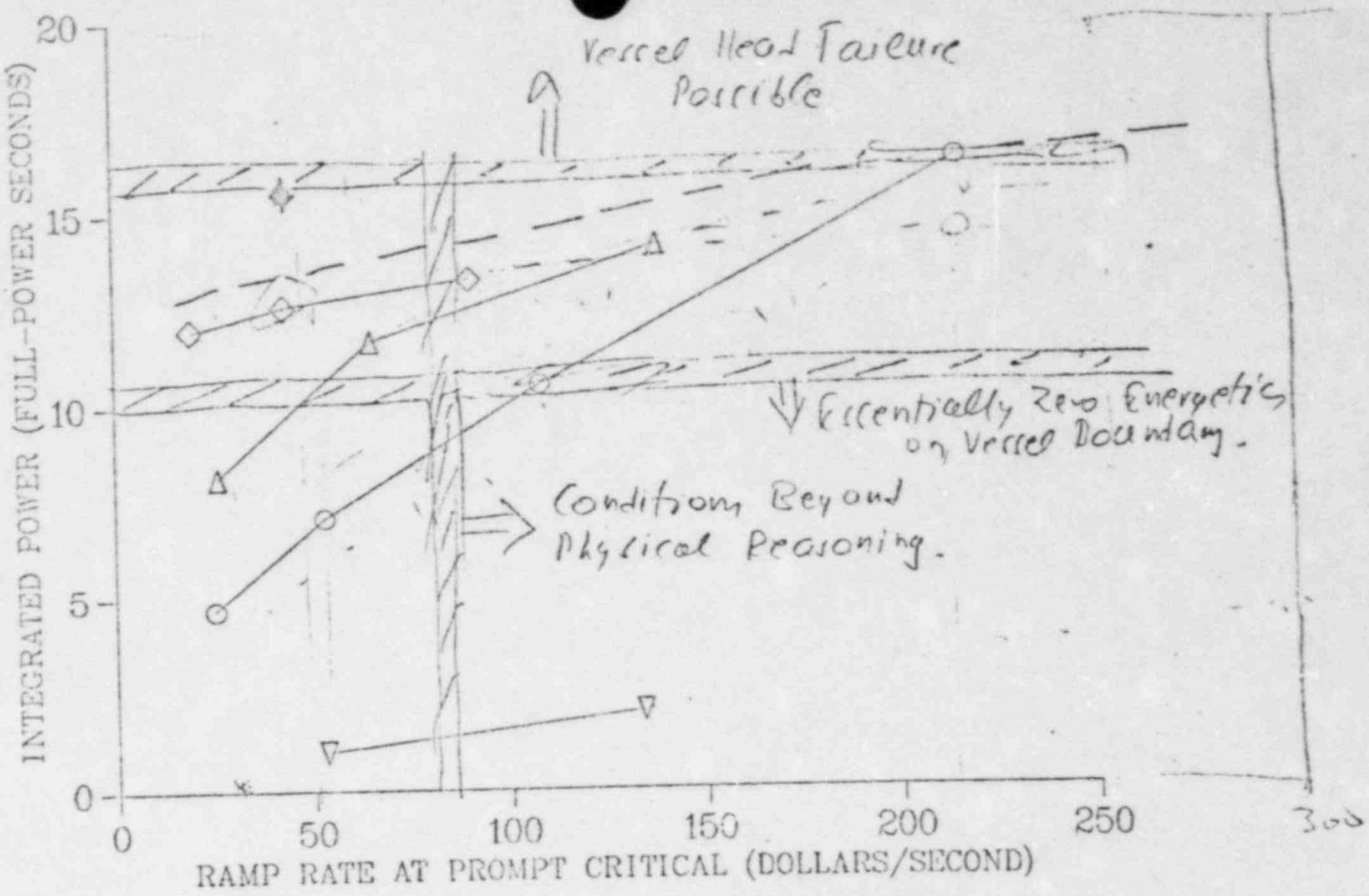

SYMBOL – CONFIGURATION

○ – 0 UNIFORM, SLUMP TO MIDPLANE, ALL DRIVERS, FI
◇ – 2 UNIFORM, SLUMP TO BOTTOM, CENTRAL 3 DRIVERS, 66% FI
△ – 3 UNIFORM, SLUMP TO BOTTOM, CENTRAL 1 DRIVER, FI
▽ – 5 UNIFORM, SLUMP TO BOTTOM, ALL DRIVERS, 70% FI –

Fig 15

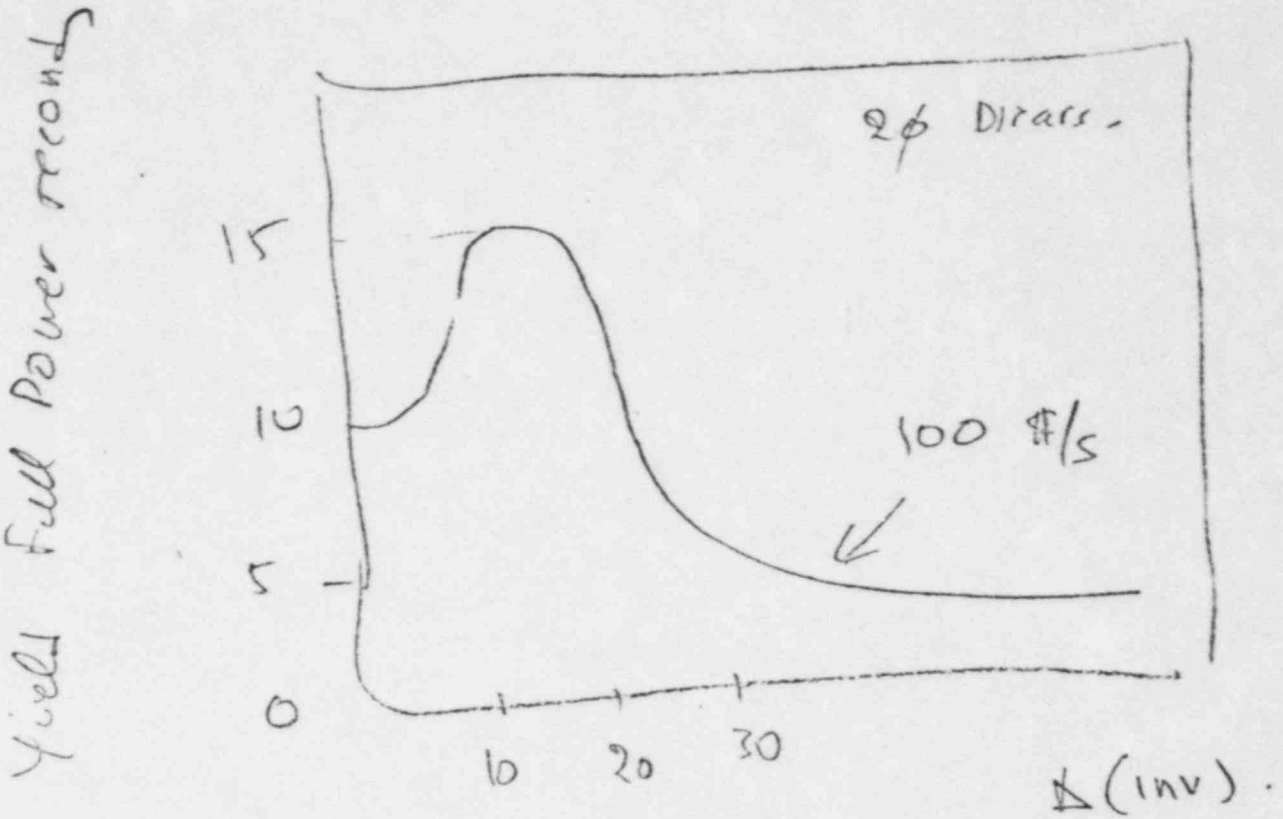

Fig. 16.

II.7

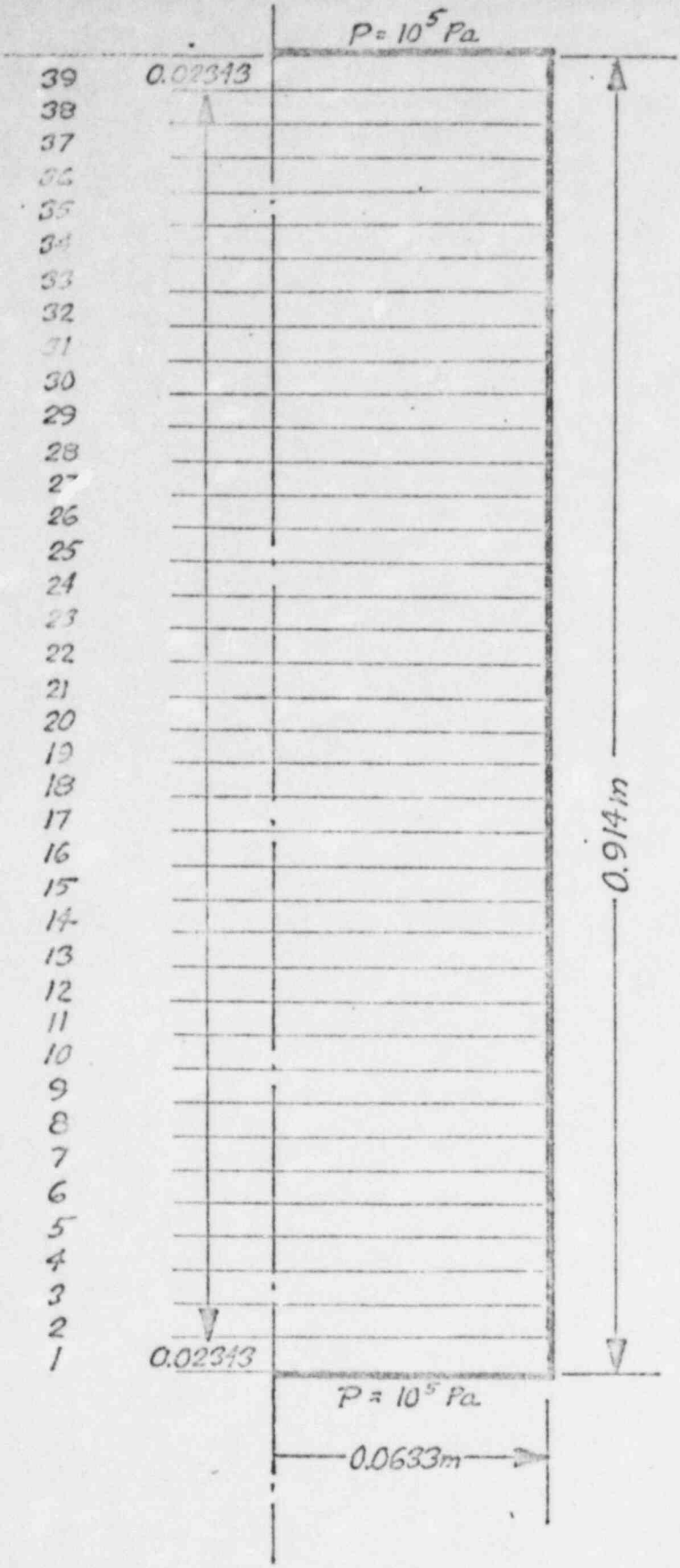

Fig 1 SIMMER-II MODEL FOR 1-D DISASSEMBLY ANALYSIS

WORTH OF FUEL AND STEEL 1DD31B

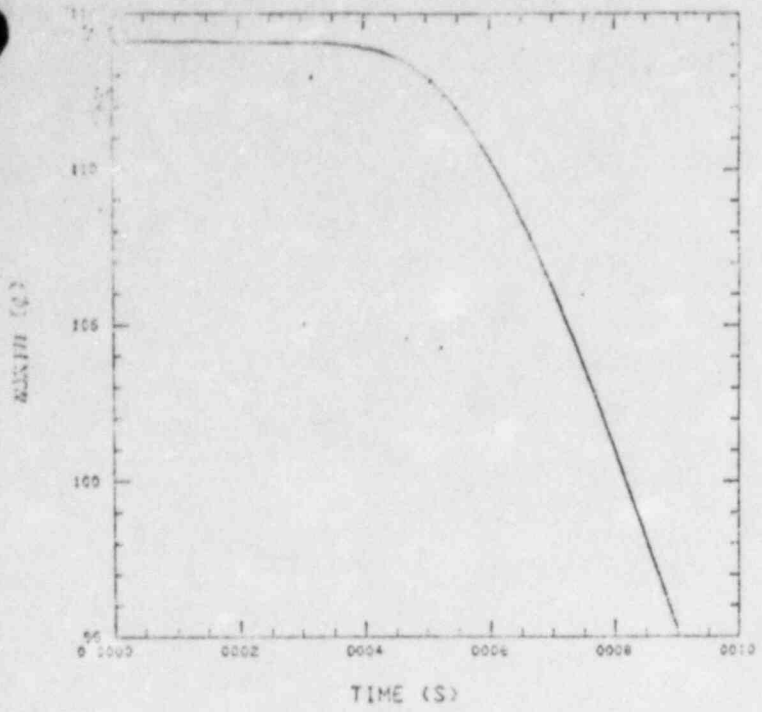

Fig 2

LIQ FUEL TEMP 1DD31B

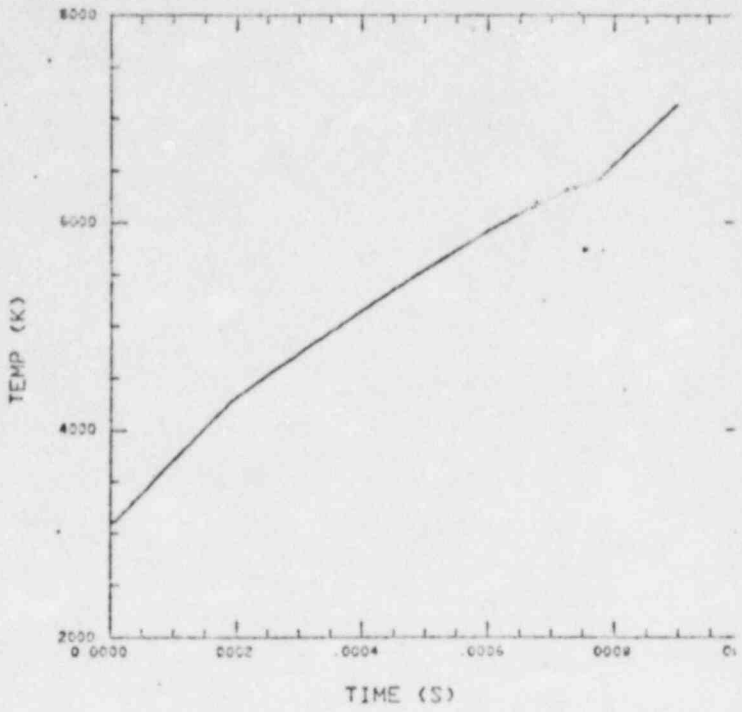

Fig 3

PRESS AT CENTER 1DD31B

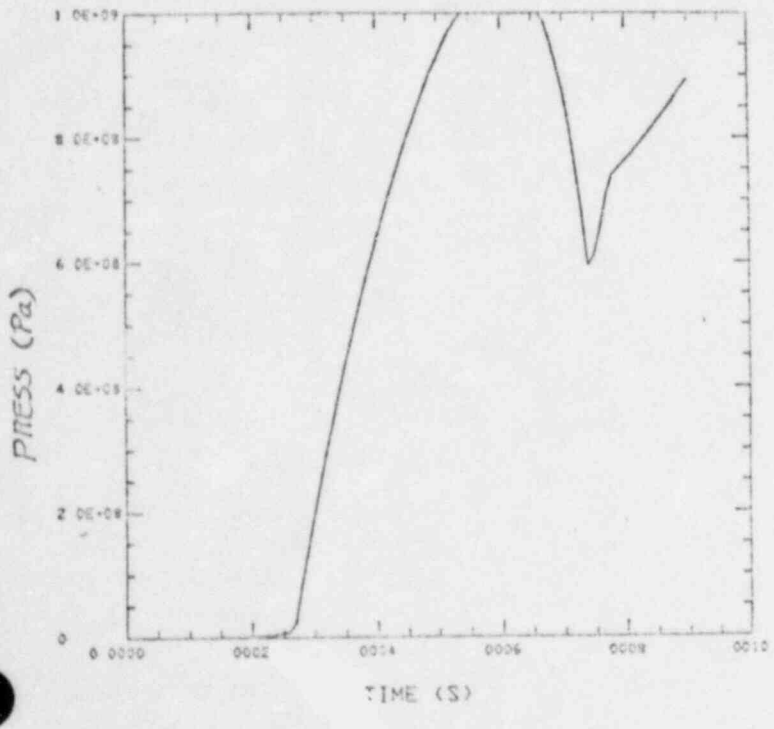

F. 4

ALPHG AT CENTER 1DD31B

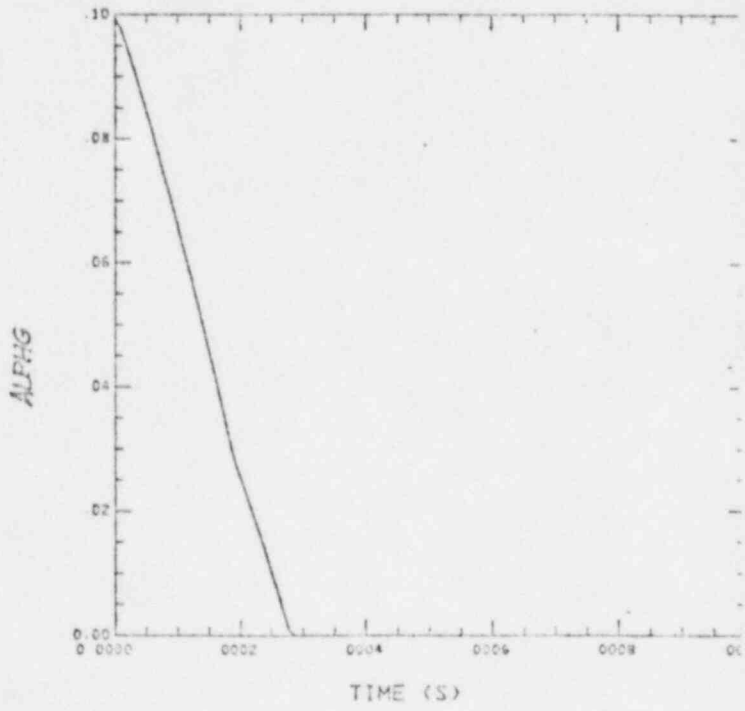

Fig 5

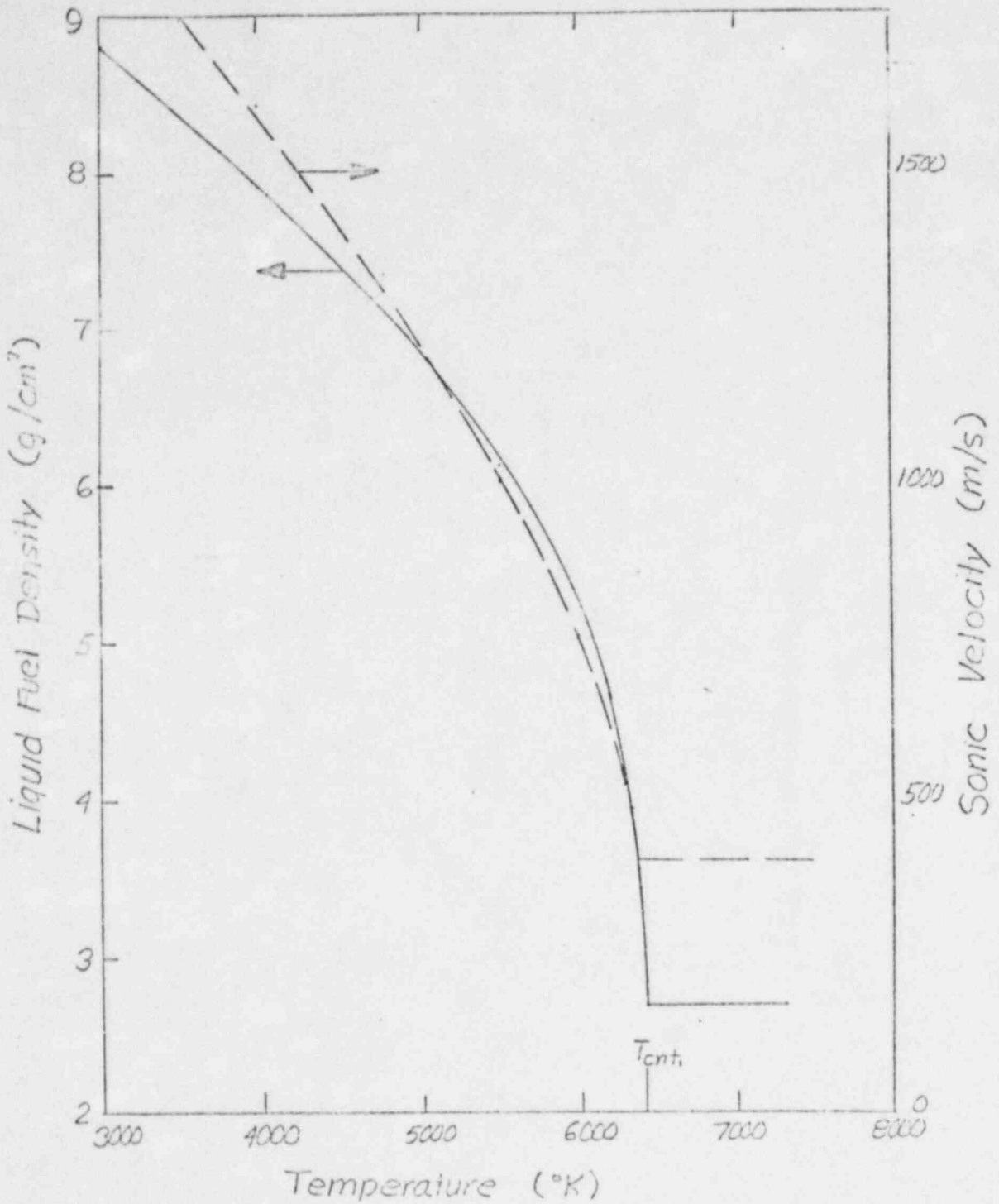
9
8
7
6
5
4
3
2
Liquid Fuel Density (g/cm³)
1500
1000
500
0
Sonic Velocity (m/s)
3000
4000
5000
6000
7000
8000
T cnt.
Temperature (°K)

Fig 6

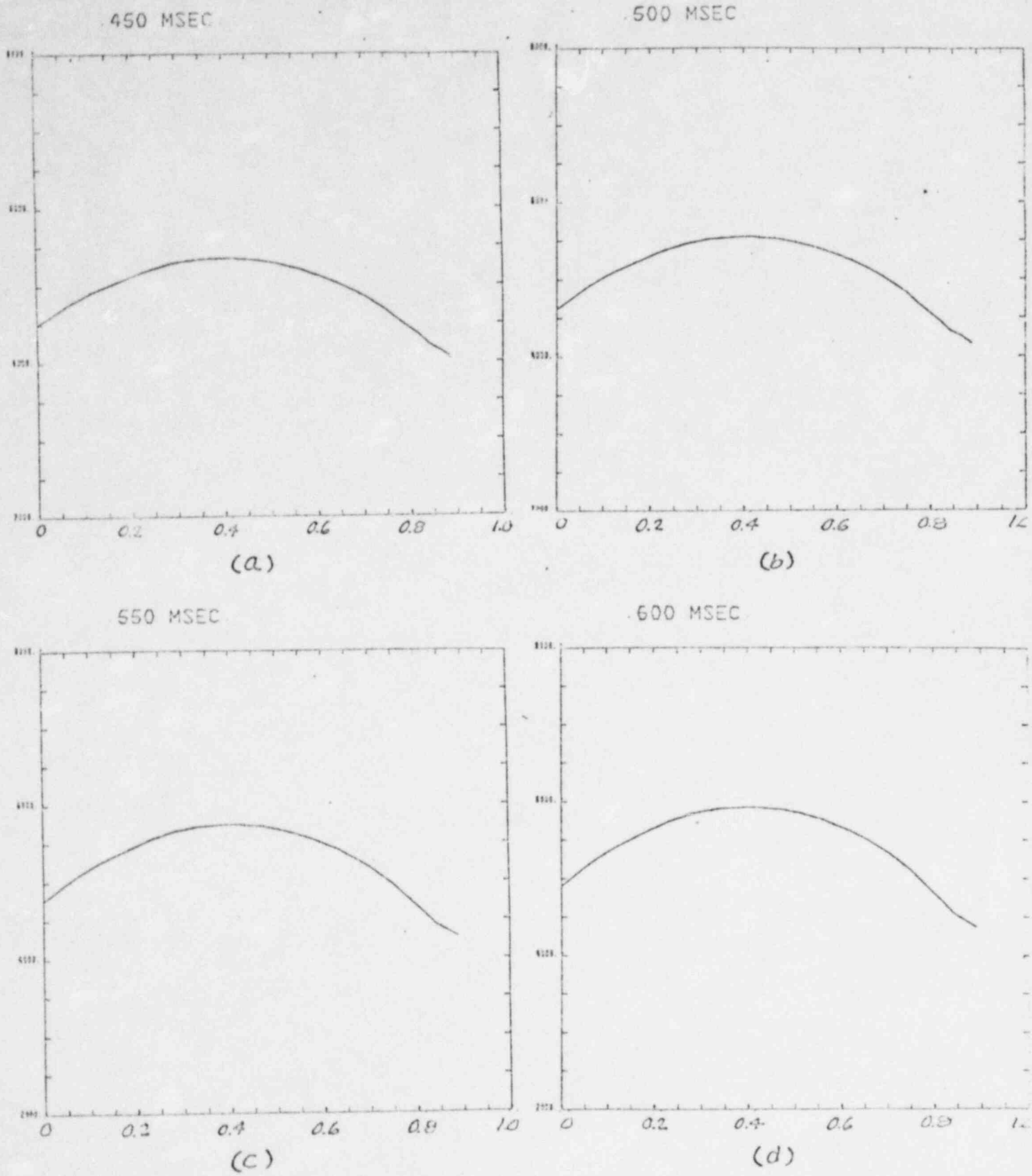

Fig 7 Temperature (K)

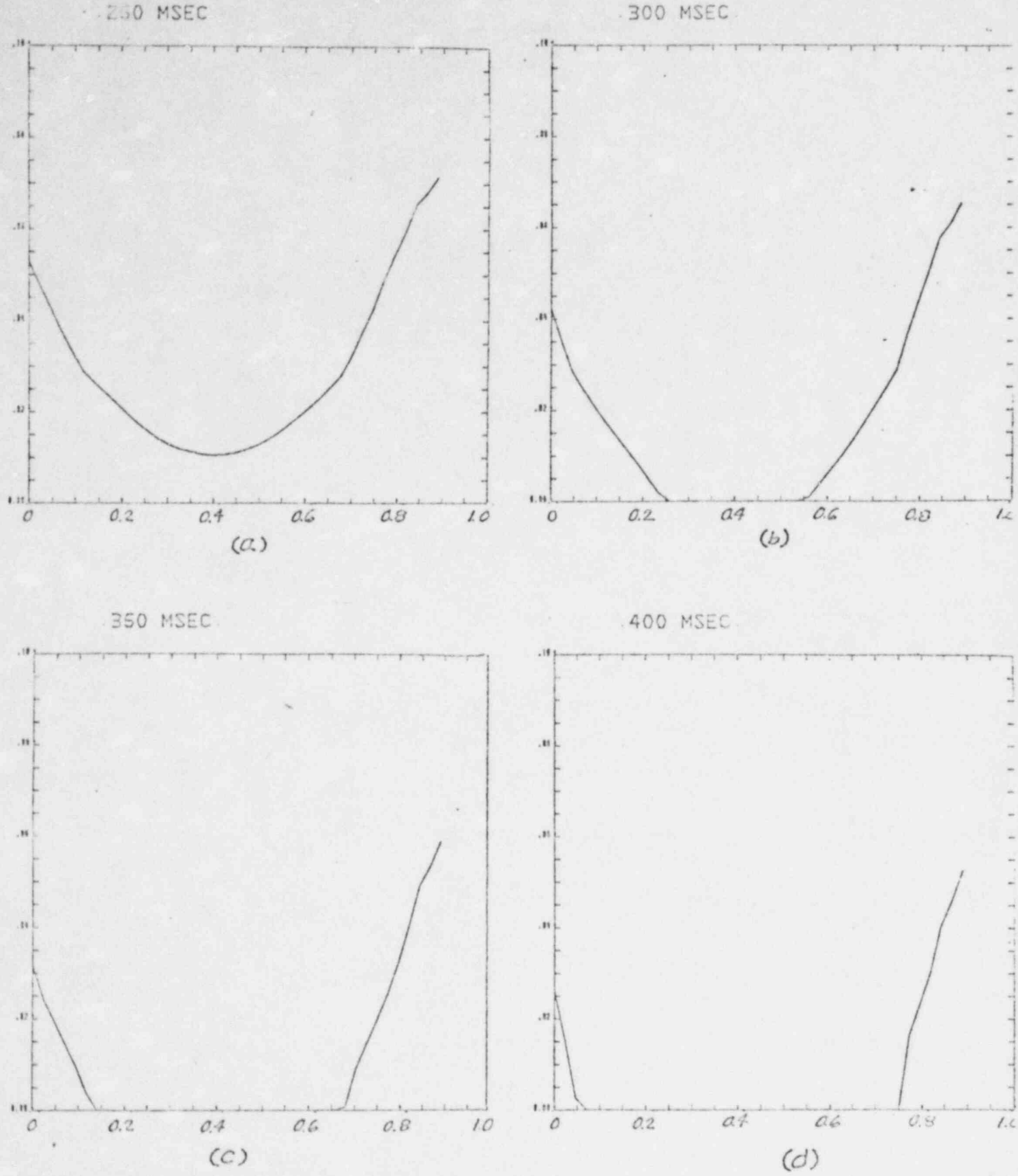

Fig 8 Void Fraction

450 MSEC

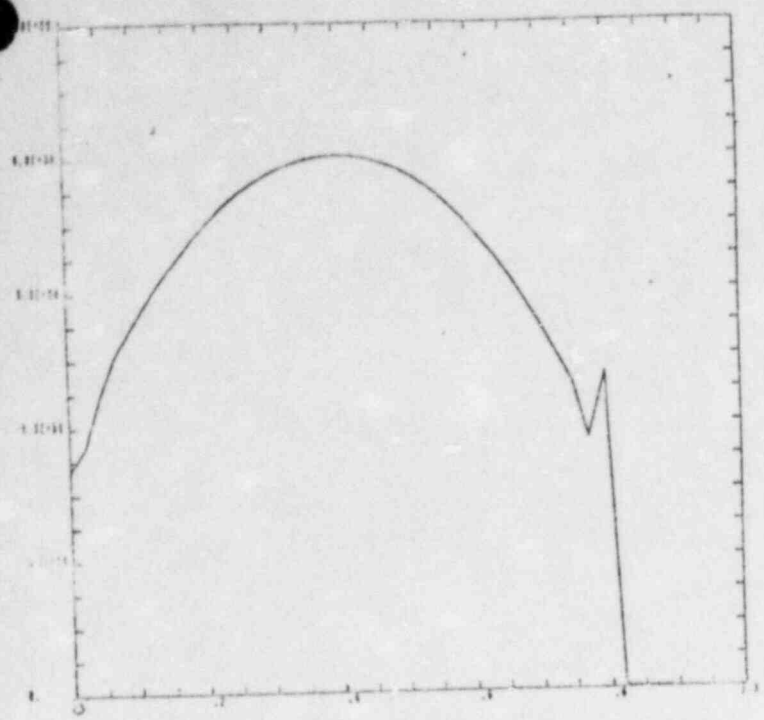

(a)

500 MSEC

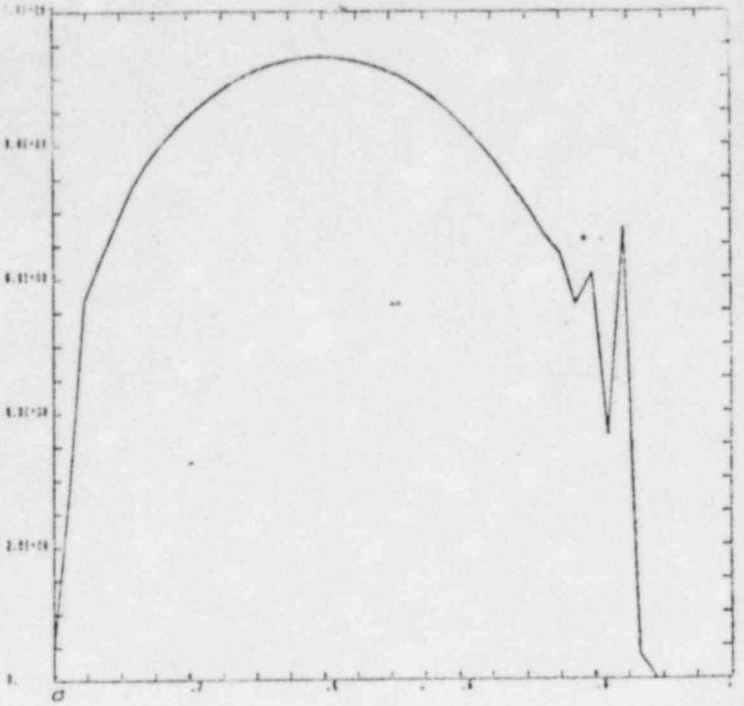

(b)

550 MSEC

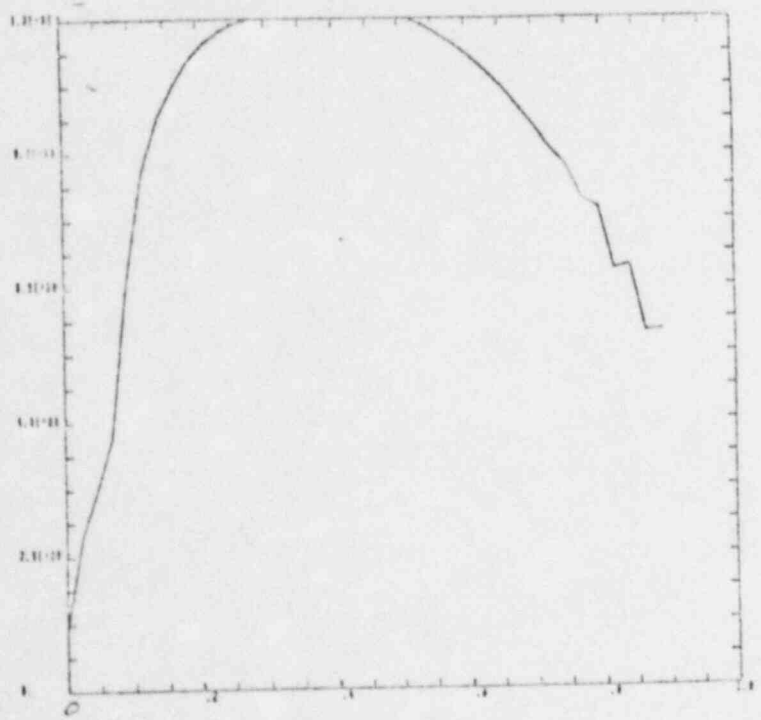

(c)

600 MSEC

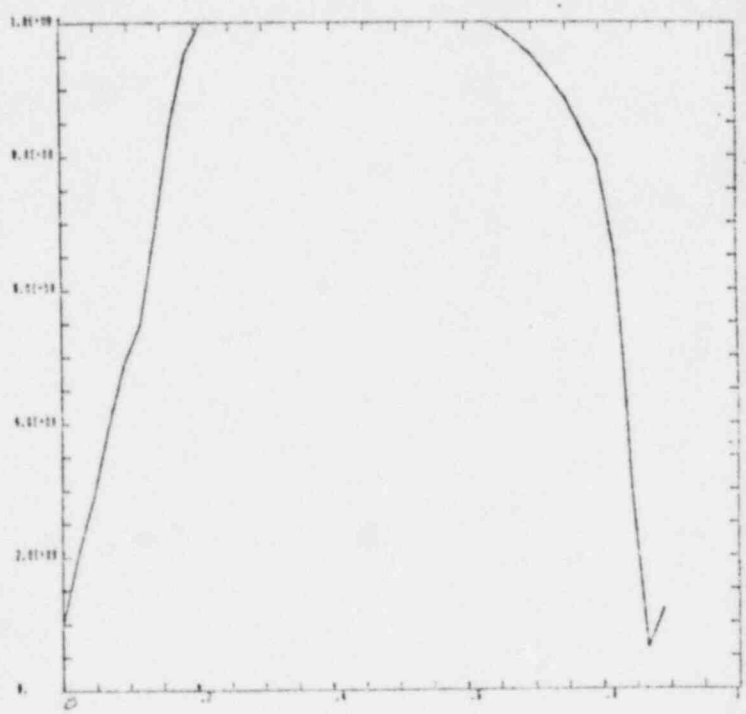

(d)

Fig 9 Pressure (Pa)

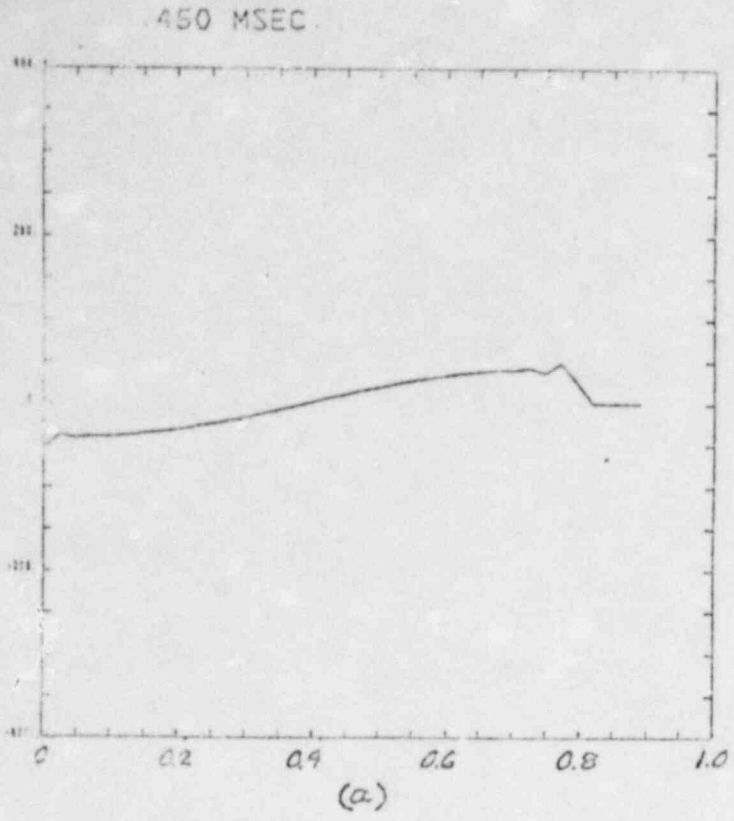

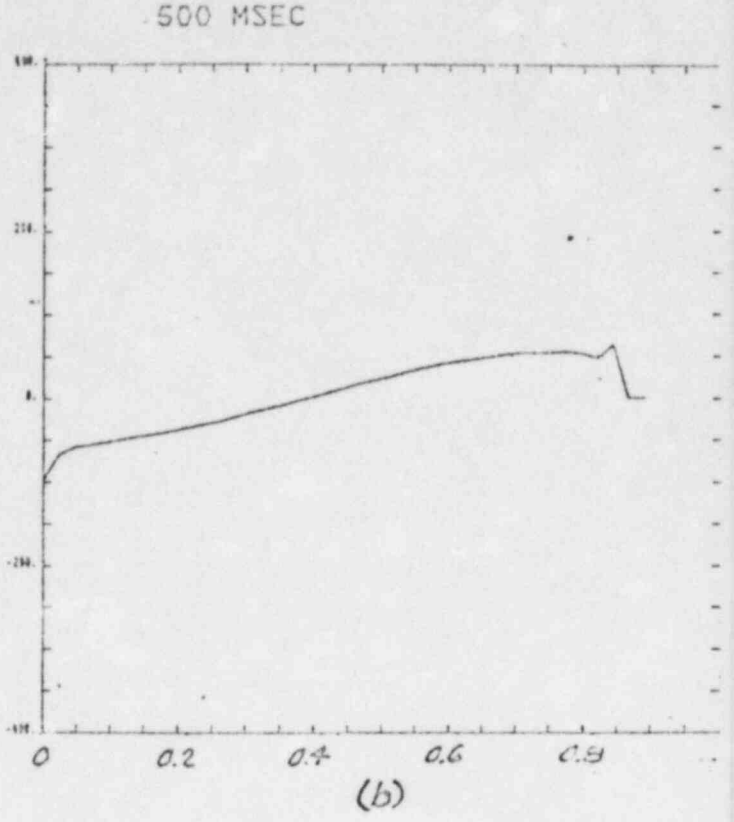

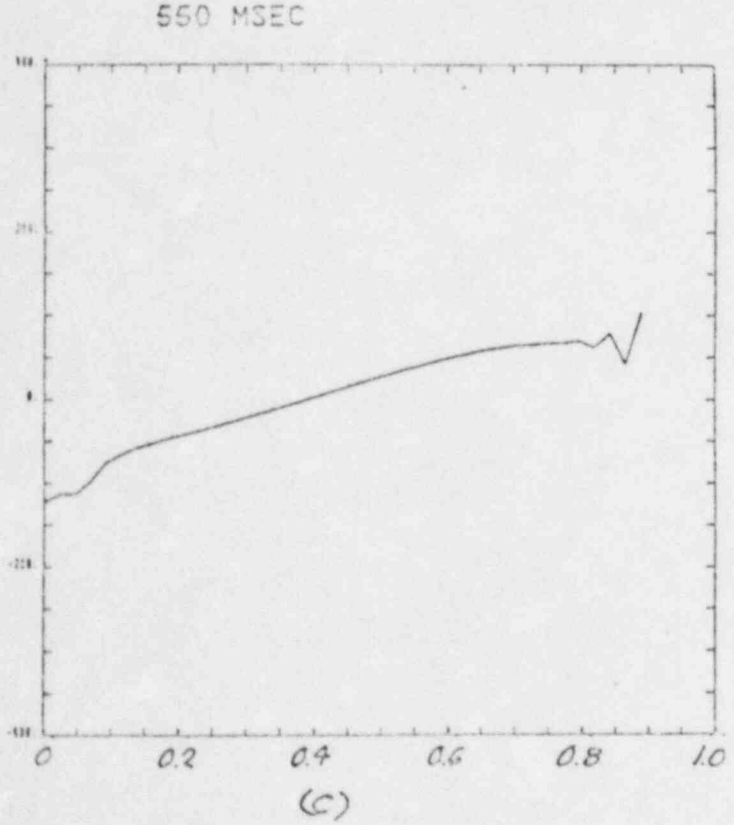

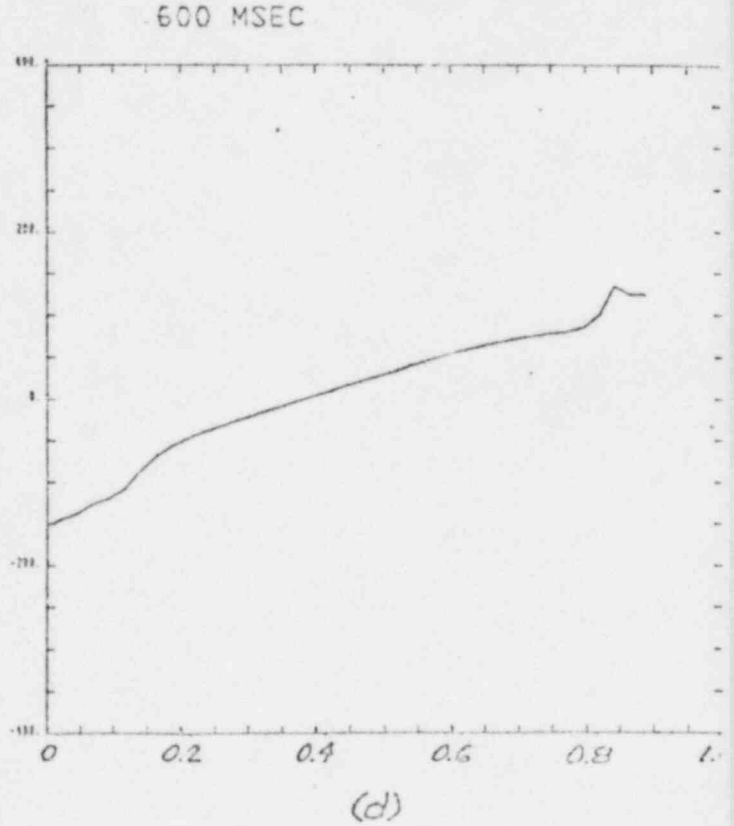

Fig 10 Velocity (m/s)

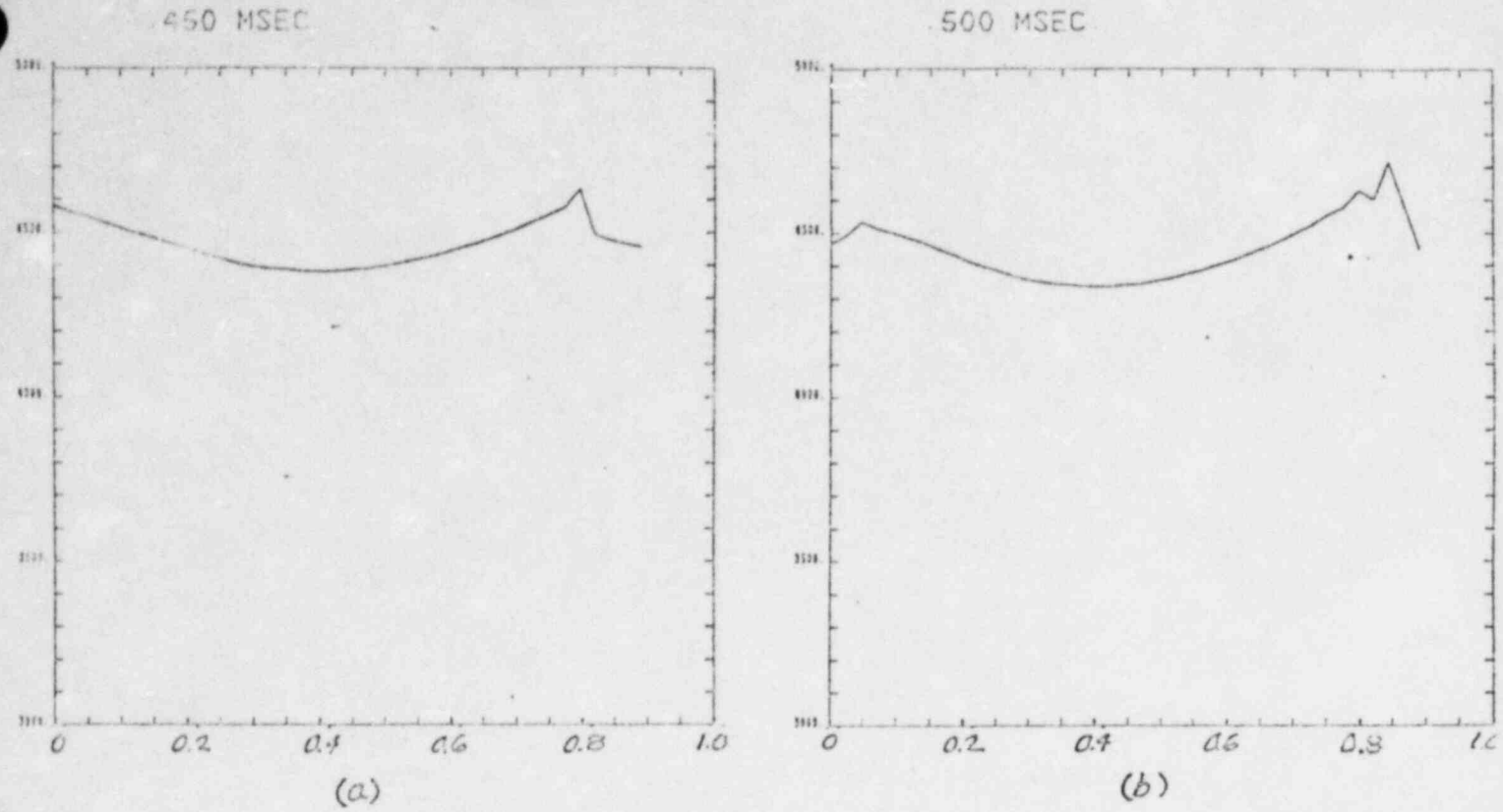

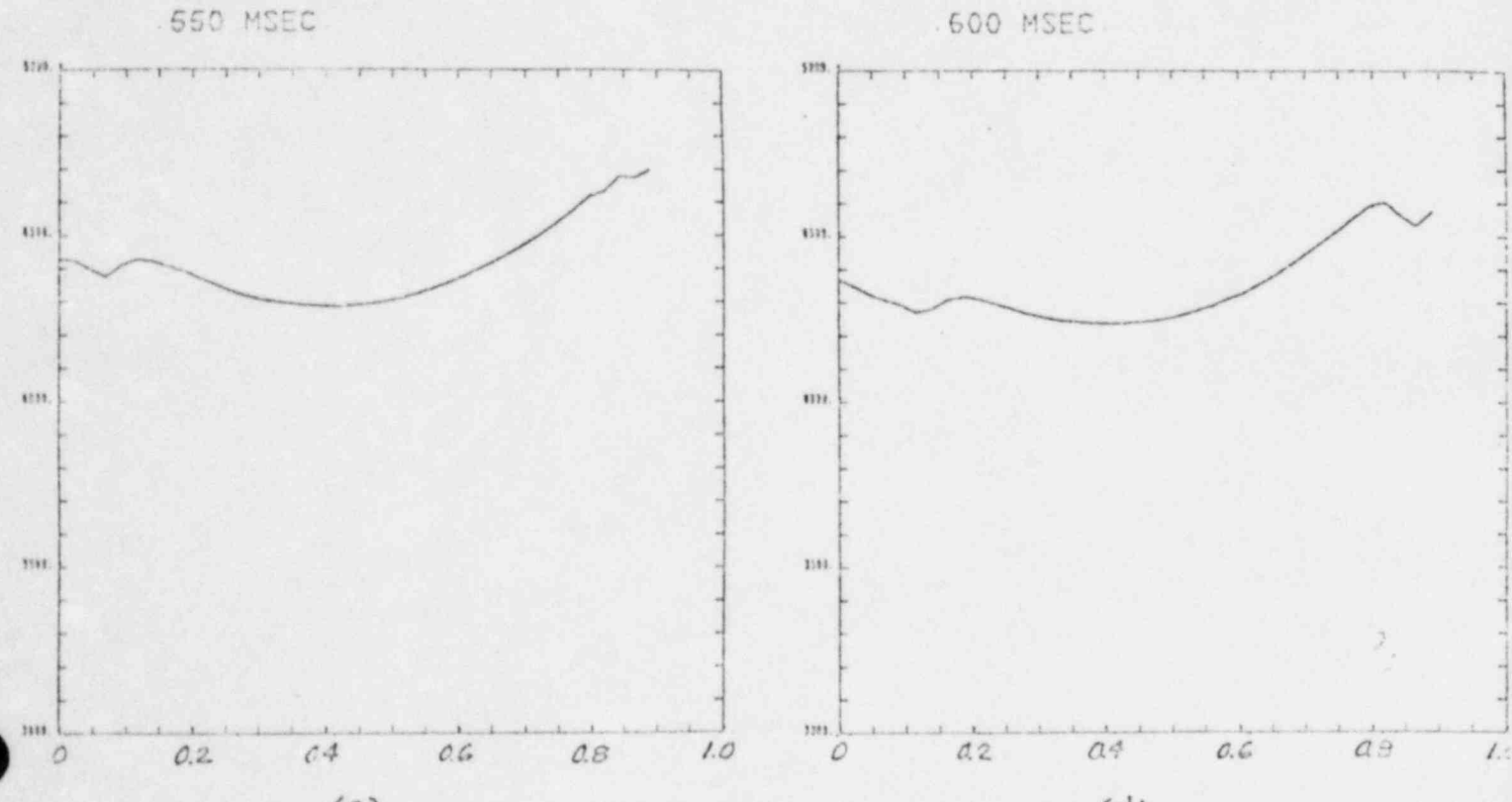

Fig II Fuel Smear Density (kg/m³)

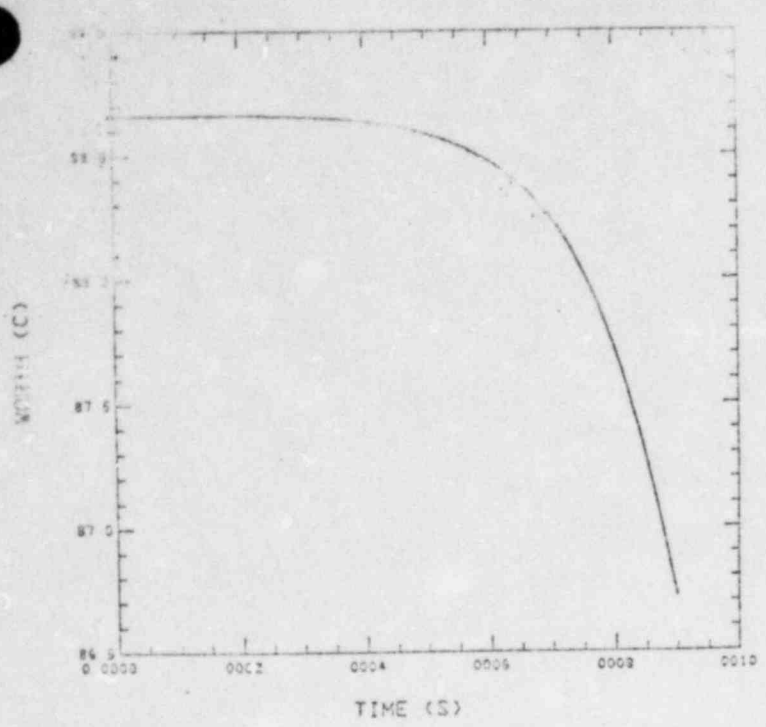

Fig 12

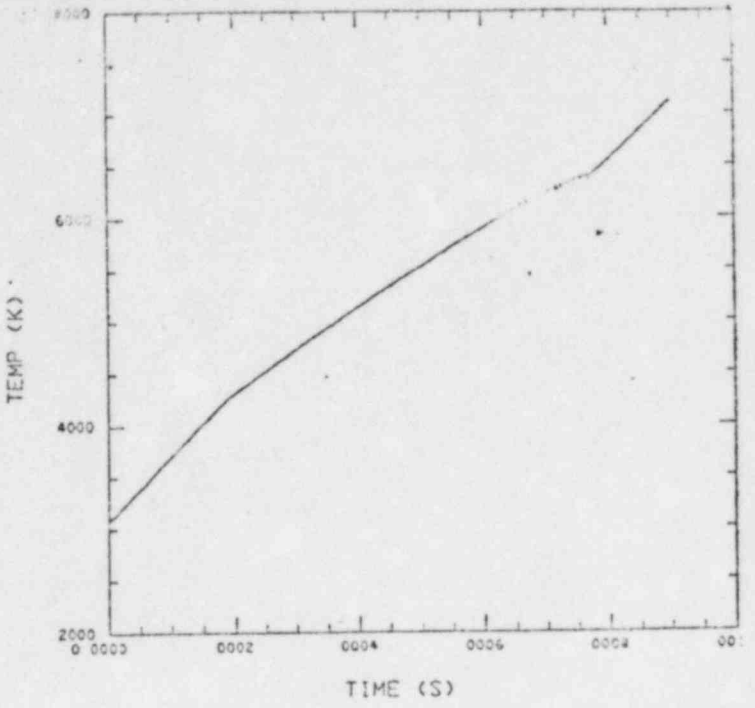

Fig 13

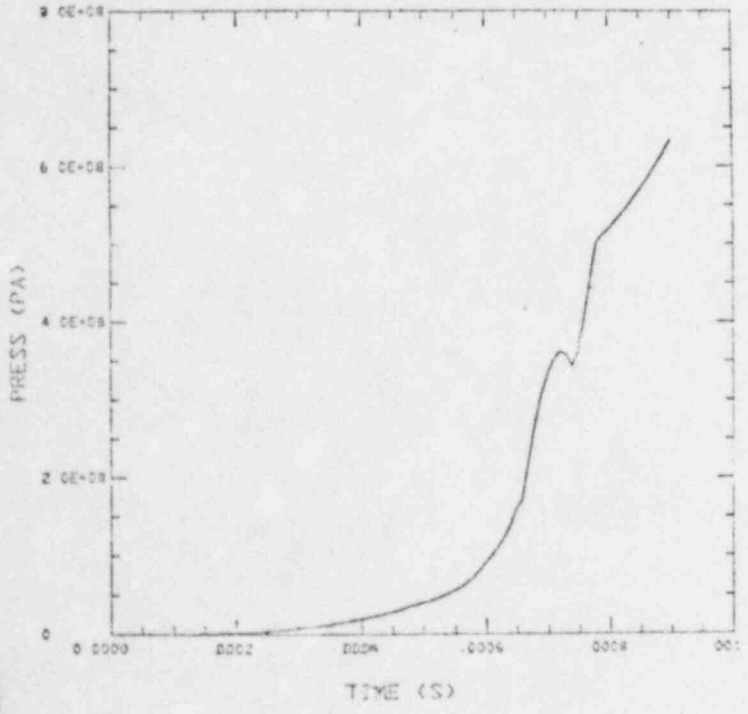

Fig 14

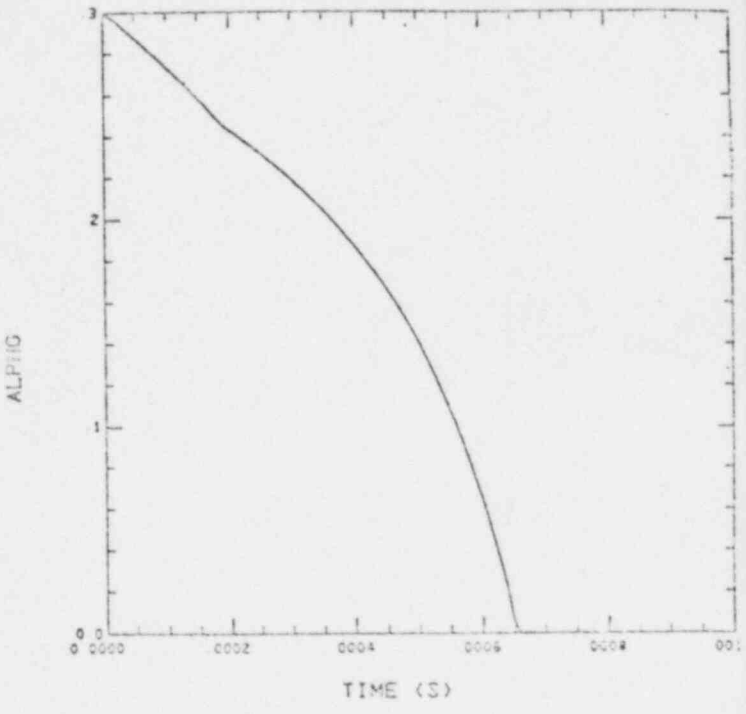

Fig 15

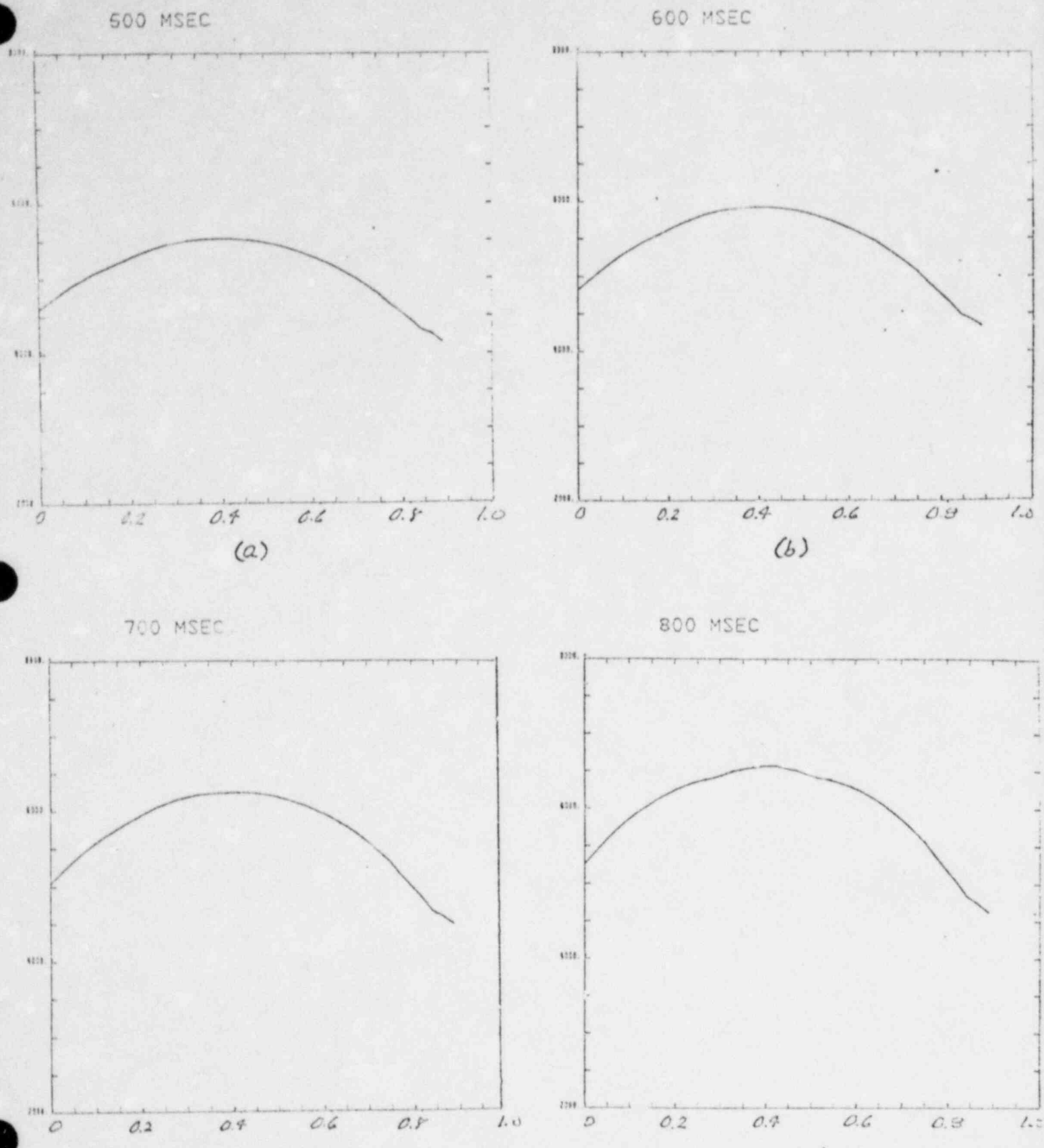

Fig 16 Temperature (K)

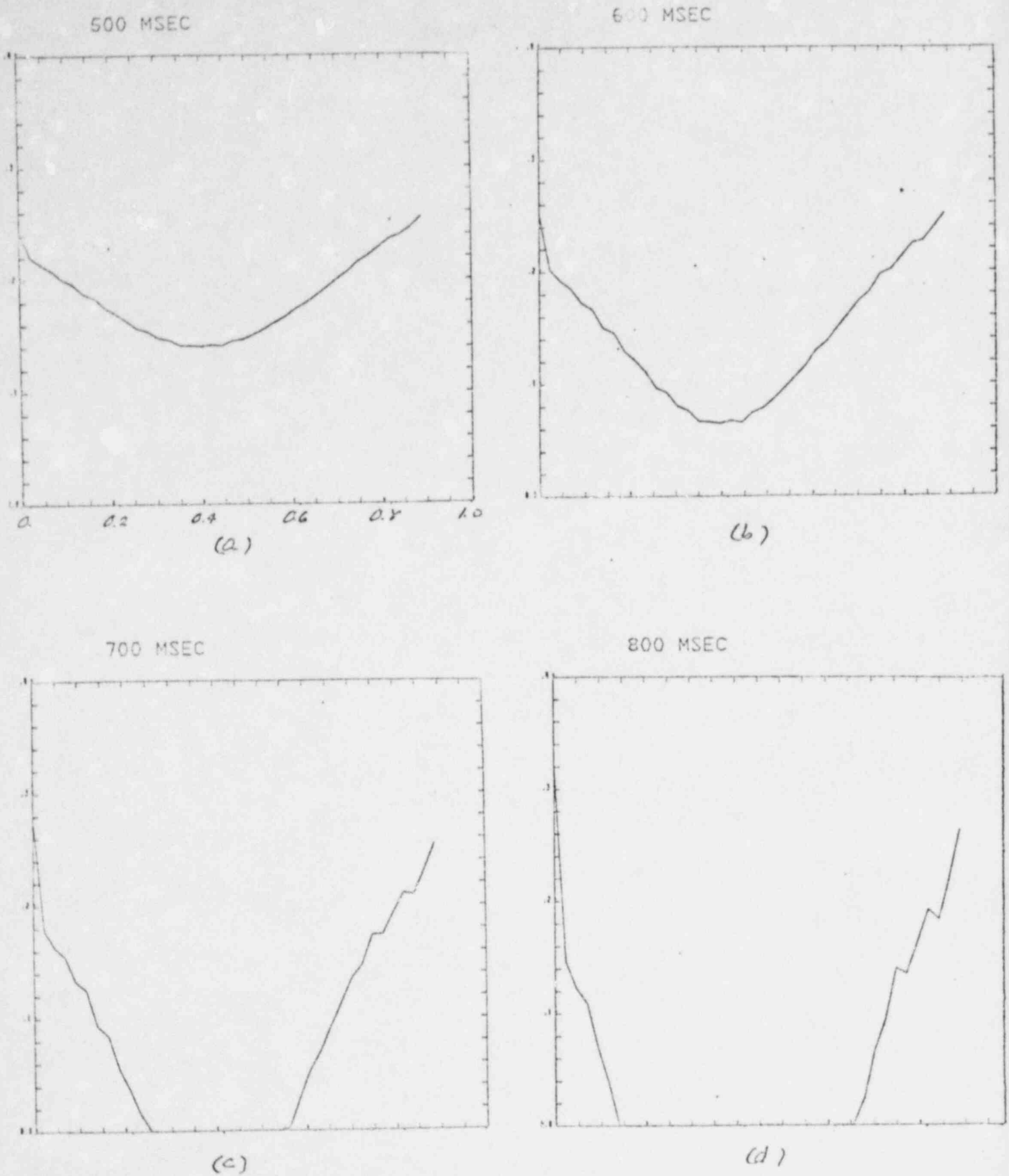

Fig 17 Void Fraction

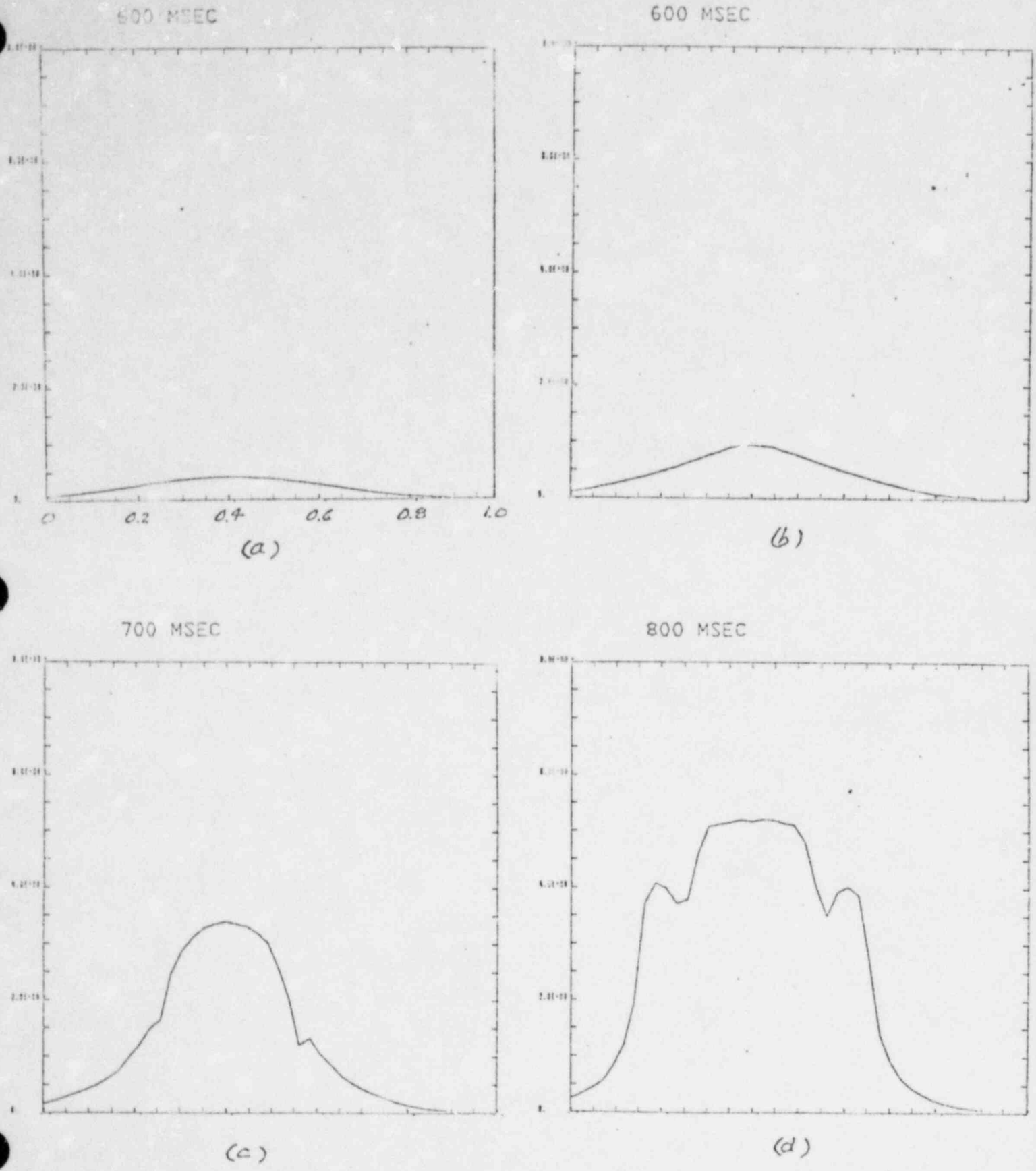

Fig 15 Pressure (Pa)

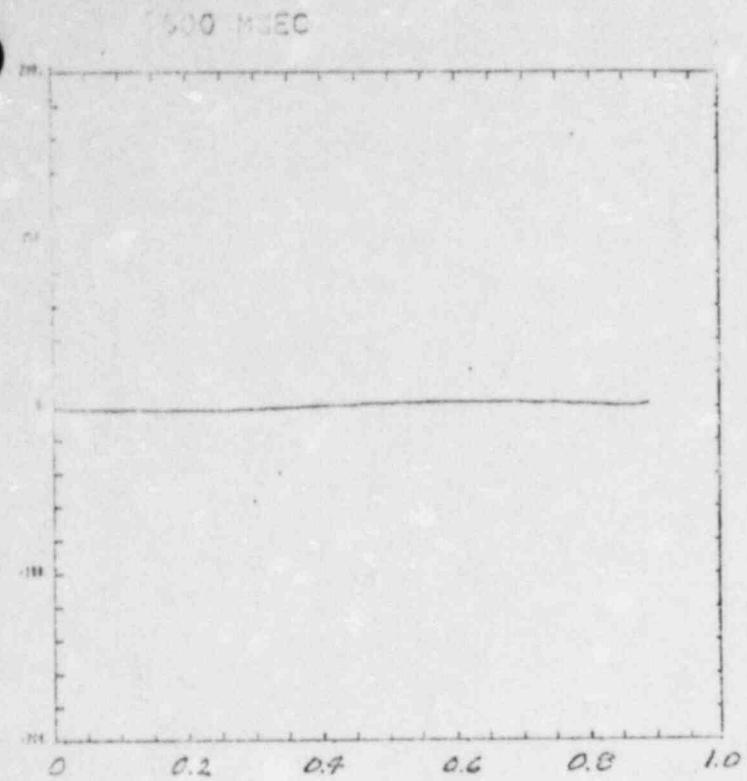

(a)

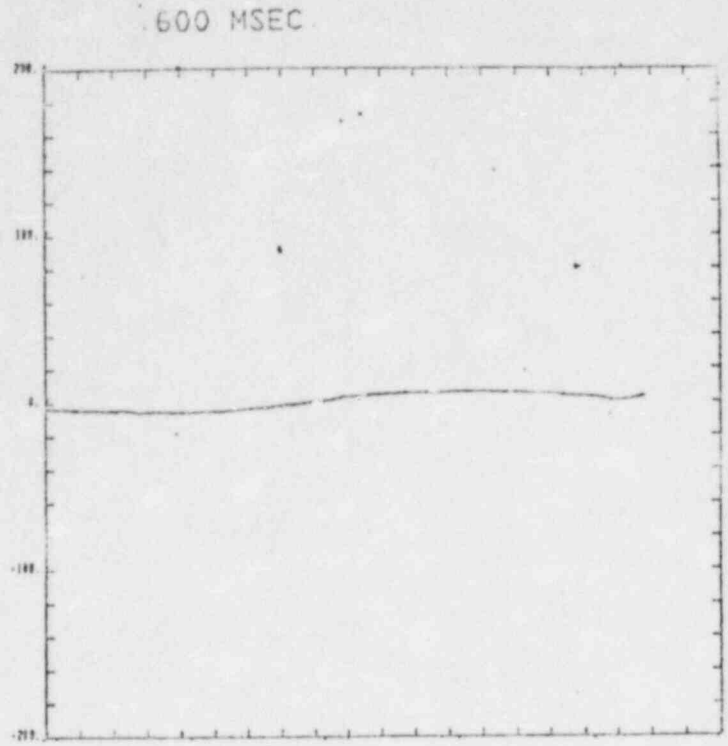

(b)

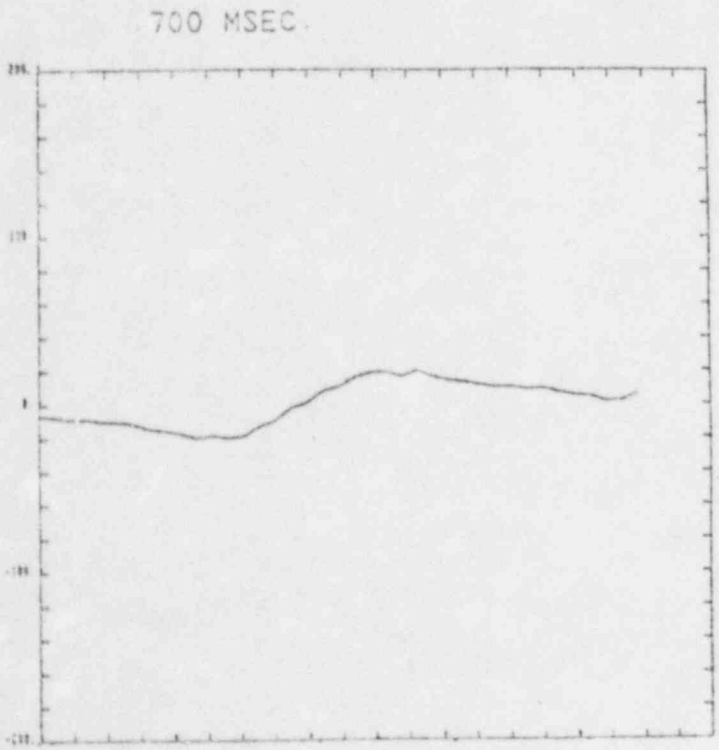

(c)

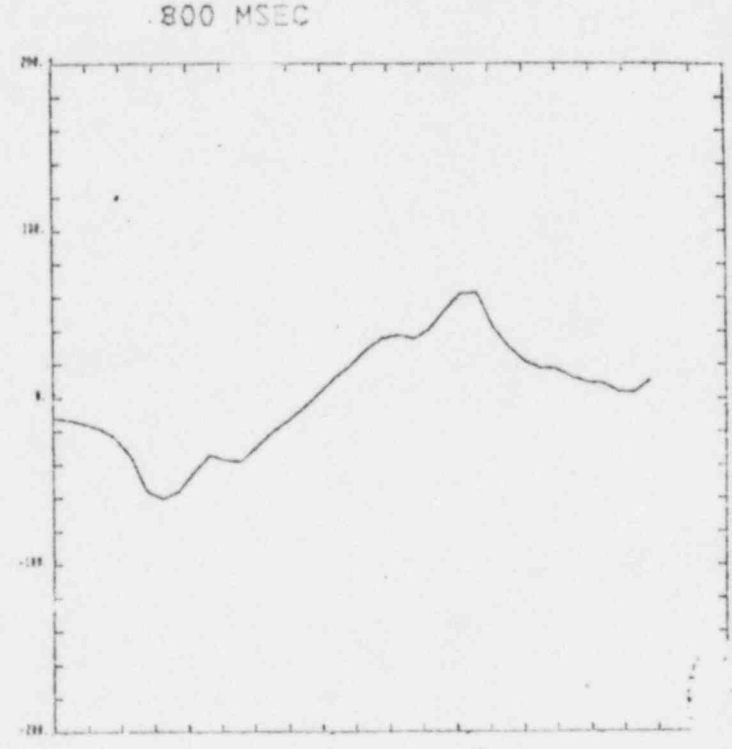

(d)

Fig 19 Velocity (m/s)

500 MSEC

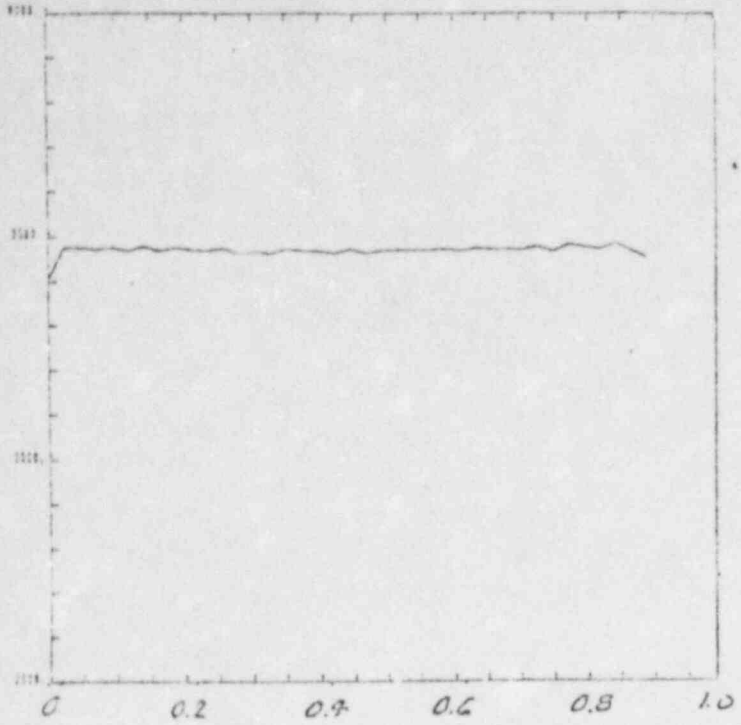

(a)

600 MSEC

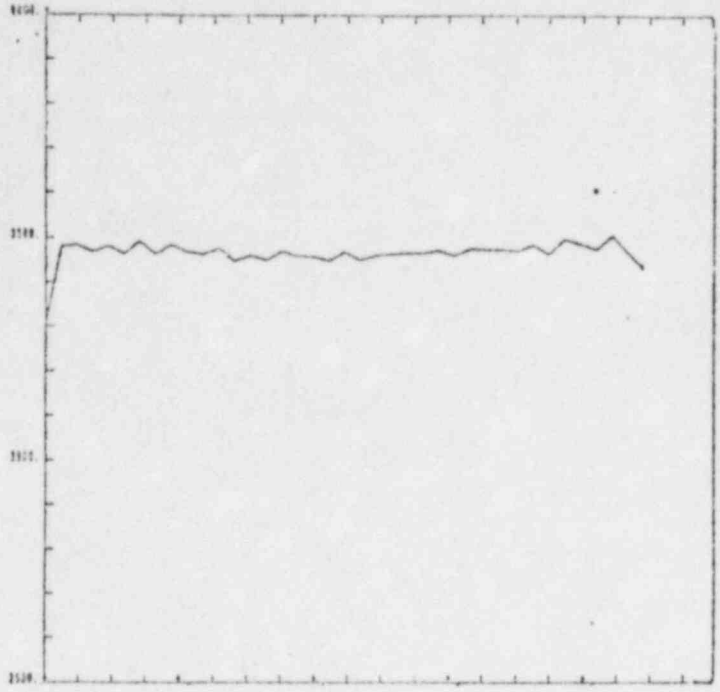

(b)

700 MSEC

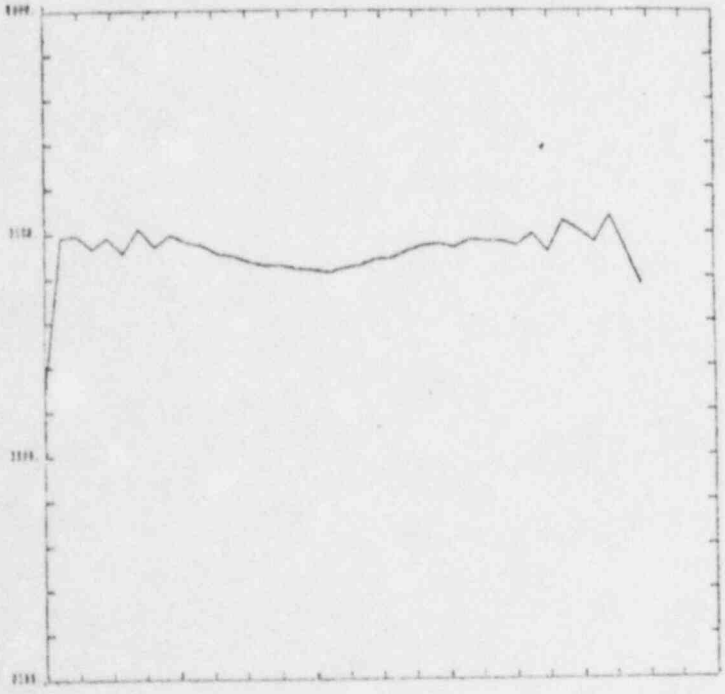

(c)

800 MSEC

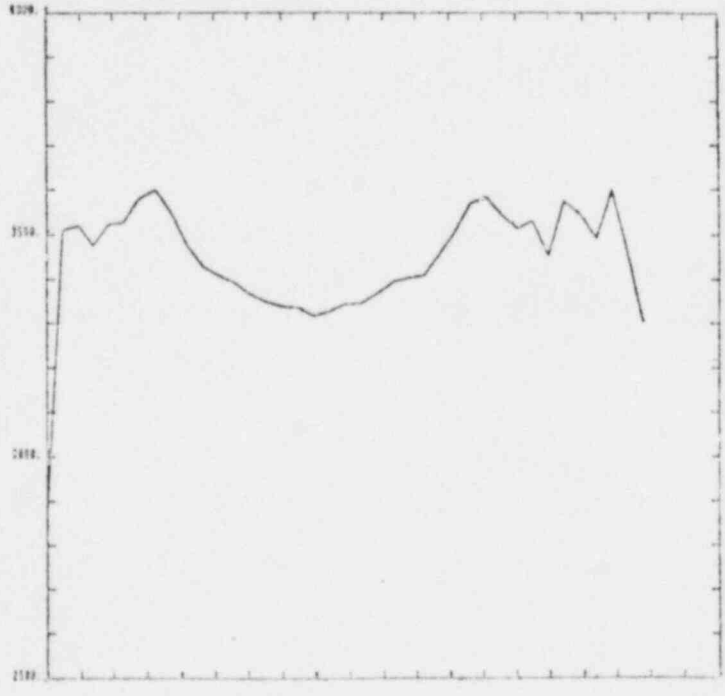

(d)

Fig 20. Fuel Smear Density (kg/m^3)

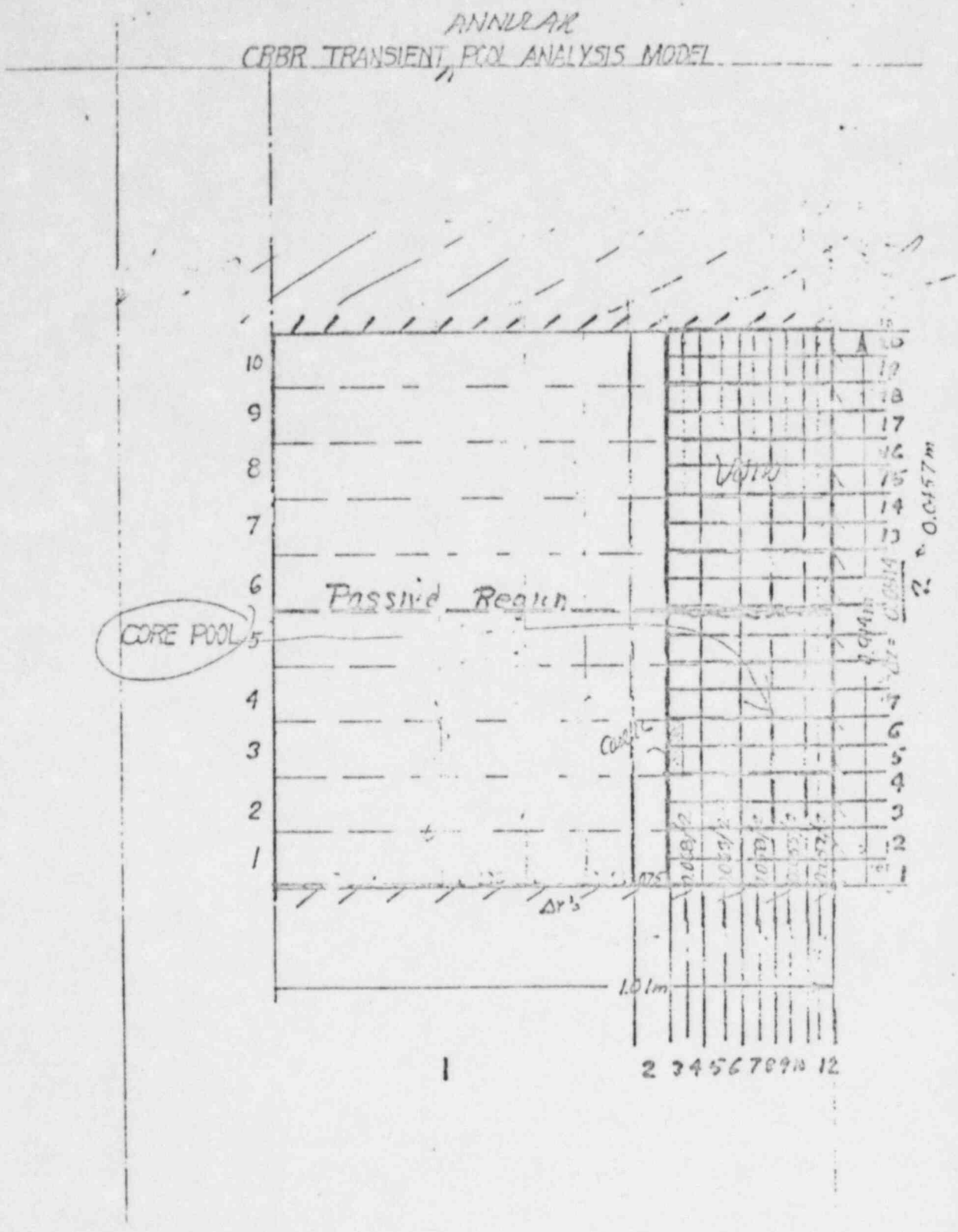
ANNULAR
CRBR TRANSIENT POOL ANALYSIS MODEL
Void
Passive Region
CORE POOL
Δr's
1.01m
0.0457m
1 2 3 4 5 6 7 8 9 10 11 12

Fig 1

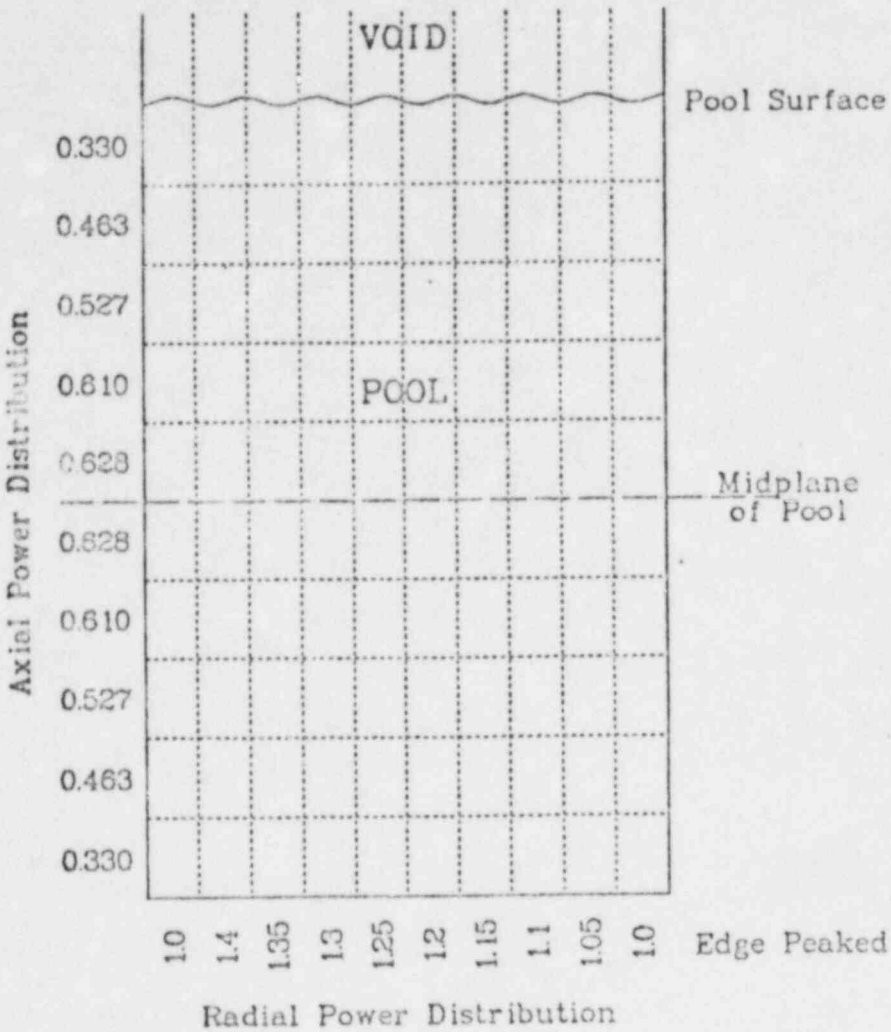
VOID
Pool Surface
0.330
0.463
0.527
0.610
POOL
0.628
Midplane of Pool
0.628
0.610
0.527
0.463
0.330
Axial Power Distribution
1.0
1.4
1.35
1.3
1.25
1.2
1.15
1.1
1.05
1.0
Edge Peaked
Radial Power Distribution

Fig 2

VOLUME FRACTION OF LIQUID
TIME 000MS

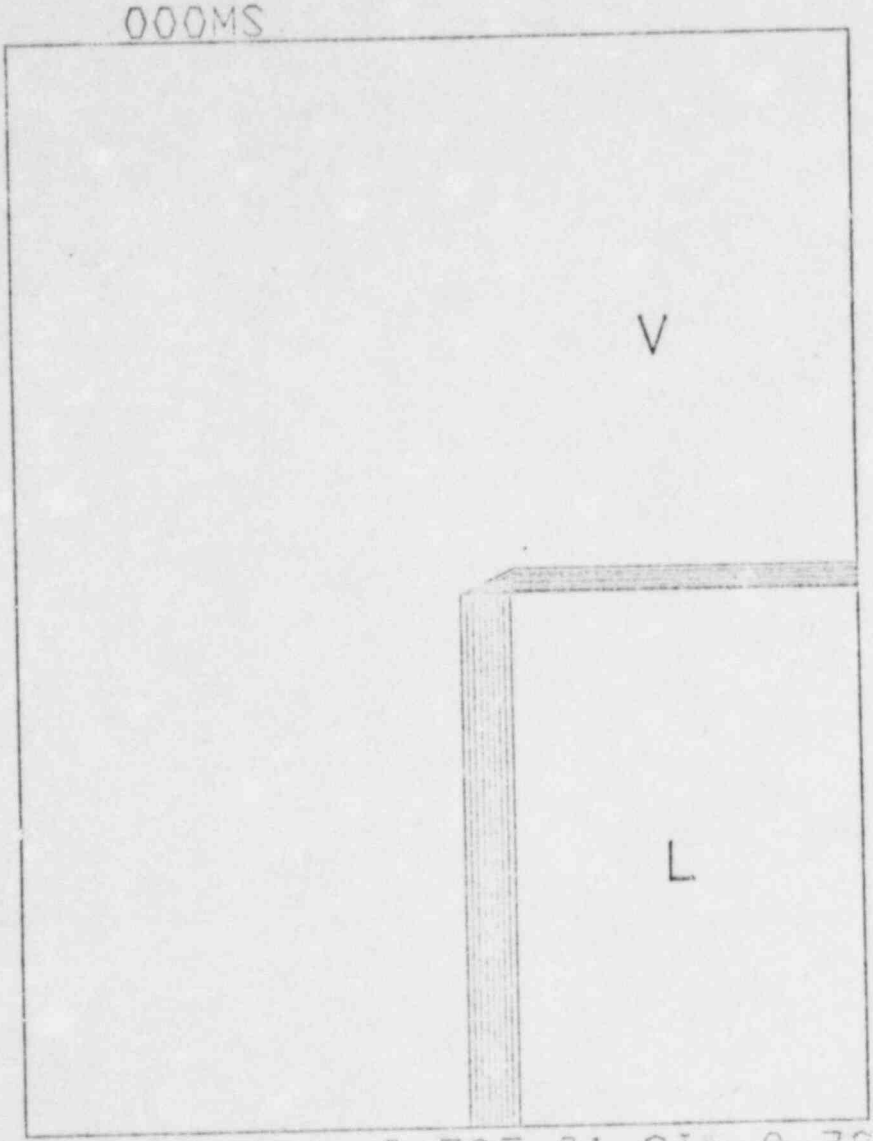

MIN= 1 90E-06 MAX= 9 78E-01 CI= 9 78E-02

Fig 3a

VOLUME FRACTION OF LIQUID
TIME 20.000MS

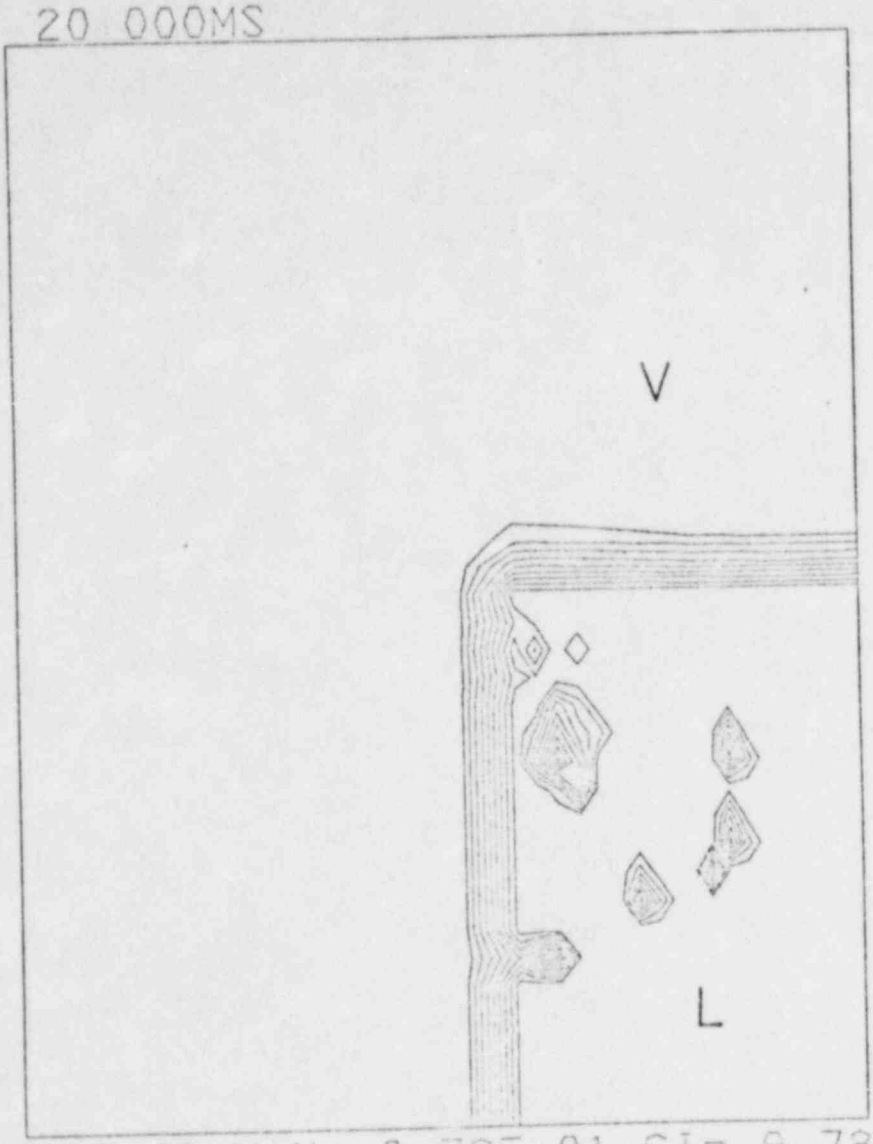

MIN= 1.90E-06 MAX= 9.78E-01 CI= 9.78E-02

Fig 3b

VOLUME FRACTION OF LIQUID
TIME 40 000MS

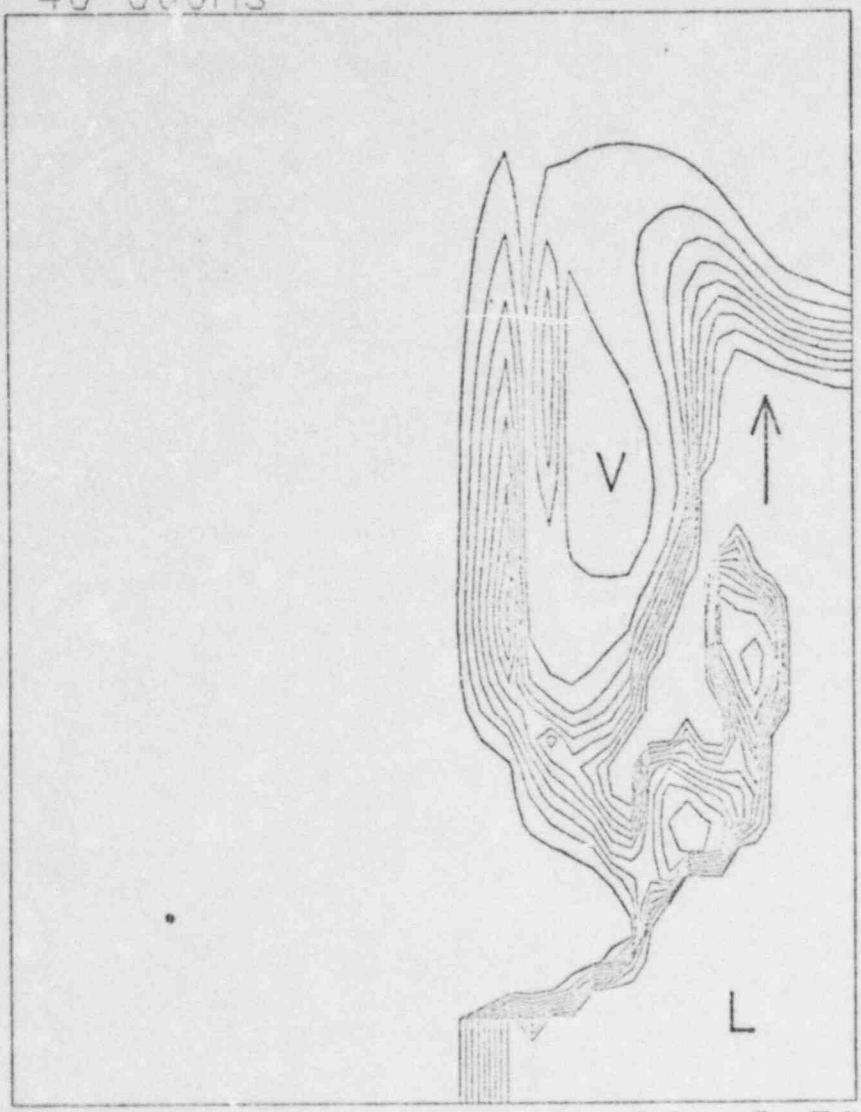

MIN= 1 90E-06 MAX= 9 78E-01 CI= 9 78E-02

Fig 3c

VOLUME FRACTION OF LIQUID
TIME 60 000MS

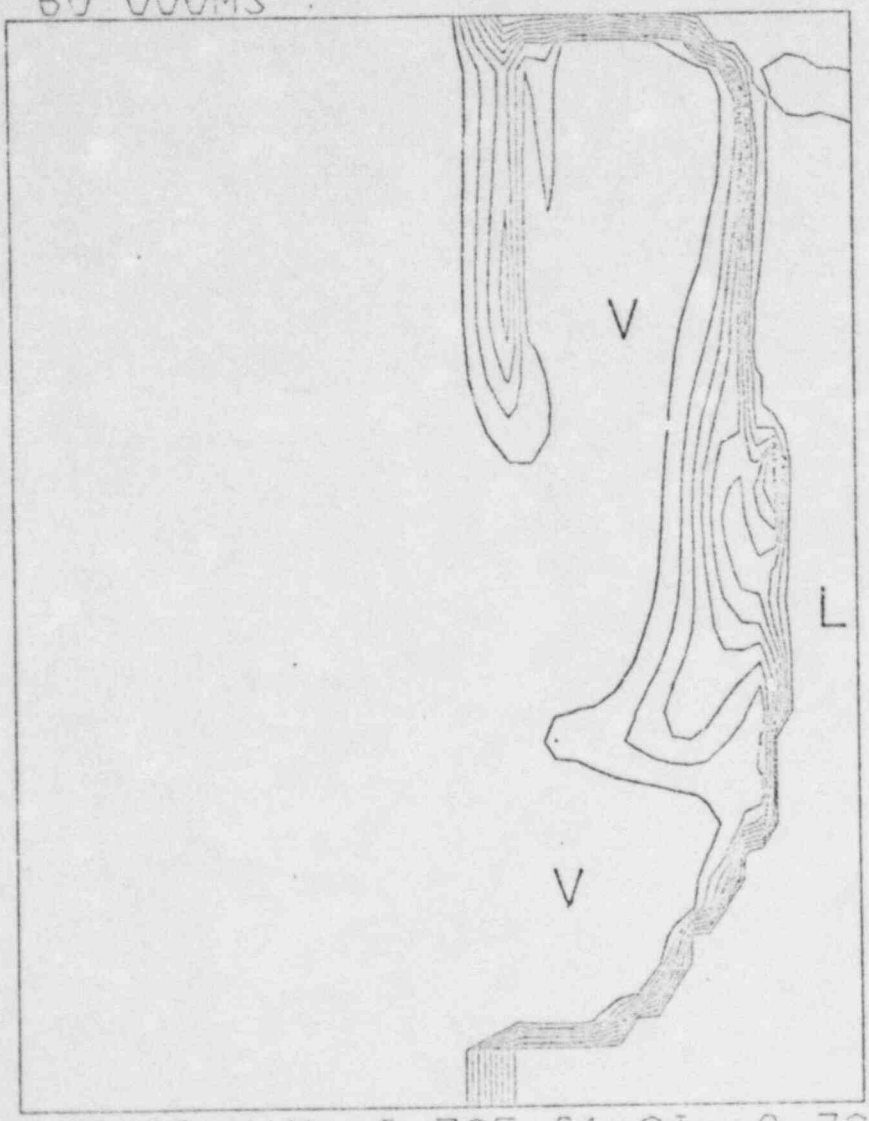

MIN= 1 90E-05 MAX= 9 78E-01 CI= 9 78E-02

Fig 3d

VOLUME FRACTION OF LIQUID
TIME 80 000MS

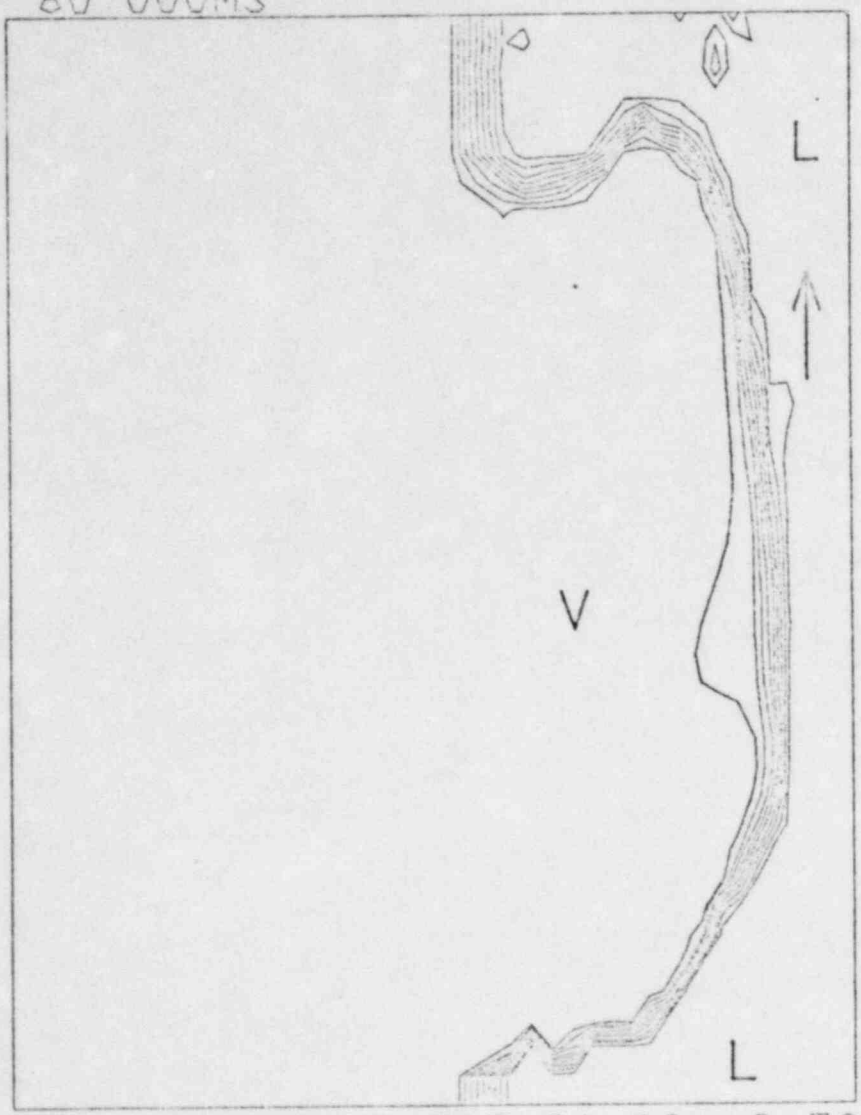

MIN= 1 90E-05 MAX= 9 78E-01 CI= 9 78E-02

Fig 3e

VOLUME FRACTION OF LIQUID
TIME 100 000MS

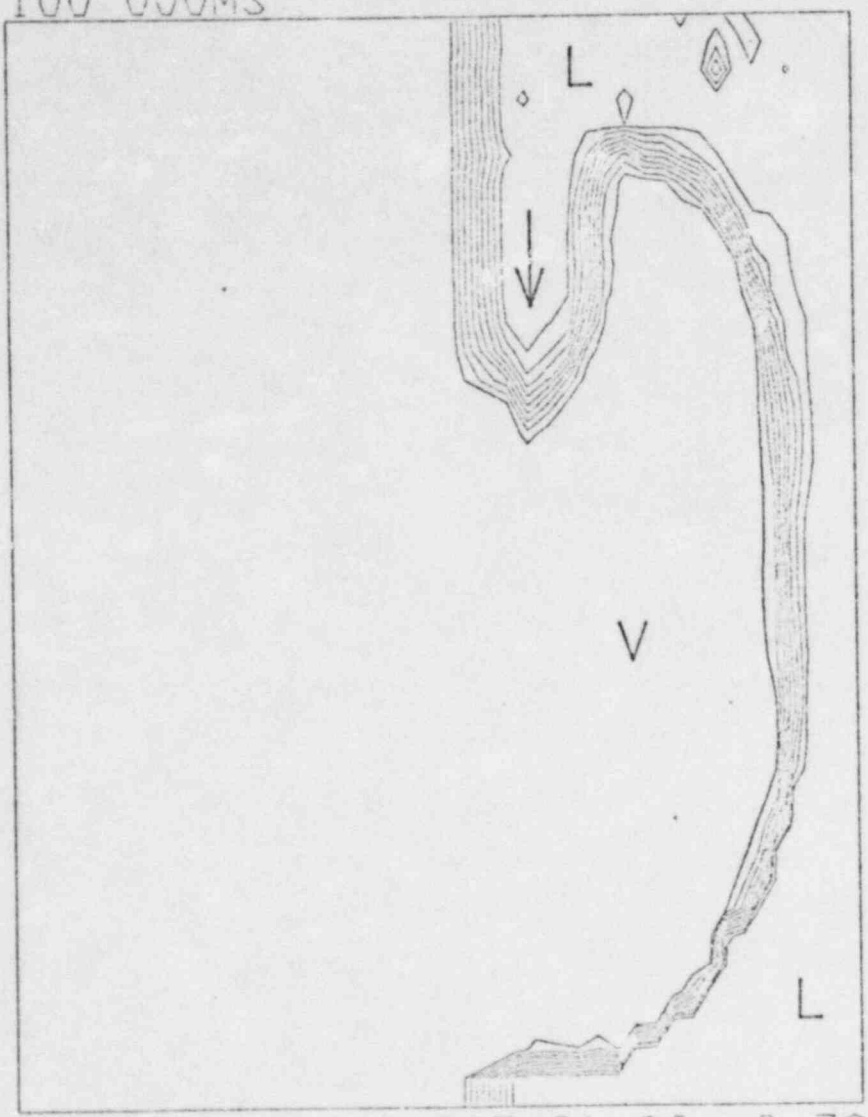

MIN= 1 90E-05 MAX= 9 78E-01 CI= 9 78E-02

Fig 3f

VOLUME FRACTION OF LIQUID
TIME 120 000MS

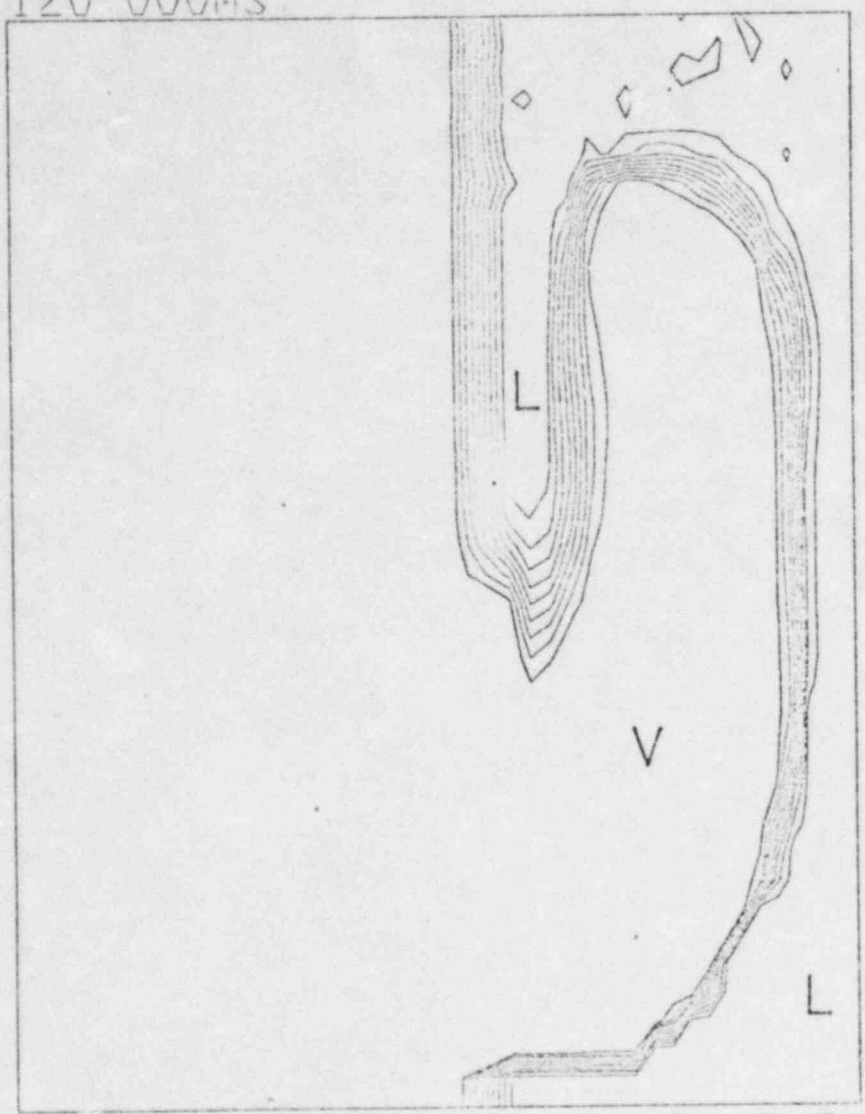

MIN= 1 90E-05 MAX= 9 78E-01 CI= 9 78E-02

Fig 39

VOLUME FRACTION OF LIQUID
TIME 140 000MS

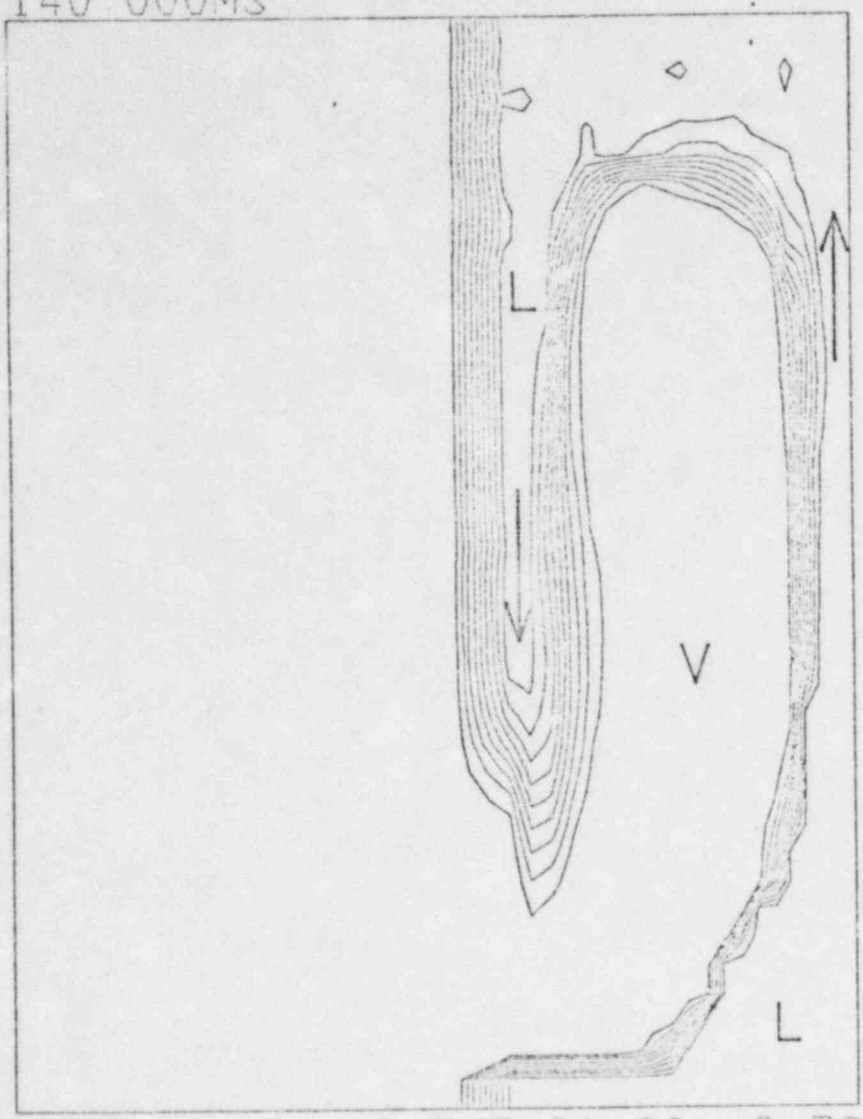

MIN= 1 90E-05 MAX= 9 78E-01 CI= 9 78E-02

Fig 3h

VOLUME FRACTION OF LIQUID
TIME 160 000MS

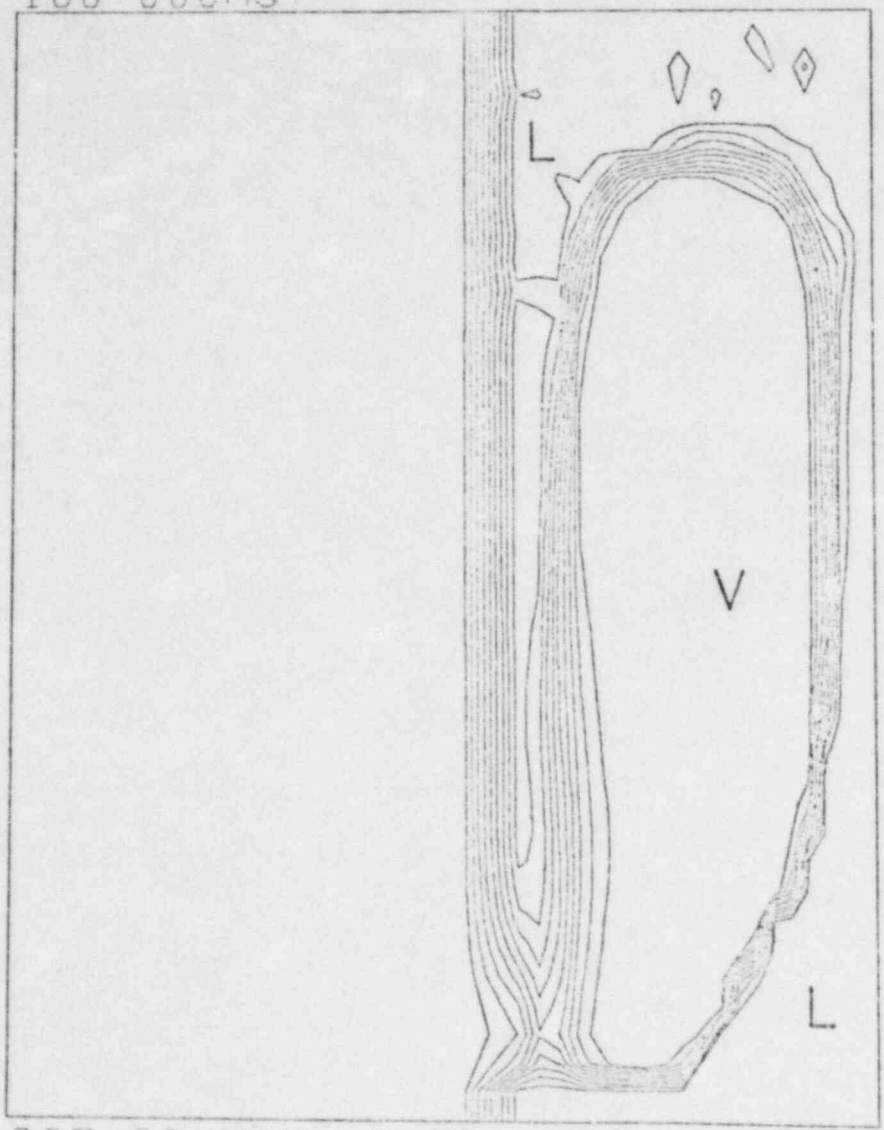

MIN= 1 90E-06 MAX= 9 78E-01 CI= 9 78E-02

Fig 3i

VOLUME FRACTION OF LIQUID
TIME 180 000MS

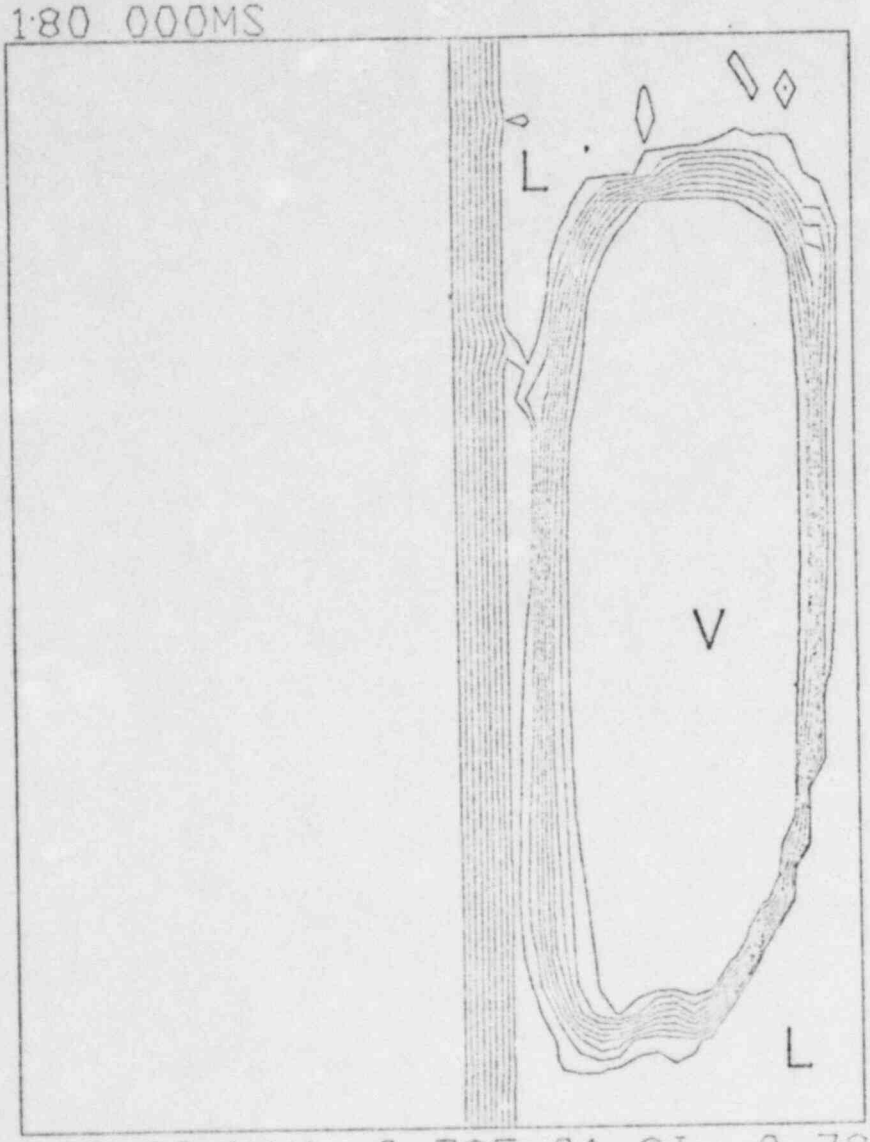

MIN= 1 90E-05 MAX= 9 78E-01 CI= 9 78E-02

Fig 3j

VOLUME FRACTION OF LIQUID
TIME 200 000MS

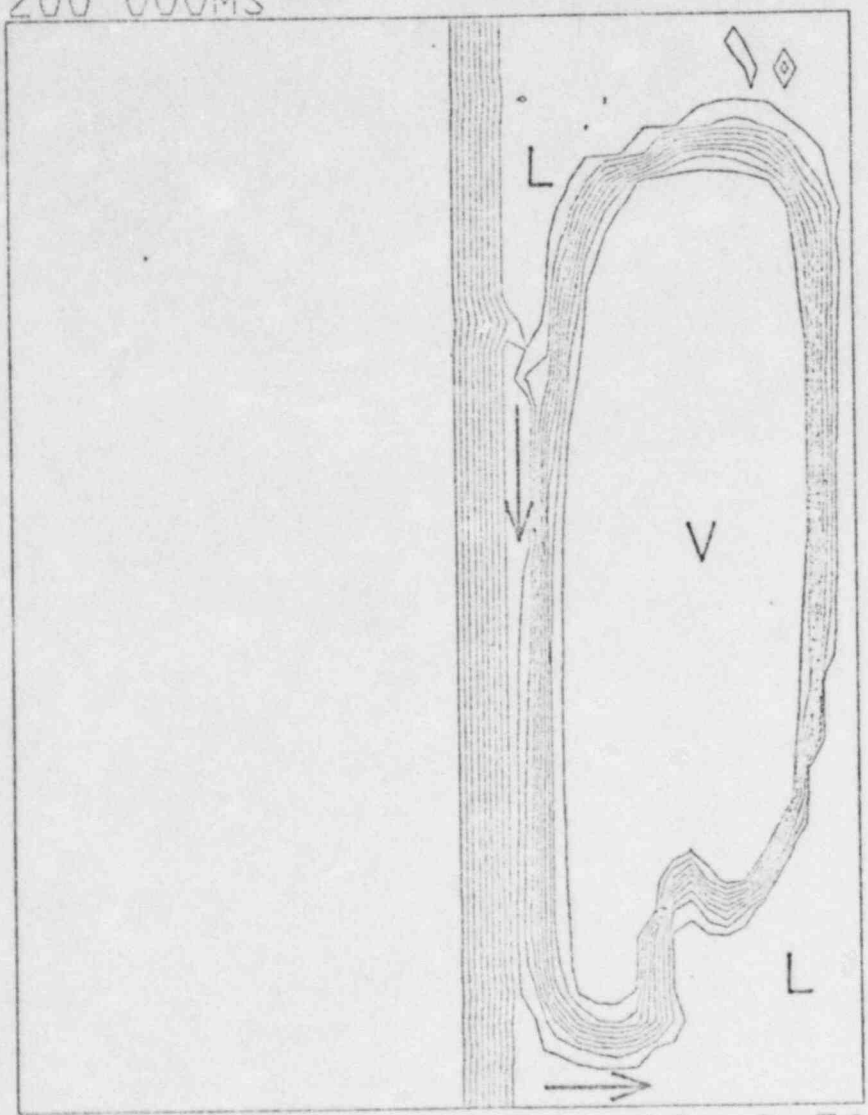

MIN= 1 90E-06 MAX= 9 78E-01 CI= 9 78E-02

Fig 3k

VOLUME FRACTION OF LIQUID
TIME 240.000MS

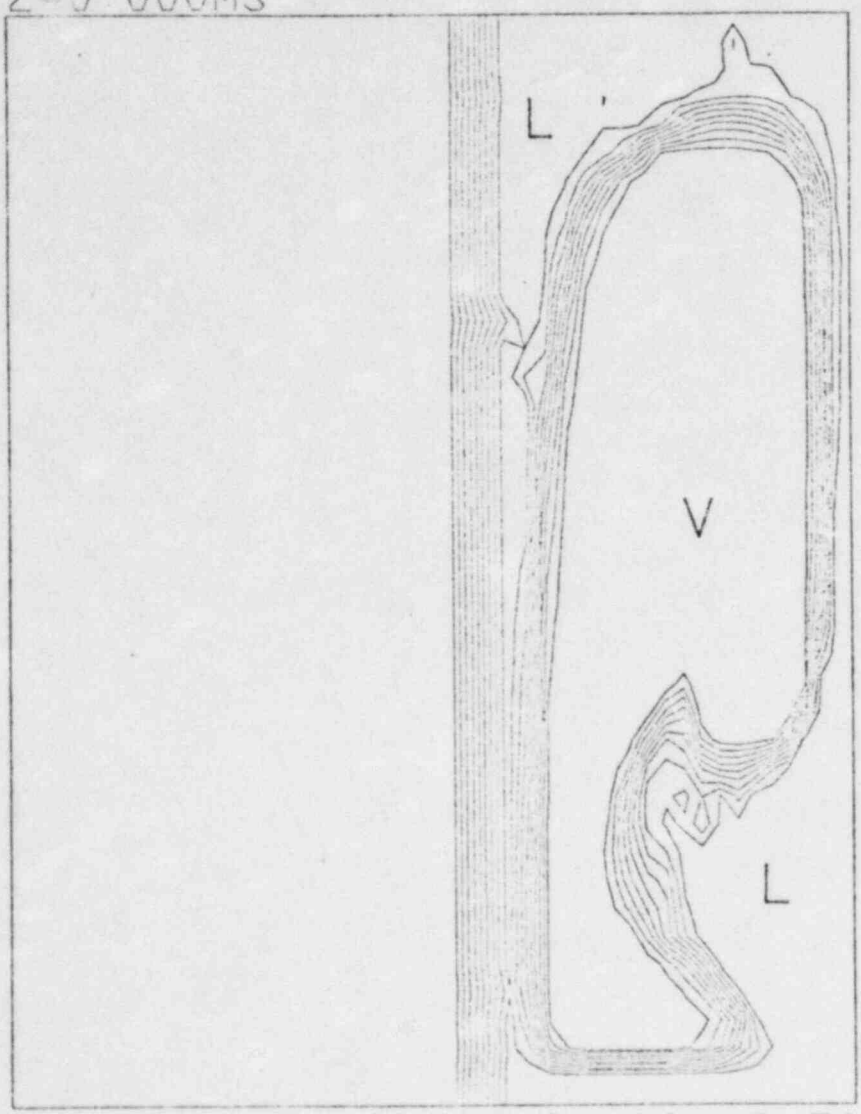

MIN= 1.90E-06 MAX= 9.78E-01 CI= 9.78E-02

Fig 31

VOLUME FRACTION OF LIQUID
TIME 280 000MS

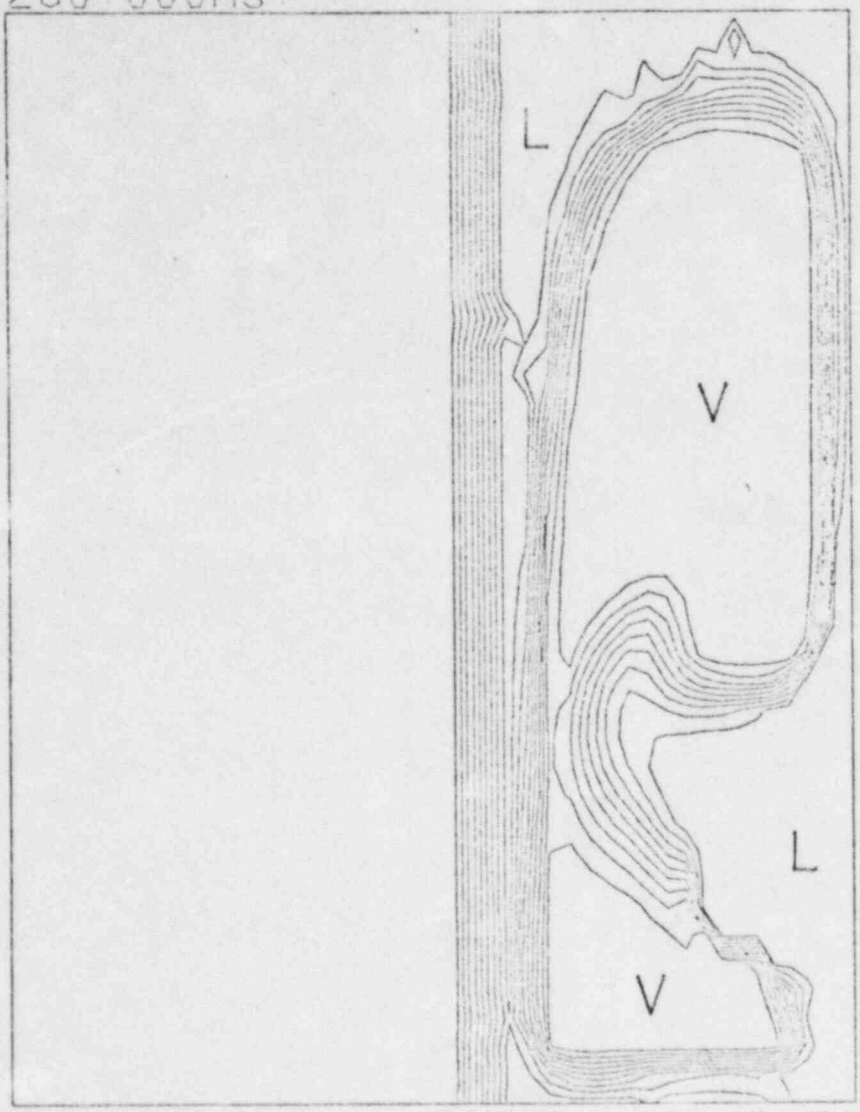

MIN= 1 90E-06 MAX= 9 78E-01 CI= 9 78E-02

Fig 3m

VOLUME FRACTION OF LIQUID
TIME 320 000MS

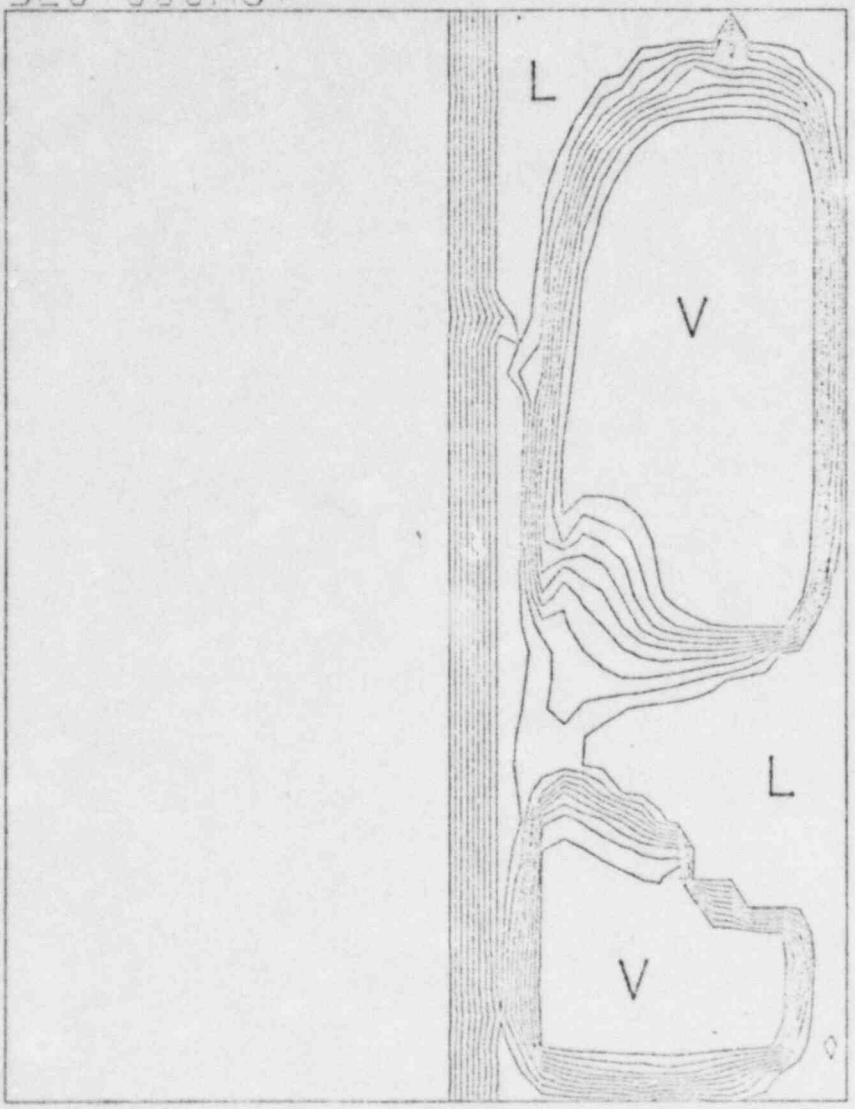

MIN= 1 90E-06 MAX= 9 78E-01 CI= 9 78E-02

Fig 3n

VOLUME FRACTION OF LIQUID
TIME .360 000MS

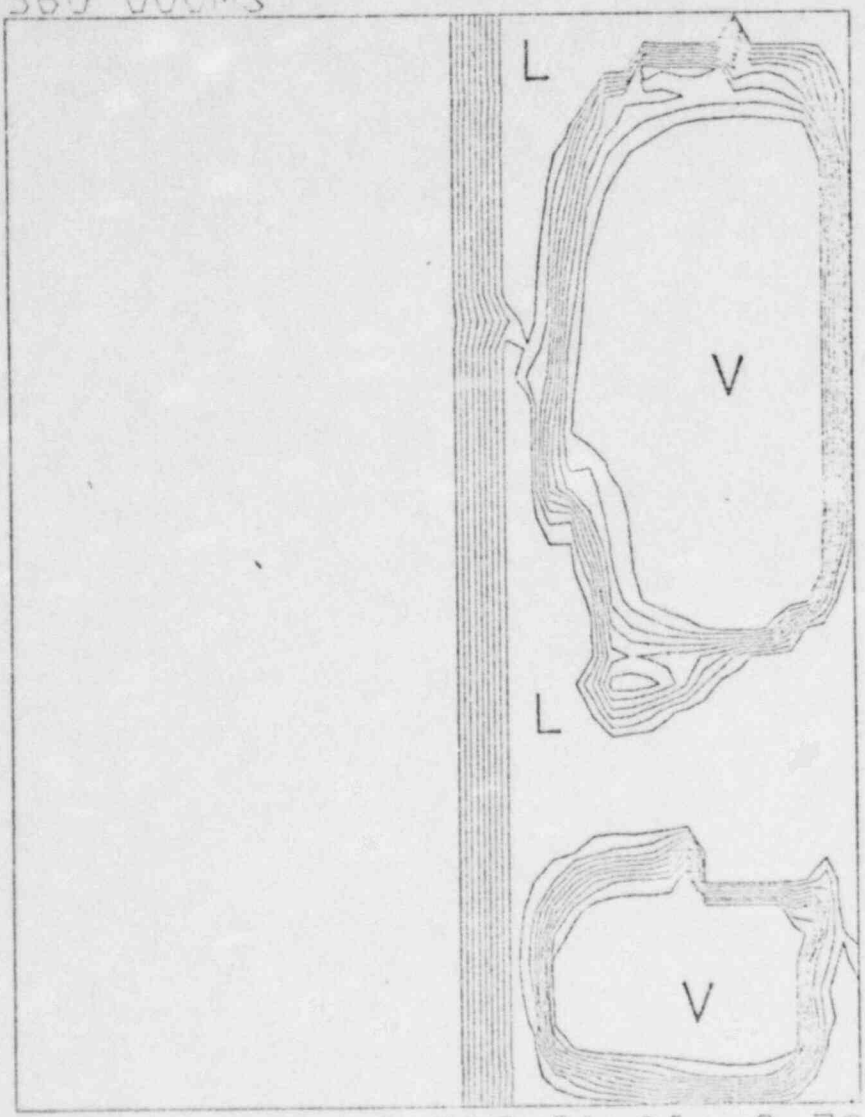

MIN= 1 90E-06 MAX= 9 78E-01 CI= 9 78E-02

Fig 3σ

VOLUME FRACTION OF LIQUID
TIME 400 000MS

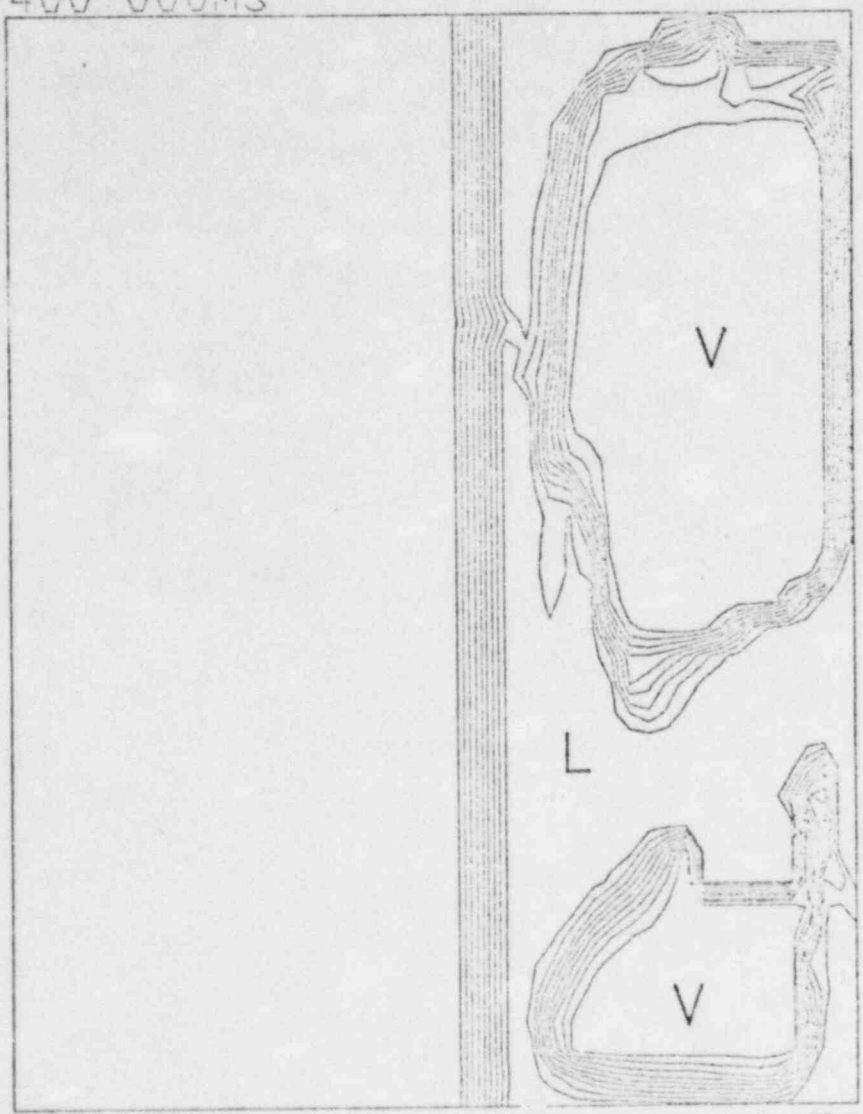

MIN= 1 90E-06 MAX= 9 78E-01 CI= 9 78E-02

Fig 3p

VOLUME FRACTION OF LIQUID
TIME 440.000MS

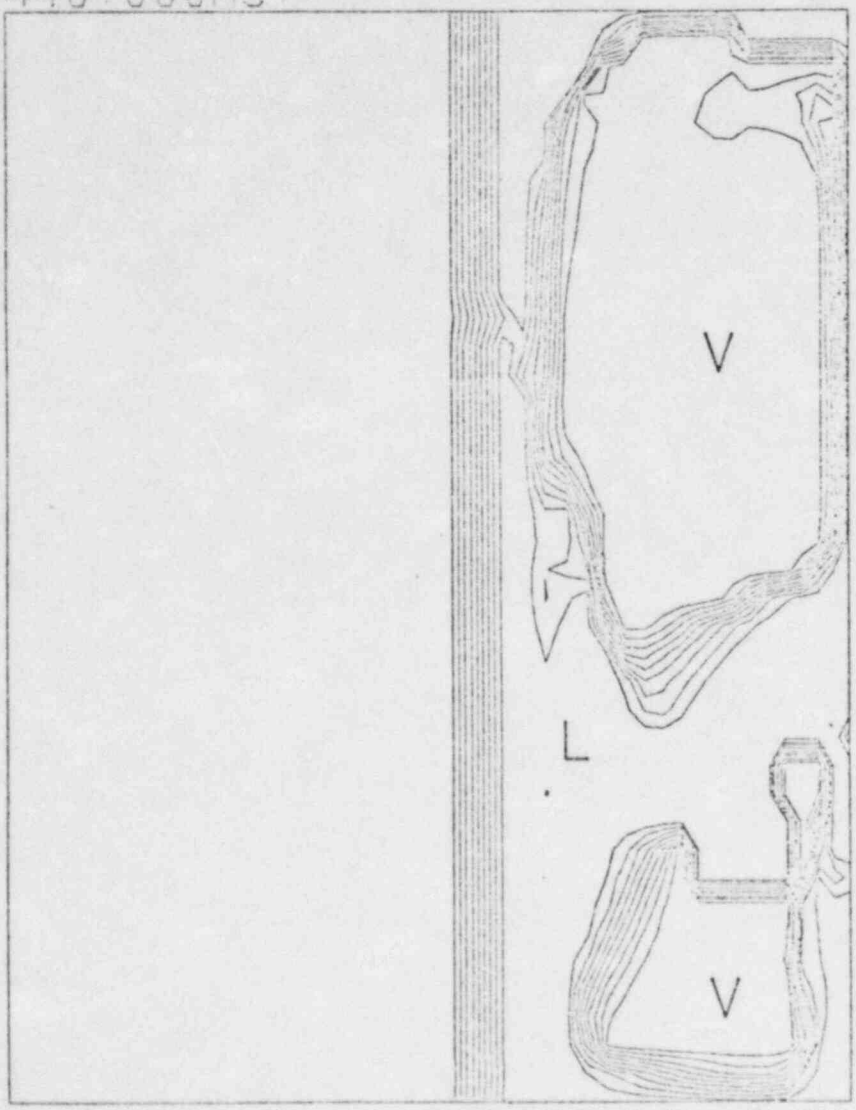

MIN= 1.90E-06 MAX= 9.78E-01 CI= 9.78E-02

Fig 39

VOLUME FRACTION OF LIQUID
TIME 480.000MS

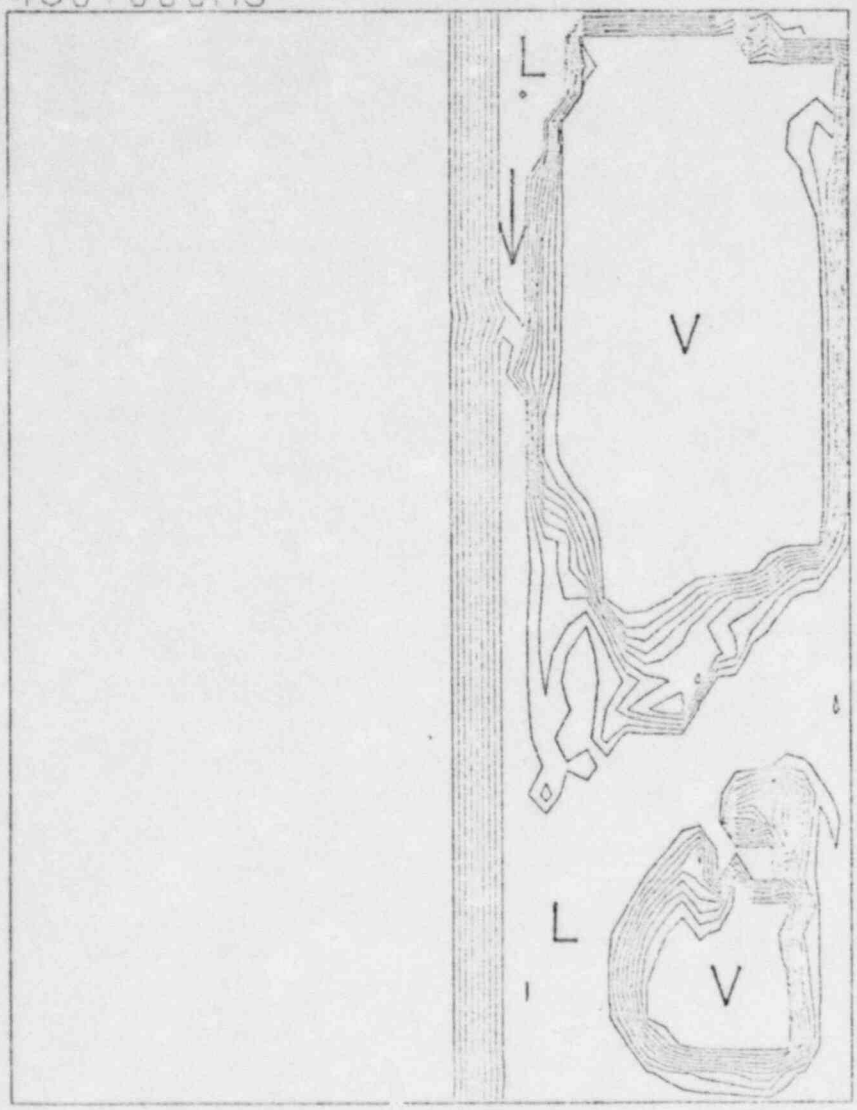

MIN= 1.90E-06 MAX= 9.78E-01 CI= 9.78E-02

Fig 3r

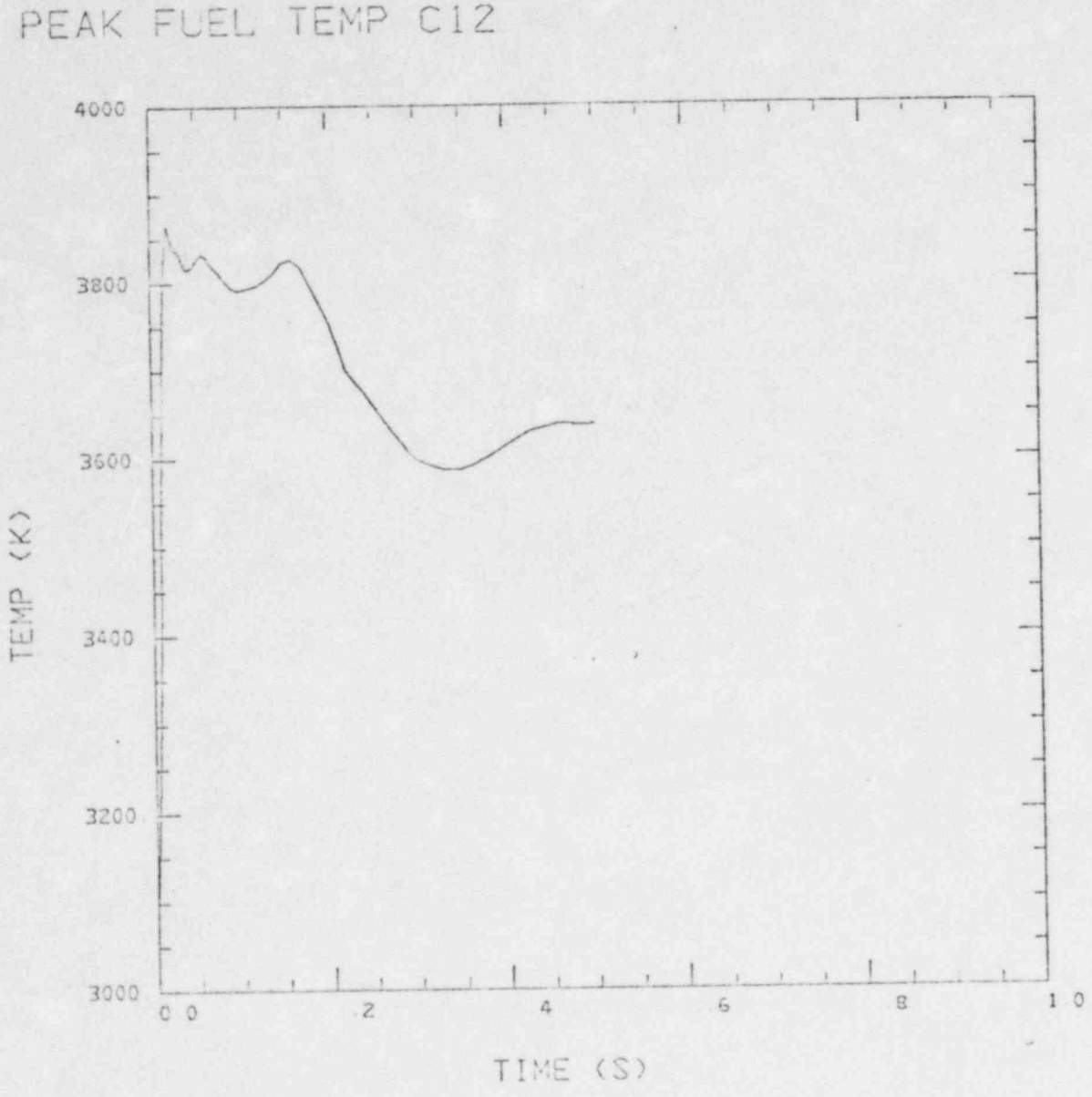
PEAK FUEL TEMP C12
4000
3800
3600
3400
3200
3000
TEMP (K)
0 0
2
4
6
8
1 0
TIME (S)

Fig 4

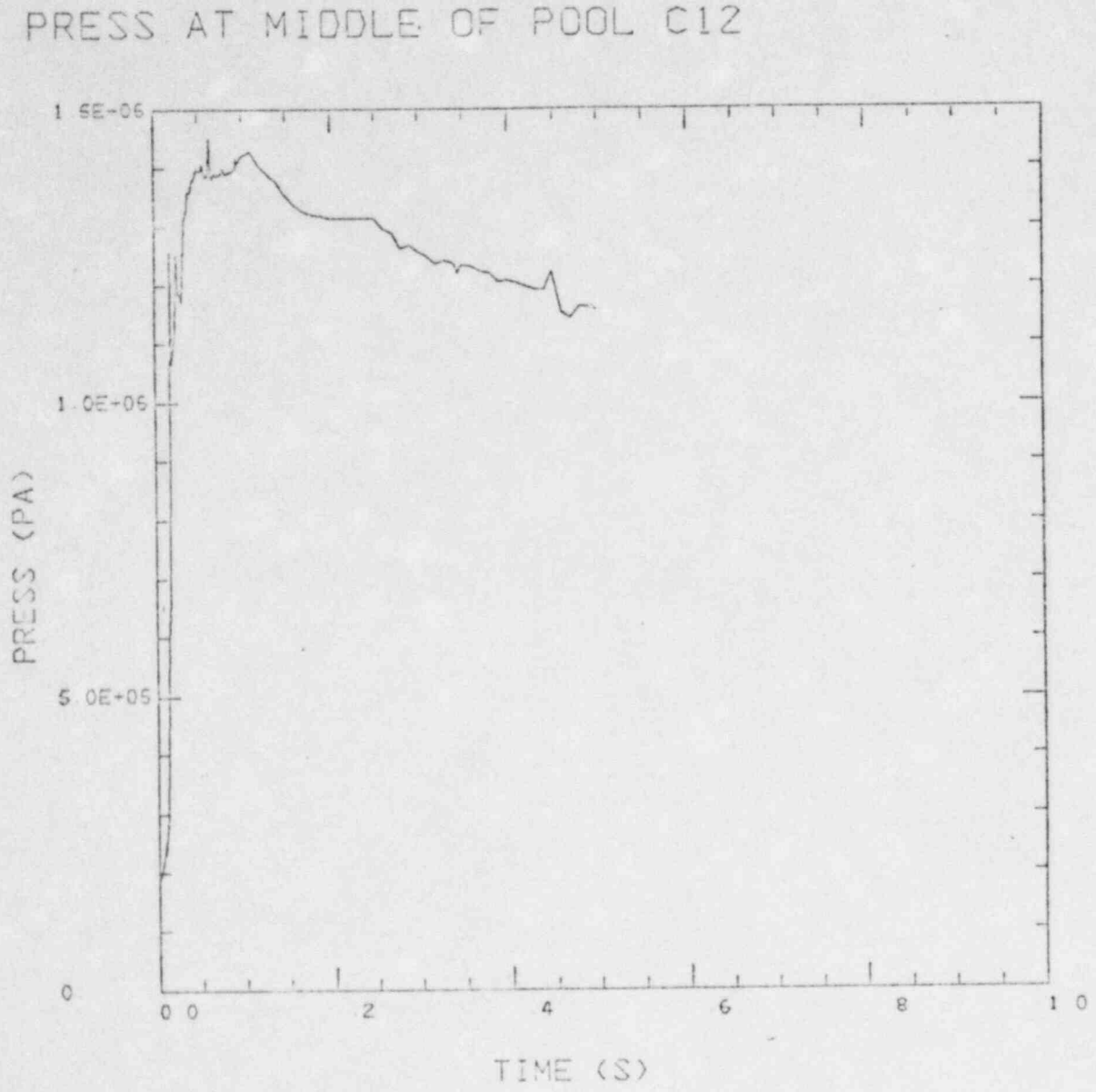
PRESS AT MIDDLE OF POOL C12
1.5E+06
1.0E+06
5.0E+05
0
PRESS (PA)
0.0
2
4
6
8
10
TIME (S)

Fig 5

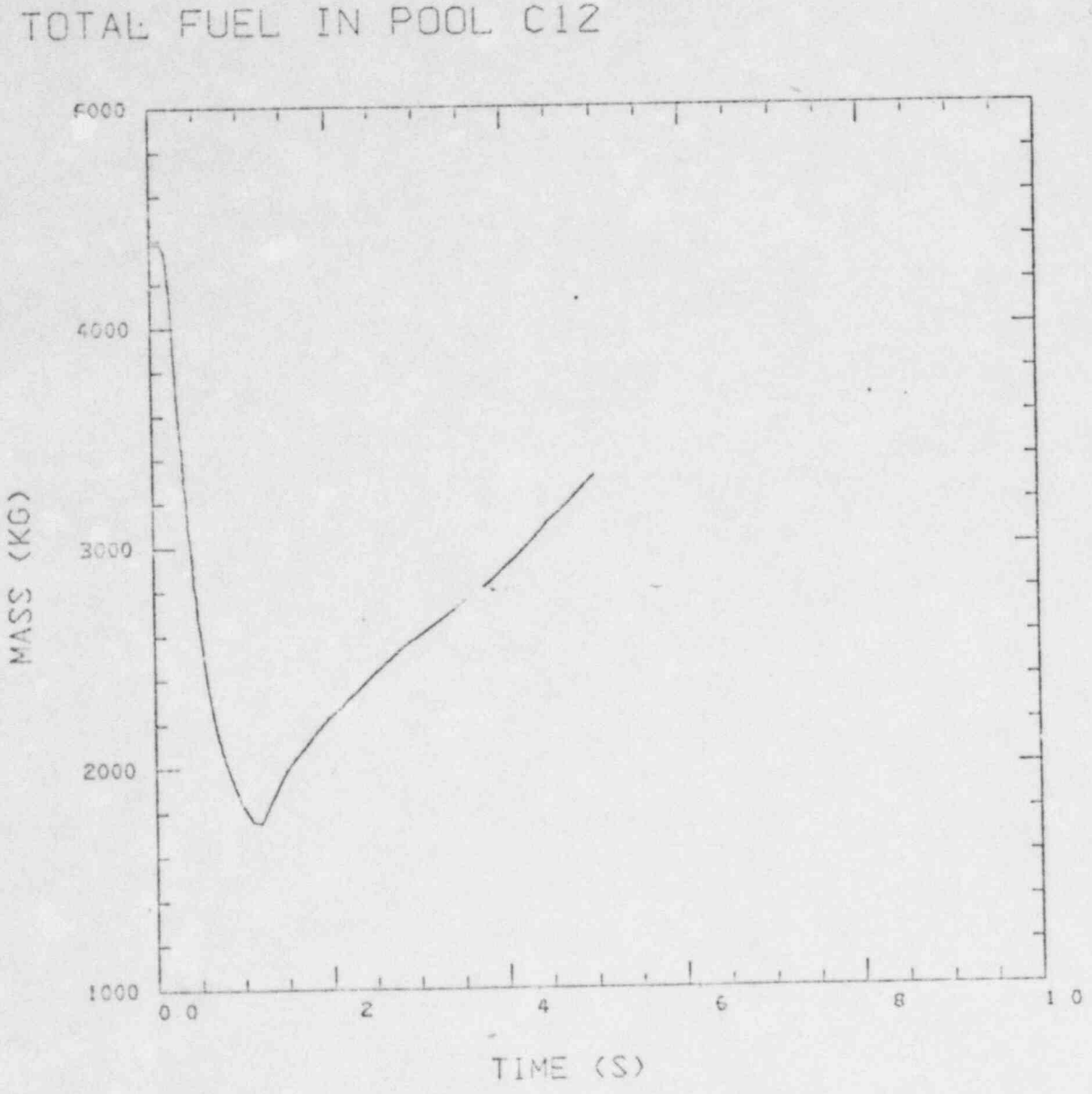
TOTAL FUEL IN POOL C12
5000
4000
3000
2000
1000
MASS (KG)
0 0
2
4
6
8
1 0
TIME (S)

Fig 6

REACTIVITY vs POOL DEPTH FOR SLUMPING OF DRIVERS 3 and 4 - CRBR

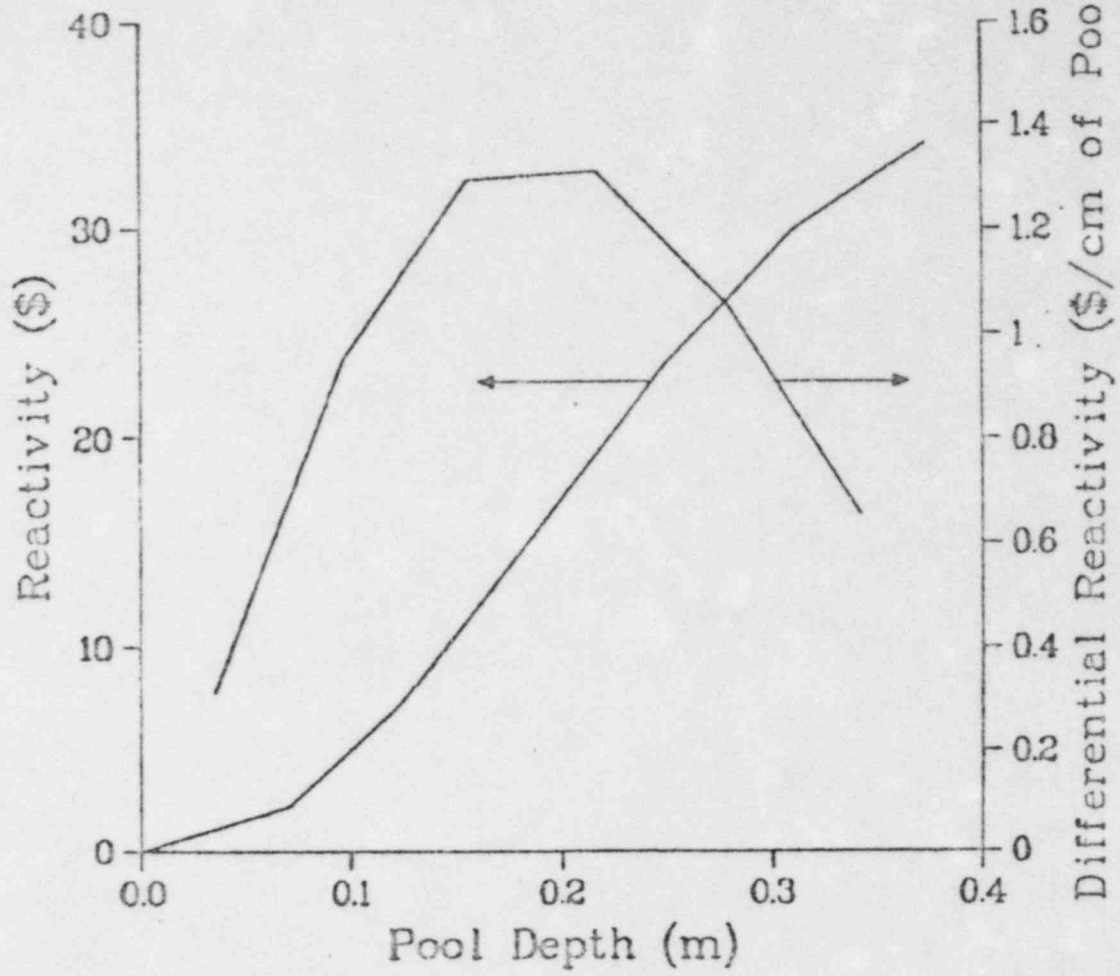

Fig 7

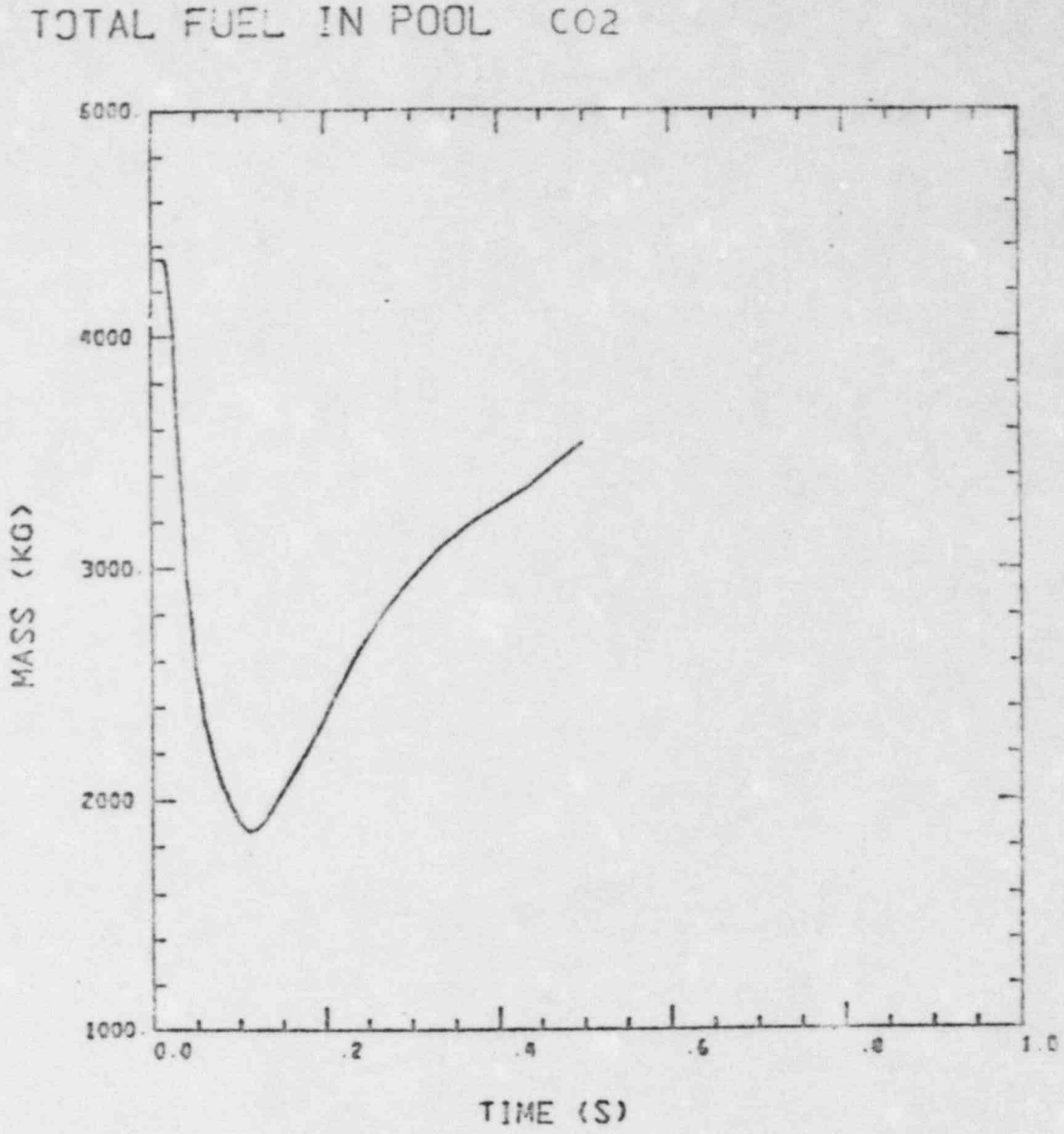
TOTAL FUEL IN POOL CO2
5000.
4000
3000.
2000
1000.
MASS (KG)
0.0
.2
.4
.6
.8
1.0
TIME (S)

Fig 8

TOTAL FUEL IN POOL C04

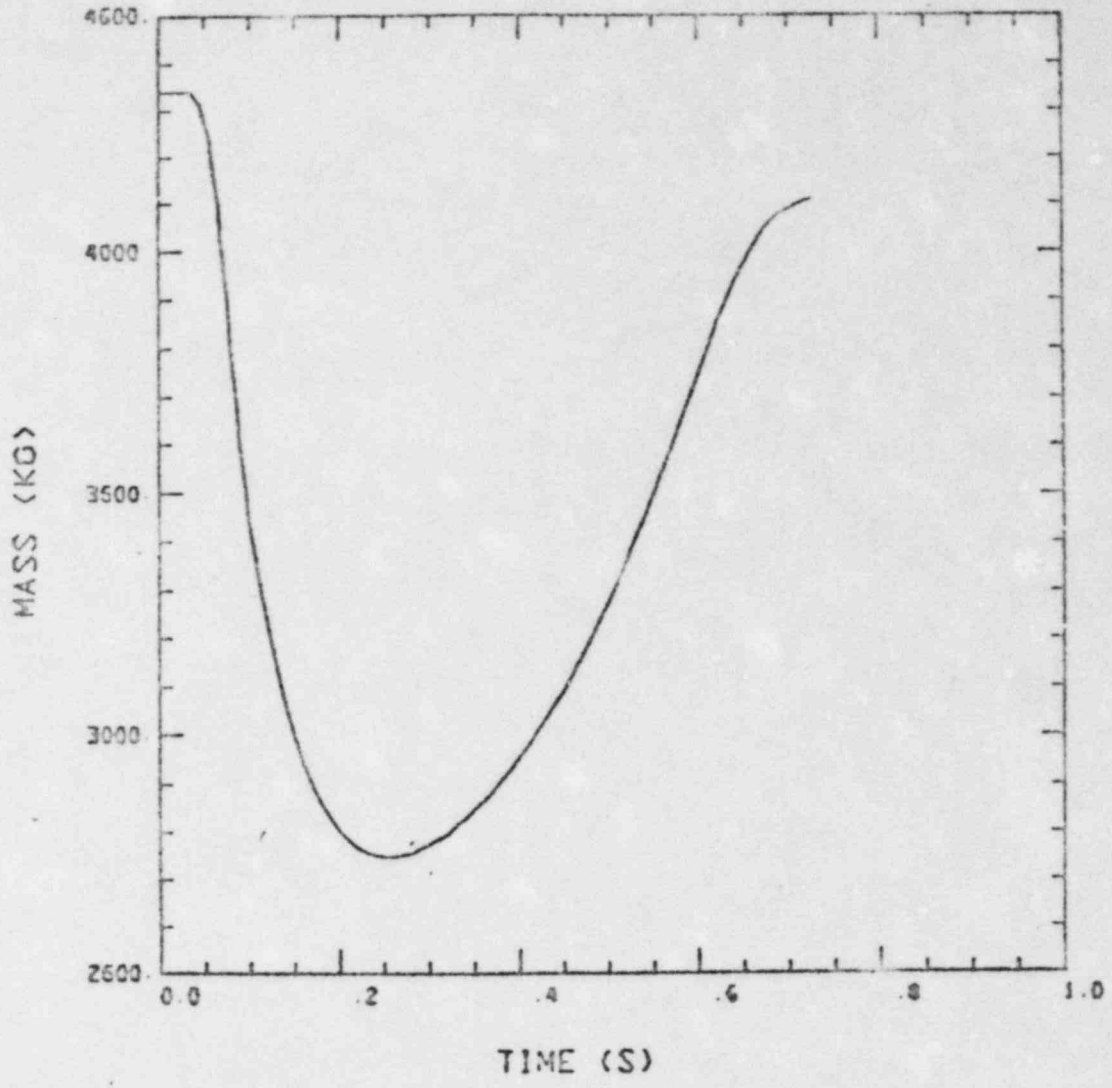

Fig 9

TOTAL FUEL IN POOL C06

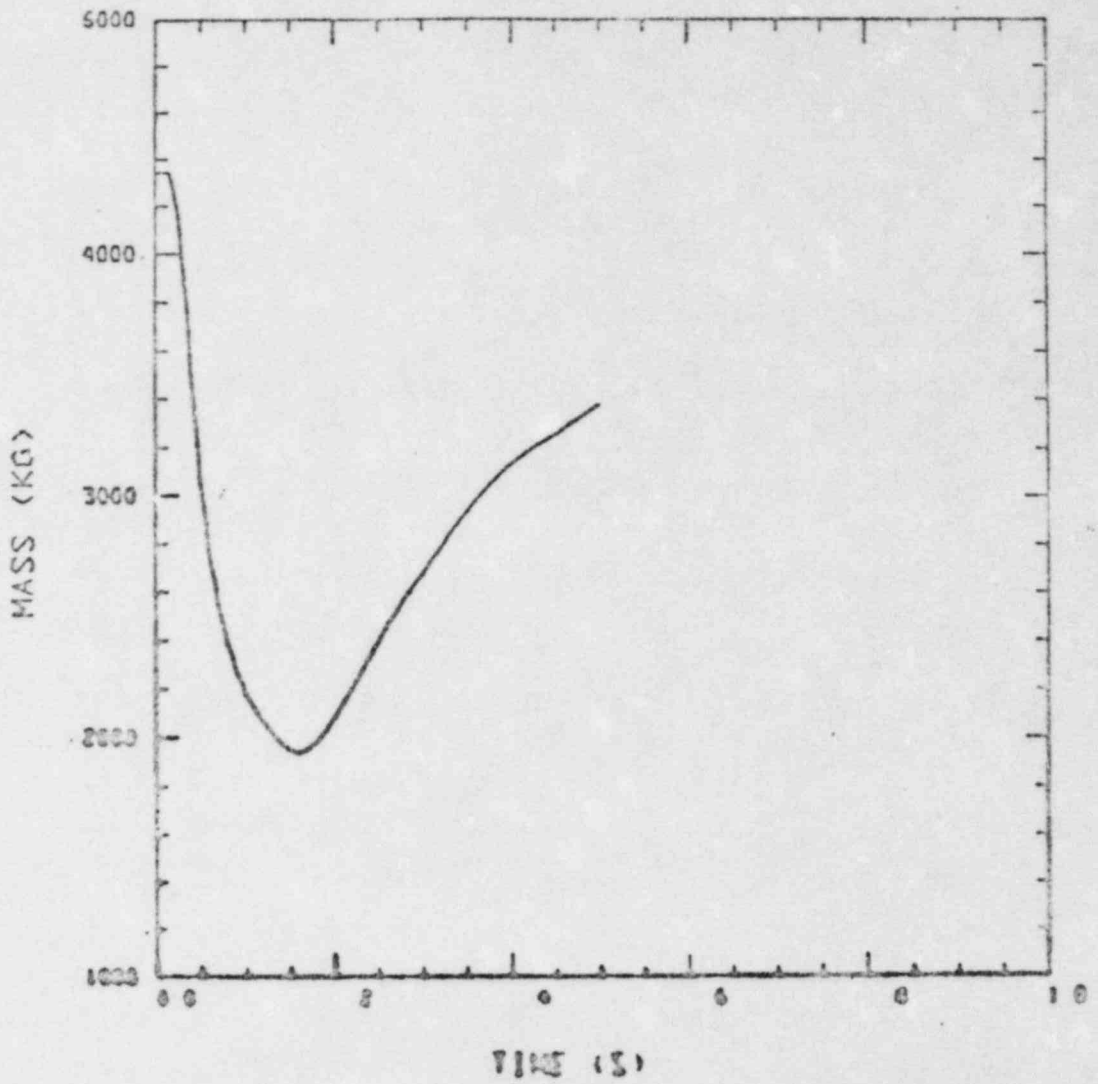

Fig 10

B.II.7

TOTAL FUEL IN POOL C08

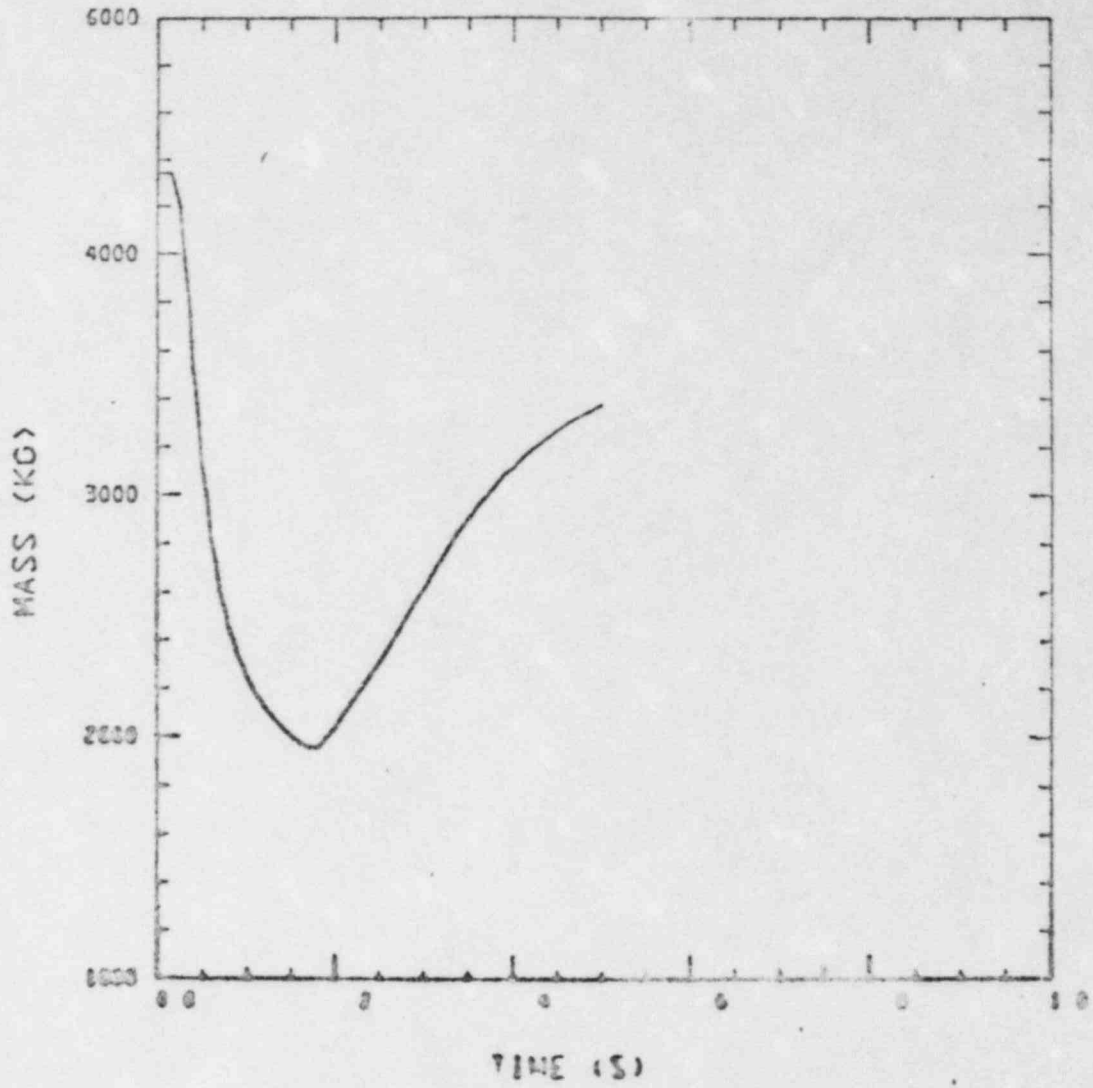

Fig 11

TOTAL FUEL IN POOL C10

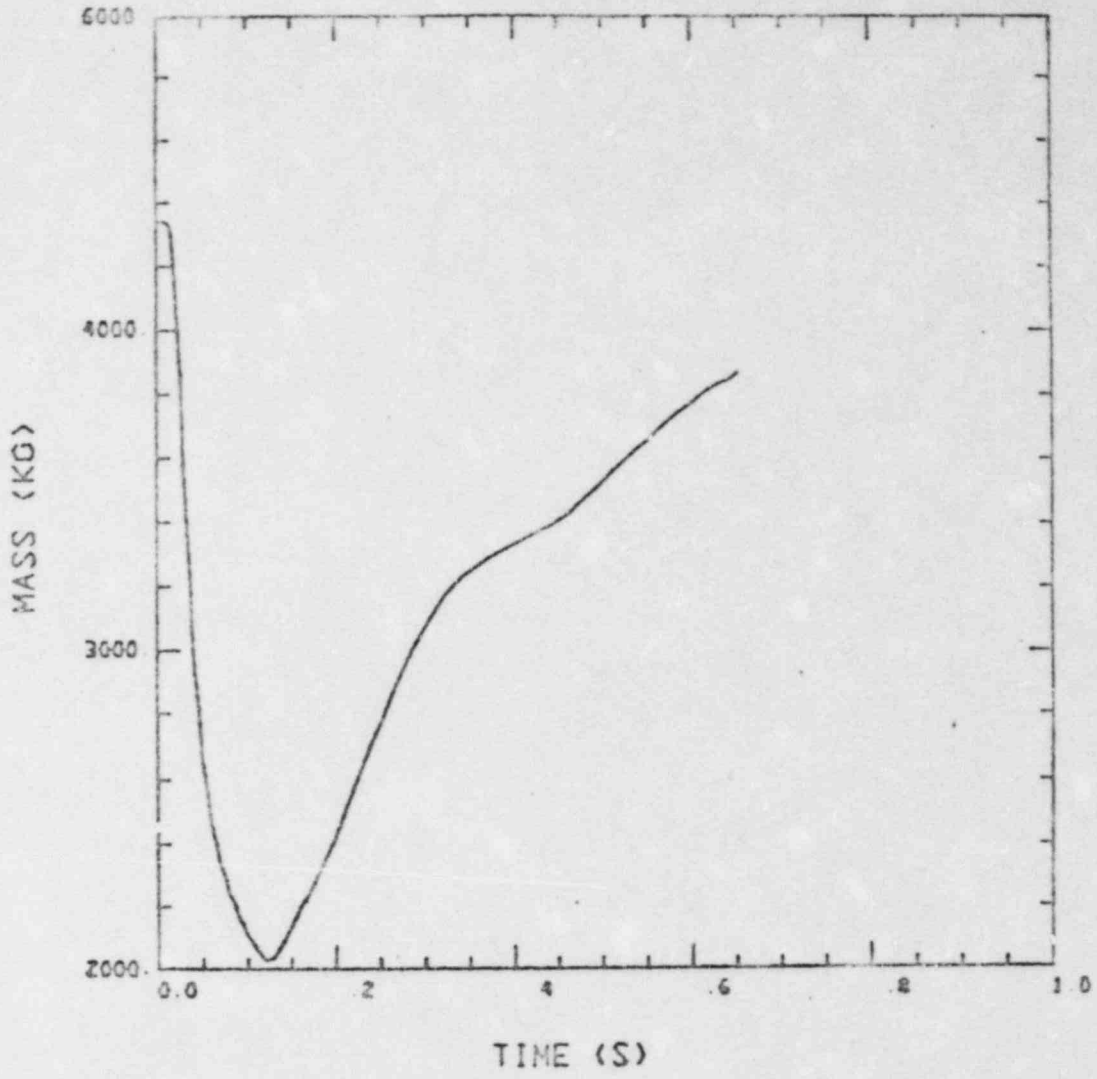

Fig 12

B.II.7

TOTAL FUEL IN POOL C14

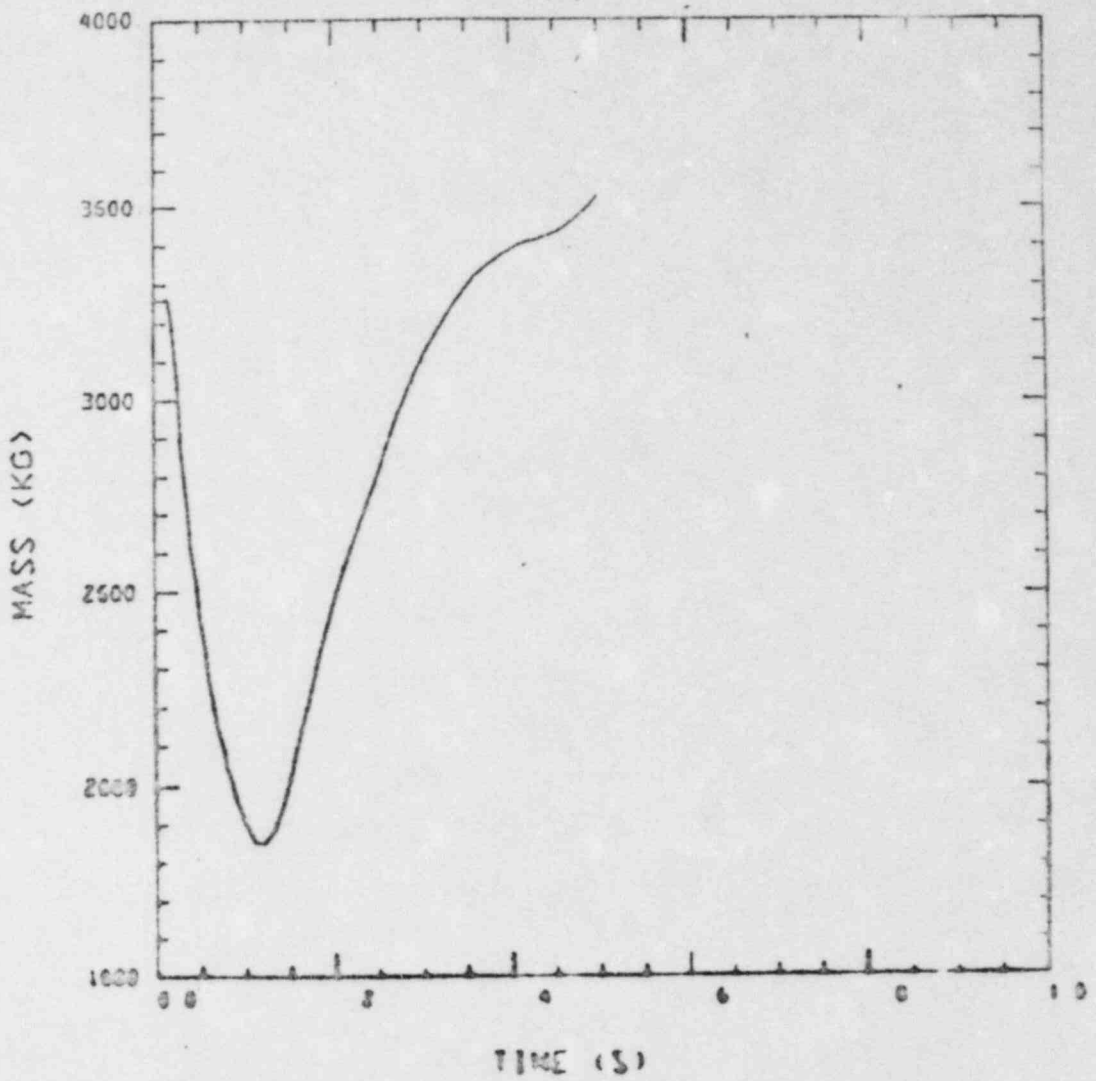

Fig 13

BII.7

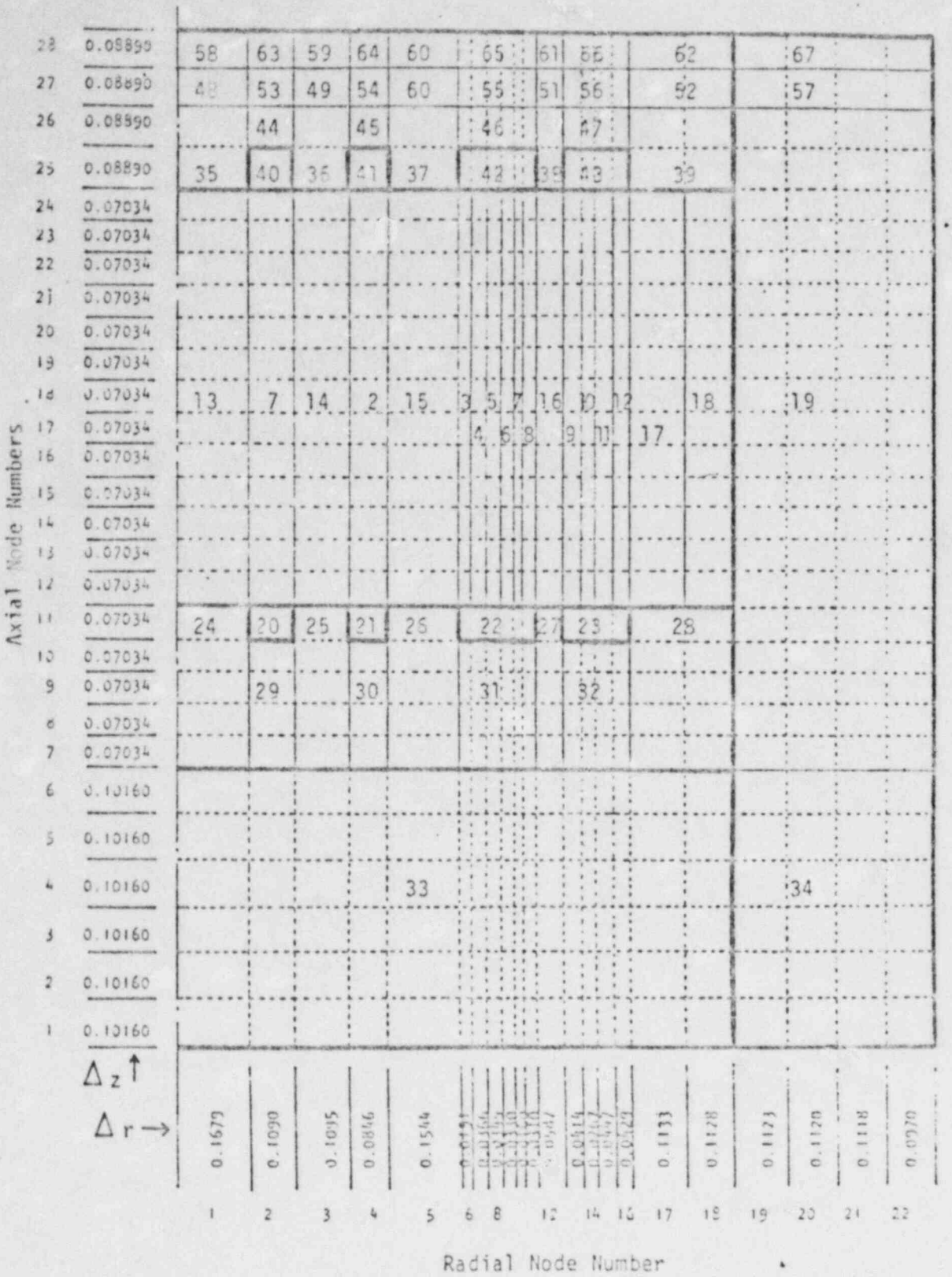

Fig. 1. Calculational model for SIMMER-II analysis of ~~sup fuel-coolant~~ cylindrical pool behavior during hypothetical core disruptive accidents in the CRBR

CII.7

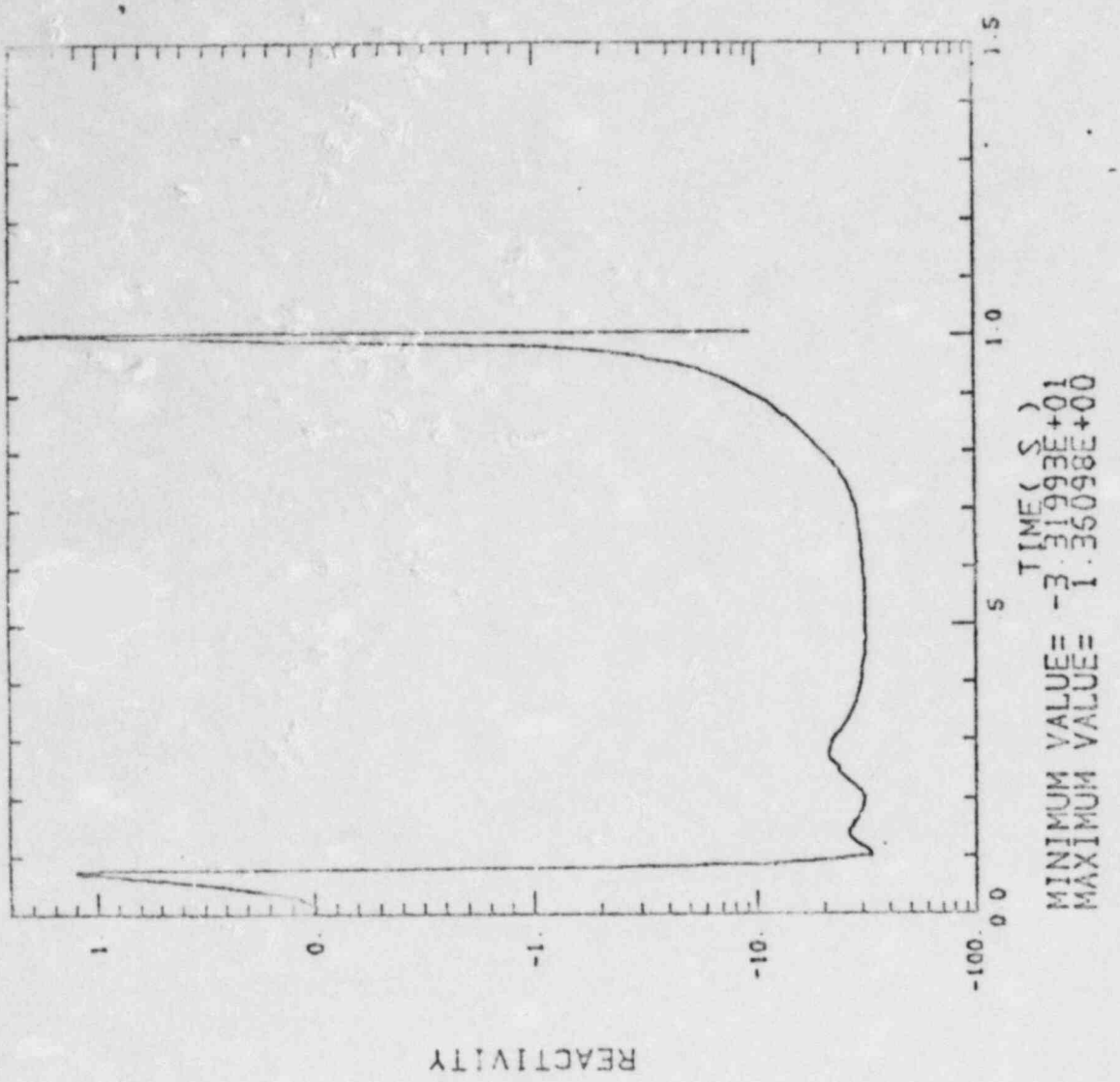
REACTIVITY
1
0
-1
-10
-100
0.0
.5
1.0
1.5
TIME(S)
MINIMUM VALUE= -3.31993E+01
MAXIMUM VALUE= 1.36098E+00

Fig 2

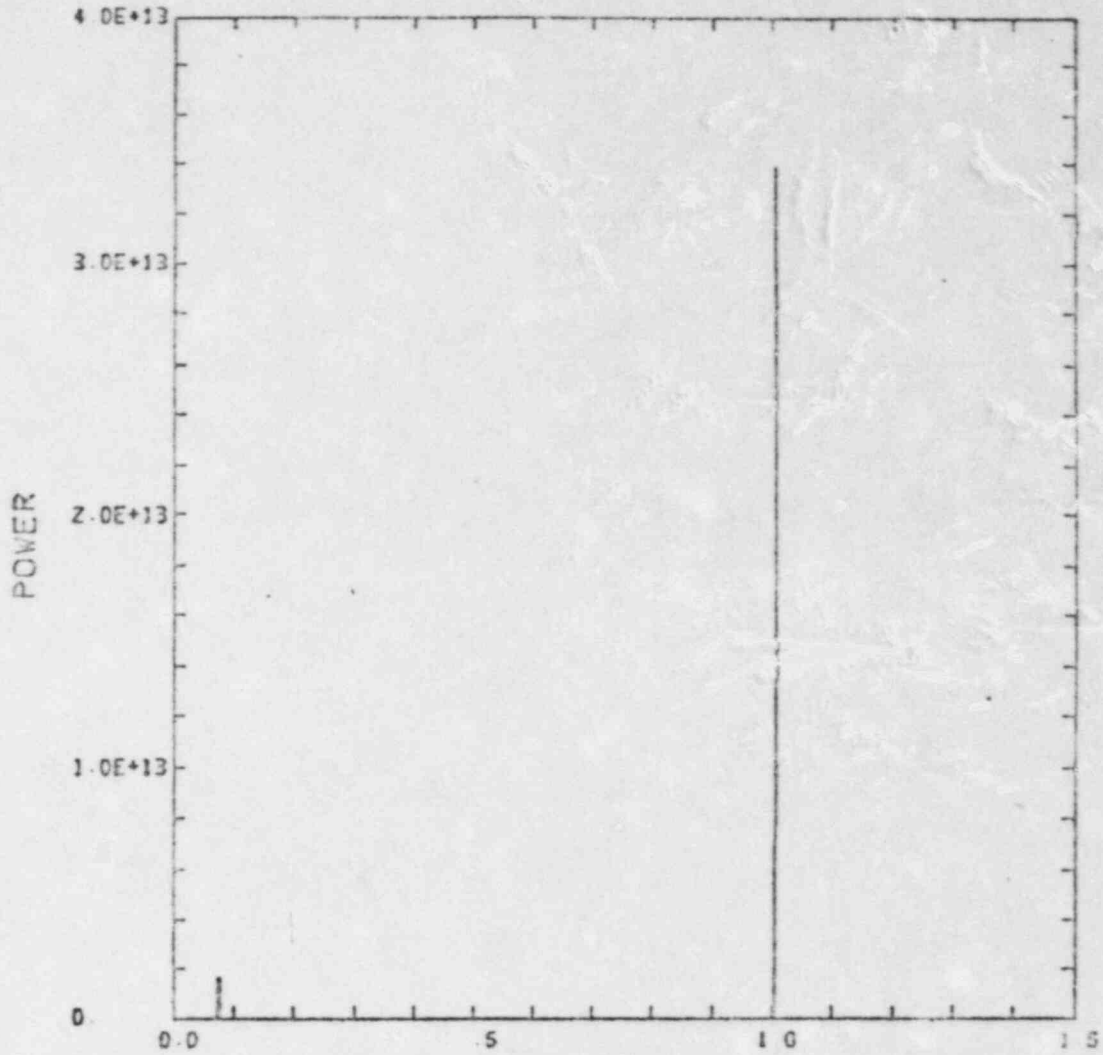

MINIMUM VALUE= 8.67754E+07
MAXIMUM VALUE= 3.39567E+13

Fig 3

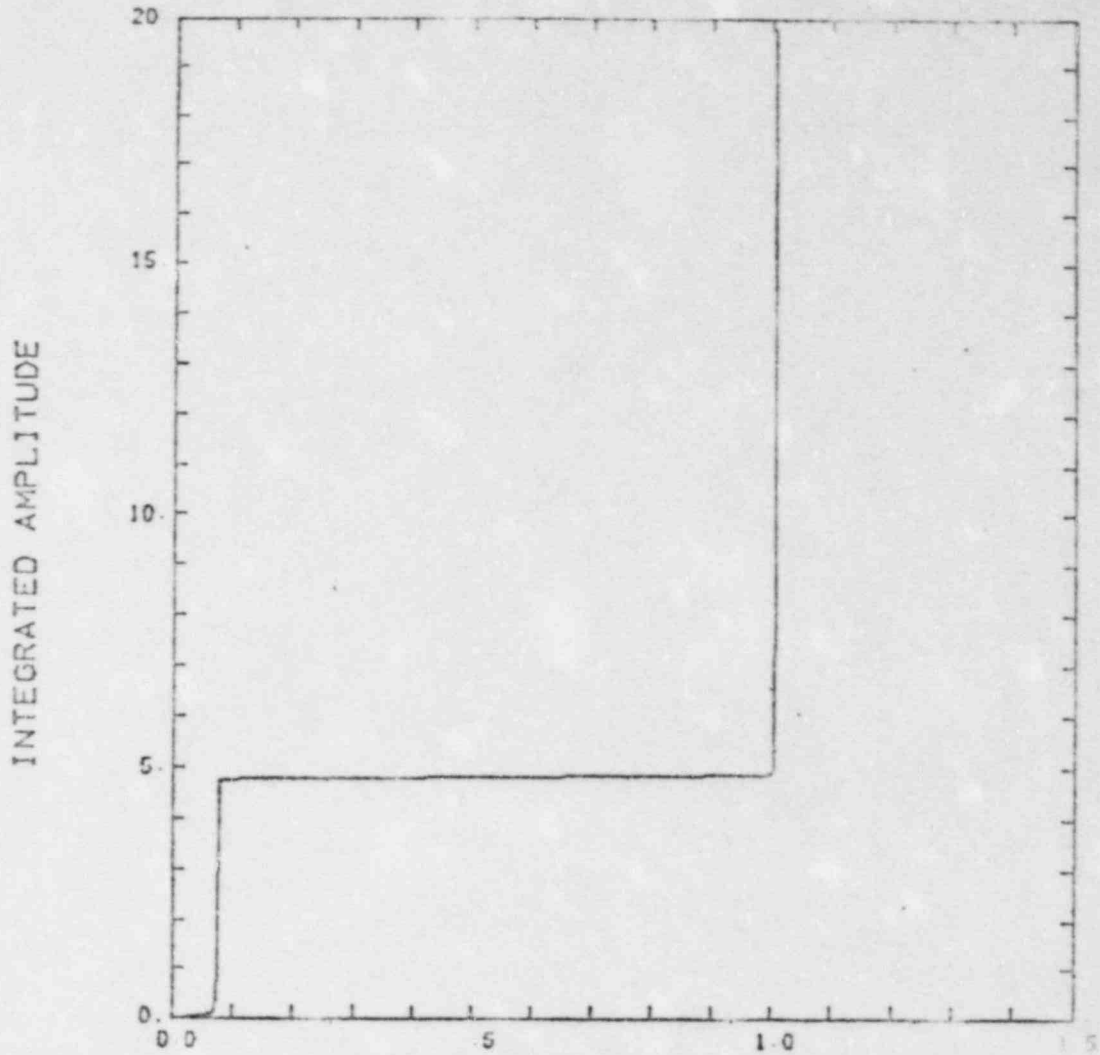
INTEGRATED AMPLITUDE
20
15
10
5
0.
0.0
.5
1.0
TIME(S)
MINIMUM VALUE= 9.99997E-05
MAXIMUM VALUE= 1.98206E+01

Fig 4

CII.7

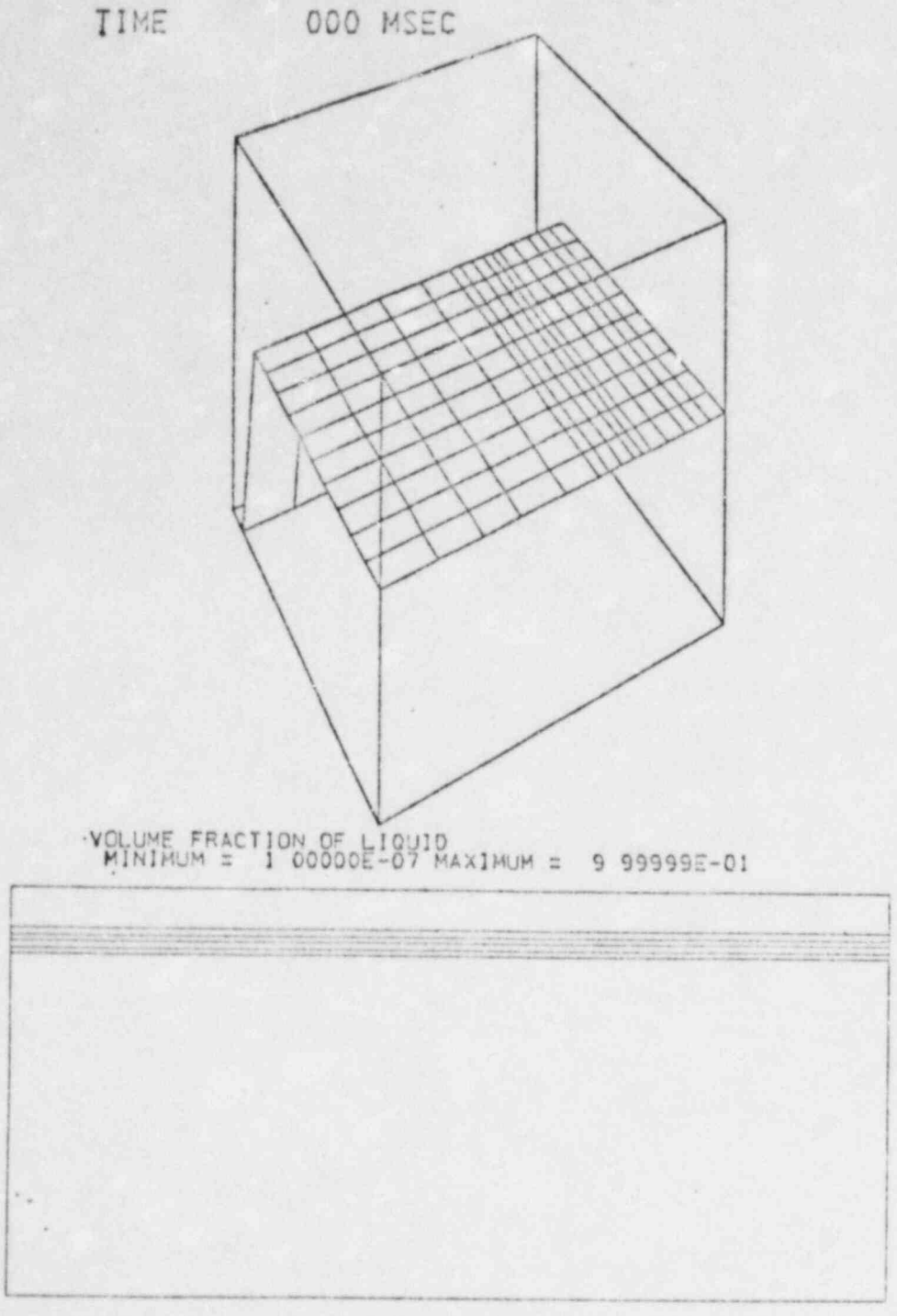
TIME 000 MSEC
VOLUME FRACTION OF LIQUID
MINIMUM = 1 00000E-07 MAXIMUM = 9 99999E-01

Fig 5a

TIME 100 000 MSEC

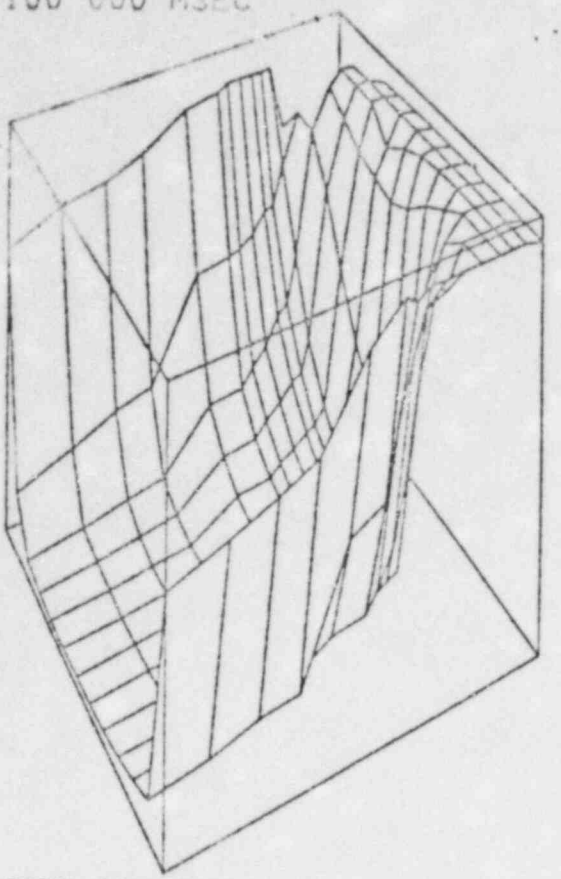

VOLUME FRACTION OF LIQUID
MINIMUM = 1 00000E-07 MAXIMUM = 9 99999E-01

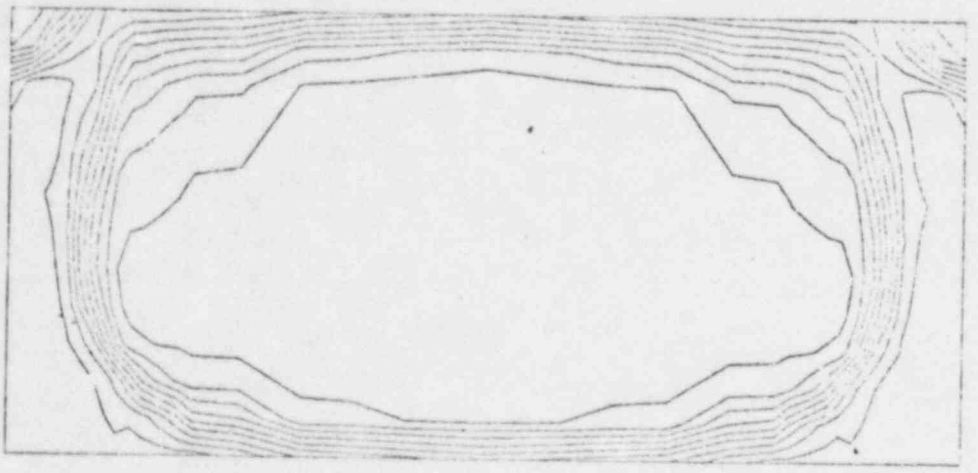

Fig 5b

TIME 200 000 MSEC

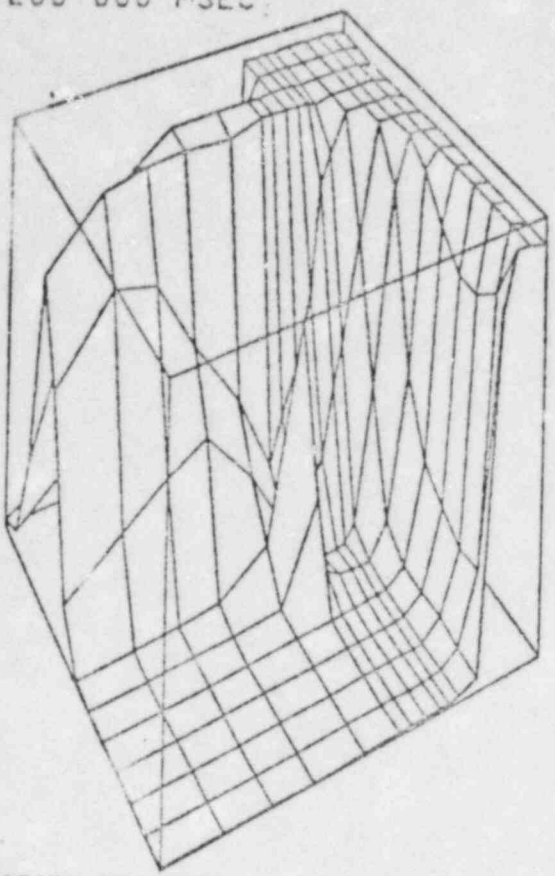

VOLUME FRACTION OF LIQUID
MINIMUM = 1.00000E-07 MAXIMUM = 9.99999E-01.

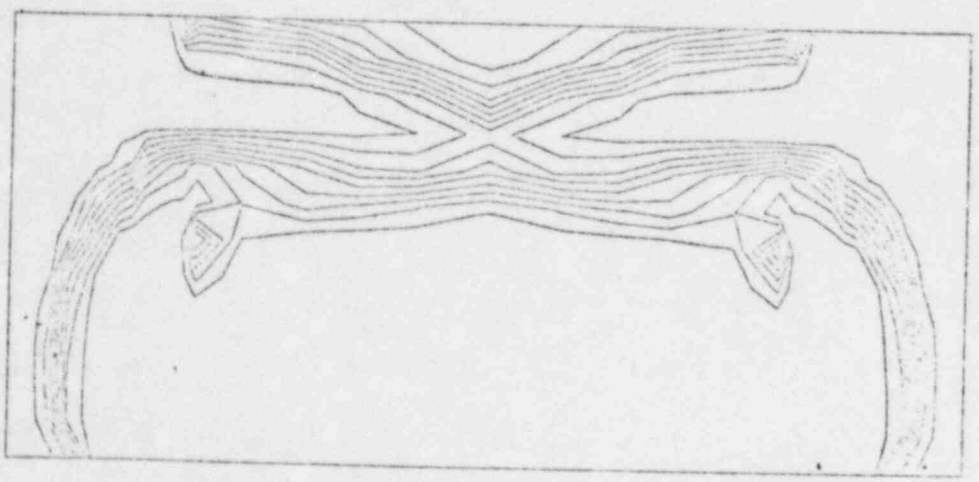

Fig 5c

TIME 400 000 MSEC

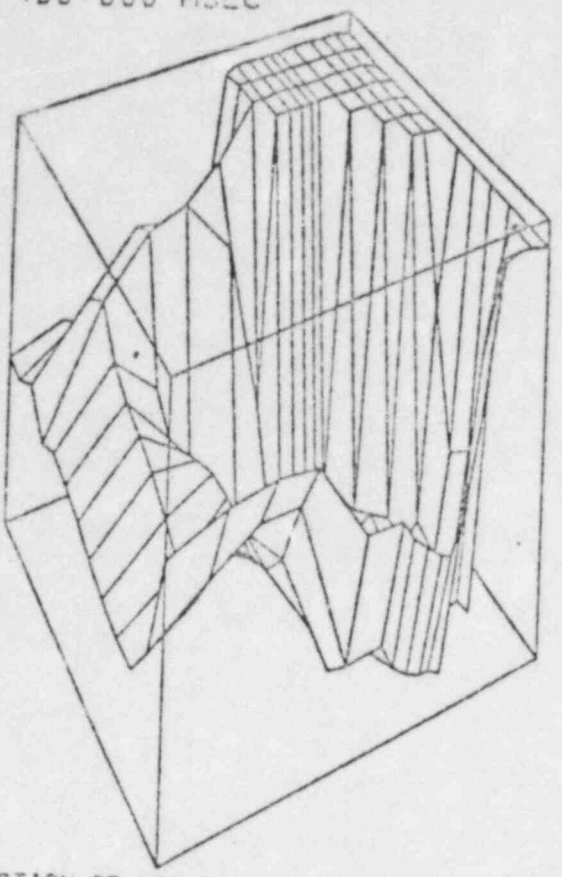

VOLUME FRACTION OF LIQUID
MINIMUM = 1 000DOE-07 MAXIMUM = 9 99999E-01

Fig 5d

TIME 600 000 MSEC

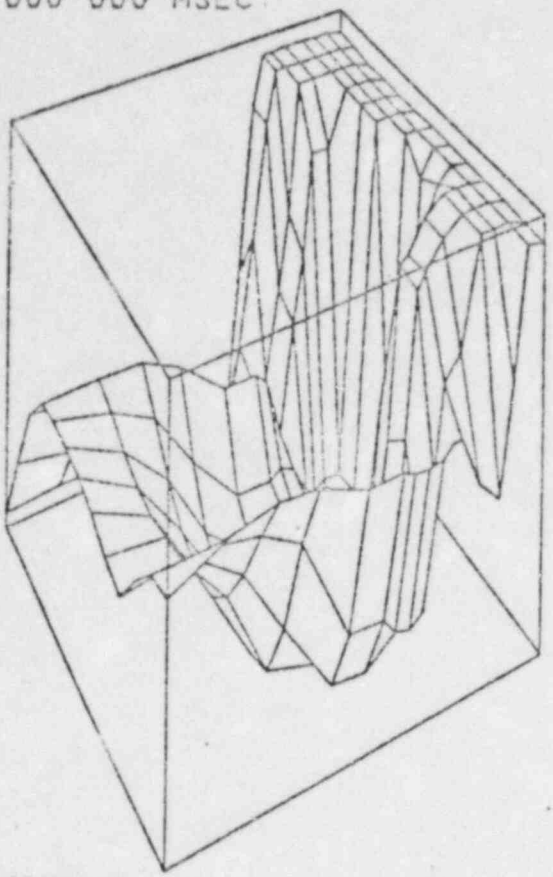

VOLUME FRACTION OF LIQUID
MINIMUM = 1 00000E-07 MAXIMUM = 9 99999E-01

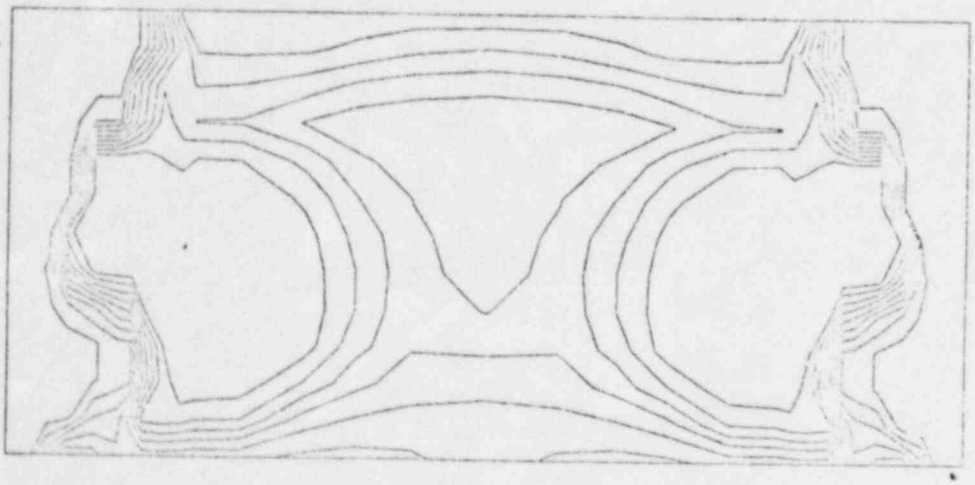

Fig 5e

TIME 800 000 MSEC

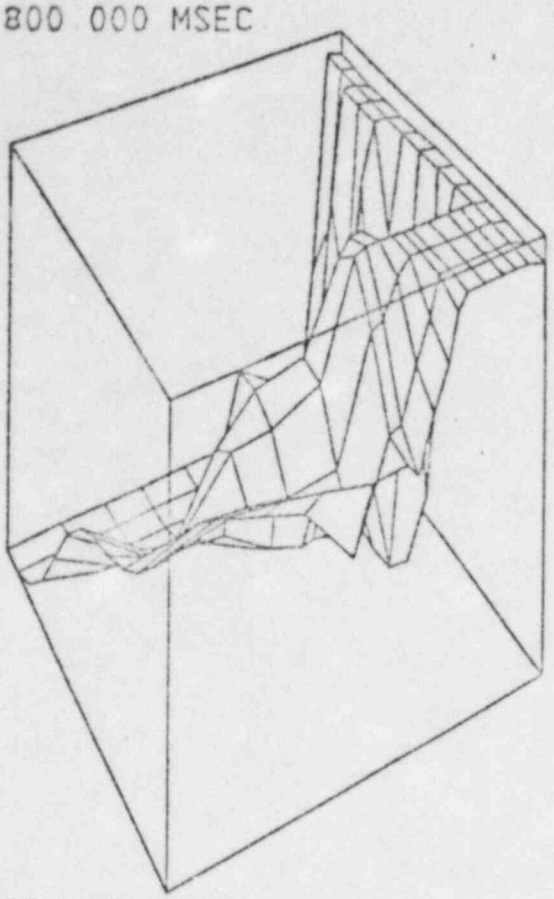

VOLUME FRACTION OF LIQUID
MINIMUM = 1 00000E-07 MAXIMUM = 9 99999E-01

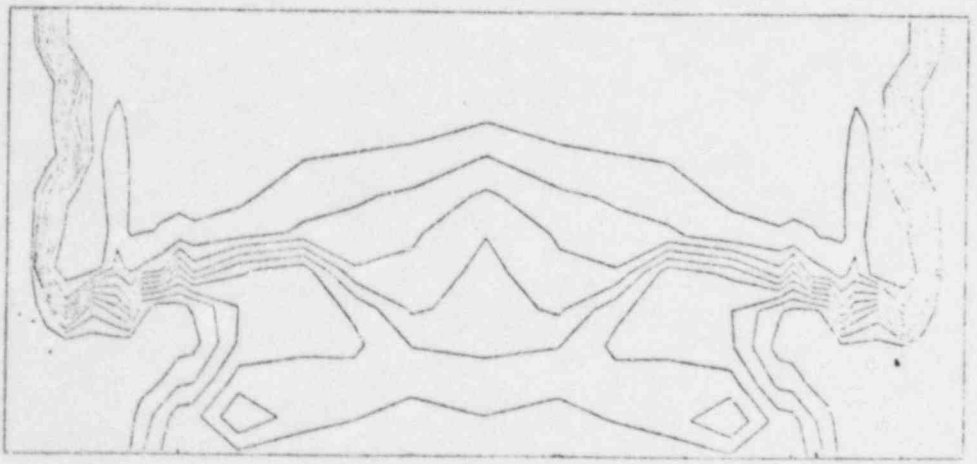

Fig 5f

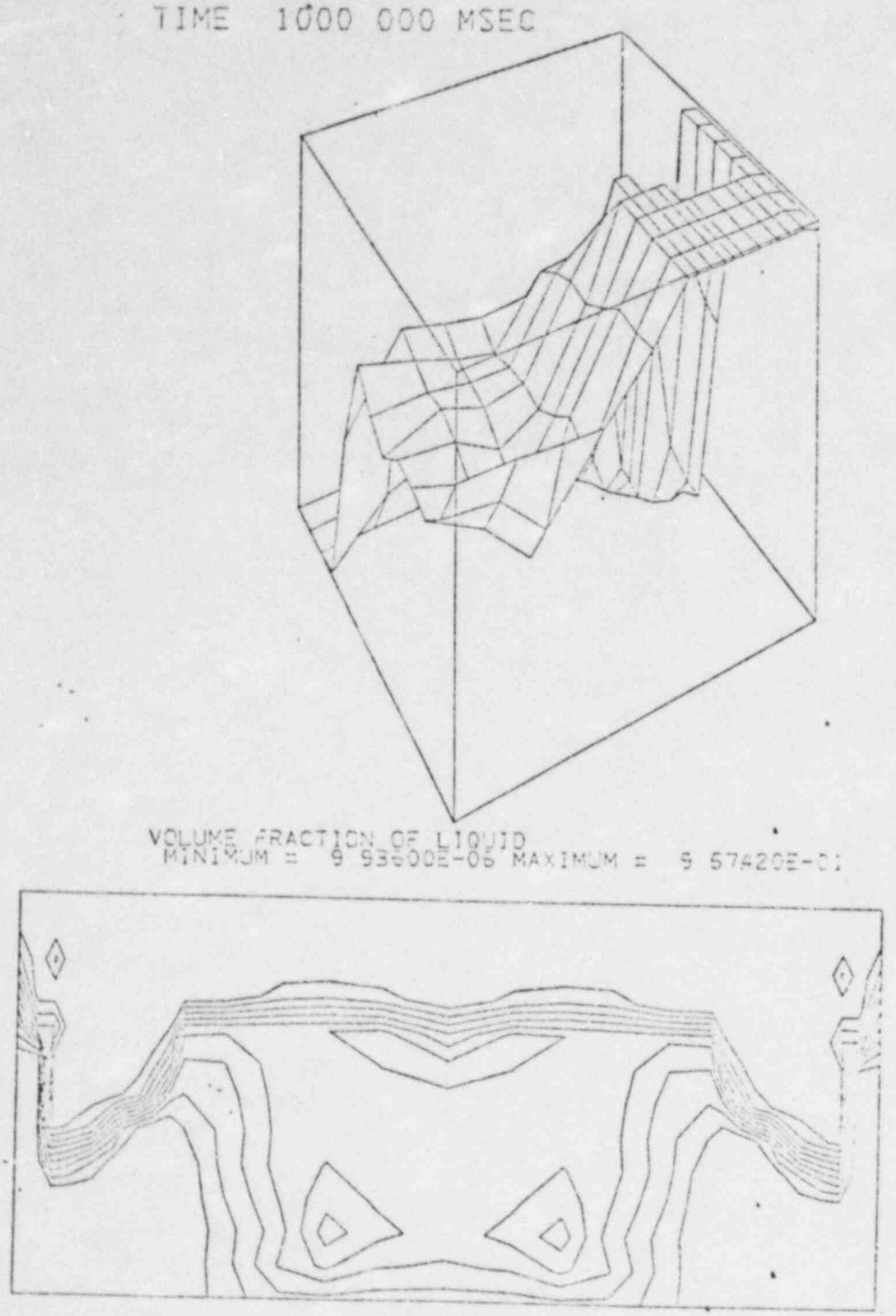
TIME 1000 000 MSEC
VOLUME FRACTION OF LIQUID
MINIMUM = 9 9360DE-06 MAXIMUM = 9 57420E-01

Fig 59

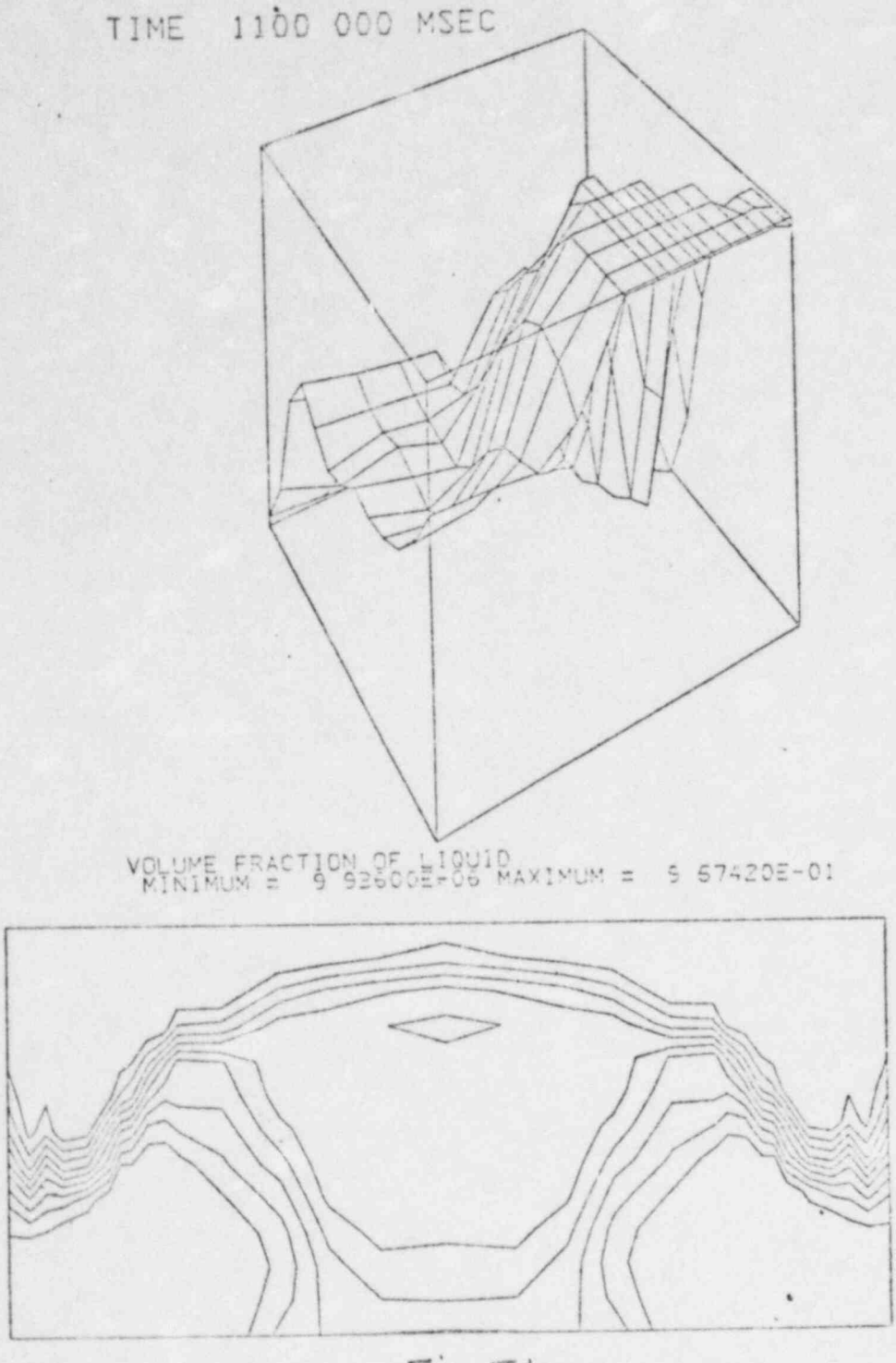
TIME 1100 000 MSEC
VOLUME FRACTION OF LIQUID
MINIMUM = 9 92600E-06 MAXIMUM = 5 67420E-01

Fig 5h

TIME 1200 000 MSEC

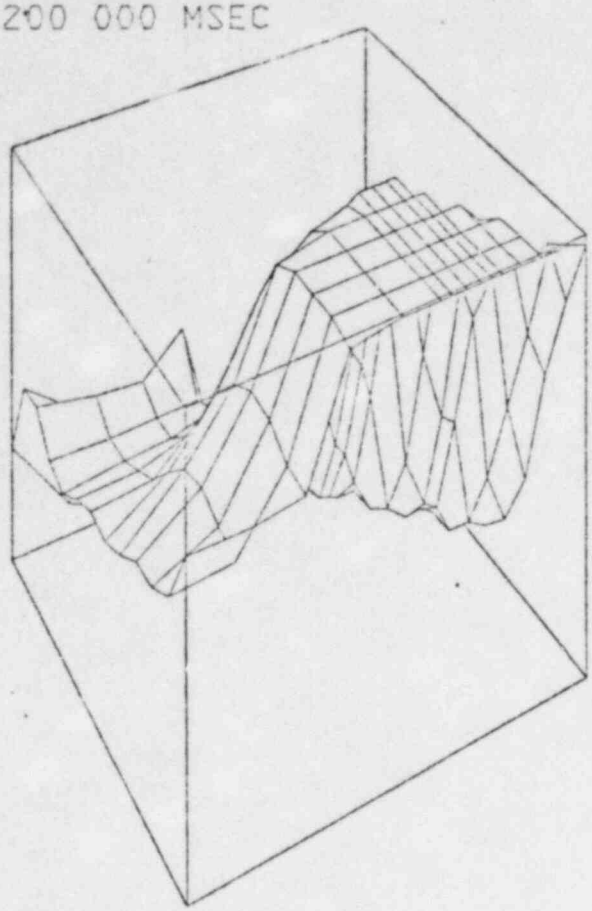

VOLUME FRACTION OF LIQUID
MINIMUM = 9 93600E-06 MAXIMUM = 9 57420E-01

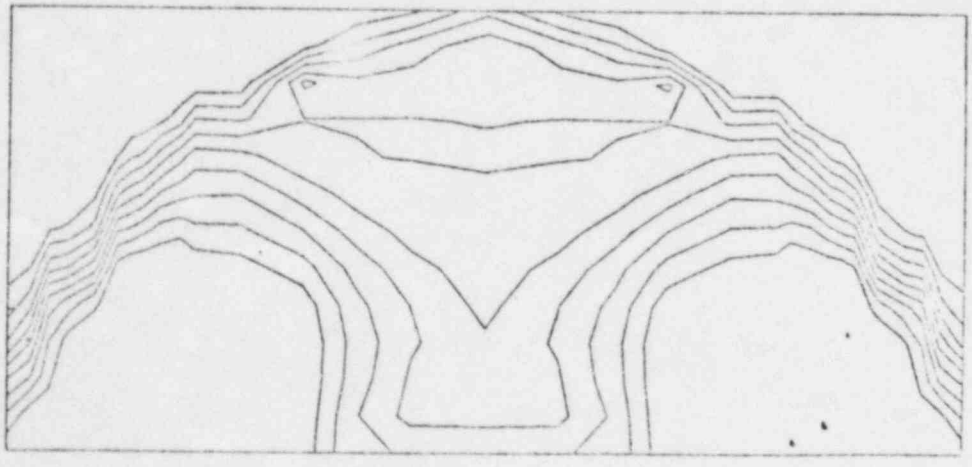

Fig 5i

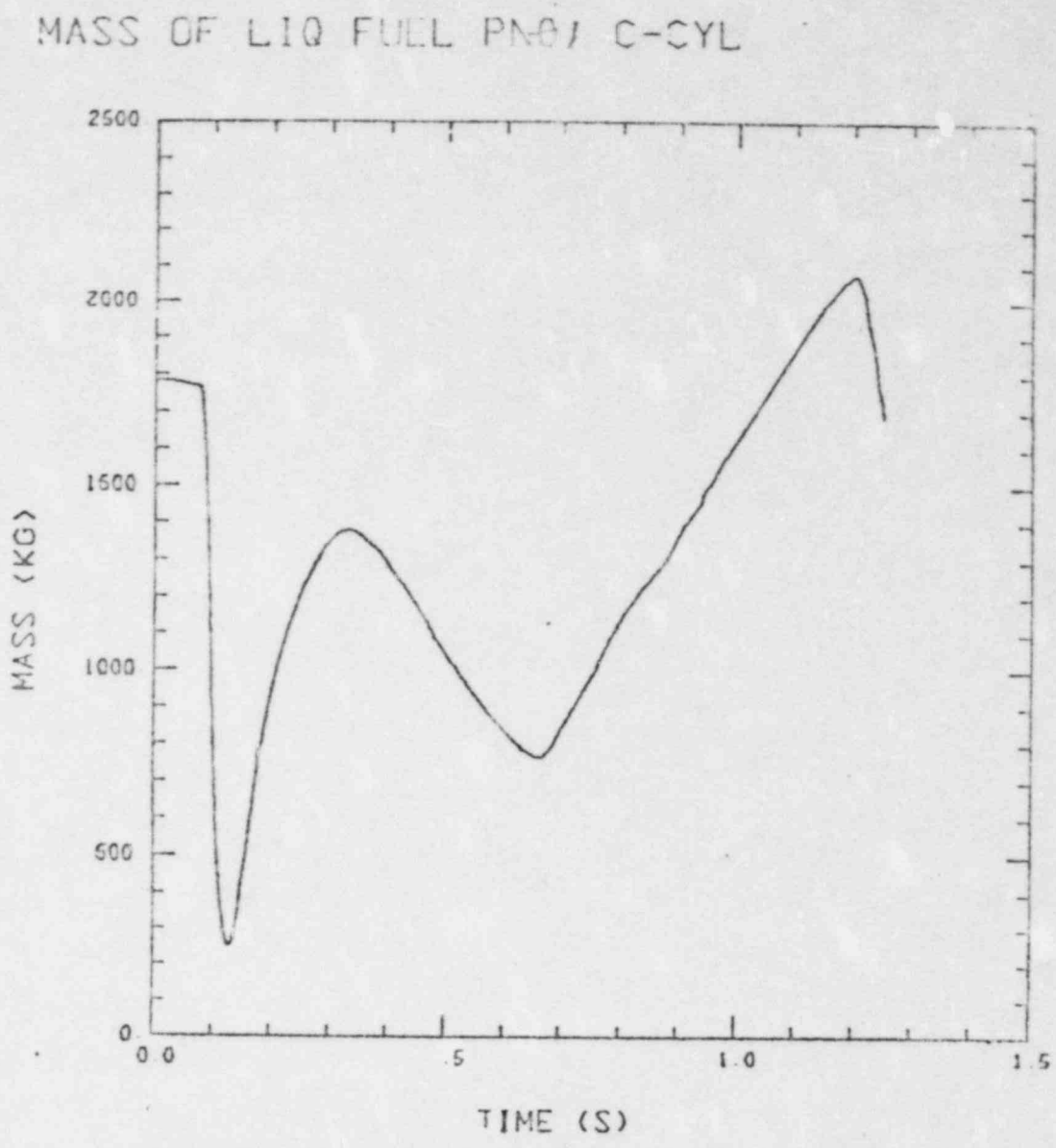
MASS OF LIQ FULL PN01 C-CYL
2500
2000
1500
1000
500
0
MASS (KG)
0.0
.5
1.0
1.5
TIME (S)

Fig 6

C.II.7

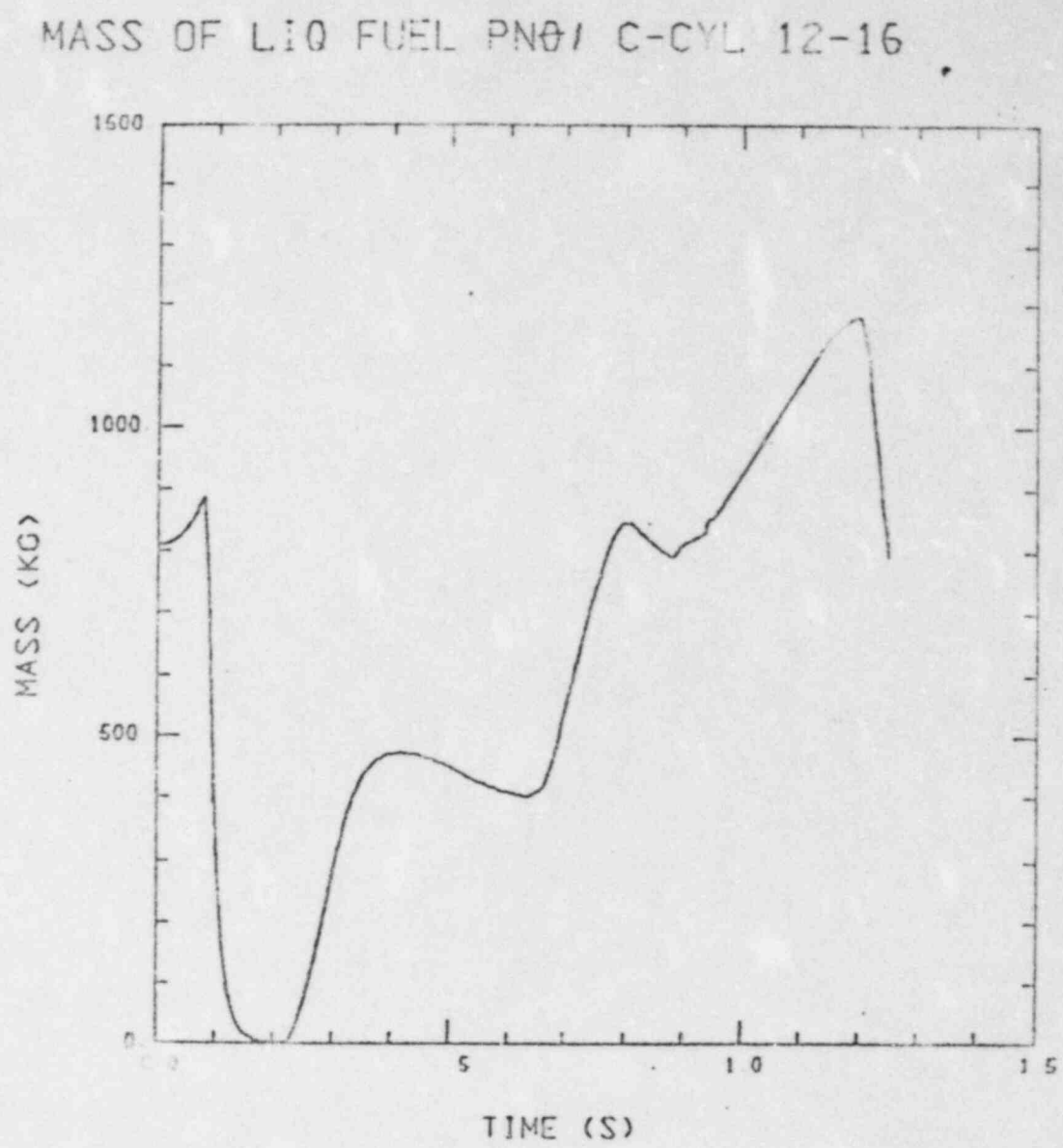
MASS OF LIQ FUEL PN01 C-CYL 12-16
1500
1000
500
0
MASS (KG)
0.0
5
10
15
TIME (S)

Fig 7

CII.7

AVERAGE VOID PNO1 C-CYL 12-16

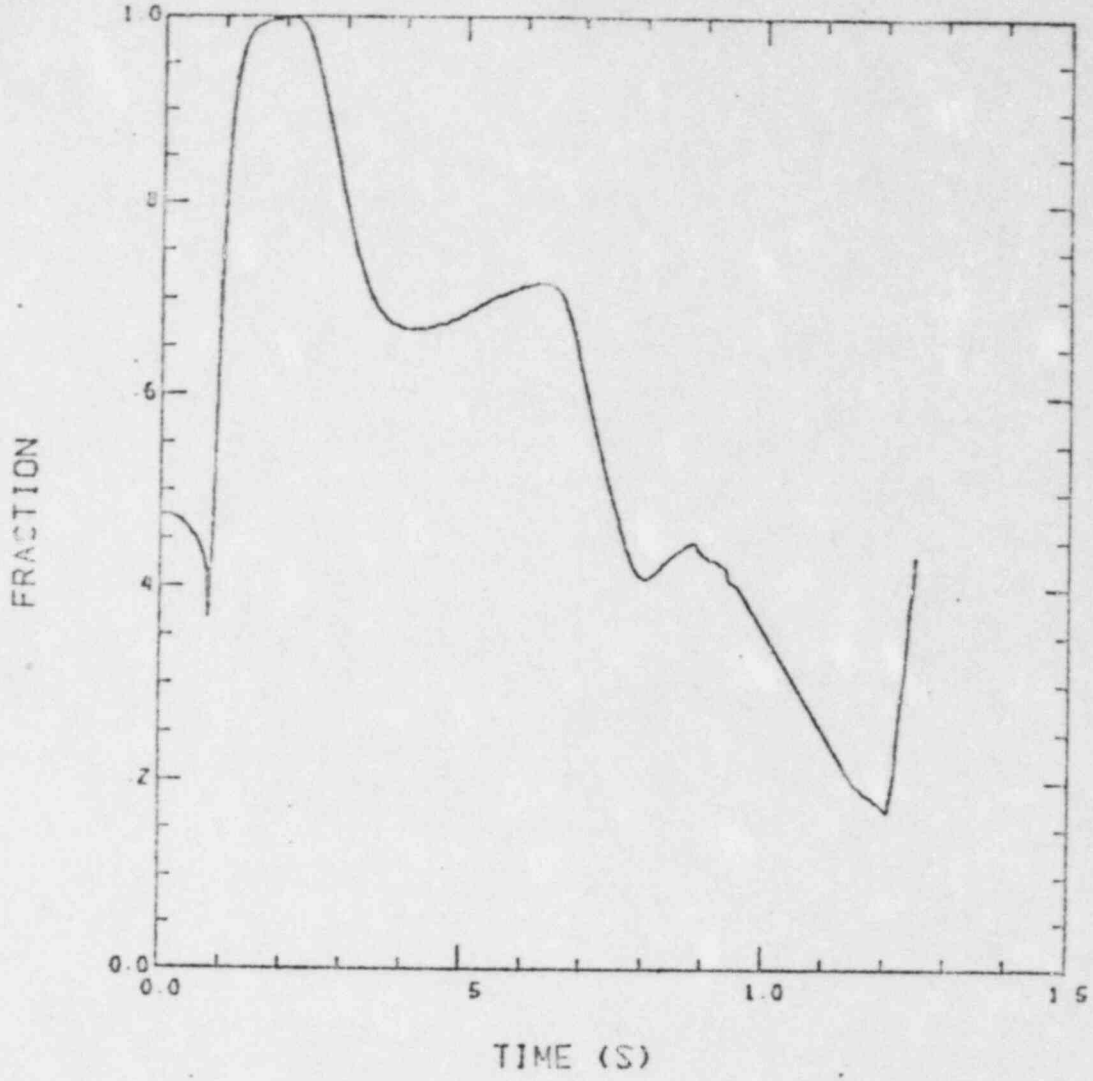

Fig 8

CZ.7

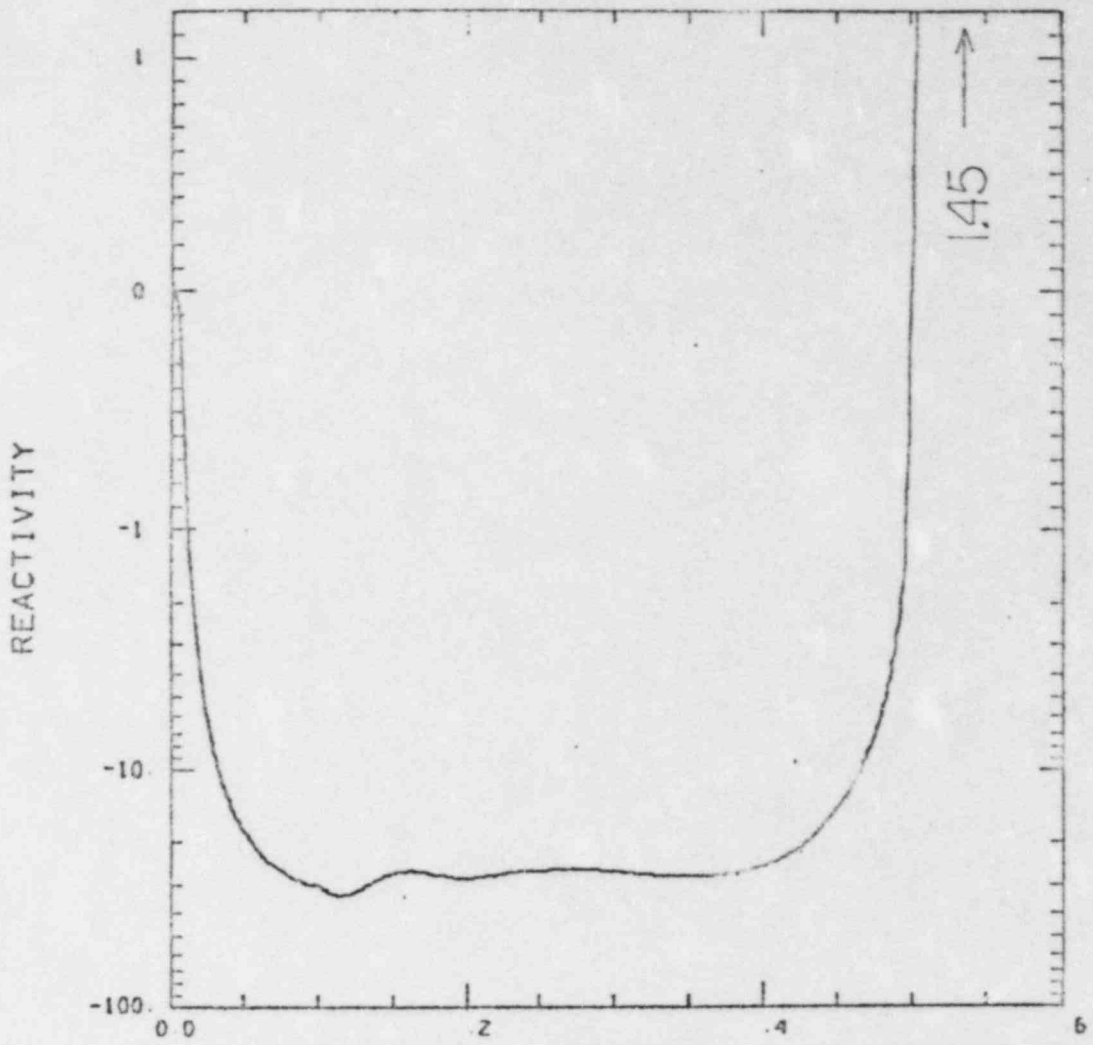

MINIMUM VALUE= -3.36598E+01
MAXIMUM VALUE= 1.33364E+00

Fig 9

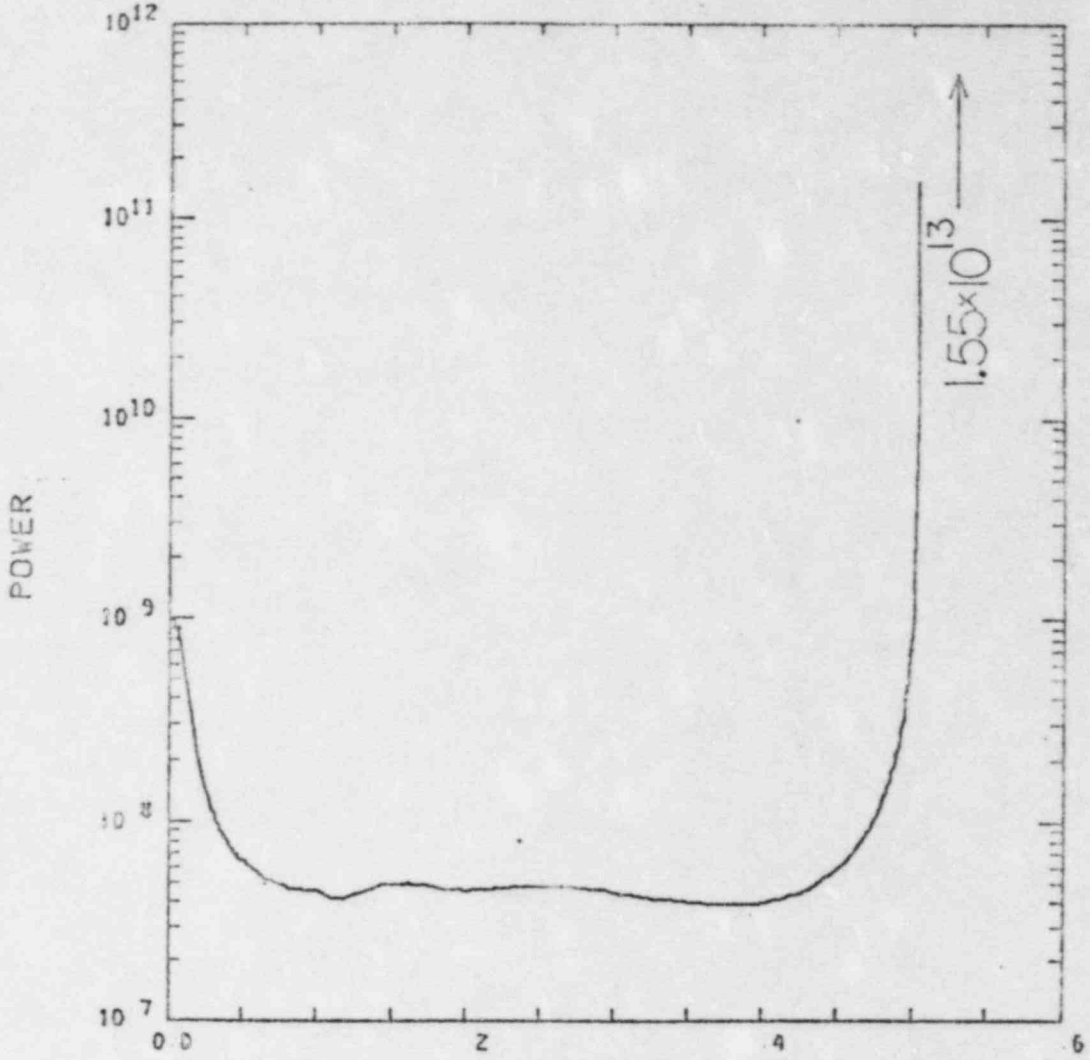

MINIMUM VALUE= 3.92035E+07
MAXIMUM VALUE= 1.56205E+11

Fig 10

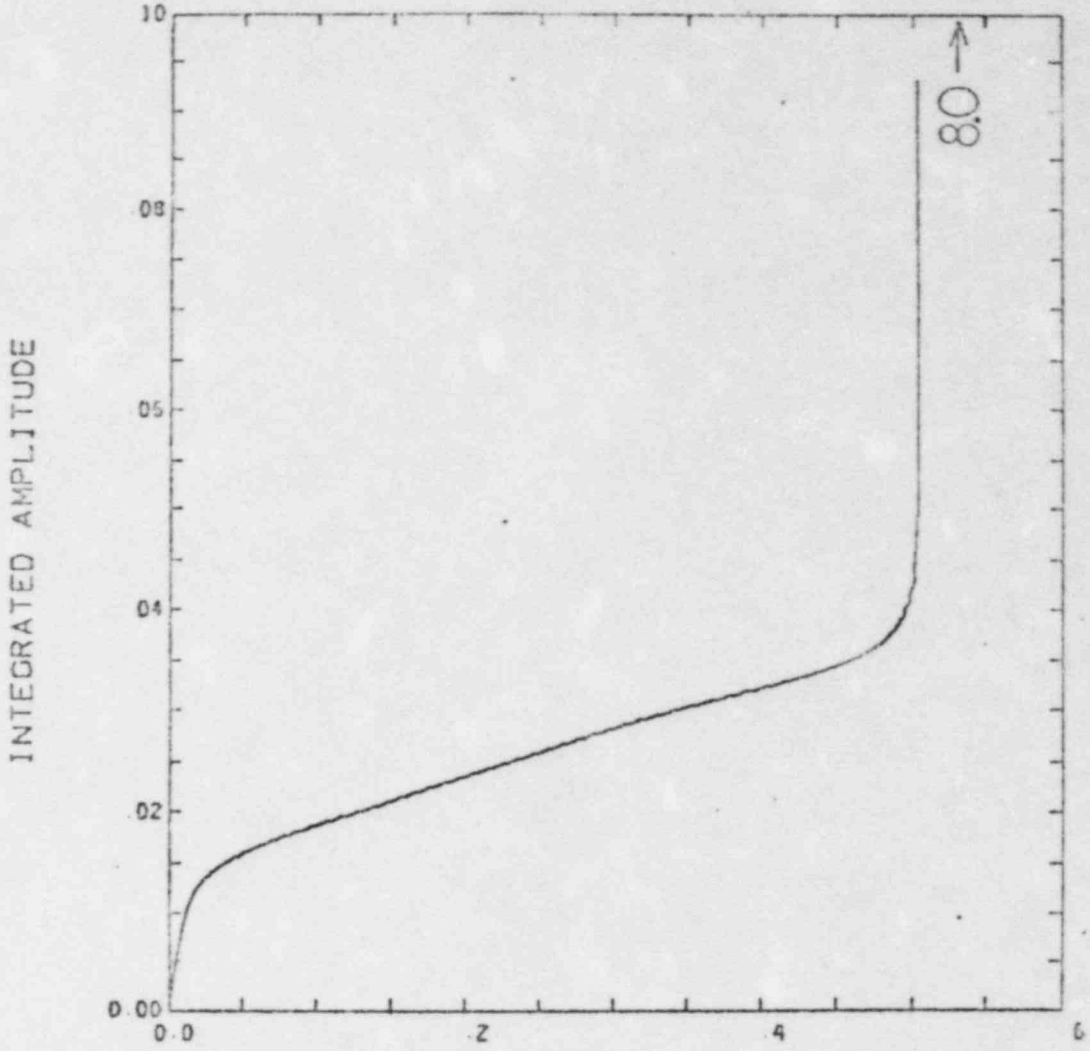
INTEGRATED AMPLITUDE
1.0
.8
.6
.4
.2
0.00
0.0
2
4
6
TIME(S)
.80
MINIMUM VALUE= 1.01541E-03
MAXIMUM VALUE= 9.31988E-02

Fig 11

CL.7

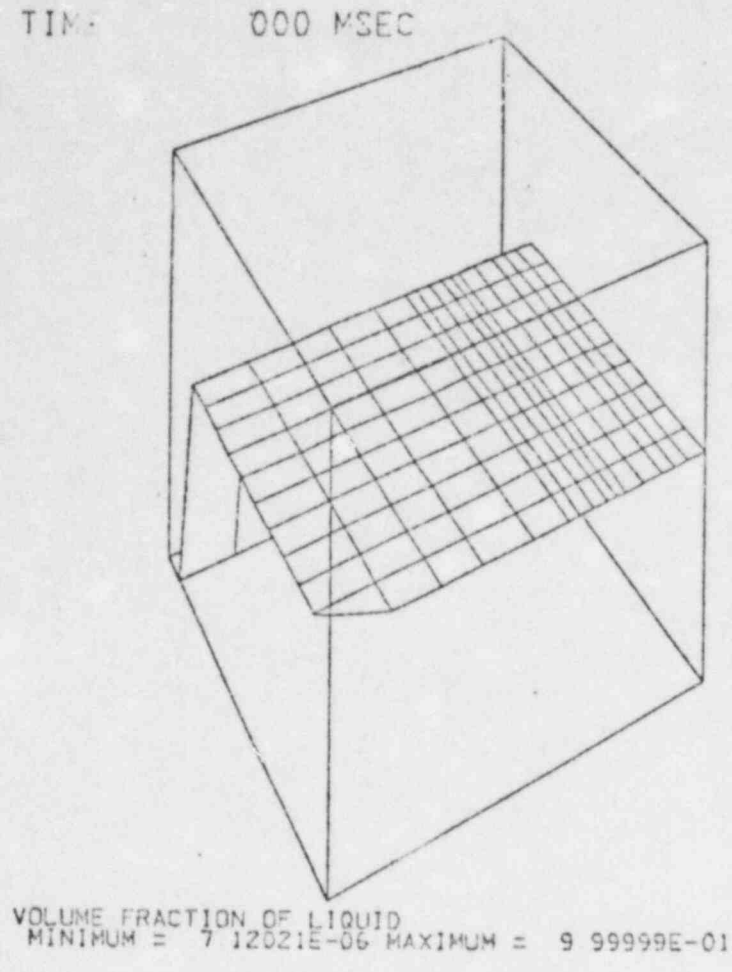
TIM
000 MSEC
VOLUME FRACTION OF LIQUID
MINIMUM = 7 12021E-06 MAXIMUM = 9 99999E-01

Fig 12a

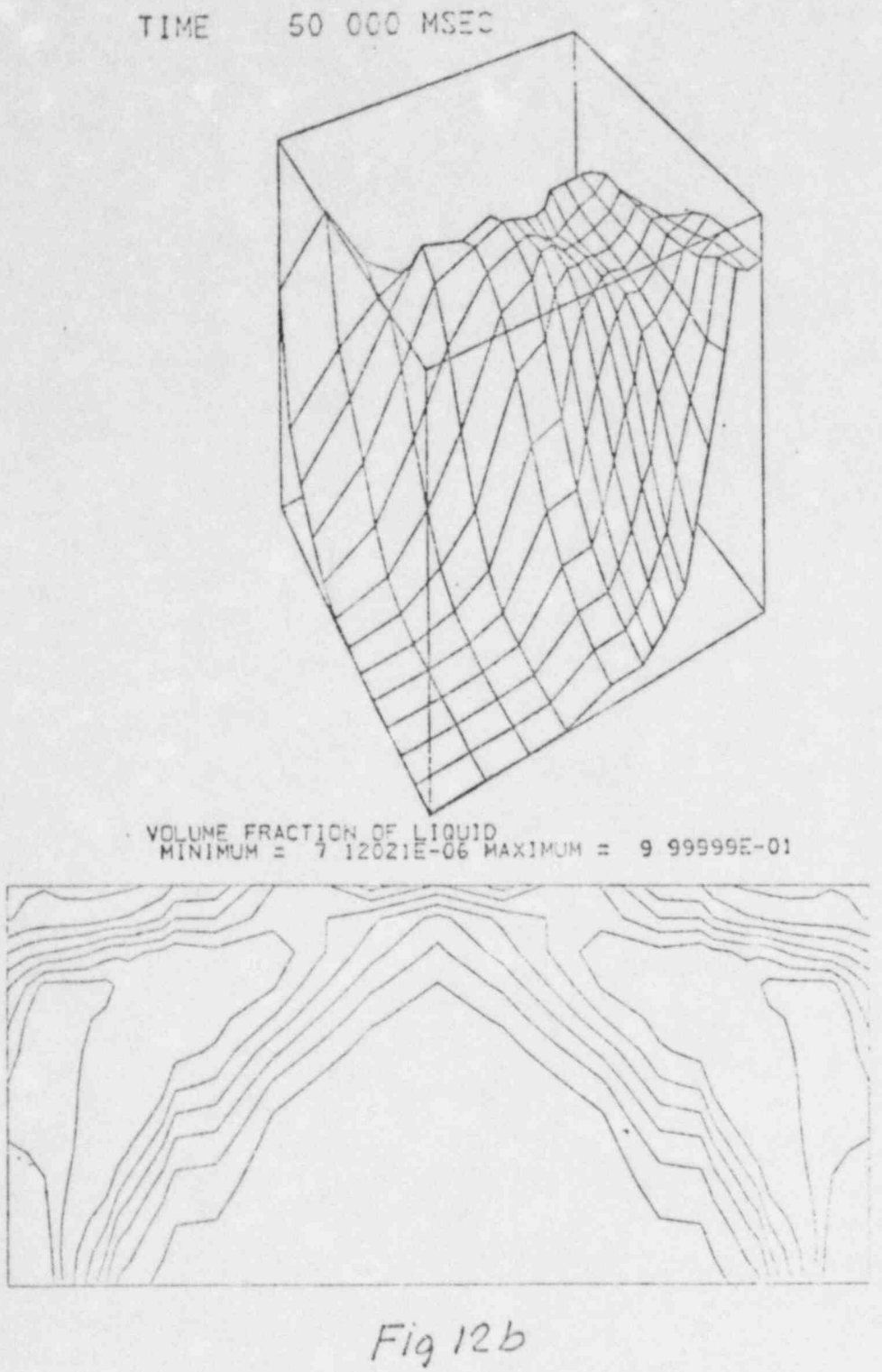
TIME 50 000 MSEC
VOLUME FRACTION OF LIQUID
MINIMUM = 7 12021E-06 MAXIMUM = 9 99999E-01

Fig 12b

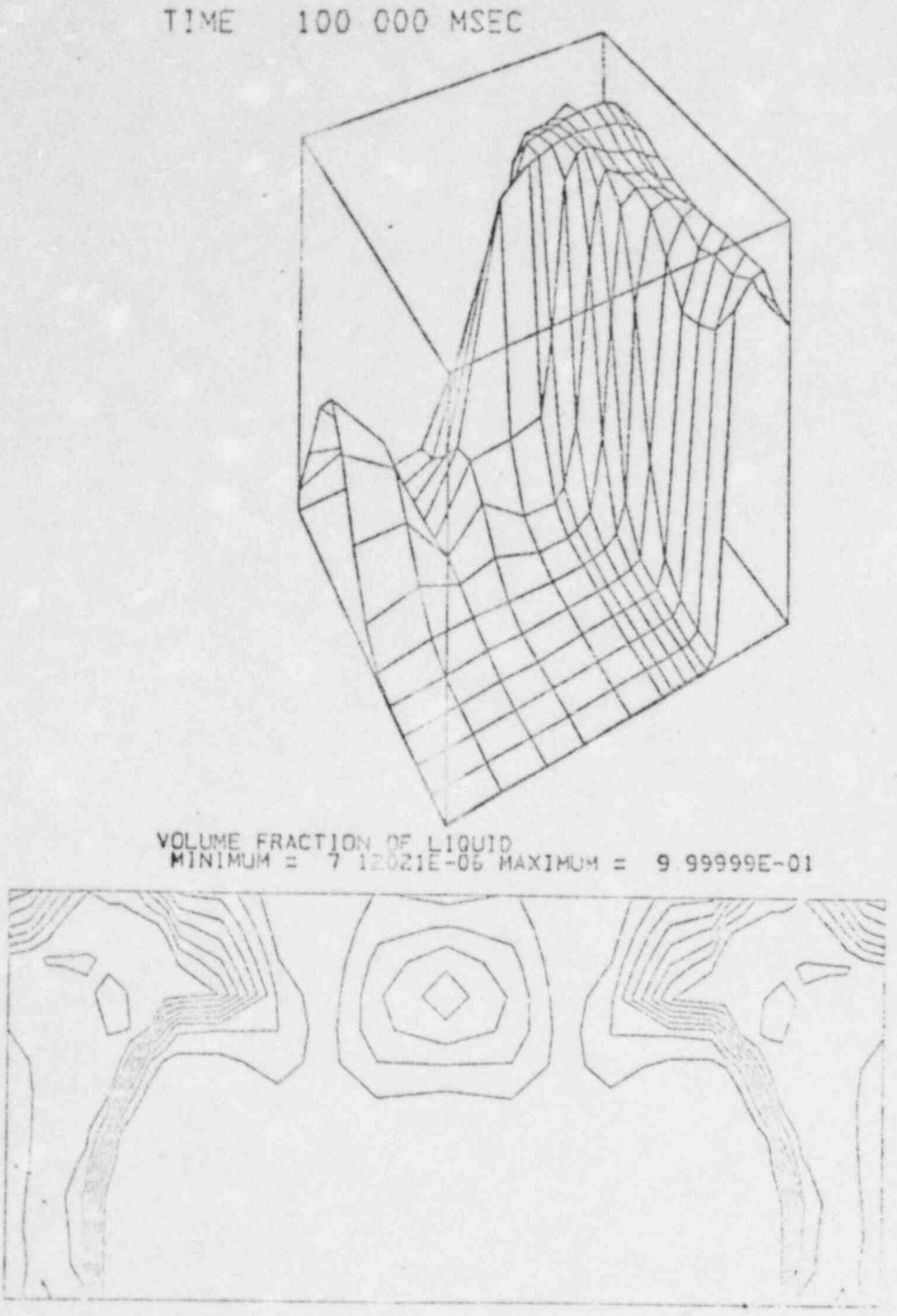
TIME 100 000 MSEC
VOLUME FRACTION OF LIQUID
MINIMUM = 7 12021E-06 MAXIMUM = 9 99999E-01

Fig 12c

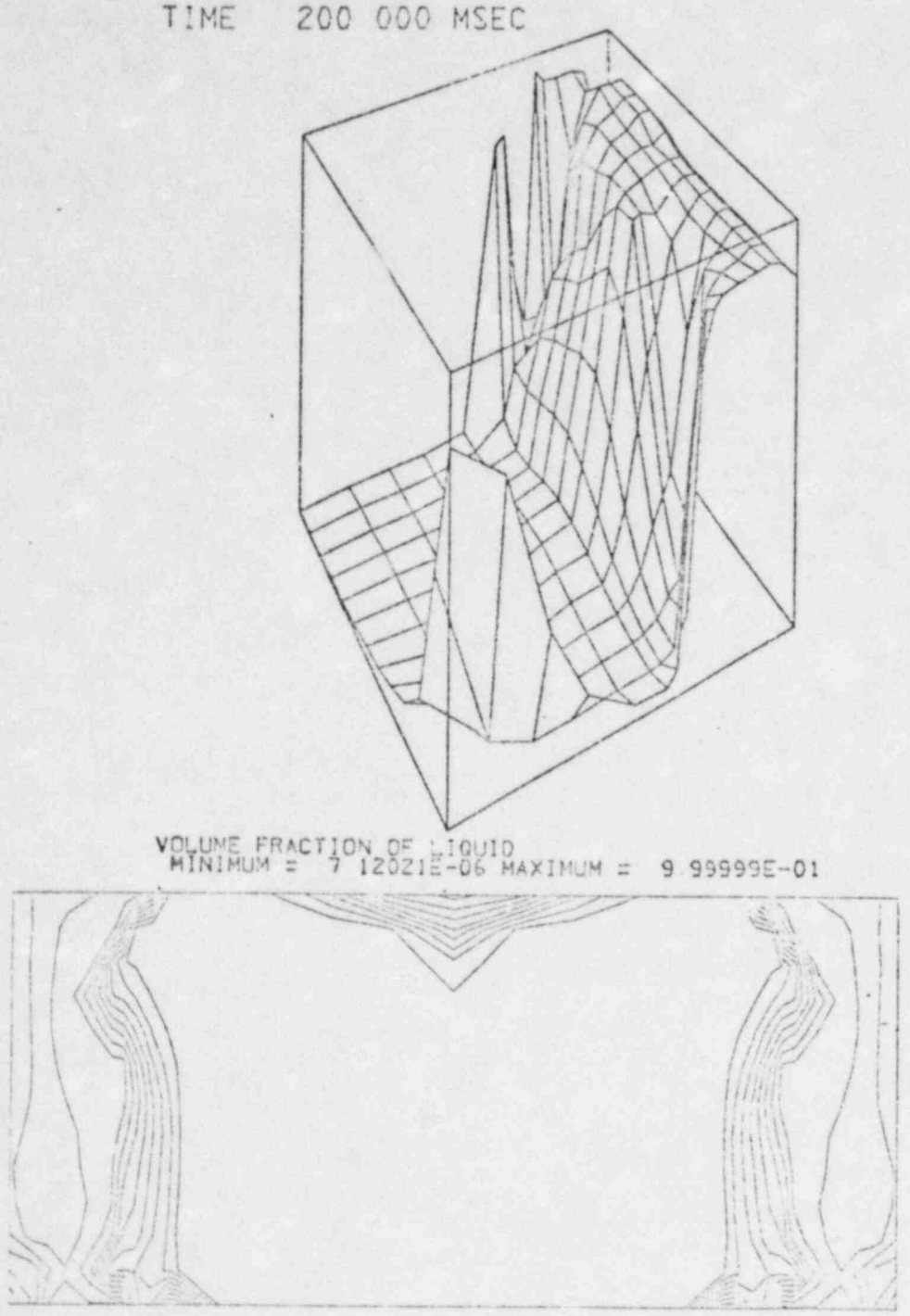
TIME 200 000 MSEC
VOLUME FRACTION OF LIQUID
MINIMUM = 7 12021E-06 MAXIMUM = 9 99999E-01

Fig 12 d

TIME 300 000 MSEC

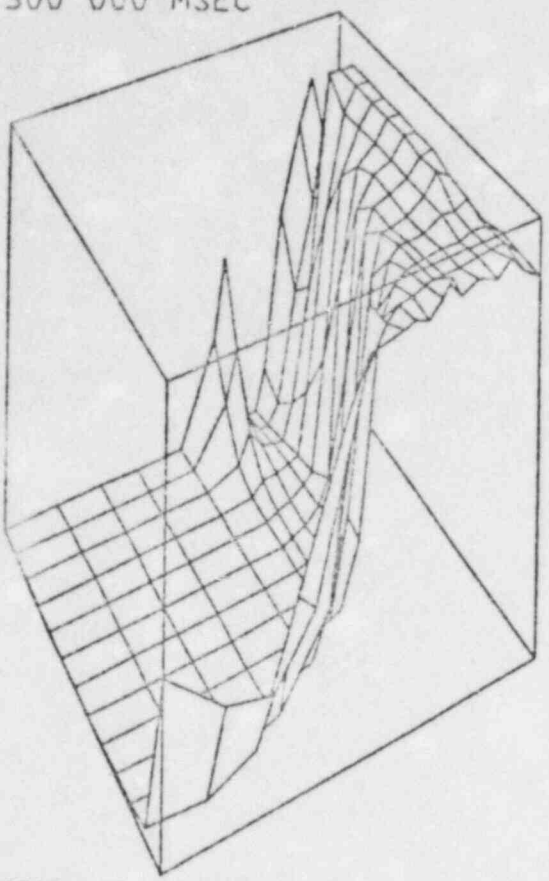

VOLUME FRACTION OF LIQUID
MINIMUM = 7.1202E-06 MAXIMUM = 9.99999E-01

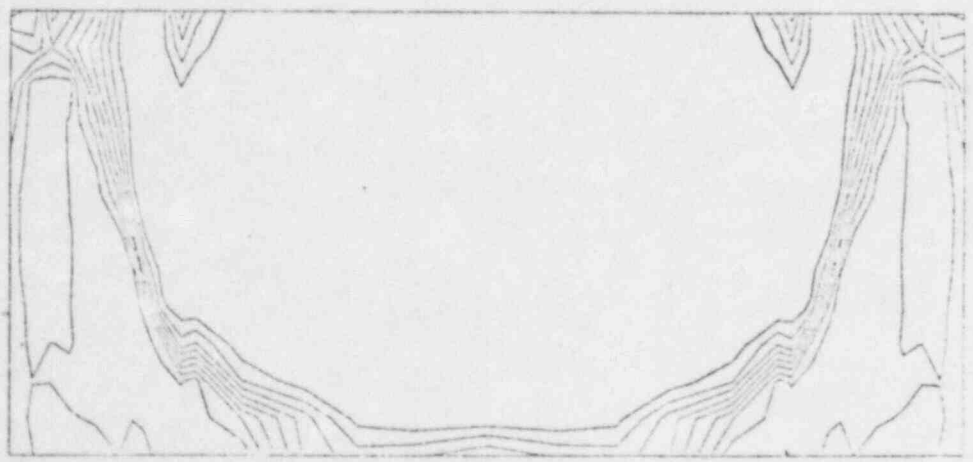

Fig 12e

TIME 400 000 MSEC

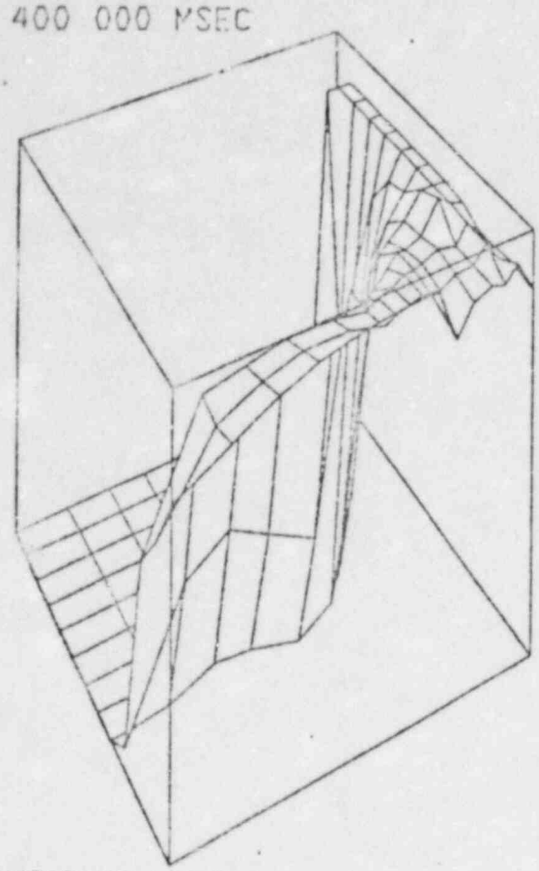

VOLUME FRACTION OF LIQUID
MINIMUM = 7.12021E-06 MAXIMUM = 9.99999E-01

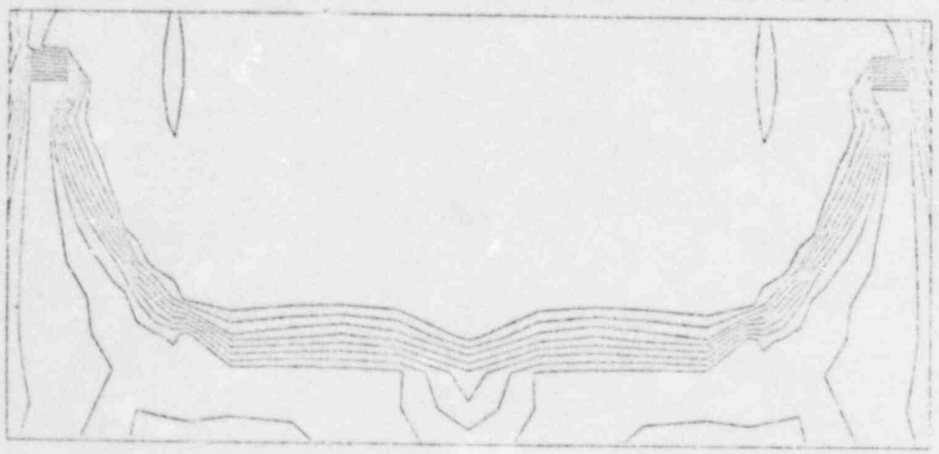

Fig 12f

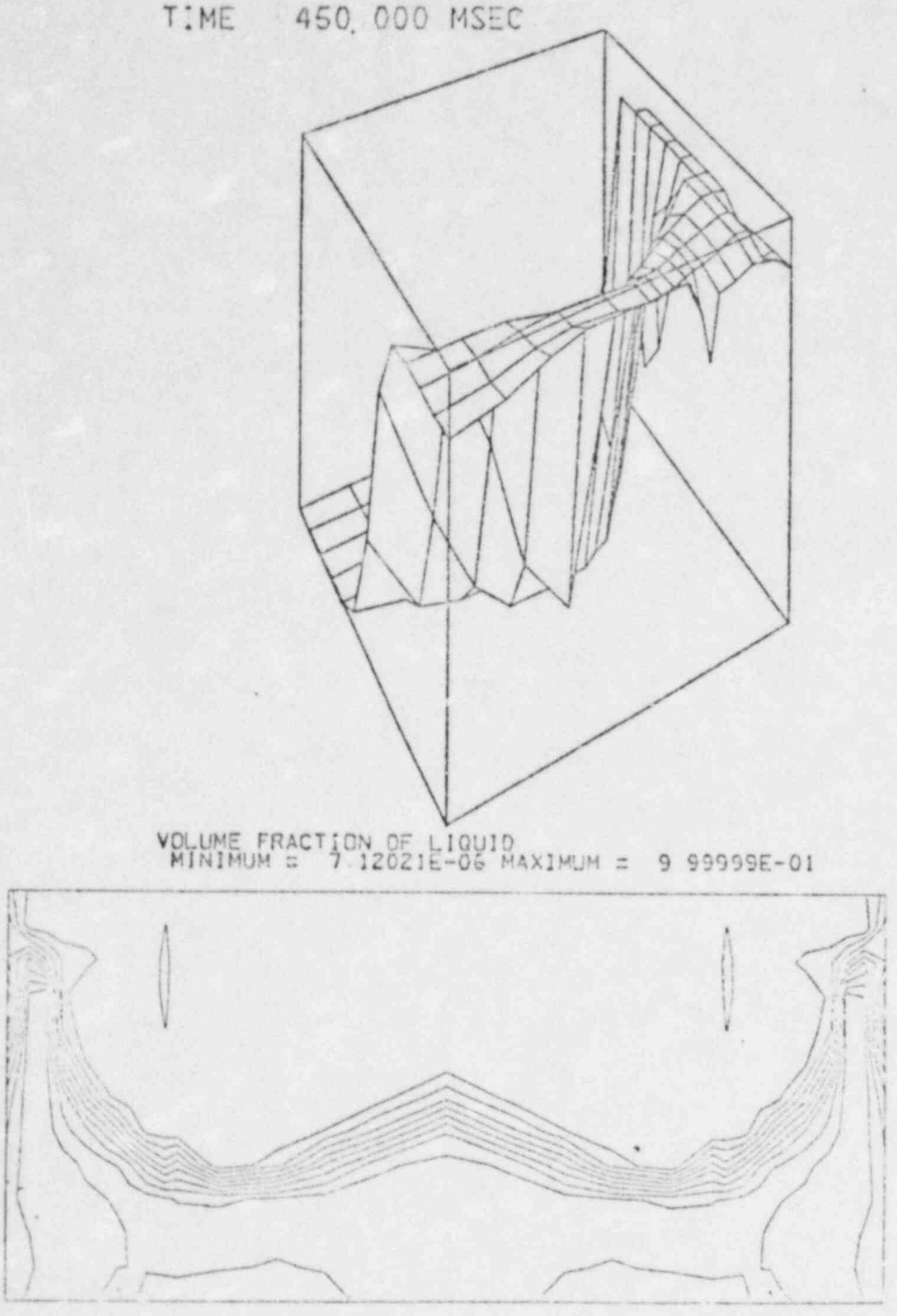
TIME 450.000 MSEC
VOLUME FRACTION OF LIQUID
MINIMUM = 7.12021E-06 MAXIMUM = 9.99999E-01

Fig 129

TIME 500 000 MSEC

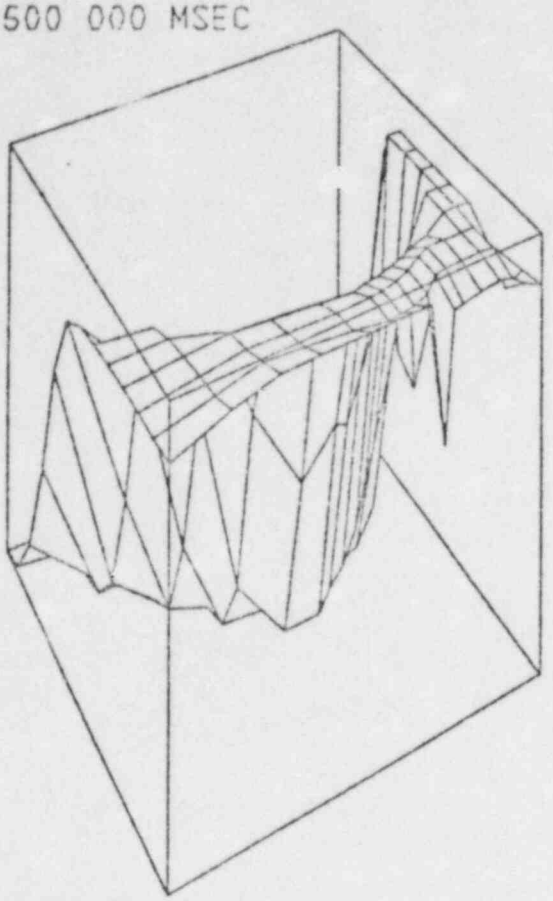

VOLUME FRACTION OF LIQUID
MINIMUM = 7 1Z021E-06 MAXIMUM = 9 99999E-01

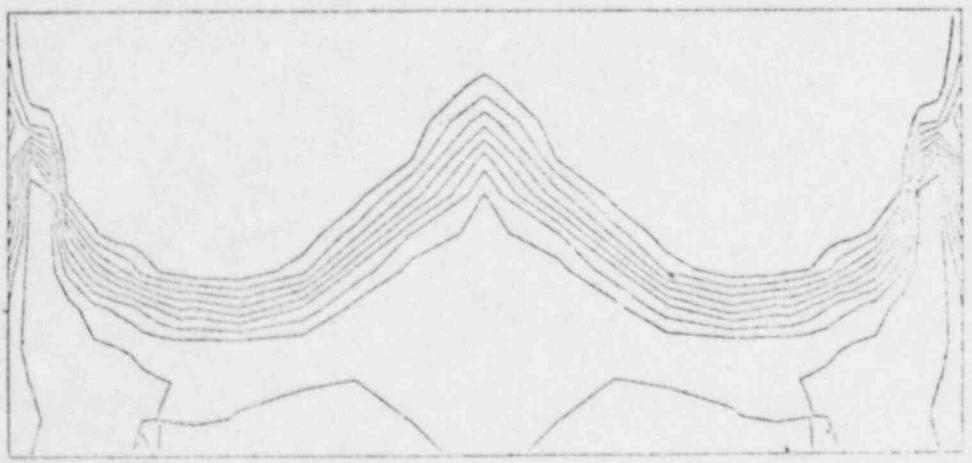

Fig 12 h

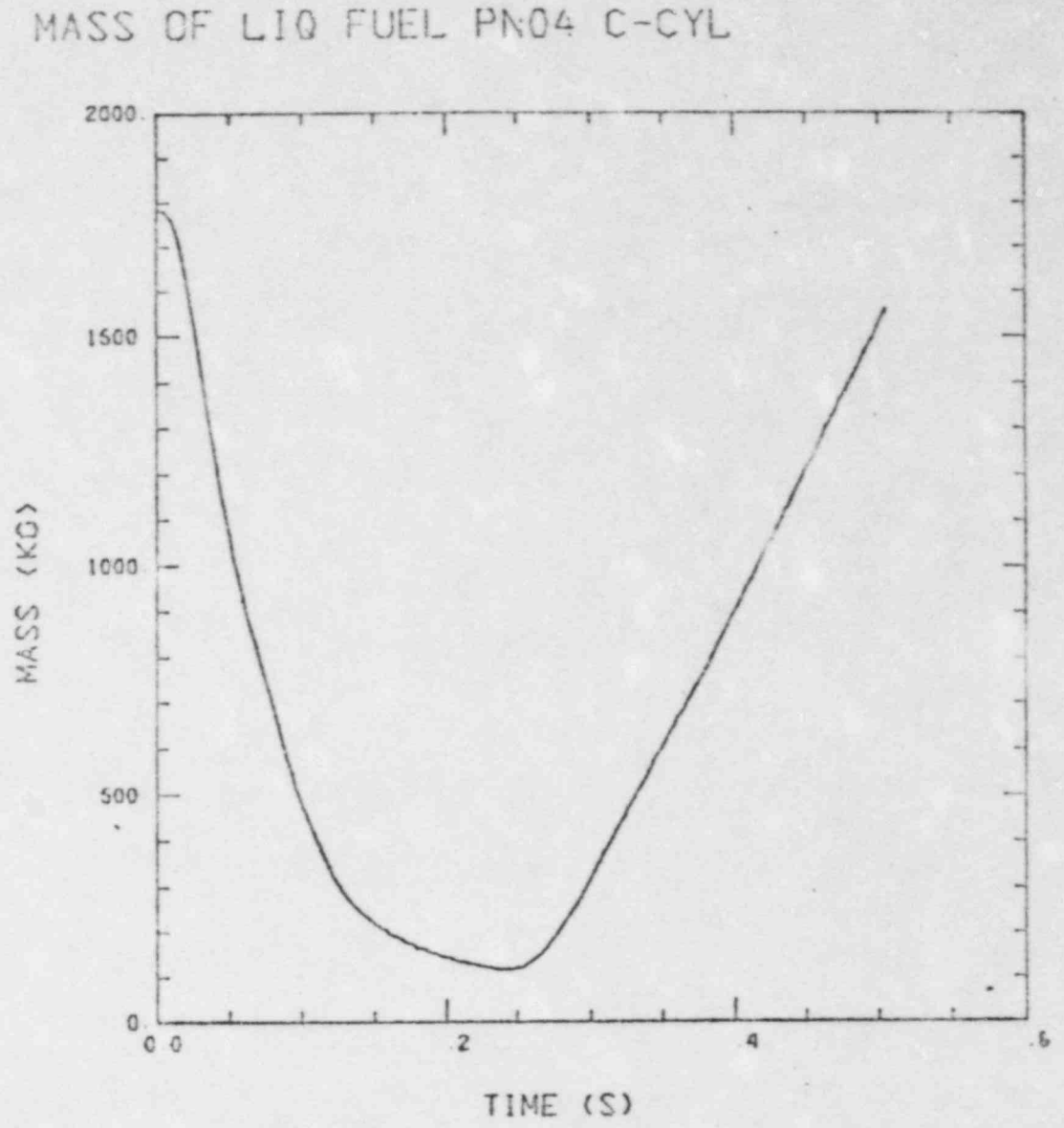
MASS OF LIQ FUEL PN04 C-CYL
2000.
1500
1000
500
0.
MASS (KG)
0.0
.2
.4
.6
TIME (S)

Fig 13

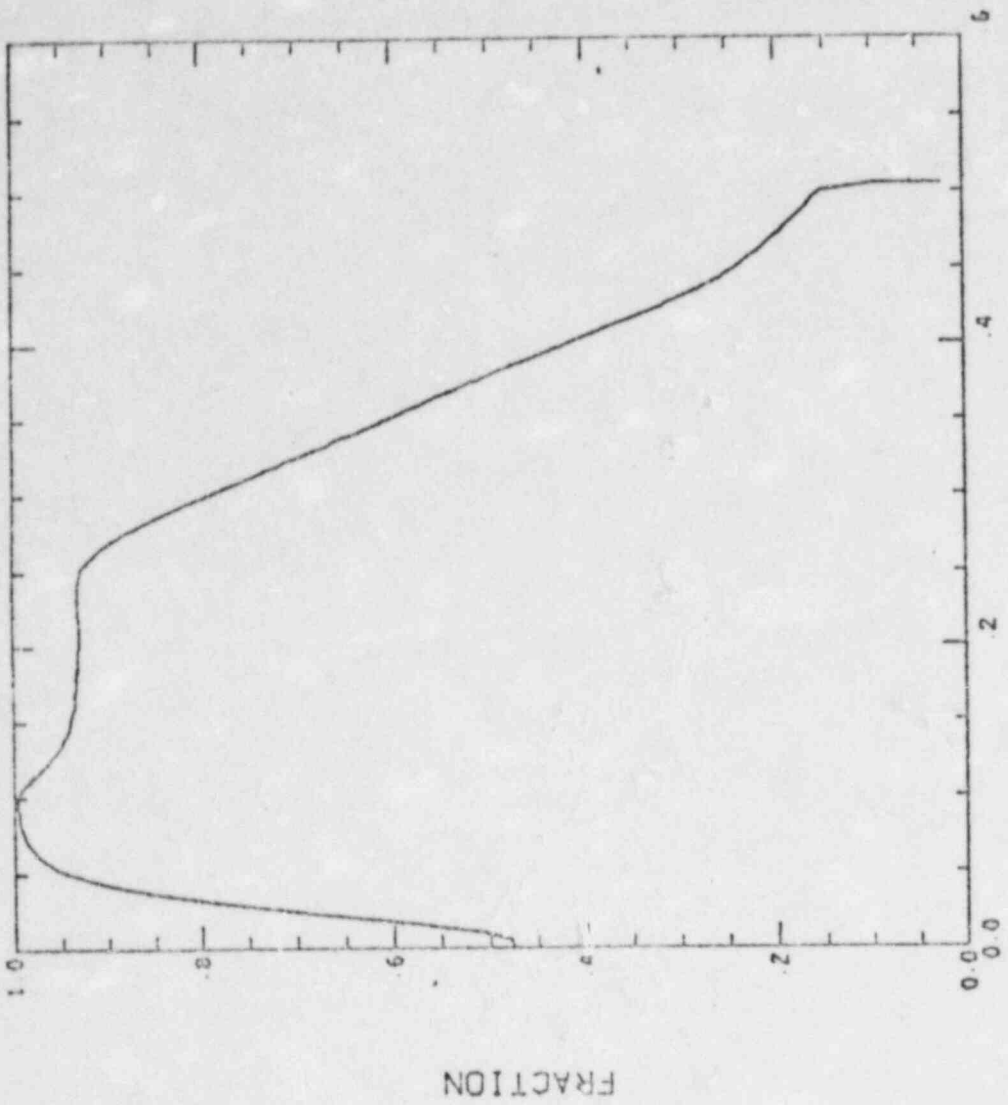

Fig 14

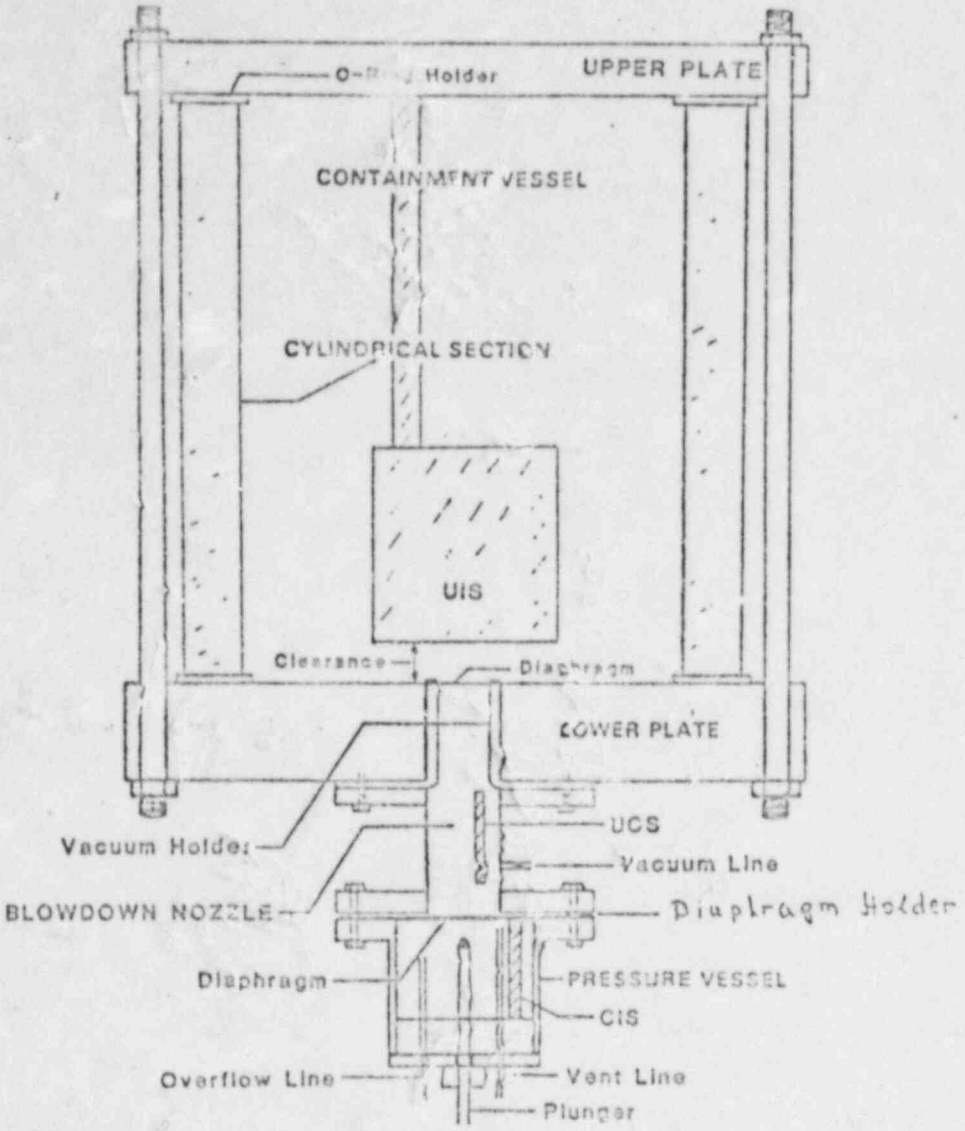

Figure 15 Scaled schematic of the test section including terminology of key components. Dimensions (ϕ = diameter, h = height, d = thickness, all in cm): Cylindrical Section ϕ = 91.4, h = 123.8; O-ring Holders d = 1.27; UIS ϕ = 27.6, h = 40.6; Clearance, S-series h = 5.0, DS-series (initial) h = 1.0 cm; Vacuum Holders, VH1 ϕ = 14.94, h = 20.3, VH2 ϕ = 11.43, h = 21.6; Blowdown Nozzle Section ϕ = 12.24, h = 22.8; Diaphragm Holder d = 0.6, Pressure Vessel ϕ=30.5, h = 30.5; Plunger ϕ = 1.3, h = 45.7; Vent Line ϕ = 0.6, Overflow Line ϕ = 0.6.

VH1 & VH2

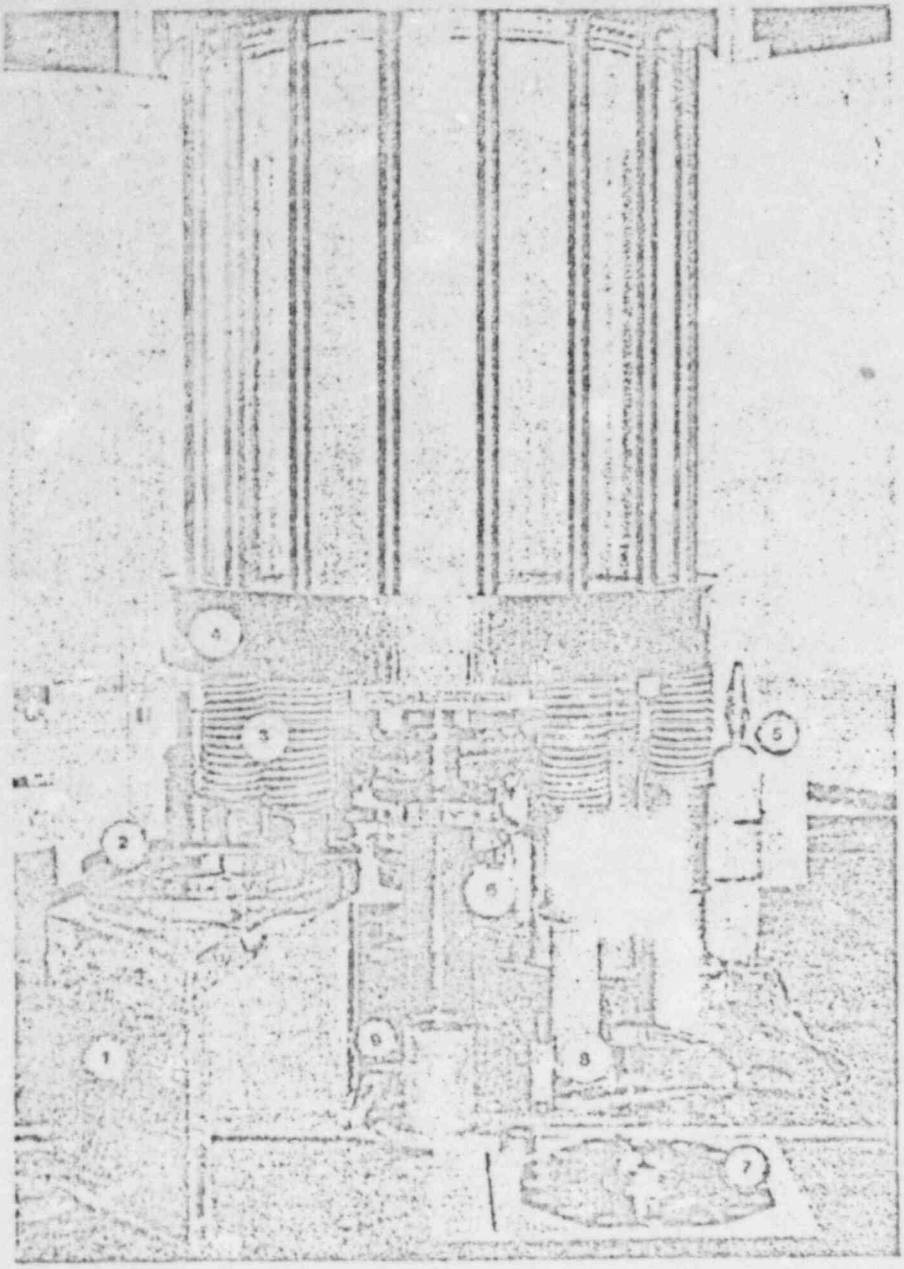

Figure 16 The Omega experimental facility and components. Legend: 1-Insulation, 2-Heaters, 3-Springs, 4-Lower Plate, 5-Nitrogen Tank, 6-Hydraulic Cylinder, 7-Steel Diaphragm, 8-Plunger System, 9-Vacuum Holder.

LA53

Dr. Charlie Bell

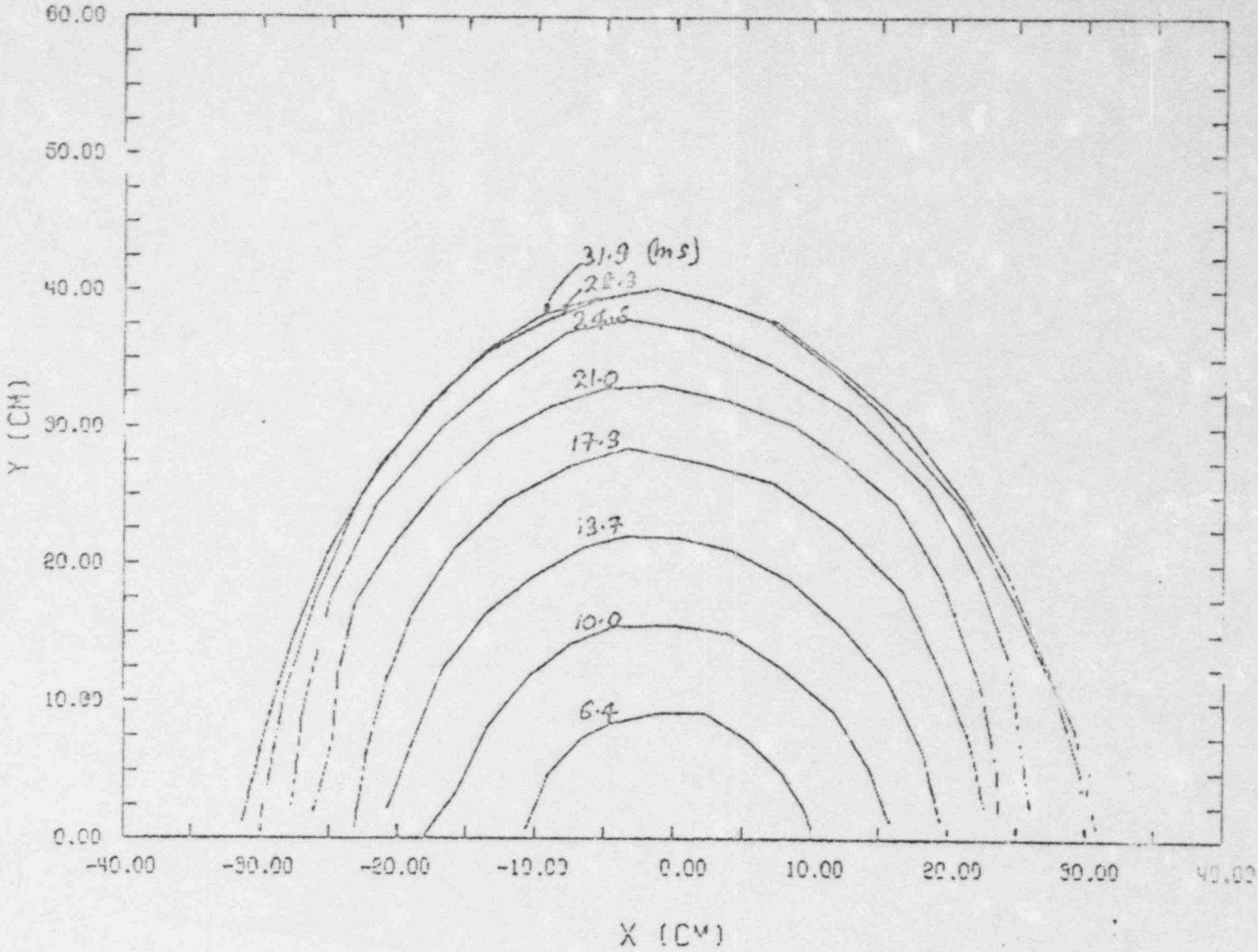

Fig 17

CII.7

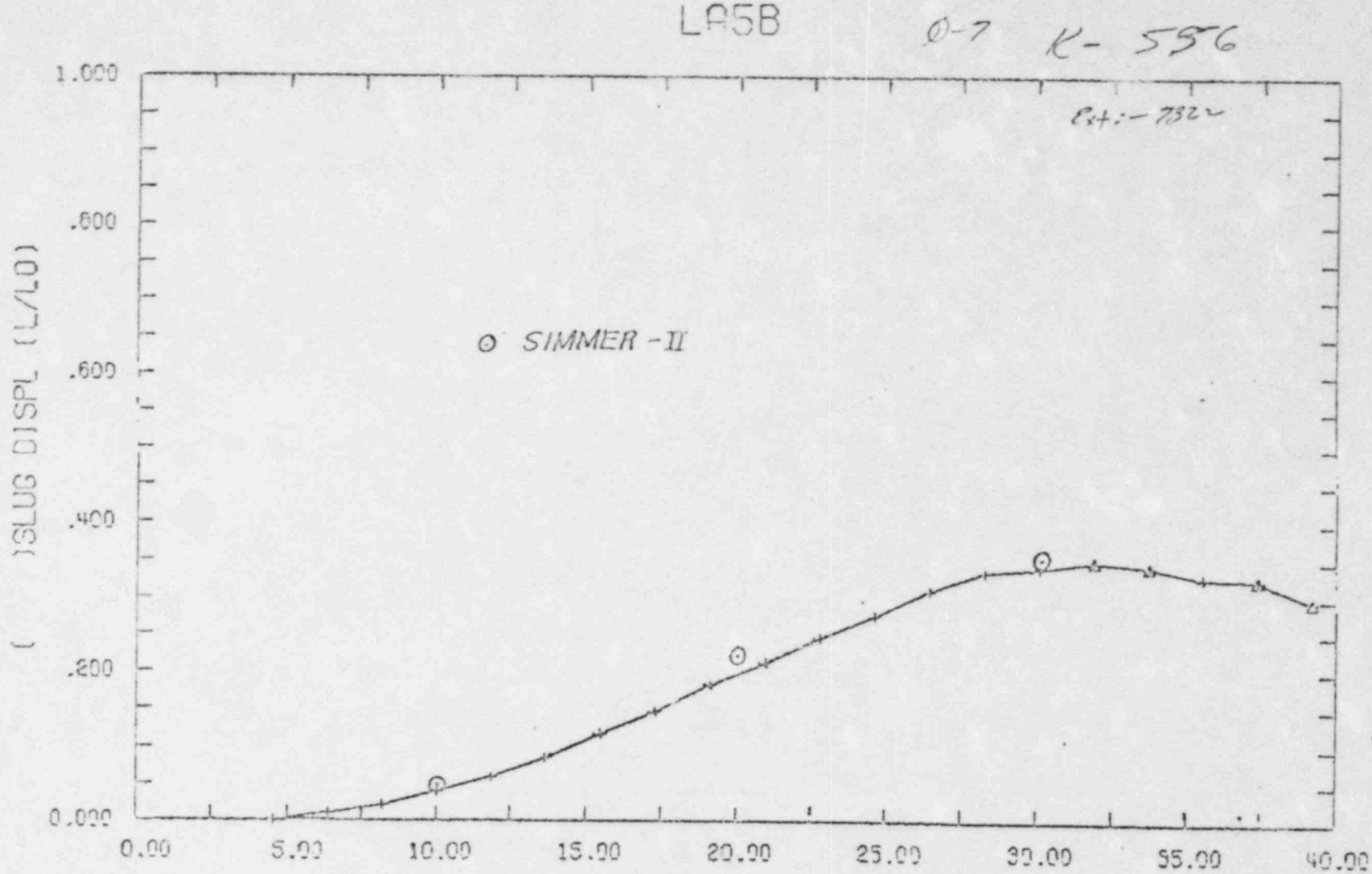
LA5B
0-7 K- 556
Ref:- 7826
SIMMER-II
1.000
.800
.600
.400
.200
0.000
SLUG DISPL (L/LO)
0.00
5.00
10.00
15.00
20.00
25.00
30.00
35.00
40.00
TIME (MSEC)

Fig 18

CII.7

LASS

Dr. Charlie Bell

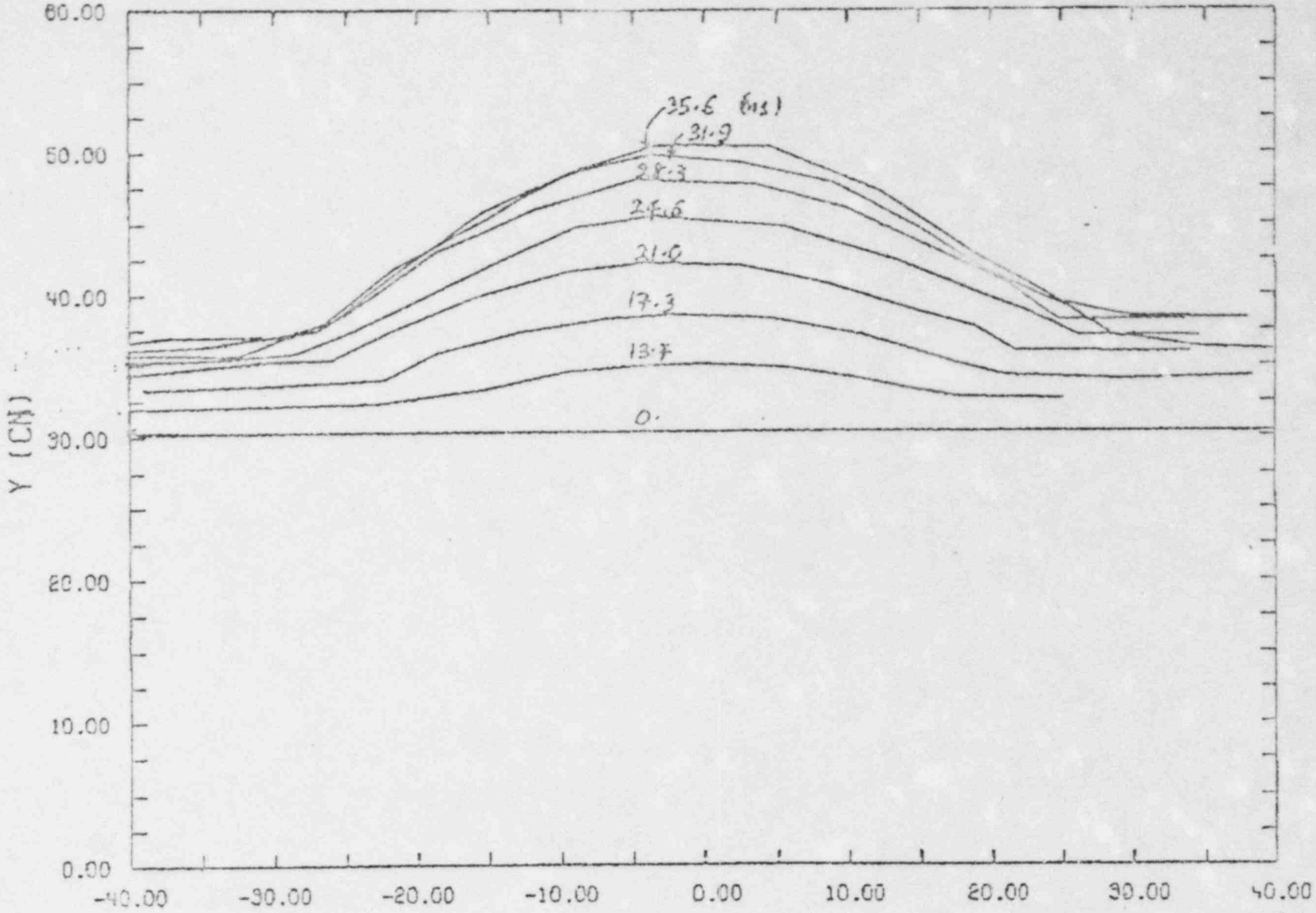

Fig 19

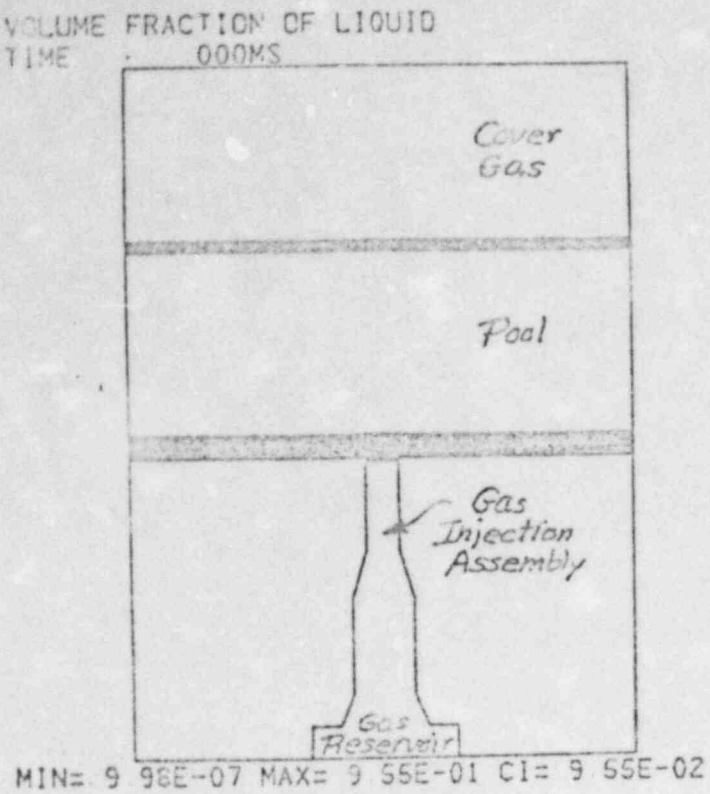

Fig 20a

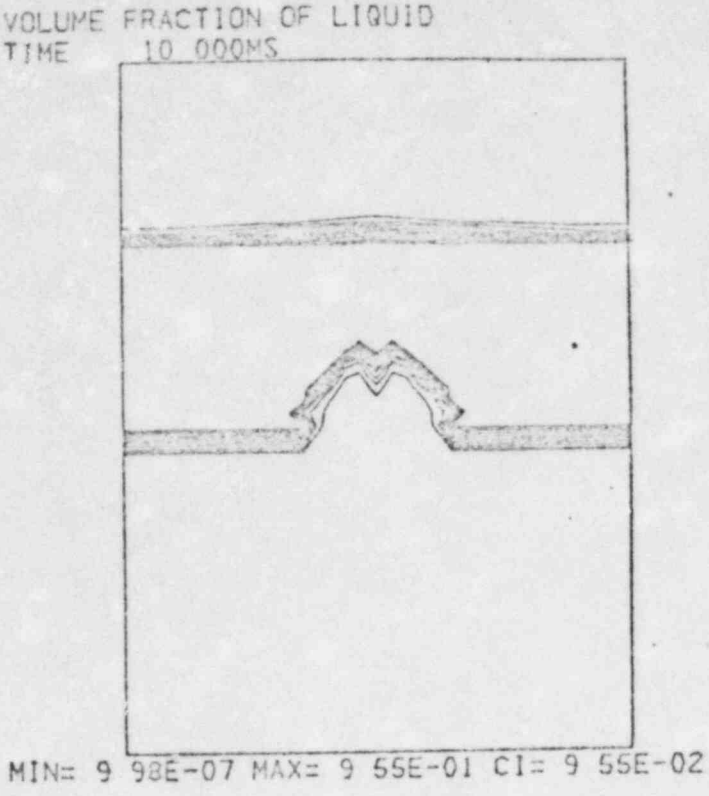

Fig 20b

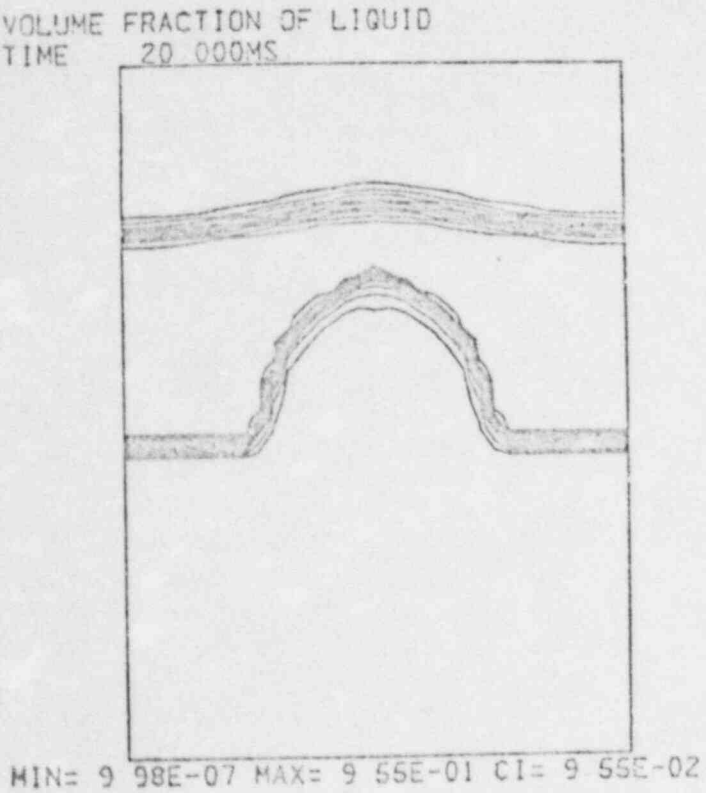

Fig 20c

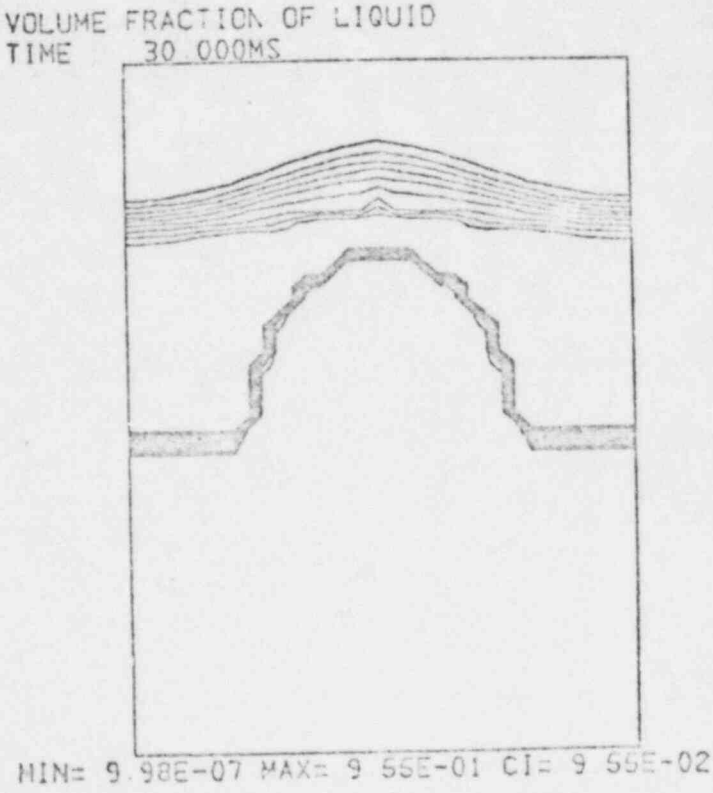

Fig 20d

VOLUME FRACTION OF LIQUID
TIME 40 000MS

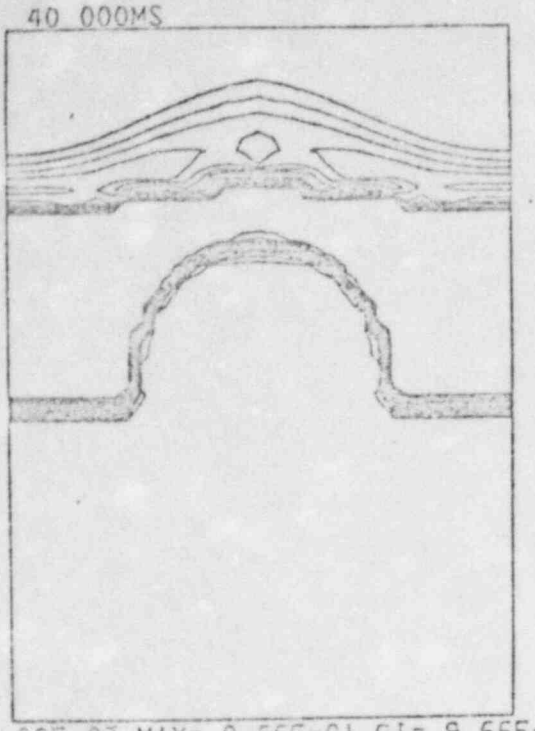

MIN= 9 98E-07 MAX= 9 55E-01 CI= 9 55E-02

Fig 20e

VOLUME FRACTION OF LIQUID
TIME 50 000MS

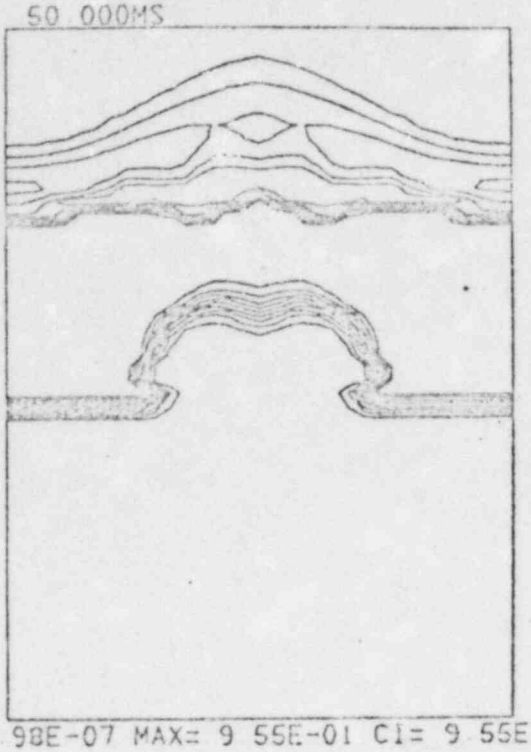

MIN= 9 98E-07 MAX= 9 55E-01 CI= 9 55E-02

Fig 20f

VOLUME FRACTION OF LIQUID
TIME 60 000MS

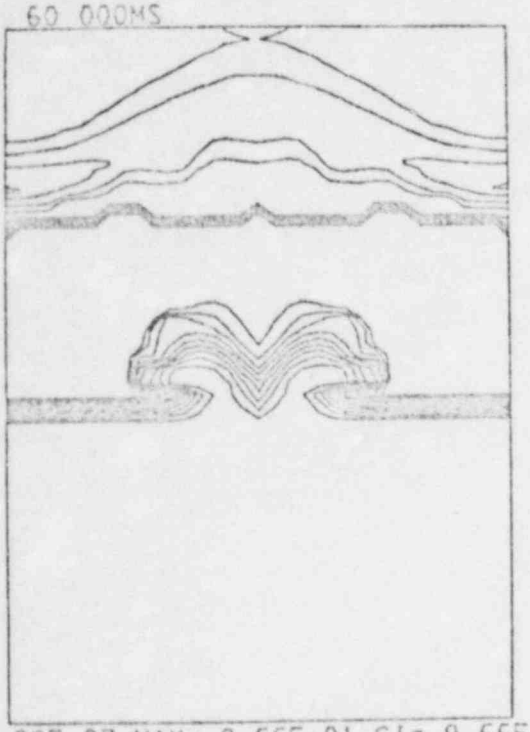

MIN= 9 98E-07 MAX= 9 55E-01 CI= 9 55E-02

Fig 20g

VOLUME FRACTION OF LIQUID
TIME 70 000MS

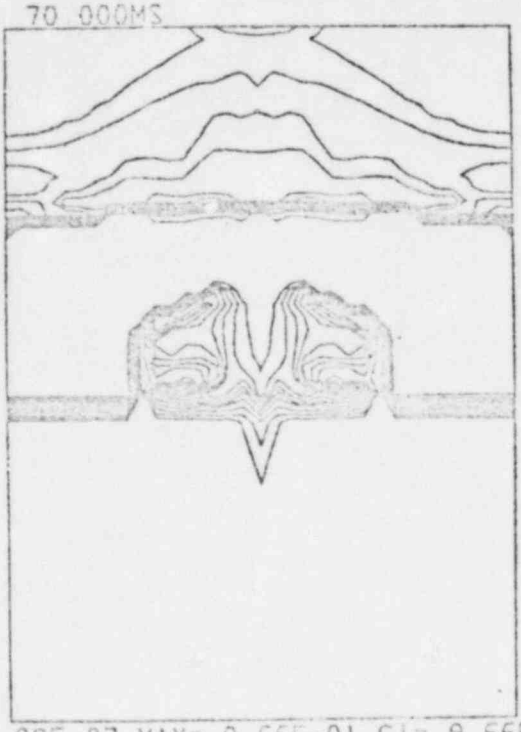

MIN= 9 98E-07 MAX= 9 55E-01 CI= 9 55E-02

Fig h

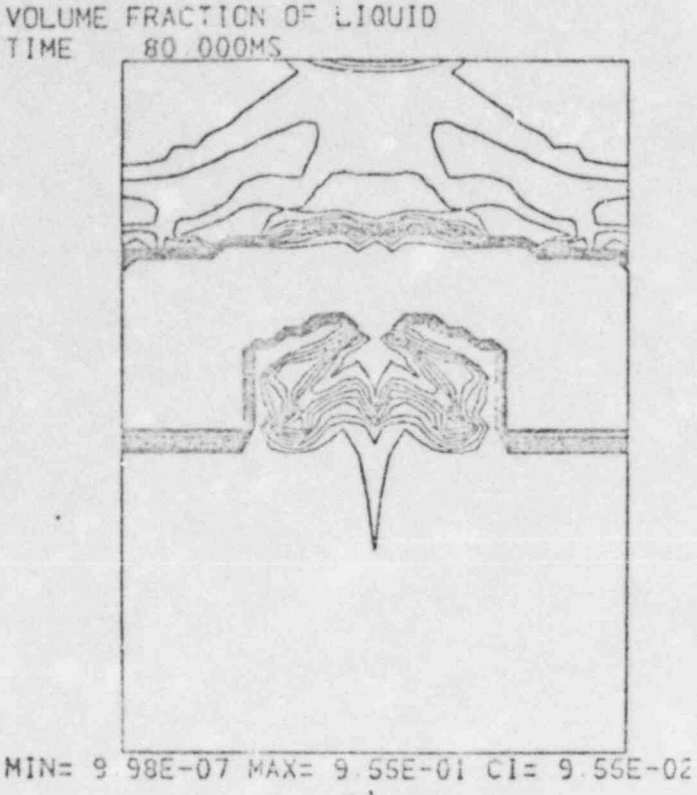
VOLUME FRACTION OF LIQUID
TIME 80.000MS
MIN= 9.98E-07 MAX= 9.55E-01 CI= 9.55E-02

Fig 20 i

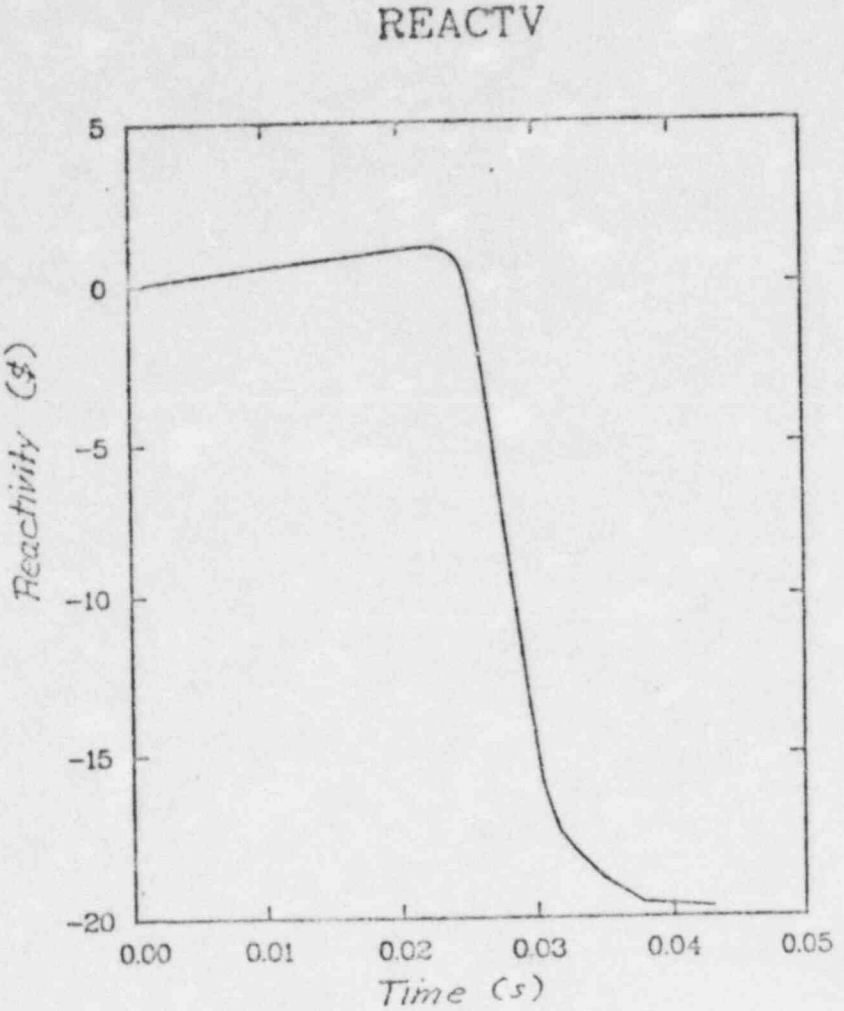

Fig 1

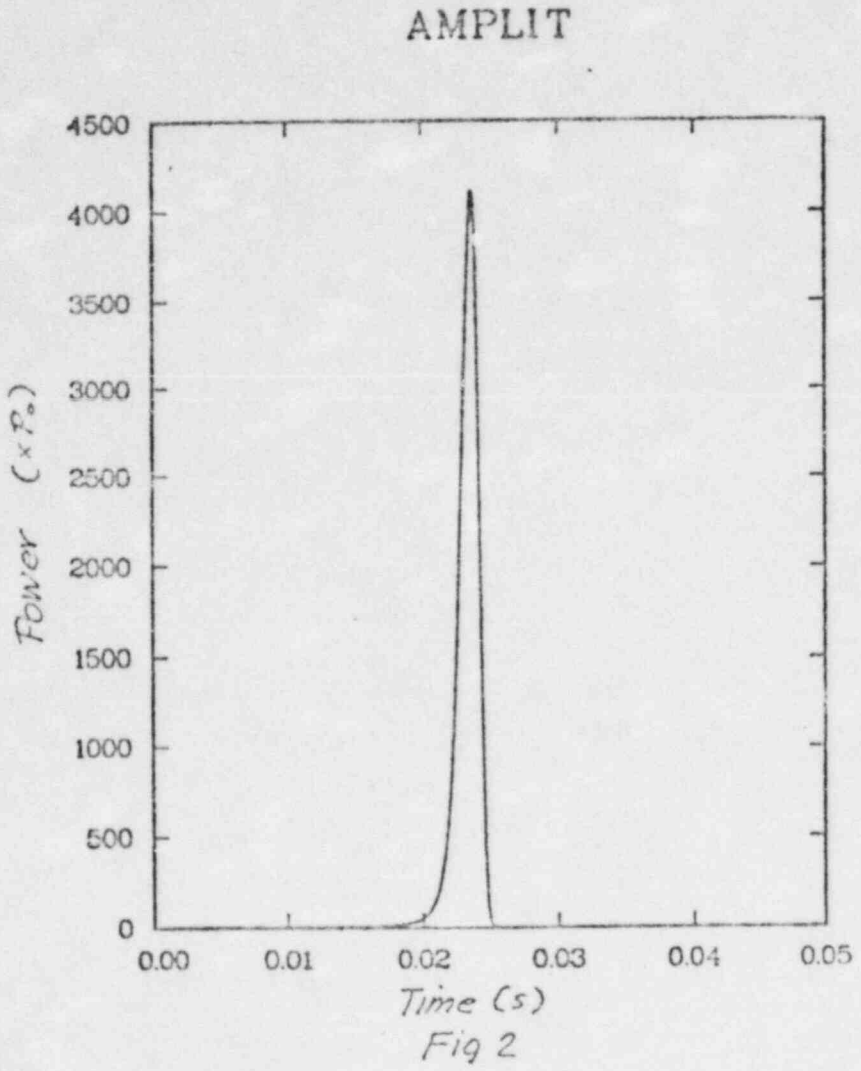
AMPLIT
4500
4000
3500
3000
2500
2000
1500
1000
500
0
Power (x P°)
0.00
0.01
0.02
0.03
0.04
0.05
Time (s)

Fig 2

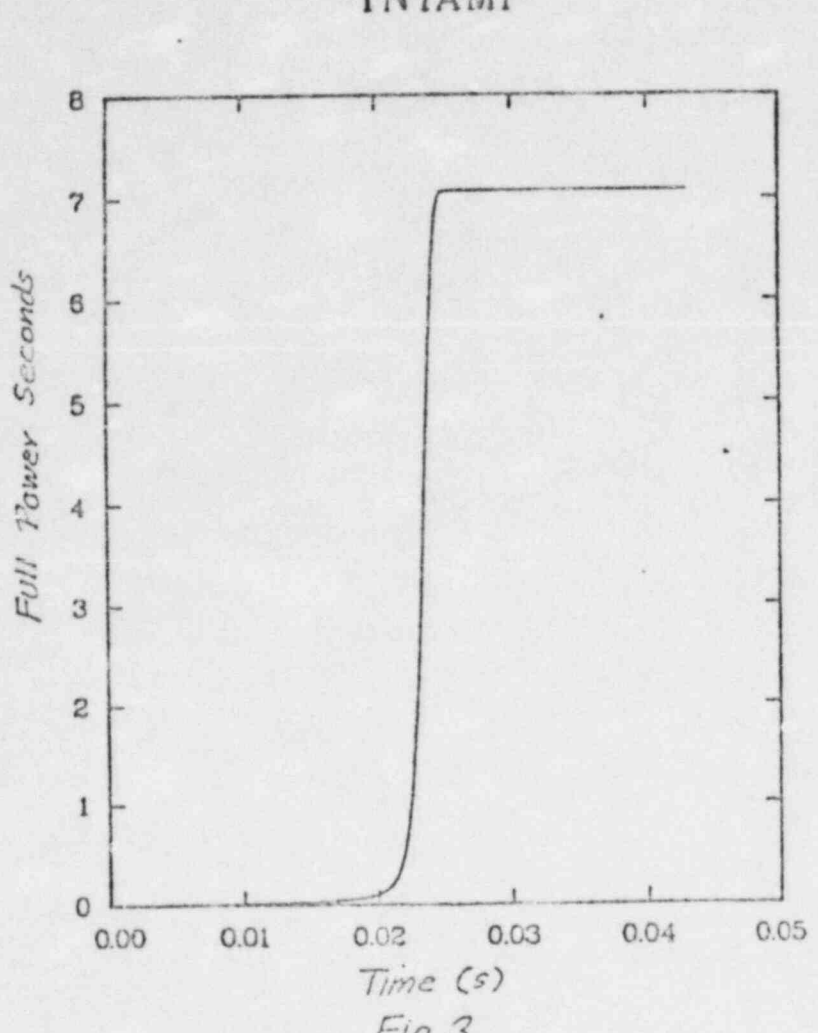
INTAMP
Full Power Seconds
0
1
2
3
4
5
6
7
8
0.00
0.01
0.02
0.03
0.04
0.05
Time (s)

Fig 3

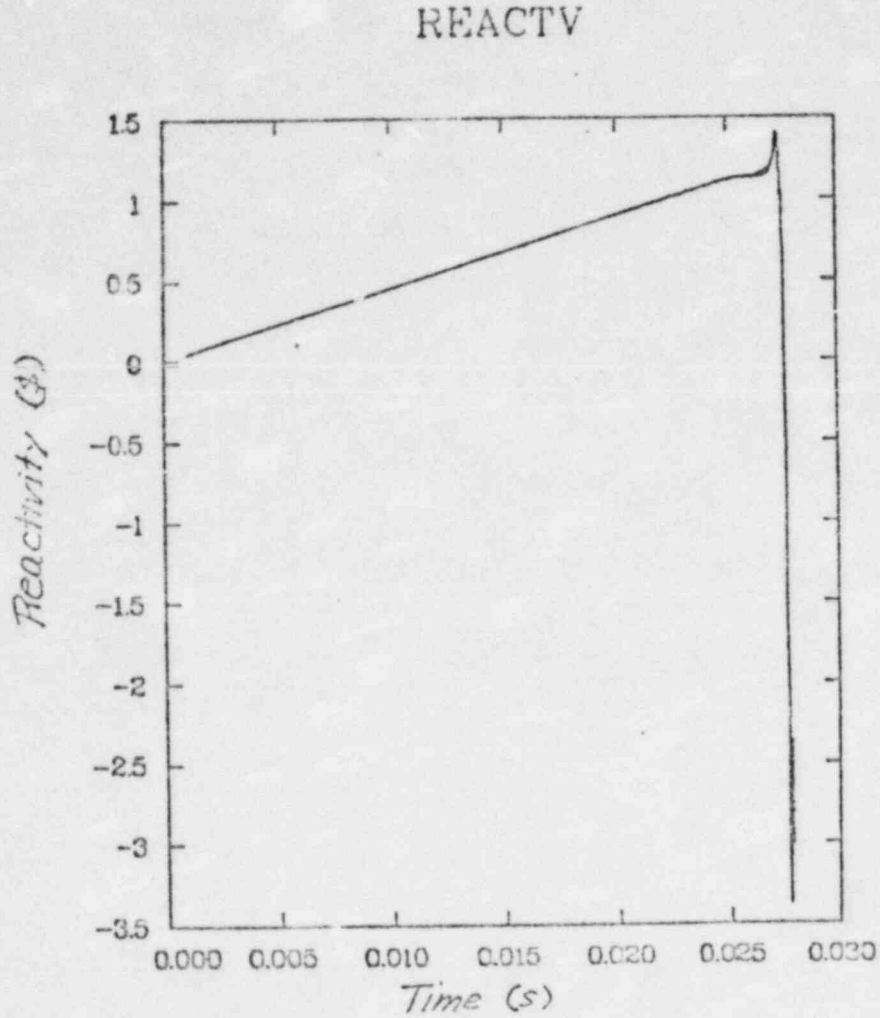
REACTV
1.5
1
0.5
0
-0.5
-1
-1.5
-2
-2.5
-3
-3.5
Reactivity ($)
0.000
0.005
0.010
0.015
0.020
0.025
0.030
Time (s)

Fig 4

AMPLIT

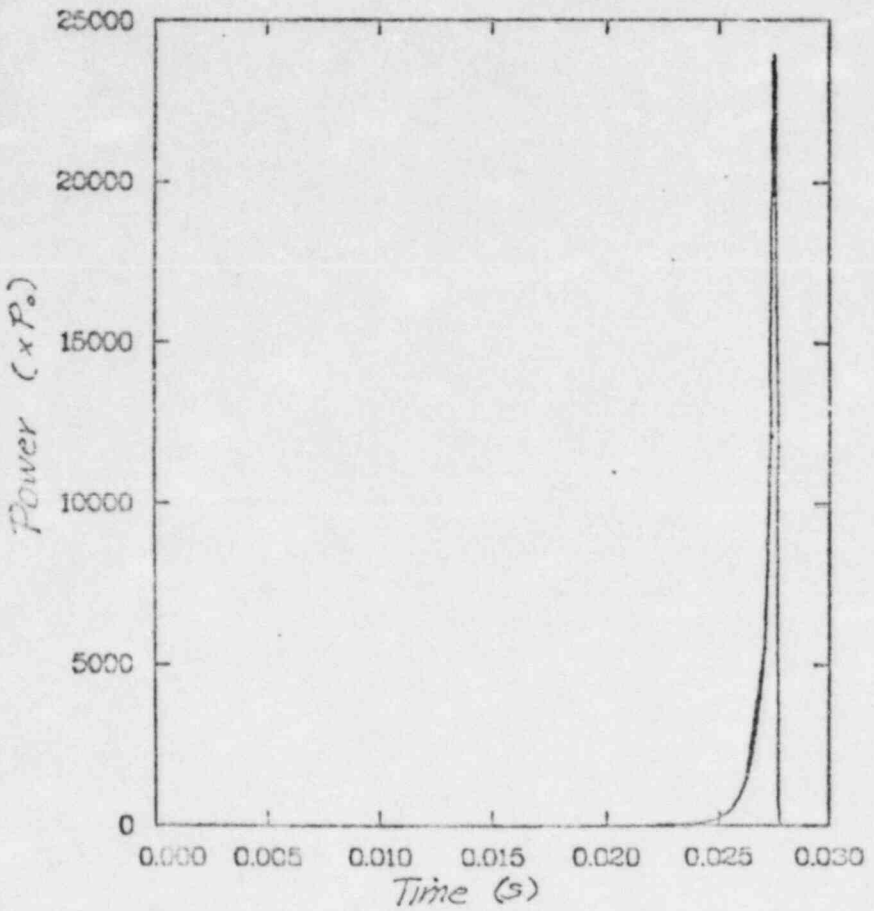
25000
20000
15000
10000
5000
0
Power (x P₀)
0.000
0.005
0.010
0.015
0.020
0.025
0.030
Time (s)

Fig 5

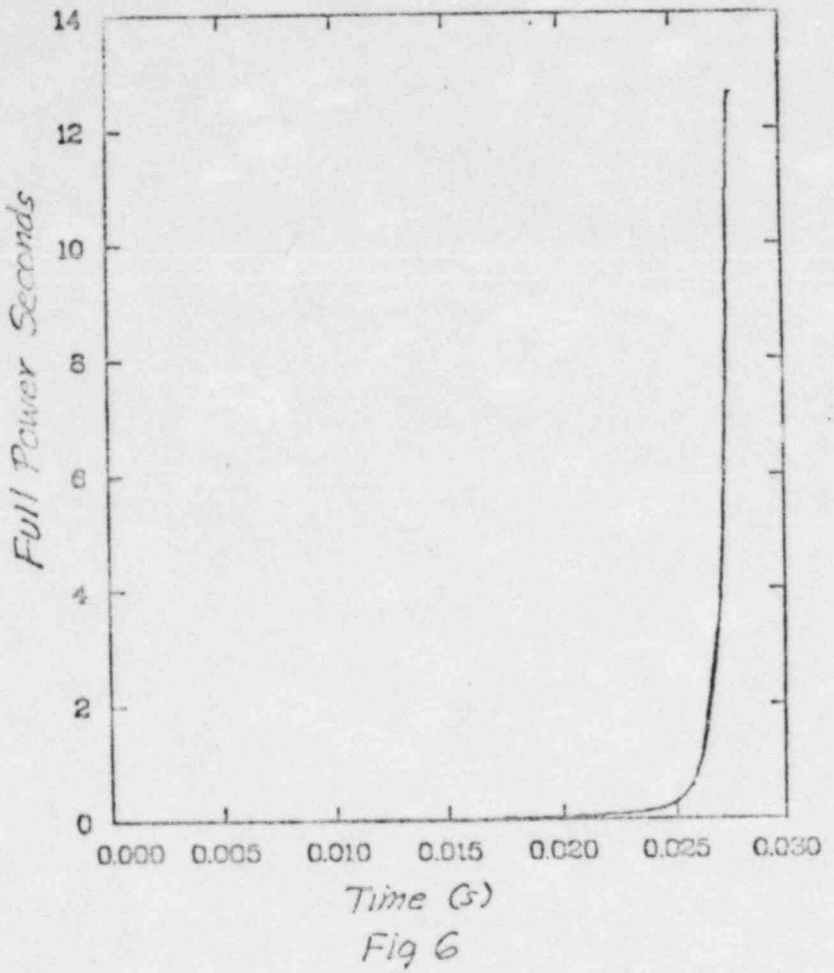
INTAMP
Full Power Seconds
0
2
4
6
8
10
12
14
0.000
0.005
0.010
0.015
0.020
0.025
0.030
Time (s)

Fig 6

1. QUALITATIVE PROBABILISTIC RESULTS.

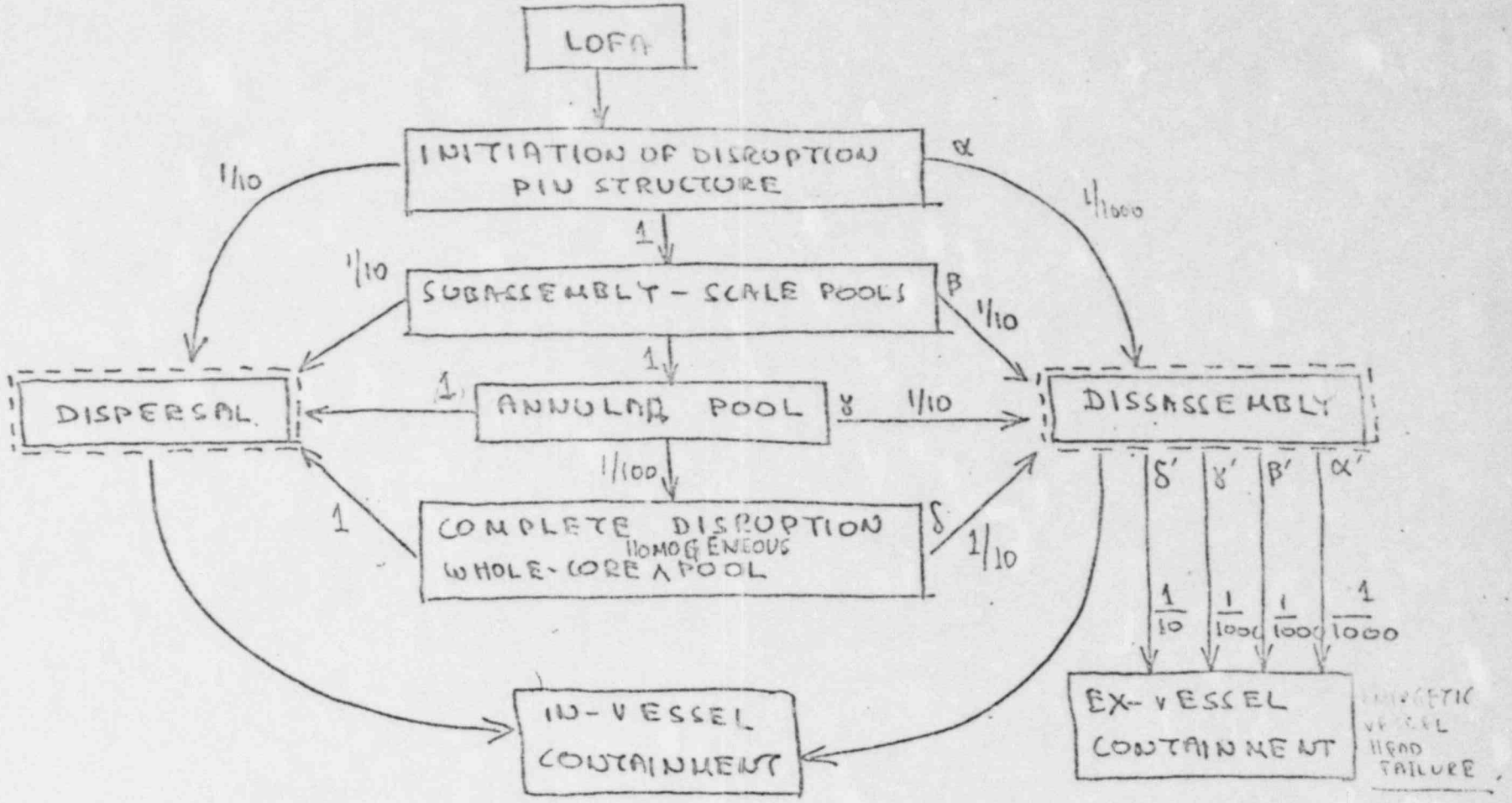

$10^{-4} + 10^{-4} + 10^{-4} + 10^{-6} \ll 10^{-3}$

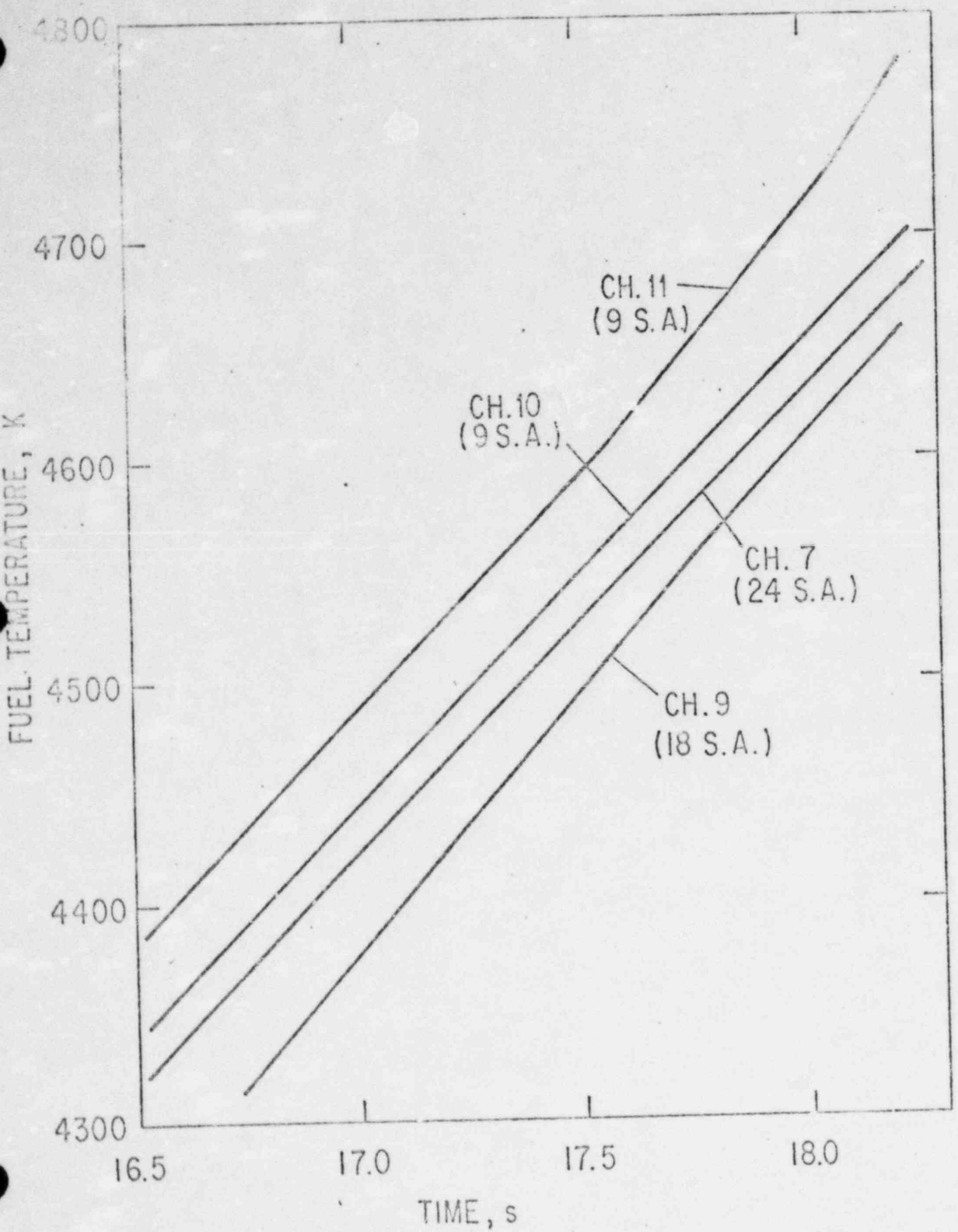
4800
4700
4600
4500
4400
4300
FUEL TEMPERATURE, K
CH. 11
(9 S.A.)
CH. 10
(9 S.A.)
CH. 7
(24 S.A.)
CH. 9
(18 S.A.)
16.5
17.0
17.5
18.0
TIME, s

Fig 1

III

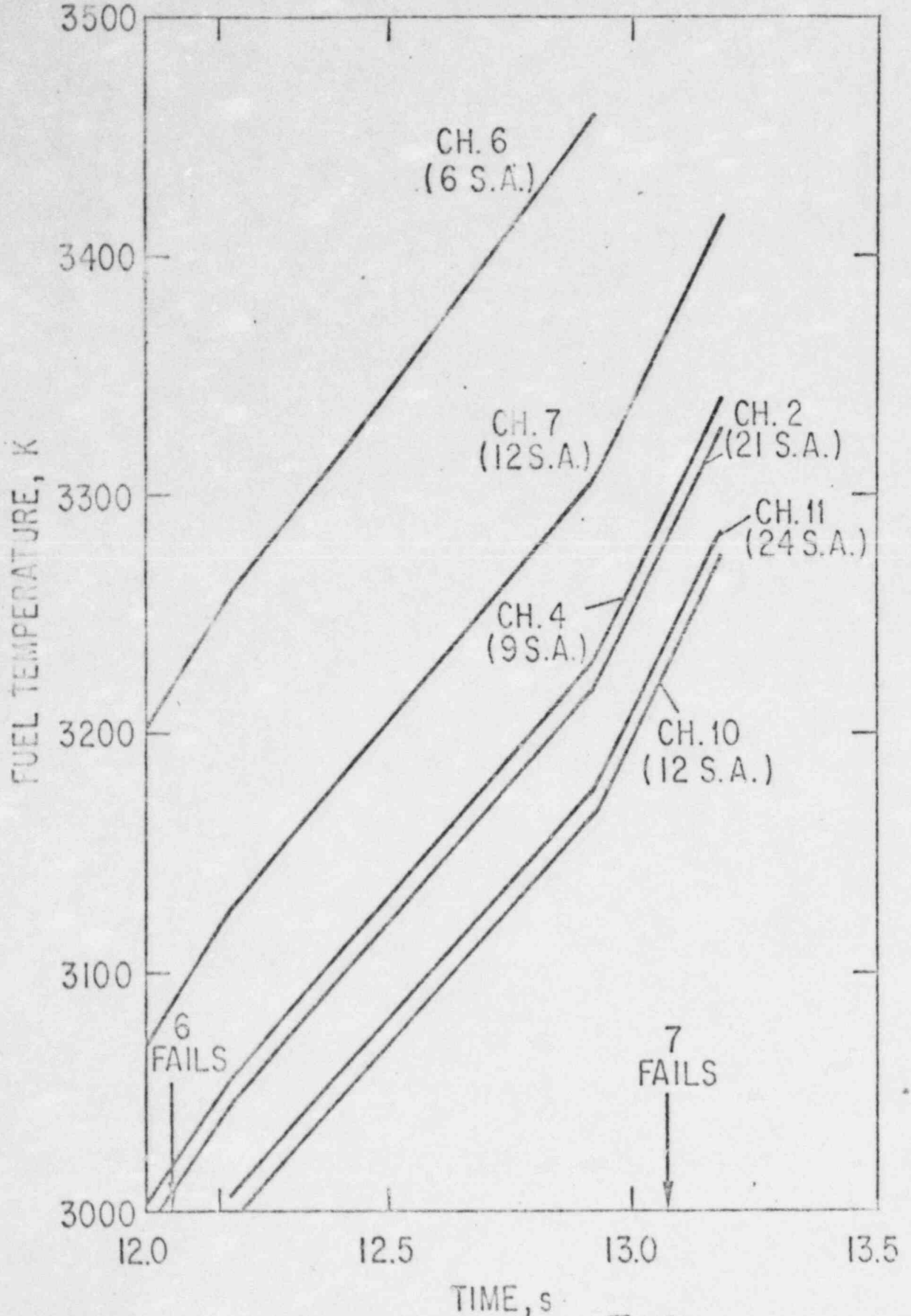
3500
3400
3300
3200
3100
3000
FUEL TEMPERATURE, K
12.0
12.5
13.0
13.5
TIME, s
CH. 6
(6 S.A.)
CH. 7
(12 S.A.)
CH. 2
(21 S.A.)
CH. 11
(24 S.A.)
CH. 4
(9 S.A.)
CH. 10
(12 S.A.)
6
FAILS
7
FAILS

Fig 2

III

Fig. 3 Fuel Temperature vs. Transient Time for a 12 ¢/s TOP Accident in the CRBR EOC-3 Core

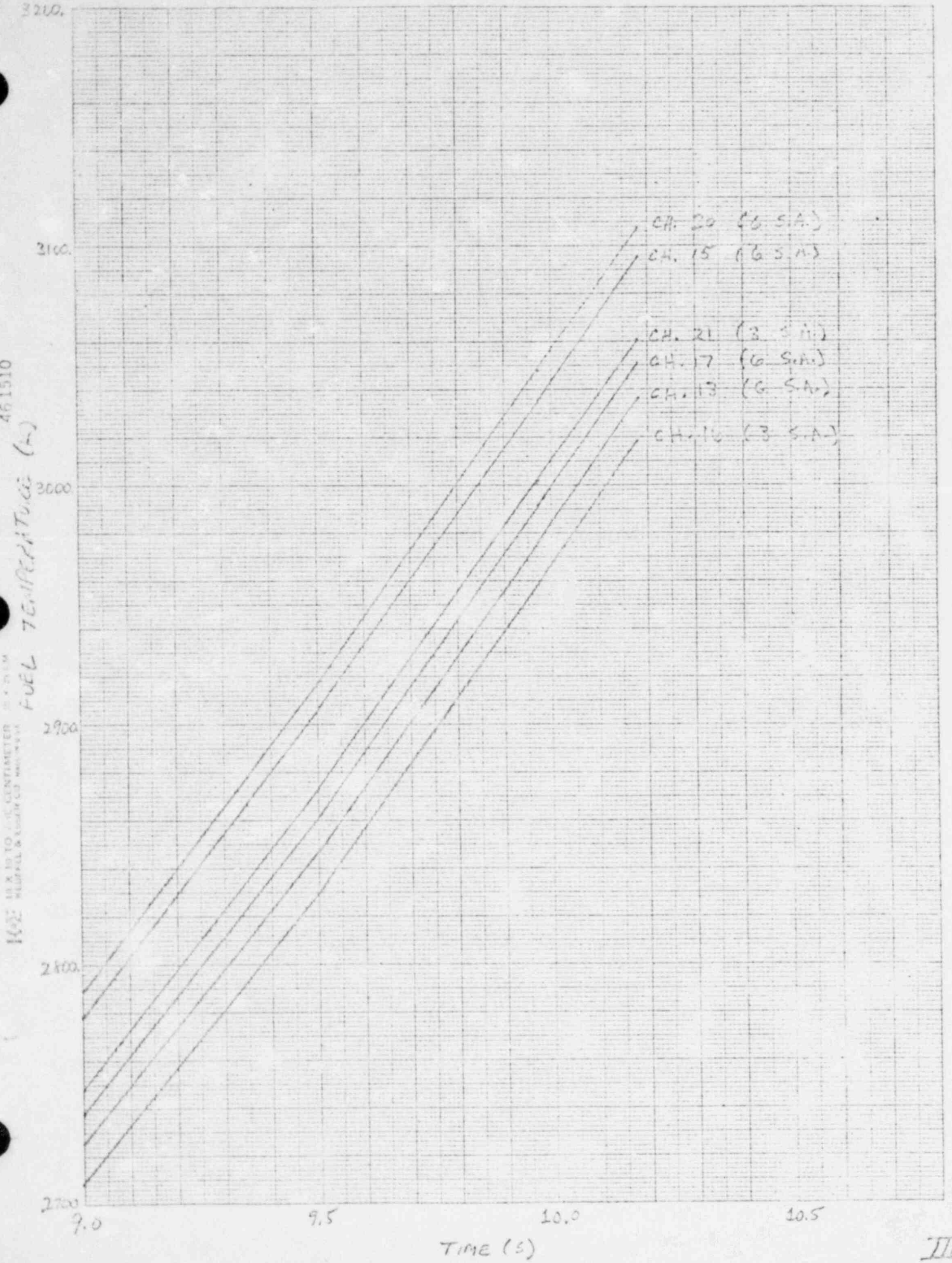

Fig. .4 Specific Sweepout Inferred from the L8 Experiment Compared with Calculated Values from Standalone PLUTO2

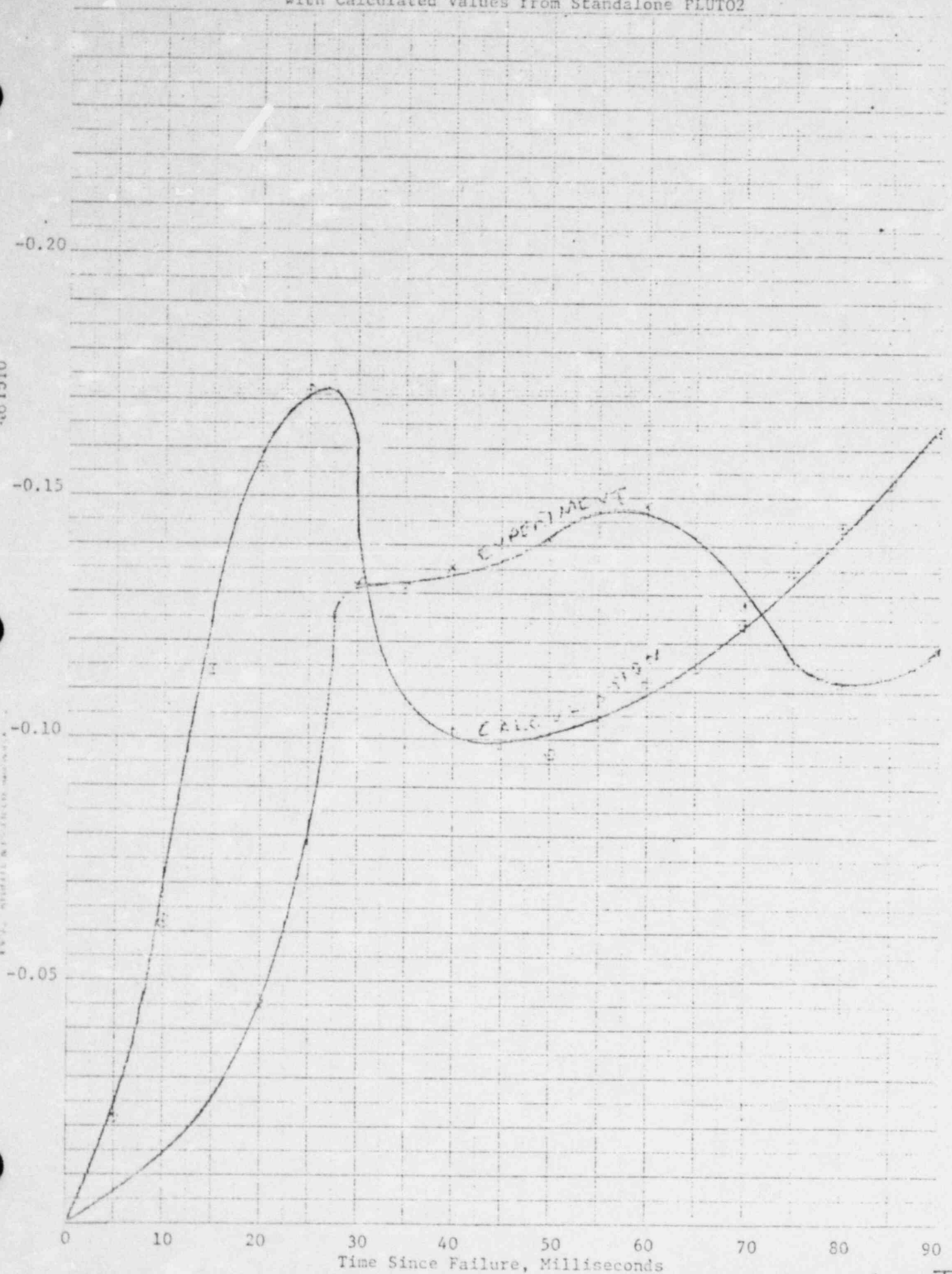

III

Fig. 5 Grams Fuel per Pin Ejected in L8 Experiment and in 10 ¢/s TOP Transient(~ 68 Grams)

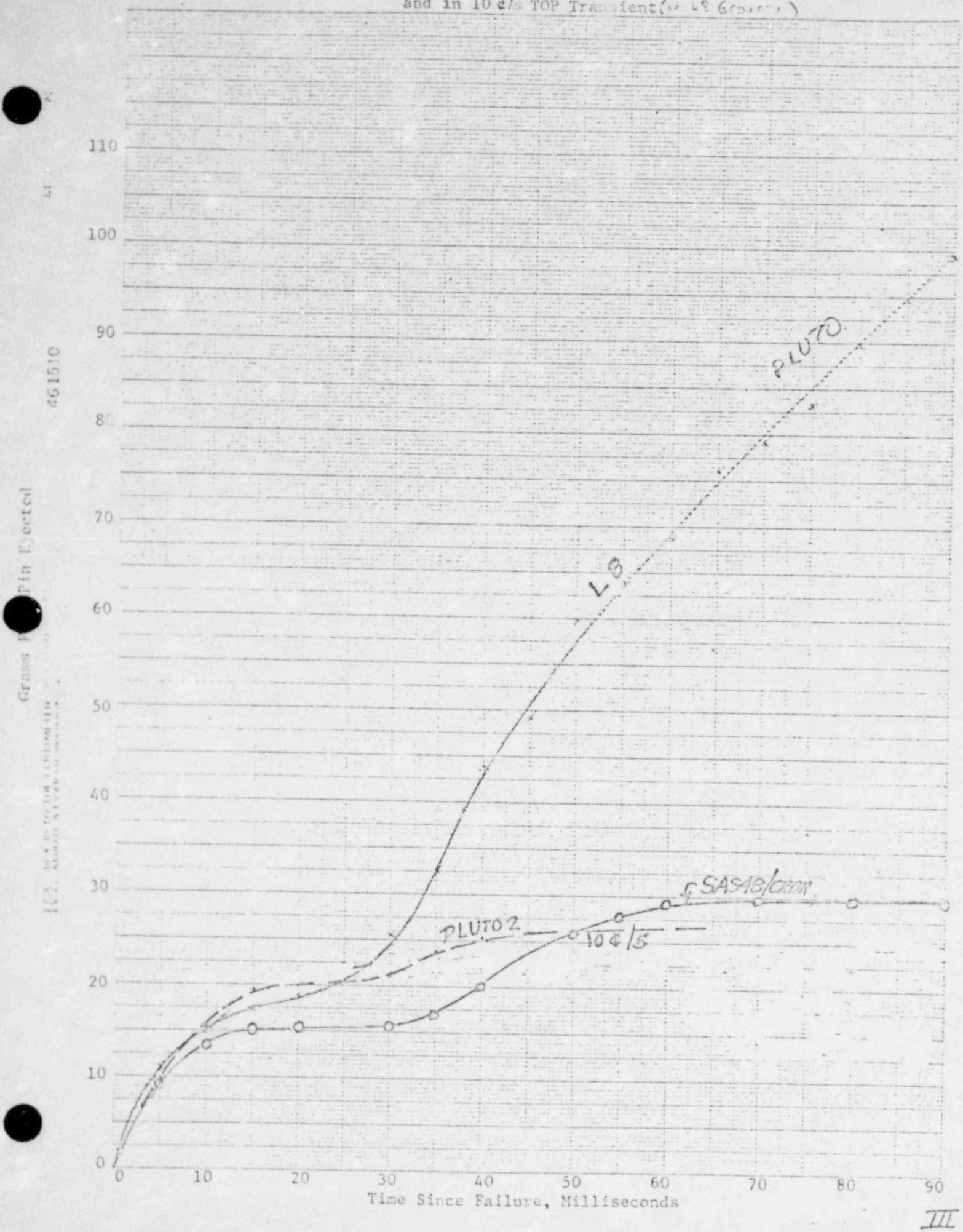

III

Fig. 6 Specific Sweepout for 10 ¢/s TOP Calculated by Standalone PLUTO2 and by PLUTO2 in SAS4A

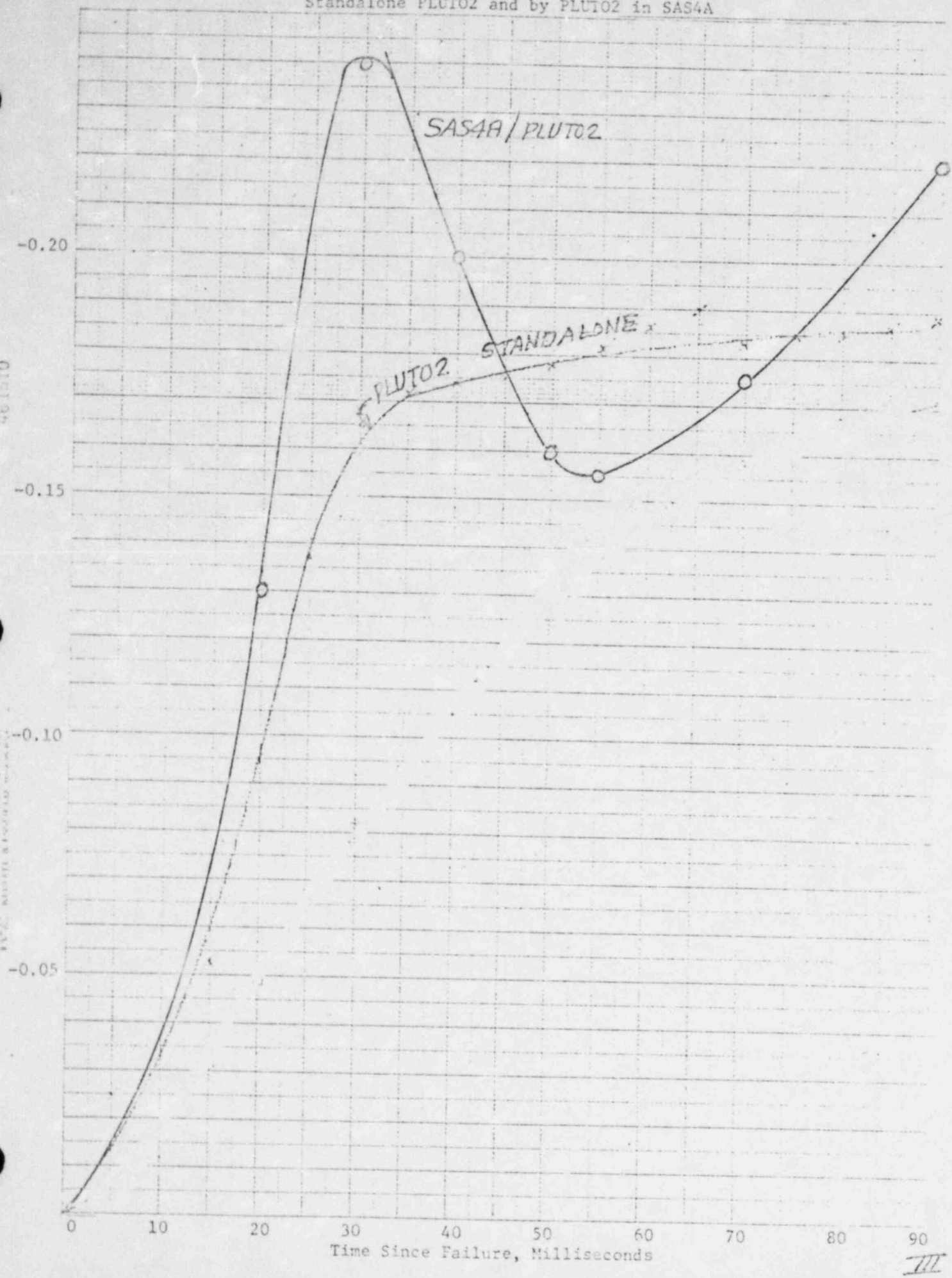

Fig. 7 Reactivity Effects in a High Power Subassembly for a 12 ℓ/s TOP in the CRBR

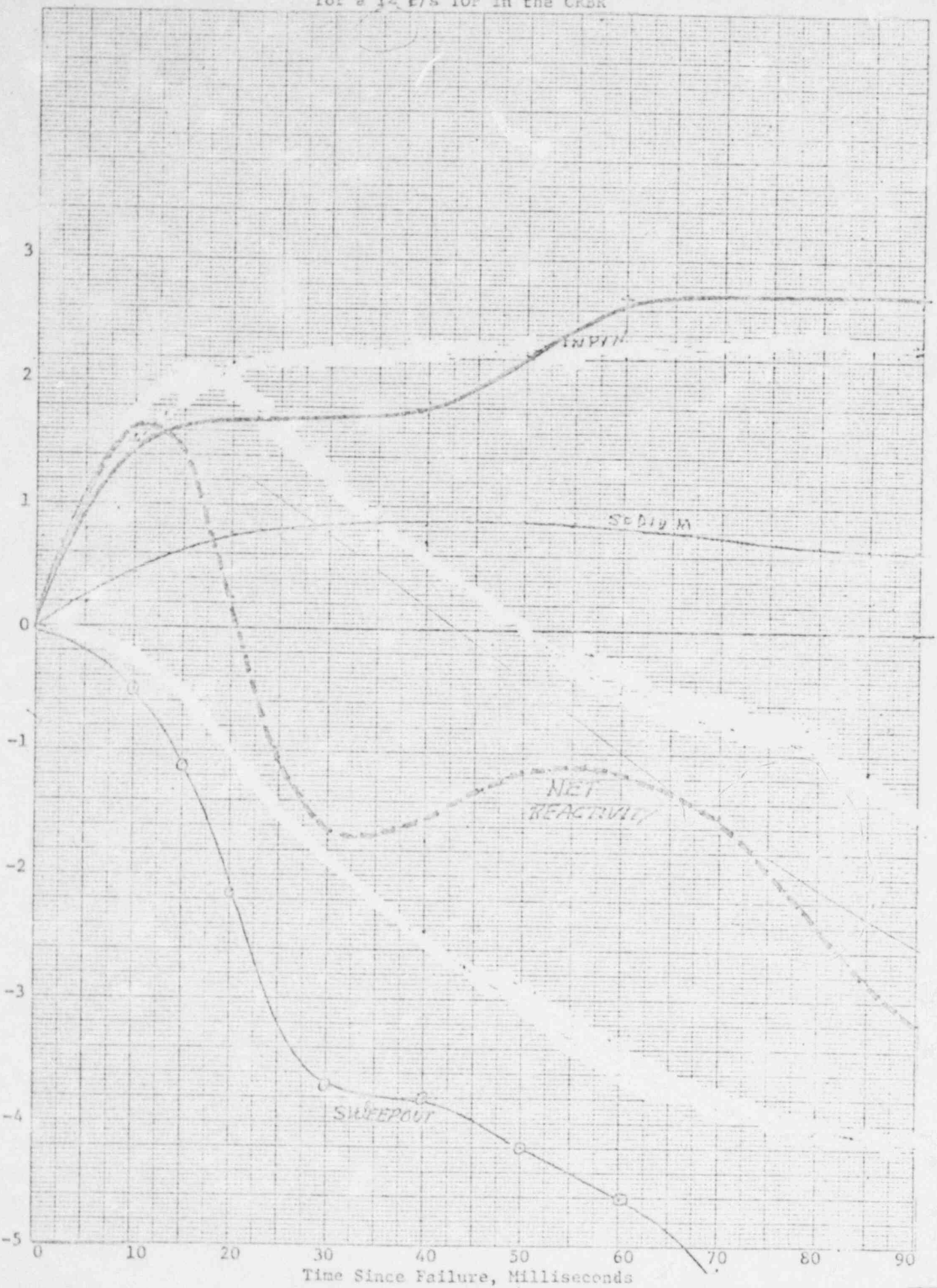

461510

Reactivity, ¢ Per Subassembly

K-E 10 X 10 TO THE CENTIMETER 46 1510
KEUFFEL & ESSER CO. MADE IN U.S.A.

III

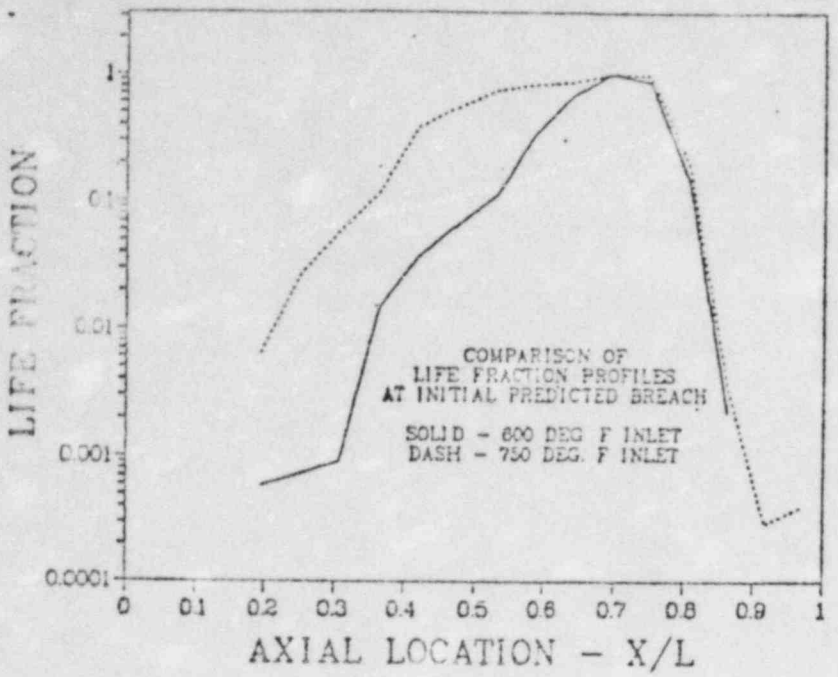

Figure 1. Axial profiles of calculated life fractions are shown for two inlet temperatures.

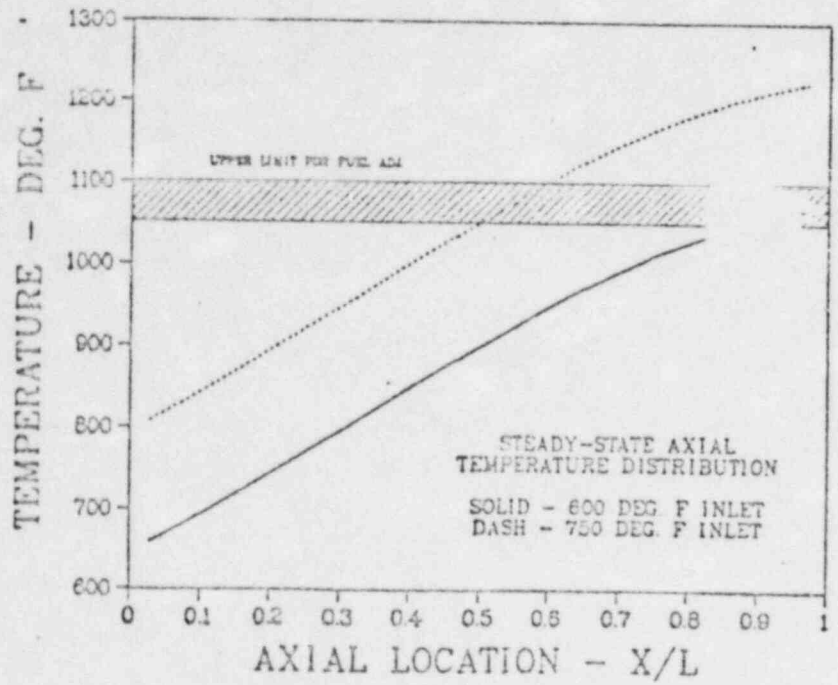

Figure 2. Steady-state cladding midwall temperatures are shown as a function of axial location for two inlet temperatures.

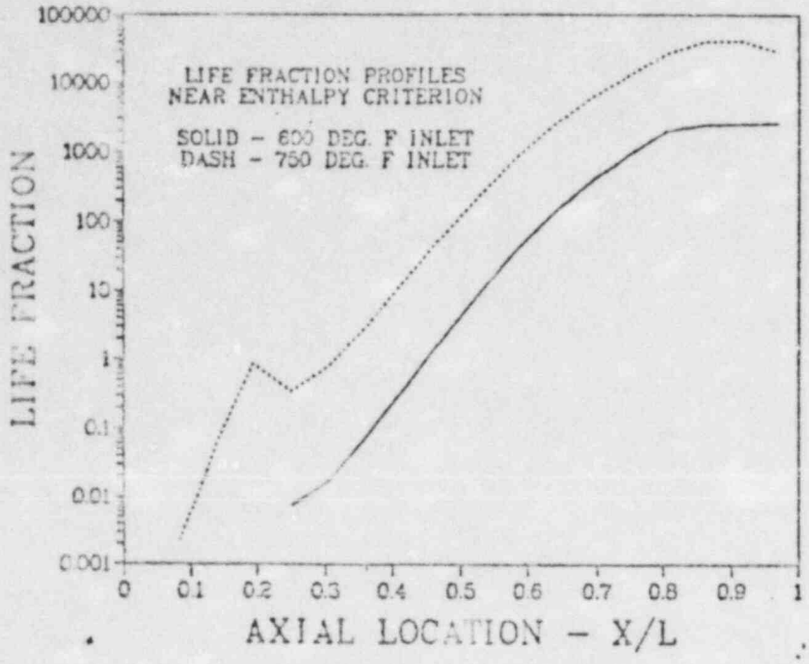

Figure 3. Life fraction profiles are shown for two inlet temperatures at a time near achievement of a peak fuel enthalpy of 1140 kJ/kg.

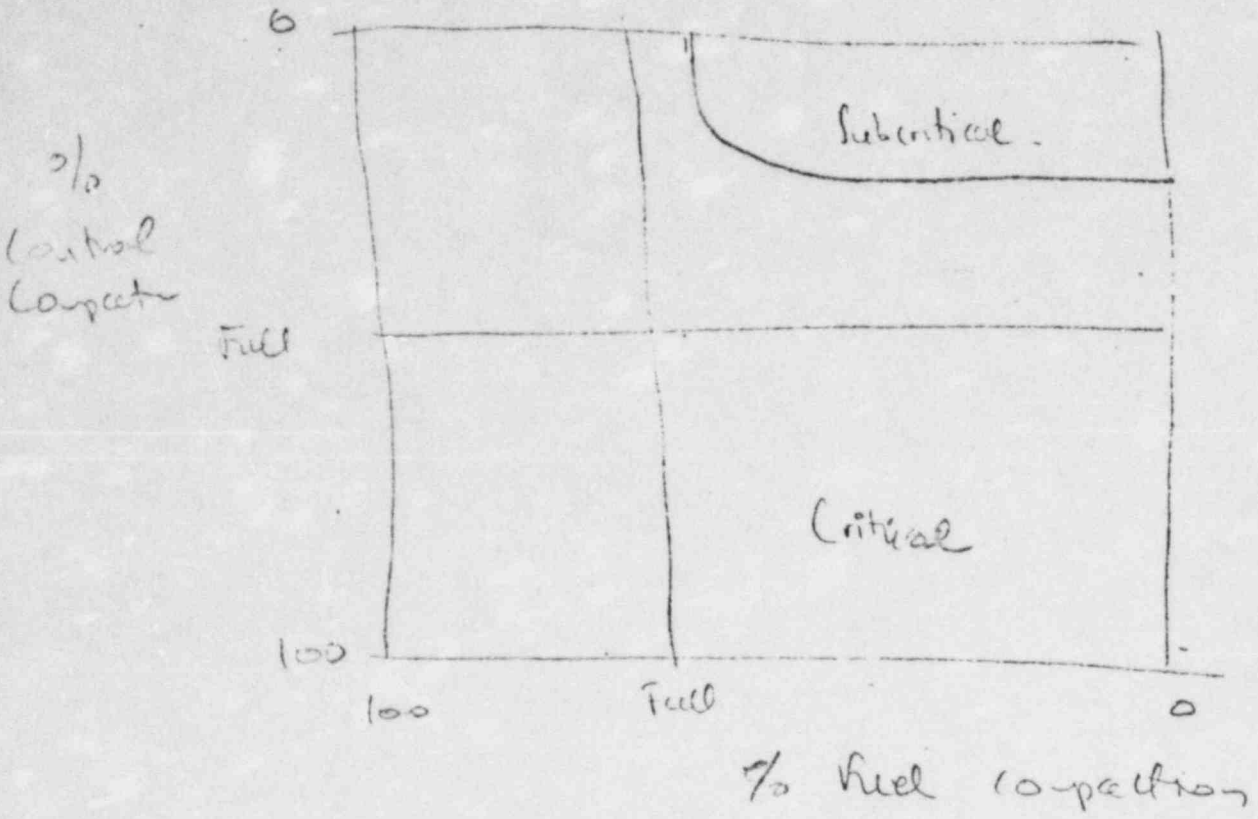
0
% Control Capacity
Full
Subcritical
Critical
100
100
Full
0
% fuel capacity

Fig 1.

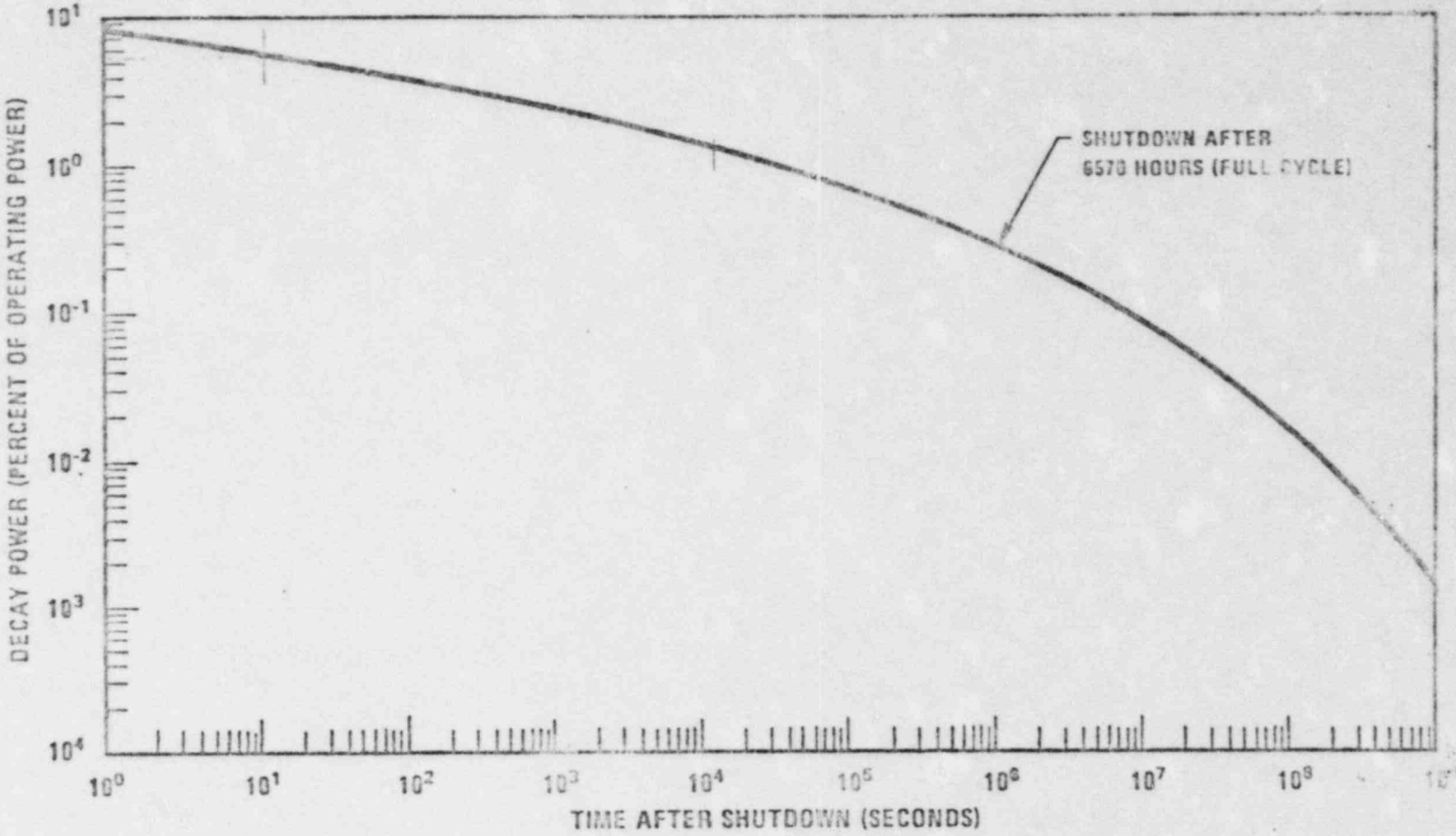

Decay Power after Shutdown Equilibrium Cycle Conditions Maximum Values.

Fig 2

IV

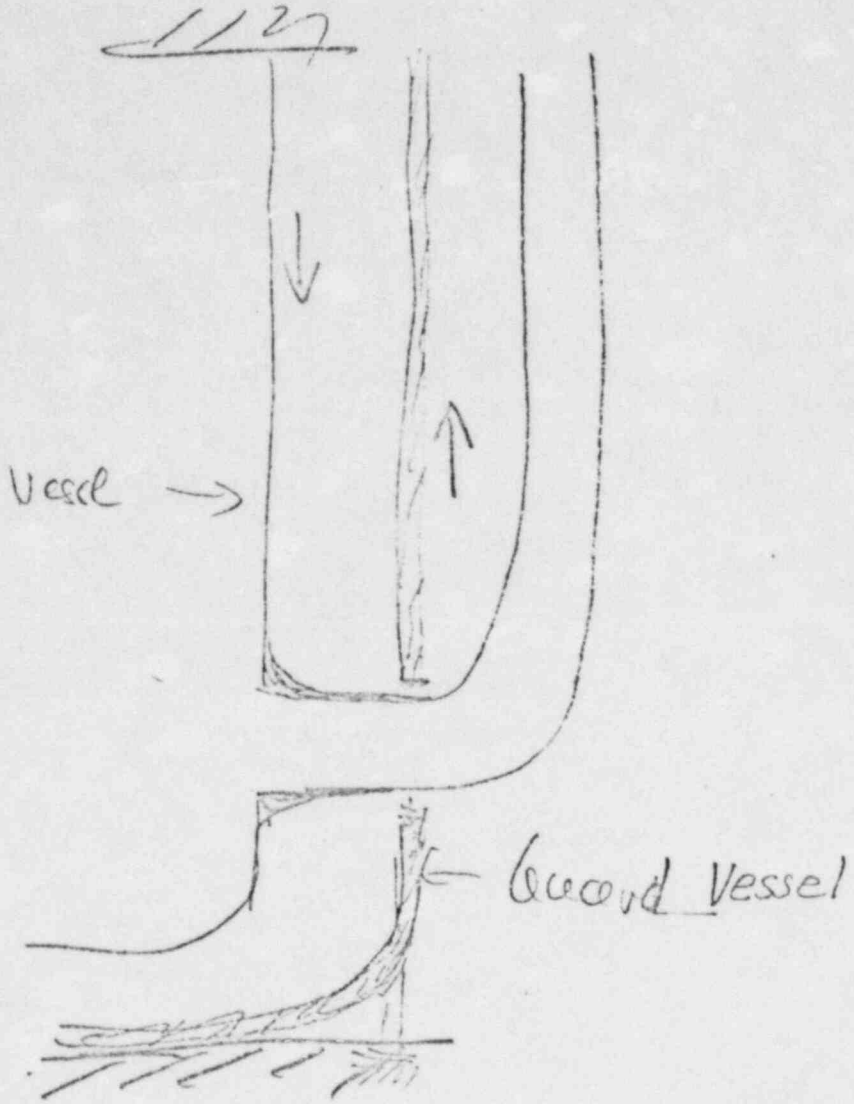

IV fig 3.

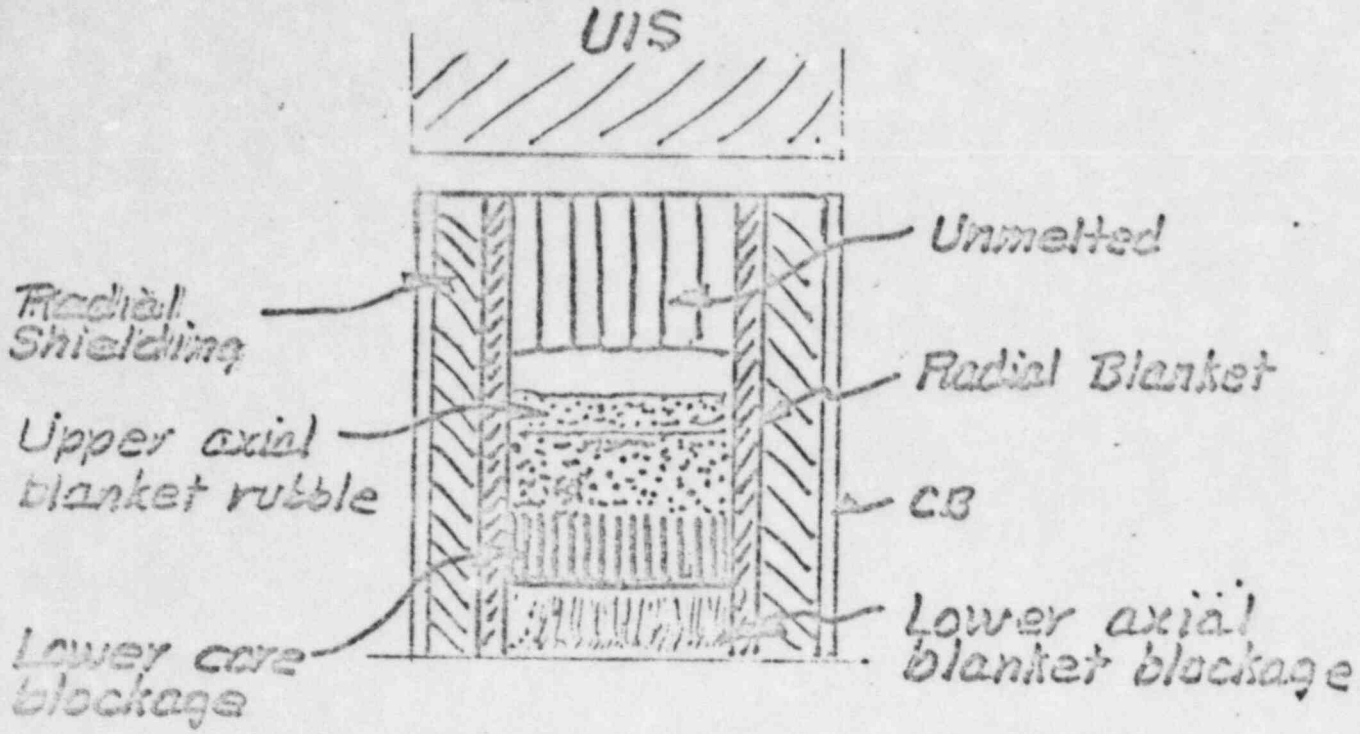

Fig 4

○ Power → Rapid melting → Gravity fall

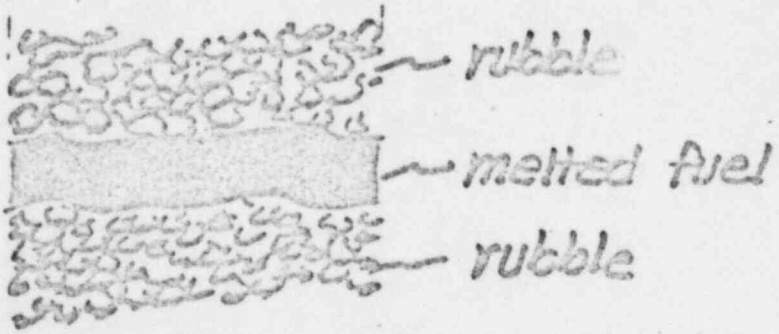

Fig 5

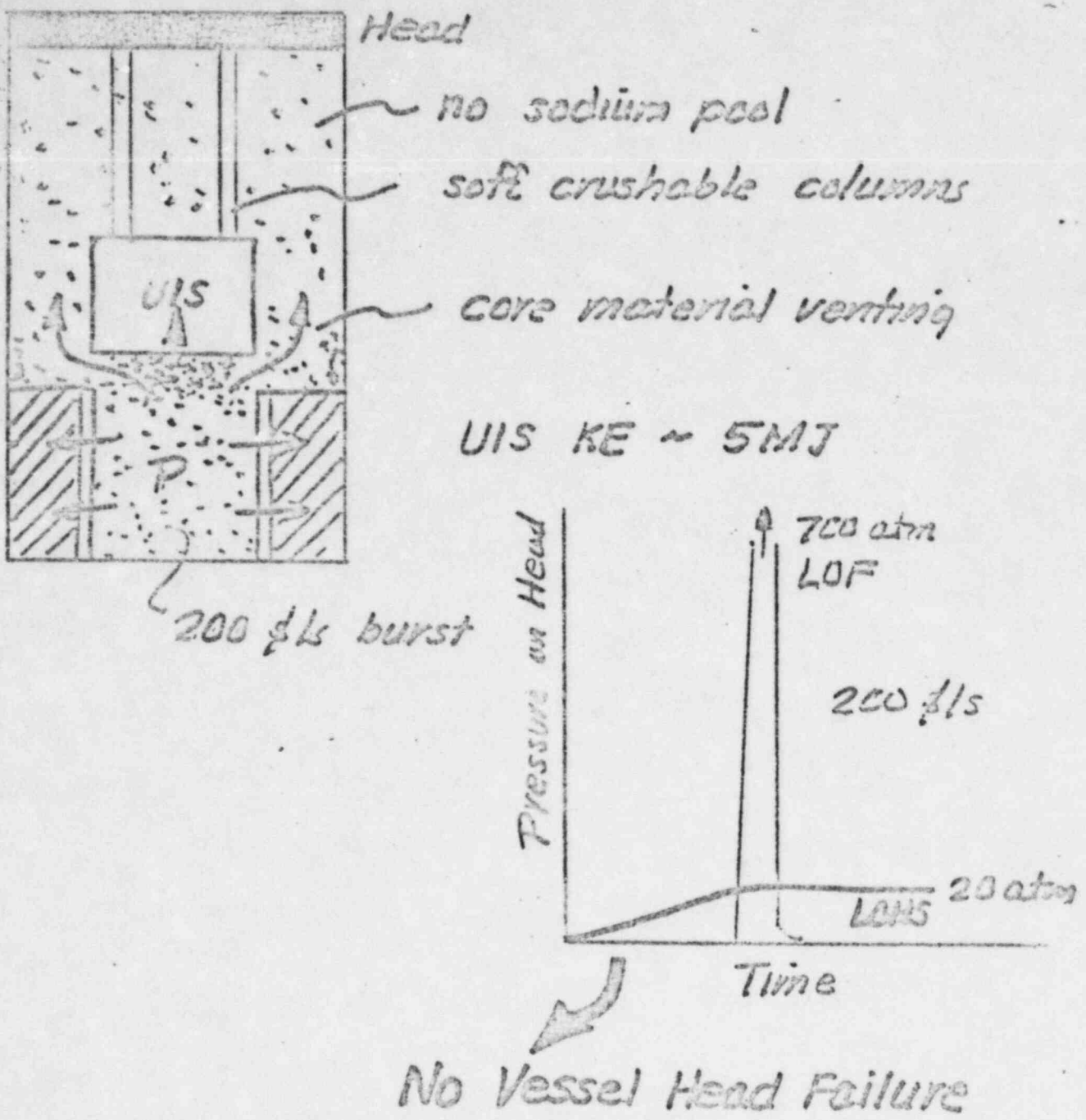
Head
no sodium pool
soft crushable columns
UIS
core material venting
UIS KE ~ 5MJ
P
200 ft/s burst
Pressure on Head
700 atm
LOF
200 ft/s
20 atm
LOHS
Time
No Vessel Head Failure

Fig 6

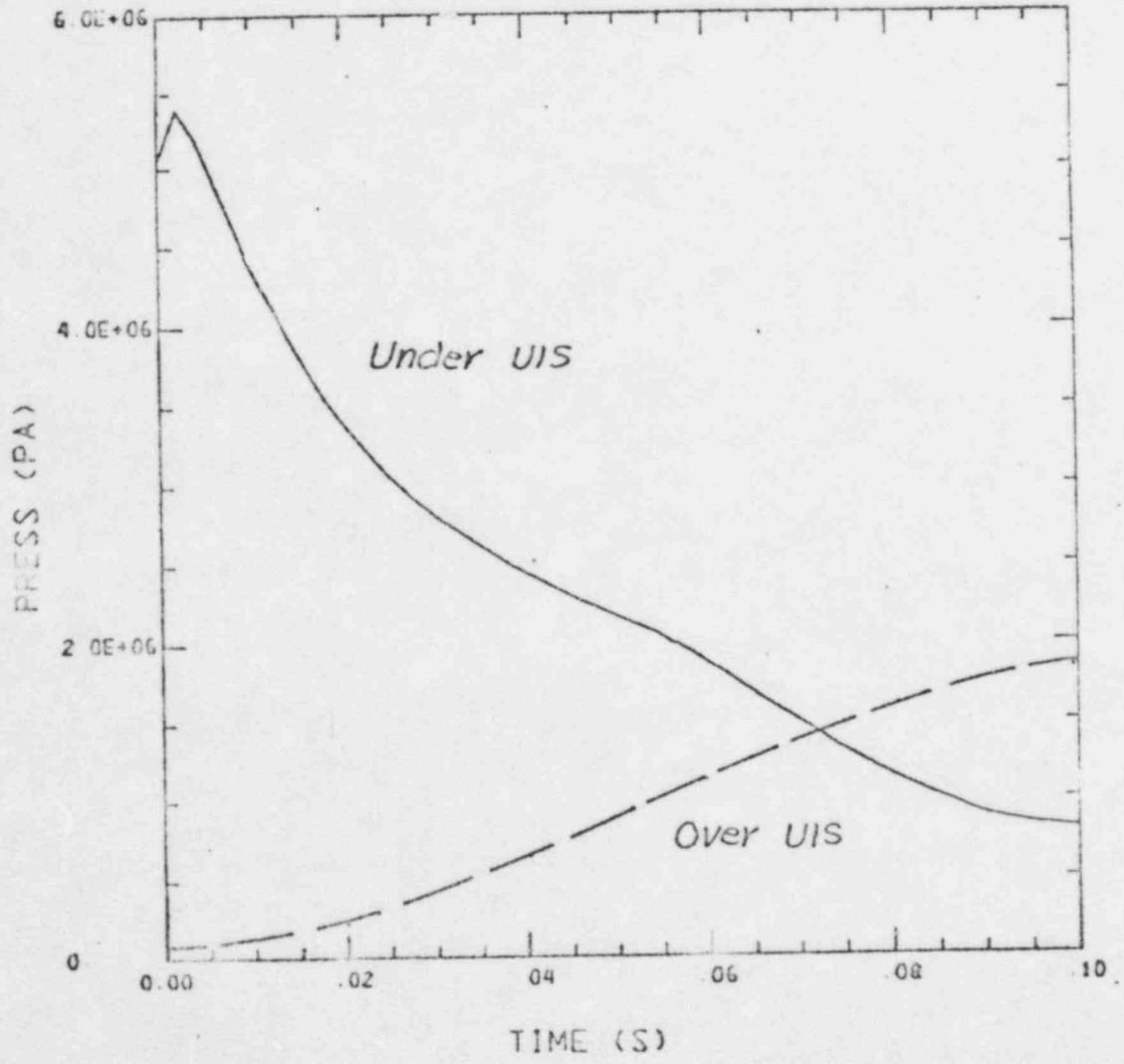
6.0E+06
4.0E+06
2.0E+06
0
PRESS (PA)
Under UIS
Over UIS
0.00
.02
.04
.06
.08
.10
TIME (S)

Fig 7